Transformer Engineering

Design, Technology, and Diagnostics

Second Edition

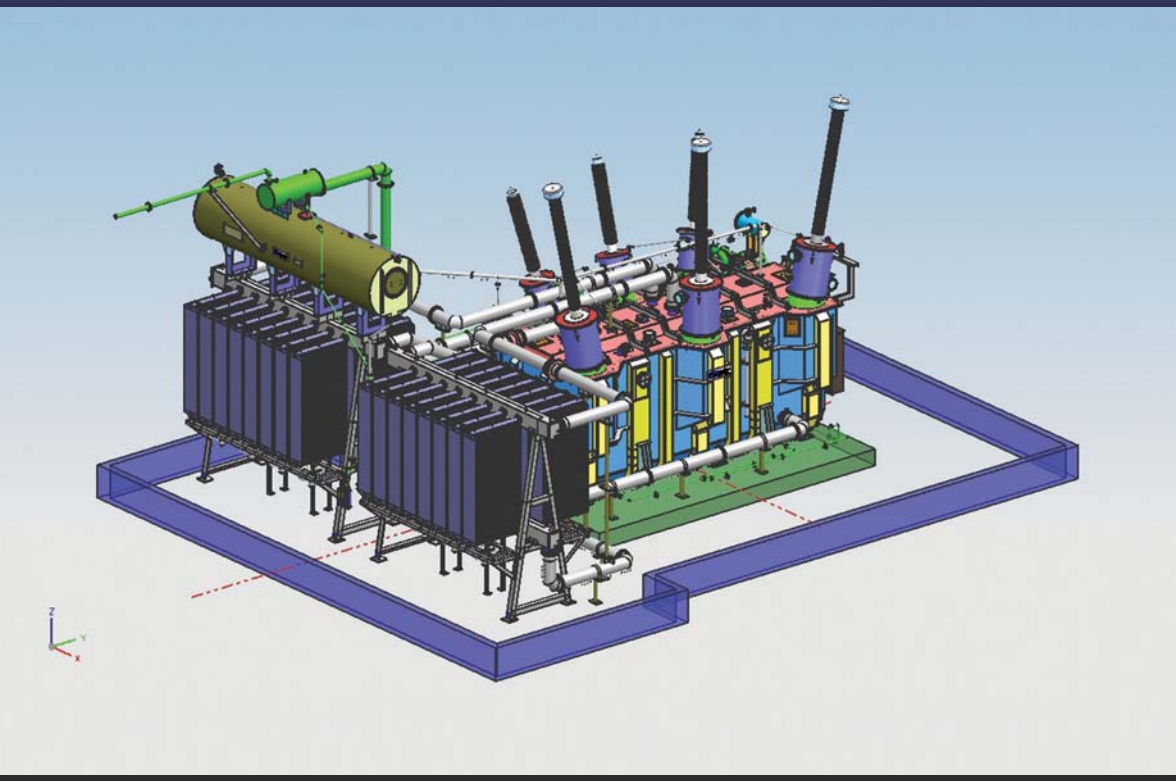

CRC Press
Taylor & Francis Group

S.V. Kulkarni
S.A. Khaparde

Transformer Engineering

Design, Technology, and Diagnostics

Second Edition

Transformer Engineering

Design, Technology, and Diagnostics

Second Edition

S.V. Kulkarni
S.A. Khaparde

CRC Press
Taylor & Francis Group
Boca Raton London New York

CRC Press is an imprint of the
Taylor & Francis Group, an **informa** business

CRC Press
Taylor & Francis Group
6000 Broken Sound Parkway NW, Suite 300
Boca Raton, FL 33487-2742

Version Date: 20120803

International Standard Book Number-13: 978-1-4398-5418-1 (eBook - PDF)

Visit the Taylor & Francis Web site at
http://www.taylorandfrancis.com

and the CRC Press Web site at
http://www.crcpress.com

Contents

Preface to the Second Edition

There have been considerable advancements in various aspects of transformer engineering since the publication of the first edition in 2004. Improvements can be clearly seen in computational capabilities and monitoring/diagnostic techniques. Such new developments and encouraging feedback received on the first edition prompted the authors to embark on the task of writing the second edition.

Three new chapters have been introduced in the second edition, Electromagnetic Fields in Transformers: Theory and Computations, Transformer–System Interactions and Modeling, and Monitoring and Diagnostics. The chapter on Recent Trends in Transformer Technology has been completely revised to reflect the latest and emerging trends in the various facets of the transformer technology. Chapter 6 on short-circuit strength aspects has been updated to bring more clarity on failure mechanisms involving buckling, tilting, and spiraling phenomena. Various factors of safety are defined along with procedures for calculating them. An appendix explaining a step-by-step procedure for designing a transformer is added, which should be beneficial to engineers in the transformer industry and the student community. A few improvements have been incorporated in the other chapters as well.

Understanding the basics of electromagnetic fields is an essential prerequisite for doing advanced computations. Chapter 12 explains the field theory relevant to transformer engineering in a simple manner. Concepts from vector algebra and vector calculus are first explained followed by corresponding examples which help understand the behavior and distribution of fields inside transformers. Properties of insulating and magnetic materials used in transformers are explained from a fundamental electromagnetic perspective. Finite element method (FEM) is widely used for analysis and optimization of

transformers. While using commercial software, the knowledge of the FEM theory helps researchers and practicing engineers solve complex problems and easily interpret field solutions. The theory of FEM is explained through the solution of one-dimensional and two-dimensional problems that represent typical electrostatic and magnetostatic fields encountered in transformers. After explaining static, time-harmonic and transient formulations, advanced coupled field computations involving electromagnetic fields and external networks/other physical fields are elaborated. Brief theory/procedures for dealing with hysteresis and magnetization/magnetostrictive forces are also given at the end.

The second new chapter covers relevant theory and explanations required for understanding the effects of transformer–system interactions. The chapter starts with the modeling aspects of transformers essential for steady-state analysis of power systems. The usefulness of magnitude-regulating and phase-shifting transformers is demonstrated through examples. The section on harmonics briefly covers their sources and effects, followed by modeling strategies for analyzing them. Ferroresonance phenomena can be detrimental to transformers; the system conditions causing ferroresonant conditions are enumerated. Adverse effects of arc-furnace loads and geomagnetic disturbances are explained later. Internal resonances due to system transients including very fast transient overvoltages are also described. Effects of switching operations involving vacuum circuit breakers on distribution transformers are highlighted. At the end, low-, mid-, and high-frequency models of transformers used for transient studies/investigative analysis are elaborated.

A considerable amount of research and development efforts by the academic community, utility engineers, and transformer specialists have led to the availability of advanced diagnostic tools. After summarizing conventional tests on oil and windings, the chapter Monitoring and Diagnostics comprehensively covers techniques for detecting partial discharges (PD), insulation degradation, and winding displacements/deformations. Methods based on electrical, acoustic, and ultra high frequency signals are practiced for PD diagnostics. Dielectric response methods used for the condition assessment of insulation are categorized into time domain and frequency domain methods. Background theory for understanding these two types of approaches is described along with diagnostic procedures. Finally, frequency response analysis, used widely for detection of winding irregularities, is thoroughly explained.

Thus, the focus of the second edition is also on diagnostic aspects and transformer–system interactions, and therefore, it is expected to help readers comprehend operational/maintenance issues and solutions in addition to the intricacies of transformer design and the applications of advanced numerical field computations.

S. V. Kulkarni
S. A. Khaparde
(For comments and suggestions, contact: svk@ee.iitb.ac.in)

Foreword to the First Edition

It is a great pleasure to welcome this new book from Prof. S. V. Kulkarni and Prof. S. A. Khaparde, and I congratulate them for the comprehensive treatment given in the book to nearly all aspects of transformer engineering.

Everyone involved in or with the subject area of this book, whether from academics or industry, knows that the last decade has been particularly dynamic and fast changing. Significant advances have been made in design, analysis, and diagnostic techniques for transformers. The enabling factors for this technological leap are extremely competitive market conditions, tremendous improvements in computational facilities, and rapid advances in instrumentation. The phenomenal growth and increasing complexity of power systems have put tremendous responsibilities on the transformer industry to supply reliable transformers. The transformer as a system consists of several components, and it is absolutely essential that the integrity of all these components individually and as a system is ensured. A transformer is a complex three-dimensional electromagnetic structure and it is subjected to a variety of stresses, dielectric, thermal, electrodynamic, etc. In-depth understanding of various phenomena occurring inside the transformer is necessary. Most of these can now be simulated on computers so that suitable changes can be made at the design stage to eliminate potential problems.

I find that many of these challenges in the design and manufacture of transformers, to be met in fast-changing market conditions and technological options, are discussed in this book. There is a nice blend of theory and practice in almost every topic discussed in the text. The academic background of the authors has ensured that a thorough theoretical treatment is given to important topics. A number of landmark references are cited at appropriate places. The previous industry experience of S. V. Kulkarni is reflected in many discussions in the book. Various theories have been supported in the text by reference to actual practices.

For example, while deliberating on various issues of stray loss estimation and control, the relevant theory of eddy currents has been explained. This theoretical basis is then used to explain various design and manufacturing practices established in the industry to analyze and minimize the stray losses in the windings and structural components. The design and manufacturing practices and processes have significant impact on the performance parameters of transformers and the same have been identified in the text while discussing various topics.

Wherever required, a number of examples and case studies are given which are of great practical value. The knowledge of zero-sequence characteristics of transformers is very important for utilities. It is essential to understand the difference between magnetizing and leakage zero-sequence reactances of the transformer. These two types of zero-sequence reactances are explained in the book for three-phase three-limb, three-phase five-limb and single-phase three-limb transformers with numerical examples. One may not find such a detailed treatment to zero-sequence reactances in the available literature. The effect of tank on the zero-sequence reactance characteristics is clearly explained.

The discussions on the sympathetic inrush phenomenon, part-winding resonance, short-circuit withstand characteristics, and noise reduction techniques should also be quite useful to the readers. With the increase in network complexity and severity of loads in some cases, the cooperation between the transformer manufacturers and users (utilities) is very critical. The design reviews with the involvement of users at various stages of contract should help in enhancing the reliability of transformers. I am happy to note that such areas of cooperation are identified at appropriate places in the text.

The book propagates the use of modern computational tools for optimization and quality enhancement of transformers. I know a number of previously published works of the authors in which the Finite Element Method (FEM) has been applied for the stray loss control and insulation design of the transformers. The use of FEM has been aptly demonstrated in the book for various calculations along with some tips, which will be helpful to a novice in FEM.

The book is therefore a major contribution to the literature. The book will be extremely helpful and handy to the transformer industry and users. It will also be useful for teaching transformers to undergraduate and postgraduate students in universities. The thorough treatment of all important aspects of transformer engineering given in the book will provide the reader all the necessary background to pursue research and development activities in the domain of transformers.

It is anticipated that this book will become an essential reference for engineers concerned with design, application, planning, installation and maintenance of power transformers.

H. Jin Sim, PE
VP, Waukesha Electric Systems
Past Chairman, IEEE Transformers Committee

Preface to the First Edition

In the last decade, rapid advancements and developments have taken place in the design, analysis, manufacturing, and condition monitoring technologies of transformers. The technological leap will continue in the forthcoming years. The phenomenal growth of power systems has put tremendous responsibilities on the transformer industry to supply reliable and cost-effective transformers.

There is a continuous increase in the ratings of generator transformers and autotransformers. Further, the ongoing trend of using higher system voltages for power transmission increases the voltage rating of transformers. An increase in current and voltage ratings needs special design and manufacturing considerations. Advanced computational techniques have to be used which should be backed up by experimental verifications to ensure the quality of design and manufacturing processes. Some of the vital design challenges are stray loss control, accurate prediction of winding hot spots, short-circuit withstand and reliable insulation design. With increasing MVA ratings, the weight and size of large transformers approach or exceed transport and manufacturing capability limits. Also, due to ever increasing competition in the global marketplace, there are continuous efforts to optimize material content. Therefore, the difference between withstand levels and corresponding operating stress levels is reducing. Similarly, the guaranteed performance figures and actual test values can be close nowadays. All these reasons demand greater efforts from researchers and designers for the accurate calculation of various stress levels and performance figures. In addition, a strict control of manufacturing processes is required. Manufacturing variations of components should be monitored and controlled.

Many books on transformers are now more than 10 years old. Some of these books are still relevant and widely referred to for understanding the theory and

operation of the transformers. However, a comprehensive theoretical basis together with applications of modern computational techniques is necessary to face the challenges of fast changing and demanding conditions. This book is an effort in that direction. The principles of various physical phenomena occurring inside transformers are explained elaborately in the text, which can also be used as a basis for teaching undergraduate and postgraduate students in universities. Wherever required, adequate references have been quoted so that the readers can go into more depth of the phenomena. In fact, a large number of very useful references (more than 400) is one of the hallmarks of this book. Some of the references, which are classical ones, date back to the early part of the last century. Using these references, many of the theories useful for transformer engineering are explained. Some of the most recent works have also been discussed to give readers a feel of the latest trends in the transformer technology.

Prof. S. V. Kulkarni worked in the transformer industry for 11 years before joining academics. He has vast experience in design and development of transformers from a small distribution range up to 400 kV class 300 MVA ratings. He had ample opportunities to investigate a number of problems in transformer works and sites. A few such case studies and site investigations, in which he was actively involved in the last decade, have been incorporated at appropriate places in the text. Also, he realized that there are some aspects of transformer engineering which have not been given adequate treatment in the presently available books. Hence, the emphasis of this book is more on these aspects, magnetizing asymmetry, zero-sequence reactance characteristics, stray losses and related theory of eddy currents, short-circuit forces and withstand, part winding resonance phenomenon, insulation design, and design aspects of transformers for rectifier, furnace and HVDC applications. The book would be particularly useful to

- Transformer designers and researchers engaged in optimization and quality enhancement activities in today's competitive environment
- Utility engineers who would like to learn more about the system interaction aspects of transformers in an interconnected power system to improve specifications and employ diagnostic tools for condition monitoring
- Undergraduate and postgraduate students who wish to understand practical issues in transformer design and pursue research for finding solutions

In Chapter 1, in addition to transformer fundamentals, various types of transformers in a typical power system are explained along with their features.

There is a trend to use better materials to reduce core losses. Many times the expected loss reduction is not obtained with these better grades. The design and manufacturing practices and processes have significant impact on the core performance, which are highlighted in Chapter 2. Three-phase three-limb core has inherent magnetizing asymmetry that results sometimes into widely different no-load currents and losses in three phases of the transformer during the no-load loss measurement by the three-wattmeter method. It is shown that one of the

three wattmeters can read negative depending upon the magnitude of asymmetry between the phases and the level of excitation. Even though the inrush current phenomenon is well understood, the sympathetic inrush phenomenon, in which the magnetization level of a transformer is affected due to energization of another interconnected transformer, is not well-known. The factors influencing the phenomenon are elucidated in the chapter. The phenomenon was investigated by Prof. S. V. Kulkarni in 1993 based on switching tests conducted at a site in Mumbai.

Chapter 3 is devoted to the leakage reactance of transformers, which can be calculated by either analytical or numerical methods. Procedures for its calculation for various types and configurations of windings, including zigzag and sandwich windings, are explained. The reactance for complex winding configurations can be easily calculated by using the *finite element method* (FEM), which is a widely used numerical method. The chapter gives exhaustive treatment to zero-sequence characteristics of the transformers. Procedures for the calculation of the magnetizing zero-sequence and leakage zero-sequence reactances of the transformers are illustrated through examples (such a treatment is scarcely available in the published literature). The effect of the presence of a delta winding on the zero-sequence reactance is also explained.

In order to accurately estimate and control the stray losses in windings and structural parts, in-depth understanding of the fundamentals of eddy currents starting from the basics of electromagnetic fields is desirable. The theory of eddy currents given in Chapter 4 is self-contained and useful for the conceptual understanding of the phenomena of stray losses in the windings and structural components of transformers described in Chapters 4 and 5, respectively. Stray losses in all the conducting components of the transformers have been given an elaborate treatment. Different analytical and numerical approaches for their estimation are discussed and compared. A number of useful guidelines, graphs and equations are given which can be used by practicing engineers. A few interesting phenomena observed during the load loss test of transformers are explained (e.g., half-turn effect). Various shielding arrangements used for effective stray loss control are discussed and compared.

A high failure rate of transformers due to short circuits is a major concern for transformer users. The success rate during short-circuit tests is far from satisfactory. The static force and withstand calculations are well-established. Efforts are being made to standardize and improve the dynamic short-circuit calculations. Precautions that can be taken at the specification, design, and manufacturing stages of transformers for improvement in short-circuit withstand have been elaborated in Chapter 6. Various failure mechanisms and factors that decide the withstand strength are explained.

Although, the methods for calculating impulse distribution are well-established, failures of large transformers due to part-winding resonances and very fast transient overvoltages have attracted the attention of researchers. After explaining the methods for calculation of series capacitances of commonly used

windings, analytical and numerical methods for transient analysis are discussed in Chapter 7. The results of three different methods are presented for a typical winding. Methods for avoiding winding resonances are also explained.

Chapter 8 elaborates insulation design philosophy. Various factors that affect insulation strength are summarized. Procedures enumerated for estimation of bulk oil and creepage withstand would be very useful to designers. Steps for designing major and minor insulation systems are presented.

Chapter 9 deals with thermal aspects of transformer design. After explaining the modes of heat transfer, various cooling systems are described. Insulation aging processes and life expectancy are also discussed. Many failures of large transformers in the recent past have been attributed to the static electrification phenomenon which is explained at the end.

Various types of loads and tests, which decide structural design aspects, are discussed in Chapter 10. Tank stiffening arrangements are elaborated. This material is scarcely available in the literature. Due to increasing environmental concerns, many users specify lower noise levels. Different noise level reduction techniques are discussed and compared.

Chapter 11 is devoted to four special types of transformers: rectifier transformers, HVDC converter transformers, furnace transformers, and phase-shifting transformers. Their design aspects and features, which are different from conventional distribution and power transformers, are enumerated.

The text concludes with Chapter 12 by identifying current research and development trends. The chapter is intended to give enough pointers to readers desirous of pursuing research in transformers.

At the end, we would like to say that even though the transformer is a mature product, there are still many design, manufacturing, and power system interaction issues that continue to haunt researchers. This book provides answers to many of these issues and tries to give directions for solving some of the remaining ones. It encompasses most of the important aspects of transformer engineering including the recent advances in research and development activities. It also propagates the use of advanced computational tools such as FEM for optimization and quality enhancement of the transformers.

S. V. Kulkarni
S. A. Khaparde

Acknowledgments

We thank our institute for providing support and nice ambience to write the second edition. It was a major task that resulted in the addition of more than 50% of the pages to the first edition, and the work would not have taken this shape without the active support of students. Current Ph.D. students, Amit Bakshi, Ketan Badgujar, and Ajay Pal Singh Baghel, have contributed significantly to some of the new topics in the second edition. The efforts of Amit in proofreading the entire text are greatly appreciated. Interactions with Dr. G. B. Kumbhar helped considerably in refining the sections dealing with the theory and applications of the finite element method. Dr. R. S. Bhide and Dr. A. S. Bhangaonkar gave useful comments on Chapters 12 and 14, respectively. Special thanks are due to Dr. S. R. Kannan for reviewing Chapters 13 and 14; his comments on discussions dealing with various monitoring and diagnostic aspects were extremely useful.

Master's level students (Ragini Agarwal, Chikku Abraham, Vinod Parmar, Makarand Kane, R. Venkataswamy, Md. Maoyafikuddin, V. Ramayya, Rani Chacko, G. Suryanarayana, Dipak Gawai and Ved Manu) helped in many ways. The excellent quality of the figures in the new chapters is due to their efforts. Prasad Bodhayan, who did a summer internship in the institute, contributed to refining some discussions in Chapter 5. Kaushik Kalyanaraman gave useful editorial comments on Chapter 12.

Prof. S. V. Kulkarni started his professional career with Crompton Greaves Limited; the rich and ample experience gained while working in the industry (1990–2001) is thankfully acknowledged. He is grateful to all his erstwhile senior colleagues (C. R. Varier, T. K. Mukherjee, D. A. Koppikar, S. V. Manerikar, B. A. Subramanyam, G. S. Gulwadi, K. Vijayan, V. K. Lakhiani, P. V. Mathai, A. N. Kumthekar and K. V. Pawaskar) for support and practical guidance. Thanks are also due to Crompton Greaves Limited for providing the picture for the cover.

Throughout the book, many practical aspects of transformer engineering are discussed. Therefore, it was very essential to get the contents reviewed by experts from the transformer industry. Many practicing specialists gave very useful suggestions and comments that helped refine the discussions on industry practices (K. Vijayan: Chapters 8 and 9, G. S. Gulwadi: Chapters 1 and 8, V. D. Deodhar, V. K. Reddy and Parmatma Dubey: Chapter 10, Dr. B. N. Jayaram: Chapter 7, Dr. G. Bhat and Dr. Sachin Paramane: Chapter 9). V. S. Joshi had given important suggestions while reviewing the first edition; he helped in the second edition as well with his useful comments on some of the new discussions. Others who gave constructive comments while the first edition was being finalized are Prof. J. Turowski, P. Ramachandran, Prof. L. Satish and M. W. Ranadive. A few of our colleagues in the electrical engineering department supported us by proofreading the first edition. Sainath Bongane, Sachin Thakkar

and G. D. Patil, who were research associates working with us, substantially helped in the editorial work. Also, Dr. G. B. Kumbhar, Dr. A. P. Agalgaonkar and Dr. M. U. Nabi, who were Ph.D. students at that time, also contributed in refining some discussions.

Nora Konopka, Taylor & Francis, gave us full encouragement; she and her colleague, Jessica Vakili, patiently supported this effort. The efforts of Karen Simon and her team in proofreading are appreciated.

Zarine Arya provided useful editorial services and her efforts are hereby acknowledged.

Writing a book is an arduous task requiring complete support from family members. Particular mention must be made of the encouragement and backing provided by Sushama S. Kulkarni. Anandchaitanya S. Kulkarni allowed his father to work even on weekends; thanks are due to the little one for his patience and sacrifice.

S. V. Kulkarni
S. A. Khaparde

1

Transformer Fundamentals

1.1 Perspective

Transformers are static devices that transfer electrical energy from one circuit to another by the phenomenon of electromagnetic induction without any change in frequency. They can link circuits that have different voltages, which is one of the enabling factors for the universal use of the alternating current (AC) system for the transmission and distribution of electrical energy. Hence, transformers ensure that various components of the power system, viz. generators, transmission lines, distribution networks and loads, can all be operated at their most suitable voltage levels. As transmission voltages are increased to higher levels in some parts of a power system, transformers again play a key role in interconnecting the different parts of the system at different voltage levels. Transformers are therefore vital links between the generating stations and the points of utilization in any system.

The transformer is an electromagnetic conversion device in which the electrical energy received by its primary winding is first converted into magnetic energy, which is re-converted into electrical energy in other circuits (secondary winding, tertiary winding, etc.). Thus, the primary and secondary windings are not connected electrically, but coupled magnetically. A transformer is termed either a step-up or a step-down transformer depending upon whether the secondary voltage is higher or lower than the primary voltage. Transformers can be used to either step-up or step-down voltage depending upon the need and application; hence, their windings are referred as high-voltage/low-voltage or high-tension/low-tension windings instead of primary/secondary windings.

***Magnetic circuits*:** A transfer of electrical energy between two circuits takes place through a transformer without the use of moving parts; a transformer

therefore has higher efficiency and lower maintenance cost than rotating electrical machines. Better grades of materials for cores are continuously being developed and introduced. Different types of silicon steels have been introduced in the following chronological order: non-oriented, hot-rolled grain oriented, cold-rolled grain oriented (CRGO), Hi-B, mechanically scribed and laser scribed. The last three types are improved versions of the CRGO class of materials. The saturation flux density has remained more or less constant around 2.0 Tesla for the CRGO grades; however, the sophisticated technologies and processes used while manufacturing the better grades have resulted in significant improvements in the watts/kg and volt-amperes/kg characteristics in the rolling direction. Transformer designers have a limited choice of grades of material; for a grade chosen based on a cost-benefit analysis, the performance of the core can be further optimized by using efficient design and manufacturing technology. The non-mitred construction used earlier was replaced by a better mitred type many decades ago, and now a far superior step-lap construction is almost universally used. A considerable increase in energy costs over the years is mainly responsible for the development (and consequent increase in the use) of the better grades of material for cores: these not only reduce the core loss but also help in reducing the noise levels of transformers. The use of amorphous steel materials results in a substantial reduction in the core loss, to the tune of 60-70% when compared to the CRGO grades. Since the manufacturing technology required for handling this brittle material has to be quite sophisticated, its use is limited to transformers with lower ratings.

***Windings*:** Paper-covered conductors are commonly used in the windings of medium and large power transformers. These conductors can be of individual-strip, bunch or continuously transposed cable (CTC) type. For the low voltage side of distribution transformers, wherein far fewer turns are involved, the use of copper or aluminum foils may be preferred. To enhance the short-circuit withstand capability, a work-hardened copper material is commonly used instead of a soft annealed type, particularly for higher-rating transformers. In generator transformers with high current ratings on the lower voltage (LV) side, CTC conductors are mostly used, which result in a better space factor and reduced eddy loss in windings. CTC conductors can be of the epoxy-bonded type to enhance their short-circuit strength. Conductors with thermally upgraded insulating paper are suitable for hot-spot temperatures of about 110°C, which help in coping with overload conditions. Moreover, a better life expectancy is possible with their use. For better mechanical properties, epoxy diamond dotted paper can be used as the interlayer insulation for multi-layer windings. High temperature superconductors are expected to be available commercially in the near future. Issues such as economic viability, manufacturability, and reliability need to be addressed prior to their large-scale deployment.

***Insulation and cooling*:** Inter-winding insulation structures consist of a number of oil ducts formed by suitably spaced insulating cylinders. Pre-compressed

pressboards, manufactured using high quality materials and processes, are used in high voltage transformers. Well-profiled angle rings, angle caps, and other special insulation components are also widely used.

Mineral oil has traditionally been the most commonly used electrical insulating medium and coolant in transformers. Studies have proved that the oil-barrier insulation system is suitable even at voltages rated higher than 1000 kV. The high dielectric strength of oil-impregnated papers and pressboards is the main reason for the widespread use of mineral oil in transformers. Silicone oil is an alternative; it is non-toxic and fire-resistant. A comparatively higher cost is an inhibiting factor in its widespread use. Transformers with biodegradable natural and synthetic esters are employed in environmentally sensitive locations.

There have been considerable advancements in the technology of gas-immersed transformers. SF6 is a non-flammable gas and has excellent dielectric properties. Hence, SF6 transformers are preferred for fire-hazard-free applications. Due to the low specific gravity of SF6 gas, gas-insulated transformers are lighter than oil-immersed transformers. The dielectric strength of SF6 gas is a function of the operating pressure; the higher the pressure, the higher the dielectric strength is. However, the heat capacity and thermal time constant of SF6 gas are less than those of oil, resulting in a lower overload capacity of SF6 transformers. Environmental concerns, sealing problems, lower cooling capability, and the present high cost of manufacture are the challenges that have to be overcome for widespread use of SF6 transformers.

Dry-type resin cast and resin impregnated transformers use class *F* or *C* insulation. The high cost of resins and their lower heat dissipation capability limit the use of these materials to transformers that have lower ratings. Dry-type transformers are primarily used for indoor applications in order to minimize fire hazards. Nomex paper insulation, which has a temperature withstand capacity of 220°C, is widely used in dry-type transformers. The initial cost of a dry-type transformer may be 60 to 70% higher than that of an oil-cooled transformer at current prices, but its overall cost at the present level of energy rates can be quite comparable to that of the oil-cooled transformer.

***Design*:** With the rapid development of digital computers, designers are freed from the drudgery of routine calculations. Computers are widely used for the optimization of designs. Within a few minutes, today's computers can work out a number of designs (by varying flux density, core diameter, current density, etc.) and come up with an optimum design. One of the major benefits of computers is in the area of analysis. Using commercial 2-D/3-D field computation software, any kind of engineering analysis (electrostatic, electromagnetic, structural, thermal, etc.) can be performed to optimize the design of transformers or to enhance their reliability.

***Manufacturing*:** In manufacturing technology, the superior techniques listed below are used to reduce manufacturing time and at the same time to improve product quality:

- A high degree of automation for slitting/cutting operations to achieve better dimensional accuracy for core laminations
- Step-lap joints for core construction to achieve lower core loss and noise level
- Core building without top yoke
- Automated winding machines for distribution transformers
- Vapor phase drying for effective and fast drying
- Low frequency heating for the drying process of distribution transformers
- Pressurized chambers to protect windings and insulating parts from pollution and dirt
- Vertical machines for winding large-capacity transformer coils
- Isostatic clamping for accurate sizing of windings
- High-frequency brazing for joints in the windings and connections.

***Accessories*:** Bushings and the tap changer (off-circuit or on-load) are the most important accessories of a transformer. The technology of bushing manufacture has advanced from the oil-impregnated paper (OIP) type to the resin impregnated paper (RIP) type, both of which use porcelain insulators. Silicone rubber bushings are also available for oil-to-air applications; due to the high elasticity and strength of silicone rubber, the strength of these bushings against mechanical stresses and shocks is higher. Oil-to-SF6 bushings are used in GIS (gas-insulated substation) applications.

The service reliability of on-load tap-changers (OLTC) is of vital importance; failures of transformers due to tap-changer problems are common. A majority of the failures reported in service are due to mechanical problems related to the drive system. Several monitoring methods are used for enhancing the service reliability of OLTCs, which include measurement of contact resistance, monitoring of drive motor torque/current, acoustic measurements, dissolved gas analysis, and temperature rise measurements.

***Diagnostic techniques*:** Several offline and online diagnostic tools are available for monitoring in-service transformers to provide information about their operating conditions. Dissolved gas analysis is widely used in conjunction with routine tests on oil and winding insulation. Frequency response analysis is being widely used to assess the mechanical condition of windings. Recently, online partial discharge monitoring techniques based on acoustic and ultra-high frequency sensors have also been deployed. Advanced time- and frequency-domain methods are becoming popular for the diagnostics of insulation. However, the higher costs of the advanced instruments required for this purpose inhibit their widespread use. An important factor that must be kept in mind is that field experience with some of the monitoring techniques is limited. A close cooperation between manufacturers and users is necessary for developing good monitoring and diagnostic systems for transformers.

Transformer technology is developing at a tremendous rate and computerized operations have replaced manual work in the design office. Continuous improvements in materials and manufacturing technologies along with the use of advanced computational tools have contributed towards making transformers more efficient, compact and reliable. Advanced diagnostic tools and several emerging trends in transformer applications are expected to fulfill a number of existing and emerging requirements of utilities and end-users.

1.2 Applications and Types of Transformers

Before the invention of transformers, in the initial days of the electrical industry, power was distributed through direct current (DC) at low voltages. Voltage drops in electrical lines limited the use of electricity to only urban areas where consumers were served using distribution circuits of small length. All the electrical equipment had to be designed for the same voltage. Development of the first transformer around 1885 dramatically changed transmission and distribution systems. The power generated with alternating currents at low voltages could be stepped up for transmission purposes to higher voltages (with lower currents), reducing voltage drops and transmission losses. The use of transformers made it possible to transmit power economically to areas hundreds of kilometers away from generating stations. Step-down transformers then reduced the voltage at the receiving stations for the distribution of power at various standardized voltage levels for its use by end-consumers. Transformers have made AC systems flexible because the various parts and equipment of the power system can be operated at economical voltage levels with suitable voltage ratios. A single-line diagram of a typical power system is shown in Figure 1.1. Voltage levels are different in different countries. Transformers can be broadly classified into several types, some of which are based on location and broad function, and others according to their applications:

1.2.1 Transformers classified according to location and broad function

***a. Generator transformers*:** The power generated at a generating station (usually at a voltage in the range of 11 to 25 kV) is stepped up by a generator transformer to a higher voltage (220, 345, 400 or 765 kV) for its transmission over long distances. Generator transformers are important and critical components of any power system. They usually have uniform loads and are designed with higher losses since the cost of supplying power is cheapest at the generating station. Lower noise levels are usually not specified since the generators supplying the transformers are even noisier.

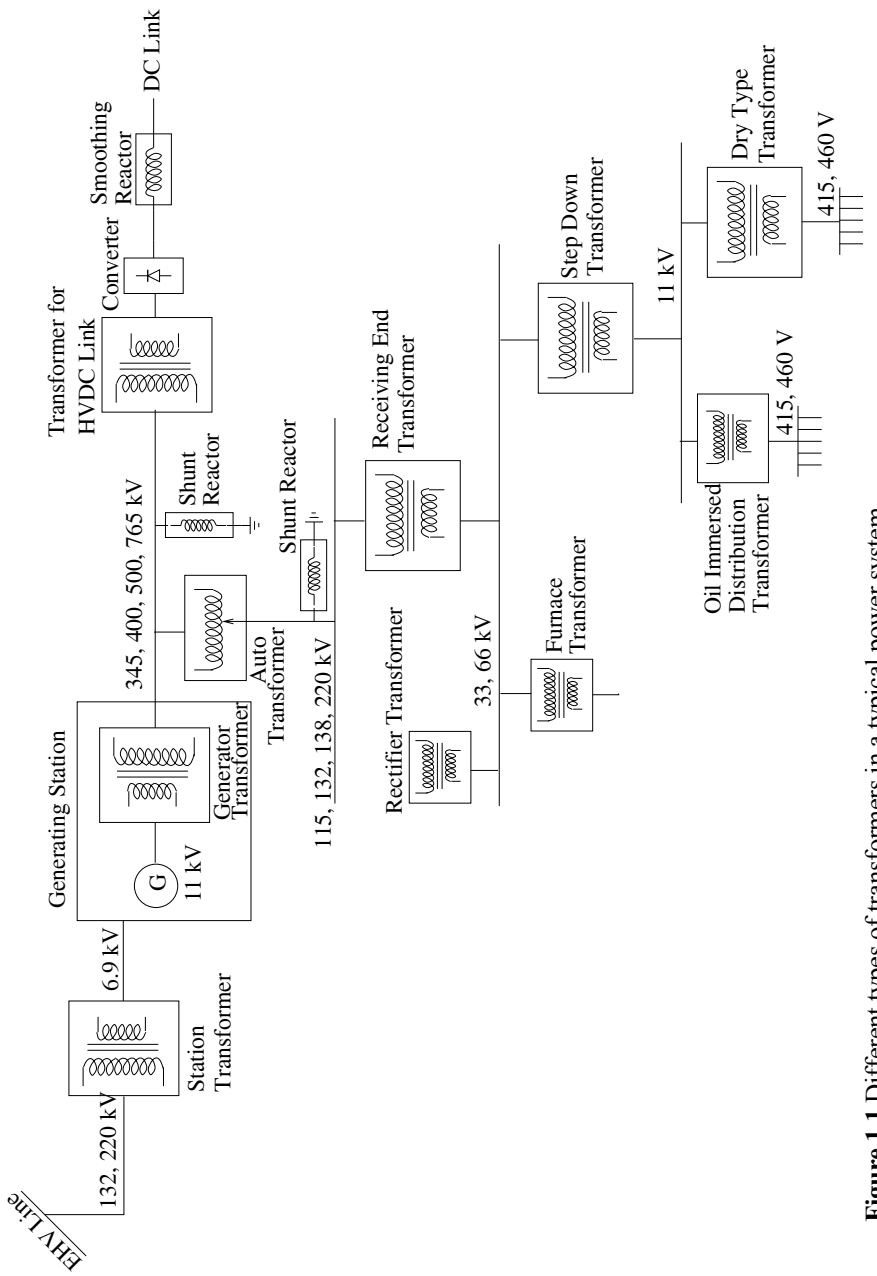

Figure 1.1 Different types of transformers in a typical power system.

A tap-changing mechanism with off-circuit taps, suitable for a small variation in the HV voltage (e.g., ± 5%), is preferred since the voltage can be easily controlled through the field excitation of the generator. Generator transformers having an on-load tap changing mechanism are used for reactive power control. They may be provided with a compact unit-cooler arrangement for want of space in the generating stations; such transformers have only one rating with oil-forced and air-forced cooling. Alternatively, oil-to-water heat exchangers can be used for the same reason. It may be economical to design the tap winding as a part of the main HV winding and not as a separate winding. This may be permissible since axial short-circuit forces are generally lower due to a small tapping range. Special care has to be taken while designing high current LV lead terminations to eliminate hot-spots in the structural parts in their vicinity. A CTC conductor with epoxy bonding is commonly used for the LV winding to minimize eddy losses and to provide higher short-circuit strength. The overexcitation conditions specified by the users have to be considered while designing generator transformers.

***b. Unit auxiliary transformers*:** These are step-down transformers with their primary winding connected to the generator output directly. The secondary voltage is of the order of 6.9 kV for supplying power to various auxiliary equipment in the generating station.

***c. Station transformers*:** These transformers are required to supply power to auxiliary equipment during the setting-up operation of generating stations and subsequently during each start-up operation. The rating of these transformers is small, and their primary winding is connected to a high voltage transmission line. This may result in a smaller conductor size for the HV winding, necessitating special measures for increasing the short-circuit strength. A split-secondary winding arrangement is often employed to achieve economical circuit breaker ratings.

***d. Interconnecting transformers or autotransformers*:** These transformers are used to interconnect two systems operating at different system voltages (e.g., 400 kV and 220 kV, 345 kV and 138 kV). There is no electrical isolation between their primary and secondary windings; some volt-amperes are conductively transformed and the remaining are inductively transformed. The design of an autotransformer becomes more cost-effective as the ratio of the secondary winding voltage to the primary winding voltage approaches unity. Autotransformers are characterized by a wide tapping range and a loaded or unloaded delta-connected tertiary winding. The unloaded tertiary winding acts as a stabilizing winding by providing a path for third-harmonic currents. Synchronous condensers or shunt reactors are connected to the tertiary winding, if required, for reactive power compensation. An adequate conductor area and a proper supporting arrangement should be provided to the unloaded tertiary

winding to help it withstand short-circuit forces under asymmetrical fault conditions.

***e. Receiving station transformers*:** These are step-down transformers that reduce a transmission or sub-transmission voltage to a primary feeder level voltage (e.g., 220 kV/33 kV transformers). They can be used to feed industrial plants directly. Loads on them vary in a wider range, and it is expensive for the generator to supply the power lost in them in the form of no-load and load losses. The farther the location of transformers from the generating station, the higher the cost of supplying the losses is. Automatic tap changing on load is usually necessary, and the tapping range is generally higher to account for a wide variation in the voltage. A lower noise level is usually specified for those transformers that are close to residential areas.

***f. Distribution transformers*:** Using distribution transformers, the primary feeder voltage is reduced to an actual utilization voltage (~ 415 or 460 V) for domestic/industrial use. Several types of transformers fall into this category due to many different arrangements and connections. The load on these transformers varies widely, and they are often overloaded. A lower value of no-load loss is desirable to improve their all-day efficiency. Hence, the no-load loss is usually capitalized with a high rate at the tendering stage. Since very little supervision is possible, users expect a minimum level of maintenance on these transformers. The cost of supplying losses and reactive power is highest for these transformers.

1.2.2 Transformers classified according to specific applications

In this chapter, only the main features of these transformers are highlighted; details of some of them are discussed in subsequent chapters.

***a. Phase shifting transformers*:** These are used to control power flow over transmission lines by varying the phase angle between the input and output voltages of the transformer. Through a proper tap-change, the output voltage can be made either to lead or lag the input voltage. The total phase-shift required directly affects the rating and size of the transformer. Presently, two distinct types of core construction are used, viz. a single-core design and a two-core design. The single-core design is used for small phase-shifts and lower MVA / voltage ratings, while the two-core design is employed for bulk power transfer with higher ratings of phase-shifting transformers. The design consists of two transformers, one associated with the line terminals and the other with the tap-changer.

***b. Earthing or grounding transformers*:** These are used to provide a neutral point that facilitates grounding and detection of earth faults in an ungrounded part of the network (e.g., delta-connected systems). Their windings are usually connected in a zigzag manner, which helps in eliminating third harmonic voltages in the lines. These types of transformers have an additional advantage

since they are not affected by the DC magnetization problems normally associated with power electronic converters.

***c. Transformers for rectifier and inverter circuits*:** These are otherwise normal transformers except for their special design and manufacturing features which enable them to counter harmonic effects. Due to extra harmonic losses, the operating flux density in their core is kept lower (around 1.6 Tesla). The winding conductor dimensions need to be smaller to reduce eddy losses, and a proper de-rating factor has to be applied depending upon the magnitudes of various harmonic components. Thermal design aspects need to be carefully looked at for eliminating hot-spots. For the transformers used in high voltage direct current (HVDC) systems, the design of their insulation system is a challenging task because of combined AC-DC voltage stresses.

***d. Furnace duty transformers*:** These transformers are used to feed the arc or induction furnaces, which are characterized by a low secondary voltage (80 to 1000 V) and a high current (10 to 60 kA) depending upon their MVA rating. A non-magnetic steel material is invariably used for the termination of LV leads and for the tank portion in their vicinity to eliminate hot spots and minimize stray losses. For applications involving very high currents, LV terminals in the form of U-shaped copper tubes having suitable inside and outside diameters are designed so that they can be cooled by oil/water circulation from inside. In many cases, a booster transformer is used along with the main transformer to reduce the rating of the tap-changer.

***e. Freight loco transformers*:** These are mounted in the engine compartments of locomotives, and their primary winding is connected to an overhead line. The primary voltage is stepped down to an appropriate level for feeding to a rectifier; the output DC voltage of the rectifier drives the locomotive. The structural design of the transformers has to be good enough to take care of locomotive vibrations. The mechanical natural frequencies of the whole structure need to be analyzed to eliminate resonant conditions.

***f. Hermetically-sealed transformers*:** The construction of these transformers is such that it does not permit any outside atmospheric air to get into the tank. It is completely sealed without any breathing arrangement, obviating the need for periodic filtration and related maintenance activities. These transformers are filled with mineral oil or synthetic liquid as a cooling and dielectric medium, and they are sealed completely with an inert gas (nitrogen) layer between the medium and the top tank plate. A welded cover construction is used for the tank to eliminate bolted joints and related leakage problems. Variations in the medium volume are absorbed by the inert gas layer. The tank is designed for high-pressure conditions at elevated temperatures. In another type of sealed construction, the use of inert gas is avoided; the expansion of the medium is absorbed by deformations of the structure used for the cooling arrangement, which can be an integral part of the tank.

***g. Outdoor and indoor transformers*:** Most transformers are suitable for outdoor duty and are designed to withstand atmospheric pollutants. The creepage distance of the bushing insulators is decided according to the pollution level. The higher the pollution level, the greater the creepage distance that is required between the live terminal and ground. On the other hand, transformers for indoor applications are kept in a weatherproof and properly ventilated room. Standards define the minimum level of ventilation required for effective cooling. Adequate clearances should be kept between the walls and the transformer to eliminate the possibility of higher noise levels due to reverberations.

There are other types of transformers, which have applications in electronics, electric heaters, traction, etc. Some of the applications have a significant impact on the design of the transformers. The duty (load) can be very onerous. For example, the winding current densities in transformers with frequent motor-starting duty have to be lower due to the high starting currents of the motors (which can be of the order of 6 to 8 times the full load current).

1.2.3 Reactors

Shunt and series reactors are very important components of the power system. The design of reactors, which have only one winding, is similar to that of transformers in many aspects. Their special features are highlighted below.

***a. Shunt reactors*:** These are used to compensate for the capacitive volt-amperes generated during no-load or light-load conditions in high voltage transmission networks, thereby helping to maintain the voltage profile within desirable limits. Shunt reactors are installed at a number of places along the length of the transmission line. They can be either permanently connected or of a switched type. Those that are permanently connected may result in poor voltage levels and increased losses under normal operating conditions. Hence, the switched types are better since these are connected only when the voltage levels need to be controlled. When connected to the tertiary winding of a transformer with a suitable rating, they become cost effective. The voltage drop due to a high impedance value between the HV winding and the tertiary winding must be taken into account while deciding the voltage rating of the reactors connected to the tertiary winding.

Shunt reactors can be of coreless (air-core) or gapped-core (magnetic circuit with non-magnetic gaps) design. The flux density in the air-core reactors has to be lower as the flux path is not well constrained. Eddy losses in the winding and stray losses in the structural conducting parts are higher in this type of design. In contrast, the gapped-core design is compact due to a higher permissible flux density. The gaps between core packets can be suitably designed to achieve a desired reactance value. Shunt reactors are usually designed to have constant impedance characteristics up to 1.5 times the rated voltage to minimize harmonic currents in overvoltage conditions.

***b. Series reactors*:** These reactors are connected in series with generators, feeders, and transmission lines to limit fault currents under short-circuit conditions. These reactors should have linear magnetic characteristics under fault conditions. They should be designed to withstand the mechanical and thermal effects of short circuits. The winding of series reactors used for transmission lines is of the fully insulated type since both the ends should be able to withstand lightning voltages. The value of the series reactors has to be judiciously chosen because a higher value reduces the power transfer capability of the lines. Smoothing reactors used in HVDC transmission systems smoothen out the ripple in the DC voltage.

1.3 Principles and the Equivalent Circuit

1.3.1 Ideal transformer

Transformers work on the principle of electromagnetic induction, according to which a voltage is induced in a coil linking to a changing flux. Figure 1.2 shows a single-phase transformer consisting of two windings, wound on a magnetic core and linked by a mutual flux ϕ_m. The transformer is in no-load condition with its primary connected to a source of sinusoidal voltage of frequency f Hz. The primary winding draws a small excitation current, i_0 (instantaneous value), from the source to set up the flux ϕ_m in the core. All the flux is assumed to be contained in the core (no leakage). Windings 1 and 2 have N_1 and N_2 turns respectively. The instantaneous value of the induced electromotive force in winding 1 due to the mutual flux is

$$e_1 = N_1 \frac{d\phi_m}{dt}. \tag{1.1}$$

Equation 1.1 gives the circuit viewpoint; there is a flux-viewpoint also [1], in which the induced voltage (counter electromotive force) is represented as $e_1 = -N_1(d\phi_m / dt)$. An elaborate explanation for both the viewpoints is given in [2]. If the winding is further assumed to have zero resistance (with its leakage reactance already neglected), then

$$v_1 = e_1. \tag{1.2}$$

Since v_1 (instantaneous value of the applied voltage) is sinusoidally varying, the flux ϕ_m must also be sinusoidal in nature varying with frequency f. Let

$$\phi_m = \phi_{mp} \sin \omega t \tag{1.3}$$

where ϕ_{mp} is the peak value of mutual flux ϕ_m and $\omega = 2\pi f$ rad/sec. After substituting the value of ϕ_m in Equation 1.1, we obtain

$$e_1 = N_1 \omega \phi_{mp} \cos \omega t. \tag{1.4}$$

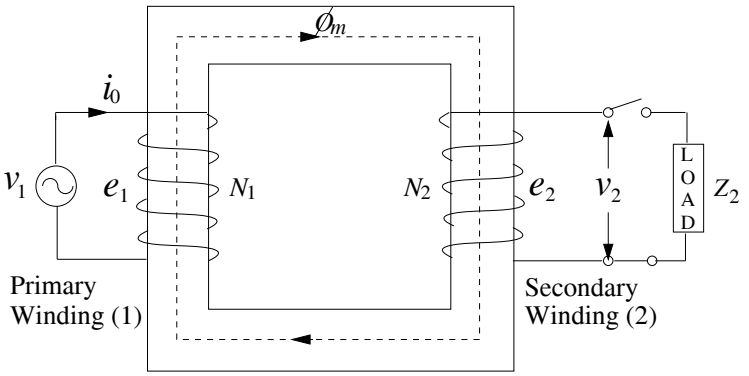

Figure 1.2 Transformer in no-load condition.

The root mean square (r.m.s.) value of the induced voltage, E_1, is obtained by dividing the peak value in Equation 1.4 by $\sqrt{2}$,

$$E_1 = 4.44\ \phi_{mp}\ f\ N_1. \tag{1.5}$$

Equation 1.5 is known as the *emf equation* of the transformer. For a given number of turns and frequency, the flux (and flux density) in its core is entirely determined by the applied voltage.

The voltage induced in winding 2 due to the mutual flux (ϕ_m) is given by

$$e_2 = N_2 \frac{d\phi_m}{dt}. \tag{1.6}$$

The ratio of the two induced voltages can be derived from Equations 1.1 and 1.6,

$$e_1/e_2 = N_1/N_2 = a \tag{1.7}$$

where a is known as the ratio of transformation. Similarly, the r.m.s. value of the induced voltage in winding 2 is

$$E_2 = 4.44\ \phi_{mp}\ f\ N_2. \tag{1.8}$$

The exciting current (i_0) is of only a magnetizing nature (i_m) if the *B-H* curve of the core material is assumed to be anhysteretic (without hysteresis) and if the eddy current losses in the core are neglected. The magnetizing current (i_m) is in phase with the mutual flux in the absence of hysteresis. Furthermore, the magnetic characteristics are assumed linear.

Now, if the secondary winding in Figure 1.2 is loaded, a current is set up in it as per Lenz's law such that the secondary magnetomotive force (mmf), i_2N_2, opposes the mutual flux, thus tending to reduce it. In an ideal transformer

$e_1 = v_1$, and therefore for a constant value of the applied voltage, the induced voltage and the corresponding mutual flux must remain constant. This can happen only if the primary winding draws more current (i_1') for neutralizing the demagnetizing effect of the secondary ampere-turns. In r.m.s. notation,

$$I_1' N_1 = I_2 N_2 . \tag{1.9}$$

Thus, the total primary current is the vector sum of the no-load current (i.e., the magnetizing component, $\hat{I}_m$, since the core losses are neglected) and the load current ($\hat{I}_1'$),

$$\hat{I}_1 = \hat{I}_1' + \hat{I}_m . \tag{1.10}$$

For an infinitely permeable magnetic material, the magnetizing current is zero. Equation 1.9 then becomes

$$I_1 N_1 = I_2 N_2 . \tag{1.11}$$

Thus, for an ideal transformer with its no-load current neglected, the primary ampere-turns are equal to the secondary ampere-turns. The same result can also be obtained by applying Ampere's law, which states that the magnetomotive force around a closed path is given by

$$\oint \mathbf{H} \cdot d\mathbf{l} = i \tag{1.12}$$

where i is the current enclosed by the line integral of the magnetic field intensity **H**. For the present case,

$$\oint \mathbf{H} \cdot d\mathbf{l} = \oint (\mathbf{B}/\mu) \cdot d\mathbf{l} = i_1 N_1 - i_2 N_2 . \tag{1.13}$$

If the relative permeability of the magnetic path is assumed as infinite, the integral value is zero. Hence, in the r.m.s. notations,

$$I_1 N_1 - I_2 N_2 = 0 \tag{1.14}$$

which is the same result as in Equation 1.11.

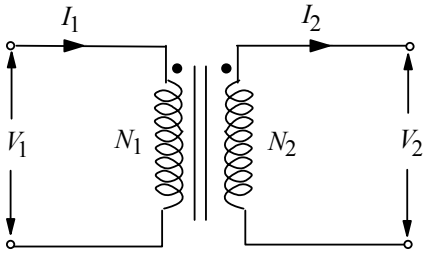

Figure 1.3 Schematic representation of an ideal transformer.

Thus, an ideal transformer (zero winding resistance, no leakage flux, infinite permeability, zero core losses) can be summarized as

$$\frac{E_1}{E_2} = \frac{V_1}{V_2} = \frac{N_1}{N_2} = \frac{I_2}{I_1} \tag{1.15}$$

and

$$V_1 I_1 = V_2 I_2 . \tag{1.16}$$

A schematic representation of the transformer in Figure 1.2 is shown in Figure 1.3. The polarities of voltages depend upon the directions in which the primary and secondary windings are wound. It is a common practice to put a dot at the end of the windings such that their dotted ends are positive at the same time, meaning thereby that the voltage drops from the dotted to the unmarked terminals are in phase. Also, the currents flowing from the dotted to the unmarked terminals produce mmfs that act along the same direction in the magnetic circuit.

If the secondary winding in Figure 1.2 is loaded with an impedance Z_2,

$$Z_2 = V_2 / I_2 . \tag{1.17}$$

Substituting from Equation 1.15 for V_2 and I_2,

$$Z_2 = \frac{(N_2/N_1)\, V_1}{(N_1/N_2)\, I_1} . \tag{1.18}$$

Hence the impedance, when referred to the primary winding (1), is

$$Z_2' = \frac{V_1}{I_1} = (N_1 / N_2)^2 Z_2 . \tag{1.19}$$

Similarly, any impedance Z_1 in the primary circuit can be referred to the secondary side as

$$Z_1' = (N_2 / N_1)^2 Z_1 . \tag{1.20}$$

It can be summarized from Equations 1.15, 1.16, 1.19 and 1.20 that for an ideal transformer, voltages are transformed in the ratio of the turns, currents in the inverse ratio of the turns, and impedances in the square ratio of the turns, whereas the volt-amperes and power remain unchanged.

The ideal transformer transforms direct voltage, that is, the DC voltages on the primary and secondary sides are related by the turns ratio. This is theoretically correct since it is assumed to have infinite core permeability with linear (non-saturating) characteristics permitting the flux to rise without limit

under a DC voltage application. When a DC voltage (V_{d1}) is applied to the primary winding with the secondary winding open-circuited,

$$V_{d1} = N_1(d\phi_m / dt)\,. \tag{1.21}$$

Thus, $(d\phi_m / dt)$ is constant (flux permitted to rise with time without any limit) and is equal to (V_{d1} / N_1). Voltage at the secondary of the ideal transformer is

$$V_{d2} = N_2(d\phi_m / dt) = (N_2 / N_1)\, V_{d1}\,. \tag{1.22}$$

However, for a practical transformer, in the steady-state condition the primary current has a value of V_{d1}/R_1, and the magnetic circuit is driven into saturation. Eventually, this reduces the values of the induced voltages E_1 and E_2 to zero. This is because, in saturation, there is hardly any change in the flux even though the current may still be increasing till the steady-state condition is reached. The value of the steady-state current, V_{d1}/R_1, is high enough to damage the transformer.

1.3.2 Practical transformer

The analysis presented for an ideal transformer is merely to explain the fundamentals of transformer action; such a transformer does not exist and the equivalent circuit of a real (practical) transformer, as shown in Figure 1.4, is now developed. Whenever a magnetic material undergoes a cyclic magnetization, two types of losses, eddy and hysteresis losses, occur in it. These losses are always present in transformers as the flux in their ferromagnetic core is of an alternating nature. A detailed explanation of these losses is given in Chapter 2.

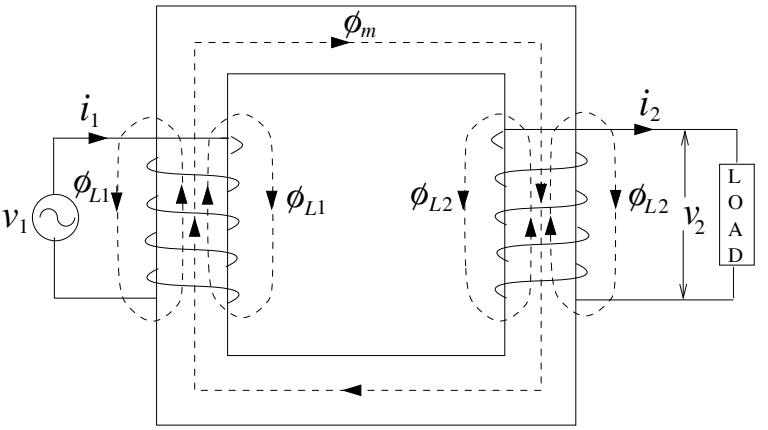

Figure 1.4 Practical transformer.

The hysteresis loss and eddy loss can be minimized by using a better grade of core material and thinner laminations, respectively. The total no-load current, I_0, consists of the magnetizing component (I_m) responsible for producing the mutual flux, ϕ_m, and the core-loss component (I_c) which accounts for the active power drawn from the source to supply the losses. The core-loss component is in phase with the induced voltage and leads the magnetizing component by 90°. With the secondary winding open-circuited, the transformer behaves as a highly inductive circuit, and hence the no-load current lags behind the applied voltage by an angle slightly less than 90° (I_m is usually much greater than I_c). In the equivalent circuit shown in Figure 1.5 (a), the magnetizing component is represented by the inductive reactance, X_m, whereas the loss component is indicated by the resistance, R_c.

Let R_1 and R_2 be the resistances of windings 1 and 2, respectively. In a practical transformer, some part of the flux linking the primary winding does not link the secondary winding. This flux component is proportional to the primary current and is responsible for a voltage drop which is represented by the inductive reactance X_{L1} (leakage reactance) and it is put in series with the primary winding of the ideal transformer. Similarly, a leakage reactance, X_{L2}, is added in series with the secondary winding of the ideal transformer to take into account the voltage drop due to the flux linking only the secondary winding. One can omit the ideal transformer from the equivalent circuit, if all the quantities are referred to either the primary or the secondary side of the transformer. For example, in the equivalent circuit of Figure 1.5 (b), all quantities are referred to the primary side,

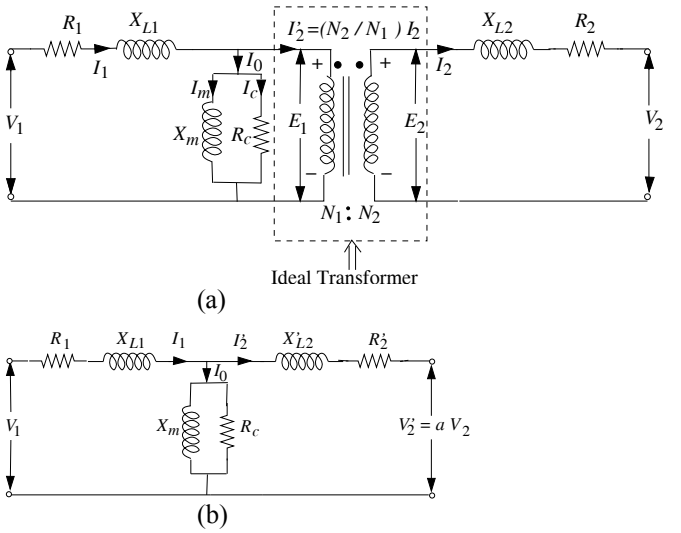

Figure 1.5 Equivalent circuit.

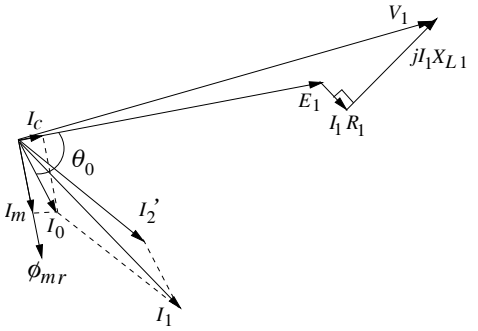

(a) Primary side (b) Secondary side

Figure 1.6 Vector diagrams.

$$X'_{L2} = X_{L2}\left(N_1 / N_2\right)^2 \tag{1.23}$$

and

$$R'_2 = R_2\left(N_1 / N_2\right)^2 . \tag{1.24}$$

This equivalent circuit is a passive lumped-T representation, valid generally for the sinusoidal steady-state analysis at power frequencies. For higher frequencies, capacitive effects must be considered, as discussed in Chapter 7. For transient analyses, all the reactances in the equivalent circuit should be replaced by the corresponding inductances.

While drawing a vector diagram, it must be remembered that all the involved phasors must be of the same frequency. The magnetization (*B-H*) curve of the core materials used in transformers is nonlinear and therefore it introduces higher order harmonics in the magnetizing current for an applied sinusoidal voltage of fundamental frequency. In the vector diagrams of transformers, however, a linear *B-H* curve is assumed (harmonics are not considered). The aspects related to core magnetization and losses are described in Chapter 2. For Figure 1.5 (a), the following equations can be written:

$$V_1 = E_1 + (R_1 + jX_{L1})\, I_1 \tag{1.25}$$

and

$$V_2 = E_2 - (R_2 + jX_{L2})\, I_2 . \tag{1.26}$$

Vector diagrams for the primary and secondary voltages/currents are shown in Figure 1.6. The output terminal voltage, V_2, is taken as a reference vector along the x-axis. The power factor angle of the load is denoted by θ_2. The induced voltages are in phase and lead the mutual flux ϕ_{mr} (r.m.s. value of ϕ_m) by 90°

in conformance with Equations 1.1 and 1.6. The magnetizing component (I_m) of the no-load current (I_0) is in phase with ϕ_{mr}, whereas the loss component (I_c) leads ϕ_{mr} by 90° and is in phase with the induced voltage E_1. The core loss is given as

$$P_c = I_c E_1 \tag{1.27}$$

or

$$P_c = I_c^2 R_c . \tag{1.28}$$

The mutual reactance, X_m, is

$$X_m = \frac{E_1}{I_m} . \tag{1.29}$$

The magnitude of the secondary current referred to the primary side (I_2') is the same as that of the secondary current (I_2), since the turns of the primary and secondary windings are assumed to be equal for the sake of simplicity. There is a finite phase shift between the terminal voltages V_1 and V_2 due to voltage drops in the leakage impedances. The voltage drops in the resistances and leakage reactances are exaggerated in the vector diagrams. The voltage drop across the winding resistances is typically less than 0.5% of the terminal voltage for large power transformers, whereas the voltage drop in the leakage impedances is much higher. For small distribution transformers (up to 5 MVA), the value of the leakage impedance is around 4% to 7% and for power transformers it can be anywhere in the range of 8% to 20% depending upon the voltage regulation and system protection requirements. The lower the percentage impedance is, the lower the voltage drop. However, the required ratings of the circuit breakers will be higher.

1.3.3 Mutual and leakage inductances

The leakage flux ϕ_{L1} shown in Figure 1.4 is produced by the current i_1, which links to winding 1 only. Similarly, the leakage flux ϕ_{L2} is produced by the current i_2, which links to winding 2 only. The primary leakage inductance is

$$L_{L1} = N_1 \frac{d\phi_{L1}}{di_1} . \tag{1.30}$$

The differential reluctance offered to the path of leakage flux is

$$\Re_{L1} = N_1 \frac{di_1}{d\phi_{L1}} . \tag{1.31}$$

Equations 1.30 and 1.31 give

$$L_{L1} = \frac{N_1^2}{\Re_{L1}} \quad . \tag{1.32}$$

Similarly, the leakage inductance of the secondary winding is

$$L_{L2} = \frac{N_2^2}{\Re_{L2}} \, . \tag{1.33}$$

Let us derive the expression for the mutual inductance, *M*. Using Equation 1.6,

$$e_2 = N_2 \frac{d\phi_m}{dt} = N_2 \frac{d\phi_m}{di_m} \frac{di_m}{dt} = M_{21} \frac{di_m}{dt} \tag{1.34}$$

where,

$$M_{21} = N_2 \frac{d\phi_m}{di_m} = N_2 \frac{N_1}{\Re_m} \, . \tag{1.35}$$

M_{21} represents flux linkages in the secondary winding due to the magnetizing current (i_m) in the primary winding divided by i_m . The reluctance offered to the path of the mutual flux (ϕ_m) is denoted by $\Re_m$. Similarly,

$$M_{12} = N_1 \frac{N_2}{\Re_m} \, . \tag{1.36}$$

Thus, the mutual inductance is given by

$$M = M_{12} = M_{21} = \frac{N_1 N_2}{\Re_m} \, . \tag{1.37}$$

Let $\Re_1$ represent the total reluctance of the parallel paths of two fluxes, viz. the leakage flux, ϕ_{L1} , of winding 1 and ϕ_m . Also let

$$k_1 = \frac{\Re_1}{\Re_m} \, . \tag{1.38}$$

The self inductance, L_1 , of winding 1, when $i_2 = 0$, is

$$L_1 = \frac{N_1^2}{\Re_1} = \frac{N_1^2}{\Re_1} \frac{\Re_m}{\Re_m} \frac{N_2}{N_2} = \frac{aM}{k_1} \, . \tag{1.39}$$

Similarly let

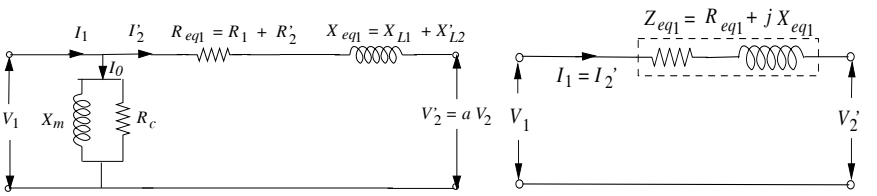

(a) (b)

Figure 1.7 Simplified equivalent circuit.

$$k_2 = \frac{\Re_2}{\Re_m} \tag{1.40}$$

and we obtain

$$L_2 = \frac{M}{ak_2}. \tag{1.41}$$

Hence,

$$M = \sqrt{k_1 k_2}\sqrt{L_1 L_2} = k\sqrt{L_1 L_2}\,. \tag{1.42}$$

Coefficient $k = \sqrt{k_1 k_2}$ is a measure of coupling between the two windings. From the definitions of k_1 and k_2 (e.g., $k_1 = \frac{\Re_1}{\Re_m} = \frac{1/\Re_m}{1/\Re_1} = \frac{1/\Re_m}{1/\Re_m + 1/\Re_{L1}}$), it follows that $0 \le k_1 \le 1$ and $0 \le k_2 \le 1$, giving $0 \le k \le 1$. For $k = 1$, the windings are said to have a perfect coupling with no leakage flux, which is possible only for the ideal transformer discussed previously.

1.3.4 Simplified equivalent circuit

Since the no-load current and voltage drop in the leakage impedance are usually small, it is often permissible to simplify the equivalent circuit of Figure 1.5 (b) by doing some approximations. Terminal voltages (V_1, V_2) are not appreciably different from the corresponding induced voltages, and hence little error is introduced if the no-load current is made to correspond to the terminal voltage instead of the induced voltage. For example, if the excitation branch (consisting of X_m in parallel R_c) is shifted to the input terminals (excited by V_1), the approximate equivalent circuit will be as shown in Figure 1.7 (a). Such an equivalent circuit is derived for a sample design in Appendix A. If we totally neglect the no-load excitation current, as it is much less as compared to the full load current, the circuit can be further simplified as shown in Figure 1.7 (b). This simplified circuit, in which a transformer can be represented by just the

impedance, Z_{eq1}, is considered to be sufficiently accurate for a modeling purpose in power system studies. Since R_{eq1} is much smaller than X_{eq1}, a transformer can be represented just as a series reactance in most cases.

1.4 Representation of a Transformer in a Power System

As seen in the previous section, the ohmic values of resistance and leakage reactance of the transformer depend upon whether they are referred on the LV side or the HV side. A great advantage is realized by expressing voltage, current, impedance, and volt-amperes in per-unit or percentage of the corresponding base values. The per-unit quantities, once expressed on a particular base, are the same when referred to either side of the transformer. Thus, the value of the per-unit impedance remains the same on either side obviating the need for any calculations by using Equations 1.19 and 1.20. This approach is very handy in power system calculations, where a large number of transformers, each having a number of windings, are present.

Per-unit values are derived by choosing a set of base values for the above-mentioned quantities. Although the base values can be chosen arbitrarily, it is preferable to use the rated quantities as the base values. The per-unit quantity (p.u.) is related to the base quantity by the following relationship:

$$Per\text{-}unit\ quantity = \frac{Actual\ value\ of\ the\ quantity}{Base\ value\ of\ the\ quantity}. \tag{1.43}$$

The actual and base values must be expressed in the same unit. Usually, the base values of voltage and volt-amperes are chosen first, from which the other base quantities are determined. The base values of voltages on the LV side and HV side are denoted by V_{bL} and V_{bH}, respectively. The corresponding values of base currents for the LV side and HV side are I_{bL} and I_{bH}, respectively. If the rated voltage of the LV winding is taken as the base voltage (V_{bL}) for the LV side,

$$\text{p.u. rated voltage on LV side} = \frac{\text{Rated voltage of LV side}}{V_{bL}} = 1.0. \tag{1.44}$$

Hence, the per-unit values of rated quantities are equal to unity when rated quantities are chosen as the base quantities. Per-unit quantities are ratios and dimensionless, which have to be multiplied by 100 to obtain percentage values.

The value of base impedance on the LV side is

$$Z_{bL} = \frac{V_{bL}}{I_{bL}} = \frac{V_{bL}^2}{V_{bL}\ I_{bL}} = \frac{V_{bL}^2}{(VA)_b} \tag{1.45}$$

where $(VA)_b$ denotes base volt-amperes. Similarly for the HV side,

$$Z_{bH} = \frac{V_{bH}^2}{(VA)_b}. \tag{1.46}$$

For the simplified equivalent circuit of Figure 1.7, the total equivalent resistance referred to the primary (LV) side can be expressed in per-unit notation as

$$(R_{eq1})_{pu} = \frac{R_{eq1}}{Z_{bL}}. \tag{1.47}$$

If R_{eq2} is the total equivalent resistance of the windings referred to the secondary (HV) winding, it follows from Equations 1.24 and 1.47 that

$$(R_{eq1})_{pu} = \frac{R_{eq2}\left(N_1/N_2\right)^2}{Z_{bL}} = \frac{R_{eq2}}{Z_{bL}\left(N_2/N_1\right)^2} = \frac{R_{eq2}}{Z_{bH}} = (R_{eq2})_{pu} = (R_{eq})_{pu}. \tag{1.48}$$

Similarly, it can easily be verified that the per-unit values of impedances on the LV and HV sides are equal.

The per-unit impedance can be expressed as

$$(Z_{eq})_{pu} = (Z_{eq1})_{pu} = \frac{Z_{eq1}}{Z_{bL}} = \frac{Z_{eq1}\ I_{bL}}{Z_{bL}\ I_{bL}} = \frac{Z_{eq1}\ I_{bL}}{V_{bL}}. \tag{1.49}$$

Thus, $(Z_{eq})_{pu}$ denotes the per-unit value of the leakage impedance voltage drop on the LV (or HV) side. For example, if 1000/100 V transformer has $(Z_{eq})_{pu}$ of 0.1, the voltage drop across the equivalent leakage impedance referred to the LV side is 0.1 times 100 volts, i.e., 10 volts; the corresponding voltage drop on the HV side is 100 volts (= 0.1×1000). Similarly,

$$(R_{eq})_{pu} = (R_{eq1})_{pu} = \frac{R_{eq1}}{Z_{bL}} = \frac{R_{eq1}\ I_{bL}\ I_{bL}}{Z_{bL}\ I_{bL}\ I_{bL}} = \frac{R_{eq1}\ I_{bL}^2}{V_{bL}\ I_{bL}}. \tag{1.50}$$

Thus, the per-unit value of the equivalent resistance, $(R_{eq})_{pu}$, is the ratio of the ohmic loss at the rated current to the rated volt-amperes. For example, $(R_{eq})_{pu}$ of 0.02 for 50 kVA, 1000/100 V transformer means that the total ohmic loss at the rated current is 0.02 times (2% of) 50 kVA, i.e., 1000 watts.

Another advantage of using the per-unit system is that the impedances of transformers of the same type (irrespective of their ratings) lie usually within a small known range of per-unit values although the ohmic values may be widely different. For large power transformers, the base voltages are usually expressed

in kV and the base volt-amperes in MVA. Hence, the base impedances on LV and HV sides can be calculated as

$$Z_{bL} = \frac{(\text{kV})_{bL}^2}{(\text{MVA})_b} \quad \text{and} \quad Z_{bH} = \frac{(\text{kV})_{bH}^2}{(\text{MVA})_b}. \tag{1.51}$$

For three-phase transformers, the total three-phase power in MVA and line-to-line voltage in kV have to be taken as the base values. It can be shown that when ohmic value of impedance is transferred from one side to the other, the multiplying factor is the ratio of squares of line-to-line voltages of both sides irrespective of whether the transformer connection is star-star or star-delta [3].

1.5 Open-Circuit and Short-Circuit Tests

Parameters of the equivalent circuit can be determined by open-circuit (no-load) and short-circuit (load) tests. The open-circuit test determines the shunt parameters of the equivalent circuit of Figure 1.5. The circuit diagram for conducting the test is shown in Figure 1.8 (a). The rated voltage is applied to one winding and the other winding is kept open. Usually, LV winding is supplied since a low voltage supply is generally available. The no-load current is a very small percentage (0.2 to 2%) of the full load current; lower percentage values are observed for larger transformers (e.g., the no-load current of a 300 MVA transformer can be as small as 0.2%). Also, the leakage impedance value is much smaller than those of the shunt branch parameters. Therefore, the voltage drop in the LV resistance and leakage reactance is negligible as compared to the rated voltage ($\therefore V_1 \cong E_1$ in Figure 1.5, and θ_0 can be taken as the angle between V_1 and I_0). The input power measured by the wattmeter consists of the core loss and the primary winding ohmic-loss. If the no-load current is 1% of the full load current, the ohmic-loss in the primary winding resistance is just 0.01% of the load loss at the rated current; the value of the winding loss is negligible as compared to the core loss. Hence, the entire wattmeter reading can be taken as the core loss. The equivalent circuit of Figure 1.5 (b) is simplified to that shown in Figure 1.8 (b).

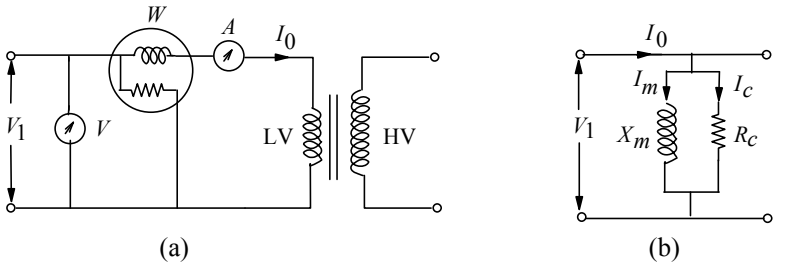

Figure 1.8 Open-circuit test.

The no-load loss, P_c, measured by the wattmeter is

$$P_c = V_1 I_0 \cos\theta_0 . \tag{1.52}$$

From the measured values of P_c, V_1 and I_0, the value of no-load power factor can be calculated from Equation 1.52 as

$$\cos\theta_0 = \frac{P_c}{V_1 I_0} . \tag{1.53}$$

With reference to the vector diagram of Figure 1.6, the magnetizing component (I_m) and the core loss component (I_c) of the no-load current (I_0) are

$$I_c = I_0 \cos\theta_0 \tag{1.54}$$

$$I_m = I_0 \sin\theta_0 . \tag{1.55}$$

The shunt parameters of the equivalent circuit are calculated as

$$R_c = \frac{P_c}{I_c^2} \quad \text{or} \quad R_c = \frac{V_1^2}{P_c} \tag{1.56}$$

$$X_m = \frac{V_1}{I_m} . \tag{1.57}$$

These values refer to the LV side, since the measuring instruments are placed on the LV side. If required, they can be referred to the HV side by using the operator a^2, i.e., $\left(N_1/N_2\right)^2$. The value of magnetizing reactance is very high as compared to the leakage reactance. For a no-load current of 0.2% (and with the assumption that $I_0 \cong I_m$), the value of X_m is 500 per unit.

A short-circuit test is done to measure the load loss and leakage impedance of the transformer. In this test, usually the LV winding is short-circuited and a voltage is applied to the HV winding in order to circulate the rated currents in both the windings; the applied voltage required for the purpose is called the impedance voltage of the transformer. For a transformer having 10% leakage impedance, the voltage required to circulate the rated currents is 10% of the rated voltage, with one of the windings short-circuited. The circuit diagram for the short-circuit test is shown in Figure 1.9 (a), in which the LV winding (secondary winding 2) is short-circuited. For an applied voltage of 10% and assuming for the equivalent circuit of Figure 1.5 (b) that the primary and referred secondary leakage impedances are equal, 5% of the voltage appears across the shunt parameters. With a no-load current of 2% at the rated voltage, the total current drawn by the two shunt elements for a 5% voltage is just 0.1% of the rated current (assuming linear B-H characteristics). Hence, the shunt

parameters can be neglected giving the simplified circuit of Figure 1.9 (b) for the short-circuit test. Since the core loss varies approximately in the square proportion of the applied voltage, with 5% voltage across R_c, it is just 0.25% of the core loss at the rated voltage. Hence, the entire loss measured by the wattmeter is almost equal to the load loss of the transformer.

The parameters of the equivalent circuit, viz. $R_{eq1}(= R_1 + R_2^{'})$, $X_{eq1}(= X_{L1} + X_{L2}^{'})$ and $Z_{eq1}(= R_{eq1} + jX_{eq1})$ can now be determined from the measured quantities of power (P_L), voltage (V_{SC}), and current (I_{SC}) as

$$Z_{eq1} = \frac{V_{SC}}{I_{SC}} \tag{1.58}$$

$$R_{eq1} = \frac{P_L}{I_{SC}^2} \tag{1.59}$$

$$X_{eq1} = \sqrt{Z_{eq1}^2 - R_{eq1}^2}\ . \tag{1. 60}$$

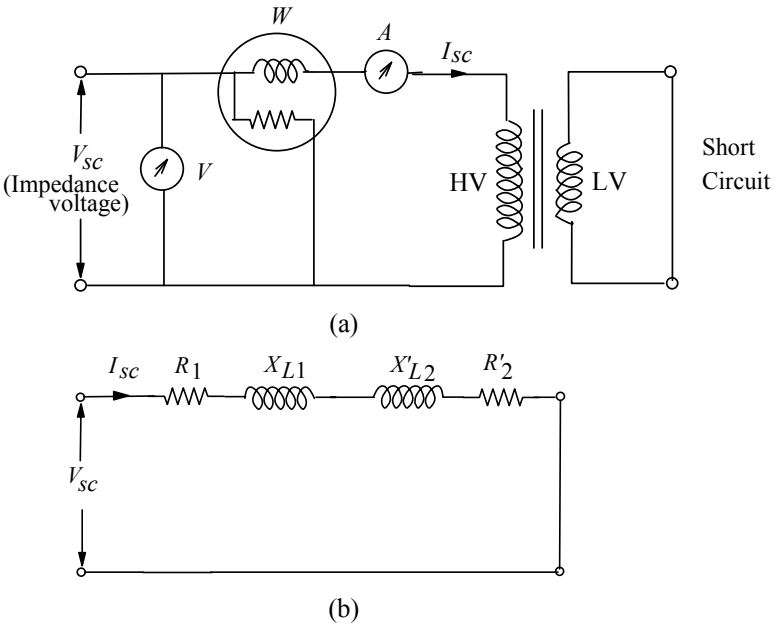

Figure 1.9 Short-circuit test (with LV terminals short-circuited).

R_{eq1} is the equivalent AC resistance referred to the primary (HV) winding, which accounts for the losses in the DC resistance of the windings, the eddy losses in the windings and the stray losses in structural parts. It is not practical to apportion the stray losses to the two windings. Hence, if the resistance parameter is required to be known for each winding, it is usually assumed that $R_1 = R_2^{'} = (1/2)\ R_{eq1}$. Similarly, it is assumed that $X_{L1} = X_{L2}^{'}$, although it is not strictly true. Since % R is much smaller than % Z, in practice the percentage reactance (% X) is taken to be the same as the percentage impedance (% Z). This approximation, however, may not be true for small distribution transformers.

1.6 Voltage Regulation and Efficiency

Since many electrical devices and appliances operate most effectively at their rated voltage, it is necessary that the output voltage of a transformer be within narrow limits when the magnitude and power factor of loads vary. Voltage regulation is an important performance parameter of transformers as it determines the quality of electricity supplied to consumers. The voltage regulation for a specific load is defined as a change in the magnitude of the secondary voltage after removal of the load (the primary voltage being held constant) expressed as a fraction of the secondary voltage corresponding to the no-load condition.

$$\text{Regulation (p.u.)} = \frac{V_{2oc} - V_2}{V_{2oc}} \tag{1.61}$$

where V_2 is the secondary terminal voltage at a specific load and V_{2oc} is the secondary terminal voltage when the load is removed. For the approximate equivalent circuit of Figure 1.7 (b), if all the quantities are referred to the secondary side, the voltage regulation for a lagging power factor load is given as [4]

$$\text{Regulation (p.u.)} = \frac{I_2 R_{eq2} \cos\theta_2 + I_2 X_{eq2} \sin\theta_2}{V_{2oc}} + \frac{1}{2}\left(\frac{I_2 X_{eq2} \cos\theta_2 - I_2 R_{eq2} \sin\theta_2}{V_{2oc}}\right)^2 \tag{1.62}$$

where R_{eq2} and X_{eq2} are the equivalent resistance and leakage reactance of the transformer referred to the secondary side respectively. The secondary load

current (I_2) lags behind the secondary terminal voltage (V_2) by angle θ_2 . For a full load condition, with the rated values taken as base quantities,

$$\text{Regulation (p.u.)} = \varepsilon_r \cos\theta_2 + \varepsilon_x \sin\theta_2 + \frac{1}{2}(\varepsilon_x \cos\theta_2 - \varepsilon_r \sin\theta_2)^2 \qquad (1.63)$$

where, $\varepsilon_r = \dfrac{I_2 R_{eq2}}{V_{2oc}}$ represents the per-unit resistance drop and $\varepsilon_x = \dfrac{I_2 X_{eq2}}{V_{2oc}}$ represents the per-unit leakage reactance drop. For a leading power factor load (I_2 leads V_2 by angle θ_2),

$$\text{Regulation (p.u.)} = \varepsilon_r \cos\theta_2 - \varepsilon_x \sin\theta_2 + \frac{1}{2}(\varepsilon_x \cos\theta_2 + \varepsilon_r \sin\theta_2)^2 . \qquad (1.64)$$

The square term is usually small and may be neglected, simplifying Equations 1.63 and 1.64 as

$$\text{Regulation (p.u.)} = \varepsilon_r \cos\theta_2 \pm \varepsilon_x \sin\theta_2 . \qquad (1.65)$$

The efficiency of a transformer, like any other electrical device, is defined as

$$\eta = \frac{\text{output power}}{\text{input power}} . \qquad (1.66)$$

The percentage efficiency of transformers is in the range of 95 to 99%. For large power transformers with low loss designs, the efficiency can be as high as 99.7%. There is a possibility of error if the efficiency is determined from the measured values of output and input powers. It is therefore determined using the values of their losses measured by the open-circuit and short-circuit tests. The efficiency is then given as

$$\eta = \frac{\text{output power}}{\text{output power} + \text{losses}} \qquad (1.67)$$

$$\therefore \eta = \frac{V_2 I_2 \cos\theta_2}{V_2 I_2 \cos\theta_2 + P_c + P_L} = \frac{V_2 I_2 \cos\theta_2}{V_2 I_2 \cos\theta_2 + P_c + I_2^2 R_{eq2}} . \qquad (1.68)$$

Although the load power factor has some effect on the mutual flux and hence the core loss, the effect is insignificant, allowing us to assume that the core loss is constant irrespective of the load condition. For assumed constant values of P_c and V_2 , the condition for maximum efficiency at a given load power factor can be derived by differentiating the expression of η with respect to I_2 and equating it to zero:

$$\frac{d\eta}{dI_2} = \frac{d}{dI_2}\left[\frac{V_2 I_2 \cos\theta_2}{V_2 I_2 \cos\theta_2 + (P_c + I_2^2 R_{eq2})}\right] = 0 . \tag{1.69}$$

Solving it further, we obtain

$$P_c = I_2^2 R_{eq2} . \tag{1.70}$$

Thus, the efficiency is maximum at a load at which the load loss value equals the constant core (no-load) loss value. Further,

$$\frac{I_2^2}{I_{2FL}^2} = \frac{P_c}{I_{2FL}^2 \; R_{eq2}} \tag{1.71}$$

where I_{2FL} is the full-load (rated) current and $I_{2FL}^2 R_{eq2}$ is the corresponding load loss. Therefore, the per-unit load at which the maximum efficiency occurs is

$$(per\text{-}unit \;\; load)_{\eta_{\max}} = \frac{I_2}{I_{2FL}} = \sqrt{\frac{P_c}{(P_L)_{FL}}} . \tag{1.72}$$

The value of maximum efficiency can be calculated by substituting the value of I_2 from Equation 1.72 in Equation 1.68. Similarly, it can easily be shown that the efficiency for a given load condition (i.e., constant I_2) is maximum for the unity power factor condition ($\cos\theta = 1$).

Example 1.1

A single-phase transformer is designed to operate at 220/110 V, 60 Hz. What will be the effect on the transformer performance if the frequency reduces by 5% to 57 Hz and the primary voltage increases by 5% to 231 volts?

Solution:

The emf equation is

$$V_1 = 4.44 \, \phi_{mp} \, f \, N_1 .$$

Now $\phi_{mp} = B_{mp} \; A_c$

where B_{mp} is peak value of the flux density in the core (wb/m^2)

A_c is cross-sectional area of the core in m^2.

Hence, for a given number of turns (N_1) and core area (A_c),

$$\frac{(231)_{57Hz}}{(220)_{60Hz}} = \frac{4.44\,(B_{mp})_{57Hz} \times A_c \times 57 \times N_1}{4.44\,(B_{mp})_{60Hz} \times A_c \times 60 \times N_1}$$

$$\frac{(B_{mp})_{57Hz}}{(B_{mp})_{60Hz}} = \frac{231 \times 60}{220 \times 57} = 1.10\,.$$

Thus, with the reduced frequency and higher applied voltage, the flux density in the core increases. This increase will in turn increase the no-load current, the core loss and the noise level of the transformer. This example shows that the operating peak flux density in the core has to be correctly chosen depending on specified overexcitation conditions by the user.

Example 1.2

Tests on 31.5 MVA, 132/33 kV star/delta 3-phase transformer gave following results (loss values given are for three phases):

- Open-circuit test: 33 kV, 5.5 A, 21 kW
- Short-circuit test: 13.2 kV, 137.8 A, 100 kW

Calculate: a) equivalent circuit parameters referred to the LV side
b) efficiency at full load and half of full load with unity power factor
c) regulation at full load with 0.8 lagging power factor

Solution:

a) Unless otherwise stated, the specified values of voltages should be taken as line-to-line values. The equivalent circuit representation is on a per-phase basis, and hence per-phase values of the losses should be used in the calculations.

The open-circuit test is performed on the LV side with the application of the rated voltage of 33 kV. For the delta connected LV winding, the line and phase voltages are equal; the phase current is the line current divided by $\sqrt{3}$. Hence, we obtain

$$\text{Per-phase no-load excitation current} = \frac{5.5}{\sqrt{3}} = 3.2 \text{ A}$$

$$\text{Per-phase core loss} = \frac{21000}{3} = 7000 \text{ W}$$

$$\text{Core-loss component} = I_c = I_0 \cos\theta_0 = \frac{P_c}{V_1} = \frac{7000}{33000} = 0.21 \text{ A}$$

$$\text{Magnetizing component} = I_m = \sqrt{I_0^2 - I_c^2} = \sqrt{3.2^2 - 0.21^2} = 3.19 \text{ A}.$$

The values of the core-loss resistance and the magnetizing reactance referred to the LV side are calculated as

$$R_c = \frac{V_1}{I_c} = \frac{33000}{0.21} = 157\ \text{k}\Omega$$

$$X_m = \frac{V_1}{I_m} = \frac{33000}{3.19} = 10.34\ \text{k}\Omega$$

$$\text{LV side base impedance} = \frac{\text{kV}^2}{\text{MVA}} = \frac{33^2}{(31.5/3)} = 103.7\ \Omega\ .$$

Thus, the per-unit value of X_m is 100 $\left(= 10.34\ \text{k}\Omega / 103.7\ \Omega\right)$.

Now the short-circuit test is performed on the HV side (the applied voltage of 13.2 kV is a fraction of the rated HV voltage, i.e. 132 kV).

Per-phase applied voltage to the star-connected HV winding $= \frac{13200}{\sqrt{3}} = 7621$ V

For the star connection, the phase and line currents are equal (=137.8 A).
Now, the ohmic value of the leakage impedance and resistance referred to the HV side can be calculated as

$$Z_{eqH} = \frac{V_{sc}}{I_{sc}} = \frac{7621}{137.8} = 55.3\ \Omega\ .$$

Per-phase value of the load-loss = $\frac{100000}{3}$ W

$$R_{eqH} = \frac{P_L}{I_{sc}^2} = \frac{100000/3}{137.8^2} = 1.755\ \Omega$$

$$\therefore X_{eqH} = \sqrt{Z_{eqH}^2 - R_{eqH}^2} = \sqrt{55.3^2 - 1.755^2} = 55.27\ \Omega\ .$$

Now, the equivalent circuit quantities calculated on the HV side can be referred to the LV side using the transformation ratio a,

$$a = \frac{N_1}{N_2} \cong \frac{V_{pL}}{V_{pH}}$$

where V_{pL} and V_{pH} are the phase voltages of the LV and HV windings respectively.

$$\therefore R_{eqL} = a^2 R_{eqH} = \left[\frac{33000}{132000/\sqrt{3}}\right]^2 \times 1.755 = 0.329\ \Omega\ .$$

Similarly,

$$X_{eqL} = a^2 X_{eqH} = \left[\frac{33000}{132000/\sqrt{3}}\right]^2 \times 55.27 = 10.36\ \Omega .$$

In per-unit quantities,

$$\varepsilon_r = (R_{eqL})_{pu} = \frac{R_{eqL}}{Z_{bL}} = \frac{0.329}{103.5} = 0.0032$$

$$\varepsilon_x = (X_{eqL})_{pu} = \frac{X_{eqL}}{Z_{bL}} = \frac{10.36}{103.5} = 0.1 .$$

We could have directly found the value of $(R_{eqL})_{pu}$ by using line-to-line and 3-phase quantities in Equation 1.50 as

$$(R_{eqL})_{pu} = \frac{100\times10^3}{31.5\times10^6} = 0.0032 .$$

Similarly, we can directly infer the value of $(X_{eqL})_{pu}$, which is almost equal to $(Z_{eqL})_{pu}$, from the short-circuit test results because the applied voltage of 13.2 kV is able to circulate the rated currents in the windings.

$$(X_{eqL})_{pu} = (X_{eqH})_{pu} = (X_{eq})_{pu} = \frac{13.2\times10^3}{132\times10^3} = 0.1 .$$

b) Efficiency can be worked out either by using per-phase or 3-phase quantities. The percentage efficiency at the full load and unity power factor $(\cos\theta = 1)$ condition can be calculated by using Equation 1.68 as

$$\eta_{FL} = \frac{31.5\times10^6\times1}{31.5\times10^6\times1 + (21\times10^3 + 100\times10^3)}\times100 = 99.62\ \%$$

and at half the full load,

$$\eta_{0.5FL} = \frac{0.5\times31.5\times10^6\times1}{0.5\times31.5\times10^6\times1 + (21\times10^3 + (0.5)^2\times100\times10^3)}\times100 = 99.71\% .$$

The maximum efficiency occurs at a load of 45.8% $(=\sqrt{21/100}\times100)$ as per Equation 1.72.

c) Regulation at the full load and 0.8 power factor lagging condition is calculated from Equation 1.63 as

$$\text{Regulation} = (\varepsilon_r \cos\theta_2 + \varepsilon_x \sin\theta_2) + \frac{1}{2}(\varepsilon_x \cos\theta_2 - \varepsilon_r \sin\theta_2)^2$$

$$= (0.0032 \times 0.8 + 0.1 \times 0.6) + \frac{1}{2}(0.1 \times 0.8 - 0.0032 \times 0.6)^2 = 0.066.$$

Example 1.3

A 500 kVA single-phase transformer is designed to have a resistance of 1% with its maximum efficiency occurring at 250 kVA load. Find the efficiency of the transformer when it is supplying a full load at 0.8 lagging power factor.

Solution:

The percentage resistance is given as

$$\%R = \frac{Load\ loss\ at\ full\ load}{Base\ VA} \times 100$$

$\therefore$ Load loss at full load = $\frac{1}{100}\left[500 \times 10^3\right] = 5000$ W.

Now from Equation 1.72, for the same terminal voltage,

$$\frac{I_{\eta_{max}}}{I_{FL}} = \frac{250}{500} = \sqrt{\frac{P_c}{5000}}$$

$\therefore P_c$ = No-load loss= 1250 W.

Total loss at full load = 1250 + 5000 = 6250 W.

Efficiency at full load and 0.8 power factor =

$$\frac{output\ power}{output\ power + losses} \times 100 = \frac{500 \times 0.8}{500 \times 0.8 + 6.25} \times 100 = 98.5\%\ .$$

All-day efficiency: Distribution transformers supply loads that vary over a wide range. Their performance cannot be judged only by the efficiency value calculated as in the above example. For them, a parameter called *all-day efficiency* is more relevant, which is defined as

$$\eta_{all-day} = \frac{(output)_{\text{kWh}}}{(input)_{\text{kWh}}} = \frac{(output)_{\text{kWh}}}{(output)_{\text{kWh}} + (losses)_{\text{kWh}}}\ . \tag{1.73}$$

The output and losses are computed for a period of 24 hours using the corresponding load cycle. The no-load loss is constant (i.e., independent of loading conditions); hence it is important to design the distribution transformers

with a lower value of the no-load loss so that a higher value of the all-day energy-efficiency is achieved.

Why rating in volt-amperes? The rating of transformers is expressed in volt-amperes and not in watts because the rated output is limited by the losses, which depend on the voltage (no-load loss) and the current (load loss), and are almost unaffected by the load power factor. The amount of heat depends on the r.m.s. values of the current and the voltage and not on the power factor. Hence, the power delivered through a transformer may not be a unique value. The rating of a transformer is therefore not expressed in terms of the power rating (watts); it is defined in terms of the apparent power (volt-amperes) that it can deliver.

Let us now prove that the load power factor does not influence the losses. The phasor diagram for the equivalent circuit of Figure 1.7 (b), wherein the secondary quantities are referred to the primary side and the shunt branch is neglected, is shown in Figure 1.10. The apparent power across the series impedance in Figure 1.7 (b) is given by,

$$P + jQ = \left(\overline{V}_1 - \overline{V}_2'\right)\overline{I}_1^* = \left(V_1\angle\alpha - V_2'\angle 0\right)I_1\angle\theta = V_1I_1\angle\left(\alpha+\theta\right) - V_2'I_1\angle\theta\,. \tag{1.74}$$

Writing the right hand side in the Cartesian system and rearranging the terms,

$$P + jQ = V_1I_1\cos\left(\alpha+\theta\right) - V_2'I_1\cos\left(\theta\right) + j\left(V_1I_1\sin\left(\alpha+\theta\right) - V_2'I_1\sin\left(\theta\right)\right). \tag{1.75}$$

Thus, the real part of the power is

$$P = V_1I_1\cos\left(\alpha+\theta\right) - V_2'I_1\cos\left(\theta\right) = I_1\left(V_1\cos\left(\alpha+\theta\right) - V_2'\cos\left(\theta\right)\right). \tag{1.76}$$

The bracketed right hand side of Equation 1.76 is the difference between the projections of phasors V_1 and V_2' on I_1 phasor in Figure 1.10, which is nothing but the I_1R_{eq1} drop. Therefore, the real power P is

$$P = I_1\left(I_1R_{eq1}\right) = I_1^2R_{eq1}\,. \tag{1.77}$$

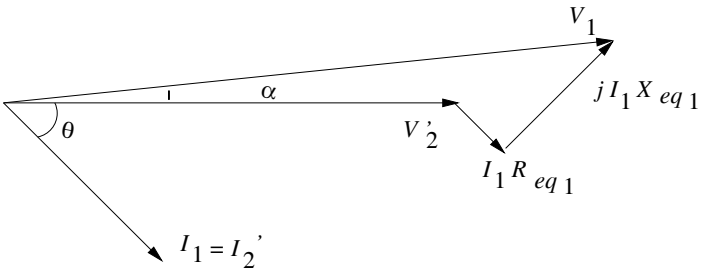

Figure 1.10 Vector diagram corresponding to the circuit in Figure 1.7 (b).

Thus, we obtained the expected expression for the load loss occurring in the transformer, which is independent of the load power factor (θ). Also, if the shunt parameters are made to correspond to the applied voltage as shown in Figure 1.7 (a), then the no-load loss is also independent of the load power factor for a given value of load VA. Hence, under the assumptions made the losses in the transformer do not change as the load power factor varies. Hence, the rating of transformers is expressed in volt-amperes and not watts. Contrary to this, the losses in motors vary with the power factor of the rotor circuit. For example, in induction motors, the loss is a function of the slip and hence the mechanical load on the shaft; the rotor side power factor changes with the slip. Hence, the rating of motors is expressed in watts.

For the transformer, if the shunt branch is connected after the primary series impedance as in Figure 1.5 (b), it can be proved that the load loss is a function of the load power factor (the dependence is usually neglected since the no-load current is a small fraction of the rated load current). Likewise, the voltage across the shunt parameters is a function of the load and its power factor, and hence the core loss depends on them. This is also explained by the fact that the loss in the core is actually decided by the vector sum of the mutual flux and the leakage flux; the latter's phase being governed by the load power factor. Thus, the core loss in actual operating conditions is a function of the load power factor (as discussed in Section 5.12); however, the effect may usually be small and neglected.

1.7 Parallel Operation of Transformers

For supplying a load in excess of the rating of an existing transformer, another transformer is usually connected in parallel with it since replacing it with a single larger unit is a costly alternative. The cost of a spare smaller rating transformer is also lower. Also, it is preferable to have a parallel transformer in case of emergencies; at least half the load can be supplied when one of the transformers is taken out of the service. For paralleling of transformers, their primary windings are connected to source bus-bars and secondary windings are connected to the load bus-bars. Various conditions that must be fulfilled for paralleling of transformers are given below.

1. The line voltage ratios of the transformers must be equal (*at each tap*): If the transformers connected in parallel have slightly different voltage ratios, then due to the inequality of the induced emfs in the secondary windings, a circulating current flows in the loop formed by the secondary windings under the no-load condition; the circulating current may be much higher than a normal no-load current. When the secondary windings are loaded, this circulating current will tend to produce unequal loadings on the two transformers, and it may not be possible to supply the full load (one of the transformers may get overloaded).

2. The transformers should have equal per-unit leakage impedances and the same ratio of the equivalent leakage reactance to the equivalent resistance (X/R): If the ratings of both transformers are the same, their per-unit leakage impedances should also be the same for equal loading. If the ratings are unequal, their per-unit leakage impedances based on their own ratings should be equal so that the currents carried by them will be proportional to their ratings. In other words, for unequal ratings, the numerical (ohmic) values of their impedances should be in inverse proportion to their ratings to have the currents in them in line with their ratings. A difference in the *X/R* ratio of the two components of their per-unit impedances results in different phase angles of the currents carried by them; one of the transformers works with a higher power factor and the other with a lower power factor than that of the combined output, and the real power will not be proportionally shared by them.

3. The transformers should have the same polarity: The transformers should be properly connected with regard to their polarity. If they are connected with incorrect polarities then the two emfs, induced in the secondary windings that are in parallel, will act together in the local secondary circuit and produce a short circuit.

The previous three conditions are applicable to both single-phase as well as three-phase transformers. In addition to these three conditions, two more conditions need to be fulfilled for the parallel operation of three-phase transformers:

4. The transformers should have the same phase sequence: The phase sequence of the line voltages of both the transformers must be identical. If the phase sequence is incorrect, pairs of phase windings will be short-circuited in every cycle.

5. The transformers should have the zero relative phase displacement between the secondary line voltages: Windings can be connected in a variety of ways that produce different phase displacements of the secondary voltages with respect to the primary voltages. The winding connections can be classified into distinct vector groups. Each vector group notation consists of an uppercase letter denoting the connection of the three phases of the HV winding, followed by a lowercase letter denoting the connection of the three phases of the LV winding, and lastly a *clock number* representing the displacement of the line-to-ground voltage phasor of any phase of the LV winding with respect to the corresponding HV winding phasor placed at 12 o'clock. Commonly used three-phase connections can be classified into four groups:

Group 1: Zero phase displacement (Yy0, Dd0, Dz0)
Group 2: 180° phase displacement (Yy6, Dd6, Dz6)
Group 3: –30° phase displacement (Yd1, Dy1, Yz1)
Group 4: +30° phase displacement (Yd11, Dy11, Yz11)

Letters y (or Y), d (or D), and z represent star, delta, and zigzag connections respectively. In order to have zero relative phase displacement of the secondary-

side line voltages, the transformers belonging to the same group can be paralleled. For example, a Yd1-connected transformer can be connected in parallel with a Dy1-connected transformer. A transformer belonging to group 1 or group 2 can be paralleled only with its group-mate. On the other hand, a transformer from group 3 can be paralleled with a transformer from group 4 by reversing the phase sequence of one of them. For example, a Yd11-connected transformer (group 4) can be paralleled with a Dy1-connected transformer (group 3) by reversing the phase sequence of both primary and secondary terminals of the Dy1-connected transformer.

Many other vector groups are also used; these along with the above four groups are described through phasor diagrams in Appendix B.

References

1. Say, M. G. *The performance and design of alternating current machines*, 2nd edition, Sir Isaac Pitman and Sons, London, 1955.
2. Toro, V. D. *Principles of electrical engineering,* 2nd edition, Prentice Hall, New Delhi, 1977.
3. Stevenson, W. D. *Elements of power system analysis,* 4th edition, McGraw-Hill, Tokyo, 1982, pp. 138–162.
4. MIT Press, *Magnetic circuits and transformers,* 14th edition, John Wiley and Sons, New York, 1962, pp. 259–406.

2

Magnetic Characteristics

The magnetic circuit is an important active part of transformers, which transfers electrical energy from one circuit to another. It is in the form of a laminated iron core structure which provides a low reluctance path to the magnetic flux produced by an excited winding. Most of the flux is contained in the core, which reduces stray losses in structural parts. Due to research and development efforts [1] by steel and transformer manufacturers, materials with improved characteristics have been developed and employed with better core building technologies. In the early days of transformer manufacturing, inferior grades of laminated steel (according to today's standards) were used with associated high losses and magnetizing volt-amperes. Later, it was found that an addition of silicon (4 - 5%) improved the performance characteristics of the material significantly, due to a marked reduction in its eddy loss on account of an increase in resistivity and permeability. Its hysteresis loss also reduced due to a decrease in the area of the *B-H* loop. Since then the silicon steels have been in use as the core material in most transformers.

The addition of silicon also helps to reduce aging effects. Although silicon makes the material brittle, the deterioration in the property is not to an extent that can pose problems during the core building process. Subsequently, a manufacturing technology with the cold rolling process was introduced, wherein material grains are oriented in the direction of rolling. This technology has remained the backbone of developments for many decades, and newer materials introduced in recent times are no exceptions. Different material grades were introduced in the following sequence: non-oriented, hot-rolled grain-oriented (HRGO), cold-rolled grain-oriented (CRGO), high permeability cold-rolled grain-oriented (Hi-B), mechanically scribed, and laser scribed. Laminations with lower thickness are manufactured and used to take advantage of their lower eddy

loss. Currently, laminations with thickness in the range of 0.23 mm to 0.35 mm are used for power transformers. The thickness of laminations used in small transformers can be as high as 0.50 mm. The lower the thickness of laminations, the higher the core building time is, since the number of laminations for a given core area increases. An inorganic coating (generally glass film and phosphate layer) having thickness of 0.002 to 0.003 mm is provided on both the surfaces of laminations, which is sufficient to withstand induced voltages having magnitude of a few volts.

Since the core is in the vicinity of high voltage windings, it is grounded; otherwise it can acquire a high potential due to capacitively transferred voltages from the windings. If the core is sectionalized by ducts (of about 5 mm) for the cooling purpose, individual sections have to be grounded. Since the capacitance between any two touching laminations is very large due to their large surface area and a very small insulating gap between them, the capacitive reactance between them is negligible. Therefore, all the laminations within each section remain almost at the same potential. Hence, each of the sections is grounded at only one point. Some users prefer to ground the core outside tank through a separate bushing for the monitoring purpose as explained in Section 14.8.

All internal structural parts of transformers (e.g., frames) are grounded. While designing the grounding system, due care must be taken to avoid multiple grounding connections forming loops in which troublesome circulating currents may be induced. The tank is grounded externally by a suitable arrangement. The frames, used for clamping the yokes and supporting windings, are generally grounded by connecting them to the tank at one point by means of a copper or aluminum strip. If the frame-to-tank connection is done at two places, a closed loop thus formed may link an appreciable amount of stray leakage flux. A large circulating current induced in the loop can eventually burn the connecting strips.

2.1 Construction

2.1.1 Types of core

A part of the core, that is surrounded by windings, is called a limb or leg. The other part, which is not surrounded by windings, but is essential for completing the path of flux, is called the yoke. This construction (termed the core type) is more common and has the following distinct advantages: construction is simpler, cooling is better, and repair is easy. The shell-type construction, in which the cross section of windings in the plane of the core is surrounded by the limbs and yokes, is also used. It has a distinct advantage that a sandwich arrangement of the LV and HV windings can be used to obtain a very low impedance value, if desired, which is not easily possible in the core-type construction. In this book, most discussions are related to the core-type construction, and wherever required a reference to the shell-type construction has been made.

The core construction mainly depends on technical specifications, manufacturing limitations, and transport considerations. It is economical to have all the windings of the three phases in one core frame. A three-phase transformer is cheaper (by about 20 to 25%) than three bank-connected single-phase transformers. But from the spare-unit consideration, users find it more economical to buy four single-phase transformers as compared to two three-phase transformers. Also, if the three-phase rating is too large to be manufactured (weights and dimensions exceeding manufacturing capabilities) and transported, there is no option but to manufacture and supply single-phase units. Figure 2.1, shows various types of core constructions.

In a single-phase three-limb core (Figure 2.1(a)), the windings are placed around the central limb, called the main limb. Its flux is equally divided between the yokes; the cross-sectional area of the yokes and end limbs is 50% of the main limb area. The arrangement is similar to the shell-type construction. The zero-sequence impedance is equal to the positive-sequence impedance in single-phase three-limb transformers connected in a bank.

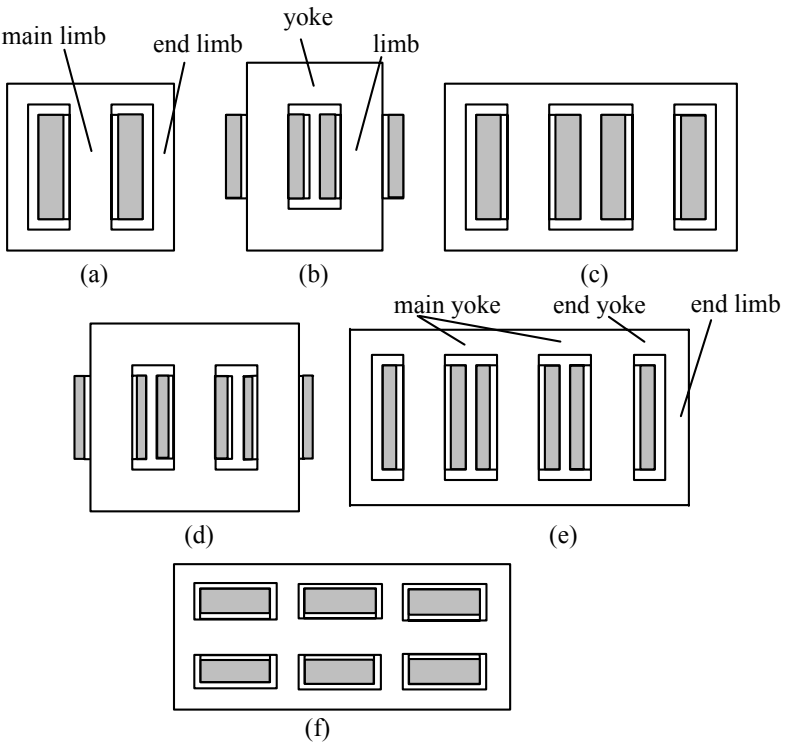

Figure 2.1 Various types of cores.

In few single-phase transformers, the windings are split into equal parts which are placed around two limbs as shown in Figure 2.1(b). This construction is sometimes adopted for very large ratings. Magnitudes of short-circuit forces are lower because of the fact that ampere-turns/height are reduced. The area of the limbs and yokes is the same. Similar to the single-phase three-limb construction, one can have additional two end limbs and two end yokes as shown in Figure 2.1(c) to obtain the single-phase four-limb arrangement with a reduced height for the transportability purpose.

The three-phase three-limb construction shown in Figure 2.1(d) is commonly used in small and medium rating transformers. In each phase, the limb flux returns through the yokes and the other two limbs. The cross-sectional areas of all the limbs and yokes are usually kept equal. The yokes can be provided with a small additional area as compared to the limbs for reducing the no-load loss. However, there may be an additional loss due to imperfect joints between the yokes and the limbs due to their different cross-sectional areas. Hence, the reduction in the no-load loss may not be significant. The provision of an extra yoke area may improve the performance under over-excitation conditions. Eddy losses in structural parts, due to the flux leaking out of the saturated core, are reduced to some extent [2, 3]. The three-phase three-limb construction has an inherent three-phase asymmetry resulting in unequal no-load currents and losses in the three phases; the phenomenon is discussed elaborately in Section 2.5.1. One can build a symmetrical core structure by connecting it in a star or delta fashion so that the windings of the three phases are electrically as well as physically displaced by 120 degrees. This construction results into minimum core weight and tank volume, but is seldom used because of complexities in manufacturing it.

In large power transformers, in order to reduce the height for transportability, the three-phase five-limb construction depicted in Figure 2.1(e) is employed. The magnetic path consisting of the end yoke and the end limb has higher reluctance than that of the main yoke. Hence, as the flux starts rising, it first takes the low reluctance path of the main yoke. Since the main yoke is not large enough to carry all the flux from the limb, it saturates and forces the remaining flux into the end limb. Since the spilling over of the flux to the end limb occurs near the flux peak and also due to the fact that the ratio of reluctances of these two paths varies due to nonlinear properties of the core, the fluxes in both the main yoke and end yoke/end limb paths are non-sinusoidal even though the main limb flux is varying sinusoidally [2, 4]. Extra losses occur in the yokes and end limbs due to the corresponding flux harmonics. In order to compensate these extra losses, it is a normal practice to keep the main yoke area as 60% and the end yoke/end limb area as 50% of the main limb area. The zero-sequence impedance is much higher for the three-phase five-limb construction than the three-limb construction due to the low reluctance path provided by the yokes and end limbs to the in-phase zero-sequence fluxes, and its value is close to but less than the positive-sequence impedance value. This is true if the

applied voltage during the zero-sequence test is small enough so that the yokes and end limbs are not saturated. The aspects related to zero-sequence impedances for various types of core constructions are elaborated in Chapter 3. Figure 2.1 (f) shows a typical 3-phase shell-type construction.

2.1.2 Analysis of overlapping joints and the building factor

While building a core, the laminations are placed in such a way that the gaps between the laminations at joints between limbs and yokes are overlapped by the laminations in the next layer. This is done so that there is no continuous gap at joints when laminations are stacked one above the other (Figure 2.2). The overlapping distance is kept around 15 to 20 mm. Two types of joints are shown in Figure 2.3. Non-mitered joints, in which the overlap angle is 90°, are simple from the manufacturing point of view, but the loss in their corners is more since the flux in them is not along the direction in which grains are oriented. Hence, the non-mitered joints are used for very small transformers. These joints were commonly adopted in the earlier days when non-oriented materials were commonly used even for larger transformers.

In mitered joints, the angle of overlap (α) is of the order of 30° to 60°; the most commonly used angle is 45°. The flux crosses at the joints along the direction of the grain orientation, minimizing losses in them. For air-gaps of equal length, the excitation requirement with mitered joints is $\sin\alpha$ times that with non-mitered joints [5].

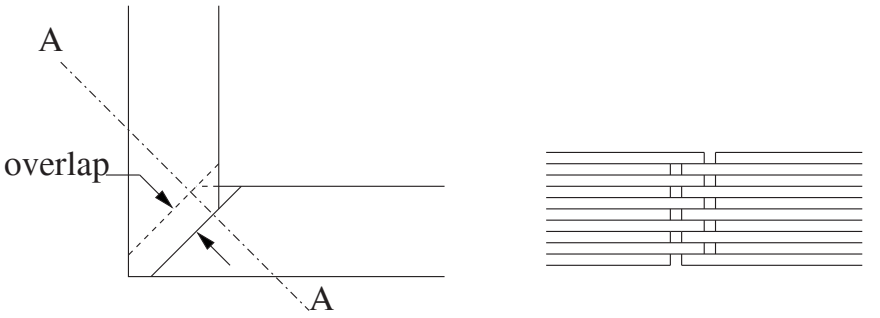

(a) Overlap at corner (b) Cross section A-A

Figure 2.2 Overlapping at joints.

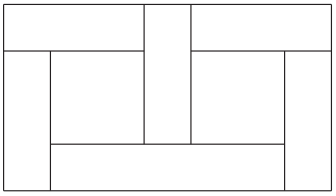

Non-mitered joint

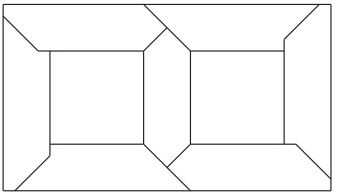

Mitered joint

Figure 2.3 Commonly used joints.

Better grades (Hi-B, scribed, etc.) having specific loss (watts/kg) about 15 to 20% lower than conventional CRGO materials (termed hereafter as CGO grades, e.g., M4) are regularly used. However, it is generally observed that the use of these better grades may not give expected loss reductions if a proper value of *building factor* is not used in loss calculations. The factor is defined as

$$Building\ \ factor = \frac{Built\ \ transformer\ \ core\ \ loss\ \ (watts/kg)}{Material\ \ Epstein\ \ core\ \ loss\ \ (watts/kg)}. \tag{2.1}$$

The building factor increases with the quality of the grade from CGO to Hi-B to scribed (domain refined). This is because of the fact that the penalties for deviations of flux, at the joints, away from the direction of the grain orientation are higher for the better grades. The factor is also a function of the operating flux density; it usually deteriorates rapidly for the better grades at higher flux densities. Hence, the cores built with better grades may not give expected benefits in line with Epstein measurements done on a single lamination sheet. Therefore, appropriate building factors should be used based on experimental /test data.

Single-phase two-limb transformers give significantly better performances than three-phase cores; the building factor can be as low as 1.0 for the domain-refined grades and even less than 1.0 for the CGO grades [6]. The lower values of losses are due to lightly loaded joints and spatial redistributions of flux in the limbs and yokes across the width of the laminations. Needless to say, the higher the proportion of the weight of the joints in the total core weight the higher the losses are. Also the loss contribution due to the joints is higher with 90° joints as compared to that with 45° joints since there is over-crowding of flux lines at the inner edge and the flux is not along the direction of the grain orientation while passing from the limb to the yoke in the former case. The smaller the overlapping length the better the core performance is; but the improvement may not be noticeable. It is also reported in [6, 7] that the gap at the core joint has a significant impact on the no-load loss and current. As compared to 0 mm gap, the increase in loss is 1 to 2% for 1.5 mm gap, 3 to 4% for 2.0 mm gap, and 8 to 12% for 3 mm gap. These figures highlight the need for maintaining minimum gaps at the core joints.

The lesser the laminations per lay the lower the core loss is. Experience shows that the constructions with 2 laminations per lay give loss advantage of 3 to 4% as compared to those with 4 laminations per lay. Advantage of 2 to 3% is further achieved when only 1 lamination per lay is used. As the number of laminations per lay reduces, the manufacturing time for core building increases. Hence, the construction with 2 laminations per lay is commonly used.

Analyses of various factors affecting the core loss have been adequately reported in the related literature. A core model based on a lumped circuit approximation is elaborated in [8] for three-phase three-limb transformers. The length of equivalent air gap is varied as a function of the instantaneous value of the flux in the laminations. Anisotropic material properties are also taken into account in the model. An analytical formulation based on the finite difference method is used in [9] to calculate the spatial flux distribution and core loss. The method takes into account the magnetic anisotropy and nonlinearity. The effects of overlapping lengths and the number of laminations per lay on the core loss have been analyzed in [10] for wound core distribution transformers.

Joints between limbs and yokes contribute significantly to the core loss due to cross-fluxing and crowding of flux lines in them. Hence, a higher proportion of the weight of the joints in the total weight leads to an increased loss. Due to lower cross-sectional areas as compared to the main limb area, the weight of the joints in single-phase three-limb, single-phase four-limb and three-phase five-limb constructions is less. However, the corresponding benefit in the core loss is negated by an increased overall weight (due to additional end limbs and yokes).

The building factor is usually in the range of 1.1 to 1.25 for three-phase three-limb cores with mitered joints. A higher height-to-width ratio of the core windows results in a decreased proportion of the weight of the joints; the core loss decreases giving a lower value of the building factor. Single-phase two-limb and single-phase three-limb cores have been shown [11] to have fairly uniform flux distributions and lower levels of total harmonic distortions as compared to single-phase four-limb and three-phase five-limb cores.

Step-lap joints are replacing mitered joints due to their superior performance [12, 13]. A typical step-lap joint consists of a group of laminations (normally 5 to 7) stacked with a staggered joint as shown in Figure 2.4.

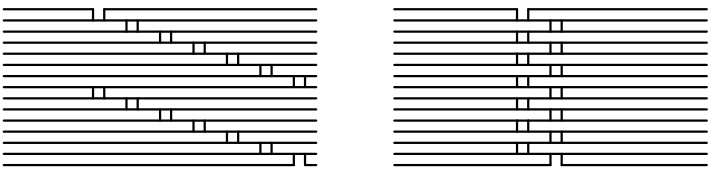

Step-lap joint Conventional mitered joint

Figure 2.4 Step-lap and conventional joints.

It is shown in [13] that, for an operating flux density of 1.7 T, the flux density in the mitered joint in the core sheet area shunting the air gap rises to 2.7 T (heavy saturation), while in the gap the flux density is about 0.7 T. Contrary to this, in the step-lap joint with 6 steps, the flux almost avoids the gap in which the observed flux density value is just 0.04 T; the flux gets redistributed just about equally in the laminations of the other five steps with a flux density close to 2.0 T in them. This explains why there is a marked improvement in the no-load performance figures (current, loss and noise) in the constructions with step-lap joints.

2.2 Hysteresis, Eddy, and Anomalous Losses

2.2.1 Classical theory

Hysteresis and eddy current losses together constitute the no-load loss according to the classical theory. As discussed in Chapter 1, the loss due to the no-load current flowing in the primary winding is negligible. Also, at the rated flux density condition on no-load, since most of the flux is confined to the core, negligible losses are produced in the structural parts due to near absence of stray flux. The hysteresis and eddy losses arise due to successive reversals of the magnetization in the iron core excited by a sinusoidal voltage source at a particular frequency f (cycles/second).

The eddy loss, occurring on account of eddy currents produced due to induced voltages in laminations in response to an alternating flux, is proportional to the square of the thickness of laminations, the square of the frequency and the square of the effective (r.m.s.) value of the flux density.

The hysteresis loss is proportional to the area of the hysteresis loop; a typical loop is shown in Figure 2.5(a).

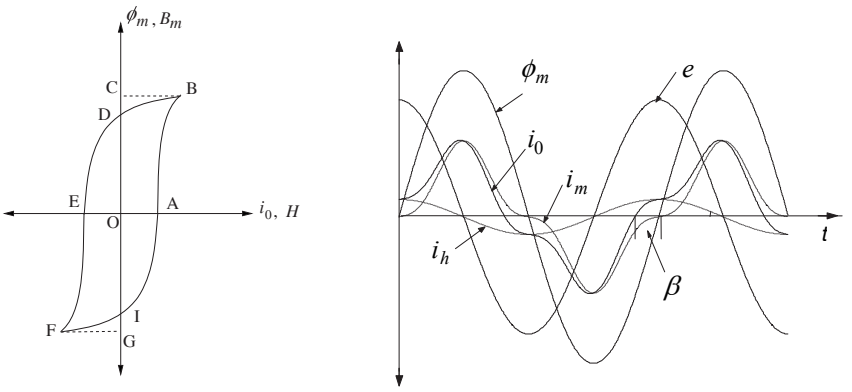

a. Hysteresis loop b. Waveforms

Figure 2.5 Hysteresis loss.

Let e, i_0 and ϕ_m denote the induced voltage, the no-load current and the core flux, respectively. According to Equation 1.1, e leads ϕ_m by 90°. Due to the hysteresis phenomenon, i_0 leads ϕ_m by the hysteresis angle (β) as shown in Figure 2.5 (b). Energy, either supplied to the magnetic circuit or returned back by the magnetic circuit, is given by

$$Energy = \int e\, i_0\, dt = \int N\, \frac{d\phi_m}{dt}\, i_0\, dt = \int N\, i_0\, d\phi_m\,. \tag{2.2}$$

If we consider the first quadrant of the hysteresis loop, the area OABCDO represents the supplied energy. The induced voltage and the current are positive for path AB. For path BD, the energy represented by the area BCD is returned to the source since the two quantities are having opposite signs giving a negative value of energy. Thus, the area OABDO represents the energy loss in the first quadrant, whereas the area ABDEFIA represents the total hysteresis loss in one cycle. The loss has a constant value per cycle meaning thereby that it is directly proportional to frequency; the higher the frequency, i.e., cycles/second, the higher the loss is. The non-sinusoidal current, i_0, can be resolved into two components: i_m and i_h. The i_h component, which is in phase with *e*, represents the hysteresis loss, and i_m is the non-sinusoidal magnetizing component.

The eddy loss (P_{eddy}) and the hysteresis loss ($P_{hysteresis}$) are given by

$$P_{eddy} = k_1\, f^2\, t^2\, B_{rms}^2 \tag{2.3}$$

$$P_{hysteresis} = k_2\, f\, B_{mp}^n \tag{2.4}$$

where

t is the thickness of the core laminations

k_1 and k_2 are constants which are material dependent

B_{rms} is the rated effective flux density corresponding to the actual r.m.s. voltage on the sine wave basis

B_{mp} is the actual peak value of the flux density

n is the *Steinmetz* constant having a value of 1.6 to 2.0 for hot-rolled laminations and a value of more than 2.0 for cold-rolled laminations due to the use of higher operating flux density in them.

In r.m.s. notations, when the hysteresis loss component (I_h) shown in Figure 2.5 (b) is added to the eddy loss component, we get the total core loss current (I_c). In practice, Equations 2.3 and 2.4 are not used by designers for calculation of the no-load loss. There are at least two approaches generally used; based on test results/experimental data, either the building factor of the entire core is

determined or an empirical factor is derived for accounting the effect of the weight at the joints separately:

$$No\ load\ loss = W_t \times K_b \times w \tag{2.5}$$

or $$No\ load\ loss = (W_t - W_c) \times w + W_c \times w \times K_c \tag{2.6}$$

where,

w is watts/kg for a particular operating peak flux density as given by the supplier (Epstein core loss for a single lamination),

K_b is the building factor,

W_c denotes the weight of the joints out of the total weight of W_t, and

K_c represents the extra loss occurring at the joints (whose value is higher for smaller core diameters).

2.2.2 Inclusion of anomalous loss

As discussed earlier, the core loss in transformers is usually classified into two components, viz. the eddy loss and the hysteresis loss, according to the classical theory. The hysteresis loss is due to the irreversible nature of the magnetic characteristics (*B*-*H* curves) when *H* is repeatedly cycled between $-H_m$ to $+H_m$ as explained earlier The eddy loss arises due to induced voltages on account of a changing magnetic induction *B*; the voltages lead to currents circulating in closed loops. These eddy currents cause a resistive loss.

The core losses can be calculated by simple formulae given by Equations 2.3 and 2.4 which assume a non-domain structure of the material. They also assume sinusoidal variation of *B*. Therefore, the classical theory tends to underestimate the core loss. The difference between the measured core loss and the calculated hysteresis loss is the apparent eddy loss, and the difference between the apparent and classical eddy loss values is the anomalous loss. In the grain-oriented transformer steel under normal working conditions, the anomalous loss can be about one-half of the total core loss [14].

Many efforts have been made in the literature for describing the three components of the core loss using a theory based on magnetic domains. A change in magnetization of the core material occurs because of the motion of the domain walls and the rotation of the domain magnetization. The hysteresis loss is caused by the resistance to the domain wall motion due to defects (impurities or dislocations in crystallographic structure) and internal strains in the material. A physical reasoning for the separation of the core loss into the three components is explained using a statistical loss theory in [15].

Hysteresis loss: This loss corresponds to the area enclosed by the DC hysteresis loop. It represents the energy expenditure per cycle of the loop as discussed earlier. Imperfections in the material cause an increase in the energy expenditure during the magnetization process, in the form of a kind of internal friction to the

domain wall motion. A numerical implementation of the hysteresis model based on the domain theory is discussed in Section 12.7.6.

Eddy losses: The eddy loss in a lamination can be calculated using the classical theory which assumes uniform flux throughout its thickness. According to the theory, the instantaneous eddy loss per unit volume is expressed in terms of the rms value of the flux density (B) as

$$P_E = \frac{d^2}{12\rho}\left(\frac{dB}{dt}\right)^2 \tag{2.7}$$

where d indicates the thickness of a single lamination and ρ is the resistivity of its material. When the magnetic induction B is sinusoidally varying, d/dt is replaced by $j\omega$ and the above expression becomes numerically equal to that in Equation 4.94 with $B = B_0/\sqrt{2}$,

$$P_E = k_e\left(f\,B_0\right)^2 \tag{2.8}$$

where, $k_e = \pi^2 d^2/(6\rho)$. The above expression is of the same form as Equation 2.3. Thus, the classical eddy currents are proportional to the square of the thickness of the lamination and to the square of the frequency of supply. The loss is inversely proportional to resistivity of the material.

Anomalous loss or microscopic eddy current loss: The measured power losses for ferromagnetic materials are usually two or three times the value calculated by using the classical eddy current theory [16]. This problem is referred to as the *eddy current anomaly*. Several attempts to explain this anomaly are based on non-uniform magnetization in the core materials due to the presence of magnetic domains. The model proposed in [17] has been frequently used in the literature for interpreting anomalous losses. It assumes an infinite lamination containing a periodic array of longitudinal domains and calculates the eddy current loss using Maxwell's equations. The model gives an excess loss in terms of microscopic eddy currents associated with the domain wall motion. The discrepancies between the losses given by the model and measurements have been related to effects such as the presence of irregularities in the wall motion, domain multiplications, and wall bowing [18].

A statistical approach has been found to give reasonably accurate results. The anomalous loss results from the domain wall motion, which can be expressed as [15]

$$\frac{dW_A}{dt} = \left(\frac{GdbH_0}{\rho}\right)^{\frac{1}{2}}\left(\frac{dB}{dt}\right)^{\frac{3}{2}} \tag{2.9}$$

where, G is a dimensionless coefficient representing a damping effect of the eddy currents (≈ 0.136), b indicates the width of the lamination, and d and ρ represent the thickness and resistivity of the lamination, respectively. H_0 characterizes the statistical distribution of the internal domain wall field and takes into account the grain size. It should be noted that this formula will give inaccurate results if the skin effect is not negligible. For electrically *thick* (i.e., the thickness is much greater than the skin depth) sheets, the formula does not hold.

2.3 Excitation Characteristics

The excitation current of transformers can be calculated by one of the following two methods. In the first method, the magnetic circuit is divided into many sections, within each of which the flux density can be assumed to be of constant value. The corresponding value of the magnetic field intensity (H) is obtained for the lamination material (from its magnetization curve) and for the air gaps at joints. The excitation current can then be calculated as the total magnetomotive force required for all magnetic sections (n) divided by the number of turns (N) of the excited winding,

$$I_0 = \frac{\sum H_n l_n}{N}$$

where l_n is the length of each magnetic section.

It is not practically possible to calculate the no-load current by estimating ampere-turns required in different parts of the core to establish a given flux density. The calculation is mainly complicated by joints. Hence, designers prefer the second method, which uses empirical factors derived from test results. They generally refer the VA/kg (volt-amperes required per kg of material) versus induction (flux density) curve of the lamination material. The VA/kg value is multiplied by a factor (which is based on test results), representing additional excitation requirements at the joints, to obtain the VA/kg value of the built core. In that case, the no-load line current for three-phase transformers can be calculated as

$$No\ load\ current = \frac{VA/kg\ of\ built\ core \times core\ weight\ in\ kg}{\sqrt{3} \times rated\ voltage}. \qquad (2.10)$$

Generally, manufacturers test transformers of various ratings with different core materials at voltage levels below and above the rated voltage and derive their own VA/kg versus induction curves.

As seen from Figure 2.5 (b), the magnetization current is rich in harmonics due to nonlinear magnetic characteristics. For a typical CRGO material, usually observed ranges of various harmonics are as follows. For a fundamental component of 1 per-unit, 3rd, 5th and 7th harmonic components are 0.3 to 0.5 per-

unit, 0.1 to 0.3 per-unit and 0.04 to 0.1 per-unit, respectively. Higher harmonic components are usually insignificant. The effective value of the total no-load current is given as

$$I_0 = \sqrt{I_1^2 + I_3^2 + I_5^2 + I_7^2 + - - - -}\,.$$

In the above equation, I_1 is the effective (r.m.s.) value of the fundamental component (50 or 60 Hz) whereas I_3, I_5 and I_7 are the effective values of the 3rd, 5th and 7th harmonics, respectively. The effect of higher harmonics of diminishing magnitudes have a small influence on the effective value of the resultant no-load current (e.g., 0.4 per-unit, i.e., 40%, 3rd harmonic current increases the resultant by only about 8%). Since the no-load current is typically 0.2 to 2% of the full load current, harmonics in it do not appreciably increase the I^2R loss in the excited winding except during extreme saturation levels. The currents harmonics do not contribute to the core loss if the applied voltage is sinusoidal.

If current harmonics are modified or constrained, the flux density in the core is modified. For example, if the third harmonic current is suppressed by isolating the neutral, the flux density will be flat-topped for a sinusoidal excitation current as shown in Figure 2.6 (the hysteresis phenomenon is neglected for simplicity). For this case, the flux can be expressed as

$$\phi_m = \phi_{mp1}\sin\omega t + \phi_{mp3}\sin 3\omega t + \phi_{mp5}\sin 5\omega t + \phi_{mp7}\sin 7\omega t + - -$$

where ϕ_{mp1}, ϕ_{mp3}, ---, etc. represent the peak values of the fundamental and harmonic components. The induced voltage per turn is

$$e = \frac{d\phi}{dt} = \omega\begin{bmatrix}\phi_{mp1}\cos\omega t + 3\phi_{mp3}\cos 3\omega t + 5\phi_{mp5}\cos 5\omega t \\ + 7\phi_{mp7}\cos 7\omega t + - - - -\end{bmatrix}. \qquad (2.11)$$

The induced voltage as seen in Figure 2.6 is peaky in nature with a pronounced third harmonic component (only the third harmonic component is shown for clarity). Thus, even a small deviation of the flux from the sinusoidal nature introduces appreciable harmonic components in the voltage (3rd harmonic flux component of 15% results in the 3rd harmonic voltage component of 45%). This results in an increase of the eddy loss but the hysteresis loss reduces as the maximum value of the flux density waveform, being flat-topped, is reduced. The net effect on the total core loss will depend on the relative changes in the eddy and hysteresis losses.

2.4 Over-Excitation Performance

The value of the operating flux density in the core has a very significant impact on the overall size, material cost and performance of the transformer. For the currently available various grades of the CRGO material, although losses and magnetizing volt-amperes are lower for the better grades, viz. Hi-B material (M0H, M1H, M2H), laser scribed, mechanical scribed, etc., as compared to the CGO grades (M2, M3, M4, M5, M6, etc.), the saturation flux density has remained the same (about 2.0 T).

The peak operating flux density (B_{mp}) is limited by over-excitation conditions specified by users. The slope of the *B-H* curve of the CRGO grades significantly worsens after about 1.9 T (a small increase in the flux density results in a substantial increase in the drawn magnetizing current). Hence, 1.9 T can be termed knee-point of the *B-H* curve. It has been shown in Example 1.1 that the simultaneous over-voltage and under-frequency conditions increase the flux density in the core. Hence, for an over-excitation condition (over-voltage and under-frequency) of α%, the operating peak flux density of $\left[1.9/(1+\alpha/100)\right]$ can be chosen. For a 10% continuous over-excitation specification, B_{mp} of 1.73 T $\left[=1.9/(1+0.1)\right]$ can be the upper limit.

For a power system, in which a voltage profile is well maintained, a continuous over-excitation condition of 5% may be specified. In this case, B_{mp} of 1.8 T may be used as long as the core temperatures and noise levels are within their permissible limits; the step-lap core construction performs better than the mitered type under overexcitation conditions.

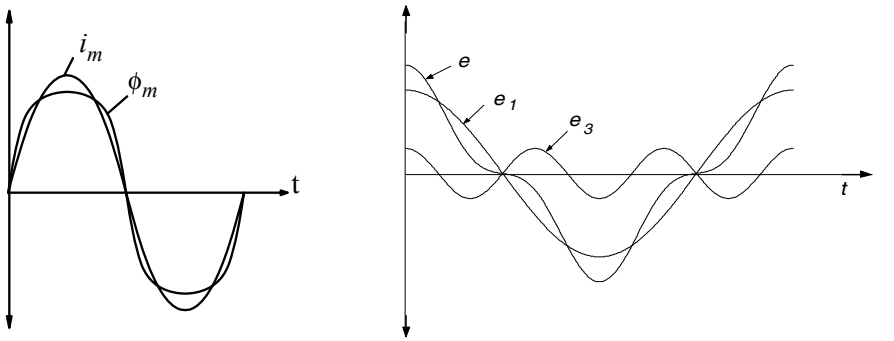

Figure 2.6 Waveforms of flux and voltage for sinusoidal magnetizing current.

The core is likely to get saturated under most of the over-excitation conditions. The spill-over flux from it returns through a predominantly high reluctance path. The over-excitation must be extreme and of a sufficiently long duration to produce damaging effects in the core laminations which can withstand temperatures of about 800 °C (they are annealed at this temperature during their manufacture), but the insulation in their vicinity, viz. press-board insulation (class A: 105 °C) and core bolt insulation (class B: 130 °C), may get damaged. Since the spill-over flux flows only during the part of each cycle when the core is saturated, it is in the form of pulses with a higher harmonic content which increases the eddy loss and temperature rise in the windings and structural parts. Guidelines for permissible short-time over-excitations of transformers are given in [19, 20]. Generator transformers are more susceptible to overvoltages due to over-speeding of generators due to load rejection conditions.

2.5 No-Load Loss Test

The hysteresis loss is a function of the average voltage or maximum flux density, whereas the eddy loss is a function of the r.m.s. voltage or r.m.s. flux density. Hence, the total core loss is a function of the voltage wave-shape. If the sine-wave excitation cannot be ensured during the test, the following correction procedure can be applied to derive the value of no-load loss on the sine wave basis [21, 22]. When a voltmeter corresponding to the mean value is used, the reading is proportional to the maximum value of the flux density in the core. Hence, if the applied non-sinusoidal voltage has the same maximum flux density as that of the desired sine-wave voltage, the hysteresis loss will be measured corresponding to the sine wave. Its r.m.s. value may not be equal to the r.m.s. value of the sine wave, hence the eddy loss has to be corrected by using a factor,

$$K_e = \frac{(\text{actual r.m.s. voltage of the applied voltage})^2}{(\text{r.m.s. voltage on the sine wave basis})^2}.$$

The true core loss of the transformer (P_c) on the sine wave basis is then calculated from the measured loss (P_m) as

$$P_c = \frac{P_m}{P_h' + K_e P_e'} \tag{2.12}$$

where P_h' and P_e' are the hysteresis and eddy loss fractions of the total core loss, respectively. The following values are usually taken for these two fractions,

$P_h' = 0.5$ and $P_e' = 0.5$ for cold rolled steel

$P_h' = 0.7$ and $P_e' = 0.3$ for hot rolled steel

The calculation according to Equation 2.12 is recommended in ANSI Standard C57.12.90-1999. For highly distorted waveforms (with multiple zero crossings per period), a correction which can be applied to this equation is given in [23].

According to IEC 60076-1 (Edition 2.1, 2000), the test voltage has to be adjusted according to a voltmeter responsive to the mean value of the voltage but scaled to read the r.m.s. voltage of a sinusoidal wave having the same mean value. Let the reading of this voltmeter be V_1. At the same time, a voltmeter responsive to the r.m.s. value of the voltage is connected in parallel with the mean value voltmeter, and let its reading be V. The wave shape of the test voltage is satisfactory if the readings V_1 and V are within 3% of each other. If the measured no-load loss is P_m then the corrected no-load loss (P_c) is given as

$$P_c = P_m(1+d) \tag{2.13}$$

where $d = \dfrac{V_1 - V}{V_1}$ (usually negative)

The method given in [24] allows the determination of the core loss from the measured data under a non-sinusoidal excitation without an artificial separation of the hysteresis and eddy losses. Harmonic components are taken into account. The computed results have been compared with the IEC method.

A voltage regulator with a large capacitor bank is better than a conventional rotating machine source from the point of view of obtaining as sinusoidal voltage as possible for core loss measurements.

The no-load loss test and the calculation of shunt parameters of the equivalent circuit have been elaborated in Chapter 1. Now, special topics/case studies related to the no-load test are discussed.

2.5.1 Asymmetrical magnetizing phenomenon

Unlike in a bank of three single-phase transformers having independent magnetic circuits, the different phases are wound on a common magnetic circuit in the three-phase three-limb construction. The excitation currents and powers drawn by the three phases are not the real requirements by the corresponding magnetic sections of the core. The current drawn by each phase winding is a function of the requirements of all the three phases. Consider a three-phase three-limb core shown in Figure 2.7. Let the magnetomotive forces required to produce instantaneous values of fluxes (ϕ_r, ϕ_y and ϕ_b) in the path between points P_1 to P_2 for the phase windings (r, y and b) be NI_r', NI_y' and NI_b', respectively. There is an inherent asymmetry in the core as the length of magnetic path between the points P_1 and P_2 for y phase is less than that for the phases r and b. Let the currents drawn from the supply be I_r, I_y and I_b.

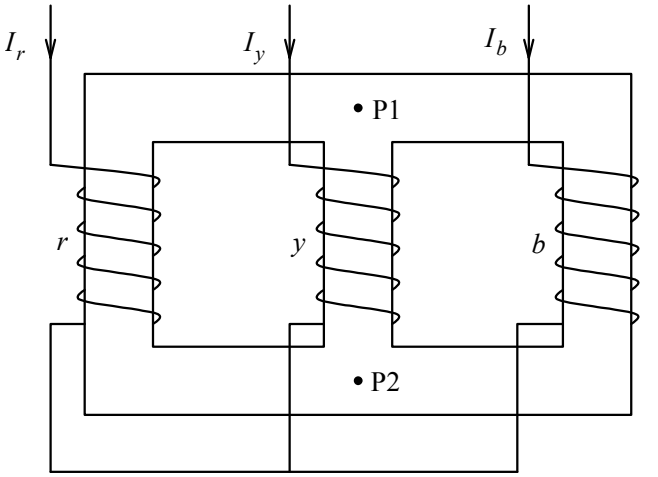

Figure 2.7 Three-phase three-limb core with Y-connected primary.

The following equations can be written:

$$NI_r - NI_y = NI_r^{'} - NI_y^{'} \tag{2.14}$$

$$NI_y - NI_b = NI_y^{'} - NI_b^{'} \tag{2.15}$$

$$NI_b - NI_r = NI_b^{'} - NI_r^{'} . \tag{2.16}$$

For a Y-connected winding (star-connected without grounded neutral),

$$I_r + I_y + I_b = 0 . \tag{2.17}$$

It follows from Equations 2.14 to 2.17 that

$$I_r = I_r^{'} - (1/3)\,(I_r^{'} + I_y^{'} + I_b^{'}) = I_r^{'} - I_z \tag{2.18}$$

$$I_y = I_y^{'} - (1/3)\,(I_r^{'} + I_y^{'} + I_b^{'}) = I_y^{'} - I_z \tag{2.19}$$

$$I_b = I_b^{'} - (1/3)\,(I_r^{'} + I_y^{'} + I_b^{'}) = I_b^{'} - I_z \tag{2.20}$$

where I_z is the zero-sequence component of the currents required to establish the required magnetomotive forces,

$$I_z = (1/3)\,(I_r^{'} + I_y^{'} + I_b^{'}) . \tag{2.21}$$

The magnitude of I_z increases with the asymmetry. The magnetomotive force, NI_z, is responsible for producing a zero-sequence flux in the space outside the

core between the points P_1 and P_2 [25]. The magnitude of this flux is quite small as compared to the mutual flux in the core. For convenience, the reluctance of the magnetic path for the phase *y* between P_1 and P_2 is taken as half of that for the extreme phases (*r* and *b*). For a sinusoidal three-phase applied voltage, the established mutual flux is also sinusoidal, and the required excitation currents contain harmonics as explained earlier. Therefore, the currents in the three-phases can be expressed as (with higher order harmonics neglected)

$$I_r^{'} = I_c \cos\omega t + I_1 \sin\omega t - I_3 \sin 3\omega t \tag{2.22}$$

$$I_y^{'} = 0.5I_c \cos(\omega t - 120^0) + 0.5I_1 \sin(\omega t - 120^0) - 0.5I_3 \sin 3(\omega t - 120^0) \tag{2.23}$$

$$I_b^{'} = I_c \cos(\omega t - 240^0) + I_1 \sin(\omega t - 240^0) - I_3 \sin 3(\omega t - 240^0) \tag{2.24}$$

where I_c is the core loss component, and a negative sign is taken for the third harmonic components [26] to obtain a peaky nature of the excitation current (for a sinusoidal flux, the excitation current is peaky in nature due to nonlinear magnetic characteristics). Substituting these expressions in Equation 2.21,

$$I_z = 0.167I_c \cos(\omega t + 60^0) + 0.167I_1 \sin(\omega t + 60^0) - 0.833I_3 \sin(3\omega t)\,. \tag{2.25}$$

After substituting this expression of I_z and the expressions of $I_r^{'}$, $I_y^{'}$ and $I_b^{'}$ from Equations 2.22 to 2.24 in Equations 2.18 to 2.20, the excitation currents drawn from the source are

$$I_r = 0.928I_c \cos(\omega t - 9^0) + 0.928I_1 \sin(\omega t - 9^0) - 0.167I_3 \sin(3\omega t) \tag{2.26}$$

$$I_y = 0.667I_c \cos(\omega t - 120^0) + 0.667I_1 \sin(\omega t - 120^0) + 0.333I_3 \sin(3\omega t) \tag{2.27}$$

$$I_b = 0.928I_c \cos(\omega t + 129^0) + 0.928I_1 \sin(\omega t + 129^0) - 0.167I_3 \sin(3\omega t)\,. \tag{2.28}$$

Since the neutral is isolated, the sum of the 3rd harmonic currents in three phases has to be zero; this condition is satisfied by the above three equations. The essence of the mathematical treatment can be understood by the vector diagrams of the fundamental and third harmonic components shown in Figure 2.8. The magnitudes of I_r and I_b are almost equal and these are greater than the magnitude of I_y. The current I_y, though smallest of all the three currents, is higher than the current required to excite the middle phase alone ($I_y > I_y^{'}$). The currents in the outer phases are slightly less than that needed to excite the outer limbs alone ($I_r < I_r^{'}$ and $I_b < I_b^{'}$). In actual practice, the currents I_r and I_b

may differ slightly due to minor differences in the characteristics of magnetic paths (e.g., unequal air gap lengths at joints). The third harmonic component drawn by the *y* phase is greater than that of the r and b phases.

Since the applied voltage is assumed to be sinusoidal, only the fundamental component contributes to the power. The wattmeter of the r phase reads negative if I_z is large enough to cause the angle between V_r and I_r to exceed 90°. A negative power value is measured in one of the phases during the no-load loss test when yoke lengths are comparable to limb heights increasing the asymmetry between the middle and outer phases.

It has been proved in [27] that when the reluctance of the central phase is half that of the outer phases,

$$I_r : I_y : I_b = 1 : 0.718 : 1. \tag{2.29}$$

The effect of change in the excitation is illustrated for the r phase in Figure 2.9. The no-load test is usually carried out at 90%, 100% and 110% of the rated voltage. The magnetizing component of the excitation current is more sensitive to an increase in flux density as compared to the core loss component. Consequently as the voltage is increased, the no-load power factor decreases. The value of I_z also increases, and hence the possibility of the negative power phenomenon increases with an increase in the applied voltage. When the angle between V_r and I_r is 90°, the r phase wattmeter reads zero, and if it exceeds 90° the wattmeter reads negative.

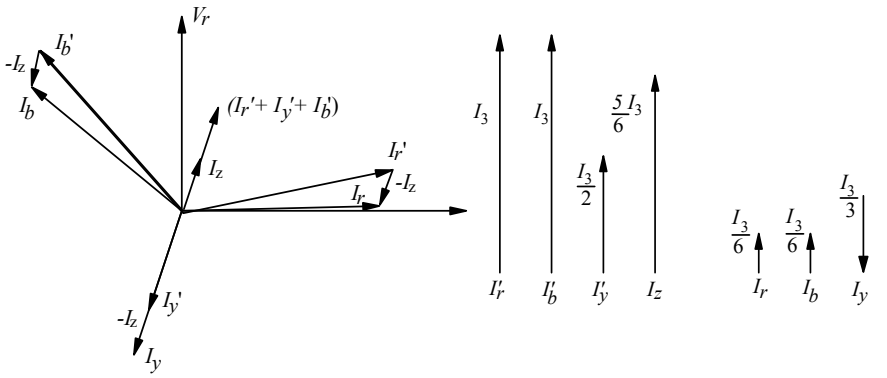

a. Fundamental components b. Third harmonic components

Figure 2.8 Magnetizing asymmetry.

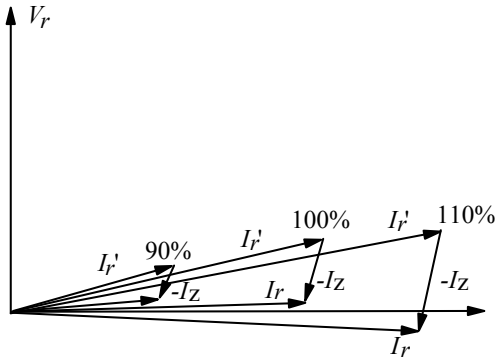

Figure 2.9 Effect of excitation level.

The magnetizing asymmetry phenomenon described above has been analyzed by using mutual impedances between three phases in [28]. It is shown that phase currents and powers are balanced if mutual impedances Z_{ry}, Z_{yb} and Z_{br} are equal. These impedances depend on the number of turns and disposition of windings, their connections, and more importantly on the dimensions and layout of the core. Because of the unbalanced mutual impedances in the three-phase three-limb construction ($Z_{ry} = Z_{yb} \neq Z_{br}$), the total no-load power is redistributed between the three phases. The form of asymmetry occurring in the phase currents and powers is different for the three-limb and five-limb constructions. It is reported in [28] that there is star point displacement in the five-limb transformers, which tends to reduce the unbalance caused by the inequality of the mutual impedances.

If the primary winding is delta-connected, a similar analysis can be performed for which a measured line current is the difference between the currents of the corresponding two phases. It can be proved that when the delta-connected winding is energized, for the Yd1 or Dy11 connection, the line current drawn by the r phase is higher than the currents drawn by the y and b phases, which are equal ($I_{r-L} > I_{y-L} = I_{b-L}$) [29]. For the Yd11 or Dy1 connection, the line current drawn by the b phase is higher than the currents drawn by the r and y phases, which are equal ($I_{b-L} > I_{y-L} = I_{r-L}$). It should be noted that, for the delta connected primary winding also, the magnetic section corresponding to the y phase requires the least magnetizing current, i.e., ($I_y' < I_r',\ I_b'$), but the phasor additions of the phase currents results into a condition in which I_{y-L} equals the line current of one of the outer phases.

2.5.2 Magnetic balance test

This test is performed at works or site as an investigative test to diagnose the core and windings. In this test, a low voltage (say, 230 V) is applied to a winding of one phase with all other windings kept open-circuited. Voltages induced in the corresponding windings of the other two phases are measured. When the middle phase (*y*) is excited, the voltages induced in the *r* and *b* phases should be in the range of 40 to 60% of the applied voltage. Some deviation from the expected value of 50% may be observed since the reluctance values corresponding to the two outer phases may differ slightly on account of minor differences in air gaps at joints. When the *r* (or *b*) phase is excited, the *y*-phase induced voltage may be as high as 90% and the voltage induced in the *b* (or *r*) phase may be as low as 10% for healthy core conditions. The addition of the r.m.s. values of the induced voltages in the unexcited phases need not necessarily be equal to the voltage applied to the excited phase. This phenomenon may be due to nonlinear *B-H* characteristics and the presence of harmonics in the fluxes of the unexcited limbs at the low applied voltage during the test; the phenomenon is not yet clearly understood.

The results of the magnetic balance test should be taken as indicative and some other tests should be performed to confirm the inferences drawn. The test can be carried out at various stages of manufacturing, viz. before and after connections, before final tests, before dispatch; the test results can be used as a reference signature for future comparisons. If the voltages measured do not fall in the expected range, a problem in the core or windings can be suspected. Let us suppose that there is an inter-turn fault in the *r* phase. When a low voltage is applied to the *y* phase winding, a much higher voltage is induced in the *b* phase winding as compared to that of the *r* phase, giving an indication of a fault in the phase *r* winding. A high current circulating in the faulty section, opposes the magnetizing flux thereby reducing the induced voltage in the faulty phase. For the test, the core should be demagnetized because a slight magnetization (e.g., after a resistance measurement test) can give erratic results. The demagnetization can be achieved by a repeated application of a variable AC voltage which is slowly reduced to zero.

2.5.3 Trouble shooting by no-load loss test

Suppose, it is suspected that during an impulse test a particular winding has failed. Inter-turn faults may not result in appreciable changes in the transfer functions (e.g., impedances) of the windings; appreciable disturbances are not noticeable in the recorded impulse waveforms. Inter-turn faults can be detected and located using the results of no-load loss tests. Therefore, it is usually recommended to do the no-load loss test after high voltage dielectric tests for detecting any fault developed in the windings. The no-load loss value shoots up if there is a turn-to-turn short circuit. In order to locate the exact position of the

fault, parallel conductors are electrically separated at both ends, and then resistance values are measured between all the points available ($1, 1', 2, 2', 3, 3'$) as shown in Figure 2.10; the winding is assumed to have 3 parallel conductors per turn.

Let us assume that each of the parallel conductors is having a resistance of 0.6 ohms. If the fault is at a location 70% from the winding bottom between conductor 1 of one turn and conductor 3 of the next turn, the measured values of resistances between $1-3$ and $1'-3'$ will be 0.36 ohms ($2\times 0.3\times 0.6$) and 0.84 ohms ($2\times 0.7\times 0.6$), respectively. The voltage corresponding to one turn circulates very high currents since these are limited only by the above resistances; the reactance of individual conductors is very small. An increase in the no-load loss value corresponds approximately to the loss in these two resistive paths due to the induced circulating currents.

2.5.4 Effect of impulse test on no-load loss

A slight increase of about few % in the no-load loss value is sometimes observed after impulse tests due to partial breakdowns of interlamination insulations (particularly at edges) resulting into an increased eddy loss. The phenomenon has been analyzed in [30], wherein it is reported that voltages are induced in the core by electrostatic as well as electromagnetic inductions. A loss increase to the tune of 2% is possible. The phenomenon is harmful to the extent that it increases the loss which, however, may not increase further in field. Application of an adhesive at the edges can prevent partial and localized damages to the core during the high voltage test.

2.6 Impact of Manufacturing Processes

For building cores of various ratings of transformers, different lamination widths are required. Since lamination rolls are available in some standard widths from suppliers, slitting operations are inevitable. It is obvious that in most cases full widths cannot be utilized and the scrap of the leftover material has to be minimized by a meticulous planning exercise. A manufacturer having a wide product range can use the leftover pieces of the cores of large transformers for the cores of small distribution transformers.

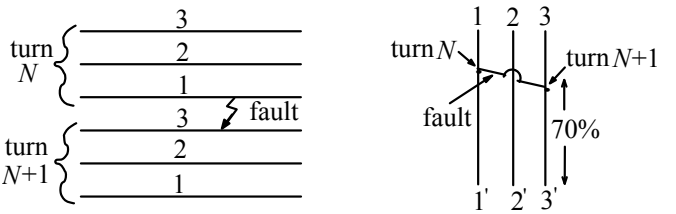

Figure 2.10 Troubleshooting during no-load loss test.

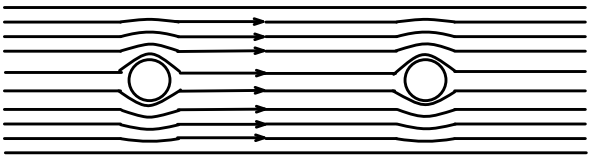

Figure 2.11 Effect of yoke bolts.

The next operation is the cutting of laminations in different shapes (e.g., mitered joint in Figure 2.3). Finally, the corner protrusions of the built core are cut because they do not carry any flux, and they may contribute to the noise level of the transformer due to their vibrations.

In bolted yoke constructions, holes are punched in the yoke laminations. The flux in the region of the holes is distorted as shown in Figure 2.11. This leads to an increase in the core loss. Boltless yoke constructions perform better; a special clamping arrangement consisting of fiber-glass/stainless steel bands is adopted. The boltless yoke construction results in better utilization of the core material and reduction in the core loss. Small guiding holes are needed to facilitate the placement of laminations and core-building. In order to strengthen the bonding of laminations, suitable epoxy resin is applied at their edges, which also results in reduction of the noise level.

The processes of slitting, cutting, and punching result in edges having burrs, which not only worsen the stacking factor but also result into short-circuiting of adjacent laminations, and therefore an increase in the eddy loss occurs. The upper limit of an acceptable burr level is about 20 microns. A low burr level improves the stacking factor of the core and reduces its loss. A high stacking factor (which is typically about 0.97 to 0.98) increases the core area leading to a cost-effective design. The staking factor, which is decided by the lamination coating and burrs, is different than the space factor ($\approx$ 0.88 to 0.90) which is defined as the useful magnetic area divided by the area of the core circle. Burrs can be removed by passing the laminations through a de-burring process. A thin coating of varnish may be applied at the edges to cover up the scratches developed during the de-burring process.

The above processes and multiple handling of laminations result in the development of mechanical strains inside the laminations, disturbing the original grain orientation and thereby causing an increase in the core loss. This effect can be mitigated by annealing the laminations at a temperature of about 800°C under an inert gas atmosphere. If state-of-the-art lamination slitting and cutting machines with a high degree of automation are used, handling of the laminations is reduced substantially and hence the annealing process is not considered necessary.

Limbs are generally made of a large number of steps in order to maximize the useful magnetic area for a given core diameter. Yokes on the other hand may have lesser number of steps to provide good axial supports to the windings. The mismatch in the numbers of limb and yoke steps may result into an extra loss at their joint.

One question which may be commonly asked by production and planning departments is: Can materials of different grades be mixed to overcome the problem of non-availability of a particular grade in sufficient quantity? Needless to say, one can mix only a better grade material, which can give marginal reduction in the no-load loss. Actually, the grade mixing should not be encouraged. In exceptional cases, however, mixing of a better grade may be allowed to minimize shop inventory problems.

2.7 Inrush Current

2.7.1 Theory

If it were possible to switch on transformers at the exact instant of a voltage wave that corresponds to the actual flux density in the core, there would not be any transient during the switching operations. In actual practice, a transient phenomenon in the form of an inrush current is unavoidable since the instant of switching cannot be easily controlled and the instant of switching favorable to one phase is not so to the other two phases.

When a transformer is switched off, the excitation current follows the hysteresis curve to zero, whereas the flux density value changes to a non-zero value B_r as evident from the hysteresis loop in Figure 2.5 (point D). For a residual flux density of $+B_r$, maximum inrush current is drawn when a transformer is switched on at the instant when the applied voltage is zero as shown in Figure 2.12. If the transformer was not switched off, the excitation current (i) and the flux density would have followed the dotted curves. As per the *constant flux linkage theorem*, the magnetic flux in an inductive circuit cannot change suddenly; the flux just after closing the switch (at $t = 0^+$) must remain equal to the flux just before closing the switch (at $t = 0^-$). Hence, the flux density, instead of starting from the negative maximum value ($-B_{mp}$), starts from $+B_r$ and reaches the peak positive value of ($B_r + 2B_{mp}$) driving the core into a deep saturation condition.

For an applied sinusoidal voltage, the flux density is sinusoidal and the magnetizing current is peaky in nature. The same result can be obtained by solving the following governing equation:

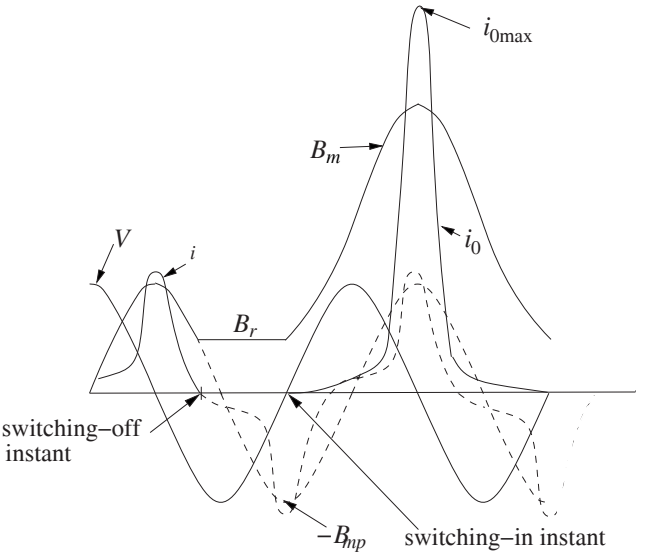

Figure 2.12 Case of maximum inrush current.

$$V_p \sin(\omega t + \theta) = i_0 R_1 + N_1 \frac{d\phi_m}{dt} \tag{2.30}$$

where

V_p = peak value of the applied voltage

θ = angle at which the voltage is switched on

i_0 = instantaneous value of the magnetizing current

ϕ_m = instantaneous value of the flux at any time t

R_1 = primary winding resistance

N_1 = primary winding turns.

The solution of the equation is quite straightforward when linear magnetic characteristics are assumed and the core loss is neglected. The solution is obtained by using the initial condition that at $t = 0$, $\phi_m = \pm\phi_r$,

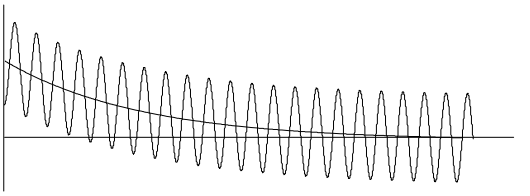

Figure 2.13 Flux wave.

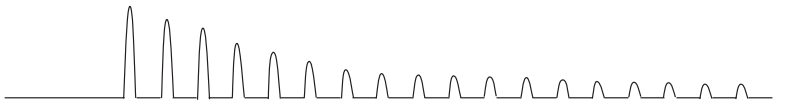

Figure 2.14 Typical inrush current waveform.

$$\phi_m = (\phi_{mp}\cos\theta \pm \phi_r)\, e^{\frac{-R_1}{L_1}t} - \phi_{mp}\cos(\omega t + \theta)\,. \tag{2.31}$$

For $\theta = 0$ and the residual flux of $+\phi_r$, the waveform of flux (flux density) is shown in Figure 2.13. It can be observed from Equation 2.31 that the flux waveform has a transient DC component which decays at a rate determined by the time constant of the primary winding (i.e., L_1 / R_1), and a steady-state AC component viz. $-\phi_{mp}\cos(\omega t + \theta)$. A typical inrush current waveform is shown in Figure 2.14 for a phase switched on at the most unfavourable instant (i.e., at zero crossing of the applied voltage wave).

It can be observed that the current waveform is completely offset in the first few cycles with the wiping out of alternate half cycles because the flux density is below the saturation value for these half cycles, resulting in very small current values. Hence, the inrush current is highly asymmetrical and has a predominant second harmonic component which is used by differential protection schemes to restrain relays from operating.

In practice the time constant (*L/R*) of the circuit is not constant; the value of *L* changes with the flux density value. During the first few cycles, the core can be in a deep saturation state and therefore *L* is small. Hence, the initial rate of the decay of the inrush current is high. As the winding and core losses damp the circuit and the flux density falls, *L* increases slowing down the decay. Hence, the decay starts with a high initial rate which progressively reduces; the total phenomenon lasts for a few seconds. Smaller transformers have higher decay rates because of smaller time constants. In general, inrush currents in less efficient (high loss) transformers have high decay rates [31].

While deriving Equation 2.31, linear magnetic characteristics are assumed, which is a major approximation. Accurate procedures for the calculation of inrush currents in single-phase transformers is given in the literature [32, 33] in which nonlinear magnetic characteristics are elaborately represented. For three-phase transformers, the analysis is more involved [34, 35, 36]. Inrush currents can be calculated in the harmonic domain for single-phase and three-phase transformers using operational matrices as given in [37]. Overvoltages in HVDC systems following inrush current transients are dealt in [38], wherein an inductive AC system impedance, due to generators, transformers and transmission lines, is shown to resonate with filters. If the resulting resonance frequency of the combination is equal to or close to a harmonic component of the inrush current of the same frequency, overvoltages occur.

2.7.2 Estimation of magnitude of first peak

A transformer user is generally interested in knowing the maximum value and decay rate of the inrush currents. For the saturation flux density of 2.03 T, the flux of magnitude ($2.03 \times A_c$) is contained in the core with A_c as its net area. The remaining flux spills out of the core, which returns through a predominantly high reluctance non-magnetic path. The ampere-turns required to produce the air flux are so large that they can be also assumed to produce 2.03 T in the core. For the worst instant of switching it can be written that

$$\phi_{air} = \mu_0 H A_w = 2\phi_{mp} + \phi_r - 2.03 A_c \tag{2.32}$$

where A_w is the mean area enclosed by a winding turn. Hence, the maximum inrush current (i.e., the first peak), $i_{0\max}$, drawn by the energized winding with N_1 turns and h_w height can be calculated for a single-phase transformer from the following equation as

$$H = \frac{N_1 \, i_{0\max}}{h_w} \tag{2.33}$$

where H is the magnetic field intensity.

$$\therefore i_{0\max} = \frac{h_w H}{N_1} = \frac{(2\phi_{mp} + \phi_r - 2.03 A_c) \, h_w}{\mu_0 \, A_w \, N_1} = \frac{(2B_{mp} + B_r - 2.03) A_c \, h_w}{\mu_0 \, A_w \, N_1} . \tag{2.34}$$

For three-phase transformers, the calculation of inrush currents needs more explanation. Let us consider the following three cases:

1) For a delta-connected primary winding, each of the phases is independently connected to the network, and the inrush phenomenon corresponding to the flux of each phase takes place as in single-phase transformers. This results in the same value of the phase inrush current as that of the single-phase transformer, but in terms of line currents the severity is less. Under normal operating conditions, the line current is $\sqrt{3}$ times the phase current. During the inrush condition, only one phase, which is switched at or near the worst instant of switching, is having high inrush current; hence the line current is almost equal to the phase current. Hence, the per-unit line inrush current of the three-phase transformer with a delta-connected primary winding is 0.577 times ($1/\sqrt{3}$ times) the corresponding inrush current of the single-phase transformer.

2) For a bank of three single-phase transformers having independent magnetic circuits, with star-connected primary and delta-connected secondary windings, the current distribution expressed in terms of the maximum inrush current

($i_{0\max}$) of the single-phase transformer is shown in Figure 2.15. It is assumed that the phase a has the maximum transient inrush current.

Since the delta allows the flow of zero-sequence currents, it holds the neutral voltage at a stable value and maintains normal line-to-neutral voltages across the phases. The presence of the delta also ensures the full single-phase transient in the phase that has maximum inrush current (the phase a in this case). Two-thirds of the required single-phase inrush current ($2\, i_{0\max}/3$) flow in the phase a on the star side and the remaining one-third flows on the delta side. Hence, the maximum inrush current in this case is $2/3$ times that of the single-phase transformer. The phases *b* and *c* do not get magnetized since the currents in them are equal and opposite on the star and delta sides.

3) A three-phase three-limb transformer (in which the phases are magnetically interlinked) can be treated as consisting of three independent single-phase transformers [22, 34] under inrush transients; for a star-connected primary winding, the inrush phenomenon is similar to that of Case 2, irrespective of whether the secondary winding is star- or delta-connected. Maximum inrush current is approximately equal to two-thirds of that corresponding to the single-phase operation.

2.7.3 Estimation of decay pattern

Equation 2.34 is an approximate formula giving maximum possible inrush current. Practicing engineers may be interested in knowing inrush current peak values for the first few cycles or the time after which the inrush current reduces to a value equal to the rated current. The procedures for estimating inrush current peaks for first few cycles are given in [39, 40]. The procedures are generally applicable for a few tens of initial cycles.

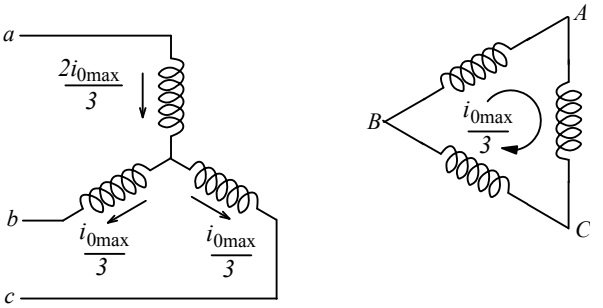

Figure 2.15 Inrush in a star-delta bank of transformers.

Example 2.1

Calculate inrush current peaks for the first 5 cycles for a 31.5 MVA, 132/33 kV, 50 Hz, Yd1 transformer, when energized from its 132 kV winding having 920 turns, mean diameter of 980 mm and height of 1250 mm. The peak operating flux density is 1.7 T for the core area of 0.22 m^2. The sum of system and winding resistances is 0.9 ohms.

Solution:

The transformer is assumed to be energized at an instant when the applied voltage to one of the phases is at zero value and increasing. It is also assumed that the residual flux is in the same direction as that of the initial flux change, thus giving maximum possible value of the inrush current. After the core saturates, the inrush current is limited by the air core reactance of the excited winding, X_s, which can be calculated using a standard formula.

Step 1:

$$X_s = \frac{\mu_0 N^2 A_w}{h_w} \times 2 \times \pi \times f \tag{2.35}$$

N = number of turns of the excited winding = 920 turns

A_w = area inside the mean turn of the excited winding

$$= \frac{\pi}{4}(mean\ diameter)^2 = \frac{\pi}{4}(0.980)^2 = 0.754\ \text{m}^2$$

h_w = height of the excited winding = 1.25 m

$$\therefore X_s = \frac{4\pi \times 10^{-7} \times 920^2 \times 0.754}{1.25} \times 2 \times \pi \times 50 = 202 \text{ ohms.}$$

Step 2:

Now angle θ is calculated [39], which corresponds to the instant at which the core saturates,

$$\theta = K_1 \cos^{-1}\left\{\frac{B_s - B_{mp} - B_r}{B_{mp}}\right\} \tag{2.36}$$

where B_s is the saturation flux density = 2.03 T

B_{mp} is the peak value of the operating flux density in the core = 1.7 T

B_r is the residual flux density = 0.8 × B_{mp} = 1.36 T

(For cold rolled materials, the maximum residual flux density can be taken as 80% of the rated peak flux density, whereas for hot rolled materials it can be taken as 60% of the rated peak flux density.)

K_1 = correction factor for the saturation angle = 0.9

$$\therefore \theta = 0.9 \times \cos^{-1}\left\{\frac{2.03 - 1.7 - 1.36}{1.7}\right\} = 2.0 \text{ radians.}$$

Step 3:

The inrush current peak for the first cycle is calculated as [39],

$$i_{0\max} = \frac{K_2\, V\sqrt{2}}{X_s}(1 - \cos\theta) \tag{2.37}$$

where V is the r.m.s. value of the applied alternating voltage

K_2 is a correction factor for the peak value = 1.15

$$\therefore i_{0\max} = \frac{1.15 \times (132000/\sqrt{3})\sqrt{2}}{202}(1 - \cos 2.0) = 869 \text{ amperes.}$$

The current calculated by Equation 2.34, for the core area of 0.22 m^2, is

$$i_{0\max} = \frac{(2 \times 1.7 + 1.36 - 2.03) \times 0.22 \times 1.25}{4\pi \times 10^{-7} \times 0.754 \times 920} = 861 \text{ amperes,}$$

which is very close to that calculated by the more accurate method.

Step 4:

After having calculated the value of inrush current peak for the first cycle, the residual flux density at the end of the first cycle is calculated. The residual component of the flux density reduces due to losses in the circuit, and hence it is a function of damping provided by the losses in the transformer. The new value of the residual flux density can be calculated as [39]

$$B_r(new) = B_r(old) - B_{mp} \times \frac{K_3 R}{X_s}\left[2(\sin\theta - \theta\cos\theta)\right] \tag{2.38}$$

where R = sum of the transformer winding resistance and the system resistance
= 0.9 ohms

K_3 = correction factor for the decay of inrush = 2.26

$$\therefore B_r(new) = 1.36 - 1.7 \times \frac{2.26 \times 0.9}{202}\left[2(\sin 2.0 - 2.0\cos 2.0)\right] = 1.3 \text{ T}$$

Steps 2, 3 and 4 are repeated to calculate the peaks of subsequent cycles. The inrush current peaks for the first 5 cycles are 869 A, 846 A, 825 A, 805 A and 786 A on the single-phase basis. Since it is a star-delta connected three-phase three-limb transformer, actual line currents are approximately two-thirds of these values (579 A, 564 A, 550 A, 537 A and 524 A).

The inrush current phenomenon may not be harmful to the transformer (although repeated switching on and off in a short period of time is not advisable). The behavior of transformers under inrush conditions continues to attract attention of researchers. The differences in forces acting on the windings during the inrush and short-circuit conditions are enumerated in [41]. An inrush current may result in the inadvertent operation of overload and differential relays, tripping the transformer out of the circuit as soon as it is switched on. Relays that discriminate between inrush and fault conditions are used:

1) Since inrush currents have a predominant second harmonic component, differential relays with a second harmonic restraint are used to prevent their mal-operation.

2) Differential relays with higher pick-ups can be used to reduce their sensitivity to asymmetrical waves; furthermore, a time delay can be added to override high initial peaks.

A technique for discriminating inrush currents from internal fault currents is described in [42]; it uses a combination of the wavelet transform and neural network approaches. The ability of the wavelet transform to extract the required information from transient signals simultaneously in the time and frequency domains is exploited for the purpose. High inrush currents may cause excessive momentary dips in system voltages affecting operations of various electrical equipment. A switching-on operation of a transformer in an interconnected network can affect already energized transformers as explained below.

2.7.4 Sympathetic inrush phenomenon

It has long been known that transient magnetizing inrush currents, sometimes reaching magnitudes as high as six to eight times the rated currents, can flow in transformers during their energization. It is generally not appreciated, however, that the other transformers, already connected to the network near the transformer being switched, may also have a transient magnetizing current of an appreciable magnitude at the same time. In order to understand how energizing of a transformer affects the operating conditions of the other interconnected transformers, consider a network as shown in Figure 2.16.

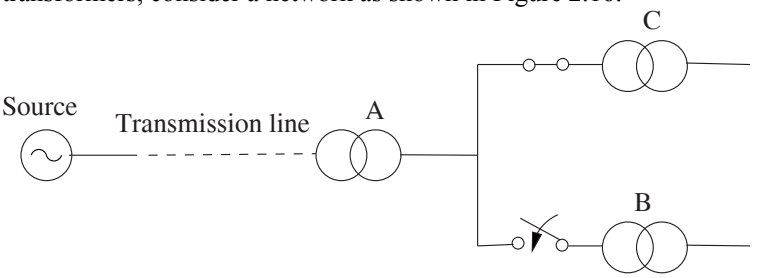

Figure 2.16 Sympathetic inrush.

When transformer B is switched on to the network already feeding similar transformers (C) in its neighborhood, the transient magnetizing inrush current of the switched-on transformer also flows into these other transformers and produces in them a DC flux which is superimposed on their normal AC magnetizing flux. This gives rise to increased flux density values and higher magnetizing currents in them [22, 43, 44]. These *sympathetic* inrush currents are substantially less than their usual inrush currents. Depending on the magnitude of the decaying DC component, this sympathetic (indirect) inrush phenomenon leads to increased noise levels in these connected transformers due to a higher flux density value in the core for the transient period. It may also lead to mal-operations of protective equipment. An increase in the noise level of an upstream power transformer during the energization of a downstream distribution transformer (fed by the power transformer) has been analyzed in [45]; the analysis is supported by noise level measurements carried out during switching operations.

Let us now analyze the case of parallel transformers shown in Figure 2.17 (a). The transformers may or may not be paralleled on the secondary side. The DC component of the inrush current of the transformer being energized flows through the transmission line resistance (between the source and the transformer) producing a DC voltage drop across it. The voltage drop forces the core of the already energized transformer towards saturation in a direction opposite to that of the transformer which is being switched on, resulting in a buildup of the magnetizing current in it; this rate of the buildup is the same as the rate at which the DC component of the magnetizing current is decreasing in the transformer being switched-on. When the two parallel transformers are similar and the magnitudes of the DC components of the currents in both the transformers become equal, there is no DC component in the line feeding both the transformers. However, there is a DC component circulating in the loop circuit between them, whose rate of decay is very slow due to high inductance and small resistance values of the windings of the two transformers. The waveforms of the currents are shown in Figure 2.17 (b).

Since the line current feeding the transformers becomes symmetrical (waveform I_c) devoid of the second harmonic component, differential relaying with a second harmonic constraint needs to be provided to each transformer separately instead of protecting them as a unit [46]. The phenomenon is more severe when transformers are fed from a weak system (i.e., transformers connected to a common feeder with a limited fault level and a high internal resistance). For a further discussion on the phenomenon, refer Section 13.6.

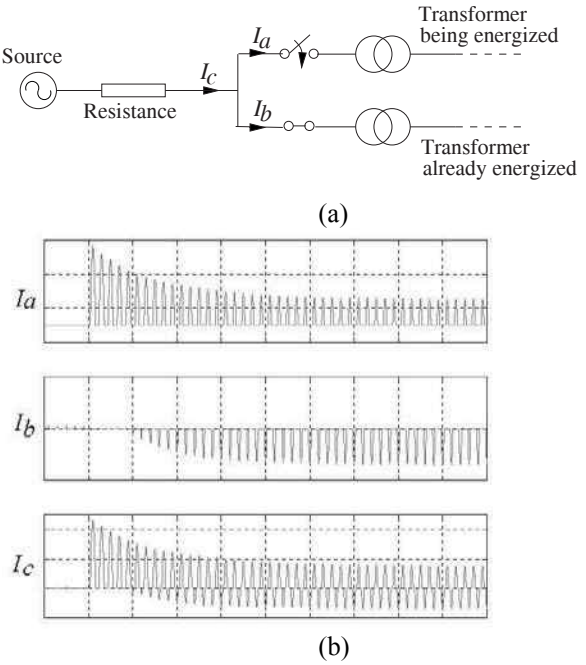

Figure 2.17 Inrush currents in parallel transformers.

2.7.5 Factors affecting inrush phenomenon

Various factors affecting the inrush current phenomenon are now summarized:

A. Switching-on angle (α)

The inrush current decreases when the switching-on angle (on the voltage wave) increases. It is maximum for $\alpha = 0°$ and minimum for $\alpha = 90°$.

B. Residual flux density

The inrush current is significantly aggravated by the residual flux density which depends upon core material characteristics and the power factor of the load when the transformer was switched off. The instant of switching-off has an effect on the residual flux density depending upon the type of the load [22]. The total current is made up of the magnetizing current component and the load current component. The current interruption generally occurs at or near zero of the total current waveform. The magnetizing current passes through its maximum value before the instant at which total current is switched-off for no load, lagging load and unity power factor load conditions, resulting in maximum value of the residual flux density as per the *B-H* curve of Figure 2.5. For leading

loads, if the leading component is less than the magnetizing component, at zero of the resultant current the magnetizing component will have reached the maximum value resulting in maximum residual. On the contrary, if the leading current component is more than the magnetizing component, the angle between the peak of the magnetizing current and the zero of the resultant current will be more than 90°. Hence, at the interruption of the resultant current, the magnetizing component will not have reached its maximum, resulting in a lower value of the residual flux density.

The type of the core material also decides the value of the residual flux density. Its maximum value is usually taken as about 80% and 60% of the saturation value for the cold-rolled and hot-rolled materials, respectively. It is also a function of joint characteristics; its values for mitered and step-lap joints will be different.

C. Series resistance

The resistance of the line between the source and the transformer has a predominant effect on the inrush phenomenon. The damping effect provided by the resistance not only reduces the peak initial inrush current but also hastens its decay rate. Transformers near generators usually have inrush transients lasting for a long period of time because of a low value of the available resistance. Similarly, large power transformers tend to have inrush currents with a slow decay rate since they have a large value of inductance in comparison to the resistances of their primary winding and the connected system.

Consider a series circuit of two transformers, with T feeding T1, as shown in Figure 2.18. When transformer T1 is energized, transformer T experiences sympathetic inrush. The resistance of the line between T and T1 contributes mainly to the decay of the inrush current of T1 (and T) [47], and not the resistance on the primary side of T.

For a parallel connection of two transformers (e.g., Figure 2.17), the sympathetic inrush phenomenon experienced by the transformer already energized is due to the coupling between the transformers on account of the DC voltage drop in the transmission line feeding them. Hence, the higher the transmission line resistance the higher the sympathetic inrush is [48].

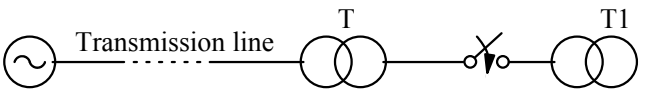

Figure 2.18 Sympathetic inrush in series connection.

D. Inrush under load

If a transformer is switched on with load, the inrush peaks are affected to some extent by the load power factor. Under heavy load conditions with the power factor close to unity, the peak value of the inrush current is lower, and as the power factor reduces (to either lagging or leading), the peak value is higher [32].

2.7.6 Mitigation of inrush current

Inrush currents in saturated core conditions are limited by the air-core reactance of the excited windings and hence they are usually lower than the peak short-circuit currents due to faults. Since transformers are designed to withstand mechanical effects of short-circuit forces, inrush currents may not be considered to be dangerous, although they may unnecessarily cause protective equipment like relays and fuses to operate.

One of the natural ways of reducing inrush currents is to switch-in transformers through a closing resistor. The applied rated voltage is reduced to a low value (e.g., 50%) because of the resistor, thus reducing the inrush current. The resistor is subsequently bypassed to apply the full voltage to the transformer [38, 49]. Its value should be small enough to allow the passage of the normal magnetizing current.

If possible, transformers should be switched from their high voltage side; a higher value of the air core reactance of the outer HV winding (on account of its larger size) reduces the inrush current.

Since residual flux is one of the main reasons for high inrush currents, any attempt to reduce it helps in mitigating the phenomenon. When a transformer is being switched off, if a capacitor of suitable size is connected across it [31], a damped oscillation will result, causing an alternating current to flow in the transformer winding. The amplitude of the current decreases with time, gradually reducing the area of the traversed hysteresis loop, eventually reducing both the current and the residual flux to zero. For small transformers, a variable AC source can be used to demagnetize the core. The applied voltage is slowly reduced to zero for the purpose.

Various schemes for controlled closing at favorable instants have been proposed in [50]. In these methods, each winding is closed when the prospective and dynamic (transient) core fluxes are equal, thus, resulting in an optimal energization without the inrush transients.

2.8 Influence of the Core Construction and Winding Connections on No-Load Harmonic Phenomenon

The excitation current is a small percentage of the rated current in transformers. With the increase in rating of transformers, the percentage no-load current usually reduces. The harmonics in the excitation current may cause interference

with communication systems and result in inadvertent tripping of protective equipment. Due to nonlinear magnetic characteristics, it can be said that:

1) for a sinusoidal applied voltage, the flux is sinusoidal and the magnetizing current is peaky in nature with a pronounced third harmonic component;

2) if the magnetizing current is constrained to have the sinusoidal nature, the flux wave will be flat-topped. The induced voltages in windings will be peaky in nature having a pronounced third harmonic component.

The harmonic phenomenon in a three-phase transformer depends on the type of magnetic circuit (separate or interlinked) and the type of winding connections (star/delta/zigzag). Let us consider the following common cases.

a) *Yy connection* (*isolated neutral*): Since the neutral is isolated, third harmonic currents cannot flow in phases and lines making the magnetizing current almost sinusoidal (if higher harmonics are neglected). This results in a flat-topped flux wave. For transformers having independent magnetic circuits (bank of single-phase transformers), there is a low reluctance magnetic path available (in the form of the end limbs) for the third harmonic flux. Due to the corresponding induced third harmonic voltages in the three phases, the neutral gets shifted. Since the frequency of third harmonic voltages is thrice the fundamental frequency, the neutral voltage also oscillates at three times the fundamental frequency causing fluctuations in the line to neutral voltages. For the third harmonic flux of x % of the fundamental component, the third harmonic voltage is $3x$ % of the fundamental frequency voltage as explained in Section 2.3. This increases voltage stresses due to higher resultant r.m.s. line to neutral voltages. Hence, Yy transformers with independent magnetic circuits are not usually preferred. The behavior of three-phase five-limb transformers is similar to that of banks of single-phase transformers since the third harmonic fluxes can flow in the outer path consisting of the end yokes and end limbs, subject to the condition that the fluxes should not be high enough to cause the saturation of this magnetic path. These disadvantages of a Yy connection are to a large extent overcome in three-phase three-limb transformers. The third harmonic fluxes, which flow in the same direction in all the three phases, have to return through the surrounding non-magnetic paths having high reluctance values. This reduces the fluxes and the associated effects such as neutral instability.

For the same reason, a moderate single-phase load can be supplied between the line and neutral terminals in three-phase three-limb transformers without causing an undue unbalance between the phase voltages. A disadvantage, however, is that the flux returning through the paths outside the core causes additional stray losses in the structural parts.

In star-connected windings, the line-to-line voltages are free of third harmonic components because these components present in the phase to neutral voltages cancel each other. Sometimes a delta-connected tertiary winding is

provided in Yy transformers so that the third harmonic currents can flow in the closed delta, making the flux and voltage waveforms almost sinusoidal.

b) *Yy connection with neutral*: If the system and transformer neutrals are grounded, the third harmonic voltages will practically disappear due to the fact that there is a path available for the third harmonic currents to flow. This connection is equivalent to the application of independent excitations to the three phases. Its main disadvantage is that the third harmonic currents cause interference in communication circuits running parallel to power lines. If a delta-connected tertiary winding is provided, the third harmonic ground currents will be reduced but not completely eliminated; the current shared by the tertiary winding depends on the relative values of the impedances offered by the two paths.

c) *Yd and Dy connections*: Due to the presence of a delta-connected winding, these connections are free of the third harmonic voltage problems associated with the Y connections. The neutral is also stabilized permitting a moderate single-phase load between the line and neutral terminals. For a delta-connected primary winding under a no-load condition, although the phases carry a circulating third harmonic current, the lines are free of it (this is not strictly true because the magnitude of the third harmonic currents in the three phases are not necessarily equal due to the magnetizing asymmetry as described in Section 2.5.1).

2.9 Transformer Noise

Transformers located near residential areas should have sound levels as low as possible. A low noise transformer is being increasingly specified by transformer users; noise levels specified can be 10 to 15 dB lower than the prevailing levels mentioned in the international standards (e.g., NEMA-TR1: Sound levels in transformers and reactors, 1993-R2000). An in-depth understanding of sources of noise is essential for designing low-noise transformers. The core, windings, and cooling equipment are the three main sources of noise in the transformer. The origin of the core noise is discussed in this chapter. The other two sources are discussed in Chapter 10 along with the techniques commonly employed for reducing noise levels.

The core vibrates due to magnetic and magnetostrictive forces. Magnetic forces appear due to non-magnetic gaps at the joints between limbs and yokes. The force per unit cross-sectional area is given as

$$\sigma = \frac{B_m^2}{2\mu_0} = \frac{B_{mp}^2}{4\mu_0}\left(1+\cos 2\omega t\right) \tag{2.39}$$

where B_{mp} is the peak value of the flux density in the gap

μ_0 is the permeability of the free space, and

ω is the fundamental angular frequency.

The magnetic force depends on the kind of interlacing used between the limb and yoke; it is highest when there is no overlapping of the laminations (continuous air gap). The overlapping reduces the flux density (and the force) in the gap, since the flux is shunted away from the gap into the laminations. The magnetic force is less for 90° overlapping (non-mitered joints), which further reduces for 45° overlapping (mitered joints). The step-lap joints give the best noise performance since the flux density in the gap reduces to a very less value as discussed in Section 2.1.2.

The forces produced by the magnetostriction phenomenon are much higher than the magnetic forces in transformers. A change in configuration of a magnetizable material in a magnetic field is due to the magnetostriction phenomenon which leads to periodic changes in the length of the material when subjected to alternating fields. This causes the core to vibrate; the vibrations are transmitted through the oil and tank structure to the surrounding air, which finally results in a characteristic humming sound. The magnetostriction phenomenon is characterized by the coefficient of magnetostriction ε,

$$\varepsilon = \frac{\Delta l}{l} \tag{2.40}$$

where l is the length of the lamination sheet and Δl denotes its change. The coefficient ε depends on the instantaneous value of the flux density according to the expression [51, 52]

$$\varepsilon_{(t)} = \sum_{\upsilon=1}^{n} K_\upsilon B^{2\upsilon} \tag{2.41}$$

where B is the instantaneous value of the flux density, and K_υ denotes coefficients which depend on the level of the magnetization, the type of the lamination material and its treatment.

With the increasing exponent (order number υ), the coefficients K_υ usually are decreasing. The magnetostriction force is given by

$$F = \varepsilon_{(t)} E A \tag{2.42}$$

where E is the modulus of elasticity in the direction of the force and A is the cross-sectional area of the lamination sheet. The previous two equations indicate that the magnetostriction force varies with time and contains even harmonics of the power frequency (120, 240, 360, …, Hz for the power frequency of 60 Hz). Therefore, the noise also contains all harmonics of 120 Hz. The amplitudes of the core vibration and the noise increase manifold if the fundamental mechanical natural frequency of the core is close to 120 Hz. The natural frequencies of the

core can be calculated approximately by analytical/empirical formulae or by a more accurate numerical technique such as the finite element method.

A typical magnetostriction curve is shown in Figure 2.19. Variations in the dimension are not linearly proportional to the flux density. The value of the magnetostriction can be positive or negative, depending on the type of the magnetic material, and the mechanical and thermal treatments. It is usually positive (an increase in the length by a few microns with an increase in the flux density) for CRGO materials at annealing temperatures below 800°C, and as the annealing temperature is increased (≥ 800°C), it can have negative values [53]. Mechanical stresses may change its sign. The magnetostriction coefficient is minimum along the rolling direction and maximum along the 90° direction.

Most of the noise transmitted from the core is from the yoke region because the noise due to vibrations of the limb is effectively damped by the windings surrounding it. Hence, empirical or semi-empirical formulae used for the calculation of the noise level have the yoke flux density as a predominant variable. The quality of yoke clamping has a significant influence on the noise level. Apart from the yoke flux density, other factors which decide the noise level are the limb flux density, the type of the core material, the leg-center (the distance between the centers of two adjacent phases), the core weight, the frequency of operation, etc. The higher the flux density, leg center, core weight and frequency, the higher the noise level is.

The noise level is closely related to the operating peak flux density and the core weight. The change in the noise level as a function of these two factors can be expressed as [54]:

$$\Delta N = 10\ log_{10}\left[\left(\frac{B_2}{B_1}\right)^8\left(\frac{W_2}{W_1}\right)^{1.6}\right]. \tag{2.43}$$

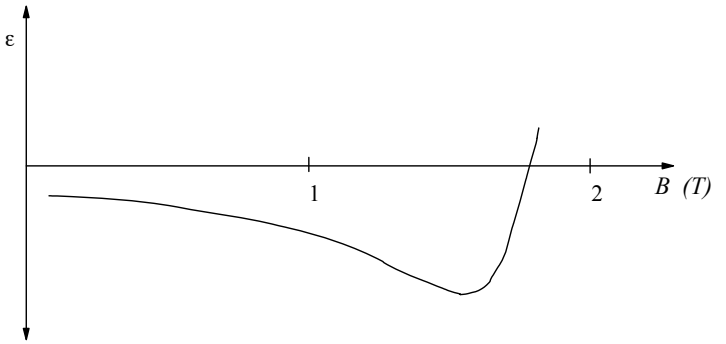

Figure 2.19 Magnetostriction curve.

If the core weight is assumed to change with the flux density approximately in the inverse proportion, for a flux density change from 1.6 T to 1.7 T, the increase in the noise level is 1.7 dB [$\approx 64\, log_{10}(1.7/1.6)$]. Hence, one of the ways of reducing noise is to design the transformer with a lower operating flux density. For a flux density reduction of 0.1 T, the noise level reduction of about 2 dB can be obtained. This method results in an increase of material content and it may be justified economically if the user has specified a higher no-load loss capitalization, in which case the natural choice is to use a lower value of flux density. The use of step-lap joints gives an appreciable noise level reduction (4 to 5 dB). The noise performance of step-lap joints is compared with that of mitered joints in [55]. A reinforced yoke construction (i.e., a higher yoke area as compared to the area of the limb) can also lead to a reduction in the noise level; the method has the advantage that the conductor content does not go up since the mean diameters of the windings do not increase. The bonding of laminations by adhesives and the placement of anti-vibration pads/damping elements between the core and tank can give a further reduction in the noise level. The use of Hi-B/scribed material gives typically a reduction of 2 to 3 dB. When a noise level reduction of the order of 15 to 20 dB is required, some of these methods are necessary but not sufficient, and hence methods involving changes in the structural design are adopted (which are discussed in Chapter 10).

In gapped core shunt reactors, vibrations can be quite high as compared to transformers due to the magnetic forces between consecutive magnetic packets (sections) which are separated by a non-magnetic gap of a few tens of millimeters. The alternating magnetic field in the core is responsible for these pulsating forces which can be calculated by Equation 2.39. Hence, the core is designed to have a high stiffness value to eliminate excessive vibrations. The non-magnetic gaps are created and supported by placing non-magnetic materials such as stone spacers or ceramic blocks having a high modulus of elasticity. The dimensional stability and core tightness can be further ensured by placing an epoxy impregnated polyester material and a fiberglass cloth of 2 to 3 mm between the last limb packet and the top/bottom yoke. These additional components are hardened when subjected to heating cycles during the processing stage, leading to good bonding between the yoke and the limb packet. It should also be ensured that the fundamental mechanical natural frequency of the vibration of the core structure is sufficiently higher than twice the power frequency.

2.10 Rotational Core Losses

The core losses in electromagnetic devices take place by two means. The first one is the alternating power loss which occurs when flux changes cyclically in magnitude, but does not vary in angular direction in space. The second is the rotational loss which occurs when the flux density and magnetic field intensity

vectors rotate in the plane of a lamination. Generally, the loss due to the rotational flux is much higher than that due to the alternating flux [56].

Rotational flux occurs at a T-joint (i.e., intersection of the middle limb and top/bottom yoke) of the core in three-phase three-limb transformers and in back-iron portions of the stator in AC rotating machines. Although the rotational core loss density is higher in T-joints of the transformers due to highly anisotropic nature of the CRGO materials, the contribution of the losses in the total core loss is not substantial because of the smaller volume of the T-joints. On the contrary, the rotational loss density is lower in rotating machines but the % volume of the back-iron portions is high resulting in a significant contribution of the rotational loss in their total core loss.

In the T-joint regions, the flux changes its path at different time instants in a magnetizing cycle because the three limbs are excited by a three-phase source. The rotating flux at a T-joint in a three-phase three-limb core is shown in Figure 2.20(a). The different arrows at a point in the joint region correspond to flux densities at various time instants in an AC cycle. The flux plot has been obtained through 2-D FEM simulations using a commercial software program. It should be noted that in the remaining core portions the flux does not rotate in space as evident from Figure 2.20(b). Variations in the direction are due to flux transfer between laminations or due to rotation in the planes of the laminations [56]. Similar to the case of the alternating core loss, the total rotational core loss density can generally be separated into three components: rotational hysteresis, eddy, and anomalous losses [57],

$$P_r = P_{hr} + P_{er} + P_{ar} \tag{2.44}$$

where, P_r is the rotational loss and P_{hr}, P_{er}, and P_{ar} are the rotational hysteresis, eddy current and anomalous losses per unit volume, respectively.

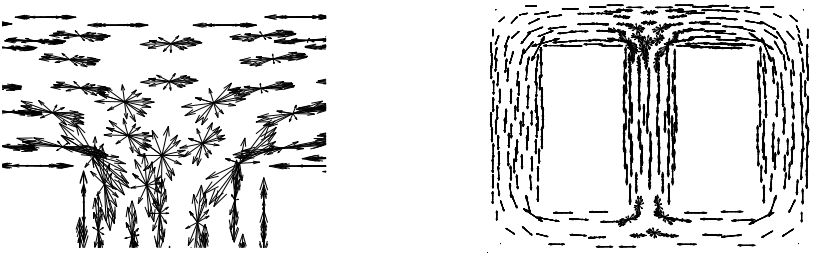

(a) (b)

Figure 2.20 Rotational flux in a T-joint.

For slowly rotating H_r and B_r in the plane of a lamination with an angle θ between the two (B_r lags H_r by θ), the rotational hysteresis loss per unit volume is [56],

$$P_{hr} = \int_0^{2\pi} B_r H_r \sin\theta \, d\alpha \tag{2.45}$$

where, α is the angle that H_r makes with a reference direction.

The rotational eddy current loss per unit volume in thin laminations with a purely circular rotating magnetic flux density can be calculated by [57],

$$P_{er} = 2k_{er}\left(fB\right)^2$$

where, f is the magnetizing frequency and B is the magnitude of the flux density. k_{er} is the coefficient of eddy current loss which is the same for both rotational and alternating eddy current losses ($=\pi^2 d^2/6\rho$).

The rotational anomalous loss can be expressed as [57, 58]

$$P_{ar} = k_{ar}\left(fB\right)^{3/2}$$

where, k_{ar} is the coefficient of the rotational anomalous loss which is a function of flux density; the coefficient reduces to zero in a saturated core condition.

References

1. Baehr, R. Up-to-date possibilities for further improvement of power transformer magnetic circuit features, *International Summer School of Transformers, ISST'93*, Lodz, Poland, 1993.
2. Koppikar, D. A., Kulkarni, S. V., Khaparde, S. A., and Arora, B. A modified approach to overfluxing analysis of transformer, *International Journal of Electrical Power & Energy Systems*, Vol. 20, No. 4, 1998, pp. 235–239.
3. Koppikar, D. A., Kulkarni, S. V., and Khaparde, S. A. Overfluxing simulation of transformer by 3D FEM analysis, *Fourth Conference on EHV Technology*, IISc Bangalore, India, 1998, pp. 69–71.
4. Bean, R. L., Chackan, N., Moore, H. R., and Wentz, E. C. *Transformers for the electric power industry*, McGraw–Hill, New York, 1959, p. 103.
5. Karsai, K., Kerenyi, D., and Kiss, L. *Large power transformers*, Elsevier Publications, Amsterdam, 1987, p. 41.
6. Girgis, R. S., teNijenhuis, E. G., Gramm, K., and Wrethag, J. E. Experimental investigations on effect of core production attributes on transformer core loss performance, *IEEE Transactions on Power Delivery*, Vol. 13, No. 2, April 1998, pp. 526–531.

7. Lofler, F., Pfutzner, H., Booth, T., Bengtsson, C., and Gramm, K. Influence of air gaps in staked cores consisting of several packages, *IEEE Transactions on Magnetics*, Vol. 30, No. 3, March 1994, pp. 913–915.
8. Elleuch, M. and Poloujadoff, M. New transformer model including joint air gaps and lamination anisotropy, *IEEE Transactions on Magnetics*, Vol. 34, No. 5, September 1998, pp. 3701–3711.
9. Mechler, G. F. and Girgis, R. S. Calculation of spatial loss distribution in stacked power and distribution transformer cores, *IEEE Transactions on Power Delivery*, Vol. 13, No. 2, April 1998, pp. 532–537.
10. Olivares, J. C., Kulkarni, S. V., Canedo, J., Driesen, J., and Escarela, R. Impact of joint design parameters on transformer losses, *International Journal of Power and Energy Systems*, Vol. 23, No. 3, 2003, pp. 151–157.
11. teNyenhuis, E. G., Mechler, G. F., and Girgis, R. S. Flux distribution and core loss calculation for single phase and five limb three phase transformer core designs, *IEEE Transactions on Power Delivery*, Vol. 15, No. 1, January 2000, pp. 204–209.
12. Loffler, F., Booth, T., Pfutzner, H., Bengtsson, C., and Gramm, K. Relevance of step–lap joints for magnetic characteristics of transformer cores, *Proceedings IEE – Electrical Power Applications*, Vol. 142, No. 6, November 1995, pp. 371–378.
13. Mechler, G. F. and Girgis, R. S. Magnetic flux distributions in transformer core joints, *IEEE Transactions on Power Delivery*, Vol. 15, No. 1, January 2000, pp. 198–203.
14. Brailsford, F. and Fogg, R. Anomalous iron losses in cold-reduced grain-oriented transformer steel, *Proceedings of IEE*, Vol. 111, 1964, pp. 1463–1467.
15. Bertotti, G. Physical interpretation of eddy current losses in ferromagnetic materials — 1: theoretical consideration, *Journal of Applied Physics*, Vol. 57, 1985, pp. 2110–2117.
16. Chikazumi, S. *Physics of Magnetism,* John Wiley & Sons, Inc., New York, 1964.
17. Pry, R. H. and Bean, C. P. Calculations of energy loss in magnetic sheet material using a domain model, *Journal of Applied Physics*, Vol. 29, 1958, pp. 532–533.
18. Graham, C. D. Physical origin of losses in conducting ferromagnetic materials, *Journal of Applied Physics*, Vol. 53, 1982, pp. 8276–8280.
19. Alexander, G. W., Corbin, S. L., and McNutt, W. J. Influence of design and operating practices on excitation of generator step-up transformers, *IEEE Transactions on Power Apparatus and Systems*, Vol. PAS-85, No. 8, August 1966, pp. 901–909.
20. Gantner, J. and Birch, F. H. Transformer overfluxing protection, *Electra*, No. 31, Report of Working Group 01 of CIGRE Study Committee No. 34 (Protection), pp. 65–74.

21. Camilli, G. A flux voltmeter for magnetic tests, *AIEE Transactions*, 1926, pp. 721–728.
22. Blume, L. F., Boyajian, A., Camilli, G., Lennox, T. C., Minneci, S., and Montsinger, V. M. *Transformer engineering*, John Wiley and Sons, New York, and Chapman and Hall, London, 1951.
23. Arseneau, R. and Moore, W. J. M. A method for estimating the sinusoidal iron losses of a transformer from measurements made with distorted voltage waveforms, *IEEE Transactions on Power Apparatus and Systems*, Vol. PAS-103, No. 10, October 1984, pp. 2912–2918.
24. Tran-Quoc, T. and Pierrat, L. Correction of the measured core losses under distorted flux, *IEEE Transactions on Magnetics*, Vol. 33, No. 2, March 1997, pp. 2045–2048.
25. Walker, C. S. The excitation requirements of 3-phase core-type 3-legged Y-connected transformers, *AIEE Transactions*, December 1957, pp. 1113–1119.
26. Kemp, P. *Alternating current waveforms*, Chapman and Hall Limited, Second Edition, London, 1952.
27. Brailsford, F. Current and power relationships in the measurement of iron losses in a three-limb transformer core, *Proceedings IEE*, Vol. 101, Pt. 2, 1954, pp. 409–416.
28. Parion J. I. Magnetizing asymmetry in three-phase core-type transformers, *Electrical Energy*, July 1957, pp. 330–336.
29. Nene, A. S., Kulkarni, S. V., and Vijayan, K. Asymmetrical magnetizing phenomenon of three phase core type transformers, *International Conference on Transformers*, *TRAFOTECH-1994,* Bangalore, India, January 1994, pp. IV 21–26.
30. McWhirter, J. H., Specht, T. R., and Albright, W. D. Effect of impulse testing on transformer iron loss, *AIEE Transactions*, February 1957, pp. 1275–1279.
31. Blume, L. F., Camilli, G., Farnham, S. B., and Peterson, H. A. Transformer magnetizing inrush currents and influence on system operation, *AIEE Transactions*, Vol. 63, 1944, pp. 366–375.
32. Lin, C. E., Cheng, C. L., Huang, C. L., and Yeh, J. C. Investigation of magnetizing inrush current in transformers —Part I: Numerical simulation, *IEEE Transactions on Power Delivery*, Vol. 8, No. 1, January 1993, pp. 246–254.
33. Finzi, L. A. and Mutschler, W. H. The inrush of magnetizing current in single-phase transformers, *AIEE Transactions*, Vol. 70, 1951, pp. 1436–1438.
34. Yacamini, R. and Abu-Nasser, A. The calculation of inrush currents in three-phase transformers, *Proceedings IEE*, Vol. 133, Pt. B, No. 1, January 1986, pp. 31–40.

35. Macfadyen, W. K., Simpson, R. R. S., Slater, R. D., and Wood, W. S. Method of predicting transient current patterns in transformers, *Proceedings IEE*, Vol. 120, No. 11, November 1973, pp. 1393–1396.
36. Nakra, H. L. and Barton, T. H. Three phase transformer transients, *IEEE PES Winter Meeting*, New York, 1974, Paper T-74-243-2.
37. Rico, J. J., Acha, E., and Madrigal, M. The study of inrush current phenomenon using operational matrices, *IEEE Transactions on Power Delivery*, Vol. 16, No. 2, April 2001, pp. 231–237.
38. Yacamini, R. and Abu-Nasser, A. Transformer inrush currents and their associated overvoltages in HVDC schemes, *Proceedings IEE*, Vol. 133, Pt. C, No. 6, September 1986, pp. 353–358.
39. Specht, T. R. Transformer magnetizing inrush current, *AIEE Transactions*, Vol. 70, 1951, pp. 323–328.
40. Holcomb, J. E. Distribution transformer magnetizing inrush current, *AIEE Transactions*, December 1961, pp. 697–702.
41. Adly, A. A. Computation of inrush current forces on transformer windings, *IEEE Transactions on Magnetics*, Vol. 37, No. 4, July 2001, pp. 2855–2857.
42. Mao, P. L. and Aggarwal, R. K. A novel approach to the classification of the transient phenomenon in power transformers using combined wavelet transform and neural network, *IEEE Transactions on Power Delivery*, Vol. 16, No. 4, October 2001, pp. 654–660.
43. Elmore, W. A. *Protective relaying: theory and applications*, Marcel Dekker, New York, 1994, p. 146.
44. Rudenburg, R. *Transient performance of electric power system,* First Edition, McGraw-Hill Book Company, Inc., 1950, pp. 640–641.
45. Kulkarni, S. V. Influence of system operating conditions on magnetizing inrush phenomenon of transformer, *International Conference on Transformers*, *TRAFOTECH-94,* Bangalore, India, January 1994, pp. VI 19–23.
46. Mason, C. R. *Art and science of protective relaying,* John Wiley & Sons, Inc., New York, 1956, pp. 259–261.
47. Bronzeado, H. and Yacamini, R. Phenomenon of sympathetic interaction between transformers caused by inrush transients, *Proceedings IEE—Science, Measurement and Technology*, Vol. 142, No. 4, July 1995, pp. 323–329.
48. Hayward, C. D. Prolonged inrush currents with parallel transformers affect differential relaying, *AIEE Transactions*, Vol. 60, 1941, pp. 1096–1101.
49. Holmgrem, B., Jenkins, R. S., and Riubrugent, J. Transformer inrush current, *CIGRE 1968*, Paper No. 12-03.
50. Brunke, J. H. and Frohlich, K. J. Elimination of transformer inrush currents by controlled switching—Part I: Theoretical considerations, *IEEE Transactions on Power Delivery*, Vol. 16, No. 2, April 2001, pp. 276–285.

51. Krondl, M. and Kronauer, E. Some contributions to the problem of transformer noise, *Bulletin Oerlikon*, No. 356, pp. 1–15.
52. Majer, K. Evaluation of transformer noise and vibrations, *International Summer School of Transformers, ISST'93*, Lodz, Poland, 1993.
53. Foster, S. L. and Reiplinger, E. Characteristics and control of transformer sound, *IEEE Transactions on Power Apparatus and Systems*, Vol. PAS-100, No. 3, March 1981, pp. 1072–1075.
54. Brandes, D. Noise levels of medium power transformers, *Elektrizitatswirtschaft*, No. 11, 1977.
55. Weiser, B., Pfutzner, B., and Anger, J. Relevance of magnetostriction and forces for the generation of audible noise of transformer cores, *IEEE Transactions on Magnetics*, Vol. 36, No. 5, September 2000, pp. 3759-3777.
56. Moses, A. J. Importance of rotational losses in rotating machines and transformers, *Journal of Material Engineering and Performance*, Vol. 1, 1992, pp. 235–244.
57. Zhu, J. G. and Ramsden, V. S. Improved formulations for rotational core losses in rotating Electrical Machines, *IEEE Transactions on Magnetics,* Vol. 34, 1998, pp. 2234–2242.
58. Fiorillo, F. and Rietto, A. M. Rotational and alternating energy loss vs. magnetization frequency in Si-Fe laminations, *Journal of Magnetism and Magnetic Materials*, Vol. 83, 1990, pp. 402–404.

3

Impedance Characteristics

The leakage impedance of a transformer is one of the most important specifications that has significant impact on its overall design. It consists of resistive and reactive components, and it has been introduced and explained in Chapter 1. This chapter focuses on the reactive component (leakage reactance), whereas Chapters 4 and 5 deal with the resistive component. The load loss (and hence the effective AC resistance) and the leakage impedance are derived from the results of the short-circuit test. The leakage reactance is then calculated from the impedance and the resistance (Section 1.5). Since the resistance is much lower than the reactance in transformers, the latter is almost equal to the leakage impedance.

The material cost of the transformer changes when the specified impedance value is changed. The cost is minimum for a particular value of the impedance when all other specified performance figures are held constant. The impedance value, at which the cost is minimum, varies with the rating and other specifications of the transformer. It will be expensive to design the transformer with an impedance value below or above the optimum. If the impedance is low, short-circuit currents and forces are high, which necessitates use of a lower current density value thereby increasing the material content. On the other hand, a high impedance value increases the eddy loss in the windings and the stray loss in the structural parts significantly resulting in higher values of the load loss and winding/oil temperatures; which again will force the designer to increase the conductor content and/or upgrade the cooling equipment. The percentage impedance, which is specified by transformer users, can be as low as 2% for small distribution transformers and as high as 20% for large power transformers. Impedance values outside this range are specified for special applications.

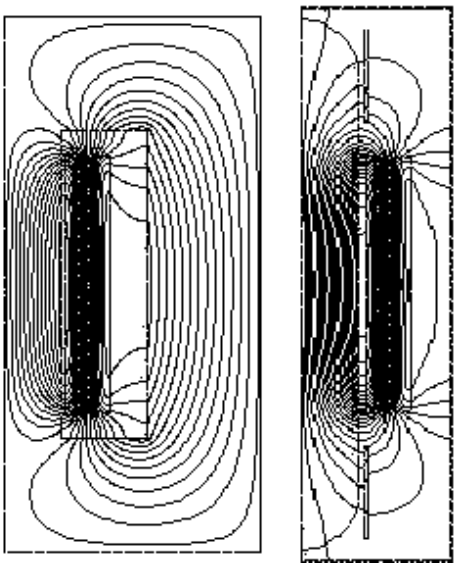

(a) (b)

Figure 3.1 Leakage field in a transformer.

3.1 Reactance Calculation

3.1.1 Concentric primary and secondary windings

A transformer is a 3-D electromagnetic structure with the leakage field appreciably different in the core-window cross section (Figure 3.1 (a)) as compared to that in the cross section perpendicular to the window (Figure 3.1 (b)). Reactance ($\cong$ impedance) values, however, can be estimated reasonably close to test values by considering only the window cross section. A high level of accuracy of 3-D calculations may not be necessary since the tolerance on reactance values is usually in the range of $\pm$ 7.5% or $\pm$ 10%.

For uniformly distributed ampere-turns along the LV and HV windings with equal heights, the leakage field is predominantly axial, except at the winding ends where there is fringing of the leakage flux which returns through a shorter path. A typical leakage field pattern shown in Figure 3.1 (a) can be replaced by a set of parallel flux lines of equal height as shown in Figure 3.2 (a). The equivalent height (H_{eq}) is obtained by dividing the winding height (H_w) by Rogowski factor K_R (<1.0),

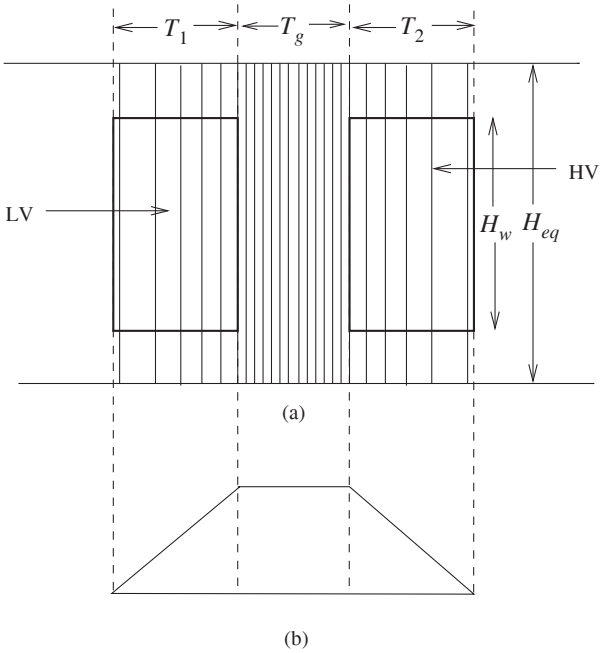

Figure 3.2 (a) Leakage field with equivalent height.
(b) Magnetomotive force or flux density diagram.

$$H_{eq} = \frac{H_w}{K_R}. \tag{3.1}$$

The leakage magnetomotive (mmf) distribution across the cross section of the LV and HV windings is of the trapezoidal form as shown in Figure 3.2 (b). The mmf at any point depends on the ampere-turns enclosed by a flux contour at that point; it increases linearly with the enclosed ampere-turns from a value of zero at the inside diameter of the LV winding to the maximum value of one per-unit (the total ampere-turns of the LV or HV winding) at its outside diameter. In the gap (T_g) between the windings, since the flux contour at any point encloses the entire LV (or HV) ampere-turns, the mmf has a constant value. The mmf starts reducing linearly from the maximum value at the inside diameter of the HV winding until it becomes zero at its outside diameter. The core is assumed to have an infinite permeability value, thus, requiring no magnetizing mmf, and therefore the primary and secondary mmfs exactly balance each other. The flux density distribution is of the same form as that of the mmf distribution. Since the magnetic properties are assumed to be ideal, no mmf is expended in the return path of the flux through the core. Hence, for a closed contour of flux at a distance x from the inside diameter of the LV winding, it can be written that

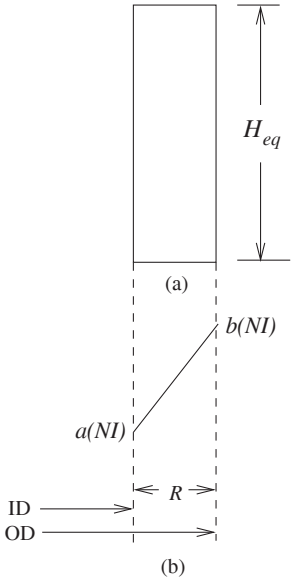

Figure 3.3 (a) Flux tube.
(b) MMF diagram.

$$\left(\frac{B_x}{\mu_0}\right)H_{eq} = (NI)_x \tag{3.2}$$

or

$$B_x = \frac{\mu_0 (NI)_x}{H_{eq}}. \tag{3.3}$$

For deriving the formula for the leakage reactance, let us first obtain a general expression for the flux linkages of a flux tube having the radial depth R and the height H_{eq}. The ampere-turns enclosed by a flux contour at the inside diameter (ID) and outside diameter (OD) of this flux tube are $a(NI)$ and $b(NI)$, respectively as shown in Figure 3.3 (b), where NI are the rated ampere-turns. Such a general formulation is useful when a winding is split radially into a few sections separated by gaps. The r.m.s. value of the flux density at a distance x from the ID of this flux tube can now be inferred from Equation 3.3 as

$$B_x = \frac{\mu_0}{H_{eq}}\left[\left(a + \frac{b-a}{R}x\right)NI\right]. \tag{3.4}$$

The flux linkages of an incremental flux tube of the width dx placed at x are

$$d\psi = N_x \phi_x = N_x B_x A, \tag{3.5}$$

where A is the area of flux tube given by

$$A = \pi(ID + 2x)\,dx\,. \tag{3.6}$$

Substituting Equations 3.4 and 3.6 in Equation 3.5, we obtain

$$d\psi = \left\{\left(a + \frac{b-a}{R}x\right)N\right\}\left\{\frac{\mu_0}{H_{eq}}\left[\left(a + \frac{b-a}{R}x\right)NI\right]\right\}\left[\pi(ID + 2x)dx\right]. \tag{3.7}$$

Hence, the total flux linkages of the flux tube are given by

$$\psi = \int_0^R d\psi = \frac{\mu_0 \pi N^2 I}{H_{eq}} \int_0^R \left(a + \frac{b-a}{R}x\right)^2 (ID + 2x)dx\,. \tag{3.8}$$

After integration and a few arithmetic operations, we obtain

$$\psi = \frac{\mu_0 \pi N^2 I}{H_{eq}} \frac{R}{3}\left[(a^2 + ab + b^2)ID + \frac{(a^2 + ab + b^2)3R}{2} - \frac{2a^2 + ab}{2}R\right]. \tag{3.9}$$

The last term in the square bracket can be neglected without introducing an appreciable error to arrive at a simple formula for the regular design use,

$$\psi = \frac{\mu_0 \pi N^2 I}{H_{eq}} \frac{R}{3}(a^2 + ab + b^2)\left[ID + \frac{3R}{2}\right]. \tag{3.10}$$

The term $\left[ID + \frac{3R}{2}\right]$ is approximately equal to the mean diameter (D_m) of the flux tube for large diameters of windings/gaps with comparatively lower values of their radial depths.

$$\therefore \psi = \frac{\mu_0 \pi N^2 I}{H_{eq}} \frac{R}{3}(a^2 + ab + b^2)\,D_m\,. \tag{3.11}$$

Now, let

$$ATD = \frac{R}{3}(a^2 + ab + b^2)\,D_m \tag{3.12}$$

which corresponds to the area of the mmf (ampere-turns) diagram. The leakage inductance of a transformer with n flux tubes can now be given as

$$L = \frac{\sum_{k=1}^{n} \psi}{I} = \frac{\mu_0 \pi N^2}{H_{eq}} \sum_{k=1}^{n} ATD\,, \tag{3.13}$$

and the corresponding expression for the leakage reactance X is

$$X = 2\pi f \frac{\mu_0 \pi N^2}{H_{eq}} \sum_{k=1}^{n} ATD. \tag{3.14}$$

The percentage leakage reactance, with the base impedance as Z_b, is given by

$$\begin{aligned} \%X &= \frac{X}{Z_b} \times 100 = \frac{IX}{V} \times 100 = 2\pi f \frac{\mu_0 \pi IN^2}{H_{eq} V} \sum_{k=1}^{n} ATD \times 100 \\ &= 2\pi f \frac{\mu_0 \pi (NI)}{H_{eq} (V/N)} \sum_{k=1}^{n} ATD \times 100 \end{aligned} \tag{3.15}$$

where V is the rated voltage and the term (V/N) is volts/turn of the transformer. Substituting $\mu_0 = 4\pi \times 10^{-7}$ and adjusting the constants so that the dimensions used in the formula are in units of centimeters (H_{eq} in cm and $\sum ATD$ in cm^2), we obtain

$$\%X = 2.48 \times 10^{-5} f \frac{(Ampere\ Turns)}{H_{eq}(Volts/Turn)} \sum_{k=1}^{n} ATD. \tag{3.16}$$

After having derived the general formula, we will now apply it for a simple case of a two winding transformer shown in Figure 3.2. The constants a and b have the values of 0 and 1 for the LV winding, 1 and 1 for the gap, and 1 and 0 for the HV winding, respectively. If D_1, D_g and D_2 are the mean diameters and T_1, T_g, and T_2 are the radial depths of the LV winding, the gap and the HV winding, respectively, using Equation 3.12 we have

$$\sum ATD = \frac{1}{3}(T_1 \times D_1) + (T_g \times D_g) + \frac{1}{3}(T_2 \times D_2). \tag{3.17}$$

The value of H_{eq} is calculated by Equation 3.1, for which the Rogowski factor K_R is given by

$$K_R = 1 - \frac{1 - e^{-\pi H_w / (T_1 + T_g + T_2)}}{\pi H_w / (T_1 + T_g + T_2)}. \tag{3.18}$$

For taking into account the effect of the core, a more accurate but complex expression for K_R can be used as given in [1]. For most cases, Equation 3.18 gives sufficiently accurate results.

For autotransformers, transformed ampere-turns should be used in Equation 3.16 (the difference between the turns corresponding to the phase voltages of the HV and LV windings multiplied by the HV winding current) and the calculated impedance is multiplied by the autofactor,

$$K_A = 1 - \frac{V_{LV}}{V_{HV}} \tag{3.19}$$

where V_{LV} and V_{HV} are the rated line voltages of the LV and HV windings respectively.

3.1.2 Sandwich windings

The reactance formula derived in the previous section can also be used for sandwich windings in core- or shell-type transformers with slight modifications. Figure 3.4 shows a configuration of such windings with two sections. The mean diameter of the windings is denoted by D_m. If there are N turns and S sections in the windings, then remembering the fact that the reactance is proportional to the square of turns, the reactance between the LV and HV windings corresponding to any one section (having N/S turns) is given by

$$\%X_S = 2.48\times10^{-5} f \frac{NI}{H_{eq}(V/N)} \frac{1}{S^2} \sum_{k=1}^{n} ATD \tag{3.20}$$

where

$$\sum_{k=1}^{n} ATD = \frac{1}{3}(T_1 \times D_m) + (T_g \times D_m) + \frac{1}{3}(T_2 \times D_m) = D_m\left[T_g + \frac{T_1 + T_2}{3}\right]. \tag{3.21}$$

If the sections are connected in series, the total reactance is S times that of a single section,

$$\%X = 2.48\times10^{-5} f \frac{NI}{H_{eq}(V/N)} \frac{1}{S} \sum_{k=1}^{n} ATD\,. \tag{3.22}$$

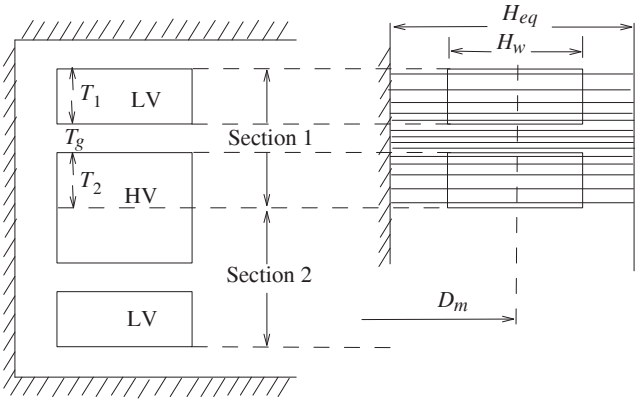

Figure 3.4 Sandwich winding.

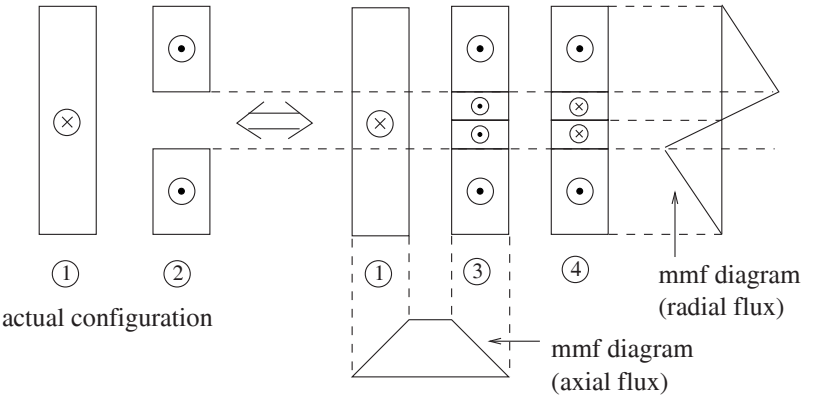

Figure 3.5 Unequal AT/m distribution.

Similarly, if the sections are connected in parallel, the formula can be derived by taking the number of turns as N and the current as I/S for a single section.

3.1.3 Concentric windings with nonuniform distribution of ampere turns

Since varying amounts of turns in the tap winding are excluded at different tap positions, the ampere-turns per unit height (AT/m) of the LV winding differ from those of the HV winding in the tap zone. This results in a higher amount of radial flux in such zones. When taps are in the main body of a winding (i.e., no separate tap winding), it is preferable to put taps symmetrically in the middle or at the ends of the winding to minimize the radial flux. If taps are provided only at one end, the arrangement causes an appreciable asymmetry and a higher radial component of the leakage flux resulting into increased eddy losses and axial short-circuit forces. For different values of AT/m along the height of the LV and HV windings, the reactance can be calculated by resolving the AT distribution as shown in Figure 3.5. The effect of the gap in winding 2 can be accounted for by replacing it with windings 3 and 4. Winding 3 has the same AT/m distribution as that of winding 1, and winding 4 has AT/m distribution such that the addition of the ampere-turns of windings 3 and 4 along their height gives the same ampere-turns as that of winding 2. The total reactance is the sum of the two reactances, the reactance between windings 1 and 3 calculated by Equation 3.16 and the reactance of winding 4 calculated by Equation 3.22 (for the sections connected in series).

Since Equation 3.22 always gives a finite positive value, a nonuniform AT distribution (unequal AT/m of the LV and HV windings) always results in a higher value of the reactance. An increased value of the reactance can be correlated with the fact that the effective height of the windings in Equation 3.16 is reduced if we take the average of the heights of windings 1 and 2. For

example, if the tapped-out section in one of the windings is 5% of the total height at the tap position corresponding to the rated voltage, the average height is reduced by 2.5%, giving an increase in the reactance of 2.5% compared to the case of the uniform AT/m distribution.

3.2 Different Approaches for Reactance Calculation

The first approach is based on the fundamental definition of the inductance of a coil, i.e., flux linkages (ψ) per unit current (I),

$$L = \frac{\psi}{I} = \frac{N\phi}{I} \tag{3.23}$$

and this approach has been used in Section 3.1 for finding the leakage inductance (Equations 3.13).

In another energy-based approach, it is calculated as

$$L = \frac{2\,W_m}{I^2} \tag{3.24}$$

where W_m is the stored magnetic energy by the current I flowing in a closed path. Now, we will see that the use of Equation 3.24 leads us to the same formula of the reactance as given by Equation 3.16.

The energy per unit volume in the magnetic field in the free space, with linear magnetic characteristics ($H = B/\mu_0$), when the flux density is increased from 0 to B, is

$$w = \int_0^B H\, dB = \int_0^B \frac{B}{\mu_0}\, dB = \frac{B^2}{2\mu_0}. \tag{3.25}$$

A detailed discussion on the magnetic energy is available in Chapter 12. The differential energy dW_x for a cylindrical ring of height H_{eq}, thickness dx and diameter ($ID + 2x$) is

$$dW_x = \frac{B_x^2}{2\mu_0} \times (volume\ of\ cylindrical\ ring) = \frac{B_x^2}{2\mu_0} \pi\ (ID + 2x)\ H_{eq}\ dx\,. \tag{3.26}$$

Now the value of B_x can be substituted from Equation 3.4 for the simple case of the flux tube with $a = 0$ and $b = 1$ (with reference to Figure 3.3),

$$dW_x = \frac{\mu_0 \pi (NI)^2 x^2 (ID + 2x) dx}{2\,R^2 H_{eq}}. \tag{3.27}$$

For the winding configuration of Figure 3.2, the total energy stored in the LV winding (with the term R replaced by the radial depth T_1 of the LV winding) is

$$W_1 = \frac{\mu_0 \pi (NI)^2}{2 T_1^2 H_{eq}} \int_0^{T_1} x^2 (ID + 2x) dx = \frac{\mu_0 \pi (NI)^2}{2 H_{eq}} \frac{1}{3} \left\{ ID + \frac{3T_1}{2} \right\} T_1 . \qquad (3.28)$$

As seen in Section 3.1.1, the term in the brackets can be approximated as the mean diameter (D_1) of the LV winding to obtain

$$W_1 = \frac{\mu_0 \pi (NI)^2}{2 H_{eq}} \frac{1}{3} D_1 T_1 . \qquad (3.29)$$

Similarly, the energy in the HV winding can be calculated as

$$W_2 = \frac{\mu_0 \pi (NI)^2}{2 H_{eq}} \frac{1}{3} D_2 T_2 . \qquad (3.30)$$

Since the flux density is constant in the gap between the windings, the energy in it can be directly calculated as

$$W_g = \frac{B_g^2}{2\mu_0} \times (volume\ of\ cylindrical\ gap) = \frac{1}{2\mu_0} \left[\frac{\mu_0 (NI)}{H_{eq}} \right]^2 \pi D_g T_g H_{eq} \qquad (3.31)$$

$$\therefore W_g = \frac{\mu_0 \pi (NI)^2}{2 H_{eq}} D_g T_g . \qquad (3.32)$$

Substituting the values of the energies from Equations 3.29, 3.30 and 3.32 in Equation 3.24, we have

$$L = \frac{2 W_m}{I^2} = \frac{2 (W_1 + W_2 + W_g)}{I^2} = \frac{\mu_0 \pi N^2}{H_{eq}} \left[\frac{1}{3} (T_1 D_1 + T_2 D_2) + T_g D_g \right] . \qquad (3.33)$$

If the term in the brackets is substituted by $\sum ATD$ according to Equation 3.17, we see that the above expression derived from the energy viewpoint is the same as that in Equation 3.13 obtained from the flux linkages.

In yet another approach, when numerical methods like finite element method (FEM) are used, the field solution is usually obtained in terms of the magnetic vector potential, and the leakage inductance is given as

$$L = \frac{1}{I^2} \int_{vol} \mathbf{A} \cdot \mathbf{J}\, dv , \qquad (3.34)$$

where **A** is the magnetic vector potential and **J** is the current density vector. Equation 3.34 can be derived [2] from Equation 3.24,

$$L = \frac{2\,W_m}{I^2} = \frac{1}{I^2}\int_{vol} \mathbf{B}\cdot\mathbf{H}\; dv = \frac{1}{I^2}\int_{vol} \mathbf{A}\cdot\mathbf{J}\; dv\,. \tag{3.35}$$

The leakage reactance between two windings in a transformer can also be calculated as

$$X_{12} = X_1 + X_2 - 2M_{12} \tag{3.36}$$

where X_1 and X_2 are the self reactances of the windings and M_{12} is the mutual reactance between them. It is difficult to calculate the self and mutual reactances which depend on saturation effects. Also, since the values of $(X_1 + X_2)$ and $2M_{12}$ are nearly equal and are much higher than the leakage reactance X_{12}, a small error in the calculation of them results in a large error in the estimation of X_{12}. Hence, it is always easier to calculate the leakage reactance of a transformer directly instead of using the formulae in terms of the self and mutual reactances. Therefore, for finding the effective leakage reactance of a system of windings, the total power of the system is expressed in terms of the leakage impedances instead of the self and mutual impedances. Consider a system of windings 1, 2, …, n, with the leakage impedances Z_{jk} between the pairs of the windings j and k. For a negligible magnetizing current (as compared to the rated currents in the windings) the total power can be expressed as [3]

$$P + jQ = -\frac{1}{2}\sum_{k=1}^{n}\sum_{j=1}^{n} \hat{Z}_{jk}\,\hat{I}_j\,\hat{I}_k^* \tag{3.37}$$

where $\hat{I}_k^*$ is the complex conjugate of $\hat{I}_k$. Winding resistances can be neglected in comparison with much larger leakage reactances. When the current vectors of the windings are parallel (in phase or phase-opposition), the expression for Q (which is given by the imaginary part of the previous equation) becomes

$$Q = \mathrm{Im}\left[-\frac{1}{2}\sum_{k=1}^{n}\sum_{j=1}^{n} \hat{Z}_{jk}\,\hat{I}_j\,\hat{I}_k^*\right] = -\frac{1}{2}\sum_{k=1}^{n}\sum_{j=1}^{n} X_{jk}\,I_j\,I_k\,. \tag{3.38}$$

Equation 3.38 gives the total reactive volt-amperes consumed by all the leakage reactances of the system of the windings. The effective or equivalent leakage reactance of the system of n windings, referred to the source (primary) winding carrying the current I_p, is given by

$$X_{eff} = \frac{Q}{I_p^2} \quad \text{in } \Omega. \tag{3.39}$$

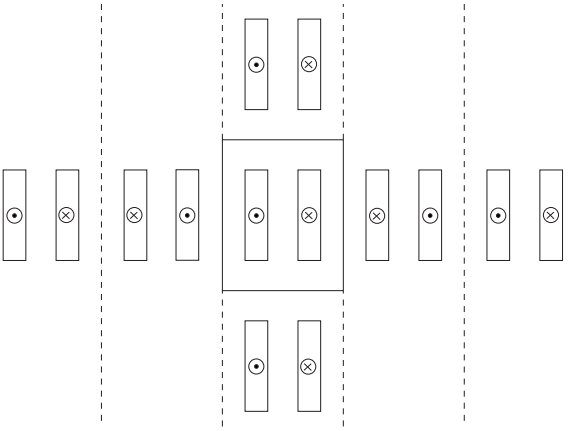

Figure 3.6 Method of images.

If the currents and X_{jk} are expressed in per-unit in Equation 3.38, the value of Q (calculated when the rated current flows in the primary winding) gives directly the per-unit reactance of the transformer consisting of n windings. The use of this reactive KVA approach is illustrated in Sections 3.6 and 3.7.

3.3 Analytical Methods

The classical method described in Section 3.1 has certain limitations. The effect of the core is neglected and it is tedious to take into account axial gaps in windings and asymmetries in distributions of ampere-turns. Some of the more commonly used analytical methods, which overcome these difficulties, are now described. The leakage reactance calculation by more accurate numerical methods (e.g., FEM) is described in Section 3.4.

3.3.1 Method of images

When computers were not available, many attempts were made to devise accurate methods of calculating axial and radial components of the leakage field, and subsequently the leakage reactance. A popular approach was to use simple Biot-Savart's law with the effect of the iron core taken into account by the method of images. The method basically works in the Cartesian (x-y) coordinate system in which windings are represented by straight coils (assumed to be of infinite dimensions along the z-axis perpendicular to the plane of the paper) placed at appropriate distances from a plane surface bounding a semi-infinite mass of infinite permeability. The effect of the iron core is represented by the images of the coils as far behind the surface as they are in the front. Parallel planes have to be added as shown in Figure 3.6 to obtain accurate results, which leads to an arrangement of infinite images in all the four directions [4]. All these

coils should give the same value of the leakage field at any point as that with the original geometry of the two windings enclosed by the iron boundary. New planes (mirrors) can be added, one at a time, until the difference between the successive solutions is negligible; usually the first three or four images are sufficient. Biot-Savart's law is then applied to this arrangement of the current distributions, which is devoid of the magnetic mass (iron), to find the value of the leakage field at any point.

3.3.2 Roth's method

A method based on double Fourier series, originally proposed by Roth, was extended in [5] to calculate the leakage reactance for an irregular arrangement of windings. The advantage of this method is that it is applicable to uniform as well as nonuniform distributions of ampere-turns of windings. The arrangement of windings in the core window can be entirely arbitrary but it should be divisible into rectangular blocks, each block having a uniform current density distribution within itself.

In this method, the core window is considered as π radians wide and π radians long, regardless of its absolute dimensions. The ampere-turn density distribution as well as the flux distribution is conceived to be consisting of components which vary harmonically along both the x and y axes. The method uses a principle similar to that of the method of images; for every harmonic the maximum value occurs at fictitious planes about which mirroring is done to simulate the effect of the iron boundary. Reactive volt-amperes (I^2X) are calculated in terms of these current harmonics for a depth of unit dimension in the z direction. The total volt-amperes are obtained by multiplying the calculated values by corresponding mean perimeters. The per-unit value of the leakage reactance is calculated by dividing I^2X by the base volt-amperes. For a reasonable accuracy, the number of space harmonics in the double Fourier series should be at least equal to 20 when the ampere-turns are symmetrically distributed in the LV and HV windings [6]. The accuracy is better with a higher number of space harmonics. Figure 3.7 shows plots of the radial flux density along the height of a transformer winding. As the number of the space harmonics is increased, the variation of the flux density becomes smooth indicating a better accuracy.

3.3.3 Rabin's method

If the effect of curvatures of the windings needs to be taken into account in Roth's formulation, the method becomes complicated, and in that case Rabin's method is more suitable [4, 7]. It solves the following Poisson's equation in cylindrical coordinates,

$$\nabla^2 \mathbf{A} = -\mu \mathbf{J} \tag{3.40}$$

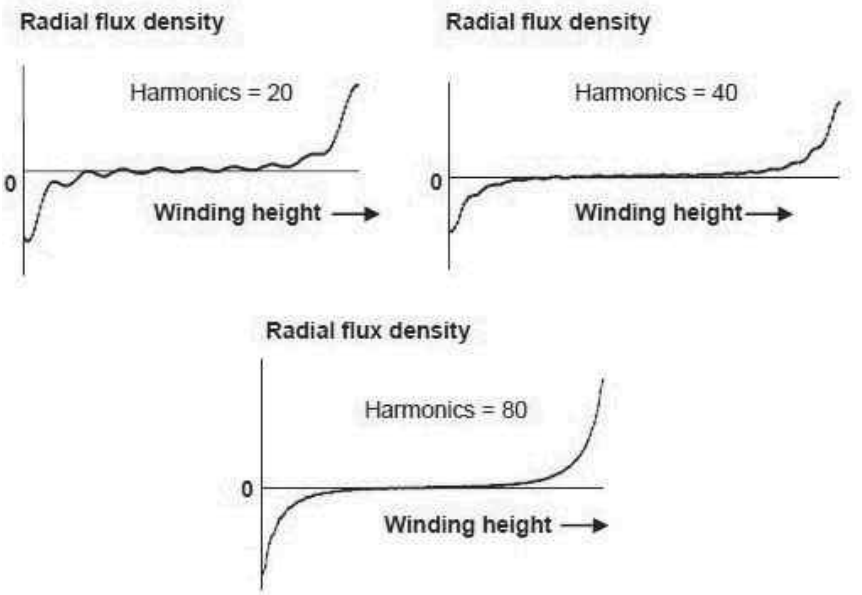

Figure 3.7 The effect of the number of space harmonics on the accuracy.

where **A** is the magnetic vector potential and **J** is the current density having only the angular component. Therefore, in cylindrical coordinates the equation becomes

$$\frac{\partial^2 A_\theta}{\partial r^2} + \frac{1}{r}\frac{\partial A_\theta}{\partial r} - \frac{A_\theta}{r^2} + \frac{\partial^2 A_\theta}{\partial z^2} = -\mu\, J_\theta \,. \tag{3.41}$$

In this method, the current density is assumed to depend only on the axial position and hence can be represented by a single Fourier series with coefficients which are Bessel and Struve functions. For a reasonable accuracy, the number of space harmonics should be about 70 [6].

3.4 Numerical Method for Reactance Calculation

The finite element method (FEM) is the most commonly used numerical method for the reactance calculation of nonstandard configurations of windings and asymmetrical/nonuniform distributions of ampere-turns, which cannot be easily and accurately handled by the classical method given in Section 3.1. The FEM analysis can be more accurate than the analytical methods described in Section 3.3. User-friendly commercial FEM software packages are now available. A 2-D FEM analysis can be integrated into routine design calculations. The main

advantage of FEM is that any complex geometry can be analyzed since its formulation depends only on the class of problem and is independent of geometrical details. It can also take into account material discontinuities easily. The theory of the FEM technique and its applications to transformers are elaborated in Chapter 12. Here, the technique is briefly illustrated when applied to calculate the leakage reactance of a transformer.

The problem geometry is divided into small elements [8, 9]. Within each element, the flux density is assumed constant so that the magnetic vector potential varies linearly within each element (a first order approximation); in Cartesian coordinates the potential can be approximated as

$$A = a + b\,x + c\,y\,. \tag{3.42}$$

For a better accuracy, the potential can be assumed to vary as a polynomial of a degree higher than one. The elements are generally of triangular or tetrahedral shape. The windings are modeled as rectangular blocks; if the distribution of ampere-turns is not uniform, they are divided into suitable sections so that the current density in each section is uniform. A typical configuration of the LV and HV windings in a transformer is shown in Figure 3.8. The main steps involved in the analysis are now outlined.

1. ***Creation of geometry***: The geometry shown in Figure 3.8 is simple. In case of complex 2-D or 3-D geometries, many commercial FEM programs allow the import of figures drawn in drafting packages, which makes it easier and less time consuming to create geometries. The problem domain has to be always bounded by a boundary (e.g., *abcda* in Figure 3.8). 2-D problems can be solved either in Cartesian or cylindrical coordinates. Since transformers are 3-D structures, both the systems lead to approximations and corresponding errors.

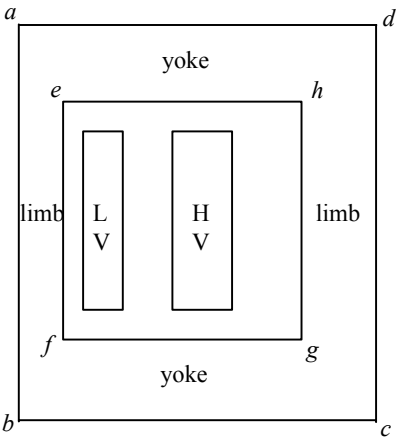

Figure 3.8 Geometry for FEM analysis.

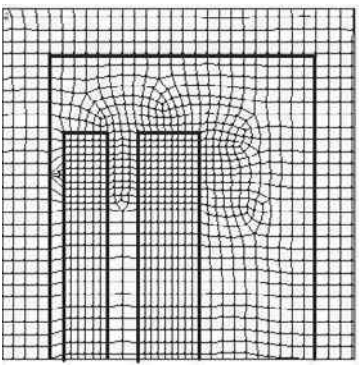

Figure 3.9 FEM mesh.

However, they give reasonably accurate results when used to calculate the leakage reactance in two dimensions. In the cylindrical coordinate system, line *ab* represents the axis (center line) of the core and the horizontal distance between the lines *ab* and *ef* equals half the core diameter.

2. ***Meshing***: This step involves division of the geometry into small elements. For most accurate results, sizes of the elements should be as small as possible if the first order approximation is used. Thus, logically the element (mesh) size should be small only in the regions where there are significant variations in values of the flux density. Such an intelligent meshing reduces the number of elements and the computation time. An inexperienced person may not always know the regions where the solution changes significantly; hence a solution with a coarse mesh can be obtained first, and then the mesh can be refined in the regions where the solution is changing rapidly. Ideally, one has to go on refining the mesh until there is no appreciable change in the value of the solution (the flux density in this case) at any point in the geometry. For the problem domain in Figure 3.8, the radial component of the flux density changes considerably at the ends of the windings, necessitating the use of a finer mesh in these regions as shown in Figure 3.9.

3. ***Material properties***: The relative permeability (μ_r) of the core is specified as a few tens of thousands. It really does not matter whether we define it as 10000 or 50000 because almost all the energy is stored in the nonmagnetic regions (μ_r =1) outside the core. While estimating the leakage reactance, the ampere-turns of the LV and HV windings are assumed to be exactly equal and opposite (the no-load current is neglected), and hence according to Ampere's circuital law there is not a single flux contour in the core enclosing both the windings (see Chapter 12 for a detailed discussion). Other parts, including windings, are defined with μ_r of 1. It should be remembered that copper/aluminum is a non-magnetic material. Here, the conductivity of the winding material is not defined

since the effect of eddy currents in winding conductors on the leakage field is usually neglected in the reactance calculation; the problem is solved as a magnetostatic problem. Individual conductors/turns may have to be modeled for the estimation of circulating currents in parallel conductors, which is a subject of discussion in Chapter 4.

4. ***Source definition***: In this step, the density of ampere-turns for each winding or section is defined (i.e., the ampere-turns divided by the cross-sectional area).

5. ***Boundary conditions***: There are two types of boundary conditions, viz., Dirichlet and Neumann. When a potential value is prescribed on a boundary, it is called the Dirichlet boundary condition. In the present case, the Dirichlet condition is defined for the boundary *abcda* (flux lines are parallel to this boundary) with the value of the magnetic vector potential taken as zero for convenience. It should be noted that a contour passing through equal values of the magnetic vector potential is a flux line. A boundary, on which the normal derivative of a potential is specified, is said to have the Neumann condition. Flux lines cross perpendicularly at these boundaries. A boundary on which the Dirichlet condition is not defined, the Neumann condition gets automatically specified in the FEM formulation. If the core is not modeled, no magnetic vector potential should be defined on the boundary *efgh* (iron-air boundary). The flux lines then impinge perpendicularly on this boundary, which is in line with the valid assumption that the core is infinitely permeable for the problem under consideration. When the core is not modeled, one reference potential may have to be defined; zero potential can be specified at a point in the gap between the two windings along their center line in the present case.

6. ***Solution***: Formations of element level coefficient matrices, the assembly of the global coefficient matrix and the imposition of boundary conditions are done in this step; commercial FEM programs do these things internally. For a detailed explanation of the FEM procedure, refer to Chapter 12.

7. ***Post-processing***: A leakage field plot (Figure 3.1a) can be obtained and studied in this step. The total stored energy is calculated as

$$W_m = \frac{1}{2} \int_{vol} \mathbf{A} \cdot \mathbf{J} \, dv \, . \tag{3.43}$$

If the problem is solved in Cartesian coordinates, the energy per unit length in the z direction is obtained. In order to obtain the total energy, the magnitude of the energy for each section of the geometry is multiplied by the corresponding mean turn length (i.e., $\pi \times$ mean diameter). Finally, the leakage inductance can be calculated using Equation 3.24.

Example 3.1

Relevant dimensions (in mm) of a 31.5 MVA, 132/33 kV, 50 Hz, Yd1 transformer are indicated in Figure 3.10. The value of volts/turn is 76.21. The transformer is having 0% to +10% taps on the HV winding. It is having a linear-type on-load tap changer; 10% tapping turns are placed symmetrically in the middle of the HV winding for giving the total voltage variation of 10%. It is required to calculate the leakage reactance of the transformer at the nominal tap position (corresponding to the HV voltage of 132 kV) by the classical method and the FEM analysis.

Solution:

We will calculate the leakage reactance by the method given in Section 3.1.3 as well as by the FEM analysis.

1. Classical method

At the nominal tap position, TAP winding has zero ampere-turns since all its turns are cut out of the circuit. This results into an unequal AT/m distribution between the LV and HV windings along their heights.

$$\text{HV current} = \frac{31.5\times10^6}{\sqrt{3}\times132\times10^3} = 137.78 \text{ A.}$$

$$\text{HV turns} = \frac{132\times10^3/\sqrt{3}}{76.21} = 1000 \text{ and LV turns} = \frac{33\times10^3}{76.21} = 433 .$$

The HV winding is replaced by a winding (HV1) with uniformly distributed ampere-turns (1000 turns are distributed uniformly along the height of 1260 mm) and a second winding (HV2) having the distribution of ampere-turns such that the superimposition of the ampere-turns of both the windings gives that of the original HV winding.

We will first calculate the reactance between the LV and HV1 windings by using the procedure given in Section 3.1.

$$T_1 = 7.0 \text{ cm}, \; T_2 = 5.0 \text{ cm}, \; T_3 = 10.0 \text{ cm}, \; H_w = 126.0 \text{ cm} .$$

Equations 3.18 and 3.1 give

$$K_R = 0.944 \quad \text{and} \quad H_{eq} = H_w / K_R = 126/0.944 = 133.4 \text{ cm} .$$

The term $\sum ATD$ is calculated as per Equation 3.17,

$$\sum ATD = \frac{1}{3}\times7.0\times67.6 + 5.0\times79.6 + \frac{1}{3}\times10.0\times94.6 = 871.1 \text{ cm}^2 .$$

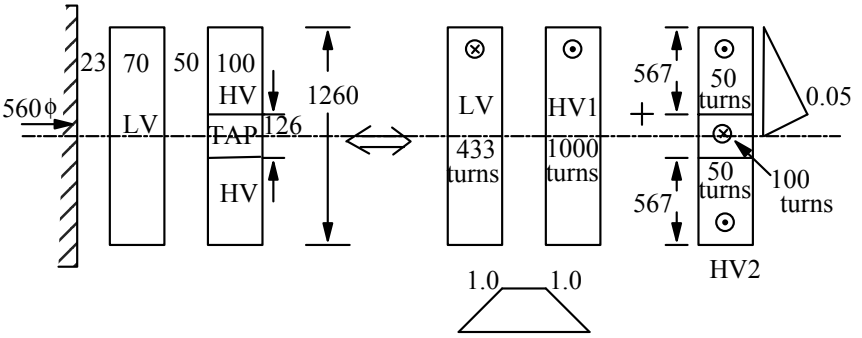

Figure 3.10 Details of the transformer in Example 3.1.

The leakage reactance can be calculated from Equation 3.16 as

$$X_{\text{LV\_HV1}} = 2.48\times10^{-5}\times50\times\frac{(137.78\times1000)}{133.4\times76.21}\times871.1 = 14.64\%\,.$$

The winding HV2 is made up of two sections. The AT diagram for the top section is shown in Figure 3.10. The section has two windings, each having ampere-turns of 0.05 per-unit [$=(50\times137.78)/(1000\times137.78)$]. For this section,

$$T_1 = 56.7 \text{ cm}, T_g = 0.0 \text{ cm}, T_2 = 6.3 \text{ cm}, H_w = 10.0 \text{ cm}\,.$$

It is to be noted here that the winding height for the calculation is the dimension in the radial direction, which is equal to 10.0 cm. Equations 3.18 and 3.1 give

$$K_R = 0.213 \text{ and } H_{eq} = H_w/K_R = 10/0.213 = 47.0 \text{ cm}\,.$$

The term ATD is calculated for each part using Equation 3.12, the corresponding values of a and b, and the mean diameter of the HV winding,

$$\sum ATD = \frac{56.7}{3}\times0.05^2\times94.6 + 0.0\times0.05^2\times94.6 + \frac{6.3}{3}\times0.05^2\times94.6 = 5.0\,.$$

The leakage reactance of the section can be calculated from Equation 3.16 as

$$X_S = 2.48\times10^{-5}\times50\times\frac{(137.78\times1000)}{47.0\times76.21}\times5.0 = 0.24\%\,.$$

The HV2 winding comprises of two such sections connected in series. Hence, the total reactance contributed by the HV2 winding is two times the reactance of a single section as explained in Section 3.1.2.

$$\therefore X_{\text{HV2}} = 2\times0.24 = 0.48\%\,.$$

Therefore, the total reactance is

$$X = X_{\text{LV\_HV1}} + X_{\text{HV2}} = 14.64 + 0.48 = 15.12\% .$$

2. FEM analysis

The analysis is done as per the steps outlined in Section 3.4. The winding to yoke distance is 130 mm for this transformer. The stored energies in the different parts of the geometry as given by the FEM analysis are:

LV winding:	438 J
HV winding:	773 J
HV winding - center gap:	87 J
Remaining portion:	1205 J

The energy stored in the core is negligible; the total energy obtained is 2503 J. Using Equation 3.24, the leakage inductance is calculated as

$$L = \frac{2 \times 2503}{(137.78)^2} = 0.264 \text{ H.}$$

The value of the base impedance is

$$Z_b = \frac{\text{kV}^2}{\text{MVA}} = \frac{132^2}{31.5} = 553.1\ \Omega .$$

$$\therefore X = \frac{2\pi \times 50 \times L}{Z_b} \times 100 = \frac{2\pi \times 50 \times 0.264}{553.1} \times 100 = 15.0\% .$$

Thus, the values of the leakage reactance given by the classical method and the FEM analysis are in close agreement.

Example 3.2

Calculate the leakage reactance of a transformer having 10800 ampere-turns in each of the LV and HV windings. The rated voltage and current of the LV winding are 415 V and 300 A, respectively. The two windings are sandwiched into 4 sections as shown in Figure 3.11. Relevant dimensions (in mm) are given in the figure. The value of volts/turn is 11.527. The mean diameter of the windings is 470 mm.

Solution:

The leakage reactance will be calculated by the method given in Section 3.1.2 and the FEM analysis.

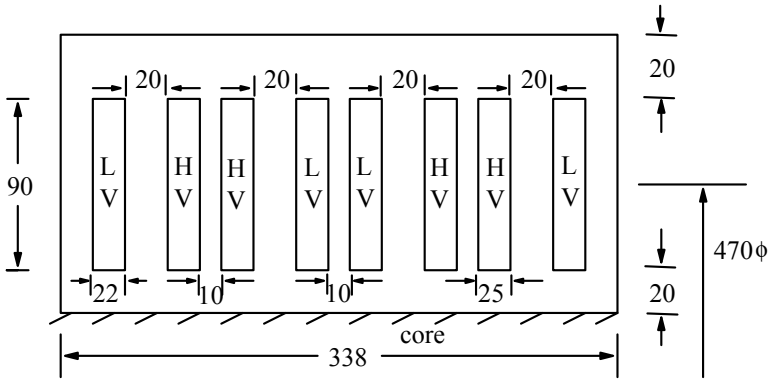

Figure 3.11 Details of the transformer in Example 3.2.

1. Classical method

The whole configuration consists of four sections, each having 1/4 part of both the LV and HV windings. For each section,

$$T_1 = 2.2 \text{ cm},\ T_g = 2.0 \text{ cm},\ T_2 = 2.5 \text{ cm},\ H_w = 9.0 \text{ cm}.$$

Equations 3.18 and 3.1 give

$$K_R = 0.767 \text{ and } H_{eq} = H_w / K_R = 9/0.767 = 11.7 \text{ cm}.$$

The term $\sum ATD$ is (Equation 3.17)

$$\sum ATD = \frac{1}{3} \times 2.2 \times 47.0 + 2.0 \times 47.0 + \frac{1}{3} \times 2.5 \times 47.0 = 167.6.$$

The leakage reactance between the LV and HV windings can be calculated from Equation 3.22 with 4 sections,

$$\%X = 2.48 \times 10^{-5} \times 50 \times \frac{10800}{11.7 \times 11.527} \times \frac{1}{4} \times 167.6 = 4.16\%.$$

2. FEM analysis

The geometry as given in Figure 3.11 is modeled and an analysis is carried out according to the steps outlined in Section 3.4. The stored energy in the different parts of the geometry is:

LV (all 4 parts):	1.44 J
HV (all 4 parts):	1.66 J
Remaining portion:	5.26 J

The total energy is 8.36 J. Using Equation 3.24, the leakage inductance is calculated as

$$L = \frac{2 \times 8.36}{(300)^2} = 0.000186 \text{ H.}$$

The base impedance value is

$$Z_b = \frac{\text{Rated voltage}}{\text{Rated current}} = \frac{415}{300} = 1.38\ \Omega .$$

$$\therefore X = \frac{2\pi \times 50 \times L}{Z_b} \times 100 = \frac{2\pi \times 50 \times 0.000186}{1.38} \times 100 = 4.23\% .$$

3.5 Impedance Characteristics of Three-Winding Transformers

A three-winding (three-circuit) transformer is required when actual loads or auxiliary loads (reactive power compensating devices such as shunt reactors or condensers) are required to be supplied at a voltage different from the primary and secondary voltages. An unloaded tertiary winding is commonly used for the stabilizing purpose as discussed in Section 3.8.

The characteristics and issues related to the leakage field (efficiency, regulation, parallel operation, and short-circuit currents) of a multi-circuit transformer cannot be analyzed in the same way as that for a two-winding transformer. The leakage reactance characteristics of a three-winding transformer can be represented by an equivalent circuit, for doing which it is assumed that each winding has its own individual leakage reactance. When the magnetizing current is neglected (which is justified in the calculations related to leakage fields) and if all the quantities are expressed in the per-unit or percentage notation, the magnetically interlinked circuits of the three-winding transformer can be represented by electrically interlinked circuits as shown in Figure 3.12. The equivalent circuit can be either a star or mesh network. The star equivalent circuit is more commonly used and is discussed here.

The percentage leakage reactances between pairs of windings can be expressed in terms of their individual percentage leakage reactances (all expressed on a common base of volt-amperes) as

$$X_{12} = X_1 + X_2 \tag{3.44}$$

$$X_{23} = X_2 + X_3 \tag{3.45}$$

$$X_{31} = X_1 + X_3 . \tag{3.46}$$

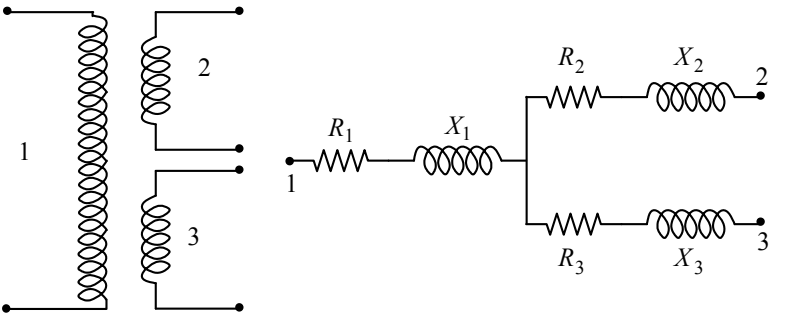

Three-winding transformer Star equivalent circuit

Figure 3.12 Representation of a three-winding transformer.

It follows from the above three equations that the individual reactances in the star equivalent circuit are given by

$$X_1 = \frac{1}{2}\left[X_{12} + X_{13} - X_{23}\right] \tag{3.47}$$

$$X_2 = \frac{1}{2}\left[X_{12} + X_{23} - X_{13}\right] \tag{3.48}$$

$$X_3 = \frac{1}{2}\left[X_{13} + X_{23} - X_{12}\right]. \tag{3.49}$$

A rigorous derivation of the above three equations and the evolution of the star equivalent circuit is given in [10].

Similarly, the percentage resistances can be derived as

$$R_1 = \frac{1}{2}\left[R_{12} + R_{13} - R_{23}\right] \tag{3.50}$$

$$R_2 = \frac{1}{2}\left[R_{12} + R_{23} - R_{13}\right] \tag{3.51}$$

$$R_3 = \frac{1}{2}\left[R_{13} + R_{23} - R_{12}\right]. \tag{3.52}$$

Note that these percentage resistances represent the total load loss (the addition of the DC-resistance I^2R loss in windings, the eddy loss in windings and the stray loss in structural parts).

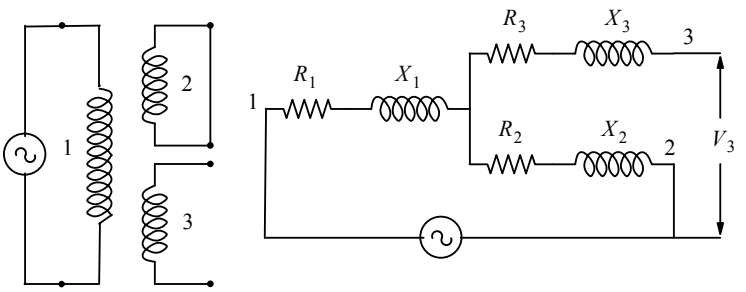

Figure 3.13 Mutual effect in star equivalent network.

The leakage reactances in the star equivalent network are basically the mutual load reactances between different circuits. For example, the reactance X_1 in Figure 3.12 is the common or mutual reactance to the loads in circuits 2 and 3. A current flowing from circuit 1 to either circuit 2 or 3 produces voltage drops across R_1 and X_1, and hence affects the voltages in circuits 2 and 3. When a voltage is applied to winding 1 with winding 2 short-circuited as shown in Figure 3.13, the voltage across the open-circuited winding 3 is equal to the voltage drop across the leakage impedance, Z_2, of circuit 2.

The individual leakage reactance of a winding can be negative. The total leakage reactance between a pair of windings cannot be negative but the mutual effect between two circuits may be negative when a load current flows [11]. Negative impedances are virtual values, and they reproduce faithfully the terminal characteristics of transformers. The three windings are interlinked, and hence a load current flowing in a winding affects the voltages in the other two windings, sometimes in a surprising way. For example, a lagging load on a winding may increase the voltage magnitude of another winding due to the presence of a negative value of a leakage reactance (capacitive reactance) in the equivalent circuit.

Similarly, a negative resistance may appear in the star equivalent network of an autotransformer with a tertiary winding or of a high efficiency transformer whose stray loss is much higher as compared to the ohmic losses in its windings (e.g., when a lower value of the current density is used for the windings).

In Chapter 1, we have seen how the regulation of a two-winding transformer is calculated. The calculation of the voltage regulation of a three-winding transformer is explained with the help of the following example.

Example 3.3

Find the voltage drop between the terminals of a three-winding transformer, when the load on the IV winding is 70 MVA at 0.8 lagging power factor, and the load on the LV winding is 30 MVA at 0.6 lagging power factor. The transformer data is:

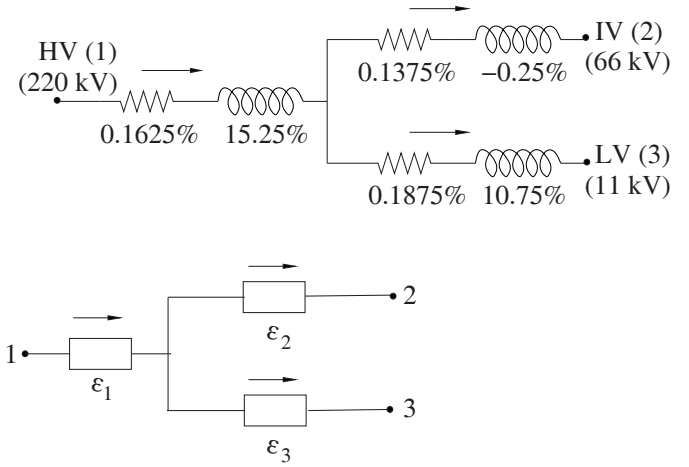

Figure 3.14 Star equivalent circuit and regulation (Example 3.3).

Rating: 100/100/30 MVA, 220/66/11 kV
Results of short circuit tests referred to 100 MVA base:

$$\text{HV-IV} \;:\; R_{1-2} = 0.30\%, \quad X_{1-2} = 15.0\%$$
$$\text{HV-LV} \;:\; R_{1-3} = 0.35\%, \quad X_{1-3} = 26.0\%$$
$$\text{IV-LV} \;:\; R_{2-3} = 0.325\%, \; X_{2-3} = 10.5\%$$

Solution:

The star equivalent circuit derived using Equations 3.47 to 3.52 is shown in Figure 3.14. It is to be noted that although the HV, IV and LV windings are rated for different MVA values, for finding the equivalent circuit, we have to work on a common MVA base (in this case it is 100 MVA).

The IV winding is loaded to 70 MVA; let the constant K_2 denote the ratio of the actual load to the base MVA,

$$K_2 = 70/100 = 0.7 .$$

Similarly, for the LV winding which is loaded to 30 MVA,

$$K_3 = 30/100 = 0.3 .$$

The voltage drops for circuits 2 and 3 are calculated using Equation 1.65,

$$\varepsilon_2 = K_2(R_2 \cos\theta_2 + X_2 \sin\theta_2) = 0.7(0.1375\times 0.8 + (-0.25)\times 0.6) = -0.03\%$$
$$\varepsilon_3 = K_3(R_3 \cos\theta_3 + X_3 \sin\theta_3) = 0.3(0.1875\times 0.6 + 10.75\times 0.8) = 2.61\% .$$

The effective power factor ($\cos\theta_1$) and the effective load taken as a fraction (K_1) of the base MVA for the primary (220 kV) circuit are determined by solving the following two equations:

$$K_1 \cos\theta_1 = K_2 \cos\theta_2 + K_3 \cos\theta_3 = 0.7\times 0.8 + 0.3\times 0.6 = 0.74 \tag{3.53}$$

$$K_1 \sin\theta_1 = K_2 \sin\theta_2 + K_3 \sin\theta_3 = 0.7\times 0.6 + 0.3\times 0.8 = 0.66 \tag{3.54}$$

Solving these two equations we obtain

$$K_1 = 0.99,\ \ \cos\theta_1 = 0.75,\ \ \ \sin\theta_1 = 0.67\,.$$

Therefore, the primary circuit voltage drop (regulation) is

$$\varepsilon_1 = K_1(R_1\cos\theta_1 + X_1\sin\theta_1) = 0.99\left(0.1625\times 0.75 + 15.25\times 0.67\right) = 10.23\%\,.$$

Now, the voltage drops between the terminals can be calculated as

$$\varepsilon_{1-2} = \varepsilon_1 + \varepsilon_2 = 10.23 + (-0.03) = 10.2\%$$

$$\varepsilon_{1-3} = \varepsilon_1 + \varepsilon_3 = 10.23 + 2.61 = 12.84\%$$

$$\varepsilon_{2-3} = -\varepsilon_2 + \varepsilon_3 = 0.03 + 2.61 = 2.64\%\,.$$

While calculating ε_{2-3}, a minus sign is used for ε_2 as the drop in the voltage is in the direction opposite to the direction of the corresponding current flow.

When there are more than three windings, transformers cannot be in general represented by a pure star or mesh equivalent circuit. The equivalent circuit should have $n(n-1)/2$ independent impedance links, where n is the number of windings. A four-winding transformer has six independent links with four terminal points. The procedure for determining the values of impedances in the equivalent circuit of a transformer having four or more windings is given in [1, 12, 13].

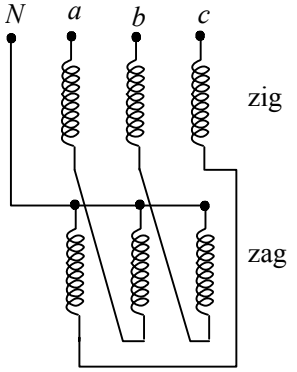

Figure 3.15 A zigzag connection.

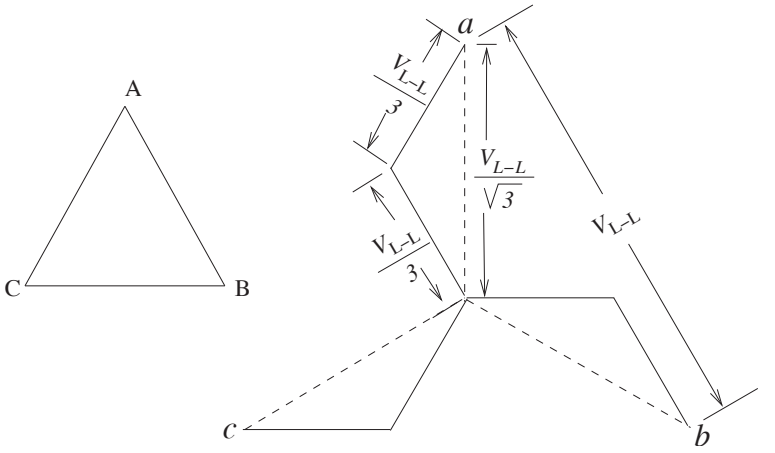

Figure 3.16 Vector diagram of a delta-zigzag transformer.

3.6 Reactance Calculation for Zigzag Transformers

A zigzag connection, in which the windings on different limbs are cross-connected, is shown in Figure 3.15. It is termed zigzag or interconnected star winding because the zig winding of one phase is connected in series with the zag winding of one of the other two phases. The vector diagram of a delta-zigzag transformer is shown in Figure 3.16. The interconnection of the windings of different phases introduces a phase shift of 30° (or 150°) between the zig (or zag) winding and the corresponding line-to-neutral voltage ($V_{L-N} = V_{L-L} / \sqrt{3}$). The zig and zag windings have 15.47% more turns than conventional windings to obtain the same magnitude of phase/line voltages. Hence, zigzag transformers are costlier than conventional transformers, but its use is essential in some cases. Their main characteristics and advantages are as follows:

- They can be used as an earthing transformer in a delta-connected system or an ungrounded star-connected system, wherein a neutral point is not available for the earthing (grounding) purpose. Consider a zigzag transformer connected to a delta-connected source as shown in Figure 3.17. For a single line-to-ground fault, a zero-sequence current flows in the ground circuit allowing a protection system to act. The voltages of the two healthy line terminals are maintained at their respective line-to-neutral voltage levels. In the absence of the grounded neutral connection, the voltages of the healthy phases increase to the line-to-line voltage level, stressing insulation systems of the connected equipment. Thus, the zigzag earthing transformers not only aid the protection system but also reduce the voltage stresses under asymmetrical fault conditions.

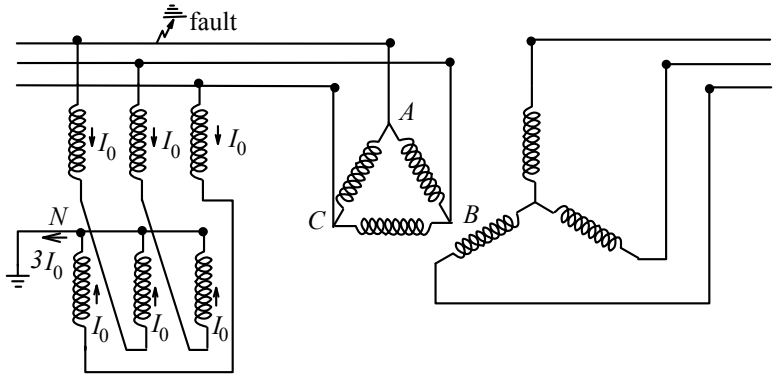

Figure 3.17 A zigzag earthing transformer.

- Zigzag transformers offer a specific advantage when used in applications consisting of power electronic converters. The DC magnetization due to asymmetry in firing angles is cancelled in each limb due to opposite directions of the DC currents flowing in its zig and zag windings. Similarly, the DC magnetization inherent in a three-pulse mid point rectifier connection is eliminated if the secondary winding is of zigzag type [14].
- Earthing transformers offer a low impedance path to zero-sequence currents under asymmetrical fault conditions because the only magnetic flux produced by the currents is the leakage flux; the magnetizing flux in each limb is zero due to the equal and opposite currents flowing in its zig and zag windings as shown in Figure 3.17. Owing to a very low impedance of the earthing transformer, it may be necessary to limit currents under fault conditions by connecting a resistor between the neutral and the earth. Under normal operating conditions, only a small exciting current flows in the windings of the earthing transformer.
- Third harmonic voltage components present in the zig and zag windings are cancelled in the lines.

The reactance of a transformer consisting of zigzag and star (or delta) windings can be calculated from reactive volt-amperes. Consider the star-zigzag transformer shown in Figure 3.18. The currents I_a, I_b and I_c are assumed to flow from the line terminals to the neutral for convenience. The corresponding vector diagram is also shown in the figure.

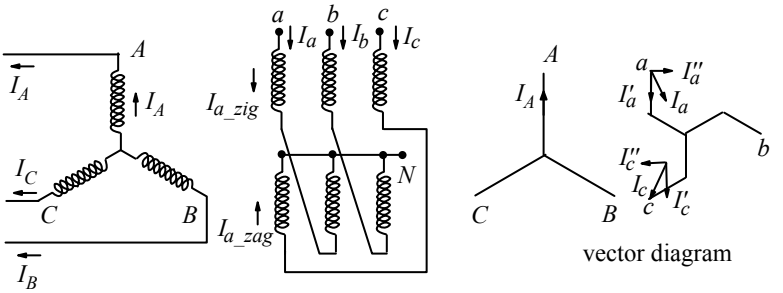

Figure 3.18 Reactance calculation of a transformer having a zigzag winding.

All the currents are resolved into two mutually perpendicular sets of components. Since the vector sum of all ampere-turns is zero on each limb, the sum of all the components indicated by prime is zero and the sum of all the components indicated by double prime is also zero. The current of the phase *A* of the star connected winding (I_A) is taken as the reference vector, and all the other currents are resolved in the directions along and perpendicular to this vector. Since I_A is the reference vector, I'_A and I''_A have the values 1 p.u. and 0 p.u., respectively, in per-unit notations. I_{a_zig} is in phase with I_a, whereas I_{a_zag} is in phase with I_c. The zig and zag windings have 0.577 p.u. ampere-turns (1.1547 $\times$ 0.5). Also, the currents I_a and I_c are at an angle of 30° with respect to the reference vector. The direction of I_c (I_{a_zag}) has been reversed in the vector diagram so that at any instant the corresponding ampere-turns of the zag winding oppose that of the star winding. Thus, we can write

$$I'_A = 1, \tag{3.55}$$

$$I''_A = 0, \tag{3.56}$$

$$(I_{a\_zig})' = (I_{a\_zag})' = -0.577 \cos 30° = -0.5, \text{ and} \tag{3.57}$$

$$(I_{a\_zig})'' = -(I_{a\_zag})'' = 0.577 \sin 30° = 0.289. \tag{3.58}$$

Equations 3.55 to 3.58 satisfy the following two equations as required by the condition that the vector sum of all the ampere-turns on the limb of the phase *A* is zero:

$$I'_A + (I_{a\_zig})' + (I_{a\_zag})' = 0 \text{ and} \tag{3.59}$$

$$I''_A + (I_{a\_zig})'' + (I_{a\_zag})'' = 0. \tag{3.60}$$

The vectors of the currents in the windings resolved into two mutually perpendicular sets can be used in conjunction with Equation 3.37 to calculate reactive volt-amperes (Q). The resistances of the windings are neglected since they are much lower than the reactances. The expressions of Q for the two sets are added algebraically,

$$Q = -\frac{1}{2}\sum_{k=1}^{n}\sum_{j=1}^{n} X_{jk}(I_j)'(I_k)' - \frac{1}{2}\sum_{k=1}^{n}\sum_{j=1}^{n} X_{jk}(I_j)''(I_k)''. \tag{3.61}$$

The expression of Q for the phase A having three windings, star, zig, and zag, denoted by numbers 1, 2, and 3, respectively, is

$$\begin{aligned} Q = &-\frac{1}{2}\{2X_{12}I_1'I_2' + 2X_{13}I_1'I_3' + 2X_{23}I_2'I_3'\} \\ &-\frac{1}{2}\{2X_{12}I_1''I_2'' + 2X_{13}I_1''I_3'' + 2X_{23}I_2''I_3''\} \end{aligned} \tag{3.62}$$

where X_{12}, X_{13}, and X_{23} are the per-unit leakage reactances between the corresponding windings. Substituting from Equations 3.55 to 3.58, and remembering that $I_1 = I_A$, $I_2 = I_{a\_zig}$ and $I_3 = I_{a\_zag}$,

$$\begin{aligned} Q = &-\{X_{12}\times 1\times(-0.5) + X_{13}\times 1\times(-0.5) + X_{23}\times(-0.5)\times(-0.5)\} \\ &-\{0 + 0 + X_{23}\times 0.289\times(-0.289)\} \end{aligned}.$$

Since the currents and reactances are expressed in the per-unit notation, the value of Q directly gives the per-unit reactance of the star/zigzag transformer.

$$\therefore Q = X_{\text{star\_zigzag}} = \frac{1}{2}[X_{12} + X_{13}] - \frac{1}{6}X_{23}. \tag{3.63}$$

Thus, the leakage reactance of a transformer having star- (or delta-) and zigzag-connected windings can be computed easily, once the leakage reactances between the pairs of the windings are calculated using a common VA base.

Example 3.4

Find the leakage reactance of a 31.5 MVA, 132/11 kV, 50 Hz, star/zigzag transformer whose various relevant dimensions (in mm) are indicated in Figure 3.19. The value of volts/turn is 76.39.

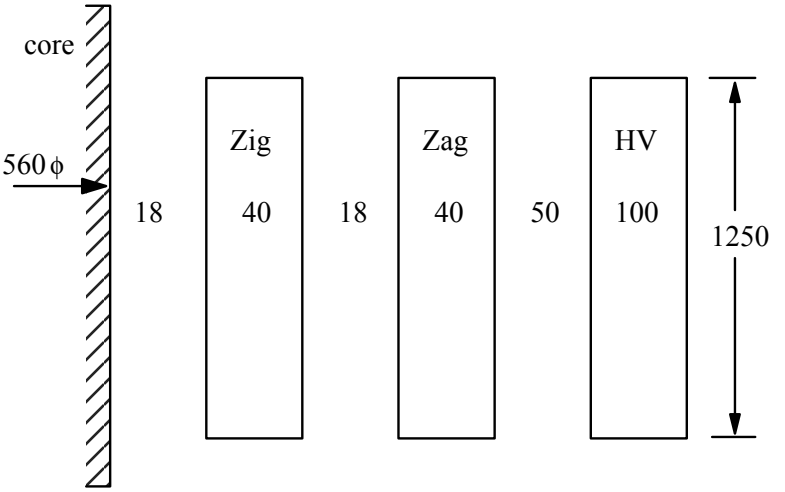

Figure 3.19 Dimensions of the star/zigzag transformer in Example 3.4.

Solution:

Let us first calculate the leakage reactances between the pairs of the windings, zig and zag, zig and HV, and zag and HV by the procedure given in Section 3.1.1 for concentric windings.

Reactance between the zig and zag windings:

$$T_1 = 4.0 \text{ cm},\ T_g = 1.8 \text{ cm},\ T_2 = 4.0 \text{ cm},\ H_w = 125.0 \text{ cm}$$

Equations 3.18 and 3.1 give $K_R = 0.975$ and $H_{eq} = 125/0.975 = 128.2$ cm.

Equation 3.17 gives

$$\sum ATD = \frac{1}{3} \times 4.0 \times 63.6 + 1.8 \times 69.4 + \frac{1}{3} \times 4.0 \times 75.2 = 310 \text{ cm}^2.$$

The reactance needs to be calculated using a common MVA base. The base volt-amperes are taken as 31.5 MVA. The corresponding current and turns of the HV winding should be used in the reactance formula.

$$\text{HV current} = \frac{31.5 \times 10^6}{\sqrt{3} \times 132 \times 10^3} = 137.78 \text{ A}$$

$$\text{HV turns} = \frac{132 \times 10^3 / \sqrt{3}}{76.39} = 998.$$

The leakage reactance is calculated using Equation 3.16 as

$$X_{\text{zig\_zag}} = 2.48\times10^{-5}\times50\times\frac{(137.78\times998)}{128.2\times76.39}\times310 = 5.4\%\,.$$

Similarly, the other two reactances can be calculated as follows.

Reactance between the zig and HV windings:

$$T_1 = 4 \text{ cm},\ T_2 = 10.8 \text{ cm},\ T_3 = 10 \text{ cm}\,.$$

$$\therefore K_R = 0.937,\ H_{eq} = 133.4 \text{ cm},\ \sum ATD = 1262.2 \text{ and } X_{\text{zig\_HV}} = 21.1\%\,.$$

Reactance between the zag and HV windings:

$$T_1 = 4 \text{ cm},\ T_2 = 5 \text{ cm},\ T_3 = 10 \text{ cm}\,.$$

$$\therefore K_R = 0.95,\ H_{eq} = 131.4 \text{ cm},\ \sum ATD = 851.9 \text{ and } X_{\text{zag\_HV}} = 14.5\%\,.$$

By using Equation 3.63, we obtain the reactance of the star/zigzag transformer as

$$X_{\text{star\_zigzag}} = \frac{1}{2}\left[X_{\text{HV\_zig}} + X_{\text{HV\_zag}}\right] - \frac{1}{6}X_{\text{zig\_zag}}$$

$$= \frac{1}{2}\times\left[21.1+14.5\right] - \frac{1}{6}\times5.4 = 16.9\%\,.$$

***Zigzag/zigzag transformer*:** The reactance of zigzag/zigzag transformers can also be calculated by using reactive volt-amperes. Consider a zigzag/zigzag transformer shown in Figure 3.20.

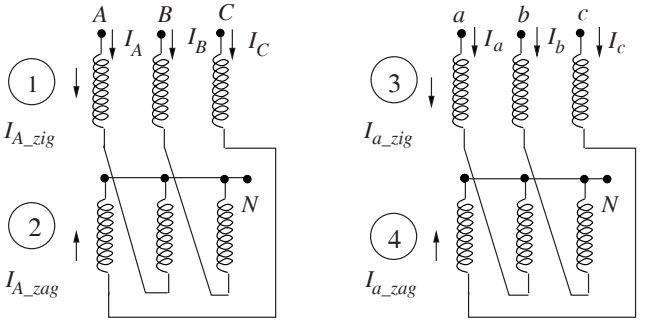

Figure 3.20 Zigzag/zigzag transformer.

The directions of the currents in the windings are shown in the figure. The per-unit ampere-turns on the limb corresponding to phase *A* are given as

$$\left(I_{A\_zig}\right)' = \left(I_{A\_zag}\right)' = 0.577\cos 30^{\circ}$$

$$\left(I_{A\_zag}\right)'' = -\left(I_{A\_zig}\right)'' = 0.577\sin 30^{\circ}$$

$$\left(I_{a\_zig}\right)' = \left(I_{a\_zag}\right)' = -0.577\cos 30^{\circ}$$

$$\left(I_{a\_zig}\right)'' = -\left(I_{a\_zag}\right)'' = 0.577\sin 30^{\circ}.$$

By using Equation 3.61, where $n = 4$ and remembering that $I_1 = I_{A\_zig}$, $I_2 = I_{A\_zag}$, $I_3 = I_{a\_zig}$, $I_4 = I_{a\_zag}$, we obtain

$$Q = \frac{-1}{2}\left\{\begin{matrix} 2X_{12}I_1'I_2' + 2X_{13}I_1'I_3' + 2X_{14}I_1'I_4' + 2X_{23}I_2'I_3' \\ + 2X_{24}I_2'I_4' + 2X_{34}I_3'I_4' \end{matrix}\right\}$$

$$\frac{-1}{2}\left\{\begin{matrix} 2X_{12}I_1''I_2'' + 2X_{13}I_1''I_3'' + 2X_{14}I_1''I_4'' + 2X_{23}I_2''I_3'' \\ + 2X_{24}I_2''I_4'' + 2X_{34}I_3''I_4'' \end{matrix}\right\}.$$

After substituting the values of in-phase and quadrature components of I_1, I_2, I_3 and I_4 obtained earlier, we have

$$Q = X_{Zigzag\_zigzag} = \frac{1}{3}\left[X_{13} + X_{24} + \left(\frac{X_{14} + X_{23}}{2}\right) - \left(\frac{X_{12} + X_{34}}{2}\right)\right]. \qquad (3.64)$$

3.7 Zero-Sequence Reactances

The theory of symmetrical components is commonly used in power system analyses. Unlike in rotating machines, the positive-sequence and negative-sequence reactances are equal in static devices such as transformers. Under symmetrical loading conditions, only positive-sequence reactances need to be considered. During asymmetrical loadings/disturbances or single-phase faults, the response of the system is mainly decided by zero-sequence reactances in the resultant network. It is relatively easy to understand and calculate positive-sequence reactances as compared to zero-sequence reactances in transformers. The zero-sequence reactance of a transformer may differ considerably from its

positive-sequence reactance depending upon the type of its magnetic circuit and winding connections.

The zero-sequence reactance seen from the terminals of a delta-connected winding is infinite, since zero-sequence currents cannot flow as there is no return path; the zero-sequence test will in fact measure a high capacitive reactance between the three phases and the ground (i.e., the winding to ground stray capacitances of the three phases are in parallel under the test condition).

In order to measure the zero-sequence reactance of a transformer having a star-connected winding, a suitable voltage is applied between the short-circuited line terminals of the winding and the neutral as shown in Figure 3.21. The zero-sequence reactance ($\cong$ impedance) of the star-connected winding with the grounded neutral is calculated as

$$X_0 = \frac{V}{(I/3)} = 3\frac{V}{I}. \tag{3.65}$$

Two types of zero-sequence reactances can be measured for a winding:

1. The open-circuit or magnetizing reactance with terminals of all other windings kept open-circuited
2. The short-circuit or leakage reactance with terminals of only one other winding short-circuited.

The influence of the type of the core construction and winding connections on these reactances and the procedures for their calculation are now discussed.

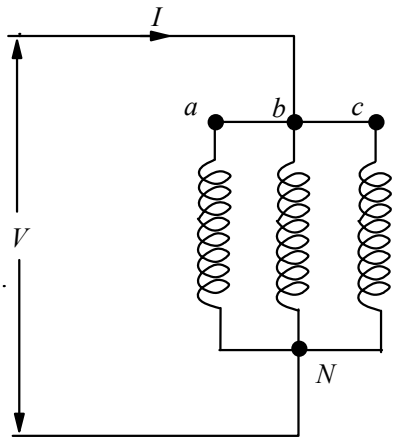

Figure 3.21 Measurement of zero-sequence impedance.

3.7.1 Open-circuit zero-sequence reactance without delta winding

A. Three-phase three-limb transformers

For a three-phase three-limb transformer, since the zero-sequence fluxes in the three limbs are in the same direction, they have to return through a path outside the core. In this case, the tank acts as an equivalent delta winding, and the open-circuit zero-sequence reactance is the one between the tank and the excited winding. Since the gap/area between the excited winding and the tank is much higher than the gap/area between the LV and HV windings, the open-circuit zero-sequence reactance is considerably higher than the short-circuit positive-sequence reactance (the usual leakage impedance between the windings), although it is much lower than the open-circuit positive sequence reactance obtained by the standard open-circuit test discussed in Chapter 1. The tank influences the zero-sequence reactance in the following way. It provides a lower reluctance return path (as compared to air) to the zero-sequence flux, which has the effect of increasing the reactance; on the other hand the tank enclosing the three phases acts as a short-circuited winding reducing the reactance. The latter effect is more dominant and hence the zero-sequence reactance inside the tank is appreciably less than that without it [15]. However, the zero-sequence reactance is much larger than the positive-sequence impedance as mentioned earlier.

The reactance between the excited winding and the tank can be calculated by the procedure given in Section 3.1.1 with the latter represented as an equivalent (fictitious) winding with zero radial depth (contribution of the tank to the AT diagram area can be neglected due to its small thickness). The winding-tank gap can be taken as the equivalent distance which gives approximately the same area of the space between them. The zero-sequence reactance is then calculated by using Equation 3.16 as

$$\%X_0 = 2.48\times10^{-5} f \frac{(Ampere\times Turns)}{H_{eq}\times(Volts/Turn)}\times(\frac{1}{3}\times T_w \times D_w + T_g \times D_g) \quad (3.66)$$

where

T_w = radial depth of the excited winding in cm

D_w = mean diameter of the excited winding in cm

T_g = gap between the excited winding and the tank in cm

D_g = mean diameter of the gap between the excited winding and the tank in cm.

When sufficient voltage is applied during the test, the zero-sequence flux passing through the tank usually saturates it. If the test is done at a voltage magnitude which does not saturate the tank made generally from mild steel material, its higher permeability will increase the reactance. Hence, the reactance calculated using Equation 3.66 has to be suitably corrected by an

empirical factor which can be derived based on a set of measurements at various voltage levels. The correction factor depends on the applied voltage as shown in Figure 3.22 [16]. The curve in the figure has the same nature as that of the permeability versus magnetic field intensity graph derived from the measurements on a typical grade of mild steel material (Figure 3.23) [17].

B. Three-phase five-limb and single-phase three-limb transformers

In a three-phase five-limb transformer, the zero-sequence flux has a return path through the end yokes and the end limbs, and hence the open-circuit zero-sequence reactance equals the open-circuit positive-sequence reactance (a high value) unless the voltage applied is such that the yokes and the end limbs saturate. For an applied zero-sequence voltage close to the rated value of the excited winding, the yokes and the end limbs will be completely saturated; their area is too less to carry the zero-sequence flux of all the three phases at the rated voltage. This results in a lower value of the open-circuit zero-sequence reactance, which can be close to that for the three-phase three-limb construction.

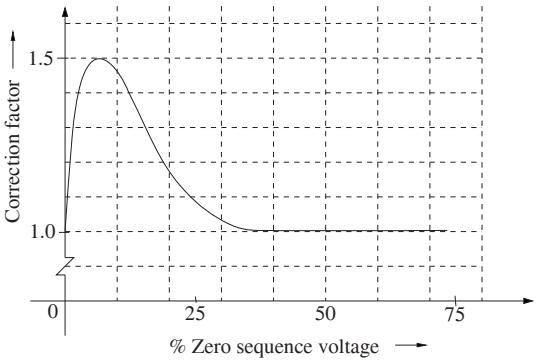

Figure 3.22 Correction factor for the zero-sequence reactance [16].

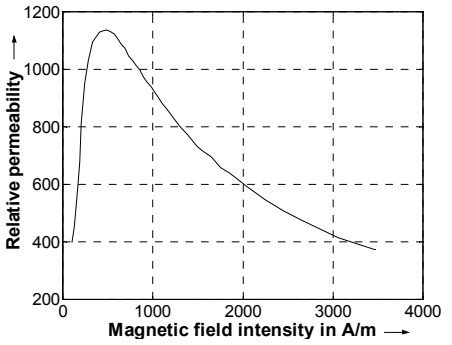

Figure 3.23 Variation of μ_r with field intensity in mild steel material [17].

For single-phase three-limb transformers, since the zero-sequence flux returns through the end limbs, the open-circuit zero-sequence reactance is equal to the open-circuit positive-sequence reactance (~ infinite value). Thus, for a bank of three single-phase transformers, the zero-sequence characteristics are usually identical to the positive-sequence characteristics [18].

3.7.2 Open-circuit zero-sequence reactance with a delta-connected winding

With one delta connected secondary winding, a zero-sequence current circulates in the closed delta. Thus, the transformer acts as if it is short-circuited regardless of whether the winding is loaded or not. Let us again consider the following two cases.

A. Three-phase three-limb transformers

When zero-sequence voltage is applied to the star-connected winding, zero-sequence currents flow in the delta-connected winding and the tank which acts as an equivalent short-circuited (delta) winding. In order to estimate the current division between these two windings and the zero-sequence reactance, we will use the method described in Section 3.2 for a composite system of windings. Let the star-connected primary winding, the delta connected secondary winding and the tank be represented by notations 1, 2, and 3 respectively. Applying Equation 3.38, for the present case of the three windings (one star- and two delta-connected windings), we obtain the per-unit value of zero-sequence reactance as

$$Q = X_0 = -\frac{1}{2}\left[2X_{12}I_1(-I_2) + 2X_{23}(-I_2)(-I_3) + 2X_{13}I_1(-I_3)\right]. \qquad (3.67)$$

The currents in windings 2 and 3 are assigned a negative sign as their direction is opposite to that of the current in the primary winding. Since the magnetizing current can be neglected,

$$I_1 = I_2 + I_3\,. \qquad (3.68)$$

If the magnitude of the applied zero-sequence voltage is such that the rated current flows in the primary winding (i.e., I_1 has a value of 1 per-unit), then

$$I_3 = 1 - I_2\,. \qquad (3.69)$$

$$\therefore Q = X_{12}\,I_2 - X_{23}\,I_2\,(1 - I_2) + X_{13}\,(1 - I_2)\,. \qquad (3.70)$$

The currents are distributed in the windings in such a way that the total energy is minimized. Hence, differentiating Q with respect to I_2 and equating the derivative to zero, we have

$$\frac{dQ}{dI_2} = X_{12} - X_{23} + 2X_{23}I_2 - X_{13} = 0 . \tag{3.71}$$

$$\therefore I_2 = \frac{X_{13} + X_{23} - X_{12}}{2X_{23}} . \tag{3.72}$$

The above value of I_2 when substituted in Equation 3.69 gives the current flowing through the tank as

$$I_3 = \frac{X_{23} + X_{12} - X_{13}}{2\ X_{23}} . \tag{3.73}$$

The delta-connected secondary winding can either be the inner or outer winding.

If the delta-connected winding (2) is the outer winding:

$$X_{13} \cong X_{12} + X_{23} . \tag{3.74}$$

Substituting the expression of X_{13} in Equations 3.72 and 3.73, we obtain

$$I_2 \cong 1 \quad \text{and} \quad I_3 \cong 0 . \tag{3.75}$$

Substituting these values of I_2 and I_3 in Equation 3.70, the value of zero-sequence reactance is obtained as

$$X_0 = Q \cong X_{12} . \tag{3.76}$$

Thus, with the outer delta-connected winding, the zero-sequence reactance is approximately equal to the short-circuit positive-sequence reactance (X_{12}) because the outer delta-connected winding shields the tank and no current flows in the latter. The phenomenon can be understood by referring to Figure 5.38 (a) wherein the leakage field is constrained to return through the limb to make the total flux linked to the outer short-circuited winding equal to zero.

If the delta-connected winding (2) is the inner winding:

$$X_{23} \cong X_{21} + X_{13} = X_{12} + X_{13} . \tag{3.77}$$

Substituting this expression of X_{23} in Equations 3.72 and 3.73, we obtain

$$I_2 \cong \frac{X_{13}}{X_{23}} \quad \text{and} \quad I_3 \cong \frac{X_{12}}{X_{23}} . \tag{3.78}$$

Putting these expressions I_2 and I_3 in Equation 3.70, we have

$$X_0 = Q \cong \frac{X_{13}}{X_{23}} X_{12} . \tag{3.79}$$

Thus, with the inner delta-connected winding, the zero-sequence reactance is always less than the (short-circuit) positive-sequence reactance (X_{12}). This is due to the fact that, in this case, $X_{23} > X_{13}$ since the outer star-connected winding (1) is closer to the tank. In this case, as the effect of the tank is not hampered, the reactance reduces; the presence of an additional short-circuited winding has the effect of reducing the impedance seen from the source end in any system of windings.

It should to be noted that Equations 3.74 and 3.77 are approximately valid; for accurate calculations, the expressions of I_2 and I_3 in Equations 3.72 and 3.73, respectively, have to be directly substituted in Equation 3.70.

The value of the measured positive-sequence impedance is the same irrespective of which winding is excited. However, as discussed in this section, the measured zero-sequence impedance depends on whether the inner or outer winding is excited. For this reason, the zero-sequence tests are not *reciprocal* for three-phase three-limb units.

B. Three-phase five-limb and single-phase three-limb transformers

For a three-phase five-limb transformer, the value of zero-sequence reactance is equal to that of the short-circuit positive-sequence reactance between the windings until the applied voltage saturates the yokes and the end limbs. At such a high applied voltage, it acts as a three-limb transformer, and the zero-sequence reactance can be calculated accordingly.

For a single-phase three-limb transformer, the zero-sequence reactance is equal to the short-circuit positive-sequence reactance between the star- and delta-connected windings, since a current flows in the closed delta (as if short-circuited) and a path is available for the flux in the magnetic circuit.

Example 3.5

Calculate the positive-sequence and zero-sequence reactances of a 2 MVA, 11/0.433 kV, 50 Hz, Dyn11 transformer whose various relevant dimensions in mm are indicated in Figure 3.24. The value of volts/turn is 15.625.

Solution:

The short-circuit positive-sequence (leakage) reactance is calculated by the procedure given in Section 3.1.1 for concentric windings.

The Rogowski factor is calculated by Equation 3.18 as

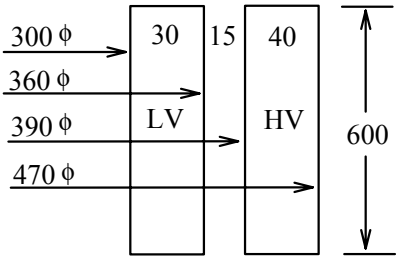

Figure 3.24 Dimensions of 2 MVA transformer.

$$K_R = 1 - \frac{1 - e^{-\pi 60.0/(3.0+1.5+4.0)}}{\pi 60.0/(3.0+1.5+4.0)} = 0.955 .$$

The equivalent winding height according to Equation 3.1 is

$$H_{eq} = H_w / K_R = 60 / 0.955 = 62.8 .$$

$\sum ATD$ is calculated using Equation 3.17,

$$\sum ATD = \frac{1}{3} \times 3.0 \times 33.0 + 1.5 \times 37.5 + \frac{1}{3} \times 4.0 \times 43.0 = 146.6 .$$

For calculating the reactance, either the LV or HV ampere-turns are used (their values are equal since the magnetizing ampere-turns are neglected).

$$\text{LV current} = \frac{2 \times 10^6}{\sqrt{3} \times 433} = 2666.67 \text{ A} \quad \text{and LV turns} = \frac{433/\sqrt{3}}{15.625} = 16 .$$

The positive-sequence leakage reactance is given by Equation 3.16,

$$\%X_p = 2.48 \times 10^{-5} \times 50 \times \frac{(2666.67 \times 16)}{62.8 \times 15.625} \times 146.6 = 7.9\% .$$

Since the delta-connected HV winding is the outer winding, the zero-sequence reactance of the star-connected winding is approximately equal to the positive-sequence leakage reactance as explained in Section 3.7.2. However, during the actual test, one usually gets the value of zero-sequence reactance higher than the positive-sequence leakage reactance by an amount corresponding to the voltage drop in the neutral bar. The reactance of a neutral bar having rectangular dimensions ($a \times b$) is given by the expression [19, 20]:

$$X_n = 2\pi f \times 0.002 L_b \left\{ \log_e \frac{2L_b}{D_s} - 1 + \frac{D_s}{L_b} \right\} \times 10^{-6} \quad (3.80)$$

where

L_b is the length of the bus-bar in cm, and

D_s is the geometric mean distance from itself = $0.2235 \times (a + b)$ cm.

For the bus-bar dimensions, a = 5 cm, b = 0.6 cm, length = 50 cm,

$$D_s = 0.2235 \times (5 + 0.6) = 1.2516 .$$

$$\therefore X_n = 2\pi \times 50 \times 0.002 \times 50 \times \left\{ \log_e \frac{2 \times 50}{1.2516} - 1 + \frac{1.2516}{50} \right\} \times 10^{-6}$$

$$= 107 \times 10^{-6} \Omega.$$

The base impedance on the LV side is

$$Z_b = \frac{(0.433)^2}{2} = 0.0937 .$$

Since the zero-sequence current flowing in the neutral bar is three times that flowing in each of the phases, the bar contributes three times the value of X_n in the zero-sequence reactance.

$$\therefore \% \; X_n = \frac{3 \times 107 \times 10^{-6}}{0.0937} \times 100 = 0.34 \% .$$

Hence, the measured zero-sequence reactance would be close to

$$(X_0)_{actual} = 7.9 + 0.34 = 8.24 \% .$$

3.7.3 Short-circuit zero-sequence reactance

This is applicable when the secondary winding is short-circuited while doing the zero-sequence test on the primary winding (e.g., a star/star transformer).

A. Three-phase three-limb transformers

The procedure for the calculation of the short-circuit zero-sequence reactance of three-phase three-limb transformers is now explained with the help of an example.

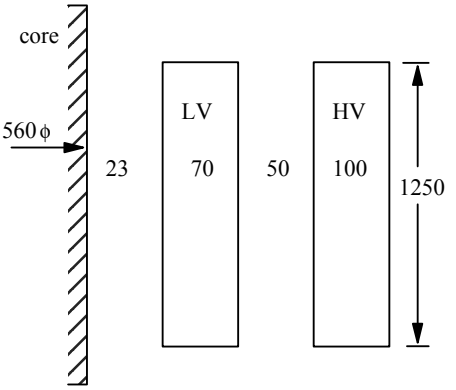

Figure 3.25 Dimensions of the transformer in Example 3.6.

Example 3.6

The relevant dimensions (in mm) of a 31.5 MVA, 132/33 kV, 50 Hz, YNyn transformer are given in Figure 3.25. The volts/turn is 83.93. Calculate the zero-sequence reactance of the LV and HV windings, and the parameters of the zero-sequence network.

Solution:

The value of the positive-sequence leakage reactance can be calculated like in the previous examples as 12.16%. Let the inner 33 kV winding and the outer 132 kV winding be denoted by numbers 1 and 2 respectively.

$$X_p = (X_p)_{12} = (X_p)_{21} = 12.16\% .$$

The open-circuit zero-sequence reactance of the LV and HV windings can be calculated by using the procedure given in Section 3.7.1 (and Equation 3.66) with the average LV-to-tank and HV-to-tank distances of 400 mm and 250 mm (for this transformer) respectively. Let us first calculate the open-circuit reactance as seen from the LV winding.

$$T_1 = 7 \text{ cm},\ T_g = 40 \text{ cm},\ T_2 \approx 0,\ H_w = 125 \text{ cm},\ K_R = 0.88,\ H_{eq} = 142 \text{ cm},$$

$$\text{HV current} = 137.78 \text{ A},$$

$$\text{HV turns} = \frac{132 \times 10^3 / \sqrt{3}}{83.93} = 908,$$

$$(X_z)_{1\_oc} = \frac{2.48 \times 10^{-5} \times 50 \times (137.78 \times 908)}{142 \times 83.93} \times \left(\frac{1}{3} \times 7.0 \times 67.6 + 40 \times 114.6 \right)$$

$$= 61.73\% .$$

Similarly,

$$(X_z)_{2\_oc} = \frac{2.48\times10^{-5}\times50\times(137.78\times908)}{137.2\times83.93}\times\left(\frac{1}{3}\times10\times94.6+25\times129.6\right)$$
$$= 47.89\% .$$

The zero-sequence reactance as seen from the inner LV winding with the outer HV winding short-circuited is the same as the positive-sequence leakage reactance (if the reactance contributed by the neutral bar is neglected),

$$(X_z)_{12\_sc} = X_p = 12.16\% .$$

The zero-sequence reactance as seen from the HV winding with the LV winding short-circuited is calculated using Equation 3.79,

$$(X_z)_{21\_sc} = X_p \times \frac{(X_z)_{2\_oc}}{(X_z)_{1\_oc}} = 12.16\times\frac{47.89}{61.73} = 9.44\% .$$

The zero-sequence network [18] of this two winding transformer is shown in Figure 3.26 which satisfies all the calculated zero-sequence reactance values, $(X_z)_{1\_oc}$, $(X_z)_{2\_oc}$, $(X_z)_{12\_sc}$ and $(X_z)_{21\_sc}$.

For example, the zero-sequence reactance as seen from the (excited) HV winding with the short-circuited LV winding is

$$(X_z)_{21\_sc} = -0.835 + (13.0 \,//\, 48.73) = -0.835 + \frac{13.0\times48.73}{13.0+48.73} = 9.43\% ,$$

which matches closely with the value calculated previously.

In a similar way, the zero-sequence reactance of a three-winding three-phase three-limb transformer can be estimated as demonstrated by the following example.

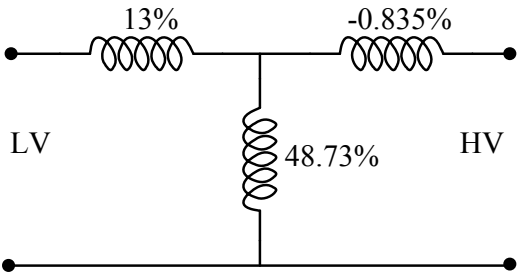

Figure 3.26 The zero-sequence network of the two-winding transformer in Example 3.6.

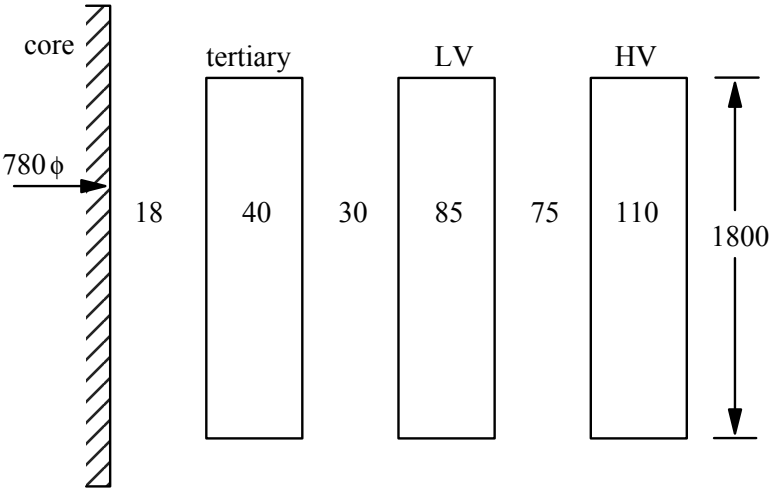

Figure 3.27 Dimensions of the three-winding transformer in Example 3.7.

Example 3.7

The relevant dimensions (in mm) of a 100 MVA, 220/66/11 kV, 50 Hz, YNynd1 transformer are given in Figure 3.27. The volts/turn is 160. Calculate the zero-sequence reactance of the transformer as seen from the HV winding with the LV winding short-circuited (and in the presence the delta-connected tertiary winding).

Solution:

Let the tertiary (11 kV), LV (66 kV) and HV (220 kV) windings be denoted by numbers 1, 2, and 3 respectively. The short-circuit positive-sequence reactances for the three pairs of the windings are calculated as

$$(X_p)_{12} = 6.0\%, \quad (X_p)_{23} = 14.6\%, \quad \text{and} \quad (X_p)_{13} = 22.64\%.$$

The open circuit zero-sequence reactances of the tertiary, LV and HV windings with an average distance of 250 mm between the HV winding and the tank are calculated as

$$(X_z)_{1\_oc} = 64.81\%, \ (X_z)_{2\_oc} = 57.71\%, \text{ and } (X_z)_{3\_oc} = 40.93\%.$$

The various zero-sequence reactances between the pairs of the windings are now obtained using Equation 3.79:

1. Zero-sequence voltage is applied to the HV winding, the LV winding is open-circuited, and the tertiary-delta is closed,

$$(X_z)_{31\_sc} = \frac{(X_z)_{3\_oc}}{(X_z)_{1\_oc}} \times (X_p)_{31} = \frac{40.93}{64.81} \times 22.64 = 14.3\% .$$

2. Zero-sequence voltage is applied to the LV winding, the HV winding is open-circuited, and the tertiary-delta is closed,

$$(X_z)_{21\_sc} = \frac{(X_z)_{2\_oc}}{(X_z)_{1\_oc}} \times (X_p)_{21} = \frac{57.71}{64.81} \times 6.0 = 5.34\% .$$

3. Zero-sequence voltage is applied to the HV winding, the LV winding is short-circuited, and the tertiary-delta is open,

$$(X_z)_{32\_sc} = \frac{(X_z)_{3\_oc}}{(X_z)_{2\_oc}} \times (X_p)_{32} = \frac{40.93}{57.71} \times 14.6 = 10.36\% .$$

The zero-sequence reactances of the three windings can now be calculated by using equations given in Section 3.5,

$$(X_z)_1 = \frac{1}{2} \times \left[(X_z)_{21\_sc} + (X_z)_{31\_sc} - (X_z)_{32\_sc} \right] = 4.64\%$$

$$(X_z)_2 = \frac{1}{2} \times \left[(X_z)_{21\_sc} + (X_z)_{32\_sc} - (X_z)_{31\_sc} \right] = 0.7\%$$

$$(X_z)_3 = \frac{1}{2} \times \left[(X_z)_{31\_sc} + (X_z)_{32\_sc} - (X_z)_{21\_sc} \right] = 9.66\% .$$

The zero-sequence star equivalent network of the three-winding transformer is shown in Figure 3.28. Using the network, the zero-sequence reactance of the transformer if measured from the HV side with the LV winding short-circuited and tertiary-delta closed can be determined as

$$(X_z)_{3\_21} = 9.66 + (0.7 \,//\, 4.64) = 10.27\% .$$

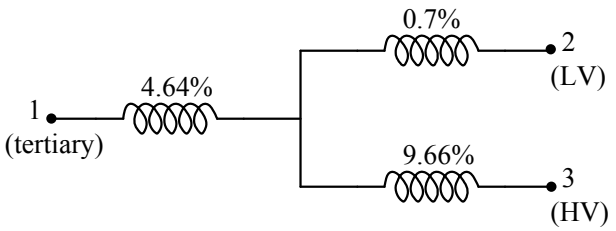

Figure 3.28 Zero-sequence star equivalent circuit.

Here, the system of four windings (i.e., the tertiary, LV and HV windings plus an imaginary winding representing the currents flowing in the tank) is converted into the equivalent three-winding system which takes into account the effect of the tank while calculating the short-circuit zero-sequence reactance between any two of the tertiary, LV and HV windings. Hence, the calculation of $(X_z)_{3\_21}$ by the star equivalent circuit of Figure 3.28 is an approximate way. Actually, the problem needs to be solved with an additional delta-connected winding representing the tank.

Let us now calculate the reactance by treating the tank as the fourth winding. The zero-sequence reactance can be calculated by the procedure given in Section 3.2 (i.e., the reactive kVA approach). Let I_1, I_2 and I_4 be the currents flowing through the tertiary, LV and equivalent delta (tank) windings respectively. The current flowing through the HV winding (I_3) is 1 per-unit and we know that

$$I_3 = 1 = I_1 + I_2 + I_4 .$$

The expression for Q is

$$Q = -\frac{1}{2}\begin{pmatrix} 2(X_p)_{12}(-I_1)(-I_2) + 2(X_p)_{13}(-I_1)I_3 + 2(X_p)_{14}(-I_1)(-I_4) \\ +2(X_p)_{23}(-I_2)I_3 + 2(X_p)_{24}(-I_2)(-I_4) + 2(X_p)_{34}I_3(-I_4) \end{pmatrix}.$$

The reactance between the tank and any other winding has already been calculated (e.g., $(X_p)_{14} = (X_z)_{1\_oc} = 64.81\,\%$). By putting the values of all the reactances and using $I_1 = 1 - I_2 - I_4$, the above expression becomes

$$Q = \left(22.64 - 14.04\,I_2 - 46.52\,I_4 + 13.1\,I_2\,I_4 + 6\,I_2^2 + 64.81\,I_4^2\right).$$

In order to have a minimum energy state, we differentiate the above expression with respect to I_2 and I_4, and equate the derivatives to zero and obtain two simultaneous equations. These two equations are solved to give

$$I_2 = 0.8747 \text{ and } I_4 = 0.2705 .$$

Putting these values in the expression for Q, we have $(X_z)_{3\_21} = 10.21\%$, which is close to that calculated by using the star equivalent circuit (i.e., 10.27%).

The methods described for the calculation of zero-sequence reactances can give reasonably accurate results and should be refined by empirical correction factors, if required, based on the results of tests conducted on a number of transformers. For more accurate calculations, numerical methods like FEM can be used [21, 22], in which the effect of the tank saturation on the zero-sequence reactance can be exactly simulated. The tank material should be modeled by defining its conductivity and nonlinear B-H characteristics. In power

transformers, tank shunts of a CRGO material are commonly put on the inner tank wall to reduce stray losses due to the leakage field. As explained earlier, the tank acts as an equivalent delta winding and reduces the zero-sequence reactance. The shunts provide an alternative low reluctance path to the zero-sequence flux and mitigate the effect of the tank. The magnetic shunts on the tank wall, therefore, have the effect of increasing the zero-sequence reactance. In such cases, an FEM analysis is essential for correct estimation of the reactance.

B. Three-phase five-limb and single-phase three-limb transformers

Since short-circuit reactances are much smaller than open-circuit reactances, the applied zero-sequence voltages, required to circulate rated currents, are usually much smaller than the rated voltages. Hence, in three-phase five-limb transformers, the yokes and the end limbs (which provide a path for the zero-sequence flux) do not saturate. Therefore, there will not be any currents flowing in the tank since all the flux is contained within the core. Hence, the short-circuit zero-sequence reactance is equal to the short-circuit positive-sequence reactance (the usual leakage reactance) in the three-phase five-limb transformers.

In single-phase three-limb transformers, their yokes and end limbs provide a path for the zero-sequence flux, and hence the zero-sequence reactance is equal to the positive-sequence reactance.

The above inferences can be drawn by analyzing the zero-sequence network in Figure 3.26. The shunt reactance is very high (~ infinity) due to a low reluctance value of the path provided by the end limbs and yokes in single-phase three-limb and three-phase five-limb transformers; the shunt branch now represents the magnetizing reactance in place of the reactance representing the imaginary (short-circuited) tank winding. This makes the short-circuit zero-sequence reactance equal to the corresponding positive-sequence (leakage) reactance with the HV winding excited and the LV winding short-circuited (or with the LV winding excited and the HV winding short-circuited).

3.8 Stabilizing Tertiary Winding

As mentioned earlier, in addition to primary and secondary windings, transformers are many times provided with an additional tertiary winding. It can be used for the following purposes:

- Static capacitors or synchronous condensers can be connected to the tertiary winding for injection of reactive power into the system for maintaining its voltage profile within certain limits.
- Auxiliary equipment in the substation can be supplied at a voltage level which is different and lower than that of the primary and secondary windings.

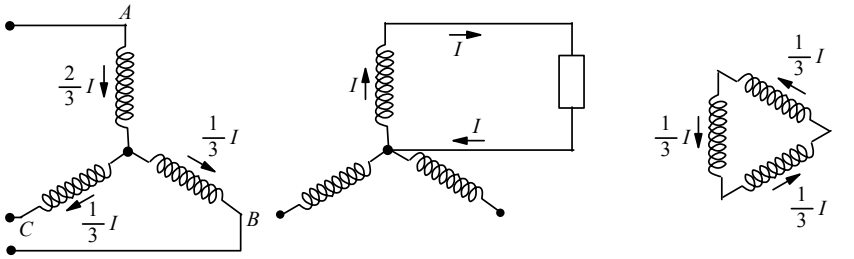

Figure 3.29 Unbalanced load.

- Three windings may be required for interconnecting three transmission lines operating at different voltages.

In these applications, the tertiary winding (which may be a star- or a delta-connected winding) is loaded. Sometimes an additional delta-connected tertiary winding is provided in transformers with the star- or auto-star-connected primary and secondary windings, which is usually not designed to take any load. Such an unloaded delta-connected winding is used for the stabilizing purpose as described below.

- Third harmonic magnetizing currents flow in the closed delta, making the induced voltages and the core flux almost sinusoidal (refer to Section 2.8).
- The winding stabilizes the neutral point; the zero-sequence impedance is lower and an unbalanced load can be taken without creating an undue unbalance in the phase voltages. Under asymmetrical loading conditions, the currents flow in such a way that the ampere-turns of the three windings balance each other as shown in Figure 3.29 for the case of a single-phase loading condition. The load on each phase of the tertiary winding is one-third of the single-phase load. Hence, the rating of the tertiary winding is usually one-third of the rating of the main windings.
- It can prevent the interference in telephone lines caused by third harmonic currents and voltages of transmission lines and earth circuits.

In the previous section, we have seen that the zero-sequence characteristics of three-phase three-limb transformers and three-phase five-limb transformers/banks of single-phase transformers are different. The magnetic circuit of the three-phase three-limb type acts as if open-circuited offering a high reluctance to the zero-sequence flux, and hence a lower zero-sequence reactance is obtained. It should be remembered that the higher the reluctance of a magnetic circuit the lower is the reactance reflected in its equivalent electric circuit. Three phase three-limb construction is not suitable for significantly unbalanced conditions since the resulting zero sequence flux has to complete its path through the tank structure which gets overheated due to induced eddy currents.

The five-limb and the shell form constructions are better-suited for unbalanced operations, since there is a path for the zero-sequence flux in them.

The magnetic circuit of three-phase five-limb transformers/banks of single-phase transformers can be visualized as a closed one giving a very high value of the zero-sequence reactance. If a delta-connected stabilizing winding is added to these three types of transformers, three-phase three-limb transformers, banks of three single-phase three-limb transformers, and three-phase five-limb transformers, the difference between the zero-sequence reactance characteristics of the three-phase three-limb transformers and that of the other two types diminishes. As long as one delta-connected winding is present, it makes a very little difference whether it is an effectively open or closed magnetic circuit from the zero-sequence reactance point of view.

A frequently asked question is whether the stabilizing winding can be dispensed with in the three-phase three-limb star-star (or auto-star) connected transformers with the grounded neutral condition. This is because, as seen in the previous section, the high reluctance nonmagnetic path offered to the zero-sequence flux results in a lower zero-sequence reactance as compared to the positive-sequence reactance, and thus to some extent the effect of the stabilizing winding is achieved. Whether or not the stabilizing winding can be omitted depends mainly on whether the zero-sequence and third harmonic characteristics are compatible with the system into which the transformer is going to be installed. If these two characteristics are not adversely affected in the absence of the stabilizing winding, it may be omitted [23]. Away from distribution points, in transmission networks the loading of the three phases of transformers is more or less balanced. Also, if the telephone-interference problem due to harmonic currents is within limits, and if the zero-sequence currents during asymmetrical fault conditions are large enough to be easily detected, the provision of the stabilizing winding in the three-phase three-limb transformers can be reviewed. This is because, since the stabilizing winding is generally unloaded, its conductor dimensions tend to be smaller. Such a winding becomes weak and vulnerable under asymmetrical fault conditions, which is a subject of discussion in Chapter 6.

Consequences of omitting the stabilizing winding in banks of three single-phase transformers/three-phase five-limb transformers can be significant. The zero-sequence reactance will be higher, and if the disadvantages of its high value cannot be tolerated, the stabilizing winding cannot be omitted. A low voltage stabilizing winding, with its terminal brought out, helps in very large transformers for carrying out tests such as the no-load loss test in the manufacturer's works. In the absence of this winding, it may not be possible to do the test if the manufacturer does not have a high-voltage source or a suitable step-up transformer. Alternatively, a star-connected auxiliary winding can be provided for the testing purpose, whose terminals can be buried inside the tank after the testing.

References

1. Blume, L. F., Boyajian, A., Camilli, G., Lennox, T. C., Minneci, S., and Montsinger, V. M. *Transformer engineering*, John Wiley and Sons, New York, and Chapman and Hall, London, 1951.
2. Hayt, W. H. *Engineering electromagnetics*, McGraw-Hill Book Company, Singapore, 1989, pp. 298–301.
3. Garin, A. N. and Paluev, K. K. Transformer circuit impedance calculations, *AIEE Transactions — Electrical Engineering*, June 1936, pp. 717–729.
4. Waters, M. *The short circuit strength of power transformers*, Macdonald, London, 1966, pp. 24–25, p. 53.
5. Boyajian, A. Leakage reactance of irregular distributions of transformer windings by method of double Fourier series, *AIEE Transactions — Power Apparatus and Systems,* Vol. 73, Pt. III-B, 1954, pp. 1078–1086.
6. Sollergren, B. Calculation of short circuit forces in transformers, *Electra*, Report no. 67, 1979, pp. 29–75.
7. Rabins, L. Transformer reactance calculations with digital computers, *AIEE Transactions — Communications and Electronics,* Vol. 75, Pt. I, 1956, pp. 261–267.
8. Silvester, P. P. and Ferrari, R. L. *Finite elements for electrical engineers*, Cambridge University Press, New York, 1990.
9. Andersen, O. W. Transformer leakage flux program based on Finite Element Method, *IEEE Transactions on Power Apparatus and Systems*, Vol. PAS-92, 1973, pp. 682–689.
10. Rothe, P. S. *An introduction to power system analysis*, John Wiley and Sons, New York, 1953, pp. 45–50.
11. Boyajian, A. Theory of three-circuit transformers, *AIEE Transactions*, February 1924, pp. 508–528.
12. Starr, F. M. An equivalent circuit for the four-winding transformer, *General Electric Review*, Vol. 36, No. 3, March 1933, pp. 150–152.
13. Aicher, L. C. Useful equivalent circuit for a five-winding transformer, *AIEE Transactions — Electrical Engineering*, Vol. 62, February 1943, pp. 66–70.
14. Schaefer, J. *Rectifier circuits: theory and design*, John Wiley and Sons, New York, 1965, pp. 12–19.
15. Christoffel, M. Zero-sequence reactances of transformers and reactors, *The Brown Boveri Review*, Vol. 52, No. 11/12, November/December 1965, pp. 837–842.
16. Clarke E. *Circuit analysis of AC power systems*, Vol. II, John Wiley and Sons, New York, Chapman and Hall, London, 1957, p. 153.
17. Jha, S. K. *Evaluation and mitigation of stray losses due to high current leads in transformers*, M. Tech Dissertation, Department of Electrical Engineering, IIT-Bombay, India, 1995.

18. Garin, A. N. Zero phase sequence characteristics of transformers, *General Electric Review*, Vol. 43, No. 3, March 1940, pp. 131–136.
19. Copper Development Association, *Copper for busbars*, Publication No. 22, January 1996, p. 53.
20. Schurig, O. R. Engineering calculation of inductance and reactance for rectangular bar conductors, *General Electric Review*, Vol. 36, No. 5, May 1933, pp. 228–231.
21. Allcock, R., Holland, S., and Haydock, L. Calculation of zero phase sequence impedance for power transformers using numerical methods, *IEEE Transactions on Magnetics*, Vol. 31, No. 3, May 1995, pp. 2048–2051.
22. Ngnegueu, T., Mailhot, M., Munar, A., and Sacotte, M. Zero phase sequence impedance and tank heating model for three-phase three-leg core type power transformers coupling magnetic field and electric circuit equations in a Finite Element software, *IEEE Transactions on Magnetics*, Vol. 31, No. 3, May 1995, pp. 2068–2071.
23. Cogbill, B. A. Are stabilizing windings necessary in all Y-connected transformers, *AIEE Transactions — Power Apparatus and Systems*, Vol. 78, Pt. 3, 1959, pp. 963–970.

4

Eddy Currents and Winding Stray Losses

The load loss of a transformer consists of the loss due to the ohmic resistance of windings (I^2R losses) and some additional losses. These additional losses are generally known as stray losses which occur due to the leakage field of windings and the field of high current carrying leads/bus-bars. The stray losses in the windings are further classified as eddy and circulating current losses. The remaining stray losses occur in structural steel parts. There is always some amount of leakage field in all types of transformers, and in large power transformers, which may be limited in size due to transport and space restrictions, the stray field strength increases with the rating much faster than in small transformers. The stray flux impinging on conducting parts (winding conductors and structural components) induces eddy currents in them. The stray loss in windings can be substantially high in large transformers if conductor dimensions and transposition methods are not chosen properly.

Today's designer faces challenges like higher loss capitalization rates and optimum performance requirements. In addition, there could be constraints on the dimensions and weight of the transformer. If the designer lowers the current densities in the windings to reduce the DC resistance loss (i.e., the I^2R loss), the eddy loss in them increases due to increased conductor dimensions. Hence, the winding conductors are usually subdivided using a proper transposition method to minimize the stray loss.

In order to accurately estimate and control the stray losses in windings and structural parts, an in-depth understanding of the fundamentals of eddy currents is desirable. Hence, the theory of eddy currents is described in the initial part of this chapter. The eddy loss and circulating current loss in windings are analyzed

in subsequent sections. Methods for the evaluation and control of these two losses are also described. The remaining components of the stray losses that occur in structural components are elaborated in Chapter 5.

4.1 Field Equations

The differential forms of Maxwell's equations, valid for static as well as time-dependent fields and also for free space as well as material bodies, are

$$\nabla \times \mathbf{E} = -\frac{\partial \mathbf{B}}{\partial t} \tag{4.1}$$

$$\nabla \times \mathbf{H} = \mathbf{J} + \frac{\partial \mathbf{D}}{\partial t} \tag{4.2}$$

$$\nabla \cdot \mathbf{B} = 0 \tag{4.3}$$

$$\nabla \cdot \mathbf{D} = \rho \tag{4.4}$$

where $\mathbf{H}$ = magnetic field strength (A/m)
$\mathbf{E}$ = electric field strength (V/m)
$\mathbf{B}$ = flux density (Wb/m^2)
$\mathbf{J}$ = current density (A/m^2)
$\mathbf{D}$ = electric flux density (C/m^2)
ρ = volume charge density (C/m^3).

There are three constitutive relations,

$$\mathbf{J} = \sigma \mathbf{E} \tag{4.5}$$

$$\mathbf{B} = \mu \mathbf{H} \tag{4.6}$$

$$\mathbf{D} = \varepsilon \mathbf{E} \tag{4.7}$$

where μ = permeability of material (henrys/m)
ε = permittivity of material (farads/m)
σ = conductivity (mhos/m).

The ratio of the conduction current density ($\mathbf{J}$) to the displacement current density ($\partial \mathbf{D}/\partial t$) is given by the ratio $\sigma/(j\omega\varepsilon)$, which is very high even for a poor metallic conductor (where ω is frequency in rad/sec). Since our analysis is for the power frequency, the displacement current density is neglected for the analysis of eddy currents in the conducting parts of transformers (copper, aluminum, steel, etc.). Hence, Equation 4.2 is simplified to

$$\nabla \times \mathbf{H} = \mathbf{J}. \tag{4.8}$$

The principle of conservation of charge gives the point form of the continuity equation,

$$\nabla \cdot \mathbf{J} = -\frac{\partial \rho}{\partial t}. \tag{4.9}$$

For slow time-varying fields in the present analysis of eddy currents in a conductor, displacement currents are neglected:

$$\nabla \cdot \mathbf{J} = 0. \tag{4.10}$$

The first-order differential Equations 4.1 and 4.8 involving both **H** and **E** are combined to give a second-order equation in **H** or **E** as follows. Taking the curl of both sides of Equation 4.8 and using Equation 4.5 we obtain,

$$\nabla \times \nabla \times \mathbf{H} = \nabla \times \sigma \mathbf{E}.$$

For a constant value of conductivity (σ), using vector algebra the equation can be simplified as

$$\nabla (\nabla \cdot \mathbf{H}) - \nabla^2 \mathbf{H} = \sigma \nabla \times \mathbf{E}. \tag{4.11}$$

Using Equation 4.6, with linear magnetic characteristics (i.e., constant μ), Equation 4.3 can be rewritten as

$$\nabla \cdot \mathbf{B} = \nabla \cdot \mu \mathbf{H} = \mu \nabla \cdot \mathbf{H} = 0 \tag{4.12}$$

which gives

$$\nabla \cdot \mathbf{H} = 0. \tag{4.13}$$

Using Equations 4.1 and 4.13, Equation 4.11 is simplified to

$$\nabla^2 \mathbf{H} = \sigma \frac{\partial \mathbf{B}}{\partial t} \tag{4.14}$$

or

$$\nabla^2 \mathbf{H} - \mu \sigma \frac{\partial \mathbf{H}}{\partial t} = 0 \tag{4.15}$$

which is known as a *diffusion equation*. Now, in the frequency domain, Equation 4.1 can be written as follows (the field quantities are phasors as well; caps are not put on their top for brevity):

$$\nabla \times \mathbf{E} = -j\omega \mathbf{B} \tag{4.16}$$

where the term $j\omega$ appears because the partial derivative of a sinusoidal field quantity with respect to time is equivalent to multiplying the corresponding phasor by $j\omega$. Using Equation 4.6 we have

$$\nabla \times \mathbf{E} = -j\omega\mu\,\mathbf{H}\,. \tag{4.17}$$

Taking the curl of both sides of the equation,

$$\nabla \times \nabla \times \mathbf{E} = -j\omega\mu\,\nabla \times \mathbf{H}\,. \tag{4.18}$$

Using Equation 4.8 we obtain

$$\nabla \times \nabla \times \mathbf{E} = -j\omega\mu\,\mathbf{J}\,. \tag{4.19}$$

Following the steps similar to those used for arriving at the diffusion Equation 4.15 and using the fact that $\nabla \cdot \mathbf{E} = (1/\varepsilon)\,\nabla \cdot \mathbf{D} = \rho/\varepsilon = 0$ (since no volume charge density is present) we have

$$\nabla \times \nabla \times \mathbf{E} = -\nabla^2 \mathbf{E} = -j\omega\mu\,\mathbf{J}\,. \tag{4.20}$$

Substituting the value of **J** from Equation 4.5,

$$\nabla^2 \mathbf{E} = j\omega\mu\sigma\,\mathbf{E}\,. \tag{4.21}$$

Now, let us assume that the vector field **E** has component only along the *x* axis.

$$\therefore \nabla^2 E_x = j\omega\mu\sigma E_x\,. \tag{4.22}$$

The expansion of the operator ∇ leads to a second-order partial differential equation,

$$\frac{\partial^2 E_x}{\partial x^2} + \frac{\partial^2 E_x}{\partial y^2} + \frac{\partial^2 E_x}{\partial z^2} = j\omega\mu\sigma E_x\,. \tag{4.23}$$

Suppose, if we further assume that E_x is a function of z only (i.e., it does not vary with x and y), then Equation 4.23 reduces to the following ordinary differential equation,

$$\frac{d^2 E_x}{dz^2} = j\omega\mu\sigma E_x\,. \tag{4.24}$$

We can write the solution of Equation 4.24 as

$$E_x = E_{xp}\,e^{-\gamma z} + E_{xp}\,e^{+\gamma z} \tag{4.25}$$

where E_{xp} is the amplitude factor, and γ is the propagation constant which can be expressed in terms of the attenuation constant α and the phase constant β,

$$\gamma = \alpha + j\beta\,. \tag{4.26}$$

Substituting the value of E_x from Equation 4.25 in Equation 4.24 we obtain

$$E_{xp}\,\gamma^2\,e^{-\gamma z} + E_{xp}\,\gamma^2\,e^{+\gamma z} = j\omega\mu\sigma\,(E_{xp}\,e^{-\gamma z} + E_{xp}\,e^{+\gamma z})\,, \tag{4.27}$$

which results in

$$\gamma^2 = j\omega\mu\sigma\ . \tag{4.28}$$

$$\therefore \gamma = \pm\sqrt{j\omega\mu\sigma}\ . \tag{4.29}$$

If the field E_x is incident on a surface of a conductor at $z = 0$ and is attenuated inside the conductor ($z > 0$), then only the plus sign has to be taken for γ .

$$\therefore \gamma = \sqrt{j\omega\mu\sigma} = \sqrt{\omega\mu\sigma} \times \sqrt{1\angle 90°} = \sqrt{\omega\mu\sigma} \times 1\angle 45°\ . \tag{4.30}$$

$$\therefore \gamma = (1+j)\sqrt{\frac{\omega\mu\sigma}{2}}\ . \tag{4.31}$$

Substituting $\omega = 2\pi f$, we obtain

$$\gamma = (1+j)\sqrt{\pi f\mu\sigma}\ . \tag{4.32}$$

Hence,

$$\alpha = \beta = \sqrt{\pi f\mu\sigma}\ . \tag{4.33}$$

The electric field intensity in the complex exponential notation in Equation 4.25, which is assumed to be along the *x* axis and is traveling or penetrating inside the conductor in +*z* direction, becomes

$$E_x = E_{xp}\,e^{-\gamma z} \tag{4.34}$$

which in the time domain can be written as

$$E_x = E_{xp}\,e^{-\alpha z}\cos(\omega t - \beta z)\,. \tag{4.35}$$

Substituting the values of α and β from Equation 4.33, we obtain

$$E_x = E_{xp}e^{-z\sqrt{\pi f\mu\sigma}}\cos(\omega t - z\sqrt{\pi f\mu\sigma})\,. \tag{4.36}$$

The conductor surface is represented by $z = 0$. Let $z > 0$ and $z < 0$ represent the regions corresponding to the conductor and the loss-free dielectric medium respectively. The source field at the surface of the conductor which establishes fields in it is

$$(E_x)_{z=0} = E_{xp}\cos\omega t\,.$$

Making use of Equation 4.5, which says that the current density within a conductor is directly related to the electrical field intensity, we can write

$$J_x = \sigma E_x = \sigma E_{xp} e^{-z\sqrt{\pi f \mu \sigma}} \cos(\omega t - z\sqrt{\pi f \mu \sigma}) . \tag{4.37}$$

Equations 4.36 and 4.37 tell us that away from the source at the surface and with penetration into the conductor, there is an exponential decrease in the electric field intensity and the conduction current density. At a distance of penetration $z = 1/\sqrt{\pi f \mu \sigma}$, the exponential factor becomes $e^{-1} (= 0.368)$, indicating that the value of the field (at this distance) reduces to 36.8% of that at the surface. This distance is called as the skin depth or the depth of penetration,

$$\delta = \frac{1}{\sqrt{\pi f \mu \sigma}} = \sqrt{\frac{2}{\omega \mu \sigma}} . \tag{4.38}$$

All the fields at the surface of a good conductor decay rapidly as they penetrate a few skin depths into it. Comparing Equations 4.33 and 4.38, we obtain the relationship,

$$\delta = \frac{1}{\alpha} = \frac{1}{\beta} \quad \text{and} \quad \gamma = \alpha + j\beta = \frac{1}{\delta} + \frac{j}{\delta} = (1 + j) \times \frac{1}{\delta} . \tag{4.39}$$

The skin depth is a very important parameter in describing the behavior of a conductor subjected to electromagnetic fields. The conductivity of copper conductor at 75°C (the temperature at which the load loss of transformers is usually calculated and guaranteed) is 4.74×10^7 mhos/m. Copper, being a non-magnetic material, has relative permeability of 1. Hence, the skin depth of copper at the power frequency of 50 Hz is

$$\delta_{Cu} = \frac{1}{\sqrt{\pi \times 50 \times \mu_0 \mu_r \times \sigma}} = \frac{1}{\sqrt{\pi \times 50 \times 4\pi \times 10^{-7} \times 1 \times 4.74 \times 10^7}} = 0.0103 \text{ m}$$

or 10.3 mm. The corresponding value at 60 Hz is 9.4 mm. For aluminum, whose conductivity is approximately 61% that of copper, the skin depth at 50 Hz is 13.2 mm. Most of the structural elements inside a transformer are made of either mild steel (MS) or stainless steel (SS) material. For a typical grade of MS material with relative permeability of 100 (assuming that it is saturated) and conductivity of 7×10^6 mho/m, the skin depth is $\delta_{MS} = 2.69$ mm at 50 Hz. Non-magnetic stainless steel is commonly used for structural components in the vicinity of fields due to high currents. For a typical grade of SS material with relative permeability of 1 (non-magnetic) and conductivity of 1.136×10^6 mho/m, the skin depth is $\delta_{SS} = 66.78$ mm at 50 Hz.

4.2 Poynting Vector

Poynting's theorem is the expression of the law of conservation of energy applied to electromagnetic fields. When the displacement current is neglected, as in the previous section, Poynting's theorem can be mathematically expressed as [1, 2]

$$-\oint_s (\mathbf{E}\times\mathbf{H})\cdot\mathbf{n}\,\mathrm{d}s = \int_v \mathbf{H}\cdot\frac{\partial\mathbf{B}}{\partial t}\mathrm{d}v + \int_v \mathbf{J}\cdot\mathbf{E}\,\mathrm{d}v \tag{4.40}$$

where v is the volume enclosed by the surface s and $\mathbf{n}$ is the unit vector normal to the surface directed outwards. Using Equation 4.5, the above equation can be modified as

$$-\oint_s (\mathbf{E}\times\mathbf{H})\cdot\mathbf{n}\,\mathrm{d}s = \int_v \mathbf{H}\cdot\frac{\partial\mathbf{B}}{\partial t}\mathrm{d}v + \frac{1}{\sigma}\int_v |\mathbf{J}|^2\,\mathrm{d}v\,. \tag{4.41}$$

This is a simpler form of Poynting's theorem which states that the net inflow of power is equal to the sum of the power absorbed by the magnetic field and the ohmic loss. The Poynting vector is given by the vector product,

$$\mathbf{P} = \mathbf{E}\times\mathbf{H} \tag{4.42}$$

which expresses the instantaneous density of power flow at a point.

Now, with $\mathbf{E}$ having only an x component which varies as a function of z only, Equation 4.17 becomes

$$\frac{\partial E_x}{\partial z} = -j\omega\mu H_y\,, \qquad H_x = 0\,, \quad H_z = 0\,. \tag{4.43}$$

Substituting the value of E_x from Equation 4.34 and rearranging we obtain

$$H_y = \frac{1}{-j\omega\mu}\times\frac{\partial}{\partial z}(E_{xp}e^{-\gamma z}) = \frac{\gamma E_x}{j\omega\mu} \tag{4.44}$$

The ratio of E_x to H_y is defined as the intrinsic impedance,

$$\eta = \frac{E_x}{H_y} = \frac{j\omega\mu}{\gamma}\,. \tag{4.45}$$

Substituting the value of γ from Equation 4.30 we obtain

$$\eta = \frac{j\omega\mu}{\sqrt{j\omega\mu\sigma}} = \sqrt{\frac{j\omega\mu}{\sigma}}\,. \tag{4.46}$$

Using Equation 4.38, the above equation can be rewritten as

$$\eta = \sqrt{j}\left[\frac{1}{\delta}\sqrt{\frac{2}{\sigma}}\right]\frac{1}{\sqrt{\sigma}} = \frac{\sqrt{1\angle 90°}\times\sqrt{2}}{\sigma\delta} = \frac{\sqrt{2}\angle 45°}{\sigma\delta}\,. \tag{4.47}$$

Now, Equation 4.36 can be rewritten in terms of the skin depth as

$$E_x = E_{xp}e^{-z/\delta}\cos(\omega t - z/\delta)\,. \tag{4.48}$$

Using Equations 4.45 and 4.47, H_y can be expressed as

$$H_y = \frac{\sigma\delta}{\sqrt{2}}E_{xp}e^{-z/\delta}\cos(\omega t - \frac{z}{\delta} - \frac{\pi}{4})\,. \tag{4.49}$$

Since **E** is in the *x* direction and **H** is in the *y* direction, the Poynting vector, which is a cross product of **E** and **H** according to Equation 4.42, is in the *z* direction.

$$\therefore P_z = E_x H_y = \frac{\sigma\delta}{\sqrt{2}}E_{xp}^2 e^{-2z/\delta}\cos(\omega t - z/\delta)\cos(\omega t - \frac{z}{\delta} - \frac{\pi}{4}) \tag{4.50}$$

Using the identity $\cos A\cos B = 1/2\left[\cos(A+B)+\cos(A-B)\right]$, the above equation simplifies to

$$P_z = \frac{\sigma\delta}{\sqrt{2}}E_{xp}^2 e^{-2z/\delta}\left[\frac{1}{2}\left\{\cos(2\omega t - \frac{2z}{\delta} - \frac{\pi}{4}) + \cos\frac{\pi}{4}\right\}\right]. \tag{4.51}$$

The time average Poynting vector is then given by

$$(P_z)_{avg} = \frac{1}{2}\frac{\sigma\delta}{\sqrt{2}}E_{xp}^2 e^{-2z/\delta}\cos\frac{\pi}{4} = \frac{\sigma\delta}{4}E_{xp}^2 e^{-2z/\delta}\,. \tag{4.52}$$

Thus, it can be observed that at a distance of one skin depth ($z = \delta$), the power density is only 0.135 ($= e^{-2}$) times its value at the surface. This is an important fact for the analysis of eddy currents and losses in structural components of transformers. If the eddy losses in the tank of a transformer due to the incident leakage field emanating from windings are being analyzed by using FEM, there should be at least two or three elements in one skin depth for obtaining accurate results.

Let us now consider a conductor with a field E_{xp} and the corresponding current density J_{xp} at the surface as shown in Figure 4.1. The fields have the value of 1 p.u. at the surface. The total power loss in the height (i.e., length) *h* and the width *b* is given by the value of power crossing the conductor surface [2] within the area ($h \times b$),

$$P = \int_S (P_z)_{avg}\, dS = \int_0^b \int_0^h \left[\frac{\sigma\delta}{4} E_{xp}^2 e^{-2z/\delta} \right]_{z=0} dx dy = \frac{\sigma\delta bh}{4} E_{xp}^2 = \frac{\delta bh}{4\sigma} J_{xp}^2 . \tag{4.53}$$

The total current in the conductor is determined by integrating the current density over the infinite depth of the conductor. Using Equations 4.34 and 4.39 we obtain

$$I = \int_0^\infty \int_0^b J_x\, dy\, dz = \int_0^\infty \int_0^b \frac{E_x}{\sigma} dy\, dz = \int_0^\infty \int_0^b \frac{E_{xp}\, e^{-\gamma z}}{\sigma} dy\, dz$$

$$= \int_0^\infty \int_0^b J_{xp}\, e^{\frac{-(1+j)z}{\delta}} dy\, dz = \frac{J_{xp} b\delta}{1+j} = \frac{J_{xp} b\delta}{\sqrt{2}\angle 45^\circ}. \tag{4.54}$$

If this total current is assumed to be uniformly distributed in one skin depth, the uniform current density can be expressed in the time domain as

$$J_u = \frac{J_{xp}}{\sqrt{2}} \cos\left(\omega t - \frac{\pi}{4} \right). \tag{4.55}$$

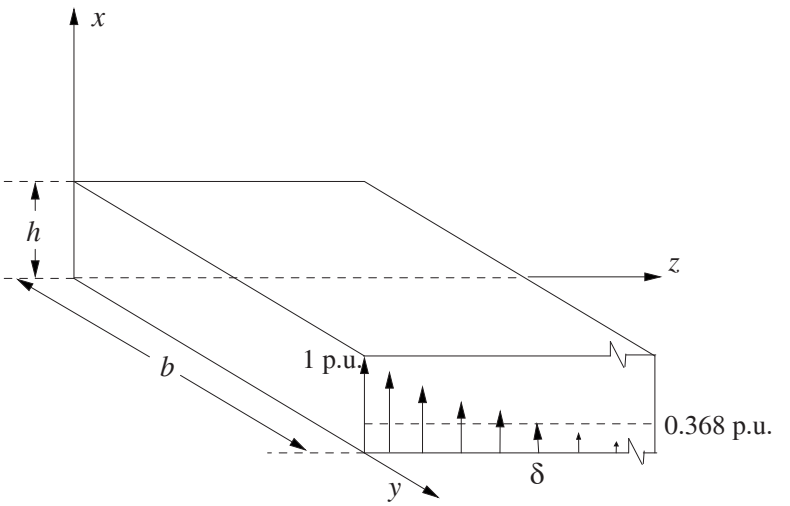

Figure 4.1 Penetration of field inside a conductor.

The total ohmic power loss is given by

$$P = \frac{1}{\sigma}\int_{v} J_u^2 \, \mathrm{d}v = \frac{1}{\sigma}\left(\frac{J_{xp}^2}{2}\cos^2\left(\omega t - \frac{\pi}{4}\right)\right) bh\delta \, . \tag{4.56}$$

The average value of power can be expressed as

$$P_{avg} = \frac{bh\delta}{2\sigma} J_{xp}^2 avg\left(\cos^2\left(\omega t - \frac{\pi}{4}\right)\right) = \frac{bh\delta}{2\sigma} J_{xp}^2 avg\left(\frac{1}{2}\left\{1 + \cos 2\left(\omega t - \frac{\pi}{4}\right)\right\}\right). \tag{4.57}$$

Since the average value of a cosine term over an integral number of periods is zero we have

$$P_{avg} = \frac{\delta bh}{4\sigma} J_{xp}^2 \tag{4.58}$$

which is the same as Equation 4.53. Hence, the average power loss in a conductor may be computed by assuming that the total current is uniformly distributed in one skin depth. This is an important result which can be used while calculating eddy current losses in conductors by numerical methods. When a numerical method such as FEM is used for estimating stray losses in the tank of a transformer, it is important to have the element size less than the skin depth of the tank material as explained earlier. With the overall dimensions of the field domain in meters, it is difficult to have very small elements inside the tank thickness. Hence, it is convenient to use analytical results to simplify the numerical analysis. For example, Equation 4.58 is used in [3] for the estimation of tank losses by 3-D FEM analysis. The method assumes uniform current density in the skin depth allowing the use of relatively larger element sizes. The above-mentioned problem of modeling and analysis of small skin depths can also be handled by using the concept of surface impedance. The intrinsic impedance can be rewritten from Equation 4.46 as

$$\eta = R + jX = \sqrt{\frac{j\omega\mu}{\sigma}} = 1\angle 45° \sqrt{\frac{\omega\mu}{\sigma}} = \sqrt{\frac{\omega\mu}{2\sigma}} + j\sqrt{\frac{\omega\mu}{2\sigma}} \, . \tag{4.59}$$

The real part of the impedance, called *surface resistance*, is given by

$$R = \sqrt{\frac{\omega\mu}{2\sigma}} \, . \tag{4.60}$$

After calculating the r.m.s. value of the tangential component of the magnetic field intensity (H_{rms}) at the surface of the tank or any other structural component in the transformer by either numerical or analytical methods, the specific loss per unit surface area can be calculated by the following expression [4],

$$P = R\,H_{rms}^2 = \sqrt{\frac{\omega\mu}{2\sigma}}\;H_{rms}^2\,. \tag{4.61}$$

Thus, the total losses in the transformer tank can be determined by integrating the specific loss over its internal surface.

4.3 Eddy Current and Hysteresis Losses

All the analysis done previously assumed linear material (*B*-*H*) characteristics meaning that the permeability (μ) is constant. The material used for structural components in transformers is usually magnetic steel (mild steel), which is a ferromagnetic material having a much larger value of relative permeability (μ_r) as compared to that of free space (for which μ_r =1). The material has nonlinear *B*-*H* characteristics and the permeability itself is a function of *H*. Moreover, the characteristics also exhibit hysteresis. Equation 4.6 ($\mathbf{B} = \mu\mathbf{H}$) has to be suitably modified to reflect the nonlinear characteristics and the hysteresis phenomenon.

The core properties are generally expressed in terms of its permeability and losses. In an alternative way, the properties can be described by a single quantity known as complex (or elliptic) permeability. With the help of this type of representation, it is possible to represent the core by a simple equivalent electric circuit and the core losses can be expressed as a function of frequency.

If *B* is assumed to be a sinusoidal quantity, *H* will be non-sinusoidal due to a typical shape of the hysteresis loop. In the complex permeability representation, the harmonics are neglected, and only the fundamental components of *B* and *H* are considered. The magnetic field intensity (*H*) and the current are in phase, whereas the flux density (*B*) and the voltage are in perfect quadrature relationship; the voltage *V* leads *B* or flux by 90 degrees according to Equation 1.1 which in the time-harmonic form becomes [5]:

$$\hat{B} = \left(\frac{-j}{N\omega A_c}\right)\hat{V}\,.$$

Here, $\hat{B}$ and $\hat{V}$ are phasors, and A_c is the cross-sectional area having magnetic path length *l* with *N* turns wound around it. In this discussion on complex permeability, caps are put on phasor quantities. We also know that

$$\hat{H} = \left(\frac{N}{l}\right)\hat{I}$$

$$\therefore \hat{\mu} = \frac{\hat{B}}{\hat{H}} = \left(\frac{-jl}{N^2\omega A_c}\right)\hat{Z}\,.$$

The above equation represents the complex permeability in terms of impedance. If $\hat{Z}$ is purely reactive, $\hat{\mu}$ turns into a real quantity representing a lossless case, but if $\hat{Z}$ is a complex quantity, then $\hat{\mu}$ has an imaginary component as well, representing the lossy nature of the material. $\hat{B}$ lags $\hat{H}$ by a hysteresis angle as shown in Figure 2.5 (b), with $\hat{H}$ having only the fundamental component (in the phasor notation, all the quantities vary sinusoidally at one frequency). In other words, we have achieved linearization with the hysteresis losses accounted in an approximate but reasonable way. In this formulation, where harmonics introduced by saturation are ignored, a functional relationship between *B* and *H* is now realized in which the permeability is made independent of *H* resulting in a linear system [6].

Let B_0 and H_0 be the peak values of the corresponding phasors. The relationship between B_0 and H_0 can be expressed as

$$\mu = B_0/H_0 = \sqrt{(\mu')^2 + (\mu'')^2} \quad \text{and} \quad \theta = \tan^{-1}(\mu''/\mu') \tag{4.62}$$

where μ' and μ'' are the real and imaginary components of the complex permeability. Here, the complex permeability is represented as

$$\hat{\mu} = \mu e^{-j\theta}. \tag{4.63}$$

For the sinusoidal magnetic field intensity, $H_0 \sin \omega t$, the flux density phasor can be expressed as [6]

$$\hat{B} = H_0(\mu' \sin \omega t + \mu'' \cos \omega t).$$

Using this equation, we obtain an elliptic *B*-*H* curve as shown in Figure 4.2. The equation of the ellipse in the Cartesian form is [6]

$$B = \mu' H \pm \mu'' \sqrt{H_0^2 - H^2}. \tag{4.64}$$

When $H = H_0$, $B = \mu' H_0$ the slope of the line joining the origin and the point Q on the ellipse is μ'. On the other hand, when $H = 0$, $B = B_r = \pm \mu'' H_0$ the slope of the line joining the point P and the *y* axis intercept (B_r) is in fact μ''. Thus, the real and imaginary components of the complex permeability can be determined from the aforesaid properties, if the *B*-*H* loop the material under investigation is determined experimentally.

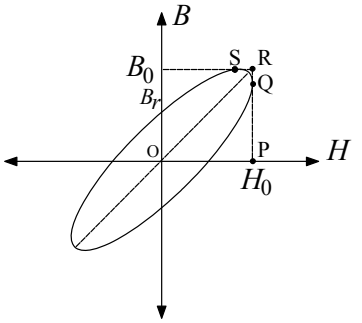

Figure 4.2 Elliptic hysteresis loop.

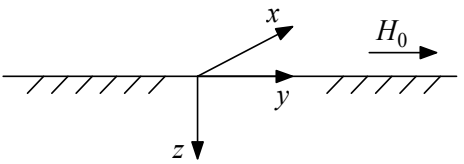

Figure 4.3 Infinite half space.

The area of the ellipse, ($\pi\mu'' H_0^2$), gives the hysteresis loss per unit volume in one cycle. If there were no hysteresis losses, the phasors $\hat{B}$ and $\hat{H}$ would be in phase, and the permeability has only the real component and the ellipse collapses into a straight line.

Let us now find the expressions for the eddy and hysteresis losses for an infinite half-space shown in Figure 4.3. The infinite half-space is an extension of the geometry shown in Figure 4.1 in the sense that the region of the material under consideration extends from $-\infty$ to $+\infty$ in the x and y directions, and from 0 to ∞ in the z direction. Similar to Section 4.1, we assume that **E** and **H** vectors have components in only the x and y directions respectively, and that they are a function of z only. The diffusion Equation 4.15 can be rewritten for this case in terms of the complex permeability as

$$\frac{d^2 H_y}{dz^2} = j\omega(\mu e^{-j\theta})\sigma H_y \,.$$

A solution satisfying boundary conditions,

$$H_y = H_0 \text{ at } z = 0 \text{ and } H_y = 0 \text{ at } z = \infty$$

is given by

$$H_y = H_0 e^{-kz} \tag{4.65}$$

where the constant k is

$$k = \sqrt{j\omega\sigma\mu e^{-j\theta}} = (1+j)\sqrt{\frac{\omega\mu\sigma}{2}}\; e^{-j\theta/2} = \frac{\alpha + j\beta}{\delta} \tag{4.66}$$

and

$$\alpha = \cos(\theta/2) + \sin(\theta/2) \text{ and } \beta = \cos(\theta/2) - \sin(\theta/2)\,. \tag{4.67}$$

$$\therefore H_y = H_0\, e^{-(\alpha+j\beta)z/\delta}. \tag{4.68}$$

Using Equation 4.8 and the fact that $H_x = H_z = 0$ we have

$$J_x = -\frac{d}{dz}(H_y) = H_0\,\frac{\alpha+j\beta}{\delta}\, e^{-(\alpha+j\beta)z/\delta}. \tag{4.69}$$

The time average density of the eddy and hysteresis losses is determined by computing the real part of the complex Poynting vector evaluated at the surface [1],

$$P_{e+h} = \frac{1}{2} Re\left[\mathbf{E}\times\mathbf{H}^*\right]_{z=0}. \tag{4.70}$$

Now,

$$\mathbf{E} = \left(J_x/\sigma\right)_{z=0}\mathbf{a}_x = \frac{H_0}{\sigma\delta}(\alpha+j\beta)\mathbf{a}_x \tag{4.71}$$

and

$$\mathbf{H} = H_0\,\mathbf{a}_y \tag{4.72}$$

$$\therefore P_{e+h} = \frac{1}{2}\mathrm{Re}\left[\frac{H_0}{\sigma\delta}(\alpha+j\beta)H_0\,\mathbf{a}_z\right] = \frac{1}{2}\left[\frac{H_0^2}{\sigma\delta}\right]\alpha. \tag{4.73}$$

In the absence of hysteresis ($\theta = 0$), $\alpha = \beta = 1$ according to Equation 4.67. Hence, the eddy loss per unit surface area is given by

$$P_e = \frac{1}{2}\left[\frac{H_0^2}{\sigma\delta}\right]. \tag{4.74}$$

Substituting the expression for the skin depth from Equation 4.38 and using the r.m.s. value of the magnetic field intensity (H_{rms}) at the surface we obtain

$$P_e = \frac{1}{2}\left[\frac{2H_{rms}^2}{\sigma}\right]\sqrt{\frac{\omega\mu\sigma}{2}} = \sqrt{\frac{\omega\mu}{2\sigma}}\; H_{rms}^2 \tag{4.75}$$

which is the same as Equation 4.61, as it should be in the absence of hysteresis (for linear *B*-*H* characteristics).

4.4 Effect of Saturation

In a transformer, the structural components (mostly made from a magnetic steel material) are subjected to a leakage field and/or a high current field. The incident field is predominantly concentrated in the skin depth near the surface. Hence, the structural components may be in a state of saturation depending upon the

magnitude of the incident field. The eddy current losses predicted by the calculations based on a constant value of the relative permeability are usually smaller than experimental values. Thus, although the magnetic saturation is part and parcel of the hysteresis phenomenon, it is considerably more important in its effect on the eddy current losses. The step function magnetization curve, as shown in Figure 4.4 (a), is the simplest way of taking the saturation into account for an analytical solution of eddy current problems. It can be expressed by the equation,

$$\mathbf{B} = (\text{sign of } \mathbf{H})\, B_s \tag{4.76}$$

where B_s is the saturation flux density. The magnetic field intensity **H** at the surface is sinusoidally varying with time $(= H_0 \sin \omega t)$. The extreme depth to which the field penetrates and beyond which there is no field is called the depth of penetration δ_s. This depth of penetration has a different connotation compared to that in the linear case discussed earlier. In this case, the depth of penetration is simply the maximum depth the field will penetrate at the end of each half period. A plate having thickness much larger than its depth of penetration is considered a thick one and it can be represented as an infinite half space; the corresponding depth of penetration is given by [1, 7, 8]

$$\delta_s = \sqrt{\frac{2H_0}{\omega \sigma B_s}}\,. \tag{4.77}$$

It can be observed that for this nonlinear case with step magnetization characteristics, the linear permeability in Equation 4.38 is replaced by the ratio B_s / H_0. Further, the expression for the average power per unit area can be derived as

$$P_e = \frac{8}{3\pi}\,\frac{H_0^2}{\sigma\,\delta_s} = 1.7\,\frac{H_0^2}{2\sigma\,\delta_s}\,. \tag{4.78}$$

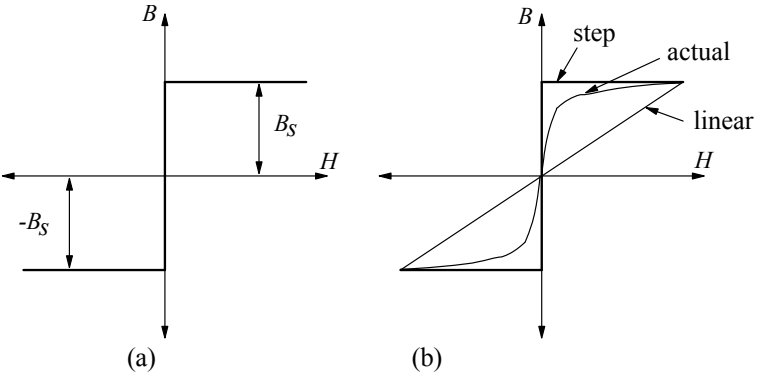

Figure 4.4 Step-magnetization.

Comparing this with Equation 4.74, it can be noted that if we put $\mu = B_s / H_0$, δ_s will be equal to δ and in that case the loss in the saturated material is 70% higher than the loss calculated with linearly approximated *B-H* characteristics. Practically, the actual *B-H* curve is between the linear and step characteristics, as shown in Figure 4.4 (b). In [7], it is pointed out that as we penetrate inside the material, each succeeding inner layer is magnetized by a progressively smaller number of exciting ampere-turns because of the shielding effect of the eddy currents in the region between the outermost surface and the layer under consideration. In step-magnetization characteristics, the flux density has the same magnitude irrespective of the magnitude of mmf. Due to this departure of the step curve response from the actual response, the value of B_s is replaced by $0.75 \times B_s$. From Equations 4.77 and 4.78, it is clear that $P_e \propto \sqrt{B_s}$, and hence the constant 1.7 in Equation 4.78 reduces to $1.7 \times \sqrt{0.75}$, i.e., 1.47. As per Rosenberg's theory, the constant is 1.33 [7]. Hence, in the simplified analytical formulations, linear characteristics are assumed after taking into account the nonlinearity by a linearization coefficient which is in the range of 1.3 to 1.5. For example, a value of 1.4 is used for the coefficient in [9] for the calculation of losses in the tank and the other structural components in transformers.

After having discussed the fundamentals of eddy currents, we will now analyze eddy current and circulating current losses in windings in the following sections. Analysis of stray losses in structural components, viz. the tank, frames, flitch plates, high current terminations, etc., is covered in Chapter 5.

4.5 Eddy Losses in Transformer Windings

4.5.1 Expression for the eddy loss

Theory of eddy currents explained in the previous sections will be useful while deriving the expression for the eddy loss occurring in windings. The losses in a transformer winding due to an alternating current are more than that due to a direct current of the same effective (r.m.s.) value. There are two different approaches for analyzing this increase in losses. In the first approach, we assume that the load current in the winding is uniformly distributed in the conductor cross section (similar to the direct current) and, in addition to the load current, there exist eddy currents which produce extra losses. Alternatively, one can calculate losses due to the combined action of the load current and the eddy currents. The former method is more suitable for the estimation of the eddy loss in windings, in which the eddy loss due to the leakage field (produced by the load current) is calculated separately and then added to the DC I^2R loss. The latter method is preferred for calculating circulating current losses, in which the resultant current in each conductor is calculated first, followed by the calculation of losses (which give the total of the DC I^2R loss and the circulating current loss). We will first analyze the eddy

losses in windings in this section; the circulating current losses are discussed in the next section.

Consider a winding conductor, as shown in Figure 4.5, which is placed in an alternating magnetic field along the *y* direction having the peak amplitude of H_0. The conductor can be assumed to be infinitely long in the *x* direction. The current density J_x and the magnetic field intensity H_y are assumed as functions of *z* only. Rewriting the (diffusion) Equation 4.15 for the sinusoidal variation of the field quantity and noting that the winding conductor, either copper or aluminum, has constant permeability (linear *B-H* characteristics),

$$\frac{d^2 H_y}{dz^2} = j\omega\mu\sigma H_y . \tag{4.79}$$

A solution satisfying this equation is

$$H_y = C_1 e^{\gamma z} + C_2 e^{-\gamma z} \tag{4.80}$$

where γ is defined by Equation 4.32. In comparison with Equation 4.65, Equation 4.80 has two terms representing waves traveling in both $+z$ and $-z$ directions (which is consistent with Figure 4.5). The incident fields on both the surfaces, having the peak amplitude of H_0, penetrate inside the conductor along the *z* axis in opposite directions. For the present case, the boundary conditions are

$$H_y = H_0 \text{ at } z = +b \text{ and } H_y = H_0 \text{ at } z = -b . \tag{4.81}$$

Using these boundary conditions, we can obtain the expression for the constants as

$$C_1 = C_2 = \frac{H_0 e^{\gamma b} - H_0 e^{-\gamma b}}{e^{2\gamma b} - e^{-2\gamma b}} = \frac{H_0}{e^{\gamma b} + e^{-\gamma b}} . \tag{4.82}$$

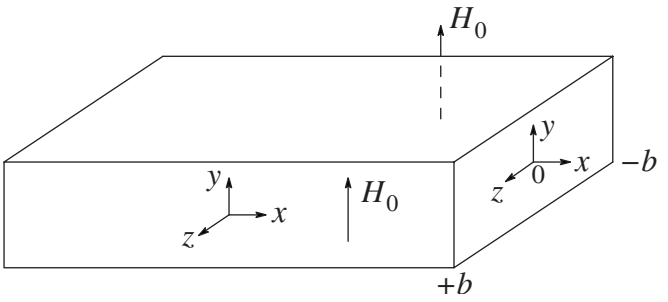

Figure 4.5 Estimation of eddy loss in a winding conductor.

Putting these values of the constants in Equation 4.80 we obtain

$$H_y = \frac{H_0(e^{\gamma z} + e^{-\gamma z})}{e^{\gamma b} + e^{-\gamma b}} = H_0 \frac{\cosh \gamma z}{\cosh \gamma b} . \tag{4.83}$$

Using Equation 4.8 and the fact that $H_x = H_z = 0$, the current density is

$$J_x = -\frac{dH_y}{dz} = -\gamma H_0 \frac{\sinh \gamma z}{\cosh \gamma b} . \tag{4.84}$$

The loss produced per unit surface area (of the *x*-*y* plane) of the conductor in terms of the peak value of the current density $\left(|J_x|\right)$ is given by

$$P_e = \frac{1}{2\sigma} \int_{-b}^{+b} |J_x|^2 dz . \tag{4.85}$$

Now, using Equation 4.39 we obtain

$$|J_x| = \left| -\gamma H_0 \frac{\sinh \gamma z}{\cosh \gamma b} \right| = H_0 \left| -\frac{1+j}{\delta} \frac{\sinh(1+j)z/\delta}{\cosh(1+j)b/\delta} \right|$$

$$= H_0 \left| -\frac{1+j}{\delta} \times \frac{\sinh(z/\delta)\cos(z/\delta) + j\cosh(z/\delta)\sin(z/\delta)}{\cosh(b/\delta)\cos(b/\delta) + j\sinh(b/\delta)\sin(b/\delta)} \right|$$

$$= \frac{\sqrt{2}H_0}{\delta} \left[\frac{(\sinh(z/\delta)\cos(z/\delta))^2 + (\cosh(z/\delta)\sin(z/\delta))^2}{(\cosh(b/\delta)\cos(b/\delta))^2 + (\sinh(b/\delta)\sin(b/\delta))^2} \right]^{1/2}$$

$$= \frac{\sqrt{2}H_0}{\delta} \left[\frac{\left(e^{z/\delta} - e^{-z/\delta}\right)^2 \cos^2(z/\delta) + \left(e^{z/\delta} + e^{-z/\delta}\right)^2 \sin^2(z/\delta)}{\left(e^{b/\delta} + e^{-b/\delta}\right)^2 \cos^2(b/\delta) + \left(e^{b/\delta} - e^{-b/\delta}\right)^2 \sin^2(b/\delta)} \right]^{1/2}$$

$$= \frac{\sqrt{2}H_0}{\delta} \left[\frac{\left(e^{2z/\delta} + e^{-2z/\delta}\right) - 2\left(\cos^2(z/\delta) - \sin^2(z/\delta)\right)}{\left(e^{2b/\delta} + e^{-2b/\delta}\right) + 2\left(\cos^2(b/\delta) - \sin^2(b/\delta)\right)} \right]^{1/2}$$

$$= \frac{\sqrt{2}H_0}{\delta} \left[\frac{\cosh(2z/\delta) - \cos(2z/\delta)}{\cosh(2b/\delta) + \cos(2b/\delta)} \right]^{1/2} . \tag{4.86}$$

Substituting this magnitude of the current density in Equation 4.85 we have

$$P_e = \frac{1}{2\sigma}\,\frac{2H_0^2}{\delta^2}\int_{-b}^{+b}\frac{\cosh(2z/\delta)-\cos(2z/\delta)}{\cosh(2b/\delta)+\cos(2b/\delta)}\,dz\,. \tag{4.87}$$

$$\therefore P_e = \frac{H_0^2}{\sigma\delta}\left[\frac{\sinh(2b/\delta)-\sin(2b/\delta)}{\cosh(2b/\delta)+\cos(2b/\delta)}\right] \tag{4.88}$$

or

$$P_e = \frac{H_0^2}{\sigma\delta}\left[\frac{e^{\xi}-e^{-\xi}-2\sin\xi}{e^{\xi}+e^{-\xi}+2\cos\xi}\right] \tag{4.89}$$

where $\xi = 2b/\delta$.

When $2b >> \delta$, i.e., $\xi >> 1$, Equation 4.89 can be simplified to

$$P_e \approx \frac{H_0^2}{\sigma\delta}\,. \tag{4.90}$$

Equation 4.90 gives the expression for the eddy loss per unit surface area of a conductor with its dimension, perpendicular to the applied field, much greater than the depth of penetration. Such a case, with the field applied on both surfaces of the conductor, is equivalent to two infinite half spaces. Therefore, the total eddy loss given by Equation 4.90 is two times that of the infinite half space analyzed earlier (Equation 4.74). For such thick conductors/plates (windings made of copper bars, structural components made from a magnetic steel material having sufficiently large thickness, etc.), the resultant current distribution is greatly influenced and limited by the effect of its own field and the currents are said to be *inductance-limited* [1] (currents are confined to the surface layers).

Now, let us analyze the case when the conductor thickness is much smaller than its depth of penetration, which is usually the case for rectangular paper insulated conductors used in transformers. For $2b << \delta$, i.e., $\xi << 1$, Equation 4.89 can be simplified to

$$P_e = \frac{H_0^2}{\sigma\delta}\left[\frac{\left(1+\xi+\frac{\xi^2}{2!}+\frac{\xi^3}{3!}\cdots\right)-\left(1-\xi+\frac{\xi^2}{2!}-\frac{\xi^3}{3!}\cdots\right)-2\left(\xi-\frac{\xi^3}{3!}\cdots\right)}{\left(1+\xi+\frac{\xi^2}{2!}+\frac{\xi^3}{3!}\cdots\right)+\left(1-\xi+\frac{\xi^2}{2!}-\frac{\xi^3}{3!}\cdots\right)+2\left(1-\frac{\xi^2}{2!}\cdots\right)}\right]$$

$$= \frac{H_0^2}{\sigma\delta}\left[\frac{\left(4\frac{\xi^3}{3!}+\cdots\right)}{4+4\frac{\xi^4}{4!}+\cdots}\right]. \tag{4.91}$$

Neglecting the higher order terms and substituting the expression of δ from Equation 4.38 we have

$$P_e = \frac{H_0^2}{\sigma\delta}\frac{\xi^3}{6} = \frac{H_0^2}{\sigma\delta}\frac{8b^3}{6\delta^3} = \frac{H_0^2}{\sigma}\frac{8b^3\omega^2\mu^2\sigma^2}{24} = \frac{1}{3}(\mu H_0)^2\sigma\omega^2 b^3 . \qquad (4.92)$$

Now, if the thickness of the winding conductor is *t*, then substituting $b = t/2$ in Equation 4.92 we obtain

$$P_e = \frac{1}{3}B_0^2\sigma\omega^2\left(\frac{t}{2}\right)^3 = \frac{\omega^2 B_0^2 t^3\sigma}{24} . \qquad (4.93)$$

It is more convenient to find an expression for the mean eddy loss per unit volume (since the volume of the conductor in the winding is usually known). Hence, dividing by t and finally substituting ρ (resistivity) as $1/\sigma$, we obtain the expression for the eddy loss in the winding conductor per unit volume as

$$P_E = \frac{\omega^2 B_0^2 t^2}{24\rho} . \qquad (4.94)$$

In the case of thin conductors, the eddy currents are said to be *resistance-limited* since they are restricted by lack of space or high resistivity [1]. In other words, since the field of the eddy currents is negligible for thin conductors, the behavior is dominated by resistive effects. Equation 4.94 matches exactly with that derived in [10] by ignoring the magnetic field produced by the eddy currents. These currents are 90° out of phase with the uniformly distributed load current flowing in the conductor, which produces the leakage field and is also responsible for the DC I^2R loss in windings. The eddy currents are shown to be lagging by 90° with respect to the load (source) current for a thin circular conductor in a later part of this section. The total current flowing in the conductor can be visualized to be a vector sum of the eddy current (I_{eddy}) and load current (I_{load}) components, having the magnitude of $\sqrt{(I_{eddy})^2 + (I_{load})^2}$, because these two current components are 90° out of phase in a thin conductor. This is a very important and convenient result because it means that the I^2R losses due to the load current and the induced eddy currents can be calculated separately and then added later for thin conductors.

Equation 4.94 is a very well-known and useful formula for the calculation of the eddy loss in windings. If we assume that the leakage field in windings is in the axial direction only, we can calculate the mean value of the eddy loss in the whole winding by using the theory in Section 3.1.1. The axial leakage field for an inner winding (having radial depth R and height H_W) varies linearly from its inside diameter to outside diameter as shown in Figure 4.6. The

thickness of the conductor, the dimension perpendicular to the axial field, is usually small. Hence, the same value of flux density (B_0) can be assumed along its two vertical surfaces. The position of the conductor changes along the radial depth as the turns are wound. Hence, in order to calculate the mean value of the eddy loss of the whole winding, we have to first calculate the mean value of B_0^2 . The r.m.s. value of the ampere turns change linearly from 0 at the inside diameter (ID) to NI at the outside diameter (OD). The peak value of the flux density at a distance x from the inside diameter is

$$B_x = \frac{\sqrt{2}\,\mu_0}{H_W}\left[\left(\frac{x}{R}\right)NI\right]. \tag{4.95}$$

The mean flux density value, which gives the same overall loss, is given by

$$(B_0^2)_{mean} = \frac{1}{R}\int_0^R \left[\frac{\sqrt{2}\,\mu_0 NI}{H_W}\right]^2 \frac{x^2}{R^2}\,dx\,. \tag{4.96}$$

Simplifying we obtain

$$(B_0^2)_{mean} = \frac{(B_{gp}^2)}{3} \tag{4.97}$$

where B_{gp} is the peak value of the flux density in the LV-HV gap,

$$B_{gp} = \frac{\sqrt{2}\,\mu_0 NI}{H_W}\,. \tag{4.98}$$

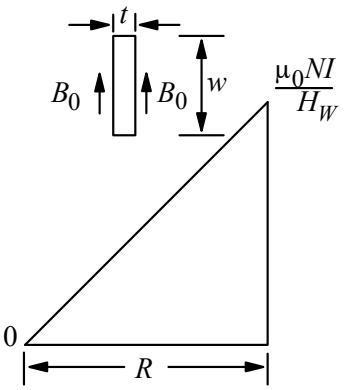

Figure 4.6 Leakage flux density distribution in a winding.

Hence, using Equations 4.97 and 4.94, the mean eddy loss per unit volume of the winding due to the axial leakage field is expressed as

$$(P_E)_{mean} = \frac{\omega^2 t^2}{24\rho}\,\frac{B_{gp}^2}{3}. \tag{4.99}$$

If we are interested in determining the mean value of the eddy loss in a section of a winding in which ampere-turns are changing from $a(NI)$ at ID to $b(NI)$ at OD, where NI are rated r.m.s. ampere-turns, the expression for the mean value of B_0^2 can be determined by using a procedure similar to that given in Section 3.1.1,

$$(B_0^2)_{mean} = \frac{(B_{gp}^2)}{3}\left[a^2 + ab + b^2\right] \tag{4.100}$$

and the mean eddy loss per unit volume in the section is

$$(P_E)_{mean} = \frac{\omega^2 t^2}{24\rho}\,\frac{(B_{gp}^2)}{3}\left[a^2 + ab + b^2\right]. \tag{4.101}$$

Equation 4.101 tells us that for a winding consisting of a number of layers, the mean eddy loss of the layer adjacent to the LV-HV gap is higher than that of the other layers. For example, in the case of a 2-layer winding,

$$(B_0^2)_{mean} = \frac{(B_{gp}^2)}{3}\left[\left(\frac{1}{2}\right)^2 + \frac{1}{2}\times 1 + 1^2\right] = 1.75\frac{(B_{gp}^2)}{3} \quad \text{(for the second layer)}$$

indicating that the mean eddy loss in the second layer close to the gap is 1.75 times the mean eddy loss for the entire winding. Similarly, for a 4-layer winding,

$$(B_0^2)_{mean} = \frac{(B_{gp}^2)}{3}\left[\left(\frac{3}{4}\right)^2 + \frac{3}{4}\times 1 + 1^2\right] = 2.31\frac{(B_{gp}^2)}{3} \quad \text{(for the fourth layer)}$$

giving the mean eddy loss in the 4th layer as 2.31 times the mean eddy loss for the entire winding. Hence, it is always advisable to calculate the total loss ($I^2R + eddy$) in each layer separately and estimate its temperature rise. Such a calculation procedure helps designers in taking countermeasures to eliminate high temperature rise problems in windings. Also, the temperatures measured by fiber-optic sensors (if installed) will be closer to the calculated values when this calculation procedure is adopted.

Eddy loss calculated by Equation 4.99 is approximate since it assumes that the leakage field is entirely in the axial direction. As seen in Chapter 3, there

exists a radial component of the leakage field at winding ends and in winding zones where ampere-turns per unit height are different for the LV and HV windings. For small distribution transformers, the error introduced by neglecting the radial field may not be appreciable, and Equation 4.99 is generally used with some empirical correction factor applied to the total calculated stray loss value. Analytical/numerical methods, described in Chapter 3, need to be used for the correct estimation of the radial field. The amount of effort required for obtaining the accurate eddy loss value might not be justified for small-distribution transformers. For medium- and large-power transformers, however, the eddy loss due to the radial field has to be estimated and the same can be determined by using Equation 4.94, for which the dimension of the conductor perpendicular to the radial field is its width w. Hence, the eddy losses per unit volume due to the axial (B_y) and radial (B_x) components of the leakage field are

$$(P_E)_{axial} = \frac{\omega^2 B_y^2 t^2}{24\rho} \tag{4.102}$$

$$(P_E)_{radial} = \frac{\omega^2 B_x^2 w^2}{24\rho}. \tag{4.103}$$

Thus, the leakage field incident on a winding conductor (see Figure 4.7) is resolved into two components, viz. B_y and B_x, and losses due to these two components are calculated separately by Equations 4.102 and 4.103, and then added. This is permitted because the eddy currents associated with these two perpendicular components do not overlap (since the angle between them is 90°).

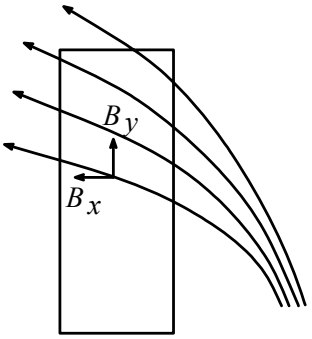

Figure 4.7 Winding conductor in a leakage field.

We have assumed that the conductor dimension is very much less than the depth of penetration while deriving Equation 4.94. This is particularly true in the case of the loss due to the axial field. The conductor thickness used in transformers mostly falls in the range of 2 to 3.5 mm and is considerably less than the depth of penetration of copper and aluminum, which is 10.3 mm and 13.2 mm, respectively, at 50 Hz. The conductor width is usually closer to the depth of penetration. If the conductor width is equal to the depth of penetration ($w = 2b = \delta$), Equation 4.89 becomes

$$(P_e)_{2b=\delta} = \frac{H_0^2}{\sigma\delta}\left[\frac{e^1 - e^{-1} - 2\sin 1}{e^1 + e^{-1} + 2\cos 1}\right] = \frac{1}{6.24}\frac{H_0^2}{\sigma\delta} \quad : \textit{from the exact equation.}$$

Comparing this value with that given by Equation 4.92,

$$(P_e)_{2b=\delta} = \frac{H_0^2}{\sigma\delta}\frac{\xi^3}{6} = \frac{1}{6}\frac{H_0^2}{\sigma\delta} \quad : \textit{from the approximate equation,}$$

an error of just 4% is obtained, which is acceptable. Hence, it can be concluded that the eddy loss due to the radial field can also be calculated with reasonable accuracy from Equation 4.103 for the conductor width comparable to the depth of penetration.

For thin circular conductors of radius of R, if the ratio R/δ is small, we can neglect the magnetic field of eddy currents. If the total current in the conductor is $I\cos\omega t$, the uniform current density is given by

$$J_0 = \frac{I}{\pi R^2}\cos\omega t \tag{4.104}$$

and the eddy current density at any radius r inside the conductor is [8]

$$J_e = \frac{I}{2\pi\delta^2}\left[\frac{1}{2} - \frac{r^2}{R^2}\right]\sin\omega t\,. \tag{4.105}$$

Thus, it can be observed from Equations 4.104 and 4.105 that for thin conductors (exhibiting resistance-limited behavior), the eddy currents lag the exciting current that produces the field responsible for them by 90°. Contrary to this, for thick conductors (with the thickness or radius much larger than the depth of penetration), the eddy currents lag the exciting current by 180° (this is an inductance-limited behavior in which the currents are confined to the surface layers).

The power loss per unit length of the thin circular conductor can be determined by using Equations 4.104 and 4.105 as (J_0 and J_e are 90° apart, square of their sum is equal to the sum of their squares)

$$P_1 = \int_0^R \left[\frac{|J_0|^2 + |J_e|^2}{2\sigma} \right] 2\pi r\, dr = \frac{I^2}{2\pi R^2 \sigma} + \frac{I^2 R^2}{96\pi \sigma \delta^4} . \quad (4.106)$$

The power loss per unit length due to the exciting current alone is

$$P_2 = \left(\frac{I}{\sqrt{2}} \right)^2 \times \frac{1}{\sigma} \times \frac{1}{\pi R^2} . \quad (4.107)$$

Therefore, the ratio of the effective AC resistance to the DC resistance of the thin circular conductor can be deduced from Equations 4.106 and 4.107 as

$$\frac{R_{AC}}{R_{DC}} = \frac{P_1}{P_2} = 1 + \frac{1}{48} \left(\frac{R}{\delta} \right)^4 \qquad \cdots \textit{for thin circular conductors} . \quad (4.108)$$

For thick circular conductors ($R >> \delta$), the effective resistance is that of an annular ring of diameter $2R$ and thickness δ, since all the current can be assumed to be concentrated in one depth of penetration as discussed in Section 4.2. Hence, the effective AC resistance per unit length is

$$R_{AC} = 1/(2\pi R \delta \sigma) \quad (4.109)$$

and

$$\frac{R_{AC}}{R_{DC}} = \frac{R}{2\delta} \qquad \cdots \textit{for thick circular conductors} . \quad (4.110)$$

4.5.2 Methods of estimation

As said earlier, the axial and radial components of a leakage field distribution can be estimated by analytical or numerical methods. Accurate estimation of the eddy loss due to the radial component by means of empirical formulae is not possible. Analytical methods [11, 12] and 2-D FEM [13, 14] can be used to calculate the eddy loss due to axial and radial leakage fields. It is assumed that the eddy currents do not have influence on the leakage field (i.e., a case of thin conductors). The FEM analysis is commonly used for the eddy loss calculations. The winding is divided into many sections. For each section the corresponding ampere-turn density is defined. The value of conductivity is not defined for these sections. The values of B_y and B_x for each conductor can be obtained from the FEM solution, and then the axial and radial components of the eddy loss are calculated for each conductor by using Equations 4.102 and 4.103, respectively. The B_y and B_x values are assumed to be constant over the conductor cross-section and are taken as equal to the corresponding values at its center. In cylindrical coordinates, B_y and B_x components are replaced by B_z

and B_r components, respectively. The total eddy loss for each winding is calculated by integrating the loss components of all its conductors.

Sometimes a quick but reasonably accurate estimate of the eddy loss is required. At the tender design stage, an optimization program may have to work out hundreds of options to arrive at an optimum design. In such cases, expressions for the eddy loss in windings for standard configurations can be determined using a multiple regression method in conjunction with an Orthogonal Array Design of Experiments technique [15]. However, due to rapid developments in computing facilities, it is now possible to integrate more accurate analytical or 2-D numerical methods into design optimization programs.

For cylindrical windings in core-type transformers, two-dimensional methods give sufficiently accurate eddy loss values. For getting the most accurate results, three-dimensional magnetic field calculations have to be performed [16, 17, 18]. Once a three-dimensional field solution is obtained, the three components of the flux density (B_x, B_y and B_z) are resolved into two components, viz. the axial and radial components; this approach enables the use of Equations 4.102 and 4.103 for the eddy loss evaluation.

For distribution transformers whose LV winding is made using a thick rectangular bar conductor, each and every turn of the winding has to be modeled (with the value of conductivity defined) in the FEM analysis. This is because the thickness of the bar conductor is usually comparable to or sometimes more than the depth of penetration, and its width is usually more than 5 times the depth of penetration. With such a conductor having large dimensions, a significant modification of the leakage field occurs due to the eddy currents, which cannot be neglected in the calculations.

4.5.3 Optimization of losses and elimination of winding hot spots

While designing a winding, if the designer increases conductor dimensions to reduce the DC resistance (I^2R) loss, the eddy loss increases. Hence, optimization of the sum of the I^2R and eddy losses should be done.

The knowledge of flux density distribution within a winding helps in choosing proper dimensions of its conductor. This is particularly important for windings having tappings within their body; high values of radial field in the tap zone can cause excessive loss and temperature rise problems. For minimization of radial flux, balancing of ampere-turns per unit height of the LV and HV windings should be done (for various sections along their height) at the average tap position. The winding with taps can be designed with different conductor dimensions in the tap zone to minimize the risk of hot spots. Guidelines are given in [19] for choosing the conductor width for eliminating hot spots in windings. For 50 Hz frequency, the maximum width that can be used is usually in the range of 12 to 14 mm, whereas for 60 Hz it is of the order of 10 to 12 mm.

This guideline is useful in the absence of a detailed calculation of temperature rise distribution in the part of the winding where a hot spot is suspected. For calculating the temperature rise of a disk or a turn, its I^2R loss and eddy loss should be added. An idle winding between the LV and HV windings links the high gap flux resulting in a substantial amount of eddy loss in it. Hence, its conductor dimensions should be properly decided.

In gapped core shunt reactors, there is considerable flux fringing between consecutive limb packets (separated by a non-magnetic gap), resulting in appreciable radial flux causing excessive losses in their winding if its distance from the core is small or if the conductor width is large.

One of the most logical ways of reducing the eddy loss of a winding is to subdivide winding conductors into a number of parallel conductors. If a conductor having thickness t is subdivided into two insulated parallel conductors, each of thickness $t/2$, the eddy loss due to the axial leakage field reduces by a factor of $1/4$ (according to Equation 4.102). However, there is a limitation imposed on the minimum value of thickness that can be used from the short-circuit withstand considerations. Also, if the width to thickness ratio of a rectangular conductor is more than about 6, there may be difficulty in winding it. The subdivision of the conductor also impairs the winding space factor in the radial direction. This is because each individual parallel conductor in a turn has to be insulated increasing the total insulation thickness in the direction. In order to improve the space factor, sometimes a bunch conductor is used in which usually two or three parallel conductors are bunched in a common paper covering. The advantage is that each conductor needs to be insulated with a lower paper insulation thickness because of the outermost common paper covering. A single bunch conductor is also easier to wind, since no crossovers are required at ID and OD of the winding. In contrast to this, for example in the case of two parallel conductors, the conductors are usually crossed over at ID and OD of each disk for the ease of winding. Three rectangular strip conductors and the corresponding bunch conductor are shown in Figure 4.8. For a strip conductor having radial thickness of 2 mm and paper covering of 0.5 mm, the total radial dimension of the three strip conductors is 9 mm, whereas for a bunch conductor having individual radial insulation of 0.175 mm and common outermost radial insulation of 0.325 mm, the total radial dimension is 7.7 mm ($=3\times(2+2\times 0.175)+2\times 0.325$) giving 15% improvement in the space factor.

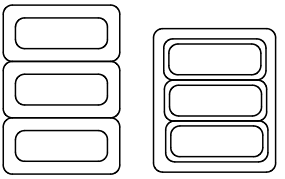

Figure 4.8 Strip and bunch conductor.

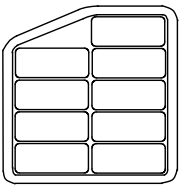

Figure 4.9 CTC conductor.

For a continuously transposed cable (CTC) conductor, in which a number of small rectangular conductors are transposed at regular intervals, it is possible to use much smaller thickness (as low as 1.2 mm) and width (as low as 3.8 mm), reducing the eddy loss considerably. Cost-benefit analysis has to be done to check the advantage gained by the reduction of losses vis-à-vis a higher cost of the CTC conductor. For a transformer specification with a high value of the load loss capitalization (dollars per kW of the load loss), the CTC conductor may give a lower total capitalized cost (i.e., the sum of material and loss costs) particularly in large transformers. The LV winding in large generator transformers is usually designed using a CTC conductor to minimize the eddy loss and improve productivity. A typical CTC conductor is shown in Figure 4.9.

One more way of reducing the eddy loss is by the use of a combination of two conductors with different widths along the winding height. At the winding ends, there may be an appreciable eddy loss due to the fact that the radial flux is incident perpendicularly on the wider conductor dimension (width). This loss can be decreased by reducing the conductor width for few disks at the ends using FEM-based calculations. The width of the conductor for the remaining middle portion, which has predominantly an axial field, is increased to have the same overall height, so that the I^2R losses are maintained approximately constant. Such an arrangement can give reduction in the winding loss ($I^2R + eddy$) by about 1 to 2% in large transformers.

In another method, end disks can have fewer turns per disk (one or two turns less compared to the remaining disks) in the HV winding having a large number of turns per disk. A conductor with higher thickness and lower width can be used for these disks so that I^2R loss is kept approximately constant and the eddy loss is reduced. This scheme is useful when the increase in the axial eddy loss due to a higher thickness is smaller than the decrease in the radial eddy loss due to a lower width (which may be particularly true at the ends since a reduction in the axial field value is accompanied by an increased radial field).

In both these methods, ampere-turns of the HV and LV windings per unit height should be equal (for various sections along their height); otherwise there will be an extra radial flux and the corresponding losses, nullifying the advantages gained.

A combination of strip and CTC conductors can be used to minimize the winding losses. A CTC conductor is used for a few top and bottom disks reducing the eddy loss, whereas the remaining disks are wound using a strip conductor. This technique requires establishment of a proper method for making the joint between the two types of conductors.

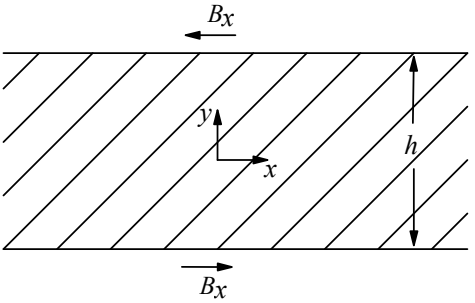

Figure 4.10 Foil winding analysis.

4.5.4 Eddy loss in foil windings

In small transformers, foil windings (made up of thin sheets of copper or aluminum) are popular because of the simplicity obtained in winding operations. A metal foil and an insulation layer can be wound simultaneously on a special machine and the whole process can be mechanized. In these windings, the eddy loss due to the axial leakage field is insignificant because of the thinness of the foil. On the contrary, radial field at the ends of the winding results in a substantial amount of the (radial) eddy loss.

The eddy loss in a foil winding can be evaluated by analytical or numerical methods. The eddy current density has been obtained as a solution of an integral equation of Fredholm type for a two winding transformer in [20]. For specific transformer dimensions given in the paper, the coefficient for the additional loss is 1.046; i.e., the eddy loss is 4.6% of the DC I^2R loss. In another approach [21], a boundary-value field problem formulated in terms of the magnetic vector potential in cylindrical coordinates is solved using modified Bessel and Struve functions. For symmetrically placed LV (foil) and HV windings, the additional loss factor reported in the paper is 5.8%. For an asymmetrical arrangement of windings, this loss would increase.

In [22], the foil winding is assumed a vertical section of an infinitely wide and deep conducting plate which is assumed symmetrically penetrated on both sides by plane electromagnetic waves. The geometry is given in Figure 4.10, where h is the height of the foil winding and B_x denotes the value of the flux density at the winding ends. The induced eddy current density (with the vertical dimensions specified with respect to the middle of the winding height) is [22]

$$J_e = \frac{B_x}{\mu_0 \delta} e^{\left[-\left(\frac{h}{2}-y\right)/\delta\right]} \left[\cos\left(\frac{\pi}{4} - \frac{\frac{h}{2}-y}{\delta}\right) + j\sin\left(\frac{\pi}{4} - \frac{\frac{h}{2}-y}{\delta}\right)\right]. \quad (4.111)$$

The eddy loss in terms of the peak value of the current density is given as

$$P_e = \frac{1}{2\sigma}\int_v |J_e|^2 dv \,. \tag{4.112}$$

It is clear from Equations 4.111 and 4.112 that

$$P_e \propto |J_e|^2 \propto e^{\left[-2\left(\frac{h}{2}-y\right)\Big/\delta\right]} \,. \tag{4.113}$$

Hence, the eddy loss is maximum at $y = h/2$ (at the two winding ends) since at this height the exponential term has the maximum value of 1,

$$e^{\left[-2\left(\frac{h}{2}-y\right)\Big/\delta\right]} = 1$$

whereas its value is just 0.0067 at $y = (h/2) - 2.5\delta$, which means that more than 99% of the induced eddy loss occurs in just 2.5δ depth from the winding ends. For an aluminum foil winding, whose skin depth is 13.2 mm at 50 Hz, almost all the eddy loss is concentrated in 33 mm from the winding ends. The foil winding eddy current density distribution calculated by Equation 4.111 for a typical transformer is shown in Figure 4.11.

Thus, the current density at the ends can be about 1.5 to 2 times the uniform current density, resulting in local heating of 2.25 to 4 times that in the middle portion of the winding. Hence, the temperature rise at the foil winding ends should be carefully assessed.

Usually, there is no temperature rise problem in foil windings since the thermal conductivity of aluminum/copper is quite good, and the winding edges are generally well exposed to the cooling medium. If a transformer with a foil winding is supplying a power electronic load, there is an increase in the heating effect at the ends of the winding on account of harmonics [23].

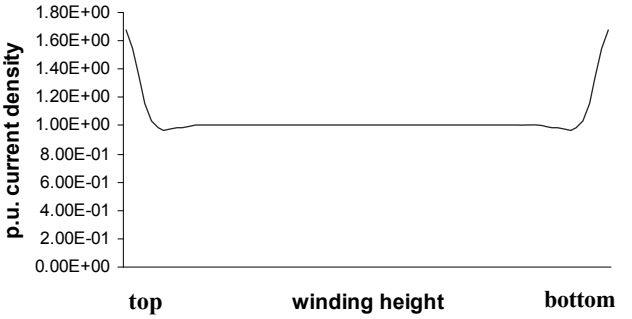

Figure 4.11 Eddy current distribution in a foil winding.

With the rapid development in computational facilities, numerical tools such as FEM can be easily applied to analyze the eddy loss distribution in foil windings without having to do any approximations as in analytical formulations. It is actually a three-dimensional problem; the loss in the foil winding calculated in the core-window cross section is lower than that calculated in the region outside the window. The radial flux at winding ends is usually more in the region outside the window, and hence the additional loss factor may be of the order of 10 to 15%. The position of the foil winding affects its eddy loss significantly. If it is the outer winding, the radial flux density at its ends reduces resulting in reduction of the eddy loss [24].

4.6 Circulating Current Loss in Transformer Windings

We have seen that the leakage field is responsible for extra losses in windings in addition to the DC I^2R loss. If the windings have a single solid conductor then eddy currents flow causing the eddy loss, and no circulating current loss appears. In the windings with large current ratings, conductors have to be subdivided into a number of parallel conductors to reduce the eddy loss to an acceptable/optimum value. Without a proper transposition arrangement, the leakage flux linked by these parallel conductors is different, inducing different voltages in them. Since the conductors are paralleled at their ends, there will be net induced voltages in the loops formed by these conductors resulting in circulating currents. These circulating currents flow back and forth within the parallel conductors and thus do not flow outside the winding. The appearing value of the circulating current loss adds to the other stray loss components.

The circulating current loss depends very much on the physical locations of the conductors in the leakage field. This loss can be avoided if the locations of each conductor at various positions along the winding height are such that all the conductors link an equal amount of leakage flux. Such a winding is said to have an ideal transposition scheme in which each conductor occupies the position of every other conductor. This can be achieved by doing suitable transpositions between the parallel conductors. In the absence of transpositions, the advantage gained through the eddy loss reduction (by subdivision of conductors) will be lost due to the circulating current loss. Inaccurate or inadequate transpositions introduce circulating currents in windings, which can be calculated by either analytical or numerical methods.

4.6.1 Analytical methods

Analytical formulae are given in [25] to calculate the circulating current loss for various types of windings. In this formulation, the ampere-turn diagram is assumed to have a trapezoidal form. The leakage flux density (B) at the inside of the conductor and in the paper covering is calculated. Integrating this value of B over the thickness, the flux/cm is obtained. The voltage gradient is then

calculated as the sum of the resistance drops of the load current and the stray currents (the eddy plus circulating currents), and the reactive drop induced by the flux. The circulating current component is calculated assuming that it is uniform in the whole cross section of the conductor. The effect of circulating currents on the leakage field has been neglected in this approximate method. Hence, it gives a higher value of the circulating current loss than that observed in practice.

It is shown in the paper that the circulating current loss for an untransposed layer winding is the same as the eddy loss in an equivalent one solid conductor. In other words, if a winding conductor having thickness t is split into two conductors each having thickness $t/2$, the circulating current loss for the untransposed case of these two conductors is the same as the eddy loss in the equivalent one conductor having thickness t. Hence, if a winding conductor is subdivided into parallel conductors which are untransposed, the total stray loss in the winding (eddy and circulating losses) will theoretically remain unchanged.

In order for each conductor to occupy the original position of every other conductor over an equal distance, various transposition schemes are used depending upon the type of winding and its conductor. Two such schemes are shown in Figure 4.12 for a layer winding with four parallel conductors. In both cases, each conductor occupies all four positions over an equal distance and hence all the conductors link the same value of leakage field (assuming that the field is entirely in the axial direction) resulting in no circulating currents.

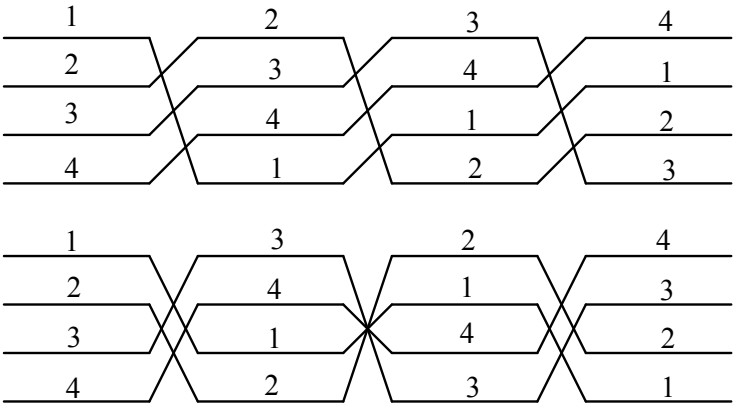

Figure 4.12 Transposition schemes in a layer winding.

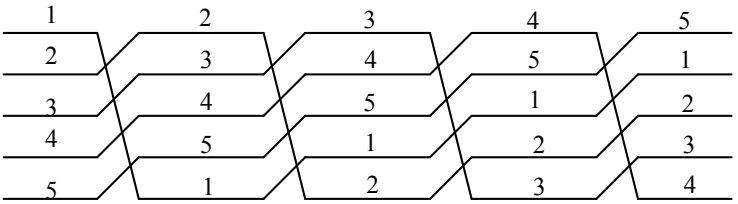

Figure 4.13 Transposition scheme for 5 parallel conductors.

In general, for *n* parallel conductors one ideally needs $n-1$ transpositions equally spaced along the winding height. For example, in the case of 5 parallel conductors, there should be 4 transpositions as shown in Figure 4.13. At every transposition, the top conductor is brought to the bottom position. A thin rectangular copper strip of nearly the same cross-sectional area (as that of the conductor) can be used to join the two cut parts of the conductor by a brazing operation. Alternatively, the conductor can be brought to the bottom position without the cutting and brazing operations by providing a slanting support made from an insulation material.

There is one more scheme [26, p. 147 of 25] which can be used in small transformers in which only 3 transpositions are done in place of $n-1$ transpositions in order to reduce the manufacturing time. A typical scheme is shown in Figure 4.14 for 12 parallel conductors. In this scheme, parallel conductors are divided into four groups for the middle transposition, and hence the number of parallel conductors has to be a multiple of 4.

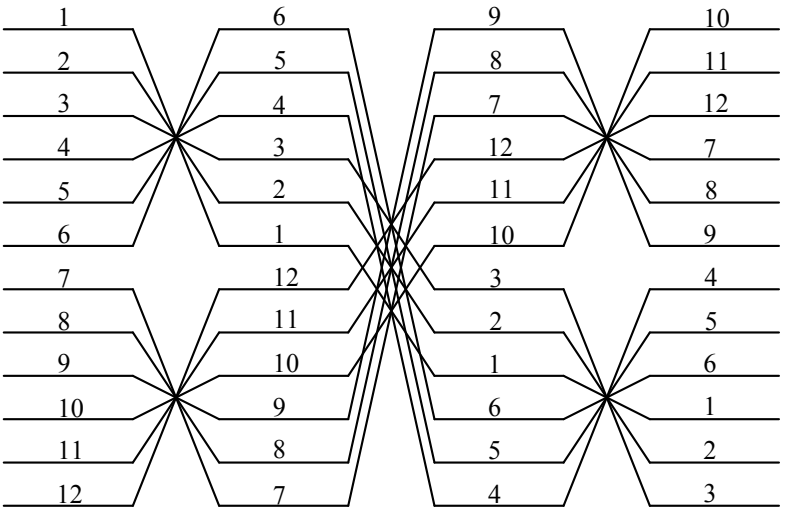

Figure 4.14 Transposition scheme for 12 parallel conductors.

This is not a perfect transposition scheme since none of the conductors is occupying the original position of every other conductor. But each conductor occupies 4 positions so that the average value of the field, linked by it, is not much different than that of the others when only the axial field is considered. The transposition scheme may be used with caution in small transformers when the radial field at ends and within the body of windings is insignificant.

In the discussion of paper [25], Rabins and Cogbill have given a very useful and quick method to check the correctness of any transposition scheme. According to this method, for each conductor a sum

$$s = \sum \frac{N_p}{N} p(p-1)$$

is calculated where p is a particular position and N_p is the number of turns (out of total turns N) in position p. Let us apply the method to evaluate the transposition scheme given in Figure 4.14. Conductor 1 in Figure 4.14 occupies positions 1, 6, 9 and 10 for which $s_1 = 0.25\times(1\times0+6\times5+9\times8+10\times9) = 48$. Similarly, the value of s for the remaining conductors can be determined. Here, it is assumed that the conductor occupies each of the 4 positions for 25% of the winding height. If this is not true or if a transposition is missed by one turn or one disk by mistake during manufacturing, the corresponding number of turns in each position should be taken. Closeness of s values for all the parallel conductors is a good indicator of the correctness of the transposition scheme. The average of the s values for all the conductors is calculated (s_{avg}). The circulating current (P_{cc}) loss is expressed in terms of the winding eddy loss (P_{eddy}) as

$$P_{cc} = P_{eddy}\left(\frac{45}{5n^2-1}\right)\left(\frac{t+t_i}{t}\right)^2\left[\frac{1}{n}\sum_1^n (s_n - s_{avg})^2\right] \qquad (4.114)$$

where t and t_i is the thickness of the conductors and the thickness of the insulation between adjacent conductors, respectively. For example, if the values of t and t_i are 2.3 mm and 0.5 mm, respectively, for the winding shown in Figure 4.14, $P_{cc} = 0.0206\,P_{eddy}$, which is negligible. This indicates that the transposition scheme given in Figure 4.14, although not a perfect one, is sufficiently good to reduce the circulating current loss to a very low value. It should be noted that the calculation accounted for the axial leakage field only. Hence, the method may be used for small transformers only, when the radial field in them is low. The transposition scheme will not be effective if there is a significant radial field in any part of the winding. Also, at the middle transposition, the conductors have to be properly supported while they are being

transposed, which otherwise may be vulnerable when subjected to short circuit forces.

Now, let us analyze continuous disk windings having a number of turns in the radial direction with each turn having two or more parallel conductors. Usually, the number of parallel conductors in a continuous disk winding is less than that in a layer winding. Hence, the problem of circulating currents is less ominous in continuous disk windings since the radial depth of each of the turns is smaller. A continuous disk winding, having N_d turns/disk and n parallel conductors per turn and crossovers between the conductors at the inside and outside diameters of every disk, is equivalent to a multi-layer winding having N_d layers with each layer having n parallel conductors transposed at its center (at the mid-height position).

A continuous disk winding with 8 parallel conductors and 3 turns per disk is shown in Figure 4.15. Kaul's formula [25] for estimation of the circulating current loss for such a continuous winding with n parallel conductors is

$$P_{cc} = 2.4\times10^{6}\times\frac{1}{180}(kR)^{4}\left[1-\frac{5}{n^{2}}+\frac{4}{n^{4}}\right]\times(I^{2}R\ Loss) \tag{4.115}$$

where

R = radial depth of the insulated turn = $n(t+t_i)$

$$k = 0.48\times10^{-4}\times\sqrt{\frac{h_c}{h_w}\,\frac{t}{(t+t_i)}\,\frac{f}{\rho}} \tag{4.116}$$

ρ = resistivity of the conductor material (copper or aluminum)

h_c = total length (height) of copper or aluminum in the axial direction

h_w = length (height) of the winding in the axial direction.

Ratios h_c / h_w and $t/(t+t_i)$ define the space factors of the winding in the axial and radial directions, respectively. Let us calculate the circulating current loss for the winding shown in Figure 4.15 with the following parameters:

$f = 50$ Hz

$t = 2.4$ mm, $t_i = 0.7$ mm

$h_c / h_w = 0.8$

$\rho = 0.0211\times10^{-6}$ ohm-m (copper conductor).

$\therefore R = 8\times(2.4+0.7)\times10^{-3} = 0.0248$ m

and

.

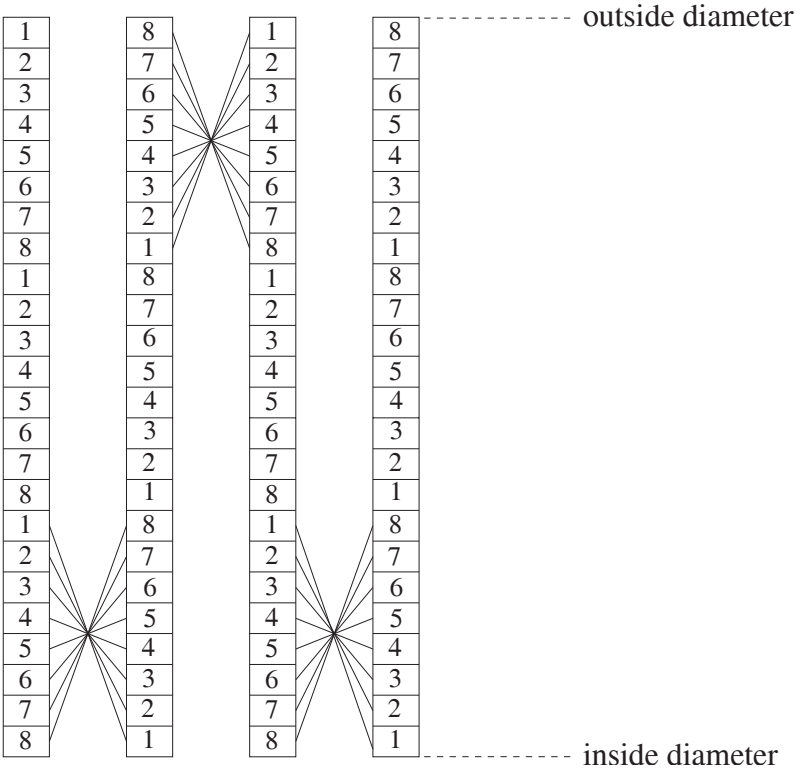

Figure 4.15 Continuous disk winding.

$$k = 0.48\times10^{-4}\times\sqrt{0.8\times\frac{2.4}{2.4+0.7}\times\frac{50}{0.0211\times10^{-6}}} = 1.839\,.$$

The circulating current loss in the winding is

$$P_{cc} = 2.4\times10^{6}\times\frac{1}{180}(1.839\times0.0248)^{4}\left[1-\frac{5}{8^2}+\frac{4}{8^4}\right]\times(I^2R\ Loss)$$

$$= 0.053\times(I^2R\ Loss)\,.$$

For I^2R loss of 130 kW for this winding (for all three-phases), the total circulating current loss is about 6.9 kW, which is a significant value. This circulating current loss can be almost eliminated by doing the group transpositions at appropriate places similar to that for the layer winding shown in Figure 4.14.

It should be noted that in the analytical methods discussed so far, only the axial leakage field is considered and the effect of the radial leakage field is neglected. Due to this assumption the calculation is easy, and the extra loss on account of circulating currents can be determined quickly while the transformer design is in progress. Although these methods may not give the accurate loss value, designers can use them to check the correctness of the chosen transposition scheme.

4.6.2 Method based on multi-winding transformer theory

This method is based on circuit equations of a multi-winding transformer. Let us consider the layer winding shown in Figure 4.14. The LV winding, consisting of 12 parallel conductors, can be considered as made of 12 windings. Hence, along with the HV winding, we have a system of 13 windings. The following circuit equations can be written for the system in terms of per-unit short-circuit (leakage) impedances between the pairs of windings [27],

$$V_{13} - V_1 = -I_1 Z_{13-1} - I_2 \frac{Z_{13-1} + Z_{13-2} - Z_{1-2}}{2} - I_3 \frac{Z_{13-1} + Z_{13-3} - Z_{1-3}}{2} - \cdots\cdots - I_{12} \frac{Z_{13-1} + Z_{13-12} - Z_{1-12}}{2} \tag{4.117}$$

$$V_{13} - V_2 = -I_1 \frac{Z_{13-2} + Z_{13-1} - Z_{1-2}}{2} - I_2 Z_{13-2} - I_3 \frac{Z_{13-2} + Z_{13-3} - Z_{2-3}}{2} - \cdots\cdots - I_{12} \frac{Z_{13-2} + Z_{13-12} - Z_{2-12}}{2}. \tag{4.118}$$

Similarly, the remaining 10 equations for $V_{13} - V_3$, $V_{13} - V_4, \cdots\cdots, V_{13} - V_{12}$ can be written. If the load loss test is performed by applying the impedance voltage to the HV winding (number 13) with the remaining 12 LV windings short-circuited, then

$$I_1 + I_2 + I_3 + \cdots\cdots + I_{13} = 0 \tag{4.119}$$

and

$$V_1 = V_2 = V_3 = \cdots\cdots = V_{12} = 0\,. \tag{4.120}$$

The leakage impedance between pairs of windings can be calculated by using the conventional formulae of Section 3.1.1 considering the four distinct positions occupied by each of these 12 LV windings along their height. The per-unit leakage impedance ($R + jX$) is calculated with the transformer MVA rating taken as the base. A more accurate estimate of the leakage impedance can be made by using FEM [28]. This combined method, in which FEM is used in

conjunction with the multi-winding theory, is an accurate method in two dimensions. The following system of 12 equations can be easily solved to give the currents flowing in the parallel conductors:

$$[I]_{12\times1} = [Z]^{-1}_{12\times12} \times [V]_{12\times1}. \tag{4.121}$$

Let us now calculate the circulating current loss for a transformer whose LV winding has 12 parallel conductors. The dimensions are shown in Figure 4.16. The transformer specification and relevant design details are:

10 MVA, 33/6.9 kV, star/star, 50 Hz
Volts/turn = 46.87, Z = 7.34%
LV conductor: thickness = 2.3 mm, insulation between conductors = 0.5 mm, area of one conductor = 22.684×10^{-6} m^2
Total conductor area = 12 × area of one conductor = 272.21×10^{-6} m^2
Mean diameter of the LV winding = 0.495 m
Turns in the LV winding = 85
LV winding volume for 3 phases = $272.21\times10^{-6} \times (\pi\times0.495\times85\times3)$
= 0.1079 m^3

Currents calculated by the method are given in Table 4.1. The currents in parallel conductors are almost equal. The total loss (I^2R + circulating current loss) calculated by the above method based on the multi-winding transformer theory is 21.882 kW (for all 3 phases) out of which the I^2R loss is 21.87 kW. Thus, the circulating current loss is 12 watts, which is just 0.055% of the I^2R loss, suggesting that the transposition scheme is good enough to reduce substantially the circulating current loss. Hence, it can be used for small rating transformers with low radial fields in windings as mentioned earlier. We had calculated for the same transformer the circulating current loss by the method of Rabins and Cogbill as

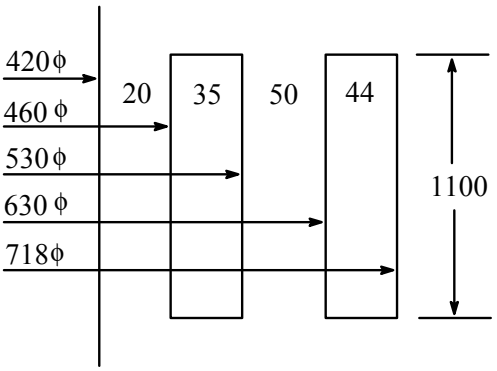

Figure 4.16 Details of 10 MVA transformer.

Table 4.1 Current Distribution in Parallel Strands

Conductor	1	2	3	4	5	6
Current (A)	68.97	69.0	69.08	69.08	69.0	68.97
Conductor	7	8	9	10	11	12
Current (A)	69.08	69.0	68.97	68.97	69.0	69.08

$P_{cc} = 0.0206\ P_{eddy}$.

The total eddy loss in the LV winding can be determined using Equation 4.99.

$$P_{eddy} = \frac{\omega^2 t^2}{24\rho}\ \frac{B_{gp}^2}{3} \times volume$$

$$B_{gp} = \sqrt{2}\ \frac{\mu_0 NI}{H_w} = \sqrt{2}\ \frac{4\pi \times 10^{-7} \times 85 \times 836.74}{1.1} = 0.1149\ \text{T}$$

$$\therefore P_{eddy} = \frac{(2\pi \times 50)^2 (0.0023)^2}{24 \times 0.0211 \times 10^{-6}}\ \frac{0.1149^2}{3} \times 0.1079 = 489.55\ \text{W}.$$

Hence,

$$P_{cc} = 0.0206 \times 489.55 = 10\ \text{W}.$$

The above answer matches closely with that calculated from the method based on the multi-winding transformer theory (12 W).

4.6.3 FEM analysis

As mentioned earlier, the analytical methods which consider only the axial leakage field are approximate. The effect of radial fields at winding ends or at tap breaks on circulating currents cannot be accounted by these methods. Also, the effect of circulating currents on the main leakage field is neglected. These effects are dominant in large power transformers as well as low-voltage high-current transformers (e.g., furnace transformers). Hence, for more accurate estimation of the circulating current loss and for arriving at a good transposition scheme, a numerical method such as FEM is used [28, 29].

In [29], it has been concluded that in the case of windings without any transpositions or with inadequate transpositions, the analytical formulations give much higher and inaccurate circulating current losses. This is particularly true when the number of parallel conductors is more. This is due to the fact that in such cases, the effect of the field due to large circulating currents significantly affects the leakage field, and this effect is neglected in the analytical formulations.

In the FEM analysis, a time-harmonic formulation is used and all conductors are modeled. It requires a considerable amount of modeling efforts. The conductors are defined as stranded meaning that the eddy currents in them are neglected. Hence, the loss given by FEM analysis is the total of the I^2R loss and the circulating current loss. In [30], the circulating currents and the corresponding losses have been calculated for a continuous disk LV winding with 12 parallel conductors by using 2-D FEM analysis and the analytical method based on the multi-winding transformer theory described earlier. The impedance voltage is applied to its HV winding which is modeled as one rectangular block with the definition of the ampere-turn density. The transposition scheme of this winding was not good. The currents calculated by both methods are close, and are compared in Figure 4.17. The circulating current losses calculated by the two methods are also in agreement. When the transposition scheme was changed to the ideal one, in which each of the twelve parallel conductors occupied the original position of every other conductor over an equal distance, the load loss of the transformer reduced by an amount close to the calculated value of the circulating current loss, thus verifying the results of the calculations by the two different methods.

In [17, 18], leakage field distribution is obtained by 3-D FEM analysis. The voltages that circulate currents between parallel conductors are determined by integrating the flux density components over the three dimensions taking into account the transpositions between parallel conductors.

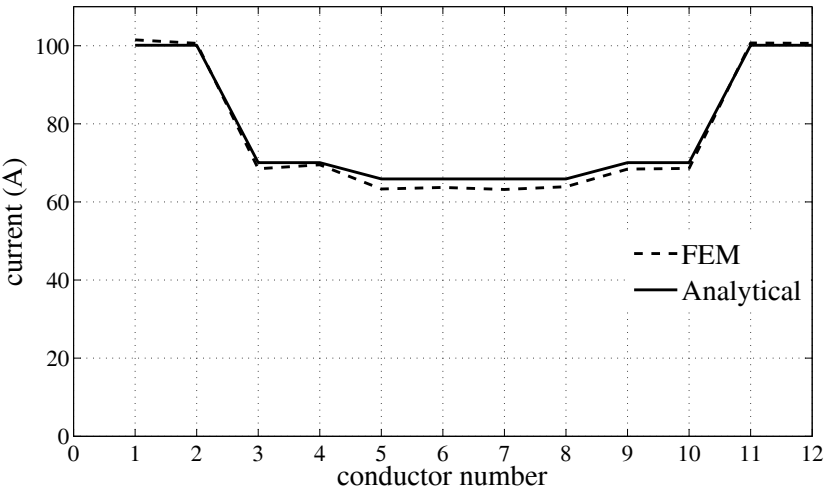

Figure 4.17 Currents in conductors of a continuous disk winding.

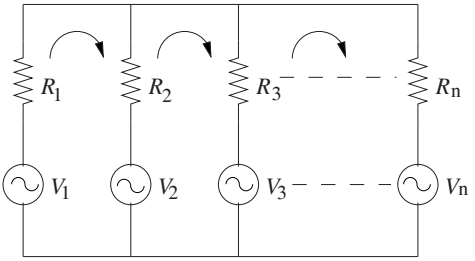

Figure 4.18 Equivalent circuit for calculation of circulating currents.

Based on these voltages and the resistances of the conductors, the circulating currents in the corresponding loops are calculated from the solution of the circuit shown in Figure 4.18. The path of circulating currents is assumed to be resistive because of low values of inductances between parallel conductors (due to adequate transpositions), small spacings between the conductors, and the one-turn path of the currents. It is reported in [17] that a significant reduction in circulating current losses can be achieved by deciding correct locations of transpositions based on such 3-D field calculations.

Until now, we considered only radially placed parallel conductors. There can be axially placed parallel conductors also. If the radial field is symmetrical at both ends and if there are two parallel conductors placed axially as shown in Figure 4.19, the net leakage field enclosed by the loop formed by the two conductors is zero (since the radial field is in opposite directions at the top and bottom ends of the winding). Hence, there will not be any circulating currents on account of the radial field, obviating any need of transpositions in the axial direction. If the radial field is significantly different at the top and bottom ends, the axial transpositions (i.e., exchanging of axial positions) may be required at pre-determined locations determined using FEM. For this case, the approximate analytical formulations, which consider only axial field, cannot be used.

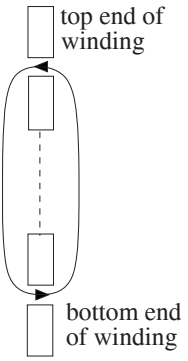

Figure 4.19 Axially placed parallel conductors in a winding.

References

1. Stoll, R. L. *The analysis of eddy currents*, Clarendon Press, Oxford, 1974.
2. Hayt, W. H. *Engineering electromagnetics*, McGraw-Hill Book Company, Singapore, 1989, pp. 336–363.
3. Dexin, X., Yunqiu, T., and Zihong, X. FEM analysis of 3-D eddy current field in power transformer, *IEEE Transactions on Magnetics*, Vol. 23, No. 5, May 1987, pp. 3786–3788.
4. Holland, S. A., O'Connell, G. P., and Haydock, L. Calculating stray losses in power transformers using surface impedance with finite elements, *IEEE Transactions on Magnetics*, Vol. 28, No. 2, March 1992, pp. 1355–1358.
5. Macfadyen, K. A. Vector permeability, *Journal IEE,* Vol. 94, Pt. III, 1947, pp. 407–414.
6. Subbarao, V. *Eddy currents in linear and nonlinear media*, Omega Scientific Publishers, New Delhi, 1991.
7. Agarwal, P. D. Eddy current losses in solid and laminated iron, *AIEE Transactions,* Vol. 78, May 1959, pp. 169–181.
8. Hammond, P. *Applied electromagnetism,* Pergamon Press, Oxford, 1971.
9. Turowski, J., Turowski, M., and Kopec, M. Method of three-dimensional network solution of leakage field of three-phase transformers, *IEEE Transactions on Magnetics*, Vol. 26, No. 5, September 1990, pp. 2911–2919.
10. Bean, R. L., Chackan, N., Moore, H. R., and Wentz, E. C. *Transformers for the electric power industry*, McGraw-Hill Book Company, New York, 1959, pp. 396–402.
11. Boyajian, A. Leakage reactance of irregular distributions of transformer windings by method of double Fourier series, *AIEE Transactions — Power Apparatus and Systems,* Vol. 73, Pt. III-B, 1954, pp. 1078–1086.
12. Rabins, L. Transformer reactance calculations with digital computers, *AIEE Transactions — Communications and Electronics,* Vol. 75, Pt. I, 1956, pp. 261–267.
13. Andersen, O. W. Transformer leakage flux program based on finite element method, *IEEE Transactions on Power Apparatus and Systems*, Vol. PAS- 92, 1973, pp. 682–689.
14. Kulkarni, S. V., Gulwadi, G. S., Ramachandran, R., and Bhatia, S. Accurate estimation of eddy loss in transformer windings by using FEM analysis, *International Conference on Transformers, TRAFOTECH-94,* Bangalore, India, January 1994, pp. I7–I10.
15. Kulkarni, S. V. and Ramachandrudu, B. Orthogonal array design of experiments for analysis of key performance parameter of transformer, *First World Congress on Total Quality Management,* Organized by Royal Statistical Society and Sheffield Hallam University, Sheffield, U.K., 10-12 April 1995, pp. 201–204.

16. McWhirter, J. H., Oravec, J. J., and Haack, R. Computation of magnetostatic fields in three dimensions based on Fredholm integral equations, *IEEE Transactions on Magnetics*, Vol. MAG-18, No. 2, March 1982, pp. 373–378.
17. Girgis, R. S., Yannucci, D. A., and Templeton, J. B. Performance parameters of power transformers using 3D magnetic field calculations, *IEEE Transactions on Power Apparatus and Systems*, Vol. PAS-103, No. 9, September 1984, pp. 2708–2713.
18. Girgis, R. S., Scott, D. J., Yannucci, D. A., and Templeton, J. B. Calculation of winding losses in shell form transformers for improved accuracy and reliability — Part I: Calculation procedure and program description, *IEEE Transactions on Power Delivery,* Vol. PWRD-2, No. 2, April 1987, pp. 398–410.
19. Kozlowski, M. and Turowski, J. Stray losses and local overheating hazard in transformers, *CIGRE 1972*, Paper No. 12-10.
20. Mullineux, N., Reed, J. R., and Whyte, I. J. Current distribution in sheet and foil wound transformers, *Proceedings IEE,* Vol. 116, No. 1, January 1969, pp. 127–129.
21. El-Missiry, M. M. Current distribution and leakage impedance of various types of foil-wound transformers, *Proceedings IEE*, Vol. 125, No. 10, October 1978, pp. 987–992.
22. Turowski, J. Additional losses in foil and bar wound transformers, *IEEE PES Winter Meeting and Symposium,* New York, January 25-30, 1976, Paper No. A-76-151-1.
23. Genon, A., Legros, W., Adriaens, J. P., and Nicolet, A. Computation of extra joule losses in power transformers, *ICEM 88*, pp. 577–581.
24. Ram, B. S. Loss and current distribution in foil windings of transformers, *Proceedings IEE — Generation, Transmission and Distribution*, Vol. 145, No. 6, November 1998, pp. 709–716.
25. Kaul, H. J. Stray current losses in stranded windings of transformers, *AIEE Transactions,* June 1957, pp. 137–149.
26. de Buda, R. G. Winding transpositions for electrical apparatus, U. S. Patent No. 2710380, June, 1955.
27. Rothe, F. S. *An introduction to power system analysis,* John Wiley, New York, 1953, pp. 45–50.
28. Isaka, S., Tokumasu, T., and Kondo, K. Finite element analysis of eddy currents in transformer parallel conductors, *IEEE Transactions on Power Apparatus and Systems,* Vol. PAS-104, No. 10, October 1985, pp. 2731–2737.
29. Koppikar, D. A., Kulkarni, S. V., Ghosh, G., Ainapure, S. M., and Bhavsar, J. S. Circulating current loss in transformer windings, *Proceedings IEE — Science, Measurement and Technology*, Vol. 145, No. 4, July 1998, pp. 136–140.

30. Kulkarni, S. V., Palanivasagam, S., and Yaksh, M. Calculation of circulating current loss in transformer windings using FE analysis, *ANSYS Users Conference*, Pittsburgh, USA, August 27-30, 2000.

5

Stray Losses in Structural Components

The previous chapter covered the theory and fundamentals of eddy currents. It also covered in detail the estimation and reduction of stray losses in windings, viz., the eddy loss and the circulating current loss. This chapter covers estimation of remaining stray losses, which predominantly consist of stray losses in structural components. Various countermeasures for the reduction of these stray losses and elimination of hot spots are discussed.

The stray loss problem becomes increasingly important with growing transformer ratings. Ratings of generator transformers and interconnecting auto-transformers are steadily increasing over last few decades. Stray losses of such large units can be appreciably high, which can result in unacceptable temperatures, affecting their life. This problem is particularly severe in large auto-transformers, wherein the actual impedance on an equivalent two-winding basis is high giving a substantial value for the stray leakage field. In the case of large generator transformers and furnace transformers, stray loss due to high current-carrying leads can become excessive, causing hot spots. To become competitive in the global marketplace it is necessary to optimize material costs, which usually leads to reduction in overall size of the transformer as a result of reduction in electrical and magnetic clearances. This has the effect of further increasing stray losses if effective shielding measures are not implemented. The size of a large power transformer is also limited by transportation constraints. Hence, the magnitude of stray field incident on structural parts increases much faster with growing ratings of transformers. It is very important for a transformer designer to know and estimate accurately all the stray loss components because each kW of load loss may be capitalized by users from

US$ 750 to US$ 2500. In large transformers, a reduction of the stray losses by even 3 to 5 kW can give a competitive advantage.

Stray losses in structural components may form a large part (> 20%) of the total load loss if not evaluated and controlled properly. A major part of stray losses occurs in structural parts with large areas (e.g., tank plates). Due to inadequate shielding of these parts, stray losses may increase the load loss of the transformer substantially, impairing its efficiency. It is important to note that the stray loss in some clamping elements with smaller areas (e.g., flitch plates) is lower, but the incident field on them can be high leading to unacceptable local high temperatures seriously affecting the life of the transformer.

Until 1980, much work was done in the area of stray loss evaluation by analytical methods. These methods have certain limitations and cannot be applied to complex geometries. With the advent of numerical methods such as the finite element method (FEM), calculation of eddy loss in various metallic components of the transformer is now easier and less complicated. Some of the complex 3-D problems when solved by using 2-D formulations (with major approximations) lead to significant inaccuracies. Availability of commercial 3-D FEM software packages since 1990 have enabled designers to simulate the complex electromagnetic structure of transformers for control of stray loss and elimination of hot spots. However, FEM analysis may require a considerable amount of time and effort. Hence, wherever possible, a transformer designer would prefer fast analysis with sufficient accuracy to decide various countermeasures for stray loss reduction. It may be preferable, for regular design use, to calculate some of the stray loss components by analytical/hybrid (analytically-numerical) methods or by some formulae derived on the basis of one-time detailed analysis. Thus, the method of calculation of stray losses should be judiciously selected; wherever possible, the designer should be given equations/curves or analytical computer programs providing quick and reasonably accurate solutions.

Computation of stray losses is not a simple task because the transformer is a highly asymmetrical and 3-D structure. The computation is complicated by

- magnetic non-linearity,
- difficulty in quick and accurate computation of stray field and its effects,
- inability of isolating exact stray loss components from tested load-loss values,
- limitations of experimental verification methods for large power transformers.

Stray losses in various clamping structures (frames, flitch plates, etc.) and the tank due to the leakage field emanating from windings and due to the field of high current-carrying leads are discussed in this chapter. The methods used for estimation of these losses are compared. The efficacies of various methods used for stray loss control are discussed. Some interesting phenomena observed during three-phase and single-phase load loss tests are also reported.

5.1 Factors Influencing Stray Losses

As ratings of transformers increase, the proportion of stray losses in their load loss may increase significantly. These losses in structural components may exceed the stray losses in windings in large power transformers (especially autotransformers). A major portion of these stray losses occurs in structural components with a large area (e.g., tank plates) and core clamping elements (e.g., frames). The high magnitude of stray flux usually does not permit designers to disregard the nonlinear magnetic characteristics of steel elements. Stray losses in structural steel components depend in a very complicated manner on parameters such as stray flux levels, frequency, resistivity, nature of excitation, etc.

In the absence of hysteresis and nonlinearity of magnetic characteristics, the expression for the eddy loss per unit surface area of a plate, subjected to (on one of its surfaces) a magnetic field of r.m.s. value (H_{rms}), has been derived in Chapter 4 as

$$P_e = \sqrt{\frac{\omega\mu}{2\sigma}}\, H_{rms}^2 \,. \tag{5.1}$$

Hence, the total power loss in a steel plate having permeability μ_s can be given in terms of the peak value of the field (H_0) as

$$P = \iint_S \sqrt{\frac{\omega\mu_s}{2\sigma}}\, \frac{H_0^2}{2}\, ds \qquad \text{….. } \textit{linear characteristics.} \tag{5.2}$$

This equation assumes a constant permeability value. It is necessary to take into account the nonlinear magnetic saturation effect in structural steel parts because their surfaces are often saturated due to the skin effect phenomenon. Non-linearity of magnetic characteristics can be taken into account by a linearization coefficient as explained in Section 4.4. Thus, the total power loss with the consideration of nonlinear characteristics can be given by

$$P = a_l \iint_S \sqrt{\frac{\omega\mu_s}{2\sigma}}\, \frac{H_0^2}{2}\, ds \qquad \text{….. } \textit{nonlinear characteristics.} \tag{5.3}$$

The term a_l in the above equation is the linearization coefficient. Equation 5.3 is applicable to a simple geometry of a plate excited by a tangential field on one of its sides. It assumes that the plate thickness is sufficiently larger than the depth of penetration (skin depth) so that it becomes a case of infinite half space. For magnetic steel, as discussed in Section 4.4, the linearization coefficient has been taken as 1.4 in [1]. For non-magnetic steel, the value of the coefficient is 1 (i.e., a_l=1).

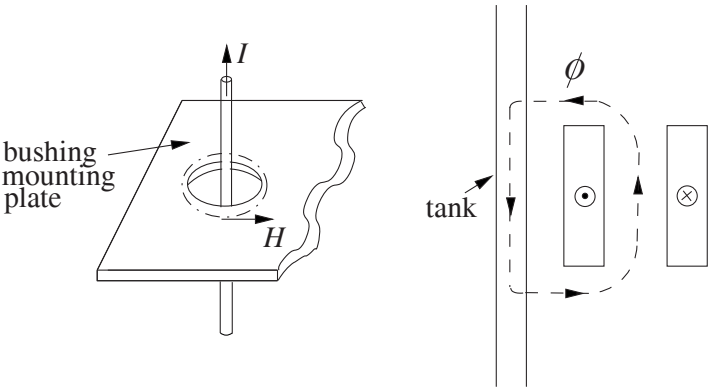

(a) (b)

Figure 5.1 Types of excitation.

5.1.1 Type of surface excitation

In transformers, there are predominantly two kinds of surface excitations as shown in Figure 5.1. In case (a), the incident field is tangential (e.g., bushing mounting plates). In this case, the incident tangential field is directly proportional to the source current since the strength of the magnetic field (H) on the plate surface can be determined approximately by the principle of superposition [2]. In case (b), for estimation of stray losses in the tank due to an incident leakage field, only the normal (radial) component of the field (ϕ) can be considered as proportional to the source current. Actually, the relationship between the source current and the tangential field component is much more complicated. In many analytical formulations, the loss is calculated based on the tangential components (two orthogonal components in the plane of the plate), which need to be evaluated from the normal component of the incident field with the help of Maxwell's equations. The estimated values of these two tangential field components can be used to find the resultant tangential component and thereafter the tank loss according to Equation 5.3.

Let us use the theory of eddy currents described in Chapter 4 to analyze the effect of different types of excitations on the stray loss magnitude and distribution. Consider a structural component as shown in Figure 5.2 (similar to that of a winding conductor of Figure 4.5) which is placed in an alternating magnetic field in the y direction having peak amplitudes of H_1 and H_2 at its two surfaces. The structural component can be assumed to be infinitely long in the x direction. Further, it can be assumed that the current density J_x and magnetic field intensity H_y are functions of z only. Proceeding in a way similar to that in Section 4.3 and assuming that the structural component has linear magnetic characteristics, the diffusion equation is given by

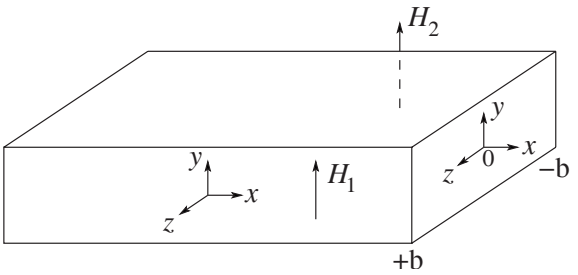

Figure 5.2 Stray loss in a structural component.

$$\frac{d^2H_y}{dz^2} = j\omega\mu\sigma H_y \,. \tag{5.4}$$

The solution of this equation is

$$H_y = C_1 e^{\gamma z} + C_2 e^{-\gamma z} \tag{5.5}$$

where γ is the propagation constant given by Equation 4.39, viz. $\gamma = (1+j)/\delta$, δ being the depth of penetration or skin depth. Now, for the present case the boundary conditions are

$$H_y = H_1 \text{ at } z = +b \text{ and } H_y = H_2 \text{ at } z = -b \,. \tag{5.6}$$

Using these boundary conditions, we can obtain expressions for the constants as

$$C_1 = \frac{H_1 e^{\gamma b} - H_2 e^{-\gamma b}}{e^{2\gamma b} - e^{-2\gamma b}} \quad \text{and} \quad C_2 = -\frac{H_1 e^{-\gamma b} - H_2 e^{\gamma b}}{e^{2\gamma b} - e^{-2\gamma b}} \,. \tag{5.7}$$

Substituting these expressions of the constants back into Equation 5.5, we obtain

$$H_y = \left[\frac{H_1 e^{\gamma b} - H_2 e^{-\gamma b}}{e^{2\gamma b} - e^{-2\gamma b}}\right] e^{\gamma z} - \left[\frac{H_1 e^{-\gamma b} - H_2 e^{\gamma b}}{e^{2\gamma b} - e^{-2\gamma b}}\right] e^{-\gamma z} \,. \tag{5.8}$$

Since $\nabla \times \mathbf{H} = \mathbf{J}$ and $\mathbf{J} = \sigma\mathbf{E}$, and only the y component of $\mathbf{H}$ and the x component of $\mathbf{J}$ are non-zero, we obtain

$$E_x = -\frac{1}{\sigma}\frac{dH_y}{dz} \,. \tag{5.9}$$

$$\therefore\ E_x = -\frac{\gamma}{\sigma}\left\{\left[\frac{H_1 e^{\gamma b} - H_2 e^{-\gamma b}}{e^{2\gamma b} - e^{-2\gamma b}}\right] e^{\gamma z} + \left[\frac{H_1 e^{-\gamma b} - H_2 e^{\gamma b}}{e^{2\gamma b} - e^{-2\gamma b}}\right] e^{-\gamma z}\right\} \,. \tag{5.10}$$

In terms of complex vectors, the (time average) power flow per unit area of the plate (in the *x*-*y* plane) can be calculated with the help of Poynting's theorem [3]:

$$P + jQ = (1/2)\left(E_x H_y^*\right)_{z=b} - (1/2)\left(E_x H_y^*\right)_{z=-b}. \tag{5.11}$$

Substituting the values of H_y and E_x from Equations 5.8 and 5.10, the value of eddy loss per unit area of the plate can be calculated. Figure 5.3 shows the plot of the normalized eddy loss, $P/(H^2/2\sigma\delta)$, versus the normalized plate thickness $(2b/\delta)$ for three different cases of the tangential surface excitation.

Case 1 ($H_1 = H$ and $H_2 = 0$): As expected, the eddy loss for this case decreases with an increase in the plate thickness until it becomes about two times the skin depth. This condition represents a configuration wherein a current carrying conductor is placed parallel to a conducting plate (e.g., a mild steel tank plate/ pocket). For this case (see Figure 5.3), the normalized active power approaches unity as the thickness and hence the ratio $2b/\delta$ increases. This is because it becomes a case of an infinite half space, and the power loss equals $H^2/(2\sigma\delta)$. It should be remembered that H, H_1, and H_2 denote peak values.

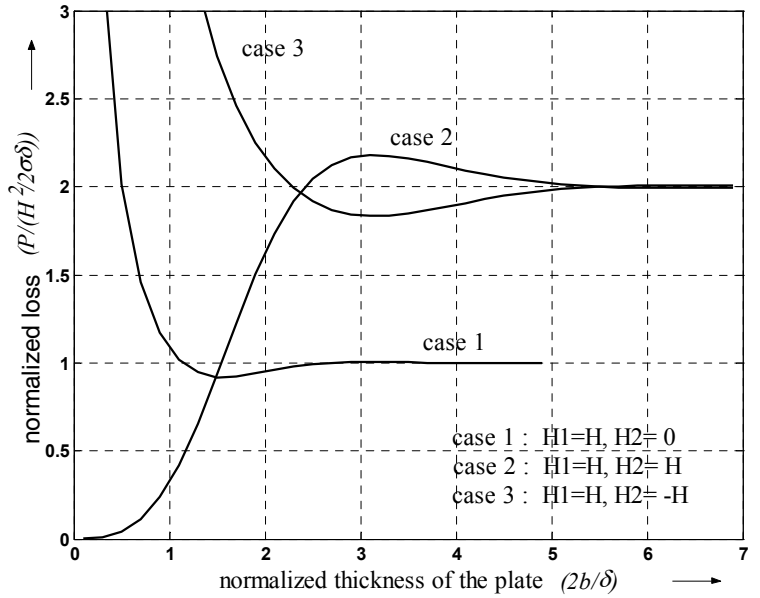

Figure 5.3 Eddy loss in a structural plate for different surface excitations.

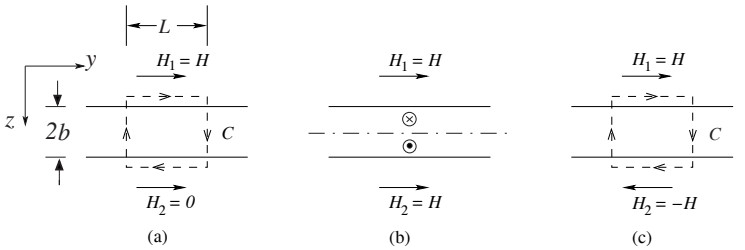

Figure 5.4 Explanation for curves in Figure 5.3.

The plot also shows that the active power loss is very high for a thin plate. A qualitative explanation for this behavior can be given with reference to Figure 5.4 (a). Consider a contour C shown in the figure. By applying Ampere's circuital law to the contour we obtain

$$\oint_C \mathbf{H} \cdot \mathbf{dL} = \int_S \mathbf{J} \cdot \mathbf{ds} . \tag{5.12}$$

Noting that **H** is only in the y direction with $H_1 = H$ and $H_2 = 0$, the equation simplifies to

$$H\,L = I .$$

As the thickness $2b$ decreases, the same amount of current passes through a smaller cross section of the plate and thus through a higher resistance, resulting in more loss.

Case 2 ($H_1 = H_2 = H$): Here, the eddy loss increases with an increase in the plate thickness. This situation arises in lead terminations/bushing mounting plates, wherein currents pass through holes in them. In this case, as the thickness increases, normalized active power loss approaches 2 because, for $2b/\delta >> 1$, the problem reduces to that of two infinite half-spaces, each excited by the peak value of the field (H) on their surfaces. Therefore, the total loss adds up to 2 per-unit. As the thickness decreases, the active power loss decreases in contrast with Case 1. As shown in Figure 5.4 (b), the currents in two halves of the plate are in opposite directions (as forced by the boundary conditions of H_1 and H_2). For a sufficiently small thickness, the effects of these two currents tend to cancel each other reducing the loss to zero.

Case 3 ($H_1 = -H_2 = H$): Here, the eddy loss decreases with an increase in the thickness. For a very high thickness value, much greater than the skin depth, the loss approaches the value corresponding to two infinite half-spaces, i.e., $H^2/(\sigma\delta)$. As the thickness decreases, the power loss attains very high values.

For the representation given in Figure 5.4 (c), an explanation similar to that for Case 1 can be given. The application of Ampere's circuital law gives twice the value of current (i.e., $2HL = I$) as compared to Case 1. Hence, as the thickness ($2b$) decreases, the current has to pass through a smaller cross section of the plate and thus through a higher resistance causing more loss.

In the previous three cases, it is assumed that the incident magnetic field intensity is tangential to the surface of a structural component (e.g., a bushing mounting plate). If the field is incident radially, the loss behavior is different. Based on a number of 2-D FEM simulations involving a configuration in which the leakage field from windings is radially incident on a structural component (e.g., a tank plate or a flitch plate), the typical curves are presented in Figure 5.5. The figure gives the variation of the loss in the structural component as the thickness is increased, for three different types of materials: magnetic steel, non-magnetic steel, and aluminum. The curves are similar to those given in [4] wherein a general formulation is used for estimation of losses in a structural component for any kind of spatial distribution of the incident magnetic field. Let us now analyze the graphs of the three different materials given in Figure 5.5.

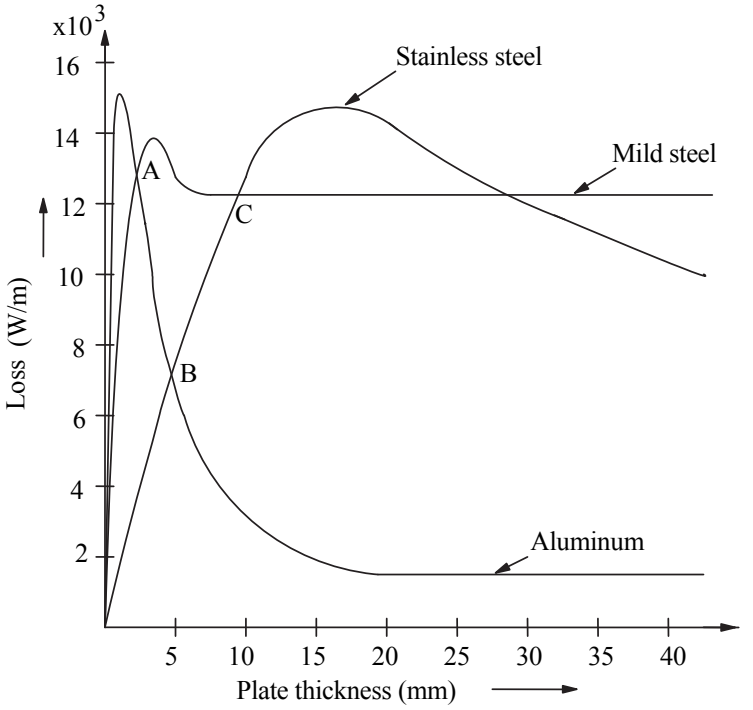

Figure 5.5 Loss in different materials for radial excitation.

1) **Magnetic steel**: We can assume that the magnetic steel plate is saturated due to its small skin depth. The value of its relative permeability corresponding to a saturation condition is therefore taken (i.e., $\mu_r = 100$). With $\sigma = 7 \times 10^6$ mho/m, its skin depth is 2.69 mm at 50 Hz. It can be seen from the graph that the power loss approaches the maximum value in about two skin depths and thereafter remains constant. This behavior is in line with the theory of eddy currents elaborated in Chapter 4. Since the eddy currents and losses are concentrated at the surface only, increasing the plate thickness beyond few skin depths does not change the effective resistance offered to the eddy currents and hence the loss remains constant (at a value which is governed by Equation 4.74).

2) **Aluminum**: In the case of aluminum with $\mu_r = 1$ and $\sigma = 29 \times 10^6$ mho/m, the skin depth at 50 Hz is 13.2 mm. It can be observed from the graph that the loss first increases with thickness and then reduces. The phenomenon can be analyzed qualitatively from the supply terminals as an equivalent R-L circuit. A thin plate exhibits resistance-limited behavior as discussed in Section 4.5.1, and its effective resistance is greater than the inductive reactance. Hence, the equivalent circuit behaves as a predominantly resistive circuit, for which the loss can be given as $P = (V^2/R)$, where V is the supply voltage. An increase in the thickness of the aluminum plate leads to a decrease in its resistance value, due to an increased cross section available for the eddy currents, and hence the loss increases. This is reflected in Figure 5.5 by the near-linear increase in the loss with the plate thickness.

Upon further increase of the plate thickness, the resistance continues to decrease while the inductance gradually increases, and the circuit behavior changes gradually from that of a purely resistive one to that of a series $R - L$ circuit. The power loss undergoes a peak, and starts to decrease as the circuit becomes more inductive. Finally, when the thickness is near or beyond the skin depth, the field and the eddy currents are almost entirely governed by the inductive effects (inductance-limited behavior). The field does not penetrate any further when the plate thickness is increased. The equivalent resistance and inductance of the circuit become independent of the increase in the thickness. The power loss also approaches a constant value as the thickness increases significantly in excess of the skin depth making it a case of an infinite half space. Since the product ($\sigma \cdot \delta$) is much higher for the aluminum plate than that for the mild steel plate, the constant (minimum) value of the loss for the former is much lower; the loss is inversely proportional to the product ($\sigma \cdot \delta$) according to Equation 4.74. The curves of aluminum and mild steel intersect at about 3 mm (point A).

3) **Non-magnetic stainless steel**: Its behavior is similar to that of the aluminum plate, both being non-magnetic materials. The curve is more flat as compared to aluminum as the skin depth of stainless steel is much higher. For a typical grade of stainless steel material with relative permeability of 1 and conductivity of

1.136×10^6 mho/m, the skin depth is 66.78 mm at 50 Hz. Another difference is the fact that as the thickness is increased, the loss approaches a constant value which is higher than that of the aluminum plate but lower than that of the magnetic steel plate since the product ($\sigma\cdot\delta$) for stainless steel lies between those of mild steel and aluminum. The intersection point (B) of the curves for stainless steel and aluminum occurs at about 5 mm and the intersection point (C) of the curves for stainless steel and mild steel occurs at about 10 mm. The location of intersection points depends on the configuration being analyzed and the nature of the incident field.

With the increase in the plate thickness, the values of losses in the mild steel (MS), aluminum (AL), and stainless steel (SS) plates stabilize to 12.2 kW/m, 1.5 kW/m and 5.7 kW/m, respectively, for particular values of currents in the windings. A thick plate is equivalent to an infinite half space and the three loss values should actually be in proportion to $(1/\sigma\delta)$ for the same tangential field excitation (H_0), according to Equation 4.74. The magnitude and nature of eddy currents induced in these three types of plates are different, which makes the value of H_0 different for these cases. Also, the value of H_0 is not constant along the surface. Hence, the losses in the plates are not in the exact proportion of their corresponding ratios $(1/\sigma\delta)$. Nevertheless, the expected trend can be observed; the losses follow the relationship $(loss)_{MS} > (loss)_{SS} > (loss)_{AL}$ since $(1/\sigma\delta)_{MS} > (1/\sigma\delta)_{SS} > (1/\sigma\delta)_{AL}$.

A few general conclusions can be drawn based on the above discussion:

1. When a plate made of non-magnetic and highly conductive material (aluminum or copper) is used in the vicinity of the field due to high currents or the leakage field from windings, its thickness should be comparable to the skin depth (i.e., 13.2 mm for aluminum and 10.3 mm for copper at 50 Hz) to reduce the loss in it to a low value. For the field due to a high current source, the minimum loss value is obtained for a thickness of [5],

$$t_{\min} = \frac{\pi}{2}\delta . \tag{5.13}$$

For aluminum (with $\delta = 13.2$ mm), we get the value of $t_{\min}$ as 20.7 mm at 50 Hz. The ratio $t_{\min}/\delta$ corresponding to the minimum loss value is 1.57. This agrees with the graph of Figure 5.3 corresponding to Case 1 (assuming that tangential field value $H_2 \cong 0$, which is a reasonable assumption for a thickness 50% more than δ), for which the minimum loss is obtained for the normalized thickness of 1.57. For the case of radial incident field also (Figure 5.5), the loss reaches a minimum value at the thickness of about 20 mm. For $t < (0.5\times\delta)$, the loss becomes substantial and may lead to overheating of the plate. Hence, if aluminum or copper is used as an electromagnetic shield, it should have

sufficient thickness to eliminate its overheating and minimize the stray loss in the shielded structural component. A sufficiently high thickness value ensures that its effective resistance is close to the minimum value.

2. Since the skin depth of mild steel (2.69 mm) is usually much less than the thickness required from mechanical design considerations, one may not be able to reduce its thickness to control the eddy loss. Hence, either magnetic shunts (made of low reluctance steel material) or electromagnetic or eddy current shields (aluminum or copper) are used to minimize the stray losses in structural components made of mild steel material in medium and large transformers.

3. From Figure 5.5, it is clear that the loss in a stainless steel plate is less than a mild steel plate for lower values of thickness. Hence, when a structural component is made of stainless steel, its thickness should be as small as possible (permitted from mechanical design considerations) in order to obtain a lower loss value. Thus, if a mild steel flitch plate is replaced by a stainless steel one, the stray loss in the latter is lower only if its thickness is $\leq$ 10 mm.

5.1.2 Effect of load, temperature, and frequency

Generally, it is expected that the load loss test be conducted at the rated current. For large power transformers the tested load loss value at a lower current value when extrapolated to the rated condition in the square proportion may result in a value less than the actual one. This is because the stray losses in structural components, which form an appreciable part of the total load loss in large power transformers, may increase more than the square proportion. With increasing winding currents and leakage field values, saturation effects in the mild steel material used for structural components increase. If a magnetic or electromagnetic shield is not adequately designed, it is less effective at higher currents increasing stray losses. The exponent of the current for stray losses may even be of the order of 2.3 to 2.5 instead of 2 in such a case [2]. Hence, depending upon the proportion of stray losses in the total load loss, the latter will be higher than that extrapolated with the exponent of 2. Hence, it is preferable to do the load loss test on large transformers at the rated current. If the test plant is having some limitation, the test can be done at a lower current value subject to agreement between the user and manufacturer of the transformer.

It should be noted that Equation 5.2 or 5.3 can be used for a plate excited by a tangential field on one side, the plate thickness being sufficiently larger than the skin depth so that it becomes a case of an infinite half space. By using an analytical approximation for the magnetization curves of a commonly used mild steel material, Equation 5.2 or 5.3 for the power loss per unit surface area in a massive steel element, subjected to the tangential field of H_0 at the surface, can be rewritten in terms of the source current I as [6]

$$P_e \propto I^{1.6} \times f^{0.5} \times \sigma^{-0.5}. \tag{5.14}$$

The above equation is valid when H_0 is proportional to I, which is true, for example, in the case of bushing mounting plates. The current exponent of 1.5 is reported in [4] for calculation of the loss in bushing mounting plates.

For stray losses in magnetic steel plates subjected to the field of high current carrying bars, the exponent of the current is slightly less than 2. The exponent is a function of the distance between the bar and the plate [7] ($=1.975-0.154\log_{10} h$, where h is the distance from the center of the bar to the plate surface in inches). For aluminum plates, the exponent value is 2 [7, 8].

The power loss per unit area for an incident flux ϕ, which is radial in nature (incident normally on the plate), is given by [6]

$$P_e \propto \phi^{2.8} \times f^{1.9} \times \sigma^{0.9} . \tag{5.15}$$

Equation 5.15 is applicable to the case of a tank plate subjected to the stray leakage field emanating from windings. The inter-winding gap flux is proportional to the currents in the windings. For a tank plate penetrated by a part of stray (leakage) field originating from the windings, the relation between this radial field and the winding current is [9]

$$\phi \propto I^{\kappa} \tag{5.16}$$

where κ is in the range of 0.8 to 0.9. Hence, Equation 5.15 can be rewritten in terms of the current as

$$P_e \propto I^{\eta} \times f^{1.9} \times \sigma^{0.9} \tag{5.17}$$

where η, the exponent of the current, is in the range of 2.2 to 2.5, which is in line with the value of 2.3 given in [2]. Hence, some stray loss components increase with the load current having an exponent greater than 2. Since these losses generally do not form the major part of load losses (if adequate shielding is done) and other stray losses vary with the current exponent of 2 or less than 2, the load loss dependence on the current is not much different than the square proportion. This is particularly true when the load loss test is done at or below the rated currents. In overloading conditions, however, the load loss may increase with the current exponent > 2.

Losses due to high current fields (e.g., in bushing mounting plates) vary in direct proportion of $\sqrt{f\rho}$ according to Equation 5.14. From Equation 5.17, it is clear that the stray losses in a tank plate vary almost in the inverse proportion of resistivity and square proportion of frequency. Since the eddy losses in windings are also inversely proportional to resistivity (see Equation 4.94), the total stray losses may be assumed to vary in the inverse proportion of resistivity (because the winding eddy losses and the tank losses form the major part of stray losses for most of the transformers). Furthermore, for simplicity in calculations, they are assumed to vary in the inverse proportion of resistivity of the winding

conductor. Thus, the total stray losses in transformers can be related to resistivity as

$$P_{stray} \propto \frac{1}{\rho} \quad or \quad P_{stray} \propto \sigma . \tag{5.18}$$

Since metals have positive temperature coefficients of resistance (resistivity increases with temperature), the stray losses can be taken to vary in the inverse proportion of temperature. If the load loss is guaranteed at 75°C, the stray loss component of the measured load loss at temperature t_m is converted to 75°C by the formula (for windings made using copper)

$$P_{stray\_75°C} = P_{stray\_t_m} \times \frac{235 + t_m}{235 + 75} . \tag{5.19}$$

For an aluminum conductor the constant 235 is replaced by 225. Contrary to stray losses, the DC I^2R loss in windings varies in direction proportion of resistivity and hence the temperature. Therefore, for the copper conductor,

$$P_{I^2R\_75°C} = P_{I^2R\_t_m} \times \frac{235 + 75}{235 + t_m} . \tag{5.20}$$

The I^2R loss at t_m (obtained by converting the value of the I^2R loss corresponding to the DC resistance test done at temperature t_r to temperature t_m) is subtracted from the measured value of the load loss at t_m to calculate $P_{stray\_t_m}$. In order to calculate the I^2R loss at t_m, the average winding temperature should be accurately determined. This is done by taking the average of top and bottom cooler temperatures. A substantial error may occur if, after oil processing and filtration cycles at about 50 to 60°C, sufficient time is not provided for oil to settle down to a lower temperature value close to the ambient temperature. In such a case, the temperature of windings may be quite different than the average of the top and bottom cooler temperatures. Hence, it is preferable to wait until the oil temperature settles as close to the ambient temperature or until the difference between the top and bottom oil temperatures is small enough (the difference should not exceed 5°C as specified in ANSI Standard C57.12.90-1993) for accurate measurements. For a forced oil cooling system, a pump may be used to mix the oil to minimize the difference between top and bottom oil temperatures.

Regarding the effect of frequency variation on the total stray losses, it can be said that since the eddy loss in windings is proportional to the square of frequency, the stray loss in tank plates is proportional to frequency with an exponent less than 2 according to Equation 5.17, and the stray loss due to fields of high currents varies with $f^{0.5}$ according to Equation 5.14, the total stray loss

varies with frequency with an exponent x, whose value depends on the proportion of these losses in the total stray loss.

$$\therefore P_{stray} \propto f^{x}. \tag{5.21}$$

If the winding eddy loss and the stray losses in all structural components are treated separately, the winding eddy loss is taken to vary with frequency in the square proportion, whereas remaining stray losses can be assumed to vary with frequencies having an exponent close to 1. According to IEC 61378 Part-1, 1997, *Transformers for industrial applications*, the winding eddy losses are assumed to depend on frequency with the exponent of 2, whereas stray losses in structural parts are assumed to vary with frequencies with the exponent of 0.8. The frequency conversion factors for various stray loss components are reported and analyzed in [10].

For a transformer subjected to non-sinusoidal duty, at higher frequencies the skin depth is lower than the thickness of winding conductors. Hence, the relationship given by Equation 4.90 or 5.1 is more valid (the frequency exponent of 0.5) instead of that given by Equation 4.94 (the frequency exponent of 2 when the thickness is less than the skin depth). Therefore, at higher frequencies the exponent for the winding eddy loss reduces from 2 to a lower value [11].

5.2 Overview of Methods for Stray Loss Estimation [12]

After having seen the basic theory of stray losses in structural components, we will now take a look at how methods of their computation have evolved from approximate 2-D analytical methods to the present day advanced 3-D numerical methods.

5.2.1 2-D methods

A method is given in [13] for estimating leakage field, in which any kind of current density distribution can be resolved into space harmonics by a double Fourier series. The leakage field distribution in the core window obtained by this method can be used to calculate the approximate value of losses in flitch plates and the first step of the core (in addition to the eddy losses in windings). A two-dimensional axisymmetric finite element formulation based on the magnetic vector potential is used in [14] to obtain losses in the tank. A computer program based on a 2-D FEM formulation for skin effect and eddy current problems is presented in [15]. The formulation is suitable for both Cartesian and axisymmetric 2-D problems. In [16], an analogy between magnetic field equations for 2-D Cartesian and axisymmetric problems is presented, and usefulness of this analogy for numerical calculations has been elaborated. The relation between the finite element and finite difference methods is also clarified. Results of measurements of flux densities and eddy currents on a 150

MVA experimental transformer are reported. In [17], a 2-D finite element formulation based on the magnetic vector potential is presented, which takes into account the varying distance between the outer winding and the tank by a correction factor. A 2-D FEM-based approach is used to obtain static magnetic field solutions in [18], and losses in the tank are calculated by analytical formulae. The paper has reported test results of tank losses with magnetic and eddy current shielding. The geometric parameters affecting the tank losses are explained through graphs. It is recommended in [19] to analyze the stray losses as a complete system and not on an individual component basis. For example, the placement of magnetic shunts on tank surfaces has the effect of reducing stray losses in the clamping elements of the core since the leakage field is oriented more towards the tank. The magnetic tank shunts also increase the radial field at the ends of the outermost winding and may increase its eddy loss if the width of its conductor is high enough to compensate the reduction in the eddy loss due to reduced axial field at the ends. A number of 2-D FEM simulations are done to understand the effect of magnetic and non-magnetic tank shields on other stray loss components. The simulations have shown that the effectiveness of magnetic shunts is dependent on permeability of their material, indicating that they should have adequate thickness so that the permeability does not reduce due to saturation.

In this era of 3-D calculations, 2-D methods are preferred for routine calculations of stray losses. These 2-D methods can be integrated into transformer design optimization programs, particularly for computing eddy losses in windings.

5.2.2 3-D analytical formulations

A quasi 3-D formulation given in [20] obtains radial flux density distribution on the tank surface by using the method of images. The approach does not consider the effect of the eddy currents induced in the tank on the incident field. This assumption is made to simplify the analytical formulation. From this radially incident peak value of the flux density (for example in the z direction), the tangential components of the magnetic field intensity (H_x and H_y) are calculated using Maxwell's equations. The resultant peak value ($H_0 = \sqrt{H_x^2 + H_y^2}$) is used to calculate the power loss per unit area using the assumption of step-magnetization characteristics (similar to the theory given in Section 4.4). The total losses in the tank are calculated by integrating the loss over its entire area. The method given in [21] calculates 3-D magnetic flux density distribution on the tank wall using a 2-D solution obtained for one phase in a three-phase transformer.

These analytical methods cannot be applied to complicated tank shapes and for finding the effects of tank shielding accurately. For such cases 3-D numerical methods are commonly used.

5.2.3 3-D numerical methods

The advent of high speed and large memory computers has made possible the application of numerical methods such as FEM, *finite difference method*, *boundary element method*, etc., for the calculation of 3-D fields inside transformers and accurate estimation of the stray losses. The boundary element method (BEM) is suitable for open boundary problems involving structural parts of non-magnetic stainless steel, wherein it is difficult to determine boundary conditions [22, 23]. For such open boundary conditions, some researchers have used the integral equation method (IEM) [24]. In order to make the generation of the mesh easier, IEM with surface impedance modeling is proposed in [25]. An improved $\mathbf{T}-\Omega$ (electric vector potential–magnetic scalar potential) formulation is used in [26], wherein the problem region is divided into source, non-conductive and conductive regions simplifying computational efforts.

An overview of methods for eddy current analyses is presented in [27]. The paper compares methods that are based on differential formulations (analytical methods, the finite difference method, the reluctance network method), integral formulations (the volume integral method, the boundary element method), and variational/weighted residual methods (FEM) on attributes such as accuracy, ease of use, practicality and flexibility. Advantages of BEM for transient and open boundary problems are enumerated in the paper. There is continuous ongoing development in 3-D numerical formulations, which started gaining importance in 1980s, for improving their modeling capabilities and accuracy for the analysis of eddy currents.

After having seen the different approaches for the calculation of stray losses, we will now discuss in detail each stray loss component and its control.

5.3 Core Edge Loss

Core edge loss occurs due to flux impinging normally on core laminations. The amount and the path of the leakage field in the core depend on the relative reluctances of the alternative magnetic circuits. Load conditions of the transformer also have significant influence; the phase angle between the leakage field and the magnetizing field decides the loading of the magnetic circuit and the total core losses during operation at site. During factory tests, the leakage flux path in the core depends largely on whether the inner or the outer winding is short-circuited as explained in Section 5.12.2. The incident leakage flux density on the limb and the clamping elements is appreciable in generator transformers due to relative closeness of the limb from the inter-winding gap as compared to autotransformers. Hence, there are more possibilities of hot spots being generated in these parts in them. However, the stray loss value may be of the same order in both types of transformers due to more leakage field in autotransformers on an equivalent two-winding basis.

In large transformers, the radially incident flux may cause considerable eddy currents to flow in core laminations resulting in local hot spots. The flux penetration phenomenon is different in a laminated core structure as compared to a solid one. In a solid block of finite dimensions, the eddy currents tending to concentrate at the edges can complete their path through the side faces, and the field is confined to the surface (skin depth) in all the faces. In the laminated case, there is restriction to the flow of eddy currents and the field penetrates much deeper as compared to the solid case. The leakage flux penetration into the laminated core poses an anisotropic and three-dimensional nonlinear field problem. The problem is formulated in terms of a **T**-Ω formulation in [28]. The solution is expressed in the form of three different characteristic modes, two associated with the core surfaces and the third describing the flux penetration into the interior. All three modes are represented in a network model by complex impedances, and then the current distribution and losses are derived from the solution of the network. The core discontinuities (holes) are accounted by changes in appropriate impedances. Thus, the method provides a means of studying effects of core steps, holes, ducts, and discontinuities (due to lapped joints). The network has to be modified with any change in the geometry or the type of excitation. The formulation in the paper has been verified on two experimental models of a core [29, 30]. Approximate formulae for finding the loss and temperature rise due to an incident field are also given. The effect of the type of the flitch plate (magnetic or non-magnetic) on the core edge loss is also explained. A non-magnetic (stainless steel) flitch plate increases the core edge loss since it allows (due to its higher skin depth) the flux to penetrate through it and impinge on the laminations. Hence, although the use of the non-magnetic flitch plate may reduce the loss in it (assuming that its thickness is sufficiently small as explained in Section 5.1.1), the core edge loss usually increases.

The first step of the core is usually split into two or three parts to reduce the edge loss in large transformers. If the stack height of the first step of the core is less than about 12 mm, slitting may have to be done for the next step also. The use of a laminated flitch plate for large generator transformers and autotransformers is preferable since it also acts as a magnetic shunt (as described in Section 5.5).

The evaluation of exact stray loss in the core poses a challenge to transformer designers. With the developments in 3-D FEM formulations which allow anisotropic modeling of permeability and conductivity, the computational difficulties can be overcome now.

5.4 Stray Loss in Frames

Frames (also called yoke beams), serving to clamp yokes and support windings, are generally in the vicinity of a stray magnetic field of windings. Due to their large surface area and efficient cooling, hot spots seldom develop in them. The

stray loss in frames has been calculated by the finite difference method and an analytical method in [31]. The losses in frames made from mild steel, aluminum and non-magnetic steel are compared. It has been shown that the losses in the frames and the tank have a mutual effect on each other. Non-magnetic steel is not recommended as a material for frames. It is expensive and difficult to machine, and the stray loss is lower only if its thickness is sufficiently small. A quick and reasonably accurate calculation of the frame loss can be done by using the reluctance network method (RNM) [32].

The loss in frames due to a leakage field can be reduced by either aluminum shielding or by use of non-metallic platforms for supporting windings. In distribution transformers, the stray loss in the tank may not be much since the value of the leakage field is low. But the loss in frames due to currents in low voltage leads running parallel to them can be significant. For example, the current of a star-connected LV winding of a 2 MVA, 11/0.433 kV transformer is 2666.67 A, which can result in stray loss in the frames of the order 1 kW (which is substantial for a 2 MVA transformer). Non-metallic frames can be used (after thorough assessment of their short circuit withstand capability) for eliminating the stray loss.

Another way of minimizing this loss is by having a go-and-return arrangement of LV winding leads passing close to the frame. These two leads can be either firmly supported from the frame or they can pass through a hole made in the frame as shown in Figure 5.6. The net field responsible for eddy current losses in the metallic frame is negligible as the two currents are in opposite directions.

A single lead may be allowed to pass through a hole in the frame with a non-magnetic insert (e.g., stainless steel material with high resistivity) as shown in Figure 5.7 up to a certain value of the current.

In power transformers, sometimes a frame of non-magnetic material (stainless steel) is used. As explained in Section 5.1.1, its thickness should be as small as mechanically possible; otherwise its loss may exceed the corresponding value for the frame made from a (magnetic) mild steel material.

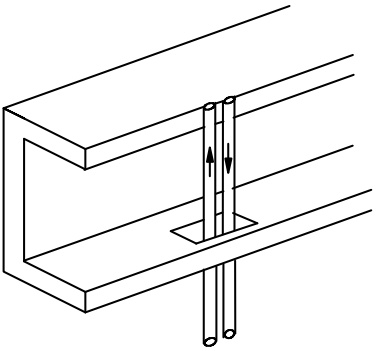

Figure 5.6 Go-and-return arrangement.

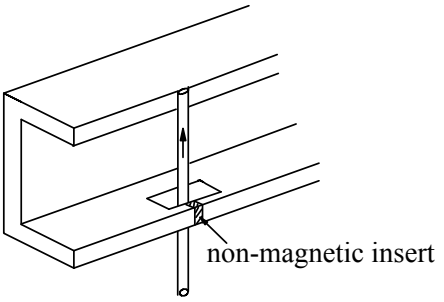

Figure 5.7 Nonmagnetic insert.

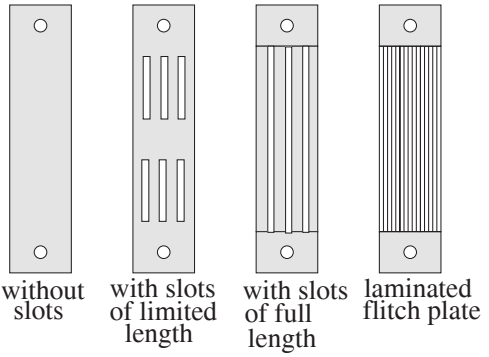

Figure 5.8 Types of flitch plates.

5.5 Stray Loss in Flitch Plates

Stray flux departing radially from the inner windings hits fittings such as flitch plates mounted on the core. On the surface of a flitch plate (which holds core laminations together vertically), the stray flux density may be much higher than that on the tank. Hence, although the losses occurring in it may not form a significant part of the total load loss of the transformer, a local temperature rise can be much higher due to a high value of incident flux density and poorer cooling conditions. The loss density may attain levels that may lead to a hazardous hot-spot if the material and type of flitch plate are not selected properly. Higher temperatures can cause deterioration of insulation in the vicinity of the flitch plate, thereby seriously affecting the transformer life.

There are a variety of flitch plate designs being used in power transformers as shown in Figure 5.8. For small transformers, mild steel flitch plates without any slots are generally used because the incident field is not large enough to cause hot spots. As the incident field increases in larger transformers, plates with slots at the top and bottom ends can be used (where the incident leakage field is higher). Sometimes, flitch plates are provided with slots in the portion corresponding to the tap zone in taps-in-body designs. These slots of limited length may be adequate if the incident field on the flitch plates is not high. Fully slotted plates are even better, but they are weak mechanically, and their manufacturing process is complicated. The plates can be made of non-magnetic stainless steel having high resistivity only if their thickness is small as explained in Section 5.1.1. When the incident leakage field on the flitch plate is very high, as in large generator transformers, the best option would be to use a laminated flitch plate. It consists of a stack of CRGO laminations, which are usually held together by epoxy molding to make the assembly mechanically strong. The top and bottom ends of laminations are welded to solid (non-magnetic) steel pads which are then locked

to the frames. A laminated flitch plate not only minimizes its own eddy loss but it also acts as a magnetic shunt reducing the loss in the first step of the core.

There are very few investigations reported in the literature that analyze stray losses in flitch plates. An approximate but practical method for calculation of the loss and temperature rise of a flitch plate is given in [4], which makes certain approximations based on the experimental data given in [33]. The field strength at the inner surface of the LV winding is assumed to vary periodically with a sinusoidal distribution in space along its height, and the non-sinusoidal nature is taken into account by multiplying the calculated loss by an empirical factor. The eddy current reaction is neglected in this analytical formulation. For a fully slotted flitch plate, the formulation is modified by considering that the plate is split into distinct parts. A more accurate 2-D/3-D FEM analysis is reported in [34], in which many limitations of analytical formulations are overcome. The paper describes details of statistical analysis, *orthogonal array design of experiments*, used in conjunction with 2-D FEM for quantifying the effect of various factors influencing the flitch plate loss. This Section contains results of the authors' paper [34] © 1999 IEEE. Reprinted, with permission, from *IEEE Transactions on Power Delivery*, Vol. 14, No. 3, July 1999, pp. 996–1001. The dependence of the flitch plate loss on the axial length of windings, the core-LV gap, the clearance between the windings and the yokes and the LV-HV gap is observed to be high. The flitch plate loss varies almost linearly with the LV-HV gap. A quadratic surface derived by multiple regression analysis can be used by designers for quick and approximate estimation of the flitch plate loss. The analysis can help in deciding the type and the material of the flitch plate to reduce its loss and eliminate hot spots. The effectiveness of the number and length of the slots in reducing the loss can be ascertained accurately by 3-D field calculations. In the paper, an in-depth analysis of eddy current paths has been reported for slotted mild steel and stainless steel flitch plates, having dimensions of 1535 mm $\times$ 200 mm $\times$ 12 mm, used in a single-phase 33 MVA, 220/132/11 kV autotransformer. For this analysis, a mild steel (MS) flitch plate with $\mu_r = 1000$ and $\sigma = 4 \times 10^6$ mho/m has been studied. The corresponding skin depth is 1.1 mm at 50 Hz. The results obtained are summarized in Table 5.1. The loss values shown are for one fourth of the plate.

Table 5.1 Loss in the MS Flitch Plate [34]

Case number	Description	Loss in watts
1	No slots	120
2	1 slot throughout	92
3	3 slots throughout	45
4	7 slots throughout	32
5	1 slot of 400 mm length	100
6	3 slots of 400 mm length	52
7	7 slots of 400 mm length	45

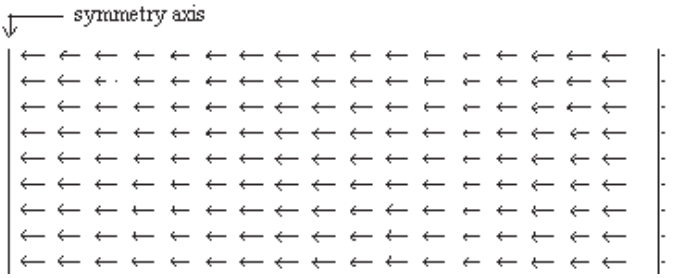

Figure 5.9 Eddy currents in the MS plate with no slots [34].

The eddy loss in a plate with 7 slots throughout is approximately 4 times less than that with no slots. The loss should reduce approximately by a factor of (n+1) for n slots (i.e., by 8 times for 7 slots) since it is proportional, theoretically, to the width square (if a plate width of 4w is divided by 3 slots into 4 plates of width w, then the loss should theoretically reduce by a factor of $(4w)^2$ divided by $4w^2$, i.e., 4). The reason for this discrepancy can be explained as follows. In the mild steel plate, the patterns of the eddy currents are complex. The incident radial flux changes its direction immediately once it penetrates inside the plate due to a very small skin depth. Therefore, the eddy loss in it occurs due to both the radial incident field as well as the axial field inside it. Figure 5.9 and Figure 5.10 show the eddy current patterns in the plate cross section, taken at 0.5 mm inside the surface facing the windings, in no-slots and 3-slots cases, respectively. The eddy current pattern does not change in this cross section after the introduction of slots. The pattern indicates the predominance of the axial field at 0.5 mm inside the surface. The corresponding eddy current loops in the thickness of the plate are shown in Figure 5.11. This explains why slots are less effective in the MS plate and the reduction of the loss is not by 8 times in 7-slots case.

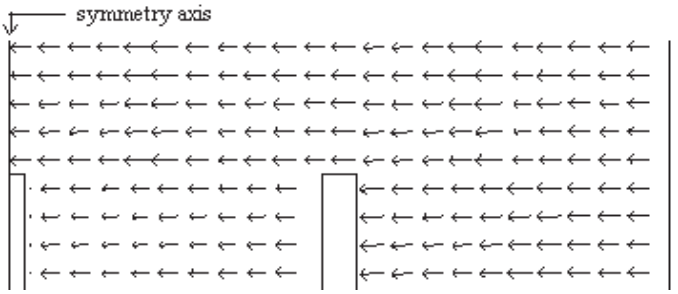

Figure 5.10 Eddy currents in the MS plate with 3 slots [34].

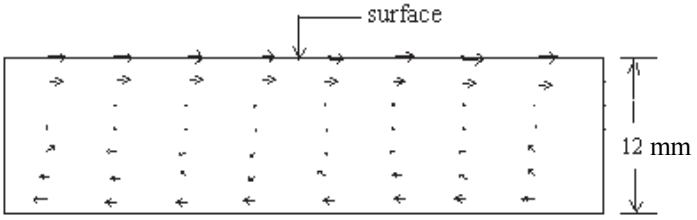

Figure 5.11 Eddy currents across thickness of the MS plate with 3 slots [34].

For a nonmagnetic stainless steel (SS) flitch plate ($\mu_r = 1$, $\sigma = 1.13 \times 10^6$ mho/m), due to its large penetration depth (67 mm at 50 Hz), the incident field penetrates through the plate and impinges on the core first step. Figure 5.12 and Figure 5.13 show the eddy currents in the plate cross section, taken at 0.5 mm inside the surface facing the windings, in no-slots and 3-slots cases, respectively. The introduction of the slots distorts the eddy current pattern significantly.

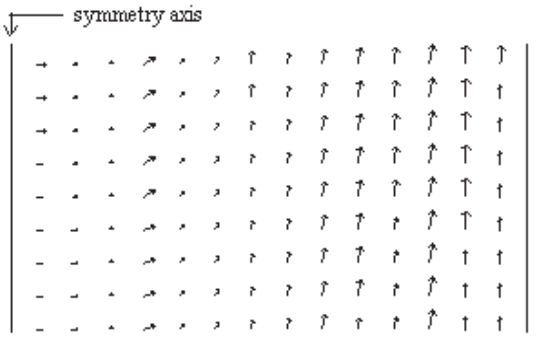

Figure 5.12 Eddy currents in the SS plate with no slots [34].

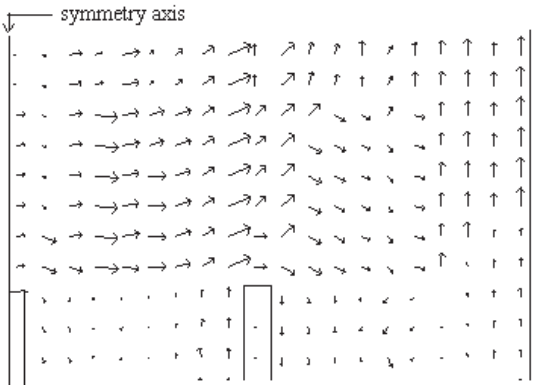

Figure 5.13 Eddy currents in the SS plate with 3 slots [34].

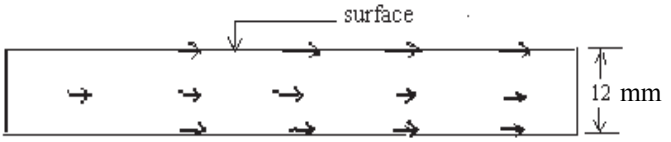

Figure 5.14 Eddy currents across thickness in the SS plate with 3 slots [34].

The pattern of the eddy currents suggests that the radial field dominates at the cross section, 0.5 mm inside the surface. Eddy current loops are absent in the plate thickness (refer to Figure 5.14). The eddy current loops are parallel to the plate surface on which the flux is incident, corroborating the fact that the eddy loss in the SS plate is predominantly due to the radial field. This behavior explains as to why the slots are effective in the SS plate. In this case, the loss should have been reduced approximately by a factor of (n+1). However, the reduction in the loss is more (12 times) than expected (8 times) if we analyze the first two entries in Table 5.2. The additional loss reduction is due to a reduced area available for the induced eddy currents on account of 5-mm wide slots.

Due to higher resistivity of SS, the losses in the SS plate are lower than the MS plate. If results from Tables 5.1 and 5.2 are compared for the *no-slots* case, it can be seen that the SS plate loss is not significantly lower than the MS plate loss for 12 mm thickness. With a greater thickness, the loss in the SS plate may exceed the loss in the MS plate, which is in line with the graphs in Figure 5.5. It shows that in order to obtain lower losses with a SS material, its thickness should be as small as possible with due considerations to mechanical design requirements. With the SS plate, the shielding effect is not available. Hence, although losses in the flitch plate are reduced, the stray loss in the first step of the core may increase substantially if it is not split. Therefore, thicker flitch plates with a low value of incident flux density should be made of MS material.

A laminated flitch plate (consisting of M4 grade CRGO laminations) has also been analyzed through 3-D FEM analysis by taking anisotropy into account. The direction along the flitch plate length is defined as a soft direction and other two directions are defined as hard directions. The loss in the laminated flitch plate is 2.5 watts, which is much lower than that of the SS plate. Hence, laminated flitch plates are preferred in large power transformers, particularly generator transformers, wherein the incident flux density on a flitch plate can be high.

Table 5.2 Loss in the SS Flitch Plate [34].

Case Number	Description	Loss in watts
1	No slots	98
2	7 slots throughout	8
3	7 slots 400 mm long	11
4	3 slots 400 mm long	17

The eddy loss distribution obtained by the 3-D FEM electromagnetic analysis is used for the estimation of the temperature rise of the flitch plate by 3-D FEM thermal analysis [34, 35]. The heat generation rates (watts/m^3) for various zones of the flitch plate are obtained from the 3-D FEM electromagnetic analysis. The computed temperatures have been found to be in good agreement with that obtained by measurements. Thus, the method of combined 3-D electromagnetic and thermal FEM analysis can be used for the analysis of the eddy loss and temperature rise of a flitch plate. Nowadays, commercial FEM software packages are available having multi-physics capability. Hence, the temperature rise can be determined more easily without manual interface between the electromagnetic and thermal analyses.

5.6 Stray Loss in Tank

The stray loss in tank plates forms a major part of the total stray loss in large power transformers. Stray flux departing radially from outer windings gives rise to eddy current losses in the tank. Though the stray flux density impinging on a tank surface is usually low, the tank loss may be high due to its large surface area. Hot spots seldom develop in the tank, since the heat is carried away by oil. A good thermal conductivity of the tank material also helps to mitigate hot spots. The loss is controlled by magnetic/eddy current shields.

Methods for estimation of the tank loss have evolved from approximate analytical methods to the present day more accurate 3-D numerical methods. The radial incident flux density at various points on the tank is computed in [36] by neglecting the effect of eddy currents on the incident field. It is assumed that the ampere-turns of windings are concentrated at the longitudinal center of each winding in the form of a current sheet, and the field at any point on the tank is calculated by superimposition of the fields due to all the windings. The tank loss is calculated using the estimated value of the radial field at each point. The analytical formulation in [37] determines the field in air without the presence of the tank, from the geometrical details of the transformer and the currents in its windings. Based on this field and the coefficient of transmission, the tangential component of the magnetic field strength on the inner surface of the tank is determined. The specific power loss at a point is then calculated by using the value of the active surface resistance of the tank material. The total losses are determined by summing the specific losses on the surface of the tank. The analytical method, presented in [38], takes into account hysteretic and nonlinear behavior of the tank material by using complex permeability. A current sheet, a sum of trigonometric functions between the core and tank (both treated as infinite half spaces), represents the mmf of windings. The calculated value of the radial component of the flux density at the tank surface is corrected by a coefficient accounting for the influence of eddy currents. The tank loss is found by Poynting's vector. The method can be applied for a specific tank shape only. The effect of magnetic/eddy current shields on the tank wall is not considered in

the method. The analytical approach in [39] expresses the incident flux density (obtained by any method) on the tank in terms of double Fourier series. Subsequently, after getting the field and eddy current distribution within the tank plate, the loss is evaluated by using a volume integral. The results are verified by an experimental setup in which a semi-circular electromagnet is used to generate radial field on the tank plate.

Thus, since the 1960s the research reported for the calculation of the tank loss has been mainly concentrating on various analytical methods involving intricate formulations, which approximate 3-D geometries for simplicity. Transformer designers prefer fast interactive design with sufficient accuracy to enable them to decide the method for reducing stray losses. The reluctance network method [1] can fulfill the requirements of very fast estimation and control of the tank stray loss. It is based on a 3-D network of reluctances. The reluctances are calculated from various geometrical dimensions and electrical parameters of the transformer. There are two kinds of elements, viz. magnetic resistances for nonconducting areas and magnetic impedances for conducting parts. The first ones are calculated purely from the geometrical dimensions of the elements, whereas the latter ones take into account analytically the skin effect, eddy current reactions with phase shifts, nonlinear permeability of ferromagnetic metals, and the effect of eddy current shields (if placed on the tank wall). Hence, the method is a hybrid method, in which the analytical approach described above is used, for the portion of the geometry involving eddy currents, in conjunction with a numerical formulation.

The equivalent reluctance of ferromagnetic steel can be determined with the help of the theory of eddy currents explained in Chapter 4. For a magnetic field applied on its surface in the y direction, and assuming that the field is a function of z only (Figure 5.15), the amplitude of flux per unit length in the x direction is

$$\phi_0 = \mu \int_0^\infty H_y \, dz \, . \tag{5.22}$$

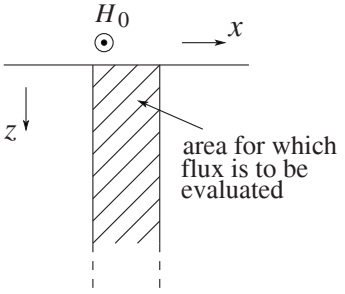

Figure 5.15 Equivalent reluctance for tank.

In line with Section 4.3, for the peak value of the magnetic field intensity (H_0) at the surface, we can write from Equation 4.68 for linear *B-H* characteristics $(\alpha = \beta = 1)$,

$$\phi_0 = \mu \int_0^\infty H_0 e^{-(1+j)z/\delta} dz \tag{5.23}$$

$$\therefore \phi_0 = \mu H_0 \frac{\delta}{1+j}. \tag{5.24}$$

If $\Re$ is the equivalent reluctance per unit length at the surface of the tank in the *y* direction, then

$$H_0 \times 1 = \Re \times \phi_0. \tag{5.25}$$

From Equations 5.24 and 5.25, we have

$$\Re = \frac{1}{\mu\delta} + j\frac{1}{\mu\delta} \quad \cdots\cdots \textit{ linear characteristics.} \tag{5.26}$$

The above equation gives the value of complex reluctance per unit length in the *y* and *x* directions (per unit surface area) along the surface of the tank (with the tank thickness along the *z* direction) for linear material characteristics. It is assumed that the tank thickness is more than three times the corresponding skin depth. Let us now derive the same for nonlinear characteristics of magnetic steel using elliptic permeability (Section 4.3), for which the value of magnetic field is given by (Equation 4.68),

$$H_y = H_0 e^{-(\alpha + j\beta)z/\delta}$$

where, $\alpha = \cos\theta/2 + \sin\theta/2$ and $\beta = \cos\theta/2 - \sin\theta/2$.

$$\therefore \phi_0 = \mu e^{-j\theta} \int_0^\infty H_0 e^{-(\alpha+j\beta)z/\delta} dz = \mu(\cos\theta - j\sin\theta) \times H_0 \frac{\delta}{\alpha + j\beta}.$$

Therefore, the equivalent reluctance per unit length at the surface of the tank in the *y* direction is given by

$$\Re = \frac{H_0}{\phi_0} = \frac{\alpha\cos\theta - \beta\sin\theta}{\mu\delta} + j\frac{\beta\cos\theta + \alpha\sin\theta}{\mu\delta}.$$

So far, we have not considered the effect of saturation harmonics on the value of the reluctance. We know that $\mu\delta = \frac{B_s}{H}\sqrt{\frac{2}{\omega\sigma(B_s/H)}} \propto \sqrt{B_s}$ and hence it must be multiplied by a factor of 1.4 as suggested in Chapter 4. Also, the value of θ for magnetic steel was found to be approximately 40^0 from an experimentally

measured *B-H* loop of mild steel having peak flux density of 0.6 T at 50 Hz (see reference 17 of Chapter 3). Hence, the final expression of the reluctance per unit length at the surface of the tank in the *y* direction is

$$\Re \cong 0.43 \times \frac{1}{\mu\delta} + j0.92 \times \frac{1}{\mu\delta}.$$

This is close to the expression, with semi-empirical correction factors, given in [32],

$$\Re \cong 0.52 \times \frac{1}{\mu\delta} + j0.86 \times \frac{1}{\mu\delta} \quad \cdots\cdots \textit{ nonlinear characteristics.} \tag{5.27}$$

The above reluctance expression must be used with peak values of magnetic field. While dealing with rms values, the expression must be divided by $\sqrt{2}$,

$$\Re \cong (0.37 + j0.61)/\mu\delta.$$

Proper values of these elements (real and complex reluctances), corresponding to the transformer parameters and the frequency of the supplied voltage, are placed into a network scheme along with the voltage sources which model magnetomotive forces in the windings. All the network elements are expressed in per unit (relative) values referred to the data of the interwinding gap. Power losses are calculated from the surface field strength according to Equation 5.3, with a semi-empirical linearization coefficient of 1.4 for mild steel. The 3-D reluctance network method has been verified [40, 41] on various ratings of power transformers from 31.5 MVA up to 315 MVA. The method is based on the assumption of four-quarter symmetric structure of a three-phase transformer. Subsequently, the method has been further improved [42] to model asymmetric structures. Due to increased number of nonstandard reluctance elements, they are first expressed with the help of analytical formulae and then introduced into the matrix equation of the entire 3-D model.

As compared to analytical and semi-analytical methods, numerical methods can give more accurate results but higher computational efforts are required. Numerical methods can be combined with analytical formulations to reduce computational efforts. The 3-D FEM formulation reported in [43] uses a complex magnetic vector potential. Eddy current losses in steel materials are computed by combining a numerical method with an analytical formulation because of the discretization problem due to a very thin skin depth of magnetic steel. A power transformer has dimensions of a few meters, whereas skin depths are in millimeters resulting in errors due to a poor aspect ratio of finite elements. A method of modeling the tank wall and other fittings with surface elements is outlined in [44], which obviates the need of having complex layers of thin elements for taking into account the skin effect. The basis of the formulation has

been explained in Section 4.2. The surface impedance element modeling approach helps to calculate the tank loss efficiently and accurately.

The presence of the tank has some influence on the stray loss in other structural components (frames, flitch plates, etc.), which depends on the relative closeness of the tank from the windings as compared to the core. If C and T are the distances of the core and the tank from the inter-winding gap-center as shown in Figure 5.16, the fringing of the leakage flux at the ends of the windings toward the core is independent of the presence or absence of the tank with magnetic shunts if [45]

$$\frac{T}{C} \geq \frac{\pi}{(8C/h)} - 1 . \tag{5.28}$$

In this case, the stray loss in the tank can be isolated by doing the load loss test with and without it. If the tank is lined with aluminum or copper shields, its effect on stray losses in other structural components is more pronounced. A much higher distance between the tank and the outside winding is required [45] to make the tank's influence negligible, which is governed by the relation $T \geq h$.

Another important aspect related to the electromagnetic field calculations of a tank wall is the analysis of temperature rise of the bolted joint between the tank and the cover. The currents induced in the two parts due to leakage and high current fields are forced to complete their path through flange bolts. The bolts are overheated if the induced currents are large. The flow of these induced currents through the bolts can be avoided by completely isolating them from the tank and the cover. This results in a number of problems. First, the induced currents may concentrate in larger cross-sectional areas of flanges causing local overheating which leads to deterioration of gaskets over a period of time.

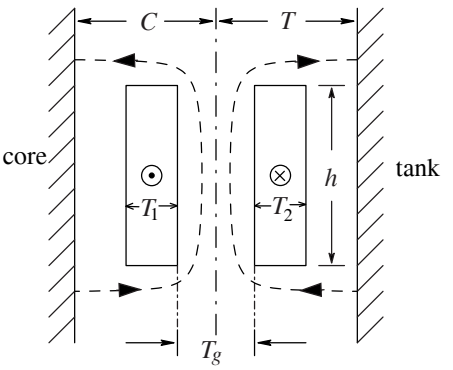

Figure 5.16 Effect of a tank wall on other stray losses.

Second, due to a bad electromagnetic contact between the tank and the cover, there is an increase in the magnetic voltage drop (magnetomotive force), leading to a greater magnetic field strength on the bolt surface, which may give rise to excessive local eddy current losses in the magnetic steel bolts (the use of highly resistive nonmagnetic bolts may mitigate the effect; however this is a costly option). Also, the condition that the tank and the cover should be at the same electrical (ground) potential is not satisfied. This phenomenon of an overheating hazard in the case of bad electromagnetic contact has been investigated in [46] by representing the bolted joint by an equivalent reluctance. The local eddy currents in these bolts may cause dangerous hot spots, damaging the gaskets/seal between the flanges. Hence, a better option would be to connect the two parts by metallic strips (links) made of high conductivity materials such as aluminum or copper to maintain both parts at the same electrical potential and to provide a low resistance alternative path to the induced currents in them. The electrical connection through metallic bolts cannot be relied upon (either due to presence of paint or a bad contact resistance). The number of connecting links to be used depends on the amount of leakage field/high current field. For small transformers with a low field at the tank surface, two connecting links may be enough. When links are not used, a large value of mmf is concentrated in the air gap between the tank and the cover due to its high reluctance value. As a conductive link is introduced, a current flows through it due to the emf induced by the aforesaid magnetic field between the tank and the cover. This current in turn produces a magnetic field which opposes the incident magnetic field. Thus the magnetic field strength on the bolt surface is reduced, reducing the excessive local eddy losses occurring in it.

Currents flowing in these connecting links can be hundreds of amperes in large power transformers (say, 300 MVA rating). These currents are high particularly in a bell type of tank construction (described in Chapter 10), in which the curb (flanged) joint is at the position of the bottom yoke. A typical leakage field plot is shown in Figure 5.17. The construction is not suitable for providing an effective shielding arrangement. This is because if a vertical magnetic shunt is placed with its bottom end at point B, its length will be lower than a desired value. An additional small vertical shunt placed between points C and D will result in higher temperatures on the tank surface at the locations near these points (since the flux will leave the shunt and enter the tank at these locations). Hence, it is always preferable to have a magnetic shunt in one piece between a point at which the flux enters the tank to a point where it leaves the tank. Therefore, it is advisable to have the curb joint as low as possible (in a bell construction) or as high as possible (in a conventional construction wherein the curb joint is at top). If this is not possible, a complex arrangement of shunts as shown in Figure 5.18 may have to be tried. The shunt S_2, which can be fixed to the shunt S_1, overlaps on the shunts S_1 and S_3 shielding the curb joint.

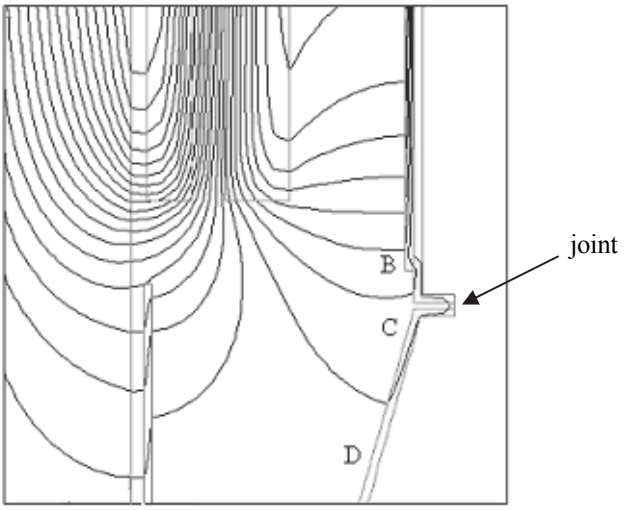

Figure 5.17 Leakage field plot for a bell tank.

When high current leads pass near a curb joint region of the tank, excessive heating of bolts may occur resulting in deterioration of gaskets. In such cases, either an adequate number and size of external links connecting the tank and the cover should be used (for shunting the currents) or the values of the currents should be controlled by careful positioning of the leads. The arrangement of Figure 5.18 is not useful for fields due to high current leads.

5.7 Stray Loss in Bushing Mounting Plates

As the transformer rating increases, the current in its low and high voltage sides increases. This leads to an increase in eddy currents in structures that surround the bushings.

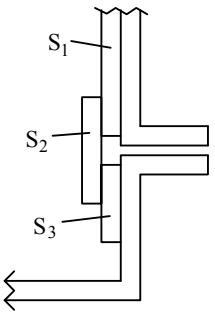

Figure 5.18 Shielding of a curb joint.

Bushing mounting plates are made of mild steel (MS) or stainless steel (SS) material. As the rating increases, the eddy current loss and the related heating effects increase. The loss and temperature rise of an MS plate (being a magnetic material) are more, and hence for higher ratings SS plates are used. But compared to MS material, SS material is expensive; hence, instead of using an SS plate, an MS plate with SS inserts is used up to a certain current value.

An experimental analysis of eddy current phenomenon in the structure that surrounds the high current bushings of a large capacity transformer is presented in [47]. A basic model with a conducting current of 20 kA is constructed to investigate the eddy current phenomenon. An eddy current probe is used for the direct measurement of the magnitude and phase of eddy currents. A 2-D formulation is used to estimate eddy current patterns. The formulation is based on a few approximations, and experimentally measured data is used for calculations. An analytical method is presented in [32, 48] to determine and prevent hot spots in bushing mounting plates. The instantaneous value field intensity at any point on the plate surface is calculated as a vector sum of field intensities due to currents in conductors of three-phases. Equation 5.3 is used to calculate the loss if the plate thickness is sufficiently larger than the skin depth (the calculated loss value is multiplied by 2 since the plate is excited on its both surfaces). If the thickness is smaller than the skin depth, a correction factor based on Figure 5.3 can be used corresponding to Case 2 (excitation of the plate by same field on both surfaces).

A formula for calculating the permissible r.m.s. value of the bushing current is given in [48], above which there is a possibility of excessive overheating,

$$I_{\max} = 2460 \times d \times \left[\sqrt{1 + 3.9 \times \left(1 + \frac{2.4 \times \sqrt{t}}{d} \right)} - 1 \right] \tag{5.29}$$

where d is the center-to-center distance between the phases as shown in Figure 5.19, and t is the plate thickness; both the dimensions are in meters. This formula has been derived for a typical grade of (magnetic) structural steel having conductivity of about 7×10^6 mho/m at 20°C. For a plate of thickness 6 mm with a distance of 150 mm between the phases, the maximum permitted current is about 780 amperes. As the current rating increases, nonmagnetic inserts made from a high resistivity SS material are used as shown in Figure 5.20. Depending upon the width of the inserts, which can be in the range of 20 mm to 50 mm, the current rating can vary. For still higher currents, a mounting plate of SS is used.

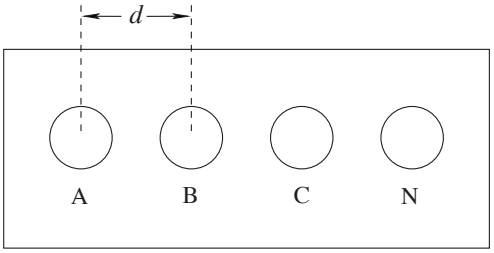

Figure 5.19 Bushing mounting plate.

Different shapes of nonmagnetic inserts have been analyzed using a 3-D FEM formulation in [49] to reduce the tank wall loss in small pad-mounted transformers. In these transformers LV leads are usually terminated on a tank wall. The results of the FEM simulation have been verified on a transformer in which T-shaped SS inserts are used.

In [35, 50], the results of the analytical formulation given in [32, 48] are compared with that of 3-D FEM analysis and experimental measurements. The loss occurring in a bushing mounting plate is calculated indirectly from the measured values of the initial temperature rise and the steady-state temperature rise. These methods, in which indirect verification of the loss is done, are described in Section 5.10. The methods are useful because it is very difficult to verify the calculation by conventional experimental measurements. This is due to the fact that the loss occurring in the plate cannot be exactly isolated from the tested load loss value of the transformer. If the conditions are simulated by using a low-voltage high-current source in a laboratory, the loss measurement is very difficult, if not impossible, at a low voltage of few volts.

5.8 Evaluation of Stray Loss Due to High Current Leads

In furnace transformers and large generator transformers, the stray loss due to induced eddy currents in structural components in the vicinity of high current leads can be substantial. They could lead to hot spots if adequate magnetic clearances are not provided or shielding measures are not taken.

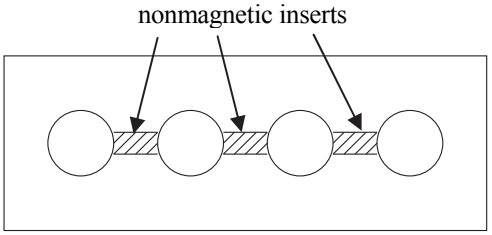

Figure 5.20 Bushing mounting plate with nonmagnetic inserts.

Techniques for evaluation of the stray loss due to a high current field have improved gradually from 2-D analytical methods to the present day 3-D numerical methods. The method discussed in [51] evaluates eddy losses in a semi-infinite solid near a filament current. Practical cases, however, involve plates of finite thickness, and hence a modification of the solution is required. An empirical formula is presented in [7] for the eddy loss calculation in steel plates based on measurements on an experimental setup. Field patterns and eddy losses due to current-carrying strip bus bars are evaluated in [5] for an aluminum sheet. The current distribution is expressed in terms of an infinite number of sinusoidal distributions with the help of Fourier integral, and then the field due to any current distribution is obtained by superimposition of fields due to sinusoidal components. In [52] also, the method first transforms the original current distribution into sinusoidal current sheets. The method is therefore quite general and can be used for different current distributions (single-phase and three-phase currents) and different shapes of conductors (filaments, rectangular conductors, etc.). A laboratory experiment has been conducted to verify the theoretical results. A method for analyzing electromagnetic fields in a system that comprises of parallel current carrying bars placed above a steel wall is presented in [53]. Current densities within the cross section of bars are computed using an integral equation technique.

All these methods, due to some assumptions and approximations, are useful for simplified 2-D geometries and cannot be applied to complex 3-D structures. With today's 3-D FEM software capabilities, 3-D problems can be easily simulated and analyzed. The analysis of eddy current patterns in the LV lead termination of a furnace transformer is done in [52] by using 3-D FEM analysis. The total eddy loss estimated by using a time-harmonic 3-D FEM formulation is in close agreement with that observed during the testing of the transformer. The arrow plot of eddy currents in the front plate of the termination is shown in Figure 5.21 (reproduced from [52] with permission from IET). The three rectangular holes in the plate carry three-phase currents of 56 kA magnitude. The plot shows the eddy currents at an instant when the R-phase current is maximum. There is a concentration of eddy currents at locations A, B, C, D, E and F. Hence, hot spots developed at these locations during the testing of the furnace transformer. Therefore, for transformers having very high currents on the LV side, magnetic clearances and the material of terminations have to be judiciously selected. In most cases, it requires 3-D analysis in the absence of data of previous proven designs.

It should be noted that time-harmonic 2-D and 3-D formulations find the time-harmonic magnetic field in and around current-carrying conductors in the presence of materials that may be conducting, magnetic, or both. Theoretically, the time-harmonic analysis is not possible for nonlinear materials because sinusoidally-varying sources do not give rise to sinusoidally-varying fields. The basis of the time-harmonic analysis is as follows [54].

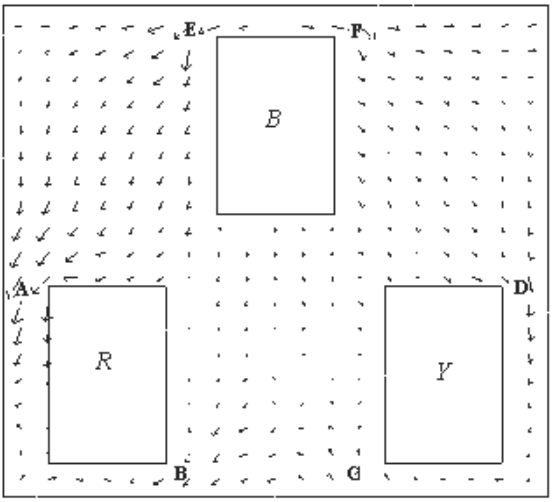

Figure 5.21 Eddy currents in the front plate of the furnace transformer [52].

In the time-harmonic formulations, the sources and fields are assumed to be time-harmonic at one specified frequency; complex phasors are used to represent them. For an eddy current analysis involving nonlinear materials, a transient formulation may have to be used. In the time-harmonic formulation based on the magnetic vector potential **A**, the solution of the following complex diffusion equation is determined.

$$\nabla^2 \mathbf{A} = \mu(-\sigma \nabla V + j\omega\, \sigma \mathbf{A}) . \tag{5.30}$$

In 2-D problems, **A** is assumed in the z direction only and is a complex quantity. The term $(-\sigma \nabla V)$ represents the source current density vector $\mathbf{J_0}$ and is referred to as the DC distribution of the current density, which is applicable to the three-phase conductors of Figure 5.21 when eddy currents in them are not considered. The other term $\left(j\omega\sigma \mathbf{A}\right)$ represents the induced eddy current density in structural components. Equating real parts and imaginary parts on both sides of the above equation we obtain

$$\nabla^2 \,\mathrm{Re}\left[\mathbf{A}\right] + \mu\omega\sigma \,\mathrm{Im}\left[\mathbf{A}\right] = -\mu\sigma \mathrm{Re}\left[\nabla V\right] \tag{5.31}$$

$$\nabla^2 \mathrm{Im}\left[\mathbf{A}\right] - \mu\omega\sigma \,\mathrm{Re}\left[\mathbf{A}\right] = -\mu\sigma \mathrm{Im}\left[\nabla V\right]. \tag{5.32}$$

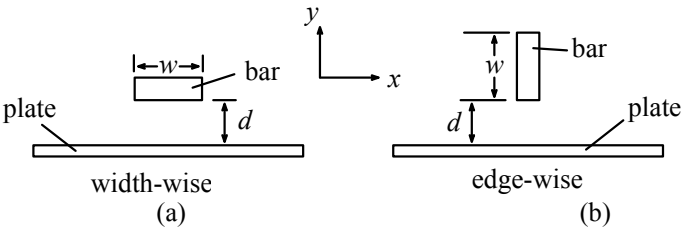

Figure 5.22 High current-carrying bar parallel to structural plate.

The solution of Equation 5.31, Re[**A**], corresponds to an instant when Re[$\mathbf{J_0}$] is at peak with Im[$\mathbf{J_0}$] as zero. Whereas, the solution of Equation 5.32, Im[**A**], corresponds to an instant when Re[$\mathbf{J_0}$] is zero with Im[$\mathbf{J_0}$] at peak. Obviously at any other time instant the solution is [54]

$$\mathbf{A}(t)=\text{Re}[\mathbf{A}]\ \cos\omega t + \text{Im}[\mathbf{A}]\ \sin\omega t\ . \tag{5.33}$$

Thus, the time-harmonic (frequency-domain) analysis technique is computationally efficient since the data required to be stored is just twice that of a static solution. For the time-domain analysis of eddy current problems involving nonlinear materials and/or nonsinusoidal excitations, the solution has to be computed at each sufficiently small time-step requiring large computational efforts and time.

After having seen some of the methods reported for analyzing the stray loss due to a field of high currents, let us see some practical aspects of design. When a high current bar runs parallel to a structural plate (e.g., tank), there are two possible configurations as shown in Figure 5.22. The configuration in which the edge (thickness) of the bar faces the plate (Case b: edgewise) is better than the other one in which the width of the bar (w) faces the plate (Case a: widthwise). General guidelines and rules given below for designing magnetic clearances are based on the results of a number of time-harmonic 2-D FEM simulations (with a mild steel plate having $\sigma = 7\times10^6$ mho/m and $\mu_r = 100$). The simulations are done with a bar current of 4 kA (r.m.s. value).

1. The edgewise configuration gives a loss advantage of about 15 to 20% over the widthwise configuration. About the same amount of advantage is reported in references [22, 4]. For a given clearance d between the bar and the plate, the edgewise configuration always results into a lower loss value. Sometimes space restrictions may not allow the edgewise placement. The losses obtained by 2-D FEM are somewhat higher than that reported in [4] (based on experimental measurements done on 1 m × 2 m plate). The difference could be because the actual loss is different due to the end effects due to the finite length of the plate in the z direction (2-D FEM calculates the loss per unit length in the z direction assuming that the plate has infinite length in that direction). Moreover, a constant value of permeability is assumed in the 2-D FEM analysis, which is not the case in reality.

Table 5.3 Loss in a Plate for a Distance of 120 mm from the Center of a Bar

Configuration	Distance of the plate from the center line of the bar (mm)	Width of the bar (mm)	Loss in the plate (watts/m)
Edgewise	120	60	586.3
Edgewise	120	80	587.8
Edgewise	120	100	589.8
Edgewise	120	120	592.3
Widthwise	120	120	579.8

2. It is generally observed that the loss in the plate (per meter length in the *z* direction) for the edgewise and widthwise configurations are approximately equal for a given distance between the center line of the bar and the plate surface (refer to Table 5.3). The plate thickness and width are 10 mm and 1000 mm respectively, whereas the bar thickness is 20 mm.

3. Theoretically, the plate loss varies in the square proportion of the bar current for linear material characteristics. An exponent of current slightly less than 2 is reported in [7] as explained in Section 5.1.2.

4. It can be seen from Figure 5.23 that the loss varies as the frequency is varied with an exponent in the range of 0.7 to 0.8. The effect of the frequency has to be considered in the case of excitation currents with high harmonic content. An exponent of 0.8 is specified for the frequency in IEC 61378 — Part 1, as explained in Section 5.1.2.

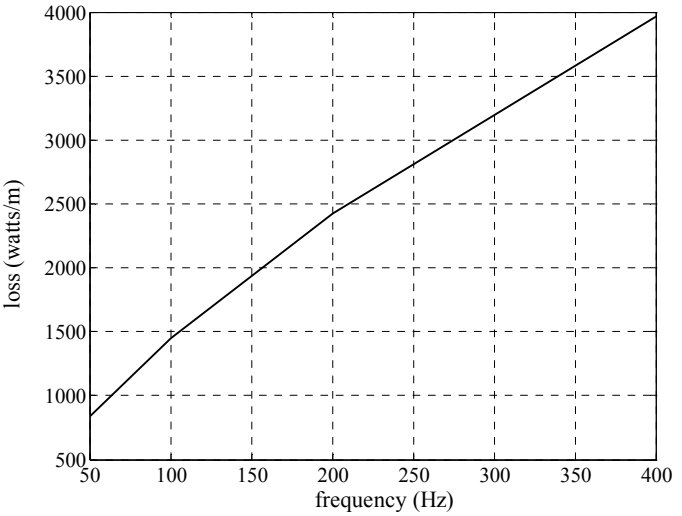

Figure 5.23 Effect of the frequency variation.

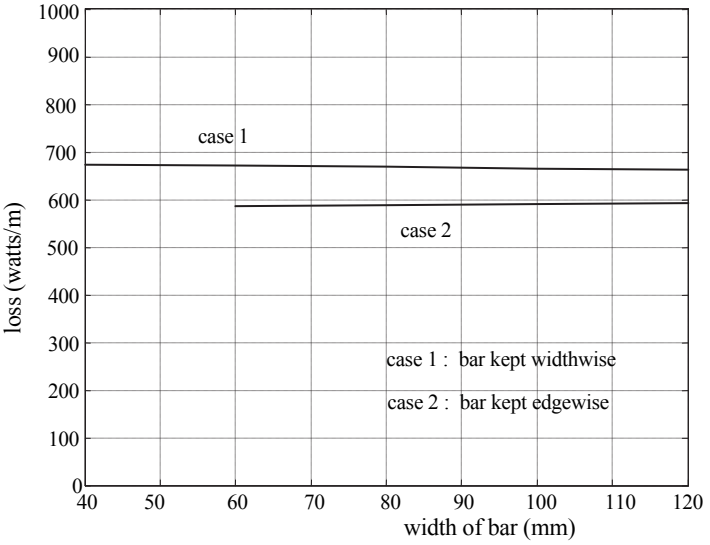

Figure 5.24 Effect of the bar width on the plate loss.

5. In the widthwise configuration, when the bar width is changed keeping the current flowing through it and its distance (*d* in Figure 5.22) from the plate constant, there is no noticeable change in the plate loss as shown in Figure 5.24 (although the loss in the bar changes). The plate loss is basically affected by the magnitude of the current and the clearance. But with an increase in the bar width (for the same current), the loss density and temperature rise in the plate reduce. Hence, for a given current with more width, the plate loss remains almost constant and one can have lower clearance for the same temperature rise. The loss in the edgewise configuration is lower than that in the widthwise configuration as explained in point 1.

6. Losses occurring in the plate are substantially influenced by variations in its material conductivity as shown in Figure 5.25 for a nonmagnetic material. For a very low conductivity value (e.g., a stainless steel material), the plate thickness is less than its skin depth. It becomes a case of resistance-limited eddy currents, and the loss increases with an increase in conductivity (this is in agreement with the discussion in Section 4.5.1 and Equation 4.93).

As conductivity increases (e.g., Al), the induced eddy currents in the plate become substantial reducing the incident field and losses in the plate. It gradually becomes a case of inductance-limited eddy currents as the skin depth becomes thin as compared to the plate thickness. The behavior is similar to that explained for aluminum material in Section 5.1.1 with reference to Figure 5.5.

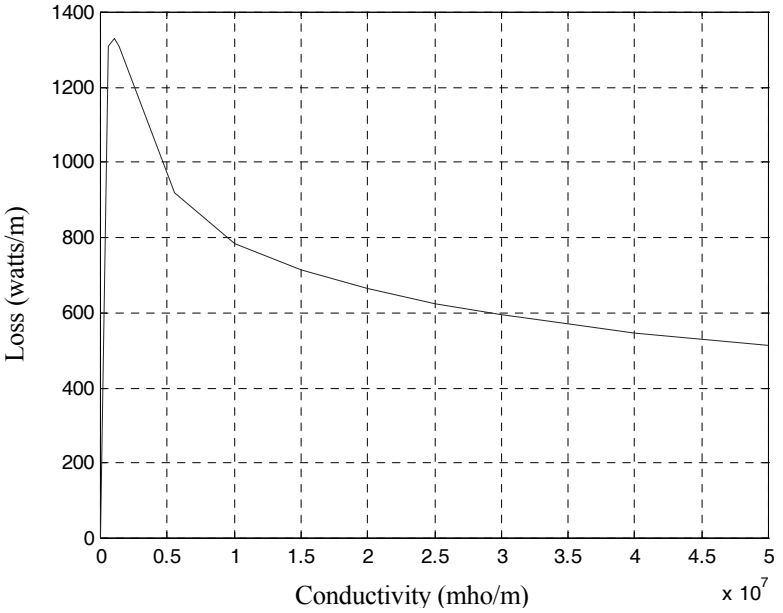

Figure 5.25 Effect of the change in conductivity of the plate.

7. For two bars carrying currents in opposite directions (go and return), there are three possible configurations as shown in Figure 5.26. The calculated loss in Case (c) is the lowest and that in Case (a) is the highest. In all the three cases, the loss increases with an increase in the distance of separation (s) between the two bars. Hence, the distance should be minimum as permitted by mechanical, thermal, and electrical considerations.

For all the configurations of the bar and the plate discussed in this section, manufacturers usually conduct experiments on various configurations and measure temperatures. Based on these measurements, clearances are standardized for various currents and configurations to limit the plate temperature rise to a specific permitted value.

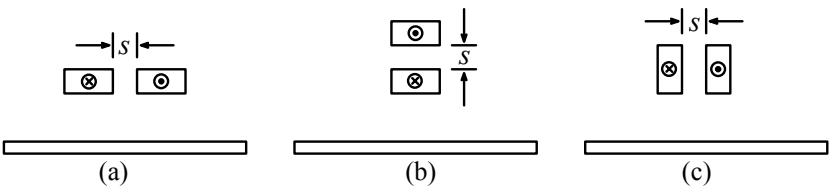

Figure 5.26 Different configurations of bars carrying go and return currents.

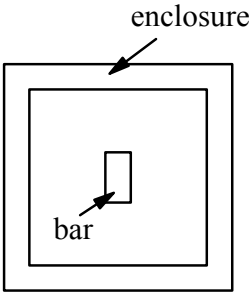

Figure 5.27 High current bar in a metallic enclosure.

When a high current bar passes through a metallic enclosure/bus-duct (see Figure 5.27), the eddy loss in the enclosure is a function of its perimeter or its distance from the bar. The higher the perimeter or the distance, the higher is the current that can be allowed to pass through the enclosure. The loss can be controlled by making the enclosure using a nonmagnetic material having high resistivity or by the use of eddy current shields (aluminium/copper shields). If three-phase bars are passing through it, the eddy loss can be reduced substantially if the bars are placed symmetrically inside the enclosure and close to each other (to make the resultant field small).

When a magnetic plate is shielded by an aluminum or a copper shield, the eddy currents induced in the shield are forced out to its edges and may cause local overheating at the edges or in structural magnetic parts close to them. Hence, the shield should be of sufficient width and should be made in one piece (without discontinuity).

5.9 Measures for Stray Loss Control

The stray loss in a structural component can be reduced in a number of ways:

- use of laminated materials
- use of high resistivity material
- reduction of flux density in the component by using materials having lower permeability
- reduction of flux density in the component by provision of a parallel magnetic path having a low reluctance and loss
- reduction of flux density in the component by diverting/repelling the incident flux by use of a shielding plate having high conductivity

These are general guidelines, and the application of these measures depends on the configuration and the type of excitation as discussed in Section 5.1. The measures for stray loss control of structural components in a transformer, except tank plates, have been discussed in previous sections. In this section, methods for reducing the stray loss in the tank are elaborated.

Three methods are commonly used for reducing stray losses in tanks. The first method uses yoke shunts which collect the leakage field coming out of the windings so that there is very little flux external to the core and windings. Second, magnetic shunts can be provided on the tank so that they carry most of the leakage flux. Third, the tank may be lined with aluminum or copper plates (shields); the eddy currents in these plates tend to shield the tank from most of the radial incident flux.

Shielding measures are not usually adopted for small distribution transformers and cost-benefit analysis is done to make the decision regarding the use of these measures [55]. The measures for stray loss control are discussed with reference to large power transformers in [56, 57, 58]. The methods for reducing the loss in various structural components due to high current and leakage fields are described briefly in [56]. An approximate formula is given for the calculation of incident radial flux density on the tank wall in [57] and the effectiveness of magnetic shunts is also investigated. The permissible values of the tangential component of the magnetic field strength on various constructional elements are given in [59] to eliminate local overheating hazards. Principles for designing tank shields are also explained.

Guidelines and useful curves are given in [60] to prevent overheating hazards in windings, the core first step, flitch plates, frames, and tank walls. The experimental results of a 37 MVA transformer are presented in [61] for various proportions of tank shielding by magnetic shunts. The effect of positioning of interphase connections of high current carrying leads on the tank loss has been explained. The effects of the tank and its shields on the magnetic field and stray loss in the windings are evaluated and compared with the corresponding measurements carried out on a 150 MVA experimental transformer in [62]. A number of findings are reported: flux density distribution varies along the circumference of the winding when placed in the tank with shields; flux density distribution in a winding may be calculated with a single-phase representation regardless of the tank and tank shield conditions; winding eddy losses in the absence of the tank are almost the same as that with the tank without any shield; winding eddy losses increase when placed in a tank with magnetic shields (shunts) and reduces when placed in a tank with aluminum shields; and circulating current losses do not depend much on the tank and its shielding conditions.

Some geometrical factors have a significant influence on tested stray losses. A small difference in the heights of the LV and HV windings can affect various stray loss components in different ways. For example, if the LV winding is taller by 1% and is placed symmetrically with respect to the HV winding height, the losses in the core clamping structures reduce, whereas the losses in the tank increase because the leakage field at ends of the windings is oriented more towards the tank. Some manufacturers may purposely adopt this design to reduce the axial short circuit forces in the LV winding (which is generally weaker if it is a layer winding). On the contrary, if the HV winding is taller, the

stray losses in the core, frames, and flitch plates increase, and those in the tank reduce. This shows that manufacturing variations in geometrical dimensions may have significant effect on the leakage field pattern and the stray losses, and this is one of the reasons why the tested load loss values of transformers, manufactured with an identical design, sometimes differ noticeably.

5.9.1 Magnetic shielding

Magnetic shunts are more effective in controlling stray losses as compared to nonmagnetic (eddy current) shields. They offer a low reluctance path to the leakage flux constraining its path in a predetermined fashion. In the case of eddy current shields, the flux repelled by them may find a path through nearby structural components negating the advantages of shielding. An ideal magnetic shunt (infinite permeability) has no magnetic voltage drop across its length. The magnetic shunts are basically useful to shield structural components from the leakage field. They are not used for shielding against the field of high currents. If magnetic shunts are of adequate thickness and are made of CRGO laminations with lower watts/kg characteristics, the losses in them are almost negligible. Usually, leftover pieces of core laminations from original rolls are used to make magnetic shunts. The height of magnetic shunts should be higher than the height of windings. The height can be decided based on the leakage field pattern obtained from an FEM analysis. The shunts can be placed on the tank from the level of the top yoke-center to the level of the bottom yoke-center in the absence of any detailed analysis. For a 360 MVA, 500 kV transformer, it is suggested in [26] that the height of the magnetic shunts should be more than that of the windings by one meter (500 mm at each end).

There are basically two types of magnetic shunts, widthwise and edgewise shunts. Widthwise shunts are placed on the tank as shown in Figure 5.28. The width of the shunts should be as small as possible to reduce entry losses at their top and bottom portions where the leakage field impinges on them radially. As the shunt width reduces, the number of shunts increases leading to a higher manufacturing time. Hence, each manufacturer arrives at a suitable width of the shunts. It can be as high as 300 mm and as small as 50 mm. The gaps between shunts have to be kept as small as mechanically possible (some space is required for their fixing arrangement on the tank) for effective shielding. By taking advantage of the fact that the incident radial flux enters the shunt (mostly in its end portions) at different points and that the (axial) flux density in the shunt (corresponding to the collected flux) is maximum at the center, a magnetic shunt of varying length can also be used as shown in Figure 5.29. Most of the incident flux can enter the shunts through their thin edges reducing the entry loss. The saving in the shunt material (laminations) thus obtained has to be compared with extra manufacturing efforts required for the purpose. An optimum design of a similar tank shield arrangement is arrived at in [63] by using the design of experiments technique in conjunction with 3-D FEM.

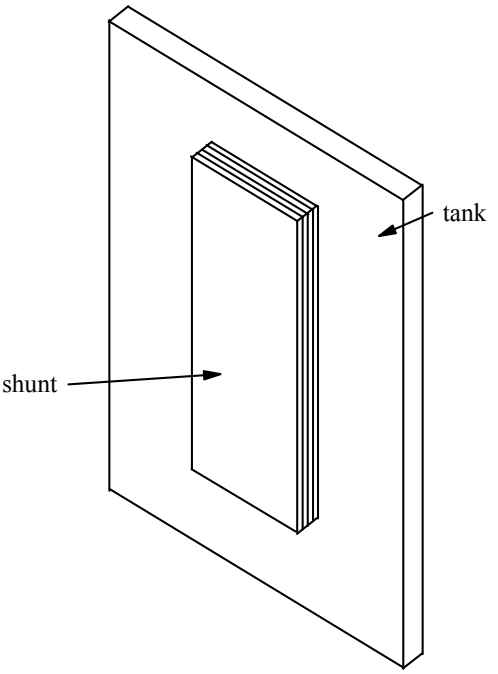

Figure 5.28 A widthwise shunt.

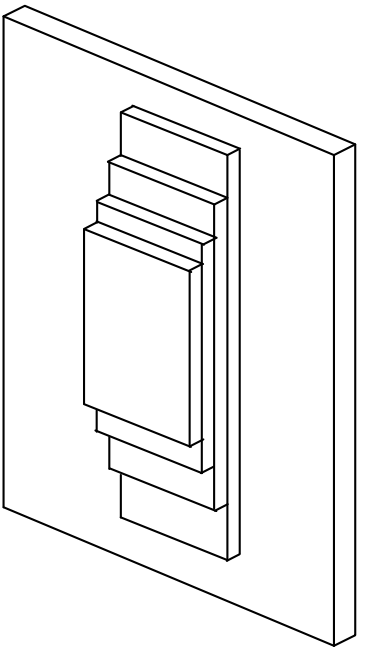

Figure 5.29 An optimum widthwise shunt.

A practical formula for the calculation of the required thickness of a widthwise tank shunt is given in [6, 32] with reference to Figure 5.16:

$$ST_{min} = \frac{C}{C+T} \frac{\sqrt{2}\,\mu_0\, N\, I \left[\frac{T_1 + T_2}{2} + T_g \right]}{h\, B} \text{ meters} \tag{5.34}$$

where B, the flux density value to be limited in shunts, can be taken as 1.7 Tesla for CRGO material and 1.4 Tesla for CRNGO material. Since the effective permeability of the widthwise shunt is less due to interlaminar nonmagnetic gaps, it is preferable to take values of B about 20% lower than the above values (i.e., 1.4 Tesla for CRGO and 1.15 Tesla for CRNGO). Under overloading conditions, shunts may get saturated and become ineffective; hence the lower value of flux density also helps under overloading conditions.

An edgewise shunt is better than a widthwise shunt because the flux is incident on the thickness (edge) of laminations resulting in negligible eddy loss in them. A typical edgewise shunt is shown in Figure 5.30. The effective permeability of laminations as seen by the incident flux is much higher for this

shunt as compared to the widthwise shunt since the flux does not encounter any non-magnetic gaps once it enters the shunt. In the widthwise shunt, due to non-magnetic gaps (however small they be), the effective permeability at the entry point reduces making it less effective as compared to the edgewise shunt. The flux distribution at the entry point is complicated. The presence of interlaminar nonmagnetic gaps reduces the average permeability in the direction normal to the laminations to a low value, and hence the flux tends to stay within a particular lamination until it saturates. The flux finds its way through the next lamination when the earlier lamination saturates and so on. Thus, it can be seen that the effectiveness of the widthwise shunts is less as compared to the edgewise shunts.

The manufacturing process of edgewise shunts is elaborate. In one of the forms, a set of laminations are epoxy moulded (like in laminated flitch plates). In another design, it can be made into a wound form. The loss advantage with the edgewise shunts has to be assessed vis-a-vis their higher cost and manufacturing time as compared to the widthwise shunts. The performances of these two types of shunts are compared in [64] by finding their effective anisotropic permeability. A substantial reduction in tank stray losses is reported in [26] by the use of edgewise shunts. It is preferable to experimentally check the quantum of stray loss reduction before standardizing the use of edgewise shunts.

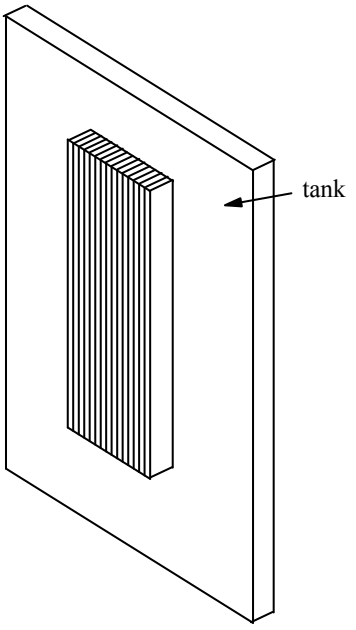

Figure 5.30 Edgewise shunt.

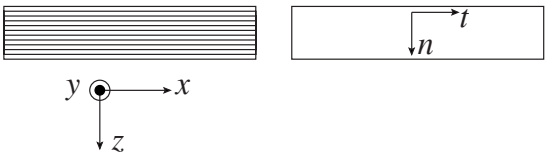

Figure 5.31 Anisotropic permeability.

For a stack of laminations subjected to a magnetic field, the directional effects of material anisotropy and the stacking factor have to be taken into account. Because of the obvious difficulties of modeling individual laminations, assemblies of laminations can be represented by solid anisotropic blocks. For a stack of laminations shown in Figure 5.31 with its stacking factor as k, the effective relative permeability across the laminations of the equivalent solid anisotropic block is [44, 65]

$$\mu_{rn}^{eff} = \mu_{rz}^{eff} \cong \frac{1}{1-k} \tag{5.35}$$

and tangential to the laminations in the x-y plane it is

$$\begin{aligned} &\mu_{rt}^{eff} = k(\mu_{rt} - 1) + 1 \cong k\mu_{rt} \\ &\Rightarrow \mu_{rx}^{eff} \cong k\mu_{rx} \quad \text{and} \quad \mu_{ry}^{eff} \cong k\mu_{ry}. \end{aligned} \tag{5.36}$$

where μ_{rx} and μ_{ry} are the relative permeabilities of the lamination material in the x and y directions, respectively (μ_{rx}, $\mu_{ry} >> 1$ and $\mu_{ry} > \mu_{rx}$, with the rolling direction along the y axis). These two values are provided by the material supplier. The stacking factor k can be calculated for the stack of laminations as the ratio of their bare thickness to insulated thickness. The reduced effective permeability across the laminations gives a correct representation of much deeper penetration of the flux in the stack of laminations. This tends to make the flux density distribution more uniform as compared to the inaccurate isotropic modeling, where the flux concentrates only in the surface layers giving a highly non-uniform flux density distribution. A 3-D FEM formulation, which takes electric and magnetic anisotropies into account, is reported in [66]. Electric conductivity and magnetic permeability are represented by tensor quantities in the Cartesian system of coordinates.

Yoke shunts are another form of magnetic shunts (flux collectors), which are placed parallel to the yoke at the top and bottom ends of the windings. These shunts can be effective since the fluxes coming out from the three phases can add up to zero in them. The yoke shunts provide an excellent means of guiding the leakage field safely back to the core minimizing stray losses in the tank and other structural components. The shunts tend to make the leakage field in the windings axial, reducing eddy losses due to the radial field at their ends. The

analysis and design of yoke shunts in large power transformers involves 3-D analysis of the leakage field because of complicated geometries and anisotropic materials. The effects of a yoke shunt are studied in [67] assuming that the shunt is connected directly to the yoke. The work is extended in [68] to include the effects of a small gap between the shunt and the yoke on the leakage field distribution. All the surfaces of magnetic circuit components are considered as magnetic equipotentials (infinitely permeable and nonsaturated). The equipotentials for all the surfaces except that of the shunt are zero. The shunt floats at a potential, which is a function of the gap between the shunt and the yoke. The leakage flux transferred to the yoke decreases as the shunt is spaced away from it. Hence, the gap must be kept sufficiently small for an effective control of the leakage field. In further work [69], the field in the gap and the yoke is analyzed. The laminated iron (yoke) is treated as a solid anisotropic block with effective permeabilities in three directions calculated using the method illustrated in [65]. The references [67, 68, 69] give useful practical guidelines for the yoke shunt design. In [70], the reluctance network method is used to study the effectiveness of yoke shunts in controlling stray losses. The effect of the gap between the windings and the yoke shunt on the stray losses in the tank and other structural components is reported. Yoke shunts can be conveniently used for three-phase five-limb and single-phase three-limb constructions, wherein the transfer of flux can be easily achieved through the yoke steps on either side of the windings. For the three-phase three-limb construction, the collection of flux by the yoke from the outer phases is not straightforward and a special transfer arrangement may be needed. Hence, yoke shunts are usually not used alone in the three-phase three-limb constructions. They are aided by either eddy current shields or magnetic shunts on the tank.

Merits and disadvantages of magnetic shunts are explained in [71]. The main disadvantage of magnetic shunts is that they cannot be used on the tank surfaces of irregular shapes. The losses measured under various combinations of shielding arrangements (i.e., yoke shunts, magnetic shunts, and eddy current shields) are reported in the paper. Some manufacturers use a wound steel pressure ring on the top of the windings, which not only acts as a clamping ring (giving mechanical stability during short circuits), but it also reduces stray losses in structural components. The ring provides a low reluctance path for the leakage field coming out of the windings and diverts it into the yoke away from the structural components. Thus, the axial component of the leakage field increases and the radial component reduces affecting the eddy loss in the windings.

A combination of horizontal and vertical magnetic shunts can also be used on the tank as shown in Figure 5.32. The vertical shunts are placed in front of the three phases, while the horizontal shunts are placed at the level of the yokes. A significant part of the incident leakage field from the three phases is effectively cancelled in the horizontal shunts if it is properly collected by them. The effectiveness of this arrangement can be enhanced by putting eddy current

shields on the short sides of the tank. The leakage flux repelled from these shields is collected by the horizontal shunts aiding the cancellation effect.

5.9.2 Eddy current shielding

Aluminum or copper shields are used for shielding structural components from the high current and leakage fields. Eddy currents induced in them repel the incident field reducing the losses in structural components. As discussed in Section 5.1, the thickness of these shields should be adequate for their effectiveness and for reducing the loss in shields themselves. In most cases, the loss in the structural component-eddy current shield combination is more than that of the structural component-magnetic shunt combination. However, eddy current shields have the advantage that they can be fitted on odd shapes of the tank unlike magnetic shunts. The weight of an eddy current shield is also usually lower than that of a magnetic shunt. For shielding a tank wall from a high current field, eddy current shields are better suited than magnetic shunts. This is because of the gaps between magnetic shunts, which reduce their effectiveness.

An analytical formulation is given in [72] for calculating the loss in the eddy current shield and the tank shielded by it. The formulation is based on a 2-D approximation; the loss in a tank plate, shielded by an aluminum shield, due to a line current is first calculated. The method is then extended to transformer windings, wherein the windings are replaced by an infinite array of line currents by using the theory of images. The eddy current loss in the shields used in air core reactors is evaluated by the image method using Fourier-Bessel integral in [73]. For finite dimensions of shields, 2-D approximations and end effects make the analytical formulations inaccurate and such problems can be simulated by 3-D numerical techniques.

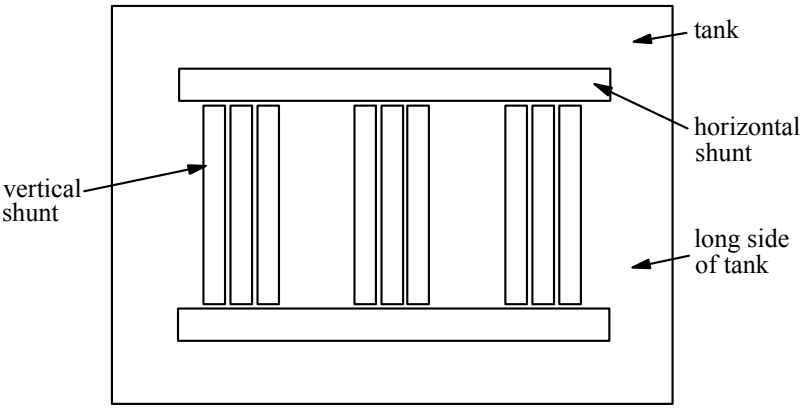

Figure 5.32 Combination of vertical and horizontal magnetic shunts.

The stray loss control by this flux rejection technique is suitable for structural components of odd shapes; shields can be suitably formed to protect the areas having complex shapes. The disadvantage of this method is that losses occur in the shields and they must be accurately evaluated. The dimensions of the shields have to be properly designed and adequate cooling needs to be provided to limit temperatures. Secondly, the diverted flux from the shields may cause overheating of the nearby unprotected structural parts. Hence, the design and positioning of the eddy current shields have to be done more carefully as compared to the magnetic shunts. The shield should of sufficient width as explained earlier in Section 5.8.

A combination of eddy current shields (provided on the tank) and yoke shunts can be used. This arrangement makes the leakage field predominantly axial (which is collected by the yoke shunts) reducing stray losses in the tank and other structural components.

5.10 Methods for Experimental Verification

Conventional search-coil/Hall-effect probe measurements have been used by many researchers for verifying the calculated values of flux densities or current densities in structural components. There are some other indirect methods of predicting the eddy loss in the structural components based on their temperature rise. One method uses measured steady-state temperatures, while the other uses the initial temperature rise. These methods are described below.

5.10.1 Steady-state temperature rise

The structural component, wherein eddy current losses need to be calculated, is allowed to reach a steady-state temperature. The component is assumed as a vertical plate. The oil film temperature, which is the average of measured values of the plate and oil temperatures, is then calculated. If the test is performed in a laboratory in air medium, then the air film temperature is determined as the average of the measured values of the plate temperature and the ambient air temperature. The properties of oil/air film (ρ, k, υ, Pr, and β) are then obtained [4] where

ρ = Density in kg m^{-3}
k = Thermal conductivity in W m^{-1} $^oC^{-1}$
υ = Kinematic viscosity in m^2 s^{-1}
Pr = Prandtl number
β = Coefficient of thermal cubic expansion in $^oC^{-1}$.

The Rayleigh number is given by

$$Ra = \frac{g \beta \Delta\theta l^3}{\upsilon^2} \text{Pr} \tag{5.37}$$

where

g = Acceleration due to gravity in m s^{-2}

l = Vertical length of the plate in m

$\Delta\theta$ = Temperature difference between the plate and the oil/air in °C.

The Nusselt number is then calculated [74, 75] from one of the following two equations:

$$Nu = 0.68 + \frac{0.67 Ra^{1/4}}{\left[1 + (0.492/\mathrm{Pr})^{9/16}\right]^{4/9}} \qquad for\ Ra < 10^9 \tag{5.38}$$

$$Nu^{1/2} = 0.825 + \frac{0.387 Ra^{1/6}}{\left[1 + (0.492/\mathrm{Pr})^{9/16}\right]^{8/27}} \qquad for\ 10^{-1} < Ra < 10^{12}. \tag{5.39}$$

The heat transfer coefficient (h) is calculated as

$$h = \frac{Nu \times k}{l} \quad \mathrm{W\ m^{-2}\ ^{\circ}C^{-1}}. \tag{5.40}$$

Finally, the loss in the plate is given by

$$P = h \times A \times \Delta\theta \tag{5.41}$$

where A is the area of the convection surface in m^2. The estimation of losses in a bushing mounting plate from the measured steady-state temperature rise and its comparison with that calculated by an analytical method and a 3-D FEM simulation are reported in [35, 50].

5.10.2 Initial temperature rise

The eddy loss in the plate can also be calculated from the initial temperature rise measured in the first few seconds of the current application. The power developed in a unit volume inside a solid can be expressed in terms of temperature θ as [6]

$$P_E = c\rho \frac{\partial\theta}{\partial t} - \left\{ k_x \frac{\partial^2\theta}{\partial x^2} + k_y \frac{\partial^2\theta}{\partial y^2} + k_z \frac{\partial^2\theta}{\partial z^2} \right\}. \tag{5.42}$$

The terms k_x, k_y and k_z are the thermal conductivities in the x, y and z directions, respectively, and c is the specific heat (J kg^{-1} $^0C^{-1}$). If the plate temperature is measured sufficiently rapidly after switching on the current (at $t = 0$) so that the temperature of the body may be considered uniform, the term inside the bracket in the above equation reduces to zero giving

$$P_E = c\,\rho \left(\frac{\partial \theta}{\partial t} \right)_{t=0} . \tag{5.43}$$

The term $(\partial\theta/\partial t)_{t=0}$ represents the gradient of the initial part of the heating curve. Thus, one can estimate power losses occurring in a structural component by a fast (say in the first 30 seconds) and accurate temperature rise measurement by using thermocouples. The loss in the bushing mounting plate has been calculated from the initial temperature rise measurements in [35, 50], which agreed well with that calculated from the steady-state temperature rise and the 3-D FEM analysis. The loss in frames is estimated from initial temperature rise measurements in [31].

The method works well for thin structural plates (5 to 6 mm thick). When the thickness increases, an appreciable error may be introduced due to faster heat transfer from the hot surface layer (wherein almost entire loss is taking place) to the inner colder layers. An improved thermometric method proposed in [76] takes into account the heat removal from the surface to its surroundings and to the interior of the structural plate by a correction factor which is a function of the plate thickness. The method sets up equations of heat flow and electromagnetic wave propagation in the material, which take into account non-uniform distributions of heat sources, variation of permeability with field strength and excitation modes of eddy currents. These equations are then solved numerically using a computer. An example of the analysis of the loss in a tank wall of a transformer is also given in the paper; measured surface field strengths are compared with those derived from the thermometric method.

5.11 Estimation of Stray Losses in Overexcitation Condition

Overvoltages appearing across the terminals of a transformer are classified according to their duration. The specification of the overvoltages is usually provided by users as 110 or 115% continuous, 125% for 1 minute, 140% for 5 seconds, and 150% for 1 second. Temporary overvoltages can occur due to the disconnection of a load at the remote end of a long transmission line, ferroresonance conditions, etc. The ferroresonant overvoltages initiated by energization processes last through several cycles or even a few seconds depending on the decay rate of the transformer inrush current. Apart from all these, there can be voltage variations due to load fluctuations. An overexcitation leading to an overfluxing condition in a transformer causes additional losses due to core saturation. The resulting spillover flux from the core can cause intense local losses in conducting parts leading to hot spots. This stray flux cuts conductors of windings and metallic structural parts and causes eddy currents to flow in them. Unlaminated structural parts can be overheated rapidly by such eddy currents, and the condition of adjacent insulation may deteriorate. To avoid these eddy current losses and hot spots, the structural parts have to be properly designed. The effects of overexcitation conditions are elaborated in [77]. Typical loss curves in

windings and structural parts as a function of overexcitation levels are given. Harmonic analysis of the excitation current at various overexcitation levels is also reported.

Finding a suitable analytical model for the purpose of studying overfluxing phenomena is a difficult task. Good working models exist for steady-state analysis. There are several methods that try to find a working model for transient studies. The models presented in [78, 79] analyze ferroresonance phenomena in distribution transformers connected via a long cable. A model based on EMTP (electromagnetic transient program) is reported in [80] for simulating a transformer under the condition of out-of-phase synchronization. A model for a three-phase, two-winding, and five-limb transformer with its supply cables is presented in [81]. In [82], an approach for studying the behavior of a transformer under overfluxing conditions is presented, which is developed by suitable modifications to the model presented in [81]. A lumped parameter approach is used for representing limb and yoke reluctances. A part of the flux fringing out of the core, and not linked to the windings, is lumped into one parameter called air-flux. This air-flux path is located between the upper and lower yokes. To take into account the saturation effect of the limbs, modification of the basic model has been done by incorporating one additional path parallel to each limb. The analysis showed that yoke reinforcement can help in controlling the path of the stray flux under overfluxing conditions.

An accurate simulation of a transformer under a saturated core condition poses a real challenge to researchers. In [83], an attempt has been made to analyze the performance of a transformer under overfluxing conditions by doing 3-D FEM based transient simulations. In this work, a 2 MVA, 11/0.433 kV transformer has been simulated under a 10% continuous overfluxing condition. The temperature rise of frames is calculated by thermal analysis which uses the loss values obtained in the electromagnetic analysis. Flux density distribution (arrow plot) is shown in Figure 5.33, which corresponds to an instant when the R phase voltage is at its positive peak, and the Y and B phase voltages are at half the negative peak value.

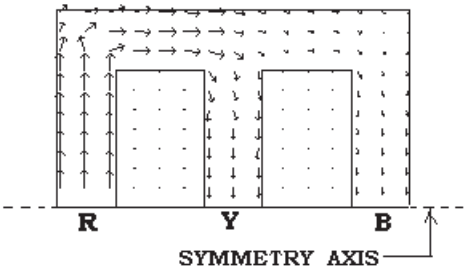

Figure 5.33 Flux density distribution during an overfluxing condition.

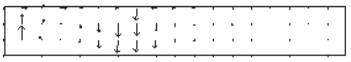

Figure 5.34 Eddy current distribution in a frame.

Some amount of flux from the yoke spills over and hits the frame part facing the yoke above the R phase winding, which is confirmed by the plot of eddy currents in the frame as shown in Figure 5.34. The effect of yoke reinforcement on the overfluxing performance has also been analyzed. The frame loss with yoke reinforcement is considerably less than that without it. The temperature rise of the frame is calculated by using the method described in Section 5.10.1. The solution is obtained by an iterative process as follows. Some initial value of temperature rise is assumed. The oil film temperature (the average of frame and oil temperatures) is calculated. The properties of oil, at this temperature, are used to calculate the Rayleigh and Nusselt numbers. The heat transfer coefficient is then calculated by using Equation 5.40, and subsequently the temperature rise ($\Delta\theta$) is calculated by Equation 5.41. The procedure is repeated until $\Delta\theta$ converges. Thus, the performance of a transformer under the overfluxing conditions can be assessed by calculating the temperature rise of various structural components by this procedure. The method described is based on some approximations. The effect of eddy currents in the core is neglected. Also, the core is modeled as an isotropic material. It needs to be modeled accurately using anisotropic properties of permeability and conductivity in the x, y and z directions. An appreciable amount of flux flows into air paths, only during the portion of the cycle when the core is saturated. Therefore, the waveform of the air-flux has pulse-like form. This type of waveform has a high harmonic content increasing eddy losses in windings considerably, which need to be calculated accurately. The simulation of an overvoltage condition, for example 125% for 1 minute, is even more challenging.

5.12 Load Loss Measurement

The dependence of stray losses on various factors has been discussed in Section 5.1. The stray losses are sensitive to the magnitude of load current, temperature, and frequency. In a very competitive market scenario, as it exists today, designers may be forced to keep a very small margin between the guaranteed and calculated values of the load loss in order to optimize the material cost. The penalty for every kW exceeded is high, and it is important to understand the effects of various design, manufacturing, and test conditions on the stray losses (and the measured load loss).

The accuracy of measurement of the load loss in power transformers is an important issue. With increasing loss capitalization rates, large power transformers may have to be designed with low losses by using improved design

and manufacturing techniques and/or by putting higher material content. This has the effect of improving further the efficiency of already very efficient transformers (as compared to most other electrical equipment) lowering their power factor. At very low power factors, a small phase angle error in current or voltage transformers can cause a large error in the measurement of the real power [58, 84, 85]. During the load loss measurement of large power transformers, where a power factor value of 0.015 is not uncommon, a phase angle error of 1 minute results in an error of 1.9% in the measured load loss. As the power factor reduces, the error increases.

Sometimes leakage reactances between windings need to be measured using a low voltage source in field as one of the investigative tests. Care should be taken that the voltage should not be too low, which otherwise results in the core operation near the origin of *B-H* curve where the permeability can be very low, decreasing the magnetizing reactance [86]. In Chapter 1, we have seen that the shunt branch in the transformer equivalent circuit is neglected while estimating the leakage reactance from the short-circuit test results. If the test is done in the field using a very low voltage source, the effect of the magnetizing reactance cannot be neglected since it may have some noticeable influence on the leakage reactance measurement.

The losses occurring in operating conditions at rated voltage and current levels can be noticeably different than those measured during the open-circuit (no-load loss) and short-circuit (load loss) tests. This is because the amount of leakage flux completing its path through the core (and causing extra stray losses in it) depends on the load power factor. At different time instants as the flux density in the core varies from zero to a peak value, the core permeability also varies. The load power factor decides the phase angle between the main (mutual) flux and the stray flux, and hence the path of the leakage flux [61, 87] and the magnitude of stray losses in the core. For example, when the load is inductive, the stray flux (in phase with the load current) lags the terminal voltage by 90°. The main flux in the core also lags the terminal voltage by approximately 90°. Hence, the main flux and the leakage flux are almost in phase. When the main flux is at its peak value, the core permeability is low and the leakage flux finds an alternate path reducing the core stray losses.

We will now discuss three typical phenomena observed during load loss measurements.

5.12.1 Half-turn effect

In single-phase transformers with unwound end limbs, (e.g., a single-phase three-limb transformer), the tested load loss value can be higher than expected due to extra losses occurring in the core on account of a half-turn effect. This phenomenon is particularly observed in autotransformers, in which high voltage (HV) and intermediate voltage (IV) bushings are fitted on the tank cover on opposite sides of the core.

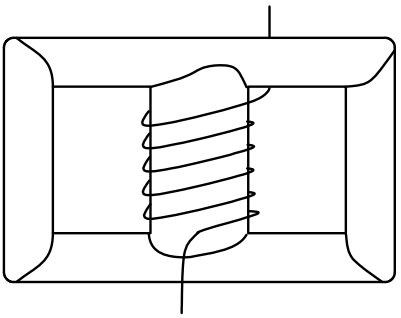

Figure 5.35 Half-turn effect in single-phase three-limb transformer.

In this case, either the common winding (IV) and/or the series winding (HV) of the autotransformer will contribute to the half-turn effect if the line lead crosses the core to the opposite side for termination. In Figure 5.35, one such arrangement of a winding is shown. In double-wound transformers (non-auto) also, the half-turn effect is present if the line and neutral terminals are not on the same side of the core for any of the two windings. The half-turn effect becomes clearly evident during the ratio test (done phase-by-phase) in three-phase three-limb transformers. For an arrangement of three phases, R, Y and B, from left to right with turns of the windings wound in the clockwise direction (looking from top), if the neutral and line leads are on opposite sides, the R phase does not have the half-turn effect as the last turn while going on the opposite side does not cross the core window. Hence, the turns ratio measured on the R phase will be less than the other two phases. Thus, if there are physically, for example 500½ turns in the winding, the R phase turns ratio will correspond to 500 turns, the Y phase turns ratio will correspond to 500½ turns (the last Y phase turn links only half the core flux while crossing), and the B phase turns ratio will correspond to 501 turns (the last B phase turn links the full core flux while crossing). During the three-phase load loss measurement on a three-phase three-limb transformer, the net flux due to these unbalances in three phases has to pass through the yokes and an external air-path since the limbs will not allow this flux in them due to the voltage source acting on the primary winding with the secondary winding short-circuited. Since the air path has extremely high reluctance, negligible flux would be set up in the entire path (the yokes plus the air-path) adding no extra loss during the load loss measurement.

In a single-phase three-limb transformer, a low-reluctance closed magnetic path consisting of the yokes and the end limbs is available for establishing an appreciable flux due to the half-turn effect as shown in Figure 5.36. The net magnetomotive force acting on the closed path is I (the current in the winding responsible for the effect) [88].

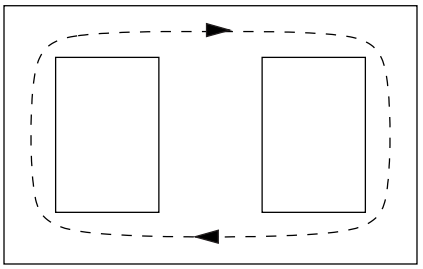

Figure 5.36 Circulating flux due to the half-turn effect.

Let us calculate the extra losses on account of this circulating flux for a 66.67 MVA, $(220/\sqrt{3})/(132/\sqrt{3})/11$ kV single-phase autotransformer having an extra half-turn in the HV series winding with 334 turns. The IV common winding has 500 turns, giving a total of 834 turns in the IV common and HV series windings (corresponding to the HV voltage of $220/\sqrt{3}$ kV). The no-load current in today's very efficient transformers with better core materials can be as low as 0.15% of the rated current. The rated current of the HV winding is 524.9 A giving a no-load current value of 0.79 A, which is required to set up the rated flux density of, for example, 1.7 T. The magnetizing ampere-turns are therefore 659 (= 0.79 × 834) to set up 1.7 T in the entire core. For a given flux density, lower ampere-turns are required for the path consisting of the yokes and the end limbs as compared to the entire core. Hence, the mmf acting on the path and having magnitude of 524.9 (i.e., the current in the HV series winding multiplied 1 turn) will set up a substantial flux density value in it resulting in an extra core loss during the load loss measurement with rated currents flowing in the windings. This approximate calculation shows that the core loss of the order of the rated no-load loss of the transformer occurs and gets additionally measured during the load loss test when the half-turn effect is present.

The phenomenon is analyzed accurately and quantitatively in [88] using a field-circuit coupled nonlinear finite-element model. The results of simulations are verified on a 40 MVA, $(220/\sqrt{3})/(132/\sqrt{3})/33$ kV single-phase auto-transformer. In three-phase five-limb transformers, the half-turn effects are cancelled due to the phasor addition of the three fluxes which are displaced by 120° with each other in balanced conditions. However, as shown in the paper, under appreciable unbalanced conditions, there would be significant amount of flux induced in the yokes and the end limbs, causing a substantial core loss and temperature rise.

During investigative tests, phase-by-phase load loss measurements are sometimes done on three-phase three-limb transformers. If one of the LV or HV windings is having the half-turn effect, during the single-phase load loss measurement test on the middle phase, the load loss value obtained is more than

those obtained during the tests on the other two phases. Also, high voltages are induced in the open-circuited windings on the extreme limbs due to the half-turn flux [88, 89].

If countermeasures are not taken, the half-turn effect will result in an unacceptable value of the load loss during the factory test and excessive temperatures in the core in service. The half-turn effect, if present, can be eliminated in the case of single-phase three-limb transformers by winding a few compensating turns on the end limbs. The direction of winding these turns should be the same on both end limbs as shown in Figure 5.37 so that the main (mutual) flux induces voltages in them in the same direction and hence they can be paralleled (connection of A_1 to B_1 and connection of A_2 to B_2). The net voltage in the loop $A_1 A_2 B_2 B_1 A_1$ is zero resulting in zero value of the circulating current, and hence the main flux flows unhindered. On the contrary, the flux due to the half-turn effect links these two windings on the two end limbs in opposite directions. This induces voltages in opposite directions in these two compensating windings causing a circulating current to flow (as shown by the arrows in Figure 5.37), which opposes its cause, the flux due to the half-turn effect. Thus, the half-turn effect is nullified and there is no extra core loss during the load loss measurement, except for small I^2R loss in the compensating turns due to the circulating current. The induced current in the compensating turns is equal to $I_1/(2n)$, where I_1 is the current in the winding having the half-turn effect during the load loss measurement and n is the number of compensating turns on each end limb. The cross section of the turns should be designed to carry the induced current.

Another way of avoiding the half-turn effect in autotransformers with the HV and IV terminals on opposite sides of the core is to take the terminal of the winding with an extra half-turn to the opposite side through the space between the core and the tank without crossing the core window. This alternative may be costly because extra space and material content are required (since adequate insulation clearances have to be provided for routing high voltage leads).

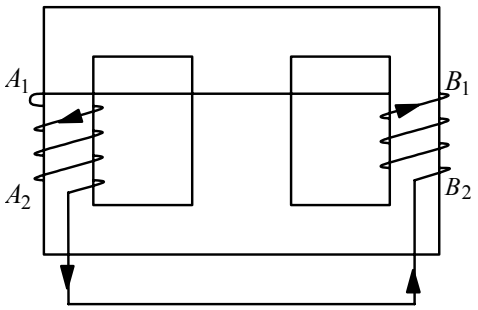

Figure 5.37 Compensating turns.

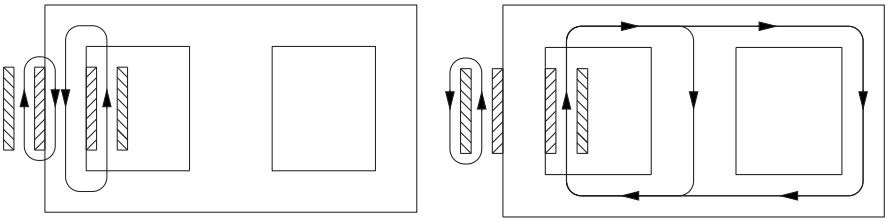

(a) Outer winding short-circuited (b) Inner winding short-circuited

Figure 5.38 Single-phase load loss measurement on three-phase transformer.

It is to be noted that the half-turn effect in three-phase five-limb transformers, which becomes significant under appreciable unbalanced load conditions, cannot be eliminated by the arrangement of compensating turns shown in Figure 5.37 since the main fluxes in the two end limbs are not in phase.

5.12.2 Single-phase load loss measurement on a three-phase transformer

In three-phase transformers with a delta connected winding, one peculiar phenomenon is observed during investigative single-phase load loss measurements. The path of leakage flux for two cases is shown in Figure 5.38. The path is influenced by the fact that the resultant flux linkages of a short-circuited winding are nearly zero.

When the inner winding is excited and the outer winding is short-circuited, the path of the leakage field predominantly consists of the leakage channel (the gap between the two windings) and the core limb of the same phase. On the contrary, when the outer winding is excited and the inner winding is short-circuited, there is no flux in the core limb of the phase under test in order to satisfy the zero resultant flux linkage condition for the inner winding. Thus, with the inner winding short-circuited, the path of the leakage field predominantly consists of the leakage channel, the yokes, the limbs of other two phases and the tank.

Let us consider a case of a delta-connected inner short-circuited winding with an impedance voltage applied to the outer star-connected winding. When the leakage flux tries to complete its path through the limbs of other two phases, voltages are induced in these phases on the delta side, which results in a circulating current in the closed delta. This current produces a counteracting flux forcing the initial flux out of the core, which is forced to complete its path through the yokes, external air-paths and the tank causing extra stray losses in the tank and I^2R loss in the delta winding. The leakage reactance also reduces. Hence, the extra losses measured or the lower value of the leakage reactance in such a case should not be mistaken as some defect in the transformer. These extra losses during the single-phase load loss measurements can be avoided by

doing them by exciting the inner delta winding and short-circuiting the outer winding.

5.12.3 Asymmetry during load loss measurement

The load loss in a transformer is usually measured by a three-wattmeter method. It is commonly observed that the readings corresponding to the three phases are appreciably different, even though the total load loss, which is the addition of the three readings, is as expected. The stray loss constitutes an appreciable part of the total loss and the stray loss components of three phases could be different due to their asymmetrical disposition with respect to the tank and other structural parts. However, a relatively small difference between these three stray loss components fails to explain significant differences between the three readings.

The major reason contributing to the phenomenon is the asymmetry of the mutual magnetic couplings between the phases as explained in [90]. A multi-port network model and time-harmonic 3D FE simulations have been employed for the purpose. Unequal mutual impedances between the phases as well as differences in their self impedances lead to the asymmetrical phenomenon. The phase currents are resolved into symmetrical components in the reported analysis to graphically explain the asymmetries in the measured currents and powers. Also, the network model is transformed into an equivalent model to represent the three-phase short-circuit test condition and to explain the trends in the currents and powers. The asymmetrical distribution is also influenced by even slight unbalanced phase differences between the voltages of the three-phase source used during the test. A more rigorous mathematical analysis of the asymmetrical phenomenon is available in [91].

References

1. Turowski, J., Turowski, M., and Kopec, M. Method of three-dimensional network solution of leakage field of three-phase transformers, *IEEE Transactions on Magnetics*, Vol. 26, No. 5, September 1990, pp. 2911–2919.
2. Jezierski, E. and Turowski, J. Dependence of stray losses on current and temperature, *CIGRE 1964*, Report 102, pp. 1–13.
3. Stoll, R. L. *The analysis of eddy currents*, Clarendon Press, Oxford, 1974.
4. Karsai, K., Kerenyi, D., and Kiss, L. *Large power transformers*, Elsevier Publication, Amsterdam, 1987.
5. Jain, M. P. and Ray, L. M. Field pattern and associated losses in aluminum sheet in presence of strip bus bars, *IEEE Transactions on Power Apparatus and Systems*, Vol. PAS-89, No. 7 September/October 1970, pp.1525 –1539.

6. Sykulski, J. K. *Computational magnetics*, Chapman and Hall, London, 1995.
7. Deuring, W. G. Induced losses in steel plates in the presence of an alternating current, *AIEE Transactions*, June 1957, pp. 166–173.
8. Allan, D. J., Mullineux, N., and Reed, J. R. Some effects of eddy currents in aluminum transformer tanks, *Proceedings IEE,* Vol. 120, No. 6, June 1973, pp. 681–685.
9. Kozlowski, M. and Turowski, J. Stray losses and local overheating hazard in transformers, *CIGRE 1972*, Paper No. 12–10.
10. Girgis, R. S., teNyenhuis, E. G., and Beaster, B. Proposed standards for frequency conversion factors of transformer performance parameters, *IEEE Transactions on Power Delivery*, Vol. 18, No. 4, October 2003, pp. 1262–1267.
11. Hwang, M. S., Grady, W. M., and Sanders, H. W. Distribution transformer winding losses due to non-sinusoidal currents, *IEEE Transactions on Power Delivery*, Vol. PWRD-2, No. 1, January 1987, pp. 140–146.
12. Kulkarni, S. V. and Khaparde, S. A. Stray loss evaluation in power transformers — A review, *IEEE PES Winter Meeting 2000*, Singapore, January 2000, Paper No. 0-7803-5938-0/00.
13. Boyajian, A. Leakage reactance of irregular distributions of transformer windings by the method of double Fourier series, *AIEE Transactions — Power Apparatus and Systems,* Vol. 73, Pt. III-B, October 1954, pp. 1078–1086.
14. Brauer, J. R. Finite element analysis of electromagnetic induction in transformers, *IEEE PES Winter Power Meeting*, New York, January 1977, Paper A77-122-5.
15. Andersen, O. W. Finite element solution of skin effect and eddy current problems, *IEEE PES Summer Power Meeting*, Mexico City, July 1977, Paper A77-616-6.
16. Sato, T., Inui, Y., and Saito, S. Solution of magnetic field, eddy current and circulating current problems, taking magnetic saturation and effect of eddy current and circulating current paths into account, *IEEE PES Winter Power Meeting*, New York, January / February 1977, Paper A77-168-8.
17. Babare, A., Di Napoli, A., and Santini, E. A method for losses evaluation in large power transformer tanks, *Electromagnetic fields in electrical engineering*, Book edited by Savini, A. and Turowski, J., Plenum Press, New York, 1988, pp. 95–100.
18. Komulainen, R. and Nordman, H. Loss evaluation and the use of magnetic and electromagnetic shields in transformers, *CIGRE 1988*, Paper No. 12–03.
19. Pavlik, D., Johnson, D. C., and Girgis, R. S. Calculation and reduction of stray and eddy losses in core-form transformers using a highly accurate finite element modeling technique, *IEEE Transactions Power Delivery*, Vol. 8, No. 1, January 1993, pp. 239–245.

20. Sironi, G. G. and Van Hulse, J. R. Eddy current losses in solid iron pieces under three-dimensional magnetic field, *IEEE Transactions on Magnetics*, Vol. MAG-14, No. 5, September 1978, pp. 377–379.
21. El Nahas, I., Szabados, B., Findlay, R. D., Poloujadoff, M., Lee, S., Burke, P., and Perco, D. Three dimensional flux calculation on a 3-phase transformer, *IEEE Transactions on Power Delivery*, Vol. PWRD-1, No. 3, July 1986, pp. 156–159.
22. Junyou, Y., Renyuan, T., Yan, L., and Yongbin, C. Eddy current fields and overheating problems due to heavy current carrying conductors, *IEEE Transactions on Magnetics*, Vol. 30, No. 5, September 1994, pp. 3064–3067.
23. Renyuan, T., Junyou, Y., Feng, L., and Yongping, L. Solutions of three-dimensional multiply connected and open boundary problems by BEM in three-phase combination transformers, *IEEE Transactions on Magnetics*, Vol. 28, No. 2, March 1992, pp. 1340–1343.
24. Renyuan, T., Junyou, Y., Zhouxiong, W., Feng, L., Chunrong, L., and Zihong, X. Computation of eddy current losses by heavy current leads and windings in large transformers using IEM coupled with improved $\mathbf{R}-\psi$ method, *IEEE Transactions on Magnetics*, Vol. 26, No. 2, March 1990, pp. 493–496.
25. Higuchi, Y. and Koizumi, M. Integral equation method with surface impedance model for 3-D eddy current analysis in transformers, *IEEE Transactions on Magnetics*, Vol. 36, No. 4, July 2000, pp. 774–779.
26. Yongbin, C., Junyou, Y., Hainian, Y., and Renyuan, T. Study of eddy current losses and shielding measures in large power transformers, *IEEE Transactions on Magnetics*, Vol. 30, No. 5, September 1994, pp. 3068–3071.
27. Krawczyk, A. and Turowski, J. Recent developments in eddy current analysis, *IEEE Transactions on Magnetics*, Vol. MAG-23, No. 5, September 1987, pp. 3032–3037.
28. Carpenter, C. J. Theory of flux penetration into laminated iron and associated losses, *Proceedings IEE*, Vol. 124, No. 7, July 1977, pp. 659–664.
29. Hemmings, R. F. and Wale, G. D. Heating in transformer cores due to radial leakage flux, Part-I: Experimental models and test results, *Proceedings IEE*, Vol. 124, No. 11, November 1977, pp. 1064–1072.
30. Carpenter, C. J., Sharples, K. O., and Djurovic, M. Heating in transformer cores due to radial leakage flux, Part-II: Computed results, *Proceedings IEE*, Vol. 124, No. 12, December 1977, pp. 1181–1186.
31. Kerenyi, D. Stray load losses in yoke-beams of transformers, *Electromagnetic fields in electrical engineering*, Book edited by Savini, A. and Turowski, J., Plenum Press, New York, 1988, pp. 113–118.
32. Turowski, J. *Technical electrodynamics*, (in Polish), WNT, Warszawa, 1993.

33. Kerenyi, D. Approximate formula for the eddy current losses induced in rectangular metal blocks by magnetic fields, *GANZ Electric Review*, No. 16, 1987, pp. 13–22.
34. Koppikar, D. A., Kulkarni, S. V., Srinivas, P. N., Khaparde, S. A., and Jain, R. Evaluation of flitch plate losses in power transformers, *IEEE Transactions on Power Delivery*, Vol. 14, No. 3, July 1999, pp. 996–1001.
35. Kulkarni, S. V. *Stray losses in power transformer: evaluation and experimental verification*, Ph.D. Dissertation, Department of Electrical Engineering, IIT-Bombay, India, 2000.
36. Vogel, F. J. and Adolphson, E. J. A stray loss problem in transformer tanks, *AIEE Transactions*, August 1954, pp. 760–764.
37. Berezovski, A. A. The calculation of stray losses in transformer tanks, *Elektrichestvo*, No. 9, 1966, pp. 1–7.
38. Valkovic, Z. Calculation of the losses in three-phase transformer tanks, *Proceedings IEE.,* Vol. 127, Pt. C, No. 1, January 1980, pp. 20–25.
39. Szabados, B., El Nahas, I., El Sobki, M. S., Findlay, R. D., and Poloujadoff, M. A new approach to determine eddy current losses in the tank walls of a power transformer, *IEEE Transaction on Power Delivery*, Vol. PWRD–2, No. 3, July 1987, pp. 810–816.
40. Koppikar, D. A., Kulkarni, S. V., and Turowski, J. Industrial verification of 3D hybrid analytically-numerical calculation of stray field and losses in 3-phase power transformers, *International Symposium on Electromagnetic Fields, ISEF '95*, Thessaloniki, Greece, September 1995, pp. 345–348.
41. Koppikar, D. A., Kulkarni, S. V., and Turowski, J. Fast 3-D interactive computation of stray field and losses in asymmetric transformers, *Proceedings IEE — Generation, Transmission and Distribution*, Vol. 147, No. 4, July 2000, pp. 197–201.
42. Zwolinski, G., Turowski, J., Kulkarni, S. V., and Koppikar, D. A. Method of fast computation of 3D stray field and losses in highly asymmetric transformers, *International Conference on Transformers, TRAFOTECH '98,* Mumbai, 23–24 January 1998, pp. I 51–58.
43. Dexin, X., Yunqiu, T., and Zihong, X. FEM analysis of 3D eddy current field in power transformer, *IEEE Transactions on Magnetics*, Vol. MAG-23, No. 5, September 1987, pp. 3786–3788.
44. Holland, S. A., O'Connell, G. P., and Haydock, L. Calculating stray losses in power transformers using surface impedance with finite elements, *IEEE Transactions on Magnetics*, Vol. 28, No. 2, March 1992, pp. 1355–1358.
45. Savini, A. and Turowski, J. Influence of structure geometry, screens and eddy currents on the critical distance of tank wall in power transformers, *Electromagnetic fields in electrical engineering*, Book edited by Savini, A. and Turowski, J., Plenum Press, New York, 1988, pp. 119–127.

46. Turowski, J. Overheating hazard in flanged bolt joints of transformers, *International Symposium on Electromagnetic Fields, ISEF'85,* Warsaw, Poland, 1985, pp. 271–274.
47. Saito, S., Inagaki, K., Sato, T., Inui, Y., Okuyama, K., and Otani, H. Eddy currents in structure surrounding large current bushings of a large capacity transformer, *IEEE Transactions on Power Apparatus and Systems*, Vol. PAS-100, No. 11, November 1981, pp. 4502–4509.
48. Turowski, J. and Pelikant, A. Eddy current losses and hot spot evaluation in cover plates of power transformers, *Proceedings IEE – Electrical Power Applications*, Vol. 144, No. 6, November 1997, pp. 435–440.
49. Olivares, J. C., Escarela, R., Kulkarni, S. V., de Leon, F., Melgoza, E., and Hernandez, O. Improved insert geometry for reducing tank wall losses in pad-mounted transformers, *IEEE Transactions on Power Delivery*, Vol. 19, No. 3, July 2004, pp. 1120–1126.
50. Kulkarni, S. V., Olivares, J. C., Escarela-Perez, R., Lakhiani, V. K. and Turowski, J. Evaluation of eddy losses in cover plates of distribution transformers, *IEE Proceedings — Science, Measurement and Technology*, Vol. 151, No. 05, September 2004, pp. 313–318.
51. Poritsky, H. and Jerrard, R. P. Eddy current losses in a semi-infinite solid due to a nearby alternating current, *AIEE Transactions*, May 1954, pp. 97–106.
52. Koppikar, D. A., Kulkarni, S. V., Khaparde, S. A., and Jha, S. K. Evaluation of eddy losses due to high current leads in transformers, *Proceedings IEE — Science Measurement and Technology*, Vol. 144, No. 1, January 1997, pp. 34–38.
53. Krakowski, M. R., Kazmierski, M., and Kersz, I. Effect of current distribution in parallel bars on electromagnetic field at nearby steel wall, *Proceedings IEE*, Vol. 136, Pt. B, No. 4, July 1989, pp. 161–167.
54. Lowther, D. A. and Silvester, P. P. *Computer aided design in magnetics*, Springer-Verlag, New York, 1985, pp. 213–215.
55. Olivares, J. C., Canedo, J., Moreno, P., Driesen, J., Escarela, R., and Palanivasagam, S. Experimental study to reduce the distribution transformer stray losses using electromagnetic shields, *Electric Power Systems Research*, 63 (2002), pp. 1–7.
56. Tagaki, T., Ishii, T., Okada, T., Kurita, K., Tamura, R., and Murata, H. Reliability improvement of 500 kV large capacity power transformer, *CIGRE 1978*, Paper No. 12–02.
57. Kerr, H. W. and Palmer, S. Developments in the design of large power transformers, *Proceedings IEE*, Vol. 111, No. 4, April 1964, pp. 823–832.
58. Beaumont R. Losses in transformers and reactors, *CIGRE 1988*, Paper No. 12–10.
59. Kozlowski, M. and Turowski, J. Stray losses and local overheating hazard in transformers, *CIGRE 1972*, Paper No. 12–10.

60. Kazmierski, M., Kozlowski, M., Lasocinski, J., Pinkiewicz, I., and Turowski, J. Hot spot identification and overheating hazard preventing when designing a large transformer, *CIGRE 1984*, Paper No. 12–12.
61. Bose, A. K., Kroon, C., and Hulsink, G. Some topics on designing transformers with low load losses, *CIGRE 1988*, Paper No. 12–05.
62. Inui, Y., Saito, S., Okuyama, K., and Hiraishi, K. Effect of tank and tank shields on magnetic fields and stray losses in transformer windings, *IEEE PES Summer Meeting*, Vancouver, Canada, July 1973, Paper No. C73-401-7.
63. Takahashi, N., Kitamura, T., Horii, M., and Takehara, J. Optimal design of tank shield model of transformer, *IEEE Transactions on Magnetics*, Vol. 36, No. 4, July 2000, pp. 1089–1093.
64. Bereza, V. L. Designing magnetic shields for transformer tanks, *Elektroteknika*, Vol. 52, No. 12, 1981, pp. 44–46.
65. Barton, M. L. Loss calculation in laminated steel utilizing anisotropic magnetic permeability, *IEEE Transactions on Power Apparatus and Systems*, Vol. PAS-99, No. 3, May/June 1980, pp. 1280–1287.
66. Silva, V. C., Meunier, G., and Foggia, A. A 3-D finite element computation of eddy current and losses in laminated iron cores allowing for electric and magnetic anisotropy, *IEEE Transactions on Magnetics*, Vol. 31, No. 3, May 1995, pp. 2139–2141.
67. Djurovic, M. and Carpenter, C. J. Three dimensional computation of transformer leakage fields and associated losses, *IEEE Transactions on Magnetics*, Vol. MAG-11, No. 5, September 1975, pp. 1535–1537.
68. Djurovic, M. and Monson, J. E. Three dimensional computation of the effect of the horizontal magnetic shunt on transformer leakage fields, *IEEE Transactions on Magnetics*, Vol. MAG-13, No. 5, September 1977, pp. 1137–1139.
69. Djurovic, M. and Monson, J. E. Stray losses in the step of a transformer yoke with a horizontal magnetic shunt, *IEEE Transactions on Power Apparatus and Systems*, Vol. PAS-101, No. 8, August 1982, pp. 2995–3000.
70. Rizzo, M., Savini, A., and Turowski, J. Influence of flux collectors on stray losses in transformers, *IEEE Transactions on Magnetics*, Vol. 36, No. 4, July 2000, pp. 1915–1918.
71. Harrison, T. H. and Richardson, B. Transformer loss reductions, *CIGRE 1988*, Paper No. 12–04.
72. Mullineux, N. and Reed, J. R. Eddy current shielding of transformer tanks, *Proceedings IEE*, Vol. 113, No. 5, May 1966, pp. 815–818.
73. Woolley, I. Eddy current losses in reactor flux shields, *Proceedings IEE*, Vol. 117, No. 11, November 1970, pp. 2142–2150.
74. Holman, J. P. *Heat transfer*, McGraw-Hill Company, Singapore, 1986.

75. Churchill, S. W. and Chu, H. H. S. Correlating equations for laminar and turbulent free convection from a vertical plate, *International Journal Heat Mass Transfer*, Vol. 18, 1975, pp. 1323–1329.
76. Niewierowicz, N. and Turowski, J. New thermometric method of measuring power losses in solid metal elements, *Proceedings IEE*, Vol. 119, No. 5, May 1972, pp. 629–636.
77. Alexander, G. W., Corbin, S L., and McNutt, W. J. Influence of design and operating practices on excitation of generator step-up transformers, *IEEE Transactions on Power Apparatus and Systems*, Vol. PAS-85, No. 8, August 1966, pp. 901–909.
78. Stuehm, D. L., Mork, B. A, and Mairs, D. D. Five-legged core transformer equivalent circuit, *IEEE Transactions on Power Delivery*, Vol. 4, No. 3, July 1989, pp. 1786–1793.
79. Mairs, D. D., Stuehm, D. L., and Mork, B. A. Overvoltages on five-legged core transformer on rural electric systems, *IEEE Transactions on Industry Applications*, Vol. 25, No. 2, March/April 1989, pp. 366–370.
80. Arthuri, C. M. Transient simulation and analysis of a three-phase five-limb step-up transformer, *IEEE Transactions on Power Delivery*, Vol. 6, No. 1, January 1991, pp. 196–203.
81. Chen, X. S. and Neudorfer, P. Digital model for transient studies of a three-phase five-legged transformer, *Proceedings IEE*, Pt. C, Vol. 139, No. 4, July 1992, pp. 351–358.
82. Koppikar, D. A., Kulkarni, S. V., Khaparde, S. A., and Arora, B. A modified approach to overfluxing analysis of transformer, *International Journal of Electrical Power and Energy Systems*, Elsevier Science Publication, Vol. 20, No. 4, 1998, pp. 235–239.
83. Koppikar, D. A., Kulkarni, S. V., and Khaparde, S. A. Overfluxing simulation of transformer by 3D-FEM analysis, *Fourth Conference on EHV Technology*, IISc Bangalore, India, 17-18 July 1998, pp. 69–71.
84. Specht, T. R., Rademacher, L. B., and Moore, H. R. Measurement of iron and copper losses in transformers, *AIEE Transactions,* August 1958, pp. 470–476.
85. Mehta, S. P. Measurement of transformer losses, *IEEE Winter Meeting*, Paper No. EHO209-7/84/0000-0043, 1983, pp. 43–52.
86. Lachman, M. F. and Shafir, Y. N. Influence of single-phase excitation and magnetizing reactance on transformer leakage reactance measurement, *IEEE Transactions on Power Delivery*, Vol. 12, No. 4, October 1997, pp. 1538–1545.
87. Bose, A. K., Kroon, C., and Wildeboer, J. The loading of the magnetic circuit, *CIGRE 1978*, Paper No. 12–09.
88. Kumbhar, G. B., Kulkarni, S. V., and Joshi, V. S. Analysis of half-turn effect in power transformers using nonlinear-transient FE formulation, *IEEE Transactions on Power Delivery*, Vol. 22, No. 1, January 2007, pp. 195–200.

89. Mohseni, H. and Hamdad, F. Overvoltage caused by winding terminal arrangement of three-phase power transformer, *International Symposium on High Voltage Engineering*, Austria, 1995, pp. 6757:1–4.
90. Escarela-Perez, R., Kulkarni, S. V., Kodela, N. K. and Olivares-Galvan, J. C. Asymmetry during load-loss measurement of three-phase three-limb transformers, *IEEE Transactions on Power Delivery,* Vol. 22, No. 3, July 2007, pp. 1566–1574.
91. Escarela-Perez, R., Kulkarni, S. V., Alvarez-Ramirez, J., and Kaushik, K. Analytical description of the load-loss asymmetry phenomenon in three-phase three-limb transformers, *IEEE Transactions on Power Delivery*, Vol. 24, No. 2, April 2009, pp. 695–702.

6

Short-Circuit Stresses and Strength

A steady increase in demand of electrical power has resulted in the addition of more generating capacity and interconnections in power systems. Both these factors have contributed to an increase in short-circuit capacity of networks, making the short-circuit duty of transformers more severe. Failure of transformers due to short circuits is a major concern for transformer users. The success rate during short-circuit tests is far from satisfactory. The test data from high power test laboratories around the world indicates that on an average practically one out of four transformers has failed during the short-circuit test, and the failure rate is above 40% for transformers above 100 MVA rating [1]. There have been efforts by manufacturers and users to improve the short-circuit withstand performance of transformers. A number of suggestions have been made in the literature for improving technical specifications, verification methods and manufacturing processes to enhance reliability of transformers under short circuits. The short-circuit strength of a transformer enables it to survive through-fault currents due to external short circuits; an inadequate strength may lead to mechanical collapse of windings, deformation/damage to clamping structures, etc. which may eventually lead to an electrical fault in it. Internal faults initiated by external short circuits are dangerous as they may involve blow-out of bushings, bursting of tanks, fire hazards, etc. Assessment of short-circuit withstand is one of the most important and challenging aspects of transformer engineering; it has been a preferential subject in many international conferences and workshops.

IEC 60076-5 standard, third edition 2006-02, specifies the limit on the change in the leakage impedance as 1% for category III (above 100 MVA rating) transformers. This specification is in line with the results of many short-circuit tests on power transformers with ratings greater than 100 MVA, in which

an increase of short-circuit inductance beyond 1% has caused significant deformations in windings. In order to meet the specification, a strict control on variations in materials and manufacturing processes has to be exercised to avoid looseness and winding movements.

This chapter first introduces the basic theory of short circuits as applicable to transformers. Thermal capability of transformer windings under short-circuit forces is also discussed. There are basically two types of forces in windings: axial and radial electromagnetic forces produced by radial and axial leakage fields, respectively. Analytical and numerical methods for calculation of these forces are discussed. Various failure mechanisms due to these forces are then described. It is very important to understand the dynamic response of a winding to axial electromagnetic forces. Practical difficulties encountered in the dynamic analysis are enumerated. Design parameters and manufacturing processes have pronounced effects on natural frequencies of a winding. Design aspects of windings and clamping structures are elucidated. Precautions to be taken during design and manufacturing of transformers for improving short-circuit withstand capability are given.

6.1 Short-circuit Currents

There are different types of faults which result into high currents, viz. single-line-to-ground faults, line-to-line faults with or without a simultaneous ground fault, and three-phase faults with or without a simultaneous ground fault. When the ratio of the zero-sequence impedance to the positive-sequence impedance is less than one, a single-line-to-ground fault results in higher fault current than a three-phase fault. It is shown in [2] that for a YNd connected transformer with a delta-connected inner winding, the single-line-to-ground fault is more severe. Except for such specific cases, usually three-phase (symmetrical) faults are most severe. Hence, it is usual practice to design a transformer to withstand a three-phase short-circuit at its terminals, the other windings being assumed to be connected to infinite systems/sources (which can ideally supply any current at a constant voltage level). The symmetrical short-circuit current for a three-phase two-winding transformer is given by

$$I_f = \frac{V}{\sqrt{3}\,(Z_T + Z_S)} \quad \text{kA} \tag{6.1}$$

where V is the rated line-to-line voltage in kV, Z_T is the short-circuit (leakage) impedance of the transformer, and Z_S is the short-circuit impedance of the system given by

$$Z_S = \frac{V^2}{S_F} \text{ ohms} \quad \text{or} \quad Z_S = \frac{S}{S_F} \text{ per-unit} \tag{6.2}$$

where S_F is the short-circuit apparent power of the system in MVA and S is the three-phase rating of the transformer in MVA. The system impedance is small as compared to the transformer impedance and is neglected, giving an extra safety margin. In per-unit quantities using sequence notations we obtain

$$I_a = \frac{V_{pF}}{Z_1}\angle 0^\circ \ , \ I_b = \frac{V_{pF}}{Z_1}\angle 240^\circ \text{ and } I_c = \frac{V_{pF}}{Z_1}\angle 120^\circ \tag{6.3}$$

where Z_1 is the positive-sequence impedance of the transformer (which is the leakage impedance offered to positive-sequence currents, calculated using the procedure given in Section 3.1 of Chapter 3) and V_{pF} is the pre-fault voltage. If the pre-fault voltages are assumed to be 1.0 per-unit (p.u.) then for a three-phase solid fault (with zero fault impedance) we obtain

$$I_a = \frac{1}{Z_1}\angle 0^\circ , \ I_b = \frac{1}{Z_1}\angle 240^\circ , \ I_c = \frac{1}{Z_1}\angle 120^\circ , \text{ and } V_a = V_b = V_c = 0 . \tag{6.4}$$

The sequence components of currents and voltages are [3]

$$I_{a1} = \frac{1}{Z_1} , \ I_{a0} = I_{a2} = 0 \text{ and } V_{a1} = V_{a2} = V_{a0} = 0 . \tag{6.5}$$

For a solid single-line-to-ground fault on phase a,

$$I_a = \frac{3}{Z_1 + Z_2 + Z_0}\angle 0^\circ , \quad I_b = I_c = 0, \quad V_a = 0 \tag{6.6}$$

$$I_{a0} = I_{a1} = I_{a2} = I_a / 3 \tag{6.7}$$

where Z_2 and Z_0 are the negative-sequence and zero-sequence impedances of the transformer, respectively. Being a static device, the positive and negative-sequence impedances of any transformer are equal ($Z_1 = Z_2$). The procedures for the calculation of Z_1 and Z_0 are given in Chapter 3.

For a line-to-line fault (between the phases *b* and *c*),

$$I_a = 0 , \qquad I_b = -I_c = -\frac{j\sqrt{3}}{Z_1 + Z_2} \tag{6.8}$$

$$I_{a1} = -I_{a2} = \frac{1}{Z_1 + Z_2}\angle 0^\circ , \quad I_{a0} = 0 \tag{6.9}$$

and for a double-line-to-ground fault,

$$I_a = 0,\ I_b = -\frac{\left(\frac{3}{2} + j\frac{\sqrt{3}}{2}\right)Z_2 + j\sqrt{3}\,Z_0}{Z_1Z_2 + Z_1Z_0 + Z_2Z_0},$$

$$I_c = -\frac{\left(\frac{3}{2} - j\frac{\sqrt{3}}{2}\right)Z_2 - j\sqrt{3}\,Z_0}{Z_1Z_2 + Z_1Z_0 + Z_2Z_0},\ V_b = V_c = 0. \tag{6.10}$$

Since a three-phase short circuit is usually the most severe fault, it is sufficient if the withstand capability against three-phase short-circuit forces is ensured. However, if there is an unloaded tertiary winding in a three-winding transformer, its design must be done by taking into account the short-circuit forces during a single-line-to-ground fault on either the LV or HV winding. Hence, most of the discussions hereafter are for three-phase and single-line-to-ground fault conditions. Based on the equations written earlier for the sequence voltages and currents for these two types of faults, we can connect the positive-sequence, negative-sequence and zero-sequence networks as shown in Figure 6.1. The solution of the resulting network yields the symmetrical components of currents and voltages in the windings under fault conditions [4].

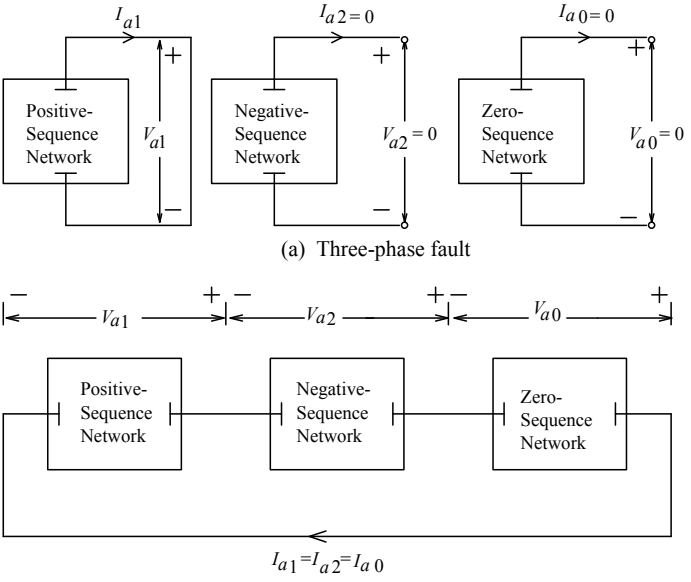

Figure 6.1 Sequence networks.

The calculation of three-phase fault currents is straightforward, whereas the calculation of single-line-to-ground fault currents requires the estimation of zero-sequence reactances and the interconnection of the sequence networks at correct points. Procedures for computation of currents under a single-line-to-ground fault condition are now described through two case studies.

Consider a case of delta/star (the HV winding in delta and the LV winding in star with grounded neutral) distribution transformer with a single-line-to-ground fault on the LV side. The equivalent network under the fault condition is shown in Figure 6.2 (a), where the three sequence networks are connected at the points of the fault (corresponding LV terminals). The impedances denoted with subscript S are the system impedances; for example Z_{1HS} is the positive-sequence system impedance on the HV side. The impedances Z_{1HL}, Z_{2HL} and Z_{0HL} are the positive-, negative- and zero-sequence impedances, respectively, between the HV and LV windings. The zero-sequence network shows open circuit on the HV system side because the zero-sequence impedance is infinitely large as viewed/measured from the delta side as explained in Chapter 3 (Section 3.7). When there is no in-feed from the LV side (no source on the LV side), system impedances are effectively infinite and the network simplifies to that given in Figure 6.2 (b). Further, if the system impedances on the HV side are very less compared to the interwinding impedances, they are neglected to give the sequence components and the fault current as (with a fault on the phase a)

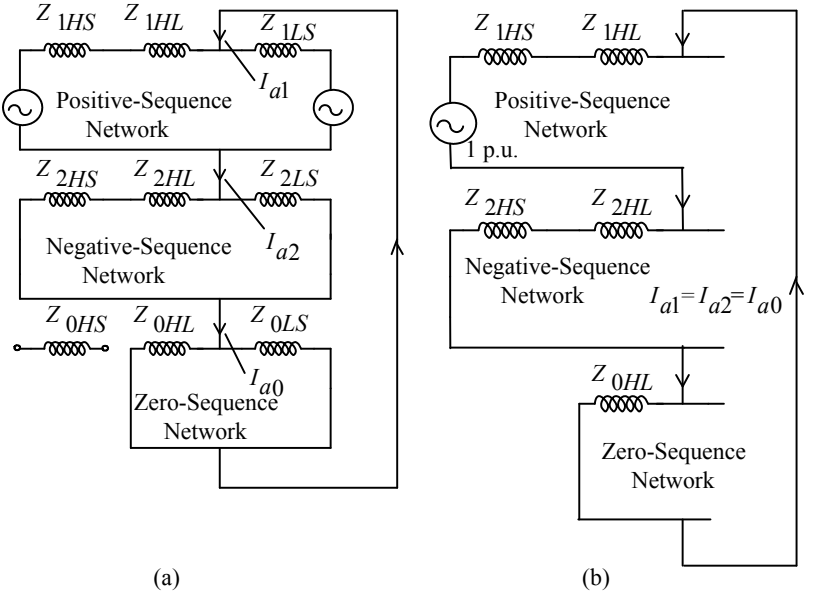

Figure 6.2 Single-line-to-ground fault on the star side of a delta/star transformer.

$$I_{a0} = I_{a1} = I_{a2} = \frac{1}{Z_{1HL} + Z_{2HL} + Z_{0HL}} \tag{6.11}$$

$$I_a = I_{a0} + I_{a1} + I_{a2} = \frac{3}{Z_{1HL} + Z_{2HL} + Z_{0HL}}. \tag{6.12}$$

Let us consider a three-winding transformer with an unloaded tertiary winding (the HV and LV windings are star-connected with grounded neutrals, and the tertiary winding is delta-connected). The corresponding sequence networks are connected as shown in Figure 6.3 (a). A single-line-to-ground fault is considered on phase a of the LV winding. Since it is a three-winding transformer, the corresponding star equivalent circuits are inserted at appropriate places in the combined network. In the positive-sequence and negative-sequence networks, the tertiary winding is shown open-circuited because it is unloaded; only in the zero-sequence network it is in the circuit since the zero-sequence currents flow in the closed delta. If pre-fault currents are neglected, both source voltages in the positive-sequence network are equal to 1 per unit. The network gets simplified as shown in Figure 6.3 (b). The positive-sequence impedance is

$$Z_1 = (Z_{1HS} + Z_{1H} + Z_{1L}) // Z_{1LS} \tag{6.13}$$

where Z_{1HS} and Z_{1LS} are the positive-sequence system impedances, and Z_{1H} and Z_{1L} are the positive-sequence impedances of the HV and LV windings, respectively, in the star equivalent circuit.

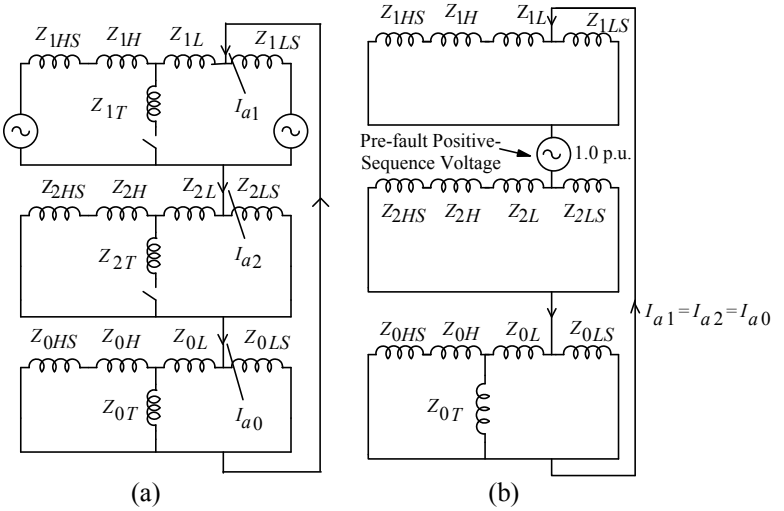

Figure 6.3 Single-line-to-ground fault in a three-winding transformer.

Similarly, the negative-sequence and zero-sequence impedances are given by

$$Z_2 = (Z_{2HS} + Z_{2H} + Z_{2L}) // Z_{2LS} \tag{6.14}$$

$$Z_0 = ([(Z_{0HS} + Z_{0H}) // Z_{0T}] + Z_{0L}) // Z_{0LS}. \tag{6.15}$$

The impedances Z_1 and Z_2 are equal because the corresponding positive-sequence and negative-sequence impedances in their expressions are equal. The total fault current is then calculated as

$$I_f = 3/(Z_1 + Z_2 + Z_0). \tag{6.16}$$

The fault current in a winding is calculated by adding the corresponding sequence currents flowing in it in the three sequence networks. For example, the current in the phase a of the HV winding is sum of the currents flowing through the impedances Z_{1H}, Z_{2H} and Z_{0H} of the positive-sequence, negative-sequence and zero-sequence networks, respectively. The tertiary winding current equals the zero-sequence current flowing through the impedance Z_{0T}.

An unloaded tertiary winding is used for the stabilizing purpose as discussed in Chapter 3. Since its terminals are not usually brought out, an external short circuit is not possible and it may not be necessary to design it for withstanding short circuits at its own terminals. However, the above analysis of a single-line-to-ground fault in a three-winding transformer has shown that the tertiary winding must be able to withstand the forces produced in it by an asymmetrical fault on the LV or HV winding. Consider a case of star/star transformer with a delta-connected tertiary winding, in which a single-line-to-ground fault occurs on the LV side whose neutral is grounded. If there is no in-feed from the LV side (i.e., no source on the LV side), with reference to Figure 6.3, the impedances Z_{1LS}, Z_{2LS} and Z_{0LS} will be infinite. There will be open circuit on the HV side in the zero-sequence network since the HV neutral is not grounded in the case being considered. If these modifications are done in Figure 6.3, it can be seen that the faulted LV winding carries all the three sequence currents, whereas the tertiary winding carries only the zero-sequence current. Since all three sequence currents are equal for a single-line-to-ground fault condition (Equation 6.7), the tertiary winding carries one third of ampere-turns of the faulted LV winding. As explained in Chapter 3, an unloaded tertiary winding is used to stabilize the neutral voltage under asymmetrical loading conditions. The load on each phase of the tertiary winding is equal to one third of the single-phase/unbalanced load applied on one of the main windings. Hence, the rating of the unloaded tertiary winding is commonly taken as one third of the rating of the main windings. The conductor size of the tertiary winding chosen according to this rule should also help the winding in withstanding forces under a single-line-to-ground fault condition. This is particularly true for the case discussed previously in which the neutral terminal

of one of the main windings is grounded (in this case the tertiary winding carries one third of the ampere-turns of the faulted winding). For the other connections of windings and neutral grounding conditions, the value of zero-sequence current flowing in the tertiary winding depends on the relative values of the impedances of the windings and the system impedances in the zero-sequence network. For example, in the above case if the HV neutral is also grounded, the zero-sequence current has another path available, and the magnitudes of the zero-sequence currents carried by the LV, HV and tertiary windings depend on the relative impedances of the parallel paths (Z_{0T} in parallel with $(Z_{0HS} + Z_{0H})$ in Figure 6.3). Hence, with the HV neutral also grounded, the forces on the tertiary winding are reduced.

As discussed in Chapter 3, an unloaded tertiary winding reduces the third harmonic component in flux and voltage waveforms by providing a path for third harmonic magnetizing currents. It also stabilizes the neutral by virtue of reduction in the zero-sequence impedance. For three-phase three-limb transformers of smaller ratings with star/star connected windings having grounded neutrals, a tertiary stabilizing winding may not be provided. This is because the reluctance offered to the zero-sequence flux is high, which makes the zero-sequence impedance low and an appreciable unbalanced load can be taken by three-phase three-limb transformers with star/star connected windings. Also, as shown in Appendix C, for such transformers the omission of stabilizing winding does not reduce the fault current drastically, and it should be detected by protection circuitry. The increase in the zero-sequence impedance due to its omission is not significant; the only major difference is the increase in the HV neutral current, which should be taken into account while designing the protection system. The removal of the tertiary winding in three-phase three-limb transformers with both HV and LV neutrals grounded eliminates the weakest link from the short-circuit design considerations and reduces the ground fault current to some extent. This results in reduction of the short-circuit stresses experienced by transformers and associated equipment. Hence, as explained in Section 3.8, the provision of the stabilizing winding in three-phase three-limb transformers should be critically reviewed if permitted by the considerations of harmonic characteristics and protection requirements.

Generator transformers are generally subjected to lower short-circuit stresses than interconnecting autotransformers. A high value of the generator impedance in series with the transformer impedance reduces the fault current magnitude for faults on the HV side of the generator transformer. There is low probability of faults on its LV side since the bus-bars of each phase are usually enclosed in a metal enclosure (bus-duct). But, since generator transformers are the most critical transformers in the whole network, it is desirable to have a higher safety factor for them. Also, out-of-phase synchronization in generator transformers can result into currents comparable to three-phase short-circuit currents. It causes saturation of the core due to which an additional magnetizing

transient current is superimposed on the fault current [5]. Considerable axial short-circuit forces are generated under these conditions [6].

The nature of a short-circuit current can be highly asymmetrical like inrush currents. It is maximum when the short circuit occurs at zero voltage instant. An asymmetrical short-circuit current has two components: a unidirectional component decreasing exponentially with time and an alternating steady-state symmetrical component at the fundamental frequency. The rate of decay of the exponential component is decided by the X/R ratio of the transformer. IEC 60076-5 (third edition: 2006-02) for power transformers specifies the asymmetry factor corresponding to switching at the zero voltage instant (the worst condition of switching). For $X/R > 14$, its value is specified as 1.8 for transformers up to 100 MVA rating, whereas it is 1.9 for transformers above 100 MVA rating. Hence, the peak value of the asymmetrical short-circuit current can be taken as

$$I_{p(asym)} = \sqrt{2} \times 1.8 \times I_{sym} = 2.55 \times I_{sym} \quad \text{for ratings up to 100 MVA}$$

$$I_{p(asym)} = \sqrt{2} \times 1.9 \times I_{sym} = 2.69 \times I_{sym} \quad \text{for ratings > 100 MVA}$$

where I_{sym} is the r.m.s. value of the symmetrical three-phase short-circuit current. The IEEE Standard C57.12.00-2000 also specifies asymmetrical factors for various X/R ratios, the maximum being 2 for the X/R ratio of 1000.

6.2 Thermal Capability During a Short-Circuit

A large current flowing in a transformer winding at the time of a short circuit increases its temperature. Because of the fact that its duration is usually very short, the temperature rise is not appreciable to cause any damage to the transformer. The IEC 60076-5 publication gives the following formulae for the highest average temperature attained by the winding after a short circuit,

$$\theta_1 = \theta_0 + \frac{2(\theta_0 + 235)}{\frac{106000}{J^2 t} - 1} \qquad \text{for copper} \tag{6.17}$$

$$\theta_1 = \theta_0 + \frac{2(\theta_0 + 225)}{\frac{45700}{J^2 t} - 1} \qquad \text{for aluminum} \tag{6.18}$$

where θ_0 is the initial temperature in °C

J is the current density in A/mm^2 during the short-circuit based on the r.m.s. value of the symmetrical short-circuit current

t is duration of the short-circuit in seconds.

While arriving at these expressions, an assumption is made that the entire heat developed during the short circuit is retained in the winding itself raising its temperature. This assumption is justified because the thermal time constant of a winding in oil-immersed transformers is very high as compared to the duration of the short circuit, which allows us to neglect the heat flow from windings to surrounding oil. The maximum allowed conductor temperature for oil-immersed transformers with the insulation system of thermal class A (i.e., 105°C) is 250°C for a copper conductor whereas the same is 200°C for an aluminum conductor. Let us calculate the temperature attained by a winding with the rated current density of 3.5 A/mm^2. If the transformer impedance is 10%, the short-circuit current density will be 35 A/mm^2 (corresponding a symmetrical short-circuit current condition). Assuming the initial winding temperature as 105°C (a worst case condition), the highest temperature attained by the winding made of copper conductor at the end of the short circuit lasting for 2 seconds (a worst case duration) is about 121°C, which is much below the limit of 250°C. Hence, the thermal withstand capability of a transformer under the short-circuit conditions is usually not a serious design issue.

6.3 Short-circuit Forces

The basic equation for calculation of electromagnetic forces is

$$\mathbf{F} = I\,\mathbf{L}\times\mathbf{B} \tag{6.19}$$

where **B** is the leakage flux density vector, I is the short-circuit current and **L** is the winding length vector. If the analysis of forces is done in two dimensions with the current density in the z direction, the leakage flux density at any point can be resolved into two components, viz. one in the radial direction (B_x) and the other in the axial direction (B_y). Therefore, there is a radial force in the x direction due to the axial leakage flux density and an axial force in the y direction due to the radial leakage flux density, as shown in Figure 6.4.

The directions of forces are readily apparent from Fleming's left hand rule also, which says that when the middle finger is in the direction of the current and the second finger in the direction of the field, the thumb points in the direction of the force (all these three fingers being perpendicular to each other).

We have seen in Chapter 3 that the leakage field can be expressed in terms of currents in the windings. Hence, forces experienced by a winding are proportional to the square of the short-circuit current, and are unidirectional and pulsating in nature. The short-circuit current having a steady state alternating component at fundamental frequency and an exponentially decaying component:

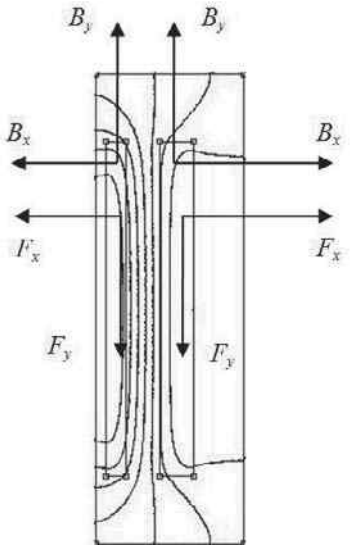

Figure 6.4 Radial and axial forces.

$$i(t) = I_m\left(e^{-\frac{R}{L}t} - \cos wt\right) = I_m\left(e^{-\frac{R}{X}wt} - \cos wt\right) \tag{6.20}$$

where I_m is the steady-state symmetrical peak value of the short-circuit current, R and X are the total resistance and leakage reactance of the transformer, respectively, t and w is the time and angular frequency, respectively. As the short-circuit force is proportional to the current, its expression is given by

$$\begin{aligned} f(t) &= F_m\left(e^{-\frac{R}{X}wt} - \cos wt\right)^2 \\ &= F_m\left(e^{-2\frac{R}{X}wt} + \frac{1}{2} + \frac{\cos 2wt}{2} - 2e^{-\frac{R}{X}wt}\cos wt\right) \end{aligned} \tag{6.21}$$

where F_m is the steady-state symmetrical peak value of the short-circuit force. Thus, the force has four components: two alternating components (one at fundamental frequency decreasing with time and other at double the fundamental frequency with a constant but smaller value) and two unidirectional components (one constant component and the other decreasing with time). The typical waveforms of the short-circuit current and force are shown in Figure 6.5. Thus, with a fully offset current the fundamental frequency component of the force is dominant during the initial cycles as seen from the figure.

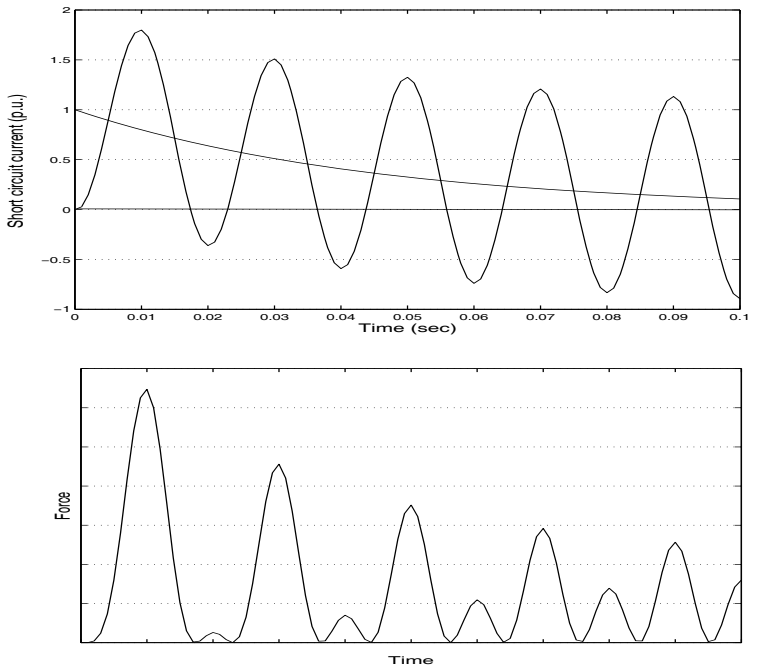

Figure 6.5 Typical waveforms of short-circuit current and force.

As described earlier, short-circuit forces are resolved into radial and axial components; this is justified since the radial and axial forces lead to the different kinds of stresses and modes of failures. Various methods have been reported in the literature for the calculation of forces in transformers. Once the leakage field is accurately calculated, the forces can be easily determined using Equation 6.19. Over the years, short-circuit forces have been studied from a static consideration, that is to say that the forces are produced by a steady current. The methods for the calculation of static forces were well documented in 1979 by a CIGRE working group [7]. The static forces can be calculated by any one of the following established methods, viz. Roth's method, Rabin's method, the method of images, and the finite element method. Some of the analytical and numerical methods for the leakage field calculations are described in Chapter 3. The withstand is checked for the first peak of the short-circuit current (with an appropriate asymmetry factor as explained in Section 6.1).

A transformer is a highly asymmetrical 3-D electromagnetic device. Under a three-phase short circuit, there is heavy concentration of field in the core window, and failures of core-type transformers mostly occur in the window region. In three-phase transformers, the leakage fields of adjacent phases affect each other. The windings on the central limb are usually subjected to higher

forces. There is a considerable variation of forces along the circumference of windings. Although, within the window, two-dimensional formulations are sufficiently accurate, three-dimensional numerical methods may have to be used for accurate estimation of forces in the regions outside the core window [8].

6.3.1 Radial forces

The radial forces produced by the axial leakage field act outwards on the outer winding tending to stretch its conductor, producing a tensile stress (also called as *hoop stress*); whereas the inner winding experiences radial forces acting inwards tending to collapse or crush it, producing a compressive stress. The leakage field pattern of Figure 6.4 indicates that due to fringing of the leakage field at the ends of the windings, the axial component of the field reduces resulting in smaller radial forces in these regions. For deriving a simple formula for the radial force in a winding, the fringing of the field is neglected; the approximation is justified because the maximum value of the radial force is important, which occurs in the middle portion of the winding.

Let us consider an outer winding that is subjected to hoop stresses. The value of the leakage field increases from zero at the outside diameter to maximum at the inside diameter (at the gap between the two windings). The peak value of the flux density in the gap is

$$B_{gp} = \frac{\sqrt{2}\mu_0 NI}{H_w} \tag{6.22}$$

where NI is the r.m.s. value of the winding's ampere-turns and H_w is the winding height in meters. The whole winding is in the average value of flux density, which is half the gap value. The total radial force acting on the winding with mean diameter of D_m (in meters) can be calculated by Equation 6.19 as

$$F_r = \left[\frac{1}{2}\frac{\sqrt{2}\mu_0 NI}{H_w}\right] \times \sqrt{2}\, NI \times \pi\, D_m = \frac{\mu_0 (NI)^2}{H_w} \times \pi\, D_m \,. \tag{6.23}$$

For the outer winding, the conductors close to the gap (at the inside diameter) experience a higher force as compared to those near the outside diameter (the force reduces linearly from its maximum value at the gap to zero at the outside diameter). The force can be considered to be transferred from conductors with high load (force) to those with low load if the conductors are wound tightly [9]. Hence, the averaging of the force value over the radial depth of the winding as done in the above equation is justified since the winding conductors share the total load almost uniformly. If the curvature is taken into account by the process of integration across the winding radial depth as done in Section 3.1.1 of Chapter 3, the mean diameter of the winding in the above equation should be replaced by its inside diameter plus two-thirds of the radial depth.

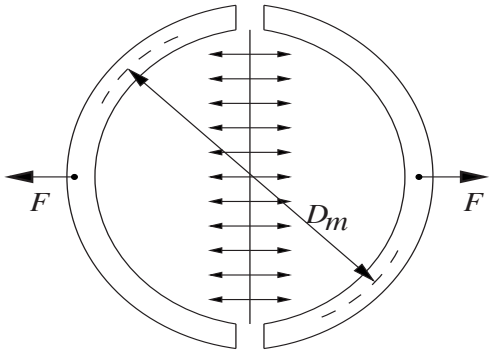

Figure 6.6 Hoop stress calculation.

The average hoop stress for the outer winding is calculated as for a cylindrical boiler shell shown in Figure 6.6. The transverse force F on the two halves of the winding is equivalent to the pressure acting on its diameter [10]; hence it will be given by Equation 6.23 with πD_m replaced by D_m. If the cross-sectional area of a turn is A_t (in m^2), the average hoop stress in the winding is

$$\sigma_{avg} = \frac{\mu_0 (NI)^2 D_m}{H_w (N \times 2 \times A_t)} = \frac{\mu_0 I^2}{2\rho\pi H_w} \times \frac{\rho\pi D_m N}{A_t} \quad . \tag{6.24}$$

Let I_r be the rated r.m.s. current and Z_{pu} be the per unit impedance of a transformer. The r.m.s. value of the short-circuit current in the winding is equal to (I_r / Z_{pu}). To take into account the asymmetry, this current value is multiplied by the asymmetry factor k. If we denote the I^2R loss per phase by P_R, the expression for σ_{avg} under the short-circuit condition is

$$\sigma_{avg} = \frac{\mu_0}{2\rho\pi H_w} \times \frac{I_r^2 k^2}{Z_{pu}^2} \times \frac{\rho(\pi D_m N)}{A_t} = \frac{\mu_0}{2\left(\sqrt{2}\right)^2 \rho\pi H_w} \times \frac{P_R \left(k\sqrt{2}\right)^2}{Z_{pu}^2} \text{ N/m}^2. \tag{6.25}$$

Substituting the values of μ_0 (= $4\pi \times 10^{-7}$) and ρ (resistivity of copper at 75°C = 0.0211×10^{-6}) we finally obtain

$$\sigma_{avg} = 4.74 \left(k\sqrt{2}\right)^2 \frac{P_R}{H_w Z_{pu}^2} \text{ N/m}^2 \tag{6.26}$$

or

$$\sigma_{avg} = 0.48\times10^{-4}\times\left(k\sqrt{2}\right)^2 \frac{P_R}{H_w Z_{pu}^2} \text{ kg/cm}^2 \quad \ldots \text{ Copper conductor} \quad (6.27)$$

where P_R is in watts and H_w in meters. It is to be noted that the term P_R is only the DC I^2R loss of the winding per phase at 75°C. Hence, with very little and basic information of the design, the average value of the hoop stress can be easily calculated. If an aluminum conductor is used, the numerical constant in the above equation will reduce according to the ratio of resistivity of copper to that of aluminum giving,

$$\sigma_{avg} = 0.29\times10^{-4}\times\left(k\sqrt{2}\right)^2 \frac{P_R}{H_w Z_{pu}^2} \quad \ldots \text{ Aluminum conductor.} \quad (6.28)$$

As mentioned earlier, the above expression of the average stress can be assumed to be applicable for an entire tightly wound disk winding without much error. This is because of the fact that although the stress is higher for the inner conductors of the outer winding, these conductors cannot elongate without stressing the outer conductors. This results in near uniform hoop stress distribution over the entire winding. In layer/helical windings having two or more layers, the layers do not firmly support each other, and there is no transfer of load between them. Hence, the hoop stress is highest for the innermost layer and it decreases towards the outer layers. For a double-layer winding, the average stress in the layer near the gap is 1.5 times higher than the average stress for the two layers considered together. Generalizing, if there are *L* layers, the average stress in k^{th} layer (from gap) is $\left[2-\left((2k-1)/L\right)\right]$ times the average stress of all the layers considered together. Thus, the design of the outer multilayer winding subjected to hoop stresses requires special design considerations.

***FEM procedure*:** FEM may be used to determine stresses generated at every point in the windings of a transformer. At each point in a winding disk, a stress tensor needs to be determined which is a 3×3 matrix, containing normal stress and shear stress components. In cylindrical coordinates, a von-Mises equivalent stress is calculated at each point in the outer winding from the stress tensor, which is given by

$$\sigma_{\text{max\_vm}} = \frac{1}{\sqrt{2}}\sqrt{\left(\sigma_r-\sigma_\phi\right)^2+\left(\sigma_\phi-\sigma_z\right)^2+\left(\sigma_z-\sigma_r\right)^2+6\tau_{r\phi}^2+6\tau_{\phi z}^2+6\tau_{zr}^2} \quad (6.29)$$

where $\sigma_{\text{max\_vm}}$ is the maximum von-Mises equivalent stress in a finite element. $\sigma_r, \sigma_\phi, \sigma_z$ are the normal stress components and $\tau_{r\phi}, \tau_{\phi z}, \tau_{zr}$ are the shear stress components of the stress tensor matrix [11]. The von-Mises stress value is used as a criterion to determine the onset of a failure in ductile materials like copper in transformer windings. According to this criterion the von-Mises stress should

be less than the yield stress of the winding material to avoid any permanent deformation. If the von-Mises equivalent stress value at any point is greater than the yield strength of the winding material, then the winding material goes into the plastic zone; otherwise it remains in the elastic zone. A safety factor corresponding to strength of the winding against the radial (tensile) short-circuit electromagnetic force can be defined as

$$\left(\mathbf{SF}\right)_{hoop} = \frac{\sigma_{\text{yield}}}{\sigma_{\text{max\_vm}}} \tag{6.30}$$

where σ_{yield} is the yield strength of the winding material (refer to Section 12.6.3 for a case study). The safety margin should be based on experience.

When the radial electromagnetic pressure is applied at the inner surface of a winding disk (with applied pressure on the outer surface being zero), the stress components induced in it are given as [12]

$$\sigma_r = \frac{a^2 P}{\left(b^2 - a^2\right)}\left(1 - \frac{b^2}{r^2}\right);\ \ \sigma_\phi = \frac{a^2 P}{\left(b^2 - a^2\right)}\left(1 + \frac{b^2}{r^2}\right);\ \ \sigma_z = 2\nu\,\frac{a^2 P}{\left(b^2 - a^2\right)}$$

where P is the average pressure acting on the inner surface of the winding, and a and b are the inner and outer radii of the winding. ν is the Poisson's ratio of the winding material. The displacements of the inner and outer surfaces of the winding disk are given as [11]

$$u_a = \frac{Pa}{E\left(b^2 - a^2\right)}\left[\left(a^2 + b^2\right) + \left(b^2 - 2\,a^2\right)\nu\right] \tag{6.31}$$

$$u_b = \frac{P\,a^2\,b}{E\left(b^2 - a^2\right)}\left(2 - \nu\right) \tag{6.32}$$

where E is the Young's modulus of elasticity of the winding material. The above two formulae give displacements close to that given by FEM (Section 12.6.3).

For an inner winding subjected to radial forces acting inwards, the average stress can be calculated by using Equations 6.24 to 6.28. However, since it can fail either by collapsing or due to bending between its supports, the compressive stresses acting on it are not simple equivalents of the hoop stresses of the outer winding. Thus, design considerations of the inner windings are quite different, and these aspects along with their failure modes are discussed in Section 6.5.

6.3.2 Axial forces

For uniform ampere-turn distribution in windings with equal heights (ideal conditions), the axial forces due to the radial leakage field at the winding ends

are directed towards the winding center as shown in Figure 6.4. Although, there are high local forces per unit length at the ends of the windings, the cumulative compressive force is maximum at their center (see Figure 6.7). Thus, both inner and outer windings experience compressive forces with no end thrust on the clamping structures (under the ideal conditions). For an asymmetry factor of 1.8, the total axial compressive force acting on the inner and outer windings taken together is given by the following expression [13]:

$$F_a = \frac{50.8 \times S}{Z_{pu} \times H_w \times f} \; kg \quad \cdots\cdots \; ideal \; conditions \tag{6.33}$$

where S is the rated power per limb in kVA, H_w is the winding height in meters, Z_{pu} is the per unit impedance, and f is the frequency in Hz. The inner winding being closer to the limb, by virtue of higher radial flux, experiences a higher compressive force as compared to the outer winding. In the absence of detailed analysis, it can be assumed that 25 to 33% of the total force is taken by the outer winding, and the remaining 75 to 67% is taken by the inner winding.

The calculation of axial forces in windings due to the radial leakage field in nonideal conditions is not straightforward. Assumptions, if made to simplify the calculations, can lead to erroneous results for nonuniform windings. Tap breaks, if present, make the computations difficult. The methods discussed in Chapter 3 should be used to calculate the radial field and the resulting axial forces. The forces at various points in a winding are added to find the maximum compressive force in it. Once the total axial force for each winding is known, the compressive stress in supporting radial spacers (blocks) can be calculated by dividing the compressive force by the total area of the radial spacers. The stress should be less than a certain limit, which depends on the material of the spacers. If the applied prestress (discussed in Section 6.8) is more than the force value, the former is considered while calculating the stress on the radial spacers.

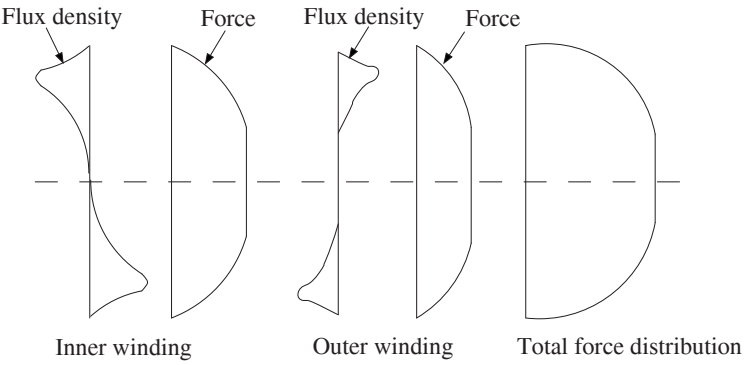

Figure 6.7 Axial force distribution.

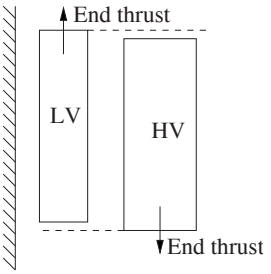

Figure 6.8 Axial asymmetry.

The reasons for a higher value of radial field and consequent axial forces are mismatch of ampere-turn distribution between the LV and HV windings, tappings in a winding, unaccounted shrinkage of insulation during drying and impregnation processes, etc. When the windings are not placed symmetrically with respect to the center line as shown in Figure 6.8, the resulting axial forces are in such a direction that the asymmetry and the end thrusts on the clamping structures increase further. It is well known that even a small axial displacement of windings or misalignment of their magnetic centers can eventually cause enormous axial forces leading to failure of transformers [14, 15]. Hence, strict sizing/dimension control is required during processing and assembly of windings so that they are symmetrically placed.

6.4 Dynamic Behavior Under Short-Circuits

The transformer windings along with the supporting clamping structure form a mechanical system having mass and elasticity. The applied electromagnetic forces are oscillatory in nature and they act on the elastic system comprising of winding conductors, insulation system, and clamping structures. The forces are dynamically transmitted to various parts of the transformer and they can be quite different from the applied forces depending upon the closeness of natural frequencies of the system and excitation frequencies. Thus, the dynamic behavior of the system has to be analyzed for determining stresses and displacements produced by short-circuit forces. The dynamic analysis, although complex, is certainly desirable for improving the understanding of the whole phenomenon and for enhancing the reliability of transformers under short-circuit conditions. The dynamic behavior is associated with time dependence of the instantaneous short-circuit current and the corresponding force, and the displacement of the windings producing instantaneous modifications of these forces. Inertia of conductors, frictional forces and reactionary forces of various resilient members of the system play an important role in deciding the dynamic response.

In the radial direction, the elasticity of copper is high and its mass is small, resulting into natural frequencies that are much higher than 50/60 Hz and

100/120 Hz (the fundamental frequency and twice the fundamental frequency of the excitation force). Hence, there exists a very remote possibility of increase in displacements by resonance effects under the action of radial forces. Therefore, these forces may be considered as applied slowly and producing maximum stress corresponding to the first peak of an asymmetrical fault current [10]. In other words, the energy stored by the displacement of windings subjected to radial forces is almost entirely elastic and the stresses in the windings correspond closely to the instantaneous values of the generated forces [16].

Contrary to the radial direction, the amount of insulation is significant along the axial direction, which is easily compressible. With the axial forces acting on the system consisting of conductors and insulation, the natural frequencies may come close to the excitation frequencies. Such a resonant condition leads to large displacements and the transformer may fail. Hence, the dynamic analysis of the mechanical system consisting of windings and clamping structures is essential and has been investigated in detail by many researchers.

The transformer windings, made up of a large number of conductors separated by insulating materials, can be represented by an elastic column with distributed mass and spring parameters, restrained by end springs representing the insulation between the windings and the yokes. Since there is heavy insulation at the ends, these springs are usually assumed as massless. When a force is applied to an elastic structure, displacements and stresses depend not only on the magnitude of the force and its variation with time, but also on the natural frequencies of the structure.

The methods for calculating the dynamic response are complex. They have to take into account the applied prestress, stiffness of clamping structure and proximity of tank/other windings. It should also take into account the effects of displacements of conductors. The method reported in [17] replaces a model of ordinary linear differential equations representing the system by an approximate equivalent model of linear difference equations with a constant time step length. Nonlinear insulation characteristics obtained from an experimental data are used to solve the difference equations by a digital computer. In [18, 19], the dynamic load and the displacement at any point in a winding are calculated by using a generalized Fourier series of the normal modes (the standing wave approach). The analysis presented can be applied to an arbitrary space distribution of electromagnetic forces with actual time variation of a fully asymmetric short-circuit current taken into account. The dynamic forces are reported to have completely different magnitudes and waveshapes as compared to the applied electromagnetic forces.

A rigorous analytical solution is possible when linear insulation characteristics are assumed. The insulation of a transformer has nonlinear characteristics. The dynamic properties of pressboard insulation are highly nonlinear and considerably different from their static characteristics. The dynamic stiffness and damping characteristics can be experimentally determined [20, 21]. The use of static characteristics was reported to be acceptable [21],

which leads to pessimistic results as compared to that obtained by using the dynamic characteristics. It was shown in [22] that the dynamic value of Young's modulus can be derived from the static characteristics. However, it is explained in [19] that this approximation may not be valid for oil-impregnated insulation. The oil provides hydrodynamic mass effect to the clamping parts subjected to short-circuit forces, and it also significantly influences the insulation's stiffness characteristics. These complexities and the nonlinearity of the systems can be effectively taken into account by numerical methods. A dynamic analysis is reported in [23] which accounts for the difference in the electromagnetic forces inside and outside the core window. It is shown that a winding displacement inside the window is distinctly different and higher than that outside the window. A simplified model is proposed in [24] whereby the physical aggregation of conductors and supports is considered as continuous elastic solid represented by a single partial differential equation.

Thus, various numerical methods are available for determining the dynamic response of a transformer under short-circuit conditions. Precise knowledge of the dynamic characteristics of various materials used in transformers is essential. The dynamic calculations can certainly increase the theoretical knowledge of the whole phenomenon, but it is difficult to ascertain the validity of the results obtained. On the contrary, it is fairly easy to calculate the natural frequencies of windings and check the absence of resonances. Hence, a more practical approach can be to check the withstand for the worst possible peak value of an asymmetrical fault current (the static calculation as explained in Section 6.3). In addition, the natural frequencies of windings should be calculated to check that they are far away from the power frequency and twice the power frequency. If the natural frequencies are close to either 50 or 100 Hz (60 or 120 Hz), they can be altered to avoid any resonance by using a different prestress value or by changing the modes of vibration by a suitable subdivision of the windings. Hence, the well-established static calculations along with the determination of natural frequencies could form a basis of short-circuit strength calculations [25, 26] until the dynamic analysis procedures are perfected and standardized.

In a typical core type power transformer, windings are commonly clamped between top and bottom clamping plates (rings) made from an insulating material. The construction of a winding is complicated and it consists of many different materials like kraft paper, precompressed boards, copper/aluminum conductors, densified wood, etc. The winding consists of many disks and insulation spacers. Thus, it is a combination of spacers, conductors and pre-compressed boards. Strictly speaking, it is having multiple degrees of freedom and is therefore considered a distributed mass system in the analysis. The winding stiffness is almost entirely governed by the insulation only. The top and bottom end insulations are considered massless linear springs. The winding can be represented by an elastic column restrained between the two end springs as shown in Figure 6.9.

The equation of motion [18, 23] is given by

$$m\frac{\partial^2 y}{\partial t^2}+c\frac{\partial y}{\partial t}-k\frac{\partial^2 y}{\partial x^2}=F(y,t) \tag{6.34}$$

where $y(x, t)$ is the displacement (from a rest position) of any point at a vertical distance x, m is the mass of the winding per unit length, c is the damping factor per unit length, k is the stiffness per unit length, and F is the applied electromagnetic force per unit length.

An expression for natural frequency, ω_n (in rad/sec), can be derived from Equation 6.34 with the boundary conditions that the displacement and velocity at any position x are zero at $t=0$, and the net force acting at positions $x=0$ (winding bottom) and $x=L$ (winding top) is zero. The expression is

$$\omega_n=\lambda_n\sqrt{\frac{K}{M}} \tag{6.35}$$

where λ_n is the eigenvalue corresponding to the n^{th} natural frequency, $M\ (=mL)$ is the total mass of the winding, L is the length (height) of the winding, and K is the winding stiffness $(=k/L)$. The stiffness per unit length of the winding is given by

$$k=\frac{A\ E_{eq}}{L_{eq}} \tag{6.36}$$

where A is the area of the insulation, E_{eq} is the equivalent Young's modulus of the winding, and L_{eq} is the equivalent length of the winding. Thus, the natural frequencies of the winding vary as a function of its mass, equivalent height, cross-sectional area and modulus of elasticity.

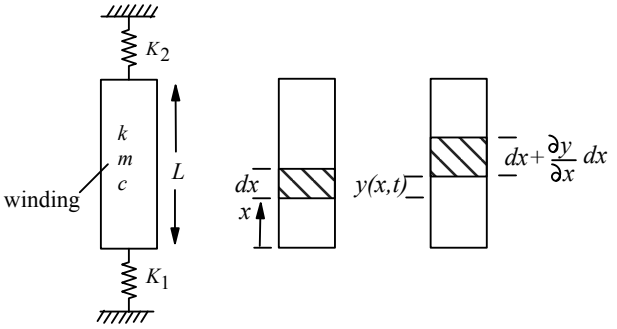

Figure 6.9 Representation of a winding [18].

The conductor material (copper) is too stiff to get compressed appreciably by the axial force. Hence, all the winding compression is due to those fractions of its height occupied by the paper and pressboard insulation. The equivalent Young's modulus can therefore be calculated from [22]

$$\frac{E_{eq}}{L_{eq}} = \frac{E_p E_b}{E_p L_b + E_b L_p} \tag{6.37}$$

where E_{eq} is the modulus of elasticity of the combined paper and pressboard insulation system, E_p is the modulus of elasticity of the paper, and E_b is the modulus of elasticity of the pressboard. The terms $L_{p,}$ L_b and L_{eq} represent the thickness of the paper, the thickness of the pressboard, and the total equivalent thickness of the paper and pressboard insulations, respectively.

The eigenvalues (λ) are calculated using the following equation [18]

$$\tan\lambda = \frac{\left(\frac{K_1}{K} + \frac{K_2}{K}\right)\lambda}{\lambda^2 - \frac{K_1 K_2}{K^2}} \tag{6.38}$$

where K_1 and K_2 are the stiffness values of the bottom- and top-end insulations, respectively. In Equation 6.38, the only unknown is λ which can be determined by an iterative method. Subsequently, the values of natural frequencies can be calculated from Equation 6.35. Another way to obtain the values of λ_n is to plot the left side and right side expressions of Equation 6.38 as a function of λ ; the intersections of the two plots gives the eigenvalues.

The natural frequencies can be more accurately calculated by numerical methods such as FEM [26]. If any of the calculated natural frequencies is close to the exciting frequencies, it can be altered by making suitable changes in the winding configuration and/or prestress value.

During vibrations of windings in the axial direction, the insulation elements like pressboard spacers or end clamping rings are mechanically stressed. At no time during the short-circuit period these elements should be stressed beyond their mechanical strength. The corresponding factor of safety can be defined for the windings against axial vibrations as

$$\left(\mathbf{SF}\right)_{dynamic} = \frac{\sigma_{\text{permissible limit}}}{\sigma_{\max}} \tag{6.39}$$

where $\sigma_{\text{permissible limit}}$ and $\sigma_{\max}$ is the maximum permissible stress limit and the maximum stress induced in some insulation element due to axial vibrations, respectively. It should be noted that the prestress (clamping pressure) value results in residual stresses which should be considered while calculating $\sigma_{\max}$.

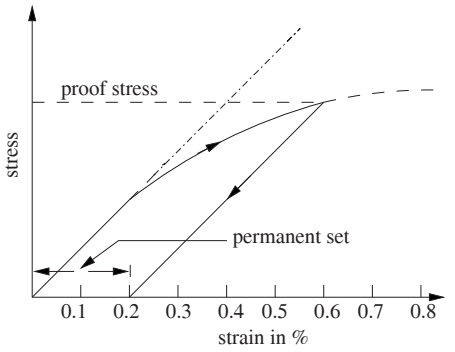

Figure 6.10 0.2% proof stress.

6.5 Failure Modes Due to Radial Forces

The failure modes of windings are quite different for inward and outward radial forces. Winding conductors subjected to outward forces experience tensile (hoop) stresses. Compressive stresses are developed in the conductors of a winding subjected to inward forces. In concentric windings, the strength of the outer windings subjected to outward forces depends on the tensile strength of the conductor; on the contrary, the strength of inner windings subjected to inward forces depends on their support structure. A radial collapse of inner windings is common, whereas an outward bursting of outer windings usually does not take place.

6.5.1 Winding subjected to tensile stresses

If a winding is tightly wound, the conductors in the radial direction in a disk winding or in any layer of a multilayer winding can be assumed to have uniform tensile stress. Since most of the space in the radial direction is occupied by the conductor material (except for the small paper covering on the conductors), the ratio of stiffness to mass is high. As mentioned earlier, natural frequencies are much higher than the excitation frequencies, and hence the chances of resonance are remote. Under a stretched condition, if the stress exceeds the yield strength of the conductor, a failure occurs. The conductor insulation may get damaged or there could be a local bulging of the winding. The conductor may even break due to improper joints. The chances of failure of windings subjected to tensile hoop stresses are unlikely if a conductor with a certain minimum 0.2% proof strength is used. The 0.2% proof stress can be defined as that stress value which produces a permanent strain of 0.2% (2 mm in 1000 mm) as shown in Figure 6.10. One of the common ways to increase the strength is the use of a work-hardened conductor; however, its hardness should not be very high since there can be difficulty in winding operation. A lower value of the current density can also be used to improve the withstand.

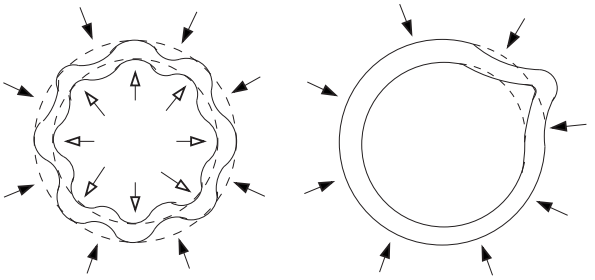

Figure 6.11 Buckling phenomena.

6.5.2 Windings subjected to compressive stresses

Conductors of inner windings, which are subjected to a radial compressive load, may fail due to bending between supports or buckling. The former case is applicable when the inner winding is firmly supported by the axially placed supporting spacers (strips), and the supporting structure as a whole has higher stiffness than conductors (e.g., if the spacers are firmly supported by the core structure). In that case, the conductors can bend between the supports all along the circumference as shown in Figure 6.11(a) if the stress exceeds the elastic limit of the conductor material. This form of failure is termed forced bending [27, discussion of 28] which has a characteristic shape sea-star [29] or pointed-star [10].

The other failure mode, i.e., buckling as shown in Figure 6.11(b), occurs when the radial compressive stress exceeds a critical value which depends on the construction of the winding. The buckling in which inner winding supports are involved is called forced buckling which occurs when the inner cylinder has a significant stiffness value as compared to the winding conductors (i.e., when a thick cylinder made from a stiff material is used).

Another type of buckling, termed free buckling, is essentially an unsupported buckling mode in which the span of the conductor buckle bears no relation to the span of axial supporting spacers. This kind of failure occurs mostly with thin winding cylinders, if the winding conductor has high stiffness as compared to that of the inner cylinders and/or if the cylinders (and the axial spacers) are not firmly supported from inside. The conductors bulge inward as well as outward at one or more locations along the circumference. There are many factors that may lead to this buckling phenomenon, viz. winding looseness, inferior material characteristics, eccentricities in windings, low stiffness of supporting structures, etc.

The strength of an inner winding against radial short-circuit forces should be checked by considering the following two stresses [29]: the first one is the stress at which permanent deformation (bending between axial spacers) will

occur, and the second one is the stress at which buckling (free or forced buckling) will occur. In the case of bending, the actual short-circuit stress should be less than the yield strength of the material. In the case of buckling, the actual stress should be less than a critical stress value which is a function of material properties as well as geometrical details.

Forced bending: A numerical procedure to determine the strength of the conductor of an inner winding, against bending between axial spacers, is now described. FEM can be used to determine the stresses induced in a winding due to radial compressive electromagnetic forces. For this, a section of a disk between two axial insulation spacers can be taken for the analysis. An assumption of plane stress can be assumed since the disk height is small as compared to its radial depth. The von-Mises equivalent stress to be calculated in each finite element for the plane stress condition is given by

$$\sigma_{\max\_vm} = \frac{1}{\sqrt{2}}\sqrt{(\sigma_x - \sigma_y)^2 + (\sigma_x)^2 + (\sigma_y)^2 + 6\,(\tau_{xy})^2} \tag{6.40}$$

where $\sigma_{\max\_vm}$ is the maximum value of von-Mises stress in a finite element. In Equation 6.40 which is for the plane stress case, the stress components viz. σ_z, τ_{xz}, and τ_{yz} are absent because their values are small enough as compared to the other stress components so that they can be neglected [30]. The factor of safety for the winding disk against bending forces can be determined as

$$(\mathbf{SF})_{Strength\_Inner\_Winding} = \frac{\sigma_{\text{yield}}}{\sigma_{\max\_vm}} \ . \tag{6.41}$$

The safety factors defined in Equations 6.30 and 6.41 are very similar, but there is a difference between them. The first safety factor (Equation 6.30) is related to the outer winding in which the hoop (tensile) stress is compared with the maximum von-Mises stress. Also, there are no constraints on the outer winding. The other safety factor (Equation 6.41) is related to the inner winding in which the compressive stress is compared with the von-Mises stress. Also, there are constraints (axial spacers) present at the inner surface of the winding.

The following FEM procedure can be used to determine the maximum von-Mises stress and hence the safety factor for the inner winding disks as defined in Equation 6.41. A 2-D vector Poisson's equation in terms of the magnetic vector potential is solved first at the time instant of the first peak of the short-circuit current. By using the relation $\mathbf{B} = \nabla \times \mathbf{A}$ and the Lorentz force equation, the radial electromagnetic forces acting on the disk are computed. The forces are converted into an average pressure value by dividing the total force by the outer surface area of the disk (i.e., disk height × π × disk outer diameter). In the subsequent structural analysis, the average pressure calculated in the electromagnetic analysis is applied on the outer surface of the disk. Various

induced stresses, as required in Equation 6.40, are obtained from the structural FEM analysis to calculate the von-Mises stress in each finite element. The factor of safety related to the strength of the inner winding can be determined using Equation 6.41. In [31], the factor of safety has been reported for a bottom conductor of the first layer in the LV-Top winding of a 200 MVA generator transformer.

***Free buckling*:** To analyze the free buckling phenomenon in an inner winding, its outermost turn can be considered as a ring with no inner supports (the outermost turn is considered because its radius is the highest and the force on it is also highest being closest to the LV-HV gap). The critical load per unit length on the outer surface of the inner winding is given by [32]

$$q_c = \frac{3EI}{R^3} \tag{6.42}$$

where E is the modulus of elasticity of the winding material, N/m^2, I is the area moment of inertia, m^4, and R is the mean radius of the ring, m. The critical pressure P_c can be obtained by dividing Equation 6.42 by the height (w) of the ring (turn) in the axial direction,

$$P_c = \frac{q_c}{w} = \frac{3EI}{R^3 w} \ . \tag{6.43}$$

The reaction force F acting at the diametrically opposite ends of the ring is

$$2F = P_c (2R) w \ \Rightarrow \ F = P_c R w . \tag{6.44}$$

The critical compressive stress is given by

$$\sigma_c = \frac{F}{A} = \frac{P_c R w}{wt} = \frac{P_c R}{t} \tag{6.45}$$

where t is the radial depth of the turn (i.e., thickness). Substituting the value of P_c from Equation 6.43 in Equation 6.45 and using the formula $I = wt^3/12$ we obtain

$$\sigma_c = \frac{E}{4}\left(\frac{t}{R}\right)^2 . \tag{6.46}$$

The factor of safety for the inner winding against radial short-circuit electromagnetic forces (free buckling) can be given as

$$(\mathbf{SF})_{Free\_Buckling} = \frac{P_c}{P_{short-circuit}} \tag{6.47}$$

where $P_{short\text{-}circuit}$ is the average pressure corresponding to a short-circuit condition.

The FEM procedure for computing the factor of safety related to free buckling is as follows. The average pressure is calculated in the same way as explained in the FEM procedure described earlier for determining the strength of an inner winding against the forced bending stresses. In the free buckling case the ring (turn) is considered unsupported, i.e., there is negligible stiffness provided by inner support structures. Therefore the ring can be considered a circular unsupported structure. In the structural FEM analysis, an axisymmetric model of the ring cross section is made. A load of 1 newton is applied at each node on the outer surface of the ring in this linear eigenvalue analysis problem. The buckling module available in commercial FEM software gives the critical load in N/m. To calculate the critical pressure value, the critical load is divided by the mean circumference of the ring. The factor of safety related to the free buckling as defined in Equation 6.47 is then calculated. The safety factor for the LV winding of a generator transformer is reported in [31].

***Forced buckling*:** The buckling can be viewed as a sequential chain of failures, initiated at the outermost conductor of the inner winding and moving towards the innermost conductor facing the core. The number of winding supports should be adequate for giving the necessary strength to the winding against the radial forces. When the supporting structures are in direct contact with the core, the inner winding can be taken as rigidly supported. On the contrary, if there is a partial or no contact with the core, the winding is only supported by an insulating cylinder made of the pressboard material, thereby reducing the effective stiffness of the support structure and increasing the chances of failure. The supports provided are effective only when the support structure as a whole is in firm contact with the core.

A winding conductor subjected to inward radial forces is usually modeled as a circular loop under uniformly distributed radial load. The critical load per unit length of the winding conductor is given by [33]

$$q_c = \frac{2E}{D_m^3}\,\frac{w\,t^3}{12}\,[N_s^2 - 4] \tag{6.48}$$

where E is the modulus of elasticity of conductor material, N_s is the total number of axially placed supports, w is the height (width) of the winding conductor, t is the thickness of the conductor, and D_m is the mean diameter of the conductor. The critical pressure is obtained by dividing Equation 6.48 by w,

$$P_c = \frac{q_c}{w} = \frac{2E}{D_m^3}\,\frac{t^3}{12}\,[N_s^2 - 4]\,. \tag{6.49}$$

By using Equations 6.45 and 6.49, the critical average compressive stress σ_{avg} can be obtained:

$$\sigma_{avg} = \frac{F}{A} = \frac{P_c R w}{wt} = \frac{P_c R}{t} = \frac{D_m/2}{t} \left\{ \frac{2E}{D_m^3} \frac{t^3}{12} [N_s^2 - 4] \right\}$$
$$= \frac{E}{12} \left(\frac{t N_s}{D_m} \right)^2 \left[\frac{N_s^2 - 4}{N_s^2} \right] \tag{6.50}$$

where A is the conductor area ($= w\,t$). For $N_s >> 1$, the expression for the minimum number of supports to be provided is

$$N_s = \frac{D_m}{t} \sqrt{\frac{12\,\sigma_{avg}}{E}} \,. \tag{6.51}$$

The term σ_{avg} is the average value of the compressive stress (in an entire disk winding or in a layer of a multi-layer winding) calculated according to Section 6.3.1. It can be observed that the higher the conductor thickness, the lower the number of required supports will be. Adoption of a higher slenderness ratio $(t\,N_s/D_m)$ allows higher critical radial compressive stresses [33]. For a winding with a low mean diameter, there is a limit up to which the conductor thickness can be increased (it is difficult to wind a thick conductor on a small former diameter). Similarly, for a given winding diameter, there is a limit on the number of axially placed supports; the radially placed spacers (between disks) on these axially placed spacers reduce the surface area available for the cooling purpose. To avoid this problem, intermediately placed axially spacers (between every two main spacers) are used, which do not have radial spacers placed on them.

The stresses induced in the inner winding during the winding process has some effect in changing the modulus of elasticity of the winding material. The strain induced during the process adds to the strain produced in the winding conductors during the impact of a radial short-circuit force. The stress corresponding to the resultant strain, i.e., one due to the winding process and the other due to the short-circuit force, gives the modified Young's modulus of elasticity which should be used to determine the critical buckling stress. Therefore, in Equation 6.50, E should be changed accordingly to take into account the stresses induced during the winding process.

***Remarks*:** An elaborate and accurate analysis of buckling behavior has been reported in the literature. The dynamic analysis of the buckling behavior of inner windings subjected to radial forces is reported in [15, 28]. FEM is used in [34] to evaluate the radial buckling strength of the windings.

The design of windings for withstanding tensile stresses is relatively easy as compared to compressive stresses. This is because for the tensile stresses, the permissible stress depends on the yield strength of the conductor material. There are fewer ambiguities once the calculated maximum stress (whose calculation is

also usually straightforward) is kept below the yield stress. The design criteria for determining the withstand of the inner windings subjected to the compressive stresses are more complicated. After drying and oil-impregnation processes, insulating components may shrink considerably. Hence, lowering clearances and tolerances provided for insulating components have to be properly decided based on manufacturing practices and variations in their dimensions observed during manufacturing. If the inner winding is not assembled on the core-limb in a tight-fit condition or if there is looseness, then wedging of insulating components is necessary. If integrity of the support structure is ensured in this manner, the inner winding can be said to be supported from the inside and the number of supports calculated by Equation 6.51 will be adequate to prevent the buckling. Some manufacturers [9] completely ignore the strength provided by the inner supporting structures and design self-supported windings. The current density used therefore has to be lower with the result that the material content and the cost of the transformer increases. Nevertheless, the reliability of the transformer is enhanced and the extra material put can be justified for large transformers. It is reported (discussion of [28]) based on the model tests that the insertion of tight-fitting insulation spacers between the core and the innermost insulating cylinder may not be an effective solution for increasing the strength because the clearances between the elements of the structure are larger than the disk displacements prior to the buckling. Thus, the practice of designing completely self-supported windings seems to be a better option.

6.6 Failure Modes Due to Axial Forces

Various types of failures occur under the action of axial compressive forces. If a layer winding is not wound tightly, some conductors may just axially pass over the adjacent conductors, which may damage the conductor insulation leading eventually into a turn-to-turn fault. In another mode of failure, if a winding is set into vibration under the action of axial forces, the conductor insulation may be damaged due to relative movement between the winding and the axially placed insulation spacers.

High axial end thrusts could lead to deformations of end clamping structures and windings. The clamping structures play the most important role in resisting axial forces during short circuits. They have to maintain an effective pressure on the windings, applied usually on the clamping ring made from a stiff insulating material (precompressed board or densified wood). The type of the insulation material used for the clamping ring depends on the dielectric stress in the end insulation regions. The densified wood material is used for low stress applications and the precompressed board, being a better material dielectrically, is used for higher stress applications and for complying stringent partial discharge requirements. When a clamping ring made of an insulating material is reinforced by a fiberglass material, an extra strength becomes available. Some

manufacturers use clamping rings made from steel. The thickness of a metallic clamping ring is smaller than that made from an insulating material. The metallic ring has to be properly grounded with a cut so that it does not form a short-circuited turn around the limb. Sharp edges of the metallic ring should be rounded off and covered with suitable insulation.

In addition to the above types of failures due to axial forces, there are two principal types of failures, viz. bending between radial spacers and tilting.

6.6.1 Bending between radial spacers

Under the action of axial forces, a winding conductor can bend between the radially placed insulation spacers as shown in Figure 6.12. The conductor bending can damage its insulation. The maximum stress in the conductor due to bending occurs at the corners of the radial spacers and is given by [10]

$$\sigma_{\max} = \frac{F_{AL}\, S^2\, y}{12\, I_0} \quad \text{kg/cm}^2 \tag{6.52}$$

where,

F_{AL} is the maximum axial bending load in kg/cm. It corresponds to the most highly stressed disk in a disk winding or turn in a helical winding (layer winding with radial spacers). The maximum axial load may usually lie in the region of nonuniform ampere-turn distribution (e.g., tap zone). The maximum axial load, calculated accurately by a method such as FEM, divided by the mean turn length (πD_m) gives the value of F_{AL}, where D_m is the mean diameter of the winding in cm.

S is the span between two radial spacers $\left(\frac{\pi D_m}{N_S} - \textit{spacer width}\right)$ in cm; N_S is the number of radial spacers.

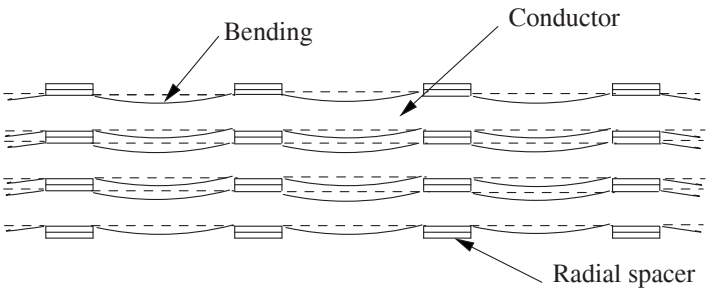

Figure 6.12 Bending between radial spacers.

y is the maximum distance from the neutral axis for the conductor in cm (i.e., half of the conductor axial width: $w/2$).

I_0 is the moment of inertia of the disk or the turn $\left(=\dfrac{n\,t\,w^3}{12}\right)$, n being the number of conductors in the radial direction, and t is the conductor radial thickness in cm.

The maximum stress in the conductor calculated by the above formula should be less than the limiting value for the type of conductor used (e.g., 1200 kg/cm^2 for soft copper).

A winding section between two radial spacers can be considered a clamped-clamped (CC) beam. The factor of safety for all types of windings against bending due to an axial short-circuit electromagnetic force is given as

$$(\mathbf{SF})_{bending} = \frac{\sigma_{\text{yield}}}{\sigma_{\text{max\_stress}}} \tag{6.53}$$

where $\sigma_{\text{max\_stress}}$ is the maximum stress given by $\dfrac{F_{AL}\,S^2}{2\,n\,t\,w^2}$, where t and w is the radial thickness and the height of the CC beam, respectively, F_{AL} is the axial load, and S is the span of the beam. $\sigma_{\text{max\_stress}}$ can be determined using FEM. In the FEM electromagnetic analysis, the axial force in each finite element is determined. The total axial force acting on the winding conductor is then determined by summing the forces in its finite elements. The total axial force is then divided by the mean circumference of the conductor to obtain the uniformly distributed load per unit circumferential length acting on the CC beam. The unsupported length of the beam is calculated by using the expression of 'S' as given above. The ends of the beam are assumed fixed, i.e., its displacements in the x and y directions and rotation are constrained at the ends. The factor of safety related to the bending has been reported for a transformer winding in [31].

6.6.2 Tilting under an axial load

The failure due to tilting under the action of axial compressive forces is one of the principal modes of failures in large power transformers. When these forces are more than a certain limit, a failure can occur due to tilting of conductors in a zigzag fashion as shown in Figure 6.13 for a disk winding. In this mode of failure, there is turning of the cross section of conductors around the perpendicular axis of symmetry. There are two kinds of forces that resist the

tilting of the conductors. The first one is due to the conductor material which resists when twisted. The second resisting force is a friction force (due to conductor corners); during the tilting phenomenon, both ends of the conductor must bite into the material of the radial spacers, producing a couple which resists tilting. The two resisting forces are usually considered separately to arrive at the critical stress and load.

The critical load and the critical stress for a disk winding, if the resistance offered by the conductor material alone is considered, are respectively [10]

$$F_{cr\_twist} = \frac{N \pi E t w^2}{6 R} \tag{6.54}$$

$$\sigma_{cr\_twist} = \frac{E}{12}\left(\frac{w}{R}\right)^2 \tag{6.55}$$

where R is the winding mean radius, w is the conductor width (the height in the axial direction), t is the conductor radial thickness, N is the number of winding turns, and E is the modulus of elasticity of the conductor material. For this case, rounded ends are assumed for the conductor so that the frictional resistance is absent. The tilting strength decreases inversely as the square of the winding radius, suggesting that large windings should be carefully designed.

If the conductor has sharp ends, the frictional force resists tilting. The critical load against the friction is [10]

$$F_{cr\_fric} = \frac{N_b N b c t^3}{6 w} \tag{6.56}$$

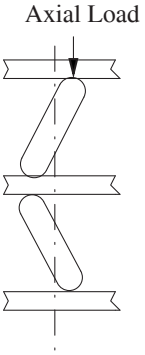

Figure 6.13 Conductor tilting in a disk winding.

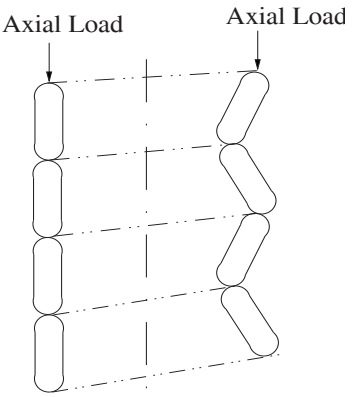

Figure 6.14 Half-tilting mode in a layer winding [35].

where N_b is the number of radial spacers (blocks), b is the width of spacers, and c is a constant which depends on the spacer material. Actually, due to the conductor corner radius, the contribution to the tilting resistance (due to friction) reduces and this reduction should be taken into account while using Equation 6.56. The critical strength of a helical winding is higher than that of a layer winding because of the additional strength offered by the radial spacers in it.

The total critical load F_{cr} is the addition of axial strengths against twisting and friction [10],

$$F_{cr} = \frac{N\pi Etw^2}{6R} + \frac{N_b N b c t^3}{6w}. \tag{6.57}$$

Analysis of a layer winding under the action of a tilting load is given in [35]. It is reported that this winding can fail in a zigzag pattern on one side only as shown in Figure 6.14 (termed as the half-tilting failure mode). It is also reported in the same paper that a disk winding can also fail in the half-tilting mode for which the winding strength is about 10% less than the corresponding full tilting strength. The critical axial force in the case of layer and helical windings are given in Equations 6.58 and 6.59, respectively [35],

$$F_{cr} = \frac{\pi}{2Rw}(3EI + GI_p) \tag{6.58}$$

$$F_{cr} = \frac{\pi}{2Rw}\left(3EI + GI_p\right) + \frac{N_b b c t^3}{6w} \tag{6.59}$$

where I and I_p are the area moment of inertia and the polar moment of inertia, respectively, and G is the shear modulus of elasticity.

The mechanical resonance frequencies in the tilting mode of failure are usually much higher than the excitation frequencies, and therefore there is no chance of a resonance condition in this mode. The conductor dimensions have a decisive role in the tilting strength. The twisting strength increases with the conductor width in the square proportion according to Equation 6.55. Equation 6.57 indicates that the risk of tilting increases for thin conductors.

When a continuously transposed cable (CTC) conductor is used, although there are two axially placed rows of conductors in one common paper covering (see Figure 4.9), it cannot be assumed that the effective tilting strength is higher. The tilting strength of a CTC conductor without epoxy bonding has been analyzed for a layer winding in [36]. Two possible modes of failures are described. The first type of failure (termed cablewise tilting), in which two adjacent cables tilt against each other, is shown in Figure 6.15 (a). If the inter-strand friction is high, the winding is forced to tilt in pairs of strands in the CTC conductor. The critical axial force for cablewise tilting failure mode is given by [36]

$$F_{cr} = \frac{E\,I\,L}{w_1\,R^2} \tag{6.60}$$

where w_1 = width (height) of an individual strand in the CTC conductor
R = mean radius of the winding
L = transposition distance in which one full transposition of all strands is completed.

The critical stress for this mode of failure, with the consideration of the conductor resistance alone, is [36]

$$\sigma_{cr\_twist} = \frac{E}{3}\left(\frac{w_1}{R}\right)^2 . \tag{6.61}$$

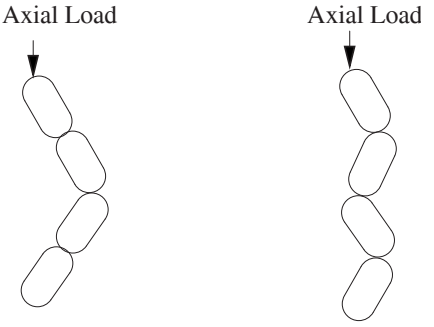

(a) Cablewise tilting (b) Strandwise tilting

Figure 6.15 Tilting in a layer winding with CTC conductor.

Comparison of Equations 6.55 and 6.61 tells us that for same strand dimensions, the CTC conductor has four times greater tilting strength; the result is obvious because the effective width of its conductor is doubled increasing the strength four times. This increase in strength is valid only when the two axially placed strands in the CTC conductor can be considered to act together under the tilting load.

In the second mode of failure (termed strandwise tilting), two axially placed strands in the CTC conductor tilt against each other as shown in Figure 6.15 (b). The critical axial force for this failure mode is given as [36]

$$F_{cr} = \frac{8GI_p}{w_1 l_c} + \frac{2EIl_c}{3R^2 w_1} + \frac{EI(L-2l_c)}{R^2 w_1} \tag{6.62}$$

where, l_c is the distance over which one strand is transposed from one position to other, w_1 is the axial height of an individual strand and R is the mean radius of the winding. The critical tilting load in this mode may be lower, reducing the effective overall tilting strength. This is because the lower of the cablewise and strandwise strengths triggers the axial instability. It is shown in [36] that while the critical stress in the cablewise tilting is independent of the number of strands in the cable (n), the critical stress in the strandwise tilting is inversely proportional to n. As the number of strands in the CTC conductor increases, the critical load limit in the strandwise tilting becomes lower than the cablewise tilting. Hence, with the increase in the number of strands in the CTC conductor, the mode of failure shifts from the cablewise tilting to the strandwise tilting.

Factors of safety for various windings, viz. disk, layer, helical (all with strip conductors), and layer and helical windings with CTC conductor against tilting can be calculated as

$$(\mathbf{SF})_{tilting} = \frac{F_{cr}}{\text{Short-circuit force}} \tag{6.63}$$

where F_{cr} is the critical axial force for a winding configuration under consideration.

The use of an epoxy-bonded CTC conductor is quite common in which the epoxy coating effectively bonds the strands increasing the resistance against the strandwise tilting. Each strand in the epoxy-bonded CTC conductor has, in addition to an enamel coating, a coat of thermosetting epoxy resin. The curing of this resin occurs at around 120°C during the processing of windings. After curing, the epoxy-bonded CTC conductor consisting of many strands can be considered one conductor with an equivalent cross section for the mechanical strength consideration. Thus, the possibility of strandwise tilting is eliminated, greatly increasing the strength of the CTC conductor against the tilting load. The

epoxy-bonded CTC conductor not only reduces the winding eddy losses (as explained in Chapter 4) but it also significantly improves the short-circuit withstand characteristics.

The critical axial force on a conductor can be determined by applying the state-space approach. The dynamic equation for the motion of the conductor, with the assumption of negligible damping and a small value of the tilt angle, is given by [37]

$$J\frac{d^2\theta}{dt^2} = \left[Fw - \left(\frac{N_b bNct^3}{6} + \frac{N\pi Etw^3}{6R}\right)\right]\theta \tag{6.64}$$

where

J = rotational inertia of the disk winding, kg.m^2
θ = tilt angle, radians
F = total axial force acting on the winding disk, newtons.

Here, a disk winding conductor is considered for analysis. The above second-order differential equation is converted into two first-order differential equations by choosing the tilt angle x_1 and the angular velocity x_2 as the state-variables, i.e.,

$$\begin{aligned} x_1 &= \theta \\ x_2 &= \dot{\theta} \end{aligned} \tag{6.65}$$

or $\dot{x}_1 = x_2$.

The resulting equations are written in the matrix form and the eigenvalues of the matrix are determined. The stability of the system is decided by checking the sign of the real part of the eigenvalues. The critical compressive force and the natural mechanical frequency of the winding are determined from the stability condition as [37]

$$F_{cr} = \left(\frac{N_b bNct^3}{6w} + \frac{N\pi Etw^2}{6R}\right);\ \omega = \sqrt{\left(\frac{N_b bNct^3}{6J} + \frac{N\pi Etw^3}{6RJ}\right)}. \tag{6.66}$$

In order to determine the initial critical tilt angle in the windings, the assumption of a small tilt angle does not work [37], and therefore the equation of motion of the conductor becomes a nonlinear differential equation,

$$J\frac{d^2\theta}{dt^2} = Fw\sin\theta - \left(\frac{\pi NEtw^3}{6R}\frac{\sin^2\theta}{\theta} + \frac{N_b bNct^3}{6}\sin\theta\right). \tag{6.67}$$

The state-space equations for this system are given as [37]

$$\dot{x}_1 = x_2$$

$$\dot{x}_2 = \left[\frac{Fw}{J} \sin x_1 - \left(\frac{N\pi Etw^3}{6RJ} \frac{\sin^2 x_1}{x_1} + \frac{N_b bNct^3}{6J} \sin x_1 \right) \right]. \tag{6.68}$$

The above two first-order differential equations are linearized by using Taylor series expansion for a small perturbation of state variables around the equilibrium point, and the resulting system is checked for the stability criterion,

$$\begin{Bmatrix} \Delta\dot{x}_1 \\ \Delta\dot{x}_2 \end{Bmatrix} = \begin{bmatrix} \frac{\partial\dot{x}_1}{\partial x_1} & \frac{\partial\dot{x}_1}{\partial x_2} \\ \frac{\partial\dot{x}_2}{\partial x_1} & \frac{\partial\dot{x}_2}{\partial x_2} \end{bmatrix} \begin{Bmatrix} \Delta x_1 \\ \Delta x_2 \end{Bmatrix} \tag{6.69}$$

where $\Delta\dot{x}_1$ and $\Delta\dot{x}_2$ are the small perturbations in the state variables. The square matrix in Equation 6.69 is the Jacobian matrix, whose eigenvalues will determine the initial critical tilt angle. If the tilt angle of the winding attains this value at its manufacturing stage or at the end of a short-circuit event, a tilting failure can occur at a smaller value of axial force in a subsequent short-circuit.

6.7 Failure Modes Due to Interactive (Combined Axial and Radial) Forces

The LV winding in a large power transformer is generally wound in a helical fashion. The winding may fail by a mechanism called a spiraling phenomenon. Helical windings have two components of the current: a circumferential component and an axial component. The spiraling occurs due to the interaction of the axial component of the current and the radial component of magnetic flux density. The result is the production of torsional electromagnetic forces on the winding. A helical winding can be split into three parts for analysis. The top and bottom ends have higher radial fields as compared to the middle portion. Hence, although the axial component of the current is same for all the three parts, the torsional forces are higher at the two ends. Since the resisting frictional force can be considered as same throughout the height of the winding, relative movements of the two end parts will occur in opposite directions because of the fact that the radial fields at the two ends are in opposite directions. The central part is almost unaffected due to small torsional forces acting on it.

Mathematically, the current density in a helical winding is given as

$$\mathbf{J} = J_\phi \, \mathbf{a}_\phi + J_z \, \mathbf{a}_z \tag{6.70}$$

where **J** is the current density in A/m^2, J_ϕ and J_z are its circumferential and axial components. The electromagnetic force density is produced in the windings by the interaction of the current density **J** and the magnetic flux density **B**. Mathematically,

$$\mathbf{F} = \mathbf{J} \times \mathbf{B} = \begin{vmatrix} \mathbf{a}_r & \mathbf{a}_\phi & \mathbf{a}_z \\ 0 & J_\phi & J_z \\ B_r & 0 & B_z \end{vmatrix} = \left(J_\phi \; B_z\right)\mathbf{a}_r + \left(J_z \; B_r\right)\mathbf{a}_\phi - \left(J_\phi \; B_r\right)\mathbf{a}_z . \tag{6.71}$$

The first term on the right side gives the radial component of the force, the second term in the circumferential direction represents the torsional force, and the last term denotes the axial component of the force. Since the radial component of the flux density B_r is maximum at the winding ends, the torsional forces are maximum at the ends. Practically also, it has been observed that in helical windings the spiraling of conductors occurs at the ends. With an increase in the helical angle the axial component of the current density increases, which in turn increases the torsional (spiraling) forces. These forces produce circumferential displacements of the helical winding [38].

The axial component of the current produces the azimuthal (ϕ) component of the magnetic flux density [39]. Although this component is lower than the axial and radial components of the magnetic field, it is present in the winding throughout its height. Although it does not contribute much to the eddy loss in the winding, stray losses in nearby structural components can be appreciable [39].

6.8 Effect of Prestress

The clamping pressure applied on the windings after the completion of core-winding assembly is called prestress. It has a significant impact on the response of windings during short circuits. Mechanical integrity of windings can be ensured if a properly chosen prestress gets maintained throughout the life of the transformers. If applied prestress is sufficient and maintained during the short-circuit duration, it may rule out the onset of free buckling due to radial forces. This is due to the transfer of axial prestress force to each disk through the radial insulation spacers [28].

The prestress value should be chosen accurately to avoid an excited resonance and large displacements of the windings. It has a significant effect in deciding the natural frequencies of the windings and their oscillations. The relationship between the natural frequencies and the prestress value can be highly nonlinear [40]. A high value of prestress reduces oscillations of the

windings. It increases the stiffness of the overall system thereby increasing the mechanical resonance frequencies. If an unprestressed natural frequency is higher than the excitation frequencies, the oscillations are reduced at higher values of the prestress. On the contrary, if the unprestressed natural frequency is lower than the excitation frequencies, a higher value of the prestress may bring them closer. Therefore, the prestress value should be judiciously chosen [19, 41, 42].

The above discussion assumes that the prestress value is constant; however, it may change due to variations in temperature, presence of moisture in insulation, and its aging. This will in turn affect the short-circuit performance of the transformer. Any change in the thickness of the materials in the windings and the end insulation regions will change the clamping pressure. Cellulose insulation is organic in nature; its thickness and stiffness may change appreciably over a period of time due to effects of temperature, moisture and aging. Coefficients of thermal expansion of winding conductors, supporting metallic structure and insulation are different; the coefficient for the insulation is the greatest amongst them. Also, with an increase in temperature, (solid) insulation material tends to shrink due to its decomposition processes. Furthermore, with variations in temperature, there is continuous exchange of moisture between oil and solid insulation. All these factors may reduce ultimately the mechanical strength and stiffness of the insulation, and change the natural frequencies; thus the problem of short-circuit withstand requires a thorough understanding of all the involved physical phenomena. The natural frequencies are reported to vary as a function of the square root of the ratio of the prestress value to the maximum electromagnetic stress in the winding [19].

The natural frequency of a winding may change during the short-circuit period due to changes in the insulation characteristics and the ratio of the prestress to the total stress. Thus, the natural frequencies measured from the free response may be different after a short circuit as compared to those measured prior to the short-circuit event. Also, during the short circuit a winding, which may be in resonance at some time experiencing a higher stress, may get detuned from the resonance due to a change in insulation characteristics at some other instant.

6.9 Short-Circuit Test

A short-circuit test can be performed by one of the following two techniques: the preset short-circuit method and the post-set short-circuit method. In the pre-set short-circuit test, a previously short-circuited transformer on its secondary side is energized from the primary side. If the secondary winding is the inner winding, the limb flux is low as explained in Section 5.12.2 (Figure 5.38) resulting in an insignificant transient inrush current, and the method will work well. If the primary winding is the inner one, there is substantial flux density in

the limb and hence the inrush current is superimposed on the short-circuit current. Since the inrush current flows through the primary winding only, it creates a significant ampere-turn unbalance between the primary and secondary windings resulting in high short-circuit forces. Depending upon the instant of closing and the core residual flux, the magnitude of the inrush current varies (as explained in Chapter 2). In order to reduce the inrush current and its effects during the test, the core can be deliberately premagnetized with the opposite polarity [43].

In the post-set short-circuit test method, the transformer is in the energized condition and its secondary winding is short-circuited. Naturally, this method is preferred as there are no inrush currents and the related problems, and also due to the fact that the test circuit represents typical site conditions during faults. However, the disadvantage of this method is that the short-circuit capacity of test stations has to be much higher [9, 44] than that in the first method to maintain the rated voltage across the transformer terminals (by overcoming the voltage drop across the series impedance between the source and the transformer) and establish the required value of the short-circuit current. If the source impedance is not negligible as compared to the transformer impedance, a higher voltage needs to be applied, subject to a limit of 1.15 p.u. on the no-load source voltage according to IEC standard 60076-5 (third edition: 2006-02). Thus, the required short-circuit capacity of the test station increases. The capacity should be at least 9 times the short-circuit power of the transformer for a 15% over-excitation condition [44]. The test stations may not have such capability, and hence short-circuit tests on large transformers are usually carried out by the pre-set method.

After the short-circuit test, the performance is considered satisfactory if the following conditions are met according to the IEC standard:

- results of short-circuit tests and measurements performed during tests do not indicate any condition of a fault
- routine tests including dielectric tests, repeated after the short-circuit test, are successful
- out-of-tank inspection does not indicate any displacement/deformation of the active part and/or support structures
- there are no traces of internal electrical discharges
- change in impedance is not more than 2% for any phase after the test for transformers up to 100 MVA rating. The corresponding value is 1% for ratings above 100 MVA. The more stringent requirement for large transformers is in line with the experience that a variation in the impedance of more than 1% in large power transformers indicates a large deformation in one or more windings, whereas a change in the impedance between 0.5% to 1% indicates a progressive movement of winding conductors [43].

To evaluate test results, the most important and conclusive diagnostic test seems to be the impedance measurement along with visual inspection [43], although advanced techniques like FRA (frequency response analysis), vibration measurements, dynamic oil pressure measurements, etc. are also used.

6.10 Effect of Inrush Current

As explained in Chapter 2, when a transformer is switched on, the magnitude of its inrush current depends on many factors, the predominant factors being the instant of switching and the residual magnetism in the core. The inrush current can be as high as six to eight times the rated current, and transformer users are always apprehensive about its repeated switching. Inrush transients are more frequent than short circuits and they last for a few seconds compared to the short circuits which are usually cleared in tens of milliseconds. The energized winding is subjected to the mechanical stresses during an inrush transient. Inrush currents are usually not taken very seriously from the mechanical design considerations. Inner windings have a lower value of air-core reactance. Therefore, a transformer switched from the inner winding experiences a higher inrush current. It is well-known that layer/helical windings are vulnerable to short circuits. Hence, if a transformer is switched on frequently from its inner layer/helical winding, forces generated due to the inrush currents may make it loose over a period of time; such a weakened winding becomes vulnerable during a subsequent short circuit event. When a transformer is switched from the outer HV winding having a higher air-core reactance value, the magnitude of the inrush current and the corresponding forces are lower.

Recent insulation failures in larger transformers, which were frequently energized under a no-load condition, have attracted attention of researchers. The impact of inrush currents on mechanical stresses of windings has been investigated in [45]. It is shown that the axial forces calculated with maximum possible inrush currents are of the same order of magnitude as that calculated with short-circuit currents, and hence the use of controlled switching strategies is generally recommended. In another paper [46], the force patterns under the short-circuit and inrush conditions are compared and shown to be significantly different from each other.

6.11 Split-Winding Transformers

Split-winding transformers have the advantage that splitting secondary windings into two parts obviates the need of having two double-winding transformers. There is a considerable saving in instrumentation (on the HV side) and space, since a transformer, with one HV winding and two LV windings, substitutes two double-winding transformers of half the power rating.

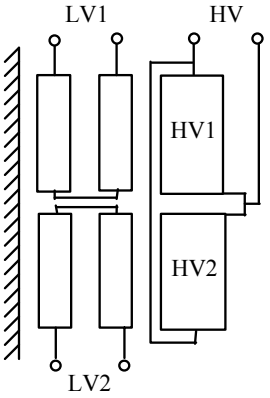

Figure 6.16 Split-winding transformer.

The arrangement also results in a considerable reduction in the values of short-circuit currents in the two separately supplied circuits, decreasing the required rating of circuit breakers. The two LV windings are placed axially with respect to each other in order to have equal impedances to the HV winding which is also split into two parts with center-line lead arrangement as shown in figure 6.16.

The split-winding arrangement requires special short-circuit design considerations. Consider the preset short-circuit method, in which a voltage is applied to the HV winding with one of the LV windings, say LV2, short-circuited. The flux density distribution is completely different in the lower and upper parts of the core limb. The flux density in the upper part is high, requiring a high value of magnetizing inrush current for the HV1 winding, whereas there is no demand for a significant magnetizing current by the HV2 winding since the flux density in the bottom part of the limb is very low due to the short-circuited inner LV2 winding. This phenomenon results into heavy distortion of fields in the core and windings of the transformer. There is considerable radial field due to an asymmetrical distribution of ampere-turns resulting into excessive axial forces and end thrusts.

The phenomenon is analyzed in [44] by means of a nonlinear magnetic model. It is recommended to do two setup tests with opposite polarity to magnetize the core in the reverse direction so that the inrush current is reduced to a harmless value during the pre-set method. If the short-circuit capacity of the test station is high enough to allow the post-set method (which eliminates the inrush currents and related problems), there is still one more characteristic of the split-winding transformer which makes the short-circuit test on it more severe than that on a conventional two-winding transformer. With the LV2 winding short-circuited, some current flows in the HV1 winding not facing directly the short-circuited LV2 winding. The current in the HV1 winding is small, in the range of 3 to 5% of that flowing in the HV2 winding [47] due to a much higher

impedance value between the HV1 and LV2 windings, but it is sufficient to cause an ampere-turn unbalance along the height of the windings. The ampere-turns of the HV2 winding are smaller than that of the LV2 winding, and corresponding to the ampere-turns of the HV1 winding there are no balancing ampere-turns in the LV1 winding (since it is open-circuited). Hence, there is a considerable distortion of the leakage field resulting into higher axial short-circuit forces [48]. For a given value of the short-circuit current, the forces are higher for the case in which only one of the LV windings is short-circuited as compared to the case when both LV windings are short-circuited. Thus, although the split-winding configuration helps in limiting the rating of circuit breakers, it poses problems for the short-circuit withstand.

The phenomenon has been accurately analyzed using coupled circuit-field simulations in [49]. The short-circuit performance of a 70-MVA, three-phase, 220/6.9/6.9-kV transformer has been analyzed under the pre-set and post-set test conditions. A 2-D axisymmetric field-circuit coupled nonlinear transient finite element model has been developed for the purpose. Also, the beneficial effect of deliberate pre-magnetization with opposite polarity is demonstrated.

6.12 Short-Circuit Withstand

The IEC 60076-5 (third edition: 2006-02) proposes that the ability to withstand dynamic effects of short circuits should be demonstrated either by a short-circuit test or by calculations/design considerations. The latter method is used if there are constraints of cost, time, logistics and test limitations [25]. In this method, the manufacturers need to provide calculations, technological choices and design margins, and demonstrate the adequacy of manufacturing processes. They have to validate dimensioning rules by reference to similar transformers which have passed the test or by reference to the tests on representative models. Comparisons of stress and strength values of the transformer with the corresponding values of the reference transformers/models should be done. The guidelines for identification of similar transformers are given in the IEC standard. This method is a sort of comprehensive design verification with involvement of the user to review material specifications, calculations of short-circuit currents and stresses for various types of faults, safety margins and quality control of manufacturing processes. The design review at different stages of design and manufacturing is important in ensuring reliability of transformers under short circuits. In order to improve the short-circuit performance of transformers, the purchaser or his representative should be involved in reviewing and assessing the quality of design and manufacturing processes at a few important stages during the execution of the whole contract. There is a lot of scope for cooperation between the transformer manufacturer and purchaser. Two major areas for cooperation are technical specifications and design review. In many cases, the purchaser may have confidence about the capability of the manufacturer based on the design review and the results of short-circuit tests on

model coils as well as full-sized transformers over a period of time. Guidelines for the demonstration of the ability of transformers to withstand dynamic effects of a short circuit are given in the IEC standard.

A short-circuit test is preferred by many purchasers to ascertain the short-circuit performance of transformers. This is because the transformer is a highly labor-intensive product and the short-circuit performance may be greatly influenced by the quality of manufacturing processes. The transformer consists of different kinds of materials whose responses to short-circuit forces are different. Two transformers having an identical design may perform differently during the short-circuit tests if the quality of manufacturing processes is not consistent. Weaknesses in design and manufacturing processes are exposed when there is a failure during the test, which may disclose some intricate failure modes based on which design and manufacturing processes can be improved. It should be remembered that, in addition to a detailed theoretical analysis with the help of advanced computational techniques, it is very much essential to correlate the results of calculations with the experimental data of short-circuit tests on transformers or their equivalent models. These tests give authentic confirmation of the assumptions or estimates of material properties, transfer of forces, clearances, etc., used in the theoretical analysis.

There are many influencing factors that determine the short-circuit stresses and withstand. These factors along with general guidelines and precautions, that can be taken at the specification, design, and production stages of transformers, are described below.

6.12.1 System configuration and transformer specification [1]

1. Limited extension of subtransmission networks thereby reducing short-circuit levels in the system.
2. High impedance grounding of the neutral of distribution and sub-transmission networks.
3. Specification of higher values of percentage impedances for critical transformers.
4. Use of transformers instead of autotransformers, if possible, even if it results in a higher cost.
5. Neutral end taps for transformers with on-load tap changing arrangement.
6. Specification of taps on more than one winding should be avoided.
7. Lower tapping range.
8. Removal of stabilizing tertiary winding from the specification for three-phase three-limb transformers up to a certain rating.
9. Specification and use of the split-winding configuration should be avoided, if possible.

The above recommendations have an impact on the power system protection and performance; hence they should be adopted after a thorough study.

6.12.2 Design

1. If the stabilizing tertiary winding is essential, its current density should be as low as possible (i.e., a massive and stiff winding).
2. For withstanding radial forces, the conductor dimensions can be chosen in such a way that the conductor can resist the compressive forces on its own, without relying on its supporting structures.
3. Whenever a CTC conductor is used for achieving lower winding stray losses and for the ease of winding, it should be epoxy-bonded to greatly enhance the resistance of the winding against buckling and tilting.
4. Windings can be made of high proof stress conductor material.
5. Use of lower current densities in windings of critical transformers.
6. Use of thicker insulating cylinders for supporting inner windings.
7. Adoption of a high slenderness ratio for the inner winding to increase its compressive strength against the radial forces.
8. Estimation of natural frequencies of windings and ensuring that there is no excited resonance.
9. Correct selection of winding arrangements to minimize short-circuit forces.
10. It is usually preferable to have taps in a separate winding and not in the body of the main winding from the short-circuit strength consideration. Further, the turns should be so arranged in the separate tap winding that when one tap-step is cut out of the circuit, the turns are uniformly removed along the height of the winding (e.g., the interleaved tap winding shown in Figure 7.15), minimizing the ampere-turn unbalance between the LV and HV windings along their height.
11. If the taps need to be provided in the body of the HV winding, their placement at its ends should be avoided. The short-circuit forces are reduced when the taps are put in the center. The forces are further reduced if they are put in two groups in the body and placed symmetrically about the center line of the winding. A relative comparison of short-circuit forces for various arrangements of tap positions is given in [10] using residual ampere-turn diagrams. The ampere-turns of the untapped winding should be reduced in the region corresponding to the tapping zone of the tap winding. The balancing of ampere-turns between the LV and HV windings in this zone should be done at the average tap position.

6.12.3 Manufacturing processes

1. Proper alignment of axially placed spacers to give adequate support to inner windings.
2. Accurate positioning of axial and radial support structures.
3. A winding should be wound tightly on the axial spacers placed on the cylinder, in which case a sufficiently thick cylinder can provide significant support to the winding for withstanding the forces that tend to buckle it.

4. Place tight-fitting wooden dowels on the core in close contact with the insulating cylinders, and radially in line with the axial supports.
5. Before use, special storage conditions are required for epoxy-bonded CTC conductors as per the supplier's instructions. Also, it is a good practice to cut a sample of the CTC conductor used for the winding, process it along with the winding, and then check its mechanical properties through a suitable testing procedure [5].
6. Strictly control manufacturing processes for windings.
7. When a double-layer winding is used to have an advantage of field cancellation due to go-and-return conductors (which reduces the associated stray losses), short-circuit forces are high both at the winding terminations and also in the leads. Hence, adequate precautions need to be taken for improving the short-circuit withstand at lead take-off points and also at the terminations. For a single-layer winding, one connection is made at the top and the other at the bottom of the winding resulting in manageable values of forces. But in this case, the route of high current leads from the winding bottom should be carefully designed to minimize the stray losses as they run parallel to the tank and other structural components before terminating on the tank cover at the top.
8. Purchase of materials from qualified suppliers with clear material specifications and quality assurance procedures.
9. Use of high density pressboard for insulation components within windings, and between windings and yokes.
10. Judicious selection of the prestress value and tight control on heights of windings with no magnetic asymmetry between them.
11. Use of clamping structures having adequate stiffness with appropriate fastening.
12. Adequate securing of leads at winding ends.
13. Adequate fastening of connections to the tap-changer and bushings.
14. Use of fiberglass reinforced clamping rings, if required.
15. Winding cylinders made of fiberglass can be used for inner windings.
16. Use of preshrunk and oil-impregnated special insulation components (e.g., angle rings/spacers).
17. Vapor phase drying of windings before the final assembly in specific cases for better dimensional control.
18. Burr-free edge rounding of spacers for eliminating the biting of the paper insulation on winding conductors.
19. Ensuring tightness of conductors in the radial direction.
20. For better sizing, windings are individually processed (heating and vacuum cycles) followed by an axial compression before the final assembly, which minimizes the possibility of any looseness in them. The designed winding height should be obtained at the final assembly stage before applying the final clamping pressure, which is achieved by inserting/removing insulation spacers (blocks).

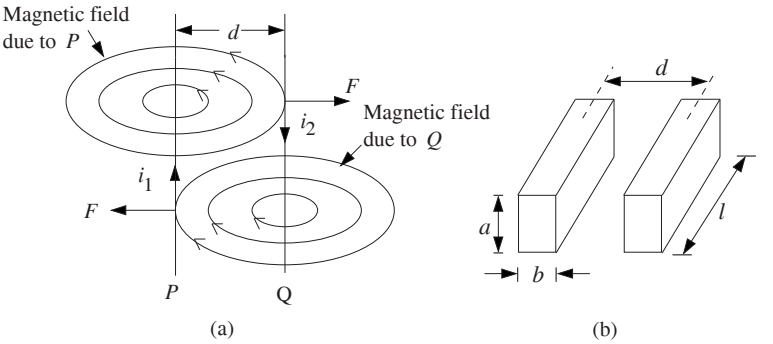

Figure 6.17 Force between parallel conductors.

Some manufacturers use an isostatic clamping process for each individual winding, in which a constant pressure value is applied on the winding uniformly and continuously throughout the drying process.

6.13 Calculation of Electrodynamic Force between Parallel Conductors

A current carrying straight conductor of length l, placed in uniform magnetic field of flux density B, experiences a mechanical force given by

$$F = B\,i\,l \sin\theta \tag{6.72}$$

where θ is the angle between the direction of the flux density vector and that of the length vector along which the current (i) flows in the conductor. Figure 6.17 (a) shows two stranded conductors (P and Q) of equal length (l) carrying currents i_1 and i_2 (in amperes), respectively, in opposite directions with a spacing of d between them (in meters). According to Fleming's left hand rule, there is a repulsive force between the conductors. If the currents are in the same direction, then the force between the conductors is attractive in nature. The force per unit length of the conductors is given by

$$f = \frac{F}{l} = \mu_0 \frac{i_1 i_2}{2\pi d} = 2\times10^{-7} \frac{i_1 i_2}{d} \text{ N/m.} \tag{6.73}$$

This is a classical formula for calculation of an electrodynamic force between two current-carrying wires. It is applicable to thin circular conductors only and is valid when the distance between the conductors is considerably larger than their dimensions. The conductors are also assumed to be rectilinear and infinitely long.

For rectangular conductors, an accurate force calculation is possible by considering the conductor cross section as a superimposition of interacting line current filaments. The force per unit length between parallel rectangular conductors shown in Figure 6.17 (b), for which $l >> d$, is

$$f = 2\times10^{-7}\,\frac{i_1 i_2}{d}\,k_s \quad \text{N/m} \tag{6.74}$$

where k_s, a function of $\left(\frac{d-b}{a+b}\right)$, is the shape factor that varies according to the dimensions and the spacing between the conductors. The value of k_s for different values of *a, b* and *d* can be obtained from the curves given in [50, 51].

In transformers, rectangular conductors/flats are used between windings and terminations. These conductors have to be supported at regular intervals to withstand short-circuit forces. Consider a rectangular conductor subjected to an electromagnetic force acting uniformly on it. Let the distance between two consecutive supports be *S*. The conductor structure, subjected to short-circuit loads, acts as a beam supported at both ends as shown in Figure 6.18. The maximum bending moment is

$$M = \frac{f S^2}{12} \tag{6.75}$$

where f is the load (force) per unit length (to be calculated by Equation 6.74).

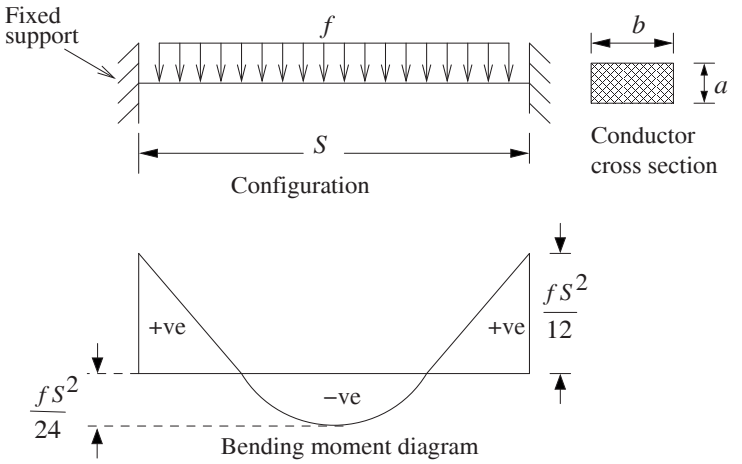

Figure 6.18 Calculation of maximum unsupported span.

Now,

$$\frac{M}{I} = \frac{\sigma}{y} \tag{6.76}$$

where $I = \frac{b\,a^3}{12}$ is the moment of inertia, $y = \frac{a}{2}$ is the maximum distance from the neutral axis for the conductor, and σ is the stress in the conductor. By putting the values of M, I and y in Equation 6.76 we obtain

$$\sigma = \frac{f\,S^2}{2\,b\,a^2} \quad \text{N/m}^2 . \tag{6.77}$$

If σ_{max} is the maximum allowable stress in the conductor in N/m^2, substituting the value of f from Equation 6.74 for the same current i (the peak value of an asymmetrical current) flowing in the two parallel conductors, we obtain the expression for the maximum allowable spacing between the consecutive supports of the conductor as

$$S = \frac{a}{i}\sqrt{1\times10^7\,\frac{\sigma_{max}\,b\,d}{k_s}} \quad \text{meters.} \tag{6.78}$$

Similarly, the maximum allowable spacing between the supports of a rectangular conductor for any other support condition can be determined.

The analysis given above is applicable for a rectilinear conductor. For more complex arrangements (e.g., bends in a conductor or two conductors in different planes), analytical formulations are possible [52]. However, any complex arrangement of conductors can be easily analyzed now using FEM.

6.14 Design of Clamping Structures

The clamping structures are provided in a transformer to prevent any movement of windings due to the forces produced at the time of a short circuit. Therefore, the clamping structures are designed such that they put the windings under a desired pressure condition. The clamping structures consist of the clamping ring, flitch plates and frames, as shown in Figure 6.19.

Stresses in clamping ring:

Bolts are provided for maintaining a constant pressure on the windings; the required pressure is applied on the clamping ring by tightening the bolts in small transformers. For large transformers, the pressure is usually applied by hydraulic jacks, and the bolts are then locked in positions or fiberglass/densified wood wedges are inserted. Under short-circuit conditions, the forces produced in the windings try to bend the portion of the ring between two consecutive bolts. The

stress on a circular clamping ring can be calculated by assuming that the structure is simply supported at the locations of the bolts. The maximum bending moment (M) and section modulus (Z) of the clamping ring are given by

$$M = \frac{F\ \pi\ D}{8\ n^2} \tag{6.79}$$

$$Z = \frac{1}{6}\ w\ t^2 \tag{6.80}$$

and the maximum bending stress is

$$\sigma_{max} = \frac{M}{Z} = \frac{6\pi F D}{8\ w\ t^2\ n^2} = \frac{3\pi F D}{4 w\ t^2\ n^2} \tag{6.81}$$

where F is the total axial force, D is the mean diameter of the ring, w is the width of the ring (half of the difference between its outer diameter and inside diameter), t is the thickness of the ring, and n is the number of clamping points.

If the stress on the clamping ring is calculated by assuming fixed-beam conditions, the bending stress is given by

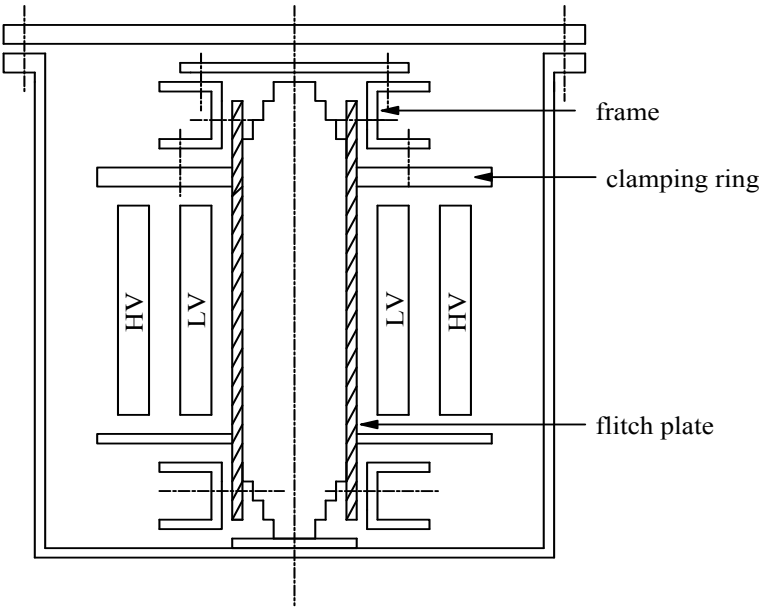

Figure 6.19 Clamping elements.

$$\sigma_{max} = \frac{6\pi F D}{12\, w\, t^2\, n^2} = \frac{\pi F D}{2\, w\, t^2\, n^2}. \tag{6.82}$$

The stress calculated by Equation 6.81 is higher than that calculated by Equation 6.82. For the design purpose, the stress can be calculated by assuming the boundary condition as the average of the simply supported and fixed beam conditions, for which $M = \pi F D/(10 n^2)$ and

$$\sigma_{max} = \frac{6\pi F D}{10\, w\, t^2\, n^2} = \frac{3\pi F D}{5\, w\, t^2\, n^2} \tag{6.83}$$

the value of which should be within the limits based on material properties and the required factor of safety.

Stresses in flitch plates and frames:

A flitch plate should be designed for withstanding the clamping force and the core-winding weight (static loads). During a short circuit, the axial forces (end thrusts) developed in windings, act on the top and bottom frames; flitch plates help to keep the frames in position. The stresses produced in the flitch plates are tensile stresses and shearing stresses. These stresses can be calculated by well-known formulae used in structural analyses.

The frames are subjected to stresses while lifting the core-winding assembly, during clamping of windings, or due to short-circuit end thrusts. Usually, short-circuit stresses decide their dimensions. The stresses in the frames are determined from the calculated values of short-circuit forces acting on them and assuming the core bolt points and locking arrangements (pins, etc.) between flitch plates and frames as support locations.

References

1. Bergonzi, L., Bertagnolli, G., Cannavale, G., Caprio, G., Iliceto, F., Dilli, B., and Gulyesil, O. Power transmission reliability, technical and economic issues relating to the short circuit performance of power transformers, *CIGRE 2000*, Paper No. 12-207.
2. Bertula, T., Nordman, H., Saunamaki, Y., and Maaskola, J. Short circuit stresses in three-limb transformers with delta connected inner winding during single-phase faults, *CIGRE 1980*, Paper No. 12-03.
3. Anderson, P. M. *Analysis of faulted power systems*, Iowa State University Press, 1976.
4. Stevenson, W. D. *Elements of power system analysis*, Fourth Edition, McGraw-Hill Book Company, 1982.

5. Babare, A., Bossi, A., Calabro, S., Caprio, G., and Crepaz, S. Electromagnetic transients in large power step-up transformers: some design and testing problems, *CIGRE 1990*, Paper No. 12-207.
6. Arturi, C. M. Force calculations in transformer windings under unbalanced mmfs by a non-linear finite element code, *IEEE Transactions on Magnetics*, Vol. 28, No. 2, March 1992, pp. 1363–1366.
7. Sollergren, B. Calculation of short circuit forces in transformers, *Electra*, Report no. 67, 1979, pp. 29–75.
8. Salon, S., LaMattina, B., and Sivasubramaniam, K. Comparison of assumptions in computation of short circuit forces in transformers, *IEEE Transactions on Magnetics*, Vol. 36, No. 5, September 2000, pp. 3521–3523.
9. Bertagnolli, G. *Short circuit duty of power transformers — The ABB approach*, Golinelli Industrie Grafiche, Italy, 1996.
10. Waters, M. *The short circuit strength of power transformers*, Macdonald and Co. Ltd., London, 1966.
11. Boresi, A. P. and Schmidt, R. J. *Advanced mechanics of materials*, John Wiley & Sons, Inc., Sixth Edition, Printed in the USA, 2003.
12. Srinath, L. S. *Advanced mechanics of solids,* Tata McGraw-Hill Publishing Company Limited, Second Edition, New Delhi, 2005.
13. Waters, M. The measurement and calculation of axial electromagnetic forces in concentric transformer windings, *Proceedings IEE*, Vol. 101, Pt. II, February 1954, pp. 35–46.
14. Norris, E. T. Mechanical strength of power transformers in service, *Proceedings IEE*, Vol. 104, February 1957, pp. 289–306.
15. McNutt, W. J., Johnson, W. M., Nelson, R. A., and Ayers, R. E. Power transformer short circuit strength: requirements, design and demonstration, *IEEE Transactions on Power Apparatus and Systems*, Vol. PAS-89, No. 8, November/December 1970, pp. 1955–1969.
16. McNutt, W. J. Short circuit characteristics of transformers, *IEEE Summer Meeting*, Portland, July 1976, Paper No. CH1159-3/76, pp. 30–37.
17. Watts, G. B. A mathematical treatment of the dynamic behavior of a power transformer winding under axial short circuit forces, *Proceedings IEE*, Vol. 110, No. 3, March 1963, pp. 551–560.
18. Patel, M. R. Dynamic response of power transformers under axial short circuit forces, Part I: winding and clamp as individual components, *IEEE Transactions on Power Apparatus and Systems*, Vol. PAS-92, September/October 1973, pp. 1558–1566.
19. Patel, M. R. Dynamic response of power transformers under axial short circuit forces, Part II: windings and clamps as a combined system, *IEEE Transactions on Power Apparatus and Systems*, Vol. PAS-92, September/October 1973, pp. 1567–1576.
20. Swihart, D. O. and Wright, D. V. Dynamic stiffness and damping of transformer pressboard during axial short circuit vibration, *IEEE*

Transactions on Power Apparatus and Systems, Vol. PAS-95, No. 2, March/April 1976, pp. 721–730.
21. Allan, D. J., Pratt, F. C., Sharpley, W. A., and Woollard, M. E. The short circuit performance of transformers — A contribution to the alternative to direct testing, *CIGRE 1980*, Paper No. 12-02.
22. Tournier, Y., Richard, M., Ciniero, A., Yakov, S., Madin, A. B., and Whitaker, J. D. A study of the dynamic behavior of transformer windings under short circuit conditions, *CIGRE 1964*, Report No. 134.
23. Hori, Y. and Okuyama, K. Axial vibration analysis of transformer windings under short circuit conditions, *IEEE Transactions on Power Apparatus and Systems,* Vol. PAS-99, No. 2, March/April 1980, pp. 443–451.
24. Quinney, D. A. Dynamic response of a power transformer winding under axial short circuit conditions, *Proceedings IEE*, Vol. 128, Pt. B, No. 2, March 1981, pp. 114–118.
25. Macor, P., Robert, G., Girardot, D., Riboud, J. C., Ngnegueu, T., Arthaud, J. P., and Chemin, E. The short circuit resistance of transformers: The feedback in France based on tests, service and calculation approaches, *CIGRE 2000*, Paper No. 12-102.
26. Lakhiani, V. K. and Kulkarni, S. V. Short circuit withstand of transformers — A perspective, *International Conference on Transformers*, *TRAFOTECH — 2002*, Mumbai, India, January 2002, pp. 34–38.
27. Steel, R. B., Johnson, W. M., Narbus, J. J., Patel, M. R., and Nelson, R. A. Dynamic measurements in power transformers under short circuit conditions, *CIGRE 1972*, Paper No. 12-01.
28. Thomson, H. A., Tillery, F., and Rosenberg, D. U. The dynamic response of low voltage, high current, disk type transformer windings to through fault loads, *IEEE Transactions on Power Apparatus and Systems*, Vol. PAS-98, No. 3, May/June 1979, pp. 1091–1098.
29. Boersma, R. and Wildboer, J. The short-circuit strength of the inner windings of transformers against radial forces, *CIGRE 1962*, Paper No. 147.
30. Crandall, S. H. and Dahl, N. C. *An introduction to the mechanics of solids,* McGraw-Hill, Inc., New York, 1978, p. 209.
31. Bakshi, A. and Kulkarni, S. V. Towards short-circuit proof design of power transformers, *The International Journal for Computation and Mathematics in Electrical and Electronic Engineering, COMPEL*, Vol. 31, No. 2, 2012, pp. 692–702.
32. Timoshenko, S. *Theory of elastic stability,* McGraw-Hill, New York, 1936.
33. Saravolac, M. P., Vertigen, P. A., Sumner, C. A., and Siew, W. H. Design verification criteria for evaluating the short circuit withstand capability of transformer inner windings, *CIGRE 2000*, Paper No. 12-208.
34. Kojima, H., Miyata, H., Shida, S., and Okuyama, K. Buckling strength analysis of large power transformer windings subjected to electromagnetic

force under short circuit, *IEEE Transactions on Power Apparatus and Systems,* Vol. PAS-99, No. 3, May/June 1980, pp. 1288–1297.
35. Patel, M. R. Dynamic stability of helical and barrel coils in transformers against axial short circuit forces, *Proceedings IEE*, Vol. 127, Pt. C, No. 5, September 1980, pp. 281–284.
36. Patel, M. R. Instability of the continuously transposed cable under axial short circuit forces in transformers, *IEEE Transactions on Power Delivery,* Vol. 17, No. 1, January 2002, pp. 149–154.
37. Bakshi, A. and Kulkarni, S. V. Eigenvalue analysis for investigation of tilting of transformer winding conductors under axial short-circuit forces, *IEEE Transactions of Power Delivery*, Vol. 26, No. 4, 2011, pp.2505–2512.
38. Wang, X., Yu, S., Zhao, Q., Wang, S., Tang, R., and Yuan, X. Effect of helical angle of winding in large power transformer, *Sixth International Conference on Electrical Machines and Systems, ICEMS* 2003, Vol. 1, pp. 355–357.
39. Janic, Z., Valkovic, Z., and Stih, Z. Helical winding's magnetic field in power transformers, Springer-Verlag 2009, pp. 161–166.
40. Madin, A. B. and Whitaker, J. D. The dynamic behavior of a transformer winding under axial short circuit forces: An experimental and theoretical investigation, *Proceedings IEE*, Vol. 110, No. 3, 1963, pp. 535–550.
41. Gee, F. W. and Whitaker, J. D. Factors affecting the choice of prestress applied to transformer windings, *IEEE Summer General Meeting*, Toronto, Canada, 1963, Paper No. 63-1012.
42. Dobsa, J. and Pirktl, E. Transformers and short circuits, *Brown Boveri Review*, Vol. 52, No. 11/12, November/December 1965, pp. 821–830.
43. Janssen, A. L. J. and te Paske, L. H. Short circuit testing experience with large power transformers, *CIGRE 2000*, Paper No. 12-105.
44. Leber, G. Investigation of inrush currents during a short circuit test on a 440 MVA, 400 kV GSU transformer, *CIGRE 2000*, Paper No. 12-104.
45. Steurer, M. and Frohlich, K. The impact of inrush currents on the mechanical stress of high voltage power transformer coils, *IEEE Transactions on Power Delivery*, Vol. 17, No. 1, January 2002, pp. 155–160.
46. Adly, A. A. Computation of inrush current forces on transformer windings, *IEEE Transactions on Magnetics,* Vol. 37, No. 4, July 2001, pp. 2855–2857.
47. Stuchl, P., Dolezel, I., Zajic, A., Hruza, J., and Weinberg, O. Performance of transformers with split winding under nonstandard operating conditions, *CIGRE 2000*, Paper No. 12-103.
48. Foldi, J., Berube, D., Riffon, P., Bertagnolli, G., and Maggi, R. Recent achievements in performing short circuit withstand tests on large power transformers in Canada, *CIGRE 2000*, Paper No. 12-201.

49. Kumbhar, G. B. and Kulkarni, S. V. Analysis of short circuit performance of split-winding transformer using coupled field-circuit approach, *IEEE Transactions on Power Delivery,* Vol. 22, No. 2, April 2007, pp. 936–943.
50. Dwight, H. B. *Electrical coils and conductors*, First Edition, McGraw-Hill Book Company Inc., New York, 1945.
51. Rodstein, L. *Electrical control equipment*, MIR Publishers, Moscow, Translated in English by G. Roberts, 1974.
52. Charles, E. D. Mechanical forces on current-carrying conductors, *Proceedings IEE*, Vol. 110, No. 9, September 1963, pp. 1671–1677.

7

Surge Phenomena in Transformers

For designing the insulation system of a transformer for withstanding overvoltage tests, voltage stresses within its windings need to be determined. For this purpose, voltage distributions within the transformer windings for the specific test voltages are calculated. For AC test voltages at power frequency, the voltage distribution is linear with respect to the number of turns and can be calculated exactly. For the calculation of the impulse voltage distribution in the windings, they are required to be simulated in terms of an equivalent circuit consisting of lumped R, L and C elements. A number of accurate methods are reported in the literature for the computation of the response of the windings to voltages, some of which are discussed in this chapter. Electric stresses in the insulation within and outside the windings are obtained by analytical or numerical techniques which are described in the next chapter.

7.1 Initial Voltage Distribution

When a step voltage impinges on the transformer winding terminals, the initial distribution in the winding depends on the capacitances between turns, between windings, and those between windings and ground. The winding inductances have no effect on the initial voltage distribution since the magnetic field requires a finite amount of time to build up as the current through an inductor cannot be established instantaneously. Thus, the inductances practically do not carry any current, and the voltage distribution is predominantly decided by the capacitances in the network, and the problem can be considered as an entirely electrostatic one. In other words, the presence of series capacitances between winding sections causes the transformer to respond to abrupt impulses as a network of capacitances for all frequencies above its lower natural frequencies

of oscillations. When the applied voltage is maintained for a sufficiently long time (50 to 100 microseconds), appreciable currents begin to flow in the inductances eventually leading to the uniform voltage distribution. Since there is difference between the initial and final voltage distributions, as shown in Figure 7.1, a transient phenomenon takes place. During this transient period, there is continual interchange of energy between electric and magnetic fields. On account of a low damping factor of the transformer windings, the transient is oscillatory. The voltage at any point in the winding oscillates about the final voltage value, reaching a maximum as shown by curve c. It is obvious that the strength of the transformer windings to lightning voltages can be significantly increased if the difference between the initial and final distributions can be minimized. This not only reduces the excessive stresses at the line end but also mitigates the oscillations thereby keeping the voltage to ground at any point in the winding insignificantly higher than the final voltage distribution.

The differential equation governing the initial voltage distribution $u_0 = u(x,0)$, for the representation of a winding shown in Figure 7.2 (wherein inductive effects are neglected), is [1]

$$\frac{d^2 u_0}{dx^2} - \frac{c_g}{c_s} u_0 = 0 . \tag{7.1}$$

In Figure 7.2, L_s, c_g and c_s denote the self inductance per unit length, the shunt capacitance per unit length to ground, and the series capacitance per unit length between adjacent turns, respectively.

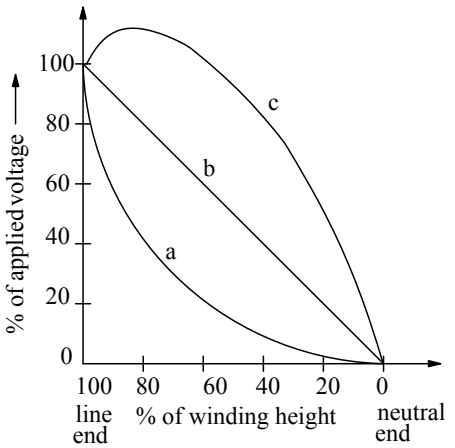

(a) initial distribution (b) final distribution (c) maximum voltage to ground

Figure 7.1 Impulse voltage distribution.

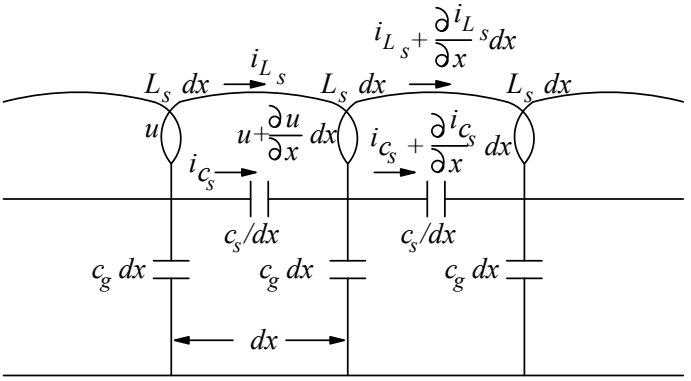

Figure 7.2 Impulse response: representation of a transformer winding.

Solution of the above equation is given by

$$u_0 = A_1 e^{kx} + A_2 e^{-kx} \tag{7.2}$$

where

$$k = \sqrt{\frac{c_g}{c_s}}\,. \tag{7.3}$$

The constants of integration A_1 and A_2 can be obtained from the boundary conditions at the line and neutral ends of the winding. For a solidly grounded neutral, we have $u_0 = 0$ for $x = 0$. Putting these values in Equation 7.2 we have

$$A_1 + A_2 = 0 \text{ or } A_1 = -A_2\,.$$

At the line end, $x = L$ (L is the winding axial length) and $u_0 = U$ (the amplitude of the step impulse voltage) giving,

$$U = A_1 e^{kL} + A_2 e^{-kL} = A_1\left(e^{kL} - e^{-kL}\right)$$

$$\therefore A_1 = -A_2 = \frac{U}{e^{kL} - e^{-kL}}\,. \tag{7.4}$$

Substituting the above expression in Equation 7.2 we obtain

$$u_0 = U\frac{e^{kx} - e^{-kx}}{e^{kL} - e^{-kL}} = U\frac{\sinh kx}{\sinh kL}\,. \tag{7.5}$$

The initial voltage gradient at the line end of the winding is given by

$$\left[\frac{du_0}{dx}\right]_{x=L} = \left[U\,\frac{k\cosh kx}{\sinh kL}\right]_{x=L} = U\,\frac{k\cosh kL}{\sinh kL} = k\,U\coth kL\,. \tag{7.6}$$

The initial voltage gradient is maximum at the line end. Since $kL > 3$ in practice, $\coth kL \cong 1$, giving the initial gradient at the line end for a unit amplitude surge ($U = 1$) as

$$\left[\frac{du_0}{dx}\right]_{max} = k\,. \tag{7.7}$$

The uniform gradient for the unit amplitude surge is $1/L$.

$$\left[\frac{du_0}{dx}\right]_{\max} = \frac{1}{L}\,k\;L = \frac{1}{L}\sqrt{\frac{c_g}{c_s}}\;\;L = \frac{1}{L}\sqrt{\frac{c_g L}{c_s/L}} = \frac{1}{L}\sqrt{\frac{C_G}{C_S}} = \frac{1}{L}\,\alpha \tag{7.8}$$

where C_G and C_S are the total ground capacitance and series capacitance of the transformer winding, respectively. The ratio $\sqrt{C_G/C_S}$ has been denoted by the distribution constant α. Thus, the maximum initial gradient at the line end is α times the uniform gradient. The higher the value of the ground capacitance is, the higher the values of α and voltage stresses at the line end.

For an isolated neutral condition, the boundary conditions,

$$\frac{du_0}{dx} = 0 \text{ at } x = 0 \text{ and } u_0 = U \text{ at } x = L$$

give the following expression for the initial voltage distribution:

$$u_0 = U\,\frac{\cosh kx}{\cosh kL}\,. \tag{7.9}$$

For the isolated neutral condition, the maximum initial gradient at the line end can be written as

$$\left[\frac{du_0}{dx}\right]_{x=L} = k\;U\;\tanh kL\,. \tag{7.10}$$

For a unit amplitude surge and $(\alpha = kL) > 3$, $\tanh kL \cong 1$. Hence, the initial gradient becomes

$$\left[\frac{du_0}{dx}\right]_{max} = k = \frac{\alpha}{L}\,. \tag{7.11}$$

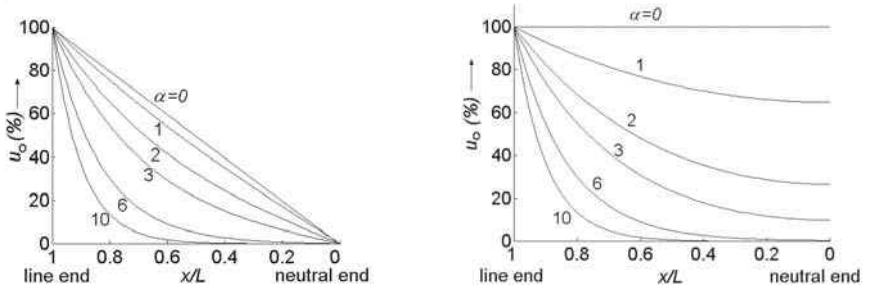

(a) Grounded neutral (b) Isolated neutral

Figure 7.3 Initial voltage distribution.

Hence, the value of the maximum initial gradient at the line end is the same for the grounded and isolated neutral conditions for abrupt impulses or very steep wave fronts. The initial voltage distribution for various values of α is plotted in Figure 7.3 for the grounded and isolated neutral conditions. The total series capacitance (C_S) and ground capacitance (C_G) of the transformer winding predominantly decide the initial stresses in it for steep fronted voltage surges. C_S consists of interturn capacitances and interdisk/intersection capacitances of the winding, whereas C_G includes the capacitance between the winding and the core/tank/other windings. Thus, the initial voltage distribution is characterized by the distribution constant,

$$\alpha = \sqrt{\frac{C_G}{C_S}} \,. \tag{7.12}$$

This parameter indicates the degree of deviation of the initial voltage distribution from the final linear voltage distribution which is decided solely by winding inductances. The higher the value of α, the higher are the deviations and amplitudes of oscillations which occur between the initial and final voltage distributions. For a conventional continuous disk winding, the value of α may be in the range of 5 to 30. Any change in the transformer design, which decreases the distribution constant of the winding, results in more uniform voltage distribution and reduces the voltage stresses between different parts of the winding. The initial voltage distribution of the winding can be made closer to the ideal linear distribution ($\alpha = 0$) by increasing its series capacitance and / or reducing its capacitance to ground. If the ground capacitance is reduced, more current flows through the series capacitances, tending to make the voltage across the various winding sections more uniform. The (ideal) uniform initial impulse voltage distribution will be achieved if no current flows through the (shunt) ground capacitances. Usually, it is very difficult and less cost effective to reduce

the ground capacitances. Insulation gaps between windings predominantly decide the ground capacitances. These capacitances depend on the radial gap and the circumferential area between the windings. These geometrical quantities are usually fixed from electrical design considerations. Hence, any attempt to decrease the distribution constant α by decreasing the ground capacitance is definitely limited. A more cost-effective way is to increase the winding series capacitance by using different types of windings as described in subsequent sections.

7.2 Ground Capacitance Calculations

In order to estimate the voltage distribution within a transformer winding subjected to impulse overvoltages, the knowledge of its effective series and ground capacitances is essential. The calculation of the capacitance between a winding and ground or between two windings is straightforward. The capacitance between two concentric windings (or between the innermost winding and the core) is given by

$$C_{gw} = \frac{\varepsilon_0 \pi D_m H}{\left(t_{oil}/\varepsilon_{oil}\right) + \left(t_{solid}/\varepsilon_{solid}\right)} \tag{7.13}$$

where D_m is the mean diameter of the gap between the two windings, t_{oil} and t_{solid} is thicknesses of the oil and the solid insulation between the two windings respectively, and H is the height of the windings (if the heights of the windings are unequal, the average height is taken in the calculation).

The capacitance between a cylindrical conductor and a ground plane is given by (Appendix D, Equation D30)

$$C = \frac{2\pi\varepsilon H}{\cosh^{-1}\left(\frac{s}{R}\right)} \tag{7.14}$$

where R and H are the radius and the length of the cylindrical conductor, respectively, and s is distance of the center of the cylindrical conductor from the plane. Hence, the capacitance between the outermost winding and the tank is

$$C_{gt} = \frac{2\pi\varepsilon_0 H}{\cosh^{-1}\left(\frac{s}{R}\right)} \left[\frac{t_{oil} + t_{solid}}{\left(t_{oil}/\varepsilon_{oil}\right) + \left(t_{solid}/\varepsilon_{solid}\right)}\right]. \tag{7.15}$$

In this case, R and H represent the radius and the height of the winding, respectively, and s is the distance of the winding axis from the tank. The capacitance between the outermost windings of two phases is half the value

given by Equation 7.15, with *s* equal to half the value of the distance between the axes of the two windings (refer to Equation D28).

7.3 Capacitance of Windings

7.3.1 Development of winding methods for better impulse response

In the initial days of transformer technology development for higher voltages, the use of electrostatic shields was quite common (see Figure 7.4). A non-resonating transformer with electrostatic shields was reported in [2, 3, 4]. It is a very effective shielding method in which the effect of the ground capacitance of an individual section is neutralized by the corresponding capacitance to the shield. Thus, the currents in the shunt (ground) capacitances are supplied from the shields and none of them have to flow through the series capacitances of the winding. If the series capacitances along the windings are made equal, uniform initial voltage distribution can be achieved. The electrostatic shield is at the line terminal potential and hence must be insulated from the winding and the tank along its height. As voltage ratings and corresponding dielectric test levels increased, it became increasingly difficult and cumbersome to design the shields. They were found to be less cost effective since extra space and material were required for insulating shields from other electrodes inside the transformer. Subsequent development of interleaved windings phased out completely the use of electrostatic shields. However, the principle of electrostatic shielding is regularly used in the form of static end rings at the line end of high voltage windings and static rings within the windings, which improve the voltage distributions and reduce the stresses locally.

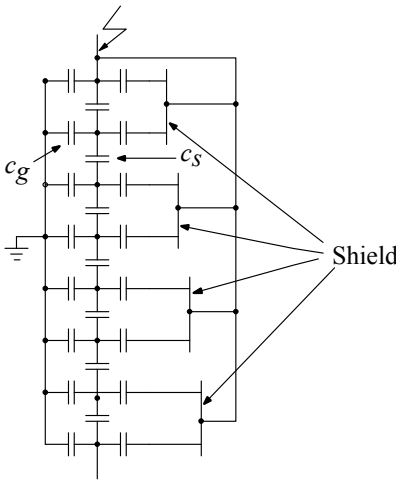

Figure 7.4 Electrostatic shields.

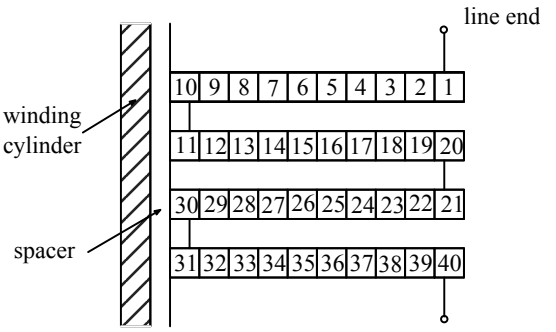

Figure 7.5 Continuous winding.

In order to understand the effectiveness of an interleaved winding, let us first analyze a continuous (disk) winding shown in Figure 7.5. The total series capacitance of the continuous winding is an equivalent of all turn-to-turn and disk-to-disk capacitances. Although the capacitance between two adjacent turns is high, all the turn-to-turn capacitances are in series, which results in a much smaller capacitance value for the entire winding. Similarly, all disk-to-disk capacitances which are also in series, add up to a small value. With an increase in the voltage class, the insulation between turns and between disks has to be increased which further worsens the total series capacitance.

An inherent disadvantage of a low series capacitance value of the continuous winding was overcome by electrostatic shielding as explained earlier until the advent of the interleaved winding. The original interleaved winding was introduced and patented by G. F. Stearn in 1950 [5]. A simple disposition of turns in some particular ways increases the series capacitance of the interleaved winding to such an extent that near uniform initial voltage distribution can be obtained. A typical interleaved winding is shown in Figure 7.6.

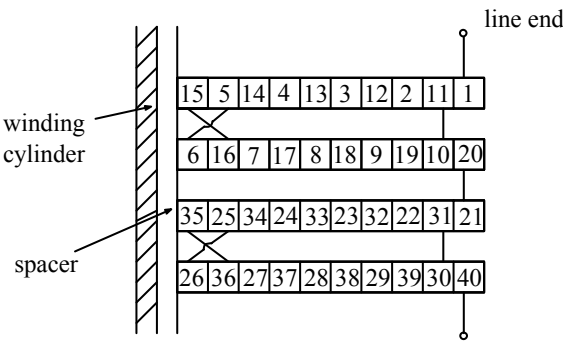

Figure 7.6 Interleaved winding.

In an interleaved winding, two consecutive electrical turns are separated physically by a turn which is electrically much farther along the winding. It is wound as a conventional continuous disk winding but with two conductors. The radial position of the two conductors is interchanged through a crossover between them at the inside diameter and appropriate conductors are joined at the outside diameter, thus forming a single circuit two-disk coil. The advantage is obvious since it does not require any additional space as in the case of complete electrostatic shielding or part electrostatic shielding (static rings). In interleaved windings, not only the series capacitance is increased significantly but the ground capacitance is also somewhat reduced because of improvement in the winding space factor. This is because the insulation within the winding in the axial direction can be reduced due to improvement in the voltage distribution, which reduces the winding height and hence the ground capacitance. Therefore, the distribution constant (α) is reduced significantly lowering stresses between various parts of the winding.

It can be seen from Figure 7.6 that the normal working voltage between adjacent turns in an interleaved winding is equal to voltage per turn times the turns per disk. Hence, one may feel that a much higher amount of turn insulation may be required, thus questioning the effectiveness of the interleaved winding. However, due to significant improvement in the voltage distribution, stresses between turns are reduced by a great extent so that the percent safety margins for the impulse stress and the normal working stress can be made of the same order. Hence, the turn-to-turn insulation is used in an effective way [6]. Since the voltage distribution is more uniform, the number of special insulation components (e.g., disk angle rings) along the winding height reduces. When a winding has more than one conductor per turn, the conductors are also interleaved as shown in Figure 7.7, for a winding with 6 turns per disk and two parallel conductors per turn, to obtain maximum benefit.

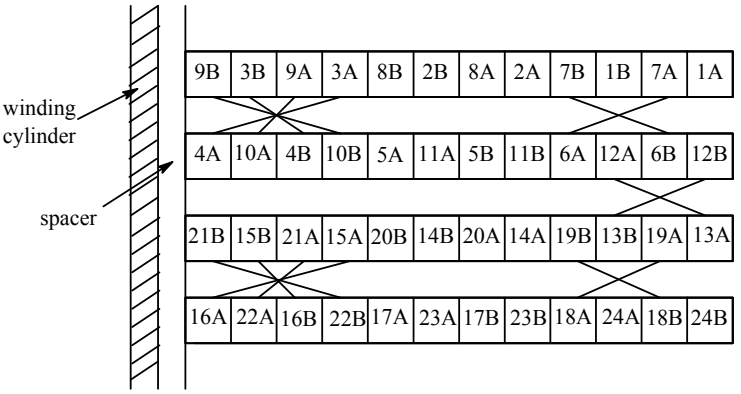

Figure 7.7 Interleaving with 2-parallel conductors per turn.

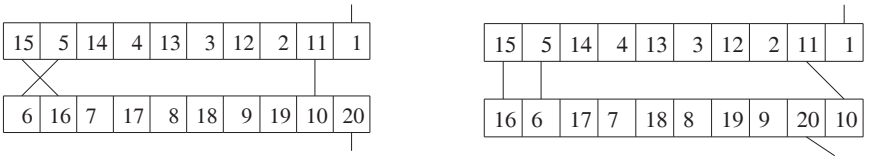

(a) Stern winding (b) Nuys winding

Figure 7.8 Two types of crossovers in interleaved winding.

In [7], the reason for improved surge characteristics of interleaved windings is explained using transmission line-like representation of the disks. There can be two types of interleaved windings with regard to the crossover connections at the inside diameter as shown in Figure 7.8. When steep impulse waves such as chopped waves or front-of-waves enter an interleaved winding, a high oscillatory voltage appears locally between turns at the center of the radial build of the disk. This phenomenon is analyzed in [8, 9] for these two types of crossovers used in the interleaved windings.

7.3.2 Turn-to-turn and disk-to-disk capacitances

For determining series capacitances of different types of windings, the calculations of turn-to-turn and disk-to-disk capacitances are essential. The turn-to-turn capacitance is given by

$$C_T = \frac{\varepsilon_0 \varepsilon_p \times \pi D_m \ (w + t_p)}{t_p} \tag{7.16}$$

where D_m is the average diameter of the winding, w is the bare width of the conductor in the axial direction, t_p is the total paper insulation thickness (both sides), ε_0 is the permittivity of free space, and ε_p is the relative permittivity of the paper insulation. The term t_p has been added to the conductor width to take into account fringing effects.

Similarly, the total axial capacitance between two consecutive disks based on geometrical considerations only is given by

$$C_{DA} = \varepsilon_0 \left[\frac{k}{t_p/\varepsilon_p + t_s/\varepsilon_{oil}} + \frac{1-k}{t_p/\varepsilon_p + t_s/\varepsilon_s} \right] \times \pi \ D_m \left(R + t_s \right) \tag{7.17}$$

where R is the winding radial depth, t_s and ε_s is the thickness and the relative permittivity of the solid insulation (radial spacers between disks) respectively, and k is the ratio of the area occupied by the oil to the total circumferential area. The term t_s is added to R to take into account fringing effects.

For the continuous winding and its variations (with static end rings/static rings between disks), there are two approaches for calculating the series capacitance. In the first approach, the voltage is assumed to be evenly distributed within the disk winding, which makes the calculation easy. However, this is a major approximation for continuous disks having low effective interturn series capacitance. The second approach, in which linear voltage distribution is not assumed within the disks for the capacitance calculation, is accurate [10, 11, 12]. The corresponding representation of capacitances for this method is shown in Figure 7.9. The total series capacitance of the winding is given by [10, 13]

$$C_S = \frac{\left[\frac{2C_{DA}}{\alpha_d}\left(\tanh 2\alpha_d\right)\right]\left[\frac{\sqrt{2}\ C_{DA}}{\alpha_d}\left(\tanh\sqrt{2}\ \alpha_d\right)\right]}{\frac{4\ C_{DA}}{\alpha_d}\left(\tanh 2\alpha_d\right)+\left(N_{DW}-2\right)\frac{\sqrt{2}\ C_{DA}}{\alpha_d}\left(\tanh\sqrt{2}\ \alpha_d\right)} \tag{7.18}$$

where C_{DA} = disk-to-disk capacitance calculated based on geometrical considerations

α_d = distribution constant of a disk = $\sqrt{\dfrac{C_{DA}}{C_T/(N_D-1)}}$

C_T = turn-to-turn capacitance

N_D = number of turns per disk

N_{DW} = number of disks in the winding.

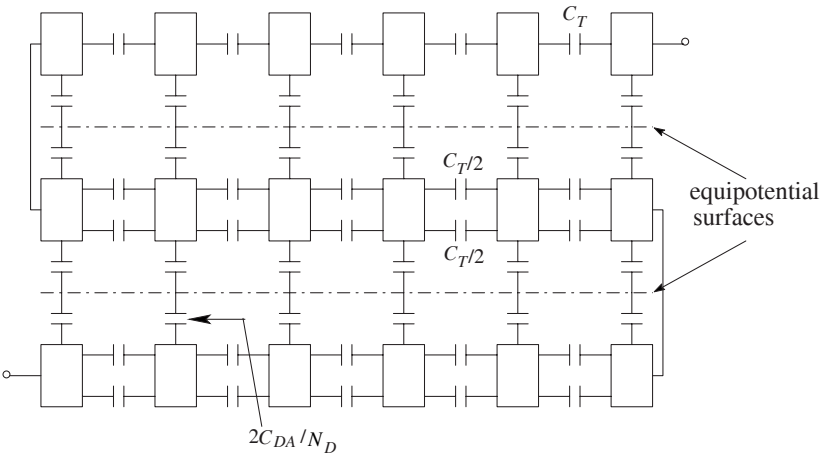

Figure 7.9 Representation of capacitances of a continuous winding.

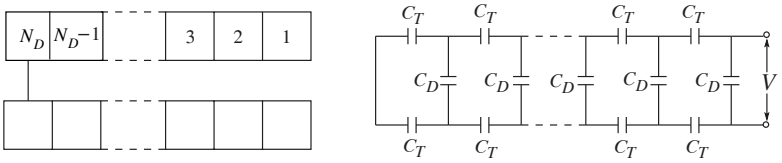

Figure 7.10 Disk-pair of a continuous winding.

The first approach, in which linear voltage distribution is assumed for capacitance calculations, is definitely approximate for continuous windings. The total series capacitance of a disk is low and also the disk-to-disk capacitance (C_{DA}) is appreciable, making the distribution constant α_d for the disk larger. Hence, the voltage distribution within any disk and within the winding is non-linear. However, the approach is easier and the expressions obtained for the capacitances of various types of windings can be easily compared. The approach is used in the following subsections for the calculation of the series capacitance of various windings including continuous windings.

7.3.3 Continuous disk winding

Let us determine the capacitance of a disk pair of a continuous winding shown in Figure 7.10 with the assumption of linear voltage distribution. The term C_T denotes the capacitance between touching turns and C_D denotes the capacitance between a turn of one disk and the corresponding turn of the other disk. If N_D is the number of turns per disk, the number of interturn capacitances (C_T) in each disk is $(N_D - 1)$. Also, the number of intersection capacitances (C_D) between the two disks is $(N_D - 1)$. The series capacitance of the disk winding is the resultant of the interturn (turn-to-turn) and interdisk (disk-to-disk) capacitances. The voltage per turn for the disk pair shown in Figure 7.10 is $(V / 2N_D)$. Using the principle that the sum of energies in the individual capacitances within the disk pair gives its entire energy, the following Equation can be written:

$$\frac{1}{2} C_T \left(\frac{V}{2N_D} \right)^2 2(N_D - 1) = \frac{1}{2} C_{TR} V^2$$

where C_{TR} = resultant interturn capacitance.

$$\therefore C_{TR} = \frac{C_T}{2N_D{}^2} (N_D - 1). \tag{7.19}$$

Now, the voltages across the first, second, and third interdisk capacitances (C_D) from the inside diameter are

$$\left(\frac{2\,V}{2\,N_D}\right),\ \left(\frac{4\,V}{2\,N_D}\right),\ \text{and}\ \left(\frac{6\,V}{2\,N_D}\right),\ \text{respectively.}$$

Hence, the expression for the voltage across C_D at the outside diameter is $2\,(N_D-1)\dfrac{V}{2\,N_D}$. The total energy stored by all such capacitances is

$$En=\frac{1}{2}\,C_D\left[\left(\frac{2\,V}{2\,N_D}\right)^2+\left(\frac{4\,V}{2\,N_D}\right)^2+\left(\frac{6\,V}{2\,N_D}\right)^2+\ldots+\left(\frac{2\,(N_D-1)\,V}{2\,N_D}\right)^2\right]. \tag{7.20}$$

Simplifying and using the identity: $1^2+2^2+3^2+\cdots+(n-1)^2=\dfrac{n(n-1)(2n-1)}{6}$

we obtain

$$En=\frac{(N_D-1)\,(2\,N_D-1)\,C_D\,V^2}{12\,N_D}=\frac{1}{2}\,C_{DR}\;V^2 \tag{7.21}$$

where C_{DR} is the resultant interdisk capacitance.

$$\therefore C_{DR}=\frac{(N_D-1)\,(2N_D-1)\,C_D}{6\,N_D}. \tag{7.22}$$

Instead of using the lumped parameter approach for the interdisk capacitances, if they are represented by a distributed capacitance C_{DU} (i.e., capacitance per unit radial depth based on the geometrical considerations only), the value of the resultant interdisk capacitance for a radial depth of *R* can be calculated as [14]

$$C_{DR}=\frac{C_{DU}\;R}{3}=\frac{C_{DA}}{3}. \tag{7.23}$$

The previous two Equations are equivalent, because if the number of turns per disk is much greater than 1 ($N_D>>1$), Equation 7.22 becomes

$$C_{DR}\cong N_D\;C_D/3=C_{DU}\;R/3.$$

The resultant series capacitance of the disk pair is given as the addition of the resultant interturn capacitance and the resultant interdisk capacitance,

$$C_{se}=\frac{C_T}{2N_D{}^2}\,(N_D-1)+\frac{C_D}{6N_D}\,(N_D-1)\,(2N_D-1) \tag{7.24}$$

or

$$C_{se} = \frac{C_T}{2N_D{}^2}\left(N_D - 1\right) + \frac{C_{DU}\ R}{3} \quad \cdots \textit{Continuous disk winding}. \tag{7.25}$$

Now, if there are N_{DW} disks in the winding, the resultant interdisk capacitance $(C_{DR})_W$ for the entire winding (with voltage V_W across it) can be calculated as

$$\frac{1}{2}\left(C_{DR}\right)_W V_W^2 = \frac{1}{2}(C_{DR})\left(\frac{V_W}{N_{DW}/2}\right)^2 \left(N_{DW} - 1\right). \tag{7.26}$$

$$\therefore \left(C_{DR}\right)_W = \frac{4\left(N_{DW} - 1\right)}{N_{DW}^2}\ C_{DR}\,. \tag{7.27}$$

Noting the fact that the expression for C_{TR} given by Equation 7.19 is for two disks, the total series capacitance for the entire winding with N_{DW} disks can be obtained by using Equations 7.19 and 7.27,

$$C_S = \frac{C_T}{N_{DW}\ N_D{}^2}\left(N_D - 1\right) + \frac{4\left(N_{DW} - 1\right)}{N_{DW}^2}\ C_{DR}\,. \tag{7.28}$$

The above expression gives the value of capacitance close to that given by Equation 7.18 for the values of disk distribution constant α_d close to 1 (almost linear distribution within a disk). For $N_{DW}, N_D >> 1$, Equation 7.28 becomes

$$C_S \cong \frac{1}{N_{DW}}\left[\frac{C_T}{N_D} + 4\ C_{DR}\right]. \tag{7.29}$$

7.3.4 Continuous winding with SER and SR

As mentioned earlier, the concept of electrostatic shielding is used in the form of a static end ring (SER) at the line end or a static ring (SR) between disks as shown in Figure 7.11.

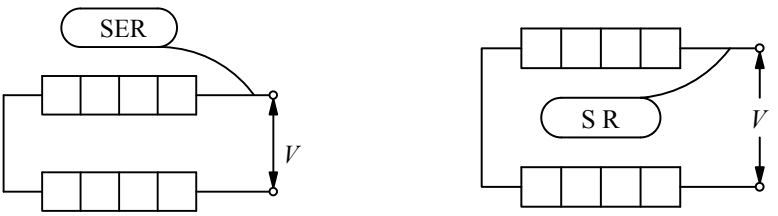

Figure 7.11 Static end ring (SER) and static ring (SR).

By providing a large equipotential surface with a good corner radius, SER reduces the stress concentration at the line end. It also improves the effective series capacitance at the line end as explained below. The closer the location of SER to the line end disk, the greater the increase in the series capacitance value is. This results in reduction of stresses appearing within the line end disk.

Let us calculate the series capacitance of a disk pair with SER as per the method given in [14]. SER is usually connected to the first turn of the winding by means of a pig-tail; hence the potential of SER is fixed to that of the line terminal (V) as shown in Figure 7.12. Let the winding radial depth be denoted by R.

The voltage at any point x of the upper section representing SER is

$$V_1(x) = V \tag{7.30}$$

and the voltage at any point x of the lower section representing the first disk is

$$V_2(x) = \frac{V}{2} + \frac{V}{2}\left[\frac{R-x}{R}\right] = V\frac{(2R-x)}{2R}. \tag{7.31}$$

Let C_{SU} be the capacitance between SER and the first disk per unit depth of the winding (based on the geometrical considerations only). Therefore, the energy stored in the capacitance C_{SU} per unit depth at point x is

$$En_x = \frac{1}{2}C_{SU}[V_1(x) - V_2(x)]^2. \tag{7.32}$$

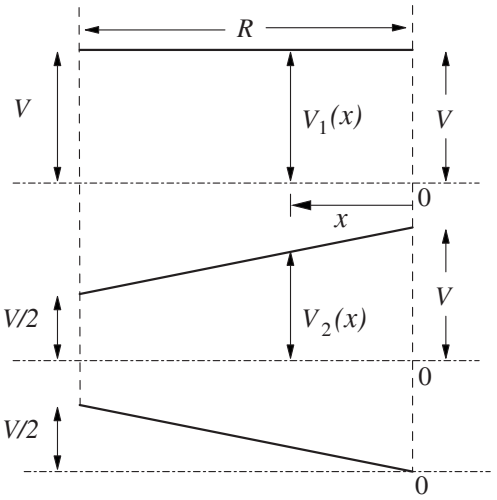

Figure 7.12 Calculation of the capacitance between SER and the line end disk.

The total energy stored by the capacitance between the first disk and SER is

$$En = \int_0^R En_x \, dx = \int_0^R \frac{1}{2} C_{SU} [V_1(x) - V_2(x)]^2 \, dx . \tag{7.33}$$

Substituting the values of $V_1(x)$ and $V_2(x)$ from Equations 7.30 and 7.31, and simplifying we obtain

$$En = \int_0^R \frac{1}{2} C_{SU} \left[V \frac{x}{2R} \right]^2 dx = \frac{1}{2} \frac{1}{12} C_{SU} \; R \, V^2 . \tag{7.34}$$

Thus, the resultant capacitance, C_{SER}, between SER and the first disk can be given by the equation

$$\frac{1}{2} C_{SER} \, V^2 = \frac{1}{2} \frac{1}{12} C_{SU} \; R \; V^2 . \tag{7.35}$$

$$\therefore C_{SER} = \frac{C_{SU} \; R}{12} . \tag{7.36}$$

Thus, the resultant capacitance between SER and the first disk is $(1/12)$ times the capacitance obtained from the geometrical consideration.

Using Equations 7.25 and 7.36, the total series capacitance of the disk pair with SER is therefore given by

$$C_{se} = \frac{C_T}{2N_D{}^2} (N_D - 1) + \frac{C_{DU} \; R}{3} + \frac{C_{SU} \; R}{12} \quad \cdots \quad with \; SER . \tag{7.37}$$

Similarly, the expression for the series capacitance of a disk-pair with SR (shown in Figure 7.11) can be determined as

$$C_{se} = \frac{C_T}{2N_D{}^2} (N_D - 1) + \frac{C_{SU} \; R}{12} + \frac{7 \; C_{SU} \; R}{12} \quad \cdots \quad with \; SR \tag{7.38}$$

where the first, second, and third terms on the right hand side of Equation 7.38 represent the interturn capacitances, the first disk to SR capacitance, and SR to the second disk capacitance, respectively. It is assumed that the gap between the first disk and SR is equal to the gap between SR and the second disk.

7.3.5 Interleaved winding

As explained earlier, an interleaved winding results in a considerable increase of series capacitance. In this type of winding, geometrically adjacent turns are kept far away from each other electrically, so that the voltage between adjacent turns

increases. By interleaving the turns in such a way, the initial voltage distribution can be made nearly uniform. The capacitances between the disks (interdisk capacitances) have very little effect on the series capacitance of this type of winding since its value is relatively low. Therefore, it is sufficient to consider only the interturn capacitances for the calculation of the series capacitance of interleaved windings. It follows that the second approach of the capacitance calculation based on the assumption of linear voltage distribution will be accurate for the interleaved windings as compared to the continuous windings.

For the interleaved winding shown in Figure 7.6, the number of interturn capacitances per disk is $(N_D - 1)$. The total number of the interturn capacitances in a disk-pair is $2(N_D - 1)$. As before, let V be the voltage applied across the terminals of the disk-pair. The voltage is assumed to be uniformly distributed over the disk-pair; the assumption is more appropriate for interleaved windings as explained earlier. The number of electrical turns between the first and second turns is 10, while that between the second and third turns is 9. This arrangement repeats alternately within the disks. Hence, for a disk-pair, the voltage across the N_D capacitances is $(V/2)$ and across the remaining $(N_D - 2)$ capacitances is $\left(\frac{N_D - 1}{N_D}\ \frac{V}{2}\right)$. The energy stored in the disk-pair is given by

$$En = \frac{1}{2} C_T \left(\frac{V}{2}\right)^2 N_D + \frac{1}{2} C_T \left[\frac{(N_D - 1)}{2N_D} V\right]^2 (N_D - 2) = \frac{1}{2} C_{se} V^2 .$$

$$\therefore\ C_{se} = \frac{C_T}{4}\left[N_D + \left(\frac{N_D - 1}{N_D}\right)^2 (N_D - 2)\right] \quad . \tag{7.39}$$

For $N_D >> 1,$ the expression simplifies to

$$C_{se} = \frac{C_T}{2}[N_D - 1] \quad \cdots \textit{interleaved winding} . \tag{7.40}$$

The interleaving of turns can give a substantial increase in the series capacitance and hence interleaved windings are used widely in high voltage transformers. As the rating of power transformers increases, higher core diameters are used increasing the voltage per turn value. Hence, a high voltage winding of a large rating transformer has usually lower turns and correspondingly lower turns per disk as compared to a high voltage winding of the same voltage class in a lower rating transformer. Since the interleaved windings are more effective for higher turns per disk, they may not be attractive for use in high-voltage high-rating transformers. Added to this, as the rating increases, the current carried by the high voltage winding increases,

necessitating the use of a large number of parallel conductors for controlling the winding eddy loss. An interleaved winding with a large number of parallel conductors is difficult from the productivity point of view. Hence, shielded-conductor (wound-in-shields) technology is adopted in high voltage windings of large power transformers. This is because the continuously transposed cable (CTC) conductor, which is ideally suited for such applications (as explained in Chapter 4), can be used with this technology.

7.3.6 Shielded-conductor winding

A shielded-conductor winding gives a modest but sufficient increase in the series capacitance and is less labor intensive as compared to an interleaved winding. The number of shielded conductors can be gradually reduced in the shielded disks from the line end, giving a possibility of achieving a tapered capacitance profile to match the voltage stress profile along the winding height [15]. This type of winding has some disadvantages, viz. reduction in the winding space factor, requirement of extra winding material (shields), disturbance in ampere-turn balance per unit height of the LV and HV windings, and an extra eddy loss in the shields.

Let us calculate the total series capacitance of a shielded-conductor disk-pair shown in Figure 7.13. For N_D turns per disk with an applied voltage of V across the disk-pair, the voltage per turn is $V/(2N_D)$. It is assumed that for shields also, the same value of voltage per turn is applicable. Out of N_D turns, the first k turns are shielded in each disk. The shield can be either floating or it can be connected to some turn. Here, the shield conductors are assumed to be floating. For the first disk the voltage of any turn is

$$V_c(i) = V - (i-1)\frac{V}{2N_D} \quad i = 1, 2, \cdots, N_D . \tag{7.41}$$

The voltage of i^{th} shield turn is (the 1st shield takes the average potential of V/2):

$$V_s(i) = \frac{V}{2} - (i-1)\frac{V}{2N_D} \quad i = 1, 2, \cdots, k . \tag{7.42}$$

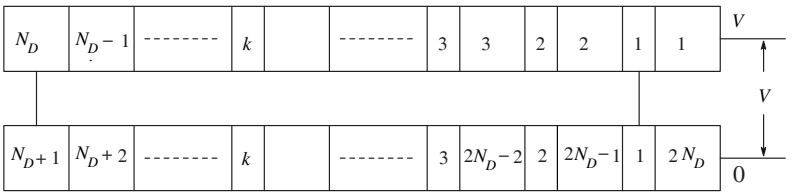

Figure 7.13 Shielded-conductor winding.

If C_{sh} denotes the capacitance between a shield turn and an adjacent disk turn, the energy between a shield turn *i* and its adjacent disk turns is

$$En_{s1} = \frac{1}{2} C_{sh} \left[\left(V_c(i) - V_s(i) \right)^2 + \left(V_c(i+1) - V_s(i) \right)^2 \right]. \tag{7.43}$$

Using the expressions from Equations 7.41 and 7.42 we obtain

$$En_{s1} = \frac{1}{2} C_{sh} \left\{ \left(\frac{V}{2} \right)^2 + \left(\frac{V}{2} - \frac{V}{2N_D} \right)^2 \right\}. \tag{7.44}$$

Similarly for the second disk, voltages of i^{th} turn and i^{th} shield are given by

$$V_c(i) = V - (2N_D - i + 1) \frac{V}{2N_D} \qquad i = 1, 2, \cdots, N_D \tag{7.45}$$

$$V_s(i) = \frac{V}{2} + (i-1) \frac{V}{2N_D} \qquad i = 1, 2, \cdots, k\,. \tag{7.46}$$

The energy between a shield turn *i* and its adjacent disk turns for the second disk can be similarly calculated as

$$En_{s2} = \frac{1}{2} C_{sh} \left\{ \left(\frac{-V}{2} \right)^2 + \left(-\frac{V}{2} + \frac{V}{2N_D} \right)^2 \right\}. \tag{7.47}$$

There are $2 \times (N_D - k - 1)$ turn-to-turn capacitances and the energy stored in each of these capacitances is

$$En_T = \frac{1}{2} C_T \left(\frac{V}{2N_D} \right)^2. \tag{7.48}$$

The expression for the energy between consecutive disks can be given by using Equations 7.21 and 7.23 as

$$En_D = \frac{1}{2} \frac{C_{DU} R}{3} V^2. \tag{7.49}$$

For the shielded-conductor winding shown in Figure 7.13, there is no contribution to the energy by the capacitances between the shield turns of the two disks at same radial depth, since their potentials are equal. For a precise calculation, the radial depth in the above equation should correspond to the radial depth of the winding excluding that of the shield turns. The total energy stored in the disk-pair with shielded-conductors is

$$En = k\, En_{s1} + k\, En_{s2} + 2 \left(N_D - k - 1 \right) En_T + En_D \tag{7.50}$$

using which the effective capacitance of the disk-pair can be calculated. A similar procedure can be followed if, through an electrical connection, the shield is attached to some potential instead of being in the floating condition. The calculation of capacitances of a shielded-conductor winding has been verified in [15] by a circuit model and also by measurements on a prototype model.

7.3.7 Layer winding

For a simple layer (spiral) winding shown in Figure 7.14, wherein an individual turn may have a number of parallel conductors depending upon the current rating, the series capacitance can be determined as follows.

Let C_T be the interturn (turn-to-turn) capacitance and N_W be the total number of turns in the winding. As before, the voltage is assumed to be uniformly distributed within the winding. The energy stored in the winding is equal to the sum of the energies stored in the individual capacitances,

$$En = \frac{1}{2} C_T \left(\frac{V}{N_W} \right)^2 (N_W - 1) = \frac{1}{2} C_S V^2 . \tag{7.51}$$

$$\therefore C_S = \frac{C_T (N_W - 1)}{{N_W}^2} \cong \frac{C_T}{N_W} \quad \cdots \quad \textit{layer winding} . \tag{7.52}$$

For a helical winding (a layer winding with radial spacers between turns), the above equation applies with C_T calculated by using Equation 7.16 with the consideration of the proportion of the area occupied by the spacers (solid insulation) and the oil.

7.3.8 Interleaved tap winding

In high-voltage high-rating transformers, when a spiral winding is used as a tap winding, the tap sections are interleaved as shown in Figure 7.15. The tap winding consists of 8 circuits (steps) giving a voltage difference between adjacent turns either corresponding to a one-circuit difference or a two-circuit difference. Thus, if there are 10 turns per circuit, the voltage difference between touching turns is either equal to 10 or 20 times the voltage per turn. This higher voltage difference necessitates the use of higher paper insulation reducing the interturn capacitance, but the reduction is more than compensated by an increased capacitive effect due to a higher voltage between the turns.

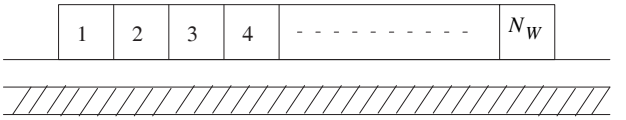

Figure 7.14 Layer winding.

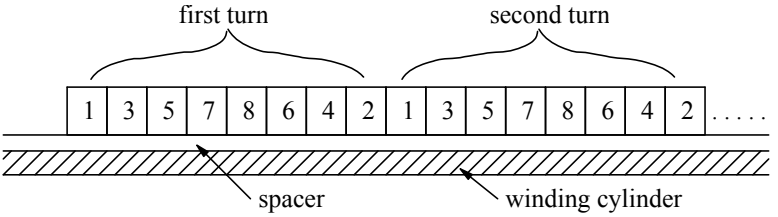

Figure 7.15 Interleaved tap winding.

Let us calculate the value of series capacitance of an interleaved winding having 8 circuits with 10 turns per circuit, giving a total number of 80 turns for the tap winding. Assuming again that the voltage is uniformly distributed within the tap winding with the voltage per turn as $V/80$, the energy stored in the winding is

$$En = 10\left\{6\left[\frac{1}{2}C_T\left(2\times10\times\frac{V}{80}\right)^2\right]+\frac{1}{2}C_T\left(10\times\frac{V}{80}\right)^2\right\}+9\left\{\frac{1}{2}C_T\left(9\times\frac{V}{80}\right)^2\right\}. \tag{7.53}$$

Simplifying and equating it to $(1/2)\,C_S\,V^2$, we obtain the effective series capacitance of the interleaved tap winding as

$$C_S \cong 4\,C_T\,. \tag{7.54}$$

Comparing this value of the series capacitance with that of the layer winding having 80 turns as given by Equation 7.52, it can be seen that the series capacitance has increased by about 320 times. The series capacitance for any other interleaved tap winding, with different turns per circuit and number of circuits, can be easily calculated by following the above procedure.

The method presented until now for the calculation of series capacitance of windings is based on the stored energy. There are few other methods reported in the literature. A rigorous analytical method is presented in [16] to calculate the equivalent series capacitance of windings. The method is also used to determine natural frequencies and internal oscillations of windings.

Analytical methods have a disadvantage that fringing effects and corresponding stray capacitances cannot be accurately taken into account. In this respect, numerical methods like FEM can give an accurate value of the capacitance. In the FEM analysis also, the capacitance is calculated from the stored energy (*En*) as

$$C = \frac{2\ En}{V^2}\,. \tag{7.55}$$

The procedure is similar to that of the leakage inductance calculation by the FEM analysis as described in Chapter 3.

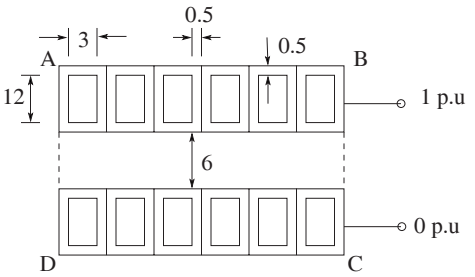

Figure 7.16 Capacitance calculation by FEM analysis.

The series capacitance of a disk-pair of a continuous disk winding and an interleaved winding is now calculated by FEM for the geometry shown in Figure 7.16 (dimensions are in mm). The gap between the two disks is 6 mm. There are 6 turns per disk, and uniform voltage distribution is assumed. The relative permittivities of oil and paper insulation are taken as 2.2 and 3.5, respectively. The geometry is enclosed in a rectangular boundary at a distance of 1 meter from the disks on all sides, so that the boundary conditions do not affect the potential distribution in the disks. The energy is calculated for the rectangular area ABCD. The values of the capacitance per unit length calculated by the analytical formulae (Equations 7.25 and 7.40) and the FEM analysis are given in Table 7.1.

7.4 Inductance Calculation

The insulation design based on only initial voltage distribution (with inductances neglected) may be acceptable for transformers of smaller voltage ratings. The difference between the initial and final (linear) distributions sets up oscillations in the winding. According to Weed's principle [17], a winding will be non-oscillating if the capacitive (initial) and inductive (final) distributions are alike; otherwise the difference will set up an oscillation under conditions favorable to it, and such an oscillation may result into much larger voltage gradients between different parts of the winding. Hence, the voltage distribution under impulse conditions should be calculated with the inclusion of inductances in the winding representation.

Table 7.1 Capacitance Calculation by Analytical Method and FEM Analysis

	Continuous winding	Interleaved winding
Analytical	57.4 pF/m	1006.8 pF/m
FEM	61.8 pF/m	1073.4 pF/m

The mutual inductance between two coaxial coil loops (A and B) of radii R_A and R_B with a distance S between them is given in SI units as [15, 18, 19]

$$L_{AB} = \frac{2\mu_0}{k} N_A N_B \sqrt{R_A R_B} \left\{ \left[1 - \frac{k^2}{2} \right] K(k) - E(k) \right\} \tag{7.56}$$

where

$$k = \sqrt{\frac{4R_A R_B}{(R_A + R_B)^2 + S^2}} \tag{7.57}$$

and N_A and N_B are the turns in sections A and B respectively, whereas $K(k)$ and $E(k)$ are the complete elliptic integrals of the first and second kinds respectively. The formula is applicable for thin circular filaments of negligible cross section. For circular coils of rectangular cross section, more accurate calculations can be done by using Lyle's method in combination with Equation 7.56 [20, 21].

The self inductance of a single turn circular coil of square cross section with an average radius of a and a square side length c is given in SI units as [15, 20]

$$L_{AA} = \mu_0 \, a \left[\frac{1}{2} \left(1 + \frac{1}{6} \left(\frac{c}{2a} \right)^2 \right) ln \left(\frac{8}{(c/2a)^2} \right) - 0.84834 + 0.2041 \left(\frac{c}{2a} \right)^2 \right]. \tag{7.58}$$

The formula applies to a relatively small cross section such that $(c/2a) < 0.2$. If the cross section is not square, it should be divided into a number of square cross sections, and then Equations 7.56 and 7.58 can be used to compute the self inductance.

The calculated self and mutual inductances should be reasonably accurate. Any difference between the calculated and measured results is mainly due to effects of field distortions and variations within the core at high frequencies [22]. For accurate results the field equations need to be solved which may not be practical. Hence, in practice, correction factors are applied to the formulae for self and mutual inductances.

Some formulations reported in the literature use customary short-circuit inductances (which are more easily and accurately calculated) in place of self and mutual inductances [23, 24]. Some others [25] use the network of inductances derived through the theory of magnetic networks, which avoids the introduction of mutual inductances in the network of lumped parameters.

7.5 Standing Waves and Traveling Waves

The transient response of a winding subjected to impulse waves was initially obtained in the literature by two different methods: the standing wave approach and the traveling wave approach. The theory of electrical waves in transmission lines cannot be directly applied to transformers due to the fact that a transformer, unlike a transmission line, has series capacitances and mutual inductances between winding sections.

Consider a single layer winding having self inductance (L_s) per unit length, shunt capacitance (c_g) per unit length to ground and series capacitance (c_s) per unit length between adjacent turns (see Figure 7.2). In this model, the mutual inductance between turns and the winding resistance are neglected for the purpose of simplifying the calculations. The set of differential equations describing the transient process taking place in the winding can be obtained by applying Kirchhoff's laws as (notations according to Figure 7.2)

$$\frac{\partial i_{L_s}}{\partial x} + \frac{\partial i_{c_s}}{\partial x} = -c_g \frac{\partial u}{\partial t} \tag{7.59}$$

$$i_{c_s} = -c_s \frac{\partial^2 u}{\partial x \partial t} \tag{7.60}$$

$$\frac{\partial u}{\partial x} = -L_s \frac{\partial i_{L_s}}{\partial t}. \tag{7.61}$$

By eliminating the currents, the above three equations can be reduced to a single differential equation in terms of voltage as

$$\frac{\partial^2 u}{\partial x^2} - L_s c_g \frac{\partial^2 u}{\partial t^2} + L_s c_s \frac{\partial^4 u}{\partial t^2 \partial x^2} = 0. \tag{7.62}$$

The solution of Equation 7.62 gives the transient voltage distribution inside the winding. Let us assume its solution in the following form [4, 26],

$$u = U e^{j\omega t} e^{j\psi x}. \tag{7.63}$$

Since the solution contains exponential terms in both time and space, it includes both standing and traveling waves.

In the standing wave approach, the expression of the assumed solution is put in Equation 7.62 which after simplification becomes

$$\psi^2 - L_s c_g \omega^2 - L_s c_s \omega^2 \psi^2 = 0. \tag{7.64}$$

$$\therefore \psi = \sqrt{\frac{L_s c_g \omega^2}{1 - \omega^2 L_s c_s}} \tag{7.65}$$

$$\omega = \frac{\psi}{\sqrt{L_s c_g \left(1 + \frac{c_s}{c_g}\psi^2\right)}}. \tag{7.66}$$

It can be seen from Equations 7.65 and 7.66 that both space frequency (ψ : the number of standing wave cycles within the space interval of 2π) and angular frequency (ω) are related to each other. With $\psi \to \infty$, the critical angular frequency of the winding is obtained as

$$\omega_{cr} = \lim_{\psi \to \infty} \frac{\psi}{\sqrt{L_s c_g \left(1 + \frac{c_s}{c_g}\psi^2\right)}} = \frac{1}{\sqrt{L_s c_s}}. \tag{7.67}$$

This is the highest frequency in time with which the winding is capable of oscillating. It is equal to the natural frequency of a single turn with its inductance L_s and capacitance c_s.

In the classical standing wave theory, the oscillations between the initial and final voltage distributions are resolved into a series of standing waves or harmonics both in space and time [1, 27, 28]. A study of the oscillations throughout the transition period from the initial to final distribution allows the calculation of the surge voltage distribution within the winding. In this approach, the waveshapes and the frequencies of standing waves (i.e., eigenfunctions or natural modes) of the winding, not connected to any source, are determined for various terminal conditions. The natural frequencies of these free oscillations are computed and the voltage distribution for each harmonic is obtained. The amplitudes of all these standing waves are then obtained for the applied wave shape, and the transient voltage distribution along the winding is finally obtained as the sum of all harmonics, a convergent infinite series. The contribution of each harmonic depends on its wave shape and natural frequency, and on its amplitude. The amplitude in turn depends on the difference between the initial and final distributions. Initially, mutual inductances were totally or partly neglected simplifying the analysis. Later on, the effect of mutual inductances was also included [29] for more accurate determination of the standing waves.

In the traveling wave theory, the incident wave is represented as an infinite series of sinusoidal components, and the resulting differential equation is analyzed to determine the conditions under which these waves can enter the winding. The method was explained in [26, 30] by its application to windings having uniformly distributed insulation, and for incoming surges with vertical wave fronts and infinite tails. The traveling wave-based analysis is superior and computationally less intensive than that based on the standing wave theory. The

solution of the original differential Equation 7.62 is assumed in the traveling wave theory as [26]

$$u = Ue^{j\omega(t-\frac{x}{v})} \tag{7.68}$$

which describes traveling waves. These waves oscillate with frequency ω and propagate at velocity v through the winding. The above solution and the previously assumed solution (Equation 7.63) are equivalent for $\psi = (-\omega/v)$. By substituting Equation 7.68 into Equation 7.62 and differentiating we obtain

$$-\left(\frac{\omega}{v}\right)^2 + L_s c_g \omega^2 + L_s c_s \omega^2 \left(\frac{\omega}{v}\right)^2 = 0 . \tag{7.69}$$

Solution of the above equation gives the velocity of propagation as

$$v = \sqrt{\frac{1}{L_s c_g} - \frac{c_s}{c_g}\omega^2} . \tag{7.70}$$

Equation 7.70 indicates that as the angular frequency (ω) increases, the velocity of the traveling wave (v) decreases. For

$$\omega_{cr} = \frac{1}{\sqrt{c_s L_s}} \tag{7.71}$$

the velocity of propagation is zero, which means at $\omega \geq \omega_{cr}$ the traveling waves cannot propagate inside the winding.

In the case of standing waves, for $\omega > \omega_{cr}$, ψ in Equation 7.65 becomes imaginary and the solution according to Equation 7.63 is transformed into

$$u = Ue^{j\omega t}e^{-\xi x} \tag{7.72}$$

where

$$\psi = j\xi = j\sqrt{\frac{L_s c_g \omega^2}{c_s L_s \omega^2 - 1}} . \tag{7.73}$$

Thus, for supercritical frequencies ($\omega > \omega_{cr}$), no standing or traveling waves exist within the winding; there is an exponential attenuation of the voltage from the winding terminal towards the interior.

A transformer winding can propagate only those oscillations having a frequency below a certain critical value. The traveling wave generally gets flattened as it travels into the winding. Unlike in transmission lines, there is no simple relationship between the wavelength and the frequency for a wave traveling through the transformer winding, and hence it cannot penetrate into the winding without distortion. Due to the presence of mutual inductances and series

capacitances between sections of the transformer winding, the form of the wave changes continuously as it penetrates inside the winding; the phenomenon is contrary to that of transmission lines, where a wave having any shape propagates without distortion, except for attenuation due to the effect of resistances. A traveling wave does not change its shape when its velocity is independent of frequency, and all natural oscillations have the same decay coefficient [31]. While both these conditions are approximately satisfied for a transmission line (and the waveshape is maintained), these are not satisfied for a transformer resulting in a major distortion of traveling waves inside the winding. Higher frequency oscillations cannot penetrate deeply into the winding and establish a standing exponential distribution (i.e., exponential attenuation of voltage from the terminal towards the interior) similar to the initial distribution of the standing wave analysis [3]. In other words, the high frequency components form a standing potential distribution and the low frequency components form a traveling wave; the splitting of incoming surge into two parts is the characteristics of the traveling wave theory. In [32], the standing wave and traveling wave approaches are compared and correlated.

The traveling component moves along the winding conductor with a velocity governed by the fundamental equation,

$$v = \frac{1}{\sqrt{\mu \varepsilon}} = \frac{c}{\sqrt{\mu_r \varepsilon_r}} \text{ m/s} \tag{7.74}$$

where μ and ε are the permeability and permittivity of the medium, respectively,

$$\mu = \mu_0 \mu_r = 4\pi \times 10^{-7} \mu_r \text{ H/m}, \qquad \varepsilon = \varepsilon_0 \varepsilon_r = 8.85 \times 10^{-12} \varepsilon_r \text{ F/m},$$

$$c = \text{velocity of light} = 3 \times 10^8 \text{ m/s}.$$

Hence, for an oil-cooled transformer with $\varepsilon_r = 3.5$ (a typical value of the resultant dielectric constant of an oil-paper-solid insulation system) and $\mu_r = 1$, the velocity of travel of a wave into the winding will be approximately equal to 160 m/μs.

7.6 Methods for Analysis of Impulse Distribution

Although the surge response of transformer windings was initially determined by the standing wave and traveling wave theories, which helped in understanding and visualizing the surge phenomena, these methods have a disadvantage in that they can basically be applied only to a uniform winding. Non-uniformities within windings, the presence of more than one winding per limb, windings of other phases, etc. are some of the complexities that cannot be handled by them. Hence, it is impractical to do the analysis by purely analytical

means for increasingly complicated present-day transformers. With the advent of computers, it became possible to solve differential equations numerically and analyze practical transformer winding configurations. A lumped parameter network is particularly well-suited for solution by computers. Using the Laplace transform, analysis of a ladder network having a finite number of uniform winding sections was done in [33]. Subsequently, the network is solved by using both digital and analog computers in [24]. The digital computer is used to calculate the coefficients of simultaneous integrodifferential equations which are then solved by an electronic analog computer. Numerical analysis reported in [22] uses the Runge–Kutta method to solve a second order differential equation representing a winding. In [34], differential equations formulate an equivalent network of a winding using a state space approach.

In [35], the transient response is calculated using a trapezoidal rule of integration through a companion network approach. It is easier to analyze a network for transient response calculations if there are no mutual couplings. Hence, the equivalent network with coupled elements is replaced by that with uncoupled elements by using the formulation given in [36]. The two circuits (coupled and uncoupled) are equivalent and have the same nodal admittance matrix. An advantage of using the companion network is that it can be analyzed using well-known methods since it is a purely resistive circuit.

The equivalent circuit representation is popularly used for finding the response of a transformer winding to high voltage surges. During transients, the windings are coupled by electric and magnetic fields. The inductances (self and mutual) and capacitances are distributed along the windings. The transients can be described by partial differential equations, but their solution is difficult. If the windings are subdivided into sections in which inductances and capacitances are lumped, the calculation becomes easier since the partial differential equations can be now replaced, with a close approximation, by ordinary simultaneous differential equations. These equations can be solved by numerical analysis using computers for complex configurations of windings. The accuracy of results obtained using the circuit representation depends predominantly on the degree of sophistication used in the winding representation. In one of the most accurate representations, each turn of the winding is represented with corresponding turn-to-turn capacitances and inductances [37]. The knowledge of interturn voltages is important for transformers subjected to very fast transient overvoltages. Such a model, although very accurate, is computationally demanding. Hence, from a practical point of view, many simplifications are done in the detailed model. A sufficient accuracy can be obtained with a network model in which the windings are lumped into R, L and C circuit components. The windings are represented by as many elements as there are disks or groups of disks with corresponding resistances, inductances (self and mutual) and capacitances (series and ground). Thus, the equivalent lumped parameter network is a series of Π circuits with mutual magnetic couplings. In such a simplified model, although an individual turn voltage cannot be

ascertained, disk voltages can be determined which can be used to decide the internal insulation between disks in the winding. Actually, the voltage stresses are the result of electric and magnetic fields which appear in the winding under surge conditions and are function of their location and time. By representing the transformer winding as a network of elements, the field problem is effectively converted into a circuit problem.

An equivalent network for a multiwinding transformer has been reported in [19] in which the conventional ladder network used for a single winding consisting of lumped elements (self and mutual inductances, series and ground capacitances) is extended for multiple windings. The method takes into account electrostatic and electromagnetic combinations of windings and therefore permits the analysis of not only the voltage response of the winding to which an impulse is applied but also transferred voltages to other windings. It is very important to calculate the transferred voltages in the case of HV windings with centerline lead arrangement. With both the ends of the LV winding grounded, the voltage at their center height (the mid-height position) of the LV winding could be oscillating and the net voltage difference between the LV and the HV windings at the center height could be more than the applied impulse magnitude. In such a case, the gap between the LV and HV windings has to be accordingly decided. A transferred surge in two-winding transformers has four components, viz. the electrostatic component decided by a network of capacitances, the electromagnetic component due to mutual inductances between windings, free oscillations of the secondary winding, and forced oscillations of the secondary winding induced by the free oscillations of the primary winding. For the free oscillations of the secondary winding, the transferred electrostatic component represents the initial distribution and the electromagnetic component represents the final distribution. These four components are also present at the terminals of the secondary and tertiary windings when the primary winding is subjected to an impulse overvoltage condition in a three-winding transformer. In [38, 39], surge transfers in three-winding transformers have been analyzed in detail. It is shown that the third and fourth components are usually insignificant and their effect is not important. The electrostatic component can be reduced to a great extent if the secondary/tertiary winding terminals are connected to an equipment (e.g., a cable of sufficient length) having a high capacitance value to ground. Even the bushing and terminal bus capacitances have the effect of reducing the transferred electrostatic component. Simple formulae are given in [40] for the calculation of transferred surge voltages in autotransformers.

In the initial works, the damping of oscillations caused by the core, winding and dielectric losses was generally not taken into account for simplifying the calculations. Subsequently, the effects of these losses were taken into account by shunt elements representing conductances between nodes and ground in the equivalent network [23]. In other words, the parameters such as winding resistances were not considered separately since their effect on damping was approximately taken into consideration by the shunt conductance elements.

In distribution transformers, winding resistances significantly reduce voltage peaks and hence they cannot be neglected. Due to availability of powerful computational facilities, complex models can be solved now. A detailed model of losses is incorporated in [37] for accurate calculations.

A method based on natural frequencies of windings is described in [41] for the calculation of impulse voltage distribution. A mathematical model representing capacitances and inductances of windings is analyzed to calculate eigenvalues and eigenvectors, based on which the temporal and spatial variations of voltage distributions in the windings are calculated.

Study of the effect of the iron core on the impulse response of windings has been studied in [19]. The effect is significant for the case of an ungrounded neutral as compared to a grounded one. It seems to indicate that there exists flux in the core when the neutral is not grounded. It has been also reported that with the inner nonimpulsed winding short-circuited, the core has negligible effect on the voltage response irrespective of the neutral grounding condition (of the impulsed winding). The main flux in the core will be cancelled by the flux produced by the inner short-circuited winding and only leakage flux contributes to the impulse response. When the winding connections/grounding conditions allow the flux to exist in the core, the losses in the core have a damping effect on peaks of the voltage response, and in this case the voltages are lower. It has been reported in [42] that a considerable variation in the core permeability results in a very moderate change in the voltage response. Hence, for determining the impulse response of a winding, air core (self and mutual) inductances (which can be easily calculated as explained in Section 7.4) are generally used and suitable correction factors based on experience/experimental measurements are applied.

In [43], a study of the behavior of a transformer winding subjected to standard impulse voltage waves chopped at different instants (on the front as well as on the tail of the waves) is presented. It is well-known that a wave chopped at an unfavorable instant may result in higher voltage stresses at line end sections of the winding as compared to voltage stresses due to a full wave of the same steepness. The instant of switching and the time to collapse of a chopped impulse predominantly decide the level of stresses.

7.7 Computation of Impulse Voltage Distribution Using State Variable Method

Accurate determination of impulse voltage distribution in a transformer winding is possible by using its equivalent circuit as explained in the previous section. The evolution of the simplified equivalent network shown in Figure 7.17 is explained in [44]. In this section, a method is elaborated for finding the impulse distribution within a single winding, which can be easily extended for multiple windings.

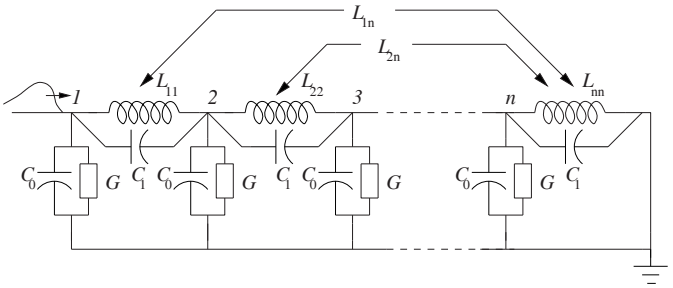

Figure 7.17 Equivalent circuit of a transformer winding.

The equivalent circuit of a transformer winding consists of a finite number of sections having elements C_0 , C_1, L_{ii}, L_{ij} and G, which are the shunt capacitance, the series capacitance, the self inductance, the mutual inductance and the shunt conductance of each section, respectively.

Due to the advancements in computational facilities, it is relatively simple to calculate the impulse voltage distribution of a winding using a state space model of the lumped parameter network as described below.

7.7.1 Derivation of differential equations

Equations for the network are formulated as [34]

$$\hat{C}\,\ddot{\hat{y}}(t) + \hat{G}\,\dot{\hat{y}}(t) + \hat{\Gamma}\,\hat{y}(t) = 0 \tag{7.75}$$

where $\hat{C}$ = nodal capacitance matrix with inclusion of the input node

$\hat{G}$ = nodal conductance matrix with inclusion of the input node

$\hat{\Gamma}$ = nodal matrix of inverse inductances with inclusion of the input node

$\hat{y}(t)$ = output vector of node voltages with inclusion of the input node.

The relationship between the nodal and branch matrices is defined by

$$\left.\begin{aligned} \hat{C} &= Q_c C_b Q_c^T \\ \hat{G} &= Q_G G_b Q_G^T \\ \hat{\Gamma} &= Q_L L_b^{-1} Q_L^T \end{aligned}\right\} \tag{7.76}$$

where Q_c , Q_G and Q_L are the incidence matrices for the capacitive, conductive and inductive elements, and C_b, G_b and L_b are the branch matrices of the capacitive, conductive and inductive elements of the network, respectively.

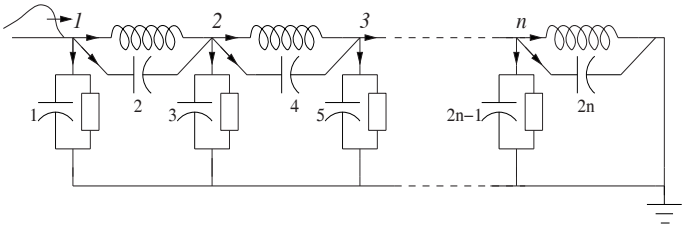

Figure 7.18 Numbering of capacitive branches.

The number of equations is reduced by excluding the input node k because its voltage is known. Therefore, Equation 7.75 can be rewritten as

$$C\,\ddot{y}(t) + G\,\dot{y}(t) + \Gamma\,y(t) = -C_k\,\ddot{x}(t) - G_k\,\dot{x}(t) - \Gamma_k\,x(t) \tag{7.77}$$

where, C = nodal capacitance matrix without the input node
G = nodal conductance matrix without the input node
Γ = nodal matrix of inverse inductances without the input node
$y(t)$ = output vector of node voltages without the input node
$x(t)$ = known voltage of the input node

C_k, G_k, Γ_k = k^{th} column of $\hat{C}$, $\hat{G}$, $\hat{\Gamma}$ with the entry of k^{th} row removed.

7.7.2 Formation of $\hat{C}$ matrix

There are $2n$ capacitive branches in the network of Figure 7.17. Therefore, the size of the branch capacitance matrix (C_b) is $2n \times 2n$. For the branches of the circuit numbered as shown in Figure 7.18 it can be written as

$$C_b = \begin{bmatrix} C_0 & 0 & 0 & \dots & 0 \\ 0 & C_1 & 0 & \dots & 0 \\ 0 & 0 & C_0 & \dots & 0 \\ \dots & \dots & \dots & \dots & \dots \\ 0 & 0 & 0 & \dots & C_1 \end{bmatrix}. \tag{7.78}$$

The corresponding incidence matrix Q_c ($n \times 2n$) is

$$Q_c = \begin{bmatrix} 1 & 1 & 0 & 0 & 0 & 0 & \dots & 0 & 0 & 0 \\ 0 & -1 & 1 & 1 & 0 & 0 & \dots & 0 & 0 & 0 \\ 0 & 0 & 0 & -1 & 1 & 1 & \dots & 0 & 0 & 0 \\ 0 & 0 & 0 & 0 & 0 & -1 & \dots & 0 & 0 & 0 \\ \dots & \dots & \dots & \dots & \dots & \dots & \dots & \dots & \dots & \dots \\ 0 & 0 & 0 & 0 & 0 & 0 & \dots & 1 & 1 & 0 \\ 0 & 0 & 0 & 0 & 0 & 0 & \dots & -1 & 1 & 1 \end{bmatrix}. \tag{7.79}$$

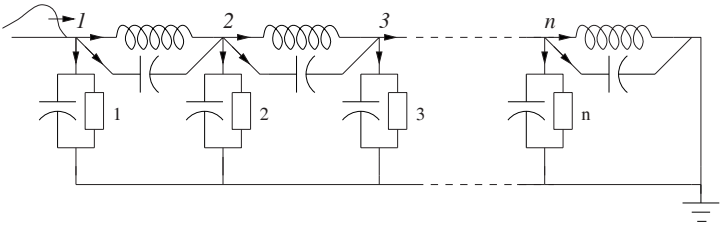

Figure 7.19 **N**umbering of conductive branches.

We can obtain $\hat{C}$ from Equation 7.76,

$$\hat{C} = Q_c C_b Q_c^T \,. \tag{7.80}$$

7.7.3 Formation of $\hat{G}$ matrix

Similarly, the branch conductance matrix (G_b) and the incidence conductance matrix Q_G of the order $(n \times n)$ for Figure 7.19 can be given as

$$G_b = \begin{bmatrix} G & 0 & 0 & \ldots & 0 \\ 0 & G & 0 & \ldots & 0 \\ 0 & 0 & G & \ldots & 0 \\ \ldots & \ldots & \ldots & \ldots & \ldots \\ 0 & 0 & 0 & \ldots & G \end{bmatrix} \tag{7.81}$$

$$Q_G = \begin{bmatrix} 1 & 0 & 0 & 0 & \ldots & 0 & 0 \\ 0 & 1 & 0 & 0 & \ldots & 0 & 0 \\ 0 & 0 & 1 & 0 & \ldots & 0 & 0 \\ 0 & 0 & 0 & 1 & \ldots & 0 & 0 \\ \ldots & \ldots & \ldots & \ldots & \ldots & \ldots & \ldots \\ 0 & 0 & 0 & 0 & \ldots & 1 & 0 \\ 0 & 0 & 0 & 0 & \ldots & 0 & 1 \end{bmatrix} \tag{7.82}$$

and

$$\hat{G} = Q_G G_b Q_G^T \,. \tag{7.83}$$

7.7.4 Formation of $\hat{\Gamma}$ matrix

Similarly, the branch inductance matrix (L_b) and the incidence inductance matrix Q_L of the order $(n \times n)$ for Figure 7.20 can be given as

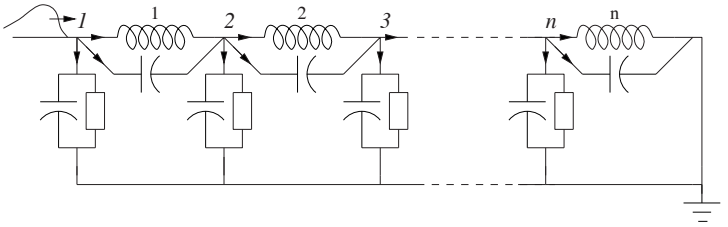

Figure 7.20 Numbering of inductive branches.

$$L_b = \begin{bmatrix} L_{11} & L_{12} & L_{13} & \dots & L_{1n} \\ L_{21} & L_{22} & L_{23} & \dots & L_{2n} \\ L_{31} & L_{32} & L_{33} & \dots & L_{3n} \\ \dots & \dots & \dots & \dots & \dots \\ L_{n1} & L_{n2} & L_{n3} & \dots & L_{nn} \end{bmatrix} \tag{7.84}$$

$$\Gamma_b = L_b^{-1} = \begin{bmatrix} \Gamma_{11} & \Gamma_{12} & \Gamma_{13} & \dots & \Gamma_{1n} \\ \Gamma_{21} & \Gamma_{22} & \Gamma_{23} & \dots & \Gamma_{2n} \\ \Gamma_{31} & \Gamma_{32} & \Gamma_{33} & \dots & \Gamma_{3n} \\ \dots & \dots & \dots & \dots & \dots \\ \Gamma_{n1} & \Gamma_{n2} & \Gamma_{n3} & \dots & \Gamma_{nn} \end{bmatrix} \tag{7.85}$$

$$Q_L = \begin{bmatrix} 1 & 0 & 0 & 0 & \dots & 0 & 0 \\ -1 & 1 & 0 & 0 & \dots & 0 & 0 \\ 0 & -1 & 1 & 0 & \dots & 0 & 0 \\ 0 & 0 & -1 & 1 & \dots & 0 & 0 \\ \dots & \dots & \dots & \dots & \dots & \dots & \dots \\ 0 & 0 & 0 & 0 & \dots & 1 & 0 \\ 0 & 0 & 0 & 0 & \dots & -1 & 1 \end{bmatrix} \tag{7.86}$$

and

$$\hat{\Gamma} = Q_L \Gamma_b Q_L^T \,. \tag{7.87}$$

7.7.5 State space model

The state space model of Equation 7.77 (without the input node) is

$$\dot{X}(t) = A X(t) + B v(t) \tag{7.88}$$

$$y(t) = F X(t) + D v(t) \tag{7.89}$$

where $X(t)$ = vector of state variables

A, F = matrices of constant coefficients
B, D = column matrices of constant coefficients
$v(t)$ = input vector of the applied impulse voltage
$y(t)$ = output vector of node voltages.

Equation 7.77 can be rewritten as

$$\ddot{y}(t)+C^{-1}G\,\dot{y}(t)+C^{-1}\Gamma\,y(t)=-C^{-1}C_k\,\ddot{x}(t)-C^{-1}G_k\,\dot{x}(t)-C^{-1}\Gamma_k\,x(t). \tag{7.90}$$

To obtain Equation 7.90 in the form of state space equations, the following state variables can be chosen,

$$X_1(t)=y(t)-\beta_0 x(t) \tag{7.91}$$

$$\begin{aligned} X_2(t)&=\dot{y}(t)-\beta_0\dot{x}(t)-\beta_1 x(t)\\ &=\dot{X}_1(t)-\beta_1 x(t)\end{aligned} \tag{7.92}$$

where $\beta_0=-C^{-1}C_k$

$\beta_1=-C^{-1}\left(G_k-GC^{-1}C_k\right).$

Now, rearranging Equation 7.92 we have

$$\dot{X}_1(t)=X_2(t)+\beta_1\,x(t). \tag{7.93}$$

Replacing $y(t)$ and $\dot{y}(t)$ in Equation 7.90 by their expressions from Equations 7.91 and 7.92, respectively, and simplifying we obtain

$$\dot{X}_2(t)=-\alpha_2\,X_1(t)-\alpha_1\,X_2(t)+\beta_2\,x(t) \tag{7.94}$$

where $\alpha_2=C^{-1}\Gamma$, $\alpha_1=C^{-1}G$,

$\beta_2=-C^{-1}\left(\Gamma_k-GC^{-1}\left(G_k-GC^{-1}C_k\right)-\Gamma C^{-1}C_k\right).$

Also, rearranging Equation 7.91 we have

$$y(t)=X_1(t)+\beta_0 x(t). \tag{7.95}$$

Equations 7.93, 7.94, and 7.95 can be written in the following matrix form,

$$\begin{bmatrix}\dot{X}_1(t)\\ \dot{X}_2(t)\end{bmatrix}=\begin{bmatrix}0 & I\\ -\alpha_2 & -\alpha_1\end{bmatrix}\begin{bmatrix}X_1(t)\\ X_2(t)\end{bmatrix}+\begin{bmatrix}\beta_1\\ \beta_2\end{bmatrix}x(t) \tag{7.96}$$

and $$[y(t)]=[I\quad 0]\begin{bmatrix}X_1(t)\\ X_2(t)\end{bmatrix}+[\beta_0]\,x(t). \tag{7.97}$$

Comparing Equations 7.96 and 7.97 with Equations 7.88 and 7.89 we obtain

$$X(t) = \begin{bmatrix} X_1(t) \\ X_2(t) \end{bmatrix}, \quad v(t) = x(t),$$

$$A = \begin{bmatrix} 0 & I \\ -\alpha_2 & -\alpha_1 \end{bmatrix}, \; B = \begin{bmatrix} \beta_1 \\ \beta_2 \end{bmatrix}, \; F = \begin{bmatrix} I & 0 \end{bmatrix} \text{ and } D = \begin{bmatrix} \beta_0 \end{bmatrix}.$$

The above analysis has converted the original 2nd order circuit Equation 7.77 to the equivalent 1st order state space system defined by Equations 7.96 and 7.97. The solution of these state space equations can be written as [45]

$$X(t) = e^{At} X(0^-) + \int_{0^-}^{t} e^{A(t-\tau)} B\, x(\tau)\, d\tau \tag{7.98}$$

where $X(0^-)$ is the state vector at t=0$^-$ and is assumed to be zero. The above expression of $X(t)$ can be evaluated analytically for simple $x(\tau)$. Alternatively, a standard built-in function in MATLAB® for a 1st order system can now be used to solve Equations 7.96 and 7.97.

After determining the values of the state variables (X) of the circuit, the node voltages can be obtained from Equation 7.97. For the sample system given in [35], the impulse response is calculated by the method. The winding consists of 12 sections; the details of lumped elements are given in Table 7.2.

The input voltage is assumed to be the standard full wave defined by

$$x(t) = x_0\left(e^{-\beta t} - e^{-\delta t}\right). \tag{7.99}$$

For (1/50) microsecond wave (which rises to its maximum value at 1 microsecond and decays to half the maximum value in 50 microseconds), when t is expressed in microseconds the values of the constants are

$$x_0 = 1.0167, \; \beta = 0.01423 \text{ and } \delta = 6.0691.$$

The calculated voltages of various nodes are plotted in Figure 7.21, which are in close agreement with those reported in [35].

Table 7.2 Inductance and Capacitance Parameters [35]

C_0	C_1
412.6 pF	120 pF

$L_{1\text{-}1}$	$L_{1\text{-}2}$	$L_{1\text{-}3}$	$L_{1\text{-}4}$	$L_{1\text{-}5}$	$L_{1\text{-}6}$
0.668 mH	0.526 mH	0.425 mH	0.344 mH	0.283 mH	0.232 mH
$L_{1\text{-}7}$	$L_{1\text{-}8}$	$L_{1\text{-}9}$	$L_{1\text{-}10}$	$L_{1\text{-}11}$	$L_{1\text{-}12}$
0.186 mH	0.139 mH	0.101 mH	0.060 mH	0.030 mH	0 mH

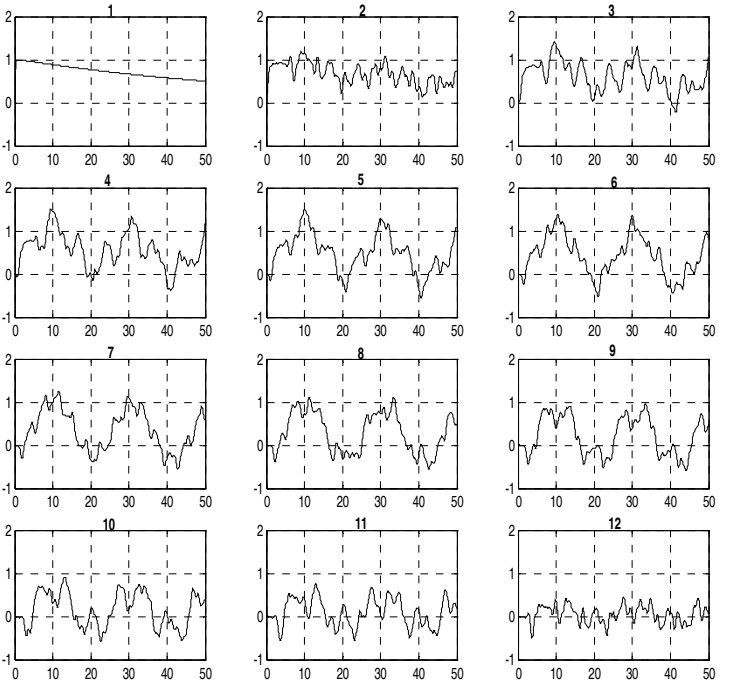

Figure 7.21 Voltage waveforms at all 12 nodes.

The results obtained for another 10-section winding are also in close agreement with that given in [46] for rectangular and chopped waves.

The voltages are also calculated using two software packages: SPICE and SEQUEL. SPICE is a general-purpose circuit simulation program for nonlinear DC, nonlinear transient, and linear AC analysis developed by the University of Berkeley, California (http://bwrc.eecs.berkeley.edu/Classes/IcBook/SPICE/).

SEQUEL is a public-domain package (a solver for circuit equations with user-defined elements), developed at IIT Bombay (see the details at http://www.ee.iitb.ac.in/~microel/faculty/mbp/sequel1.html). It allows the user to incorporate new elements in the package by simply writing a "template" to describe the model equations. SEQUEL is based on the Sparse Tableau approach, in which all variables are treated in the same manner without separating them into "current-like" and "voltage-like" variables. This makes it particularly convenient to write new element templates. It solves a (generally nonlinear) system of equations of the form,

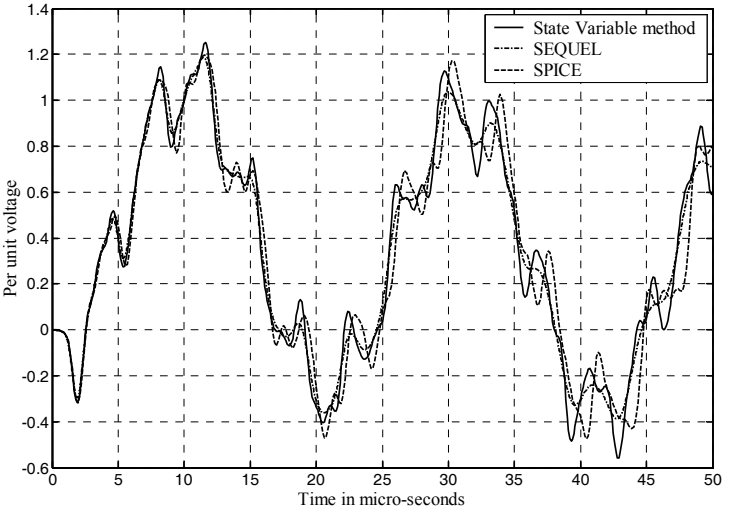

Figure 7.22 Comparison of voltage waveform at node 6 obtained using different methods.

$$f_i = (x_1, x_2, x_3, \cdots, x_n) = g_i \tag{7.100}$$

where $g_i = 0$ or $g_i = dx_j / dt$. The method employed by SEQUEL to solve the nonlinear equations is the well-known Newton-Raphson (NR) iterative method. Four discretization schemes are offered for transient simulation: (i) Backward Euler, (ii) Trapezoidal, (iii) Gear's scheme (order 2) and (iv) TR-BDF2 scheme.

The results of all 3 methods (the state variable method, SEQUEL and SPICE), shown in Figure 7.22 for node 6 of the winding with 12 sections, closely agree with each other. The state variable method can be easily extended for multiwinding transformers. The matrices in Equation 7.77 will have to be modified and the same procedure can be followed to obtain the impulse response.

7.8 Winding Design for Reducing Internal Overvoltages

7.8.1 Part winding resonance

Part winding resonance has been identified as the root cause of failures of a few power transformers. If the frequency of an exciting oscillating voltage coincides with one of the fundamental natural frequencies of a winding or its part, resonant overvoltages occur. The failures of four single-phase autotransformers in 500 kV and 765 kV systems of American Electric Power between 1968 and

1971 led to a detailed investigation of the resonance phenomenon [47, 48]. All these failures involved breakdown of off-circuit tap changers immediately after the occurrence of transmission system faults. The taps were at the neutral end of the common winding in all four failed autotransformers. After the investigations, it was concluded that the traveling waves generated by line faults contributed to the failures. Factory and field tests with nonstandard wave shapes revealed that transient voltages could be generated across tap sections significantly in excess of those during the standard tests.

Because the tap changers are usually remote from the transformer line terminals, high frequency components of the incoming surges will not usually find their way into the tap zone of the winding; instead the zone may experience transient overvoltages associated with lower frequencies of winding resonance. It is also reported in [44, 48] that the part winding fundamental natural frequencies are proportional to the volt-ampere rating (per phase) raised to a power substantially less than one and inversely proportional to the voltage rating (phase value). Hence, as the voltage rating goes up in EHV transformers, natural frequencies may become substantially lower (few kHz), thus increasing the chances of the part winding resonance.

Researchers have studied voltage transients which lead to winding resonances and the factors that can mitigate them. The voltage transients are generated by switching operations of lines or other nearby equipment in the network. The use of closing resistors or point of wave switching during switching operations may possibly mitigate the effects. A transformer should be designed such that it is as far as possible self-protecting against winding resonances. Some methods have been suggested to protect transformers from failures due to the part winding resonance phenomenon involving tap windings [47, 49], viz. connection of external arresters to windings, use of shunt capacitors, and connection of nonlinear resistors in parallel with the tap windings.

Natural frequencies of core type transformers are normally between 5 kHz to a few hundred kHz if one excludes the problem of very fast transients [50]. There is always a chance that the frequency of an external oscillating disturbance is close to one of the natural frequencies of a transformer winding. The winding natural frequencies are determined by its parameters, and these cannot be changed beyond certain limits. In certain cases, where exact natural frequencies of the network can be determined (e.g., a cable feeding a transformer in a substation), it may be possible to change the winding type to avoid resonance conditions. Every effort should be made to avoid network conditions that tend to produce oscillating voltages. If possible, parameters of the expected disturbances in the network should be made known to the transformer designer since unlimited requirements will make the transformer very costly. In this context, closer cooperation between users and manufacturers of transformers is desirable. The knowledge of precise transmission line propagation characteristics is essential for determining the amplitude of

incoming surges. Also, the terminal conditions (loading, neutral grounding, etc.) of transformers have significant impact on the resonance phenomenon.

A resonance basically is the excitation of an oscillation in a winding by an external oscillating disturbance, both having frequencies very close to each other. Analysis of the failure of a generator step-up transformer due to an internal resonance caused by an oscillating voltage excitation is reported in [51]. Oscillatory switching surges can be produced in a system by sudden voltage changes (switching operations, short line faults, etc.) at some distance from the transformer terminals. The natural frequency of a line is given by

$$f = \frac{v}{4L} \tag{7.101}$$

where v is the wave propagation velocity (300 m/μs for overhead transmission lines and 100 m/μs for cables) and L is the length of the line (i.e., the distance of the transformer from the location where a switching operation or a ground fault occurs). If the natural frequency of the line corresponds to a natural frequency of the winding, high internal overvoltages may develop. Hence, after knowing the dominant resonant frequency of the winding, the critical line length can be calculated from Equation 7.101, at which the placement of the circuit breaker should be avoided. It should be ensured as far as possible that a fault does not occur at this location.

The resonant overvoltages are basically determined by the winding design and the damping provided by the frequency-dependent winding resistance. The calculation of this resistance, although laborious, is essential. Oscillations are significantly affected by internal damping effects (i.e., winding and core losses) and external damping effects (i.e., line losses); the amplitude of oscillations decreases with an increase in the damping.

Possibility of resonant conditions in the windings can be known from the terminal and internal measurements. The resonances are of two types: a terminal resonance and an internal resonance. For a complex non-uniform winding, the terminal response may not necessarily bear a direct relation to the internal response of a particular part of the winding. In other words, a part winding resonance may significantly influence transient oscillations of a major part of the winding but its effects may not be observed in the terminal impedance plot.

Although it was known long ago that high frequency resonances exist within the transformer windings, traditionally the emphasis has been to check the response of transformers to pulse (unidirectional) test voltages since conditions leading to steady state high frequency excitations were not envisaged in the power system. Hence, the standards have been based on pulse shapes thought to be reasonably representing transient overvoltages in the system. Designers in earlier days worried only about the standard voltage shapes and not about the calculation of internal resonant frequencies which the nonstandard wave shapes may excite. The pattern of oscillations in transformer windings is

not very orderly due to nonuniformities in insulation systems and distribution of turns. It is obvious that in order to check the withstand capability against winding resonances, there is no point in increasing power frequency test voltage as it will not lead to a local high stress concentration in the winding. Also, it is observed in most of the cases that under standard test conditions, the front of the standard switching impulse waveform may rise too slowly or the tail of the standard lightning impulse waveform may fall too rapidly to excite an internal part winding resonance as compared to the possibility of resonances in actual service with lower magnitudes of surges after occurrence of line faults. Hence, the withstand can possibly be checked by suitably modifying the impulse wave shape (front and tail portions). It has been reported in [51] that certain aperiodic overvoltage wave shapes (different than wave shapes encountered in standard tests) such as fast-front long-tail switching overvoltages can result in high internal voltage stresses in transformer windings.

7.8.2 Natural frequencies of windings

For eliminating resonances in windings, an accurate determination of their frequency response characteristics is essential. These characteristics can be determined by actual measurements, which is an established technique. Its disadvantage is that the response cannot be predicted at the design stage and it is difficult to measure the internal winding response unless the winding insulation is pierced and damaged for the use of conductively coupled probes. Capacitively coupled nondestructive probes can be used after careful scrutiny of their accuracy and precision. In [52], authors have used an equivalent circuit containing lumped inductances and capacitances for determining natural frequencies of a winding. It is shown that the mutual inductances between all the sections of the winding must be taken into account to determine correctly the natural frequencies. Subsequently, the method of equivalent circuit has been used in [53] for finding oscillations of coupled windings; the natural frequencies of the primary winding of a transformer are determined with its secondary winding short-circuited. The natural frequencies of three-phase transformer windings are calculated in [54] to take into account the effects of the capacitive and inductive couplings between the windings of different phases.

Another method employs an electromagnetic scaled model to determine the natural frequencies and the voltage response of a transformer [55]; its obvious disadvantages are the high cost and time involved in building a scaled model for each transformer of interest. Hence, the most convenient and economical method is computer-based simulations. A numerical method has been presented in [56] for determining the terminal/internal impedance versus frequency characteristics for a general lumped parameter network, using which the resonant frequency characteristics and amplification factors are calculated. If a transformer winding is represented by a lumped parameter network, its response will not exactly match that of the actual one. In practice, it is sufficient

to choose the number of sections in the winding representation somewhat larger than the number of required resonant frequencies [52, 56].

7.8.3 Graded capacitance winding

The development of interleaved windings is an important milestone in the history of power transformers. Although interleaving improves dramatically the voltage distribution in the main winding, the tap (regulating) winding, if present, may be subjected to very high local voltages due to the part winding resonance phenomenon. Thus, the improvement in surge voltage response obtained by interleaving may be offset by the overvoltages on account of resonance conditions. When the main winding is fully interleaved, the design of the tap winding and the tap changer becomes critical in high voltage transformers since the voltage across the tap winding may reach unacceptable levels. The surge performance of a power transformer having taps on the HV winding has been analyzed in [57] for two cases: an interleaved winding and a non-interleaved continuous disk winding. For the first case, wherein both HV main winding and its corresponding tap winding are of interleaved type, it is reported that the voltages (with respect to ground) of various points in the HV main winding are almost linearly distributed along the length of the winding indicating a marked improvement as compared to the non-interleaved type. For both designs, the voltage across the tap winding is shown to have oscillatory nature, but in the interleaved design there is no attenuation suggesting occurrence of a part winding resonance condition in the tap winding. The peak value of the voltage is practically limited by the winding resistance under the resonance condition. It has been proved that because of a high series capacitance value due to interleaving, the resonant frequency of tap winding disks has reduced to a value of 22 kHz which is close to the excitation frequency for the standard 1.2/50 microseconds impulse wave (the impulse wave has a frequency of about 20 kHz when it reaches the tap winding). The reported study suggests that in order to eliminate the possibility of resonance conditions, resonant frequencies of different parts of the winding should be determined at the design stage, and also the winding response for a variety of input voltage waveforms, covering a wide range of frequencies of practical importance, should be studied.

Thus, interleaving may not always be the right solution for high voltage windings and it may lead to high voltages in some parts of the windings. Usually, it is thought that in order to improve the voltage distribution, it is always better to have the main winding fully interleaved. If the tap winding is of non-interleaved type, due to a substantial increase in its impedance (on account of its less series capacitance), the voltage across it can be higher. Hence, there may be a temptation to make the tap winding also interleaved, in which case there is a possibility of a part winding resonance condition as explained earlier. One of the better options can be a graded series capacitance design. The series capacitance of the main winding can be gradually reduced in 2 or 3 steps (by

changing the degree of interleaving) and its neutral end part (electrically adjacent to the tap winding) can be of continuous disk type. In this case, the tap winding can also be of continuous disk nature. The part winding resonance phenomenon can be damped to a great extent by using the graded interleaving technique. A graded interleaving scheme for a winding with two parallel conductors can be obtained by using the conductor interleaving (Figure 7.7) at line end and the turn interleaving (Figure 7.6) for subsequent disks. For the case of one conductor per turn, interleaving schemes shown in Figure 7.23 [58] and Figure 7.24 [8] can be used. The first type of interleaving, in which four disks are required to complete the interleaving, results in a much higher capacitance as compared to that in Figure 7.6 which is a two-disk interleaving method. Its capacitance can be easily calculated by the method given in Section 7.3.5. The second type is a one-disk interleaving method which results in lower series capacitance as compared to the two-disk interleaving method.

Although the series capacitance increases with the degree of interleaving, only marginal improvement in response may be obtained by complex schemes. Also the winding process becomes more difficult; hence interleaving methods involving more than four disks are rarely used in practice. The importance and usefulness of the graded capacitance approach for interleaved and shielded-conductor windings have been verified in [59]. It may be more advantageous to have a graded series capacitance scheme, rather than high series capacitances throughout the winding.

One useful scheme could be a two-disk interleaving arrangement at the line end, followed by disks with one-disk interleaving and continuous disks in sequence, with the neutral end tap section also a continuous disk winding. The phenomenon of higher voltages due to a sudden impedance (capacitance) change can be mitigated by means of this graded capacitance arrangement.

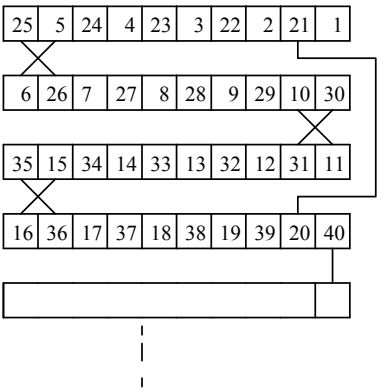

Figure 7.23 Four-disk interleaving.

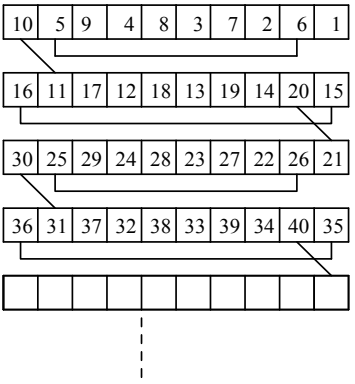

Figure 7.24 One-disk interleaving.

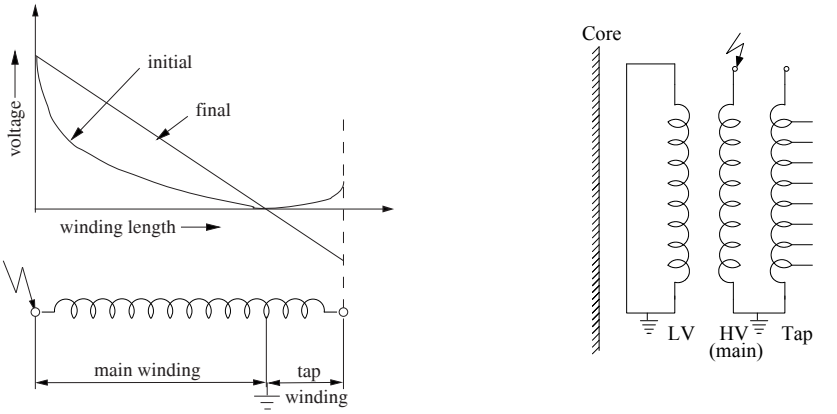

Figure 7.25 Tap winding with an open end.

For a tap winding with a large tapping range, the problem of higher stresses is more severe at its open end during the impulse test condition wherein the entire tap winding is out of circuit. The corresponding configuration and a typical voltage distribution are shown in Figure 7.25. A high difference between the initial and final voltage distributions at the open end is responsible for significant voltage oscillations. The type of the HV main winding and the tap winding can be judiciously selected to avoid a high voltage buildup in the latter as explained earlier. A reverse graded interleaving method is proposed in [60] to reduce the voltage buildup, in which the degree of interleaving is reduced from the line end to the tap end for the main winding, whereas for the tap winding it is increased from the main winding end to the open end. An increase of the series capacitance at the open end, thus obtained, substantially reduces the voltage stresses there.

7.8.4 Location of windings

Transient voltages appearing across the tap winding depend on its design and position with respect to the main winding. One of the effective ways of reducing high stresses across the tap winding or between the winding and ground, is to have the winding located between the core and the LV winding. The inner tap winding is usually of an interleaved type (as described in Section 7.3.8) having a high series capacitance value reducing the impulse voltage across it. In autotransformers, if the tap winding is placed between the HV (series) and IV (common) windings as shown in Figure 7.26 (with taps at the line end of the IV winding) it acts as a shield for the IV winding and improves the voltage distribution significantly at the IV winding line end (during an impulse test on the IV winding).

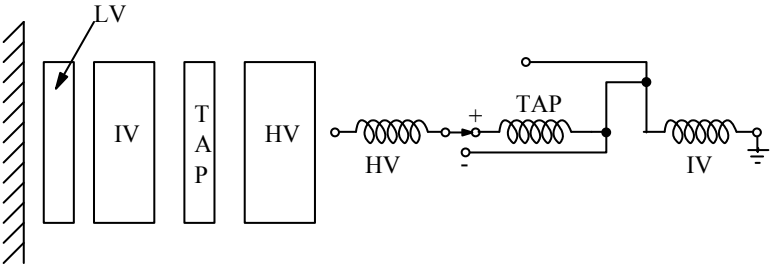

Figure 7.26 The effect of tap winding location in autotransformers.

However, the insulation of the neutral end disks of the IV winding may have to be strengthened (by special insulation components) since these face the tap winding which may be at a much higher potential.

References

1. Blume, L. F. and Boyajian, A. Abnormal voltages within transformers, *AIEE Transactions*, Vol. 38, February 1919, pp. 577–614.
2. Thomas, H. L. Insulation stresses in transformers with special reference to surges and electrostatic shielding, *Journal IEE*, Vol. 84, 1940, pp. 427–443.
3. Norris, E. T. The lightning strength of power transformers, *Journal IEE*, Vol. 95, Pt. II, 1948, pp. 389–406.
4. Heller, B. and Veverka, A. *Surge phenomena in electrical machines*, Iliffe Books Ltd., London, 1968.
5. Chadwik, A. T., Ferguson, J. M., Ryder, D. H., and Stearn, G. F. Design of power transformers to withstand surges due to lightning, with special reference to a new type of winding, *Proceedings IEE*, Pt. II, Vol. 97, 1950, pp. 737–750.
6. Grimmer, E. J. and Teague, W. L. Improved core form transformer winding, *AIEE Transactions*, Vol. 70, 1951, pp. 962–967.
7. Pedersen, A. On the response of interleaved transformer windings to surge voltages, *AIEE Transactions*, Vol. 82, June 1963, pp. 349–356.
8. Van Nuys, R. Interleaved high-voltage transformer windings, *IEEE Transactions on Power Apparatus and Systems,* Vol. PAS-97, No. 5, September/October 1978, pp. 1946–1954.
9. Teranishi, T., Ikeda, M., Honda, M., and Yanari, T. Local voltage oscillation in interleaved transformer windings, *IEEE Transactions on Power Apparatus and Systems,* Vol. PAS-100, No. 2, 1981, pp. 873–881.
10. Jayaram, B. N. The series capacitance of transformer windings, *Electrotechnics*, Indian Institute of Science, No. 28, 1961, pp. 69–87.

11. Jayaram, B. N. The equivalent series capacitance of a single disk-coil in a transformer winding, (in German), Elektrotechnische Zeitschrift — A, Vol. 94, 1973, pp. 547–548.
12. Kawaguchi, Y. Calculation of circuit constants for computing internal oscillating voltage in transformer windings, *Electrical Engineering in Japan*, Vol. 89, No. 3, 1969, pp. 44–53.
13. Jayaram, B. N. Determination of impulse distribution in transformers with a digital computer, (in German), Elektrotechnische Zeitschrift — A, Vol. 82, January 1961, pp. 1–9.
14. Karsai, K., Kerenyi, D., and Kiss, L. *Large power transformers*, Elsevier Publication, Amsterdam, 1987.
15. Del Vecchio, R. M., Poulin, B., and Ahuja, R. Calculation and measurement of winding disk capacitances with wound-in-shields, *IEEE Transactions on Power Delivery*, Vol. 13, No. 2, April 1998, pp. 503–509.
16. Chowdhuri, P. Calculation of series capacitance for transient analysis of windings, *IEEE Transactions on Power Delivery*, Vol. PWRD–2, No. 1, January 1987, pp. 133–139.
17. Weed, J. M. Prevention of transient voltage in windings, *AIEE Transactions*, February 1922, pp. 149–159.
18. Wilcox, D. J., Hurley, W. G., and Conlon, M. Calculation of self and mutual impedances between sections of transformer windings, *Proceedings IEE,* Vol. 136, Pt. C, No. 5, September 1989, pp. 308–314.
19. Miki, A., Hosoya, T., and Okuyama, K. A calculation method for impulse voltage distribution and transferred voltage in transformer windings, *IEEE Transactions on Power Apparatus and Systems,* Vol. PAS-97, No. 3, May/June 1978, pp. 930–939.
20. Grover, F. W. *Inductance calculations: working formulae and tables*, Van Nostrand Company, Inc., 1947.
21. Wirgau, K. A. Inductance calculation of an air-core disk winding, *IEEE Transactions on Power Apparatus and Systems,* Vol. PAS-95, No. 1, January/February 1976, pp. 394–400.
22. Okuyama, K. A numerical analysis of impulse voltage distribution in transformer windings, *Electrical Engineering in Japan*, Vol. 87, 1967, pp. 80–88.
23. Krondl, M. and Schleich, A. Predetermination of the transient voltages in transformers subject to impulse voltage, *Bulletin Oerlikon*, No. 342/343, December 1960, pp. 114–133.
24. McWhirter, J. H., Fahrnkopf, C. D., and Steele, J. H. Determination of impulse stresses within transformer windings by computers, *AIEE Transactions*, Vol. 75, Pt. III, February 1957, pp. 1267–1279.
25. Honorati, O. and Santini, E. New approach to the analysis of impulse voltage distribution in transformer windings, *Proceedings IEE*, Vol. 137, Pt. C, No. 4, July 1990, pp. 283–289.

26. Rudenberg, R. Performance of traveling waves in coils and windings, *AIEE Transactions*, Vol. 59, 1940, pp. 1031–1040.
27. Bewley, L. V. *Traveling waves on transmission lines*, John Wiley and Sons, Inc., New York, 1951.
28. Allibone, T. E., McKenzie, D. B., and Perry, F. R. The effects of impulse voltages on transformer windings, *Journal IEE*, Vol. 80, No. 482, February 1937, pp. 117–173.
29. Abetti, P. A. and Maginniss, F. J. Fundamental oscillations of coils and windings, *AIEE Transactions*, February 1954, pp. 1–10.
30. Rudenberg, R. Surge characteristics of two-winding transformers, *AIEE Transactions*, Vol. 60, 1941, pp. 1136–1144.
31. Glaninger, P. Modal analysis as a means of explaining the oscillatory behavior of transformers, *Brown Boveri Review*, 1-86, pp. 41–49.
32. Abetti, P. A. Correlation of forced and free oscillations of coils and windings, *AIEE Transactions*, December 1959, pp. 986–996.
33. Lewis, T. J. The transient behavior of ladder networks of the type representing transformer and machine windings, *Proceedings IEE*, Vol. 101, Pt. II, 1954, pp. 541–553.
34. Fergestad, P. I. and Henriksen, T. Transient oscillations in multi-winding transformers, *IEEE Transactions on Power Apparatus and Systems*, Vol. PAS-93, 1974, pp. 500–509.
35. Kasturi, R. and Murty, G. R. K. Computation of impulse voltage stresses in transformer windings, *Proceedings IEE*, Vol. 126, No. 5, May 1979, pp. 397–400.
36. Carlin, H. J. and Giordano, A. B. *Network theory*, Prentice-Hall, Inc., 1964.
37. De Leon, F. and Semlyen, A. Complete transformer model for electromagnetic transients, *IEEE Transactions on Power Delivery*, Vol. 9, No. 1, January 1994, pp. 231–239.
38. Abetti, P. A. Electrostatic voltage distribution and transfer in three-winding transformers, *AIEE Transactions*, December 1954, pp. 1407–1416.
39. Abetti, P. A. and Davis, H. F. Surge transfer in three-winding transformers, *AIEE Transactions*, December 1954, pp. 1395–1407.
40. Koppikar, D. A. and Vijayan, K. Transferred surge voltage in transformers, *International Conference on Transformers*, *TRAFOTECH — 94*, Bangalore, January 1994, pp. I21–I24.
41. Gupta, S. C. and Singh, B. P. Determination of the impulse voltage distribution in windings of large power transformers, *Electric Power Systems Research*, Vol. 25, 1992, pp. 183–189.
42. Fergestad, P. I. and Henriksen, T. Inductances for the calculation of transient oscillation in transformers, *IEEE Transactions on Power Apparatus and Systems*, Vol. PAS-93, 1974, pp. 510–517.

43. Munshi, S., Roy, C. K., and Biswas, J. R. Computer studies of the performance of transformer windings against chopped impulse voltages, *Proceedings IEE,* Vol. 139, Pt. C, No. 3, May 1992, pp. 286–294.
44. McNutt, W. J., Blalock, T. J., and Hinton, R. A. Response of transformer windings to system transient voltages, *IEEE Transactions on Power Apparatus and Systems*, Vol. PAS-93, March/April 1974, pp. 457–466.
45. Phillips, C. L. and Harbor, R. D. *Feedback control systems*, Prentice-Hall, Inc., 1996.
46. Waldvogel, P. and Rouxel, R. A new method of calculating the electric stresses in a winding subjected to a surge voltage, *The Brown Boveri Review*, Vol. 43, No. 6, June 1956, pp. 206–213.
47. Margolis, H. B., Phelps, J. D. M., Carlomagno, A. A., and McElroy, A. J. Experience with part-winding resonance in EHV auto-transformers: diagnosis and corrective measures, *IEEE Transactions on Power Apparatus and Systems*, Vol. PAS-94, No. 4, July/August 1975, pp. 1294–1300.
48. McElroy, A. J. On the significance of recent EHV transformer failures involving winding resonance, *IEEE Transactions on Power Apparatus and Systems*, Vol. PAS-94, No. 4, July/August 1975, pp. 1301–1307.
49. Teranishi, T., Ebisawa, Y., Yanari, T., and Honda, M. An approach to suppressing resonance voltage in transformer tap windings, *IEEE Transactions on Power Apparatus and Systems,* Vol. PAS-102, No. 8, August 1983, pp. 2552–2558.
50. Preininger, G. Resonant overvoltages and their impact on transformer design, protection and operation, *International Summer School on Transformers*, *ISST'93*, Technical University of Lodz, Poland, 1993, Paper No. 11.
51. Musil, R. J., Preininger, G., Schopper, E., and Wenger, S. Voltage stresses produced by aperiodic and oscillating system overvoltages in transformer windings, *IEEE Transactions on Power Apparatus and Systems*, Vol. PAS-100, No. 1, January 1981, pp. 431–441.
52. Abetti, P. A. and Maginniss, F. J. Natural frequencies of coils and windings determined by equivalent circuit, *AIEE Transactions*, June 1953, pp. 495–503.
53. Abetti, P. A., Adams, G. E., and Maginniss, F. J. Oscillations of coupled windings, *AIEE Transactions*, April 1955, pp. 12–21.
54. Gururaj, B. I. Natural frequencies of 3-phase transformer windings, *AIEE Transactions,* June 1963, pp. 318–329.
55. Abetti, P. A. Transformer models for determination of transient voltages, *AIEE Transactions*, June 1953, pp. 468–480.
56. Degeneff, R. C. A general method for determining resonances in transformer windings, *IEEE Transactions on Power Apparatus and Systems,* Vol. PAS-96, No. 2, March/April 1977, pp. 423–430.

57. De, A. and Chatterjee, N. Part winding resonance: demerit of interleaved high-voltage transformer winding, *Proceedings IEE — Electric Power Applications*, Vol. 147, No. 3, May 2000, pp. 167–174.
58. Schleich, A. Behaviour of partially interleaved transformer windings subjected to impulse voltages, *Bulletin Oerlikon*, No. 389/390, pp. 41–52.
59. Okuyama, K. Effect of series capacitance on impulse voltage distribution in transformer windings, *Electrical Engineering in Japan*, Vol. 87, 1967, pp. 27–34.
60. De, A. and Chatterjee, N. Graded interleaving of EHV transformers for optimum surge performance, *International Symposium on High Voltage Engineering, ISH-2001*, Bangalore, Paper No. 6-30, pp. 916–919.

8

Insulation Design

Insulation design is one of the most important aspects of transformer engineering, particularly in high voltage transformers. Sound design practices, use of appropriate insulating materials, controlled manufacturing processes and good housekeeping ensure quality and reliability of transformers. Comprehensive verification of dimensioning rules is essential for enhancing reliability as well as for material cost optimization.

Due to the steady increase in transmission system voltages over the years, the voltage ratings of power transformers have increased and hence insulation content in them contributes significantly to their cost. Also, insulation space influences the cost of active parts (i.e., the core and windings) as well as the quantity of oil. Moreover, it is also environmentally important that we optimize the transformer insulation system which is primarily made from wood products. In addition, with increasing MVA ratings, the weight and size of large transformers approach or exceed transport limits. These reasons together with the ever-increasing competition in the global market are responsible for continuous efforts to reduce insulation content in transformers. In other words, margins between withstand levels and operating stress levels are reducing. This requires greater efforts from researchers and designers for accurate calculation of stress levels at various critical electrode configurations inside the transformer under different test voltage levels and different test connections. Advanced computational tools (e.g., FEM) are being used for the calculation of stress levels. These stress levels are compared with withstand levels based on experimental/published data.

For an excellent dielectric performance, reduction in maximum electric stress in insulation is usually not enough; the following factors affecting its withstand characteristics should be given due consideration: waveforms of

applied voltages, volt-time characteristics of insulation, shapes and surface conditions of electrodes, partial discharge inception characteristics of insulation, impurities, moisture, etc. Minimization of nonuniform fields and creepage stresses, improvement in oil processing and impregnation, elimination of voids, elimination of local high stresses due to winding connections/crossovers/ transpositions, are some of the important aspects in the insulation design. Strict control of manufacturing processes is equally important; manufacturing variations of insulating components should be monitored and controlled. Proper acceptance norms and criteria have to be established by the manufacturers for the insulation processing carried out before high voltage tests.

The transformer insulation system can be categorized into major insulation and minor insulation. The major insulation consists of insulation between windings, between the windings and the core, and between high voltage leads and ground. The minor insulation consists of internal insulation within the windings, viz. interturn and interdisk insulation. This chapter gives the methodology for the design of the major and minor insulation systems. Various methods for field computations are described. Factors affecting the insulation strength are discussed. In transformers with oil-solid composite insulation system, two kinds of failures usually occur. The first type involves complete failure between two electrodes, which can be in the form of jump/bulk-oil breakdown, creepage breakdown along an oil-solid interface or combination of both. The second type is a local failure (partial discharges) which may not immediately lead to a breakdown. Sustained partial discharges lead to deterioration of the insulation system eventually resulting in a failure between two electrodes. This chapter discusses these failures and countermeasures to avoid them. It also covers various kinds of test levels and a method of conversion of these to an equivalent design insulation level (DIL) for designing the major and minor insulation systems. Statistical methods for optimization and reliability enhancement are also introduced.

8.1 Calculation of Stresses for Simple Configurations

For a uniform field in a single dielectric material between two bare electrodes, the electric stress (field strength) is given by the voltage difference between the electrodes divided by the distance between them,

$$E_u = \frac{V}{d}\,. \tag{8.1}$$

The above equation is applicable to, for example, a parallel plate capacitor with one dielectric (with end fringing effects neglected).

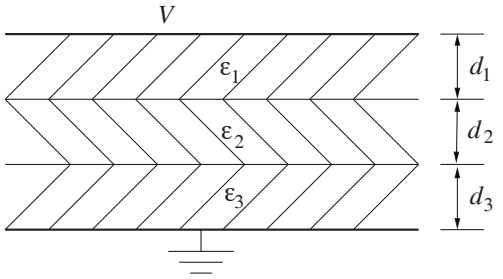

Figure 8.1 Multidielectric configuration.

For nonuniform fields (e.g., a cylindrical conductor–plane configuration), the stress (E_{nu}) is higher at the conductor surface; an increase in the stress value as compared to that under the uniform field condition is characterized by a non-uniformity factor (η),

$$\eta = \frac{E_{nu}}{E_u}. \tag{8.2}$$

The nonuniformity factor is mainly a function of the configuration.

For a multidielectric case of two parallel plates shown in Figure 8.1, the stress in any dielectric for a potential difference of V between the plates is

$$E_i = \frac{V}{\varepsilon_i\left(\frac{d_1}{\varepsilon_1}+\frac{d_2}{\varepsilon_2}+\frac{d_3}{\varepsilon_3}\right)} \qquad i = 1, 2, 3 \tag{8.3}$$

where ε_i is the relative permittivity of i^{th} dielectric. This expression for the configuration of parallel plates can be derived by using the fact that the electric field intensity is inversely proportional to permittivity (for discussions on various field quantities and the basic field theory, refer to Chapter 12). The stress value is constant within any dielectric.

For a configuration of two concentric cylindrical electrodes of radii r_1 and r_2, with a single dielectric between them as shown in Figure 8.2, the stress in the dielectric is not constant. The stress at any radius r ($r_1 < r < r_2$) is

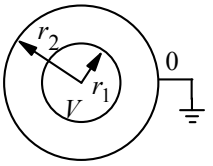

Figure 8.2 Concentric cylindrical electrodes.

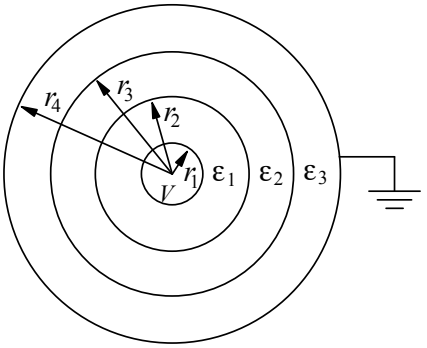

Figure 8.3 Concentric cylindrical electrodes with multiple dielectrics.

$$E = \frac{V}{r \ln \frac{r_2}{r_1}} \tag{8.4}$$

and the maximum stress occurs at the inner electrode surface given by

$$E_{\max} = \frac{V}{r_1 \ln \frac{r_2}{r_1}}. \tag{8.5}$$

For the multi-dielectric case shown in Figure 8.3, the stress at any radius r is

$$E_i = \frac{V}{r\varepsilon_i \left[\frac{1}{\varepsilon_1} \ln \frac{r_2}{r_1} + \frac{1}{\varepsilon_2} \ln \frac{r_3}{r_2} + \frac{1}{\varepsilon_3} \ln \frac{r_4}{r_3} \right]} \qquad i = 1, 2, 3. \tag{8.6}$$

For a cylindrical conductor-plane configuration (Figure 8.4), formulae for stresses at the conductor and plane surfaces are derived in Appendix D. The maximum stress on the conductor surface occurs at point P (along the shortest distance between the two electrodes) which is given by the following expression (Equation D.14 of Appendix D),

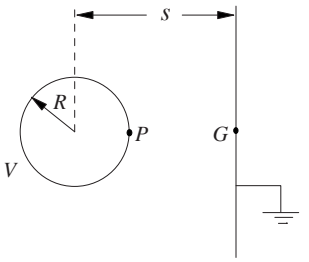

Figure 8.4 Cylindrical conductor-plane configuration.

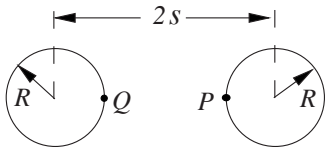

Figure 8.5 Stress between two bare cylindrical conductors.

$$E_P = \frac{V}{(s-R)} \frac{\sqrt{(s/R)^2 - 1}}{\ln\left[\sqrt{(s/R)^2 - 1} + (s/R)\right]} \tag{8.7}$$

and the maximum stress at the plane occurs at point G, whose expression is (Equation D.19),

$$E_G = \frac{V}{(s-R)} \frac{2 \times \sqrt{((s/R)-1)/((s/R)+1)}}{\ln\left[\sqrt{(s/R)^2 - 1} + (s/R)\right]}. \tag{8.8}$$

In the previous two equations, the factor multiplying the term $(V/(s-R))$ is the nonuniformity factor. For calculation of stress at any other point along the shortest distance, Equation D.22 can be used.

For the configuration of two bare cylindrical conductors shown in Figure 8.5 with a potential difference V between them, the maximum electric stress occurring at points P and Q is given as (Equations D.12 and D.13)

$$E = \frac{V}{2\,(s-R)} \frac{\sqrt{(s/R)^2 - 1}}{\ln\left[\sqrt{(s/R)^2 - 1} + (s/R)\right]}. \tag{8.9}$$

The above equation is applicable when the electrostatic field between the two conductors is not influenced by any other boundary condition (a case of two isolated conductors).

Thus, for bare leads of equal radii, the configuration is equivalent to considering a potential difference of $(V/2)$ applied between one of the conductors and a plane at a distance of s from the conductor center (the cylindrical conductor-plane configuration of Figure 8.4).

For the configuration of a paper-insulated cylindrical conductor (e.g., an insulated high voltage lead in a transformer) and a plane shown in Figure 8.6, the maximum stress in the oil at the surface of the covered conductor (at point A) is

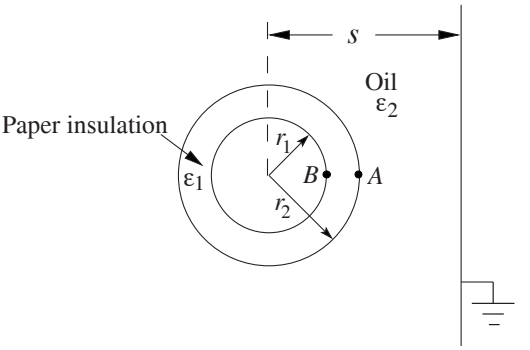

Figure 8.6 Stress between insulated lead and ground.

$$E_A = \frac{V}{r_2\varepsilon_2\left\{\dfrac{\left(\dfrac{s}{r_2}-1\right)\ln\left[\left(\dfrac{s}{r_2}\right)+\sqrt{\left(\dfrac{s}{r_2}\right)^2-1}\right]}{\varepsilon_2\sqrt{\left(\dfrac{s}{r_2}\right)^2-1}}+\dfrac{\left(\dfrac{r_2}{r_1}-1\right)\ln\left[\left(\dfrac{r_2}{r_1}\right)+\sqrt{\left(\dfrac{r_2}{r_1}\right)^2-1}\right]}{\varepsilon_1\sqrt{\left(\dfrac{r_2}{r_1}\right)^2-1}}\right\}}. \tag{8.10}$$

Similarly, the maximum stress in the paper insulation at the conductor surface (at point B) is given by the expression,

$$E_B = \frac{V}{r_1\varepsilon_1\left\{\dfrac{\left(\dfrac{s}{r_2}-1\right)\ln\left[\left(\dfrac{s}{r_2}\right)+\sqrt{\left(\dfrac{s}{r_2}\right)^2-1}\right]}{\varepsilon_2\sqrt{\left(\dfrac{s}{r_2}\right)^2-1}}+\dfrac{\left(\dfrac{r_2}{r_1}-1\right)\ln\left[\left(\dfrac{r_2}{r_1}\right)+\sqrt{\left(\dfrac{r_2}{r_1}\right)^2-1}\right]}{\varepsilon_1\sqrt{\left(\dfrac{r_2}{r_1}\right)^2-1}}\right\}}. \tag{8.11}$$

At any other point in this geometry and for more complicated electrode configurations, analytical or numerical techniques should be used for accurate field computations as described in the next section.

8.2 Field Computations

8.2.1 Analytical methods

For estimating electric stress levels at various critical electrodes, it is necessary to find electrostatic field distribution. The field distribution can be determined by a variety of methods. Classical methods such as the method of images give accurate results whenever they can be applied. For complex configurations, which exist inside a transformer, these methods cannot be applied. Initially, transformer designers had to depend on analog methods in which conducting paper and electrolytic tank analogs were used [1]. Before the advent of computers and numerical methods, these methods were widely used for multi-electrode and multidielectric material systems of transformers with two-dimensional approximations of the problems. The stressed oil volume, required for estimation of strength, was also calculated by direct plotting of equigradient lines on a conducting paper analog by using suitable instrumentation [2]. Analog methods are inconvenient, inaccurate, and expensive, and are limited in their application. They may not be relevant now due to availability of advanced computational techniques.

A conformal mapping technique such as the Schwarz-Christoffel transformation has also been widely used for relatively simple geometries within the transformers [3, 4]. In this method, the whole region of interest is mapped into a new plane in which the solution is constructed involving unknown constants in the transformation equation. The unknown constants are calculated by solving a set of nonlinear equations which describe the boundaries of the region in the original plane. Curved boundaries can also be handled in this method. Although the method is suitable for regions with a single dielectric material, for multidielectric problems an approximate solution can be obtained by converting them into a single dielectric region by using equivalent insulation distances. The method is best suited for a simply connected region containing few electrodes. For multiple connected regions with complicated electrode shapes and multiple dielectrics, this method is not suitable.

8.2.2 Numerical methods

In many cases, physical systems are so complex that analytical solutions are difficult or impossible, and hence numerical methods are commonly used for field computations. A numerical technique, the finite difference method (FDM), is used in [5, 6]; it results in a set of linear equations which are solved by direct matrix methods or iterative methods. FDM gives accurate results and can handle curved boundaries accurately if more grid points are taken on the boundary. Its main disadvantage is that the solution (potential distribution) is available at discrete points only, and hence the method presents some difficulties where quantities like stressed areas/volumes are required to be calculated [7].

One of the most powerful and popular numerical techniques today is the finite element method (FEM). It is in use for electrostatic field computations since the last four decades [8]. Usefulness of the method has already been demonstrated for magnetostatic and eddy current problems in earlier chapters. At locations where the field is changing sharply, higher order polynomials can be used to approximate the potential distribution within the corresponding elements and/or a fine mesh can be used. As the method yields a set of linear equations, solution can be obtained by direct matrix methods or iterative methods. The electric stress in any element is calculated by differentiating the approximated polynomial function. The stressed area between two equigradient lines can be derived by finding the elements in which the stresses are within the two limits of stress values.

Many adopt the charge simulation method (CSM) for electric field computations because it is suitable for unbounded regions and it has high accuracy [9]. In this method, physically distributed charges on the conductor surface are replaced by discrete fictitious line charges placed outside the space in which the field distribution has to be computed. The magnitudes of these charges are calculated in order that their integrated effect satisfies the boundary conditions exactly at some selected number of points on the boundary. The method requires proper selection and placement of a large number of charges for a reasonable accuracy. For example, a charge distribution on the surface of a high voltage electrode can be replaced by k line charges placed inside the electrode. For determining the magnitude of these charges, k points are chosen on the surface of the electrode and the condition to be satisfied is as follows. At each of these points on the electrode surface, the potential resulting from the superposition of these fictitious charges should be equal to the conductor electrode potential V_c,

$$\sum_{i=1}^{k} P_i \cdot Q_i = V_c$$

where P_i is a potential coefficient and Q_i is a discrete fictitious line charge. When the above equation is applied to all the selected points k, we obtain a system of k linear equations which are solved to obtain the magnitudes of the k charges. The electric field value at any point in the domain then can be determined easily by the superposition principle using these k charges.

CSM is not suitable for complex electrode configurations with multiple dielectrics. On the contrary, FEM is most suitable for complex but bounded problems. For electrodes with very small radius, because of the limitation on the smallest size of the element that can be used and the approximation of a curved path by small line segments, the accuracy of FEM may not be the best. Hence, advantages of CSM and FEM can be combined with elimination of their disadvantages in the combination method as reported in [10]. In this method, the

entire problem space is divided into two parts; CSM is used mainly for the open space with infinite boundary and FEM is used for the finite enclosed space.

8.3 Factors Affecting Insulation Strength

The breakdown voltage of a dielectric material is a statistically distributed quantity and varies as a function of its physical/chemical properties and impurities present in it. Failures may not always be initiated by high electrical stresses; interrelated thermal, chemical and mechanical factors may have significant influence on the breakdown processes. As compared to metals, insulating materials exhibit an erratic behavior. With aging and/or deterioration of electrical and mechanical properties, it becomes even more difficult to predict their performance. In transformers, a composite oil-solid insulation system is used. The erratic behavior of the oil is pronounced when used alone. There is a much larger scatter of its breakdown voltage as compared to that of air. The large scatter may be associated with random paths of streamers and variations in their progress in the oil [11]. Hence, large oil ducts are always subdivided by solid insulation into small ducts due to which the transformer insulation system becomes more dependable and stable.

Compared to the breakdown processes in gases, the processes that initiate and lead to breakdowns in the oil are difficult to comprehend. General models using *micro-bubble* and *weak-link theory* have been attempted. It is reported in the literature that some micro-bubbles exist in the oil even in the absence of an electric field, and the application of a field creates additional bubbles. It is suggested that discharges are ignited in these micro-bubbles. Due to dielectrophoretic forces, particles/impurities are swept from surrounding oil regions to the points of highest stress in the oil gap [12]; the corresponding theory is described in the following subsection. These particles then tend to line up along the electric field lines to create a *weak-link* in the oil gap; this phenomenon is accentuated in the presence of moisture. Transformer designers use to a great extent semi-empirical data for the insulation design as there is still no coherent theory of oil breakdown.

8.3.1 Suspended solid particle mechanism

Transformer oil may contain some amount of solid impurities in the form of fibers or dispersed particles [13]. Along with the solid impurities, bubbles generated during overload periods are also present in the oil [14]. If each of these impurities is considered as a sphere of radius r and permittivity ε, immersed in oil having permittivity ε_{oil}, then in an electric field $\mathbf{E}$ they are polarized and have induced dipole moment in them. The force they experience is given as [13, 15, 16]

$$\mathbf{F} \propto \left(r^3 \frac{\varepsilon - \varepsilon_{oil}}{\varepsilon + 2\varepsilon_{oil}} \mathbf{E} \cdot \nabla \right) \mathbf{E} .$$

If **E** is only in the *x*-direction the above expression reduces to

$$\begin{aligned} \mathbf{F} &\propto \left(r^3 \frac{\varepsilon - \varepsilon_{oil}}{\varepsilon + 2\varepsilon_{oil}} E_x \mathbf{a}_x \cdot \left\{ \mathbf{a}_x \frac{\partial}{\partial x} + \mathbf{a}_y \frac{\partial}{\partial y} + \mathbf{a}_z \frac{\partial}{\partial z} \right\} \right) E_x \mathbf{a}_x \\ &\propto \left(r^3 \frac{\varepsilon - \varepsilon_{oil}}{\varepsilon + 2\varepsilon_{oil}} E_x \frac{\partial}{\partial x} \right) E_x \mathbf{a}_x \\ &\propto r^3 \frac{\varepsilon - \varepsilon_{oil}}{\varepsilon + 2\varepsilon_{oil}} E_x \frac{\partial E_x}{\partial x} \mathbf{a}_x . \end{aligned} \qquad (8.12)$$

If $\varepsilon > \varepsilon_{oil}$, which is true for solid particles or bubbles with water vapor content, the force on the particles/bubbles is directed towards the high electric field region according to Equation 8.12. If $\varepsilon < \varepsilon_{oil}$, which is true for air bubbles (without water content), the force on the bubbles is directed towards the low electric field region. For metal particles $\varepsilon \to \infty$, therefore the quotient in the above expression reduces to unity and the force on the metallic particles, which is high in comparison to nonmetallic particles, is directed towards the high electric field region.

8.3.2 Effect of moisture and impurities

Needless to say, moisture and other impurities have a significant deteriorating effect on the dielectric strength of the transformer insulation. The moisture has a deteriorating effect on both electrical and mechanical properties of the insulation. As the moisture content in oil increases, strength reduces drastically until the saturation point, after which there is no appreciable further deterioration of the strength. Hence, percentage saturation is a decisive factor influencing the dielectric strength of the transformer oil [17, 18]. The degrading effect of the moisture is also significantly affected by the amount of other impurities present in the oil [19]. The presence of solid impurities makes the effect more significant even with low moisture content in the oil. The solid insulation has more affinity (as compared to the oil) for moisture. It has been reported in [20] that at room temperature, the reduction in the dielectric strength of the oil due to cellulose particles becomes manifold at high moisture levels.

An increase in pressure or temperature increases the quantity of a gas the oil can hold. If the oil temperature rises owing to an increase in ambient temperature or load, the oil expands and the pressure increases. When the pressure falls, the oil has more gas content than it can hold. The excess gas content eventually diffuses out of the oil after some time (a few days or weeks) depending on the ratio of the oil surface exposed to the gas and the total oil

volume. If the pressure drops suddenly, gas bubbles may be formed in the oil, reducing its dielectric strength [19].

The dielectric strength of paper insulation is largely decided by its mechanical properties. A brittle paper having lost its mechanical strength has a low dielectric strength. Aging of insulation affects its mechanical strength more significantly than the electrical strength [19]. The rate of ageing increases rapidly with an increase in temperature and the mechanical properties deteriorate. An aged transformer may have 2% to 3% of moisture.

Many studies have been reported in the literature [17, 20–23] highlighting the effects of various influencing factors, viz. temperature, pressure, impurities, moisture, electrode shape/surface, electrode metal, applied voltage and its duration, gap between electrodes, etc., on the oil breakdown strength.

The presence of moisture in the regions of high electric field regions may lead to partial discharges [24]. Moisture may loosen the clamping system and therefore reduce the ability of a transformer to withstand short-circuit forces. The various sources of moisture in a transformer are (a) residual moisture (typically 0.5% or less after factory processing), (b) ingressed moisture (during repair/installation, due to poor sealing at joints, and due to a pressure difference with respect to atmosphere), and (c) aging of cellulose insulation.

Under normal operating conditions, temperature variations in a transformer are the major cause for the transfer of moisture between paper insulation and oil. As the temperature increases, some amount of the moisture present in the paper insulation transfers to the oil, and when the temperature decreases, the moisture returns back, but at a slower rate, from the oil to the paper. The distribution of water in the layers of paper insulation is nonuniform. Water molecules migrate from hot inner layers closer to conductor surfaces to outer colder layers [25].

Free water may appear in the transformer oil when moisture in it exceeds the saturation value. This happens, for example, when a transformer is tripped on a cool day after some time of operation at high temperatures. As the temperature decreases abruptly, the water solubility in oil reduces quickly and the moisture returns to the paper but this reverse process is slower as mentioned earlier. Therefore, free water appears in the oil, which will reduce its dielectric strength.

8.3.3 Effect of time and frequency

Volt-time characteristics are specific curves representing the relationship between voltage and time-to-breakdown. These characteristics are generally governed by the fact that some amount of energy is required to cause the breakdown of a gap, and thus the breakdown voltage and the corresponding time are interdependent [26]. The higher the voltage the lower the time is to cause the breakdown. A typical volt-time curve of air insulation is shown in Figure 8.7.

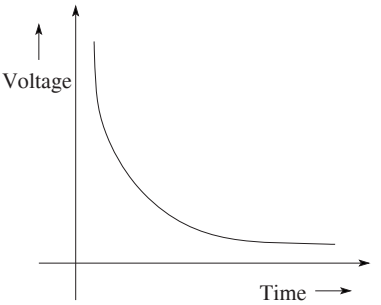

Figure 8.7 Typical volt-time curve.

In short-time power frequency overvoltage tests, the breakdown strength of solid insulation is influenced by temperature. When an alternating voltage is applied, initially the heat on account of dielectric losses is stored inside the insulation, and its temperature begins to rise. The heat is dissipated to surrounding ambient which is at a lower temperature. The insulation temperature continues to rise until a state of equilibrium is reached, wherein the heat dissipated is equal to the heat generated. But with an increase in the temperature, the resistance of the solid insulation decreases due to its negative temperature coefficient of resistance resulting in an increase of its leakage current. Losses further increase due to the increased current value, and this leads to a run-away condition resulting in an eventual breakdown. Hence, with an increase in the time of application of the voltage, the dielectric strength reduces. For most insulating materials, the infinite time strength is approximately two-thirds of the one-minute strength, and the one-second strength is about 1.6 times the one-minute strength [27].

The dependence of the oil dielectric strength on the duration of voltage application is erratic as compared to the solid insulation. Although it is difficult to obtain definite volt-time characteristics, it can be said that the dielectric strength reduces rapidly after a few seconds and remains more or less constant after a few minutes for power frequency test voltages. It requires time for impurities to get lined up and bridge the gap; hence for a very short time period of voltage application the strength is very high.

The frequency of the test voltage has a significant effect on the insulation strength; its increase results in reduction of the strength, and thus increases rapidly the severity of the power-frequency overvoltage test. As the frequency increases, the dielectric loss and the heating effect increase, reducing the strength of the solid insulation. The strength does not vary linearly with the reciprocal of the frequency [28] but approximately with an exponent of 0.137, i.e., strength $\propto (1/f^{0.137})$. The frequency has a much smaller effect on the oil strength compared to that on the solid insulation. In general, it can be concluded that an increase in the frequency has a harmful effect on the strength of

transformer insulation during the power-frequency overvoltage test. If the frequency is increased, the time of application of the test voltage should be reduced to produce the same amount of dielectric stress. Hence, standards specify the total number of cycles for the power frequency induced overvoltage test. When this test (in which the insulation is stressed to at least twice the voltage/turn) is conducted, the frequency is also increased in order to avoid core saturation. The IEC standard 60076-3, second edition: 2000, specifies that the test time should be 60 seconds for any frequency up to and including twice the rated frequency. For a test frequency higher than twice the rated frequency, the test time should be reduced and calculated in accordance with the following formula,

$$test\ duration = 120 \times \frac{rated\ \ frequency}{test\ \ frequency} \text{ seconds} \tag{8.13}$$

subject to a limit that it should not be less than 15 seconds. In other words, the number of cycles for the test is fixed; 6000 cycles for 50 Hz and 7200 cycles for 60 Hz transformer. Hence, for a 50 Hz transformer, if the test is conducted at 200 Hz, the test duration should be 30 seconds.

The effect of the time of application and frequency of the voltage (during power-frequency overvoltage tests) on the creepage strength is not significant as compared to that on the puncture of solid insulation [28]. The creepage breakdown in the absence of conducting material impurities is mostly decided by oil failure, and an increase in the frequency does not result in significant decrease of the oil strength due to a smaller heat effect [29].

Regarding impulse volt-time characteristics, two types of curves have been derived in the literature. For the first one, called full-wave volt-time curve, a full impulse wave is applied across the insulation and the breakdown may occur either on the wave-front or wave-tail portions or it may not occur if the voltage is low. A volt-time curve is plotted using these breakdown points. For the second one, the wave-front slope is varied, and for each slope value the voltage is increased till the breakdown occurs. This front-of-wave volt-time curve is of similar nature but has somewhat different values as compared to the full-wave volt-time curve.

The impulse volt-time curve of the insulation used in a transformer is drastically different than that of air insulation. Typical curves for oil and oil-impregnated pressboards are shown in Figure 8.8. The curves indicate that the oil and solid insulations have flat characteristics after few microseconds. Composite oil-solid insulation system generally has volt-time characteristics close to that of the solid insulation alone. It is reported in [30] that the dependence of dielectric strength on the impulse duration in the range of 10^{-3} to 10^{-1} seconds is small for major insulation consisting of oil-barrier system (e.g., gaps between windings).

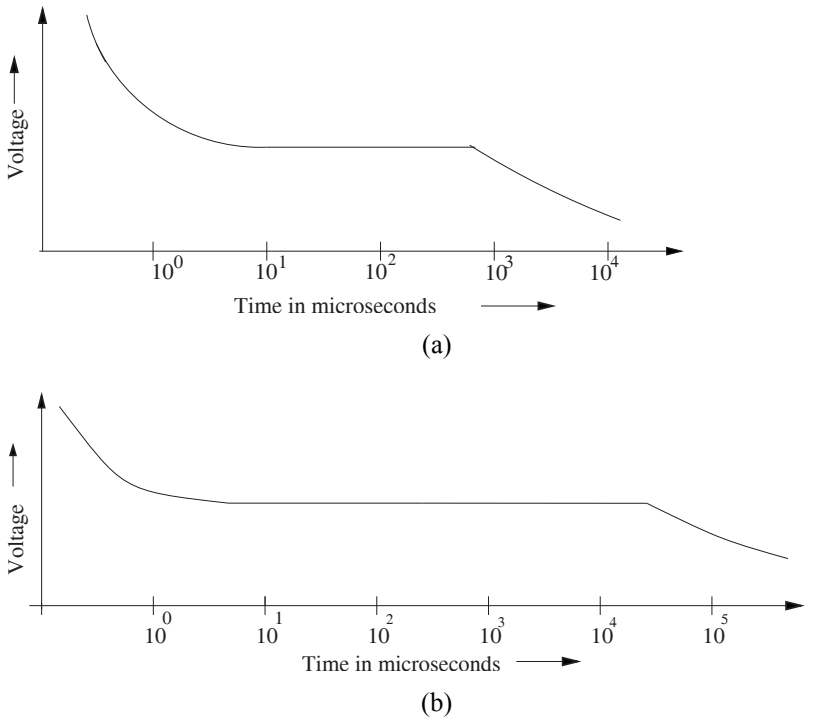

Figure 8.8 (a) Volt-time curve of oil-gap; (b) Volt-time curve of oil-impregnated pressboard.

The impulse ratio can be defined as the ratio of the impulse full wave strength to the one-minute r.m.s. AC (50 or 60 cycles) strength. Long ago, researchers reported the impulse and one-minute volt-time characteristics [31, 32, 33] and the corresponding impulse ratios. Later, the volt-time curves for partial discharge inception voltages have also been investigated. The partial discharge and breakdown volt-time curves, and corresponding impulse ratios are reported in [34] for three different configurations, viz. turn-to-turn insulation, disk-to-disk insulation and oil gaps between barriers. It has been shown that the breakdown volt-time curve, as expected, is significantly above the partial discharge volt-time curve in the microsecond range. The two curves come very close to each other in the AC long-term region of several minutes as shown by the typical curves in Figure 8.9. It means that for very short times, a partial discharge initiated is not sufficient, whereas in the longer duration of several minutes its magnitude is sufficient to cause a breakdown.

During factory testing, different dielectric tests, lightning impulse, switching impulse, and short-time/long-time power frequency tests, are carried out separately independent of each other. In actual power system operation, the

transformer may be subjected to superimposed AC and lightning impulse voltages. The dielectric strength under such superimposed AC and lightning stress levels is reported in [35]. The breakdown voltage under the superimposed stress condition can be significantly lower than the corresponding value for the lightning impulse alone.

Gas-insulated substations (GIS) are being used widely all over the world. Disconnecting switch operations in GIS generate steep front transient overvoltages characterized by a rise time of a few nanoseconds (5 to 20 ns), a short duration of several microseconds, and amplitude as high as 2.5 per unit. The 50% breakdown probability voltage of oil-paper insulation is reported to be lower for steep-fronted GIS transients than for lightning impulses [36]. Oil-paper insulated equipment like transformers or their bushings, when subjected to GIS transients, may fail at voltages below the lightning impulse level. Hence, the insulation of transformers for the GIS applications must be designed with due consideration to these steep-fronted transients.

Sometimes transformers are subjected to high frequency oscillatory overvoltages. In such cases, the damping of oscillations (defined as the ratio of two consecutive amplitudes of same polarity) has significant impact on the dielectric strength of their insulation; the strength increases with the increase in damping. For example, the breakdown strength for an undamped oscillating voltage having a frequency of 0.9 MHz is below the dielectric strength for the lightning impulse voltage, whereas with a damping ratio of 0.9 the strength is in the same range of as that for the lightning impulse voltage [37].

8.3.4 Effect of temperature

As temperature increases, the dielectric strength of most of the solid insulations reduces. Due to an increase in the dielectric loss (and the power factor), the temperature goes up further. The ohmic resistance of the insulation reduces with increasing temperature, which results in flow of more current through it. It may finally lead to a current run-away condition and an eventual breakdown.

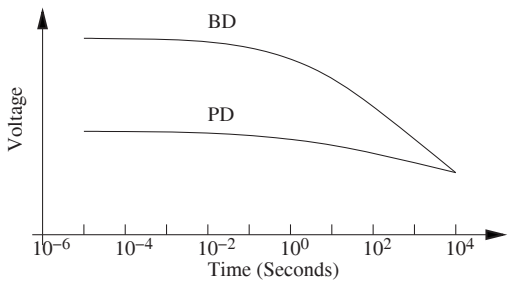

Figure 8.9 Breakdown (BD) and partial discharge (PD) volt-time curves [34].

The oil dielectric strength usually increases with temperature in the operating range. A marked improvement in the strength is observed at high temperatures for the oil containing high moisture content. The temperature effects are dynamic in the sense that a considerable amount of time is required for establishing equilibrium between moisture in the oil and that in the solid insulation made from cellulose material. During different thermal loading conditions, there is continuous interchange of moisture affecting the strength to some extent. For a reasonable temperature rise, the amount of moisture in the oil reduces, which helps to keep the transformer insulation system in a healthy condition. It is known that an increase of temperature usually increases the mobility of carriers and hence the conductivity. Hence, the breakdown voltage of the oil should decrease with an increase in its temperature; experiments conducted by many researchers show the opposite trend. Variations in the mobility of carriers, therefore, may not possibly be used to explain the results of experiments. There is some amount of gas bubbles present in the oil and their solubility increases with temperature; this explains the increase of strength with the temperature [38]. Hence, it is generally not preferable to keep a transformer idle for a long time. Even a spare transformer should be kept in a no-load condition for a reasonable amount of time periodically. The strength increases with temperature from –5°C to about 80 to 100°C; above which it reduces [27, 39]. Below –5°C, the strength increases rapidly as moisture particles in the suspension are frozen.

8.3.5 Effect of thickness

It is well-known that the dielectric strength of an insulating material does not generally increase in direct proportion to its thickness in a nonuniform field condition. The strength can be expressed in terms of the thickness by the following simple exponential formula [40]:

$$E \propto (thickness)^n \,. \tag{8.14}$$

The numerical constant n varies from 0.5 to 1.0 depending on the processing/treatment of the material and the degree of nonuniformity of the field. For an untreated insulation, n is lower as compared to a treated insulation. For better shaped electrodes giving uniform fields, its value is higher. For an electrode with a small radius, there is more crowding of equipotential lines at its surface resulting in a high stress and a low value of the breakdown voltage. The above equation indicates that as the voltage rating increases, the insulation content of the transformer increases more rapidly.

8.3.6 Stressed volume effects

The breakdown strength of the transformer oil decreases as its stressed volume increases [41]. This is also in line with the general fact that the insulation

strength reduces when its area under test increases [42]. The oil dielectric strength reduces as its stressed volume increases for both power frequency and impulse voltages [17]. Although, designers take either the stressed area or the stressed volume for strength considerations, it is generally agreed that the size of the structure is instrumental in the breakdown process. The strength calculations based on the stressed oil volume are more commonly used in the industry. The breakdown of a gap is usually initiated at the weakest spot under a high stress condition. If in some other gap a greater volume of oil is subjected to the same level of stress, it is quite probable that a still weaker spot is present, resulting in the breakdown at a lower voltage. The amount of impurities and electrode protrusions become important considerations for the area/volume effects. Usually the relationship between the breakdown strength and the stressed volume is obtained experimentally from many breakdown studies for various types of electrode configurations. The breakdown strength for a plain oil gap is expressed in terms of the stressed oil volume (for power frequency test voltages) as [12]

$$E = 17.9\left(SOV\right)^{-0.137} \text{ kVrms/mm} \tag{8.15}$$

where the stressed oil volume (SOV) is in cm^3. In [43], the 50% breakdown probability stress for one-minute power frequency voltage is calculated as

$$E = 11.5\left(SOV\right)^{(-1/9.5)} + 2.5 \text{ kVrms/mm} \tag{8.16}$$

where SOV is in cm^3. It can be verified that the strengths given by Equations 8.15 and 8.16 give the values of E of the same order for practical values of SOV (e.g., in the case of a high voltage lead to ground configuration). The design should be such that the calculated stress value should be lower than E by some experience-based margin. It is assumed in the above equations that electrodes are covered with some minimum thickness of paper insulation.

Thus, if a failure is predominantly decided by particles/impurities, a larger oil volume will provide more particles which are drawn into high stress zones, which may subsequently lead to a breakdown. However, a point is reached after which a further increase in the volume will have an insignificant effect on the strength since there is little influence of the field on remote zones unless the field divergence is low. Hence, the volume in the above equations is taken as corresponding to the region in which the calculated electric stress values are between the maximum value and 90% of the maximum value.

Equations 8.15 and 8.16 tell us that as the stressed volume increases, the dielectric strength of the insulation system reduces. If the electrode radius is increased, the stress values reduce, but at the same time the stressed oil volume increases reducing the withstand. Hence, an optimum electrode contour can be determined by studying the relative variations in the stress and strength values with different electrode contours [44].

8.3.7 Creepage phenomenon

The solid insulation is used inside a transformer at many places, viz. between turns, between layers, between disks, between a winding and ground, and between windings. The designer is confronted with mainly two types of electrical failures: puncture and creepage. The creepage strength of the solid insulation is significantly lower than its puncture strength. Along equipotential lines the creepage strength is maximum; therefore the electric field (**E**) should be normal to the insulation surface (since the equipotential lines are at right angles to the electric field). Due to complications of winding construction and connections, it is difficult to keep the field normal to the insulation surface everywhere. Also, it is not always possible to bend the solid insulation components to any desired radius. In any case, considering the fact that the electric field is actually a 3-D quantity, difficulties of having shaped insulation components normal to the field are obvious. The places where there is a field component parallel to the insulation surface, the strength is significantly reduced. When there is a failure along the surface of insulation, it is termed a creepage failure phenomenon. If the placement of the solid insulation results in stresses along its surface, much of the purpose of using it, viz. subdivision of oil ducts for higher overall strength, may be defeated.

The creepage flashover characteristics of oil-pressboard interfaces have been analyzed and reported in the literature [45, 46]. A permittivity mismatch of two insulation materials usually assists flashover phenomenon at their interface [47]. The electric field in the oil immediately adjacent to the pressboard is distorted due to the permittivity mismatch. Significant improvements can be made by matching permittivities of the oil and pressboard insulations [48]. Thus, a pressboard material having permittivity close to that of the oil not only reduces the oil stress but also results in a higher value of the flashover voltage along the oil-pressboard interfaces [49]. Hence, with a low permittivity pressboard, there is significant scope for optimization of insulation content since the electric field distribution will become more uniform in the oil-paper-pressboard insulation system of transformers. A low permittivity pressboard, manufactured by blending polymethylpentene fibers with cellulose fibers, has been used in a 765 kV, 500 MVA transformer [49].

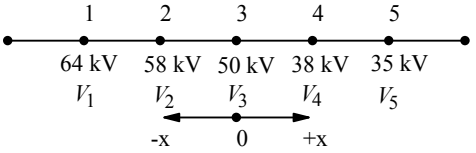

Figure 8.10 Cumulative stress calculation.

8.3.8 Cumulative stress calculations

Using calculations based on SOV, the strength of an oil gap can be calculated as discussed in Section 8.3.6; SOV-based calculations are more relevant for larger oil gaps. Another approach, in which cumulative stress calculations are done, is commonly used for the design of the insulation system of transformers. The approach is used for both creepage withstand assessment and oil gap design.

For estimating creepage withstand characteristics, cumulative stress distributions are determined along oil-solid interfaces. For a two-electrode case, finding the cumulative stress distribution is easy. The maximum stress is usually at one of the electrodes, and it reduces as we move toward the other electrode. Hence, the cumulative stress at any point is the difference between the electrode voltage and the voltage at that point divided by its distance from the electrode. For complex electrode configurations, with more than two electrodes, the maximum stress may not be at one of the extremities of the path (interface) under consideration, in which case the cumulative stress calculation should be started from the maximum stress point. The creepage stress distribution along a solid-oil interface can be calculated by using the procedure described in [50].

Let us consider a solid-oil interface shown in Figure 8.10 and assume that the potential values, calculated by some method at points 1, 2, 3, 4 and 5, spaced at 2 mm distance, are as given in the figure. It is also assumed that the stress is maximum at point 3 (7 kVrms/mm). The creepage stress is calculated for a unit length of 2 mm in either direction from point 3, and the path is extended in the direction of higher stress. Next, the cumulative stress is calculated for 4 mm length in either direction as shown in Table 8.1. The calculation procedure is continued till the entire path is traced. The calculated cumulative stress values are plotted in Figure 8.11. The withstand for each of these creepage distances (for power frequency overvoltages) can be calculated by [51]

$$E_{creep} = 15\, d_2^{-0.37} \text{ kVrms/mm} \tag{8.17}$$

Table 8.1 Cumulative Stress Calculation

Path length (mm)	Cumulative stress calculation		
	$+x$ direction	$-x$ direction	Path extended to point
2	$\frac{V_3 - V_4}{2} = 6.0$ kV/mm	$\frac{V_2 - V_3}{2} = 4.0$ kV/mm	4
4	$\frac{V_3 - V_5}{4} = 3.75$ kV/mm	$\frac{V_2 - V_4}{4} = 5.0$ kV/mm	2
6	$\frac{V_2 - V_5}{6} = 3.83$ kV/mm	$\frac{V_1 - V_4}{6} = 4.33$ kV/mm	1

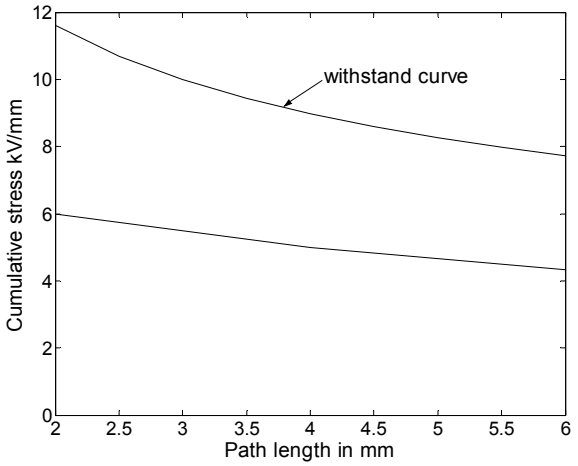

Figure 8.11 Plot of cumulative stress.

where d_2 is the creepage path length in mm. The equation is valid for a degassed oil and a good quality solid insulation with clean surface, and is in agreement with the curve deduced in [52, 12] by considering creepage field strengths for four different configurations.

It should be remembered that the calculated cumulative stress levels should be lower than the value given by Equation 8.17 by a margin depending on quality of components and manufacturing processes, i.e., the margin between the creepage withstand and creepage stress for any length should be more than a certain value fixed by the designer based on experience/established practices. Usually, the creepage strength is considered about 30% lower than the bulk oil (jump) strength [53, 54].

The reference withstand curve for bulk oil, subjected to power frequency overvoltages, is described by the following equation [12],

$$E_{oil} = 18\, d_1^{-0.38} \text{ kVrms/mm} \tag{8.18}$$

where d_1 is the oil gap in mm between covered electrodes, and the oil is considered without gases.

It is always advisable to cover the electrodes with some insulation as it improves the strength by about 15 to 20% [12]. The creep withstand calculated by Equation 8.17 is about 17 to 13% lower than the bulk oil withstand given by Equation 8.18 (for a length of 1 to 100 mm), but as a conservative value it can be taken 30% lower as mentioned earlier for any distance. The creep withstand has been taken about 21% lower than the bulk oil strength in [55].

Thus, we have seen that there are two distinct approaches for determining the withstand for bulk oil breakdown phenomena; one is based on the distance

(Equation 8.18 above) and the other is based on the stressed oil volume (Equation 8.15 or 8.16). These two approaches do not contradict each other, and the consistency of the strengths obtained from the gap length and stressed oil volume considerations has been elaborated in [12].

8.3.9 Effect of oil velocity

The velocity of oil has noticeable influence on its breakdown characteristics. It is reported in [43] that the power frequency breakdown voltage of moving oil is higher than that of stationary oil by 10 to 15% at about 5 cm/s, and it reduces and becomes equal to that of the stationary oil at a velocity of about 25 cm/s. It reduces further for higher velocities. The explanation for this particular behavior is as follows. If oil movement is more dominant than the force by which impurities are swept and drawn in high stress zones as observed in the case of stationary oil, the breakdown voltage tends to be higher as the velocity increases. When it increases beyond a certain value, reduction of the breakdown voltage may be linked to the stressed oil volume effect, wherein the probability of a large number of impurities passing through a high stress zone between the electrodes increases. This phenomenon is in line with the *weak-link* theory; the chances that weak-links of the oil (particles/impurity) may initiate a discharge are higher due to the fact that a higher volume of the oil passes through a high-stress zone [18]. Contrary to this theory, a higher velocity shortens the time for which impurities will remain in the high stress zone, and the breakdown voltage should increase as per volt-time characteristics. Hence, the breakdown voltage at higher velocities will depend on which of the two effects, the volt-time effect or the oil volume effect, is the deciding factor. For impulse conditions, the breakdown voltage does not seem to be affected by the oil velocity.

8.3.10 Processing of insulation

Removal of moisture and impurities from insulation is one of the most important manufacturing processes. Removing moisture from the oil is relatively simple, which can be done by conventional methods of filtration or heat/vacuum cycles. However, most of the moisture is in the solid insulation (it can be as high as 99%). Hence, a challenge is to make the solid insulation dry efficiently and quickly.

With an increase in the size of transformers, the time taken for processing of their insulation also increases. The time taken by a conventional hot air-vacuum process is considerably higher for large transformers with high voltage ratings. The conventional drying method may take more than 7 days for a 220 kV class transformer. The method consists of heating the assembly of the core and windings in an air medium and applying vacuum for extracting moisture. Moisture in an insulating material can be reduced by raising its temperature and/or by reducing water vapor partial pressure, i.e., by applying vacuum. The application of a vacuum speeds the moisture extraction process; heating alone

takes more time to remove a given amount of moisture from the solid insulation. Depending on the rating and voltage class of the transformer, several cycles of alternate heating and vacuum are required until the transformer insulation is dried. A moisture content of less than 0.5% is usually taken as the acceptance criterion for ending the process.

Requirement of a faster and more efficient process along with the need for better insulation performance resulted in the development and use of the kerosene vapor phase drying (VPD) method [56]. It is a fast and efficient method in which kerosene vapor at a high temperature is used as the heating medium instead of hot air (used in the conventional method). A special grade of kerosene, heated to about 130°C in an evaporator and converted into vapor form, is injected into the autoclave or transformer tank housing the assembly of the core and windings. As the process of heating is done under vacuum, the moisture extraction starts during the heating period itself. When the insulation reaches a certain desired temperature, a fine vacuum is applied to remove the remaining moisture. In the VPD process, windings and insulation systems are almost uniformly heated, whereas in the conventional process inner insulation components may not be heated adequately. The total process time in the VPD method is less than half of that for the conventional method in which, as heating is done through the medium of air in presence of oxygen, the temperature is limited to about 110°C. On the contrary, in the VPD process, the drying is done in an oxygen-free atmosphere (virtually in vacuum), and hence there are no harmful effects or loss of insulation life even at 130°C. Thus, uniform heating at a higher temperature under vacuum results in faster removal of moisture. The VPD process has another advantage that the vapor condensing on colder winding and insulation parts washes out impurities. This aspect is particularly useful when one wants to clean windings of transformers which come back to factory for repair. With uniform heating of all insulation parts, shrinkage is uniform. Furthermore, shrinkage is negligible during operation on site, ensuring the mechanical integrity of windings.

Low frequency heating (LFH) method is also used for the drying purpose, particularly for distribution and medium range power transformers. A low frequency (few mHz) impedance voltage is applied to the HV winding with the LV winding short-circuited, which results in uniform heating of the windings of the transformer (since the eddy current loss in the winding conductors, a cause of uneven temperature distribution, is almost zero). The windings are heated to 110°C and the moisture in the solid insulation is removed in less time as compared to the conventional technique, consisting of hot oil circulation and vacuum cycles, in which the operating temperature is about 60 to 80°C. The required impedance voltage is also low due to a very low frequency of operation. Generally, a current less than 50% of the rated value is required to reach a desired winding temperature. Main advantages of the technique are reduction in the process time, energy savings, and on-site applicability. At the site, after taking the (wet) transformer out of service and with its oil removed, the method can

be applied to remove the moisture in its solid insulation. This way, the problem is addressed directly since most of the moisture is in the solid insulation. The requirement of a lower voltage application goes well with the condition that the transformer is without oil.

Presence of small cellulose particles in oil has a pronounced effect on its dielectric strength. Due to the hygroscopic nature of cellulose, moisture in the oil plays a decisive role as it is absorbed into the cellulose. The cellulose particles have a deteriorating effect on the strength even when the ppm content of moisture in the oil is well within limits; the water content (saturation) in the cellulose insulation is the deciding factor. Hence, it is absolutely essential to minimize content of suspended cellulose particles and fibers in the oil. These particles usually originate from the surface of paper/pressboard insulation. The major sources of these particles are the edges of radial spacers (pressboard insulation between disks) and axial spacers (pressboard strips in the major insulation between windings) if these components do not have a machined finish. Punching operations required for making these components involve shearing of pressboards. Burrs, micro-delaminations and subsequent formation of cellulose fibers are unavoidable if punching tools are not of good quality or their maintenance is inadequate. Hence, it is always recommended to have an additional operation of milling so that the edges of the pressboard components are smooth and fiber free.

Once properly processed and impregnated with dry oil, it is important to prevent moisture from getting access to the oil impregnated solid/paper insulation. A simple and widely followed method for small and medium power transformers is to provide a breather with a dehydrating material (such as silica gel) and an oil seal. The oil seal provides isolation to the dehydrating material from the atmosphere. Thus, the transformer breathes through the dehydrating material, and hence the moisture from the atmosphere cannot get into the transformer oil. Advanced breather systems (e.g., drycol breather) are also popular in some countries.

Transformer oil deteriorates to some extent when exposed to the atmosphere. Air acts as an oxidizing agent forming sludge in the oil. Hence, many of the large transformers are equipped with an air bag fitted inside the conservator, so that the transformer oil does not come in direct contact with the outside atmosphere. Changes in oil volume on account of temperature variations are absorbed by this flexible bag thus maintaining a constant pressure. One side of this bag is in contact with the atmosphere through a dehydrating agent so that if the bag ruptures, the oil is not exposed to the atmosphere since the dehydrating breather steps into the conventional mode of operation. Actions can be initiated to replace the ruptured bag in the meantime.

Once the transformer (insulation) is processed, it is filled with dry and degassed oil (having dielectric characteristics within acceptable limits) under vacuum. Immediately after the oil filling, some air bubbles are formed in the insulation which may lead to partial discharges. Hence, a certain hold/settling

time needs to be provided before the commencement of high voltage tests. During the settling period, heavier particles/impurities settle down at the bottom and the air bubbles move up or get absorbed. After the hold time, air bubbles should be released by bleeding (through air release plugs) at the top so that the transformer is free of (trapped) air. With this, dielectrically critical areas are cleared. The hold time increases with the voltage rating of transformers. For 132 kV class transformers it should be minimum 24 to 36 hours, for 220 kV class it should be about 48 hours, and for 400-500 kV class transformers it is desirable to have the hold time of about 72 hours [57]. A lower hold time may be adopted by the transformer manufacturers based on their experience.

8.4 Test Methods and Design Insulation Level (DIL)

In service, the transformer insulation is subjected continuously to operating voltages and occasionally to overvoltages. The operating voltages decide the working voltage stress on the insulation. The overvoltages can be broadly divided into lightning overvoltages (aperiodic surges with duration of one to tens of microseconds), switching overvoltages (oscillatory surges with duration up to thousands of microseconds), and temporary overvoltages (lasting for few minutes) at or close to the power frequency. Standards on transformers have defined test levels for various voltage classes. There are basically four different types of tests: a lightning impulse test, a switching impulse test, a short duration power frequency test, and a long duration power frequency test with partial discharge measurement. While the first three tests check the insulation's overvoltage withstand capability, the long duration test is mainly intended for checking the insulation behavior under working voltage stresses. The design of insulation between various electrodes is decided by one or more of these test levels. An interdisk spacing is decided by impulse stresses, whereas the end insulation between the windings and the top/bottom yoke is predominantly decided by the power frequency test voltages. The conductor insulation is decided by either the impulse stress or the working voltage stress.

When oil and solid insulation are stressed together, two kinds of failures can usually occur. In one type, there could be a complete catastrophic failure between two electrodes (e.g., jump breakdown, creepage breakdown or combination of both). This kind of failure is uncommon if adequate clearances are provided and maintained. The second one is a local oil failure (partial discharge). In earlier days, the partial discharge (PD) measurement test was not conducted due to nonavailability of proper instrumentation. Also, many partial discharges used to result in undetected damages (since the solid insulation acted as a barrier to propagation of discharges). With the development of instrumentation and awareness of slow but damaging effects of discharges, the partial discharge test has become one of the most important tests for high voltage transformers. The international standards on transformers have defined PD limits. Some manufacturers set their internal norms much lower than those

specified in the standards in order to ensure long-term reliability of transformers. In order to obtain very low PD levels, sharp electrodes inside the transformer have to be rounded or electrostatically shielded. Processing and impregnation procedures have to be excellent for minimizing impurities and air voids. Also, the manufacturers should have proper instrumentation for the measurement of low PD levels. Ambient partial discharges in the test area and surrounding environment have to be minimized. Partial discharges lead to progressive damage of insulation resulting in an eventual failure after a time period which depends on their severity and location inside the transformer. Hence, it is advisable to eliminate sources and causes of partial discharges so that progressive deterioration of insulation becomes a remote possibility.

A transformer should be designed and manufactured such that it is partial discharge free. It should be noted that the impregnation of insulation may not be perfect and also it may not be possible to control the dielectric field uniformly at all locations. Hence, in practice some amounts of partial discharges are always there; efforts should be made to minimize them. Electric stress values below PD inception levels do not result in aging of the mechanical strength of the pressboard. In such a case, the life of the pressboard insulation is decided by the mechanical strength as affected by thermal conditions [49]. PD is usually measured either in pico-coulombs or micro-volts. Its detection and measurement of PD is difficult. Methods for locating PD sources are discussed in Section 14.3.

***Design insulation level*:** After calculating voltages at critical locations inside a transformer (within the windings, at the ends of the windings, on the surface of leads, etc.) under all test conditions, it is quite meaningful to convert these voltages to one equivalent voltage, which is usually the one-minute short duration power frequency voltage. This equivalent voltage level is called the d*esign insulation level* (DIL) which is expressed in kVrms. Thus, at any point inside the transformer, there is only one DIL, which is the maximum of the equivalent one-minute power frequency voltage levels during the four different tests. This approach is widely followed by transformer designers for simplifying the insulation design process. The conversion factors used by different manufacturers for converting the calculated voltages (under various tests) to the one-minute r.m.s. level may not be identical but they fall in a narrow range. The factors reported in [54] are given in Table 8.2.

Table 8.2 Factors for Conversion to One-Minute (r.m.s.) Power Frequency Level

Test voltage	Multiplication factor
Lightning Impulse Level (BIL)	~ (1/2.30)=0.44
Switching Impulse Level (SIL)	~ (1/1.80)=0.55
Long duration (one hour) power frequency voltage	~ (1/0.80)=1.25

The conversion factor for the one-hour power frequency test voltage is in agreement with the following equation given in [43],

$$V_t = \left(1/t\right)^{0.055} V_1 \tag{8.19}$$

where V_1 and V_t are the 50% breakdown probability voltages for 1 minute and t minutes, respectively. The equation gives V_{60}/V_1 as 0.8, which is in line with that given in Table 8.2.

The multiplication factor for BIL in Table 8.2 is in accordance with the impulse ratio (the ratio of the lightning impulse level to the power frequency level) of about 2.3, as evident from Table 8.3 which gives commonly used BIL and power frequency test levels for various voltage classes. An impulse ratio in the range of 2.3 to 2.5 is being used in the industry [11, 12] while calculating the equivalent DIL of a BIL value. This range of the impulse ratio represents an average conversion factor for the impulse voltage duration in the range of 10 to 100 microseconds. The overvoltages stressing the interdisk or interturn insulations during the impulse test may be shorter than 10 microseconds in which case the conversion factor seems conservative. The impulse ratio of 2.68 has been suggested in [30] for 1.5/40 microsecond impulse waveform while designing interwinding and interdisk insulations, giving the corresponding multiplication factor of 0.37 for BIL in Table 8.2 (in place of 0.44). A lower value may open avenues for insulation optimization since in that case the equivalent DIL value is lower. On the other hand for impulse overvoltages of more than hundreds of microseconds duration (close to switching transients), there is a risk in using the impulse ratio between 2.3 to 2.5 and therefore it should be lower. Thus, the conversion factor should be judiciously selected based on detailed analysis and experimental data. For AC voltages and non-oscillatory impulses having durations other than that of lightning, switching and long duration power frequency voltages, an interpolation is done with caution for finding DIL [53].

Having estimated the DIL at critical electrodes inside a transformer, one can proceed with the design of its insulation system.

Table 8.3 Impulse Ratios

Voltage class	BIL (kVp)	Power frequency test level (kVrms)	Impulse ratio
132 kV	550	230	2.39
220 kV	950	395	2.40
400 kV	1300	570	2.28

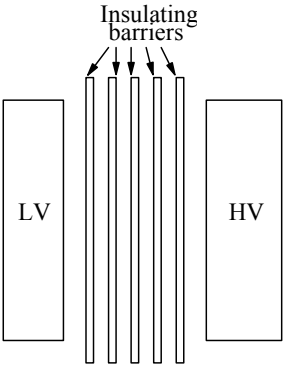

Figure 8.12 Subdivided duct between LV and HV windings.

8.5 Insulation between Two Windings

The gap between the low voltage (LV) and high voltage (HV) windings is subdivided into many oil ducts by means of solid insulating barriers (Figure 8.12). The insulation system of oil-cooled power transformers consists of a combination of oil and solid insulation (paper and precompressed board). Both of them are cheaper than most other insulating materials, and together they give much higher dielectric strength than individually.

In an oil-pressboard insulation system, since the maximum admissible stress in a good quality pressboard material for one-minute power frequency overvoltage is about 40 kVrms/mm [53], the limiting design stress values are primarily due to stress levels in the oil. In degassed oil with almost uniform field distribution (e.g., between barriers in the HV-LV gap), a typical PD inception field stress value for an 8 mm oil duct is 10 kVrms/mm for insulated winding conductors [52, 58]. Since the stress is high at winding conductor corners, the PD inception stress value for an 8 mm oil duct next to windings for degassed oil is lower, i.e., about 8.4 kVrms/mm. The allowed (design) stress values can be lower than these PD inception stress values depending on the required safety margin and the quality of manufacturing processes. Thus, the dielectric strength of the solid insulation is much higher than that of the oil. Since electric stress (E) is inversely proportional to permittivity, the oil stress is significantly higher than that in the solid insulation. The oil permittivity ($\cong 2.2$) is about half that of the solid insulation, hence the oil stress is twice the solid insulation stress in uniform fields. Since the oil has to bear a higher stress, it is recommended to make barriers as thin as possible and give more space for the oil ducts. In the oil-paper-pressboard insulation system, the strength of the insulation arrangement is predominantly decided by the strength of the oil ducts. Hence, the design of a transformer insulation system essentially means proper dimensioning of oil

ducts and oil-solid interfaces. For a given total gap between two windings, there is no advantage gained by increasing the solid insulation thickness just because its strength is higher. On the contrary, a high solid insulation thickness results in more stress in oil ducts. The barriers should be as thin as possible, if permitted from mechanical strength considerations. Barriers with a thickness of 1.5 to 2 mm are generally used for getting good mechanical stability. The lower the oil duct width, the higher the withstand stress (kV/mm) is. The number of barriers in an interwinding gap should be adequate so that larger oil gaps are avoided (oil gaps larger than 14 mm are usually not recommended in the interwinding gaps). Insulating barriers have an additional function of acting as barriers against the propagation of a discharge streamer in the oil between electrodes. The barriers break the oil path into smaller ducts and prevent the lining up of impurities in the oil.

The size of the first duct next to windings should be properly chosen. Although a small width is desirable as it gives higher kV/mm withstand value, thermal considerations may not allow the use of duct width below 6 mm. The first duct is usually of 6 to 10 mm size. Withstand for the ducts (the first duct and the other ducts in the HV-LV gap) can be determined by referring to published curves [52, 58] for four types of gaps, degassed oil between barriers, gas saturated oil between barriers, a degassed first oil duct, and a gas-saturated first oil duct. The maximum stress in the first duct has to be accurately determined (say, by FEM). Breakdown gradients obtained for a typical configuration are given in [30]. The values of breakdown gradients for a yoke-end-line-lead arrangement (the line terminal at the yoke end of a winding) are lower than those for a centerline-lead arrangement (the line terminal taken at the midpoint of the winding stack with two parallel branches). This is because the field distribution in the first duct at the line terminal is more nonuniform for the former as compared to the latter arrangement. Actual design values should be lower than the breakdown values depending on the margin to be kept. The HV-LV (*HILO*) gap value is usually based on the average stress expressed as [59],

$$E_{av} = \frac{DIL}{(HILO\ gap - 0.5 \times solid\ insulation)}. \tag{8.20}$$

It typically has a value of about 6 kVrms/mm. A manufacturing tolerance is added to the *HILO* gap calculated by the above expression. For a winding-to-end-limb clearance (e.g., in a single-phase three-limb construction) or an innermost-winding-to-core clearance, a lower value of E_{av} is used due to the presence of sharp corners of the core. In some critical cases, an electrostatic shield is used around the core/end limb facing the windings. The phase-to-phase insulation design is very similar but the stresses due to switching impulse and power frequency test levels need to be considered; most of the time the voltages between phases are 150% of phase-to-ground voltage levels.

8.6 Internal Insulation

Internal/minor insulation consists of all insulation components within the windings, viz. conductor paper covering, insulation between layers in the radial direction, insulation between turns or disks in the axial direction, and special insulating components that are placed close to the insulated conductors.

In addition to withstanding short and long duration overvoltages during tests at manufacturer's works and operation at site, the conductor insulation has to withstand continuous working voltage stresses. This is an important criterion for deciding the conductor insulation in the case of interleaved main and tap windings. In such windings, physically adjacent turns are electrically many turns apart, resulting in significantly higher working stress. The conductor paper covering in such cases is predominantly decided by this working stress. For example, in a disk winding the total stressed paper area can be calculated as

$$A_s = M_t \; k \; (N_t - 1) \; w \; N_d \; N_p \tag{8.21}$$

where M_t = mean turn length of the winding,

N_t = number of turns per disk, w = width of the winding conductor,

k = multiplying factor which depends on the degree of interleaving (= 2 for conductor interleaving shown in Figure 7.7),

N_d = number of disks per phase, N_p = number of phases.

The higher the stressed paper area, the lower the allowed working voltage stress is. Figure 8.13 gives the allowed voltage per mm of paper insulation thickness between turns as a function of the stressed paper insulation area. The voltage per mm allowed is usually in the range of 2400 to 4000 V/mm. The voltage per turn of the transformer, corresponding to a continuous overvoltage condition, is divided by the paper insulation thickness between two turns. The value obtained should be less than that given by Figure 8.13 (the y axis values are not marked since they depend on design practices).

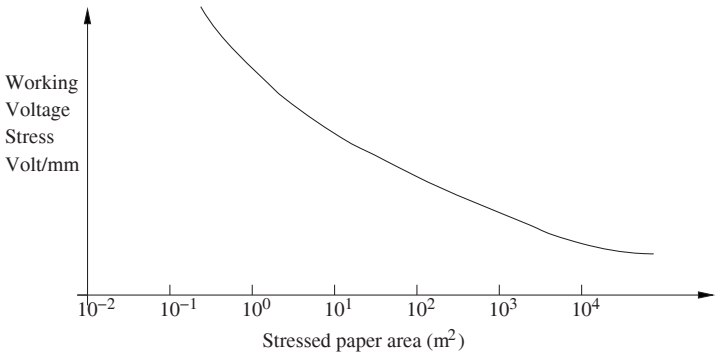

Figure 8.13 Working voltage stress.

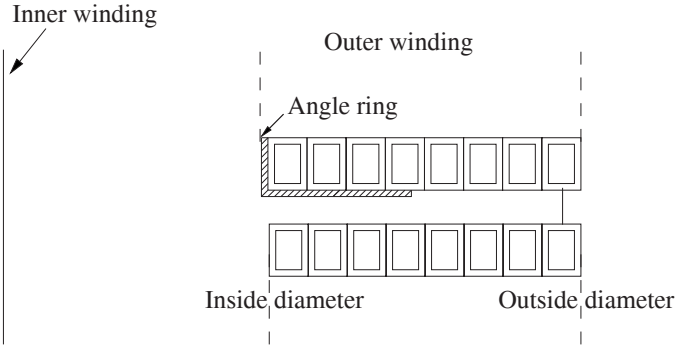

Figure 8.14 Angle ring at the inside diameter of an outer winding.

Considering primarily the lightning impulse stresses, special insulating components are placed closely hugging paper-insulated winding conductors. These are usually placed at line end disks or turns, where the resultant stress at the disk corner is high. This solution is beneficial as compared to increasing the conductor paper insulation which would reduce the series capacitance, increase the winding temperature rise and reduce the winding space factor. These special insulating components inside the winding are called as disk angle rings (Figure 8.14) or disk angle caps (Figure 8.15). Since they are closely fitted to winding conductors, the oil stress is reduced (since the oil duct shifts away from the conductors). Thus, they are doing the same function as achieved by increasing the conductor radius. If these are made from layers of paper insulation, they become flexible and can easily take the shape of the conductor eliminating oil voids between them and the paper covered conductors. On the contrary, if they are made from molded solid insulation, small oil voids may exist, which then will have higher stresses. The withstand strength of the voids is also high because of their small dimensions. In any case, it is always preferable to have angle rings/caps closely fitting the conductors to eliminate voids.

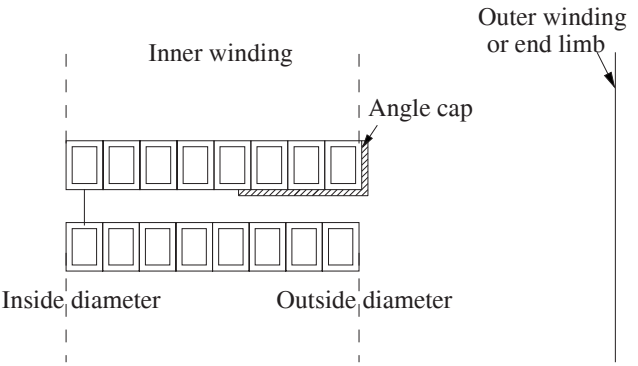

Figure 8.15 An angle cap placed at the outside diameter of an inner winding.

Angle caps are used to protect the winding corners from another winding or an end limb as shown in Figure 8.15. Angle rings/caps made from molded material are usually available in a sector form, which have to be overlapped by doing proper chamfering. The overlapping distance is usually kept as 30 to 40 times the thickness of the angle rings/caps.

Although it is essential to achieve near-uniform initial impulse voltage distribution, what is more important from the insulation design point of view is obtaining uniform dielectric stresses in relation to corresponding strength values. Generally, it is very difficult to obtain equal initial impulse voltages between disks/turns throughout the winding; the insulation should be designed such that the margin between the strength and the stress is in the same range of values along the winding height. This is an ideal design which may not be possible since, for cooling purposes, adequate interdisk or interturn gaps are kept at the neutral end even though the stresses are low. It is not advisable to increase the turn or disk insulation, where stresses are high, without detailed calculations. There could be failure even if extra insulation is provided because the increase in the strength may not be commensurate with the increase in the stress due to a reduced series capacitance value.

8.7 Design of End Insulation

In the composite oil-solid insulation system, the strength of an insulation arrangement is predominantly determined by the strength of oil gaps. The solid insulation is used to subdivide long oil gaps (having lower dielectric strengths) into smaller ones. While assessing the end insulation design, the strengths of oil gaps and solid-oil interfaces are evaluated. FEM is commonly used for estimation of electrostatic field distribution. A typical end insulation arrangement is shown in Figure 8.16. The electric stress distributions along various contours between the windings and between the yokes and the windings are examined [60]. Two such contours are shown in the figure by dotted lines.

For each oil duct within a selected contour (e.g., A-C), the cumulative field distribution is determined by integrating the field along the contour starting from the maximum value as described in Section 8.3.8. If in an oil gap, the maximum stress is at one of the extreme ends, the calculations are greatly simplified since the cumulative stress at any point with a distance of d from the point of maximum stress on the contour is calculated as the voltage difference between the two points divided by d. In this case the cumulative stress is

$$E_{(d)} = \frac{1}{d}\int_0^d E_{(x)}\,dx\,. \tag{8.22}$$

The cumulative oil stress values for each oil gap along the contour A-C are plotted and compared with a reference strength/withstand curve, described by a formula such as Equation 8.18, as shown in Figure 8.17.

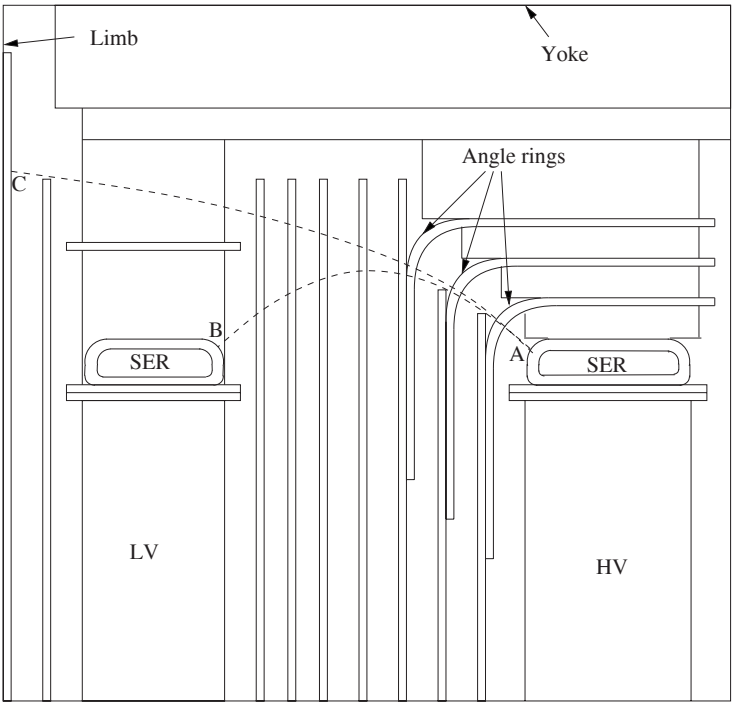

Figure 8.16 Typical end insulation arrangement of a power transformer.

An end insulation arrangement is optimum if the minimum margin between the withstand and stress curves is approximately same for all the ducts. The task of insulation designers is to adjust the barriers/angle rings in such a way that the minimum margin in each resulting oil duct is greater than some fixed safety margin value and that these minimum margins are in the same range of values.

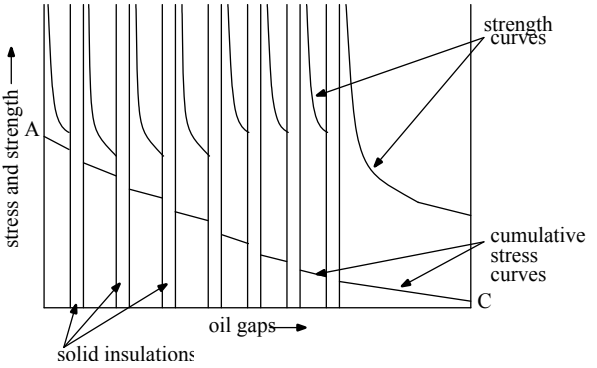

Figure 8.17 Analysis of oil ducts in end insulation region.

The minimum safety margin is a function of quality of insulation and technology of drying/oil impregnation processes. Usually a safety margin of 25 to 35% in critically stressed parts of the transformer insulation is considered as sufficient to pass successfully the long duration (one hour) induced overvoltage test without partial discharges and also the impulse test [61].

The placement of angle rings/caps is an important aspect of the end insulation design. They divide larger oil ducts into smaller ones increasing the withstand of the total gap and the resulting oil ducts. The angle rings/caps should be placed along the equipotential lines; otherwise higher creepage stresses along their surface may reduce the overall dielectric strength. As we go away from the winding corner, the radius of an angle ring/cap should be more so that it lies along an equipotential line and the creepage stress on its surface is minimized. The angle rings/caps with a fixed and small radius of 2 to 3 mm are cheaper than the contoured ones with a much higher radius. However, the creepage stress on the noncontoured angle rings/caps can be high, reducing the overall strength of the insulation arrangement. In order to optimize end insulation clearances, contoured angle rings/caps need to be used which reduce not only the creepage stresses but also the oil duct sizes in high stress zones thereby improving their withstand. The effectiveness of a contoured angle ring can be clearly seen from Figure 8.18. The creepage stress along the portion AB of the contoured angle ring is much less than that along the corresponding portion CD of the noncontoured angle ring. The first angle ring/cap should be close to the winding for having a smaller first oil duct width.

Apart from an effective subdivision of oil ducts by barriers/angle rings (caps)/solid washers, it is necessary to reduce electric stresses at winding corners. The stress can be reduced by placing a static end ring (SER) at the end of the winding (see Section 7.3.4 for a discussion on SERs). The inner and outer diameters of the SER have to be flush with the corresponding diameters of the winding, and it should be as close to the winding end disk/turn as possible all along the circumference.

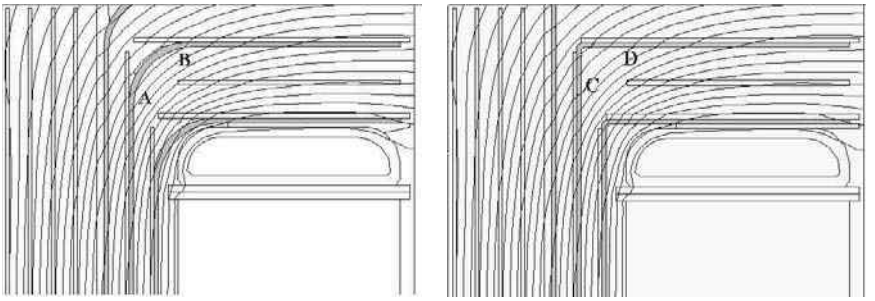

(a) Contoured angle ring (b) Noncontoured angle ring

Figure 8.18 Effectiveness of contoured angle ring.

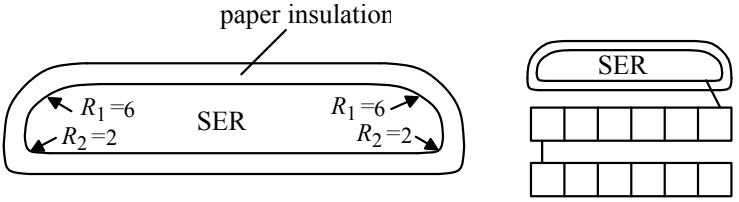

Figure 8.19 Static end ring.

In low voltage windings, if the SER is dispensed with, a turn or disk angle ring/cap is usually placed on the last turn/disk, which reduces the stress in the oil duct immediately next to it.

A typical sketch of an SER is shown in Figure 8.19. The inner radius (R_2) close to the winding disk is usually standardized to 2 mm, whereas the outer radius (R_1) can be at least 6 mm and it may be more as the voltage rating and radial depth of the winding increases. The paper insulation thickness is of the order of 3 mm. A static ring (SR) may be placed between two disks of a winding, particularly between the second and third disks and between the fourth and fifth disks from the line end of a continuous disk winding since the lightning impulse voltage appearing across these disks can be high.

Sometimes, the LV winding height is kept greater (by a few mm) than the HV winding height. The stress at the LV corner facing the HV winding is lower in this case compared to the case wherein the LV winding height is equal to or shorter than the HV winding height.

8.8 High Voltage Lead Clearances

In high voltage transformers, the clearances between leads and ground, between leads, etc. have to be judiciously selected. Consider a high voltage insulated lead near a ground plane as shown in Figure 8.20. The maximum electric stress in the paper insulation and the oil can be calculated by the well-known formulae given in Section 8.1. The complete stress distribution can be accurately analyzed by using FEM.

The oil duct strength can be computed on the basis of the stressed oil volume (SOV) theory. The stressed volume between the maximum stress and the contour of 90% of the maximum stress for a cylindrical lead-plane configuration can be calculated by the following approximate formula [62],

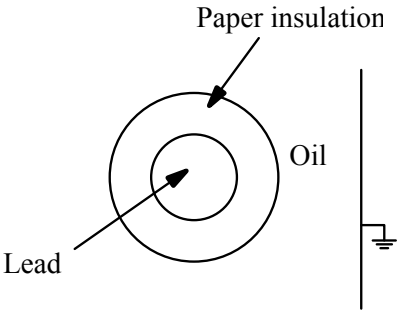

Figure 8.20 High voltage lead insulation.

$$SOV = \frac{\pi r^2}{18} l \tag{8.23}$$

where r is the bare lead radius and l is the effective lead length. A more accurate formula for a bare lead is given in [63]. SOV for a covered lead and/or for a complex configuration of electrodes can be calculated by using FEM. The 50% breakdown probability stress for one-minute power frequency voltage can be calculated from the SOV value through Equation 8.16. The safe withstand value is lower than this breakdown stress value and can be decided by the transformer manufacturer depending on the acceptable value of the percentage breakdown probability and the quality of manufacturing processes (which decide the level of impurities) [43, 64]. The margin kept is also a function of manufacturing practices and required working tolerances. For example, a lead-to-tank clearance may actually be less than that specified in the drawing. Mechanical tolerances, lowering clearances and magnetic clearances may dominate over the dielectric design considerations in lower voltage ratings.

An increase in breakdown voltage for a lead-to-ground configuration can be obtained by one or more of the following means: an increase in the clearance, an increase of the bare lead diameter, an increase in the thickness of the paper insulation, and placement of barriers to subdivide the oil duct. The first option is obviously not cost effective as it increases the material cost and the size of the transformer. Out of the remaining three options, the paper covering has significantly more impact in improving the withstand [65]. With an increase in the paper insulation, more voltage is dropped across it, reducing the stress in the oil. Thermal considerations and manufacturing time are also the deciding factors while standardizing the bare diameter, the paper insulation thickness, and the clearance for various DILs. When the electrode is not sharp, barriers can be put along equipotential lines to enhance the strength.

It should be noted that the increase of either the bare lead diameter or the paper thickness increases SOV, but the reduction in strength due to an increased SOV is not significant as compared to the reduction in the stress value because of the logarithmic relationship between the strength and SOV.

When there is a row of tap leads facing a winding or a tank wall, the maximum stress is less compared to that in an isolated lead case. The extent of the stress reduction has to be assessed for the worst configuration (giving minimum reduction) and then the electrical clearances can be standardized accordingly using the isolated lead-to-ground clearances. The clearance of the row of tap leads to ground is usually lower as compared to that of the isolated lead to ground case.

The above analysis has assumed a smooth ground plane. When the ground electrode is not smooth and is having sharp corners, it becomes difficult to standardize the clearances. It is preferable to have at least 2 mm radius at the corners. With this minimum corner radius, in the absence of detailed analysis, 1 mm of oil gap per kVrms of the DIL seems to be a safe design criterion (i.e., an average stress of 1 kVrms/mm). A value of about 1.4 kVrms/mm or more can be used, based on experience.

In some cases due to nearness of high voltage electrodes to the tank, the electric field at its surface may be high and therefore the tank surface should be covered with proper insulation [53].

The above analysis holds good for jump clearances in oil between a lead and ground. There is one more design consideration when leads are supported by a solid insulation piece fixed to a grounded part as shown in Figure 8.21 (equipotential lines obtained from an FEM analysis are also displayed). In this case, the cumulative creepage stress on the pressboard surface and the corresponding withstand are calculated using the procedure given in Section 8.3.8. For nonhomogeneous field distributions (involving sharp electrodes), the rule of 1 mm of creepage path per kVrms may be followed in the absence of detailed analysis.

Sometimes insulating barriers are placed close to high voltage leads in high stress zones. The combined effects of the oil velocity and particles sweeping towards high stress zones, as discussed in Section 8.3.9, have a definite role to play in power frequency breakdowns. The barriers make the oil flow restricted in the high stress zones so that the probability of the occurrence of breakdown phenomena (in which floating particles are drawn into high stress zones helping breakdown processes) is reduced to a great extent. Hence, the barriers can be quite effective when used to subdivide large oil gaps in the high stress zones. They should be placed close to the electrode along equipotential lines. If there is an appreciable creepage stress along their surface (due to improper placement), the overall strength may not improve.

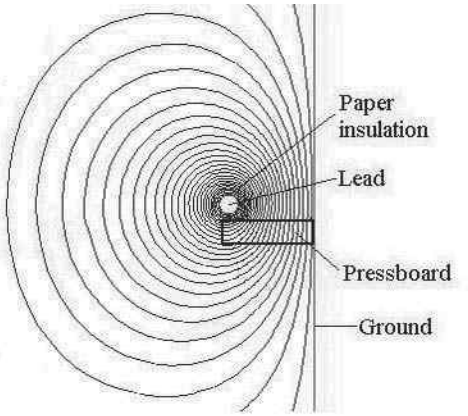

Figure 8.21 Optimum creepage distance calculation by FEM analysis.

Nonuniform field patterns exist in the vicinity of high voltage leads between winding terminations and lower bushing connections. Covering the leads with thick paper insulation may not help much as the stress in the oil may not be reduced significantly. Also, too much insulation on the leads limits their thermal capability. The scatter of the breakdown voltage for such a wide oil duct can be much higher resulting in lower dielectric strength. The modern lead exit systems [54] consist of pressboard barrier systems which divide the oil gap into smaller gaps. The lead is covered by a thin layer of molded pressboard.

8.9 Statistical Analysis for Optimization and Quality Enhancement

8.9.1 Parameter design

Optimization of an insulation system requires identification of factors having significant influence on stresses and strengths. Orthogonal array design of experiments is a technique that allows the effect of several parameters to be determined efficiently. The analysis of relative effects of the different factors can be done by decomposition of variance which is commonly called as analysis of variance (ANOVA).

An approach for the optimization of major insulation of a 400 kV class of transformer has been described in [66]. Figure 8.22 shows a sectional view of transformer windings, in which the insulation arrangement of two disks of its HV winding is depicted. The factors affecting maximum oil stress and strength are viz. the conductor radius (R), the conductor paper covering (PC), the disk angle ring thickness (DAR), the HV-LV gap, the duct width between the disks,

the first oil duct width and the voltage difference between the disks. The quantification of the effect of these factors has been reported in [66], which is based on 36 FEM simulations for specific combinations of the above seven factors. Such an analysis helps designer to do *parameter design*, i.e., choosing an optimum combination of the factors. A quadratic surface is generated by using multiple regression analysis to express the oil stress in terms of the factors, which has been used further for the tolerance design as explained below.

8.9.2 Tolerance design

Insulation optimization cannot be done in isolation without due consideration to variations usually observed during the manufacturing processes. The tolerance design methodology can be used to identify critical insulation components whose manufacturing variation needs to be controlled. For this, the deviations in dimensions of all (control) factors are first determined by choosing random samples from the manufacturing site. The standard deviation (SD) can be calculated from the data. For the tolerance design, three levels of the factors can be taken around the mean (m) as $m-\sqrt{3/2}\ SD$, m, and $m+\sqrt{3/2}\ SD$ [67]. Either FEM simulations can be used to obtain the oil stress values for the specific combinations of the factors or the quadratic surface generated earlier (at the parameter design stage) can be used expediting the analysis. The subsequent ANOVA analysis can reveal the relative effects of manufacturing variations in the factors on the stress values. This can help in identifying manufacturing processes that need to be controlled on priority to help reliability enhancement/optimization efforts. The extra investment needed to improve a particular process can also be justified by such analysis.

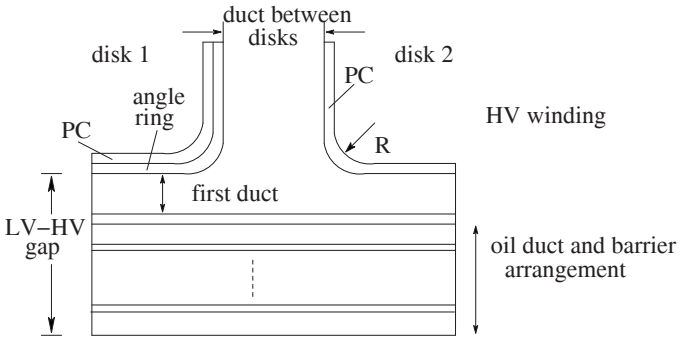

Figure 8.22 Insulation arrangement between two disks.

References

1. McDonald, D. The electrolytic analogue in the design of high voltage power transformers, *Proceedings IEE*, Vol. 100, Pt. II, 1953, pp. 145–166.
2. Birke, P. V., Lackey, J., and Palmer, S. Determination of highly stressed volumes in oil dielectrics, *IEEE Transactions on Electrical Insulation*, Vol. EI-7, No. 3, September 1972, pp. 139–144.
3. Cockcroft, J. D. The effect of curved boundaries on the distribution of electrical stress around conductors, *Journal IEE*, Vol. 66, 1928, pp. 385–409.
4. Fogaras, L. and Lampe, W. Calculation of electrical field strength around transformer winding corners, *IEEE Transaction on Power Apparatus and Systems*, Vol. PAS-87, No. 2, February 1968, pp. 399–405.
5. Galloway, R. H., Ryan, H. M., and Scott, M. F. Calculation of electric fields by digital computer, *Proceedings IEE*, Vol. 114, No. 6, June 1967, pp. 824–829.
6. Wexler, A. Computation of electromagnetic fields, *IEEE Transactions on Microwave Theory and Techniques*, Vol. MTT-17, No. 8, August 1969, pp. 416–439.
7. Rele, A., Palmer, S., and Birke, P. V. Dielectric stress calculations for EHV transformer winding, *IEEE PES Summer Meeting*, Vancouver, Canada, 1973, Paper No. C-73-396-9.
8. Andersen, O. W. Laplacian electrostatic field calculations by finite elements with automatic grid generation, *IEEE Transactions on Power Apparatus and Systems*, Vol. PAS-92, September/October 1973, pp. 1485–1492.
9. Singer, H., Steinbigler, H., and Weiss, P. A charge simulation method for the calculation of high voltage fields, *IEEE Transactions on Power Apparatus and Systems*, Vol. PAS-93, 1974, pp. 1660–1668.
10. Okubo, H., Ikeda, M., Honda, M., and Yanari, T. Electric field analysis by combination method, *IEEE Transactions on Power Apparatus and Systems*, Vol. PAS-101, October 1982, pp. 4039–4048.
11. Tschudi, D. J., Krause, C., Kirch, H. J., Franchek, M. A., and Malewski, R. Strength of transformer paper-oil insulation expressed by the Weidmann oil curves, *CIGRE 1994*, WG 33.03.
12. Nelson, J. K. An assessment of the physical basis for the application of design criteria for dielectric structures, *IEEE Transactions on Electrical Insulation*, Vol. 24, No. 5, October 1989, pp. 835–847.
13. Kuffel, E., Zaengl, W. S., and Kuffel, J. *High voltage engineering: Fundamentals*, Second Edition, Newnes, Butterworth-Heinemann Publication, Oxford, 2000.
14. Oommen, T. V., Petrie, E. M., and Lindgren, S. R. Bubble generation in transformer windings under overload conditions, *Minutes of the Sixty-Two Annual International Conference of Doble Clients,* Sec. 8–5.1, 1995.

15. Griffiths, D. J. *Introduction to electrodynamics*, Third Edition, Prentice Hall, New Jersey, 1999.
16. Sheng, P. and Wen, W. Electrorheology: statics and dynamics, *Solid State Communications,* Vol. 150, Issue 21–22, 2010, pp. 1023–1039.
17. Nelson, J. K., Salvage, B., and Sharpley, W. A. Electric strength of transformer oil for large electrode areas, *Proceedings IEE*, Vol. 118, No. 2, February 1971, pp. 388–393.
18. Krause, C. Dielectric strength of transformer oil: impact of oil flow, moisture and cellulose particles, *WICOR Insulation Conference*, Rapperswil, Switzerland, September 1996.
19. Norris, E. T. High voltage power transformer insulation, *Proceedings IEE*, Vol. 110, No. 2, February 1963, pp. 428–440.
20. Miners, K. Particles and moisture effect on dielectric strength of transformer oil using VDE electrodes, *IEEE Transactions on Power Apparatus and Systems*, Vol. PAS-101, No. 3, March 1982, pp. 751–756.
21. Zein El-Dine, M. E. and Tropper, H. The electric strength of transformer oil, *Proceedings IEE*, Vol. 103, Pt. C, 1956, pp. 35–45.
22. Maier, G. The electric strength of insulating oil with power-frequency voltage, switching surges and standard impulses, *The Brown Boveri Review*, Vol. 54, No. 7, July 1967, pp. 368–376.
23. Kamata, Y. and Kako, Y. Flashover characteristics of extremely long gaps in transformer oil under non-uniform field conditions, *IEEE Transactions on Electrical Insulation*, Vol. EI-15, No. 1, February 1980, pp. 18–26.
24. Du, Y., Zahn, M., Lesieutm, B. C., Mamishev, A. V., and Lindgren, S. R. Moisture equilibrium in transformer paper-oil systems, *IEEE Electrical Insulation Magazine*, Vol. 15, Jan.–Feb. 1999, pp. 11–20.
25. Chakravorti, S. Moisture equilibrium and its effect on transformer Part I: Moisture in oil-paper composite insulation of transformer, *Invited lecture at TRAFOTECH-2010, Mumbai*, Jan. 17, 2010.
26. Peek, F. W. The effect of transient voltages on dielectrics: Law of impulse spark-over and time lag, *AIEE Transactions*, October 1930, pp. 1456–1469.
27. Blume, L. F., Boyajian, A., Camilli, G., Lennox, T. C., Minneci, S., and Montsinger, V. M. *Transformer engineering*, John Wiley and Sons, New York, and Chapman and Hall, London, 1951.
28. Montsinger, V. M. Effects of time and frequency on insulation test of transformers, *AIEE Transactions*, Vol. 43, February 1924, pp. 337–347.
29. Vogel, F. J. Insulation tests of transformers as influenced by time and frequency, *AIEE Transactions*, Vol. 43, February 1924, pp. 348–355.
30. Lokhanin, A. K., Morozova, T. I., Voevodin, I. D., Beletsky, Z. M., Kuchinsky, G. S., and Kaplan, D. A. Problems of coordination of dielectric strength of extra high-voltage power transformer major insulation, *CIGRE 1970*, Paper No. 12-06.

31. Vogel, F. J. Factors influencing the insulation coordination of transformers, *AIEE Transactions*, June 1933, pp. 411–416.
32. Montsinger, V. M. Coordination of power transformers for steep–front impulse waves, *AIEE Transactions – Electrical Engineering*, Vol. 57, April 1938, pp. 183–195.
33. Bellaschi, P. L. and Teague, W. L. Dielectric strength of transformer insulation, *AIEE Transactions – Electrical Engineering*, January 1937, pp. 164–171.
34. Ikeda, M., Yanari, T., and Okubo, H. PD and BD probability distribution and equi-probabilistic V-t characteristics of oil-filled transformer insulation, *IEEE Transaction on Power Apparatus and Systems*, Vol. PAS-101, No. 8, August 1982, pp. 2728–2735.
35. Kamata, Y., Endoh, K., Furukawa, S., Endoh, F., Nonomura, K., Iwata, Y., Horiuchi, S., and Takasu, N. Dielectric strength of oil-immersed transformer insulation with superimposed AC and lightning impulse voltage, *IEEE Transaction on Electrical Insulation*, Vol. 25, No. 4, August 1990, pp. 683–687.
36. Vandermaar, A. J., Wang., M., Neilson, J. B., and Srivastava, K. D. The electrical breakdown characteristics of oil-paper insulation under steep front impulse voltages, *IEEE Transaction on Power Delivery*, Vol. 9, No. 4, October 1994, pp. 1926–1933.
37. Breitfelder, D., Buckow, E., Knorr, W., and Peschke, W. Dielectric strength of transformer oil under impulse and high frequency voltage stress, *International Symposium on High Voltage Engineering, ISH'87*, Braunschweig, Germany, August 1987.
38. Rasaruk. M. and Petcharaks, K. Thermal effect on AC breakdown characteristic of transformer oil under inhomogeneous fields, *IEEE Power Engineering Society Winter Meeting, 2000*, Vol. 3, 23-27 January 2000, pp. 2176–2180.
39. Clark, F. M. *Insulating materials for design and engineering practice,* John Wiley and Sons, Inc., New York, 1962.
40. Clark, F. M. and Montsinger, V. M. Dielectric strength — Thickness relation in fibrous insulation, *General Electric Review*, Vol. 28, No. 5, May 1925, pp. 286–290.
41. Wilson, W. R. A fundamental factor controlling the unit dielectric strength of oil, *AIEE Transactions*, February 1953, pp. 68–74.
42. Hill, L. R. and Schmidt, P. L. Insulation breakdown as a function of area, *AIEE Transactions*, Vol. 67, 1948, pp. 442–446.
43. Ikeda, M., Teranishi, T., Honda, M., and Yanari, T. Breakdown characteristics of moving transformer oil, *IEEE Transaction on Power Apparatus and Systems*, Vol. PAS-100, No. 2, February 1981, pp. 921–928.
44. Kato, K., Han, X., and Okubo, H. Insulation optimization by electrode contour modification based on breakdown area/volume effects, *IEEE*

Transactions on Dielectrics and Electrical Insulation, Vol. 8, No. 2, April 2001, pp. 162–167.
45. Anderson, J. G. and Liao, T. W. The propagation mechanism of impulse creepage discharges over oil-immersed surfaces, *AIEE Transactions*, May 1955, pp. 218–226.
46. Okubo, H., Okamura, K., Ikeda, M., and Yanabu, S. Creepage flashover characteristics of oil/pressboard interfaces and their scale effects, *IEEE Transactions on Power Delivery,* Vol. PWRD-2, No. 1, January 1987, pp. 126–132.
47. Anker, M. U. Effect of test geometry, permittivity matching and metal particles on the flashover voltage of oil/solid interfaces, *IEEE Transactions on Power Apparatus and Systems*, Vol. PAS-102, No. 12, December 1983, pp. 3796–3802.
48. Taylor, R. J. Effect of permittivity matching on the flashover of solid/liquid interfaces, *Proceedings IEE*, Vol. 124, No. 10, October 1977, pp. 899–904.
49. Kamata, Y., Ohe, E., Endoh, K., Furukawa, S., Tsukioka, H., Maejima, M., Fujita, H., Nozaki, M., Ishizuka, F., and Hyohdoh, K. Development of low-permittivity pressboard and its evaluation for insulation of oil-immersed EHV power transformers, *IEEE Transactions on Electrical Insulation*, Vol. 26, No. 4, August 1991, pp. 819–825.
50. Nelson, J. K. Some steps toward the automation of the design of composite dielectric structures, *IEEE Transactions on Dielectrics and Electrical Insulation*, Vol. 1, No. 4, August 1994, pp. 663–671.
51. Derler, F., Kirch, H. J., Krause, C., and Schneider, E. Development of a design method for insulating structures exposed to electric stress in long oil gaps and along oil / transformerboard surfaces, *International Symposium on High Voltage Engineering*, *ISH'91*, Dresden, Germany, August 1991.
52. Moser, H. P. *Transformerboard*, Scientia Electrica, Vermont, USA, 1979.
53. Tschudi, D. J. AC insulation design: paper-oil insulation systems, *WICOR Insulation Conference*, Rapperswil, Switzerland, September 1996.
54. Dahinden, V., Schultz, K., and Kuchler, A. Function of solid insulation in transformers, *TRANSFORM 98*, April 1998, Munich, Germany, pp. 41–54.
55. Aubin, J. and Malewski, R. Safety margin of internal insulation of EHV power transformers, *International Symposium on High Voltage Engineering, ISH'95*, Graz, Austria, August 1995.
56. Grieder, H. Drying transformers with kerosene vapour, *Brown Boveri Review,* 2/3-73, 1973, pp. 117–122.
57. Kawamura, T. Proposals on standardization on the site installation to secure the reliability of transformer insulation, *CIGRE 1976*, Paper 12-01.
58. Weidmann, H. Catalogue, pp. A41-5, A41-6.
59. Lakhiani, V. K. and Kulkarni, S. V. Insulation design of EHV transformers — A review, *International Insulation Conference, INSUCON 2002*, Berlin, Germany, June 2002, pp. 283–287.

60. Tschudi, D., Dahinden, V., and Derler, F. Dielectric strength assessment of power transformer insulation, *International Symposium on High Voltage Engineering*, *ISH'95*, Graz, Austria, August 1995.
61. Vailles, C., Malewski, R., Dia-Do, X., and Aubin, J. Measurement of dielectric stress in EHV transformer insulation, *CIGRE 1994*, Paris, France, WG 33.03.
62. Kawaguchi, Y., Murata, H., and Ikeda, M. Breakdown of transformer oil, *IEEE Transactions on Power Apparatus and Systems*, Vol. PAS-91, January/February 1972, pp. 9–19.
63. Palmer, S. and Sharpley, W. A. Electric strength of transformer insulation, *Proceedings IEE*, Vol. 116, No. 12, December 1969, pp. 2029–2037.
64. Ikeda, M. and Menju, S. Breakdown probability distribution on equi-probabilistic V-T characteristics of transformer oil, *IEEE Transaction on Power Apparatus and Systems*, Vol. PAS-98, No. 4, July-August 1979, pp. 1430–1437.
65. Rengarajan, S. and Satyanarayana, S. Computation and analysis of HV lead clearance to tank wall in large power transformers using stressed oil volume concept, *International Symposium on High Voltage Engineering*, *ISH'95*, Graz, Austria, August 1995, pp. 1042:1–4.
66. Koppikar, D. A., Kulkarni, S. V., and Dubey, A. K. Optimization of EHV Transformer Insulation by Statistical Analysis, *International Symposium on High Voltage Engineering*, *ISH'97,* Montreal, August 1997, Vol. 6, pp. 289–292.
67. Phadke, M. S. *Quality engineering using robust design*, Prentice-Hall International, Inc, New Jersey, USA, 1989.

9

Cooling Systems

The magnetic circuit and windings are the principal sources of losses and resulting temperatures in various parts of a transformer. The losses in the core and the windings, and the stray losses due to leakage and high current fields, are mainly responsible for heat generation within the transformer. Sometimes loose electrical connections inside the transformer, leading to a high contact resistance, cause higher temperatures. Excessive temperatures due to heating of curb bolts, that are in the path of a stray field, can damage gaskets (refer to Chapter 5). The heat generated due to all these losses must be dissipated without allowing the core, winding, and structural parts of the transformer to reach temperatures that will cause deterioration of its insulation. If the insulation is subjected to temperatures higher than the allowed values for a long time, it looses insulating properties; in other words, the insulation is aged, severely affecting the transformer life. There are two principle characteristics of the insulation, viz. the dielectric strength and the mechanical strength. The dielectric strength remains high up to a certain temperature after which it drops rapidly. At this point the insulation material becomes brittle and loses its mechanical strength. Thus, it is primarily the mechanical strength that is affected by higher temperatures and aging, which in turn affects the dielectric strength. Hence, the dielectric strength alone cannot always be depended upon for judging the effect of temperature on the insulation [1].

Accurate estimation of temperatures on all surfaces is very critical in the design of transformers to decide the operating flux density in the core and the current densities in the windings/connections. It helps in checking the adequacy of cooling arrangements provided for the active parts and in ensuring reliable

operation of the transformer; the insulation life can be estimated under overload conditions and corrective actions can be taken in advance.

The values of maximum oil and winding temperatures depend on the ambient temperature, the transformer design, loading conditions and the cooling provided. The limits for the ambient temperature and the corresponding limits for oil temperature and winding temperature rise are specified in the international standards. As the ambient temperature varies from country to country, the limits could be different for different countries. For example in IEC 60076-2 (second edition: 1993), maximum ambient temperature of 40°C is specified with a limit on the top oil temperature rise of 60°C. In a country where the maximum ambient temperature is 50°C, the top oil temperature rise limit may be correspondingly reduced to 50°C. If the installation site is more than 1000 m above the sea level, the allowable temperature rise for the transformer is reduced according to the guidelines given in the standards because air density reduces with an increase in altitude lowering the effectiveness of cooling. Altitude basically affects the convective heat transfer (because of lower buoyancy effect) and not the radiation. A corresponding reverse correction is applied when the altitude of the factory location is above 1000 m and the altitude of the site is below 1000 m.

In oil cooled transformers, the oil is the medium for both cooling and insulation. Heat from the core, windings and structural components in the transformer is dissipated by means of oil circulation. The heat is finally transmitted either to atmospheric air or water. In the subsequent sections, modes of heat transfer and their application in different cooling configurations are discussed.

9.1 Modes of Heat Transfer

The heat transfer rate is the rate of flow of thermal energy from a hotter body to a colder body. Whenever there exists a temperature difference within a medium or between different media, heat transfer occurs. The heat transfer mechanism in a transformer takes place by three modes: conduction, convection and radiation. In the oil-cooled transformers, the convection mode plays the most important role, and the conduction mode is least important. Rigorous mathematical treatment for expressing these modes of heat transfer is difficult and hence designers mostly rely on empirical formulae.

9.1.1 Conduction

Conduction is a process of heat transfer across a stationary medium such as a solid or fluid. Almost all the types of transformers are either oil or gas filled, and heat flows from their core and windings into the cooling medium. From the core, heat can flow directly, but from the winding it flows through the insulation provided on the winding conductor. In large transformers, at least one side of

insulated conductors is exposed to the cooling medium, and the heat flows through a small thickness of the conductor insulation. But in small transformers the heat may have to flow through several layers of conductors and insulation materials before reaching the cooling medium.

The temperature drop across the insulation due to the conduction heat transfer mechanism can be calculated by the following basic thermal law:

$$\Delta\theta = Q \times R_T \tag{9.1}$$

where Q is the heat flow (power loss) in W, and R_T is thermal resistance in °C/W. $\Delta\theta = T_2 - T_1$, where T_1 is the temperature of oil and T_2 is the temperature of the winding conductor. The thermal resistance is given by

$$R_T = \frac{t_i}{k \times A} \tag{9.2}$$

where t_i is the insulation thickness in m, A is the cross-sectional area in m^2, and k is the thermal conductivity in W/(m °C). If q denotes heat flux per unit transfer area, the temperature drop across the insulation can be rewritten as

$$\Delta\theta = \frac{q \times t_i}{k}\,. \tag{9.3}$$

It should be noted that the thermal conductivity of oil-impregnated paper insulation is temperature dependent and its proper value should be taken in the calculations [2].

9.1.2 Radiation

Any body at a raised temperature compared to its surroundings radiates heat energy in the form of waves. The heat dissipation from a transformer tank occurs by means of both radiation and natural convection modes. The cooling of radiators also occurs by radiation, but it is far less than that by convection. Because of closeness of radiator fins, the entire surface of radiators does not participate in the heat transfer mechanism by radiation. Thus, the effective area for radiation can be taken as the outside envelope surface of the radiators. The emissivity of the radiating surface affects the radiation. The heat transfer in watts by radiation is expressed by the Stephan-Boltzmann law:

$$P_R = \eta\, E\, A_R \left(T_s^4 - T_a^4\right) \tag{9.4}$$

where $\eta = 5.67 \times 10^{-8}$ W/(m^2 °K^4) is the Stephan-Boltzmann constant, E is the surface emissivity factor, A_R is the surface area for radiation in m^2, T_s is the

average temperature of the radiating surface in °K, and T_a is the ambient air temperature in °K.

Surface emissivity is a property that depends on several factors like surface finish, type of paint applied on the surface, etc. When the emissivity factor is less than unity, the effective radiating surface is correspondingly less. For tank and radiators painted with grey colour having emissivity of 0.95, the effective radiating area is usually assumed to be that of the outside envelope without introducing much error.

For outdoor installation, there is an effect of solar radiation during day time. The net heat transfer from the transformer to its surrounding is less as some heat due to solar radiation is absorbed by the tank.

9.1.3 Convection

The oil, being a liquid, has one important mechanical property in that its volume changes with temperature and pressure [3]. Changes in volume with temperature provide the essential convective or thermosiphon cooling. Changes in volume with pressure affect the amount of transferred vibrations from the core to the tank.

The heat dissipation from the core and windings in a transformer occurs mainly due to convection. When a heated surface is immersed in a fluid, heat flows from the surface to the cooling medium. Due to the increase in the fluid temperature, its density (or specific gravity) reduces. The fluid (oil) in an oil-cooled transformer, rises upwards and transfers its heat to outside ambient air through the tank and radiators. The rising oil is replaced by the colder oil from the bottom, and thus continuous oil circulation occurs. The convective heat transfer is expressed by the relationship:

$$Q = h A \left(T_{surface} - T_{fluid} \right) \tag{9.5}$$

where Q is the heat flow in W, h is the heat transfer coefficient in W/(m^2 °C), A is the surface area in m^2, and the temperatures $T_{surface}$ and T_{fluid} are in °C. Since h depends on geometry as well as fluid properties, its estimation is very difficult. However, many empirical correlations are available, which can be used in the majority of design calculations.

The heat dissipation from the transformer tank to ambient air occurs similarly but the warmed air after cooling does not come back and its place is occupied by a new quantity of fresh air. In the case of a tank plate, heat dissipation by convection and radiation mechanisms are comparable since the surface area available for the convective cooling is the same as that for the radiation cooling. The heat dissipated by the tank through the convection and radiation modes is also usually calculated by empirical relations in which the resultant effect of both mechanisms is taken into account.

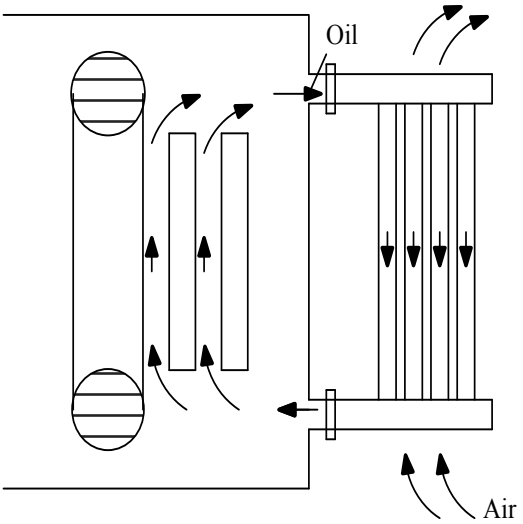

Figure 9.1 ONAN cooling.

9.2 Cooling Arrangements

9.2.1 ONAN/OA cooling

In small rating transformers, the tank surface area may be able to dissipate heat directly to the atmosphere, while bigger rating transformers usually a require much larger dissipating surface in the form of radiators/tubes mounted directly on the tank or mounted on a separate structure. If the number of radiators is small, they are preferably mounted directly on the tank so that the arrangement results in smaller overall dimensions.

When the number of radiators is large, they are mounted on a separate structure and the arrangement is called a radiator bank. The radiators are mounted on headers, which are supported from the ground. In this case, strict dimensional control of pipes and other fittings is required in order to avoid oil leakages.

Oil is kept in circulation by gravitational buoyancy in the closed-loop cooling system as shown in Figure 9.1. The heat developed in active parts is passed onto the surrounding oil through the surface transfer (convection) mechanism. The oil temperature increases and its specific gravity drops, due to which it flows upwards and then into the coolers. The oil heat is dissipated along the colder surfaces of the coolers, which increases its specific gravity, and it flows downwards and enters the transformer tank from the inlet at the bottom level. Since the heat dissipation from the oil to atmospheric air is by natural means (the circulation mechanism for the oil is the natural thermosiphon flow in the cooling equipment and windings), the cooling is termed ONAN (oil natural and air natural) or the OA type of cooling.

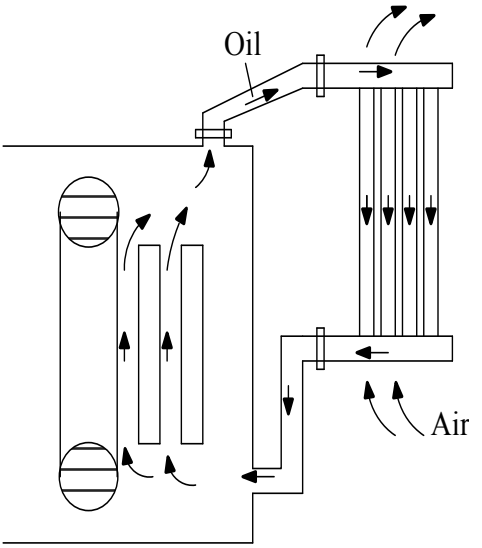

Figure 9.2 Arrangement for a high thermal head.

In the arrangement consisting of radiator banks, higher thermal heads can be achieved by adjusting the height of support structures. The thermal head can be defined as the difference between the centers of gravity of fluids in the tank and radiator bank. Although it is difficult to obtain high thermal heads in tank-mounted radiators, a reasonable amount of thermal head is achieved by an arrangement as shown in Figure 9.2. When the radiators are mounted at a higher height, the buoyancy effect on the cooling-loop increases, resulting in an increase of the rate of oil flow and heat dissipation in the cooling equipment. However, it is to be noted that the increase in the flow rate also results in an increased frictional pressure loss, thereby offsetting the advantage obtained by the additional thermal head due to the height difference.

9.2.2 ONAF/FA cooling

As the transformer rating increases, the total loss to be dissipated also increases. One way of increasing the heat dissipation is to increase the heat transfer coefficient between the radiator outside surface and air. When Equation 9.5 is applied for a radiator, $T_{surface}$ corresponds to its outside wall surface temperature. However, the temperature drop across the radiator plate is very small; hence $T_{surface}$ can be considered as the oil temperature itself. If fans are used to blow air onto the cooling surfaces of the radiators, the heat transfer coefficient is significantly increased. For a given set of ambient air and oil temperatures, a compact arrangement is possible since fewer radiators are

required to cool the oil. This type of cooling is called the ONAF (oil natural and air forced) or FA type of cooling.

If there is a particular case in which either ONAN or mixed ONAN/ONAF cooling can be specified, the ONAN cooling has the following advantages (although it may take more space):

- It is more reliable as no cooler controls are involved and it requires less maintenance.
- The cost increase due to extra radiators is, to a large extent, compensated by the reduction in cost due to the absence of fans and control circuitry.
- It is particularly useful when low noise transformers are required. Absence of fans makes it easier to achieve a required low noise level.
- There is no cooler loss.
- Winding losses are also reduced (although marginally) because of lower temperatures at fractions of the rated load as compared to the mixed cooling.
- Most of the time, when the load on the transformer is less than its full rating, temperatures inside it are low and its life increases (gain of life).

Thus, in cases where the ONAN rating is 75% or more (it is closer to the ONAF rating), the ONAN cooling can be specified instead of the mixed ONAN/ONAF cooling based on cost-benefit analysis.

There are two typical configurations for mounting fans in ONAF cooling. One method is to mount fans below radiators for blowing air from bottom to top. Larger capacity fans can be used since it is easy to design the support structures for them. In this system the fans can either be supported directly from the radiators or they can be ground mounted. Care should be taken that the fans mounted on radiators do not produce appreciable vibrations. Usually, sufficient surface of radiators is covered in the air-flow cones created by the fans; the remaining surface is taken to be naturally cooled. In the second method, fans are mounted on the side of radiators. These fans are relatively smaller in size compared to the first arrangement since the number of fans is usually greater for this configuration. Both configurations have some advantages and issues; selection of a particular scheme depends design and manufacturing practices.

9.2.3 OFAF/FOA cooling

As discussed previously, the flow rate inside the windings under ONAN and ONAF cooling arrangements is governed by the natural balance between the viscous resistance and the thermosiphon pressure head. Normally this flow rate is relatively low. Because of this, the heat carrying (or dissipating) capacity of the oil is low. The heat carrying capacity can be defined as

$$Q = \dot{m} C_p \left(T_{out} - T_{in}\right) \tag{9.6}$$

where Q is the heat flow in W, $\dot{m}$ is the mass flow rate in kg/s, C_p is the specific heat in J/(kg °C), and the temperatures T_{out} and T_{in} are in °C. For given

transformer oil inlet (T_{in}) and top oil (T_{out}) temperatures, the only way to increase the heat dissipation capability is to increase $\dot{m}$. This necessitates the use of an external pump to circulate the oil in high rating transformers. Also, in order to get a higher heat transfer rate, fans have to be always operating. This type of cooling is called OFAF (oil forced and air forced) or FOA cooling. There are basically two types of pump designs: an axial flow in-line type and a radial flow type for circulating oil against low and high frictional head losses, respectively. The axial flow type is used with mixed cooling (ONAN/ONAF/ OFAF) since it offers less resistance when switched-off. The radial flow type pumps, which offer very high resistance to oil flow under a switched-off condition, are used with oil-to-air heat exchangers (unit cooler arrangement) or oil-to-water heat exchangers, in which no natural cooling is provided. The head required to be developed for these two types of compact heat exchangers is high and the radial flow pump can cater to this requirement well.

In an OFAF cooling arrangement, when fans are mounted on the sides of radiators, they should be uniformly distributed over their height, whereas for an ONAF cooling more fans should be mounted at the top of their height. This is because in the OFAF condition, the temperature difference between top and bottom portions of the radiators is small as compared to that under the ONAF condition.

When oil is forced into the transformer (Figure 9.3), its flow is governed by resistances of available paths as well as buoyancy. Hence, some of the oil may not enter either the windings or the core, and may form a parallel path outside these active parts. Thus, the top oil temperature may reduce because of the mixture of the hot oil coming from the windings and the cool oil coming from the pump. This in turn reduces the effectiveness of the radiators. The heat dissipation rate can be improved if the oil is forced by pumps and is directed into the windings through predetermined paths as shown in Figure 9.4. This type of cooling is termed ODAF (oil directed and air forced) type of cooling. The ODAF cooling is used in large rating power transformers. One disadvantage of the ODAF cooling is increased pressure loss because of the ducting system used for directing the oil flow. For each winding, the oil flow rate is required to be determined accurately. In the absence of proper oil flow rates, an unreasonable temperature rise may result. Additionally, any blockage or failure of the ducting system leads to higher temperatures.

Generally, the higher the pump capacity (and the greater the oil velocity) the higher the rate of heat dissipation is. Hence, high capacity pumps were used permitting greater loss densities (use of higher current densities in the windings and/or a higher flux density in the core), leading to a lower material cost and smaller size of the transformers. The trend continued until a number of large transformers failed due to a phenomenon called static electrification which is explained in Section 9.6. Hence, the oil pump capacity should be judiciously selected.

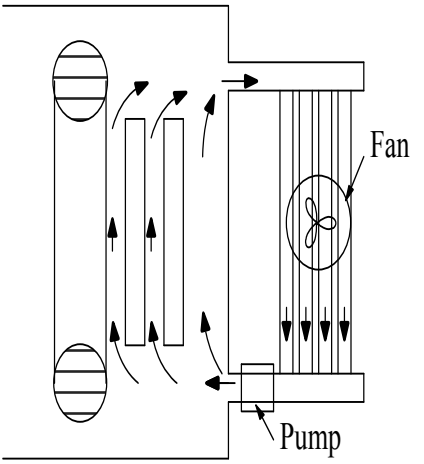

Figure 9.3 OFAF cooling.

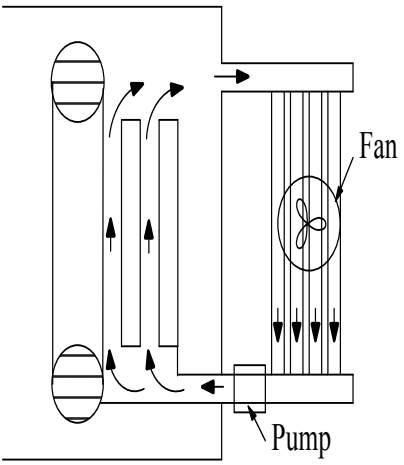

Figure 9.4 ODAF cooling.

9.2.4 Unit coolers

As mentioned earlier, sometimes an OFAF cooling arrangement is provided through compact heat exchangers when there is a space constraint at site. In these units, an adequate surface area is provided by means of finned tubes. Usually, about 20% standby cooling capacity is provided. A disadvantage of these coolers is that there is only one rating available (with running of the fans and the pumps). If the system of the fans and pumps fails (e.g., failure of auxiliary supply), an ONAN rating is not available. Hence, the continuity of auxiliary supply to the fans and pumps is required to be ensured.

9.2.5 OFWF cooling

For most of the transformers installed in hydropower stations, where there is an abundance of water, oil-to-water heat exchangers are used. As the surface heat transfer coefficient of water is greater than that of air, such a type of cooling results in smaller radiators. This type of cooling is termed water forced (WF) cooling. Depending on the type of oil circulation, the transformer cooling system is termed OFWF or ODWF type of cooling. During operation, it is very important to ensure that the oil pressure is always more than the water pressure so that the possibility of water leaking into the oil is eliminated. A dedicated differential pressure gauge and a corresponding protection circuit are used to trip the transformer if a specific value of the pressure difference is not maintained during the operation.

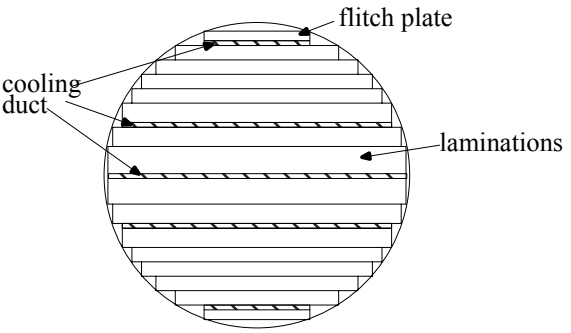

Figure 9.5 Core cooling ducts.

9.3 Dissipation of Core Heat

As the transformer core size increases, it becomes more important to decide the positions of cooling ducts in it. These cooling ducts (shown in Figure 9.5) reduce its surface temperature rise relative to that of the oil as well as the temperature rise of its interior relative to that at the surface. It is necessary to maximize the core area to have an optimum design. The cooling ducts reduce the core area, and hence their number should be minimized. This requires accurate determination of the temperature profile of the core and effective placement of the cooling ducts. The complicated geometry of the boundary surface between the core and the oil, and the anisotropy of the thermal conductivity of the laminated core, are some of the complexities involved in the computations.

A general formulation of the approximated 2-D problem of temperature distribution in rectangular cores subjected to linear boundary conditions (thermal resistance being independent of heat flow and oil temperatures) is given in [4]. The method described in [5] solves the 2-D problem by transforming Poisson's equation of heat conduction into Laplace's equation. The method can be applied to any arbitrary shape due to the use of a functional approximation. The paper also reports an electrical analog method which uses the analogy between electrical potential difference and temperature difference, between electrical current and heat flow, and between electrical conductivity and thermal conductivity. The calculation of temperature distribution in the core is a complex 3-D problem with nonuniform heat generation. Furthermore, the properties of core are anisotropic in the sense that the thermal conductivity along the plane of laminations is quite different from that across them. The problem can be solved by using a 3-D finite element thermal formulation with the anisotropic thermal material properties taken into account.

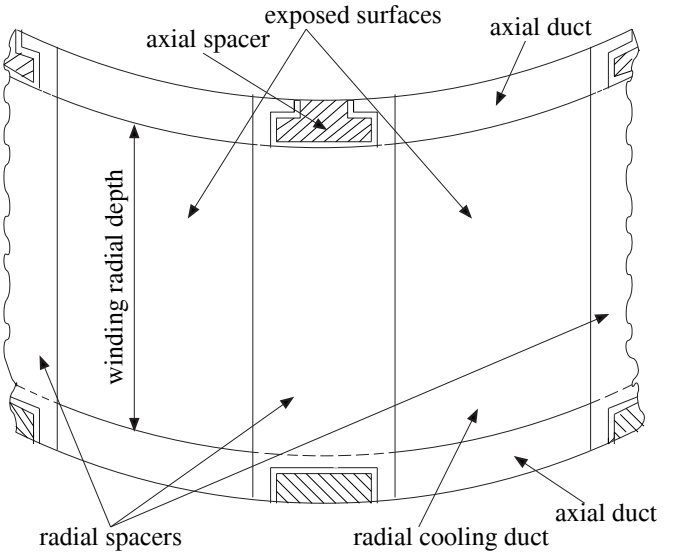

Figure 9.6 Effect of radial spacers on cooling.

The surface of the core is usually in contact with the insulation between it and the frames. Hence, the limit on the core surface temperature is the same as that for the windings. For the interior portions of the core which are in contact with only oil (film), the limit is 140°C. In most cases, the temperature difference between the core interior (e.g., mid-location between two cooling ducts) and the surface is about 15 to 20°C.

9.4 Dissipation of Winding Heat

Radial spacers (pressboard insulations between disks/turns) cover about 30 to 40% of the winding surface, making the covered area ineffective for the convective cooling. The arrangement is shown in Figure 9.6. Thus, although a large spacer width may be required from short-circuit withstand considerations, it is counterproductive for cooling. Hence, while calculating gradients, only uncovered surface areas of windings are taken into account.

Heat from the covered winding area is transferred to the uncovered area by the thermal conduction process increasing the thermal load on the uncovered surfaces. Contrary to the width of radial spacers, cooling is improved with an increase in their thickness. Hence, radial spacers may not be required from insulation considerations in low voltage windings, but they are essential for providing cooling ducts.

A required spacer thickness bears a specific relationship with the radial depth of the winding. For a given radial depth, a certain minimum thickness of

radial spacers is required for effective cooling (otherwise the resistance to oil flow in the duct between two disks/turns is higher and the oil largely flows through the axial ducts at inside and outside diameters resulting in higher temperatures at the middle portion of the radial depth).

When the winding radial depth is large, the usual practice of providing two axial ducts at the inside and outside diameters (along with the radial ducts) may not be enough. Hence, an additional axial cooling duct may be provided in the middle of the radial depth as shown in Figure 9.7, so that the thickness of the radial spacers can be lower. With this arrangement, the axial space factor of the winding improves (due to reduction of insulation along the winding height), but the radial space factor worsens. Hence, the design and dimensioning of the axial and radial spacers have to be judiciously done, which may also depend on manufacturing practices.

Axial ducts play an important role in dissipation of heat from the windings. The higher the axial duct width, the better the oil flow conditions are; this statement is true for windings without radial ducts. In large transformers with radial cooling ducts between disks/turns, the relative values of the thicknesses of the axial ducts (at the inside and outside diameters of the winding) and the radial ducts decide the oil velocity within the winding and the rate of heat dissipation.

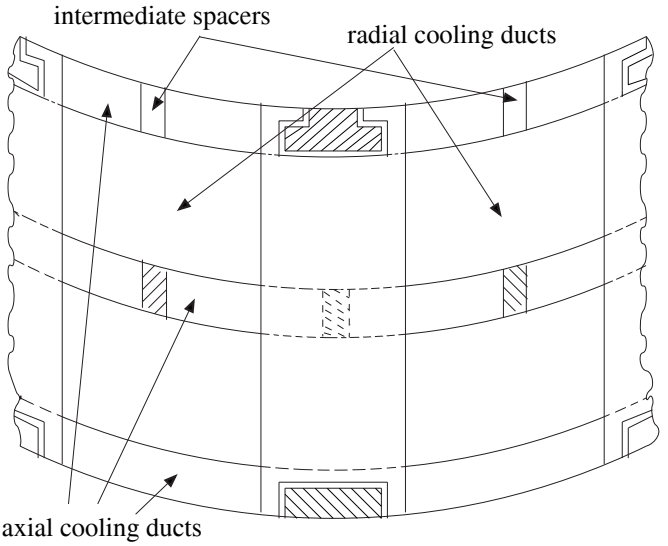

Figure 9.7 Axial cooling ducts.

The axial duct at the winding outside diameter is usually of the order of 10 to 12 mm, whereas the duct at the winding inside diameter is kept equal to or below 8 mm from the dielectric strength consideration (as explained in Chapter 8). Thus, the thermal and dielectric requirements are in conflict while designing the thickness of the inner axial duct. A size less than 6 mm is not preferred from the thermal consideration. Narrow ducts or manufacturing deficiencies result in high flow resistances, thereby leading to unacceptable temperatures within the winding.

In power transformers, a guided oil flow is commonly used to cool their windings effectively. The oil guiding is achieved through washers as shown in Figure 9.8. The washers have to be accurately cut to required dimensions so that there is proper sealing at desired locations eliminating oil leakages. If oil guiding strips are used, they have to be securely held to the innermost conductor (sealing at the inside diameter) or the outermost conductor (sealing at the outside diameter) along the circumference. The location and number of these oil guiding components have to be properly selected. Oil flow through multiple passages has been studied in [6], in which the oil flow rates are shown to be different in upper ducts as compared to lower ducts. Similar trends are reported in [7] for SF6 flow rates in gas cooled transformers. The effects of the number of radial ducts between two consecutive oil guiding washers, the width of radial ducts and the width of axial ducts on the winding temperatures have been reported in [8] based on FEM simulations.

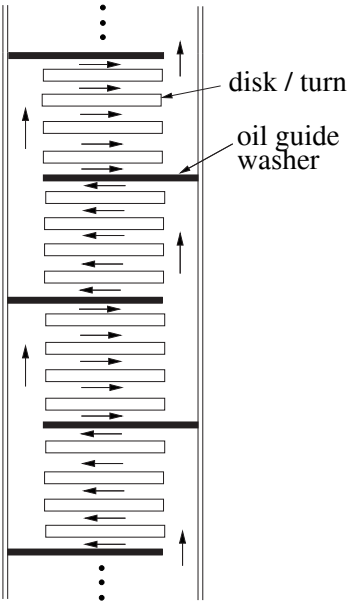

Figure 9.8 Directed oil flow in a winding.

When winding gradients are calculated by simple formulae, an average loss per disk (in a disk winding) or per turn (in a layer winding) is considered, which is calculated by adding the average eddy loss in the disk or turn to its I^2R loss. The effects of winding curvature can be neglected. The average temperature rise of the winding above the average oil temperature is then calculated as the sum of the temperature drop across the conductor paper insulation and the surface temperature drop. It is to be noted that the heat flux per unit surface area used in these calculations should be determined by considering only the exposed horizontal surface area of the winding (not covered by the radial spacers).

Although temperature rise calculations in transformers have been heavily relying on empirical factors, there have been continuous efforts for determining the temperatures through accurate formulations. Equations governing the distributions of interlayer temperatures and duct-oil velocities under thermal and hydrodynamic conditions are derived in [9] for a layer-type transformer winding. A resistive-network analog computer has been used in the iterative solution of equations. The finite difference method is used in [10] to find a numerical solution for a disk-type transformer winding. A general network method is described in [11], in which interconnecting flow paths or ducts are represented by a network diagram, each element of which corresponds to a single path with nodes placed at the junctions. A solution is obtained by a numerical procedure that predicts the temperature distribution in ducts. The temperature distribution in a winding does not vary linearly with its height as usually assumed. Variations in temperatures with the winding height is close to a linear distribution in a forced oil cooling condition, whereas for naturally oil cooled transformers (ONAN and ONAF) it can be significantly nonlinear [12].

9.5 Aging and Life Expectancy

As explained earlier, the insulation properties and hence the life of a transformer is basically decided by the mechanical strength of its insulation under normal aging processes. Brittleness in paper insulation is strongly conducive to dielectric failure by various mechanisms. The period of time after which the deterioration of an insulating material becomes critical is called the service life or life expectancy. The service life of a transformer can be calculated by using the Montsinger formula applicable to the 80 to 140°C range of temperatures,

$$\text{Life} = De^{-p\theta} \text{ years} \tag{9.7}$$

where D is a constant expressed in years, p is a constant expressed in °C^{-1}, and θ is temperature in °C. It is generally recognized that the rate of aging as measured by the tensile strength of class A insulation doubles for each 5 to 10°C increase in the temperature [1]. It was reported in 1930 [13] that the aging of the tensile strength is doubled for approximately each 8°C increase in the temperature. Subsequent tests reported [14] on paper insulation confirmed this

aging rate. During discussions in the CIGRE Transformer Working Group in 1961, 6°C was considered to be a more correct value [15] and is now used widely by transformer designers and users. It should be remembered that the paper insulation life can be considered to reach half for a 6°C rise when the moisture content in the insulation is within acceptable limits (typically less than 0.5% by weight); a higher moisture content will increase the rate of aging many times.

Hence, for the temperature range of 80 to 140°C, the life expectancy is taken to be halved for an increase in the temperature of 6°C. This means that if a service life of N years applies for a temperature of θ °C, the temperature of $(\theta + 6)$ °C will reduce the life by $(N/2)$ years. With these figures, the constant p in the Montsinger formula can now be determined. Rewriting Equation 9.7 as

$$N = De^{-p\theta} \text{ years} \tag{9.8}$$

$$\frac{N}{2} = De^{-p(\theta+6)} \text{ years} \tag{9.9}$$

and taking the ratio of the above two equations we obtain

$$2 = e^{p6}$$

$$\therefore\ p = 0.1155°\ \text{C}^{-1}. \tag{9.10}$$

If the life expectancy at some temperature θ_b is chosen to be normal, then that is applicable to an arbitrary temperature θ can be related to this normal life expectancy. The ratio of these two life expectancies is called as the aging factor or the relative reduction of life, and is given using the Montsinger relation as [2]

$$K_{ag} = \frac{De^{-0.1155\,\theta_b}}{De^{-0.1155\theta}} = e^{0.1155(\theta-\theta_b)}. \tag{9.11}$$

The limits on maximum values of currents and temperatures are given in standards, which are applicable to loading beyond the nameplate rating. For example, according to the IEC Standard 60076-7: 2005, the limits are given separately for three categories of transformers: distribution, medium power and large power transformers. For each of these, the limits are specified for three types of loadings, viz. normal cyclic loading, long-time emergency cyclic loading and short-time emergency loading. The limits are lower for large power transformers. Under normal cyclic loading conditions, 150% current and hot spot temperatures up to 120°C (for metallic parts in contact with cellulose insulating materials) are allowed for distribution and medium power transformers, whereas for large power transformers the corresponding limits are 130% and 120°C. For all transformers the top oil temperature limit of 105°C is specified under normal cyclic loading conditions, whereas the limit of 115°C is

specified for long-time emergency cyclic loading and short-time emergency loading.

Pure oil, free from impurities and sealed from the atmosphere, can withstand temperatures up to 140°C [3] which is the flash point of oil. Generally, the temperature of structural components and other metallic parts should be limited to 135 to 140°C, provided this temperature occurs over a small surface area of a few cm^2 that is in contact with a bulk quantity of oil [2].

It is generally accepted that a continuous operation with the hot spot temperature of 98°C results in a normal use of life or rate of degradation. This is the temperature at which the insulation of a transformer deteriorates at the normal rate. Thus, if we choose 98°C as the temperature corresponding to the normal life expectancy, then the aging factor applicable to an arbitrary temperature θ can be given as

$$K_{ag} = e^{0.1155(\theta - 98)}. \tag{9.12}$$

If the ambient temperature (θ_a) is appreciably varying during the period under consideration, the weighted ambient temperature should be taken for the hot spot temperature calculation. The weighted ambient temperature θ_{awt} is that temperature which lasts for the same time t and causes the same loss of expectancy as the ambient temperature $\theta_a(t)$ which is varying in magnitude with time. For equal reduction of life expectancy the following equation holds

$$t\, e^{0.1155\,\theta_{awt}} = \int_0^t e^{0.1155\,\theta_a(t)}\, dt. \tag{9.13}$$

The weighted ambient temperature can be fixed once and for all in a given climatic condition. This temperature, when calculated by Equation 9.13, is such that the extra loss of life during the summer season is compensated by the gain of life in the winter season.

The temperature rise limits set by the standards are in line with the hot spot limit for the normal aging of a transformer. The hot spot limit of 98°C is applicable to the average winding temperature rise of 55°C above ambient temperature (for transformers without thermally upgraded insulation). The corresponding limit is 95°C according to the IEEE standard C57.91: 1995, and the limit is 110°C for a thermally upgraded insulation (for transformers with 65°C average winding rise); i.e., the maximum (hottest spot) winding temperature rise of 80°C is allowed above the average ambient temperature of 30°C for the normal aging conditions.

The steady-state hot spot temperature is calculated as the sum of the ambient external cooling medium temperature, the temperature rise of top oil above the cooling medium and the hot spot winding gradient. Let us assume that the hot spot gradient is 1.1 times the average gradient (which is the difference

between the average winding temperature rise and the average oil temperature rise). For yearly weighted average ambient temperature of 20°C, and top oil rise and average winding rise limits of 60°C and 65°C, respectively (according to the IEC standard 60076-2: 1993), the hot spot temperature is

$$\text{hot spot temperature} = 20 + 60 + (65 - 0.8 \times 60) \times 1.1 \cong 98\,^{\circ}\text{C}$$

where the average oil temperature rise is taken as 80% of the top oil temperature rise, which is usually true for natural oil circulation. For forced oil conditions, the hot spot temperature is lower since the average oil temperature rise is closer to the top oil temperature rise. Thus, it can be seen that if the temperature rise of the oil and windings are within the limits set by the standards, the hot spot temperature will not be exceeded and a certain transformer life (of few decades), with the normal aging processes, can be expected. If the hot spot gradient is 1.3 times the average gradient, the top oil rise and the average winding rise should be lower so that the hot spot temperature limit is not exceeded. Thus, based on the calculated value of the hot spot gradient, designer may have to limit the top oil rise and average winding rise values.

Example 9.1

The loading of a transformer is such that the hot spot temperature does not exceed 92°C for 18 hours in a day. For the remaining 6 hours, during peak load periods, the transformer can be overloaded. What will be the temperature corresponding to the allowed overload condition?

Solution:

Here, the objective is to have a normal use of life over the whole period of the day. Transformer gains life during the lower load period of 18 hours and this gain of life can be utilized to allow an overload. The temperature θ during the overload period of 6 hours is given by

$$24 = 18\, e^{0.1155\,(92-98)} + 6\, e^{0.1155\,(\theta-98)} = 18 \times 0.5 + 6\, e^{0.1155\,(\theta-98)}$$

$$\therefore e^{0.1155\,(\theta-98)} = \frac{24 - 18 \times 0.5}{6} = 2.5$$

$$\therefore \theta = \frac{\ln(2.5)}{0.1155} + 98 = 106\,^{\circ}\text{C}.$$

If the thermal time constant of the transformer is considered, the duration of the overload can be higher than the one calculated above. The usual values of thermal time constants for transformers lie in the range of 1 hour to 8 hours; lower values are for the forced cooled transformers and higher values are for the naturally cooled transformers. The thermal time constants of windings

considered alone are much lower (in the range of few minutes to tens of minutes).

Example 9.2

Estimate the relative extent of insulation aging of a transformer winding subjected to a temperature of 136°C for 3 hours during a day.

Solution:

The aging factor calculated by Equation 9.12 is

$$K_{ag} = e^{0.1155(136-98)} = 80.6 .$$

Hence, the operation of the transformer at 136°C for 3 hours is equivalent to $3 \times 80.6 = 241.8$ hours (approximately 10 days) of operation with the normal aging processes.

Here again, the thermal time constant is ignored which results into a very conservative calculation. For accurate calculations the IEC standard 60076-7: 2005 or IEEE standard C57.91: 1995 can be used.

Example 9.3

A transformer is loaded in such a way that its hot spot temperature is about 86°C during most of the time in a day. For a few hours during the peak load period we want to overload the transformer so that its hot spot temperature rise is limited to 120°C. How long should the period of the overload last, if the resulting loss of life has to be kept the same as that with normal aging processes?

Solution:

The relative loss of life can be calculated by Equation 9.12,

$$K_{ag} = e^{0.1155(\theta-98)}$$

At 86°C hot spot temperature, the relative loss of life is 0.25 and at 120°C, its value is 12.7. Suppose, the transformer is operated for x hours at 86°C, and then at 120°C for $(24 - x)$ hours. Therefore, the value of x can be calculated by the following equation,

$$0.25 \times x + 12.7 \times (24 - x) = 24 \quad \Rightarrow \quad x = 22.55 \text{ hours.}$$

Therefore, the overloading can be done for approximately 1.5 hours.

It is well-known that the paper aging is highly dependent on temperature, water and oxygen. The thermally upgraded paper is less affected by the presence of water and oxygen as compared to the normal paper, and hence its use is technically beneficial [16]. The thermally upgraded paper can be used for

increasing the overloading capability and life of a transformer. Many transformer manufacturers are using it but the use is still not widespread. Furfural analysis of commonly available thermally upgraded kraft papers has been reported in [17]; it is suggested to have a detailed knowledge of the thermally upgraded paper and its behavior during aging processes before its use is made in transformers.

Most of the earlier work is based on the use of the tensile strength for assessing the remaining useful life; a reduction in tensile strength to 50% of its original value is used as the criterion. A more precise DP (degree of polymerization) method, which is now widely getting acceptance, can give the same information more conveniently.

Transformers subjected to a non-sinusoidal duty deserve special attention. Hot spot temperatures and loss of life should be accurately estimated [18]. A suitable derating factor has to be used to compensate the effects of harmonics.

Online monitoring is necessary to sense incipient faults in transformers. Most faults of thermal nature can occur due to malfunctioning of fans/radiators or overloading. The load on a transformer and the ambient temperature can be remotely monitored. The modified IEEE thermal model reported in [19] can be used to calculate the top oil temperature of the transformer at any instant using the load current, ambient temperature and previous top oil temperature values through a linear regression algorithm. The predicted temperature can be continuously compared (or for example, at every 15 minutes) with the measured value. Some kind of fault or abnormality can be suspected inside the transformer if the measured temperature is higher than the predicted one.

9.6 Direct Hot Spot Measurement

The rate of deterioration of winding insulation increases as its temperatures increase. Hence, it is necessary to know the hottest conductor temperature in order to ensure an expected life for the insulation and the transformer. The oil temperature is usually high at the top. Also, there are higher loss densities in the winding at the top because of the eddy loss due to a radial leakage field. In addition, an extra insulation may have been provided to line-end turns at the top. All these reasons lead to having hot spots at disks/turns in the top portion of the winding. The hot spot is usually assumed to be present at the second disk/turn from the top. The hot spot winding gradient can be about 1.1 to 1.3 times the average winding gradient over the average oil rise.

The winding temperature is traditionally measured by a winding temperature indicator (WTI) which uses the principle of thermal imaging. A thermometer-type sensor which measures the top oil temperature is placed in a tank pocket and is surrounded by a heater coil carrying a current in proportion of the load current. After proper adjustment of settings, the device reads the hot spot temperature of the winding. The settings are specified by designers based on the calculated value of the hot spot gradient. Since the actual value of the hot

spot gradient is a function of many design and manufacturing parameters, viz. winding eddy loss density, effectiveness of cooling ducts provided, etc., the accuracy of winding hot spot temperature measurement by WTI may not always be good. Hence, the direct hot spot measurement technique is being increasingly specified and used. In this method a sensor, made of photo-luminescent material and attached to the end of an optical fiber, is in thermal contact with the winding. The sensor is usually placed between an insulated conductor and a radial spacer. The fiber-optic cable is brought out of the tank up to the instrument through a hole made in the tank with a proper oil-sealing arrangement. A pulse of light from the light emitting diode (LED) in the instrument is sent to the sensor through the fiber-optic cable, which stimulates the sensor material to fluoresce. Depending on the decay time of the returning fluorescent signal, which is a function of the conductor temperature, the instrument calculates and displays the corresponding hot spot temperature by a lookup table approach. By using the fiber-optic sensor, accurate measurement of hot spot temperatures can be done, however the sensor insertion method is critical. The requirements of the measurement system are that the sensor should be sufficiently small, the signal transmission system should not degrade the dielectric strength of the transformer, and the components used should withstand thermal, mechanical, and chemical rigors of the transformer environment [20].

It is important to accurately calculate the loss density and corresponding gradients at various critical locations in windings and thereafter predict locations of hot spots. The hot spot temperatures measured at these locations by the direct hot spot measurement technique should be reasonably close to the calculated values. The calculations are complicated by the fact that resistivity of the conductor changes as the temperature along the winding height changes. The I^2R loss of the winding is directly proportional to resistivity, whereas the winding eddy loss is inversely proportional to resistivity. Hence, generally as the oil temperature increases from bottom to top, the I^2R loss increases while the eddy loss tends to reduce. Since the I^2R loss is the dominant component, losses are higher at the top. The stray leakage field and the corresponding winding eddy losses are different along the winding radial depth, as explained in Chapter 4, and this variation should be taken into account during the calculation of hot spot temperatures.

9.7 Static Electrification Phenomenon

Generation of static charges, caused by oil streaming on a solid insulating component, is responsible for streaming or static electrification phenomenon in transformers. This phenomenon occurs due to the friction between the oil and solid dielectric components of the transformers. Depending on the type of oil and its velocity, high levels of localized electrostatic charges (due to charge separation) can be generated leading to very high voltages inside the

transformer. Such an overvoltage, depending on where it occurs inside the transformer, could trigger a sequence of electrical discharges and arcing. Failures in some of the large high voltage transformers and autotransformers have been attributed to the occurrence of electrostatic charges. When the voltage and power ratings of the transformer increase, tendency is to use high oil flow rates for the cooling purpose and to improve the insulation resistance. From the standpoint of static electrification, these improvements result in an increase of charging tendency. The accumulation of charges leads to production of a strong DC field, which may stress the insulation to an unacceptable level. If high voltage transformers are manufactured with reduced dimensions and kg/MVA values, chances of electrostatic charging are higher. The reduction in the weight-to-power ratio usually results in greater oil velocities and more labyrinths aiding the static electrification phenomenon.

When oil flows through insulation ducts, charge separation occurs at the interface of the solid insulation and the oil. The charge separation also occurs in the other regions of the flow system such as radiator pipes and pumps. It has been observed that paper/pressboard insulation structure acquires a negative charge and the oil carries a positive charge. The lower part of the insulation arrangement (i.e., bottom end insulation) may accumulate a high negative charge leading to development of an excessive DC voltage [21, 22]. As the oil flows up through the windings, it becomes more and more positively charged, and the upper tank may act as a reservoir for the positive charge. There is charge relaxation in every part of the flow system which mitigates the effect. The static charge distribution in the system is determined by the balance of the charge separation and charge relaxation processes [23]. The radiator pipes are efficient charge dissipating devices.

There are many factors which influence the static electrification phenomenon:

- *Moisture content*: Moisture has a significant effect on the charging tendency; drying out causes the charge density to increase, while addition of moisture reduces it. Since transformers are operated with low moisture levels in oil (below 10 ppm at the time of new oil filling), high charging tendencies may be experienced [24].
- *Temperature*: There is an increase in charging tendency with temperature since the dryness of oil increases. Hence, it may be advisable to reduce the flow rate during the warming-up process.
- *Flow rate*: The charging tendency increases with greater flow rates. The increase varies somewhere between the second and fourth power of the oil flow velocity. The average flow rate involved in one of the failures was 20 cm/s over an average typical cross section [25]; the flow rate in the windings was 45 to 60 cm/s, and in the pumps and piping in the heat exchangers it was more than 4.5 m/s. The consideration of static electrification decides the upper limit of the oil flow rate in forced oil cooled transformers, and thus impacts the cooling system design.

- *Turbulence*: The charge motion or generation depends on turbulence in oil.
- *Surface condition*: The charge generation/separation process is enhanced with increasing roughness of the solid insulation.
- *Pumps*: Pumps can be substantial sources of charge generation [26].
- *Orifices*: Orifice effects have been demonstrated to generate charges.
- *Fields*: The AC and DC fields have definite impact on the static electrification, which is investigated in [27].

Some of the methods reported for reducing charging tendency are clay filtration of oil and the addition of charge suppressors to oil [24]. Charge reduction by addition of charge suppressers is not a viable solution as it increases the electrical conductivity of oil. The oil flow can be reduced in the susceptible temperature range by operating the cooling system using automatic control.

In addition to incorporating pumps that operate at low flow velocities, the effect of changing the location of pumps may also be a consideration if the pumps prove to be the prime sources of charge generation. The pumps can be mounted at the top of radiators to allow more distance for charge relaxation in the oil prior to entering the bottom of the transformer.

9.8 Recent Trends in Computations

The governing equations of fluid flow are based on conservation laws of physics [28], viz. conservation of mass, momentum and energy. Three dimensional Navier-Stokes equations describe fluid flow and heat transfer in any domain and the same can be applied for transformers also. Commercial software programs generally solve these dimensional form of equations for which material properties need to be defined. On the other hand, equations in nondimensional form are preferred by researchers. In this approach, the effect of flow and fluid properties are taken into account while defining nondimensional parameters. The advantage of the dimensionless numbers is the applicability of the results to other similar heat transfer problems. The Navier-Stokes equations can be rewritten in the nondimensional form in which the following three dimensionless parameters characterize fluid flow in the cooling circuit of a transformer: Reynolds number, Grashof number and Prandtl number.

Reynolds number (*Re*) is uL/v where u is the velocity of oil (m/s), L is the characteristic length (m) and v is kinematic viscosity (m^2/s). It represents the ratio between the inertia and viscous forces acting on a fluid body, and is used to determine whether the flow in the cooling channels of the windings is laminar ($Re<2100$) or turbulent ($Re>4000$). If the Reynolds number is high, heat transfer is better with a corresponding increase in the pressure drop which has to be compensated by a higher pump capacity in OFAF systems.

The second nondimensional parameter, Grashof number ($Gr=g\beta\Delta TL^3/v^2$), is the ratio of the buoyancy and viscous forces. Here, g is the gravitational accelera-

tion (m/s^2), β is the coefficient of thermal expansion for fluid (K^{-1}), ΔT is the temperature difference between the fluid (either air or oil) and the winding. A larger *Gr* means a stronger buoyancy force indicating the dominance of natural convection over forced convection.

Prandtl number expresses the ratio between the momentum diffusivity (kinematic viscosity) and the thermal diffusivity. The thicknesses of the thermal and hydrodynamic boundary layers are related by this parameter [29]. The kinematic viscosity of fluid indicates the rate at which momentum diffuses through the fluid on account of molecular motion. The thermal diffusivity is indicative of the rate of heat diffusion in the fluid. For the two cooling fluids in a transformer, i.e., oil (cooling active parts) and air (cooling the oil in radiators), the Prandtl number is usually of the order of 100 and 0.7, respectively.

In order to accurately model the temperature distribution inside the windings of a transformer, a strong coupling between the cooling fluid and the solid components (active parts) is required, which can be modeled through a conjugate heat transfer approach. It allows an accurate modeling of the active materials that influence overall conduction and convection modes. Two approaches are essentially used to study temperature gradients, hot spot locations, and mass flow distribution in windings, viz. the thermohydraulic network-based model and the computational fluid dynamics (CFD) based simulations.

***Thermohydraulic Network Model*:** The guided oil flow arrangement shown in Figure 9.8 is considered for explaining the model. A winding section between any two consecutive washers is known as a pass. Without loss of generality, one pass can be taken for the analysis, as shown in Figure 9.9, to simulate 2-D axisymmetric temperature field in a winding disk, and to determine the bulk oil temperatures and flow distribution. The coolant flows are treated 1-D (either in the vertical or horizontal direction as shown in the figure) in the cooling ducts with a constant mass flow rate between nodes of the network.

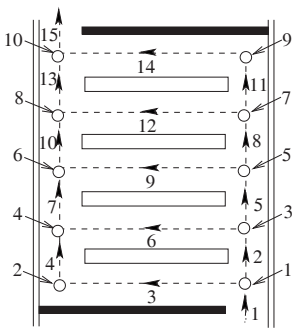

Figure 9.9 Thermohydraulic network model [30].

For each pass, the input data are the pressure and total mass flow rate at its entrance, and all geometric parameters. Pressure is associated with nodes and mass flow rate with horizontal/vertical paths. The oil velocity can vary in a horizontal duct due to non-uniformities in cross-sectional areas and its temperature-dependent properties; the mass flow rate is therefore considered as the main variable [30]. The output data are the pressure and mass flow rate distribution in various cooling ducts within the pass, and the pressure and the mass flow rate at the pass-outlet become the input data for the next pass. The principle of conservation of mass flowing into and out of each junction is used to formulate equations of the hydraulic network [30]. In each closed loop, the sum of the pressure drops is zero.

***CFD Model*:** This allows comprehensive 3-D analysis in contrast with the previous approach which assumes circular symmetry. 3D models generated in a typical CAD software can be imported into a mesh generator where geometry is discretized into a number of computational cells (or grid cells). There are many discretization methods, but the most commonly used are the finite difference method, the finite volume method, and the finite element method. It is cumbersome to apply the finite difference approach for irregular boundaries. Traditionally, commercial solvers were mostly FEM based. Most of the commercial CFD solvers, now, are based on the finite volume method of discretization of governing equations. Basic laws of physics are used to ensure conservation of fluxes at discretized smaller control volumes as well as over the complete computational domain. Necessary boundary conditions such as pressure, velocity, mass flow, temperature and/or heat fluxes are set at the boundaries.

Temperature-dependent oil properties are generally used in CFD analysis. The heat generation rate in each disk, calculated from electromagnetic analysis, is used as an input for the CFD analysis. The effect of axial and radial spacers can be determined. It is also possible to optimize the number of discs per pass and determine locations of oil guiding washers to improve the oil flow distribution in the winding. To reduce computational burden, an angular sector can be considered for the analysis purpose with rotational periodicity at its boundaries [31]. CFD model, thus generated, is given as an input to the CFD solver. From the solution, pressure drops and local temperatures are extracted for the estimation of flow losses and hot spot temperatures.

References

1. Blume, L. F., Boyajian, A., Camilli, G., Lennox, T. C., Minneci, S., and Montsinger, V. M. *Transformer engineering*, John Wiley and Sons, New York, and Chapman and Hall, London, 1951.
2. Karsai, K., Kerenyi, D., and Kiss, L. *Large power transformers*, Elsevier Publication, Amsterdam, 1987.

3. Norris, E. T. High voltage power transformer insulation, *Proceedings IEE*, Vol. 110, No. 2, February 1963, pp. 428–440.
4. Higgins, T. J. Formulas for calculating temperature distribution in transformer cores and other electrical apparatus of rectangular cross section, *AIEE Transactions — Electrical Engineering*, Vol. 64, April 1945, pp. 190–194.
5. Rele, A. and Palmer, S. Cooling of large transformer cores, *IEEE Transactions on Power Apparatus and Systems*, Vol. PAS-91, No. 4, July/August 1972, pp. 1527–1535.
6. Nakamura, Y., Jia, W., and Yasuhara, M. Incompressible flow through multiple passages, *Numerical Heat Transfer*, Pt. A, Vol. 16, 1989, pp. 451–465.
7. Nakadate, M., Toda, K., Sato, K., Biswas, D., Nakagawa, C., and Yanari, T. Gas cooling performance in disk winding of large-capacity gas-insulated transformer, *IEEE Transactions on Power Delivery*, Vol. 11, No. 2, April 1996, pp. 903–908.
8. Kamath, R. V. and Bhat, G. Numerical simulation of oil flow through cooling ducts of large transformer winding, *International Conference on Transformers, TRAFOTECH-1998*, Mumbai, India, 1998, pp. I1–I5.
9. Allen, P. H. G. and Allan, D. J. Layer-type transformer-winding cooling factors derived from analogue solution of the governing equations, *Proceedings IEE*, Vol. 110, No. 3, March 1963, pp. 523–534.
10. Preiningerova, S. V. and Pivrnec, M. Temperature distribution in the coil of a transformer winding, *Proceedings IEE*, Vol. 124, No. 3, March 1977, pp. 218–222.
11. Oliver, A. J. Estimation of transformer winding temperatures and coolant flows using a general network method, *Proceedings IEE*, Vol. 127, Pt. C, No. 6, November 1980, pp. 395–405.
12. Pierce, L. W. An investigation of the thermal performance of an oil filled transformer winding, *IEEE Transactions on Power Delivery*, Vol. 7, No. 3, July 1992, pp. 1347–1358.
13. Montsinger, V. M. Loading transformers by temperature, *AIEE Transactions*, Vol. 49, 1930, pp. 776–792.
14. Clark, F. M. Factors affecting the mechanical deterioration of cellulose insulation, *AIEE Transactions — Electrical Engineering*, Vol. 61, October 1942, pp. 742–749.
15. Hochart, B. *Power transformer handbook*, Butterworths and Co. Publishers Ltd., London, 1987.
16. Shroff, D. H. A review of paper aging in power transformers, *Proceedings IEE*, Vol. 132, Pt. C, No. 6, November 1985, pp. 312–319.
17. Morais, R. M., Mannheimer, W. A., Carballeira, M., and Noualhaguet, J. C. Furfural analysis for assessing degradation of thermally upgraded papers in transformer insulation, *IEEE Transactions on Dielectrics and Electrical Insulation*, Vol. 6, No. 2, April 1999, pp. 159–163.

18. Emanuel, A. E. and Wang, X. Estimation of loss of life of power transformers supplying nonlinear loads, *IEEE Transactions on Power Apparatus and Systems*, Vol. PAS-104, No. 3, March 1985, pp. 628–636.
19. Lesieutre, B. C., Hagman, W. H., and Kirtley Jr, J. L., An improved transformer top-oil temperature model for use in an on-line monitoring and diagnostics system, *IEEE Trans. on Power Delivery*, Vol. 12, No. 1, 1997, pp. 249–256.
20. McNutt, W. J., McIver, J. C., Leibinger, G. E., Fallon, D. J., and Wickersheim, K. A. Direct measurement of transformer winding hot spot temperature, *IEEE Transactions on Power Apparatus and Systems*, Vol. PAS-103, No. 6, June 1984, pp. 1155–1162.
21. Higaki, M., Kako, Y., Moriyama, M., Hirano, M., Hiraishi, K., and Kurita, K. Static electrification and partial discharges caused by oil flow in forced oil cooled core type transformers, *IEEE Transactions on Power Apparatus and Systems*, Vol. PAS-98, No. 4, July/August 1979, pp. 1259–1267.
22. Shimizu, S., Murata, H., and Honda, M. Electrostatics in power transformers, *IEEE Transactions on Power Apparatus and Systems*, Vol. PAS-98, No. 4, July/August 1979, pp. 1244–1250.
23. Tamura, R., Miura, Y., Watanabe, T., Ishii, T., Yamada, N., and Nitta, T. Static electrification by forced oil flow in large power transformers, *IEEE Transactions on Power Apparatus and Systems*, Vol. PAS-99, No. 1, January/February 1980, pp. 335–343.
24. Oommen, T. V. Static electrification properties of transformer oil, *IEEE Transactions on Electrical Insulation*, Vol. 23, No. 1, 1988, pp. 123–128.
25. Crofts, D. W. The static electrification phenomena in power transformers, *IEEE Transactions on Electrical Insulation*, Vol. 23, No. 1, 1988, pp. 137–146.
26. Howells, E., Zahn, M., and Lindgren, S. R. Static electrification effects in transformer oil circulating pumps, *IEEE Transactions on Power Delivery*, Vol. 5, No. 2, April 1990, pp. 1000–1006.
27. Miyao, H., Higaki, M., and Kamata, Y. Influence of AC and DC fields on streaming electrification of transformer oil, *IEEE Transactions on Electrical Insulation*, Vol. 23, No. 1, 1988, pp. 129–135.
28. Versteeg, H. K. and Malalasekera, W. *An introduction to computational fluid dynamics: The finite volume method*, Longman Scientific and Technical, England, 1995, pp. 10–15.
29. Holman, J. P. *Heat transfer*, McGraw - Hill Company, Singapore, 1986.
30. Zhang, J. and Li, X. Coolant flow distribution and pressure loss in ONAN transformer windings — Part I: Theory and model development, *IEEE Transactions on Power Delivery*, Vol. 19, No. 1, 2004, pp.186–193.
31. Torriano, F., Chaaban, M., and Picher, P. Numerical study of parameters affecting the temperature distribution in a disc-type transformer winding, *Applied Thermal Engineering*, Vol. 30, 2010, pp. 2034–2044.

10

Structural Design

10.1 Importance of Structural Design

The tank of a transformer is a closed structure which is made from steel plates. It behaves like a plate structure. Stiffeners are usually provided on all the sides and also on the top cover of the tank to reduce stresses and deflections in its plates under various types of loads. The tank is designed for a pressure value higher than the operating one, as specified by the applicable standards. The design and fabrication of the tank is complicated due to transport and site restrictions (on its dimensions and weight). Apart from pressure and vacuum loads, the transformer structure has to withstand other loads such as lifting, jacking, haulage, etc. Its strength against seismic loads may also need to be ascertained.

Its design becomes further complicated due to accessories and fittings connected or mounted on it. These include conservator and radiator mounting arrangements, cooler pipes, turrets which house bushings, support arrangement for control box housing controls for fans and pumps, support structures for the tap changer drive mechanism, valves for sampling/draining/filtration, cable trays or conduits for auxiliary wiring, inspection covers for getting access to important parts inside the transformer such as bushings (for making connections) and the tap changer, the cable box, bus duct terminations, etc. Certain simplifying assumptions are done while analyzing the strength of the tank with all these fittings under various loading conditions.

The stress analysis of a transformer structure can be done by mainly two approaches: an analytical method and a numerical method. Analytical methods are used for determining the stiffening requirements to limit stresses and deflections for simple tank constructions. The tank shapes are usually complex and the application of analytical methods is difficult. For example, if the tank is

not rectangular and if there are many pockets (extruding structures) or openings, numerical methods such as FEM are used to determine the stresses and deflections under various loading conditions.

10.2 Different Types of Loads and Tests

10.2.1 Loads

The transformer tank should be capable of withstanding the following loads:

Lifting and jacking: The tank is designed to facilitate handling of the transformer. For this purpose, lifting lugs and jacking pads (as shown in Figure 10.1 (a)) are provided on the tank. Lifting lugs, provided towards the top of the tank, are used to lift the structure by a crane. Jacking pads, provided toward the base of the tank, are used for handling the transformer in the absence of the crane, especially at site. Generally, four jacking pads/lifting lugs are used.

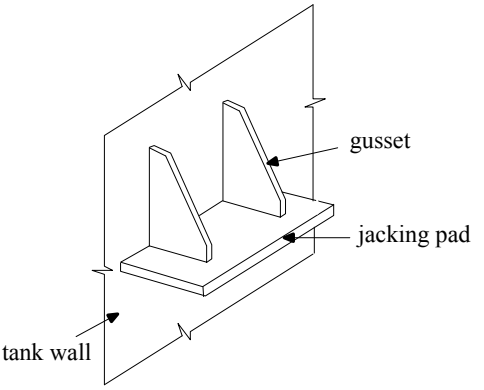

(a) Jacking pad

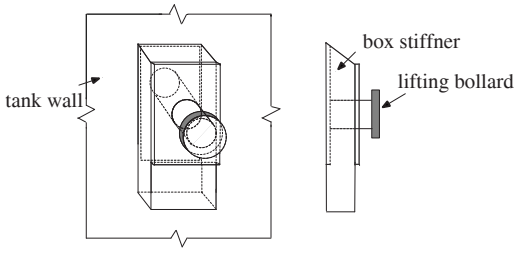

(b) Lifting bollard

Figure 10.1 Jacking pad and lifting bollard.

Lifting lugs are used for distribution transformers, wherein the loads are less. Lifting bollards are used for medium and large power transformers as shown in Figure 10.1 (b). Ride-over (transport) lugs are provided for the purpose of supporting the transformer on a floorless wagon during transport.

Haulage load: For local movements of the transformer at the place of installation, rollers and haulage lugs are provided. The haulage lugs are provided on the lower portion of the tank, whereas the rollers are provided under the base plate. Usually, four rollers are provided but for large transformers six or eight rollers may be provided. In place of rollers, a solid under-base is sometimes provided to facilitate skidding over rails or pipes.

Seismic and wind loads: The transformer has to be designed for a specified seismic acceleration and a wind load. The seismic and wind loads are very important design considerations for bushings, supporting structures of the conservator, and radiators. It is very difficult, if not impossible, to conduct the seismic test on a transformer. Seismic tests on bushings are usually specified and can be done. Special care has to be taken for bushings because they have a high cantilever load.

Transient pressure rise: When an internal fault takes place in an oil-filled transformer, a large volume of decomposed gases may be generated due to arcing. Under these conditions, the tank structure has to withstand a rapid rise of pressure if the pressure relief device does not act immediately. If the tank is not designed with an adequate factor of safety, it may rupture leading to a fire hazard and serious environmental impact due to oil outflow. The tank should be designed in such a way that it is within the elastic limit under the pressure rise conditions. It should not be too rigid or too flexible in order to avoid its bursting. Special devices such as sudden pressure relays are used which can act quickly under such transient pressure rise conditions.

10.2.2 Tests

The following tests are conducted to check the strength of a transformer structure:

Leak test: This test is meant to check whether the welded joints of the tank structure are leak proof or not. The test is conducted by pressurizing the tank using air pressure. A soap solution is sprayed over all the welded joints under specified pressure conditions. Any leak due to weld defects (cracks, pin holes, etc.) leads to bubble formation.

Vacuum test: The leak test (done with pressurized air) is followed by the vacuum test. A specified vacuum is applied to the tank for at least an hour. Permanent deflections measured after removal of the vacuum should be within the limits specified by users/standards, which depend on the tank size. The tank

is then cleared for shot-blasting and painting processes. This test is important because oil filling is done under specified vacuum conditions (either at works or site). In addition, the drying and impregnation may be done in the tank itself (e.g., in the vapor phase drying process). The vacuum may be partial or full depending on the voltage class and size of the transformer, and the user specifications.

Pressure test: This test is usually done after all the dielectric tests are completed in the manufacturer's works. The accessories such as bushings are removed and a pressure of 5 psi higher than the maximum operating pressure is generally applied to check the pressure withstand capability of the tank. All the welded joints are checked manually; if any oil leakage is noticed, the oil is drained and weld defects are rectified. Gasket leaks, if any, are also rectified.

Dye-penetration test: This test is conducted for load bearing members to detect weld defects. In this test, the surface to be tested is cleaned thoroughly and a dye (usually of pink color) is applied to the weld surface. The dye is left there for some time, typically 30 minutes, and then it is wiped clean. During this period, if there are any weld defects in the surface being tested, the dye due to capillary action penetrates through. After this, another solution known as developer is sprayed on the surface. This developer brings out the dye that has penetrated inside and leaves pink marks on the locations where the weld defects are present. This test is useful to detect weld integrity of load-bearing members such as jacking pads and lifting lugs/bollards.

10.3 Classification of Transformer Tanks

Depending upon the position of the joint between the upper and lower parts, we have two types of construction: the conventional tank and the bell tank.

Conventional tank: This type of construction has a top cover as shown in Figure 10.2 (a). Since the joint is usually above the top yoke level, it facilitates proper placement of magnetic shunts on the tank wall for an effective stray-loss control. The disadvantage is that the core and the windings are not visible on site when the cover is removed. Hence, for inspection of the core-winding assembly, a crane with higher capacity is required to remove the assembly from the tank.

Bell tank: In this construction, shown in Figure 10.2 (b), the joint between the two parts is at the bottom yoke level to facilitate the inspection of the core-winding assembly on site after the bell is removed. Thus, it consists of a shallow bottom part and a bell-shaped top cover. The bell construction may not be convenient for proper placement of magnetic shunts if the joint is at such a height from the bottom that it comes in the path of the leakage field. This may lead to a bolt overheating problem (as discussed in Chapter 5).

For the above two types of tank, either a plain or a shaped tank can be used.

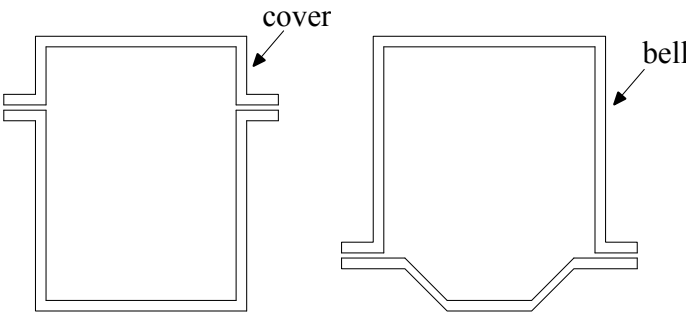

(a) Conventional tank (b) Bell tank

Figure 10.2 Types of tanks.

Plain tank: This kind of tank has rectangular shape and is simple in construction. It facilitates standardization, and the design of stiffeners is also straightforward. It usually leads to higher oil and steel quantity in high voltage transformers. If special detachable (bolted) bushing pockets are used for a center line lead HV winding arrangement, some saving in oil quantity can be achieved. This is usually done in large high voltage transformers.

Shaped tank: In order to save oil quantity, the tank is shaped so that its volume reduces. The tank shaping is mainly influenced by electrical clearances (between high voltage leads and the grounded tank), transport considerations, tap changer mounting arrangements, etc. The lower portion of the tank may be truncated in order to facilitate the loading of a large transformer on some specific type of wagon (in the case of rail transport) and/or to reduce oil quantity. The tank walls may be curved/stepped to reduce the tank size and volume. A shaped tank has the advantage that the curved portions of its walls give a stiffening effect. However, its design is more complex, requiring greater engineering and manufacturing efforts. Also, placement of magnetic shunts or eddy current shields on it may be cumbersome.

The joint between the two parts of the tank can be either bolted or welded type, which gives the following two types of construction.

Bolted construction: This construction, although preferred for easy serviceability, has a major disadvantage in that leaks can develop if gaskets deteriorate over a period of time. Oil leakage problems can occur if there is unevenness in the plates that are bolted or if the gaskets are overcompressed. The bolted joint may also lead to overheating hazards in large transformers as discussed in Chapter 5.

Welded construction: This type of construction eliminates probable leakage points since the two parts of the tank are welded together. It can thus ensure

leak-proof joints throughout the service life of the transformer. But if a problem or fault develops inside the transformer, a dewelding operation has to be done and there is a limit on the number of times one can do the de-welding and subsequent welding operations. C-shaped clamps are used during the welding operation and a thin gasket is provided between the two curbs so that the welding spatters do not enter inside the tank. Some arrangement is provided inside the tank at the top for arresting the buckling of the cover under lifting loads.

Depending on whether the tank is totally sealed from the outside atmosphere or is in contact with the atmosphere, the following two types of construction exist.

Breathing tank construction: Ambient temperature and load variations result in change of oil volume. The conservator fitted on the tank top allows these volume changes. It is partially filled with oil and it communicates with the atmosphere through a breather containing a moisture-absorbing material. In order to eliminate the contact of oil with the atmosphere, a constant oil pressure system is used in which a flexible bag (membrane) fitted inside the conservator communicates with the outside air. The air bag contracts or expands depending on changes in the oil volume. This construction is commonly used for large power transformers.

Sealed tank construction: In this type of arrangement, free space (filled usually with nitrogen gas) is provided in the tank for oil expansion based on the maximum expected oil temperature. The contact of oil with the outside atmosphere is totally eliminated. The tank is designed to withstand the pressure variations due to changes in the oil volume. The construction has a disadvantage in that with a sudden fall in temperature, gases may be released from the oil, seriously affecting the dielectric strength of the insulation system. Higher clearances have to be provided between electrodes separated by the combined oil and gas spaces (as compared to conventional clearances for oil immersed electrodes).

There are some special types of tank construction based on their application and features, as given below.

Corrugated tank: This construction is used in small distribution transformers to obviate the need of providing radiators separately. Corrugations are made by folding a steel sheet continuously on a special purpose machine. These corrugations are then welded on a steel frame to form a tank wall. The corrugations provide an adequate cooling surface and also play the roll of stiffeners. In distribution transformers, the use of the corrugated tanks can reduce the manufacturing (fabrication) time substantially.

Cover-mounted construction: In this type of construction, the core and the windings are attached to the tank cover. Lifting lugs/bollards are provided on the frames. The construction facilitates connections from the windings to cover

mounted accessories like an in-tank type OLTC and small bushings. Access to the lifting lugs/bollards is provided through inspection openings on the cover. The complete core-winding assembly with the top cover can be lifted by means of the lifting lugs/bollards and lowered into the tank. The whole arrangement can be made compact and simpler. For the servicing purpose, the untanking of the core-winding assembly is possible without removing the bushing connections.

Perforated tank: This type of tank is used in dry-type transformers, wherein it is used just as an enclosure to house the active parts. The perforations allow the flow of air for cooling the inside active parts. The construction generally consists of detachable panels which cannot take any lifting load. The absence of oil and the presence of perforations usually lead to higher noise levels in dry transformers as compared to oil-cooled transformers, and special measures need to be taken to reduce them.

10.4 Tank Design

The mechanical design is taken up after the electrical design of a transformer is finalized. The mechanical design requires the following inputs: core dimensions (the diameter, the center-to-center distance, etc.), details of windings, design insulation levels at various electrodes (as described in Chapter 8), details of the tap changer, details of accessories (bushings, radiators, fans, pumps, protection devices, etc.), weight and size limitations during transport and on site, etc. The designer has to keep in mind the requirements of tank shielding arrangements. The tank dimensions and profile are decided in a layout drawing drawn to scale considering electrical clearances, magnetic clearances, transport size limits, and manufacturability. The design of stiffeners is an important aspect of the tank design. An effective stiffening arrangement can reduce the tank plate thickness. The stiffeners are designed in such a way that the weight of the tank is minimum and at the same time it is able to withstand specified loads. Stiffeners are of the following types (as shown in Figure 10.3):

Flat stiffeners: These stiffeners, which have a low section modulus, are suitable for tanks in small transformers. They are more compact compared to other types of stiffeners.

T stiffeners: These stiffeners offer a higher section modulus compared to the flat stiffeners but lower than the box stiffeners (for the same cross-sectional area). They occupy more space compared to the flat stiffeners but are compact when compared with box stiffeners. They are useful in the cover area where less space is available due to accessories such as bushings, turrets, etc. because of which the box stiffeners cannot be used. These are also useful for stiffening a dome-shaped cover or an irregular cover where stiffening is difficult with the other types of stiffeners.

Box stiffeners: For large power transformers, the flat and T-type stiffeners are not suitable because their number increases. The box stiffeners give a much higher value of the section modulus, and hence they are used in large transformers. Aesthetically, they look better than the other stiffeners. The box stiffeners can also be used for other purposes. A lifting bollard can be embedded into a box stiffener for the lifting purpose. A jacking arrangement can be achieved if a plate is provided (with gussets) at the bottom of a box stiffener. It can also be used to provide an extra gas space in sealed transformers.

Usually, stiffening is done vertically. Sometimes horizontal stiffeners are also provided. The stiffeners are designed to uniformly distribute the lifting load. The location of stiffeners on the tank may be affected by space restrictions. The dimensions and location of a stiffener depend not only on the strength considerations but also on the various fittings and accessories which have to be mounted on the tank.

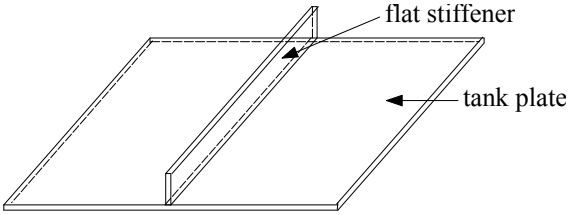

(a) Flat stiffener

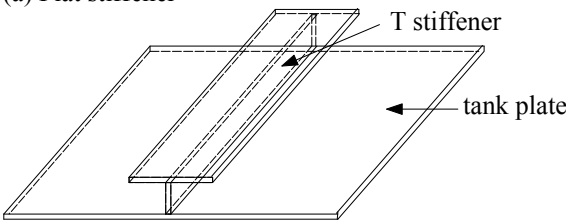

(b) T stiffener

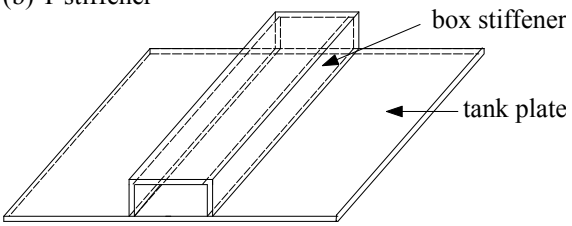

(c) Box stiffener

Figure 10.3 Types of stiffeners.

The stiffeners can be designed as simply supported or fixed support structures. In the simply supported case, the stiffeners are terminated at some distance from the top or bottom edge of the tank plates, which may result in higher deflections. If the stiffener ends are anchored to the top curb and the bottom plate (in a conventional tank) then it is termed a fixed support stiffener, and this arrangement gives lower deflections. The T stiffeners and the flat stiffeners can be terminated on the curb whereas the box stiffeners cannot be terminated on it because of the space requirement for bolting operations. For practical reasons one has to leave some space between the termination of the box stiffener and the curb. In such cases, the box stiffener can be tied to the curb by means of a gusset.

Since many accessories are mounted on the top cover, an adequate space may not be available for its stiffening. In such cases, higher cover plate thickness needs to be used with the application of flat or T stiffeners wherever possible.

The base plate of a tank is usually much thicker than its vertical plates. It is designed to carry a total load corresponding to the sum of the entire core-winding assembly weight, the oil head, and the test pressure. The base plate can be stiffened by cross channels to reduce its thickness. The box stiffeners may also be used sometimes for stiffening of the base plate.

A number of small local stiffeners are provided under extended projections/pockets and shaped tank parts.

10.5 Methods of Analysis

The design of a tank structure comprises mainly the analysis of the combined behavior of plates and stiffeners.

10.5.1 Analytical method

In an analytical method, which can be applied to plain rectangular tanks, each side plate is divided into many panels. One side of a rectangular tank with three vertical stiffeners is shown in Figure 10.4. The center line of a stiffener is taken as the panel boundary. Hence, for the purpose of analysis there are four panels. These panels are subjected to loads such as pressure and vacuum. as described earlier.

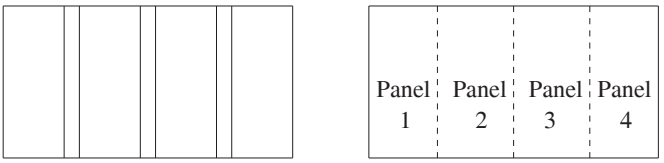

Figure 10.4 One side of a rectangular tank.

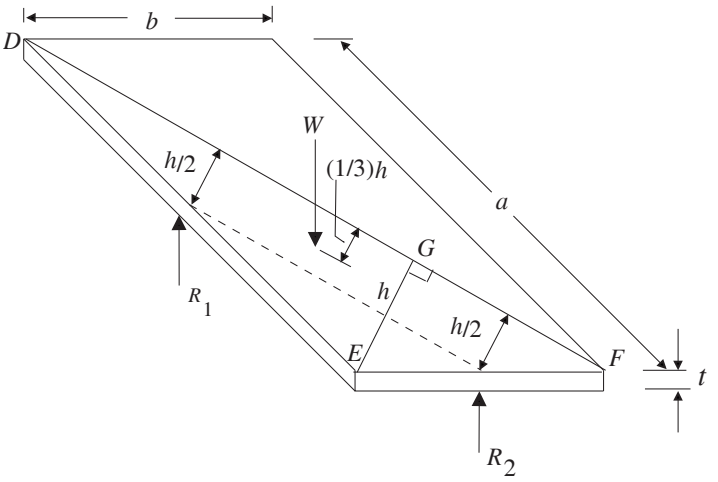

Figure 10.5 Rectangular simply supported plate under uniform load.

The stress analysis of each panel can be done by using the theory of plates. The stress calculation for simply supported and fixed type of rectangular plates is an integral part of the transformer tank design. Let us first analyze a simply supported plate.

Consider a rectangular plate of dimensions $a \times b$ and thickness t as shown in Figure 10.5. Let the load per unit area be w; hence the total load on the plate is wba. The load on the plate area on one side of the diagonal is (1/2) wba, which is denoted by W. This load acts on the centroid of the triangular area DEF. The centroid is at a distance of (1/3) h from DF.

Experiments on the simply supported rectangular plate show that the plate has a tendency to curl up at the corners, and the resultant pressure on each edge acts at its midpoint. The diagonal DF is the most critical section when one side of the plate is not very much longer than the other side [1]. The moment arm for the two reactions R_1 and R_2 is same. From the conditions of symmetry and equilibrium, their sum is equal to (1/2) wba.

The bending moment about DF is

$$M = (R_1 + R_2)\left(\frac{1}{2}h\right) - W\left(\frac{1}{3}h\right). \tag{10.1}$$

Substituting the expressions for the reactions and load, we obtain

$$M = \frac{1}{2}\, wba\left(\frac{1}{2}h - \frac{1}{3}h\right) = \frac{1}{12}wbah. \tag{10.2}$$

The length of *DF* is $\sqrt{a^2 + b^2}$. Therefore, the average bending moment per unit length of the diagonal is

$$M_1 = \frac{1}{12} \frac{wbah}{\sqrt{a^2 + b^2}}. \tag{10.3}$$

From the similarity of triangles *FGE* and *FED*, we have

$$\frac{EG}{EF} = \frac{ED}{DF}.$$

$$\therefore h = \frac{ab}{\sqrt{a^2 + b^2}}. \tag{10.4}$$

Substituting the expression of *h* in Equation 10.3 we obtain

$$M_1 = \frac{1}{12}\left[\frac{a^2}{(a^2 + b^2)}\right] wb^2. \tag{10.5}$$

The section modulus (*z*) of the plate per unit length along the diagonal is equal to (1/6) t^2. Accordingly, the bending stress at the surface of the plate across the diagonal *DF* in the simply supported case is

$$\sigma_{ss} = \frac{1}{2}\left[\frac{w\, a^2 b^2}{(a^2 + b^2)\, t^2}\right] \quad \text{..... } \textit{Simply supported case}. \tag{10.6}$$

The analysis for a plate with fixed edges is complicated. The deflection for a fixed plate is symmetrical and maximum at its centre. The ratio of two adjacent sides play an important role in deciding the deflection, and the bending moment at various locations is calculated by using analytical methods [2]. The maximum bending moment divided by the section modulus gives the maximum bending stress in the plate. For the panels of a tank side as shown in Figure 10.4, three sides can be approximately considered as fixed and the fourth (top) side can be considered as simply supported. The analysis for this case is given in [2].

In order to simplify the calculations, it can be assumed that the behavior of the tank plate is between the simply supported and fixed edge conditions. The stresses calculated under these two conditions are multiplied by empirical factors to calculate the resultant stress (σ_r),

$$\sigma_r = k_1\, \sigma_{ss} + k_2\, \sigma_{fe} \tag{10.7}$$

where σ_{ss} and σ_{fe} are stresses for the simple supported and fixed edge conditions, respectively. k_1 and k_2 are empirical constants such that $k_1 + k_2 = 1.0$.

The numerical methods give accurate stress and deflection values without recourse to simplifying assumptions as done in the analytical methods.

10.5.2 Numerical method

For problems involving complex geometries, material properties and boundary conditions, the designer depends on numerical methods which can give accurate stress distribution in the tank structure. The finite element method (FEM) is a very effective numerical analysis tool for the simulation of structural components under various loading conditions. The FEM analysis can be used for material optimization, reliability enhancement, failure analysis and corrective actions, verification of new designs, etc. Before the advent of FEM, many approximations had to be made in the analytical methods for complex tank geometries, and it was almost impossible to predict the exact performance of the structures under given loading conditions. It was not possible for the designer to know the margin or factor of safety for new designs. Due to this ignorance factor, the designer had to put extra material thereby increasing the transformer cost. Using FEM, it is possible to detect high stress zones and take suitable corrective/preventive actions. The FEM analysis can be used to investigate problems like vibrations, buckling, non-linear behaviour, etc.

In FEM, a given problem domain is divided into a number of elements, that are straight lines for 1-D domains, triangular or quadrilateral elements for 2-D domains, and tetrahedral or cubical elements for 3-D domains. The transformer tanks can be considered as 2-D shells and can be discretized into 2-D shell elements. The required solution function is approximated over an element by interpolation between the values at its nodes. The interpolating functions may be linear or higher order polynomials. Let u_i and v_i be the x and y components of displacements at the nodes of a triangular element, respectively (i = 1, 2, 3). The vector $\{U\} = (u_1\ v_1\ u_2\ v_2\ u_3\ v_3)^{\mathrm{T}}$ then represents the nodal displacements. The displacements over the entire element area may be given as [3]

$$\begin{Bmatrix} u(x,\ y) \\ v(x,\ y) \end{Bmatrix} = \begin{bmatrix} N_1 & 0 & N_2 & 0 & N_3 & 0 \\ 0 & N_1 & 0 & N_2 & 0 & N_3 \end{bmatrix} \{U\} \tag{10.8}$$

where $N_i(x, y)$ are the interpolating functions. Using standard symbols [3], the strain vector $\{\varepsilon\} = (\varepsilon_x \quad \varepsilon_y \quad \gamma_{xy})^{\mathrm{T}}$ is related to the displacements as

$$\begin{Bmatrix} \varepsilon_x \\ \varepsilon_y \\ \gamma_{xy} \end{Bmatrix} = \begin{Bmatrix} \dfrac{\partial u}{\partial x} \\ \dfrac{\partial v}{\partial y} \\ \dfrac{\partial u}{\partial y} + \dfrac{\partial v}{\partial x} \end{Bmatrix} = \begin{bmatrix} \dfrac{\partial N_1}{\partial x} & 0 & \dfrac{\partial N_2}{\partial x} & 0 & \dfrac{\partial N_3}{\partial x} & 0 \\ 0 & \dfrac{\partial N_1}{\partial y} & 0 & \dfrac{\partial N_2}{\partial y} & 0 & \dfrac{\partial N_3}{\partial y} \\ \dfrac{\partial N_1}{\partial y} & \dfrac{\partial N_1}{\partial x} & \dfrac{\partial N_2}{\partial y} & \dfrac{\partial N_2}{\partial x} & \dfrac{\partial N_3}{\partial y} & \dfrac{\partial N_3}{\partial x} \end{bmatrix} \{U\}$$

or $\{\varepsilon\} = [B]\{U\} \Rightarrow \boldsymbol{\varepsilon} = \mathbf{B}\mathbf{U}$. (10.9)

The potential energy of the element (*e*) is dependent on the displacements over the element area. According to Equation 10.8, it becomes a function of the nodal displacement vector **U**. In the absence of internal (body) forces, initial strains and initial stresses, it is given by

$$E = \frac{1}{2}\int_V (\boldsymbol{\varepsilon}^{\mathrm{T}} \mathbf{D}\, \boldsymbol{\varepsilon})\, dV - \mathbf{F}^{\mathrm{T}}\mathbf{U} = \frac{1}{2}\int_V (\mathbf{U}^{\mathrm{T}}\, \mathbf{B}^{\mathrm{T}} \mathbf{D}\, \mathbf{B}\, \mathbf{U})\, dV - \mathbf{F}^{\mathrm{T}}\mathbf{U} \tag{10.10}$$

where **D** is an elasticity matrix containing the appropriate material properties, **F** is the nodal load vector, and *V* is the element volume. Minimizing the above expression gives the governing equation which determines the solution, i.e.,

$$\partial E/\partial U = \mathbf{K}^{(e)}\mathbf{U} - \mathbf{F} = 0 \tag{10.11}$$

where $\mathbf{K}^{(e)} = \int_V \mathbf{B}^T \mathbf{D}\, \mathbf{B}\, dV$. This forms the element equation.

All such element equations are combined by first replacing the element-wise nodal quantities by the corresponding global nodal quantities, and adding all the element equations. This forms the global system of linear equations,

$$\mathbf{K}\ \bar{\mathbf{U}} = \bar{\mathbf{F}} \tag{10.12}$$

where $\bar{\mathbf{U}}$ and $\bar{\mathbf{F}}$ are the global displacement and load vectors, and **K** is the global stiffness matrix. The above linear system of equations is a large and sparse system of equations, solved normally by the iterative methods especially suited for solving such systems. The solutions can be refined for obtaining more accurate solutions by using a finer mesh with smaller elements, using higher order interpolating functions over the elements, or both.

***Material and geometric nonlinearities*:** During a pressure/vacuum test the applied pressure takes the tank walls beyond the linear elastic region and a continued loading may cause their permanent deformations. Geometric nonlinearity is exhibited by a wall when the geometry changes appreciably (more than the wall thickness) due to a deformation. The problem must be solved

iteratively, reformulating the stiffness matrix to reflect the new geometry at each step. The simulation methodology in the geometric nonlinear analysis is similar to that in a linear static analysis. Time varying loads are applied in increments; if the deflections are very large, finer load increments are given.

A large deflection (X) in a flat square plate, assumed fixed at all its edges, can be approximately calculated by [4]

$$X = 0.818w\left(\frac{pw}{Et}\right)^{1/3}$$

where w is half-width of the square plate, p is the applied uniform pressure, E is the modulus of elasticity, and t is the plate thickness

Material nonlinearity needs to be considered when the material properties of a structure change during the loading. Solutions must be obtained iteratively, reformulating the stiffness matrix to account for the new changes in material properties in each step. A nonlinear stress-strain curve at different load levels or the slope of the curve after the yield point of the material (i.e., the tangent modulus) should be assigned to the model. The algorithm involves iterations at each time step.

10.6 Overpressure Phenomenon in Transformers

The problem of explosions of oil-insulated equipment as a result of low-impedance internal faults has been a major concern. When an internal fault takes place inside an oil filled transformer, arcing produces a large amount of decomposed gas increasing the tank pressure rapidly. The pressure relief device may not be able to keep up with the gas generation rate and the tank can rupture [5]. The severity of an internal fault depends mainly on the arc energy and the tank expansion coefficient. The higher the arc energy and the lower the tank expansion coefficient, the higher the severity is. The arc voltage is not related very much to the arc current and is mainly a function of the arc length, the electrode shape and the pressure [6, 7]. Since the oil is relatively incompressible, and since the bottom plate and the side plates of the tank act together as a rigid structure, the tank cover is usually subjected to the overpressures [8]. In order to reduce such consequences, it is necessary to determine the resulting overpressures for different faults and geometrical parameters of the transformer.

The use of flange-reinforcing measures such as C-shaped clamps and joint reinforcement beams [6] increases the strength of tanks against excessive overpressures. In a 3-phase split-type transformer the major part of the tank is divided into three parts (one part per phase), with a common ducting for connections, to take care of transport limits. The pressure rise in such a configuration may reach an excessive level due to a small expansion coefficient

and kinetic energy of oil. A diaphragm type conservator, which is a pressure reducing structure, is suggested as a countermeasure.

The phenomenon has been studied both analytically and experimentally. Different formulations are proposed for predicting the overpressures during a low impedance fault. In [9], the results of analysis and experimental work are combined to obtain a semi-empirical equation for the peak pressure in the air space of a pole-type distribution transformer. It is reported that the arc length and $(i^2t)_{arc}$ are the most significant variables, the former being generally beyond control. However, this semi-empirical equation is probably only valid for geometrically similar transformers and hence may not be generalized. A comprehensive explanation of different failure modes in distribution transformers is given in [10]. The overpressure phenomenon is studied using high speed photography and it is shown experimentally that the arc depth under oil plays an important role in its motion, compression of the air space and the resulting overpressure. It is also reported that the maximum pressure exerted on the transformer tank cover depends on two principal parameters. One is the arc energy expended per unit volume of the air space, and another is the efficiency of the process by which the arc energy is converted into the kinetic energy.

The equations for the static pressure within the faulted oil-filled distribution transformer as a result of arcing and gas generation are given in [5]. The equations are derived under known conditions such as tank dimensions, air space, specific fuses and pressure relief devices, and unknown quantities such as the fault current magnitude, the arc length and location, and gas temperatures. The finite difference approach is proposed in [11] to study the phenomenon of arcing in oil insulated equipment. The solution of the proposed method is compared with that of an analytical formulation for an infinite cylinder filled with oil. The application of the finite difference method for the analysis of low-impedance faults in a cylindrical pole-type distribution transformer is given in [12].

10.7 Seismic Analysis

An earthquake is a dynamic phenomenon which occurs due to the release of energy below the ground because of instability of the earth's internal structure. The source of earthquake is a sudden displacement of ground on both sides of a fault which results from a rupture of a crystal rock. The size of earthquake is measured by the amount of strain energy released at the source. The earthquake produces random ground motions which are characterized by simultaneous but statistically independent horizontal and vertical components. A moderate earthquake may persist for 15 sec to 30 sec and a severe one for 60 sec to 120 sec. The vibration of ground motion may be magnified many fold in the equipment. The magnification depends on the characteristic frequency of vibration of the system consisting of soil, foundation and equipment.

Transformers are important elements of power supply systems. It is very essential that utmost care is taken while designing their tank and accessories for seismic withstand. Anchorage failure, bushing failure, conservator bracket deformation, oil leakage and other miscellaneous damages can occur if they are not adequately designed. Certain accessories and protection devices (e.g., buchholz relays) may malfunction during an earthquake giving a false indication of a fault inside the transformer. The main principle for improving strength under earthquake conditions is that the natural frequency of the transformer and its parts should be above 30 Hz ensuring a lower acceleration factor.

Design for seismic conditions is based on the seismic zone where the equipment would be installed. The transformer user should provide information to the transformer manufacturer about the seismic activity in terms of maximum accelerations, response spectra or time histories. The seismic zone of a place defines the intensity of an earthquake which is likely to hit that place. As per IEEE C57.114-1990 (IEEE seismic guide for power transformers and reactors), typical values of maximum horizontal ground acceleration range from 0.1 g (zone 1) to 0.5 g (zone 4), where g is the acceleration due to gravity. If the transformer is not ground mounted, the acceleration at the mounting location has to be considered.

Although seismic withstand can be most accurately checked by a laboratory test, it is very difficult to conduct the test on a product like transformer. Hence, the following three calculation methods are commonly used for checking the seismic withstand of transformers.

***Seismic coefficient method*:** This is an approximate method in which normal static stress calculations are done with certain seismic accelerations applied to the center of gravity of structures. Seismic coefficients are applied separately to various vulnerable components such as bushings, conservators, radiators, etc., which are mostly the overhanging or extended portions of the transformer structure. This method does not take into consideration the natural frequencies of the structure or its components.

***Response spectrum method*:** As per IEEE C57.114-1990, when the natural frequencies of a transformer are lower than about 30 Hz, the static method should not be used and one has to take into account the natural frequencies of the structure. The response spectrum method determines the dynamic response which depends on the natural frequencies of the structure. The transformer needs to be analyzed as a spring-mass model using a response spectrum curve with an appropriate damping factor. The response of the structure to an earthquake due to each mode of vibration is calculated, and the total response is determined by combining the individual modal responses (square root of sum of squares technique). A numerical method like FEM needs to be used for this purpose. The FEM analysis gives stresses, accelerations and displacement plots which help in identifying weak structures that need to be strengthened.

***Time history method*:** This method is computationally very intensive and requires actual earthquake data. This method can be used for analysis of structures which underwent an earthquake whose time history is known.

Since it is not possible to test the seismic withstand of transformers by an actual test, experimental investigations have been done to evaluate their natural frequencies and mode shapes of vibrations. The results of a multipoint random excitation test and a forced vibration test are compared with that of FEM analysis in [13]. A significant global deformation mode is reported at a frequency of about 3.5 Hz. The results of experimental tests on a buchholz relay are compared with that of the numerical analysis. In another reference [14], the efficacy of the amplification and response factors for a bushing given in IEC standard (IEC 61463, Ed. 1.1, Bushings — Seismic qualification) is examined.

The design precautions suggested by IEEE C57.114-1990 include placing the transformer and interconnected accessories/equipment on a strong and common foundation to reduce differential movement during an earthquake and firm anchoring of the transformer by welding its base to the structural steel members embedded in or firmly fixed to a concrete foundation.

***Seismic simulation procedure*:** The general process for performing a single-point response spectrum analysis consists mainly of modal and spectral analysis. The modal solution gives a series of natural frequencies and mode shapes. Spectrum solutions are obtained for a given base excitation. The excitation input could be in the form of frequency vs. acceleration for a given damping value. Usually 2% damping (typically used for mild steel material) is accounted for in the response spectrum unless otherwise specified. Seismic loading is specified in terms of displacement, velocity, or acceleration (having different frequency components). The loading in the vertical direction is considered to be 80% of those in the horizontal directions according to IEEE C57.114-1990 and IEEE 693-2005 standards. This loading has to be combined suitably with the modal response to compute the deflections and stresses in the structure.

The spectrum analysis is based on a mode-superposition approach where the responses of the higher modes, corresponding to frequencies greater than 50 Hz, are neglected. Different regions in a component can vibrate at different frequencies with associated mode shapes. Hence, if the excitation has a wide frequency band, the mass participating may approach 100%. However, since higher order modes are not generally extracted to reduce computational burden, and because of constrained degrees of freedom in the system, the participating mass will be less than 100%. The number of modes used in the transient solution for seismic loads should be able to capture at least 90% mass participation in the direction of the seismic load to obtain a reasonably accurate solution. Due to the truncation of the high frequency modes and the constraints, if less than 90% of mass participates in the solution, a missing mass correction procedure is adopted [15]. The missing modes are considered by performing a static analysis, and the effect of missing load vectors is then combined with the results obtained from the

response spectrum method. The missing-mass response and the modal responses are combined using the square root of the sum of the squares (SRSS) method [16].

10.8 Transformer Noise: Characteristics and Reduction

With the growing consciousness of the ill effects of noise pollution, many users specify low noise levels for transformers. While the trend of ever increasing transformer ratings implies corresponding higher noise levels, noise-reducing measures have to be adopted to make the transformers quieter. By using modern design methods and materials, noise emissions from transformers can be economically lowered to acceptable levels. In order to reduce noise levels, it is very important to know and understand the sources of the noise. The pressure generated by vibrations of the core and windings in a transformer is transmitted to tank surfaces though the oil medium. Since the oil is relatively incompressible, the noise is transmitted without appreciable damping. The tank responds to these noise waves depending on its natural frequencies and mode shapes of vibrations.

The principal source of the transformer noise is the magnetic core, which has been discussed in Chapter 2. In this chapter the other two sources of noise, load-controlled noise and equipment noise, are discussed.

10.8.1 Load-controlled noise

This noise is emitted by a loaded transformer in addition to its no-load noise. It is caused by electromagnetic forces between its LV and HV windings, resulting from the leakage field, and is proportional to the square of the load current. These forces cause vibrations of the windings and consequent acoustic radiations having frequency of 100 or 120 Hz (twice the power frequency). Axial vibrations of the windings mainly contribute to the noise (radial vibrations can be significant only for winding diameters greater than 6 meters [17]). The contribution of the load-controlled noise to the overall noise level of the transformer becomes significant when the operating flux density in the core is lower than 1.4 T. At such a low value of flux density, the noise from the core is considerably reduced. The other sources of the load-controlled noise are the vibrations of tank walls and the magnetic shunts placed on them. If the shunts are rigidly anchored to the tank walls, the noise due to their vibrations is usually low.

The vibration amplitudes produced by a given axial compressive force depend on the mass, modulus of elasticity and damping characteristics of the windings. Pressboard and other insulating materials play an important role in deciding the response. The noise can be kept as low as possible by using a pressboard material with a high damping coefficient and applying a proper value of prestress to the windings. The natural frequencies of the windings should be

away from the frequencies of the exciting compressive forces (i.e., twice the power frequency and its multiples), since a resonance amplifies the vibrations and noise.

A loaded transformer represents a typical magneto-mechanical system immersed in a fluid (oil). For developing a numerical method for accurate calculation of the load-controlled noise, the electromagnetic field, the mechanical displacement field, the acoustic pressure field, and their couplings have to be considered as one system. Due to the complexity of this multi-field problem, a combination of the finite element and boundary element methods is used in [18] for the prediction of the load-controlled noise.

10.8.2 Noise due to cooling equipment

Fan noise is a result of vortex flows in the vicinity of its blades. The noise is a function of its air delivery, blade size and speed. While the noise due to the core produces frequencies in the range of 100 to 600 Hz, the frequencies associated with the noise due to the cooling equipment (fans and pumps) are usually below and above this frequency range in the sound spectrum. In general, high flow speeds of cooling medium in fans and pumps should be avoided.

Since the noise of a fan is a function of its speed and circumferential velocity, a low speed fan has a lower noise level. As the speed is lowered, the air delivery also reduces, necessitating an increase in number of fans. Many times, the noise level specified is so low that it may not be possible to get a suitable fan. Therefore, ONAN (OA) cooling should be specified/used in place of mixed ONAN/ONAF (FA) cooling for small and medium rating power transformers, even if it results in an increase in the number of radiators.

A radiator also contributes to noise due to transferred tank vibrations transmitted through cooler pipes that connect it to the tank (structure-borne vibration). Pipe-work and supporting structures should be designed such that there is no resonance.

10.8.3 Noise level reduction

It is pointed out in Chapter 2 that the reduction in noise level is not significant if the operating peak flux density in the core is reduced. A lower value of the operating flux density also results in a higher material cost and size of the transformer. Hence, other cost-effective noise reduction methods are commonly used as described below.

There are different ways by which the noise can be reduced. Methods like stiffening the bracing or supporting parts and adding cushions between parts in a transformer have long been known and used [19] for reducing vibrations and noise. Barrier walls and total sound-proof enclosures have also been used [20]. An easy but somewhat expensive way would be to put the transformer in a closed room whose walls and floor are massive. The noise reduces as it tries to pass through a massive wall. The noise can also be reduced by building a free-

standing enclosure of concrete and steel plates around the transformer. However, this method has some disadvantages (e.g., a large area is needed for the transformer installation). The use of sound insulation panels is another way of achieving reduced noise levels without any additional space requirement. The closely fitting sound insulation panels described in [21] are mounted between reinforcing channels (stiffeners). The assembly consists of a resilient steel sheet, a steel plate and weights. The steel sheet connects the steel plate to the stiffeners. The weights are placed at the boundaries of the plate and the sheet to avoid the transmission of structure borne vibrations from the stiffeners to the steel plate. The noise level reduction of 14 dB is reported by the use of these insulation panels. The development of a vibration controlled sound insulation panel, capable of reducing the noise generated from a transformer by 12 to 13 dB, is reported in [22]. The panel consists of highly damped plates which are mounted on the side walls of the transformer tank with isolating rubber pieces placed in-between.

A substantial reduction in the noise level (of the order of 15 dB) can also be obtained by using a double tank design. The transformer is contained in the inner tank which is supported inside the outer tank in this construction. Both tanks are suitably insulated from each other to reduce the structure-borne sound. Glass wool is placed in the space between the two tanks for an effective noise reduction.

Active noise control is one more technique in which an anti-phase noise signal is generated and superimposed on the noise emitted by the transformer. This requires very sophisticated instrumentation and computational facilities. The active control scheme implemented with digital signal processing is reported in [23]; noise levels can be reduced by 5 to 15 dB.

In dry-type distribution transformers (resin impregnated or cast resin), due to the absence of oil and the presence of openings/perforations on the tank (for an effective air circulation and cooling), the noise level can be higher. Hence, the core limbs can be of bolted construction in addition to the bolted yokes to give more rigidity to the core structure and reduce the noise emanating from it.

The techniques for reducing noise in transformers can be summarized as below.

- Reduction in core flux density: This reduces noise by 3 to 5 dB for a reduction in flux density of 10% (or approximately 2 dB reduction per 0.1 T). The method has adverse effects on the cost and size of transformers.
- Hi-B grade and scribed core materials give 2 to 3 dB reduction as compared to non-Hi-B grades.
- Avoidance of core resonance by calculation of core resonant frequencies: The core natural frequencies should not coincide with the excitation frequencies as discussed in Chapter 2.
- Increased core damping: By application of a suitable viscoelastic or adhesive coating to core laminations, the noise level can be reduced.

- It should be ensured that any links or attachments to the core are flexible so that they do not transmit vibrations.
- Step-lap joint: It gives a reduction by about 4 to 5 dB as compared to the mitred construction, for the commonly used flux densities (1.6 to 1.7 T).
- Corner protrusions of built cores should be cut since they may contribute to noise due to vibrations (also they are not useful as they do not generally carry any flux).
- The clamping pressure on the core should be adequately distributed so that no appreciable length of the core is left unclamped. If limbs/yokes are clamped with resin-glass or fiber-glass tapes, the pitch (distance between two tapes) should be small so that adequate and uniform pressure is applied.
- To reduce the structure-borne vibrations, the core-winding assembly should be isolated from the tank base by using oil compatible antivibration pads between them. The pads are also put between the frames and the tank. Such isolations can give a noise level reduction of 2 to 4 dB.
- Sound insulation panels placed between tank stiffeners can give a reduction of 5 to 15 dB.
- An increased tank wall mass, achieved by putting sand in hollow braces on the wall, can give an appreciable noise level reduction.
- Double tank design: The inner and outer tanks are suitably insulated from each other to eliminate structure-borne vibrations. Also, suitable sound absorbent wool is placed between the two tanks. The noise reduction is about 15 dB.
- Complete concrete or brick wall enclosures: The noise reduction is about 20 to 30 dB, but the method is rather expensive.
- Active phase cancellation technique: The sound emitted by a transformer is overlaid by externally applied anti-phase sound. A noise level reduction of 5 to 15 dB may be possible.
- If the transformer noise level required is too low to get a fan with a lower noise level, ONAN (OA) cooling may be specified/used in place of mixed ONAN/ONAF (FA) cooling for small and medium rating transformers.

Some precautions which need to be taken at site for noise level control are:

- The reflecting surfaces should not coincide with half the wavelength of frequencies of noise emitted by the transformer [24] (to avoid standing waves and reverberations/echoes).
- Fire walls are sometimes placed adjacent to the transformer. It may not be possible to place them at a location so that no undesirable reflections occur. In such cases a sound-absorbent material, suitable for outdoor use, may have to be applied on the walls.
- A dry type distribution transformer is mostly located in a room inside a building. With the walls of the room having a low sound absorption coefficient, the sound emitted by the transformer reflects back and forth

between the walls. This may lead to a considerable increase in the noise level. These aspects should be duly considered by the user (while designing the room) and manufacturers (while designing the transformer).

- If simple barrier walls are used for obstructing the noise, they are not effective at the edges. The walls have to be extended at right angles on one or both ends with an application of sound-absorbent material for better results.
- The transformer should not be mounted on a foundation on which adjacent walls are also mounted because the vibrations from the transformer may be transmitted through the foundation to the walls. The vibration of these walls will increase the overall noise level.
- A solid connection between a vibrating transformer and any solid structure in the vicinity should be avoided (flexible connections can be used as far as possible).
- The tank base can be isolated from the supporting ground/foundation by a suitable vibration damper to reduce structure-borne vibrations.

10.8.4 Noise simulation and prediction methodology

As discussed earlier, transformer noise can be classified into two categories: the noise due to the core and the noise due to forces associated with the windings. The periodic repulsive forces between the LV and HV windings can produce appreciable noise if the windings are loosely wound. Tank resonances and cooling fans also contribute to the total noise. Apart from the magnetostriction effect in the core which is a main source of the noise in a transformer, transverse relative motion of the core laminations also produces noise [25], due to the presence of small gaps between the laminations since they may not have uniform and flat surfaces.

The compressive stress introduced in the laminations along the flux direction should be avoided as it increases the level of noise output [26]. If laminations are not perfectly flat, the clamping forces by core-bolts try to flatten them; this additional compressive stress generated in comparison with flat laminations, has been found to produce more noise. Moreover, the temperature gradients during operation lead to compressive stresses along the direction of flux [26] and the corresponding noise.

An accurate modeling of core laminations is essential to understand and/or predict the noise due to the magnetostriction phenomenon. Three distinct approaches are reported in [25] for this purpose. The core structure can be treated as a single solid block, an assembly of several bocks (steps), or a fully laminated structure. In the second and third cases, sliding interface surfaces are modeled between each pair of steps and between each pair of laminations, respectively, except at bolted positions. Although the computational burden is highest for the third case, the computed mechanical natural frequencies are closest to the experimental results [25]. Therefore, in order to model a

transformer for vibro-acoustic analysis in an FEM software program, it is important to model the laminations individually with definition of correct properties of the core material. Also, various physical environments such as structural, fluid dynamic and acoustics have to be coupled in a proper way so that a precise model can be made for the analysis.

The computational burden can be substantially reduced if the acoustic analysis is limited to determining noise due to the core in an open boundary situation (without the tank enclosure). The procedure is as follows. 3-D electromagnetic simulations are carried out to obtain core displacements as a function of flux distribution (flux density Vs displacement curve should be fed to the FEM software based on tested material data). Mechanical modal analysis is performed to determine natural frequencies and mode shapes of the core structure. Harmonic analysis is subsequently performed to obtain overall core displacements considering excitation with core natural frequencies. The core displacements along with their frequency components are then taken into a boundary element solver wherein a sound-radiating surface and measurement locations are defined. Pressure fluctuations, thus obtained, are converted to dB scale and noise values are calculated at all nodal points defined on the boundary wall.

10.8.5 Noise level measurement

Noise levels are commonly measured in decibels (dB) by comparing the pressure generated by the noise source with some standard level. The noise level is measured on A-weighted scale which closely follows the sensitivity of the human ear. There are basically two methods for noise measurement: a sound pressure measurement technique and a sound intensity measurement technique. The details of test methods and acceptable test environment conditions are given in IEC standard 60076-10 (Determination of sound levels, First Edition, 2001). Sound pressure is a scalar quantity and requires simple instrumentation.

Sound intensity is a vector quantity and the method measures directional sound. It is therefore less affected by background noise. Hence, the sound intensity method can give more accurate measurements in the presence of background noise. However, sound intensity measurements require better skills and more sophisticated instrumentation. The information about the location and characteristics of noise sources can be obtained by studying the measured frequency spectrum.

Apart from the design challenges discussed previously, the measurement of low noise levels poses a difficult problem. The minimum level of noise that can be measured is limited by the ambient noise conditions in the test area. Special enclosures may have to be used to shield the instruments/test setup and the transformer from the high ambient noise.

10.9 Transport Vibrations and Shocks

A transformer may be subjected to impact loading during transportation by ship/road. Damages may occur in some critical components, e.g., shearing of locating pins or locating posts, winding deformations, and loosening of locknuts and other supports/bolted connections. A low velocity impact acceleration-time diagram is generally used for design of components to represent shock loading which may occur accidentally during transport of heavy structures. During sea transport the transformer may experience an impact in any direction (i.e., x, y or z). The force time diagram has an ascending zone where the acceleration rises from zero to peak and a descending zone when the impact reduces. Though the impact is considered to act in only one direction at a time, to account for randomness in the direction of the impact, different combinations of load cases are considered during the analysis. The data from the shock recorder, which goes along with the transformer assembly to record the level of shocks during transport, are used to decide the time and amplitude of the shock load. Various design combinations are analyzed during the transient analysis to make sure that the internal assembly withstands the shock levels.

References

1. Seely, F. B. and Smith, J. O. *Advanced mechanics of materials,* John Wiley and Sons, New York, London, 1952.
2. Timoshenko, S. and Woinowsky-Krieger, S. *Theory of plates and shells,* McGraw-Hill Inc., Singapore, 1959.
3. Zienkiewicz, O. C. *Finite element method*, McGraw-Hill, London, 1977.
4. Ugural A. C. *Stresses in plates and shells,* McGraw-Hill, 1999.
5. Goodman, E. A. and Zupon, L. Static pressures developed in distribution transformers due to internal arcing under oil, *IEEE Transactions on Power Apparatus and Systems*, Vol. PAS-95, No. 5, September/October 1976, pp. 1689–1698.
6. Kawamura, T., Ueda, M., Ando, K., Maeda, T., Abiru, Y., Watanabe, M., and Moritsu, K., Prevention of tank rupture due to internal fault of oil-filled transformer, *CIGRE 1988*, Paper No. 12-02.
7. Tagaki, T., Ishii, T., Okada, T., Kurita, K., Tamura, R., and Murata, H. Reliability improvement of 500 kV large capacity power transformer, *CIGRE 1978*, Paper No. 12-02.
8. Hamel, A., Dastous, J. B., and Foata, M. Estimating overpressures in pole-type distribution transformers — Part I: Tank withstand evaluation, *IEEE Transactions on Power Delivery*, Vol. 18, No. 1, January 2003, pp. 113–119.
9. Mahieu, W. R. Prevention of high-fault rupture of pole-type distribution transformers, *IEEE Transactions on Power Apparatus and Systems*, Vol. PAS-94, No. 5, September/October 1975, pp. 1698–1707.

10. Barkan, P., Damsky, B. L., Ettlinger, L. F., and Kotski, E. J. Overpressure phenomena in distribution transformers with low impedance faults: experiment and theory, *IEEE Transactions on Power Apparatus and Systems*, Vol. PAS-95, No. 1, January/February 1976, pp. 37–47.
11. Foata, M., Iordanescu, M., and Hardy, C. Computational methods for the analysis of explosions in oil-insulated equipment, *IEEE Transactions on Power Systems*, Vol. 3, No. 1, February 1988, pp. 286–293.
12. Dastous, J. B., Foata, M., and Hamel, A. Estimating overpressures in pole-type distribution transformers — Part II: Prediction tools, *IEEE Transactions on Power Delivery*, Vol. 18, No. 1, January 2003, pp. 120–127.
13. Bellorini, S., Bettinali, F., Salvetti, M., Gatti, F., Zafferani, G., and Monzani, O. Mechnical seismic behavior of power transformers, *CIGRE 1998,* Paper No. 12-212.
14. Bellorini, S., Bettinali, F., Salvetti, M., and Zafferani, G. Seismic qualification of transformer high voltage bushings, *IEEE Transactions on Power Delivery*, Vol. 13, No. 4, October 1998, pp. 1208–1213.
15. Subramanian, K. V., Sridhar, G. P., Kushwaha, H. S., Reddy, G. R. Application of residual mass correction in time history analysis, *Transactions of the 14th International Conference on Structural Mechanics in Reactor Technology*, Lyon, France, August 17–22, 1997, Paper K21/5, pp. 317–324.
16. Richard, M. and Wang, Y. Evaluation of modal combination methods for seismic response spectrum analysis, *Proceedings of the 15th International Conference on Structural Mechanics in Reactor Technology*, 1999, pp. 225–232.
17. Reiplinger, E. Study of noise emitted by power transformers based on today's viewpoint, *CIGRE 1988,* Paper No. 12-08.
18. Rausch, M., Kaltenbacher, M., Landes, H., Lerch, R., Anger, J., Gerth, J., and Boss, P. Combination of finite and boundary element methods in investigation and prediction of load-controlled noise of power transformers, *Journal of Sound and Vibration*, 250 (2), 2002, pp. 323–338.
19. George, R. B. Power transformer noise: its characteristics and reduction, *AIEE Transactions,* March 1931, pp. 347–353.
20. Murray, C. S. Transformer audio noise problems on an electric power system, *AIEE Transactions,* Vol. 68, 1949, pp. 740–752.
21. Kanoi, M., Hori, Y., Maejima, M., and Obta, T. Transformer noise reduction with new sound insulation panel, *IEEE Transactions on Power Apparatus and Systems*, Vol. PAS-102, No. 9, September 1983, pp. 2817–2825.
22. Ebisawa, Y., Hirai, K., Suda, K, and Ikeda, M. Development of new type sound insulation panel for transformers, *International Conference on Transformers, Transformer-97*, Kolobrzeg, May 1997, pp. 37–42.

23. Teoh, C., Soh, K., Zhou, R., Tien, D., and Chan, V. Active noise control of transformer noise, *International Conference on Energy Management and Power Delivery*, EMPD '98. Vol. 2, March 1998, pp. 747–753.
24. http://www.federalpacific.com/: Understanding transformer noise.
25. Masti, R. S., Desmet, W., and Heylen, W. On the influence of core laminations upon power transformer noise, *Proceedings of the International Conference on Noise and Vibration Engineering*, Leuven, Belgium, 2004, pp. 3851–3862.
26. Thompson, J. E., Magnetostriction and transformer noise, *Journal of the Institution of Electrical Engineers*, Vol. 9, Issue 98, Feb. 1963, pp. 72–74.

11

Special Transformers

11.1 Rectifier Transformers

Duties of rectifier transformers serving special industrial loads are more stringent than conventional transformers. Electrical energy in the form of direct current is required in electrolytic processes used in aluminum smelters and chemical plants (producing chlorine, soda, etc.). Various methods used for converting AC into DC in earlier days included use of motor-generator sets, rotary converters, and mercury arc rectifiers. Due to rapid developments in power electronic converters and switching devices, transformers with modern static converters (rectifiers) are being widely used for current ratings as high as hundreds of kilo-amperes. Design and manufacture of transformers for the rectifier duty poses certain challenges. Complex winding arrangements, high currents and associated stray field effects, additional losses and heating effects due to harmonics, the necessity of maintaining constant direct current, etc. are some of the special characteristics of the rectifier transformers.

11.1.1 Bridge connection

One of the most popular rectifier circuits, three-phase six-pulse bridge, is shown in Figure 11.1. It gives a 6-pulse rectifier operation with the r.m.s. value of the secondary current for an ideal commutation condition (zero overlap angle) as

$$I = \sqrt{\frac{1}{2\pi}\int_0^{2\pi} i^2 d\theta} = \sqrt{\frac{1}{2\pi}\left[I_d^2 \frac{2\pi}{3} + I_d^2 \frac{2\pi}{3}\right]} = I_d \sqrt{\frac{2}{3}} \qquad (11.1)$$

where I_d is the direct current. For a transformer with unity turns ratio, the r.m.s. value of the primary current is also given by the above expression.

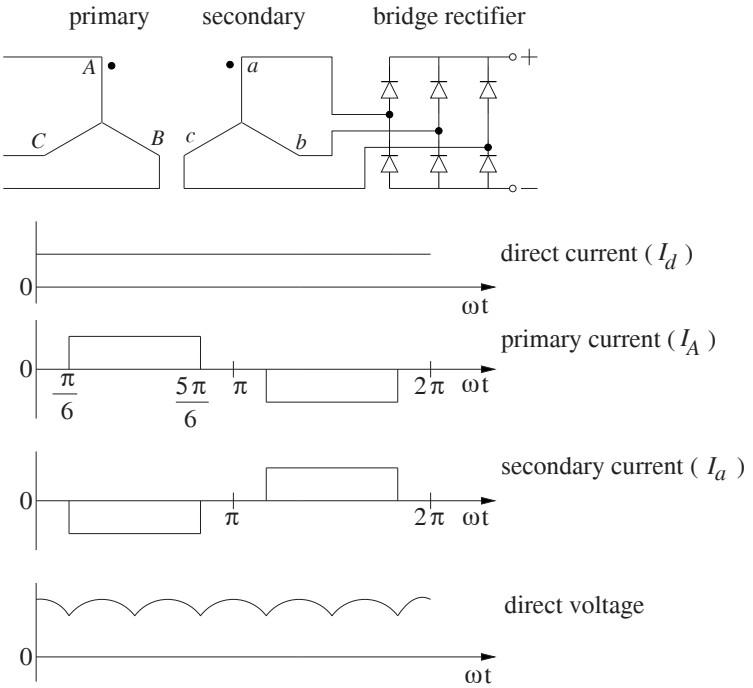

Figure 11.1 Bridge connection.

The average value of the direct voltage is

$$V_d = \frac{1}{\pi/3} \int_{-\pi/6}^{+\pi/6} \sqrt{2}\, E \cos\theta \, d\theta = \frac{3\sqrt{2}}{\pi} E \tag{11.2}$$

where E is the line-to-line r.m.s. voltage.

The secondary winding does not carry any direct current (the average value over one cycle is zero). The ratings of both primary and secondary windings are equal, which can be obtained by using Equations 11.1 and 11.2 as

$$P = \sqrt{3}\, E\, I = 1.047\ V_d\, I_d = 1.047\ P_d \tag{11.3}$$

Thus, in the bridge connection the capacity of the transformer is well utilized because the required rating of ($1.047\ P_d$) is the minimum value for the 6-pulse operation. The bridge connection is simple and widely used.

11.1.2 Interphase transformer connection

When the current requirement increases, two or more rectifier systems need to be paralleled. The paralleling is done with the help of an interphase transformer

which absorbs at any instant the difference between the direct voltages of the individual systems so that there are no circulating currents. Two 3-pulse rectifier systems (operating with a phase displacement of 60°) paralleled through an interphase transformer are shown in Figure 11.2.

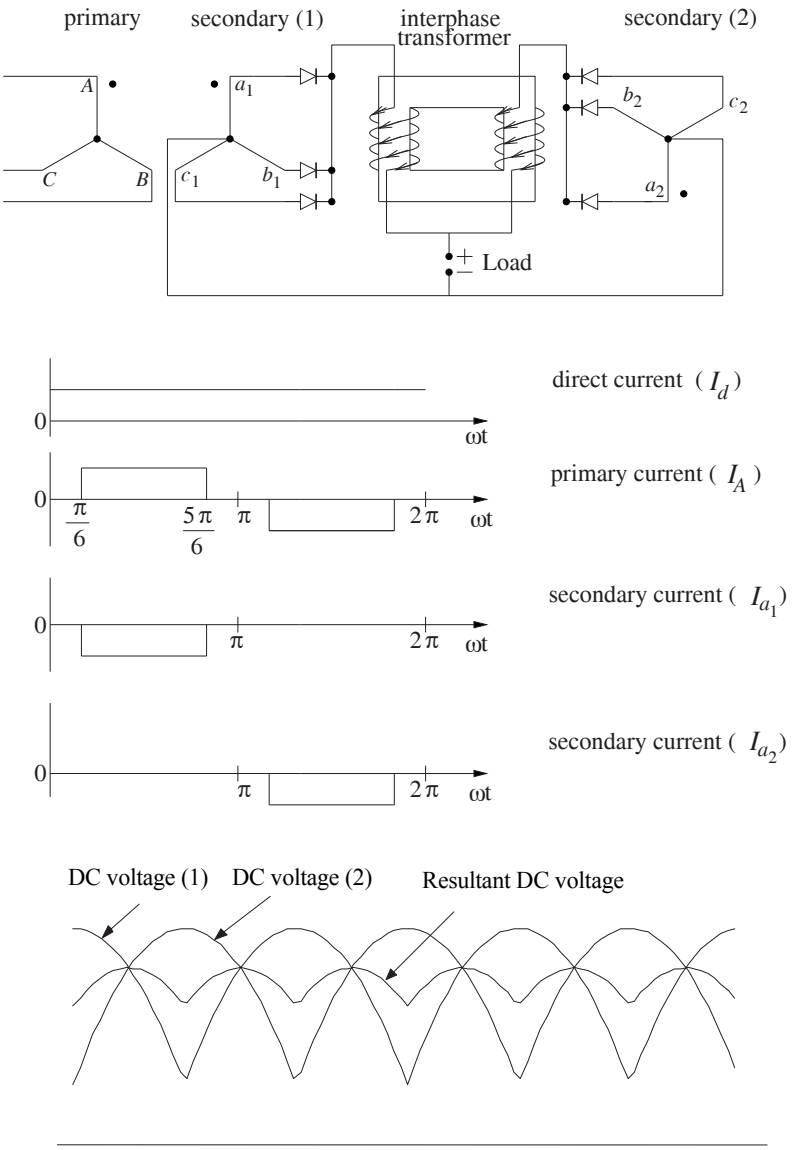

Figure 11.2 Interphase transformer: arrangement and waveforms.

The difference between the instantaneous values of direct voltages of the two systems is balanced by the voltage induced in the windings of the interphase transformer. Since both the windings are linked with the same magnitude of magnetic flux, the voltage difference is equally divided between them. The output DC voltage at any instant is the average of the DC voltages of the two systems. Thus, the paralleling of the two 3-pulse systems results in a system with 6-pulse performance. The r.m.s. value of the secondary current is

$$I_s = \sqrt{\frac{1}{2\pi}\left[\left(\frac{I_d}{2}\right)^2 \frac{2\pi}{3}\right]} = \frac{I_d}{2}\sqrt{\frac{1}{3}} \tag{11.4}$$

where I_d is the total direct current (sum of the direct currents of the two rectifier systems). Each secondary conducts for one third of each cycle, and it can be proved that the rating of the two secondary windings considered together is $1.48\,P_d$. Since the primary winding carries the current pulses in both half cycles, it is utilized efficiently (compared to the secondary windings). The r.m.s. value of its current is

$$I_p = \sqrt{\frac{1}{2\pi}\left[\left(\frac{I_d}{2}\right)^2 \frac{2\pi}{3} + \left(\frac{I_d}{2}\right)^2 \frac{2\pi}{3}\right]} = \frac{I_d}{2}\sqrt{\frac{2}{3}}\,. \tag{11.5}$$

The corresponding primary rating is $1.047\ P_d$, the minimum value which can be obtained for the 6-pulse performance. Since the flux in the magnetic circuit of the interphase transformer is alternating with 3 times the supply frequency when two 3-pulse systems are paralleled or with 6 times the supply frequency when two 6-pulse systems are paralleled, the core losses are higher. Hence, the operating flux density in the interphase transformer is designed to be around 50 to 67% of the value used in the conventional transformers [1].

If a 12-pulse operation is desired, two 6-pulse rectifier systems operating with a phase displacement of 30° are combined through an interphase transformer. In this case, the time integral of the voltage to be absorbed is smaller as compared to that in the 6-pulse operation (due to smaller voltage fluctuations in the ripple). Also, the frequency of the voltage is 6 times the supply frequency. Hence, the size and cost of the interphase transformer is reduced. When a 12-pulse system is obtained through one primary winding (usually star connected) and two secondary windings (one in star and the other in delta connection), it may be difficult to get the ratio of turns of the two secondary windings equal to $1/\sqrt{3}$ (because of their low number of turns). Therefore, the required 30° phase displacement is obtained by having two primary windings, one connected in star and the other in delta, and two secondary windings are connected either in star or delta. One such arrangement is shown in Figure 11.3.

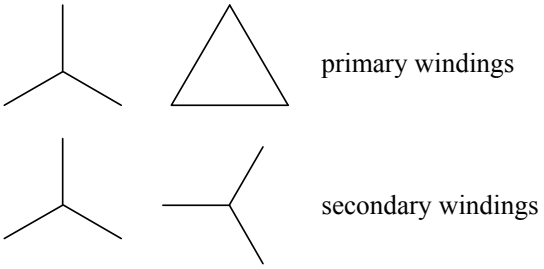

Figure 11.3 Twelve-pulse operation.

Since the two primary windings are displaced by 30°, it is necessary to have an intermediate yoke [2] to absorb the difference between the two limb fluxes ϕ_1 and ϕ_2 (see Figure 11.4). The intermediate yoke area should be corresponding to the difference of the two fluxes (which is about 52% of the main limb area).

Under the balanced condition of the two paralleled rectifier systems, the currents (average values) in both the windings of the interphase transformer are equal. This results in equal flux in the same direction in both the limbs forcing the corresponding field lines to return through the high reluctance nonmagnetic path outside the core (a substantial portion of DC ampere-turns is absorbed along the nonmagnetic return path). Another way to explain the phenomenon is that since net ampere-turns are zero in the window (since currents are directed in opposite directions), flux lines in the closed magnetic path are absent. Hence, the flux density in the core is low under the balanced condition. A slight imbalance in currents of the two systems results in a nonzero value of ampere-turns acting on the closed magnetic path, which may drive the core into saturation [3]. Thus, the interphase transformer draws a high excitation current under imbalanced conditions. This is one more reason (apart from higher core losses) for keeping a lower value of the operating flux density.

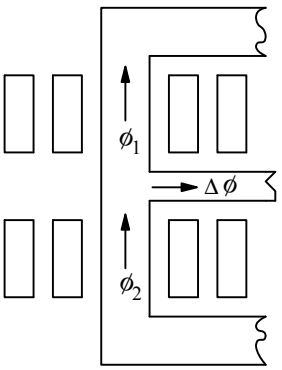

Figure 11.4 Intermediate yoke arrangement.

Although the interphase transformer connection has disadvantages, viz. a higher rating of its secondary winding and saturation of its magnetic circuit due to unbalance between two paralleled systems, it competes well with the bridge connection in a certain voltage-current range. The application of the interphase transformers is not restricted to paralleling of two systems; for example, with a three-limb core, three systems can be paralleled [1]. If the pulse number has to be further increased (e.g., 24-pulse operation), the required phase shift is obtained by using zigzag connections or phase shifting transformers [1, 2].

The IPT-system is mostly used for the parallel operation of two controlled rectifiers (i.e., with thyristors). The system comprising controlled rectifiers is often a closed-loop control system in which firing angles of thyristors are varied according to load requirements. The difference in voltages to be absorbed by the IPT does not remain constant. The difference increases with the firing angle. Hence, the probability of the IPT to walk into saturation increases, and therefore it is beneficial to use the transformer (IPT) as a separate entity for absorbing the variable voltage difference. The parallel operation of two uncontrolled rectifiers (using power diodes) is an open-loop system in which the voltage difference is constant for a particular load requirement. The five-legged rectifier transformer (FLRT) system is mostly employed for such applications. The voltage control is achieved in the system by providing supply through a three-phase auto-transformer. The IPT system is costlier and bulkier compared to that with the FLRT system due to the additional magnetic circuit. However, the system allows fine and better controllability compared to the FLRT system.

A simplified reluctance model for a five-legged transformer has been derived in [4] to analyze its zero-sequence characteristics. The open-circuit zero-sequence inductance of the transformer has been shown to be a function of the inductances contributed by the flow of magnetic flux through the end-legs. An analytical formulation for the zero-sequence characteristics of a three legged transformer is also developed and compared with that of the five-legged transformer. An in-depth analysis of the five-legged system is presented in [5] with an explanation of the role played by the end-legs. The system is compared with the conventional system and the IPT-like behavior of the end-legs, ensuring equal current sharing is investigated. The results of the analytical models are verified with that of coupled field-circuit analysis and with experimental measurements; a 12V, 5000A hexa-phase rectifier system consisting of a five-legged transformer is used for the purpose [4, 5].

11.1.3 Features of rectifier transformers

Rectifier transformers are used in applications where the secondary voltage is required to be varied over a wide range at a constant current value. It is extremely difficult and uneconomical to have taps on the secondary winding because of its very low number of turns and a high current value. The taps are either provided on the primary winding, or a separate regulating transformer

(autotransformer) is used feeding the primary of the main transformer, which can be accommodated in the same tank. Various circuit arrangements that can be used to regulate the secondary voltage are elaborated in [6].

For higher pulse operations, extended delta connections are shown to be more advantageous than zigzag connections, as they result in lower eddy losses and short-circuit forces [7].

The output connections, which carry very high currents, increase the impedance of the transformer significantly. The increase in the impedance value due to these connections can be calculated for a single conductor according to Equation 3.80. For go-and-return conductors of rectangular dimensions, the impedance can be calculated using the formulae given in [8].

For large rating rectifier transformers, the field due to high currents causes excessive stray losses in the structural parts made from magnetic steel. Hence, these parts are usually made from nonmagnetic steel.

Rectifier transformers are subjected to harmonics due to non-sinusoidal current duties. Hence, sometimes the pulse number is decided by harmonic considerations. Due to harmonics, more elaborate loss calculations are required for the rectifier transformers compared to the conventional transformers [9].

Sometimes the core of the rectifier transformer supplying power electronic loads is designed to have a small gap in the middle of each limb [7] to limit the residual flux and to keep the magnetizing reactance reasonably constant. This feature also limits the inrush current thereby protecting the power electronic devices. Under normal operating conditions, the core flux fringing out in the gap between the two core parts hits the inner winding causing high eddy losses. In order to mitigate this effect, the windings may also have to be designed with a gap at the location facing the core gap.

Because of possibilities of rectifier faults, special design and manufacturing precautions are taken for rectifier transformers. It is generally preferred to design the rectifier transformers with larger core area with corresponding smaller number of turns to reduce short-circuit forces [10]. Disk-type windings are preferred since they have better short-circuit strength compared to layer windings. Quality of drying/impregnation processes and integrity of clamping/support structures have to be very good. The paper insulation on winding conductors can also be strengthened.

11.2 Converter Transformers for HVDC

There has been a steady increase in high voltage direct current (HVDC) transmission schemes in the world because they offer many advantages compared to HVAC systems [11, 12]. The converter transformer is one of the most important and costly components of the HVDC transmission system. The converter transformer design has much in common with that of the conventional power transformer except for a few special design aspects on which this section elaborates.

11.2.1 Configurations

A standard 12-pulse converter configuration can be obtained using star-star and star-delta connections with one of the following arrangements: 6 single-phase two-winding, 3 single-phase three-winding and 2 three-phase two-winding constructions. The arrangements are shown in Figure 11.5.

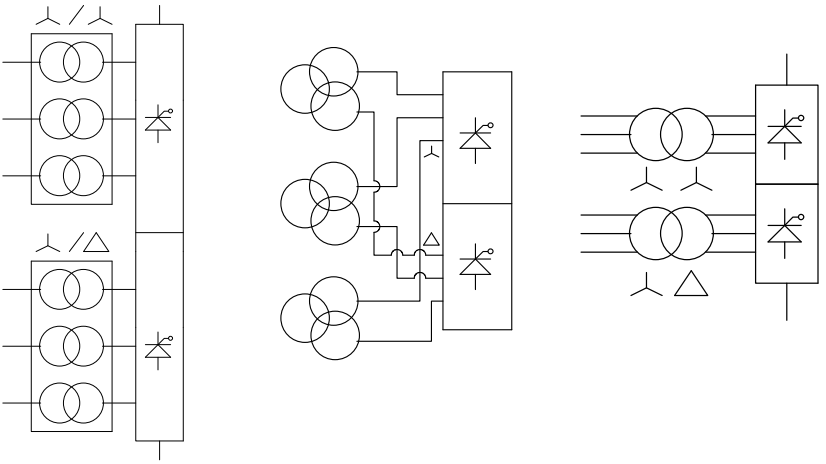

(a) 1-ph 2-winding (b) 1-ph 3-winding (c) 3-ph 2-winding

Figure 11.5 Configurations of converter transformers.

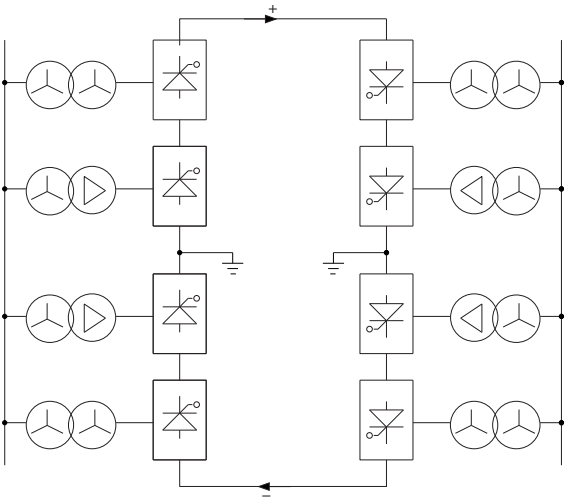

Figure 11.6 Schematic diagram of a bipolar 12-pulse configuration.

The weight and size of an individual transformer are highest and the overall cost (with all transformers considered) is lowest in the three-phase two-winding configuration, whereas the weight and size of an individual transformer are lowest and the overall cost is highest in the single-phase two-winding configuration. Since the cost of a spare transformer in the single-phase two-winding configuration is lowest (that of only one of the six transformers), it is more commonly used.

11.2.2 Insulation design

A simplified schematic diagram for bipolar (double) 12-pulse operation is shown in Figure 11.6. The windings connected to the converters and that connected to the AC side are generally termed as the valve and AC windings, respectively. Since the potentials of the valve winding connections are determined by the combination of conducting valves at any particular instant, the entire valve winding has to be fully insulated. Also, unlike the AC windings, both terminals of the valve windings experience the full DC voltage of the bridge to which they are connected. Hence, the end insulation gaps are higher resulting in greater radial leakage field at the two ends of the windings. The winding eddy loss due to the radial leakage field can be much higher than that in the conventional transformer, if the conductor dimensions are not chosen properly.

Thus, in addition to the normal AC voltage, the valve windings are subjected to a direct voltage depending on their position with respect to ground. Under an AC voltage, the potential distribution is in inverse proportion to capacitances, or electric stresses are inversely proportional to permittivities of different insulating materials in a multi-dielectric system. Since the permittivity of oil is about half of solid insulation, the stress in oil is more under the AC voltage condition in the conventional transformers. Since the dielectric strength of the oil is much less as compared to that of the solid insulation, the insulation design problem reduces mainly to designing of oil ducts as elaborated in Chapter 8. Contrary to AC conditions, under DC voltage conditions the voltage distribution is in direct proportion to resistances, or electric stresses are directly proportional to resistivities of involved insulating materials. At lower temperatures the resistivity of solid insulating materials used in transformers is much higher than that of the oil. The ratio of the resistivity of a high quality pressboard to that of the oil is about 100 at 20°C, which reduces to as low as 3.3 at 90°C [13]. This is because the fall in the resistivity of the pressboard with temperature is much higher than that of the oil [14]. Such a large variation in the ratio of the two resitivities increases the complexity of insulation design.

Thus, under DC conditions at lower temperatures, most of the voltage is distributed across the solid insulation, and stress in it greatly exceeds that in the oil. The oil ducts have practically only AC voltage across them, whereas solid insulations (barriers, washers, supporting and clamping components, etc.)

generally have a preponderance of DC voltage with a certain amount of superimposed AC voltage. Therefore, the number of pressboard barriers is greater in converter transformers as compared to conventional transformers. However, the proportion of solid insulation cannot be higher than a certain value because the composite oil-solid system has to withstand AC voltage tests as well.

Let the symbols ε and ρ denote relative permittivity and resistivity, respectively. With voltage V across two parallel plates shown in Figure 11.7, under AC field conditions the stresses in the oil and the solid insulation are

$$E_1 = \frac{V}{d_1 + \frac{\varepsilon_1}{\varepsilon_2} d_2} \cdots \textit{for oil} \qquad E_2 = \frac{V}{d_2 + \frac{\varepsilon_2}{\varepsilon_1} d_1} \cdots \textit{for solid} \tag{11.6}$$

and under DC field conditions the stresses are

$$E_1 = \frac{V}{d_1 + \frac{\rho_2}{\rho_1} d_2} \cdots \textit{for oil} \qquad E_2 = \frac{V}{d_2 + \frac{\rho_1}{\rho_2} d_1} \cdots \textit{for solid} . \tag{11.7}$$

For nonuniform field conditions involving complex electrode shapes, the techniques described in Chapter 8 should be used to calculate the stresses.

Under steady-state DC conditions, space charges are accumulated at the boundary of the oil and the solid insulation. When there is polarity reversal, in which the applied DC voltage changes from $+V$ to $-V$, an equivalent of the voltage difference $2V$ is applied. As the time required for reversing the polarity of the applied voltage is much shorter than the space charge relaxation time [15], the voltage due to space charge is not affected during the time of polarity reversal. Therefore, using Equations 11.6 and 11.7, the stresses in the oil and the solid insulation under the polarity reversal condition can be given by

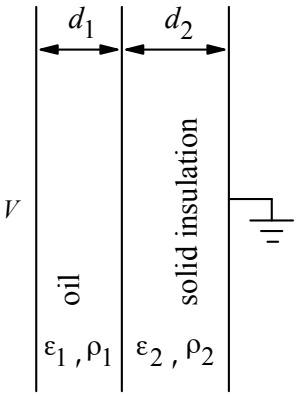

Figure 11.7 Oil-solid insulation system.

$$E_1' = \frac{V}{d_1 + \frac{\rho_2}{\rho_1} d_2} - \frac{2V}{d_1 + \frac{\varepsilon_1}{\varepsilon_2} d_2} \quad \cdots \textit{for oil} \tag{11.8}$$

$$E_2' = \frac{V}{d_2 + \frac{\rho_1}{\rho_2} d_1} - \frac{2V}{d_2 + \frac{\varepsilon_2}{\varepsilon_1} d_1} \quad \cdots \textit{for solid} . \tag{11.9}$$

Thus, under the polarity reversal condition, the oil gap is stressed more (since $\rho_2 >> \rho_1$ and $\varepsilon_1/\varepsilon_2 \cong 0.5$). It can be easily seen from the above equations that the smaller the stress across the oil gap before the polarity reversal, the more the stress is across it after the polarity reversal. The voltage distribution under various conditions is shown in Figure 11.8. The voltage across the oil gap is much higher during the polarity reversal condition (Case 3) as compared to Case 2 of the steady-state DC voltage condition (prior to the polarity reversal).

For the oil-solid composite insulation system, superimposition of a relatively low DC voltage on an AC voltage has very little effect on the partial discharge inception voltage [14-17]; this is due to the fact that most of the DC voltage is dropped across the solid insulation, which has a high DC withstand voltage. If, however, the DC voltage magnitude is within the range of the breakdown voltage, the breakdown behavior of the entire system is determined by the DC voltage. Although the converter transformers are stressed by combined AC and DC voltages during service conditions, it is not considered necessary to test them with superimposed voltages [18]. Conventional power frequency and impulse tests are generally sufficient in addition to pure DC voltage tests and the polarity reversal test.

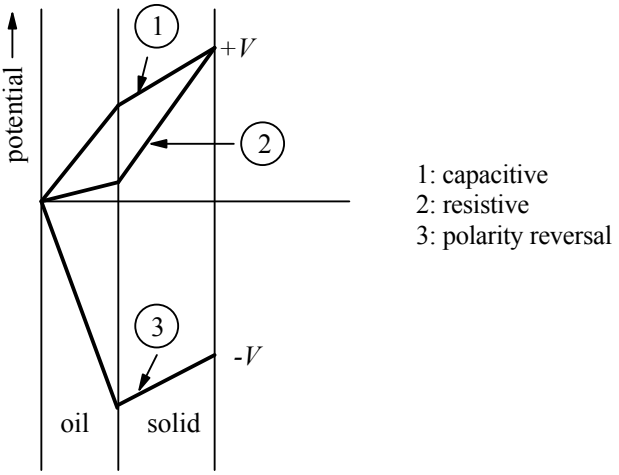

Figure 11.8 Voltage distribution under various conditions [15].

As in the case of AC insulation design (Chapter 8), the stresses under DC voltage conditions can be calculated accurately by numerical methods. The field distribution is generally calculated for a worst case condition, say at 20°C, since at this temperature the ratio of the resistivity of the solid insulation to that of the oil is high resulting in a high stress value in the solid insulation. The density of equipotential lines in barriers/cylinders is much higher compared to that in the oil, necessitating an increase in their thickness compared to that in conventional transformers. The shape and placement of barriers and the width of the resulting oil ducts would have already been decided by the requirements of AC design and thermal considerations [13]. Hence, it is obvious that the high strength of the solid insulation cannot be fully utilized from the DC design consideration if the stress in the oil gap (having a lower strength) has to be kept low under the AC and polarity reversal conditions [19]. Discontinuities in solid insulations result in higher tangential (creep) stresses along the solid-oil interfaces, and hence these should be properly looked at while finalizing the insulation design.

The insulation design of the converter transformers is complicated by the fact that the ratio of resistivities of the solid insulation and the oil, which varies considerably as explained earlier, is greatly influenced by a number of factors [18], such as temperature, field strength, moisture, time, and aging (contrary to the conventional transformers where the corresponding ratio of permittivities does not exceed about 2 and is practically independent of external factors).

The volt-time characteristics of the oil under DC voltage conditions are reported in [15, 20] for plane-plane electrodes; the DC breakdown voltage shows a rapid rate of decrease for stressing time until 100 seconds, after which there is hardly any decrease. The long-time breakdown voltage ($t \rightarrow \infty$) is 70 to 80% of the one-minute breakdown voltage [20]. Under combined AC-DC voltage conditions, the AC breakdown voltage of the oil decreases as the DC voltage increases. The DC 1-minute withstand voltage of the oil gap is about 20 to 30% lower than the AC 1-minute withstand voltage [16, 20, 21]; on the contrary the oil-impregnated paper/solid insulation withstands more DC voltage than AC voltage [16]. A higher DC strength of the solid insulation can be partly explained by the absence of partial discharges which lower the strength in the case of AC voltages. Even if there are oil voids in the solid insulation, the stress in them is too low under the DC voltage to initiate partial discharges.

It is reported in [22] that the dielectric strength of the converter transformer insulation under the polarity reversal condition is similar to that under switching impulse stresses. An equivalent AC power frequency voltage test has been suggested for the polarity reversal test.

From the typical schematic shown in Figure 11.6, it is clear that when a number of converters are connected in series, the line (AC side) windings are connected in parallel across the same lines and the inductively transferred overvoltage to ground increases cumulatively from one converter bridge to the next higher bridge because the valve (DC side) windings are connected in series

(although voltages across the valve windings remain almost the same for all the converters).

11.2.3 Other design aspects

***On-load tap changer* (*OLTC*):** The OLTC of a converter transformer plays a crucial role in HVDC transmission systems. Its tap position is adjusted to obtain a voltage condition that minimizes the reactive power requirement of HVDC converters (i.e., the firing angle of converters is kept as minimum as possible). Hence, the OLTC is an important constituent of the HVDC control scheme. The number of OLTC operations in a converter transformer is usually much higher than that in a conventional power transformer for the same reason. The OLTC is used for effective control of the DC voltage and the power flowing through the HVDC line.

***Leakage impedance*:** The leakage impedance of the converter transformer is the principal component of the commutating reactance, which limits the rate of rise of the loop current during the small overlap period when current is transferred from one valve to another. Thus, the leakage impedance helps in preventing instantaneous current transfer which otherwise would result in high di/dt values damaging the valves. The leakage impedance value has to be judiciously selected; a higher value reduces the rate of rise of the loop current during the current commutation process, but increases the overlap angle and the reactive power demand of the converters. The permissible tolerance on the impedance value of the converter transformers is usually lower than that on the impedance of the conventional transformers to reduce distortions in DC voltage waveforms and noncharacteristic harmonics.

***DC bushings*:** Creepage requirements of DC bushings are higher. The DC creepage withstand of an insulator can be about 30% lower than the AC withstand. While for conventional transformers, a creepage distance of about 31 mm/kV is specified for very heavily polluted areas, the creepage distance of as high as 40 mm/kV may be specified for DC bushings in the converter transformers.

***Harmonics*:** One of the most severe duties of the converter transformers is the presence of harmonics. Due to harmonics, eddy losses in windings and stray losses in structural components are higher in the converter transformers than in the conventional transformers. For a 6-pulse operating condition, the harmonics generated are $6k \pm 1$, where k is an integer. For a 12-pulse operating condition, the harmonics generated are $12k \pm 1$. Thus, the higher the pulse number the higher is the frequency of the lowest order harmonic produced. But as the pulse number increases, the number of transformers required is more and also the complexity of transformer connections increases. For a 24-pulse operating condition, use of zigzag windings or an extended delta connection is required.

Under normal operating conditions, the current in the converter transformer windings has a stepped waveform. It is still an AC current since it is symmetrical about the *x* axis. Nonuniformities or asymmetries in valve firing angles produce DC magnetization of the transformer core increasing the magnetizing current, and the windings carry a DC current component corresponding to the level of DC magnetization. Although with modern firing controls, the DC magnetization is much lower, careful design of the magnetic circuit is necessary to avoid excessive losses and noise in the core.

Due to harmonics and possibilities of DC magnetization, the operating flux density in the converter transformer is less than that in the conventional transformer, and its value is around 1.6 Tesla. A high harmonic content produces greater noise, and some special measures for noise control may have to be adopted as described in Chapter 10.

The leakage field in converter transformers contains appreciable harmonic content which results into high eddy losses in windings and structural parts. The losses in the windings can be controlled by using subdivided conductors or CTC (continuously transposed cable) conductors. If the CTC conductors are used, they are an epoxy-bonded type having high short-circuit strength as explained in Chapter 6. The magnetic or eddy current shielding techniques, discussed in Chapter 5, have to be used to minimize losses and to eliminate hot spots in the tank and other structural components. The load loss of a 213 MVA single-phase converter transformer has been measured at a number of frequencies between 60 Hz and 6 kHz in the work reported in [23]; the corresponding harmonic load loss factors are given for accounting extra losses due to harmonics.

***Short-circuit withstand*:** Due to possibility of maloperations of valves resulting in high currents, the short-circuit withstand design of the converter transformers deserves more attention. Quality of processing (drying and impregnation) and integrity of clamping/support structures have to be ensured. The windings of the converter transformers need to be adequately braced. The current density of the windings can be lower to enhance their strength against short-circuit forces.

11.3 Furnace Transformers

A transformer supplying an arc furnace has to deliver unusually high currents over a wide range of voltage. Power ratings between 50 and 100 MVA are quite common now with the secondary currents of more than 50 kA. Furnace transformers have special features for handling very high currents compared to conventional transformers. Since the LV winding current is high, its voltage is better controlled by providing taps on the HV winding.

An arc furnace has three electrodes connected to the secondary terminals of the furnace transformer which has to be specially designed to withstand frequent short circuits on the secondary side. Currents drawn in the arc furnace are characterized by wide fluctuations and unbalanced conditions, which lead to

problems of voltage drops, harmonics, etc. (details are given in Section 13.4) These effects can be mitigated by supplying furnaces directly from a high voltage transmission line having high capacity (i.e., an adequate short-circuit level at the supply point) through a furnace transformer. In such a case, when the voltage ratio is high, suitable measures should be taken for protecting the secondary winding against the electrostatically transferred voltages from the high voltage primary winding. These measures are connection of a surge arrester, or a capacitor, between the secondary terminals and a ground and placement of an electrostatic shield between the primary and secondary windings.

The leakage reactance of the furnace transformer affects the furnace operation since it is added to the reactance of the high current connections between the transformer secondary terminals and electrode tips. The higher the reactance, the lower the useful service currents are, thereby reducing the efficiency of the operation. Hence, the leakage reactance needs to be kept as small as practically possible with due consideration to the short-circuit withstand of windings and clamping/support structures. Also, a certain minimum value of reactance is required in the furnace circuit to stabilize arcs. In large furnace installations, the low voltage connections usually provide the necessary reactance. For smaller installations, a reactor may have to be added in series with the primary winding to give a sufficient reactance value for the stability. The series reactor, which may be housed in the tank of the furnace transformer, is usually provided with taps so that the reactance value can be varied for an optimum performance. Hence, depending on the rating of furnace installation and its inherent reactance, the leakage reactance of the furnace transformer has to be judiciously selected to meet the stability and efficiency requirements.

Although the core-type construction is common, the shell-type construction is also used [24] because one can get a desired low impedance value by suitably interleaving the primary and secondary windings. The furnace transformers are provided with a separate regulating (tap) winding. The variation of the percentage reactance over the entire tapping range depends on the disposition of the windings. The effects of various dispositions on the percentage reactance and the performance of furnaces are analyzed in [25].

The melting process of a furnace requires initially more power to break down and melt the furnace charge. The power required afterward for refining the molten metal is lower. The variable power input requirement is achieved by varying the supply voltage to the electric arc furnace over a wide range continuously using an OLTC. Its use is essential where temporary interruptions in supply for changing taps is not desirable. Since the regulation required is generally fine, an OLTC with a large number of steps is required. Due to frequent operations, its oil quality should be regularly checked. It is preferable to place the OLTC in a separate compartment so that its maintenance can be carried out without having to lower the oil to an extent that windings are exposed [26].

The commonly used arrangements for the voltage regulation are shown in Figure 11.9. Arrangement (a), which consists of taps at the neutral end of the primary winding, is used for low rating furnace transformers (5 to 10 MVA). The cost of the OLTC is minimum due to lower voltage and current values (the primary voltage may be of the order of 33 or 66 kV). The disadvantage of this arrangement is that the step voltage is not constant throughout the range of voltage regulation. For a fixed primary voltage, when the tap position is changed for varying the secondary voltage the voltage per turn changes, which results in nonuniform step variations in the secondary voltage from one tap to another.

Arrangement (b), used for larger furnace applications, eliminates the disadvantage of the previous arrangement. A separate autotransformer is used for the voltage regulation. The step voltage is uniform throughout since the voltage per turn is independent of the tap position for a given input voltage applied to the primary winding of the autotransformer which may be supplied directly from a system at 66 or 132 kV. The OLTC voltage class is higher than that of arrangement (a) and three single-phase tap changers may have to be used. Also, the autotransformer and the furnace transformer are usually housed in separate tanks, thereby increasing the cost and size of the total system.

The most popular arrangement used for medium and large power furnace applications consists of a furnace transformer with a booster arrangement as shown in Figure 11.9 (c). The booster transformer on the output side boosts or bucks the fixed secondary voltage of the main transformer. The primary winding of the booster transformer is supplied from the tap winding of the main transformer, and the supply voltage is selected such that it results in the least onerous operating conditions for the OLTC. Hence, the OLTC cost is low in this arrangement. Also, the variation in the secondary voltage is the same from one tap position to another throughout the range of regulation. Usually, the main and booster transformers are placed in the same tank minimizing the length of connections between the secondary windings of the two transformers. The amount of structural steel required is also reduced.

The booster transformer rating is much smaller than that of the main transformer, being sufficient for the regulation purpose only. Although the diameters of the two cores are different, the magnetic circuits of the two transformers have generally the same center-to-center distance and equal window heights to facilitate the connections between their secondary windings. If one wants to reduce the core material content, the center-to-center distance of the booster transformer can be lower, but the connections become complicated. Since the currents of the secondary windings of the main and booster transformers are equal, the same conductor type and size are generally used for both windings.

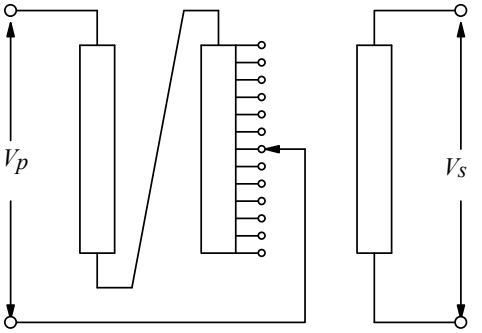

(a) Taps on primary winding

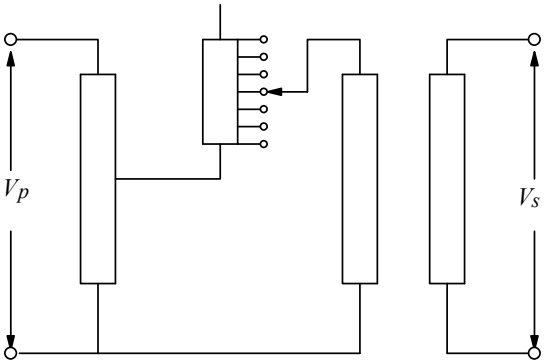

(b) Regulation by autotransformer

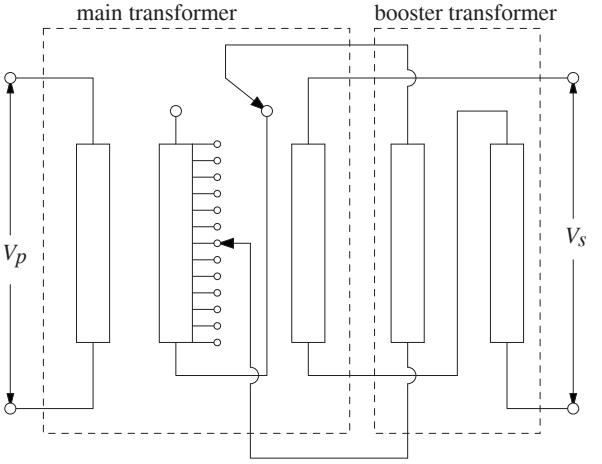

(c) Booster arrangement

Figure 11.9 Types of furnace transformers.

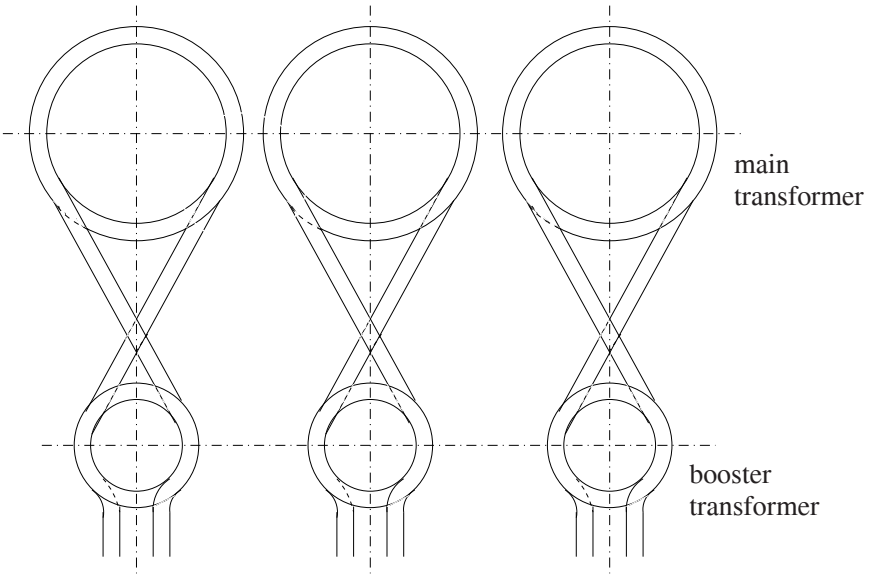

Figure 11.10 Figure eight connection.

Also, the two windings are often connected in a figure eight fashion (Figure 11.10) avoiding extra connections between them. A special arrangement is required to lift the two core-winding assemblies simultaneously.

Since the current carried by the secondary windings is quite high, a continuously transposed cable (CTC) conductor is used which minimizes the eddy losses, gets rid of the transposition problems, and improves the winding space factor. The material of structural parts supporting high current terminations and tank parts in the vicinity of high current fields should be non-magnetic steel. Analysis of a high current termination in a large furnace transformer is reported in [27], wherein excessive losses and hot spots observed during the tests have been analyzed by 3-D FEM analysis. Suitable modifications in magnetic clearances and the tank material eliminated the hot spots.

The secondary winding of a furnace transformer is made up of a number of parallel coils arranged vertically and connected by vertical copper bars. A go-and-return arrangement is used for the input and output connections (placed close to each other) reducing the magnetic field and associated stray losses in the nearby structural parts. A delta-connected secondary winding is preferable since the current to be carried by it is reduced. Many times, both the ends of each phase of the secondary winding are brought out through the terminals and the delta connections are made at the furnace (i.e., the connections are automatically formed by the metallic charge in the furnace). This minimizes the inductive voltage drops in the leads and can achieve a better phase balance

between the electrode currents. Due to heavy connections, some unbalance may exist which has to be minimized by some specific arrangements [25]. The secondary winding terminals are usually located on the vertical side of the tank (instead of the top cover) resulting in lower lengths of the connections, stray losses, and the transformer cost. The LV (secondary) winding is invariably the outermost winding and the HV (primary) winding can be placed next to the core. In such a case, the regulating (tap) winding is between the HV and LV windings. Such a disposition of windings reduces variations in the percentage impedance as the tap position is changed from the minimum to the maximum in variable flux designs.

Small furnace transformers are naturally cooled with radiators. For large ratings and where there are space restrictions, forced oil cooling with an oil-to-water heat exchanger can be used. The oil pressure is always maintained higher than the water pressure (so that the water does not leak into the oil if a leakage problem develops). The LV terminations may be in the form of U-shaped copper tubes of certain inside and outside diameters so that they can be water cooled from inside. These copper tubes can be cooled by oil as well [26].

11.4 Phase Shifting Transformers

In a complex power transmission network, a phase shifting transformer (PST) can be used to control the flow of active power and to improve transient stability in a very efficient way as elaborated in Section 13.1.2. It has been successfully used to control and increase the power flow between two large systems [28]; in this case the option of using a PST was finalized after its comparison with other options such as an HVDC link and series capacitors. The PST provides a well-defined phase shift (advance or retard) between the primary (source) and secondary (load) terminals as shown in Figure 11.11. In the phase-advance mode, the voltage vector at the output of the PST is made to lead the input voltage vector by adding a leading quadrature voltage to the source voltage. In the phase-retard mode, a lagging quadrature voltage is added to the source voltage so that the voltage vector at the output of the PST lags the input voltage.

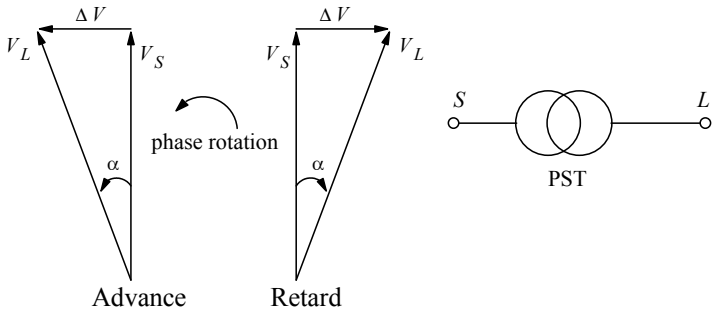

Figure 11.11 Advance mode and retard mode.

Normally, the phase shift can be varied during operation in definite steps by use of an OLTC. The sign of the phase shift can be inverted by using an OLTC having a reversing switch. These transformers can be constructed with many different winding configurations depending on the rated voltage, the power output, and the amount of required phase shift.

The rated power that decides the PST size is given by [29]

$$S_{eq} = 3\times\left\{ V_{ph}\times 2\sin(\alpha/2) \right\}\times I_{SL} = 3\,V_{ph}\;I_{SL}\times 2\sin(\alpha/2) \qquad (11.10)$$

where V_{ph} is the line-to-ground voltage, I_{SL} is the line current flowing from the source to the load, and the term in the brackets is the voltage between *S* and *L* terminals expressed in terms of the phase shift angle α. Hence, the required maximum value of the phase shift angle decides the rating and size of the PST. Depending on the voltage/power rating, phase shift angle requirements, connected system's short-circuit capability and OLTC performance, two distinct designs of PST are used, viz. single-core design and double-core design.

The simpler single-core design is generally used at lower voltages for small phase shifts and small ratings of PSTs. Figure 11.12 shows the arrangement of a PST with a delta-connected exciting winding. In this configuration, the regulating winding of each phase is wound on the same core limb as the exciting winding. The phase shift between the source (*S*) and load (*L*) terminals is achieved by connecting the regulating winding as shown in the figure. Its voltage is in phase with that of the exciting winding between the other two phase terminals. The voltage magnitudes of the *S* and *L* terminals are equal under the no-load condition. The phasor diagram shows the phase shift advancement obtained for the load terminal voltage with respect to the source terminal voltage. If an OLTC with a reversing switch is used, one can obtain a phase-advance position as well as a phase-retard position.

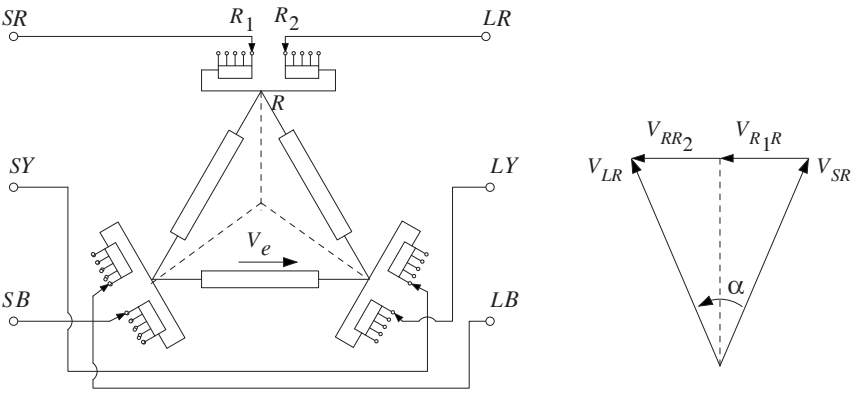

Figure 11.12 Delta configuration of PST and phasor diagram.

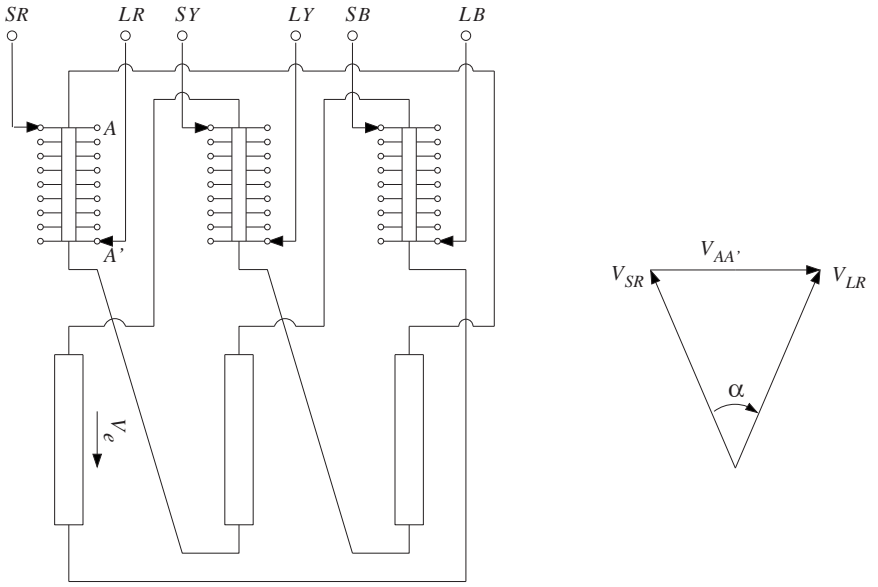

Figure 11.13 Delta-hexagonal PST (with retard phase shift).

A special case of the configuration shown in Figure 11.12 is the design with only one tap winding and one OLTC with a reversing switch, which can be used for smaller phase shifts.

Another configuration that uses the single-core design is shown in Figure 11.13. The arrangement, known as delta-hexagonal PST, generally has an OLTC with linear regulation, i.e., without a reversing switch. The regulating winding is wound on the same core limb as the main exciting winding. The regulating winding of the *R* phase is located between the main windings of the *Y* and *B* phases and produces a phase shift (retard) as shown in the figure.

The two configurations of the single-core design discussed above have line-end regulation. The tap changer and the regulating (tap) winding are directly exposed to system disturbances (overvoltages/short-circuit currents). Hence, the cost of the OLTC increases. Additional impedances may have to be connected to the load side terminals to protect the tap changer from short-circuit currents because no transformer impedance is present at zero phase angle. If an OLTC with a reversing switch is used in the arrangement shown in Figure 11.12, during the switch operation, the tap winding is momentarily disconnected from the main winding. Its potential is then decided by the potentials of adjacent windings and the capacitances between the windings and between the windings and ground. This problem of high recovery voltage can be tackled [29, 30] by using shields between the windings or by using a tie-in resistor (which connects the tap winding to a fixed potential during the reversing operation).

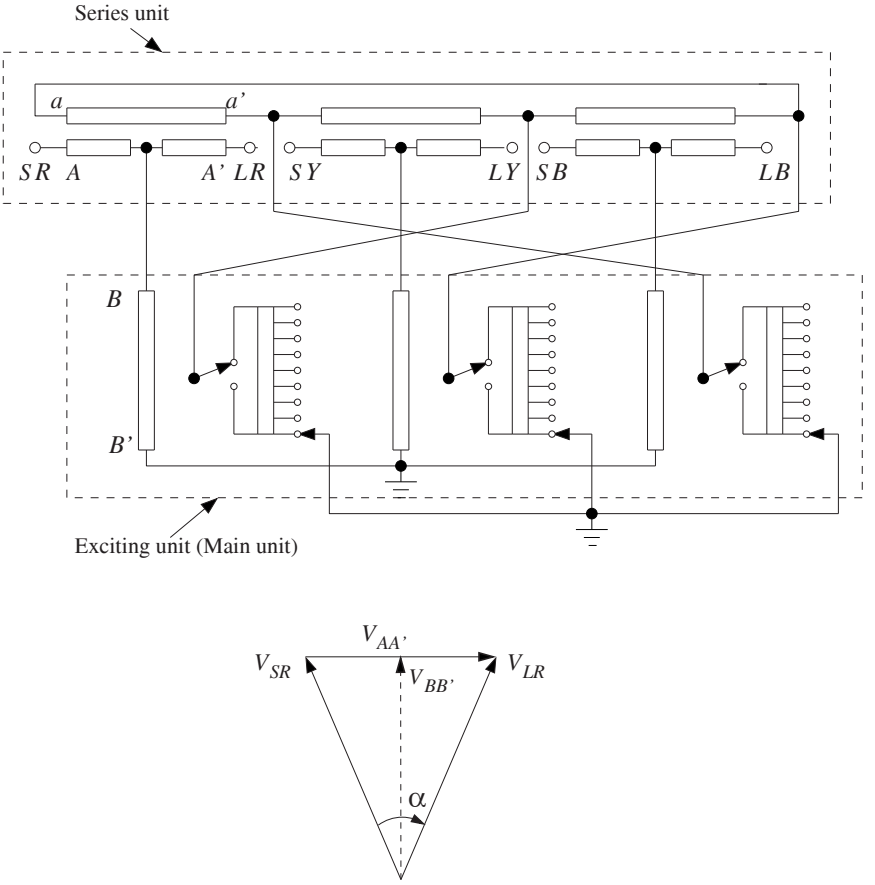

Figure 11.14 Commonly used configuration for two-core design PST.

The two-core design shown in Figure 11.14 is popularly used for large PST ratings and phase shifts. This type of PST basically consists of a series unit and an exciting unit, which are enclosed in separate tanks. When the design is used for smaller ratings and lower voltages, both units can be enclosed in the same tank.

The winding of each phase of the series unit, between the source and load terminals, is split into two halves, and the main winding of the exciting unit is connected to the connection point of these two split windings. The advantage of this arrangement is that the tap winding in the exciting unit and the winding aa' in the series unit can be designed independently (the windings AA' and BB' form a part of the HV network). The voltage level of the tap winding and the aa' winding can be suitably chosen to reduce the tap changer cost.

It is clear from the phasor diagram that the voltage $V_{BB'}$ also changes with the phase angle α because the exciting winding (BB′) is located electrically in the middle of the series winding. For $\alpha = 0°$, $V_{AA'}$ becomes zero and the three voltages V_{SR}, V_{LR} and $V_{BB'}$ become equal. Thus, the condition $\alpha = 0°$ gives the highest exciting voltage $V_{BB'}$, and the corresponding voltage at the tap winding is also maximum. The OLTC has to be designed for the step voltage corresponding to this highest voltage.

In order to achieve rapid and smooth control of the power flow, static phase shifters can be used, which employ tap changers consisting of static devices like thyristors. One such scheme, reported in [31], is shown to minimize the subsynchronous resonances in large turbine-generators occurring due to capacitive series compensation of lines. Applications of static phase shifters in power systems are reported in [32]. By augmenting an existing conventional phase shifter with a small static phase shifter (thus giving a hybrid phase shifter), dynamic performance can be improved.

The calculation of currents in phase shifting transformers under system fault conditions requires more elaborate treatment as compared to that for conventional transformers. The equivalent circuit model and the positive-sequence, negative-sequence and zero-sequence networks under the fault analysis are explained in [33]. The reported method can be used to calculate currents under various fault conditions.

References

1. Schaefer, J. *Rectifier circuits: theory and design*, John Wiley and Sons, Inc., New York, 1965.
2. Pelikan, T. and Isler, J. Rectifier transformers for heavy currents, *The Brown Boveri Review*, Vol. 48, No.3/4, March/April 1961, pp. 215–228.
3. Wells, R. Rectifier interphase transformers and current balance, *Electrical Review*, Vol. 207, No. 14, October 1980, pp. 45–46.
4. Bhide, R. S., Kulkarni, S. V., and Bhandarkar, P. Analytical description for zero-sequence characteristics of five-legged core construction in Transformers, *Proceedings of IET — Electric Power Applications*, Vol. 4, No. 6, July 2010, pp. 407–417.
5. Bhide, R. S., Kulkarni, S. V., and Bhandarkar, P. Analysis of five-legged transformer used for parallel operation of rectifiers by coupled circuit-field approach, *IEEE Transactions on Power Delivery*, Vol. 26, No. 2, April 2011, pp. 607–616.
6. Coppadoro, F. Voltage regulation of transformers for silicon rectifiers, *Brown Boveri Review*, Vol. 8-72, August 1972, pp. 416–421.

7. Andersen, O. W. Large transformers for power electronic loads, *IEEE Transactions on Power Delivery*, Vol. 12, No. 4, October 1997, pp. 1532–1537.
8. Copper Development Association, *Copper for busbars*, Publication 22, June 1996, p. 53.
9. Crepaz, S. For an improved evaluation of conventional losses of transformers for converters, *IEEE Transactions on Industry Applications*, Vol. IA-11, No. 2, March/April 1975, pp. 165–171.
10. Kasermann, P. Oerlikon rectifier transformers, *Bulletin Oerlikon*, No. 336/337, 1959, pp. 134–139.
11. Arrillaga, J. *High voltage direct current transmission*, Peter Peregrinus Ltd., London, 1983.
12. Kimbark, E. W. *Direct current transmission*, John Wiley and Sons, New York, 1971.
13. Tschudi, D. J. DC insulation design: paper-oil insulation systems, *WICOR Insulation Conference*, Rapperswil, Switzerland, September 1996, pp. 1–9.
14. Ganger, B., Falkenhagen, H., and Kury, H. Contributions to the problem of insulation stresses in HVDC converter transformers, *Direct Current*, Vol. 2, No. 1, February 1971, pp. 15–29.
15. Takahashi, E., Tsutsumi, Y., Okuyama, K., and Ogata, F. Partial discharge characteristics of oil-immersed insulation systems under DC, combined AC-DC and DC reversed polarity voltage, *IEEE Transactions on Power Apparatus and Systems*, Vol. PAS-95, No. 1, January/February 1976, pp. 411–420.
16. Kurita, K., Hyuga, S., Ikemoto, N., Oka, Y., Sudo, Y., Hirano, M., Kako, Y., and Kiwaki, H. Converter transformer, DC reactor and transductors for 125 kV 37.5 MW thyristor converter, *Hitachi Review*, Vol. 21, No. 4, pp. 146–156.
17. Hessen, P. and Lampe, W. Insulating problems in HVDC converter transformers, *Direct Current*, Vol. 2, No. 1, February 1971, pp. 30–44.
18. Wahlstrom, B. Voltage tests on transformers and smoothing reactors for HVDC transmission, *Electra*, Report No. 46, 1976, pp. 19–38.
19. Kull, U. The behavior of a laminated oil-paper dielectric with high direct voltages, *The Brown Boveri Review*, Vol. 55, No. 4/5, April/May 1968, pp. 215–221.
20. Ohshima, I., Motegi, S., Honda, M., Yanari, T., and Ebisawa, Y. HVDC breakdown of transformer oil and the effect of space charge on it, *IEEE Transactions on Power Apparatus and Systems*, Vol. PAS-102, No. 7, July 1983, pp. 2208–2215.
21. Ganger, B. E. The breakdown voltage of oil gaps with high DC voltage, *IEEE Transactions on Power Apparatus and Systems*, Vol. PAS-87, No. 10, October 1968, pp. 1840–1843.
22. Hasegawa, T., Yamaji, K., Hatano, M., Kouan, T., and Hosokawa, N. Dielectric strength of transformer insulation at DC polarity reversal, *IEEE*

Transactions on Power Delivery, Vol. 12, No. 4, October 1997, pp. 1526–1531.
23. Forrest, J. Harmonic load losses in HVDC converter transformers, *IEEE Transactions on Power Delivery*, Vol. 6, No. 1, January 1991, pp. 153–157.
24. Grundmark, B. Large furnace transformers, *ASEA Journal*, December 1972, pp. 151–156.
25. Bonis, P. and Coppadoro, F. Transformers for arc furnaces, *Brown Boveri Review*, Vol. 60, No. 10/11-73, October/November 1973, pp. 456–467.
26. Hochart, B. *Power transformer handbook*, Butterworth and Co. Ltd., London, 1987.
27. Koppikar, D. A., Kulkarni, S. V., Khaparde, S. A., and Jha, S. K. Evaluation of eddy losses due to high current leads in transformers, *Proceedings IEE - Science Measurement and Technology*, Vol. 144, No. 1, January 1997, pp. 34–38.
28. Patel, B. K., Smith, H. S., Hewes, T. S., and Marsh, W. J. Application of phase shifting transformers for Daniel-Mcknight 500 KV interconnection, *IEEE Transactions on Power Delivery*, Vol. PWRD-1, No. 3, July 1986, pp. 167–173.
29. IEEE Standard C57.135-2001™, IEEE guide for the application, specification, and testing of phase-shifting transformers.
30. Kramer, A. and Ruff, J. Transformers for phase angle regulation considering the selection of on-load tap changers, *IEEE Transactions on Power Delivery*, Vol. 13, No. 2, April 1998, pp. 518–525.
31. Iravani, M. R. and Mathur, R. M. Damping subsynchronous oscillations in power systems using a static phase shifter, *IEEE Transactions on Power Systems*, Vol. PWRS-1, No. 2, May 1986, pp. 76–83.
32. Iravani, M. R., Dandeno, P. L., Nguyen, K. H., Zhu, D., and Maratukulam, D. Applications of static phase shifters in power systems, *IEEE Transactions on Power Delivery*, Vol. 9, No. 3, July 1994, pp. 1600–1608.
33. Del Vecchio, R. M., Poulin, B., Feghali, P. T., Shah, D. M., and Ahuja R. *Power transformer design principles: with applications to core-form power transformers*, Gordon and Breach Science Publishers, Canada, 2001, pp. 499–542.

12

Electromagnetic Fields in Transformers: Theory and Computations

A transformer is a complex 3-D electromagnetic device. Although a static device and simple enough in principle, it is built from a complex assembly of several components such as the core, windings, insulation, tank, and several accessories. A three-phase transformer is a multiphase structure having materials with nonlinear characteristics and anisotropic properties. Superimposition of various physical fields (electromagnetic, thermal, structural, acoustic, fluid, etc.) poses a real challenge to its designer. Many times, there are conflicting design requirements for these different fields. Advanced field computations involving coupled analysis of the electromagnetic field and the other fields are generally essential for its quality enhancement and optimization.

Owing to tremendous advances in computational facilities, accurate field computations in electromagnetic devices are now possible. Various numerical techniques are available for tackling electromagnetic and coupled problems. Numerical techniques can be categorized into methods based on differential formulations (e.g., the finite difference method), integral formulations (e.g., the boundary element method) and variational/Galerkin formulations (e.g., the finite element method). The finite element method (FEM) has emerged as the most popular numerical method, and many commercial 2-D and 3-D FEM packages are available. Applications of this technique for the design and analysis of the transformers have been cited in earlier chapters at appropriate places. Many manufacturers develop their own customized FEM programs for optimization and reliability enhancement of transformers. 2-D FEM, which is widely used for estimation of eddy losses and short-circuit forces in windings, can be integrated into electrical design optimization programs.

While the commercial software make field computation possible for engineers who may not have adequate knowledge of the electromagnetic field theory, interpretation and post-processing of results could be difficult. Also, in

order to obtain accurate values of field variables and related performance figures, source and boundary conditions have to be defined correctly. The mesh size has to be small enough in the areas where the spatial rate of change of a field variable is high. Many times 2-D approximations have to be done since 3-D field computations are computationally demanding. Nonlinear transient 3-D problems may have convergence problems. The knowledge of the product, fields and numerical techniques is essential for doing reasonable 2-D approximations. Commercial software programs offer alternative formulations for 3-D simulations; competence in computational electromagnetics is certainly necessary to apply them. Numerical results need to be verified by approximate analytical or empirical formulae at least initially while using commercial software.

The above discussion underlines the need of giving an adequate exposure of the field theory and FEM to transformer engineers. This is exactly the motivation of this chapter; basics of electromagnetics as relevant to transformer engineering are discussed first. The idea is not to describe the field theory in detail; it is exhaustively covered in numerous textbooks on the subject [1–4]. Rather, emphasis is given on summarizing the pertinent theory that would be useful to the engineers while analyzing various electromagnetic phenomena in transformers. After giving a brief introduction to Maxwell's equations, the second section describes the mathematical concepts which are the main foundations of the field theory. Later, potentials used for solving electrostatic, magnetostatic, and time varying problems are elaborated. The most popular numerical technique, FEM, is then explained with examples. Various field formulations and their applications for performance assessment of transformers, under steady state and transient conditions, are then summarized. Coupled field problems in transformers, involving interaction between electromagnetic fields and circuits and/or physical fields, are also described. The coupled problems in transformers involving circuit-field, magnetic-thermal, and magnetic-structural phenomena are then elucidated. Lastly, the performance figures that can be computed using the technique are elaborated. This exposure to the field and FEM theory in this chapter is expected to help researchers and practicing engineers to solve complex as well as practical electromagnetic and coupled problems in transformers.

12.1 A Perspective

As discussed earlier, the transformer is a complex 3-D structure in which many physical fields like thermal, fluid, structural, acoustic, etc., exist in addition to electric and magnetic fields. If these fields can be represented accurately by an equivalent lumped parameter representation, their spatial distribution is not required to be known. However, it is a well-known fact that practical products such as transformers cannot be reliably designed and/or optimized without the precise knowledge of fields inside them. Empirical formulae fail to represent distributions of the fields in space, particularly so in the problem regions with high gradients. End effects, sharp corners, material nonlinearities and hysteretic

properties, and material anisotropies make the expressions/formulae almost ineffective. They are generally derived for near-uniform field conditions with linear and isotropic material properties. Also, the geometry is assumed as infinite in extent in at least one if not two dimensions.

12.1.1 Analytical techniques

The above discussion highlights the necessity of computing field distributions inside transformers by either analytical or numerical methods. Before the advent of numerical methods, analytical techniques, such as the double-Fourier method (discussed in Chapter 3), method of images (used in Appendix D), separation of variables, Schwarz-Christoffel transformation, etc., were used for the computation of 2-D electrostatic and magnetostatic fields inside transformers. However, there are certain limitations of these analytical methods. These formulations are not geometry independent, their mathematical formulation is intensive, it is very difficult to handle nonlinear and anisotropic materials, multiple materials cannot be easily handled, and their application to 3-D geometries is almost ruled out. For 2-D geometries consisting of a single material with linear and isotropic properties and homogenous Dirichlet and/or Neumann boundary conditions they can work very well with reasonably good accuracy. For such cases, they should be used since their integration into design or optimization programs is straightforward (as compared to the numerical techniques); they are computationally very efficient as well. Often the analytical methods may lead to simple expressions like the ones derived using the method of images in Appendix D for determining the stress and voltage distribution. Their application may sometimes lead to closed-form expressions and solutions that are exact, in which case the dependence of the field on various factors is readily apparent.

12.1.2 Numerical methods

Numerical methods have become an integral part of design and development activities of power transformers. These are now indispensable for evaluation and improvement of performance parameters at the design stage, reliability enhancement, and investigative/failure analysis. Existing designs can be improved and new designs can be verified, obviating the need of costly and time-consuming experimental approach. Also, since it is possible to find stress levels at various points, factors of safety can be determined, thus opening optimization possibilities.

The numerical methods do not generally give exact solutions in the sense that there is always an associated error which is a function of the number of variables selected and/or the order of the approximating polynomial expression chosen for the variables. The error by itself is not a problem and is in a way inevitable. However, it is important to have control over the error, e.g. by choice of an appropriate scheme in which the error is smaller or by using some appropriate *smoothing* or *correcting* techniques. Let us suppose that the electrostatic field distribution inside a parallel plate capacitor has to be

determined without consideration of fringing fields at the ends of its plates. Actually this is a trivial problem whose exact solution is available (the electric field intensity being equal to the voltage difference between the plates divided by the distance separating them). It is considered here for explaining the topic under discussion. Let us assume that the solution is 10 kV/mm. If the problem is solved by a numerical technique, say FEM, one may not obtain the solution exactly as 10 kV/mm everywhere between the plates. However, the error can be controlled by choosing a fine mesh size. Thus, the solutions can be obtained within engineering accuracy requirements (solution values such as 9.995, 10.005, etc. are accurate enough for the design purpose). The moment the problem is redefined with the requirement of consideration of the fringing fields, it becomes almost an intractable problem for the analytical methods and for the numerical methods there is hardly any additional order of difficulty in solving it.

The popular numerical methods being used by researchers and practicing engineers are the finite difference method (FDM), FEM, the boundary Element method (BEM), the charge simulation method (CSM), and the method of moments (MOM). Textbooks on computational electromagnetics [5–11] can be referred to obtain comprehensive understanding of the methods. Here, few comments are made on the methods with particular reference to their utility for transformer engineering.

FDM: This is the simplest numerical method with various numerical schemes that are the result of convenient manipulations of Taylor series expansions, by which differential equations are converted into difference equations. The problem domain is discretized to form a rectangular or square grid. The potential at each grid point is then expressed in terms of the potentials of the points surrounding it. Thus, there will be as many equations as there are unknown potentials in the grid. Solving these equations, with known boundary conditions, leads to the determination of all the unknowns. Potential at any intermediate point, which is not on the grid, can be calculated by interpolation. The main disadvantage of the method is that irregular boundaries cannot be easily handled compared to the other methods. Hence, its application to transformers is limited; however, its variant known as the reluctance network method [12] has been successfully applied for the stray loss evaluation as highlighted in Chapter 5.

The finite difference time domain method (FDTD) is an extension of FDM for simulation of high frequency electromagnetic phenomena. One may wonder about its applicability to transformers, a low frequency device. It can be used successfully for the simulation and diagnostics of partial discharges (PD) propagating in the form of high frequency electromagnetic waves. The theory and implementation aspects of the method for PD diagnostics are elaborated in Section 14.3. The method is conceptually simple as compared to the other methods (FEM and MOM) that can be used for the purpose.

***BEM*:** It is an integral equation method in which the field variable to be determined appears under the integral in the governing integro-differential

equation. By using Green's identity [13], the volume integral is converted into a surface integral, reducing the dimension of the problem by one order, this being the method's major advantage. In transformers, BEM can be used for finding dielectric stresses in insulation. The surface enclosing the problem volume in 3-D (or the contour enclosing the problem surface in 2-D) is discretized into elements with associated nodes, and the problem is formulated in terms of the potential (u) and its normal derivative (du/dn) on the boundary nodes. Generally, either u or du/dn is known on them. Using the integral equation, n equations are set up, solution of which leads to determination of the unknowns. Once all the boundary variables are known, the potential at any point within the domain can be evaluated using them. BEM is being used for the calculation of electric fields for the purpose of insulation design; a few commercial BEM software programs are also available.

The method has another distinct advantage in that it is ideally suited for open boundary problems obviating the need of defining fictitious boundaries. On the contrary, FEM requires that the problem domain be bounded. The major disadvantages of BEM are the resulting square matrix to be solved is fully populated compared to a highly sparse matrix in FEM and nonlinearities cannot be easily handled. Hence, the best features of the two techniques can be combined using a hybrid FEM-BEM formulation to determine noise levels in transformers as highlighted in Chapter 10 (Section 10.8.1).

Another integral method, CSM, has also been used for electric field computations in transformers; its brief theory and a few references have been given in Section 8.2. However, in comparison with FEM and other techniques, its application is rather limited to only electrostatic field problems.

***FEM*:** This method is the most popular numerical technique because of the following capabilities and features:

- Its formulation can handle geometric complexities,
- Anisotropic, nonuniform and nonlinear media can be handled,
- Availability of several commercial software makes its applicability to real-life transformer problems easier,
- The method is easily amenable to solving problems that involve coupling of electromagnetic fields with circuits and/or other physical fields.

Many of the case studies presented in various chapters are FEM based. The method can be used to calculate the following parameters and performance figures:

- Inter-turn/inter-disk/inter-section/inter-winding capacitances,
- Dielectric stresses in insulation,
- Self and mutual inductances between turns/disks/sections of a winding,
- Eddy current losses in windings and structural parts,
- Proximity effects between winding conductors, between high current carrying bars,
- Circulating current losses in windings,

- Forces in windings and current-carrying bars/terminations,
- Mechanical deformations in windings and clamping structures,
- Mechanical natural frequencies of windings,
- Temperature profile of the core, oil, windings, and structural parts,
- Mechanical stresses in the tank under pressure and vacuum conditions,
- Deflections and stresses in tanks and overhanging parts under seismic accelerations,
- Oil velocities in different zones within windings,
- Magnetostriction and load-controlled noise levels.

The theory of FEM is described in Section 12.4. Many of the basics of electromagnetic fields and potentials used in various FEM formulations are discussed in the following two sections.

12.2 Basics of Electromagnetic Fields Relevant to Transformer Engineering

The objective of this section is to give an adequate exposure to the theory of electromagnetic fields, as required for better understanding of fields in transformers. The concepts are not given in an orderly fashion when compared to standard textbooks on the electromagnetic fields. Here, it is assumed that the reader has some background in the field theory.

12.2.1 An overview of Maxwell's equations

The principles of operation of all electromagnetic devices including transformers can be well understood with the help of four Maxwell's equations along with the continuity equation and the Lorentz force equation. Maxwell's equations in the differential form are given by

$$\nabla \cdot \mathbf{D} = \rho \tag{12.1}$$

$$\nabla \cdot \mathbf{B} = 0 \tag{12.2}$$

$$\nabla \times \mathbf{E} = -\frac{\partial \mathbf{B}}{\partial t} \tag{12.3}$$

$$\nabla \times \mathbf{H} = \mathbf{J} + \frac{\partial \mathbf{D}}{\partial t}. \tag{12.4}$$

The continuity equation is

$$\nabla \cdot \mathbf{J} = -\frac{\partial \rho}{\partial t} \tag{12.5}$$

and the Lorentz force equation is

$$\mathbf{F} = Q(\mathbf{E} + \mathbf{v} \times \mathbf{B}) . \tag{12.6}$$

In addition, there are three constitutive relations that have to be used while applying the above set of equations for modeling any electromagnetic phenomenon:

$$\mathbf{J} = \sigma \mathbf{E} \tag{12.7}$$

$$\mathbf{B} = \mu \mathbf{H} \tag{12.8}$$

$$\mathbf{D} = \varepsilon \mathbf{E} . \tag{12.9}$$

The various terms in the above equations are:

$\mathbf{H}$ = magnetic field strength (A/m)
$\mathbf{E}$ = electric field strength (V/m)
$\mathbf{B}$ = flux density (Wb/m^2)
$\mathbf{J}$ = current density (A/m^2)
$\mathbf{D}$ = electric flux density (C/m^2)
ρ = volume charge density (C/m^3)
Q = charge (C)
$\mathbf{v}$ = velocity (m/s)
μ = permeability (henrys/m)
ε = permittivity (farads/m)
σ = conductivity (mhos/m).

Maxwell's equations as given above are said to be in *point* or *differential* form; the involved partial derivatives will in general vary from point to point for fields varying as a function of space. At the interface of two material media, the involved fields may be discontinuous; their partial derivatives at the interface cannot then be defined (since infinite). For example, the normal component of the electric field intensity vector is discontinuous at a dielectric-dielectric interface; it is inversely proportional to the dielectric constant (relative permittivity) in uniform field conditions. Hence, at interfaces the following Maxwell's equations in the integral form are used to derive the boundary conditions for determining the relationships between the tangential/normal components of fields on both sides:

$$\oint_s \mathbf{D} \cdot d\mathbf{s} = \int_v \rho_v dv \tag{12.10}$$

$$\oint_s \mathbf{B} \cdot d\mathbf{s} = 0 \tag{12.11}$$

$$\oint_l \mathbf{E} \cdot d\mathbf{l} = -\frac{\partial}{\partial t} \int_s \mathbf{B} \cdot d\mathbf{s} \tag{12.12}$$

$$\oint_l \mathbf{H} \cdot d\mathbf{l} = \int_s \left(\mathbf{J} + \frac{\partial \mathbf{D}}{\partial t} \right) \cdot d\mathbf{s} \,. \tag{12.13}$$

Many of the above equations and variables have also been defined elsewhere in some other chapters. However, they are given here for the sake of completeness to supplement further discussions in this chapter. By the end of this section, our objective is to understand the equations and be able to appreciate their relevance to transformers. Many of the published research papers that deal with the field computations in transformers use these equations.

12.2.2 Preliminaries

***Coordinate systems*:** In order to calculate the value of a field variable at any point in space, we need a reference coordinate system. Most often orthogonal coordinate systems are used because of simplicity and convenience. Out of about 20 known 3-D orthogonal coordinate systems, the most commonly used ones are Cartesian (x, y, z), cylindrical (r, ϕ, z) and spherical (r, θ, ϕ). In an orthogonal coordinate system any point in 3-D space is thought of as the intersection of three surfaces perpendicular to each other (e.g., surfaces x = constant, y = constant and z = constant in Cartesian system).

A Cartesian system is easy to visualize and is a general system that can be used for any arbitrary 3-D problem in which there are no symmetries. In transformers, an analysis involving all three phases would necessitate the use of a Cartesian system. When 2-D approximation is done (i.e., analysis in the x-y plane), the structure is assumed to be of infinite extent in the z direction, and the field quantities and performance figures are calculated per unit length in the z direction. Such an approximation may be justified for windings with large diameters.

The cylindrical system is ideally suited for axisymmetric problems wherein the whole structure is symmetric about an axis. For such symmetrical problems, 3-D field distribution is obtained from 2-D axisymmetric analysis since field quantities do not vary with ϕ direction. There is no single common axis even in single-phase transformers due to the planar nature of the core structure. If only the leakage field is of interest in a single-phase transformer (e.g., during a short-circuit test condition which results into a small amount of flux in the core), its windings can be modeled in the cylindrical system with one of the boundaries representing the core with a flux-normal condition. If, however, core conditions are also under investigation, the yoke geometry needs to be suitably modified for an accurate representation as demonstrated in [14].

The spherical system is perfectly suited for modeling fields radiating from a point source. This system has a limited number of applications in transformers. Although a spherical symmetry does not exist in the transformers, an analysis in spherical coordinates may form a part of initial studies undertaken for understanding partial discharge propagation inside a transformer.

Field quantities are classified as vectors or scalars. Scalars (e.g., voltage, temperature) are the quantities that can be denoted by just a number; they are independent of the coordinate system being used. Vectors (e.g., force, flux density, current density) are quantities that have magnitude as well as direction; their representation changes when a different coordinate system is used. For example, if the flux density at a point (3, 4, 5) in a Cartesian system is $1\mathbf{a}_x + 3\mathbf{a}_y + 5\mathbf{a}_z$, the corresponding points and the vector representation in the other two systems will be (5, 53.13°, 5) and $3.0\mathbf{a}_r + 1.0\,\mathbf{a}_\phi + 5\mathbf{a}_z$ (cylindrical system), and ($5\sqrt{2}$, 45°, 53.13°) and $5.66\mathbf{a}_r - 1.414\mathbf{a}_\theta + 1.0\,\mathbf{a}_\phi$ (spherical system). Here, the components in cylindrical and spherical systems are obtained by taking the dot product of the vector in a Cartesian system with the corresponding unit vectors in the two systems.

It should be noted that current flowing through a winding is a scalar quantity. However, the associated length vector $d\mathbf{l}$ takes care of the representation of the current direction. Thus, the current in any operation involving a dot or cross product is always accompanied by its corresponding length vector (e.g., force on a differential current element is given by $d\mathbf{F} = I\,d\mathbf{l}\times\mathbf{B}$). This brings us to the types of products involving vectors, which are discussed next.

Dot and cross products: Many times these products involve contours, surfaces, and volumes. A number of field variables are obtained by integrating the products over these geometrical entities. Volume is a scalar quantity, whereas contours and surfaces are vectors. A contour is a length vector; a surface has its area as the magnitude and the unit normal to it as the direction. Needless to say that for arbitrarily shaped contours or surfaces, the corresponding unique direction can be defined for each of their infinitesimal elements. A closed contour encloses an open surface, and a closed surface encloses a volume. Hence, in the divergence theorem, a volume integral is equivalent to a closed surface integral, and in Stokes' theorem an open surface integral is related to a closed contour integral. For a closed surface, the normal at any point on it is in the outward direction, whereas for an open surface the corresponding contour integral in conjunction with the right-hand rule decides its direction.

The result of a dot product is a scalar quantity. If $\mathbf{A}$ and $\mathbf{B}$ are two vectors, then the dot product is defined as $\mathbf{A}\cdot\mathbf{B}=|\mathbf{A}||\mathbf{B}|\cos\theta$ (i.e., the product of their magnitudes multiplied by the cosine of the smaller angle between them). If field distributions inside a transformer are known, various quantities of interest can be calculated, such as $\int \mathbf{B}\cdot d\mathbf{s}$ gives the flux crossing the surface $\mathbf{s}$, $-\int \mathbf{E}\cdot d\mathbf{l}$ gives the potential difference between two points calculated along the (open) contour $\mathbf{l}$, $\oint \mathbf{H}\cdot d\mathbf{l}$ gives the current enclosed by the (closed) contour $\mathbf{l}$, etc. If two vectors are orthogonal (perpendicular) to each other, their dot product is zero, whereas their interaction yields a maximum value when the angle between them is zero.

Along an equipotential line, the potential difference between any two points is zero, which is confirmed by the fact that $-\int \mathbf{E} \cdot d\mathbf{l}$ is zero (since **E** lines are orthogonal to equipotential lines), and the mutual flux through a cross section (surface) of the core, computed using $\int \mathbf{B} \cdot d\mathbf{s}$, is maximum since the angle between **B** (flux density) and $d\mathbf{s}$ is zero.

The cross (vector) product of **A** and **B** vectors, **A** × **B**, is a vector whose magnitude is the area of the parallelogram formed by them and is in the direction perpendicular to the plane containing the two vectors (the direction of the right thumb as the fingers of the right hand rotate from **A** to **B**), i.e., $\mathbf{A} \times \mathbf{B} = |\mathbf{A}||\mathbf{B}| \sin\theta \, \mathbf{a}_n$. Axial and radial forces in windings are calculated using the cross product $\mathbf{F} = \mathbf{J} \times \mathbf{B}$ as elaborated in Chapter 6.

Del operator: This operator is used to represent partial differentiations of scalars and vectors, as in the basic gradient, divergence and curl operations. It is defined in the Cartesian and cylindrical systems as

$$\nabla = \frac{\partial}{\partial x}\mathbf{a}_x + \frac{\partial}{\partial y}\mathbf{a}_y + \frac{\partial}{\partial z}\mathbf{a}_z \qquad \text{Cartesian system} \qquad (12.14)$$

$$\nabla = \frac{\partial}{\partial r}\mathbf{a}_r + \frac{1}{r}\frac{\partial}{\partial \phi}\mathbf{a}_\phi + \frac{\partial}{\partial z}\mathbf{a}_z \qquad \text{cylindrical system} \qquad (12.15)$$

Description of various operators used in the spherical system is not given in the text since the system is rarely used for analyzing transformers.

12.2.3 Gradient and electrical scalar potential

The gradient operator gives the maximum rate of change of a scalar field and the direction in which the maximum occurs; the outcome of the gradient operation is a vector. The gradient of an electric scalar potential (voltage) in Cartesian coordinates is defined as (the discussions in this text will be for Cartesian system unless specified otherwise),

$$\nabla V = \frac{\partial V}{\partial x}\mathbf{a}_x + \frac{\partial V}{\partial y}\mathbf{a}_y + \frac{\partial V}{\partial z}\mathbf{a}_z . \qquad (12.16)$$

The above equation resolves the gradient, in any arbitrary direction, along the corresponding coordinate axes.

It can easily be inferred that

$$\mathbf{E} = -\nabla V . \qquad (12.17)$$

This equation is valid for electrostatic systems. For time-varying fields, the equation has to be modified as explained later. The electric field intensity vector (**E**) is directed from a higher potential to a lower potential (**E** lines can be said to

originate from positive charges and terminate on negative charges). On the contrary, the *gradient* is from a lower potential to a higher potential (e.g., the gradient of a hill at a point is its upward slope at that point). Hence, it is logical that **E** is negative of ∇V. The integral form of the above equation is

$$V = -\int \mathbf{E} \cdot d\mathbf{l} \,. \tag{12.18}$$

The above equation can be used to calculate voltage drop along a contour. It is difficult to express an arbitrarily shaped contour in terms of a single vector and hence the contour can be approximated as being made of n segments. If i^{th} segment has the two end points as (x_{i1}, y_{i1}) and (x_{i2}, y_{i2}), this segment can be written in the vector form as $(x_{i2} - x_{i1})\mathbf{a}_x + (y_{i2} - y_{i1})\mathbf{a}_y$. Let the electric field at the segment location be $\mathbf{E}_i = E_{ix}\mathbf{a}_x + E_{iy}\mathbf{a}_y$. Then the voltage drop across the contour will be

$$-\sum_{i=1}^{n}\left[E_{ix}(x_{i2} - x_{i1}) + E_{iy}(y_{i2} - y_{i1})\right].$$

Consider an equipotential surface (like any electrode surface inside a transformer). A position vector $d\mathbf{P}$ joining two points on it can be expressed as $dx\,\mathbf{a}_x + dy\,\mathbf{a}_y + dz\,\mathbf{a}_z$. For the equipotential surface,

$$dV = 0 = \frac{\partial V}{\partial x}dx + \frac{\partial V}{\partial y}dy + \frac{\partial V}{\partial z}dz$$

$$\therefore 0 = \nabla V \cdot d\mathbf{P} \,.$$

The dot product is zero implying that the two vectors are orthogonal. Therefore, ∇V, and therefore **E** is along the normal direction to the equipotential surface. Thus, **E** lines are always perpendicular to any equipotential surface. If $\mathbf{a}_n$ is the unit vector in the normal direction, the gradient has the maximum component along it (since both are in the same direction). Hence, the maximum rate of change of the voltage $(\partial V/\partial n = \nabla V \cdot \mathbf{a}_n)$ at any point on an equipotential surface is in the direction of the normal at that point.

One of the applications of the dot product is that we can determine the component of a vector in a particular direction, by taking the dot product of the vector with the unit vector in that direction. For example, the component of $\mathbf{E}_i$, as defined above along the x direction is given by $\mathbf{E}_i \cdot \mathbf{a}_x$ which results in the scalar quantity E_{ix}. This mathematical operation is particularly useful for finding creepage stress along the surface of an insulating component.

12.2.4 Divergence

Divergence gives the net outflow of flux from a closed surface per unit volume as the volume shrinks to zero. The divergence of field **A** at point *P* in Cartesian coordinates is defined as

$$\nabla \cdot \mathbf{A} = \frac{\partial A_x}{\partial x} + \frac{\partial A_y}{\partial y} + \frac{\partial A_z}{\partial z} \tag{12.19}$$

and in cylindrical coordinates it is given as

$$\nabla \cdot \mathbf{A} = \frac{1}{r}\frac{\partial}{\partial r}(rA_r) + \frac{1}{r}\frac{\partial A_\phi}{\partial \phi} + \frac{\partial A_z}{\partial z}. \tag{12.20}$$

Let us prove the equivalence of divergence in different coordinate systems. Consider a vector function

$$\mathbf{D} = \frac{1}{x}\left\{ y\mathbf{a}_x + y^2\mathbf{a}_y + (zx - y)\mathbf{a}_z \right\}.$$

To express the same function in cylindrical coordinates we need to obtain D_r, D_ϕ and D_z. This can be done by determining the component of **D** in the r, ϕ and z directions, for which we have to take the dot product of **D** with $\mathbf{a}_r, \mathbf{a}_\phi$ and $\mathbf{a}_z$ [1]. Thus, we obtain in the cylindrical system

$$\mathbf{D} = \left(\sin\phi + r\sin^2\phi\tan\phi\right)\mathbf{a}_r + \left(-\sin\phi\tan\phi + r\sin^2\phi\right)\mathbf{a}_\phi + \left(z - \tan\phi\right)\mathbf{a}_z.$$

Similarly, **D** can be converted into spherical coordinates. Thus, **D** expressions are different in various coordinate systems. Using Equations 12.19 and 12.20, we obtain the expressions for divergence in the Cartesian and cylindrical coordinate systems as

$$\nabla \bullet \mathbf{D}_{Cartesian} = -\frac{y}{x^2} + \frac{2y}{x} + 1$$

$$\nabla \bullet \mathbf{D}_{cylindrical} = \frac{1}{r}\left\{ \begin{array}{l} \sin\phi + 2r\sin^2\phi\tan\phi - \sin\phi\sec^2\phi - \cos\phi\tan\phi \\ +2r\sin\phi\cos\phi \end{array} \right\} + 1.$$

Note that these expressions are equivalent and each one can be transformed into another by standard formulae. Now, consider a point P (3, 4, 5) in Cartesian co-ordinates. Its coordinates in the cylindrical system are (5, 53.13°, 5). $\nabla \cdot \mathbf{D}$ calculated at P using the above two expressions comes out to be the same (= 3.22) as it ought to be!

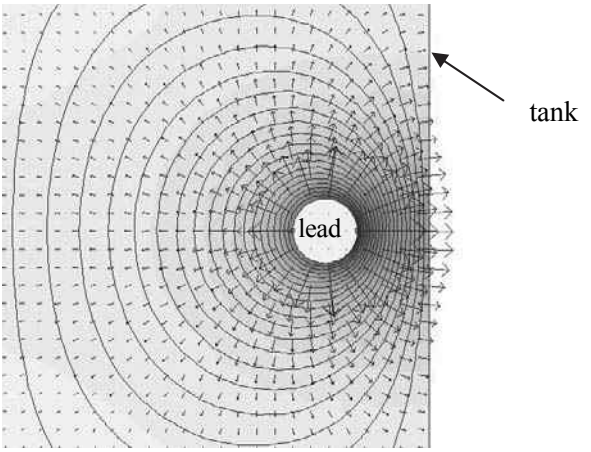

Figure 12.1 Electric field between high voltage lead and tank.

Now, let us understand the first Maxwell's equation, $\nabla \cdot \mathbf{D} = \rho_v$. The units of ∇, **D** and ρ_v are m $^{-1}$, C m^{-2}, and C m^{-3}, respectively. We know that the lines of **E** (and **D**) fields originate from positive charges and terminate on negative charges. Thus, if we consider a small volume around a positive charge, since one line will originate from it and end on a negative charge somewhere else (since for every charged particle there always exists an oppositely charged particle), the divergence of the field will be positive at the point where the positive charge exists. Non-zero divergence at a point indicates existence of a *flow source* which can be either positive or negative.

In transformers, the divergence is non-zero at many points. For example, consider the electric field between a high voltage lead and a tank plate in a transformer as shown in Figure 12.1, which is analyzed as an electrostatic field (at an instant when the voltage difference between them is maximum). The **E** lines (shown by arrows) are perpendicular to the equipotential lines. The lead is taken as a bare one for simplicity. It is known that the electric field intensity inside a good conductor is practically zero; for very high conductivity (i.e., negligible resistance) the voltage drop between any two points within the conductor is close to zero. When the lead is positive with respect to the tank, for every **E** line emanating from the lead and terminating on the tank, we can associate a positive divergence on the lead and a negative divergence on the tank (and vice versa when the lead is at negative potential in the next half cycle). Since the insulation between the two electrodes does not have any charges (it is considered as ideal with only bound charges), the divergence of the electric field at any point in it is zero. The electric field lines crossing the insulation from the lead to the tank pass through all such points; however, no new line emanates from these points.

The origin of the electric and magnetic fields is the electric charge. Charges at rest lead to electrostatic fields, which may exist in the transformers under only special conditions, e.g., static electrification (refer to Chapter 9). Moving charges at constant velocity (DC currents) result into steady magnetic fields, which again are not common in the transformers except under specific circumstances, e.g., DC magnetization of the core, which may happen due to rectifier loads, geomagnetic disturbances, the transient DC component in inrush currents, etc. Accelerated charges are responsible for time-varying electric and magnetic fields. For example, time-varying acceleration of charges from a source to a load results in a sinusoidal current rising from zero (maximum acceleration) to its peak value (zero acceleration) in the first quarter of each cycle.

There are principally two types of charges: the free charges (electrons) that constitute current in conductors and the bound charges in insulating materials. It should be noted that the volume charge density appearing in the first Maxwell's equation, $\nabla \cdot \mathbf{D} = \rho_v$, is on account of free charges. We will discuss the bound charges later while understanding the polarization phenomenon in dielectrics. In the electrostatic field plot of Figure 12.1, the lines of **D** or **E** field originate or terminate on the free charges which reside on the electrode surfaces. Applying the divergence theorem, we have

$$\int_v \nabla \cdot \mathbf{D}\, dv = \oint_s \mathbf{D} \cdot d\mathbf{s}\,. \tag{12.21}$$

However,

$$\int_v \nabla \cdot \mathbf{D}\, dv = \int_v \rho_v\, dv = Q$$

$$\therefore \oint_s \mathbf{D} \cdot d\mathbf{s} = Q \tag{12.22}$$

which is the Gauss law. Since **D** has only the normal component (D_n) at the conductor surface, it is straightforward to derive the relation $D_n = \rho_s$ from the Gauss law [1] where ρ_s is the surface charge density.

The second Maxwell's equation, $\nabla \cdot \mathbf{B} = 0$, also involves a divergence operation. It means that the magnetic field lines (**B**, **H**) always close on themselves; no magnetic monopoles exist. Since, from any point in the field, no line originates, its divergence is always zero. If we now apply the divergence theorem to the equation, we obtain

$$\int_v \nabla \cdot \mathbf{B}\, dv = 0 = \oint_s \mathbf{B} \cdot d\mathbf{s}\,. \tag{12.23}$$

Thus, it should be noted that, while the closed surface integral of $\mathbf{B} \cdot d\mathbf{s}$ is always zero to satisfy the divergence-free condition, the open surface integral of

$\mathbf{B} \cdot d\mathbf{s}$ yields the flux crossing the open surface as discussed during the explanation of the dot product. If we assume a small cube around a point with the magnetic field directed normally to any of the two opposite sides, the remaining four sides will not contribute to the closed surface integral (since **B** and $d\mathbf{s}$ are orthogonal) and the contributions of the two opposite sides will be equal but opposite in sign (since the unit normal vectors on the two sides are the corresponding outward vectors which have opposite directions). Thus, the closed surface integral is always zero.

It must be emphasized that the first two Maxwell's equations are valid for time-varying fields. **B** and **D** vectors can in general be a function of time.

12.2.5 Curl

The curl is a measure of circulation of a vector field. The curl of a vector field is a vector; it may be interpreted as the circulation per unit area. Circulation is a concept from fluid dynamics, and it measures the ability of the field to rotate. Mathematically, it is determined as

$$\nabla \times \mathbf{A} = \begin{vmatrix} \mathbf{a}_x & \mathbf{a}_y & \mathbf{a}_z \\ \dfrac{\partial}{\partial x} & \dfrac{\partial}{\partial y} & \dfrac{\partial}{\partial z} \\ A_x & A_y & A_z \end{vmatrix}. \tag{12.24}$$

The concept of the curl can be understood from Equation 12.4. There are two vortex sources, the conduction current density, **J**, and the displacement current density, $\partial \mathbf{D}/\partial t$, that give rise to circulation of the **H** field. There is a separate discussion on the current densities later. Let us assume that we are dealing with a low frequency electromagnetic phenomenon ($\omega\varepsilon << \sigma$) allowing us to neglect $\partial \mathbf{D}/\partial t$. This gives us Ampere's law in differential form,

$$\nabla \times \mathbf{H} = \mathbf{J}. \tag{12.25}$$

By taking the surface integral on both sides,

$$\int_s (\nabla \times \mathbf{H}) \cdot d\mathbf{s} = \int_s \mathbf{J} \cdot d\mathbf{s}.$$

And applying Stokes' theorem to the left side of the above equation, we obtain

$$\oint_l \mathbf{H} \cdot d\mathbf{l} = I. \tag{12.26}$$

This is Ampere's law in its integral form, a very useful equation in comprehending field distributions in transformers. The leakage field plot in Figure 3.1(a) can be understood with the help of Equation 12.26. The field plot

corresponds to a balanced ampere-turns condition; LV and HV ampere-turns are equal and opposite, which amounts to neglecting the magnetization current (which is much smaller than the rated current flowing in the windings during the short-circuit test condition as elaborated in Section 1.5). Since the net ampere-turns enclosed in the core window are zero, we find that there is not a single flux contour enclosing both the windings, which is in agreement with Equation 12.26 (it should be understood that I in the equation corresponds to ampere-turns when multiple turns are involved). If $\mathbf{H} \cdot d\mathbf{l}$ is integrated along any contour in the core region encircling both the windings, we can surmise from the plot that the result of the integration would be zero (there are two sets of lines; one set of lines enclosing LV turns are in the counterclockwise direction while the other set of lines enclosing HV turns are in the clockwise direction in the core region).

I, in Equation 12.26, is a vortex source which is responsible for creating circulation (vortex) of the **H** field around it, with decreasing magnitude of the field away from the source. The circulation of the **H** field, i.e., $\oint \mathbf{H} \bullet d\mathbf{l}$, is maximum in planes perpendicular to the current direction. Since the magnitude of the **H** field, as shown in Figure 12.2 for an infinitely long filamentary current I along the z-axis, is constant on any circular contour, we choose a circular path for simplifying the integration. Since this path encloses the whole current, in cylindrical coordinates

$$\int H_\phi \mathbf{a}_\phi \cdot r d\phi \mathbf{a}_\phi = H_\phi r \int d\phi = 2\pi r H_\phi \;\Rightarrow\; \mathbf{H} = \frac{I}{2\pi r}\mathbf{a}_\phi . \tag{12.27}$$

This expression tells us that the value of field reduces as we go away from the current source. This is analogous to the case of diminishing waves that originate from a point where a stone is vertically dropped in a pond of water. Equation 12.27 is sometimes useful to determine an approximate value of the **H** or **B** field near a current carrying lead inside a transformer. However, the presence of a metallic object or a boundary in its vicinity and a significant deviation of the current source from the ideal filamentary nature introduce errors in the calculation.

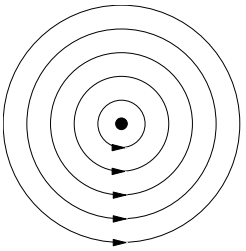

Figure 12.2 Magnetic field due to a line current source.

The curl operator appears in another Maxwell's equation, $\nabla \times \mathbf{E} = -\dfrac{\partial \mathbf{B}}{\partial t}$, which is in fact the most important one from the point of view of understanding the working principle of transformers. It is point or differential form of Faraday's law of electromagnetic induction. Here the vortex source, $-(\partial \mathbf{B}/\partial t)$, is a time varying field. It causes the circulation of the **E** field around it. Here again, as in the case of the previous curl equation, the concept is better understood in the integral form of the equation (Faraday's law). Taking the surface integral,

$$\int_s (\nabla \times \mathbf{E}) \cdot d\mathbf{s} = \int_s \left(-\frac{\partial \mathbf{B}}{\partial t} \right) \cdot d\mathbf{s} \,. \tag{12.28}$$

For a static device such as a transformer, ***s*** does not change with time,

$$\int_s \frac{\partial}{\partial t} (\mathbf{B} \cdot d\mathbf{s}) = \int_s \left[\left(\frac{\partial \mathbf{B}}{\partial t} \right) \cdot d\mathbf{s} + \mathbf{B} \cdot \left(\frac{\partial \mathbf{s}}{\partial t} \right) \right] = \int_s \left(\frac{\partial \mathbf{B}}{\partial t} \right) \cdot d\mathbf{s} \,.$$

Hence, Equation 12.28 can be rewritten as

$$\int_s (\nabla \times \mathbf{E}) \cdot d\mathbf{s} = -\int_s \frac{\partial}{\partial t} (\mathbf{B} \cdot d\mathbf{s}) \,.$$

Since the partial derivative with respect to time and the surface integration are two independent operations, we can interchange them:

$$\int_s (\nabla \times \mathbf{E}) \cdot d\mathbf{s} = -\frac{\partial}{\partial t} \int_s \mathbf{B} \cdot d\mathbf{s} = -\frac{\partial \phi}{\partial t} \,.$$

And applying Stokes' theorem to the left hand side of the above equation, we have

$$\oint_l \mathbf{E} \cdot d\mathbf{l} = -\frac{\partial \phi}{\partial t} \,. \tag{12.29}$$

However, $\oint_l \mathbf{E} \cdot d\mathbf{l}$ is an electromotive force (an induced voltage *e*). Thus, we obtain Faraday's law (for a single turn case) as

$$e = -\frac{\partial \phi}{\partial t} \,.$$

For *N* turns, the law becomes

$$e = -N\frac{\partial \phi}{\partial t}\,. \tag{12.30}$$

The minus sign is in accordance with Lenz's law which states that the direction of the induced emf is such that the flux generated by the induced current opposes the change in the flux, and this is the field viewpoint (see Section 1.3.1); in the circuit viewpoint the minus sign is dropped, and using the expression $L = N\phi/i$, the corresponding induced voltage (drop) is written as $e = L\,di/dt$ which opposes the applied time-varying voltage in the circuit.

The Maxwell's equation under discussion and its integral form (Equations 12.3 and 12.29, respectively) describe nonconservative fields; work is done in carrying a charge around a closed path in them and it is dependent on the path traversed. For a given changing magnetic field the polarity of the voltage induced in an encircling loop depends on whether the loop in traversed in the clockwise or counterclockwise direction. Hence, the polarity of the voltage induced in a transformer coil reverses if the direction of winding it is reversed. For the star-connected LV and HV windings in a transformer, if they are wound in opposite directions the vector group obtained is Yy6 instead of Yy0.

The net induced voltage in a closed path is due to the work done by the time-varying field. Contrary to this, in an electrostatic field, no work is done when a charge is taken around a closed path. In the field plot of Figure 12.1, $\oint \mathbf{E}\cdot d\mathbf{l}$ is zero for any closed path since it is an electrostatic field distribution. The dot product $\mathbf{E}\cdot d\mathbf{l}$ along any contour gives the potential difference between its two end points. However, if the contour is a closed one, we come back to the same point from where we started the integration and the potential difference has to be zero. Also, the calculated potential difference between any two points in an electrostatic field is independent of the path of integration. Let us consider a closed contour in an electrostatic field, as shown in Figure 12.3.

$$\int_{C_1} \mathbf{E}\cdot d\mathbf{l} + \int_{C_2} \mathbf{E}\cdot d\mathbf{l} = 0 \quad \text{or} \quad \int_{P_1}^{P_2} \mathbf{E}\cdot d\mathbf{l} \text{ along } C_1 + \int_{P_2}^{P_1} \mathbf{E}\cdot d\mathbf{l} \text{ along } C_2 = 0 \quad \text{or}$$

$$\int_{P_1}^{P_2} \mathbf{E}\cdot d\mathbf{l} \text{ along } C_1 = -\int_{P_2}^{P_1} \mathbf{E}\cdot d\mathbf{l} \text{ along } C_2\,.$$

$$\therefore \int_{P_1}^{P_2} \mathbf{E}\cdot d\mathbf{l} \text{ along } C_1 = \int_{P_1}^{P_2} \mathbf{E}\cdot d\mathbf{l} \text{ along } C_2\,. \tag{12.31}$$

Thus, the line integral between any two points in electrostatic fields is independent of the path of the integration. In electrostatic fields, we associate the result of the integration to the corresponding potential difference. On the other hand, in the presence of a time-varying field, the integration in the encircling loop is said to give an induced voltage.

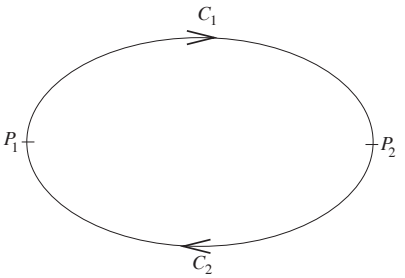

Figure 12.3 Contour integral in an electrostatic field.

For the time-varying case, using Equation 12.29, we obtain for the same closed contour,

$$\int_{P_1}^{P_2} \mathbf{E} \cdot d\mathbf{l} \text{ along } C_1 - \int_{P_1}^{P_2} \mathbf{E} \cdot d\mathbf{l} \text{ along } C_2 = -\frac{\partial \phi}{\partial t}. \tag{12.32}$$

Imagine a conducting wire in the place of the loop such that the two ends of the wire are very close but insulated from each other. The voltage induced in this wire will correspond to one turn voltage according to the emf equation of the transformer (Section 1.3.1). The two voltages in the left side of the above equation will be equal and opposite in sign giving the one turn voltage as required by the right hand side. The above example also proves that the induced voltage calculated between any two points in a time-varying field is a function of the path of integration.

What happens to the induced voltage in a short-circuited wire-loop in a time-varying field? If we measure the voltage across any two points of the wire-loop, it will be zero. The induced voltage is balanced by the corresponding resistive drop. The leakage inductance of the short-circuited wire-loop is negligible since it is a one-turn coil with a thin cross section.

12.2.6 Current densities and continuity equation

The rate of flow of electric charges is termed as *current*. However, a more fundamental field perspective is *current density*. The general notion that currents are governed by Ohm's law is not always true. There are three types of current densities: conduction, convection and displacement.

Until now we have discussed only one type of current density, i.e., the conduction current density (**J**). The conduction current in a conductor is due to flow of charges caused by the applied field and is governed by Ohm's law. The conduction current density is given by Equation 12.7, i.e., $\mathbf{J} = \sigma\mathbf{E}$. This is also known as the differential or point form of Ohm's law. When this is extended to conductor geometry it leads to the more familiar integral form of Ohm's law i.e.,

$V = IR$. Needless to say, the conductors of transformer windings have only the conduction current in them.

The term convection is derived from thermodynamics. As the name suggests the convection current is set up due to flow or motion of charges, but it is not governed by Ohm's law. It does not involve conductors and it flows through an insulating medium or vacuum. The convection current density is given by

$$\mathbf{J} = \rho_v \mathbf{v} . \tag{12.33}$$

Here ρ_v is the volume charge density and $\mathbf{v}$ is the velocity of the charges. In oil insulated and cooled transformers, charges generated in oil (e.g., due to a static electrification phenomenon as described in Chapter 9) can move under natural buoyancy condition or due to pump action, resulting in a convection current density. If applicable, $\mathbf{J}$ in Equation 12.4 accounts for both conduction and convection current densities.

We need to understand the continuity equation as highlighted in Section 12.2.1, before discussing the displacement current density. The equation is based on the law of conservation of charge [1]. If we start with the point form of Ampere's law and take the divergence of each side,

$$\nabla \cdot \nabla \times \mathbf{H} = 0 = \nabla \cdot \mathbf{J} . \tag{12.34}$$

Thus, $\nabla \cdot \mathbf{J}$ needs to have zero value since the divergence of the curl is always zero. However, this condition is in contradiction with the continuity equation which requires that $\nabla \cdot \mathbf{J}$ must be equal to $-\partial \rho_v / \partial t$ for time-varying fields. Thus, Ampere's law is not consistent with the continuity equation. Maxwell resolved this ambiguity by introducing a new term, the displacement current density, $\partial \mathbf{D} / \partial t$, which finally led to Equation 12.4 which can be shown to satisfy the continuity equation [1, 2]. The additional term $\partial \mathbf{D} / \partial t$ can easily be correlated to the term $-\partial \rho_v / \partial t$ in the continuity equation. Without displacement current density, propagation of electromagnetic waves and currents flowing through capacitors cannot be explained. In transformers, the term becomes indispensible when partial discharge propagation needs to be analyzed for monitoring and diagnostics purposes. Capacitors are an inherent part of any lumped equivalent circuit used for analyzing the response of transformers subjected to high frequency transients. Although, the displacement current density does not explicitly appear in these lumped circuit analyses, it should be remembered that the currents flowing through the capacitors (insulators) can be comprehended only by using it. For alternating currents, the plates of capacitors get alternately charged with positive and negative charges leading to a non-zero $\partial \mathbf{D} / \partial t$ term which becomes increasingly significant as the frequency increases ($\partial / \partial t$ becomes $j\omega$ in the time-harmonic analysis involving sinusoidally varying

quantities). Let us see the implication of the continuity equation in the lumped equivalent circuit representation of a transformer winding, shown in Figure 7.17. It should be remembered that the continuity equation is the point or differential form of Kirchhoff's current law (KCL). Conduction currents flow in the conductors (i.e., resistors and inductors). Through the series and shunt capacitances, displacement currents flow satisfying the continuity equation and KCL at every node.

12.2.7 Fields in materials

After having understood Maxwell's equations and the continuity equation, let us now discuss the remaining two constitutive relationships, viz. $\mathbf{D} = \varepsilon \mathbf{E}$ and $\mathbf{B} = \mu \mathbf{H}$; the first constitutive relationship $\mathbf{J} = \sigma \mathbf{E}$ has already been discussed. Various types of materials are used in transformers, whose material properties widely differ from each other and from that of the free space.

A. Dielectric materials

The dielectric constant of any insulating (dielectric) medium is a function of polarizability. In the absence of any field, the atoms of a material are unpolarized; i.e., the centers of the positive charge (nucleus) and the negative charge (orbiting electrons) coincide. When an electric field is applied, the two centers are separated by a small distance forming an electric dipole. A polarized dielectric slab is shown in Figure 12.4 (a) [15]. Any electric field is directed from a higher (positive) to a lower (negative) potential. Hence, the positive charges shift in the direction of the field and the negative charges in the opposite direction, forming many atomic dipoles in the slab. The positive and negative charges of adjacent dipoles cancel each other's effect giving a net polarization which produces a layer of positive charges on one surface and a layer of negative charges on the other, as shown in Figure 12.4 (b). These surface charges are of bound type; they do not have sufficient energy to leave the dielectric medium (they can get liberated in exceptional or abnormal conditions due to an excessive electric field, heating, friction, or any combination of these). Having understood the polarization, now consider a parallel-plate capacitor with a certain potential difference between its plates as shown in Figure 12.4 (c). It has free-space medium in which we have a field distribution defined by,

$$\mathbf{D} = \varepsilon_0 \mathbf{E} . \tag{12.35}$$

When a depolarized dielectric slab is now introduced between the plates, it is polarized due to the electric field within the plates of the capacitor and the (bound) surface charges induce additional free charges of opposite polarity on the plates as shown in Figure 12.4 (d) with bold font.

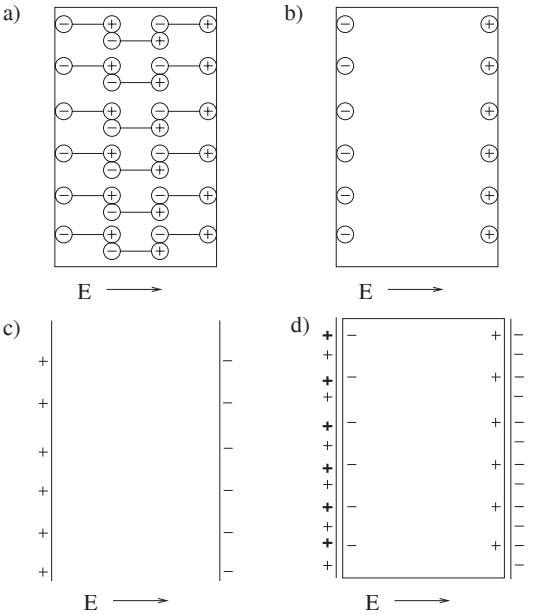

Figure 12.4 Dielectric material.

It should be noted that the plates, being good conductors, have abundant free charges; the induced negative charges, for example, will repel a few more free electrons making the left hand side plate more positively charged. For a given applied voltage, the surface charges will increase with an increase in the capacitance between the plates. The electric flux density vector, **D**, increases; new field lines of the vector will originate from the induced positive charges on the left side plate and terminate on the induced negative charges of the other plate. The increase is a function of polarizability of the material expressed by the polarization vector (**P**),

$$\mathbf{D} = \varepsilon_0 \mathbf{E} + \mathbf{P} \,. \tag{12.36}$$

For isotropic and linear dielectrics, since **P** is linearly related to **E**, it can be expressed as

$$\mathbf{P} = \chi_e \varepsilon_0 \mathbf{E}$$

where χ_e is called the electric susceptibility of the material, which is a dimensionless quantity. Putting this expression in Equation 12.36, we obtain

$$\mathbf{D} = \varepsilon_0 \mathbf{E} + \chi_e \varepsilon_0 \mathbf{E} = (\chi_e + 1)\varepsilon_0 \mathbf{E} = \varepsilon_r \varepsilon_0 \mathbf{E} = \varepsilon \mathbf{E} \tag{12.37}$$

where $\varepsilon_r = (\chi_e + 1)$ is called the relative permittivity or the dielectric constant of the material. It can be said that the dielectric constant of an insulating medium is a direct measure of its charge-storing capability. In transformers, the dielectric constant of solid insulation is about twice that of mineral oil; this is indicative of the fact that the electric susceptibility of the former is greater than the latter. $\varepsilon (= \varepsilon_r \varepsilon_0)$, called the permittivity, is a scalar, which is the case for the commonly used dielectric materials in transformers, such as oil, pressboard, fiberglass and epoxy (in ferroelectric materials, the relationship between **P** and **E** is nonlinear as well as hysteretic, making ε a nonscalar quantity). The use of relative permittivity, ε_r, as defined by Equation 12.37, renders the consideration of bound charges and polarization unnecessary in most of the (field) computations in transformers involving the dielectric materials. Since the dielectric materials used in the transformers do not exhibit hysteretic behavior, no energy is lost on account of it. This is in sharp contrast with the hysteresis losses that occur in the core and structural components made from ferromagnetic steel, as explained later.

Equation 12.4 in a time-harmonic form becomes,

$$\nabla \times \mathbf{H} = \mathbf{J} + j\omega\varepsilon_0\varepsilon_r \mathbf{E} = (\sigma + j\omega\varepsilon_0\varepsilon_r)\mathbf{E} .$$

The above equation can be rewritten as

$$\nabla \times \mathbf{H} = j\omega\varepsilon_0 \left(\varepsilon_r - j\frac{\sigma}{\omega\varepsilon_0} \right) \mathbf{E} .$$

Thus, dielectric losses on account of moisture and other (conducting) impurities make the dielectric constant (relative permittivity) a complex quantity, i.e., $\hat{\varepsilon}_r = \varepsilon_r' - j\varepsilon_r''$. The permittivity expression becomes,

$$\hat{\varepsilon} = \varepsilon_0 \left(\varepsilon_r - j\frac{\sigma}{\omega\varepsilon_0} \right). \tag{12.38}$$

The real part ε_r' equals ε_r, and the imaginary part $\varepsilon_r'' (= \sigma/\omega\varepsilon_0)$ is called a loss factor or loss index which is frequency-dependent. Thus, the imaginary part represents the dielectric loss (this is in contrast with the representation of an impedance in a circuit, in which the real component, *R*, represents losses). The complex permittivity is temperature-dependent as well since the electrical conductivity of the insulation is a function of temperature. The dissipation factor or loss tangent is defined as

$$\tan\delta = \frac{\varepsilon''}{\varepsilon'} = \frac{\varepsilon_r''}{\varepsilon_r'} = \frac{\sigma}{\omega\varepsilon_0\varepsilon_r} .$$

Dielectric materials are equivalently represented as a parallel combination of R and C for circuit analysis. For an ideal (lossless) dielectric material, $\sigma = 0$, making it a purely capacitive circuit element whose dielectric constant becomes a real number. The losses in a practical dielectric material increase with an increase in its conductivity (moisture) and temperature, and the frequency of the applied voltage. Insulating materials have a negative temperature coefficient of resistance; the resistive element of the R-C representation reduces with an increase in their temperature, leading to a higher (leakage) current through the resistor and the loss increases.

When an alternating voltage having rms value V and frequency ω is applied across a dielectric material, represented by an equivalent R-C circuit, the dielectric loss is given by

$$P = \omega C V^2 \tan\delta . \tag{12.39}$$

The real and imaginary parts of the complex permittivity vary as a function of frequency. Understanding the frequency-dependence of the dielectric constant is necessary for a diagnostic tool known as frequency domain spectroscopy as discussed in Section 14.6.

The dielectric constant of mineral oil is generally expressed in the form given by Equation 12.38,

$$\left(\hat{\varepsilon}_r\right)_{oil} = 2.2 - j\frac{\sigma}{\omega\varepsilon_0}$$

where the real part has been substituted by its usual dielectric constant, i.e., 2.2. It means that the real part is taken as independent of the frequency for the oil. On the other hand, the expression for paper and pressboard insulations cannot generally be expressed in such a simple form. Because of various intricate polarization processes, more elaborate models are employed; the expression becomes more complicated with both real and imaginary components exhibiting frequency-dependent behavior (see Section 14.6.3). For the paper/pressboard insulation, the imaginary component is generally much lower than the real component except if the moisture is unacceptably high.

Insulation systems used in most high voltage equipment including transformers are of multi-dielectric nature. As explained in Section 12.2.1, the Maxwell's equations in the integral form are used to derive the relationships between the field vectors on both sides of a dielectric-dielectric interface. The application of the integral form of a curl equation to a closed path and of a divergence equation to a shallow pillbox, at the interface, gives the boundary condition for the tangential components and the normal components, respectively, of the field vectors. The application of Equations 12.12 and 12.10 yields, for an interface between two dielectrics (denoted by 1 and 2), the following boundary conditions for the tangential components and the normal components, respectively [1, 2],

$$E_{1t} = E_{2t} \tag{12.40}$$

and

$$D_{1n} - D_{2n} = \rho_s$$

where ρ_s is the free surface charge density. Generally, the free charges do not exist at the interface (unless deliberately placed) yielding $D_{1n} = D_{2n}$ which can be written in the following form

$$\frac{E_{1n}}{E_{2n}} = \frac{\varepsilon_2}{\varepsilon_1} = \frac{\varepsilon_{r2}}{\varepsilon_{r1}}. \tag{12.41}$$

Equations 12.40 and 12.41 tell us that the tangential electric field is continuous and the normal electric field is discontinuous, respectively, across the interface between two dielectrics. It is clear from Equation 12.41 that, for an oil-pressboard interface in transformers, the normal component **E** is nearly double in the oil as compared to that in the solid, at the interface, since $\varepsilon_{pressboard} \cong 2\varepsilon_{oil}$. Furthermore, since the dielectric strength of the pressboard is much higher than that of the oil, the design of the oil-pressboard insulation systems mainly involves proper dimensioning of the oil ducts, as elaborated in Chapter 8. On similar lines, since the dielectric constant of the oil is about twice that of air, higher stresses appearing across air bubbles, if present, lead to partial discharges which can deteriorate the insulation strength considerably. It should be stated here that, for a single dielectric between two electrodes, the electric field (stress) distribution is independent of its dielectric constant, although the breakdown strength depends on its properties.

The boundary conditions can be derived in the same way for a conductor-dielectric interface using the fact that no fields (either electric or magnetic) can exist within perfect conductors; the fields in the dielectric (medium 2) will be

$$D_{2t} (\text{and } E_{2t}) = 0 \quad \text{and}$$

$$D_{2n} = \varepsilon_2 \; E_{2n} = \rho_s .$$

The tangential component of **E** is zero along any equipotential surface, which requires the corresponding tangential component in the dielectric medium to have zero value, due to the continuity condition above for a conductor-dielectric interface. Thus, these conditions reinforce the discussion in Section 12.2.4 on the characteristics that the electric flux (**E**) is normal to the surface of (perfect) conductors and the value of the electric flux density (**D**) is equal to the surface charge density. The energy in an electric field is given by

$$W_E = \frac{1}{2}\int_v \mathbf{D}\cdot\mathbf{E}\, dv = \frac{1}{2}\int_v \varepsilon E^2 \, dv . \tag{12.42}$$

It should be noted that $(1/2)\varepsilon E^2$ is the energy density, J m^{-3}. Based on the earlier discussion on polarization, the energy can also be expressed as

$$W_E = \frac{1}{2}\int_v \varepsilon_0 \varepsilon_r E^2 \, dv = \frac{1}{2}\int_v \varepsilon_0 E^2 \, dv + \frac{1}{2}\int_v PE \, dv \, . \tag{12.43}$$

The energy density in the dielectric, $(1/2)PE$, is on account of the polarization phenomenon; this energy can be likened to the way energy is stored in a stretched spring (the work is done by the electric field in polarizing the dielectric). The stored energy increases by ε_r times after a dielectric is introduced in free space.

B. Magnetic materials

Magnetic materials can be broadly classified into three major groups: diamagnetic, paramagnetic, and ferromagnetic, depending upon their relative permeability (μ_r) values; materials from each of these groups are commonly used in transformers. Although the differences in behavior of these various types of materials in magnetic fields can be comprehensively explained using quantum theory, we will analyze them briefly through a simple atomic model. An electron orbiting around a nucleus is equivalent to a tiny current loop, with the current direction being opposite to that of the electron motion. It is a type of bound current, denoted by I_b, which is said to establish a magnetic dipole moment, **m**, while circulating around a closed path enclosing a differential area $d\mathbf{s}$,

$$\mathbf{m} = I_b d\mathbf{s} \qquad \text{(A-m}^2\text{)}. \tag{12.44}$$

The orbiting electron experiences a torque (**T**) in an external magnetic field (**B**), which tends to align the magnetic field produced by the loop with the external field,

$$\mathbf{T} = \mathbf{m} \times \mathbf{B} \qquad \text{(N-m)}. \tag{12.45}$$

The other two types of spins are electron spin and nuclear spin, with the corresponding bound currents and magnetic moments, related by Equation 12.44. However, the magnetic moment due to the nuclear spin is negligible as compared to the orbital and spin magnetic moments.

In diamagnetic materials, the intrinsic magnetic moment of each atom is zero since the orbit and spin magnetic moments cancel each other completely in the absence of an external magnetic field. However, under the action of a field, the spin moment exceeds slightly the orbital moment [15], resulting in a small net moment that opposes the applied field; hence, we have relative permeability which is less but very close to 1 in diamagnetic materials. Copper is such a material with the value of μ_r as 0.999991. Thus, a copper specimen will be repelled if brought closer to a bar magnet.

In paramagnetic materials, the two moments do not cancel each other, resulting in a net moment for the atom even in the absence of an external field. However, due to random orientation of the atoms, the materials have no overall magnetic moment. When an external field is applied, the torques acting on the atomic dipoles tend to align them along the field, giving a higher field magnitude inside the material as compared to the applied field. However, this increase is negligibly small, resulting in μ_r little higher than 1; aluminum is a paramagnetic material having μ_r of 1.00000065. Hence, it is attracted, although very weakly, to magnets. For practical purposes, both copper and aluminum are considered as nonmagnetic materials with μ_r of 1.0. It should, thus, be reemphasized that although copper and aluminum are good electrical conducting materials, their magnetic property is as bad as that of air.

In ferromagnetic materials, due to interatomic interactions in their crystal lattice, the moments of a large number of atoms get aligned in a direction forming magnetic domains. Due to random orientations of the domains, the net magnetic moment of a ferromagnetic material is zero. However, when an external field is applied, the domains oriented along the field direction grow at the expense of their neighbors, increasing substantially the internal magnetic field. This property gives the ferromagnetic materials a substantially higher value of permeability as compared to the other two types of materials. When the applied field is removed, an entirely random orientation of the domains is not achieved, and therefore a residual field remains in the material. Also, the state of the material is dependent on its magnetic history, leading to hysteretic properties which have been elaborately discussed in Chapter 2 while describing the nature of the *B-H* curve of the core material (CRGO steel) which is of ferromagnetic type.

Ferrites fall under another category of materials known as ferrimagnetic substances, in which the moments of adjacent atoms are unequal and oriented in opposite directions giving a net magnetic moment which is less as compared to that in the ferromagnetic materials. However, they have higher resistivity and therefore lower induced eddy currents, which makes them suitable for use in small high frequency transformers used for power electronic applications.

Having understood qualitatively the behavior of the commonly used magnetic materials in the transformers, we will now quantify the contribution of magnetic diploes as a distributed source of the field. The magnetization vector, **M**, can be defined as the magnetic dipole moment (**m**) per unit volume. Since **m**, as defined in Equation 12.44 has the unit of A-m^2, the unit of **M** is A/m. The additional magnetic field contributed by the bound currents (corresponding to orbital, spin and nuclear moments) is governed by the following equation [1],

$$I_b = \oint \mathbf{M} \cdot d\mathbf{l} \tag{12.46}$$

where, the integration is done over any closed contour lying within the magnetic material. For an arbitrary closed contour, **M** may have an orientation different than

that of the contour along the path of the integration. Equation 12.46 determines the total bound current enclosed by the contour. The corresponding differential or point form of the equation is

$$\nabla \times \mathbf{M} = \mathbf{J}_b \,. \tag{12.47}$$

As a result of the action of the magnetic moments, the magnetic field **B** changes (decreases in diamagnetic materials and increases in the other types that we have discussed) and is defined by,

$$\mathbf{B} = \mu_0 (\mathbf{H} + \mathbf{M}) \,. \tag{12.48}$$

The presence of the magnetic material adds the component $\mu_0 \mathbf{M}$ to the free-space field $\mu_0 \mathbf{H}$. All the discussed magnetic effects of the material are accounted in **M**, which explains why it is multiplied by μ_0.

For linear isotropic magnetic media, **M** and **H** are linearly related,

$$\mathbf{M} = \chi_m \mathbf{H} \tag{12.49}$$

where χ_m is the magnetic susceptibility of the material. Therefore, we have

$$\mathbf{B} = \mu_0 (\mathbf{H} + \chi_m \mathbf{H}) = \mu_0 (1 + \chi_m) \mathbf{H} = \mu_0 \mu_r \mathbf{H} \tag{12.50}$$

where the well-known and previously discussed material property, μ_r, has now been defined as

$$\mu_r = 1 + \chi_m \,. \tag{12.51}$$

In a way, it quantifies the ability (susceptibility) of the magnetic material to respond to an applied field. For diamagnetic and paramagnetic materials, the value of magnetic susceptibility is a very small negative and positive real number, respectively, which makes their μ_r value practically equal to 1. It is worth mentioning here that a perfect diamagnetic material (e.g., a superconducting material) has $\chi_m = -1$. Thus, when placed in a magnetic field, a perfect diamagnetic material, with free space surrounding it, would not have any field inside it; the magnetic field lines would surround the material without going into it (the reluctance offered by the material to the flux is theoretically infinite on account of zero permeability). The situation is similar to a case wherein a perfect electrical conductor is placed in an electrostatic field; being an equipotential surface (and since no electric field can exist inside a perfect conductor) the electric field lines go parallel to the surface of the conductor.

In ferromagnetic materials, the value of μ_r can be 3 to 4 orders higher than that of air. Most of the electric devices, including transformers, are driven by voltage sources. For a given applied voltage and the corresponding flux density

(**B**), a ferromagnetic material would then have a low value of the **H** field inside it. Since, the current drawn from the voltage source to set up the flux density is equal to the line integral of $\mathbf{H} \cdot d\mathbf{l}$, the ampere-turns expended for the purpose are reduced. This also underlines the need of minimizing the (unavoidable) air gaps at the joints between the limbs and yokes in the magnetic circuit of transformers.

Defining the permeability as

$$\mu = \mu_0 \mu_r \tag{12.52}$$

we obtain the well-known relationship from Equation 12.50 viz. $\mathbf{B} = \mu \mathbf{H}$. The relative permeability, μ_r, expressed and used in the form given by Equation 12.51, obviates the need of considering bound currents and magnetization in field computations in transformers.

In the above discussions, it is implicitly assumed that the medium is isotropic. For an anisotropic material, the permeability must be defined by a 3 × 3 matrix; the constitutive relation then must be written in the matrix form as,

$$\begin{Bmatrix} B_x \\ B_y \\ B_z \end{Bmatrix} = \begin{bmatrix} \mu_{xx} & \mu_{xy} & \mu_{xz} \\ \mu_{yx} & \mu_{yy} & \mu_{yz} \\ \mu_{zx} & \mu_{zy} & \mu_{zz} \end{bmatrix} \begin{Bmatrix} H_x \\ H_y \\ H_z \end{Bmatrix}. \tag{12.53}$$

A laminated core is an excellent example of an anisotropic structure. The permeability of the structure is highest along the direction of the grain orientation. Along the orthogonal direction (to the grain orientation) in the plane of laminations, the permeability is lower. It is least in the direction perpendicular to the plane of laminations because of the nonmagnetic coating on the surface of the laminations. When the coordinate axes are aligned along the crystal axes, the off-diagonal elements in the square matrix are zero, greatly simplifying the analysis. The entries of the diagonal matrix can be calculated using Equations 5.35 and 5.36 in Section 5.9.1. In the absence of the alignment, the off-diagonal elements will be non-zero meaning thereby that all the three magnetic field intensity components would decide the value of the magnetic flux density component along any of the three axes.

We have earlier seen the representation of permittivity as a complex number to account for the lossy nature of dielectric materials. Likewise, permeability can be represented as a complex quantity; its imaginary part is indicative of the eddy and hysteresis losses occurring in the ferromagnetic materials that are subjected to alternating fields. With increase in frequency, the induced fields and corresponding eddy currents increase, reducing the value of the field in the material and its effective permeability. A magnetic material, whose losses are neglected, is characterized by real permeability. The expression for complex permeability and the graphs showing the frequency-dependence of its real and imaginary components are given in Section 13.10.3 of Chapter 13. Such

characteristic curves are important while, for example, analyzing response of the core to high frequency excitations.

In transformers, boundary conditions at interfaces between different types of magnetic materials need to be determined for field computations. Using Maxwell's Equations 12.11 and 12.13 in the integral form, we can determine the boundary conditions for the normal and tangential components of the field vectors on both sides of the interface between two magnetic materials as [1, 2],

$$B_{1n} = B_{2n} \tag{12.54}$$

$$H_{1t} = H_{2t} \,. \tag{12.55}$$

Thus, the normal component of **B** and the tangential component of **H** are continuous across the boundary. The condition specified in Equation 12.55 is derived based on an assumption that there are no surface currents in either of the materials.

Let us consider that fields are oriented in two media as shown in Figure 12.5 (a). The media are assumed to be isotropic with fields **H** and **B** in the same direction. Expressing the normal and tangential components in the above two equations in terms of the corresponding magnitudes of the fields and dividing one equation by the other, we have

$$\frac{H_1 \sin\theta_1}{H_2 \sin\theta_2} = \frac{\mu_1 H_1 \cos\theta_1}{\mu_2 H_2 \cos\theta_2} \quad \Rightarrow \quad \frac{\tan\theta_1}{\tan\theta_2} = \frac{\mu_1}{\mu_2} = \frac{\mu_{r1}}{\mu_{r2}} \,. \tag{12.56}$$

Let us understand the relevance of Equation 12.56 for magnetic field distributions in transformers. For example, the leakage field plot shown in Figure 3.1 (a) has been obtained with core material constants defined as relative permeability = 5000 and electrical conductivity = 0. It should be noted that the conductivity has been defined as zero because in that analysis the primary objective was to determine the leakage impedance of the transformer (and not the eddy current losses in core, which anyway cannot be calculated accurately using the 2-D approximation). Also, the effect of eddy currents in the core on the leakage field is small and therefore neglected. Here, we have a core-air interface (actually it is core-oil interface in the oil-cooled and -insulated transformers; however, the magnetic properties of oil and air are alike). Putting the values of the constants for the interface shown in Figure 12.5 (b), we obtain $\tan\theta_1 = 5000 \tan\theta_2$. For any practical value of θ_1 (between 0° and 90°), the value of θ_2 will be very close to zero, meaning thereby that flux lines must impinge on high permeability materials at right angles as can be seen in the field plot of Figure 3.1 (a).

The energy stored in a magnetic field for linear material characteristics is

$$W_M = \frac{1}{2}\int_v \mathbf{B}\cdot\mathbf{H}\, dv = \frac{1}{2}\int_v \mu H^2\, dv = \frac{1}{2}\int_v \frac{B^2}{\mu} dv \tag{12.57}$$

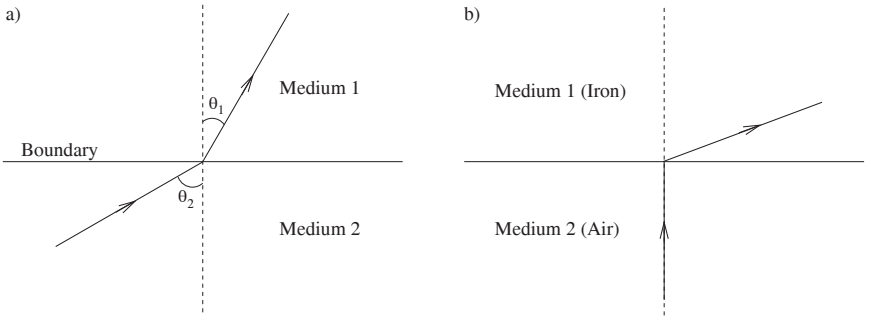

Figure 12.5 (a) Boundary conditions: Magnetic field. **(b)** Core-air interface.

where $(1/2)\mu H^2$ or $(1/2)B^2/\mu$ is the energy density, J m^{-3}. It is assumed here that the material has isotropic properties. For a nonlinear *B-H* curve, wherein the permeability is a function of *B,* i.e., $B = \mu(B)H$, the expression for the magnetic energy is modified to

$$W_M = \int_v \int_0^B H\, dB\, dv \tag{12.58}$$

where, $\int H\, dB$ is the energy density. It is the area under the *B-H* curve calculated with reference to the *B* axis. For example, in Figure 2.5(a) depicting a hysteresis loop, Equation 12.58 can be applied to understand how some energy is lost when the loop is traversed. From point A to point B, the energy stored in the material is proportional to the area OABCDO, which is positive. From point B to point D, a part of the stored energy is returned back to the source since *dB* is negative while performing the integration; the returned energy being proportional to the area BCDB. Thus, the area OABDO represents the hysteresis loss of the first quadrant.

For linear characteristics, the energy density expression is simplified to $\int_0^B H\, dB = \int_0^B \frac{B}{\mu} dB = \frac{B^2}{2\mu}$ or $\mu H^2/2$, which is in line with Equation 12.57; the density is numerically equal to half the rectangular area *BH*. The other half is termed co-energy as identified in Figure 12.6. Thus, $\int H\, dB$ represents energy while $\int B\, dH$ represents co-energy. The concept of co-energy is useful in finding numerically the values of forces. It is not very difficult to understand why $\int H\, dB$ represents the energy stored in a magnetic circuit. The energy is given as

$$Energy = \int V\, I\, dt = \int (N\, d\phi/dt)\, I\, dt = \int N\, A\, dB\, I = \int N\, A\, dB\, (Hl/N) = v \int H\, dB$$

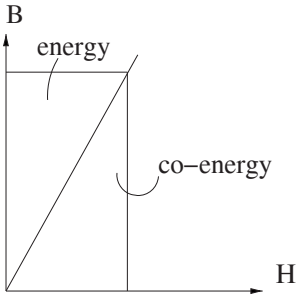

Figure 12.6 Energy and co-energy.

where the terms used carry the usual meanings with volume (v) being the product of the area (A) and length (l) of the magnetic circuit in which the flux density has been established by the applied voltage V.

With this, we have covered many important concepts of electromagnetic fields which are generally relevant to the transformer engineering. Maxwell's equations and the continuity equation have been discussed. Although a passing reference was made to the force density in winding conductors, i.e., $\mathbf{J} \times \mathbf{B}$, the Lorentz force equation and different methods of computing various forces in transformers are elaborately discussed in Section 12.7.7. In the next few sections, we will now use most of the discussed electromagnetic theory to understand how fields can be computed, interpreted and analyzed in transformers.

12.3 Potential Formulations

Maxwell's equations form a set of first order partial differential equations in terms of the field vectors **E**, **H**, **D** and **B**. The current densities, **J** and $\partial \mathbf{D}/\partial t$, and the volume charge density, ρ_v, are the sources. For obtaining the field solution, we need to manipulate these equations to obtain a second order partial differential equation (PDE) in just one variable. Instead of formulating in terms of one of the field vectors, it is computationally attractive to write the PDE in terms of a suitable potential function. Four potentials are commonly used in the field formulations: electric scalar potential (V), magnetic scalar potential (Ω), electric vector potential (**T**) and magnetic vector potential (**A**). We have discussed until now only the electric scalar potential while deliberating on static electric fields. We will now discuss the formulations based on these potentials and their applications to transformers.

12.3.1 Electric Scalar Potential (V)

In electrostatic fields, charges are at rest leading to zero current and magnetic field. Equation 12.3 is therefore reduced to

$$\nabla \times \mathbf{E} = 0 .$$

E and V are related by Equation 12.17, i.e., $\mathbf{E} = -\nabla V$. This relationship is consistent with the above equation since the curl of the gradient of a scalar variable is always zero.

Using Equation 12.9, Maxwell's first equation can be rewritten as

$$\nabla \cdot \varepsilon \mathbf{E} = \rho_v \qquad \Rightarrow \qquad \nabla \cdot \varepsilon \left(-\nabla V\right) = \rho_v .$$

Or,

$$\frac{\partial}{\partial x}\varepsilon_x \frac{\partial V}{\partial x} + \frac{\partial}{\partial y}\varepsilon_y \frac{\partial V}{\partial y} + \frac{\partial}{\partial z}\varepsilon_z \frac{\partial V}{\partial z} = -\rho_v . \tag{12.59}$$

For a homogeneous and isotropic material, $\varepsilon_x = \varepsilon_y = \varepsilon_z = \varepsilon$, and ε is not a function of the independent variables (*x, y, z*),

$$\frac{\partial^2 V}{\partial x^2} + \frac{\partial^2 V}{\partial y^2} + \frac{\partial^2 V}{\partial z^2} = -\frac{\rho_v}{\varepsilon} \tag{12.60}$$

or,

$$\nabla^2 V = -\frac{\rho_v}{\varepsilon} . \tag{12.61}$$

This is Poisson's equation governing electrostatic field distributions, whose solution determined either by an analytical or a numerical technique yields voltage distribution. It should be remembered that ∇^2 operator is in different forms in cylindrical and spherical coordinates. The equation is in the differential or point form; when the operator operates on $V(x, y, z)$, the result at any point inside the problem domain is equal to $-\left(\rho_v/\varepsilon\right)$ if the (free) charge density is present at that point, and the result is zero otherwise. Thus, for a complex arrangement of electrodes, finding analytically such a polynomial function describing V is practically impossible, underlining the need of a numerical approach for computing field distributions. The main advantage of computing V instead of **E** is obvious; the number of unknowns at a point in the problem domain reduces from three (E_x, E_y and E_z) to one. In exceptional cases, ρ_v is not equal to zero. While calculating electric field distributions in transformers, it is invariably zero and we need to solve Laplace's equation,

$$\nabla^2 V = 0 . \tag{12.62}$$

For a 2-D domain containing nonhomogeneous materials, such as a multiple dielectric insulation system in Figure 8.16, the governing PDE takes the form

$$\frac{\partial}{\partial x}\varepsilon\frac{\partial V}{\partial x}+\frac{\partial}{\partial y}\varepsilon\frac{\partial V}{\partial y}=0\,.$$

For the system shown in the figure, the field distribution is obtained for a worst-case potential difference between the electrodes, making it a case of electrostatic field distribution. Once the solution is obtained, **E** is calculated as

$$\mathbf{E}=-\nabla V=-\frac{\partial V}{\partial x}\mathbf{a}_x-\frac{\partial V}{\partial y}\mathbf{a}_y\,. \tag{12.63}$$

A contour in an approximated 2-D domain actually represents a surface in the corresponding 3-D geometry. Consider an equipotential line in a 2-D domain. If the orientation of the coordinate system is such that the *x*-direction is along the line, $\partial V/\partial x=0$ along it. Substituting this condition in the above equation we are left with only the normal (*y* directed) component of **E**. Thus, we have again proved that **E** lines are normal to equipotential surfaces; the electric flux flows normal to equipotential lines in electrostatic fields. It should be noted that the term *flux* is used to denote field vectors and not potentials.

It may be appropriate here to discuss about commonly specified boundary conditions while seeking solution to a field problem. When potential is specified along a boundary, it is termed Dirichlet boundary condition. If the normal derivative $\partial V/\partial n$ of the potential is defined, it is known as a Neumann boundary condition. If the specified potential or its derivative is zero, it is known as a homogeneous boundary condition; a nonzero value is classified as a nonhomogeneous boundary condition. Many times symmetry conditions are exploited to reduce the size of field problems. On lines in 2-D and surfaces in 3-D domains, about which the problems are symmetrical, the boundary condition to be specified is $\partial V/\partial n=0$. The equipotential lines impinge normally on such boundaries.

There is another electric scalar potential-based formulation for calculating numerically the losses in imperfect dielectric materials. These materials are generally represented by a parallel R-C circuit, which means that both conduction and displacement current densities should be accounted in the field model. Taking the divergence of both sides of Equation 12.4 and noting that the divergence of the curl of a vector quantity is identically zero, we obtain

$$\nabla\cdot\left(\mathbf{J}+\frac{\partial\mathbf{D}}{\partial t}\right)=0\,.$$

This divergence-free condition is obvious because currents flow in closed paths. Using the constitutive relationships in Equations 12.7 and 12.9, and the relation $\mathbf{E}=-\nabla V$ (the time-varying term is absent since the influence of magnetic effects on the electric field can be neglected, i.e., $\nabla\times\mathbf{E}=0$ [16]), we obtain

$$-\nabla\cdot\left(\sigma\nabla V\right)-\nabla\cdot\left(\frac{\partial}{\partial t}\left(\varepsilon\nabla V\right)\right)=0\,.$$

In the time-harmonic form, wherein V is a phasor, the equation becomes

$$-\nabla\cdot\left(\left(\sigma+j\omega\hat{\varepsilon}\right)\nabla\hat{V}\right)=0$$

which is the governing PDE in this case. It should be noted that the permittivity constant in this case is complex, i.e., $\hat{\varepsilon}=\varepsilon'-j\varepsilon''$, which gives

$$-\nabla\cdot\left(\left(\sigma_{eff}+j\omega\varepsilon'\right)\nabla\hat{V}\right)=0$$

wherein, the effective conductivity is defined as $\sigma_{eff}=\sigma+\omega\varepsilon''=\sigma+\omega\varepsilon'\tan\delta$, with $\tan\delta=\varepsilon''/\varepsilon'$ as discussed in Section 12.2.7-A.

12.3.2 Magnetic Vector Potential

The magnetic vector potential (**A**) is now discussed before the magnetic scalar potential since the former is very commonly and naturally used for most 2-D magnetic field problems. We will now use Maxwell's second equation, $\nabla\cdot\mathbf{B}=0$, to understand the genesis of **A**. In fact it is interesting to note that each of the four Maxwell's equations leads to the understanding of the origin of one of the four potential functions. Since, the divergence of the curl of a vector quantity is always zero, the vector **B** can always be written as the curl of another vector, say **A**,

$$\mathbf{B}=\nabla\times\mathbf{A}\,. \tag{12.64}$$

Using Equation 12.64 and the Biot–Savart law for the magnetic flux density, we can obtain the expressions for **A** [1, 2] at a point due to a current distribution as,

$$\mathbf{A}=\int_{l}\frac{\mu_0 I\ d\mathbf{l}}{4\pi R}\quad\text{(Line current)}\qquad\mathbf{A}=\int_{v}\frac{\mu_0\mathbf{J}\ dv}{4\pi R}\quad\text{(Volume current)} \tag{12.65}$$

where R is the distance of the point from the elemental length/volume. It can be observed from the above expressions that the direction of **A** is the same as that of the current flow and its magnitude reduces with an increase in distance from the source. In 2-D field analysis of transformers (or any other electrical machine), one would always take a cross section perpendicular to the direction of flow of currents. The direction of **A**, i.e., the direction of the current flow, gets fixed as the z-direction in Cartesian coordinates (and the ϕ direction in cylindrical coordinates). That leaves us with only one unknown at any point where the potential needs to be determined, i.e., the magnitude of the potential. In other words, the formulation results in a single degree of freedom, A_z. Once the solution is obtained, the two components (B_x and B_y) of the flux density vector can be

easily determined by taking the curl of the magnetic vector potential. This greatly simplifies the computational burden and also leads to better visualization of fields. Compared to this, if the field problem is formulated in terms of either **B** or **H**, the number of unknowns would be the *x* and *y* components of the field at these points, doubling the number of unknown variables. Hence, formulations based on the magnetic vector potential are popularly used for solving 2-D static, time-harmonic, transient and coupled magnetic field problems. For 3-D problems, they are not that attractive as explained later while discussing the magnetic scalar potential.

For time varying fields, using Equations 12.3 and 12.64, we have

$$\nabla\times\mathbf{E} = -\frac{\partial\mathbf{B}}{\partial t} = -\frac{\partial\left(\nabla\times\mathbf{A}\right)}{\partial t} \quad \text{or}$$

$$\nabla\times\mathbf{E} + \nabla\times\frac{\partial\mathbf{A}}{\partial t} = 0 \qquad \Rightarrow \qquad \nabla\times\left(\mathbf{E} + \frac{\partial\mathbf{A}}{\partial t}\right) = 0\,.$$

Since the sum of the two vector quantities in the parenthesis is curl free, it can be expressed as the gradient of a scalar. Also, in order to have consistency with the definition of the scalar potential function *V* in electrostatics, we can write

$$\mathbf{E} + \frac{\partial\mathbf{A}}{\partial t} = -\nabla V \quad \text{or} \tag{12.66}$$

$$\mathbf{E} = -\nabla V - \frac{\partial\mathbf{A}}{\partial t} \tag{12.67}$$

which reduces to Equation 12.17 for the static case. The above equation says that the electric field intensity can be due to charge accumulation (in a static case) and/or time varying currents. In transformers, for computing the electric field distribution at an instant of time with some potential difference between the electrodes having accumulation of (free) charges on them, we use $\mathbf{E} = -\nabla V$, as discussed earlier. On the contrary, while determining the magnetic field under time-varying conditions (e.g., computation of eddy currents in structural parts), the electric field will be due to the time varying component only, i.e., $\mathbf{E} = -\partial\mathbf{A}/\partial t$.

Now, let us try to understand the physical basis of the magnetic vector potential. A small test particle of mass *m* and charge *e,* moving with velocity **v**, has mechanical momentum *m***v** and electrokinetic momentum *e***A**, giving it the total momentum of *m***v** + *e***A** [3]. Thus, the unit of **A** from this definition is momentum per unit charge. The Lorentz force equation tells us that we have two types of forces on electric charges; the first one arises from stationary charges, while the second type is a force on charges moving across the magnetic field **B**, with $-\nabla V$ and $-\partial\mathbf{A}/\partial t$ (or $\mathbf{v}\times\mathbf{B}$) as the corresponding **E** vectors. Since, by definition the force is the rate of change of momentum, **E** is the rate of change of momentum per unit charge as per Equation 12.6. Comparing this definition with

that given by $-\partial \mathbf{A}/\partial t$, the unit of **A** is momentum per charge from the Lorentz equation point of view as well. The well-established name, magnetic vector potential, for **A** is rather unfortunate since a potential represents the corresponding potential energy (a scalar quantity) [17]. The correct name, electro-kinetic momentum, as defined by Maxwell, is however rarely used.

Coming back to Equation 12.64 which defines **A**, since the curl operation implies differentiation with respect to length, the commonly used unit of **A** is Wb/m. We will now derive a simple but very useful equation, which corroborates this unit. We know that the flux passing through an open surface *d***s**, bounded by a closed contour *l*, is

$$\phi = \int_s \mathbf{B} \cdot d\mathbf{s} \quad \Rightarrow \quad \phi = \int_s (\nabla \times \mathbf{A}) \cdot d\mathbf{s} .$$

Using Stokes' theorem, we obtain

$$\phi = \oint_l \mathbf{A} \cdot d\mathbf{l} . \tag{12.68}$$

It is clear from the above equation that the unit of **A** is Wb/m. Another advantage of using the magnetic vector potential-based 2-D formulation is that the flux passing through a surface can be easily calculated. Consider a problem domain in the *x*-*y* plane as shown in Figure 12.7, with the *y* direction being perpendicular to the plane of the paper. Suppose that we have obtained field solution in terms of A_z. Thus, values of the potential at points 2 and 3, i.e., A_2 and A_3, are known. We need to find the flux passing through the rectangular area 2341. Please note that for the current flowing along the *z* direction (since we have taken **A** as *z*-directed), the flux will cross the *x*-*z* plane for the case of points 2 and 3 on a line along the *x* direction. Parameters of interest are generally calculated per meter depth for 2-D problems in Cartesian system. Now, if we apply Equation 12.68 for the closed rectangular contour passing through points 1, 2, 3 and 4, we have

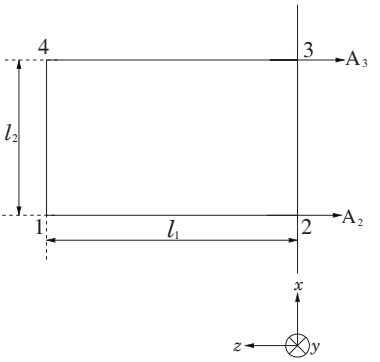

Figure 12.7 Computation of flux passing through a given surface area.

$$\phi = A_2 l_1 + 0 l_2 - A_3 l_1 - 0 l_2 = A_2 \times 1 - A_3 \times 1 = A_2 - A_3 .$$

This is an important and useful result in the 2-D analysis using the **A**-based formulation. The flux passing through any two points, in the problem domain, is simply given by the difference between the corresponding two potentials at those points. It also means that irrespective of the value of the magnetic vector potential specified on the boundary of the domain, the calculated value of the flux will be same. Anyway, we should not be concerned about the absolute values of the magnetic vector potential, if the flux distribution is being correctly determined. Thus, for the magnetostatic field analysis depicted in Figure 3.1 (a), for example, the values of the potential specified on the outermost boundary can be zero or any other value.

Having seen some of the basic definitions and concepts that helped us to comprehend the magnetic vector potential, we will now derive the governing PDEs in terms of it, for analyzing the magnetic field distributions under various operating conditions in transformers. Starting with Equation 12.4 and using Equations 12.8, 12.9, 12.64 and 12.67, we obtain

$$\nabla \times \mathbf{H} = \mathbf{J} + \frac{\partial \mathbf{D}}{\partial t} \quad \Rightarrow \quad \nabla \times \nabla \times \mathbf{A} = \mu \mathbf{J} + \mu\varepsilon \frac{\partial \left(-\nabla V - \frac{\partial \mathbf{A}}{\partial t} \right)}{\partial t} .$$

It is assumed that we are dealing with linear materials. Using the vector identity, $\nabla \times \nabla \times \mathbf{A} = \nabla \left(\nabla \cdot \mathbf{A} \right) - \nabla^2 \mathbf{A}$,

$$\nabla \left(\nabla \cdot \mathbf{A} \right) - \nabla^2 \mathbf{A} = \mu \mathbf{J} - \nabla \left(\mu\varepsilon \frac{\partial V}{\partial t} \right) - \mu\varepsilon \frac{\partial^2 \mathbf{A}}{\partial t^2}$$

or,

$$\nabla^2 \mathbf{A} - \mu\varepsilon \frac{\partial^2 \mathbf{A}}{\partial t^2} = -\mu \mathbf{J} + \nabla \left(\nabla \cdot \mathbf{A} + \mu\varepsilon \frac{\partial V}{\partial t} \right) . \tag{12.69}$$

We have until now defined only the curl of **A**. Being a vector function, both curl and divergence of **A** must be specified. The divergence of **A** is chosen according to the Lorentz gauge,

$$\nabla \cdot \mathbf{A} = -\mu\varepsilon \frac{\partial V}{\partial t} . \tag{12.70}$$

It can be proved that this gauge is consistent with the continuity equation [3]; hence the choice is not arbitrary. The condition simplifies the field computations concerning electromagnetic waves [18] (it uncouples the wave equation that is originally in a coupled form with two variables, **A** and *V*). For static problems the right side reduces to zero, and for field computations involving low

frequency electromagnetics (as in transformers) the term $\mu\varepsilon(\partial V/\partial t)$ in its phasor equivalent form, $j\omega\mu\varepsilon V$, is negligibly small (since $\mu\varepsilon$ is a very small number). Thus, for static and power frequency cases,

$$\nabla \cdot \mathbf{A} = 0 \tag{12.71}$$

which is known as the Coulomb gauge. Therefore, Equation 12.69 reduces to

$$\nabla^2 \mathbf{A} - \mu\varepsilon \frac{\partial^2 \mathbf{A}}{\partial t^2} = -\mu \mathbf{J} . \tag{12.72}$$

J in the above equation, which is the same as that in Equation 12.4, represents conduction current densities, i.e., the source current density ($\mathbf{J}_s$) and the eddy current density ($\mathbf{J}_e$),

$$\mathbf{J} = \mathbf{J}_s + \mathbf{J}_e . \tag{12.73}$$

For now, we assume that the source current density is zero. In a time-varying field, $\mathbf{E} = -\partial \mathbf{A}/\partial t$, and this **E** vector represents the (induced) eddy current density,

$$\mathbf{J}_e = -\sigma \, \partial \mathbf{A}/\partial t . \tag{12.74}$$

Substituting this expression in Equation 12.72 and rearranging, we have

$$\nabla^2 \mathbf{A} - \mu\sigma \frac{\partial \mathbf{A}}{\partial t} - \mu\varepsilon \frac{\partial^2 \mathbf{A}}{\partial t^2} = 0 . \tag{12.75}$$

It can be proved that this form of equation is satisfied by the other vectors that we have discussed, **B**, **H**, **J**, **D** and **E** [3]. Depending on whether we are analyzing a low frequency or a high frequency phenomenon, one of the two time-dependent terms in the above equation becomes negligible. What matters is the ratio of the conduction current density to the displacement current density,

$$\left| \mathbf{J} / \frac{\partial \mathbf{D}}{\partial t} \right| = \left| \frac{\sigma \mathbf{E}}{j\omega\varepsilon \mathbf{E}} \right| = \frac{\sigma}{\omega\varepsilon} . \tag{12.76}$$

The displacement current density dominates in the analysis of partial discharge (PD) propagation in the form of an electromagnetic wave through the insulation system of the transformers (due to high frequency content of PD pulses and negligible conductivity of the dielectric materials), in which case, we essentially solve the wave equation,

$$\nabla^2 \mathbf{A} - \mu\varepsilon \frac{\partial^2 \mathbf{A}}{\partial t^2} = 0 .$$

On the contrary, while determining stray losses due to induced eddy currents in the windings and structural parts in the transformers, we essentially analyze low frequency phenomena at power frequency (50/60 Hz and higher order harmonic frequencies) with a high value of electrical conductivity of the involved metallic parts. Thus, the ratio $\sigma/\omega\varepsilon$ is high, making the term representing the displacement current density negligible compared to the one due to the conduction current density, and we obtain what is known as the diffusion equation

$$\nabla^2 \mathbf{A} - \mu\sigma \frac{\partial \mathbf{A}}{\partial t} = 0 . \tag{12.77}$$

If Equation 4.21 is written in terms of **A** in the time domain, we will obtain the above equation. Equation 4.21 is a source-free diffusion equation. A peak value of the **E** field was assumed at the surface of a conductor in the analysis of eddy currents; some source, which is not in the investigated conductor domain, is responsible for the field. If, however, the source (say, current density $\mathbf{J}_s$) is also included in the domain, then $\mathbf{J} = \mathbf{J}_s - \sigma\, \partial\mathbf{A}/\partial t$. It should be noted that the sign of the induced current density is opposite to that of the source density, which is indicative of the fact that the induced current opposes the cause according to Lenz's law. The diffusion equation with the source term becomes

$$\nabla^2 \mathbf{A} - \mu\sigma \frac{\partial \mathbf{A}}{\partial t} = -\mu \mathbf{J}_s . \tag{12.78}$$

This is the governing PDE while analyzing the stray losses in metallic plates of the transformers in the vicinity of high current leads, as discussed in Section 5.8. For linear materials with sinusoidal current excitation, all the field quantities vary sinusoidally, allowing us to do time-harmonic analysis, wherein the governing PDE is rewritten with the field variables as phasors,

$$\nabla^2 \mathbf{A} - j\omega\mu\sigma\ \mathbf{A} = -\mu \mathbf{J}_s . \tag{12.79}$$

This is a quasistatic formulation which gives a solution in terms of the real and imaginary values of **A**. The computational burden is not much as explained in Section 5.8; the number of unknown variables is doubled, but we can obtain the potential value at any instant of time using Equation 5.33. However, if the material involved is nonlinear, PDE in the time domain form as given in Equation 12.78 has to be used for finding the solution (even if we have a sinusoidal excitation).

Finally, if we are dealing with static magnetic fields, for example while calculating the leakage reactance of a transformer, Equation 12.78 takes the form,

$$\nabla^2 \mathbf{A} = -\mu \mathbf{J}_s \tag{12.80}$$

which is Poisson's equation representing magnetostatic fields. It is a vector equation with the corresponding three scalar equations in Cartesian coordinates as

$\nabla^2 A_x = -\mu J_x$, $\nabla^2 A_y = -\mu J_y$ and $\nabla^2 A_z = -\mu J_z$ (where the subscript *s* is dropped for simplicity). For calculating the leakage inductance, we define the distribution of ampere-turns in the windings using the peak or rms values of the currents flowing in them (e.g., field plot in Figure 3.1 is obtained by defining just J_z, and we have only one scalar PDE). After getting the solution in terms of **A**, the energy and the inductance can be calculated using Equations 3.43 and 3.35, respectively.

Before ending the discussion on the magnetic vector potential, a remark on boundary conditions is appropriate. In two dimensions, with **A** having only the *z* component, we have

$$\mathbf{B} = \nabla \times \mathbf{A} = \begin{vmatrix} \mathbf{a}_x & \mathbf{a}_y & \mathbf{a}_z \\ \dfrac{\partial}{\partial x} & \dfrac{\partial}{\partial y} & \dfrac{\partial}{\partial z} \\ 0 & 0 & A_z \end{vmatrix} = \mathbf{a}_x \frac{\partial A_z}{\partial y} - \mathbf{a}_y \frac{\partial A_z}{\partial x}. \tag{12.81}$$

If a homogeneous Dirichlet condition is specified on a boundary along the *x* direction, i.e., $\partial A_z / \partial x = 0$, the magnetic flux density vector will have only the *x* component according to Equation 12.81. In other words, the tangential component of the vector field gets specified on the boundary. Hence the flux flows along equipotential lines in magnetic field problems, whereas it flows normal to equipotential lines in electric field problems [19] as described in the previous subsection.

12.3.3 Magnetic scalar potential

The magnetic vector potential, which is very popularly used for 2-D magnetic field problems, becomes unattractive when applied to 3-D problems. This is because there are three unknowns or three degrees of freedom (A_x, A_y and A_z) at the points in a domain where the field needs to be determined. The computational burden increases substantially, particularly for complex 3-D problems with thousands of nodes and elements in a typical numerical method. This shortcoming led to an increased usage of the magnetic scalar potential based formulations, at least for static problems.

As explained later, if there are no current sources in the domain, a magnetic scalar potential can be defined. Using Equation 12.4 and the condition that the conduction and displacement currents should be zero in the domain where the magnetic scalar potential (Ω) is defined, we have a curl-free case:

$$\nabla \times \mathbf{H} = 0.$$

Since the curl of the gradient of a scalar is identically zero, we can define the magnetic field intensity in terms of the magnetic scalar potential:

$$\mathbf{H} = -\nabla \Omega. \tag{12.82}$$

This definition of **H** is analogous to that of the electric field intensity in the electrostatic field, i.e., $\mathbf{E} = -\nabla V$, and therefore the corresponding PDE for the magnetic scalar potential is

$$\nabla \cdot \mathbf{B} = 0 \quad \Rightarrow \quad \nabla \cdot \mu \mathbf{H} = 0 \quad \Rightarrow \quad \nabla \cdot \mu\left(-\nabla \Omega\right) = 0 \quad \Rightarrow \quad -\mu \nabla^2 \Omega = 0$$

or,

$$\nabla^2 \Omega = 0 \quad \Rightarrow \quad \frac{\partial^2 \Omega}{\partial x^2} + \frac{\partial^2 \Omega}{\partial y^2} + \frac{\partial^2 \Omega}{\partial z^2} = 0 \,. \tag{12.83}$$

This is the Laplace's equation in terms of the magnetic scalar potential, which can be solved to obtain the potential, and then the field vector (**H**) using Equation 12.82. The advantage of using the scalar potential instead of the magnetic vector potential, in current-free regions, is now obvious. We just have to solve a single scalar equation instead of a vector equation which is equivalent to three scalar equations.

The condition $\nabla \times \mathbf{H} = 0$ in the integral form becomes $\oint \mathbf{H} \cdot d\mathbf{l} = 0$, which means that for the use of the magnetic scalar potential, the domain should be a current-free region and any arbitrary loop drawn in it must not enclose a current distribution. For the regions containing current distributions the scalar potential cannot be used, which is a serious limitation. To overcome this problem, a reduced scalar potential-based formulation is used for the solution of magnetostatic fields. The magnetic field intensity can be written as a sum of two components, one due to current distributions in the domain and the other representing the remaining field:

$$\mathbf{H} = \mathbf{H}_c + \mathbf{H}_m \,. \tag{12.84}$$

The term, $\mathbf{H}_c$, due to the current distributions, is defined by

$$\nabla \times \mathbf{H}_c = \mathbf{J}$$

and it is determined analytically from the current distributions, for example, by direct integration using Biot-Savart law. Having accounted the current sources, now the domain can be remodeled without them, allowing the remaining curl-free field ($\mathbf{H}_m$) to be defined in terms of reduced magnetic scalar potential (Ω_r):

$$\mathbf{H}_m = -\nabla \Omega_r \,. \tag{12.85}$$

The corresponding Laplace's equation, in the form of Equation 12.83, in terms of Ω_r, can be solved easily. After having computed Ω_r, $\mathbf{H}_m$ is calculated using Equation 12.85 and subsequently **H** is determined using Equation 12.84:

$$\mathbf{H} = \mathbf{H}_c - \nabla \Omega_r \,. \tag{12.86}$$

In the context of the reduced magnetic scalar potential, it should be noted that, the magnetic scalar potential Ω, defined previously, is called total scalar potential.

12.3.4 Electric vector potential

Another potential that has been used for magnetic field computations involving eddy currents is electric vector potential (**T**) defined by the relation:

$$\nabla \times \mathbf{T} = \mathbf{J} .$$

Subtracting this equation from Equation 12.25, we have $\nabla \times (\mathbf{H} - \mathbf{T}) = 0$, which allows us to express the vector $(\mathbf{H} - \mathbf{T})$ as the gradient of a scalar, i.e.,

$$\mathbf{H} - \mathbf{T} = -\nabla\Omega \qquad \Rightarrow \qquad \mathbf{H} = \mathbf{T} - \nabla\Omega . \tag{12.87}$$

This equation is similar to Equation 12.67, i.e., $\mathbf{E} = -\nabla V - \partial \mathbf{A}/\partial t$. Thus, it can be inferred that the vector **T** represents induced eddy currents as the term $-\partial \mathbf{A}/\partial t$ does in the **A**-based formulation. The corresponding diffusion equation in terms of **T** for the region having induced currents will have exactly the same form as that of Equation 12.77. We can obtain another diffusion equation in Ω having the same form [3]. The corresponding **T**-Ω formulation is discussed in the next section as one of the mixed potential formulations.

12.3.5 Mixed potential formulations

We have already discussed the utility of using the magnetic scalar potential for magnetostatic problems. Since the applicability of this potential is dramatically reduced in current-carrying regions, the use of the formulation based on the reduced scalar potential became popular. However, its use is not accurate in regions of high permeability. In regions where $\mu_r >> 1$ (e.g., the magnetic circuit in transformers), the value of the magnetic field intensity (**H**) vector is very small. Since it is given as the difference between the two field quantities according to Equation 12.86, a small error in calculation of these quantities results in a large error in the calculated value of **H** [6].

This difficulty can be overcome by using a mixed formulation in which the reduced scalar potential Ω_r is used in current-carrying regions and the total scalar potential Ω in current-free magnetic regions with high permeability (eddy currents in the magnetic parts cannot be modeled using this formulation). The formulation, however, requires continuity between the tangential components of **H** and between the normal components of **B** at the interface of the two regions through a proper coupling mechanism. Figure 12.8 shows a problem domain for which the mixed formulation can be used. The symmetry about the centerline is conveniently exploited and only half of the core region is modeled so that any arbitrary loop in it does not enclose any external current source, allowing us to

define the total scalar potential. For the remaining nonmagnetic part which contains a current source (i.e., winding), we can use the reduced scalar potential as shown in the figure [7].

The formulation in terms of a potential reduces computational burden in most practical problems. In electrostatic field problems, only the electric scalar potential based formulation, discussed earlier, is used for 2-D as well as 3-D problems. In 2-D electromagnetic field problems, the magnetic vector potential is widely used for static, time-harmonic and transient problems. However, for 3-D electromagnetic field computations, depending upon the problem type, one potential may be preferable over the others. Several formulations based on different potentials have been proposed in the literature. All these 3-D formulations can be broadly classified into two types of applications: static fields and time-varying fields (time-harmonic or transient).

For 3-D magnetostatic problems, the formulations based on the magnetic vector potential and the magnetic scalar potentials are widely used. The formulations based on the magnetic scalar potentials have a few advantages over those based on the magnetic vector potential since the degrees of freedom are three times less. However, there are some issues while using the magnetic scalar potentials, necessitating the use of mixed $\Omega - \Omega_r$ formulations for 3-D applications as discussed earlier.

For 3-D time-harmonic or transient problems involving eddy currents, either the electric vector potential (**T**) or the magnetic vector potential (**A**) must be used. The total domain of interest can be divided into two parts, a conducting domain with eddy currents and a nonconducting domain. The formulation based on **A** is straightforward; in the eddy current regions, the electric scalar potential (V) is considered in conjunction with **A**. In regions free of eddy currents, only **A** is considered. This **A-*V*, A** formulation is represented by the following regions and equations:

1. Thick conductors or eddy current regions: potentials used - A_x, A_y, A_z, and V

$$\nabla \times \frac{1}{\mu} \nabla \times \mathbf{A} + \sigma \nabla V + \sigma \frac{\partial \mathbf{A}}{\partial t} = 0 \cdot \tag{12.88}$$

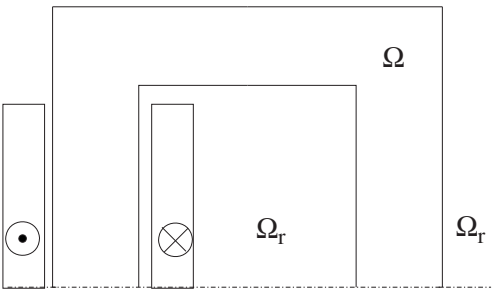

Figure 12.8 Use of total and reduced magnetic scalar potentials.

$$\nabla \cdot \left(-\sigma \nabla V - \sigma \frac{\partial \mathbf{A}}{\partial t} \right) = 0 \cdot \tag{12.89}$$

2. Stranded conductors: potentials used - A_x, A_y, A_z

$$\nabla \times \frac{1}{\mu} \nabla \times \mathbf{A} = \mathbf{J}. \tag{12.90}$$

In stranded conductors, eddy currents are neglected as explained in a later section wherein coupled field-circuit formulations are discussed.

3. Nonconducting source-free regions: potentials used - A_x, A_y, A_z

$$\nabla \times \frac{1}{\mu} \nabla \times \mathbf{A} = 0. \tag{12.91}$$

Since there are two sets of unknowns in the eddy current regions: **A** and V; the formulation has two equations (12.88 and 12.89). Equation 12.89 is the divergence-free condition corresponding to Ampere's law. The advantages of this formulation are that it can be used for multiply-connected regions, and external circuit equations can be easily coupled. In [20], a field-circuit coupled approach based on **A-***V*, **A** formulation is described, which can be used for the analysis of transient problems involving transformers. In a nonconducting source-free region, three unknowns need to be solved in the **A-***V*, **A** formulation. Hence, although this formulation is used universally for 2-D applications, it leads to a large number of unknowns in 3-D applications, which increases storage requirements as well as computational burden. Also, coils or windings need to be explicitly modeled and discretized, which further adds to the number of unknowns.

T-Ω formulations are used as alternatives to **A-***V* formulations for solving 3-D eddy current problems in transformers. The **A**-based formulation involves computation of three components of **A**, whereas in the **T-**Ω formulation, only one or at most two components of **T** need to be calculated [3, 6] in conducting regions only (in non-conducting regions, **T** is zero). The formulation is particularly advantageous for the analysis of laminated structures in transformers [21]. Short-circuit forces can also be calculated by using this mixed formulation [22]. In [23], such a formulation is used to model a 100 MVA power transformer under short-circuit transients. The paper also describes the field-circuit coupling methodology which is based on the electric vector and magnetic scalar potentials. In [24], 3-D distributions of eddy-current densities and loss densities in metallic structures near heavy current leads in a large transformer are calculated using the potentials. A disadvantage of the formulation is that the boundary conditions at conducting boundaries need to be imposed carefully. Another problem can arise from the fact that, in Equation 12.87, **T** and $-\nabla\Omega$ are of the same order leading to a larger error in the calculation of **H** if there is even a small error in calculating these two field quantities. Hence, mixed formulations using **T**, Ω and Ω_r are also used.

12.4 Finite Element Method

In various chapters of this book and specifically in Section 12.1.2, the utility of FEM for design and analysis of transformers has been highlighted. In this section, the theory of FEM and its procedures for static, time-harmonic, and transient formulations are described. Techniques for handling nonlinearity are also briefly covered. For a detailed description of the method and its applications, there are many textbooks dedicated to the subject [5, 7, 8, 9, 10, 11, 25, 26]. This section is intended to give exposure of the method to practicing transformer engineers and researchers so that they can simulate complex field problems using commercial software with better understanding; they can even develop 2-D codes for computation of various performance parameters of the transformers. The discussion on the FEM theory is restricted for two reasons to 1-D and 2-D problems. First, the procedural details for 3-D computations become unwieldy, and, secondly, practicing engineers and even researchers generally use commercial software for 3-D applications. The development of 3-D code for solving practical problems is a herculean task which involves use of sophisticated algorithms for solving large and sparse matrices, in addition to other computational complexities.

Although other numerical methods such as BEM are also being used, in this text, the theory and applications of FEM is covered as it has emerged as the most versatile method; for the other methods the readers can refer books dealing with them [5, 7, 13, 27].

12.4.1 1-D electric field problem

Let us take an illustrative example of a cylindrical capacitor that can be viewed as representing the LV-HV gap in a transformer. We have to compute the potential as well as electric field distribution in the gap and the capacitance between the two windings. In order to simplify FEM procedural details, the actual gap with combined oil-pressboard insulation is converted into an equivalent gap having only one dielectric, say, oil. If we assume a uniform field condition, which will be the case when the diameters of the windings are large, the total thickness of the pressboard (*pb*) insulation can be reduced by a factor of $\varepsilon_{pb}/\varepsilon_{oil}$, according to Equation 12.41, taking into consideration the fact that the electric field has only the radial (i.e., normal) component.

The geometry of the problem is the same as that given in Figure 8.2, wherein the radii of the two electrodes are R_1 (= 300 mm) and R_2 (= 350 mm). The dielectric between the electrodes has permittivity ε. The inner electrode is at potential V, say 300 kVp, and the outer electrode is assumed to have zero potential (this condition simulates a condition wherein the inner winding is subjected to an impulse overvoltage of 300 kV peak with the outer winding grounded). The field solution for the problem can be obtained exactly using Equation 8.4. We will

compare the results of the FEM analysis with the closed form expression. The field distribution is governed by Laplace's equation:

$$\varepsilon \nabla^2 V = -\rho = 0 \qquad \Rightarrow \qquad \varepsilon \left\{ \frac{1}{r}\frac{\partial}{\partial r}\left(r\frac{\partial V}{\partial r} \right) + \frac{1}{r^2}\frac{\partial^2 V}{\partial \phi^2} + \frac{\partial^2 V}{\partial z^2} \right\} = 0$$

with the boundary conditions,

$$V\,|_{r=300,\,0\le\varphi<2\pi} = 300 \text{ kV}$$
$$V\,|_{r=350,\,0\le\varphi<2\pi} = 0.$$

Since, V is a function of r only, the governing PDE takes the form:

$$\frac{1}{r}\frac{\partial}{\partial r}\left(\varepsilon\, r\frac{\partial V}{\partial r} \right) = 0$$

where ε has been taken inside the bracket to explain the procedure for a general case with multiple dielectrics. There are two popular approaches (a weighted residual method and a variational method) for solving the above equation [5, 7, 9, 11]. Both methods lead to the same linear system of equations and we will use the variational technique whose principles and procedure are simple to understand. The method is based on a principle that the solutions to governing PDEs (such as Laplace's equation above) are obtained when the total energy in the problem domain is minimized.

The expression for the total electrostatic energy in the cylindrical capacitor problem under consideration is given by:

$$W_e = \frac{1}{2}\int_s \varepsilon\, r \left|\nabla V\right|^2 dr\, d\phi \qquad \Rightarrow \qquad W_e = \frac{2\pi}{2}\int_l \varepsilon\, r \left|\nabla V\right|^2 dr \tag{12.92}$$

where the use is made of the fact that the integrand is independent of ϕ. Thus the problem becomes effectively one dimensional in terms of the variable *r*, with the corresponding geometry as shown in Figure 12.9 (a).

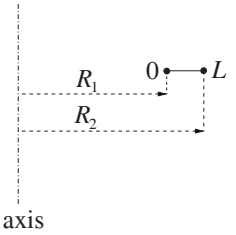

Figure 12.9 (a) 1-D geometry. (b) Finite elements.

The FEM procedure can be broadly divided into five steps: discretization of the domain, approximation of the solution, assembly of the system, imposition of boundary/source conditions, and finally solving the set of equations. Let us discretize the domain (0, L) into small subdomains which in this case will be short line segments. Let l^e (e = 1, 2, 3,…, M) denote the length of e^{th} element and M be the total number of the elements; here M = 10.

The second step is to select the interpolation functions. For simplicity we take linear functions; the voltage distribution within any element is assumed to vary linearly with the independent variable (r):

$$V^e(r) = a^e + b^e r \tag{12.93}$$

where a^e and b^e are the constants to be determined. There are two nodes associated with each element, one at r_1^e and the other at r_2^e :

$$V_1^e = a^e + b^e r_1^e \text{ and}$$

$$V_2^e = a^e + b^e r_2^e .$$

These two equations can be written in terms of matrices,

$$\begin{bmatrix} V_1^e \\ V_2^e \end{bmatrix} = \begin{bmatrix} 1 & r_1^e \\ 1 & r_2^e \end{bmatrix} \begin{bmatrix} a^e \\ b^e \end{bmatrix} \quad \Rightarrow \quad \begin{bmatrix} a^e \\ b^e \end{bmatrix} = \begin{bmatrix} 1 & r_1^e \\ 1 & r_2^e \end{bmatrix}^{-1} \begin{bmatrix} V_1^e \\ V_2^e \end{bmatrix}.$$

Substituting back into Equation 12.93, we have

$$V^e(r) = \begin{bmatrix} 1 & r \end{bmatrix} \begin{bmatrix} a^e \\ b^e \end{bmatrix} = \begin{bmatrix} 1 & r \end{bmatrix} \begin{bmatrix} 1 & r_1^e \\ 1 & r_2^e \end{bmatrix}^{-1} \begin{bmatrix} V_1^e \\ V_2^e \end{bmatrix}$$

or,

$$V^e = \sum_{j=1}^{2} N_j^e V_j^e . \tag{12.94}$$

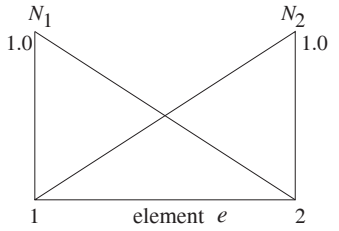

Figure 12.10 1-D Shape functions.

N_j^e denotes the interpolation or shape functions which are given by

$$N_1^e = \frac{r_2^e - r}{l^e} \quad \text{and} \quad N_2^e = \frac{r - r_1^e}{l^e} \tag{12.95}$$

where $l^e = r_2^e - r_1^e$. The functions N_j^e, which depend on the independent variable *r,* are shown in Figure 12.10. N_1^e (N_2^e) equals 1 at node 1 (2) and zero at node 2 (1); at any intermediate point its value is a fraction between 0 and 1. This is an obvious result given the expression, as in Equation 12.94, for voltage at any point within the element, $V^e = N_1^e V_1^e + N_2^e V_2^e$. For example, at node 1, $V^e = V_1^e$ leading to $N_1^e = 1$ and $N_2^e = 0$. Thus, for the nodes, $\left(N_i^e\right)_j = \delta_{ij}$, where $\delta_{ij} = 1$ when $i = j$ and $\delta_{ij} = 0$ when $i \neq j$. At any point in the element including the two end nodes, $N_1^e + N_2^e = 1$. It should be emphasized here that the shape functions defined by Equation 12.95 are not valid at any point outside the element.

The energy of an element *e* is expressed using Equations 12.92 and 12.94 as

$$W_e^e = \pi \int_{r_1^e}^{r_2^e} \varepsilon r \left|\nabla V\right|^2 dr = \pi \int_{r_1^e}^{r_2^e} \varepsilon r \left|\nabla\left(\sum_{j=1}^{2} N_j^e V_j^e\right)\right|^2 dr$$

$$= \pi \int_{r_1^e}^{r_2^e} \varepsilon r \left|\left(\sum_{j=1}^{2} \left(\nabla N_j^e\right) V_j^e\right)\right|^2 dr$$

$$= \pi \int_{r_1^e}^{r_2^e} \varepsilon r \left[\left(\nabla N_1^e V_1^e + \nabla N_2^e V_2^e\right) \cdot \left(\nabla N_1^e V_1^e + \nabla N_2^e V_2^e\right)\right] dr$$

$$= \pi \sum_{i=1}^{2} \sum_{j=1}^{2} \int_{r_1^e}^{r_2^e} \varepsilon r \left[V_i^e \nabla N_i^e \cdot \nabla N_j^e V_j^e\right] dr$$

$$\therefore W_e^e = \pi \sum_{i=1}^{2} \sum_{j=1}^{2} V_i^e \left(\int_{r_1^e}^{r_2^e} \left(\varepsilon r \frac{\partial N_i^e}{\partial r} \frac{\partial N_j^e}{\partial r}\right) dr\right) V_j^e \,.$$

Let $k_{ij}^e = \int_{r_1^e}^{r_2^e} \left(\varepsilon r \frac{\partial N_i^e}{\partial r} \frac{\partial N_j^e}{\partial r}\right) dr$ and $k^e = \begin{bmatrix} k_{11}^e & k_{12}^e \\ k_{21}^e & k_{22}^e \end{bmatrix}$

where k^e is called the elemental stiffness matrix, which depends on the geometrical details and material properties of the element. For example,

$$k_{11}^e = \int_{r_1^e}^{r_2^e} \varepsilon\, r \frac{\partial N_1^e}{\partial r} \frac{\partial N_1^e}{\partial r} dr\,.$$

Using Equation 12.95, we obtain

$$k_{11}^e = \int_{r_1^e}^{r_2^e} \varepsilon\, r \left(\frac{\partial}{\partial r} \frac{r_2^e - r}{l^e} \right) \left(\frac{\partial}{\partial r} \frac{r_2^e - r}{l^e} \right) dr \quad \Rightarrow \quad k_{11}^e = \varepsilon \frac{\left(r_2^e\right)^2 - \left(r_1^e\right)^2}{2\left(l^e\right)^2}\,.$$

Similarly, we have

$$k_{12}^e = \int_{r_1^e}^{r_2^e} \varepsilon\, r \left(\frac{\partial}{\partial r} \frac{r_2^e - r}{l^e} \right) \left(\frac{\partial}{\partial r} \frac{r - r_1^e}{l^e} \right) dr \quad \Rightarrow \quad k_{12}^e = -\varepsilon \frac{\left(r_2^e\right)^2 - \left(r_1^e\right)^2}{2\left(l^e\right)^2}$$

$$k_{21}^e = \int_{r_1^e}^{r_2^e} \varepsilon\, r \left(\frac{\partial}{\partial r} \frac{r - r_1^e}{l^e} \right) \left(\frac{\partial}{\partial r} \frac{r_2^e - r}{l^e} \right) dr \quad \Rightarrow \quad k_{21}^e = -\varepsilon \frac{\left(r_2^e\right)^2 - \left(r_1^e\right)^2}{2\left(l^e\right)^2}$$

$$k_{22}^e = \int_{r_1^e}^{r_2^e} \varepsilon\, r \left(\frac{\partial}{\partial r} \frac{r - r_1^e}{l^e} \right) \left(\frac{\partial}{\partial r} \frac{r - r_1^e}{l^e} \right) dr \quad \Rightarrow \quad k_{22}^e = \varepsilon \frac{\left(r_2^e\right)^2 - \left(r_1^e\right)^2}{2\left(l^e\right)^2}\,.$$

The elemental energy can, therefore, be expressed as

$$W_e^e = \pi \left\{ V^e \right\}^{\mathrm{T}} \left[k^e \right] \left\{ V^e \right\}$$

where, $V^e = \left\{ V_1^e \;\; V_2^e \right\}^{\mathrm{T}}$.

The following connectivity matrix gives the correspondence between the global node numbers with the local node numbers of each element,

$$\begin{array}{c} \\ 1^e \\ 2^e \end{array} \begin{array}{c} \begin{array}{cccccccccc} e_1 & e_2 & e_3 & e_4 & e_5 & e_6 & e_7 & e_8 & e_9 & e_{10} \end{array} \\ \begin{pmatrix} 1 & 2 & 3 & 4 & 5 & 6 & 7 & 8 & 9 & 10 \\ 2 & 3 & 4 & 5 & 6 & 7 & 8 & 9 & 10 & 11 \end{pmatrix} \end{array}$$

where 1^e and 2^e are the local node numbers of each finite element and 1, 2, …, 11 are the global node numbers; the number of nodes (n) and elements (M) are 11 and 10, respectively, with reference to Figure 12.9 (b). The global matrix entries can now be calculated as

$$K_{11} = k_{11}^{e_1}, \quad K_{12} = k_{12}^{e_1} = k_{21}^{e_1} = K_{21}, \quad K_{1i} = k_{i1} = 0 \quad i = 3,4,\cdots,11$$
$$K_{22} = k_{22}^{e_1} + k_{11}^{e_2} \quad K_{23} = k_{12}^{e_2} = K_{32}$$
$$K_{55} = k_{22}^{e_4} + k_{11}^{e_5} \quad \text{and so on...}$$

Thus, the global coefficient or stiffness matrix is

$$K = \begin{array}{c} \\ 1 \\ 2 \\ 3 \\ \vdots \\ 11 \end{array} \begin{array}{c} \begin{array}{ccccc} 1 & 2 & 3 & \cdots & 11 \end{array} \\ \begin{pmatrix} k_{11}^{e_1} & k_{12}^{e_1} & 0 & \cdots & 0 \\ k_{21}^{e_1} & k_{22}^{e_1} + k_{11}^{e_2} & k_{12}^{e_2} & \cdots & 0 \\ 0 & k_{21}^{e_2} & k_{22}^{e_2} + k_{11}^{e_3} & \cdots & 0 \\ \vdots & & & \ddots & \vdots \\ 0 & 0 & 0 & \cdots & k_{22}^{e_{10}} \end{pmatrix} \end{array}.$$

It is a tridiagonal and sparse matrix. Off-diagonal entries corresponding to nodes that are not directly connected via any element are zero. The energy for the whole domain is

$$W_e = \pi \{V\}^{\mathrm{T}} [K] \{V\}.$$

Here, K is a matrix of dimensions 11×11 and V is a vector of dimensions 11×1,

$$V = \{V_1 \quad V_2 \quad V_3 \quad V_4 \quad V_5 \quad V_6 \quad V_7 \quad V_8 \quad V_9 \quad V_{10} \quad V_{11}\}^{\mathrm{T}}.$$

The total energy of the system can be minimized by differentiating it with respect to nodal potential variables,

$$\left(\frac{\partial W_e}{\partial V_1} \quad \frac{\partial W_e}{\partial V_2} \quad \cdots \quad \frac{\partial W_e}{\partial V_{11}} \right)^{\mathrm{T}} = 0.$$

A set of n number of simultaneous equations obtained from the above equation can be written in matrix form as

$$[K]\{V\} = 0 \quad \Rightarrow \varepsilon [K_1]\{V\} = 0 \quad \Rightarrow \quad [K_1]\{V\} = 0$$

where $[K] = \varepsilon [K_1]$. Thus, for a problem domain with a single homogeneous material the dielectric constant does not decide the voltage distribution. If there were two dielectric materials (1 and 2) with ε_1 and ε_2 as their permittivities, the nonzero entries of $[K_1]$ corresponding to elements in dielectric-1 and dielectric-2 will be multiplied by ε_1 and ε_2, respectively.

The linear system of equations does not have a unique solution since the boundary conditions have not yet been imposed. After imposing the boundary conditions, $V_1 = 300$ kV and $V_{11} = 0$ kV, we have

$$\begin{pmatrix} 1 & 0 & 0 & \cdots & 0 & 0 \\ -121 & 244 & -123 & \cdots & 0 & 0 \\ 0 & -123 & 248 & \cdots & 0 & 0 \\ \vdots & \vdots & \vdots & \ddots & \vdots & \vdots \\ 0 & 0 & 0 & \cdots & 276 & -139 \\ 0 & 0 & 0 & 0 & 0 & 1 \end{pmatrix} \begin{Bmatrix} V_1 \\ V_2 \\ V_3 \\ \vdots \\ V_{10} \\ V_{11} \end{Bmatrix} = \begin{Bmatrix} 300e3 \\ 0 \\ 0 \\ \vdots \\ 0 \\ 0 \end{Bmatrix}$$

which after simplification becomes,

$$\begin{pmatrix} 244 & -123 & \cdots & 0 \\ -123 & 248 & \cdots & 0 \\ \vdots & \vdots & \ddots & \vdots \\ 0 & 0 & \cdots & 276 \end{pmatrix} \begin{Bmatrix} V_2 \\ V_3 \\ \vdots \\ V_{10} \end{Bmatrix} = \begin{Bmatrix} 363e5 \\ 0 \\ \vdots \\ 0 \end{Bmatrix}.$$

The solution of the above equations in kV is:

V_2	V_3	V_4	V_5	V_6	V_7	V_8	V_9	V_{10}
267.8	236.2	205.0	174.4	144.2	114.5	85.2	56.4	28.0

The voltage drop is almost linear because of a near-uniform field condition since the diameters of the two electrodes are much larger than the gap separating them.

Once V_1^e and V_2^e for each element are known, constants a^e and b^e are calculated from Equation 12.93. The electric field intensity, **E**, is computed from Equations 12.93, 12.15 and 12.17 as $\mathbf{E} = -b\,\mathbf{a}_r$. The electric field intensity in any element can also be directly calculated as $\mathbf{E}^e = \left(V_1^e - V_2^e\right) \Big/ l^e \,\mathbf{a}_r$. The values of **E** thus calculated match closely with those obtained from the closed form expression given by Equation 8.4.

For a single homogeneous cylindrical dielectric between two circular electrodes, the electric stress is highest at the surface of the inner electrode, which reduces as we approach toward the surface of the outer electrode. The insulation is not uniformly stressed and thus not effectively utilized. Hence, in OIP (oil-impregnated paper) condenser bushings, better stress distribution is achieved by insertion of floating foils made of aluminum or a semiconducting material. If edge effects are neglected, the total charge (Q) appearing on each conducting foil is the same. The electric field intensity in a section between two adjacent foils is [28]

$$E_n = \frac{Q}{2\pi\,\varepsilon\,R_n\,l_n}$$

where, R_n and l_n are the mean radius and the length of the section, respectively. Thus the stresses in all the sections can be made equal by ensuring that the product $R_n \times l_n$ is kept constant. Therefore, with increasing distance from the axis the lengths of the foils are reduced in the OIP bushings.

In the gap between the HV and LV windings in transformers, the field is almost uniform except in the ducts immediately adjacent to the windings. Hence, the stress equalization approach is not needed; the higher stresses at the conductor corners are handled by other design means as discussed in Chapter 8.

12.4.2 2-D magnetic field problem

Let us take an illustrative example of a core joint as shown in Figure 12.11. Here, it is a simplified model in which the joint is considered without gaps and the material is assumed isotropic and homogeneous, having a constant value of relative permeability ($\mu = \mu_0 \mu_r$). If we wish to set up flux density of 1.7 T in the core width of 0.15 m, the flux passing through the cross section area per meter depth is 0.255 Wb (= 1.7×0.15×1). This amount of flux can be established by using appropriate boundary conditions. On the a-b-c and d-e-f boundaries, in accordance with Equation 12.68, let us assign the value of A_z as 0.255 and 0, respectively, to establish the required flux. Equipotential lines will be normal to a-f and c-d boundaries (i.e., a Neumann boundary condition). We will now discuss the FEM procedure for solving this 2-D problem in Cartesian coordinates.

The field distribution in this case is governed by Laplace's equation:

$$-\frac{1}{\mu}\nabla^2 A_z = J_z = 0 \quad \Rightarrow \frac{1}{\mu}\left\{\frac{\partial^2 A_z}{\partial x^2} + \frac{\partial^2 A_z}{\partial y^2}\right\} = 0 .$$

The magnetic material is assumed to have homogeneous and isotropic properties; its permeability is constant. The energy stored in the magnetic field is [7]

$$W_m = \frac{1}{2\mu}\int_s \left|\nabla A_z\right|^2 ds . \tag{12.96}$$

We will choose a linear interpolating function for simplicity (the subscript z is dropped for brevity):

$$A^e(x, y) = a^e + b^e x + c^e y \tag{12.97}$$

where a^e, b^e and c^e are constants. The corresponding nodal potentials are:

$$A_1^e = a^e + b^e x_1^e + c^e y_1^e$$
$$A_2^e = a^e + b^e x_2^e + c^e y_2^e$$
$$A_3^e = a^e + b^e x_3^e + c^e y_3^e .$$

These three equations can be written in matrix form,

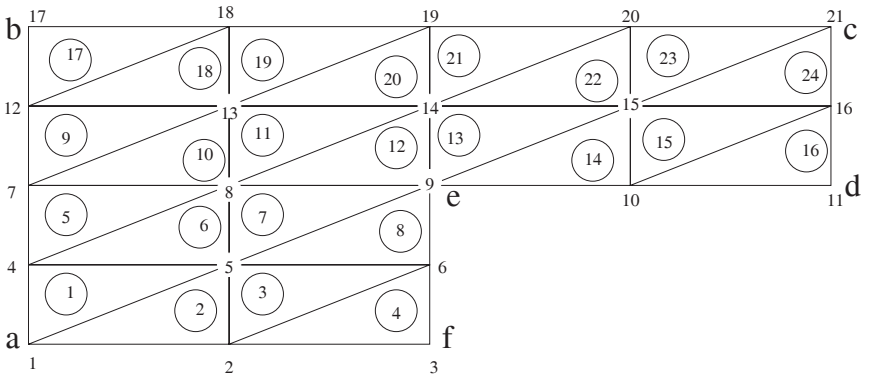

Figure 12.11 Core joint – 2-D FEM mesh.

$$\begin{bmatrix} A_1^e \\ A_2^e \\ A_3^e \end{bmatrix} = \begin{bmatrix} 1 & x_1^e & y_1^e \\ 1 & x_2^e & y_2^e \\ 1 & x_3^e & y_3^e \end{bmatrix} \begin{bmatrix} a^e \\ b^e \\ c^e \end{bmatrix} \quad \Rightarrow \quad \begin{bmatrix} a^e \\ b^e \\ c^e \end{bmatrix} = \begin{bmatrix} 1 & x_1^e & y_1^e \\ 1 & x_2^e & y_2^e \\ 1 & x_3^e & y_3^e \end{bmatrix}^{-1} \begin{bmatrix} A_1^e \\ A_2^e \\ A_3^e \end{bmatrix}.$$

Substituting back into Equation 12.97, we have

$$A^e = \begin{bmatrix} 1 & x & y \end{bmatrix} \begin{bmatrix} a^e \\ b^e \\ c^e \end{bmatrix} = \begin{bmatrix} 1 & x & y \end{bmatrix} \begin{bmatrix} 1 & x_1^e & y_1^e \\ 1 & x_2^e & y_2^e \\ 1 & x_3^e & y_3^e \end{bmatrix}^{-1} \begin{bmatrix} A_1^e \\ A_2^e \\ A_3^e \end{bmatrix}$$

$$\therefore A^e = \sum_{j=1}^{3} N_j^e A_j^e \,. \tag{12.98}$$

N_j^e denotes shape functions which are given by (the superscript *e* on coordinates is dropped for brevity),

$$\begin{aligned} N_1^e &= \frac{1}{2\Delta^e}[(x_2 y_3 - x_3 y_2) + (y_2 - y_3)x + (x_3 - x_2)y] \\ N_2^e &= \frac{1}{2\Delta^e}[(x_3 y_1 - x_1 y_3) + (y_3 - y_1)x + (x_1 - x_3)y] \\ N_3^e &= \frac{1}{2\Delta^e}[(x_1 y_2 - x_2 y_1) + (y_1 - y_2)x + (x_2 - x_1)y] \end{aligned} \tag{12.99}$$

where, $\Delta^e =$ area of the triangular element $= \frac{1}{2}\begin{vmatrix} 1 & x_1 & y_1 \\ 1 & x_2 & y_2 \\ 1 & x_3 & y_3 \end{vmatrix}$. (12.100)

The functions N_j^e, which depend of the independent variables *x* and *y,* are shown in Figure 12.12 (wherein the shaded portion is the element). Thus, N_1^e equals 1 at node 1 and it is zero at nodes 2 and 3; at any intermediate point its value is between 0 and 1. This follows from the expression in Equation 12.98, for the potential at any point within the element, $A^e = N_1^e A_1^e + N_2^e A_2^e + N_3^e A_3^e$ (e.g., at node 1: $A^e = A_1^e$, leading to N_1^e=1, $N_2^e = 0$ and $N_3^e = 0$). Thus, as in the 1-D case, for the nodes, $\left(N_i^e\right)_j = \delta_{ij}$, where $\delta_{ij} = 1$ when $i = j$ and $\delta_{ij} = 0$ when $i \neq j$. At any point in the element including the nodes, $N_1^e + N_2^e + N_3^e = 1$.

Substituting Equation 12.98 in 12.96, we have

$$W_m^e = \frac{1}{2\mu}\int_{\Omega^e}\left|\nabla\left(\sum_{j=1}^{3} N_j^e A_j^e\right)\right|^2 d\Omega \;\Rightarrow\; W_m^e = \frac{1}{2\mu}\int_{\Omega^e}\left|\left(\sum_{j=1}^{3}\left\{\nabla N_j^e\right\} A_j^e\right)\right|^2 d\Omega \text{ or}$$

$$W_m^e = \frac{1}{2\mu}\int_{\Omega^e}\left[\begin{array}{l}\left(\nabla N_1^e A_1^e + \nabla N_2^e A_2^e + \nabla N_3^e A_3^e\right)\cdot \\ \left(\nabla N_1^e A_1^e + \nabla N_2^e A_2^e + \nabla N_3^e A_3^e\right)\end{array}\right] d\Omega$$

$$\Rightarrow W_m^e = \frac{1}{2\mu}\sum_{i=1}^{3}\sum_{j=1}^{3}\int_{\Omega^e} A_i^e \nabla N_i^e \cdot \nabla N_j^e A_j^e \, d\Omega$$

$$\Rightarrow W_m^e = \frac{1}{2\mu}\sum_{i=1}^{3}\sum_{j=1}^{3} A_i^e \left(\int_{\Omega^e} \nabla N_i^e \cdot \nabla N_j^e d\Omega\right) A_j^e$$

$$\Rightarrow W_m^e = \frac{1}{2\mu}\sum_{i=1}^{3}\sum_{j=1}^{3} A_i^e \left[\int_{\Omega^e}\left(\frac{\partial N_i^e}{\partial x}\frac{\partial N_j^e}{\partial x} + \frac{\partial N_i^e}{\partial y}\frac{\partial N_j^e}{\partial y}\right) d\Omega\right] A_j^e \,.$$

The entries of the element coefficient matrix are

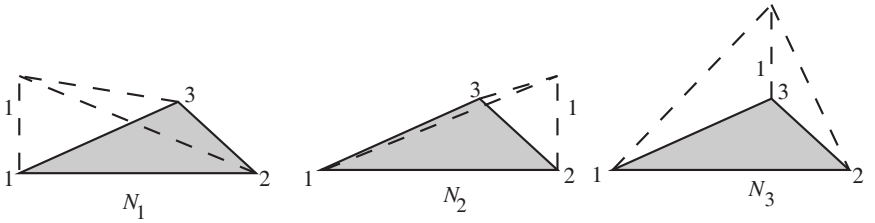

Figure 12.12 2-D shape functions.

$$k_{ij}^e = \frac{1}{\mu}\int_{\Omega^e}\left(\frac{\partial N_i^e}{\partial x}\frac{\partial N_j^e}{\partial x}+\frac{\partial N_i^e}{\partial y}\frac{\partial N_j^e}{\partial y}\right)d\Omega \text{ and} \tag{12.101}$$

$$k^e = \begin{bmatrix} k_{11}^e & k_{12}^e & k_{13}^e \\ k_{21}^e & k_{22}^e & k_{23}^e \\ k_{31}^e & k_{32}^e & k_{33}^e \end{bmatrix}.$$

The elemental energy can thus be represented as

$$W_m^e = \frac{1}{2}\left\{A^e\right\}^{\mathrm{T}}\left[k^e\right]\left\{A^e\right\} \tag{12.102}$$

where, $A^e = \left\{ A_1^e \;\; A_2^e \;\; A_3^e \right\}^{\mathrm{T}}$.

For example, $k_{11}^e = \frac{1}{\mu}\int_{\Omega^e}\nabla N_1^e \cdot \nabla N_1^e \, d\Omega$. Using Equation 12.99, we obtain

$$k_{11}^e = \frac{1}{4\mu\left(\Delta^e\right)^2}\left[(y_2-y_3)^2+(x_3-x_2)^2\right]\int_{\Omega^e} d\Omega = \frac{1}{4\mu\Delta^e}\left[(y_2-y_3)^2+(x_3-x_2)^2\right]$$

(since $\int_{\Omega^e} d\Omega = \Delta^e$, i.e., the element area).

Similarly, we have

$$k_{12}^e = \frac{1}{\mu}\int_{\Omega^e}\nabla N_1^e \cdot \nabla N_2^e d\Omega = \frac{1}{4\mu\Delta^e}\left[(y_2-y_3)(y_3-y_1)+(x_3-x_2)(x_1-x_3)\right]$$

$$k_{13}^e = \frac{1}{\mu}\int_{\Omega^e}\nabla N_1^e \cdot \nabla N_3^e d\Omega = \frac{1}{4\mu\Delta^e}\left[(y_2-y_3)(y_1-y_2)+(x_3-x_2)(x_2-x_1)\right].$$

The global coefficient matrix is of dimensions 21×21. The following connectivity matrix can be written for the first eight elements by referring to Figure 12.11 ($1^e, 2^e$ and 3^e are the local node numbers for each element, which are not shown in the figure for brevity):

$$\begin{array}{c} \\ 1^e \\ 2^e \\ 3^e \end{array}\begin{array}{c} \begin{array}{cccccccc} e_1 & e_2 & e_3 & e_4 & e_5 & e_6 & e_7 & e_8 \end{array} \\ \begin{pmatrix} 1 & 1 & 2 & 2 & 4 & 4 & 5 & 5 \\ 5 & 2 & 6 & 3 & 8 & 5 & 9 & 6 \\ 4 & 5 & 5 & 6 & 7 & 8 & 8 & 9 \end{pmatrix} \end{array}.$$

For example, a few entries of the global coefficient matrix $[K]$ are

$$K_{11} = k_{11}^{e_1} + k_{11}^{e_2}, \quad K_{12} = k_{12}^{e_2} = k_{21}^{e_2} = K_{21}, \quad K_{14} = k_{13}^{e_1} = K_{41}$$
$$K_{15} = k_{12}^{e_1} + k_{13}^{e_2} = K_{51},$$
$$K_{22} = k_{22}^{e_2} + k_{11}^{e_3} + k_{11}^{e_4}, \quad K_{21} = k_{12}^{e_2} = K_{12}, \quad K_{23} = k_{12}^{e_4} = K_{32},$$
$$K_{25} = k_{23}^{e_2} + k_{13}^{e_3} = K_{52}, \quad \text{and so on.}$$

The total energy in the whole model can now be expressed as

$$W_m = \frac{1}{2}\{A\}^{\mathrm{T}}[K]\{A\} \tag{12.103}$$

where, $\{A\}$ is a column vector of all nodal potential values,

$$\{A\} = \{A_1 \quad A_2 \quad A_3 \quad \cdots \quad A_{21}\}^{\mathrm{T}}.$$

The total energy of the system is minimized by differentiating it with respect to the nodal potential variables and equating to zero, as done in the previous example. After imposing the boundary conditions, A = 0.255 Wb/m at all nine nodes on the boundary a-b-c and A = 0 Wb/m at all five nodes on the boundary d-e-f, we obtain a set of 21 equations which can be solved to obtain the solution. The values of the magnetic vector potential thus obtained at various nodes are:

A_2	A_5	A_8	A_{13}	A_{14}	A_{15}	A_{16}
0.1303	0.1332	0.1473	0.2012	0.1473	0.1332	0.1303

The corresponding plot of equipotential lines is shown in Figure 12.13 (a). The field lines are not smooth since the mesh is not good (fine) enough. When the mesh is made dense with 3840 elements, an accurate solution is obtained whose field plot is shown in Figure 12.13 (b).

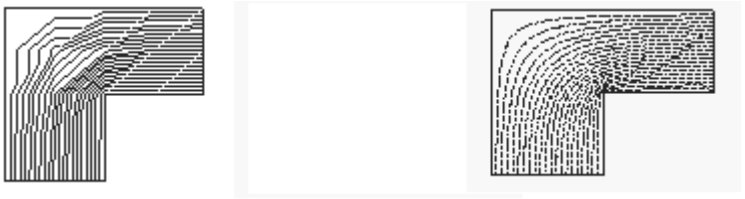

(a) (b)

Figure 12.13 (a) Equipotential (A) lines for the coarse mesh of Figure 12.11.
(b) Equipotential (A) lines for a dense mesh.

(a) (b)

Figure 12.14 (a) Equipotential (Ω) lines for the coarse mesh of Figure 12.11.
(b) Equipotential (Ω) lines for a dense mesh.

The above problem can also be formulated in terms of the magnetic scalar potential (since there is no current source in the problem domain). Equation 12.82 can be written in an integral form to express the difference in potentials on the boundaries c-d and a-f in terms of the magnetic field intensity,

$$\Omega_{\text{c-d}} - \Omega_{\text{a-f}} = -\int \mathbf{H} \cdot d\mathbf{l} \, .$$

For a flux density value of 1.7 T and an assumed value of relative permeability of 5000, the magnitude of **H** is 270.56 A/m according to Equation 12.8. Assuming that the magnitude of the vector is constant along the path of integration along a contour joining boundaries c-d and a-f (which is an approximation), we obtain for the mean core length of 0.45 m, $\Omega_{\text{c-d}} - \Omega_{\text{a-f}} = 121.75$ A. Hence, the boundary conditions can be defined as $\Omega_{\text{c-d}} = 121.75$ and $\Omega_{\text{a-f}} = 0$, and the corresponding governing PDE is given by Equation 12.83, a Laplace's equation, which can be solved by using the procedure outlined earlier. The field plots for the coarse and dense meshes are shown in Figure 12.14. The equi-Ω lines are normal to the equi-*A* lines of Figure 12.13.

12.5 FEM Formulations

12.5.1 Static formulations

Through a specific application to a PDE representing a magnetostatic formulation, we will understand the theory and procedure of the Galerkin method which is more versatile in applicability to a variety of field computation problems. In the variational method, described in the previous section, a functional (an energy expression) is minimized which has an energy interpretation. However, a functional is not guaranteed to exist for all practical problems.

Let us consider Poisson's equation for a 2-D magnetostatic case (Equation 12.80). In the weighted residual approach, the solution is obtained by weighting the residual of the governing PDE. The residual (error) for an assumed approximate solution, $\tilde{A}_z(x, y) = a + bx + cy$, is

$$r = -\frac{\partial}{\partial x}\left(\upsilon_x \frac{\partial \tilde{A}_z}{\partial x}\right) - \frac{\partial}{\partial y}\left(\upsilon_y \frac{\partial \tilde{A}_z}{\partial y}\right) - J_z \neq 0 \tag{12.104}$$

where υ is the inverse of μ. The approximation should be chosen in such a way that the residual over all points in the domain is reduced to a least possible value in a weighted integral sense. In FEM, the domain is divided into elements with corresponding nodes; hence the minimization of the residual over the domain amounts to enforcing the condition:

$$R_i = \int_S W_i \, r \, dx \, dy = 0$$

where *S* is the area of the domain and *i* is a node in the domain. The weighting functions are selected as the corresponding nodal shape functions (Equation 12.99) in Galerkin's method, which leads to the same set of equations as obtained using the variational approach. For each element, there are three nodes giving the following set of three equations

$$R_i^e = \int_s N_i^e r \, dx \, dy \qquad i = 1, 2, 3$$

where *s* represents the element area. Substituting the expression of *r* (at element level) and dropping the subscript *z* and the symbol ~ in the variable *A* for brevity, we obtain

$$R_i^e = \int_s N_i^e \left(-\frac{\partial}{\partial x}\left(\upsilon_x \frac{\partial A^e}{\partial x}\right) - \frac{\partial}{\partial y}\left(\upsilon_y \frac{\partial A^e}{\partial y}\right) - J^e \right) dx \, dy \, .$$

Integrating by parts and using the fact that we have either a Dirichlet condition or homogeneous Neumann condition or both at the boundaries, the above expression is simplified as [9]

$$R_i^e = \int_s \left(\upsilon_x \frac{\partial N_i^e}{\partial x}\frac{\partial A^e}{\partial x} + \upsilon_y \frac{\partial N_i^e}{\partial y}\frac{\partial A^e}{\partial y} \right) dx \, dy - \int_s N_i^e J^e \, dx \, dy \qquad i = 1, 2, 3.$$

Substituting the expression of A^e from Equation 12.98 in terms of the three nodal shape functions, we have

$$R_i^e = \sum_{j=1}^{3} \left\{ \int_s \left(\upsilon_x \frac{\partial N_i^e}{\partial x}\frac{\partial N_j^e}{\partial x} + \upsilon_y \frac{\partial N_i^e}{\partial y}\frac{\partial N_j^e}{\partial y} \right) A_j^e \, dx \, dy \right\} - \int_s N_i^e J^e \, dx \, dy. \tag{12.105}$$

The bracketed expression under the integral sign in the first term on the right side is present in Equation 12.101 (for $\upsilon_x = \upsilon_y = \upsilon = 1/\mu$), which resulted in the

element coefficient matrix of dimensions 3×3 in the variational formulation. We have an additional term here, involving the source J^e, which contributes to a column matrix f^e, representing sources, if the current density is nonzero in the element under consideration. It should be remembered that a global F matrix, assembled using f^e matrices, is further modified when boundary conditions are imposed. In the previous example, the source is only in the form of boundary conditions. We would have encountered the additional term in that example had there been a current density distribution in any part of the domain in Figure 12.11, since in that case the corresponding energy functional is [7]

$$I = \frac{1}{2\mu}\int_S |\nabla A|^2 \, dS - \int_S J\, A \, dS \, . \tag{12.106}$$

It is interesting to further note that the source term reduces the stored energy; the (external) source has to expend some energy to set up a given magnetic field [19].

Thus, in general, the entries of the *f* matrix are contributed by the source and boundary conditions. From the above discussion it can be concluded that, for a given problem defined by a corresponding PDE, Galerkin's method and the variational procedure lead to identical matrices at the element and global levels.

Having understood the equivalence between the two approaches, let us express Equation 12.105 in matrix form:

$$\left\{R^e\right\} = \left[k^e\right]\left\{A^e\right\} - \left\{f^e\right\} . \tag{12.107}$$

The entries of matrix k^e are determined as explained in Section 12.4. The formation of the f^e matrix involves calculation of the integral $\int N_i^e J^e \, dx \, dy$. For a triangular element with a linear (first-order) approximation of the potential function (as being considered here), such integrals can be evaluated analytically through the following closed form expression [29]:

$$\iint_s \left(N_1^e\right)^l \left(N_2^e\right)^m \left(N_3^e\right)^n \, dxdy = \frac{l!\, m!\, n!}{(l+m+n+2)!} 2\Delta^e \, . \tag{12.108}$$

It should be remembered that for higher order elements, analytical expressions of the corresponding integrals are not available and hence numerical integration techniques need to be used for the purpose [5]. For the present case, $l = 1$ and $m = n = 0$, giving

$$\int_s N_i^e J^e \, dx \, dy = \frac{J^e \Delta^e}{3} .$$

Thus, with $i = 1, 2, 3$ the elemental matrix representing the source becomes

$$\left\{f^e\right\} = \frac{J^e \Delta^e}{3}\{1 \quad 1 \quad 1\}^{\mathrm{T}} \quad \Rightarrow \quad f_i^e = J^e \frac{\Delta^{\mathrm{e}}}{3}. \tag{12.109}$$

In other words, the current in an element is apportioned equally to its three nodes in the FEM procedure. After the assembly of all the elemental equations and the enforcement of the condition that the residue is zero, we have

$$\{R\} = \sum_{e=1}^{M}\left\{R^e\right\} = \sum_{e=1}^{M}\left(\left[k^e\right]\left\{A^e\right\} - \left\{f^e\right\}\right) = 0 \qquad \Rightarrow \qquad [K]\{A\} = \{F\}.$$

If we let

$$\begin{aligned} &u_1 = y_2 - y_3;\ u_2 = y_3 - y_1;\ u_3 = y_1 - y_2 \\ &v_1 = x_3 - x_2;\ v_2 = x_1 - x_3;\ v_3 = x_2 - x_1 \end{aligned} \tag{12.110}$$

then the expressions for the entries of the 3×3 element coefficient matrix calculated earlier can be conveniently expressed as

$$k_{ij}{}^{e} = \frac{\left(u_i u_j + v_i v_j\right)}{4\Delta^{\mathrm{e}}\mu}. \tag{12.111}$$

The expression for the element area in Equation 12.100 becomes

$$\Delta^e = \frac{1}{2}\left(u_1 v_2 - u_2 v_1\right).$$

Using Equations 12.111 and 12.109, the global matrices [*K*] and [*F*] can be easily formed once the connectivity details between the elements and the global node numbers are known [9],

$$\begin{aligned} K_{n(i,e),n(j,e)} &= K_{n(i,e),n(j,e)} + k^e{}_{ij} \\ F_{n(i,e)} &= F_{n(i,e)} + f_i^e. \end{aligned} \tag{12.112}$$

It should be noted that *i* and *j* are the local node numbers of the element *e*, and $n(i,e)$ and $n(j,e)$ give the corresponding global numbers. After having calculated $\left[k_{ij}^e\right]_{3\times3}$ and $\left\{f_i^e\right\}_{3\times1}$ matrices using Equations 12.111 and 12.109, respectively, for each finite element in the problem domain, the two global matrices are assembled by executing Equation 12.112 for all the elements in a computer code. The information of connectivity details, material properties and coordinates of the nodes for each element can be obtained by drawing the problem geometry and by forming the mesh in commercial FEM software or in

the PDE toolbox of MATLAB®. There are many free/commercial mesh generators available for the purpose. The global numbers of the nodes on the outermost boundary can also be known for imposing boundary conditions later. Two dimensional FEM codes can be easily developed using this procedure.

12.5.2 Time-harmonic formulations

These formulations are used for analysis of eddy current losses in windings and structural parts of transformers. The involved materials are assumed to have linear magnetic characteristics so that for a given sinusoidal voltage/current excitation, all other voltages/currents and fields in the problem domain are also sinusoidal, allowing all of them to be treated as time-harmonic (phasor) quantities. The governing PDE for computation of eddy currents is as given by Equation 12.79. When Galerkin's method is applied, the residue for an element is obtained as

$$R_i^e = \sum_{j=1}^{3} \left\{ \int_s \left(\upsilon_x \frac{\partial N_i^e}{\partial x}\frac{\partial N_j^e}{\partial x} + \upsilon_y \frac{\partial N_i^e}{\partial y}\frac{\partial N_j^e}{\partial y} \right) \hat{A}_j^e \, dx \, dy - j\omega\sigma \int_s N_i^e \hat{A}_j^e \, dx \, dy \right\} - \int_s N_i^e \hat{J}^e \, dx \, dy.$$

The elemental level equation (again for 2-D triangular element with the first-order approximation) can be obtained as

$$\left\{R^e\right\} = \left[k^e\right]\left\{\hat{A}^e\right\} - j\omega\left[d^e\right]\left\{\hat{A}^e\right\} - \left\{\hat{f}^e\right\}. \tag{12.113}$$

The matrix k^e is identical to that in the case of the static formulation. Generally, the current density is taken as the reference phasor making the matrix $\hat{f}^e$ real (i.e., with no imaginary components) and identical to the matrix f^e in the static case. The additional matrix d^e evaluated using Equation 12.108 is

$$\left[d^e\right] = \sigma\frac{\Delta^e}{12}\begin{bmatrix} 2 & 1 & 1 \\ 1 & 2 & 1 \\ 1 & 1 & 2 \end{bmatrix}. \tag{12.114}$$

$\left[d^e\right]$ is a 3 × 3 matrix since $\hat{A} = N_1^e\hat{A}_1^e + N_2^e\hat{A}_2^e + N_3^e\hat{A}_3^e$ and there is one residual statement for each of the three nodes, thereby giving 9 terms. The entries of the matrix can be easily verified using the fact that for the diagonal elements, $l = 2$, $m = n = 0$, and for the off-diagonal elements, $l = m = 1$, $n = 0$, while using the expression in Equation 12.108. After assembling all the element equations, we have

$$[K]\{\hat{A}\} - j\omega[D]\{\hat{A}\} = \{\hat{F}\}. \tag{12.115}$$

Boundary conditions need to be imposed on this global system of equations. The set of equations containing complex variables can be directly solved using software which has such a facility. Alternatively, they need to be decomposed into two sets by equating real and imaginary parts; the sets are solved separately to obtain the real and imaginary components of the magnetic vector potential. The value of the potential can then be calculated at any time instant from these components using Equation 5.33 in Section 5.8. The eddy current losses can be estimated using the solution as explained in Section 12.7.3.

12.5.3 Transient formulations

Transient simulations are used for computing magnetic fields that vary over time, such as those caused by voltage or current surges. This approach may involve a long simulation time with many time steps if an accurate solution has to be obtained. The analysis can be either linear or nonlinear. Performance parameters such as inrush currents, dynamic short-circuit forces, etc. are calculated using transient formulations. The governing partial differential equation for a 2-D homogeneous linear medium is

$$\frac{1}{\mu}\frac{d^2A(t)}{dx^2} + \frac{1}{\mu}\frac{d^2A(t)}{dy^2} = -J(t) + \sigma\frac{\partial A(t)}{\partial t}. \tag{12.116}$$

The finite element descretization of this PDE leads to the following global system of equations:

$$[K]\{A(t)\} - [D]\frac{\partial}{\partial t}\{A(t)\} = \{F(t)\}. \tag{12.117}$$

This is a time-dependent system of ordinary differential equations. The matrices K and D are the same as in the static/time-harmonic formulations. They are independent of time for linear problems and need to be calculated only once (unlike in nonlinear transient problems wherein they have to be iteratively updated at each time step). The matrix F is also the same as earlier except for the fact that it is time-dependent being a function of J which is a time-varying quantity. To solve the above time-dependent system of equations, a suitable time-stepping scheme needs to be used. Numerical time stepping techniques, such as Euler and Runge-Kutta methods, are commonly used for time discretization. The following equation gives a generalized scheme for time stepping [7]:

$$\left[[K]-\frac{[D]}{\beta\Delta t}\right]\{A\}^{t+\Delta t}=\{F\}^{t+\Delta t}+\frac{1-\beta}{\beta}\{F\}^{t}-\left[\frac{[D]}{\beta\,\Delta t}+\frac{1-\beta}{\beta}[K]\right]\{A\}^{t}\,. \quad (12.118)$$

The value of β determines the type of the time-stepping scheme. $\beta = 0$, $\beta = 1$ and $\beta = 1/2$ lead to Euler's forward-difference algorithm, Euler's backward-difference algorithm, and the Crank-Nicholson method, respectively.

Thus, with the knowledge of the solution at the current time step and excitations (F) at the next and the current time steps, one can obtain the solution at the next time step. The process continues till the final time-instant of interest is reached. The time-step (Δt) and initial conditions $A(t=0)$ must be chosen appropriately depending on the problem type. For example, if the source is sinusoidally varying 50 Hz current signal, time step of 1 or 2 ms is generally sufficient. In the absence of residual magnetism, the initial condition $A = 0$ can be imposed at all nodes in the problem domain.

12.5.4 Axisymmetric problems

If we need to analyze leakage field/forces associated with transformer windings, a per-phase axisymmetric model with 2-D approximation is an attractive computational option. Consider a magnetostatic field problem which is symmetric about the z-axis. The corresponding PDE to be solved is Poisson's equation in cylindrical coordinates:

$$\frac{\partial}{\partial r}\left(\frac{1}{r\mu}\frac{\partial\left(rA_\phi\right)}{\partial r}\right)+\frac{\partial}{\partial z}\left(\frac{1}{\mu}\frac{\partial A_\phi}{\partial z}\right)=-J_\phi \quad (12.119)$$

which can be rewritten by multiplying and dividing the second term on the left side by r as

$$\frac{\partial}{\partial r}\left(\frac{1}{r\mu}\frac{\partial\left(rA_\phi\right)}{\partial r}\right)+\frac{\partial}{\partial z}\left(\frac{1}{r\mu}\frac{\partial\left(rA_\phi\right)}{\partial z}\right)=-J_\phi\,. \quad (12.120)$$

If we let $r = x$, $z = y$, $rA_\phi = A$, and $1/(r\mu) = \upsilon$, the transformation leads to the same form as in Equation 12.80. The boundary conditions are also correspondingly transformed, e.g., $A_\phi = c \;\Rightarrow\; A = rA_\phi = rc$, and we can apply the previous FEM procedure to this problem [9]. Thus a 2-D FEM code written for a PDE in Cartesian coordinates can be used for a PDE in cylindrical coordinates after doing a few simple transformations. The flux lines obtained from the solution are not the lines of constant A_ϕ, but rather lines of constant rA_ϕ. The solution has to be retransformed back by dividing its value at any point by the distance of the point from the axis.

12.5.5 Nonlinear problems

Nonlinear problems, involving material properties which vary as a function of field variables, are computationally more difficult. In transformers, nonlinearities are encountered while modeling the core and the structural components made from magnetic steel. The elements of [*K*] corresponding to the nonlinear regions depend on permeability values which are in turn dependent on values of the magnetic vector potential. The permeability curve of a nonlinear material can be represented by the following equation [30]:

$$H = \left(c_1 \, e^{c_2 B^2} + c_3 \right) B \tag{12.121}$$

where c_1, c_2 and c_3 are the constants which determine the shape of the *B-H* curve. The reluctivity of the material ($\upsilon = 1/\mu$) can be represented as

$$\upsilon = c_1 \, e^{c_2 B^2} + c_3 \, . \tag{12.122}$$

Generally, methods such as the Chord or Newton-Raphson method are used to solve nonlinear problems. In the chord method, an initial solution is obtained by assuming a constant value of reluctivity in the nonlinear region. Its value in all the finite elements is updated iteratively using a multiplier known as a relaxation factor (η) [7, 26],

$$\upsilon_{new} = \upsilon_{old} + \eta \left(\upsilon_{new} - \upsilon_{old} \right) . \tag{12.123}$$

Even though this method is stable and yields assured convergence, its rate of convergence can be poor.

The Newton-Raphson method, due to its quadratic convergence characteristics, is used widely to solve nonlinear problems. A procedure will now be discussed to solve a nonlinear magnetostatic problem. This formulation, for example, can be used to determine flux distribution in nonlinear core regions, if the value of the excitation current is given. Initially, with an assumed constant value of permeability in the whole nonlinear region, the solution is obtained:

$$\{ A \}_0 = [K]_0^{-1} \{ F \} .$$

The corresponding flux density distribution is obtained by using Equation 12.81,

$$B^2 = \left(\frac{\partial A}{\partial y} \right)^2 + \left(\frac{\partial A}{\partial x} \right)^2 \tag{12.124}$$

where the partial derivatives can be obtained using Equations 12.98, 12.99 and 12.110 as (superscript *e* has been dropped for brevity)

$$\frac{\partial A}{\partial x} = \frac{A_1 u_1 + A_2 u_2 + A_3 u_3}{2\Delta} \quad \text{and} \quad \frac{\partial A}{\partial y} = \frac{A_1 v_1 + A_2 v_2 + A_3 v_3}{2\Delta} \tag{12.125}$$

$$B^2 = \frac{\left(A_1 u_1 + A_2 u_2 + A_3 u_3\right)^2 + \left(A_1 v_1 + A_2 v_2 + A_3 v_3\right)^2}{4\Delta^2}. \tag{12.126}$$

Using the computed values of the flux densities, the permeability values in the nonlinear regions are updated and the residue (error), R, is then calculated as

$$\left\{ R(A) \right\}_0 = \left[K \right]_1 \left\{ A \right\}_0 - \left\{ F \right\}.$$

In the Newton-Raphson method, the Taylor series expansion is used to calculate the corrections $\{\Delta A\}$ at the end of each iteration:

$$\left\{ R(A + \Delta A) \right\} = \left\{ R(A) \right\} + \left[\frac{\partial R(A)}{\partial A} \right] \left\{ \Delta A \right\} + ...$$

Neglecting the 2nd and higher order derivatives, and making the residue with corrections equal to zero for the first iteration (index 0), we obtain

$$\left\{ 0 \right\} = \left\{ R \right\}_0 + \left[\frac{\partial \left\{ R \right\}}{\partial \left\{ A \right\}} \right]_0 \left\{ \Delta A \right\} = \left\{ R \right\}_0 + \left[J_C \right]_0 \left\{ \Delta A \right\}_0 \tag{12.127}$$

where,

$$\left[J_C \right]_0 = \left[\frac{\partial \left\{ R \right\}}{\partial \left\{ A \right\}} \right]_0$$

is called the Jacobian matrix. Suppose that we are solving a nonlinear Poisson's equation, then the residue or the error for an element is given by Equation 12.107 in which the matrix k can be split into linear (k^l) and nonlinear (υ) parts (superscript e has been dropped for brevity):

$$\left\{ R \right\} = \upsilon \left[k^l \right] \left\{ A \right\} - \left\{ f \right\}.$$

The above equation can be written in an expanded form as

$$\begin{Bmatrix} R_1 \\ R_2 \\ R_3 \end{Bmatrix} = \upsilon \begin{bmatrix} k_{11}^l & k_{12}^l & k_{13}^l \\ k_{21}^l & k_{22}^l & k_{23}^l \\ k_{31}^l & k_{32}^l & k_{33}^l \end{bmatrix} \begin{Bmatrix} A_1 \\ A_2 \\ A_3 \end{Bmatrix} - \begin{Bmatrix} f_1 \\ f_2 \\ f_3 \end{Bmatrix}.$$

The element level Jacobian matrix is

$$\begin{bmatrix} \dfrac{\partial R_1}{\partial A_1} & \dfrac{\partial R_1}{\partial A_2} & \dfrac{\partial R_1}{\partial A_3} \\ \dfrac{\partial R_2}{\partial A_1} & \dfrac{\partial R_2}{\partial A_2} & \dfrac{\partial R_2}{\partial A_3} \\ \dfrac{\partial R_3}{\partial A_1} & \dfrac{\partial R_3}{\partial A_2} & \dfrac{\partial R_3}{\partial A_3} \end{bmatrix}.$$

The first element, for example, can be expressed as

$$\frac{\partial R_1}{\partial A_1} = \upsilon k_{11}^l + \left[k_{11}^l A_1 + k_{12}^l A_2 + k_{13}^l A_3 \right] \frac{\partial \upsilon}{\partial A_1}$$

$$= \upsilon k_{11}^l + \left[k_{11}^l A_1 + k_{12}^l A_2 + k_{13}^l A_3 \right] \frac{\partial \upsilon}{\partial B^2} \frac{\partial B^2}{\partial A_1}.$$

It should be noted that $\{f\}$ is a vector of constants since the source current is fixed.

For each element, there are three residues corresponding to its three nodes, and $\{A\} = \{A_i \quad A_j \quad A_k\}^{\mathrm{T}}$. Hence, there are nine partial derivatives associated with each element, giving the dimensions of 3×3 to the Jacobian matrix of each element. The terms $\partial \upsilon / \partial B^2$ and $\partial B^2 / \partial A_1$ can be determined from Equations 12.122 and 12.126, respectively, as

$$\frac{\partial \upsilon}{\partial B^2} = c_1 c_2 e^{c_2 B^2}$$

$$\frac{\partial B^2}{\partial A_1} = \frac{2u_1 \left(A_1 u_1 + A_2 u_2 + A_3 u_3 \right) + 2v_1 \left(A_1 v_1 + A_2 v_2 + A_3 v_3 \right)}{4\Delta^2}.$$

The calculated element-level Jacobian matrices can now be combined to give a global matrix of size $n \times n$, which can be used in Equation 12.127 to give the set of corrections,

$$\{\Delta A\}_0 = -\left[J_C \right]_0^{-1} \{R\}_0. \tag{12.128}$$

Effectively, we have thus obtained a linearized global system of equations. The values of A for the next iteration are

$$\{A\}_1 = \{A\}_0 + \{\delta A\}_0.$$

The nonlinear iterations are continued until $max(\{R\})$ is less than a specified threshold value for convergence.

12.6 Coupled Fields in Transformers

As briefed in the introductory remarks of this chapter, transformers are complex electromagnetic structures having superimposition of electromagnetic, thermal, structural, fluid and acoustic fields. Additionally, they are connected to external power or distribution networks necessitating coupled solutions of the circuit equations with the set of equations, representing above physical fields, obtained through the FEM procedures. Figure 12.15 shows various coupled fields and coupling parameters in transformers [31]. For example, alternating magnetic fields produce eddy and hysteresis losses in the core and structural parts; a consequent temperature rise in them may lead to an appreciable change in the material properties (conductivity and permeability) which in turn affect the magnetic field computations. The forces on conducting parts, calculated in the magnetic domain, lead to their deformations which can be ascertained in the structural domain; the deformations change the magnetic reluctances, thus making it a coupled problem. The other couplings between the associated fields in the figure can be explained in a similar way.

Electromagnetic fields inside transformers interact with the external networks and the other physical fields. Some of the examples of such interactions are inrush current phenomena and short-circuit forces (magnetic field-circuit), saturation of magnetic circuit due to irregularities and unbalanced conditions in converters (magnetic field-power electronic circuit), hot spots in windings and structural parts due to eddy currents (magnetic-thermal), hot spots in windings due to unintended constrictions of oil flows (thermal-fluid), deformations of windings and current carrying bars or leads due to electromagnetic forces (magnetic-structural), magnetostrictive noise prediction problem (magnetic-fluid-structural-acoustic), etc. The last example involving the four coupled fields can be regarded as one of the most complicated numerical problems that confront the researchers working in the area of coupled field computations.

For realistic and accurate analyses, the interactions need to be accounted using coupled field formulations. The coupled field problems can be broadly classified into strongly (directly) and weakly (indirectly or sequentially) coupled ones [32]. This classification is mainly based on the degree of nonlinearity and relative time constants of the coupled fields. A weakly coupled problem is solved using cascaded algorithms, wherein the coupled fields are solved in successive steps (e.g., many of the magnetic-thermal problems including those in transformers).

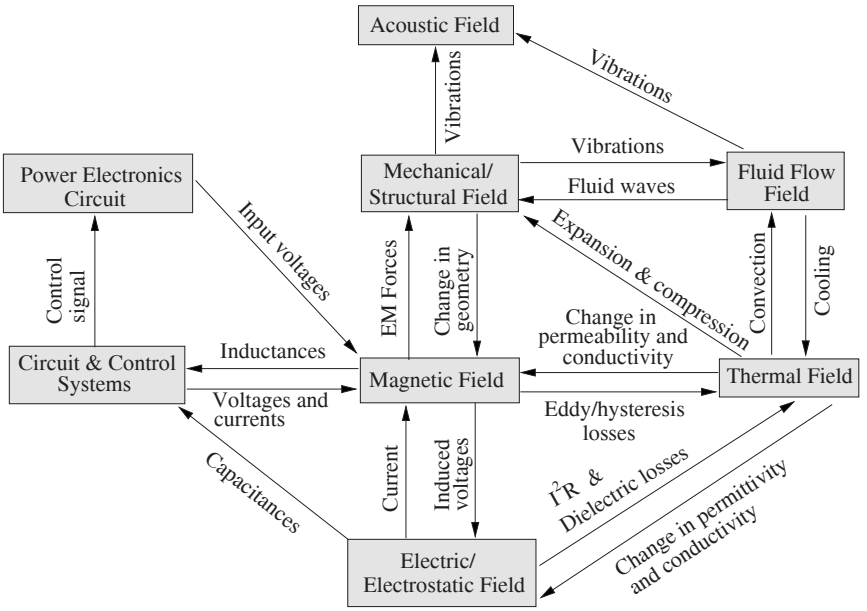

Figure 12.15 Coupled field interactions in transformers [31].

On the other hand, in the direct method, equations representing the coupled fields are solved simultaneously with all the necessary variables taken into account. The electromagnetic field-circuit problems involving nonlinearities are invariably solved by the direct approach. Core saturation problems due to network transients also fall in this category.

In transformers, both classes of problems are encountered. Strongly coupled problems include a number of phenomena in which transformers are subjected to network transients. The field part is generally formulated by using FEM, while the circuit part is represented in terms of nodal or loop equations. For analyzing the behavior of a transformer under transient conditions, such as under inrush conditions involving magnetic nonlinearities, such a field-circuit formulation is essential. Other important classes of coupled field systems are magnetic-thermal and magnetic-structural problems which, in most cases, can be solved as weakly coupled problems. In this text the phenomena in the transformers, requiring both weakly and strongly coupled formulations for their analysis, are discussed in the following sections. In the next section, strongly coupled field-circuit formulations and their applications to transformers are covered. In the subsequent sections, weakly coupled magnetic-thermal formulations and magnetic-structural formulations are discussed along with corresponding case studies. The magnetic-thermal case study is a transient one in which the output of one field is passed on to the other. On the other hand, the magnetic-structural one is a steady-state analysis in which electromagnetic forces for a worst short-circuit instant calculated

using an electromagnetic field solver are fed as the input to a structural solver to find the corresponding deformation; such weakly coupled formulations determining steady-state quantities can actually be called loosely coupled computations.

12.6.1 Coupled field-circuit formulations

Many electrical devices, including transformers, are fed by voltage sources. Coupled field-circuit formulations find many applications in transformers. A few such problems that are tackled in the literature have been cited earlier [20, 23] while discussing mixed potential formulations. In many applications, transformers are connected to power electronic circuitry. Analysis of such transformers feeding rectifier loads can be found in [33, 34]. Forces in a transformer under time varying fault conditions are analyzed in [35].

A transformer connected to an external circuit is shown in Figure 12.16. The transformer, which represents the field domain, is discretized into a number of finite elements. The current, not known in advance, may be a nonlinear function of a circuit element and/or a field variable. Such an analysis falls under the category of the coupled field-circuit type in which the current in the external circuit and the chosen potential (for example, magnetic vector potential **A**) in the field domain are interdependent. Contrary to this, if the transformer is assumed to be fed by an ideal voltage source with zero internal impedance, it becomes merely a field computation problem. Furthermore, if the transformer can be accurately represented by a circuit having lumped elements, it is just a circuit-analysis problem.

The coupled field-circuit analysis involves solving a set of interlinked field and circuit equations. We will again restrict ourselves to 2-D problems. The number of equations depends on the number of nodes representing the field domain, and circuit equations formed after the application of Kirchhoff's voltage or current law. The governing PDE for most of the magnetic field problems (static, time-harmonic and transient) in terms of the magnetic vector potential is given by Equation 12.78:

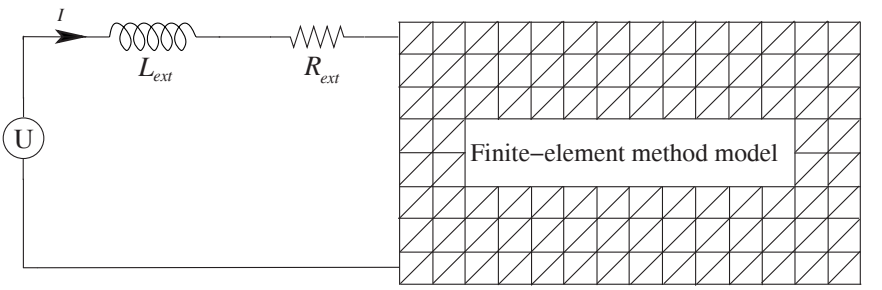

Figure 12.16 A transformer connected to an external network.

$$\nabla^2 \mathbf{A} - \mu\sigma \frac{\partial \mathbf{A}}{\partial t} = -\mu \mathbf{J} \tag{12.129}$$

where the subscript *s* for the source current density is dropped for simplicity. A typical and relatively simple coupled field-circuit problem in transformers is the computation of inrush current. Let us take a case in which a single-phase transformer is excited by a voltage source. The connecting line between the two has resistance and inductance, R_{ext} and L_{ext}, respectively, as shown in Figure 12.16.

Let us discuss modeling aspects of conductors of the excited winding (the other windings are open-circuited and hence not modeled). The conductors are modeled as either stranded or solid (massive) type. Their representation is governed by the skin effect phenomenon observed in the conductors. In Chapter 4, there is a discussion on electrically thin and thick conductors; this classification is based on the comparison of the conductor dimensions with the skin depth of its material. When the dimensions are comparable to or less than the skin depth, it is classified as a thin conductor. In other words, it is assumed that the eddy currents induced in the conductor do not have appreciable effect on the incident field that produces them. On the other hand, when the conductor dimensions are much larger than the skin depth, the effect of the induced eddy currents cannot be neglected and the conductors are called thick or massive.

In terms of modeling, we do not define the electrical conductivity of the material for a thin conductor, which automatically ensures that there are no induced currents in it. Thus, effectively, we are considering its DC resistance only. If the DC I^2R losses have to be accounted in the simulation, the corresponding resistance is added to the external circuit resistance in Figure 12.16. When the leakage reactance of a transformer is calculated using FEM, the problem is modeled as a magnetostatic one in which conductivity of the conductors in the windings is specified as zero; i.e., the eddy currents in the windings are assumed to have a negligible effect on the leakage reactance, which is a valid assumption. In fact, it is interesting to note here that even for calculating the eddy losses in windings, we again model it as a magnetostatic problem; it is assumed that the leakage field responsible for the eddy currents does not change due to them. After having calculated the leakage field the eddy losses due to its axial and radial components is calculated analytically using the formulae given by Equations 4.102 and 4.103, respectively, as discussed in Section 4.5.1. If suppose, we want to exactly calculate the eddy losses with the consideration of the effect of the eddy currents on the leakage field, each winding conductor has to be modeled separately with its electrical conductivity specified. The extra efforts, however, may not be justified since the gain in accuracy may not be appreciable for electrically thin conductors.

Therefore, returning back to the discussion of the inrush current computation, the winding conductor is modeled as a stranded type without any conductivity specified. Its DC resistance is added to R_{ext} to account for the damping effect provided by it. Equation 12.129 is simplified to the following:

$$\nabla^2 \mathbf{A} = -\mu \mathbf{J} \ .$$

For the stranded conductor in the present case, since the eddy currents are neglected, it will have uniform current density. Assuming that each turn carries I amperes of current, the magnitude of the constant average current density of the winding is

$$J = \frac{N I}{A_{cs}}$$

where, N is the number of turns and A_{cs} is the cross-sectional area of the winding; A_{cs}/N represents the cross-sectional area of one turn. The PDE takes the following form in two dimensions:

$$\frac{\partial}{\partial x}\left(\upsilon \frac{\partial A_z}{\partial x}\right) + \frac{\partial}{\partial y}\left(\upsilon \frac{\partial A_z}{\partial y}\right) = -J_z \ \Rightarrow \ \frac{\partial}{\partial x}\left(\upsilon \frac{\partial A_z}{\partial x}\right) + \frac{\partial}{\partial y}\left(\upsilon \frac{\partial A_z}{\partial y}\right) = -\frac{NI}{A_{cs}}.$$

The current density has been put in terms of *I,* which is also the current flowing in the external circuit (and hence the inrush current). This is a nonlinear Poisson's equation in which the current and potential variables are time-dependent and their values at any time instant depend on the nonlinear characteristics of the core.

After FEM discretization of the above equation, we obtain a set of equations in matrix form:

$$\left[K\right]\left\{A_z\right\} + \left[P\right]\left\{I\right\} = \left\{0\right\}. \tag{12.130}$$

$\left\{A_z\right\}$ and $\left\{I\right\}$ are column matrices with dimension $n \times 1$ and $c \times 1$, respectively, where n is the number of nodes in FEM domain and c is the number of external circuits. The ($n \times n$) global coefficient matrix, $\left[K\right]$, is the same as discussed in the previous two sections. $\left[P\right]$ is a $n \times c$ matrix. For the problem domain of Figure 12.16 with only one external circuit and corresponding one current variable, $\left\{I\right\}$ is 1×1 matrix, and $\left[P\right]$ is $n \times 1$ column matrix which is formed by assembly of elemental level matrices $\left\{P^e\right\}_{3x1}$

$$\left\{P_i^e\right\} = \frac{N}{A_{cs}} \iint N_i^e \, dxdy \quad i = 1,2,3 \tag{12.131}$$

where, N_i^e is the elemental shape function. The above expression is similar to that of the second term in Equation 12.105. Since the whole winding is modeled, in this case, by a rectangular block carrying *NI* ampere-turns, only those entries of $\left\{P\right\}$, which correspond to the nodes in the winding associated with the current *I*, are nonzero. Many of these non-zero entries are contributed by more than one

element since the corresponding nodes in the winding are common to more than one finite element. The electromotive force (emf) induced in the winding provides the magnetic coupling with the electric circuit. In 2-D, it is possible to compute the induced emf in terms of A_z, which when added to the resistive voltage drop gives the total voltage across the winding

$$V = RI + \frac{N\,l}{A_{cs}} \int_s \frac{\partial A_z}{\partial t}\, ds \tag{12.132}$$

where, R is the resistance of the winding, s is the domain of the winding, and l is the length of the domain in the z-direction.

The matrix form of the external circuit equations can be written as

$$\{U\} = \left\{\frac{d\phi}{dt}\right\} + [R_{ext}]\{I\} + [L_{ext}]\left\{\frac{d\,I}{dt}\right\}$$

The first term on the right side represents the induced voltage across the winding terminals since the resistance of the winding has already been included in R_{ext}. If the flux linkages ϕ are expressed in terms of the magnetic vector potential, the set of equations can be written as:

$$\{U\} = [G]\left\{\frac{dA}{dt}\right\} + [R_{ext}]\{I\} + [L_{ext}]\left\{\frac{d\,I}{dt}\right\} \tag{12.133}$$

where, $\{U\}$ is the vector of input voltages, $[L_{ext}]$ and $[R_{\text{ext}}]$ are the matrices of external inductances and resistances, respectively, and $[G]$ is $[P]^{\text{T}}$ (for 2-D problems with unit depth) [20], which depends on the geometrical features of the windings. For a depth of l meters in the z-direction, $[G]$ has to be multiplied by l. The matrices $[L_{ext}]$ and $[R_{\text{ext}}]$ are obtained using mesh (loop) equations. In this particular case of the inrush current computation, these along with $\{U\}, \{I\}$ and $\{dI/dt\}$ are simply 1 × 1 matrices. From Equations 12.130 and 12.133, the system of global field-circuit coupled equations can be written as

$$\begin{bmatrix} [0] & [0] \\ [G] & [L_{ext}] \end{bmatrix} \begin{Bmatrix} \{\dot{A}\} \\ \{\dot{I}\} \end{Bmatrix} + \begin{bmatrix} [K] & [P] \\ [0] & [R_{ext}] \end{bmatrix} \begin{Bmatrix} \{A\} \\ \{I\} \end{Bmatrix} = \begin{Bmatrix} \{0\} \\ \{U\} \end{Bmatrix}. \tag{12.134}$$

In this system of equations the unknowns are the values of the magnetic vector potential at various nodes and the current in the external circuit (i.e., the inrush current in the excited winding). The matrix $[K]$ is nonlinear since it is a function of υ $(= 1/\mu)$ which varies nonlinearly with B. The set of nonlinear equations can be solved using the procedure given earlier in Section 12.5.5. Eventually, the system is reduced to the form as in Equation 12.128 with an additional current

variable. The dimension of the final square matrix that is inverted to obtain the solution $\{\{A\}\ \{I\}\}^{\mathrm{T}}$ is of dimension $(n+1)\times(n+1)$. The increase of dimension by one is due to the additional circuit equation. However, the increase would be more than one if more current-carrying windings are involved as in some of the case studies discussed in appropriate chapters, viz., the sympathetic inrush phenomenon in Chapters 2 and 13, the half-turn effect in Chapter 5, and the analysis of short-circuit forces in a split-winding transformer in Chapter 6. An analysis of the effect of firing angle unbalance between paralleled rectifier systems through an interphase transformer is another such case study [36].

12.6.2 Coupled magnetic-thermal formulations

These formulations are used in transformers to calculate temperatures in windings and structural parts due to eddy currents. The details of the coupled magnetic-thermal simulation of a foil-winding transformer connected to a nonlinear load are given in [37]. Eddy losses in windings and stray losses in structural components increase due to current harmonics, giving rise to higher temperatures. The coupled magnetic-thermal analysis of a transformer subjected to current harmonics is outlined in [38], which uses a mixed frequency- and time-domain approach. A study of the electromagnetic and thermal behavior of a dry-type transformer under nonlinear loads is carried out in [39]. In [40], the temperature rise in a flitch plate is calculated due to the leakage field induced eddy current losses in a loosely coupled fashion; the losses calculated using time-harmonic 3-D FEM analysis is used to compute the steady-state temperature rise in the plate through thermal FEM analysis. The 2-D transient magnetic and thermal equations are [41]

$$\nabla\cdot\left(\frac{1}{\mu}\nabla A_z\right) = -\sigma_T\frac{V}{l} + \sigma_T\frac{\partial A_z}{\partial t} \tag{12.135}$$

$$\nabla\cdot\left(k\nabla T\right) = -q_{A_z,T} + mc\frac{\partial T}{\partial t} \tag{12.136}$$

where σ_T is the temperature-dependent electrical conductivity, T is the unknown temperature (°C), k is the thermal conductivity (W/m/°C), m is the mass density (kg/m^3), c is the specific heat (J/kg /°C), and q (varying with A_z and T) is the loss per unit volume (W/m^3). The first equation follows directly from Equation 12.78 with the magnitude of the source term $\mathbf{J}_s$ written as $|\sigma\mathbf{E}| = \sigma(V/l)$, being a voltage-fed case. Temperature distribution influences the resistance of conducting parts and therefore their losses. Thus, the above two equations are coupled by the following relations:

$$\sigma_T = \frac{\sigma_{ref}}{1+\alpha\left(T-T_{ref}\right)} \tag{12.137}$$

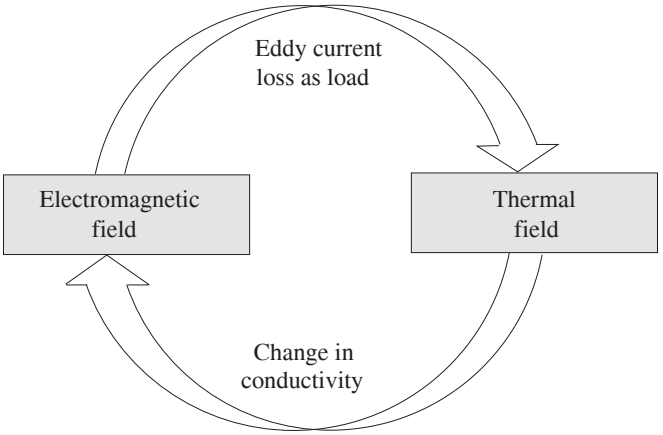

Figure 12.17 Weakly coupled magnetic-thermal model.

$$q_{A_z,\,T} = \frac{1}{s}\int \sigma_T \left(\frac{V}{l} - \frac{\partial A_z}{\partial t}\right)^2 ds \tag{12.138}$$

where σ_{ref} is the initial conductivity (S/m), α is the temperature coefficient of resistance ($^oC^{-1}$), T_{ref} and T are the initial and final temperatures of the material (^oC), l is length (m), and s is the area of a finite element (m^2). It should be noted that the calculations in 2-D are usually done for one meter depth. The conductivities corresponding to the computed temperatures are used in the electromagnetic analysis. Figure 12.17 shows the weakly coupled model under discussion.

In thermal problems, two types of boundary conditions are commonly encountered: convection and radiation. The boundary condition at the convectively cooled surface is given as [10, 42]

$$k\,\nabla(T)\cdot\mathbf{n} + h_c\,(T - T_a) = 0 \tag{12.139}$$

where T is the unknown temperature at boundary, T_a is the known ambient temperature, h_c is the convection heat transfer coefficient ($W/(m^2\text{-}^\circ C)$), and $\mathbf{n}$ is the unit normal. Similarly, the boundary condition associated with convection as well as radiation is given by [43]:

$$k\,\nabla T\cdot\mathbf{n} + h_c\,(T - T_a) + C_{rad}\left(T^4 - T_a^4\right) = 0 \tag{12.140}$$

where C_{rad} is the surface emissivity ($W\text{-}m^{-2}\text{-}^\circ C^{-4}$).

We will now see the application of the above coupled formulation to a practical problem. In low frequency devices including transformers, connections are made of parallel bars. Thermal and mechanical criteria influence the design of such connections in addition to electrical considerations. The parallel bars within

each phase may not be transposed, leading to unequal mutual impedances between them. Also, the sets of three-phase bars may not be symmetrically disposed. Due to such an asymmetrical three-phase structure, the three-phase voltages become unbalanced. All these asymmetries and proximity effects between the bars make the current sharing between them skewed. Furthermore, any current unbalance on account of an asymmetrical load (like in an arc-furnace) can deteriorate the performance. Harmonic effects may cause additional overheating. Coupled magnetic-thermal formulation is necessary to study the distribution of currents, losses and temperature in such connections.

Let us consider an arrangement of three-phase busbars as shown in Figure 12.18 for the analysis. It consists of four copper bars per phase, each having length of 0.5 m and dimensions of 80 mm × 6 mm, and a distance of 60 mm separates the phases. The bars are considered as solid conductors exhibiting skin and proximity effects. Electrical, magnetic and thermal properties used in the analysis are given in [44]. The boundary corresponding to magnetic analysis is taken sufficiently away from the bars (such that it should not influence the field of the bars) with $A_z = 0$ on it. In the thermal model, only the bars are meshed and the convection phenomenon due to air is taken into account using appropriate convection coefficients at the boundaries [44].

Since the thermal time constant is much larger than the electromagnetic time constant in this case, the two fields are coupled weakly. The rate of change in electrical properties of the material due to heating is usually low and not high enough to instantaneously change the electromagnetic behaviour significantly. Therefore, the electromagnetic field is solved as a time-harmonic problem (in the frequency-domain) while the thermal field is solved as a transient problem (in the time-domain). Figure 12.19 shows the flowchart for the analysis [45].

The electromagnetic solution is updated after solutions are obtained for few time steps in the thermal transient analysis carried out with temperature-dependent material properties. In the work, the parallel connected bars are modelled as current-fed *thick* conductors. The governing equations are [45]

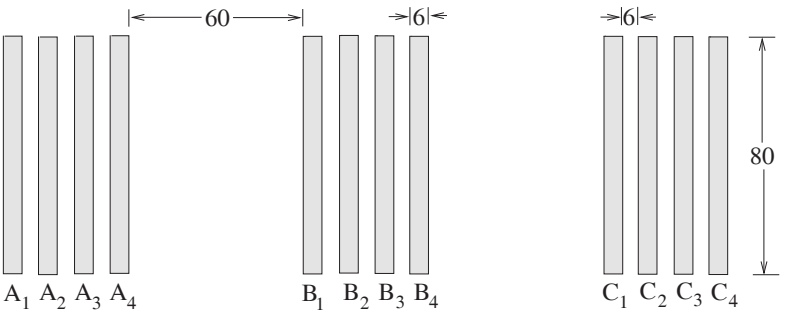

Figure 12.18 Arrangement of three-phase parallel bars [44].

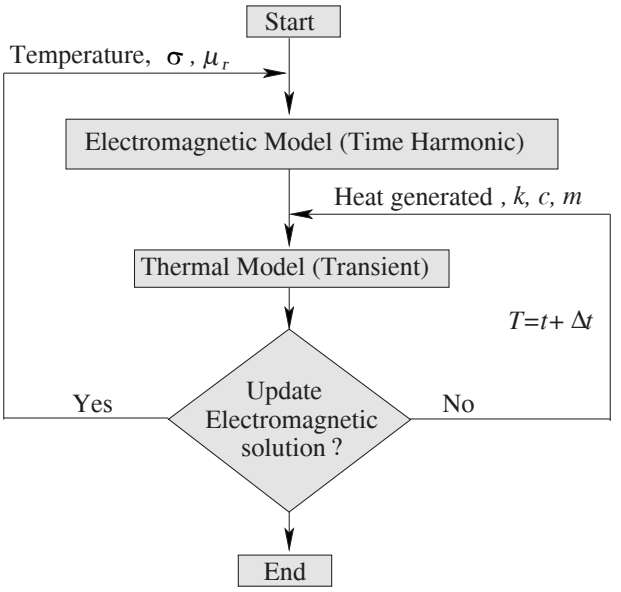

Figure 12.19 Flow chart for the coupled magnetic-thermal model.

$$\frac{1}{\mu_0}\frac{\partial^2 \hat{A}_z}{\partial x^2} + \frac{1}{\mu_0}\frac{\partial^2 \hat{A}_z}{\partial y^2} = \sigma\left(\hat{g} + j\omega\hat{A}_z\right) \tag{12.141}$$

$$\hat{I} = \int_s \sigma\left(\hat{g} + j\omega\hat{A}_z\right) ds \tag{12.142}$$

where $\hat{g} = -\left(\hat{V}/l\right)$ in V/m is representing the source current density. The first equation follows directly from Equation 12.79 with $\mu = \mu_0$ since there are no magnetic materials in the domain. The second equation integrates the source and induced current densities to obtain the total current in a busbar. This equation has to be written for each busbar in the system. The above two equations can be written in matrix form as

$$\begin{bmatrix} [K] + j\omega[D] & [W] \\ j\omega[W]^{\mathrm{T}} & [H] \end{bmatrix} \begin{Bmatrix} \{\hat{A}\} \\ \{\hat{g}\} \end{Bmatrix} = \begin{Bmatrix} 0 \\ \{\hat{I}\} \end{Bmatrix} \tag{12.143}$$

where the elements of $[K]$ matrix are calculated using Equation 12.111, and $[D]$ is same as in Equation 12.115. Further, similar to matrix P^e in Equation 12.131, the elemental level matrix W^e is given as

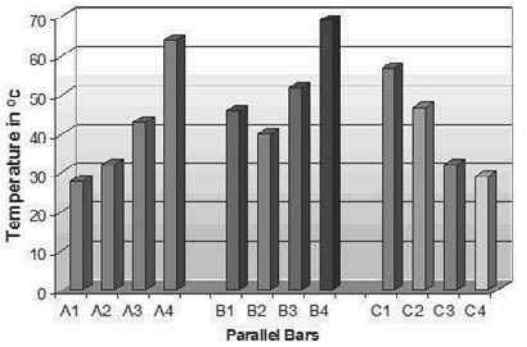

Figure 12.20 Temperature rise in busbars [44, 45].

$$\left\{W_i^e\right\} = \sigma \iint N_i^e \, dxdy \quad i = 1, 2, 3$$

and the assembly of all such elemental matrices gives one column of $[W]$. The number of columns of this matrix equals the number of the solid bars in the domain with defined electrical conductivity. $[H]$ is a diagonal matrix of the conductance of the bars, and [*I*] is the matrix of the imposed currents in the bars. The elemental joule loss (Q_e) in W/m, for the 2-D problem under consideration, is calculated using the following formula:

$$Q_e = \int_s \sigma \left(\hat{g} + j\omega \hat{A}_z\right)\left(\hat{g} + j\omega \hat{A}_z\right)^* ds \tag{12.144}$$

where * denotes a complex conjugate operation. The basis of the formula is explained in Section 12.7.3. Calculated elemental joule losses from the electromagnetic analysis are used as loads to the thermal model described by Equation 12.136. The current density distribution in the busbars is nonuniform due to the reasons discussed earlier. The calculated temperature rise in each bar after 1.5 hours is shown in Figure 12.20. Thus, using the coupled magnetic-thermal formulation, such phenomena leading to undesirable current and temperature distributions in high current terminations can be analyzed to take corrective measures while designing such systems. There are other applications of the formulation that can lead to improvements in the design of windings and structural parts as indicated in the references cited earlier.

12.6.3 Coupled magnetic-structural formulations

Magnetic-structural coupled problems in transformers involve investigation of displacements/deformations, vibrations, and noise, all these phenomena are electromagnetic in origin. Deformations of windings and connections generally

happen due to Lorentz forces, whereas the vibration of the tank is predominantly due to magnetostriction and magnetic forces associated with the core. The following system of equations represents a strongly coupled magnetic-mechanical system [46]

$$\begin{bmatrix} [K] & [C] \\ [N] & [M] \end{bmatrix} \begin{Bmatrix} \{A\} \\ \{X\} \end{Bmatrix} = \begin{Bmatrix} \{F\} \\ \{F_{ext}\} \end{Bmatrix} \tag{12.145}$$

where, $[K]$ and $[M]$ are the magnetic and mechanical global coefficient matrices, respectively, $[N]$ and $[C]$ are the coupling matrices, and $\{F\}$ and $\{F_{ext}\}$ are the column vectors representing the magnetic and mechanical source terms, respectively. $\{A\}$ and $\{X\}$ are the column vectors of unknown magnetic vector potential and mechanical displacement variables (which have 3 components at every node in the finite element domain for a 3-D problem). The term $[N]$ represents the effect of magnetic parameters on mechanical displacements, whereas $[C]$ represents the effect of mechanical displacements on magnetic parameters. Also, it can be proved that the total magnetic force (F_{mag}) can be represented by $-[N]\{A\}$ [46]. In [47], magnetic and mechanical fields are taken to be strongly coupled. On the contrary the mechanical and acoustic fields are coupled weakly for which the calculated tank surface displacements are applied as inputs to the acoustic field model to calculate the radiated transformer noise. If the effects of displacements on magnetic fields are not appreciable, $[C]$ can be neglected and the magnetic forces ($-[N]\{A\}$) affecting displacements can be added to the mechanical (external) forces:

$$\begin{bmatrix} [K] & [0] \\ [0] & [M] \end{bmatrix} \begin{Bmatrix} \{A\} \\ \{X\} \end{Bmatrix} = \begin{Bmatrix} \{F\} \\ \{F_{ext} + F_{mag}\} \end{Bmatrix}. \tag{12.146}$$

The magnetostriction phenomenon can also be considered in a weakly coupled scheme by adding the corresponding vector $\{F_{ms}\}$ to the other forces [46]:

$$\begin{bmatrix} [K] & [0] \\ [0] & [M] \end{bmatrix} \begin{Bmatrix} \{A\} \\ \{X\} \end{Bmatrix} = \begin{Bmatrix} \{F\} \\ \{F_{ext} + F_{mag} + F_{ms}\} \end{Bmatrix}. \tag{12.147}$$

For the analysis of load-controlled noise in transformers, the main coupling between the mechanical and magnetic fields is due to the volumetric force $\mathbf{f}_v$ resulting from the Lorentz forces (which cause the winding vibrations):

$$\mathbf{f}_v = \mathbf{J} \times \mathbf{B} = \left(\mathbf{J}_s - \sigma \nabla V - \sigma \frac{\partial \mathbf{A}}{\partial t} + \sigma \mathbf{v} \times (\nabla \times \mathbf{A}) \right) \times (\nabla \times \mathbf{A}) \tag{12.148}$$

where, $\mathbf{v}$ is the time derivative of the mechanical displacement.

Having briefly seen the governing equations for the coupled magnetic-structural problems in transformers, we will discuss an approach for assessing the mechanical strength of an outer transformer winding subjected to radial electromagnetic short-circuit forces. The mechanical deformation of a disk in the winding is calculated for a worst-case short-circuit instant. The problem is a loosely coupled one and Equation 12.146 is applicable here with F_{ext} being zero:

$$\begin{bmatrix} [K] & [0] \\ [0] & [M] \end{bmatrix} \begin{Bmatrix} \{A\} \\ \{X\} \end{Bmatrix} = \begin{Bmatrix} \{F\} \\ \{F_{mag}\} \end{Bmatrix}. \tag{12.149}$$

Effectively, we are solving two static problems separately. First, the magnetic system, $[K]\{A\} = \{F\}$ is solved; the corresponding PDE is $\nabla^2 \mathbf{A} = -\mu \mathbf{J}$. Since it can be approximated as a 2-D axisymmetric problem, the system of equations becomes $[K]\{A_\phi\} = \{F_\phi\}$. Once the solution $\{A_\phi\}$ is obtained, the electromagnetic forces acting on any finite element area can be computed as

$$F_z^e = 2\pi J_\phi B_r^e A^e D_c \tag{12.150}$$

$$F_r^e = 2\pi J_\phi B_z^e A^e D_c \tag{12.151}$$

where A^e is the area of the element and D_c is the distance of the centroid of the element from the axis. The expression for the average radial pressure (in Pascal or N/m^2) acting on the disk is given as

$$P_r = \frac{\sum F_r^e}{\pi D_{inner} h} \tag{12.152}$$

where, D_{inner} is the inner diameter of the disk (m) and h is the disk height (m). The average pressure acting on the disk is calculated by adding all the elemental level forces. The axial pressure can be calculated by using F_z^e and the corresponding disk area on which it acts. However, it is not used here since we are interested in calculating the radial deformation due to hoop stresses.

The total force in Equation 12.152 is divided by the number of nodes on the inner surface of the disk to obtain an elemental force value which is equally divided between the two nodes of each element lying on the surface. Thus, the two end-nodes will have half the elemental force value and the remaining nodes are subjected to the elemental force value. The nodal forces thus obtained for the entire domain form the nodal force vector F_{mag} which becomes the source term of the governing equation in the structural domain, viz. $[M]\ \{X_r\} = \{F_{mag}\}$, which is the second static problem being solved. Since the considered forces are only in the radial direction, the displacement is in the radial direction only. The corresponding PDE is [48]:

$$\frac{d^2X_r}{dr^2} + \frac{1}{r}\frac{dX_r}{dr} - \frac{X_r}{r^2} = 0\,. \tag{12.153}$$

[*M*] is formed by assembly of all the element coefficient matrices, as in

$$\left[M^e\right] = \int_{\mathrm{v}} \left[B^e\right]^{\mathrm{T}} \left[D^e\right]\left[B^e\right] d\mathrm{v} \tag{12.154}$$

where $[B^e]$ is the element strain displacement matrix, given by the relation, $\left\{\varepsilon^e\right\} = \left[B^e\right]\left\{x^e\right\}$. $\left\{\varepsilon^e\right\}$ and $\left\{x^e\right\}$ is the strain vector and the displacement vector for an element, respectively. $[D^e]$ is the elastic stress-strain constitutive matrix, which can be calculated using the procedure given in [45, 49]. Finally, various stress components in a finite element are calculated as

$$\{\sigma\} = [D]\{\varepsilon\}\,. \tag{12.155}$$

Deformations and stresses induced in a disk of the HV winding of a 200 MVA single-phase generator transformer are determined in [45, 50]. The winding disk is considered as a thick wall cylinder. When the ratio of its inner diameter to radial thickness is less than 20, it is considered as thick. The inner and outer radii of the disk are 0.945 m and 1.095 m, respectively, and the height of the disk is 13.1 mm. The axisymmetric structural model consists of the disk geometry having inner radius *a* and outer radius *b*. The mechanical properties given to the disk are: Young's modulus of elasticity, E = 119 E09 N/m^2 and Poisson's ratio, ν = 0.34. The pressure input, as calculated in the electromagnetic analysis, is applied at the inner surface of the disk, i.e., at $r = a$. The boundary conditions are viz. at $r = a$, $\sigma_r = -P_r$ and at $r = b$, $\sigma_r = 0$. Since a high prestress is applied from the top through a clamping ring, all the nodes can be considered as constrained in the *z*-(vertical) direction, i.e., $\varepsilon_{zz} = 0$ [48]. Shear stress components are zero due to radial symmetry, i.e., $\tau_{r\phi}$, $\tau_{\phi z} = 0$. The equivalent or von-Mises stress is used as a criterion for determining the onset of failures in ductile materials (as discussed in Section 6.3.1). The von-Mises stress σ_{vm} should be less than the yield stress σ_{yield} of the material. The expression for the von-Mises stress in the axisymmetric case under consideration is given as

$$\sigma_{\mathrm{vm}} = \frac{1}{\sqrt{2}}\sqrt{\left(\sigma_r - \sigma_\phi\right)^2 + \left(\sigma_\phi - \sigma_z\right)^2 + \left(\sigma_z - \sigma_r\right)^2 + 6\tau_{zr}^2}\,. \tag{12.156}$$

Generated mechanical stresses and winding deformations are computed for a worst case condition, i.e., the first peak of the short-circuit force. In the radial direction, there is less chance of a mechanical resonance as discussed in Section 6.4; therefore, the radial forces can be applied statically in the analysis. The

loosely coupled formulation can therefore be used since the problem is approximated as static and linear in both electromagnetic and structural domains.

The calculated short-circuit radial pressure as obtained from Equation 12.152 is 10.44 MPa. According to the structural FEM analysis results [50], at 10.44 MPa pressure the maximum von-Mises stress of 71.6 MPa, as shown in Figure 12.21, is much less than the yield strength of 180 MPa of the copper material used (CPR2 grade). Up to 26.30 MPa pressure, the winding disk is in the elastic region. Thus, it can be concluded that the factor of safety for this disk is about 2.5 $(=180/71.6)$. If the pressure is increased further, the inner wall of the disk starts yielding. At 30.33 MPa the whole disk goes into a plastic state. The displacements of the inner and outer surfaces calculated using FEM matched closely with those given by expressions in Equations 6.31 and 6.32, respectively.

12.7 Computation of Performance Parameters

We have seen until now in this chapter the relevant theory of electromagnetics and the finite element method. Some of the advanced computational aspects, including transient simulations, handling of nonlinearity and coupled field computations, have also been discussed. Throughout this text the applications of the field theory and the FEM technique for the design and analysis of the transformers have been pointed out at appropriate places. In this section, procedures for computation of various performance parameters, many of which have been discussed in earlier chapters, are summarized with additional comments and remarks. Computation of proximity effects, magnetic/magnetostrictive forces, and modeling of hysteresis behavior are the new topics in the section.

12.7.1 Capacitances and inductances

Inter-turn/inter-disk/inter-section/inter-winding capacitances: These capacitances are commonly calculated by using analytical formulae as enumerated in Chapter 7. These formulae cannot accurately take into account the end effects, fringing effects and complex geometries involving multiple dielectric materials. If a higher accuracy is desired in computing them, FEM is used for the purpose.

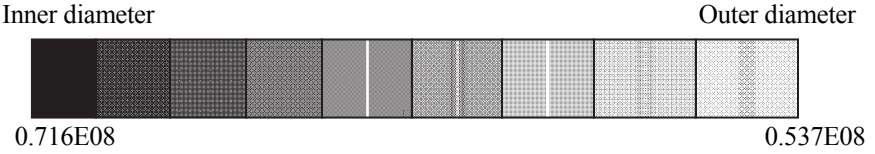

Figure 12.21 von-Mises stress distribution at 10.44 MPa pressure [50].

For a given potential difference (V) between electrodes the electrostatic energy is computed using Equation 12.42 once the FEM solution is obtained. The energy value is equated to $(1/2)CV^2$ to calculate C. This approach was used to compute the series capacitance of a disk-pair in Section 7.3.

Self and mutual inductances between turns/disks/sections of a winding: For calculation of inductances, the energy-based calculation is again a natural choice. The self-inductance of a turn or a disk or a section of a winding, when it is alone excited with current I, is simply given as

$$L_{ii} = 2W_m / I^2 . \tag{12.157}$$

The stored energy can be calculated using the expression given by Equation 3.34 in terms of magnetic vector potential and current density variables, which is a normally followed procedure since 2-D magnetic field problems are invariably solved in terms of the magnetic vector potential, or through the expression given by Equation 12.57 in terms of **B** and **H** fields. Magnetic linearity is assumed in these calculations. In commercial FEM software, the stored energy is readily available at the click of a button after the solution is obtained.

The mutual inductance between two entities (turns/disks/sections) is calculated by doing three FEM simulations: exciting the entity 1 alone, exciting entity 2 alone, and exciting both entities. Using Equation 12.157, the first two energy values give self inductances L_{11} and L_{22}. The mutual inductance can then be determined as

$$M_{12} = \frac{1}{I_1 I_2}\left(W_{12} - \frac{1}{2}L_{11}{I_1}^2 - \frac{1}{2}L_{22}{I_2}^2\right). \tag{12.158}$$

Alternatively, we can evaluate the mutual inductance through just two simulations as follows. The first FEM simulation is done with currents I_1 and I_2 and the second one with currents $-I_1$ and I_2. The corresponding two energies are given by

$$W_{m1} = \frac{1}{2}\left(L_{11}I_1^2 + 2M_{12}\, I_1 I_2 + L_{22}I_2^2\right) \tag{12.159}$$

and

$$W_{m2} = \frac{1}{2}\left(L_{11}I_1^2 - 2M_{12}\, I_1 I_2 + L_{22}I_2^2\right). \tag{12.160}$$

Manipulating the above two expressions we have

$$M_{12} = \frac{W_{m1} - W_{m2}}{2\, I_1 I_2}. \tag{12.161}$$

The calculation of the leakage inductance of a transformer using FEM has already been elaborated in Chapter 3. For the calculation of frequency-dependent self and mutual inductances, see Section 13.10.3.

12.7.2 Stresses in insulation system

This is a major application of the FEM technique in transformers. The philosophy of the design of the insulation systems and the corresponding procedures have been covered in Chapter 8. Also, while elaborating a sample design of a transformer in Appendix A, the factors influencing the inter-turn, inter-disk, inter-winding and winding-to-core insulation have been discussed. After obtaining electrostatic field distribution by FEM, the insulation withstand can be calculated using the concepts and guidelines given in Chapter 8. The insulation system design involves determining the stresses and strengths. The accuracy of computed stresses depends mainly on the mesh size, particularly at sharper electrodes. For example, if one of the electrodes in an FEM simulation has a corner radius of 1 mm, the size of the FEM mesh at the corner should be at least 0.3 mm or lower with first-order (linear) finite elements. Furthermore, the mesh size should be reduced in the next set of simulations to check that the solution obtained there does not change much. If required, quantities such as creepage stresses along an insulation surface, cumulative stresses in bulk oil, etc. can be obtained using the solution. Strengths are calculated by using concepts such as stressed oil volume (see Section 8.3.6) which can be also determined from the solution.

12.7.3 Eddy current losses in windings and structural parts

The theory of eddy currents and the procedures for calculation of eddy current losses in windings and structural parts have been adequately discussed in Chapters 4 and 5. The eddy losses in a winding are commonly calculated using 2-D magnetostatic simulations as discussed in Section 4.5.2, although more accurate calculations can be performed by using time-harmonic simulations with modeling of each conductor/turn with definition of electric conductivity as discussed in Section 12.6.1. What will be discussed here is how eddy currents and losses in windings and structural parts can be computed (through time-harmonic simulations) once the 2-D solution is available in terms of the magnetic vector potential (A), which has only the z-component.

The magnitude of the eddy current density in each finite element is

$$\hat{J}_e^e = -j\omega\sigma\,\hat{A}^e \tag{12.162}$$

which is nothing but Equation 12.74 written in the time-harmonic form, and $\hat{A}^e$, in the phasor form, is the value of the magnetic vector potential at the centroid of each element, which can be taken as the average of the three nodal values.

$$\therefore \hat{J}_e^e = -j\omega\sigma\,\frac{\hat{A}_1 + \hat{A}_2 + \hat{A}_3}{3}. \tag{12.163}$$

The loss density in W/m^3 in terms of the current density and resistivity (ρ) is

$$P_E = \rho J^2 = (1/\sigma) J^2. \tag{12.164}$$

Hence, in the time-harmonic case, the expression for the elemental eddy losses in per unit length can be expressed in terms of the rms value of the elemental current density as [51]

$$P^e = \int_{\Omega^e} P_E^e \, dx dy = \int_{\Omega^e} \frac{\hat{J}_e^e \hat{J}_e^{e*}}{\sigma} dx \, dy \, . \tag{12.165}$$

Such elemental level heat sources become input to a thermal model if temperatures need to be calculated. They can be integrated over the entire conducting domain to calculate the total eddy losses in it. If the domain is a conductor carrying the source current as well, the total elemental losses are calculated using Equation 12.165 with the term $\hat{J}_e^e$ replaced by the phasor addition of $\hat{J}_e^e$ and $\hat{J}_s^e$. The induced eddy current density has to be obtained from a formulation, in which a voltage source feeds the thick conductor; the PDE to be solved is given by Equation 12.135. The total loss in the conductor is then expressed in terms of the two E components as in Equation 12.138 (it should be noted that the loss density $= (1/\sigma) J^2 = \sigma E^2 = \sigma \hat{E} \hat{E}^*$, where J and E denote modulus of respective phasors).

12.7.4 Circulating current loss in windings

Procedures for calculation of circulating current losses in windings using analytical and FEM techniques have been elaborated in Chapter 4. Generally, as discussed there, the eddy and circulating current losses in windings are calculated separately. Parallel conductors forming a turn have to be treated as separate entities. Typically, the LV winding of a transformer is made up of parallel conductors; it is short-circuited during the load loss test with an impedance voltage applied to the HV winding. During the FEM simulation for the circulating current loss estimation, the currents in the LV and HV windings are unknown. It becomes a case of coupled field-circuit simulation; the entire HV winding is modeled as one circuit fed by a voltage source, and each of the LV conductors is treated as a different circuit. The total number of circuits in the model becomes $L_c + 1$, where L_c represents the number of LV conductors in parallel. The value of the voltage source is adjusted until rated currents are established in the winding conductors which are modeled as stranded conductors with their resistances treated as external resistances; the values of these resistances will be unequal if the mean lengths of the conductors are different. The field model accounts for the different flux linkages (and the inductances) of the parallel conductors. In an alternative approach, both resistive and inductive effects can be taken into account in the field

model, for which the conductors have to be modeled as massive ones with definition of their electrical conductivity. This way, the circulating and eddy current losses will be calculated simultaneously.

12.7.5 Proximity effects

When a winding with many conductors (turns) carries an alternating current, the distribution of the current is not uniform across the cross section of the conductors. This phenomenon is due to the skin and proximity effects. In Chapter 4, there is an elaborate discussion on skin effect/depth of penetration. We will discuss the effect briefly here to differentiate it from the proximity effect. A time-varying current in a conductor produces a time-varying magnetic field (inside and outside its cross section) inducing eddy currents in it that oppose the original current. The central portion of the conductor links a greater magnetic flux than its outer part. Hence the induced voltage is higher in the central portion. If the conductor is assumed to be made up of a number of filamentary elements, we can say that the inductance (and hence the impedance) offered by the elements in the central portion is higher tending to confine the total current to the outer surface of the conductor. The confinement of the current to the surface is characterized by the skin depth. This is an important material characteristic constant whose expression has been derived in Chapter 4 (Equation 4.38) from the first principles. Effectively, there is a decrease in the area through which the total current flows making the AC resistance higher than the corresponding DC value. The effect becomes stronger as the frequency increases.

On the other hand, the proximity effect in a conductor is due to the time-varying flux produced by currents in other conductors in its vicinity. Figure 12.22 shows the current distributions in two circular conductors for two cases obtained using time-harmonic FEM simulations.

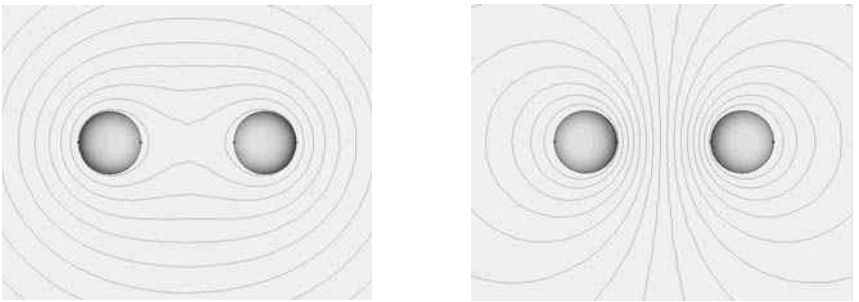

(a) Currents in same direction (b) Currents in opposite directions

Figure 12.22 Proximity effect.

When the current is carried by them in the same direction (see Figure 12.22 (a)), the portions of the two conductors in close proximity (facing each other) link more flux thereby increasing their inductance. Therefore, the current carried by the remaining portions (farther from each other) is more. Hence the total current is not only confined to the surface, which is reflected by the nonuniform current density distribution in the radial direction due to the skin effect, but it also distributes nonuniformly along the circumferential direction; in other words, the skin effect gets skewed along the ϕ direction due to the proximity effect.

In Figure 12.22 (b), wherein the currents in the two conductors are in opposite directions, using similar reasoning based on the flux linkages of the closer and farther portions, it can be surmised that the portions of the two conductors in close proximity will have higher current densities. Thus, the proximity effect makes the total current distribution more nonuniform (compared to that due to the skin effect alone) increasing the AC resistance further. The mutual impedance between the two conductors has two components. The imaginary part represents the mutual inductance corresponding to the induced voltage, while the real part is the mutual resistance accounting for an increase in the AC resistance. See Section 13.10.3 for additional comments on the mutual resistance.

The procedures outlined earlier for the calculation of self and mutual inductances do not take into account the skin and proximity effects since they are magnetostatic formulations that neglect induced fields and currents due to time-varying effects. The influence of the skin effect on the self inductance is not appreciable since it affects the internal flux of the conductor whose contribution to the self inductance is much less than that of the flux outside it. On the contrary, the mutual inductance (and the mutual resistance) between the conductors in close proximity is substantially influenced by the proximity effect. For example, when the currents flow in opposite directions in the two conductors, the closest portions of the conductors have higher current densities, effectively reducing the distance between them and therefore affecting the corresponding mutual inductance significantly. Since the skin and proximity effects are pronounced at higher frequencies, they should be considered in a more rigorous way as in [52] for determining the response of transformer windings to high frequency surges.

12.7.6 Hysteresis loss

While designing electromagnetic devices including transformers, magnetic field computations should precisely take into account the nonlinear and hysteretic behavior of their magnetic circuit. Various hysteresis models have been proposed in the literature. The Jiles-Atherton (JA) model and the Preisach model are the most frequently used hysteresis models in electromagnetic field computations. The Preisach model has been described briefly in Section 13.3.

The JA model is based on the energy balance equation. In the model, magnetization M is decomposed into two components:. reversible component

M_{rev} and irreversible component M_{irr}. The model is represented by the following first-order differential equation [53],

$$\frac{dM}{dH} = \frac{M_{an}(H) - M_{irr}(H)}{(k\delta/\mu_0) - \alpha\left(M_{an}(H) - M_{irr}(H)\right)} + c\left(\frac{dM_{an}}{dH} - \frac{dM}{dH}\right) \tag{12.166}$$

where, M is the total magnetization, H is the applied magnetic field, M_{an} is the anhysteretic magnetization, μ_0 is the magnetic permeability of free space, k is the domain wall pinning parameter which is responsible for the irreversible component of the magnetization, c is the domain wall bowing parameter which characterizes the reversible magnetization component, α is the mean field parameter, and δ is the directional parameter defined as

$$\left.\begin{array}{ll} \delta = +1 \text{ for} & dH/dt > 0 \text{ and } (M_{an}(H) - M(H)) > 0 \\ \delta = -1 \text{ for} & dH/dt < 0 \text{ and } (M_{an}(H) - M(H)) < 0 \end{array}\right\}. \tag{12.167}$$

The anhysteretic magnetization M_{an} is defined as

$$M_{an}\left(H_e\right) = M_s\left[\coth\left(\frac{H_e}{a}\right) - \left(\frac{a}{H_e}\right)\right] \tag{12.168}$$

where, M_s is the saturation magnetization and a is known as the shape factor which is temperature-dependent. H_e is the effective field:

$$H_e = H + \alpha M \tag{12.169}$$

The model depends on the values of the following five parameters: M_s, k, α, c and a. The values of these parameters can be determined by a parameter identification process using iterative or optimization techniques [54]. The model is relatively simple to implement in numerical techniques. We will describe here implementation of the JA model in the finite element method. In the original JA model, we obtain B from H. However, while using a magnetic vector potential-based FEM formulation, B is obtained directly from the computed potential at each time step. Hence, an inverse JA model proposed in [10] can be used which calculates H from B.

***Implementation of the JA hysteresis model in FEM computations*:**

The JA model can be implemented in FEM calculations using some standard iterative methods such as the Newton–Raphson technique. Another alternative is a time-stepping method using the inverse JA hysteresis model which is based on a differential reluctivity approach as described below.

For isotropic materials in two dimensions, the generalized relationship between vectors **B** and **H** can be expressed as

$$d\mathbf{H} = \upsilon_d \, d\mathbf{B} \, . \tag{12.170}$$

Here, the differential reluctivity υ_d is a scalar quantity. For anisotropic case in three dimensions, it would be a 3×3 reluctivity tensor matrix. The expression of υ_d is [10]

$$\upsilon_d = \frac{\Delta H_x \Delta B_x + \Delta H_y \Delta B_y}{\Delta B_x^2 + \Delta B_y^2} \tag{12.171}$$

Applying the Euler scheme to Equation 12.170, we have

$$\mathbf{H}(t + \Delta t) = \upsilon_d \Delta \mathbf{B} + \mathbf{H}(t) \,. \tag{12.172}$$

We can write Ampere's Law at a time instant (t+Δt) as

$$\nabla \times \mathbf{H}(t + \Delta t) = \mathbf{J}(t + \Delta t) \,. \tag{12.173}$$

Using Equations 12.172, 12.173 and 12.64, we obtain

$$\nabla \times \upsilon_d (\nabla \times \mathbf{A}(t + \Delta t)) = \mathbf{J}(t + \Delta t) + \nabla \times \upsilon_d (\nabla \times \mathbf{A}(t)) - \nabla \times \mathbf{H}(t) \,. \tag{12.174}$$

Equation 12.174 is solved iteratively incorporating the inverse JA model. At each time step, $\mathbf{B}(t+\Delta t)$ is obtained from the computed $\mathbf{A}(t+\Delta t)$ for each finite element. The inverse JA model is used to obtain $H_x(t+\Delta t)$ and $H_y(t+\Delta t)$ from $B_x(t+\Delta t)$ and $B_y(t+\Delta t)$, respectively. ΔH_x and ΔH_y can now be evaluated since $H_x(t)$ and $H_y(t)$ of the previous time step are known. Similarly, the calculated ΔB_x and ΔB_y values enable the computation of υ_d using Equation 12.171. The elemental matrices are recalculated with updated υ_d values to solve Equation 12.174 again. This procedure is repeated until convergence is reached.

***Eddy and anomalous losses in field computation*:** The total core loss consists of the hysteresis, eddy, and anomalous components as discussed in Section 2.2. The eddy loss depends on the rate of change of magnetic induction and physical dimensions of laminations. The anomalous loss varies with domain wall movement. The total magnetic field intensity $\mathbf{H}_T$ can be written as a sum of three components: the hysteretic field $\mathbf{H}_h$, the field associated with eddy currents $\mathbf{H}_{eddy}$, and the field associated with the anomalous loss $\mathbf{H}_{anomalous}$ [10, 55]. The fields associated with the eddy and anomalous losses can be calculated by using the expressions of the corresponding losses given by Equations 2.7 and 2.9, respectively. For calculating the total core loss using FEM, the total magnetic field $\mathbf{H}_T$ is used in Equation 12.173 instead of $\mathbf{H}$. The effect of the eddy current and anomalous losses on the hysteresis loop is shown in Figure 12.23(A) which has been plotted by using the values of the parameters given in [55]. The loop widens with the inclusion of the additional losses. The corresponding no-load currents computed by a FEM code are shown in Figure 12.23(B).

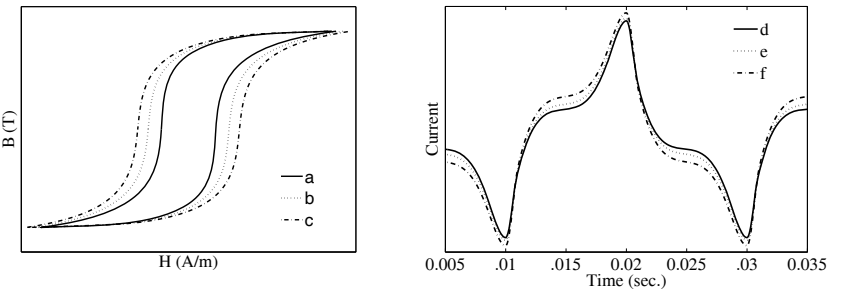

A. Dynamic hysteresis loop B. No-load current

a = static hysteresis loop
b = hyteresis with only classical eddy loss (50 Hz)
c = hyteresis with classical eddy and anomalous loss (50 Hz)
d = current with case a
e = current with case b
f = current with case c

Figure 12.23 Effect of eddy and anomalous losses.

12.7.7 Electromagnetic forces

In a transformer, the forces of electromagnetic origin occur in its windings, core, and leads. A precise knowledge of local distributions of these forces is essential for deformable bodies. On the other hand, for analyzing a moving rigid body, the total force acting on it should be computed; such a global force computation is applicable in gapped-core shunt reactors while calculating forces between core-packets.

Various methods are available to calculate different forces in transformers; computations based on Lorentz force, Virtual Work approach and Maxwell stress tensor are used to calculate short-circuit forces in windings, forces between packets of the gapped-core in shunt reactors, and magnetostrictive forces in the core of transformers, respectively. The basics of these techniques are described below.

***Lorentz force method*:** A current-carrying conductor in a magnetic field experiences a force defined by the Lorentz equation. The total force on the conductor is obtained by integrating the forces due to the magnetic field acting on each differential current-carrying element,

$$\mathbf{F} = \int_v (\mathbf{J} \times \mathbf{B})\, dv \tag{12.175}$$

where, $\mathbf{J}\times\mathbf{B}$ is the force density in an infinitesimal volume of the conductor. This method is particularly useful for determining axial and radial forces in transformer windings during short circuits as explained in Chapter 6. The method is used for the computation of forces in material media having free currents in them. However, materials subjected to magnetization forces cannot be handled by it. These forces can be analyzed by either the virtual work method or the Maxwell stress tensor approach.

***Virtual work method*:** Analytical techniques can be used for simple geometries and uniform field distributions. The forces are computed using the energy density expression,

$$W = \frac{1}{2}\frac{B^2}{\mu_0} \quad . \tag{12.176}$$

If a force is applied to move a body, having cross-sectional area A, by Δx, the incremental stored energy due to the work done by the force is

$$\Delta W = W \cdot \Delta v = \frac{1}{2}\frac{B^2}{\mu_0}\left(A\,\Delta x\right) \; . \tag{12.177}$$

The force corresponding to the additional energy is then given by

$$f = \frac{\Delta W}{\Delta x} = \frac{1}{2}\frac{B^2}{\mu_0} A \, . \tag{12.178}$$

The force per unit area on the body surface is therefore given by

$$F_s = \frac{f}{A} = \frac{1}{2}\frac{B^2}{\mu_0} \quad \text{N/m}^2 \, . \tag{12.179}$$

If a uniform flux condition is assumed in the gap between two packets of a gapped core shunt reactor, the force between them can be computed by the above formula. However, if the flux distribution is nonuniform and geometries are complex, a numerical technique such as FEM is generally applied using virtual work principles.

The classical virtual work method uses a finite difference approximation to evaluate energy derivatives. This method computes the energies in two positions of a movable body which is assumed to be displaced; a change in the stored magnetic energy divided by its displacement (say, in the x direction) gives the force acting on it as the displacement tends to be infinitesimal [56],

$$F = -\frac{\Delta W'}{\Delta x} = -\frac{W_1' - W_2'}{\Delta x}. \tag{12.180}$$

A major problem with this method is that it needs two field computations for calculating energies in two different positions. Another approach uses Coulomb's method in which energy derivatives are calculated by a virtual displacement of nodes in an FEM formulation. The forces are calculated by using either a magnetic vector potential-based formulation (an energy based approach in which flux-linkage is held constant) or a magnetic scalar potential based formulation (a co-energy based approach in which current is held constant) [26, 56].

Maxwell stress tensor: This is widely used for electromagnetic force computations. The local force distribution in the magnetized bodies (without magnetostriction) can be expressed as [57, 58]

$$\mathbf{F}_v = -\frac{1}{2}\mathbf{H}\cdot\mathbf{H}\,\nabla\mu\,. \tag{12.181}$$

On the surface of a material, $\mathbf{F}_v$ can be written in terms of normal and tangential components as

$$\mathbf{F}_v = -\frac{1}{2}(H_t^2 + H_n^2)\,\nabla\mu = -\frac{1}{2}(H_t^2 + \frac{B_n^2}{\mu^2})\,\nabla\mu\,. \tag{12.182}$$

Since, $\dfrac{\nabla\mu}{\mu^2} = -\nabla\upsilon$ (where $\upsilon = \text{reluctivity} = 1/\mu$),

$$\mathbf{F}_v = -\frac{1}{2}(H_t^2\nabla\mu - B_n^2\nabla\upsilon). \tag{12.183}$$

The force density at the surface follows from the above equation,

$$\mathbf{F}_s = -\frac{1}{2}(H_t^2(\mu_0 - \mu) - B_n^2(\upsilon_0 - \upsilon))\mathbf{n} \tag{12.184}$$

where, **n** is the unit normal vector to the surface.

In gapped-core structures, the force between two packets can be computed using Equation 12.184 with the assumption of negligible fringing effects (i.e., $H_t = 0$) as

$$\mathbf{F}_s = \frac{1}{2}(B_n^2(\upsilon_0 - \upsilon))\mathbf{n}. \tag{12.185}$$

The reluctivity υ of the core material is negligible in comparison of the reluctivity of nonmagnetic gaps between packets. Hence the magnitude of the force per unit area perpendicular to the surface can be expressed as

$$F_s = \frac{1}{2}\frac{B^2}{\mu_0}$$

which is the same as that derived earlier analytically via the energy approach, i.e., Equation 12.179.

An additional force that can occur in a core material is due to magnetostriction. In the above discussion it is assumed that any change in the permeability is due to inhomogeneous materials (i.e., $\nabla\mu \neq 0$) and it is independent of the material density (ρ). This is a valid assumption for rigid body motion. However, it is no longer valid for deformable core laminations under the action of magnetostriction forces [57]. The permeability of such materials should be expressed as a function of the material density (i.e., $\delta\mu = (\partial\mu/\partial\rho)\delta\rho$). Thus, in addition to the magnetization forces, the magnetostriction forces can also occur in a magnetic material; if there are induced eddy currents in the material, the Lorentz force also exists, and therefore a generalized expression for the force density can be written as [57]

$$\mathbf{F}_v = \mathbf{J}\times\mathbf{B} - \frac{1}{2}\mathbf{H}\cdot\mathbf{H}\nabla\mu + \nabla\left(\frac{1}{2}\mathbf{H}\cdot\mathbf{H}\rho\frac{\partial\mu}{\partial\rho}\right). \tag{12.186}$$

The total force density contains three terms; the first term represents the Lorentz force density in conducting materials, the second term indicates the magnetization force density, and the third term represents the magnetostriction force density.

It is generally convenient to express the force density in terms of a stress tensor. This approach is particularly useful in the computation of local force distributions. The divergence of the stress tensor gives the volume force density,

$$\mathbf{F} = \int_v \nabla\cdot\mathbf{T}\,dv\,. \tag{12.187}$$

The tensor is a 3×3 matrix and has a unit of N/m^2; its elements are described in [8]. It should also be remembered that the divergence of a tensor is a vector. The above expression can give all the types of forces occurring in the volume of a body. For example, magnetization and magnetostriction forces are expressed in terms of the stress tensor in [59].

Applying the divergence theorem, the volume integral in Equation 12.187 can be transformed into a closed surface integral. For magnetization forces only, the tangential (F_t) and normal (F_n) components of the force per unit area on an elemental surface can be expressed in terms of the tangential and normal field components [8, 26],

$$F_t = B_n H_t$$
$$F_n = \frac{1}{2}\left(\frac{1}{\mu_0} B_n^2 - \mu_0 H_t^2\right). \tag{12.188}$$

***Calculation of forces for noise calculation*:** The main source of noise in a transformer is core vibrations which result from the magnetizing force that acts between individual laminations and the magnetostriction force which causes a change in the length of core laminations. The contribution of magnetization forces in the noise depends on the design of core joints and corners. These forces are in the form of attractive and repulsive forces between ends of sheets facing each other in joint regions, and thus between limbs and yokes. The Maxwell stress tensor method can be implemented in an FEM formulation to compute core vibrations and noise. In [59], the magnetization forces have been calculated by applying Maxwell stress tensor locally, which is also called magnetic stress tensor. The magnetostriction forces are calculated using a magnetostriction stress tensor which is a function of the corresponding strain tensor.

References

1. Hayt, W. H. *Engineering electromagnetics*, McGraw-Hill Book Company, Singapore, 1989.
2. Sadiku, M. N. O. *Elements of electromagnetics,* Third Edition, Oxford University Press, New York, 2002.
3. Pramanik, A. *Electromagnetism: theory and applications*, Second Edition, Prentice Hall of India Private Limited, New Delhi, 2008.
4. Ida, N. *Engineering electromagnetics*, Springer, New York, 2004.
5. Sadiku, M. N. O. *Numerical techniques in electromagnetics with MATLAB*®, Third Edition, CRC Press, 2009.
6. Ida, N. *Numerical modeling for electromagnetic non-destructive evaluation*, Chapman & Hall, London, 1995.
7. Chari, M. V. K. and Salon, S. J. *Numerical methods in electromagnetism, Academic Press*, 2000.
8. Salon, S. J. *Finite element analysis of electrical machines,* Springer International Edition, New Delhi, 1995.
9. Jin, J. *The finite element method in electromagnetics*, Second Edition, John Wiley and Sons, 2002.
10. Bastos, J. P. A. and Sadowski, N. *Electromagnetic modeling by finite element methods,* Marcel Dekker, Inc., New York, 2003.
11. Bianchi, N. *Electrical machine analysis using finite elements,* CRC Press, Taylor & Francis Group, USA, 2005.
12. Sykulski, J. K. *Computational magnetics*, Chapman & Hall, 1995.

13. Poljak, D. and Brebbia, C. A. *Boundary element methods for electrical engineers,* WIT Press, Southampton, 2005.
14. Kumbhar, G. B. and Kulkarni, S. V. Analysis of short circuit performance of split-winding transformer using coupled field-circuit approach, *IEEE Transactions on Power Delivery*, Vol. 22, No. 2, April 2007, pp. 936–943.
15. Kraus, J. D. and Fleisch, D. A. *Electromagnetics with applications*, Fifth Edition, WCB/McGraw-Hill, Singapore, 1999.
16. Preis, K., Biro, O., Supancic, P., Ticar, I., and Matzenauer, G. Time-domain analysis of quasistatic electric fields in media with frequency-dependent permittivity, *IEEE Transactions on Magnetics*, Vol. 40, No. 2, March 2004, pp. 1302–1305.
17. Hammond, P. and Sykulski, J. K. *Engineering electromagnetism: physical processes and computation,* Oxford University Press, 1994.
18. Cheng, D. K. *Field and wave electromagnetics,* Second Edition, Addison-Wesley, Singapore, 1999.
19. Hoole, S. R. H. *Computer-aided analysis and design of electromagnetic devices*, Elsevier Science Publishing Co., 1989.
20. Renyuan, T., Shenghui, W., Yan, L., Xiulian, W., and Xiang, C. Transient simulation of power transformers using 3D finite element model coupled to electric circuit equations, *IEEE Transactions on Magnetics*, Vol. 36, No. 4, July 2000, pp. 1417–1420.
21. Carpenter, C. J. Theory of flux penetration into laminated iron and associated losses, *Proceedings IEE*, Vol. 124, No. 7, July 1977, pp. 659–664.
22. Renyuan, T., Yan, L., Dake, L., and Lijian, T. Numerical calculation of 3-D transient eddy current field and short circuit electromagnetic force in large transformers, *IEEE Transactions on Magnetics,* Vol. 28, No. 2, March 1992, pp. 1418–1421.
23. Bouissou, S. and Piriou, F. Numerical simulation of a power transformer using 3D finite element method coupled to circuit equation, *IEEE Transactions on Magnetics*, Vol. 30, No. 5, September 1994, pp. 3224–3227.
24. Renyuan, T., Hu, Y., Liang, Z., and Xie, D. Computation of 3-D open boundary eddy-current fields in large transformers using $\boldsymbol{T}$, ψ-φ_m method coupled with GTM, *IEEE Transactions on Magnetics*, Vol. 38, No. 2, March 2002, pp. 1257–1260.
25. Lowther, D. A. and Silvester, P. P. *Computer aided design in magnetics*, Springer-Verlag, New York, 1985.
26. Reece, A. B. J. and Preston, T. *Finite element method in electric power engineering,* Oxford University Press, UK, 2000.
27. Bondeson, A., Rylander, T., and Ingelstrom, P. *Computational electromagnetics,* Springer (India) Pvt. Ltd., New Delhi, 2007.
28. Seely, S. *Introduction to electromagnetic fields,* McGraw-Hill Book Company, Inc., New York, 1958.

29. Silvester, P. P. and Ferrari, R. L. *Finite elements for electrical engineers,* Cambridge University Press, Third Edition, Cambridge, 1996.
30. Brauer, J. Simple equations for the magnetization and reluctivity curves of steel, *IEEE Transactions on Magnetics*, Vol. 11, No. 1, January 1975, p. 81.
31. Kulkarni, S. V. Coupled field computations for analysis of intricate phenomena in transformers, Invited Paper, *Advanced Research Workshop on Transformers* ARWtr 2007, Baiona, Spain, October 28–31, 2007, pp. 172–186.
32. Hameyer, K., Driesen, J., Gersem, H. D., and Belmans, R. The classification of coupled field problems, *IEEE Transactions on Magnetics*, Vol. 35, No. 3, May 1999, pp. 1618–1621.
33. Zhou, P., Fu, W. N., Lin, D., Stanton, S., and Cendes, Z. J. Numerical modeling of magnetic devices, *IEEE Transactions on Magnetics*, Vol. 40, No. 4, July 2004, pp. 1803–1809.
34. Heiden, R. H. V., Arkadan, A. A., Brauer, J. R., and Hummert, G. T. Finite element modeling of a transformer feeding a rectified load: the coupled power electronics and nonlinear magnetic field problem, *IEEE Transactions on Magnetics*, Vol. 27, No. 6, November 1991, pp. 5217–5219.
35. Arturi, C. M. Electromagnetic force calculations on a 3-phase autotransformer under time-varying fault by a 3D non-linear finite element code, *IEEE Transactions on Magnetics*, Vol. 29, No. 2, March 1993, pp. 2010–2013.
36. Bhide, R. S., Kumbhar, G. B., Kulkarni, S. V., and Koria, J. P. Coupled circuit-field formulation for analysis of parallel operation of converters with interphase transformer, *Electric Power Systems Research*. Vol. 78, Issue 1, Jan 2008, pp 158–164.
37. Driesen, J., Deliege, G., Belmans, R., and Hameyer, K. Coupled thermo-magnetic simulation of a foil-winding transformer connected to a non-linear load, *IEEE Transactions on Magnetics*, Vol. 36, No. 4, July 2000, pp. 1381–1385.
38. Driesen, J., Belmans, R., and Hameyer, K. The computation of the effects of harmonic currents on transformers using a coupled electromagnetic-thermal FEM approach, *Proceedings of Ninth International Conference on Harmonics and Quality of Power*, Orlando, USA, Vol. 2, April 2000, pp. 720–725.
39. Lefevre, A., Miegeville, L., Fouladgar, J., and Olivier, G. 3-D computation of transformers overheating under nonlinear loads, *IEEE Transactions on Magnetics*, Vol. 41, No. 5, May 2005, pp. 1564–1567.
40. Koppikar, D. A., Kulkarni, S. V., Srinivas, P. N., Khaparde, S. A., and Jain, R. Evaluation of flitch plate losses in power transformers, *IEEE Transactions on Power Delivery*, Vol. 14, No. 3, July 1999, pp. 996–1001.
41. Driesen, J., Belmans, R., and Hameyer, K. Computation algorithms for efficient coupled electromagnetic-thermal device simulation, *IEE*

Proceedings — Science, Measurement and Technology, Vol. 149, No. 2, March 2002, pp. 67–72.
42. Garg, V. K. and Raymond, J. Magneto-thermal coupled analysis of canned induction motor, *IEEE Transactions on Energy Conversion*, Vol. 5, No. 1, March 1990, pp. 110–114.
43. Feliachi, M. and Develey, G. Magneto-thermal behavior finite element analysis for ferromagnetic materials in induction heating devices, *IEEE Transactions on Magnetics*, Vol. 27, No. 6, November 1991, pp. 5235–5237.
44. Kumbhar, G. B., Kulkarni, S. V., Escarela-Perez, R., and Campero-Littlewood, E. Applications of coupled field formulations to electrical machinery, *The International Journal for Computation and Mathematics in Electrical and Electronic Engineering,* Vol. 26, No. 2, 2007, pp. 489–523.
45. Kulkarni, S. V. Finite element method applied to design and analysis in power transformers, Part 2: Electromagnetic and coupled field computations in transformers, Tutorial in *Advanced Research Workshop on Transformers*, ARWtr2010, Santiago-de-Compostela, Spain, October 2010, pp. 85–140.
46. Delaere, K., Heylen, W., Hameyer, K., and Belmans, R. Local magnetostriction forces for finite element analysis, *IEEE Transactions on Magnetics*, Vol. 36, No. 5, September 2000, pp. 3115–3118.
47. Rausch, M., Kaltenbacher, M., Landes, H., Lerch, R., Anger, J., Gerth, J., and Boss, P. Combination of finite and boundary element methods in investigation and prediction of load-controlled noise of power transformers, *Journal of Sound and Vibration*, 250 (2), 2002, pp. 323–338.
48. Srinath, L. S. *Advanced mechanics of solids,* Tata McGraw-Hill, Second Edition, New Delhi, 2005, pp. 295–297.
49. Seshu, P. *Textbook of finite element analysis,* PHI, New Delhi, 2006.
50. Bakshi, A., Thakar, R. V., Kulkarni, S. V., and Vora, S. Mechanical stress and deformation analysis of transformer winding using finite element method, *International Conference on Transformers, TRAFOTECH-2010*, Mumbai, January 2010, pp. I-1–I-5.
51. Penabad-Duran, P. and Lopez-Fernandez, X. M. Finite element method applied to design and analysis in power transformers, Part 1: Introduction to FEM analysis, Tutorial in *Advanced Research Workshop on Transformers*, ARWtr2010, Santiago-de-Compostela, Spain, October 2010, pp. 14–83.
52. Moreau, O., Popiel, L., and Pages, J. L. Proximity losses computation with a 2D complex permeability modeling, *IEEE Transactions on Magnetics,* Vol. 34, No. 5, September 1998, pp. 3616–3619.
53. Jiles, D. C. and Atherton, D. L. Theory of ferromagnetic hysteresis, *Journal of Magnetism and Magnetic Materials*, Vol. 61, 1986, pp. 48–60.
54. Etien, E., Halbert, D., and Poinot, T. Improved Jiles-Atherton model for least square identification using sensitivity function normalization, *IEEE Transactions on Magnetics*, Vol. 44, No. 7, July 2008, pp. 1721–1727.

55. Jiles, D. C. Frequency dependence of hysteresis curves in conducting magnetic materials, *Journal of Applied Physics*, Vol. 76, No. 10, November 1994, pp. 5849–5855.
56. Coulomb, J. L. and Meunier, G. Finite elements implementation of virtual work principle for magnetic or electric force and torque computation, *IEEE Transactions on Magnetics,* Vol. 20, No. 5, September 1984, pp. 1894–1896.
57. Woodson, H. H. and Melcher, J. R. *Electromechanical Dynamics Part II: field, forces, and motion,* John Wiley & Sons, Inc., New York, 1968.
58. Reyne, G., Sabonnadiere, J. C., Coulomb, J. L., and Brissonneau, P. A survey of the main aspects of magnetic forces and mechanical behavior of ferromagnetic materials under magnetization, *IEEE Transactions on Magnetics,* Vol. 23, No. 5, September 1987, pp. 3765–3767.
59. Hilgert, T., Vandevelde, L., and Melkebeek, J. Comparison of magnetostriction models for use in calculations of vibrations in magnetic cores, *IEEE Transactions on Magnetics*, Vol. 44, No. 6, June 2008, pp. 874–877.

13

Transformer–System Interactions and Modeling

This chapter deals with modeling aspects of transformers for various steady-state and transient studies involving connected power systems. Transformers are important constituents of any power system network. Their accurate representation is necessary to determine power flow conditions in steady-state conditions and to ascertain the effect of power system transients on them. There are many steady state and transient operating conditions that affect transformers operating in power systems. Unbalanced operations, harmonics and ferroresonance conditions can be detrimental to their operation. Steeply rising voltage transients associated with gas-insulated systems can be harmful to bushings and windings. Switching operations of vacuum circuit breakers are known to cause problems to transformers. Several unexplained failures are reported in the literature [1] which may have happened due to internal resonances caused by very fast transient overvoltages or vacuum circuit breaker operations. Part winding resonance phenomena can lead to severe voltage stresses in windings. Geomagnetic disturbances result in severe saturation conditions of the magnetic circuit. Sympathetic inrush currents cause maloperation of protective devices and lead to higher noise levels in transformers. Such power system interaction aspects of transformers are discussed in this chapter. Various approaches reported in the literature for studying them are also enumerated.

13.1 Power Flow Analysis with Transformers

Transmission systems are fairly balanced and power flow calculations are done on a per phase basis. As discussed in Section 1.3.4, transformers are modeled as series elements with their leakage impedances expressed in per unit (p.u.) for

power flow and fault calculations. Since the resistive component of the leakage impedance is much smaller, particularly so in large transformers, a representation in terms of only per-unit leakage reactance values is generally adequate for power flow studies. A typical value of per-unit resistance for medium and large rating power transformers is in the range of 0.002 p.u. to 0.004 p.u. These values are much smaller than their usual leakage reactance values which are typically around 0.1 p.u. Furthermore, the values of resistances of transmission lines are also much higher; the accuracy of the calculated real (or active) power flow values in the network may not be affected much if resistances of transformers are neglected. The approximation is particularly justified for the power system planning studies. However, for knowing actual operating conditions on an existing network, the losses occurring in its various components should be taken into account. This necessitates doing power flow computations with resistances of transformers taken into consideration. It should be mentioned here that their consideration for the power flow analysis of distribution systems is certainly essential because of the fact that the R/X ratio of distribution transformers is higher than that of power transformers. A 2 MVA, 11/0.415 kV transformer has a typical R/X ratio of 0.2 which is much higher than a corresponding typical value of 0.025 for a 100 MVA, 220/66 kV transformer.

In addition to the R/X ratio, distribution systems have many other characteristics which are different than those of transmission systems. These include their radial nature in many cases, unbalanced three-phase loading, single-phase loads, and untransposed feeders/unsymmetrical spacings of conductors. This necessitates three-phase power flow computations in which the equivalent model of the transformers is dependent on their connections (vector groups) and grounding conditions (e.g., whether the neutral of a star connected winding is grounded or not). Hence, the analysis becomes complicated compared to that for transmission systems.

13.1.1 Transformer modeling for distribution systems

The modeling of a three-phase transformer is an important task while doing the power flow analysis of a distribution system. For a given transformer with its vector group, all branch voltages are expressed in terms of branch currents and self/mutual impedances using Kirchoff's Voltage Law. From the resulting matrix equation, the branch currents can be easily determined by just taking the inverse of the square matrix which relates the branch voltages with the branch currents. The next step involves writing the branch voltages in terms of the phase voltages [2], which enables us to obtain the nodal admittance matrix of the transformer as explained below using a case study.

Let us model a Yyn0 distribution transformer shown in Figure 13.1 (Y/y stands for star connection and n denotes that the neutral of the secondary winding is brought out for grounding). Branches 1, 3 and 5 represent the three-phase primary winding.

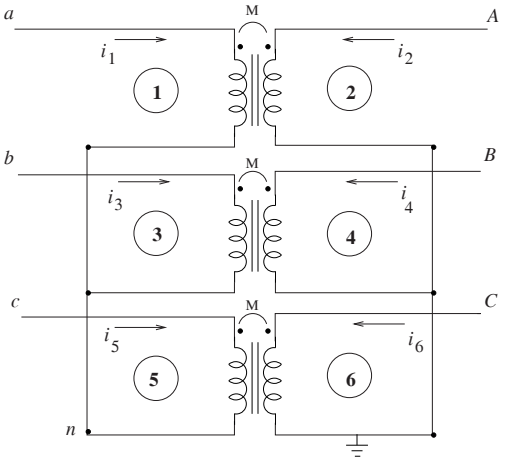

Figure 13.1 Yyn0 distribution transformer.

The branch voltages can be expressed using the following equation [2]:

$$\begin{bmatrix} v_1 \\ v_2 \\ v_3 \\ v_4 \\ v_5 \\ v_6 \end{bmatrix} = \begin{bmatrix} Z_1 & Z_m & 0 & 0 & 0 & 0 \\ Z_m & Z_2 & 0 & 0 & 0 & 0 \\ 0 & 0 & Z_1 & Z_m & 0 & 0 \\ 0 & 0 & Z_m & Z_2 & 0 & 0 \\ 0 & 0 & 0 & 0 & Z_1 & Z_m \\ 0 & 0 & 0 & 0 & Z_m & Z_2 \end{bmatrix} \begin{bmatrix} i_1 \\ i_2 \\ i_3 \\ i_4 \\ i_5 \\ i_6 \end{bmatrix} \tag{13.1}$$

where, Z_1 and Z_2 are the per-phase self impedances of the primary and secondary windings, respectively. Z_m is the mutual impedance between the primary and secondary windings. The branch currents can be determined from the above equation by taking the inverse of the square matrix [2],

$$\begin{bmatrix} i_1 \\ i_2 \\ i_3 \\ i_4 \\ i_5 \\ i_6 \end{bmatrix} = \frac{1}{Z_1 Z_2 - Z_m{}^2} \begin{bmatrix} Z_2 & -Z_m & 0 & 0 & 0 & 0 \\ -Z_m & Z_1 & 0 & 0 & 0 & 0 \\ 0 & 0 & Z_2 & -Z_m & 0 & 0 \\ 0 & 0 & -Z_m & Z_1 & 0 & 0 \\ 0 & 0 & 0 & 0 & Z_2 & -Z_m \\ 0 & 0 & 0 & 0 & -Z_m & Z_1 \end{bmatrix} \begin{bmatrix} v_1 \\ v_2 \\ v_3 \\ v_4 \\ v_5 \\ v_6 \end{bmatrix}. \tag{13.2}$$

The 6×6 matrix in the above equation is called *branch admittance matrix* ($\mathbf{Y_B}$). The neutral voltage of the ungrounded star winding with respect to ground is 1/3rd

of the summation of the phase voltages for an assumed balanced supply condition,

$$v_n = \frac{v_a + v_b + v_c}{3}. \tag{13.3}$$

Now, $v_1 = v_a - v_n = v_a - \frac{v_a + v_b + v_c}{3} = \frac{2}{3}v_a - \frac{1}{3}v_b - \frac{1}{3}v_c$.

The other branch voltages can be similarly expressed, giving

$$\begin{bmatrix} v_1 \\ v_2 \\ v_3 \\ v_4 \\ v_5 \\ v_6 \end{bmatrix} = \begin{bmatrix} 2/3 & -1/3 & -1/3 & 0 & 0 & 0 \\ 0 & 0 & 0 & 1 & 0 & 0 \\ -1/3 & 2/3 & -1/3 & 0 & 0 & 0 \\ 0 & 0 & 0 & 0 & 1 & 0 \\ -1/3 & -1/3 & 2/3 & 0 & 0 & 0 \\ 0 & 0 & 0 & 0 & 0 & 1 \end{bmatrix} \begin{bmatrix} v_a \\ v_b \\ v_c \\ v_A \\ v_B \\ v_C \end{bmatrix}. \tag{13.4}$$

Thus the branch voltages have been expressed in terms of the phase voltages using the 6×6 square matrix (say, **D**) on the right hand side in the above equation. The nodal admittance matrix Y is related to the branch admittance matrix ($\mathbf{Y_B}$) through the equation:

$$\mathbf{Y} = \mathbf{D}^{\mathrm{T}} \mathbf{Y_B} \mathbf{D}. \tag{13.5}$$

Substituting for $\mathbf{Y_B}$ and **D**, using Equations 13.2 and 13.4, respectively, we obtain

$$\mathbf{Y} = \frac{1}{Z_1 Z_2 - Z_m^{\,2}} \begin{bmatrix} 2Z_2/3 & -Z_2/3 & -Z_2/3 & -2Z_m/3 & Z_m/3 & Z_m/3 \\ -Z_2/3 & 2Z_2/3 & -Z_2/3 & Z_m/3 & -2Z_m/3 & Z_m/3 \\ -Z_2/3 & -Z_2/3 & 2Z_2/3 & Z_m/3 & Z_m/3 & -2Z_m/3 \\ -2Z_m/3 & Z_m/3 & Z_m/3 & Z_1 & 0 & 0 \\ Z_m/3 & -2Z_m/3 & Z_m/3 & 0 & Z_1 & 0 \\ Z_m/3 & Z_m/3 & -2Z_m/3 & 0 & 0 & Z_1 \end{bmatrix}.$$

Now, let Y_p be the short-circuit admittance of the transformer referred to its primary side. For a two-port network consisting of primary (1) and secondary (2) windings, we have on a per phase basis:

$$v_1 = Z_1 i_1 + Z_m i_2$$

$$v_2 = Z_m i_1 + Z_2 i_2.$$

The short-circuit admittance as seen from the primary side is the ratio of the primary current to the primary voltage when the secondary winding is short-

circuited. Hence, substituting V_2 as 0, we obtain the short circuit admittance as [2]

$$Y_p = \frac{Z_2}{Z_1 Z_2 - Z_m{}^2}. \tag{13.6}$$

Thus, the nodal admittance matrix for Yyn0 connection takes the final form as

$$\mathbf{Y} = \begin{bmatrix} 2Y_p/3 & -Y_p/3 & -Y_p/3 & -2Y_p/3 & Y_p/3 & Y_p/3 \\ -Y_p/3 & 2Y_p/3 & -Y_p/3 & Y_p/3 & -2Y_p/3 & Y_p/3 \\ -Y_p/3 & -Y_p/3 & 2Y_p/3 & Y_p/3 & Y_p/3 & -2Y_p/3 \\ -2Y_p/3 & Y_p/3 & Y_p/3 & Y_p & 0 & 0 \\ Y_p/3 & -2Y_p/3 & Y_p/3 & 0 & Y_p & 0 \\ Y_p/3 & Y_p/3 & -2Y_p/3 & 0 & 0 & Y_p \end{bmatrix}. \tag{13.7}$$

For a YNyn0 connection ($V_n = 0$ in Equation 13.3), the matrix simplifies to

$$\mathbf{Y} = \begin{bmatrix} Y_p & 0 & 0 & -Y_p & 0 & 0 \\ 0 & Y_p & 0 & 0 & -Y_p & 0 \\ 0 & 0 & Y_p & 0 & 0 & -Y_p \\ -Y_p & 0 & 0 & Y_p & 0 & 0 \\ 0 & -Y_p & 0 & 0 & Y_p & 0 \\ 0 & 0 & -Y_p & 0 & 0 & Y_p \end{bmatrix}. \tag{13.8}$$

For other standard connections, matrices are given in [2]. The influence of transformer connections on a distribution system is significant and has to be taken into account by a procedure such as the one outlined above.

The analysis assumed a nominal tap position; for an off-nominal tap ratio $1:a$ with the primary and secondary voltages expressed in per-unit, the matrix for the YNyn0 connection will be modified to

$$\mathbf{Y} = \begin{bmatrix} a^2Y_p & 0 & 0 & -aY_p & 0 & 0 \\ 0 & a^2Y_p & 0 & 0 & -aY_p & 0 \\ 0 & 0 & a^2Y_p & 0 & 0 & -aY_p \\ -aY_p & 0 & 0 & Y_p & 0 & 0 \\ 0 & -aY_p & 0 & 0 & Y_p & 0 \\ 0 & 0 & -aY_p & 0 & 0 & Y_p \end{bmatrix} \tag{13.9}$$

which is derived in the next subsection (Equation 13.17) using another procedure on per-phase basis. In the above analysis, the mutual couplings between the phases are ignored. These can however be considered by determining the mutual admittance through a procedure such as the one outlined in Section 13.10.4.

13.1.2 Regulating transformers

An important function of a transformer is to regulate the voltage at the point of its connection to the power system network. It may be needed to supply a desired voltage to a load by adjusting the tap position, thus countering voltage variations in the network due to various reasons. Tap changers can be used to control the flow of reactive and active powers as well through magnitude-regulating and phase-shifting transformers, respectively.

***Magnitude-regulating transformers*:** A regulating transformer, which can adjust the voltage magnitude, can be provided at one end of a transmission line to either increase or decrease the reactive power flowing through it. This feature is particularly useful when the reactive power flow between two systems connected via a long transmission line needs to be controlled.

Such a transformer can also be used to modify the magnitudes of reactive powers flowing through two parallel transmission lines. This useful feature of *magnitude-regulating transformers* is demonstrated through a numerical example below.

Example 13.1: Two identical transformers, each having the impedance of $j0.15$ p.u., are connected in parallel as shown in Figure 13.2. The only non-ideality considered is the leakage reactance for each transformer as shown in the figure (losses are neglected). The total load is $0.85+j0.6$ p.u. at 1.0 p.u. voltage. If a tap-changer operation changes the voltage of transformer-2 to $+1.05\angle 0^{o}$ p.u., calculate the change in the real and reactive powers associated with both transformers.

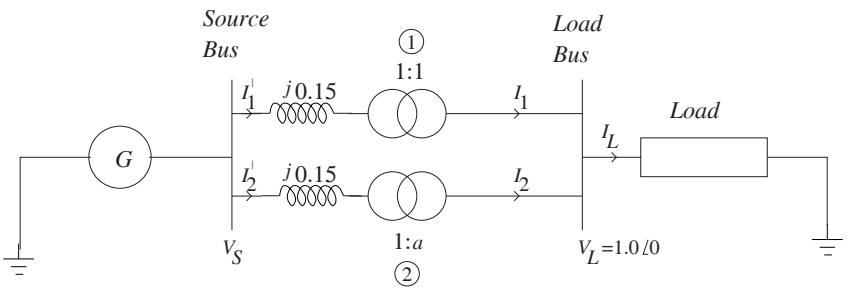

Figure 13.2 A system with a regulating transformer.

Solution: The current drawn by the load is

$$I_L = \left(\frac{S_L}{V_L}\right)^* = \left(\frac{0.85 + j0.6}{1.0}\right)^* = (0.85 - j0.6) \text{ p.u. and}$$

$$I_1 + I_2 = 0.85 - j0.6 . \tag{13.10}$$

Since transformer-1 is in the nominal tap position, the per-unit currents and voltages are equal on its both sides. Transformer-2 is in an off-nominal tap position; the per-unit value of voltage on its primary side will be $(1/a)$ times the per-unit secondary voltage (i.e., the load bus voltage), and its primary current will be a^* times the secondary current as evident from Equation 13.16 derived later while discussing the methodology for doing the power flow analysis with phase-shifting transformers (here the direction of both currents is the same, hence a^* times and not $-a^*$ times). The sending end voltage can be expressed as

$$V_S = 1\angle 0^\circ + j0.15 I_1 = \frac{1}{1.05}\angle 0^\circ + j0.15 \times 1.05 I_2 .$$

Simplifying the above equation we have,

$$j0.15 I_1 - j0.1575 I_2 = -0.0476 . \tag{13.11}$$

Solving Equations 13.10 and 13.11, we obtain

$$I_1 = 0.4354 - j0.1525$$
$$I_2 = 0.4146 - j0.4475.$$

Therefore the power flowing through each transformer can be calculated as

$$S_1 = V_L I_1^* = 0.4354 + j0.1525$$
$$S_2 = V_L I_2^* = 0.4146 + j0.4475.$$

Thus, it can be observed that an introduction of a small off-nominal voltage-magnitude setting has caused a substantial change in the reactive powers flowing through the two transformers, without a significant change in the real powers. When $a = 1$ (i.e., nominal setting), the powers associated with the two transformers can be similarly calculated as

$$S_1 = V_L I_1^* = 0.425 + j0.3$$
$$S_2 = V_L I_2^* = 0.425 + j0.3.$$

If the two transformers have identical ratings but unequal impedances, they (and the two lines) will not share equal voltamperes. In such a case, the voltamperes may nearly be equalized by suitably adjusting the voltage magnitude on one of the lines through a tap change operation.

***Phase-shifting transformers*:** Unlike the magnitude-regulating transformers, the phase shifting transformers control the flow of active power. They also improve the stability of the power system as explained later. They are deployed to control the real power flow between two systems connected via a long transmission line or for modifying the proportions of the powers shared by two transmission lines connected in parallel; the latter application is now demonstrated by an example.

Example 13.2: In the previous example, let us now assume that the transformers are of the phase-shifting type. The tapping of transformer-2 is now adjusted to obtain its voltage as $+1.0\angle 4^{o}$ p.u. (with the voltage of the other transformer remaining unchanged at $1.0\angle 0^{o}$ p.u.), calculate the change in the real and reactive powers associated with both transformers.

Solution: The current drawn by the load has been calculated in the previous example as

$$I_L = (0.85 - j0.6)\,\text{p.u.}$$

Using KCL and KVL we obtain

$$I_1 + I_2 = 0.85 - j0.6 \tag{13.12}$$

$$V_S = 1\angle 0^{\circ} + j0.15I_1 = \frac{1.0}{1.0\angle 4^{\circ}} + j0.15I_2 \times 1\angle -4^{\circ}. \tag{13.13}$$

Here $a = 4^0$ and the primary current of transformer-2 is a^* times its secondary current as explained earlier. Using the previous two equations, we have

$$I_1 = 0.1817 - j0.3148$$
$$I_2 = 0.6683 - j0.2852$$

and the loads shared by the two transformers are

$$S_1 = V_L I_1^{*} = (0.1817 + j0.3148)\,\text{p.u.}$$
$$S_2 = V_L I_2^{*} = (0.6683 + j0.2852)\,\text{p.u.}$$

Thus, it can be observed that a small change in the phase angle leads to an appreciable change in the real powers without affecting much the reactive components. The control of the active power flowing along a line in a complex interconnected network under steady-state conditions is useful for giving relief to overloaded lines. Thus, the application of phase-shifting transformers can lead to greater flexibility in operating power systems, which is particularly desirable in a deregulated market scenario. The design aspects of phase-shifting transformers are discussed in Section 11.4.

***Stability improvement using phase-shifting transformers*:** Phase-shifting transformers can also be handy in emergency conditions wherein the active power flowing through a line needs to be modulated for improving system stability.

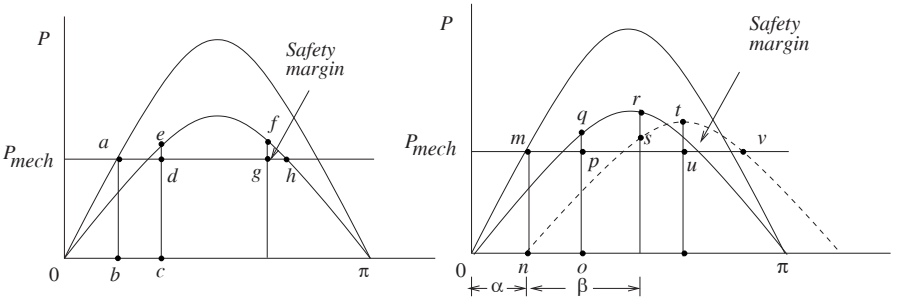

a) Without PST b) With PST

Figure 13.3 Safety margin for system stability [4].

The stability of power systems under fault conditions is usually checked using an *equal area criterion* [3]. Consider that a load (connected at bus 2) is supplied from a generator (connected to bus 1) through a set of two parallel transmission lines (between bus 1 and bus 2). The power flowing between the two busbars depends on the corresponding voltage magnitudes (V_1 and V_2), the effective reactance (X) of the two connecting lines considered together, and the power angle difference (δ) between the two voltages:

$$P = \frac{V_1 V_2}{X} \sin \delta \,. \tag{13.14}$$

If a three-phase fault occurs on one of the transmission lines close to the generator bus (1), the power transfer to load (at bus 2) during the fault period will be zero (segment *bc* in Figure 13.3a). P_{mech} represents the mechanical input to the generator. After the faulted line is tripped, a little more than 50% of the original power can be transmitted through the healthy line (assuming some overload capacity). The generator swings until point *f* at which the decelerating area *defgd* ($P_{mech} < P$) equals the accelerating area *abcda* ($P_{mech} > P$). The available safety margin corresponds to the area *fghf*. The application of a phase-shifting transformer, connected between the generator bus (*G*) and bus 1, can increase the safety margin by reducing the phase angle difference between the voltages at the busbars *G* and 2 [4]. While swinging, when the generator reaches the power angle $\alpha + \beta$, a phase-shift of α is introduced, which effectively results in shifting the electrical power output curve by α degrees toward the right side as shown in Figure 13.3b. Area *pqrstup* now balances the accelerating area *mnopm* (which is the same as *abcda*), giving an increased safety margin *tuvt* (> *fghf*). If X_T is the reactance of the phase-shifting transformer, the power flow equation under this condition becomes

$$P' = \frac{V_G V_2}{2X + X_T} \sin(\delta - \alpha) \tag{13.15}$$

(without PST: $P' = \dfrac{V_G V_2}{2X}\sin\delta$, with $V_G = V_1$).

Power flow with regulating transformers: The usual power flow algorithm needs to take into account the effect of a magnitude and/or phase change due to a regulating transformer by using a modified nodal admittance matrix. The matrix elements corresponding to the two nodes between which the transformer is connected are modified as elaborated below.

The equivalent circuit of a regulating transformer referred to its secondary winding is shown in Figure 13.4. The transformer is connected between nodes *m* and *n* of a power system network. Per-phase analysis is being done since the regulating transformers are usually deployed in transmission systems. The off-nominal tap ratio, *a*, may be real (e.g., 1.04) or imaginary (e.g. $e^{j\pi/60}$ or 3° shift). The complex powers associated with nodes *m* and *n* are

$$S_m = V_m I_m^*$$

$$S_n = aV_m I_n^* .$$

The ideal transformer in the dashed box is lossless resulting in

$$S_m = -S_n .$$

Hence, we obtain

$$I_m^* = -a\, I_n^* \quad \Rightarrow \quad I_m = -a^*\, I_n . \tag{13.16}$$

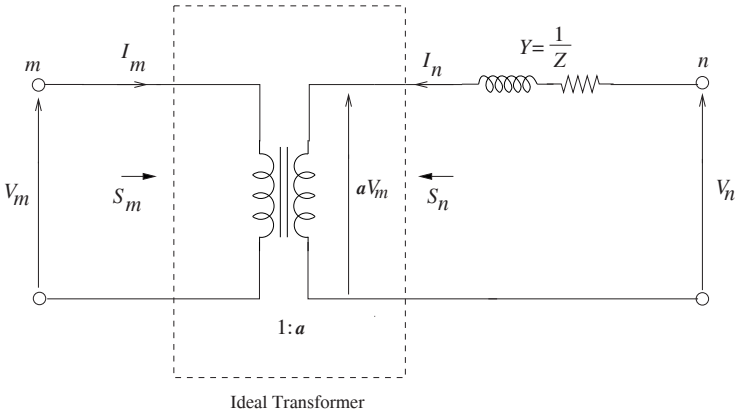

Figure 13.4 Regulating transformers.

Thus, the p.u. voltage on the secondary side is a times the corresponding voltage on the primary side. On the other hand, the p.u. current on the primary side is $-a^*$ times that of the secondary side (with the directions of the currents as shown in the figure). Now,

$$I_n = (V_n - aV_m)\ Y = (-aY)V_m + (Y)V_n .$$

Multiplying by $-a^*$ on both sides

$$-a^* I_n = I_m = (aa^*)YV_m - (a^*)YV_n .$$

The above two equations can be written in matrix notations as

$$\begin{bmatrix} Y_{mm} & Y_{mn} \\ Y_{nm} & Y_{nn} \end{bmatrix} \begin{bmatrix} V_m \\ V_n \end{bmatrix} = \begin{bmatrix} (aa^*)Y & -a^*Y \\ -aY & Y \end{bmatrix} \begin{bmatrix} V_m \\ V_n \end{bmatrix} = \begin{bmatrix} I_m \\ I_n \end{bmatrix}. \tag{13.17}$$

If the equivalent circuit is drawn with the admittance referred to the primary side ($=Y'$), it can be similarly proved that the admittance matrix is

$$\begin{bmatrix} Y_{mm} & Y_{mn} \\ Y_{nm} & Y_{nn} \end{bmatrix} = \begin{bmatrix} Y' & -\dfrac{Y'}{a} \\ -\dfrac{Y'}{a^*} & \dfrac{Y'}{aa^*} \end{bmatrix} .$$

The above matrix can be obtained by replacing Y in the admittance matrix in Equation 13.17 by $Y'/(aa^*)$ or $Y'/|a|^2$ because $Y' = Y\,|\,a\,|^2$ (when $a = 1$, $Y' = Y$ as expected since the p.u. values are same on both sides at the nominal tap).

If the turns ratio is complex (i.e., a phase-shift is involved with or without a magnitude change), the off-diagonal terms in the 2×2 admittance matrix in Equation 13.17 become unequal, and for such an asymmetrical matrix we cannot draw an equivalent pi-circuit model. When it is a real number (only magnitude change) the equivalent circuit as shown in Figure 13.5 can be drawn.

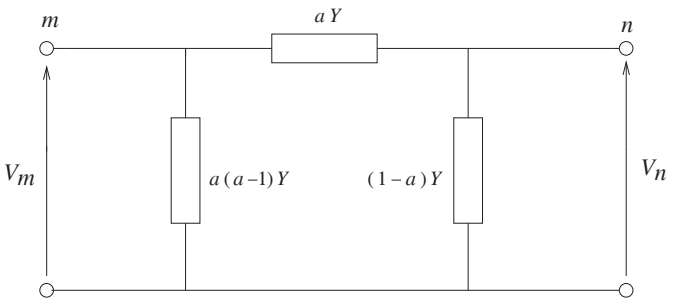

Figure 13.5 Equivalent pi-model.

Thus, putting a regulating transformer between two buses modifies the characteristics of the line between them. For doing power flow analysis, the original admittance matrix with $a = 1$ is modified (three of its four entries have to be changed). If it is a magnitude-regulating transformer, its symmetry is conserved. However, for a phase-shifting transformer, we obtain an asymmetric matrix.

The problem of not being able to get an equivalent circuit presentation for a phase-shifting transformer is overcome in [5] by a suitable manipulation of the corresponding equations so that a matrix with equal off-diagonal elements is obtained.

13.2 Harmonic Studies

Sources of harmonics: Sources producing harmonics can be divided into two categories from the point of view of transformers. External sources, mainly comprising power semiconductor devices and electric arc furnace loads, contribute to harmonics which can be detrimental to transformers. On the other hand, inherent characteristics of transformers such as magnetic nonlinearity and susceptibility of certain types of winding connections can also contribute to harmonic distortions. Overexcitation conditions leading to a core saturation condition can be detrimental to transformers as highlighted in Sections 2.4 and 5.11. Inrush current transients are additional sources of harmonics. The harmonic content in inrush currents varies with time, and peaks and nulls are usually observed for each harmonic [6].

For an ideal sine-wave voltage source, the flux set up in the core is also sinusoidal according to Equation 1.5 (with the frequency and the number of turns held constant). Due to nonlinear *B-H* characteristics, the magnetizing component of the current becomes peaky in nature, having a predominant third harmonic current as discussed in Section 2.3. The no-load current is symmetrical containing only odd harmonics. A magnetic imbalance can exist due to an asymmetry in firing angles in a connected rectifier load, in which case a DC component is present in the magnetizing current. In such a case, even harmonics are present in addition to odd harmonics. The other sources of DC magnetization are half-wave rectifier loads and unusual geomagnetically induced currents as explained in a later section.

The effects of various types of connections of windings on the no-load harmonic phenomenon have already been narrated in Section 2.8. The presence of a delta-connected winding is desirable for reducing harmonics in voltages and flux waveforms. A third harmonic current circulates inside the delta and the line currents become almost distortion-free. Moreover, the harmonic voltage of each phase is balanced by the corresponding voltage drop due to the circulating current making the line voltages free of third harmonic voltages. Thus, the transformers with a delta-connected winding can be helpful in mitigating harmonics on both

load and source sides.

Star-connected windings should be grounded to provide a path for third harmonic currents to make the voltage/flux waveforms sinusoidal. Their neutral connections should have a sufficient cross-sectional area that is suitable for the third harmonic currents. An ungrounded star connection can result in an undesirable situation in which the neutral voltage oscillates at three times the fundamental frequency (although the line voltages do not contain third harmonic components as the corresponding components in the phase voltages cancel each other).

Power electronic devices used in switched-mode power supply units, rectifiers/inverters for industrial applications and HVDC transmission systems, and reactive power compensating devices contribute to harmonic pollution of power systems. The devices are inherently nonlinear and are increasingly being used in various applications for better controllability, high efficiency and compactness.

***Effects of harmonics on transformers*:** Since the no-load current in a transformer is typically less than 1% of the rated current, the harmonics in it on account of nonlinear magnetic characteristics do not result in appreciable thermal stresses. However, there is always a possibility of resonant conditions between the system capacitance (due to connected cables and devices used for power factor improvement) and the transformer inductance at one of the harmonic frequencies while switching unloaded or lightly loaded transformers. Furthermore, under light load conditions with an increased system voltage, the harmonic distortions contributed by the transformers to the system can be appreciable.

The adverse effects of harmonics on transformers have been discussed in Chapter 11 while commenting on the special design aspects of industrial-duty rectifier transformers and HVDC converter transformers. Eddy and hysteresis losses in the core, as well as eddy losses in the windings, increase with harmonics. For any harmonic component, the eddy loss in the core and the winding conductors are proportional to the square of the product of the harmonic frequency and the corresponding amplitude of the flux density (see Equation 2.3 and Equation 4.94 respectively). The hysteresis loss varies linearly with frequency (Equation 2.4); its dependence on the flux density is more complicated, as discussed in Section 2.2.1. The increase in the eddy loss due to harmonics is more than that in the hysteresis loss. Effects of harmonics are generally more detrimental to the windings than the core.

Dielectric losses increase linearly with frequency and in the square proportion of the amplitude of the harmonic voltage (Equation 12.39); the losses are generally very small in comparison with those occurring in the active parts. Industrial duty rectifier transformers have to be often derated according to standards to increase their life expectancy; the corresponding derating factor is calculated based on amplitudes of harmonics expressed in percentage of the fundamental frequency. Harmonic-duty transformers have higher noise levels

compared to conventional transformers. Insulation stresses can be higher because of increased voltage peaks due to harmonic distortions.

Harmonics in currents directly affect equipment, like transformers, through which they flow. Harmonic voltage-drops in system impedances produce voltage distortions which affect power quality (which is essentially decided by the voltage quality). Thus, current harmonics indirectly affect power quality, and their effect is felt strongly by weak systems (a system is called weak when its effective source impedance as seen from a connected load is high). Strong systems are relatively less affected by current harmonics.

***Mitigation of harmonic effects*:** There are a number of ways by which harmonics can be eliminated or their effects can be mitigated. Lowering of flux density for the purpose is a costly proposition. Proper choice of winding connections and grounding practices is certainly a better option as highlighted earlier. An electromagnetic shield between the primary and secondary windings of each phase is able to attenuate high harmonic frequencies. Thinner and/or subdivided winding conductors are helpful in keeping their eddy loss under control at high frequencies.

External to transformers, shunt filters consisting of tuned capacitor and inductor elements are commonly used to bypass unwanted harmonics by providing a low impedance path to them. These are called *passive* filters. Today, *active* filters consisting of power electronic devices are being used for doing the same function more effectively although at a higher cost. Converters with a high pulse number should be used to eliminate lower order dominant harmonics.

***Harmonic modeling*:** As mentioned earlier, winding connections and grounding conditions have major influence on harmonics. These factors have to be taken into account in power system studies, such as power flow analysis, to obtain correct data on harmonic distortions. A simplified analysis on a per-phase basis can lead to inaccurate results. A three-phase two winding transformer, therefore, needs to be represented by a 6×6 admittance matrix, as discussed in the previous section, in the harmonic analysis of the power system. A comprehensive discussion on this aspect involving various types of connections and multiple windings is available in [7].

Another important issue is the modeling of magnetic characteristics. In harmonic studies, transformers can either be modeled as linear elements or through sophisticated algorithms that capture core nonlinearities. For practical purposes, the leakage inductance of windings is considered as constant and their resistance is taken as linear and frequency dependent; skin and proximity effects are accounted through a rigorous approach or by using empirical formulae. Modeling of frequency-dependent resistances by empirical means can be approximate. Frequency-dependent winding parameters can be accurately calculated using FEM as described in Section 13.10.3. Winding capacitances need not be modeled since at the harmonic frequencies of interest their effect is negligible.

An elaborate modeling effort is usually required for the core which consists

of a resistive component (R_c) and a reactive component (X_m), both of which are nonlinear elements. The resistive component is contributed by eddy and hysteresis losses out of which the latter are nonlinear whereas the former are linear, being resistance-limited, according to the discussion in Section 4.5.1 since *electrically* thin laminations form the core structure. An equivalent current source is commonly used to represent the total no-load current [8, 9, 10].

For a given harmonic frequency, under the no-load condition, the series impedance in the equivalent circuit of the transformer (Figure 1.5) is linear and the voltage drop across it can be calculated in the frequency domain. If the variation of the resistance and the leakage inductance with frequency is known, the harmonic analysis can account for it. The core loss resistance can be assumed as constant for simplifying the analysis in [8]. The magnetizing component of the no-load current (I_m) is a function of the induced voltage which in turn is decided by the voltage drop across the series impedance due to the total no-load current. Hence, the solution of this nonlinear problem can be determined by using an iterative technique in the time domain. The no-load current thus determined is then converted to the frequency domain using the discrete Fourier transformation (DFT) as explained in [8]. In [9], the value of the equivalent current source is determined using *finite difference method*. The measured value of the no-load power loss is used in [10] to first determine the nonlinear resistance R_c (and the lossy component of the no-load current) using an algorithm. The measured no-load current is then used to calculate the current flowing through the nonlinear inductance using magnetization characteristics in an iterative manner.

13.3 Ferroresonance

Ferroresonance is a resonant phenomenon involving an iron-core inductor and a capacitor. The capacitive and inductive reactances are equal with opposite signs during the resonance condition, and the current is limited by the circuit resistance. High currents and/or high voltages are produced if the resistance is not sufficient enough. Transformers are susceptible to the ferroresonance phenomenon as their magnetizing inductances are nonlinear since ferromagnetic materials are used for building their cores.

The phenomenon can be unpredictable and more likely to happen than a normal resonance condition (between linear inductor and capacitor elements) which occurs rarely unless the circuit is specifically tuned at a particular frequency. Since the inductive reactance varies due to the iron core, the possibility of the two reactances becoming equal increases considerably. A graphical solution of the nonlinear circuit is elaborated in [11] with a discussion on possible operating points. The phenomenon is characterized by a sudden jump or shift of the operating point from one stable state to another.

***Causes*:** The phenomenon generally occurs due to a series resonance between the connected/stray system capacitances and the magnetizing inductance of the

transformer. Series capacitors, used for compensation of voltage drops and/or reactive power control, can be problematic. Line-to-ground/line-to-line capacitances, underground cable capacitances, winding to ground capacitances of transformer windings, and bushing and circuit breaker capacitances may be involved in the phenomenon if they appear in series with the magnetizing inductance. Under normal operating conditions, these capacitances will not form a series resonant circuit; unbalanced conditions produced by the energization of only one or two phases can lead to a resonance condition. Ferroresonance is more likely to occur in such cases due to a nonlinear nature of the involved inductor, whose value is a function of the core saturation level, thus making it both voltage and frequency dependent. This gives the inductance a range of values. Hence, even if there may not be a perfect match between the two reactance values at a particular frequency, there are more possibilities that the values will come closer due to the variable nature of the inductor. The residual flux density in the core and the instant of switching also affect the phenomenon if it occurs at the time of switching-in of the transformer. A normal resonance between the linear L-C elements is a function of frequency only.

The phenomenon is more likely to happen with ungrounded primary connections as shown in Figure 13.6. The current through the only excited phase (*C*) completes its path through the line-to-ground (stray) capacitances of the incoming lines of the open phases, which may lead to ferroresonant overvoltages. A similar condition would occur if the ungrounded star-connected primary winding in the figure is replaced by a delta connected winding [12].

The grounding of the primary neutral helps in reducing the possibility of the occurrence of the phenomenon. While energizing an unloaded transformer with its primary neutral grounded, an abnormal condition arises if its two phases say, *B* and *C*, are only energized.

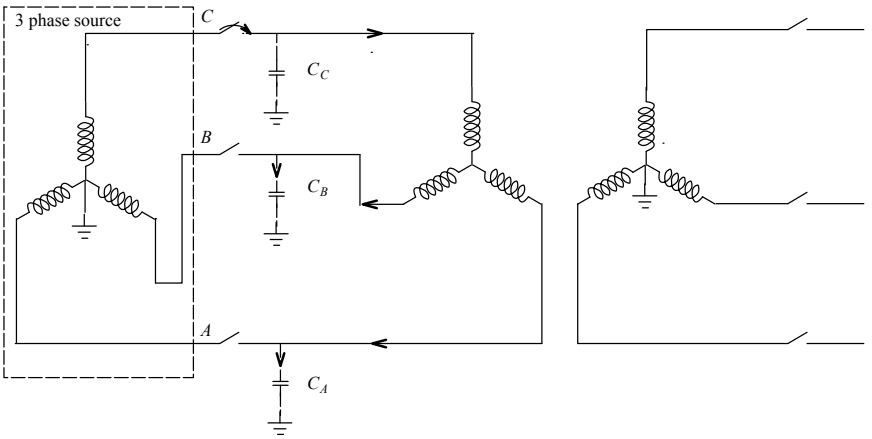

Figure 13.6 A ferroresonant condition.

If magnetic circuits of the three phases are decoupled (as in a bank of three single-phase units), the open phase (A) does not have any voltage across it. Ferroresonant overvoltages can appear in this case only if phase-to-phase capacitive couplings exist [12]. In the case of magnetically coupled phases (as in three-phase three-limb, three-phase five limb, and others), the voltage developed across the open phase allows a possibility of a series resonance between its magnetizing inductance and the line/cable capacitance C_A [13].

Thus the conditions that increase the possibility of ferroresonance can be summarized as:

- The transformer is unloaded or lightly loaded (no or little damping),
- A line or cable with a large shunt capacitance is connected to the transformer,
- An unbalanced condition is produced by single-phase connections and disconnections, fuse operations in one or two phases, delays in closing/opening of one or two phases, a break in a line/cable conductor or energization of one or two phases of star connected windings.

***Effects on transformers*:** The ferroresonance phenomenon causes the following adverse effects in transformers:

- Overheating of the core, windings, and structural parts due to overexcitation conditions leading to saturation of the magnetic circuit and the resulting spillover flux,
- Noise level increases considerably due to a substantial increase in the flux density of the core,
- A wide fluctuation in voltage magnitudes in the system can occur affecting domestic appliances and industrial systems; high levels of harmonic distortions and flickers in lighting loads are the common effects,
- Surge arresters can fail due to an excessive overheating due to overcurrents associated with ferroresonance conditions.

***Mitigation*:** Losses inherent in circuit elements provide damping effects. Most damping is, however, provided by a loaded secondary condition. An appreciable load on the secondary side can substantially mitigate the phenomenon. Hence, the system conditions with lightly-loaded or unloaded transformers supplied via highly capacitive cables/lines should be avoided. Underground cables have a relatively large ground capacitance value, which explains why the phenomenon is mostly found to occur involving them. Low-loss transformers increase the vulnerability. A damping resistor placed between the neutral of star-connected windings and ground, a smaller line/cable length between the circuit breaker and the transformer, and a core construction without magnetic coupling between phases reduce its possibility.

***Modeling*:** A deeper understanding and modeling of nonlinear magnetic circuit behavior is essential while analyzing ferroresonance phenomena. Different core

constructions are used in transformers as described in Chapter 2. The zero-sequence impedance of the transformer is influenced by the type of its magnetic topology. Ferroresonant conditions mostly involve unbalanced conditions and hence the zero-sequence characteristics play an important role in deciding the response of the transformer, necessitating a correct modeling approach for the core topology.

An analytical solution to the nonlinear ferroresonance problem has to be obtained in the time domain using a numerical integration technique. The accuracy of the solution mainly depends on how nonlinearities are considered. Determining nonlinear parameters of the model is the biggest challenge. As in the case of modeling for harmonic studies, a correct representation of the nonlinear elements (R_c and X_m) is an essential prerequisite. Although the hysteresis loss is inherently nonlinear, the core loss resistance (R_c) representing both eddy and hysteresis losses is modeled as a linear resistance to simplify the analysis. The analysis can be further simplified by a piecewise linear approach in which the nonlinear magnetization curve (with hysteresis neglected) is assumed to be consisting of two straight lines, one corresponding to the linear region and the other representing the saturation zone. However, such an oversimplification of the X_m parameter can lead to erroneous results.

The magnetic hysteresis phenomenon plays an important role in deciding the ferroresonance behavior of a transformer. Saturation, hysteresis behavior, and eddy current losses are the characteristics that need to be considered in any model for an accurate analysis of the phenomenon. Historically, the hysteresis curve was represented using rational fractions or power series approximations [14]. Two second-order rational functions with the coefficients determined from material parameters were typically used to represent hysteresis. However, such models do not consider the effects of minor loops and eddy currents. Preisach and Jiles-Atherton models are more popular these days since they yield results that reproduce more closely observed behavior.

The Preisach model is relatively more accurate in representations of minor loops [15]. In this model, a ferromagnetic material is represented as an assembly of particles, each of which could be in one of two saturation states (i.e., +Bs and –Bs). The overall behavior of a ferromagnetic material can be modeled by superposition of infinite number of rectangular type of hysteresis operators, each of which corresponds to a magnetic particle. Mathematically, it can be represented using a distribution function, known as a Preisach distribution function, which is a statistical representation of magnetic domains switching their states as the applied field changes. Using the model, the core can be represented by an equivalent hysteretic nonlinear inductor in ferroresonance studies [15]. Such an analytical model can then be used for each of the three phases in transient simulators; however, if the mutual couplings between the phases are not considered the accuracy may not be good enough. Hence, the FEM-based approach would be even better; the corresponding formulation is described briefly in Section 12.7.6.

13.4 Arc Furnace Applications

Arc furnaces are known to cause undesirable effects to the supply network. Networks with a low short-circuit ratio are severely affected; if the short-circuit power of the network at the point of connection is about 100 times the rated furnace power, the arc furnace operations do not cause appreciable system disturbances [16]. Unsymmetrical loads, poor power factors, harmonic distortions and voltage fluctuations are the main characteristics of systems with arc-furnace loads. Abrupt or periodic fluctuations of three-phase currents occur due to the random movement of the melting material, which are mostly unbalanced. The associated reactive and active power fluctuations result in excessive voltage variations. The frequency of the voltage flicker is typically 1 to 10 Hz [17]. Negative sequence currents can be substantial during the melt-down phase due to asymmetries between current magnitudes in positive and negative half cycles. Voltage fluctuations are higher during this phase as compared to several refining stages that follow. Nonlinear characteristics of the arc due to variations in its length and high levels of harmonic pollution (which may be contributed by even harmonics as well) worsen the network operating conditions [18].

Due to firings/extinctions of arcs at natural current zeros, AC arcs can be unstable. DC arcs are more stable than AC arcs and hence DC arc furnaces produce lower voltage fluctuations in the connected system; however the power electronic converters associated with them can cause a substantial harmonic pollution.

The operating point of an AC arc furnace can be determined using what is called a *circle diagram.* Let us consider a system, having R_S and X_S as resistance and reactance, respectively, feeding an arc furnace load with R_a as the arc resistance. The series circuit of R_S, X_S and R_a is fed by a constant voltage source V_S. The total circuit admittance is given by

$$Y = \frac{1}{Z} = \frac{1}{(R_s + R_a) + j(X_s)}. \tag{13.18}$$

It can be proved that the admittance Y traces a semicircle on R-X (or P-Q) plane as shown in Figure 13.7. When the arc resistance tends to infinity, the operating point is origin. When R_a plus R_S is zero, the other extreme condition, again the active power delivered to the furnace is zero (and the reactive power is maximum: point B). Since the apparent power is $S = P + jQ = V_s^2 / Z = V_s^2 Y$, for a constant system voltage V_S, S delivered by the source also traces a semicircle [18]. Further, the active power delivered by the source is

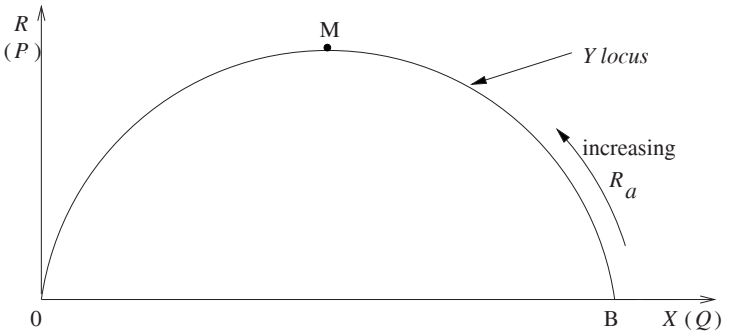

Figure 13.7 Circle diagram [18].

$$P = \frac{V_s^2 (R_s + R_a)}{(R_s + R_a)^2 + (X_s^2)}. \tag{13.19}$$

The maximum active power therefore is obtained when $R_s + R_a = X_s$, which gives $P_{\max} = V_s^2 / \left[2\left(R_s + R_a\right)\right]$ or $P_{\max} = V_s^2 / (2X_s)$. At this point (M in the figure) the reactive power Q equals $P_{\max}$, highlighting that the AC arc furnaces consume a considerable amount of reactive power. Also, it can be observed that when the operating point shifts on either side of M, a small change in the active power is accompanied by a large variation in the reactive power. Such variations in the reactive power cause considerable voltage fluctuations.

Connected equipment such as the furnace transformer need to bear the brunt of the onerous conditions associated with the arc furnace. The rating of the furnace transformer should be judiciously decided, based on a detailed study of its expected duty cycle. A load in excess of its rating may be permitted during the melt-down phase since it is followed by reduced loads during the refining stages, thus allowing to have a normal life expectancy. Its short-circuit impedance needs to be chosen after a trade-off between the short-circuit strength and the furnace's efficiency; a high impedance value reduces the impacts of the severe load conditions but reduces the short-circuit power available at the furnace, increasing its operating cycle time. The other design features of the furnace transformers are discussed in Chapter 11.

In order to minimize the effects of arc furnaces on the connected system, a suitable combination of static VAR compensators, capacitor banks, and tuned filters is used. These measures reduce voltage fluctuations, improve the power factor, and decrease harmonic distortions. It should be noted that installed capacitors can lead to severe disturbances due to a ferroresonance condition [19]. Furthermore, if vacuum circuit breakers are used, the problem of *virtual current chopping* (as discussed in Section 13.9), if any, needs to be tackled. Severity of such transient phenomena associated with arc furnace installations calls for a

detailed transient study using commercial software.

13.5 Geomagnetic Disturbances

Although the effects of solar-geomagnetic activities on power systems and equipment were known, the failure of a large generator step-up transformer in 1989 during a solar-geomagnetic disturbance created great concern and apprehension about the effects of geomagnetic currents on transformers. It is difficult to predict the magnitude and location of geomagnetic currents with a reasonable degree of accuracy [20]. Under normal excitation conditions, the exciting ampere-turns are less than 0.5% of the rated ampere-turns in large transformers. Hence, even a small amount of geomagnetically induced excitation current dramatically changes the field pattern and applies DC bias to the core flux. During solar-geomagnetic disturbances, DC currents flow in low resistance paths via neutrals of transformers and transmission lines as a result of earth surface potentials. Because of the peculiar location of the north magnetic pole with respect to the north geographic pole, the regions of North America with low earth conductivity generally have high values of earth surface potential, and the transformers in these regions are vulnerable to the geomagnetic effects [21]. The DC currents may saturate the core completely, increasing the drawn excitation current manifold, which is rich in even and odd harmonics. The stray losses in structural parts can increase to excessive values generating hot spots. Due to heavy field distortions, transposition schemes based on the assumption of axial field distribution become ineffective resulting in unacceptable circulating current values in parallel conductors. Since the reluctance to zero-sequence flux is higher in three-phase three-limb transformers, as discussed in Section 3.7, these transformers are less prone to geomagnetically induced saturation than single-phase three-limb or three-phase five-limb transformers [20].

The duration of a geomagnetic activity can be long, lasting for repeat periods of several hours [22], which may result in substantial durations of overheating in the affected transformer. Its impedance changes drastically due to field distortion and harmonics. As a result, the reactive power associated with it changes. This criterion is used in the monitoring program reported in [23] to protect transformers from the geomagnetic effects. Active and passive devices used for mitigating the effects are described in [21].

13.6 Sympathetic Inrush Phenomenon

A transformer already connected to a supply system can experience an unexpected saturation of its magnetic circuit during an inrush transient of an incoming transformer. This saturation, established by the asymmetrical voltage drop across the system resistance, caused by the DC component of the inrush current, is

responsible for the *sympathetic* or *reflected* inrush current of appreciable magnitude in the already connected transformers. This sympathetic inrush phenomenon may lead to maloperation of differential relays and may prolong temporary harmonic overvoltages. It may also lead to an increase in noise levels of the already connected transformers. The phenomenon is elaborated in Section 2.7.4; here the details of a case study will be given.

Electric and magnetic equivalent circuit-based methods [24] have been used in literature for simulating the phenomenon. However, the analysis can be performed more accurately using the coupled field-circuit approach elaborated in Chapter 12. A 31.5 MVA three-phase transformer model is used to investigate the sympathetic inrush phenomenon in [25]. A configuration consisting of two transformers connected in parallel is considered. The two transformers are modelled using FEM. The FEM field equations of the transformers are then solved simultaneously with the circuit equation of the connected network. A normal inrush current in a transformer decays usually within a few cycles but the sympathetic inrush current persists in the circuit for a relatively longer duration as evident from the comparison of waveforms in Figure 13.8 (a) and Figure 13.8 (b). The parameters affecting the magnitude and duration of the sympathetic inrush current such as resistances in the circuit, the switching-on angle, the residual flux density and load conditions, which have been discussed in Section 2.7.4, can be studied through coupled field-circuit simulations.

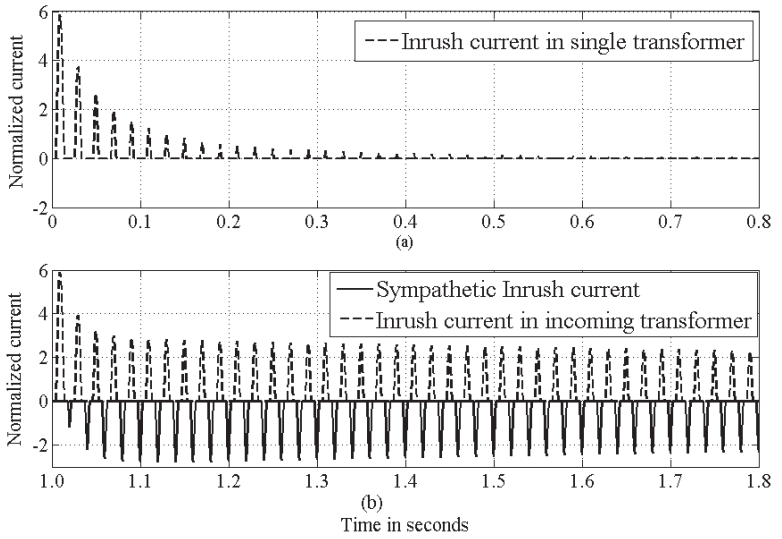

Figure 13.8 Sympathetic inrush phenomenon [25].

13.7 Internal Resonances Due to System Transients

A few failures of high voltage power transformers have been attributed to internal resonances as described in Chapter 7 (Section 7.8.1) while discussing part-winding resonance phenomena. Internal resonances are triggered when a perfect match occurs between a part or full winding natural frequency and the frequency of a sinusoidal component in the transient excitation or a high frequency component in a steeply rising overvoltage. Factory and field tests with oscillating overvoltages reveal that the transient voltages could be developed across a section of a winding (e.g., a tap section) significantly in excess of those during standard tests involving aperiodic excitations. An investigation is reported in [26] to determine the *frequency domain severity factor*, which is the ratio of the spectral density of the transient overvoltage to that of the standard impulse test waves. When the value of this factor is greater than one, the stresses imposed by the system transients would be greater than the standard tests. It is also demonstrated in the same paper that the standard chopped wave test represents correctly the stresses imposed by system transients for most of the reported cases.

Surge arresters are designed to protect transformers from aperiodic overvoltages. On the other hand, as highlighted also later in the discussion on fast transients associated with gas insulated switchgear, the arresters may not always be able to avoid internal overvoltages caused by oscillatory overvolatges; sometimes these excitations are well below their protective level [27]. In such cases only the losses occurring in the line and the transformer provide damping effects which may not be adequate. Switching operations and line faults at some distance from the transformer terminals are mainly responsible for oscillating overvoltages. Accurate simulations of transformers under such conditions at the design stage and greater cooperation between manufacturers and users are essential to avoid internal resonances.

In high rating transformers with large sizes, natural frequencies of windings tend to be lower, increasing the possibility of resonances. It has been reported in the literature [28] that a variety of oscillating overvoltages with frequencies ranging from a few tens of Hz to several kHz can strike the terminals of the transformers, making them more vulnerable to oscillatory transients. Simulation studies reported in [26] indicate that the dominant frequency of the transient voltages arriving at transformer terminals due to circuit breaker closing operations was in the 60–200 kHz range. When the distance between the circuit breaker and the transformer was reduced, the dominant frequency shifted above 200 kHz.

Internal winding resonances can be deceptive; the overvoltages generated by them may not be high enough to cause immediate breakdowns, but they can lead to sustained partial discharges with associated aging processes. In such cases, it is generally difficult to attribute eventual failures to resonance phenomena since they may not be triggered by a system transient or a lightning overvoltage.

It may not be possible to specify a new test that will represent non-standard overvoltages leading to internal resonances. Therefore, the possible influence of the cable length and the type of breaker design should be investigated at the design stage through user-manufacturer interactions.

Under resonance conditions, interturn voltage amplification factors (with respect to power frequency voltage distribution) of the order of 30 are possible. The voltage between two points in the affected winding section can become 2 to 3 times the transient voltage at the input terminal. Modeling aspects for simulations of internal overvoltages are discussed in Section 13.10.

13.8 Very Fast Transient Overvoltages

Switching operations in gas-insulated substations (GIS) can lead to very fast transient overvoltages (VFTO). Small dimensions of GIS result in fast travel times between refractions and reflections of the waves leading to frequencies in the MHz range. GIS systems are characterized by small damping due to their coaxial design and the absence of corona losses because of nearly homogenous field conditions [29]. Hence, the transformers directly connected to GIS systems are vulnerable; those connected via overhead lines to GIS are relieved of some amount of the stress due to damping effects provided by the lines. VFTOs with rise times and amplitudes of the order of 10 ns and 1.5 p.u., respectively, are typical [30]; 2.5 p.u. amplitude is possible in some unfavorable conditions. Such a steep fronted section of the wave is often followed by an oscillatory component having a frequency component in the MHz range. It not only leads to severe intersection/interturn voltages (due to highly nonlinear voltage distribution) but it may also result in a part-winding resonance condition [30].

Interturn voltages can reach high levels due to resonant conditions necessitating the computation of the transformer response using a turn-based model. A coarse disk-based model can be grossly incorrect. The basic multiconductor transmission line theory can be effectively used for evaluating the winding response as highlighted later in Section 13.10.2. The VFTO amplitude appearing across the transformer terminals is usually lower than the standard lightning impulse test level. However, the interturn voltages in the line-end winding section can reach about 25% of the applied VFTO, which makes interturn voltages much higher than those under the lightning impulse test condition [31]. Hence, the interturn insulation is generally decided by VFTO stresses.

13.9 Transients in Distribution Transformers

Internal resonances in power transformers have been discussed in Chapter 7 and Section 13.7. VFTO phenomena discussed in the previous section are also usually associated with medium or high rating transformers. This section deals

with fast transient phenomena in distribution transformers.

Vacuum circuit breakers (VCBs) are increasingly being deployed in distribution systems due to advances in the vacuum switching technology. Low maintenance costs and long life make them attractive. However, transient overvoltages can occur when small inductive currents are switched by VCBs. The chopping action before the natural current zero can lead to high overvoltages. The withstand voltage level is low due to short gaps in VCBs; a small transient recovery voltage is enough for re-ignitions which in turn lead to voltage transients in the connected network. These transients are usually rich in high frequency content. The phenomenon is more complex in three-phase circuits. A high frequency transient current from the first interrupting phase induces currents in the other phases through mutual couplings. The power frequency current with the superimposed high frequency current can also be chopped in the other phases; such a switching action is called *virtual current chopping* (VCC) [32, 33].

Switching transients involving magnetizing and inrush currents have been studied in [32, 33]. The magnetizing current being small is chopped immediately and the overvoltages are usually insignificant since the interrupted current is not high. Switching of inrush currents, although rare, can happen due to relay malfunctioning. Chopping of inrush current in one phase, at an instant when its magnitude is not low, leads to significant re-ignition overvoltages. Furthermore, the chopping of the currents in other phases, as explained earlier, results in corresponding voltage transients. An RC circuit connected on the load side of the VCB is effective in suppressing such transients.

Switching transients produced by VCBs can also result in internal overvoltages within the windings of distribution transformers. The transients are mainly influenced by the cable length separating the VCB from the transformer. Experimental investigations on distribution transformers subjected to the switching transients are reported in [34]. Transients in the form of multiple re-ignition pulse trains are typically stochastic in nature. Similar to the VFTO phenomena associated with GIS systems, interturn voltages can reach high values although the terminal voltages are not significant. RC snubber circuits are better suited as protection devices as compared to surge arresters since the overvoltage levels may be low enough so that the arresters do not operate but high enough to cause internal overvoltages which can be handled by the snubber circuits. High-loss transformers naturally are less susceptible because of the associated higher damping effects.

13.10 Low-, Mid-, and High-Frequency Models of Transformers

13.10.1 Time and frequency domain models

Time domain models: When the frequency content in transients is in the range of a few kHz, effects of the core cannot be neglected. Its nonlinear effects due to

saturation and hysteretic behavior need to be considered by using a time domain model. For simulations involving topological changes, for example, due to operation of circuit breakers, the time domain approach is well suited. The frequencies below which the core affects the response of the transformers can be easily gauged if SFRA (swept frequency response analysis) signatures are available under end-to-end (open-circuit) and end-to-end (short-circuit) conditions. Depending upon their rating, size and winding details, the two signatures will almost overlap after a certain frequency value in the kHz range [35]. This is the frequency value beyond which the core effect can be neglected. This transition frequency can be anywhere between 10 kHz and 100 kHz. Thus, the time domain models are generally essential for modeling low frequency transients up to a few kHz due to ferroresonance phenomena, overexcitation conditions and switching operations.

***Frequency domain models*:** Investigation of the high frequency behavior of the transformers is often done in the frequency domain since linearity can be assumed in the absence of the core effect at high frequencies. Beyond 100 kHz, frequency domain models are commonly used. The approach is particularly advantageous for taking into account harmonic losses in the core and windings. It should be noted that, for a linear and lossless model, both frequency and time domain approaches are equivalent [36].

Core nonlinearities can be approximately taken into consideration in the frequency domain analysis. For this, its material characteristics need to be *linearized* using a complex (elliptic) permeability based approach as explained in Chapter 4 and in Section 13.10.3 of this chapter in discussion of computation of frequency-dependent parameters. The response of a transformer to a variety of applied voltage waveforms can be determined by using the Fourier transform and the principle of superposition, provided that the core nonlinearities are either insignificant or they can be approximated by the complex permeability approach. Such time-harmonic computations for multiple frequency components in the excitation can be done by using commercial FEM software.

13.10.2 Analytical and numerical models

A transformer is a complex electromagnetic device containing a variety of materials, some of which exhibit nonlinear behavior. Skin and proximity effects, which become predominant at high frequencies, pose additional complexities. In order to take into account such subtle effects, the whole structure has to be modeled with minute details with a correct representation of material characteristics. For example, the response to VFTO transients requires a turn-based modeling approach. Such a model may become mathematically and/or computationally demanding. Therefore, some tradeoff is generally required between accuracy and simplicity of the model. Various models have been reported in the literature having varying degrees of complexity.

Deriving a black box model based on terminal measurements can be a

simple yet effective way for transient studies. In this approach an equivalent RLC network is obtained from the terminal measurements carried out in factory or field. The measured characteristics, e.g., an impedance or admittance curve in the frequency domain, can be faithfully represented by a model fine-tuned using a vector fitting technique [37]. Such a model can be used effectively by field engineers to analyze the transformer's response to system transients. However, an advanced and detailed model based on a distributed parameter approach is required for manufacturers to assess the impacts of standard and nonstandard overvoltages on windings at the design stage.

Analytical methods were used initially before the advent of numerical techniques. The main advantage of applying the analytical techniques is that it is possible to obtain closed-form formulae in which the effect of the influencing factors can be easily seen. However, these methods can be used for homogeneous winding structures only. A better approach is to have a numerical model in which the behavior is analyzed through a lumped circuit approach. Numerical values of the circuit parameters are used for the purpose. The accuracy of the model depends on how fine each section in the circuit is modeled. The highest frequency being investigated determines the corresponding shortest wavelength; the length of each section should be much smaller than this wavelength. For very high frequency transients, modeling of individual turns may become essential. The resistances, self and mutual inductances, and series and ground capacitances in the model are computed through analytical formulae or more accurately using FEM. Shunt conductances and mutual resistances are generally neglected. Once the circuit model is constructed, its analysis can be done using standard network analyzers; commercial circuit simulators can also be used for the purpose.

In recent times, transmission line-based models have also been used to study transients in transformers. Any analysis using lumped parameters has a shortcoming in that it may not be accurate enough for very high frequency transients (having very short rise and fall times). In such cases, wavelengths become comparable to winding dimensions and the response to such transients can be accurately analyzed using a model that takes into account traveling wave aspects. Depending upon the highest frequency of interest, the basic entity in the model can be a turn or a disk or a section. Each entity is then modeled as a distributed line. Single transmission line (STL) and multiconductor transmission line (MTL) models have been used for the purpose. In the former model, a single line represents the winding under investigation. For very high frequencies, the model is not as good as the MTL model which, however, requires more computational efforts. A combination of STL and MTL models can also be used in which the voltages calculated at the ends of a disk/section using the STL model are given as input to the MTL model for determining interturn voltages. Such a hybrid approach effectively reduces the size of the system of equations to be solved for determining the response in the frequency domain. The frequency domain analysis is simpler and hence preferred to obtain

quick results. However, the time domain approach may be required for certain purposes; the approach has been found to be better than the lumped circuit analysis for analyzing VFTO transients [36]. A good treatise on both STL and MTL approaches can be found in [38]. The basics of the MTL theory are given in [39].

When a circuit-model is used, one has already lost the details of the field-behavior. A field solution usually demands the corresponding variables to be functions of three-dimensional space as well as time, and hence it is computationally cumbersome. The transmission line approach is a bridge between the circuit approach and the field approach. The transmission line model has voltages and currents as functions of both distance (one dimensional space) and time. Further, the model employs distributed parameters; capacitors, inductors, and resistors are distributed throughout the line, and hence it tries to capture the field behaviour.

13.10.3 Computation of frequency-dependent parameters

R, L and C parameters can be calculated easily by various formulae if frequency-dependent effects are neglected. DC resistances of windings are calculated based on conductor dimensions. Formulae given in Section 7.4 are commonly used to calculate the self and mutual inductances of winding sections, whereas interturn, interdisk and interwinding capacitances can be calculated by using the formulae given in Sections 7.2 and 7.3. The formulae for the inductances are approximate and do not consider leakage, skin and proximity effects.

High frequency phenomena in transformers are often investigated these days, e.g., studies involving power system transients. The design of high frequency transformers used for power electronic applications also requires an understanding of the effects of high frequencies on their performance parameters. Furthermore, such investigations are useful in SFRA diagnostics. For determining the high frequency response using lumped parameter models, an accurate calculation of various equivalent circuit parameters with the inclusion of frequency-dependent effects is necessary. Thus, the damping associated with the eddy/hysteresis losses in core laminations and skin/proximity effects in winding conductors are taken into account. Constant values of self and mutual inductances were quite commonly used earlier although it was well known that they are dependent on frequency. While estimating impulse voltage distributions within transformer windings, the approximation did not matter much; sufficiently accurate results could be obtained. The calculations were usually done using inductances and capacitances. However, due to the failures of a few transformers due to internal resonances and the realization that the understanding of the resonance characteristics of the transformer windings is of paramount importance, recent studies have been incorporating frequency-dependent winding resistances and self/mutual inductances in the simulations. For understanding and determining the frequency response of transformer windings as a part of SFRA diagnostics, the

frequency dependence has to be considered for better accuracy.

The self and mutual inductances decrease as frequency increases; the rate of decrease is higher at low frequencies. This behavior is observed for both air core and iron core inductances [40]. Needless to say, the iron core inductances are higher than the air core ones in all frequency ranges; the difference between them is larger at low frequencies. The self inductances of winding sections and mutual inductances between them form the diagonal and off-diagonal elements of the corresponding inductance matrix, respectively. Equation 3.36 can be rewritten in terms of the inductances as

$$L_{ij} = L_{ii} + L_{jj} - 2M_{ij} \tag{13.20}$$

where L_{ii} and L_{jj} are the self inductances of i^{th} and j^{th} sections, respectively. L_{ij} is the leakage inductance and M_{ij} is the mutual inductance between the two sections. As already described in Section 3.2, it is not advisable to calculate the leakage inductance using the self and mutual inductances due to the error involved in subtracting one large number from another large one (the leakage inductance is very small compared to the self and mutual inductances). Hence, the leakage inductances are calculated independently of the self and mutual inductances. FEM can be used to determine the self and mutual inductances separately as elaborated in Section 12.7.1. However, the procedures described there are based on magnetostatic calculations, the frequency-dependent skin and proximity effects are not considered. Time-harmonic FEM simulations are required for the purpose.

Let us consider two coils 1 and 2. If the material conductivity is not defined, the induced voltage in the open-circuited coil 2 due to a current flowing in coil 1 is just a measure of the mutual inductance between them. With material conductivity defined, there would be an eddy loss in coil 2 on account of alternating flux produced by the coil 1 current; the loss is a measure of the mutual resistance between the two coils, and the induced voltage corresponds to the mutual impedance between them. The values of mutual resistance (R_{ij}) and mutual inductance (M_{ij}) increase with a reduction in spacing between the coils. Presence of an iron core not only increases the mutual inductance but it also increases the mutual resistance, when compared to the air core case. The mutual inductance has to be obviously higher due to a high permeability value of the iron core; the mutual resistance is also higher due to a higher induced voltage leading to a greater eddy loss in the coil 2 conductor.

The values of resistances (self and mutual) increase with frequency; the self resistance (representing the loss in a coil due to its current with all other coils open-circuited) increases due to an increased skin effect as the frequency goes up, whereas the mutual resistance increases as the induced voltage (and the eddy loss) in the other coil increases with the frequency.

The winding resistances and inductances vary with frequency due to skin and proximity effects as mentioned earlier. The frequency-dependent skin and proximity effects can be taken into account by relatively simple and reasonably

accurate formulae for determining analytically the frequency response of windings as illustrated in [41].

It is difficult to model the core, being laminated and made from a magnetic material. Various models and algorithms have been presented in the literature to model it. The principle of duality between the magnetic and electric circuits can be effectively used to model the low frequency response. The model proposed in [42] uses the duality principle by which an equivalent circuit is derived in terms of frequency-dependent complex reluctances.

The analytical determination of the winding losses due to skin/proximity effects and the core loss is approximate. This is because of the anisotropic and geometrically complex nature of the core. Hence, there is a growing tendency among researchers to use FEM for computing winding parameters. Interturn, interwinding and winding-to-ground capacitances are calculated by electrostatic FEM analysis. The capacitances are usually assumed to be frequency-independent. In the field approach, resistances and self/mutual inductances of windings can be computed with skin and proximity effects automatically considered. For these computations, core nonlinearities can be neglected; multiple time-harmonic FEM solutions are obtained with the frequency swept in the range of interest. The procedure is as follows.

A turn-based geometry is created in an FEM program. The governing equation for determining the self and mutual impedances is $\{V\} = [Z]\{I\}$, where $\{V\}$ and $\{I\}$ are the column vectors of voltages and currents, and $[Z]$ is the $n \times n$ impedance matrix, where n is the number of turns in the model. In order to compute the elements of the first column of the impedance matrix, i.e., Z_{11}, Z_{21},....., Z_{n1}, only the first turn is energized with a current magnitude of 1 ampere and the induced voltage in it and in the other turns is determined from the FEM solution. These computed induced voltages, i.e., V_1, V_2,....,V_n are then numerically equal to Z_{11}, Z_{21},....., Z_{n1} since $Z_{ji} = V_j / I_i$, where $i = 1$ and $j = 1, 2, ..., n$. Similarly, the next column of the impedance matrix is determined by energising only the 2nd turn with the same value of current, and so on to obtain all the entries of the impedance matrix. The solution is sought for a complete sweep of frequency; i.e., at each frequency we obtain a separate impedance matrix. These impedance matrices involve complex numbers; the real and imaginary parts of each entry represent the resistance and the inductive reactance, respectively. The matrices at the required frequency steps are then plugged into a standard network solver to obtain the response of the winding for a desired frequency range.

The parameters thus computed can be then used in the lumped circuit model (with a suitable number of sections) that can be connected to an external circuit/source for determining the transformer response at high frequencies. This model is good enough when the frequencies of interest are high and the core has a negligible effect or when the winding connections are such that its effect is eliminated (e.g., a short-circuited winding around it).

For an investigation requiring an accurate representation of core effects, a hybrid model can be used. The high frequency response, derived from the parameters determined from the time-harmonic simulations, can be used to find an equivalent RLC network consisting of a few elements through a vector fitting technique [37]. The equivalent circuit representing the transformer's behavior over a wide high-frequency range is then combined with a model which is valid at low frequencies taking into account the core nonlinearities.

Alternatively, in a more sophisticated approach, time-harmonic FEM simulations are used to derive the entire frequency response by representing the core and winding behavior using appropriately determined complex permeability values as described below.

Frequency-dependent core properties: Let us first see how to take into account the frequency-dependent core behavior. Generally, the effect of the core is neglected beyond 10 kHz; however the core has been found to influence the frequency response up to 100 kHz [43].

It is often convenient to include the eddy current loss in terms of complex or elliptical permeability as discussed in Section 4.3. This representation is particularly useful for the high frequency modeling of the core in diagnostic studies. When the eddy loss is also considered in addition to the hysteresis loss, the phase angle between voltage and current departs further away from 90^0 towards zero. A major problem arises due to the eddy current loss inclusion: B and H vary inside the laminations; these are generally greater near the surfaces of the laminations and smaller in the interior parts. One can overcome the difficulty by defining H at the surfaces ($=H_0$) and B by its average over the entire lamination cross section [44].

Figure 4.5 in Section 4.5 shows a rectangular conductor block of a conductor; it can as well represent a lamination sheet of thickness $2b$, placed in an alternating field along the y direction. The solution for the field problem, governed by Equation 4.79, is given by the expression in Equation 4.83:

$$H_y = \frac{H_0\left(e^{\gamma z} + e^{-\gamma z}\right)}{e^{\gamma b} + e^{-\gamma b}} = \frac{H_0}{1 + e^{-2\gamma b}}\left(e^{\gamma(z-b)} + e^{-\gamma(z+b)}\right) \tag{13.21}$$

The average magnetic flux density in the y-direction, B_y, can be determined in terms of the total magnetic flux passing through the cross section ($2b\,\Delta x$) as

$$B_{y(avg)} = \frac{\phi}{2b\,\Delta x} = \frac{\int_{-b}^{b} \mu_0 \mu_{ry} H_y \,\Delta x\, dz}{2b\,\Delta x}$$

$$= \frac{\mu_0 \mu_{ry} H_0 (1 - e^{-2\gamma b})}{\gamma b (1 + e^{-2\gamma b})} = \frac{\mu_0 \mu_{ry} H_0 (e^{+\gamma b} - e^{-\gamma b})}{\gamma b (e^{+\gamma b} + e^{-\gamma b})}$$

$$\therefore B_{y(avg)} = H_0 \frac{\mu_0 \mu_{ry}}{\gamma b} \tanh(\gamma b) . \tag{13.22}$$

Therefore, the effective complex permeability is [44]

$$\mu_y^{eff} = \mu' - j\mu'' = \frac{B_{y(avg)}}{H_0} = \mu_y \frac{\tanh(\gamma b)}{\gamma b} . \tag{13.23}$$

The negative sign of the imaginary component indicates that the phasor $\hat{B}$ lags the phasor $\hat{H}$ by the hysteresis angle. Thus, we have determined the effective complex permeability which takes into account the eddy current loss. The hysteresis loss can also be considered by using Equations 4.66 and 4.67; the expression of γ has to be changed from $(1+j)/\delta$ to $(\alpha + j\beta)/\delta$ for the purpose. The constants, α and β, are calculated using Equation 4.67 after determining θ from Equation 4.62. For this, we need to experimentally determine the *B*-*H* loop and extract the fundamental components of *B* and *H* from the measured data.

The effective permeability in the above equation can be split into real and imaginary parts using trigonometric identities (as done while deriving Equation 4.89) to give,

$$\mu' = \frac{\mu_0 \mu_r}{2\chi} \frac{\sinh 2\chi + \sin 2\chi}{\cosh 2\chi + \cos \chi} \tag{13.24}$$

$$\mu'' = \frac{\mu_0 \mu_r}{2\chi} \frac{\sinh 2\chi - \sin 2\chi}{\cosh 2\chi + \cos \chi} \tag{13.25}$$

where $\chi = b/\delta$ with δ given by Equation 4.38 and μ_r is the relative permeability at zero frequency. The frequency-dependent real and imaginary parts of the complex permeability are shown in Figure 13.9 for typical values of material parameters $\left(\mu_r = 650,\ \sigma = 5\times10^6\ S/m,\ b = 0.175\,mm\right)$.

The nature of the variation of the two components can be understood from their expressions; unlike the hyperbolic functions, the sine and cosine functions are bound within ± 1. Hence, both the components become almost equal after a certain value of χ.

Now we will see how the complex permeability representation can be used effectively in FEM-based computations. The rolling direction in the plane of lamination (*x*-*y*) is the *y* direction in this discussion.

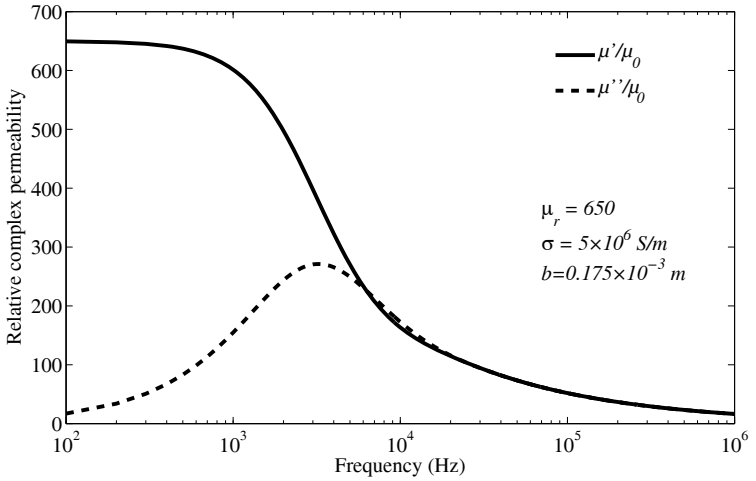

Figure 13.9 Frequency dependence of complex permeability.

For a stack of laminations, some amount of the magnetic area is lost due to the nonmagnetic insulation coating on them; the permeability values in three directions should be adjusted using Expressions 5.35 (across the laminations) and 5.36 (along the surface of the laminations) which make use of the stacking factor k (the ratio of the bare thickness to the insulated thickness of a lamination). Hence, we obtain the effective complex permeability values along the two directions in the surface of the lamination from Equation 13.23 and Equation 5.36 as [43]

$$\hat{\mu}_x^{eff} = \mu_x' - j\mu_x'' = k\mu_0\mu_{rx}\frac{\tanh(\gamma_x b)}{\gamma_x b} \tag{13.26}$$

with $\gamma_x = (1+j)\times\frac{1}{\delta_x}$ and $\delta_x = \frac{1}{\sqrt{\pi f \mu_0 \mu_{rx} \sigma}}$, and

$$\hat{\mu}_y^{eff} = \mu_y' - j\mu_y'' = k\mu_0\mu_{ry}\frac{\tanh(\gamma_y b)}{\gamma_y b} \tag{13.27}$$

with $\gamma_y = (1+j)\times\frac{1}{\delta_y}$ and $\delta_y = \frac{1}{\sqrt{\pi f \mu_0 \mu_{ry} \sigma}}$.

The effective permeability in the z direction (perpendicular to the plane of laminations) is given by Equation 5.35,

$$\mu_z^{eff} = \mu_0 \frac{1}{1-k} . \tag{13.28}$$

It should be noted that the effective permeability in the z direction is not a complex value. Thus, we have obtained the permeability tensor (refer to Equation 12.53) with three diagonal elements as given by the above three equations. The off-diagonal elements are zero since it is assumed that the coordinate axes are aligned along the crystal axes.

The permeability tensor can be used for representing the magnetic characteristics of the core portions without irregularities such as joints between limbs and yokes. At the joints, an overall effective permeability needs to be determined by 2-D FEM [43, 45]. For finding the effective permeability of the joints shown in Figure 2.4, magnetic field intensity of 1 A/m is specified in terms of a spatial derivative of the complex magnetic vector potential on the horizontal boundaries. On the vertical boundaries a homogeneous Neumann boundary condition is specified for the potential. The averaged magnetic flux density in the horizontal direction $\left(\hat{B}_x\right)$, derived from the obtained solution $\left(\hat{A}_z\right)$ and Equation 12.81, gives directly the value of the effective complex permeability of the joint region. The value is lower than the rest of the core due to the presence of the gaps [43]. This formulation serves the purpose of determining the response of transformers in the harmonic domain (e.g., SFRA). However, the model is linear and it may not be good enough for designing joints or improving their performance; inclusion of saturation and hysteresis effects is of paramount importance as discussed in Section 12.7.6.

Similarly, with reference to Figure 5.31, the effective conductivity of the laminated core can be defined using the tensor notation; i.e., the bulk material conductivity is multiplied by the stacking factor k to get the effective conductivities in the x and y directions, and the conductivity in the z direction is taken as zero; these three values give the diagonal elements of the conductivity tensor (with its off-diagonal elements as zero).

Frequency-dependent winding conductor properties: Frequency-dependent skin and proximity effects in windings can be handled in a similar way. The effects have been discussed in Section 12.7.5. At frequencies beyond a few kHz, these effects become dominant and the flux concentrates at the conductor surface (the skin effect) and its distribution gets skewed as well (the proximity effect). Effectively, this represents a diamagnetic effect (see Section 12.2.7), in which the flux is repelled from the volume of winding conductors making the relative permeability less than 1 (the conductor material, being either Cu or Al, is non-magnetic having relative permeability of 1 in the absence of the high frequency effects). The losses due to the skin and the proximity effects can be considered by using the complex permeability based approach. The diamagnetic effect makes the real part of the complex permeability less than 1, whereas its imaginary part

represents the losses. The effective complex permeability tensor of a winding conductor can be found by subjecting it to a magnetic field in all three directions [45, 46]. The diamagnetic effects do not contribute significantly at lower frequencies. As the frequency increases to a value at which the core effect becomes negligible (typically for $f > 10^6$ Hz), the winding inductance approaches its air core value and the diamagnetic effects become significant. However, if there exists a short-circuited winding during an investigative test such that there is negligible flux in the core, the diamagnetic effects influence the winding inductance even at lower frequencies [47].

The frequency-dependent core and conductor effects, thus incorporated through the corresponding effective complex permeability tensors, can then be integrated into a large-scale model [43, 47] to determine the frequency response. The core losses and the winding losses due to the skin/proximity effects are taken into account through the complex permeability representation. Furthermore, the complex permeability approach makes it possible to represent the core material as having linear characteristics (with hysteresis considered as discussed earlier). Thus, the problem can be solved through a quasi-static (time-harmonic) formulation as described in Section 12.5.2. The frequency responses of transformers thus calculated can then be compared with measured responses [45].

Frequency-dependent dielectric properties: An imperfect dielectric can be represented by a parallel circuit model consisting of a capacitor and a resistor. As explained in Section 12.2.7, by using the complex permittivity representation $\left(\hat{\varepsilon} = \varepsilon' - j\varepsilon''\right)$, the real and imaginary parts of the corresponding complex admittance ($G + j\omega C$) can be derived. The conductance G is a function of the imaginary component ε'' of the complex permittivity and the susceptance $j\omega C$ depends on the real component ε'; these two components themselves are frequency-dependent. Frequency response measurements on oil, paper and pressboard samples [48, 49] can be used in conjunction with geometrical data to calculate various admittances representing the imperfect sectional series and shunt capacitances of the equivalent ladder network of the transformer [50]. Such a model can then be used to investigate the effect of moisture, temperature and aging on the frequency response [45].

13.10.4 Transient simulations

In order to analyze a wide range of electromagnetic transient phenomena associated with transformers, a wideband, nonlinear and lossy model is needed. Manufacturers can develop such a detailed model based on the design data. The users of transformers, however, often require a simplified or reduced order model having good accuracy.

Depending upon the types of system studies, transformers have to be modeled to include many of the following parameters/details: leakage and mutual inductances, frequency-dependent skin and proximity effects, nonlinear

characteristics of the core including hysteresis, interturn and interwinding capacitances, and topological information of the core and windings. Providing accurate transformer models that are suitable for a wide variety of transient studies has always been a challenge; over the years the models have been improved and refined.

A review of transformer models for simulation of transient phenomena, such as ferroresonances, harmonic interactions and switching operations, using the electromagnetic transient program (EMTP), is given in [51]. These transients can be typically classified as low- and mid-frequency transients with frequencies usually lower than the first resonant frequency of windings, which occurs at several kilohertz. For a multi-phase multi-winding transformer, governing equations can be written using a branch impedance or admittance matrix.

Any transformer with multiple windings (n) can be represented by a matrix equation, viz. $\{V\} = [Z]\{I\}$, wherein the elements $[Z]$ can be determined using no-load excitations. If winding j is energized and all other windings are open-circuited, the impedances of j^{th} column are given as $Z_{ij} = V_i / I_j$, where $i = 1, 2, ...n$. The impedance matrix elements can also be determined using FEM simulations as demonstrated in [52]. These impedances should not be confused with the short-circuit leakage impedances between the windings, which are measured with one winding excited and another winding short-circuited, and with all other windings open-circuited.

The admittance matrix is governed by the equation $\{I\} = [Y]\{V\}$, whose elements can be determined by doing measurements with unconventional short-circuit tests or through the corresponding FEM simulations. With winding i energized and other windings short-circuited, the admittances of i^{th} column are given as $Y_{ji} = I_j / V_i$, where $j = 1, 2, ...n$.

Such matrix representations are linear in nature, and hence nonlinear circuit equivalents of the core are interfaced to them. Such models, however, cannot correctly take into account different core designs. Topology-based models are well-suited for the purpose since these are derived based on the core construction using the principle of duality.

High frequency simulations can be performed using transient programs if the frequency characteristics of transformer admittances are obtained either through a detailed physical model or through measurements [53]. Rational approximations in the form of an RLC network can be derived using the vector fitting technique [37] as mentioned previously.

13.10.5 Interfacing transformer and network models

There are two distinct approaches for analyzing transformers subjected to system transients. In the first approach, network simulators are used with an equivalent circuit representing the transformer under investigation. A few of

these approaches have been discussed previously; the accuracy depends on whether the circuit model can reproduce the field conditions in the transformer. Some of the intricate phenomena discussed in this text (e.g., sympathetic inrush transients, short-circuit forces in split-winding transformers and the half-turn effect) require the field modeling approach for achieving a desired level of accuracy. The transformer is modeled in the field domain and the external network through circuit equations. The two sets of equations are then strongly coupled by an approach which is discussed in Section 12.6.1. The complete set of equations is solved at each time step. Researchers usually develop such coupled field-circuit codes for solving complex problems. However, practicing engineers find it much easier to use commercial software for the purpose.

Numerical techniques, such as FEM, can take into account geometrical complexities, material nonlinearities, anisotropic properties, distributed effects of fields, and heterogeneous materials existing inside the transformer as discussed in Chapter 12. Network simulators, on the other hand, have models for a variety of power system components such as transmission lines and circuit breakers. Hence, the commercial FEM and network solvers can be coupled through a set of variables.

A method for coupling an electromagnetic transient program with an FEM code is described in [54]. The field model provides a set of variables in the form of an inductance matrix to the transient program. This is a weakly-coupled formulation as there is lag of one time-step in the two sets of simulations; the error on account of this one time-step delay can be reduced by having smaller time-steps. The extra computational burden due to FEM computations (as compared to that with a network solver alone) may be justified if the gain in accuracy is significant. A similar approach is presented in [55]; for energization studies of large transformers the EMTP's capability of modeling large networks is complemented by 3-D representation of nonlinear core properties in a commercial FEM program.

References

1. Lapworth, J. A., Jarman, P. N., and Breckenridge, T. Transformer internal overvoltages caused by remote energization, *CIGRE 2006,* Paper A2-305.
2. Chen, T., Chen, M., Inoue, T., Kotas, P., and Chebli, E. A. Three-phase cogenerator and transformer models for distribution system analysis, *IEEE Transactions on Power Delivery*, Vol. 6, No. 4, October 1991, pp.1671–1681.
3. Kundur, P. *Power system stability and control,* Mc-Graw Hill, New York, 1993.
4. O'Kelly, D. and Musgrave, G.. Improvement of power-system transient stability by phase-shift insertion, *Proceedings IEE,* Vol. 120, No. 2, February 1973, pp. 247–252.

5. Martinez-Velasco, J. A. Equivalent circuit of transformers with control of voltage and phase angle, *Electric Power Systems Research,* Vol. 81, 2011, pp. 1349–1356.
6. Arrillaga, J. and Watson, N. R. *Power system harmonics,* Second Edition, John Wiley & Sons, 2003.
7. Wakileh, G. J. *Power system harmonics: fundamentals, analysis and filter design*, Springer-Verlag, Berlin, 2001.
8. Dugui, W. and Zheng, X. Harmonic model of power transformer, *International Conference on Power System Technology,* POWERCON'98, 1998, pp. 1045–1049.
9. Pedra, J., Sainz, L., Lopez, R., and Bogarra, S. Transformer saturation model for the harmonic analysis on power systems, *Eighth International Conference on Harmonics and Quality of Power,* ICHQP'98, Athens, Greece, October 1998, pp. 1053–1058.
10. Wiechowski, W., Bak-Jensen, B., Bak, C. L., and Lykkegaard, J. Harmonic domain modeling of transformer core nonlinearities using the DIgSILENT PowerFactory software, *Electric Power Quality and Utilization,* Vol. XIV, No. 1, 2008, pp. 3–11.
11. Santoso, S., Dugan, R. C., Grebe, T. E., and Nedwick, P. Modeling ferroresonance phenomena in an underground distribution system, *International Conference on Power System Transients,* Rio de Janeiro, Brazil, 2001, Paper 34.
12. Buigues, G., Zamora, I., Valverde, V., Mazon, A. J., and San Martin, J. I. Ferroresonance in three-phase power distribution transformers: sources, consequences, and prevention, 19th *International Conference on Electricity Distribution,* CIRED 2007, Vienna, Session 1, August 2007, Paper 0197.
13. IEEE Working Group, Chair - Iravani, M. R. Modeling and analysis guidelines for slow transients — Part III: The study of ferroresonance, *IEEE Transactions on Power Delivery,* Vol. 15, No. 1, January 2000, pp. 255–265.
14. Rivas, J., Zamarro, J. M., Martin, E., and Pereira, C. Simple approximation for magnetization curves and hysteresis loops, *IEEE Transactions on Magnetics*, Vol. 17, No. 4, July 1981, pp. 1498–1502.
15. Rezaei-Zare, A., Sanaye-Pasand, M., Mohseni, H., Farhangi, S., and Iravani, R. Analysis of ferroresonance modes in power transformers using Preisach-type hysteresis magnetizing inductance, *IEEE Transactions on Power Delivery*, Vol. 22, No. 2, April 2007, pp. 919–929.
16. Wanner, E. and Herbst, W. Static power factor compensators for use with arc furnaces, *Brown Boveri Review,* Vol. 2, 1977, pp. 124–134.
17. Yu, H., Yue, Y., Zhifei, C., and Ling, X. Research on the calculation of the influence of arc furnace reactive impact loads on power system and the method of compensation, Proceedings of International Power and Energy Conference, IPEC 2010, October 2010, pp. 1052–1055.
18. Vervenne, I., Van Reusel, K., and Belmans, R. Electric arc furnace modeling from a power quality point of view, 3rd IEEE Benelux Young Researchers

Symposium in Electrical Power Engineering, Gheni, Belgium, April 2006, Paper No. 36.
19. Mendis, S. R. and Gonzalez, D. A. Harmonic and transient overvoltage analyses in arc furnace power systems, *IEEE Transactions on Industry Applications,* Vol. 28, No. 2, March/April 1992, pp. 336–342.
20. Ringlee, R. J. and Stewart, J. R. Geomagnetic effects on power systems, *IEEE Power Engineering Review*, July 1989, pp. 6–9.
21. Albertson, V. D., Bozoki, B., Feero, W. E., Kappenman, J. G., Larsen E. V., Nordell, D. E., Ponder, J., Prabhakara, F. S., Thompson, K., and Walling, R. Geomagnetic disturbance effects on power systems, *IEEE Transactions on Power Delivery*, Vol. 8, No. 3, July 1993, pp. 1206–1216.
22. Kappenman, J. G. Geomagnetic storms and their impact on power systems, *IEEE Power Engineering Review*, May 1996, pp. 5–8.
23. Wrubel, J. N. Monitoring program protects transformers from geomagnetic effects, *IEEE Computer Applications in Power*, January 1992, pp. 11–14.
24. Bronzeado, H. S., Brogan, P. B., and Yacamini, R. Harmonic analysis of transient currents during sympathetic interactions, *IEEE Transactions on Power Systems*, vol. 11, no. 4, November 1996, pp. 2051–2056.
25. Kumbhar, G. B. and Kulkarni, S. V. Analysis of sympathetic inrush phenomena in transformers using coupled field-circuit approach, *IEEE PES General Meeting*, Tampa, USA, June 2007.
26. Massaro, U. R. R. and Antunes, R. Electrical transient interaction between transformers and power system — Brazilian experience, *International Conference on Power System Transients* Kyoto, Japan, 2009.
27. Musil, R. J., Preininger, G., Schopper, E., and Wenger, S. The resonant effect of oscillating system overvoltages on transformer windings, *IEEE Transactions on Power Apparatus and Systems,* Vo. PAS-101, No. 10, pp. 3703–3711.
28. Lee, K. H. and Schneider, J. M. Rockport transient voltage monitoring system: analysis and simulation of recorded waveforms, *IEEE Transactions on Power Delivery,* Vol. 4, No. 3, July 1989, pp. 1794–1805.
29. Kress, K., Konig, D., and Muller, W. Traveling waves as causes of internal resonance phenomena in coils and windings, *CIGRE 1992*, Paper No. 12-303.
30. Cornick, K., Filliat, B., Kieny, C., and Muller, W. Distribution of very fast transient overvoltages in transformer windings, *CIGRE 1992*, Paper No. 12-204.
31. Nakanishi, K., Fujita, S., Kurita, H., Kishi, A., Hasegawa, T., and Shibuya, Y. High-frequency voltage oscillation in transformer windings and electrical breakdown properties of interturn insulation immersed in oil at VFT voltage, *Electrical Engineering in Japan,* Vol. 132, No. 4, 2000, pp. 45–52.

32. Ohashi, H., Mizuno, T., and Yanabu, S. Application of vacuum circuit breaker to dry type transformer switching, *IEEE PES Winter Meeting,* New York, January 1976, Paper A 76 174-3.
33. Popov, M. and van der Sluis, L. Improved calculations for no-load transformer switching surges, *IEEE Transactions on Power Delivery,* Vol. 16, No. 3, July 2001, pp. 401–408.
34. Van Craenenbroeck, T., De Ceuster, J., Marly, J. P., De Herdt, H., Brouwers, B., Van Dommelen, D. Experimental and numerical analysis of fast transient phenomena in distribution transformers, *IEEE PES Winter Meeting 2000,* Singapore, Paper 0-7803-5938.
35. Picher, P. Mechanical condition assessment of transformer windings using frequency response analysis (FRA), *CIGRE WG A2.26 Report*, 2007.
36. Degeneff, R. C., Vakilian, M., Guttierez, M., Soderberg, P., McKenny, P. J., Girgis, R. S., Schneider, J. M., and Provanzana, J. H. Modeling power transformers for transient voltage calculations, *CIGRE 1992,* Paper 12-304.
37. Gustavsen, B. and Semlyen, A. Rational approximation of frequency domain responses by vector fitting, *IEEE Transactions on Power Delivery,* Vol. 14, No. 3, July 1999, pp. 1052–1061.
38. Popov, M., van der Sluis, L., Smeets, R. P. P., and Roldan, J. L. Analysis of very fast transients in layer-type transformer windings, *IEEE Transactions on Power Delivery*, Vol. 22, No. 1, January 2007, pp. 238–247.
39. Paul, C. R. *Analysis of multiconductor transmission lines*, 2nd Edition, Wiley-IEEE Press, October 2007.
40. Mombello, E. E. Impedances for the calculation of electromagnetic transients within transformers, *IEEE Transactions on Power Delivery,* Vol. 17, No. 2, April 2002, pp. 479–488.
41. Badgujar, K. P., Gupta, A., and Kulkarni, S. V. A hybrid modeling approach for determining frequency response of transformer coils, *11th International Conference on Transformers, TRAFOSEM-2011*, New Delhi, November 2011, Session-IV, pp. 25–34.
42. Shintemirov, A., Tang, W. H., and Wu, Q. H. Transformer core parameter identification using frequency response analysis, *IEEE Transactions on Magnetics*, Vol. 46, No. 1, 2010, pp.141–149.
43. Abeywickrama, K. G. N. B., Podoltsev, A. D., Serdyuk, Y. V., and Gubanski, S. M. Computation of parameters of power transformer windings for use in frequency response analysis, *IEEE Transactions on Magnetics,* Vol. 43, No. 5, May 2007, pp. 1983-1990.
44. Macfadyen, K. A. Vector permeability, *Journal IEE,* Vol. 94, Pt. III, 1947, pp. 407–414.
45. Abeywickrama, K. G. N. B., Serdyuk, Y. V., and Gubanski, S. M. High-frequency modeling of power transformers for use in frequency response analysis, *IEEE Transactions on Power Delivery,* Vol. 23, No. 4, October 2008, pp. 2042–2049.

46. Podoltsev, A. D., Abeywickrama, K. G. N. B., Serdyuk, Y. V., and Gubanski, S. M. Multiscale computations of parameters of power transformer windings at high frequencies, Part I: small-scale level, *IEEE Transactions on Magnetics,* Vol. 43, No. 11, November 2007, pp. 3991–3998.
47. Podoltsev, A. D., Abeywickrama, K. G. N. B., Serdyuk, Y. V., and Gubanski, S. M. Multiscale computations of parameters of power transformer windings at high frequencies, Part I: large-scale level, *IEEE Transactions on Magnetics,* Vol. 43, No. 12, December 2007, pp. 4076–4082.
48. Gafvert, U. Influence of geometric structure and material properties on dielectric frequency response of composite oil cellulose insulation, *International Symposium on Electrical Insulating Materials,* Kitakyushu, Japan, June 2005, pp. 73–76.
49. Abeywickrama, K. G. N. B., Ekanayake, C., Serdyuk, Y. V., and Gubanski, S. M. Effects of the insulation quality on the frequency response of power transformers, *Journal of Electrical Engineering & Technology,* Vol. 1, No. 4, 2006, pp. 534–542.
50. Abeywickrama, K. G. N. B., Serdyuk, Y. V., and Gubanski, S. M. Exploring possibilities for characterization of power transformer insulation by frequency response analysis, *IEEE Transactions on Power Delivery*, Vol. 21, No. 3, July 2006, pp. 1375–1382.
51. Martinez, J. A. and Mork, B. A. Transformer modeling for low- and mid-frequency transients – a review, *IEEE Transactions on Power Delivery,* Vol. 20, No. 2, April 2005, pp. 1625–1632.
52. Escarela-Perez, R., Kulkarni, S. V., and Melgoza, E. Multi-port network and 3D finite-element models for accurate transformer calculations: single-phase load-loss test, *Electric Power Systems Research*, Vol. 78, Issue 11, November 2008, pp. 1941–1945.
53. Morched, A., Marti, L., and Ottevangers, J. A high frequency transformer model for the EMTP, *IEEE Transactions on Power Delivery,* Vol. 8, No. 3, July 1993, pp. 1615–1626.
54. Melgoza, E., Guardado, J. L., and Venegas, V. A method for coupling electromagnetic transients programs with finite element magnetic field solvers, *International Conference on Power System Transients, IPST'05,* Montreal, Canada, June, 2005.
55. Dennetiere, S., Guillot, Y., Mahseredjian, J., and Rioual, M. A link between EMTP-RV and FLUX3D for transformer energization studies, *Electric Power Systems Research,* Vol. 79, 2009, pp. 498–503.

14

Monitoring and Diagnostics

Due to severe competition and restructuring taking place in the power industry, there is a need to reduce maintenance costs, operate transformers as much as possible, extend their life, and prevent unplanned outages. Hence, in the recent years the monitoring and diagnostics of transformers have attracted considerable attention of researchers and practicing engineers. The monitoring can be either offline or online. The trend is more towards online techniques due to ongoing developments in computational/analysis tools and information technology.

Insulation degradation is the primary reason for aging and eventual failures of transformers. It is usually the limiting factor in the longevity of any electrical equipment including transformers. Degradation beyond a limit can become the cause of their natural end-of-life. Various impurities and mechanisms that lead to insulation degradation are moisture, conducting particles, hot-spots, oxidation and partial discharges.

The presence of moisture in the insulation system of the transformer reduces dielectric strength, leads to bubble formation at high temperatures and accelerates cellulose decomposition. Moisture in the presence of oxygen inflicts major damage to the insulation. Moisture and oxygen degrade the paper insulation to form sludge and acids. Sludge gets deposited on windings, impairing cooling efficiency. Acids accelerate the decay rate further. Hence, moisture and oxygen lead to aging of transformers and reduction in their life expectancy.

The third catalyst for insulation deterioration is temperature. Aging accelerates rapidly with temperature in the presence of high moisture content in the paper/pressboard insulation; the general guideline that the insulation life becomes half for every 6-degree temperature rise is valid when moisture in the insulation is within the acceptable limit, i.e., less than 0.5% by weight. The aging rate is much higher if the moisture is at an unacceptable level.

An oxygen inhibitor can be added to the oil for arresting its high decay rate. The inhibitor acts as a sacrificial agent since the oxygen attacks it rather than the cellulose insulation. The inhibitor may have to be periodically replenished to make up for its falling level due to the oxygen.

Transformers are typically dried by manufacturers so that the moisture to dry weight ratio is within 0.5%. On site a ratio more than 2.5% certainly calls for a dry-out operation. The limit on moisture in oil for a dry-out operation is typically 30% oil saturation [1]. The amount of moisture dissolved in oil increases with temperature. When the moisture content increases beyond the saturation value, oil can no longer hold it resulting in free water suspensions. Paper insulation is much more hygroscopic in nature than the oil. Hence, the moisture distributes unequally between the oil and the cellulose insulation; the latter has a greater amount. In fact, most of the moisture inside the transformer resides in the cellulose insulation (can be as high as 99% or more). Temperature conditions predominantly decide the moisture distribution between them. Moisture gets into the transformer during manufacturing, through various gaskets, while inspecting it at the site, via degradation of insulation due to its normal aging process, and because of rapid temperature and pressure variations. Moisture has a tendency to drift towards cooler parts (at bottom) and regions with higher electrical stresses.

Partial discharges occurring in an insulating material can be detrimental to its condition. A partial discharge is a localized breakdown that occurs without complete bridging of the insulation. The breakdown is in the form of extremely fast, nanosecond discharges. Partial discharges over an appreciable period of time, can lead to catastrophic failures. When discharges occur in insulation voids, signals in the electrical, chemical and acoustic domains are generated. Different techniques have been developed to detect such signals for determining the extent and location of discharges.

The processes of insulation degradation and the corresponding failure mechanisms in transformers are complex. The monitoring not only detects the incipient faults but also allows a change from periodic to condition-based maintenance [2]. It is important to identify key parameters that should be monitored to reduce the cost of the overall monitoring system. The high cost of monitors, reliability issues of electronic equipment, performance under adverse field conditions, and inadequate expertise in interpretation are some of the challenges that need to be overcome. There are a number of offline and online monitoring/diagnostic techniques that are currently being used and developed further. This chapter elaborates these techniques; a few of them, which are well-established and documented in technical reports/standards, will be discussed briefly. A concise summary of routine tests is given in Section 14.1. It should be stated here that the intention of the discussions in this chapter is not to give limits and values (which are given in standards and technical reports), but to highlight the importance of the discussed parameters and tests, and to give a background theory of some of the diagnostic tests.

14.1 Conventional Tests

14.1.1 Routine tests on oil

Since oil comes in contact with the active parts and the solid insulation when it flows due to natural or forced convection, various tests on its samples usually reveal the status of the health of the transformer. Incipient faults can also be detected. The tests/measurements can be done offline or by taking samples in an energized condition. A few online sensors have also been developed in recent times for monitoring oil.

Moisture: Equilibrium charts are commonly used to indirectly determine the moisture content in cellulose insulation from moisture in oil; the method can work well if they are in thermal equilibrium, which is a rare possibility during operating conditions [3]. As discussed in Section 8.3, there is migration of moisture between them as the temperature changes due to variations in load. Mineral oil has a low affinity to moisture, but the solubility increases significantly with temperature. Hence, as the temperature rises, the moisture in the cellulose insulation migrates to the oil. On the other hand, when there is a drop in the temperature (say, due to a reduction in load) the moisture tends to return to the cellulose insulation, but at a slower rate. Therefore, the oil appears to have greater moisture at lower temperatures resulting in overestimation of the moisture content in the cellulose insulation when the equilibrium charts are used.

Karl Fischer titration is another conventional technique for the measurement of moisture in cellulose. It requires careful extraction of paper/pressboard samples and their storage (until the measurement is done in a laboratory). This is an intrusive technique like the DP (degree of polymerization) test to be discussed later. The main limitation of these intrusive techniques is that the diagnosis has to be done by using paper samples collected from easily accessible parts (e.g., high voltage leads) as critical insulation areas between windings are not reachable for the purpose.

More sophisticated dielectric diagnostic methods have been in use recently, which determine the moisture in solid insulation from dielectric characteristics such as charging/discharging currents, recovery voltages, and the dissipation factor. These methods, which can be used for doing on-site diagnostics, are generally more accurate than the conventional methods. Also, the data measured using them contains much more information which can give better insight into various dielectric processes. These advanced methods are discussed in a later section.

Cellulose degradation is an irreversible process which is accelerated in the presence of moisture. Extracting moisture from the cellulose insulation by hot oil circulation may not be an efficient process. Drying through heating/vacuum cycles or vapor-phase process after a hot oil spray can make the moisture extraction faster [3, 4] since the sprayed oil can be at a higher temperature (up to 110°C) than the circulated oil (at 60-75°C). Exposed surfaces have higher

moisture content and they are effectively dried by the spray. However, unexposed insulation areas are not effectively dried by this method; a LFH (low frequency heating) technique can be used concurrently to uniformly heat the windings and the cellulose insulation in close vicinity of their conductors. Site dry-out needs to be simple and has to done using one or more of the above methods depending on available resources. Molecular sieves have been used for online drying in the field; they consist of columns with molecular sieve material which binds moisture from the oil [5]. Vapor phase drying, discussed in Chapter 8, is the most effective drying method. However, high costs and sophisticated processes associated with it preclude its use on site.

***Dielectric strength*:** Determination of the breakdown voltage (BDV) of oil samples according to the test procedures outlined in standards (e.g., IEC-60156, Insulating liquids-Determination of the breakdown voltage at power frequency-test method, Second edition, 1995-07) is an important quality check before conducting high voltage tests on a transformer in the factory or before commissioning it on site. If the strength is below a certain value, the oil needs to be processed again to improve its characteristics. The parameter is measured by applying a voltage between two electrodes having shapes as specified in the standards. The distance between them is also standardized. The method is sensitive to the presence of moisture and contaminants in the oil.

***Interfacial tension*:** It is defined as the force in dynes required to pull a small wire ring vertically up through an oil-water interface by a distance of 1 cm. Pure oil results in a clear line between the two media requiring a higher force (40–50 dynes/cm). Contaminated oil weakens the interfacial tension and lowers the corresponding force value, which may call for additional monitoring and diagnostic measures.

***Acid number*:** It is the amount of potassium hydroxide in mg required to neutralize the acid present in 1 gm of oil. A higher acid number than the limit specified in standards is indicative of an unacceptable level of acid content in the oil. This number along with the interfacial tension gives a good signal about the oil condition. The limit on the acid number is 0.4 mg [6, 7].

***Tan delta*:** Its higher value is indicative of a significant loss (resistive) component of the leakage current, which may be due to various kinds of impurities that may be present in the oil (e.g., moisture, conducting particles). It should be noted the test result can be in the form of a power factor or dissipation factor value. These indices are adversely affected by aging products and soluble polar contaminants (water molecules) in the oil; a significant increase in $\tan\delta$ is usually observed.

14.1.2 Tests on windings

***Insulation resistance test*:** The insulation resistance is measured by applying a DC voltage to the winding under test with its neutral isolated from the ground (if applicable) and all other windings short-circuited and grounded. The core and the tank are also grounded. The transformer must be de-energized for conducting the test. The measured resistance then tests the condition of the insulation between the winding and the core/tank/other windings; for a good insulation condition its value is in mega-ohms. The duration of the test is 1 minute and the measured resistance value at the end of test duration is used for future comparisons. The readings are sensitive to temperatures and the magnitude of the applied DC voltage; these parameters must be recorded and taken into account during the comparisons. The test is performed as a part of commissioning procedures to check for any ingress of moisture during transport or storage. Since the test is done with a DC voltage, all the terminals should be grounded for a sufficient amount of time after the test to drain the charges completely to ground.

Polarization index: The ratio of the measured insulation resistance after 10 minutes to that measured after 1 minute is known as polarization index. Its value is lower (≈ 1.0) for moist/contaminated insulation compared to that for dry/pure insulation (≈ 2.0) [7]. The governing theory for such a behavior is explained through an equivalent circuit model in Section 14.5.5.

14.1.3 Power factor test

This test, which helps to determine the quality of the insulation between the windings and between the windings and the core/tank/ground, is conducted using a Schering bridge or transformer-ratio-arm bridge. The corresponding capacitance and tanδ values can also be determined. The measured power factor value is indicative of losses in the total insulation system including the bushings. With aging the power factor deteriorates; the measured power factor should be compared to previous test readings to ascertain its trend. When the power factor or tanδ value is higher than the limits specified in the standards, other conventional tests, such as moisture-in-oil analysis, can be conducted to confirm the insulation status. Additionally, advanced dielectric response tests as discussed in Sections 14.5 and 14.6 can also be performed.

Any change in the capacitance between the LV and HV windings, between the LV winding and ground, and between the HV winding and ground is indicative of aging, winding deformations, dislocation of winding support structures, or a combination of these. It should be remembered that the capacitances of bushings are also part of the measured values. The method may not be sensitive enough to detect mechanical irregularities in the windings; advanced methods such as frequency response analysis (to be discussed later) should be used.

14.2 Dissolved Gas Analysis

Dissolved gas analysis is an established and proven method to detect incipient faults. Degradation of oil and cellulose insulation leads to evolution of the following key gases: hydrogen (H_2), oxygen (O_2), carbon monoxide (CO), carbon dioxide (CO_2), methane (CH_4), acetylene (C_2H_2), ethylene (C_2H_4) and ethane (C_2H_6). Since the mineral oil used in transformers has chains of hydrocarbon molecules, its decomposition leads to formation of H_2, CH_4, C_2H_2, C_2H_4 and C_2H_6 gases. On the other hand, cellulose (paper insulation) degradation is accompanied by release of O_2, CO and CO_2 gases. Since the paper is oil-impregnated, gases such as H_2 and CH_4 are also produced due to its thermal decomposition as it ages normally. Because of the production of O_2 and H_2 the degradation process of the paper insulation leads to more moisture generation which accelerates the decay further.

The dissolved gas analysis (DGA) is done using a gas chromatograph which houses different adsorption columns. The gases extracted using a suitable technique (e.g., vacuum extraction) are fed into the columns where they are adsorbed and separated. Established dissolved gas interpretation methods/ guidelines, as described below in brief, are commonly used.

***Key gas method*:** Various types of faults produce different gases. Therefore, the analysis can be done by identifying the most prominent gas that is generated. Arcing, overheated cellulose and partial discharges produce predominantly acetylene, carbon oxides and hydrogen, respectively. The generation of ethane and ethylene is generally associated with overheating of metal parts (e.g., contacts of tap changer assembly, terminations of conductors/leads, tank plates).

***IEEE method*:** A guide for interpretation of gases generated in oil-immersed transformers (IEEE Standard C57.104-1991) classifies conditions into four types depending upon the concentrations of individual key gases and the amount of the total dissolved combustible gases (TDCG). Severity increases from condition 1 to condition 4. The rate of increase of different gases in a given time interval is a better indicator than their absolute levels. Acetylene gas is the exception; a small amount of acetylene gas above a certain ppm value cannot be disregarded, although the rate may be small, as it may be indicative of high-energy arcing.

***Rogers ratio method*:** It uses three ratios of certain key gases, viz. CH_4/H_2, C_2H_2/C_2H_4 and C_2H_4/C_2H_6 , to classify an already diagnosed gas generation problem into a specific fault type. The method uses the fact that the gases begin to form in small amounts when the temperature reaches a certain level. For example, hydrogen begins to form around 150°C and increases steadily with the temperature. The concentration of acetylene, which shows up beyond 500°C [5, 8], increases significantly above 700°C. Thus, in a specific temperature range, the amount of one gas is more than that of another gas. For a certain temperature prevailing inside the transformer the ratios will have typical values enabling an

estimation of the temperature and hence the fault-type.

IEC 60599 (Mineral oil-impregnated electrical equipment in service – Guide to the interpretation of dissolved and free gases analysis, edition 2.1 2007-05) gives a method which is similar to the Rogers ratio approach. It uses the three ratios as above and considers six types of faults: partial discharge, discharges of low energy, discharges of high energy, and thermal faults of three intensities (temperature less than 300°C, between 300°C and 700°C, and greater than 700°C).

***Duval triangle method*:** This is also a popular diagnostic approach. It uses concentrations of three key gases, CH_4, C_2H_2 and C_2H_4, to suggest a probable type of fault. We can either use the total accumulated content of the key gases or the increase (over the previous DGA record) in each of the key gases to arrive at a point in the Duval triangle [1]. The location of the point in the triangle indicates the type of the fault.

DGA can be unreliable if the transformer under investigation has cooled after de-energization. Also, the analysis on a new transformer or a transformer which has been recently processed for oil-filtration can lead to erroneous diagnostic conclusions [5]. Whenever a problem is suspected from the analysis, it is recommended to analyze another sample and compare the two results. It may not be prudent to base inferences on just one analysis [6]; there can be errors in sampling and handling procedures.

DGA can be done online as well to detect a few key gases such as hydrogen, oxygen, methane, carbon monoxide, carbon dioxide, ethane, ethylene and acetylene along with the moisture in the transformer oil [9]. Ambient and top oil temperatures can also be measured. Oil samples are collected and processed every one or two hours. Advanced and compact sensors are being developed to detect the gases. There is enough experience already available with online hydrogen sensors. Portable units are available that can detect hydrogen in oil, which is indicative of mostly the occurrence of partial discharges. Investigation of dynamic behavior of the gases with changing operating conditions is possible. Online monitoring of oxygen can give a warning of air leaks [10]. Online instruments with lower costs, which measure only three key gases, hydrogen, carbon dioxide and acetylene, are also available [9].

14.3 Partial Discharge Diagnostics

14.3.1 Physics of partial discharge

A partial discharge (PD) is a transient breakdown of a part of the insulation system in high voltage equipment. By this process, the entire dielectric is not breached; that is, the breakdown does not occur between two conductors. Only a small portion of the insulation suffers a miniature breakdown. Partial discharges can be thought of as motion of charges due to a local intensification of the electric field which exceeds the breakdown strength in a small region of the

insulation. A sustained PD activity leads to an accelerated aging of the insulation and can become the cause of an eventual failure.

PD processes are complex and recorded signals are statistical in nature, and the effect of previous *discharges* on the subsequent ones cannot generally be ignored. The correlation of the physics of a PD activity with measured electrical, acoustic or chemical signals is extremely intricate due to the presence of various possible conditions and parameters that affect it. In fact, determining such correlations has been an important and integral part of diagnostic studies recently.

Presence of microscopic voids is inevitable in the manufacture of solid dielectrics such as pressboard cylindrical barriers, supports or spacers. These voids will be mostly filled with the impregnating medium which may be resin or oil. The potential difference across the insulator sets up an electric field. The void, with or without the impregnant, has a lower dielectric constant than the surrounding solid, and hence has a higher electric field across it. When the electric field exceeds its dielectric strength, a local breakdown occurs. The actual physical process is fairly intricate. Ionization has to take place as the voltage rises to peak in a half cycle, in order to generate the charges that jump across the void and reduce the overall electric field. The electrons so produced move mainly under the influence of the external electric field. These electrons get deposited on the dielectric surface, and thus effectively reduce the field inside the void, which leads to PD extinction as the voltage dips after reaching the peak. The presence of deposited charges causes the discharge pulse to occur at a smaller value of the phase angle during the next half-cycle, as the charges effectively increase the field within the void during this opposite half-cycle [11]. The process is further complicated by the generation of secondary electrons and the memory effect of the previous discharge pulse.

In a void, PD takes place when the following conditions are satisfied [12], viz. the local electric field should be greater than the breakdown field strength, electrons must be available for starting the physical process, the weak region should be enough in size for the avalanche to occur, and the duration of the applied voltage should be sufficiently long to bridge the weak dielectric region. Local field intensification also takes place in oil in the solid-oil interface due to improper stress grading or due to sharp points on the tank. When the field exceeds the oil dielectric strength, PD will result in oil

14.3.2 Diagnostic techniques

PD results in a localized and nearly instantaneous release of energy, which produces a number of effects such as local heating, generation of electromagnetic and acoustic waves, chemical reactions, among others [13]. Correspondingly, the following different methods of recording these have been developed.

***Dissolved gas analysis*:** Like many other defects, PD occurring in oil causes the generation of hydrogen gas. Hence, its trace detected during DGA may be indicative of PD activities. Detection of certain gases such as carbon monoxide or carbon dioxide may indicate the presence of partial discharges in paper insulation. Since the paper insulation can be replaced only by rewinding, even a small trace of carbon monoxide/dioxide becomes a matter of concern.

***Electrical method*:** In this technique, a large valued coupling capacitor is connected across the equipment under test, and the apparent charge provided during the PD discharge is measured by integrating the high-frequency current pulses flowing through this capacitor. The actual charge transfer across the cavity cannot be measured, and hence the apparent charge transfer has to be measured. The energy dissipated during the discharge is directly proportional to this apparent charge transfer and the square of the inception voltage [14].

A measuring impedance is connected either in series with the test specimen or with the coupling capacitor. For testing a transformer, a bushing is invariably used as the coupling capacitor. Impedance is connected between the bushing tap and ground for sensing the capacitively coupled PD signal. Alternatively, a high frequency current transformer (HFCT) is placed in the bushing turret or around the ground lead from neutral to act as a current sensor.

One common method of studying PD phenomena is *phi-q-n* analysis. Here, *phi* is the phase angle, with respect to the voltage waveform, at which the PD pulse occurs, *q* is the magnitude of the discharge pulse in pC, and *n* indicates the number of such occurrences over a period. This data acquired over a long duration can exhibit a 3-D pattern which can be used to identify the source of PD inside the transformer. Also, the evolution of the pattern over a much longer period may be used to analyze the introduction/suppression of PD sources. An appropriate statistical analysis of the measured data over many cycles can give useful information.

The method's offline nature, elaborate setup, high external/ electromagnetic interference, and difficulties in locating PD discharges are the major shortcomings. The measurements are affected by electrical interference signals from surrounding equipment. Hence, it is not attractive for on-site measurements. One more limitation is that the maximum observed amplitude of the discharge may not be indicative of either the deterioration taking place or the time to breakdown [15]. For example, a solid dielectric with an internal void breaks down after the appearance of a tree; the propagation rate for the tree is generally greatest when the detected discharge amplitude and frequency are the lowest. Continuous monitoring at the bushing tap or through a HFCT and the use of phase-resolved digital measurements over a long period with suitable statistical analysis may somewhat overcome these disadvantages.

The PD detection range for the electrical method is larger; it covers a wider area which includes, for example, tap changer and bushings. There is better correlation between instrument readings and actual PD magnitudes as compared to

that with the acoustic method which is discussed next.

***Acoustic method*:** This method involves the detection of mechanical signals emitted from the discharge as a result of pressure variations. The corresponding waves propagate through the surrounding oil and other insulating materials, which can be detected at a tank wall using piezoelectric sensors fitted externally. The acoustic sensors based on the piezoelectric effect are less expensive and the main advantage of the acoustic technique is that there is generally no interference in measurements due to signals from the electric network. However, the PD detection is possible within a radius of only about 20 to 30 cm from the source since the acoustic signals are attenuated by the media through which they travel. Hence, a number of acoustic sensors may have to be used, located judiciously around the transformer periphery. Acoustic sensors can also be placed internally using waveguides (e.g., fiberglass rods) to enhance the strength of the signals to be measured, but the system is expensive and difficult to install.

A typical acoustic PD detection system consists of a sensor, a filter, a pre-amplifier and a data acquisition system. Ambient noise of mechanical origin mainly influences the signal-to-noise ratio and sensitivity of the PD detection system. Sensors used have a typical frequency range of 70 to 150 kHz to suppress the core noise as well as the noise due to mechanical vibrations of the transformer structure [16]. The location of the PD source can be determined based on the measurement of the time of arrival and the amplitude of the signal.

The intensity of the emitted acoustic signal is proportional to the discharge energy. Therefore, a linear relationship between the peak discharge magnitude and the amplitude of the acoustic signal over a wide frequency range is possible. The shape of the detected signal depends on the source, the detection apparatus and the sensor.

Simple hardware requirements and well-established discharge-location algorithms make the method attractive. Also, being immune to electromagnetic noise, it can be effectively used for on-site condition monitoring. The main limitation of the method is that its sensitivity can be seriously hampered by signal attenuation. Also, the propagation velocity of the ultrasonic waves is strongly dependent on material properties of the media [17]. It is less sensitive to partial discharges occurring in inner windings. Furthermore, a considerable amount of expertise and experience is required for interpreting acoustic measurements since multiple signals are recorded after attenuation, reflections, and scattering.

Thus, when an acoustic wave propagates through the insulating media, its intensity decreases as a function of the distance from the source due to several mechanisms such as geometrical spreading of the wave, acoustic absorption (conversion of acoustic energy to heat) and scattering of the wave-front. It is therefore important to increase the signal-to-noise ratio through an averaging technique whereby the noise is effectively suppressed. The technique works very well when the signal and the noise are uncorrelated, the signal is of

repetitive nature, and the noise is *white* (meaning that it contains every frequency within the investigated band in equal proportions) [18]. For an effective averaging to happen, a trigger derived from a physical PD effect having higher sensitivity can be used. The electrical PD method or UHF (ultra high frequency) PD method, to be discussed next, can be used for the purpose. A UHF-triggered acoustic technique is elaborated in [18].

***UHF method*:** This technique involves detection of electromagnetic waves (300–3000 MHz) emitted by PD activities [19]. During a PD pulse, electrons from the outermost orbit are dislodged from atoms or molecules and are accelerated rapidly by the electric field. Electromagnetic radiations occur and spread in all possible directions when electrical charges are accelerated. Bad contacts and electrostatic discharges due to floating metallic parts can also result in radiations [20]. The signals are attenuated as they travel through complex arrangement of conductors and insulation due to losses and reflections. They are also reflected at tank boundaries. Because of the inverse relationship between the time-domain and frequency-domain representations of a pulse, shorter PD current pulses have more spectral energy at high frequencies [21].

Signals in the UHF range can be measured by suitable tank-mounted sensors when the discharges occur on a time scale of 1 ns or less. The sensors used in gas-insulated substations (GIS) have been successfully applied for UHF diagnostics of transformers [22]. PD sources can be located by the time-of-flight method. Signals from sensors are usually filtered and amplified, and analog-to-digital conversion is done to digitize the data.

The phase of each recorded PD pulse can be easily determined using a clock and a phase reference signal [22]. The amplitude of the pulses can be directly correlated to the energy content in the UHF signal. Neural networks can be used for pattern recognition to diagnose the characteristics of the PD source.

Dielectric windows need to be provided for enabling the UHF diagnostics of transformers. They provide a robust electrical aperture through which the UHF signals can be detected. Alternatively, the sensor can be installed through a valve, or it can be permanently positioned inside the tank. The UHF sensors must have a large bandwidth because the frequency content of the signals from a PD source can vary considerably depending on its location and the signal path. Sensitivity over the range of 500 to 1500 MHz is essential. Although immune from electrical interference, the UHF measurements may be affected by communication noise, thermal noise in the detection system, and noise due to operation of power electronic switches; denoising of UHF signals can be done using the discrete wavelet transform [23]. Efforts have been made to analyze signatures due to various types of PD sources in [24].

Analysis of corona pulses under DC and AC voltage conditions has been done in the UHF range in [25] for a point-plane electrode configuration. It has been experimentally validated that corona signals exist in a frequency range of 300 MHz to 1500 MHz. The signals received for positive and negative DC polarities

are distinct. The overall strength of a signal captured from a negative polarity discharge is stronger than that for a positive polarity discharge, on an average by about 10 dB, for the same voltage magnitude. Also, the negative polarity corona has more uniform frequency content. The corona magnitude for the positive polarity has a tendency to increase in the frequency range of 1000–1500 MHz. Correlations between the physical processes and the received signals have also been identified. The electron avalanche travel duration in the negative polarity corona is much longer than that in the burst pulses or streamers for the positive polarity corona. At higher voltages, it can be expected that a larger region around the point electrode gets depleted of electrons and, hence, forms a positive space charge. Consequently, electrons that were further away reach the positive point and thus there is an increase in the current pulse duration and a consequent increase in the lower frequency content of the spectrum. These are the possible mechanisms responsible for a changing UHF pattern with increasing voltage. The analysis of signals received for an applied AC voltage has also been done with respect to physical discharge mechanisms. Under DC voltage conditions, due to the faster accelerations of electrons and ions in negative streamers and short pulses in positive streamers, the frequencies emitted by the discharges can be expected to be in a higher range. However, these two modes are not observed in the case of AC corona. Hence, higher frequency signals may be much smaller in magnitude for AC as compared to DC. This discussion is more applicable to point-plane configurations. The analysis and experimental work needs to be extended for practical configurations encountered in transformers.

The interest in UHF detection of PD is mainly due to the possibility of online monitoring [26]. Secondly, with UHF frequencies in the range of 300 to 3000 MHz, the technique is inherently immune to noise. Very small discharges up to 10 pC can be recorded with good sensitivity. In this respect, the UHF method is much superior to the acoustic technique if discharges are confined within insulating barriers [27]. A main disadvantage of the method is that special arrangements for incorporating UHF sensors have to be made during the manufacturing stage. Also, a complicated algorithm is required for locating discharges. Hence, although the method is well-developed for GIS equipment, it is still evolving for transformers.

***FDTD method*:** Recently, numerical simulations have been attempted to gain further insight into the PD propagation to aid diagnostics. The finite difference time domain (FDTD) technique is widely used to simulate and analyze electromagnetic wave propagation phenomena. The technique is relatively easy to understand and implement compared to other methods such as FEM and *method of moments* (MOM) when applied to high-frequency computational electromagnetics.

The method belongs to the general class of time-domain numerical modeling methods in which Maxwell's equations in the differential form are simply converted into difference equations. The whole computational domain is discretized using Yee's lattice as shown in Figure 14.1.

Maxwell's time-dependent curl equations are (see Chapter 12):

$$\begin{aligned} \nabla \times \mathbf{E} &= -\mu \frac{\partial \mathbf{H}}{\partial t} \\ \nabla \times \mathbf{H} &= \sigma \mathbf{E} + \varepsilon \frac{\partial \mathbf{E}}{\partial t}. \end{aligned} \tag{14.1}$$

In Cartesian coordinates, the curl equations can be written as six scalar equations [28]:

$$\begin{aligned} \frac{\partial H_x}{\partial t} &= \frac{1}{\mu}\left(\frac{\partial E_y}{\partial z} - \frac{\partial E_z}{\partial y}\right) \\ \frac{\partial H_y}{\partial t} &= \frac{1}{\mu}\left(\frac{\partial E_z}{\partial x} - \frac{\partial E_x}{\partial z}\right) \\ \frac{\partial H_z}{\partial t} &= \frac{1}{\mu}\left(\frac{\partial E_x}{\partial y} - \frac{\partial E_y}{\partial x}\right) \\ \frac{\partial E_x}{\partial t} &= \frac{1}{\varepsilon}\left(\frac{\partial H_z}{\partial y} - \frac{\partial H_y}{\partial z} - \sigma E_x\right) \\ \frac{\partial E_y}{\partial t} &= \frac{1}{\varepsilon}\left(\frac{\partial H_x}{\partial z} - \frac{\partial H_z}{\partial x} - \sigma E_y\right) \\ \frac{\partial E_z}{\partial t} &= \frac{1}{\varepsilon}\left(\frac{\partial H_y}{\partial x} - \frac{\partial H_x}{\partial y} - \sigma E_z\right). \end{aligned} \tag{14.2}$$

Grid points are defined in the domain as $(i, j, k) = (i\Delta x, j\Delta y, k\Delta z)$. Any time and space dependent field variable can be written as $f^n(i, j, k) = f(i\delta, j\delta, k\delta, n\Delta t)$, where δ and Δt are the space and time increments, respectively. It is a usual practice to take the same space increment in all three directions.

The partial derivative of the field variable in the z direction, for example, can be written as

$$\frac{\partial f^n(i,j,k)}{\partial z} = \frac{f^n(i,j,k+1/2) - f^n(i,j,k-1/2)}{\delta}. \tag{14.3}$$

The other two partial derivatives with respect to the x and y variables can be similarly expressed. The partial derivative with respect to time is written as

$$\frac{\partial f^n(i,j,k)}{\partial t} = \frac{f^{n+1/2}(i,j,k) - f^{n-1/2}(i,j,k)}{\Delta t}. \tag{14.4}$$

Using these expressions, the six scalar equations are rewritten to obtain a system of six coupled finite difference equations in an explicit form [28]. For example, the expression for H_z is written with respect to Yee's cell in Figure 14.1 as

$$H_z^{n+1/2}(i-1/2, j+1/2, k) = H_z^{n-1/2}(i-1/2, j+1/2, k) + \frac{\Delta t}{\mu(i-1/2, j+1/2, k)\delta}\left[\begin{array}{l} E_x^n(i-1/2, j+1, k) - E_x^n(i-1/2, j, k) - \\ \left\{E_y^n(i, j+1/2, k) - E_y^n(i-1, j+1/2, k)\right\}\end{array}\right].$$

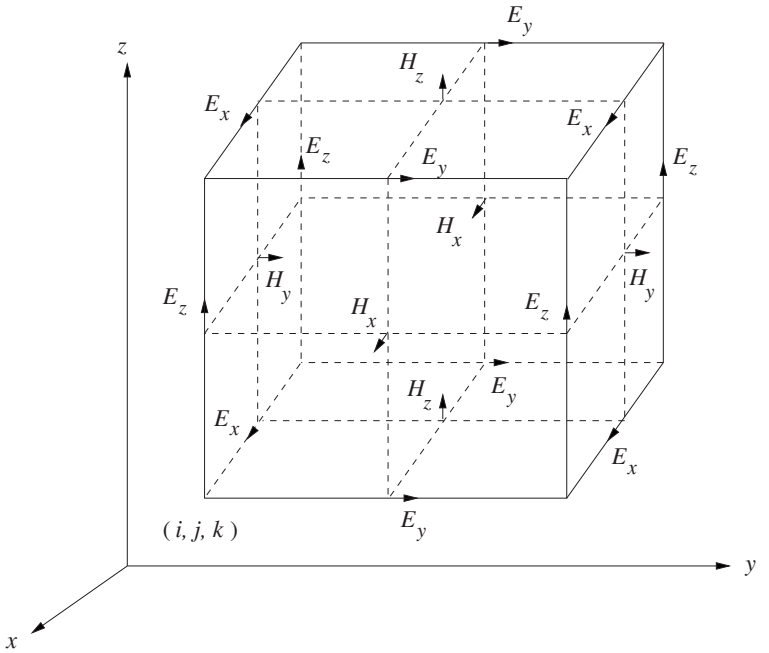

Figure 14.1 Yee's unit cell.

The difference equations written for the electric and magnetic fields at grid points are then solved in a leap-frog manner; the electric field is solved at a given time instant and then the magnetic field is solved at the next time instant, and the process is repeated until the last time instant of interest.

The cell-size must be small enough to yield reasonably accurate results at the highest frequency of interest and large enough to permit the implementation of the algorithm on a computer. The size must be much smaller than the smallest wavelength for which an accurate solution needs to obtained. Typically, the space increment δ should be 0.1λ, (10 cells in one wavelength) or less at the highest frequency (the shortest wavelength) of interest.

Once the cell size is determined, the maximum allowed time-step is determined by Courant stability condition,

$$\Delta t \leq \frac{\delta}{\sqrt{n} \cdot \mu_{\max}} \tag{14.5}$$

where n is the number of space dimensions (equals 3 for a 3-D problem domain) and $\mu_{\max}$ is the maximum wave phase velocity within the model.

While simulating propagation of electromagnetic waves from a PD source inside a transformer, an absorbing boundary condition (ABC) [29, 30] is applied to the tank for eliminating reflections so that the path between the source and the sensor location can be studied. One of the efficient ways of enforcing ABC is perfectly matched layer (PML), which is accomplished by changing μ with ε at the boundary to keep the impedance constant, as seen by the wave, for eliminating reflections [30]. Further the boundary material is made highly lossy by assigning complex values to the material constants; their imaginary parts represent the losses. The wave thus gets completely absorbed within the boundary layer.

Results of simulations of PD wave propagation in 2 dimensions are given in [30]. For the stability of the numerical results, the time step is chosen so as to satisfy the Courant Condition given by Equation 14.5. Simulations are first done for free space; subsequently PD propagation is analyzed for a scaled down problem domain with circular obstructions represeting the core and windings. The contours of E field for both cases are shown in Figure 14.2. A PD pulse is located at the center of the domain. The numerical procedure can be extended to real cases in transformers involving 3-D geometries and different material media.

For PD localization, arrival times to reach the sensors are measured and then the time differences are calculated to locate the origin of source. For determining whether the pulse has reached the installed sensors, the field value at the sensor locations is calculated and compared with a threshold value set for the sensors. For the localization, we can use either an absolute time approach or time differences of arrival (TDOA) method.

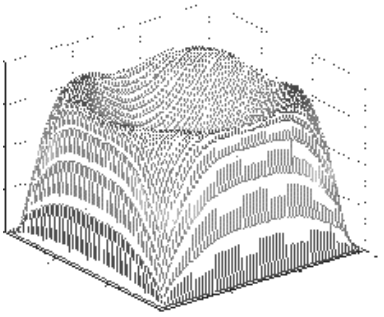

a) PD propagation: free space

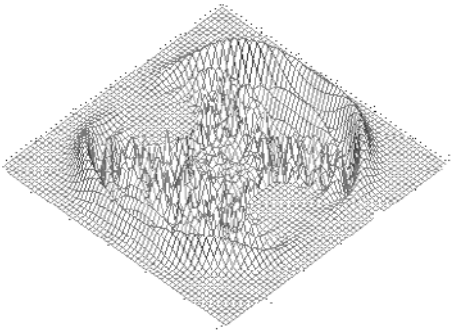

b) PD propagation: with obstructions

Figure 14.2 FDTD simulations.

In the former method the triggering instant of the PD pulse is required to be known. However, in many practical applications this instant is usually unknown. Hence the TDOA approach is commonly used, which can locate a PD source whose triggering instant is not known. The method requires more than one sensor since the difference between the arrival times at multiple sensors is used to determine the location of the PD source [30].

14.4 Degree of Polymerization and Furan Analysis

Degree of polymerization: The cellulose is made up of polymeric chains of glucose units. The number of units per chain is termed the degree of polymerization (DP). It has a definite correlation with the mechanical strength of paper insulation. Its measured value is used to study the phenomena of aging and the corresponding influencing factors. The DP of about 1200 for new paper drops to just about 200 for severely aged paper. In fact the drying processes (heating/vacuum cycles) during the manufacture of transformers lowers the DP value to about 1000 [4]. Temperature, oxygen and moisture are the main degrading agents which reduce the DP value through pyrolytic, oxidative and hydrolytic degradation processes, respectively [5]. Moisture content in the cellulose insulation increases with depolymerization. The degradation of the molecular chain results in reduction of its length and mechanical strength, and the color of the insulation changes to a darker shade. It becomes brittle and hence vulnerable under the action of short-circuit forces. Its mechanical damage may finally result in a catastrophic interturn failure.

The measured DP value can give an estimate of the remaining life of the test sample. A DP value of 200 is taken to indicate the absolute end of life as suggested in the IEEE Standard C57.91-1995 (Guide for loading mineral oil immersed transformers), which corresponds approximately to the end-point

criterion of 50% tensile strength used previously [3]. The quality of cellulose can be assessed in terms of the percentage DP loss or in terms of the percentage tensile strength (TS) loss. The degradation of cellulose is quantified in terms of a degradation variable which is a function of a reference DP value and the measured DP value after degradation. Similar expression for the variable can be derived in terms of a reference value of TS and its measured value after degradation [31].

The main disadvantage of this intrusive technique is that a paper-insulation sample is required to be taken from inside the transformer (generally from lead insulation in the top portion of the transformer) necessitating shutdown of the transformer. Also, ddegradation is usually localized in regions with high temperatures and moisture. Critical insulation parts between windings and insulation on winding conductors are not accessible for the sampling purpose. Hence, advanced diagnostic response techniques in the time-domain and the frequency-domain as discussed in Section 14.5 are commonly used these days when moisture content in the cellulose insulation needs to be estimated.

Furan analysis: A practical alternative to the DP test is furan measurement. It is, in a way, an indirect and integral method. When cellulose materials (paper and solid insulation) degrade due to thermal stresses/oxygen/moisture, the final products of the degradation process are CO, CO_2 and water. Furanic compounds are generated as intermediate products among which 2-furfural is a significant proportion. These compounds, which are dissolved in oil, can be detected using high performance liquid chromatography (HPLC) analysis. Threshold concentrations of furfural, as a function of the number of service years, are given in [32]. The rate of change of furans between tests is generally a better indicator to assess the oil condition rather than judging by just their absolute magnitude. Results of the DP test and HPLC can complement each other in assessing the condition of insulation [33]. DP and 2-furfural contents have been correlated through simple equations by researchers [3].

14.5 Time Domain Dielectric Response Methods

The moisture in cellulose insulation can be determined indirectly based on the measured moisture content of oil or directly using the Karl Fischer titration technique. There are a few issues with such conventional techniques (see Section 14.1). Since the conventional methods for measuring moisture content are not accurate enough, alternative methods based on insulation characteristics such as recovery voltages, polarization/depolarization currents and the dissipation factor have been developed. The measurements can be done in both time domain and frequency domain. This section describes time domain methods viz. a polarization depolarization current (PDC) method and a recovery voltage method (RVM); the frequency domain method, frequency domain spectroscopy (FDS), is elaborated in the next section. A reference data set needs to be generated by testing

a large number of cellulose samples at various moisture levels, temperatures and oil conductivities to assist diagnostics while applying these sophisticated methods. The dielectric response measurements are performed between the HV and LV windings or between each winding and ground, enabling diagnosis of different insulation arrangements inside the transformer.

14.5.1 Equivalent circuit representation

Insulating media are represented by a simple *R*-*C* parallel circuit representation for explaining tanδ/power factor test results. However, the polarization/depolarization processes cannot be captured by the circuit. An equivalent circuit model, as shown in Figure 14.3, is generally used to describe the polarization processes. R_0 represents the insulation resistance through which the conduction current flows and C_0 denotes the geometric capacitance representing the free space within the dielectric. The other shunt branches consisting of *R*-*C* elements represent the polarization and depolarization of the dipoles. The corresponding time constants R_iC_i are indicative of time dependencies of the involved processes.

In a polymeric dielectric material, due to the presence of inhomogeneities both on the macroscopic and microscopic or atomic levels, different relaxation times exist [34]. Corresponding to different motions of dipoles in the dielectric (some dipoles are more free to rotate than others), several different types of relaxation times are observed [35]. Some dipoles have orientations that are more favorable than others and the transitions between these orientations may be easier than the others [34]. Therefore, relaxation time constants at different locations within the dielectric can be different; these inhomogeneous characteristics are represented by the R_i-C_i elements in the equivalent circuit.

The R_0 branch and the R_i-C_i branches represent the conduction current and the polarization current, respectively. These two current components give the total leakage current of the dielectric. Higher moisture content results in a stronger polarization and a faster relaxation process.

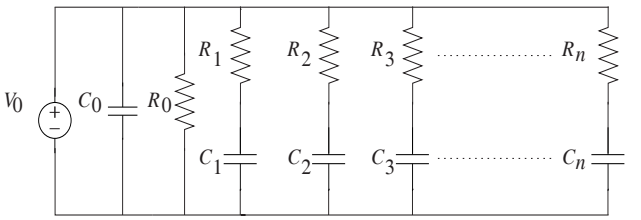

Figure 14.3 Equivalent circuit of a dielectric material.

The circuit is quite an approximation for complex insulation arrangements inside a transformer. Interfacial polarization between oil ducts and barriers has significant influence on recovery voltages and polarization currents. Hence it is suggested in [36, 37] that each oil duct and pressboard barrier should be represented separately by its own circuit. Such a modeling approach enables distinguishing the interfacial polarization and the individual response of each material. However, the circuit in Figure 14.3, which treats the insulation system as one equivalent material, is commonly used since it amenable for applying easier algorithms for diagnostics.

The equivalent series resistance of oil ducts and pressboard barriers decide the value of R_0. Since the conductivity of the pressboard material is much lower than that of the oil under normal conditions, its value is predominantly decided by the high resistance of the barriers. The resistance is experimentally determined from the difference between the polarization and depolarization currents at long times since, according to the simplified equivalent representation, it is involved only during the polarization process (at sufficiently long times due to its very high value); during the depolarization process it is bypassed due to an applied short circuit (the test procedure is described in the following subsection). C_0 is determined by dividing the capacitance value, obtained through conventional measurements, by the effective dielectric constant of the insulation system.

14.5.2 PDC and RVM techniques

***PDC technique*:** Both moisture in dielectrics and products of aging influence the polarization and conduction processes. The exact correlation between the measured response and the fundamental polarization/depolarization processes inside the dielectric is not yet perfectly understood. A polarization current flows when dipoles tend to align in the direction of the applied field. The dipoles return to their original states as a part of the relaxation process when the field is removed and the dielectric is short circuited. These charging (polarizing) and discharging (depolarizing) currents, which contain information about the geometric structure and material properties of the dielectric, are analyzed in the PDC method.

The method involves dielectric spectroscopy in the time domain. It is a sophisticated version of the insulation resistance measurement. A DC step voltage is applied to a dielectric under investigation; the duration of the voltage application is sufficiently long (typically 500 or 1000 seconds). A corresponding charging current is measured, which is a function of polarization processes and conductivity of the dielectric. When the voltage is removed and the dielectric is short circuited, a discharging current flows, whose source is the previously activated polarization.

For PDC measurements, the excitation voltage is generally applied to the HV winding and the relaxation currents are measured on the LV side of the transformer. A reference data base has to be generated by a number of tests on cellulose samples with known moisture content. The depolarization current plot then can be used to obtain an estimate of the moisture content in the oil and in the solid insulation using the calibrated data. When polarization and depolarization

currents are plotted with respect to time, a comparison between them helps to assess the condition of the insulation.

RVM: This method tries to interpret the behavior of the insulation system when not fully discharged during the depolarization process, and empirically determines the moisture content. It involves an additional step compared to the PDC method. During the DC excitation period, a polarization current flows through the test object. Water molecules present in it are polarized in the direction of the applied DC field. Afterward, for a certain amount of time (which is shorter than the charging time), the object is short circuited; a depolarization current flows during this discharging operation. Subsequently, a recovery or return voltage is measured under an open-circuit condition; the magnitude of the voltage depends on the relaxation of the remaining polarization which in turn is a function of the energy stored in the water (polar) molecules. The entire procedure is repeated for different charging times in order to obtain meaningful diagnostic data. Measurements are carried out with different charging-discharging periods, and the peak recovery voltage and its initial rate of rise are analyzed as a function of the charging period. The charging period (t_c) is typically kept double of the discharging or short-circuit period (t_d) in these measurements, which gives the method an experimental/empirical character. The recovery voltage is high for small t_c (and t_d) values due to an incomplete depolarization condition and the corresponding available energy [38]. The peak values of the recovery voltage plotted as a function of the charging time gives a characteristic curve called polarization spectrum. It takes relatively a long period of time to generate the characteristics.

If the short circuit is removed when the depolarization process is incomplete, and a voltmeter is connected across the dielectric in the RVM technique, the initial voltage measured by it is zero since C_0 immediately discharges at the start of the depolarization process. The measured recovery or return voltage then steadily increases to a value which is a function of the residual polarization and the corresponding stored energy in the R_i-C_i branches at time t_d. The magnitude of the voltage is the resultant of the residual voltages in the polarization capacitances (all C_i elements).

The polarization/depolarization currents and the recovery voltage are shown as a function of time in Figure 14.4. The instrument used should be able to measure currents in nA/pA range. Unlike in the RVM technique, the time periods for measurements of polarization and depolarization currents are generally kept same in the PDC method.

During the polarization process, the capacitance of an individual *R*-*C* shunt branch is charged to a voltage,

$$V_i = V_0 \left(1 - e^{-(t/\tau_i)}\right), \tag{14.6}$$

where $\tau_i = R_i C_i$ is the time constant associated with i^{th} shunt branch.

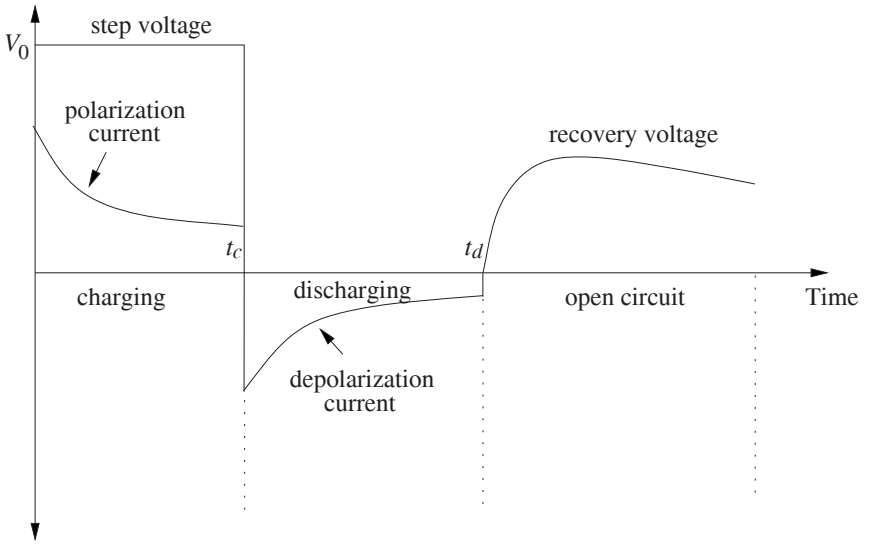

Figure 14.4 Polarization/depolarization currents and recovery voltage.

When the voltage source V_0 is removed and the dielectric is short circuited, a depolarization current flows from each of these shunt branches into the short-circuit (refer Figure 14.3). The depolarization current is a result of various relaxation processes appearing at different locations within the dielectric. The exponentially decaying depolarization current components can be summed up to give the total depolarization current as

$$I_d = \sum_{i=1}^{n} \frac{V_i}{R_i} e^{-(t/\tau_i)} \tag{14.7}$$

where, the time t is measured from the instant at which the short circuit is applied. An exponential curve fitting technique can be used to determine the values of the circuit parameters R_i and C_i [39]. Usually, about 5 to 10 R_i-C_i branches are chosen to represent the depolarization process. The depolarization current is then equal to the sum of the corresponding components of the branch currents. The last part of the measured depolarization current is assumed to be solely due to the largest time constant branch, which enables determination of its resistance and capacitance elements by a curve fitting technique. The determined largest time-constant component is deducted from the depolarization current, and the process is repeated to determine the elements of the second largest time-constant branch. The procedure is continued until the parameters corresponding to the smallest time-constant are computed [39].

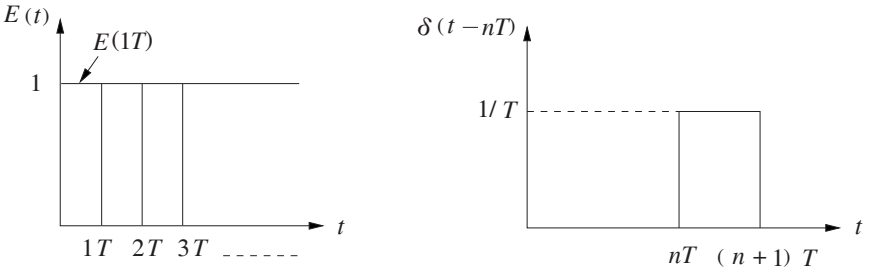

(a) Unit step function (b) Rectangular pulse

Figure 14.5 Step electric field.

14.5.3 Time domain response

In practice, dielectric systems are subjected to various time varying electric fields. The dielectric response to such excitations is influenced by time-dependent polarization processes [34]. The polarization vector, $P(t)$, lags with respect to the electric field, $E(t)$, due to a complex nature of the polarization phenomenon. In a dielectric the electric flux density vector $D(t)$ is given by

$$D(t) = \varepsilon_0 E(t) + P(t) \tag{14.8}$$

where ε_0 is the permittivity of free space and

$$P(t) = \varepsilon_0 \chi(t) E(t) \tag{14.9}$$

where $\chi(t)$ is the susceptibility of the dielectric material which contains information of different kinds of polarization processes.

Equation 14.8 is the same as Equation 12.36 with a difference that the vectors are explicitly shown as time-dependent quantities (here the vectors are not represented by boldface letters for simplicity). The first term in the equation is the induced charge density due to free space, which follows the electric field instantaneously. On the other hand, the second term follows the field with a delay on account of intricate polarization processes in the material medium.

Generally, a step electric field is applied to a dielectric system to investigate its polarization phenomenon and the state of its condition. Figure 14.5 (a) shows a unit step electric field which is approximated by a discrete function, consisting of continuous rectangular constant sections each of width T and amplitude unity,

$$E(t) = E(nT), \text{ where } nT \le t \le (n+1)T \text{ for all } n.$$

In Figure 14.5 (a), if the waveform is arbitrary, then T should tend to zero for a correct representation of $E(t)$. Further, $E(t)$ can be written as

$$E(t) = \sum_{n=0}^{\infty} E(nT)\,\delta(t-nT)\,T \tag{14.10}$$

where $\delta(t-nT)$ is a rectangular pulse of width T and amplitude $1/T$ as shown in Figure 14.5 (b), having unit area [40]. For example, from Equation 14.10,

$$E(t)\big|_{1T} = E(1T)\times\delta(t-1T)\times T = E(1T)\times\frac{1}{T}\times T = E(1T).$$

Let the response to a unit pulse $\delta(t-nT)$ be $f(t-nT)$. If $E(t)$ in Equation 14.10 is applied to a dielectric system, its response $P(t)$ can be expressed as

$$P(t) = \varepsilon_0 \sum_{n=0}^{\infty} E(nT)\,f(t-nT)\,T. \tag{14.11}$$

In Figure 14.5 (b), as $T \to 0$, $1/T \to \infty$, the pulse has unit area and it is then called impulse or Dirac delta function. Thus for a very small value of the pulse width (T), we can write $nT = \tau$ and $T = d\tau$, and Equation 14.11 becomes

$$\begin{aligned} P(t) &= \lim_{T\to 0} \varepsilon_0 \sum_{n=0}^{\infty} E(nT)\,f(t-nT)\,T \\ &= \varepsilon_0 \int_0^{\infty} E(\tau)\,f(t-\tau)\,d\tau. \end{aligned} \tag{14.12}$$

And if the upper limit is at some arbitrary time t,

$$P(t) = \varepsilon_0 \int_0^{t} E(\tau)\,f(t-\tau)\,d\tau.$$

Since a step voltage is applied with amplitude E_0 for any time instant greater than zero,

$$P(t) = \varepsilon_0 E_0 \int_0^{t} f(t-\tau)\,d\tau. \tag{14.13}$$

From Equations 14.9 and 14.13, it is evident that [41]

$$f(t) = \frac{d\chi(t)}{dt}\,. \tag{14.14}$$

Now in the time-domain diagnostic techniques (RVM and PDC), $E(t) = E_0\,1(t)$. Using Equation 14.13, $D(t)$ given in Equation 14.8 is modified to

$$D(t) = \varepsilon_0 E_0 \, 1(t) + \varepsilon_0 \, E_0 \int_0^t f(t-\tau) d\tau. \tag{14.15}$$

The polarization current density has two components: the conduction and displacement current density components (refer to Chapter 12 for a detailed discussion on these two components),

$$\begin{aligned} J_{pol}(t) &= \sigma_0 E_0 + \frac{dD(t)}{dt} \\ &= \sigma_0 \, E_0 + \varepsilon_0 E_0 \, \delta(t) + \varepsilon_0 E_0 \frac{d}{dt} \int_0^t f(t-\tau) d\tau. \end{aligned} \tag{14.16}$$

The first term represents the steady-state current density at infinite time due to the conductivity of the dielectric material (at very long times, the other components of the current density decay to zero). The Dirac delta function appears in the second term of Equation 14.16 because the time derivative of a unit step function is the Dirac delta function. Mathematically,

$$\int \delta(t) dt = 1 \text{ which implies } \frac{d\left(1(t)\right)}{dt} = \delta(t). \tag{14.17}$$

Since, $\frac{d}{dt} \int_0^t f(t-\tau) d\tau = f(t)$, Equation 14.16 becomes

$$\begin{aligned} J_{pol}(t) &= \sigma_0 \, E_0 + \varepsilon_0 E_0 \, \delta(t) + \varepsilon_0 E_0 f(t) \\ &= \sigma_0 E_0 + \varepsilon_0 E_0 \, (\delta(t) + f(t)). \end{aligned} \tag{14.18}$$

The first term on the right side of Equation 14.18 gives the conduction current density in a dielectric system and this is the steady current at infinite time. In the electric equivalent circuit of Figure 14.3, this represents the insulation resistance R_0. Its value can be calculated from the difference in the polarization and depolarization currents at long times as explained previously. The second term is the instantaneous response of the system due to "free space" in the volume of the dielectric material [34], and hence this component cannot usually be measured. In the equivalent circuit, this corresponds to the geometric capacitance C_0 which is equal to C_m / ε_r where C_m is the capacitance measured between the two terminals of the dielectric material with ε_r as its dielectric constant. For a composite dielectric system, the effective value of the dielectric constant should be used. The last term is due to the material medium, which cannot follow instantaneously the step function electric field. This term contains all the information of the different polarization processes in the dielectric material. In the equivalent circuit, the term is represented by the parallel R_i–C_i

branches, each of them corresponding to a distinct polarization process. As explained in Section 12.2.7 of Chapter 12, when a dielectric is placed in an electric field, there are two sets of lines of electric force in it. One that would exist in free space and the other that corresponds to the induced charges on the plates due to the polarized dielectric. The second set of lines is set up with a time delay; the phenomenon is manifested in terms of the time constants associated with the parallel R_i–C_i branches.

In other words, we have split the response into three terms in Equation 14.18, the first representing the conductivity, the second corresponding to the free space, and the last accounting for the intricate polarization processes in the dielectric material. It should be noted that, there is no resistance in series with C_0 in the equivalent circuit of Figure 14.3 meaning thereby that its charging is theoretically instantaneous (in practice the charging of C_0 and the decay of the current through C_0 is not instantaneous due to a source resistance). This current cannot usually be measured since it decays to zero before the measuring instrument can respond.

Therefore, after neglecting this second component and multiplying Equation 14.18 by the cross-sectional area A of the dielectric, we obtain

$$I_{pol}(t) = C_0 V\left(\frac{\sigma_0}{\varepsilon_0} + f(t)\right) \tag{14.19}$$

where C_0 and V is the capacitance and the voltage across the dielectric test specimen, respectively, and $V = E_0 d$, d being the depth of the dielectric. Substituting $C_0 = \varepsilon_0 A/d$, the first term in the above equation reduces to V/R_0, which is the current flowing through R_0 in the equivalent circuit of Figure 14.3. The term $f(t)$ represents the parallel R_i–C_i branches of the circuit.

If after time T_c (charging time), the specimen is short-circuited, a depolarization current flows. If we take the instant of application of the short circuit as the reference ($t = 0$), the total dielectric response can be obtained by using the superposition principle for which the short circuit can be represented by two equal and opposite voltage sources in series, giving [34]

$$I_{depol}(t) = C_0 V\left[f(t) - f(t + T_c)\right]. \tag{14.20}$$

14.5.4 Diagnostics

***PDC Method*:** The conditions of oil and cellulose insulation can be correlated to the parameters of the smallest time constant and the largest time constant, respectively, with reference to the circuit in Figure 14.3. A low time constant of the oil is due to high mobility of its charge carriers [39]. A better condition of the liquid and solid insulations increases the resistance and decreases the capacitance in the branches representing them; the magnitudes of the relaxation (polarization and depolarization) currents are also lower in the respective time periods. The

measurements on reclaimed oil samples in [39] showed that an improved oil condition reduced the magnitudes of the currents during the initial period; the longer time values were affected marginally since the oil reclamation dried the solid insulation to a limited extent. Thus, the oil conductivity affects the initial values of polarization and depolarization currents while the solid conductivity influences their nature at long times. Since the polarization and depolarization currents have different dependencies on the solid insulation conductivity, they have different time dependencies at longer times (the effect of the conductivity is marginalized due to the applied short circuit during the depolarization).

If we assume that the equivalent circuit in Figure 14.3 is a reasonably accurate representation, during the depolarization process the resistance R_0, representing mainly the cellulose resistance, is bypassed by the short circuit. Thus the presence and absence of the resistance during the flow of polarization and depolarization currents, respectively, leads to the different time dependencies. As indicated in Figure 14.6, a difference between them at short times is indicative of a higher oil conductivity (poor oil quality), whereas moisture content/aging of cellulose can be estimated to be on a higher side if the two curves depart from each other at long times.

***RVM*:** For a used/aged insulation system, the polarization spectrum shifts towards the left as shown in Figure 14.7, indicating low time-constants. It should be remembered that a high oil conductivity value as well as a moist cellulose condition results in the same effect [43] which may lead to a wrong diagnosis about the moisture content in the cellulose insulation. Thus, RVM diagnosis may be strongly influenced by the oil resistivity which may mask the effect of cellulose moisture on the measured quantities. The PDC technique is better in correlating measurements with the cellulose moisture.

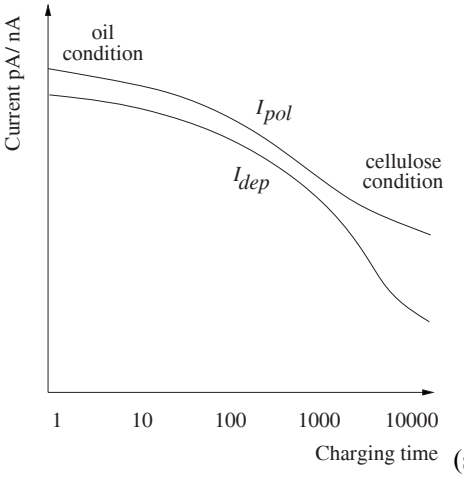

Figure 14.6 PDC curves: influences of oil conductivity and moisture. in cellulose [37, 42].

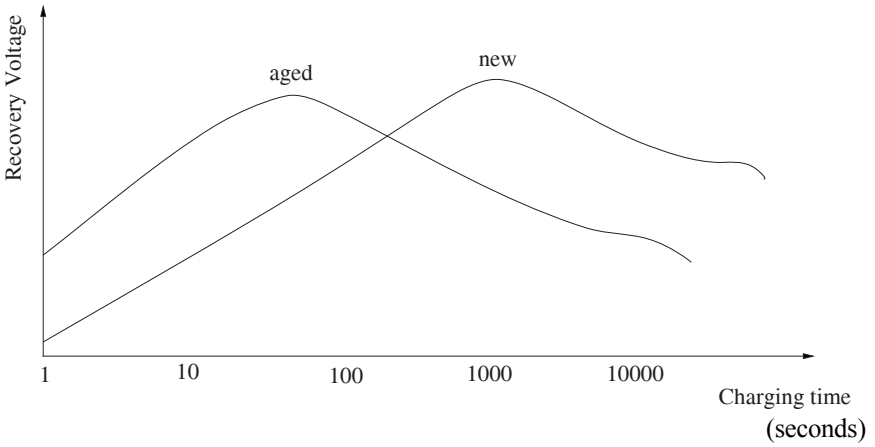

Figure 14.7 Polarization spectrums for new and aged insulation systems [42].

Polarization and depolarization processes are fast for high moisture content. Therefore, the insulation system polarizes and depolarizes almost completely within the usually chosen values of t_c and t_d values. Since the residual polarization is close to zero at the end of the short-circuit period, very low recovery voltages are measured. Therefore, the polarization spectrum shifts to smaller time constants for high moisture levels.

The polarization spectrum obtained from the RVM technique can be correlated to variation of the polarization current with the charging period [42]. Typically two peaks are observed in the polarization spectrum as explained later. The dominant maximum in the spectrum corresponds to the major exponential descend of the polarization current with the charging time. Also, the position of the dominant maximum is directly related to the time constant of the interfacial polarization between oil ducts and pressboard barriers [38, 39]. The time constant changes with the oil conductivity and the geometry (different proportions of oil and cellulose); this fact needs to taken into account while diagnosing moisture content in the cellulose insulation. The branches in the equivalent circuit with intermediate time constants represent the interfacial polarization between the oil ducts and pressboard-barriers/paper-insulation.

If the oil conductivity and geometrical details are not accounted correctly the RVM based diagnostics can be erroneous [44]. The estimation of moisture content in solid insulation may be incorrect if the diagnosis is based on the dominant peak and its position in the polarization spectrum. The presence of a subdominant peak may correspond to polarization phenomena in solid insulation, and hence the corresponding time constant should be used in conjunction with the calibration data for the moisture estimation. The second local peak has also been found to occur in the case of high oil conductivity (abnormal water content in oil); diffusion of water from oil into paper forms a moist layer at the surface of the

paper, which is responsible for the additional peak in the polarization spectrum [38]. Thus, whenever a subdominant peak is observed, the RVM diagnostics should be done with a properly calibrated data. Temperature has also been found to influence the accuracy; a suitable correction factor may have to be used.

***R_0 and C_0 Parameters*:** R_0 is indicative of the overall health of the insulation system. Its low value indicates a moist and/or aged condition. The resistance influences the polarization current at longer times; the current is lower for a better insulation condition. On the other hand, the depolarization current is almost independent of the resistance since the short circuit during the discharge period bypasses it and takes all the discharging currents from the various polarization capacitances. Thus, the resistance does not participate in the depolarization process. If the equivalent circuit of Figure 14.3 can be considered a good enough approximation, the resistance can be determined from the difference between the polarization and depolarization currents at long times. From the discussion, it is also apparent that R_0 should be affecting the subdominant peak, if any, occurring at a longer time rather than the dominant peak occurring at a shorter time in the polarization spectrum.

C_0 depends on the geometry of the insulation system and its value affects the polarization/depolarization current and the polarization spectrum. Reference curves, generated using an insulation system having different dimensional details, may have to be normalized with the geometric capacitance for the purpose of diagnostics.

14.5.5 Polarization index

We can use the equivalent circuit of Figure 14.3 to explain the basis of polarization index (PI) test described in Section 14.1.2. When a DC voltage is applied to the insulation system under investigation, the insulation resistance and PI values are a function of three independent current components:

Capacitive charging current (I_C): This corresponds to the capacitive charging current flowing through C_0 of the equivalent circuit. If the source resistance is very small, the capacitance is charged rapidly and the current decays quickly. The current disappears fast before being noticed for low capacitance test specimens.

Resistive leakage current (I_R): It represents the conduction current density on account of free charges in the insulation under test. The current is very small for good insulation, which remains at a constant value in the steady state condition. For bad insulation its value can be fairly large, which may increase with time because of the corresponding losses and consequent temperature rise, since insulating materials have negative temperature coefficient of resistance. The total current equals this component after the other two components decay to negligible values.

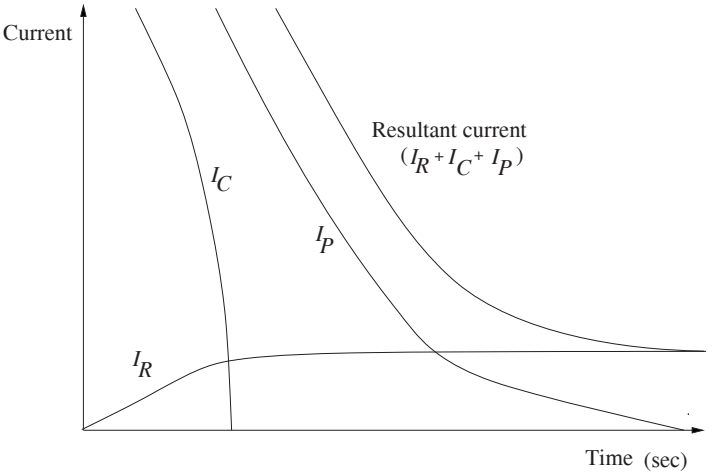

Figure 14.8 Currents components during PI test.

Polarization current (I_P): It is also termed the dielectric absorption current. The current components flowing through the R_i-C_i branches in the equivalent circuit add up to give the polarization current. In a simplified representation, the current is represented by just one R_i-C_i branch. I_P decays eventually to zero at a rate which is a function of the state of the insulation; a faster decay is observed for an insulating material which is aged, moist or contaminated.

The three components are shown in Figure 14.8 as a function of time. Now let us understand PI in the context of their variations with time. It is the ratio of the measured insulation resistance (*IR*) after 10 minutes to that measured after 1 minute, i.e., IR_{10}/IR_1. For good insulation, since the polarization current drops slowly and dominates over the conduction (resistive leakage) current, the measured resistance increases continuously in the time period of interest, and the measured PI value is higher (≈ 2.0). For bad insulation, on the contrary, a high and constant value of the conduction current masks the polarization current, giving a PI value close to 1.0.

14.6 Frequency Domain Dielectric Response Method

14.6.1 Frequency domain spectroscopy (FDS)

This is a diagnostic method in the frequency domain, in which measurements of the capacitance or the dissipation factor (tanδ) of the test specimen are typically done over the frequency range of 0.1 mHz to 1 kHz. Thus the method is an extension of tanδ and capacitance tests conducted at the power frequency (50/60 Hz). Any error in FDS measurements can be known easily by comparing the

measured value at the power frequency with that of the conventional tests. Measurements done in a wide frequency range help in making a distinction between the oil and cellulose properties as they influence different frequency zones. A single value of a diagnostic parameter at the power frequency in the conventional tests may not give a conclusive indication of a potential problem. Furthermore, there is always a possibility of making a wrong interpretation of high moisture content based on the power factor reading when the culprit actually is high oil conductivity [7].

The test involves the application of a sinusoidal voltage with variable frequency to the insulation system under investigation. The applied voltage, the current drawn, and the phase angle between these two phasors are measured to determine its capacitance and tanδ as a function of frequency. For a capacitive test object, the real and imaginary components of the complex permittivity are first determined from the FDS measurements and then the frequency dependent capacitance or dissipation factor is calculated. We will now first discuss a few basics which govern a frequency domain response before elaborating the diagnostic aspects of the method.

14.6.2 Frequency domain response

Using Equation 14.16, the current density in the frequency domain is obtained as

$$\hat{J}(\omega) = \sigma_0 \hat{E}(\omega) + j\omega \hat{D}(\omega)\,, \tag{14.21}$$

where

$$\hat{D}(\omega) = \varepsilon_0\, \hat{E}(\omega) + \hat{P}(\omega). \tag{14.22}$$

Equation 14.9 can also be rewritten in the frequency domain,

$$\hat{P}(\omega) = \varepsilon_0\, \hat{\chi}(\omega)\, \hat{E}(\omega). \tag{14.23}$$

By substituting Equations 14.22 and 14.23 in Equation 14.21, we have [41]

$$\hat{J}(\omega) = \sigma_0\, \hat{E}(\omega) + j\omega\varepsilon_0 (1 + \hat{\chi}(\omega))\hat{E}(\omega) \tag{14.24}$$

Now,

$$\hat{\chi}(\omega) = \chi'(\omega) - j\chi''(\omega). \tag{14.25}$$

The minus sign of the imaginary part of Equation 14.25 is due to the fact that the polarization vector lags behind the electric field intensity by some angle in the dielectric materials.

Since $\hat{\varepsilon}_r(\omega) = 1 + \hat{\chi}(\omega)$ and by using the relation given in Equation 14.25, we obtain

$$\begin{aligned}\hat{\varepsilon}_r(\omega) &= 1 + \left(\chi'(\omega) - j\chi''(\omega)\right) \\ &= \left(1 + \chi'(\omega)\right) - j\chi''(\omega) \\ &= \varepsilon_r'(\omega) - j\varepsilon_r''(\omega)\end{aligned} \tag{14.26}$$

It should be noted that in a dielectric material, due to the existence of several polarization processes which are weakly coupled to each other [34], we have

$$\chi'(\omega) = \sum_n \chi_n'(\omega) \qquad \text{and} \qquad \chi''(\omega) = \sum_n \chi_n''(\omega)$$

where n is the number of different polarization processes in the material. Therefore, Equation 14.24 is modified to

$$\hat{J}(\omega) = \left(\sigma_0 + j\omega\varepsilon_0\left[\varepsilon_r'(\omega) - j\varepsilon_r''(\omega)\right]\right)\hat{E}(\omega). \tag{14.27}$$

Rearranging, we have

$$\hat{J}(\omega) = j\omega\varepsilon_0\left[\varepsilon_r'(\omega) - j\left(\varepsilon_r''(\omega) + \frac{\sigma_0}{\omega\varepsilon_0}\right)\right]\hat{E}(\omega). \tag{14.28}$$

$\tan\delta$ is the ratio of the imaginary part of the permittivity to its real part (see Section 12.2.7). Hence, we have

$$\tan\delta(\omega) = \frac{\left(\varepsilon_r''(\omega) + \dfrac{\sigma_0}{\omega\varepsilon_0}\right)}{\varepsilon_r'(\omega)} = \frac{\varepsilon_0\left(\varepsilon_r''(\omega) + \dfrac{\sigma_0}{\omega\varepsilon_0}\right)}{\varepsilon_0\varepsilon_r'(\omega)} = \frac{\varepsilon''(\omega)}{\varepsilon'(\omega)}. \tag{14.29}$$

In this model, the losses due to conductivity of the dielectric and the losses during the polarization/depolarization process are represented by $\sigma_0/\omega\varepsilon_0$ and $\varepsilon_r''(\omega)$ respectively. Contributions to the total loss by these two terms cannot be differentiated or separated by a measuring instrument [34, 41]; however, they help in understanding the two different processes occurring in the dielectric material. The term $\varepsilon_r''(\omega)$ represents the losses occurring in the R_i elements of the equivalent circuit of Figure 14.3. ε' and ε'' are the real and imaginary components of the dielectric constant. For a simple *R-C* representation of a dielectric material with frequency-independent material properties,

$$\tan\delta = \frac{\sigma_0}{\omega\varepsilon_0\varepsilon_r}. \tag{14.30}$$

which is the ratio of the conduction current density to the displacement current density (Equation 12.76).

The frequency dependent complex permittivity obtained using FDS can be

correlated to the time-dependent response function measured in PDC/RVM techniques through Fourier transformation [44]. If capacitance is used as a diagnostic parameter, for an applied AC voltage at frequency ω, its measured value is a complex quantity with its real and imaginary components directly related to the corresponding components of the complex permittivity [45]:

$$C(\omega) = C'(\omega) - jC''(\omega) = k\left[\varepsilon'(\omega) - j\varepsilon''(\omega)\right]. \tag{14.31}$$

Here, constant k is a function of geometry; for a parallel plate capacitor configuration, it is the ratio of the plate area of the capacitance to the distance between the two plates. Hence, the tanδ expression can be rewritten as

$$\tan\delta = C''(\omega) / C'(\omega). \tag{14.32}$$

14.6.3 Diagnostics

The insulation structure between windings consists of barriers, spacers and oil. In the FDS method, an effective dielectric constant of such a composite insulation structure is determined using an *X-Y* model [44, 46],

$$\varepsilon_{eff} = \frac{Y}{\dfrac{1-X}{\varepsilon_{spacer}} + \dfrac{X}{\varepsilon_{barrier}}} + \frac{1-Y}{\dfrac{1-X}{\varepsilon_{oil}} + \dfrac{X}{\varepsilon_{barrier}}} \tag{14.33}$$

where X is the fraction of the length occupied by the barriers in the radial direction and Y is the fraction of the length occupied by the spacers in the circumferential direction (a similar approach has been used to determine the capacitance between consecutive disks through Equation 7.17). ε_{eff} is a complex quantity since the permittivities of the three materials in the equation are complex, and the real and imaginary components of these three quantities are frequency-dependent, which can be determined experimentally [46].

Spacers and barriers are made from pressboard (*pb*) material, hence $\varepsilon_{spacer} = \varepsilon_{barrier} = \varepsilon_{pb}$. The effective permittivity becomes,

$$\varepsilon_{eff} = \varepsilon_{pb} Y + \frac{1-Y}{\dfrac{1-X}{\varepsilon_{oil}} + \dfrac{X}{\varepsilon_{pb}}}. \tag{14.34}$$

As discussed in Section 12.2.7, it is reasonably accurate to express ε_{oil} in terms of the constant real component $(=2.2)$ and the frequency-dependent imaginary component in conformance with measured values. On the other hand, both parts of ε_{pb} are frequency dependent and an elaborate mathematical model is generally required to model intricate polarization processes.

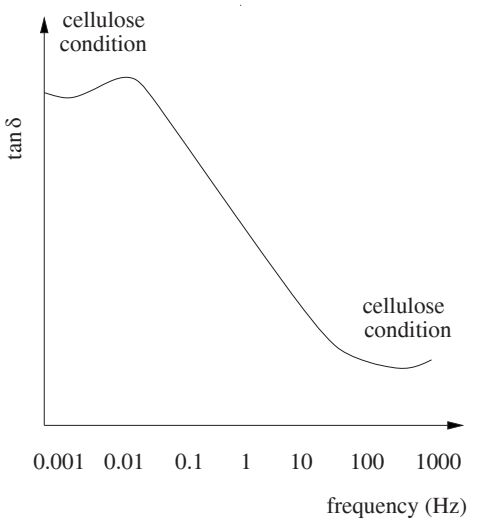

Figure 14.9 Interpretation of dissipation factor measurment [43, 46].

The effective permittivity as expressed in Equation 14.34 is used to calculate the frequency-dependent capacitance which is compared and best fitted to the corresponding measured response; the fitted model then gives the oil conductivity and the moisture content in the solid insulation. Alternatively, tanδ measurements can be used for the purpose. A typical plot of tanδ versus frequency is shown in Figure 14.9. Moisture in cellulose influences both low and high frequency regions. A higher moisture level increases tanδ values in these regions. The middle part of the curve having a sharp gradient is mainly affected by oil conductivity variations. For an insulation system with an oil-pressboard interface, a charge accumulation occurs at the pressboard surface resulting in a prominent peak in the FDS plot at low frequencies [43] — the hump to the left side of the sharp gradient. Temperature also affects the curve; a higher temperature shifts it towards higher frequencies.

The frequency-dependent real and imaginary components of the complex permittivity can also be used as diagnostic parameters. A significant increase in both ε' and ε'' is generally observed at frequencies lower than 100 Hz for aged insulation systems. An extensive experimental research work on paper and pressboard samples has been reported in [47]. The pressboard and paper samples exhibit similar FDS characteristics. It has been generally observed that for high moisture contents the curves of both ε' and ε'' shift toward higher frequencies and the minimum observed value of ε'' increases. The curve of ε' is almost unaffected by moisture in the frequency range beyond 100 Hz, and in this range the magnitude of ε' is many times higher than that of ε''. However, below 0.1 Hz the two magnitudes become comparable and ε'' may exceed ε' as the

frequency further decreases [46, 47] even at an acceptable level of moisture content, and ε'' can become substantially higher than ε' at high moisture levels.

Time-domain PDC measurements are performed quickly but they provide low frequency information. On the other hand, although the FDS method requires a much longer time period for measurements in the very low frequency range, the data up to the kHz range is available for the analysis. It is possible to combine the best of the two approaches in a single measurement setup [48] with a shorter measurement time by operating in the time domain for a very low frequency range and in the frequency domain for remaining frequencies up to a few kHz. The time domain data is processed to get the corresponding information in the frequency domain so that the characteristics in the entire frequency range are obtained.

14.7 Detection of Winding Displacements

14.7.1 Conventional methods

The loss of mechanical integrity might occur due to short-circuit forces, aging, winding shrinkage or transportation/relocation of transformers. Various methods have been used for detecting core and winding deformations. The one based on leakage reactance measurements is the simplest. However, it is an offline method requiring de-energization of the transformer.

This technique is sensitive to radial deformations as compared to other irregularities. A change in the reactance of more than certain percentage for any phase indicates a winding deformation as discussed in Section 6.9.

A change in the measured excitation (no-load) current can be used to detect core damages. However, this approach is not capable of detecting winding deformations and is highly influenced by residual magnetism if present.

14.7.2 Frequency response of stray losses

There have also been some efforts to correlate winding looseness with the frequency response of stray losses (FRSL) over a range of frequencies up to a few hundred Hz [49]. The test circuit for the measurements is the same as for the impedance measurement. In this test, an AC voltage source with variable frequency is used to measure the complex short-circuit impedances of three phases separately as a function of frequency. Analysis of the resistive part of the impedance of each phase, which represents the corresponding stray loss, is done. Comparisons between the results of the three phases can also be done to detect any abnormalities. If one of the windings is deformed or displaced, the pattern of the leakage flux and the stray losses are modified; a corresponding change in the variation of the measured AC resistance with frequency occurs, thus providing useful diagnostic information. The resistance typically increases with a frequency exponent of 1.4 to 1.8 [49]; frequency exponents for different components of the stray losses in transformers have also been elaborated in

Section 5.1. The method is best suited for detecting short circuits between parallel strands [5, 49] since the measured stray losses can increase noticeably on account of higher eddy losses in the winding. On the contrary, the usual impedance measurement test may not be able to detect this problem as the leakage field is not appreciably affected. The FRSL test, however, is not sensitive to minor displacements of windings since a limited range of lower frequencies is used.

14.7.3 Impulse frequency response analysis

The frequency response analysis (FRA) technique is a widely used method for detecting mechanical displacements of windings [50]. Its sensitivity is better than the previously discussed approaches. The frequency response of a winding can be obtained using a time-domain method (impulse FRA) or a frequency-domain method (swept FRA). The method has become popular in spite of its offline nature and skills required for interpretations. It essentially involves comparisons of measured data with reference signatures, and hence a consistent test procedure, including lead lengths, dispositions, etc., is an essential pre-requisite.

Impulse FRA (IFRA), also termed low voltage impulse (LVI) method, is adapted from the impulse test. The method has been in use in short-circuit laboratories for diagnosis but its use on site has been limited due to the difficulty in ensuring repeatability of the test procedures. The steepness of the applied voltage is adjusted to obtain a wide frequency band. Its main advantage is that, unlike in swept FRA (SFRA), it is possible to determine several transfer functions simultaneously. Its major disadvantages are inadequate data points at low frequencies, variations in precision due to different amounts of the injected power across the frequency range [51], and ambient noise affecting interpretation. The required instrumentation is also sophisticated. It, however, has a potential for online application with the impulse injected through the bushing tap.

14.7.4 Swept frequency response analysis (SFRA)

In this technique, the transfer function of a transformer winding is determined, which is essentially the plot showing the poles (or natural frequencies) as a function of frequency. The transfer function is compared with the corresponding reference signature (fingerprint) measured earlier. Changes in the overall shape and resonance frequencies (which occur due to changes of winding inductances and capacitances) are the key indicators of any winding displacement after a short circuit, aging or transport. The SFRA technique is preferred over the LVI method since the main problem with the LVI method is the difficulty in carrying out comparisons because the measurements are affected by ambient noise. SFRA can detect interturn faults because of its finer resolution in the low frequency band [51].

The main disadvantage of the SFRA technique is that each measurement requires a relatively long duration compared to the LVI method since the

measurements are carried out at discrete frequencies. It should be noted that both SFRA and LVI techniques are used to determine the transfer function of windings. In the former, the transfer function is determined by sweeping the frequency of an input sine wave, and no Fourier transformation is required. In the latter time-domain method, the transfer function is estimated from low voltage impulse test data, for which the waveforms of the input impulse voltage and the neutral current are converted into the frequency domain using Fourier transformation.

Many researchers have contributed to improving SFRA's applicability. The winding response can be measured in terms of its magnitude plot ($20\log (V_2/V_1)$), driving point impedance or transfer admittance; the magnitude plot (voltage ratio) method, being more sensitive to small deformations, is preferred [42]. The transfer function is dependent on the type of windings and their connections, terminal conditions, tap position, etc.

***SFRA procedures*:** The worldwide standardization activities for the SFRA test are underway [48]. Technical reports, a draft international standard and user manuals are available for the purpose. Generally, there can be variations in the selected frequency range, the number of frequency points chosen, and the type of connection employed by different users.

The end-to-end connection [50], the most popular one, is preferable when windings in transformers need to be checked individually. A swept frequency signal is applied to one end of the winding, and the output signal is measured at its other end. The health of the core can be diagnosed in this connection. In the second type of connection, called an end-to-end short circuit, the connections are similar to that of the previous one except for the fact that the corresponding secondary winding is short-circuited which in turn eliminates the effect of the core in the low frequency band. The response is influenced by the leakage inductance rather than the magnetizing inductance. The high frequency response is similar in both methods.

There are two other types of connections, capacitive interwinding and inductive interwinding, which are used for specific purposes. When the measurements are taken between two windings of a phase (with their other ends open circuited), the test checks the inter-winding capacitance. On the other hand when the other ends are grounded, the test checks the turns-ratio between the two windings.

A number of precautions need to be taken during the fingerprint and subsequent measurements, such as use of identical measuring circuits, impedances and testing instruments, employing shielded cable with lowest possible inductance, grounding of the shield, termination of test leads into their characteristic impedances to eliminate reflections, etc. Conclusions should not generally be based on just one set of SFRA readings; readings with alternative connections should be taken to substantiate them.

***SFRA curve characteristics*:** Figure 14.10 shows an SFRA magnitude plot (end-to-end connection) of a medium rating power transformer. The curve is

characterized by a typical pattern in which the first minimum corresponds to the resonance between the magnetizing inductance and the capacitance of the winding.

It is usually observed for the center-phase that the minimum in the SFRA curve is in the form of only one valley point (V-shape) in the low frequency region. On the other hand, there are two valley points (W-shape) in the SFRA curves of the end phases. The V-shaped minimum in the former case is slightly shifted to the left. The phenomenon is due to different magnetic lengths of the central phase and end phases. After the first minimum the curve shows an upward trend indicating capacitive behavior of the winding. It should be noted that a downward slope of the curve is indicative of inductive behavior, while an upward slope reflects a capacitive nature of the winding for a magnitude or admittance plot in the low frequency region; the trend will be opposite for an impedance plot. The magnitudes of the peak and valley points are mainly governed by the damping provided by lossy (resistive) elements. The mid frequency region is influenced by the inductances and capacitances of the winding. A number of dips and peaks can be observed in this region corresponding to parallel and series resonant conditions, respectively. The high frequency band also exhibits resonant conditions which are mainly influenced by the effect of bushing capacitances, lead inductances and stray capacitances.

***Types of comparisons*:** There are three kinds of comparisons: time-based (comparison with previously recorded signatures on the same winding), type-based (comparison with the SFRA curve of corresponding winding of another transformer of the same design and make), and phase-based (signatures of different phases of the transformer are compared). The time-based comparison is always preferred; if previous measurement records are not available, the other two types are used.

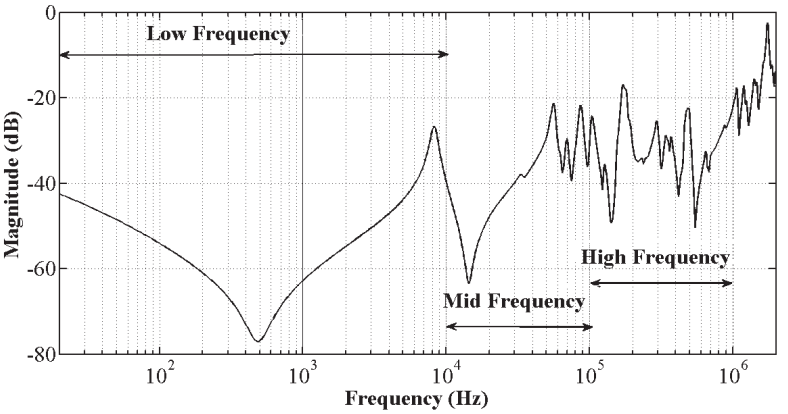

Figure 14.10 A typical SFRA signature (courtesy Reliance Power).

In the design-based comparison, it should be borne in mind that the center phase SFRA curve is different than that of the two extreme phases due to different magnetic path lengths as explained previously.

***Statistical techniques for ascertaining deviations*:** The frequency response measurement actually gives two curves, a magnitude plot and a phase plot. Although the phase plot has a good amount of information, it is difficult to use it for the diagnostic purpose. The graphical information contained in the magnitude plot is processed to determine one or more statistical indices for quantifying deviations from its reference signature.

Several statistical parameters have been proposed in the literature to identify deviations. Generally used statistical parameters [52] are correlation coefficient (CC), absolute logarithmic square error (ALSE), mean square error (MSE), root mean square error (RMSE), absolute deviation (DABS), and min-max (MM). When there is no deviation between two curves, the (ideal) values of CC, ALSE, MSE, RMSE, DABS and MM will be 1, 0, 0, 0, 0 and 1, respectively. Generally, these parameters are determined separately for three frequency regions (low, mid and high frequency bands). In practice, the parameters are used in a complementary way; any interpretation done using only one index can lead to erroneous conclusions. A few comments on their characteristics can be made [52]:

CC: Two data sets are said to be perfectly correlated (i.e., CC=1) if the two curves exactly overlap. This parameter is sensitive to sharp changes in the measured data with respect to the fingerprint data.

MSE: This index is calculated as the mean of the sum of squared deviations. The parameter is hypersensitive for deviations above one unit; deviations less than one unit are undermined.

DABS: This index is the average of the absolute difference between the individual data points. Its sensitivity towards large deviations is lower.

ASLE: This parameter is calculated by finding the average of sum of deviations between the log scaled readings of the two sets. Due to the logarithm, the scatter of its values reduces. The sensitivity of the ASLE and DABS parameters to differences in the data sets in some frequency bands may be reduced since an averaging operation is involved while calculating them.

RMSE and CSD: RMSE is just the square root of MSE for a large number of data points. CSD is a function of deviations of data points in the compared data sets from their respective average values. RMSE and CSD give similar values.

MM: For each pair of compared data points, low and high values are noted. MM is then calculated as the ratio of the sum of all low values to that of all the high values. Its sensitivity towards sharp deviations is high.

It is preferable to use the statistical parameters in a complementary way to identify deviations in SFRA data. In the absence of universally accepted values

of thresholds, the dependence on just one or two parameters may lead to wrong conclusions. Recently *t*-test was proposed in [52], which gives binary result (0 or 1); this feature can be useful in borderline cases when other statistical parameters do not exhibit similar trends. Furthermore, the *t*-test can be employed even when the sample size and/or the spot frequencies of the two SFRA data sets are different, for which the other parameters cannot be applied. It should be emphasized that an expert's opinion/intervention is usually required when the above statistical parameters are used since the parameters merely give an indication of the level of deviations; any further investigation to discern possible abnormalities/faults may involve a detailed technical analysis as discussed below.

***Deformation diagnostics*:** When statistical parameters indicate that there is an appreciable deviation, the probable irregularity inside the transformer has to be determined. Typically, such curves are split into four regions (low frequency, mid frequency, high frequency and very high frequency). A shape change or distortion in the low frequency region (up to 5000–10000 Hz) can be attributed to a core problem (e.g., residual magnetism, short-circuited laminations, mechanical displacements). Short-circuited turns also affect this zone since the main flux in the core is modified. The intermediate region, i.e., 10^4 to 10^5 Hz, responds to gross deformations/displacements of the winding. This region is governed by the resonances occurring between its inductances and capacitances. Finer and smaller winding irregularities influence the high frequency range in the MHz range. Winding leads and/or connecting leads used for the measurements influence the response in the very high frequency range. This band shifts upwards on the frequency scale for shorter lead lengths. It should be noted that this division into four regions is not sacrosanct. Also, the abovementioned core and winding problems can affect more than one region. Furthermore, these zones of frequency ranges are dependent on the transformer rating and size. For higher ratings, the zones shift to lower frequencies.

A number of researchers have attempted to correlate the effects of variations in dimensions and properties of the core, windings, connections and support structures on SFRA characteristics. The core greatly influences the low frequency region as compared to the high frequency zone. The effects of ungrounded core and multiple grounds are studied in [53]. Residual magnetism in the core affects the low frequency region significantly. Hence, SFRA measurements should not be performed immediately after de-energization of the transformer; some idle period must be allowed to eliminate the effect of core magnetization on the low frequency response [54]. The consequences of loosened turns, buckling phenomena, and axial displacements on mid and high frequency regions are experimentally demonstrated in [55].

Insulation diagnostics: SFRA can be used for the insulation diagnostics purpose [56]. The dielectric spectroscopy (FDS), which is being popularly used for the estimation of moisture content in solid insulation based on low frequency

measurements (0.1 mHz – 1 kHz), takes an appreciable amount of time. The SFRA measurements are typically carried out in 20 Hz – 10 MHz range, thus requiring lesser time. As elaborated in Section 14.6.2, the dielectric losses occurring in the insulation materials used in power transformers, due to the polarization and conduction phenomena, are taken into account by the imaginary part of the complex permittivity. Moisture content and aging affect the complex permittivity and SFRA signatures. High moisture content in the paper/pressboard insulation increases both real and imaginary parts of its complex permittivity; the real component is affected more. An increased value of the real part (and hence the capacitances of the equivalent ladder network) shifts the resonant peaks to the left on the frequency scale, whereas a higher value of the imaginary part reduces their magnitudes (due to increased losses) [56].

An increase in aging of the pressboard insulation leads to higher dielectric losses providing a greater damping effect. Thus, resonant peaks may get damped with the degradation of the cellulose material; however, the resonant peaks generally do not shift on the frequency scale since the real part is almost unaffected. Thus, in general, a deteriorated insulation condition affects the whole frequency range while we have already deliberated that the winding movements predominantly affect the mid and the high frequency response, making it possible to discriminate between the two causes using the SFRA technique [56]. An increase in temperature has also been found to affect the imaginary component more than the real component, and hence the temperature influences the damping of the resonant peaks.

Computations and simulations: Computer-based simulations are performed for aiding SFRA diagnostics. A ladder structure shown in Figure 7.17 is commonly used. Since the electric and magnetic fields coexist, and they are of distributed nature inside the transformer, for reproducing perfectly the fields and the SFRA response, it would be necessary to have infinite number of R, L and C elements. However, a reasonably accurate analysis of the ladder representation with a few sections is possible; in other words, it is practically sufficient to determine the first few dominant frequencies. Hence, although the simulated SFRA response does not generally match exactly with measurements (particularly at high frequencies), the ladder network approximation is reasonably accurate if the number of sections are chosen somewhat higher than the number of resonant frequencies of interest as discussed in Section 7.8.2.

An exhaustive parametric study can be done on the ladder network to find correlations between the variations of the values of lumped circuit elements (caused by deformations/displacements) and the natural frequencies. Minor axial and radial deformations are simulated by changing the sectional series capacitance (C_s) and the sectional ground capacitance (C_g), respectively [57]. C_s plays a dominant role in deciding the shape of the SFRA curve and the natural frequencies.

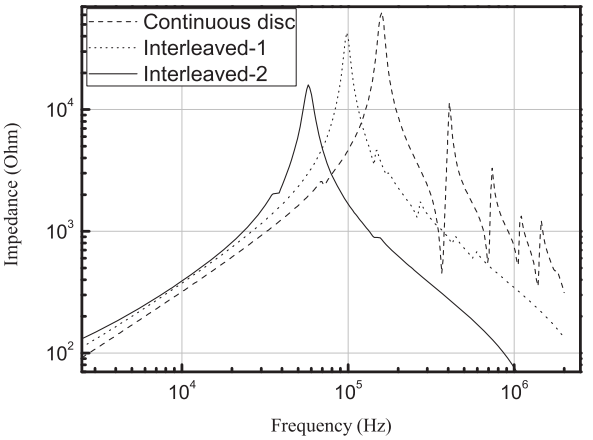

Figure 14.11 FRA curve of three coils with different series capacitance.

An increase in C_s shifts all the natural frequencies towards the low frequency zone and vice versa [58, 59, 60]. It influences the response for frequencies above 100 kHz, whereas below this frequency, its effect is not appreciable.

The winding design plays a key role in deciding the nature of the SFRA signature. Figure 14.11 shows FRA signatures of three coils, viz. continuous disk (CD), interleaved-1 and interleaved-2 coils, obtained in terms of the driving point impedance by using an LCR meter. The frequency is swept from 10^4 Hz to 2 MHz. The first resonance frequency of the CD coil is greater than 10^5 Hz, it is equal to10^5 Hz for the interleaved-1 coil, and it is less than 10^5 Hz for the interleaved-2 coil. This behavior can be logically related to the values of effective series capacitance $(C_S)_{\text{eff}}$ of the three coils; $(C_S)_{\text{eff}}$ of the interleaved-2 coil > $(C_S)_{\text{eff}}$ of the interleaved-1 coil > $(C_S)_{\text{eff}}$ of the CD coil. One more interesting point to note is that the magnitude of the first resonance peak is higher for the CD coil, it is intermediate for the interleaved-1 coil, and it is lowest for the interleaved-2 coil. The CD coil has more resonances compared to the interleaved-1 and interleaved-2 coils. This is mainly due to the fact that the CD coil has higher value of the distribution constant α ($=\sqrt{C_G/C_S}$), as defined in Section 7.1, compared to the other two coils. Due to lower series capacitances of CD windings, their SFRA signatures have, in general, more resonant peaks, and the positions of the resonant frequencies are toward the right as compared to those of the interleaved windings.

Like C_s, a change in C_g shifts the curve to the right or to the left side when it is decreased or increased, respectively. Variations in self and mutual inductances predominantly affect the low frequency zone (<100 kHz). For the frequencies between 100 kHz and 1 MHz, the resonances occurring between the involved inductances and capacitances decide the shape of the SFRA response and the

locations of natural frequencies. The resistance of the winding decides the damping effect and changes the peak values of the poles and zeros. Using such a generated knowledge base, one can infer the most probable type of deformation. Table 14.1 summarizes the effects of the various influencing parameters on the SFRA signature.

Alternatively one can take a network synthesis route [61]. From the measured SFRA data, the sectional parameters of the ladder network can be estimated and used for the diagnostics purpose. In another approach, distinct circuits have been proposed for various frequency regions [62]. The approach employs four circuit topologies; each topology is valid for a particular frequency band. In one of the recently proposed methods, frequency dependent core and winding characteristics have been incorporated using effective complex permeability values which are derived through FEM simulations [63].

Table 14.1 Effect of Variations in Parameters on SFRA Signatures

Parameter	Change	Frequency of first pole	Distance between consecutive natural frequencies	Effect on peak value of poles and zeros	Effect for frequencies lower than 100 kHz	Effect for frequencies Higher than 1 MHz	Shifting of graph
C_s	↑	↓	↓	Yes	–	Yes	←
	↓	↑	↑	Yes	–	Yes	→
C_g	↑	↓	–	Yes	–	Yes	←
	↓	↑	–	Yes	–	Yes	→
L	↑	↓	↓	Yes	Yes	–	←
	↓	↑	↑	Yes	Yes	–	→
R	↑	–	–	↓	–	–	–
	↓	–	–	↑	–	–	–

Nomenclature

↑ : Increase
↓ : Decrease
– : Almost no change
← **:** Shifting to left (toward low frequencies)
→ **:** Shifting to right (toward high frequencies)

A detailed discussion on such advanced frequency-dependent parameter computations for modeling high frequency response is available in Section 13.10.3. Once all the equivalent circuit parameters are known, the governing equations for the frequency-domain analysis need to be formulated. For the calculation of the SFRA signature (driving point impedance), the nodal admittance matrix can be computed as demonstrated in Chapter 7 (Section 7.7). At each frequency, the matrix is assembled by combining the nodal capacitance matrix, the nodal conductance matrix and the nodal matrix of inverse inductances. The first diagonal element of the inverted matrix represents the driving point admittance.

Deformation coefficient based diagnostics: One of the shortcomings of the FRA techniques is the difficulty in interpreting FRA responses since the measurements are graphical rather than numeric [64]. There have been efforts to develop diagnostic approaches that are numeric. One such technique [65] determines the location and extent of a deformation by using numerical values of deformation coefficients and charts/look-up tables, respectively. The method makes use of three capacitance measurements at a high frequency and one capacitance measurement at a low frequency for the purpose of deformation diagnostics. The low frequency measurement, done in a particular way, directly gives the extent of radial deformations, whereas the high frequency measurements help in identifying the deformed sections as well as the extent of axial deformations. The method is described in brief below.

In a certain high frequency band the behavior of a transformer winding is capacitive in nature and at such frequencies it can be represented by a ladder network consisting of sectional series capacitances (C_s) and sectional ground capacitances (C_g) as shown in Figure 14.12. Each section of the winding (1, 2, …, n) is represented by a pi (π) model with $C_g/2$ as its two legs.

The proposed method makes use of three fingerprint capacitances at a high frequency (C_{1H} , C_{2H} and C_{12H}) and one fingerprint capacitance (C_L) at a low frequency for the purpose of deformation diagnostics. C_{1H} , C_{2H} ,C_{12H} and C_L are the capacitances between the terminals 1 and 1', 2 and 2', 1 and 2, and 1 and 1', respectively.

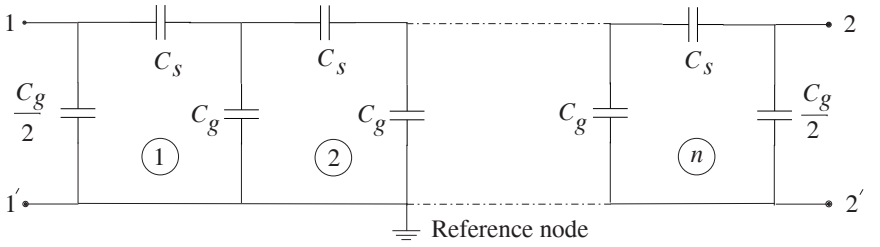

Figure 14.12 Capacitive ladder network of a winding at a high frequency.

Table 14.2 Deformation Coefficients

Section	DC value		Section	DC value
1	3.523 ↔ 3.657		5	–0.554 ↔ –0.556
2	2.685 ↔ 2.721		6	–1.650 ↔ –1.659
3	1.650 ↔ 1.659		7	–2.685 ↔ –2.721
4	0.554 ↔ 0.556		8	–3.523 ↔ –3.657

A deformation coefficient is defined as

$$\mathrm{DC} = log\left(\frac{C_{1\mathrm{H}} - C'_{1\mathrm{H}}}{C_{2\mathrm{H}} - C'_{2\mathrm{H}}}\right) \tag{14.35}$$

where, $C'_{1\mathrm{H}}$ and $C'_{2\mathrm{H}}$ are the measured capacitances between terminals 1 and 1', and 2 and 2', respectively, at the same high frequency after a deformation.

From the fingerprint values of C_{L} and $C_{12\mathrm{H}}$, the sectional series capacitance (C_s) and the sectional ground capacitance (C_g) can be derived as described in [65]. Changes in C_g and C_s can be made in the model to simulate minor radial and axial deformations, respectively, and the corresponding DC values are calculated. The DC values lie in a narrow and distinct range for each section for practical values of deformation, as demonstrated by an example given below.

Table 14.2 presents DC values for a real sized coil due to variations in the sectional ground capacitance values from +40% to −40% for its eight sections. The DC value of any section remains in a very narrow and distinct range for the simulated deformations as evident from the table. During a diagnostic investigation, the DC value calculated by Equation 14.35, using the measured terminal capacitances, is compared with the above table values to locate the deformed section. The method can be easily extended for deformation diagnostics of three-phase star and delta connected windings as demonstrated in [66].

Opening of a transformer is a major power disruption activity. The location and extent of a deformation, if determined, is important diagnostic information. Utility engineers with the help of transformer specialists can then estimate severity of the suspected deformations. A minor deformation at critical locations (e.g., the line-end of a high voltage winding) usually requires immediate opening and repair of the transformer since it can lead to a catastrophic failure. On the other hand, a deformation at the neutral end may not call for an immediate action.

Online techniques have also been proposed recently for the deformation diagnostics as highlighted in Chapter 15.

14.8 Accessories

14.8.1 On-load tap changers (OLTC)

It is well known that a large percentage of transformer failures occur due to OLTC problems. Hence, the service reliability of OLTCs is of vital importance. Substantial portion of transformer maintenance budget is generally consumed for maintaining OLTCs. The problems related to OLTCs are either of mechanical nature (faults related to drive mechanism, shaft, springs, etc.) or of electrical nature (contact wear and tear, burning of transition resistors, dielectric failures, etc.). Because of friction and contact erosion, small metal particles may get into oil to form a chain leading to a short circuit between contacts. Also, the particles may be a cause of partial discharges. Higher temperatures of arcs during switching operations lead to accelerated oil degradation.

Measurement of the contact resistance in a de-energized condition is a simple test for checking the health of OLTC contacts. The drive-motor current (or torque) can also be monitored. Any deviation from the reference signature can be an indication of an incipient problem.

DGA of OLTC-oil is another method for detecting abnormalities. Even in normal conditions, gases such as hydrogen and acetylene are usually detected. An increasing ethylene level is indicative of contact problems [9]. A high rate of generation of these gases is indicative of a deteriorating condition of the contacts. Online DGA analysis is also possible with recent advances in sensor and instrumentation technologies [9].

Vibro-acoustic signals measured by means of a wide frequency band accelerometer placed on the tank of a transformer can be used for the condition assessment of its OLTC [5]. It has been observed that the acoustic signature on account of pressure/vibration waves has a characteristic shape for every tap-change operation. A detectable change in the signature can be correlated with an abnormality inside the OLTC.

Most of the mechanical problems (excessive friction, contact problems, higher operating times, etc.) affect motor drive currents. Hence, the peak current, the average current and ampere-cycles are commonly monitored [67]:

Inrush (or peak) current: Backlash in the linkages and any additional static friction increase the inrush current (and the starting torque).

Average motor current: This parameter can be used to detect an excess in dynamic friction; it is very useful diagnostic parameter when the motor directly drives the linkages (and not through springs).

Ampere-cycles: The area under the motor current Vs time curve can be correlated to initial (inrush) conditions, average operating conditions and the total operating time to provide useful diagnostic information.

Thermal monitoring and diagnostics: The temperature difference between the main transformer tank and the OLTC compartment can be a very useful

parameter for the monitoring purpose. Temperatures in the main tank are usually higher. However, variations in normal operating conditions (load, ambient temperature, mode of cooling, etc.) can make the temperature difference the other way. The diagnosing algorithm needs to take into account these normal variations. Such an intelligent diagnostic procedure can identify correctly the condition of excessive losses due to bad contacts leading generally to a situation in which the OLTC compartment temperature becomes higher than that of the main tank.

A relatively new technique involving dynamic resistance measurements is also used to detect contact coking, long switching times, defects in transition resistors, and contact wear and tear. A DC voltage is applied to the transformer, and the tap changer is operated through all its positions [5]. The measured current fluctuations during the switching operations are used for the diagnostic purpose. An important aspect in such monitoring systems is to gain a long-term experience for evaluating such data.

14.8.2 Bushings

High voltage surges, moisture ingress, internal partial discharges and insulation degradation are the main causes for bushing failures. The health of OIP (oil-impregnated paper) condenser bushings is generally monitored by the following ways. Intrusive tests include moisture-in-oil analyses, DGA of oil samples from bushings, and depolymerization (DP) test on paper samples. These tests should be done if really required for further investigations after a high power factor problem is detected by a standard test. The dielectric response methods such as FDS and PDC are preferred for the bushings as well since these are nonintrusive techniques and have the capability of providing the required diagnostic information. Any change in polarization spectra in time or frequency domain can be used to estimate moisture content; it is difficult to obtain the diagnostic information based on the measurement of $\tan\delta$ or capacitance at one frequency value using conventional tests.

The online monitoring of the power factor of bushings can be performed by vectorially adding currents of three phases obtained using the capacitance (test) tap. Since in reality the bushings are never identical, the sum-current has a nonzero value which is unique for each set of bushings. Hence, variations in the sum-current phasor are monitored. In [68], the development of a fiber-optic instrument for the online monitoring of the dielectric dissipation factor of transformer bushings is reported. It consists of an electro-optic electric-field sensor for sensing the high voltage, capacitors for measuring the insulation current, and a signal processing unit.

14.9 Other Diagnostic Tests/Instruments

14.9.1 Excitation current test

This test is done on site by applying a suitable voltage to HV windings, one phase at a time, with all other windings open-circuited. The test has to be done before any investigative test involving a DC voltage application (otherwise residual magnetism will influence the excitation currents). Short-circuiting of core laminations, unusual asymmetries between the magnetic paths of three phases, and inter-turn faults can be detected. There is inherent asymmetry between the excitation currents of the three phases as elaborated in Section 2.5.1. If the observed asymmetry at site is pronounced as compared to factory/previous site tests, a problem in the magnetic path of one or more of the phases can be suspected. The magnetic balance test, described in Section 2.5.2, can also be used to corroborate the results of the excitation current test.

The winding ratio test can be performed along with the excitation current test. It detects any abnormality related to winding turns (e.g., short-circuited turns, open circuit conditions). The test is generally done after repair work involving OLTC mechanism or other connections.

14.9.2 Winding resistance measurement

This is a standard and simple test done using a suitable DC voltage source. The measured resistance values of the LV and HV windings are compared with factory test records. Connection/contact problems and short-circuited turns/sections can be identified. The LV side test results can be more sensitive to contact resistance problems since the LV winding has a much lower resistance value.

14.9.3 Core insulation resistance test

As discussed in Chapter 2, the core is grounded at one point. If there is any inadvertent multiple grounding, circulating currents flow which may lead to hot spots. The test helps in checking the insulation between the core and structural parts (frames and tank structure) which are also grounded. The core is either connected to a tank plate or a frame at one point or it is grounded separately outside the tank through a proper termination arrangement. The core is isolated from the ground to test its insulation by a suitable DC voltage source (typically 2.5 kV). Multiple grounds and bad insulation conditions can be detected easily.

14.9.4 Winding temperature measurement

Hottest temperatures are usually in the windings, which significantly influence the service life of transformers. It is therefore of paramount importance to monitor their temperatures. Conventional indirect methods are usually not accurate since

the hot spot temperature is estimated based on the measured top oil temperature and the load current.

The direct hot-spot temperature measurement method, which uses fiber-optic sensors, is now increasingly used on critical transformers as an online monitoring technique. The temperature of a disk/turn can be measured directly using a fiber optic sensor placed in its close vicinity. Since the measuring instrument is costly, it can be used for transformers located in one substation/area by rotation (if fiber-optic sensors are installed and brought out for these transformers). Multiple sensors have to be used if temperatures of more than one winding in a transformer need to be monitored. The technique is described in Chapter 9; the challenge for the transformer designer is to predict the hot-spot temperature and the location for fixing the location of the sensor. A distributed type fiber optic sensor, capable of measuring temperature distribution along the length of the winding, has also been reported in the literature. The application is limited, however, by high costs of the distributed sensor and possibility of its damage by mechanical stresses.

A simple yet effective temperature monitoring system, which uses a regression technique to fit a mathematical model of the winding temperature as a function of the ambient temperature, the top oil temperature and the load current, can be effectively used as an online temperature monitoring system. Measured data over a period of time is used to train the model. Once trained, the predicted temperatures by the model are then periodically compared with the measured temperatures to obtain an indication of any abnormality inside the transformer. The measured temperature would be higher than the predicted one based on the three abovementioned parameters if any problem is developing inside the transformer. Unlike the one based on the fiber optic sensor technology, the system is cost effective and nonintrusive, which can be supplied along with conventional control cubicles.

14.9.5 Corrosive sulphur test

Sulphur is present in mineral oils, amount of which depends on the crude oil used and the degree of its refining. At high temperatures, it reacts with metals to form sulphides which precipitate on cellulose insulation. There has been a noticeable number of failures due to copper sulphide formation in oil. Standards have been established to check the tendency of oils to react with copper to form the sulphide.

14.9.6 Particle count test

Presence of nonmetallic and metallic particles in oil significantly influences its dielectric strength. They can align in regions of high field intensities and cause breakdowns. Monitoring of particles is important both at the factory and site. During various manufacturing processes, cellulose particles and metal dust can get into transformers. Under operating conditions, wear of pump bearings can be a

source of metallic particles. Particle size analyzers use a light beam; based on the amount of light blocked the size and number of particles are determined [7].

14.9.7 Infrared thermography test

An infrared camera, which forms a thermal image based on radiations from a hot object, can be used to detect loose/bad electrical connections of bushings and other terminations on the tank, restricted or blocked oil flow in radiators, or any such problems which will show up as distinct temperature zones. It is a very good diagnostic tool for detecting hot spots during factory tests or site operations. However, problems in active parts inside the tank will not be visible to the camera.

14.10 Life Assessment and Refurbishment

The life assessment is a process of reviewing risks of failures for given transformer and network conditions. Factors that determine the remaining life of transformers can be categorized under three headings [69]: strategic (e.g., load increasing beyond the rating), economic (a high cost of losses or maintenance) and technical (aging, overstressing or contamination). A number of diagnostic tests are used to assess the overall health of transformers which can be then ranked considering risks of failures or life expectancy. The remaining (residual) life of the transformer can be estimated by assessing the extent of deterioration of the paper insulation through its DP test or by knowing the content of furan compounds in the oil as discussed in Section 14.4. Furan analysis gives an indication of overall health of the cellulosic insulation whereas DP indicates the extent of degradation at a specific location [33]. Both these tests can help in making decisions about the transformer refurbishment.

Recently, the refurbishment option has been given serious consideration by many users. It can slow down the insulation aging and improve the short-circuit strength. During the refurbishment, critical components such as OLTC can be upgraded, repaired, or replaced enhancing the transformer reliability. Reclamping of windings is also done if there is any looseness.

References

1. United States Department of the Interior, Bureau of Reclamation, *Transformer diagnostics*, FIST 3-31, June 2003.
2. Bengtsson, C. Status and trends in transformer monitoring, *IEEE Transactions on Power Delivery*, Vol. 11, No. 3, July 1996, pp. 1379–1384.
3. Oommen, T. V. and Prevost, T. A. Cellulose insulation in oil-filled power transformers: Part II — Maintaining insulation integrity and life, *IEEE Electrical Insulation Magazine,* Vol. 22, No. 2, March/April 2006, pp. 5–14.

4. Lundgaard, L. E., Hansen, W., Linhjell, D., and Painter, T. J. Aging of oil-impregnated paper in power transformers, *IEEE Transactions on Power Delivery*, Vol. 19, No. 1, January 2004, pp. 230–239.
5. CIGRE Working Group A2.34. *Guide for transformer maintenance*, February 2011.
6. United States Department of the Interior, Bureau of Reclamation, *Transformer maintenance*, FIST 3-30, October 2000.
7. ABB Ltd. *Service handbook for transformers,* 2006.
8. Rogers, R. R. IEEE and IEC codes to interpret incipient faults in transformers using gas in oil analysis, *IEEE Transactions on Electrical Insulation,* Vol. EI-13, No. 5, October 1978, pp. 349–354.
9. Snow, T. and McLarnon M. The implementation of continuous online dissolved gas analysis (DGA) monitoring for all transmission and distribution substations, *IEEE International Symposium on Electrical Insulation,* San Diego, CA, June, 2010.
10. Lindgren, S. R. Transformer condition assessment experiences using automated on-line dissolved gas analysis, *CIGRE* 2004, Paper A2-202.
11. Van Brunt, R. J. Physics and chemistry of partial discharges and corona: recent advances and future challenges, *IEEE Transactions on Dielectrics and Electrical Insulation*, Vol. 1, November 1994, pp. 761–784.
12. Fuhr, J. Procedure for identification and localization of dangerous PD sources in power transformers, *IEEE Transactions on Dielectrics and Electrical Insulation*, Vol. 12, No. 5, Oct. 2005, pp. 1005–1014.
13. Wang, M., Vandermaar, A. J. and Srivastava, K. D. Review of condition assessment of power transformers in service, *IEEE Electrical Insulation Magazine*, Vol.18, No. 6, November 2002, pp. 12–25.
14. Kreuger, F. H. *Partial discharge detection in high-voltage equipment*. Butterworth and Co., London, 1989.
15. Laurent, C. and Mayoux, C. Partial discharge — Part XI: Limitations to PD as a diagnostic for deterioration and remaining life, *IEEE Electrical Insulation Magazine*, Vol. 8, No. 2, March/April 1992, pp. 14–17.
16. Fuhr, J., Haessig, M., Boss, P., Tschudi, D., and King, R. A. Detection and location of internal defects in the insulation of power transformers, *IEEE Transactions on Electrical Insulation*, Vol. 28, Dec. 1993, pp. 1057–1067.
17. Lundgaard, E. Partial discharge — Part XIII: Acoustic partial discharge detection — Fundamental considerations, *IEEE Electrical Insulation Magazine*, Vol. 8, No. 4, July/August 1992, pp. 25–31.
18. Markalous, S. M., Tenbohlen, S., and Feser, K. Detection and location of partial discharges in transformers using acoustic and electromagnetic signals, *IEEE Transactions on Dielectrics and Electrical Insulation,* Vol. 15, No. 6, December 2008, pp. 1576–1583.
19. Rengarajan, S., Parmar, R. N., Bhoomaiah, A., and Kuntia, J. S. Development of an UHF detection system for partial discharge

measurement in transformer insulation, *IEEE International Symposium on Electrical Insulation,* Vancouver, June 2008, pp. 100–103.
20. Raja, K. On the UHF partial discharge measurements in transformers, *Conference on Electrical Insulation and Dielectric Phenomena*, 2003, pp. 349–352.
21. Judd, M. D., Cleary, G. P., Bennoch, C. J., Pearson, J. S. and Breckenridge, T. Power transformer monitoring using UHF sensors: Site trials, *IEEE International Symposium on Electrical Insulation*, Boston, April 2002, pp. 145–149.
22. Judd, M. D., Yang, L., and Hunter, I. B. B. Partial discharge monitoring for power transformers using UHF sensors — Part 1: Sensors and signal interpretation, *IEEE Electrical Insulation Magazine*, Vol. 21, No. 2, March 2005, pp. 5–14.
23. Yang, L., Judd, M. D., and Bennoch, C. J. Denoising UHF signal for PD detection in transformers based on wavelet technique, *Conference on Electrical Insulation and Dielectric Phenomena*, 2004, pp. 166–169.
24. Raja, K., Devaux, F., and Lelaidier, S. Recognition of discharge sources using UHF PD signatures, *IEEE Electrical Insulation Magazine*, Vol. 18, No. 5, September/October 2002, pp. 8–14.
25. Bhangaonkar, A. S., Dudani, K. K., and Kulkarni, S. V. Analysis of frequencies radiated by the point-to-plane electrode configuration under DC and AC voltages, *International Journal of Emerging Electric Power Systems* Vol. 10, No. 3, Article 6, 2009.
26. Judd, M. D., Cleary, G. P., and Bennoch, C. J. Applying UHF partial discharge detection to power transformers, *IEEE Power Engineering Review*, August 2002, pp. 57–59.
27. Raja, K. and Floribert, T. Comparative investigations on UHF and acoustic PD detection sensitivity in transformers, *IEEE International Symposium on Electrical Insulation*, Boston, 2002, pp. 150–153.
28. Sadiku, M. N. O. Numerical technique in electromagnetics with MATLAB®, Third edition, CRC press, 2009.
29. Yang, L., Judd, M. D., and Costa, G. Simulating propagation of UHF signals for PD monitoring in transformers using the finite difference time domain technique, *Conference on Electrical Insulation and Dielectric Phenomena,* 2004, pp. 410–413.
30. Abraham, C. and Kulkarni, S. V. FDTD simulated propagation of electromagnetic pulses due to PD for transformer diagnostics*, IEEE Region 10 Conference, TENCON 2008*, Hyderabad, India, November 2008.
31. Wang, Z. D. and Ding H. Z. On the degradation evolution equations of cellulose, *Cellulose*, 2008, 15, pp. 205–224.
32. Zhang, G., Wei, J., Dong, M., Mu, H., Li, H., Zhang, Y., Li, Y., and Yan, Z. Lifetime monitoring and estimation strategy for large power transformers, *International Conference on Condition Monitoring and Diagnosis,* Beijing, April 2008.

33. Shrinet, V., Patel, M. J., and Ramamoorthy, M. Role of furan and DP analysis for refurbishment of power transformer: few case studies, *CIGRE 2000*, Paper No. 12/33-09.
34. Jonscher, A. K. *Dielectric relaxation in solids*, Chelsea Dielectric Press, London, 1983.
35. Alger, S. M. *Polymer science dictionary*, Second Edition, Chapman and Hall, London, 1997.
36. Kuchler, A. and Bedel, T. Dielectric diagnostics of water content in transformer insulation systems, *ETEP,* Vol. 11, No.1, January/February 2001, pp. 65–68.
37. Der Houhanessian, V. and Zaengl, W. S. Application of relaxation current measurements to on-site diagnosis of power transformers, *IEEE Conference on Electrical Insulation and Dielectric Phenomena,* Minneapolis, USA, October 1997, pp. 45–51.
38. Urbani, G. M. and Brooks, R. S. Using the recovery voltage method to evaluate aging in oil-paper insulation, *IEEE International Conference on Conduction and Breakdown in Solid Dielectrics,* Vasteras, Sweden, June 1998, pp. 93–97.
39. Saha, T. K., Purkait, P., and Muller, F. Deriving an equivalent circuit of transformer insulation for understanding the dielectric response measurements, *IEEE Transactions on Power Delivery,* Vol. 20, No. 1, January 2005, pp. 149–157.
40. Massachusets Institute of Technology, Department of Mechanical Engineering, 2.14 Analysis and design of feedback control system: The Dirac delta function and convolution.
web.mit.edu/2.14/www/Handouts/Convolution.pdf
41. Kuffel, E., Zaengl, W. S. and Kuffel, J. *High voltage engineering: Fundamentals*, Second Edition, Butterworth-Heinemann Publication, Oxford, 2000.
42. Hassig, M., Braunlich, R., Gysi, R., Alff, J. J., Der Houhanessian, V. and Zaengl, W. S. On-site applications of advanced diagnosis methods for quality assessment of insulation of power transformers, *IEEE Conference on Electrical Insulation and Dielectric Phenomena,* Kitchner, Canada, October 2001, pp. 441–447.
43. Gafvert, U., Adeen, L., Tapper, M., Ghasemi, P., and Jonsson, B. Dielectric spectroscopy in time and frequency domain applied to diagnostics of power transformers, *6th International Conference on Properties and Applications of Dielectric Materials,* Xian, China, June 2000, pp. 825–830.
44. Gubanski, S. M. (CIGRE Task Force). Dielectric response methods for diagnostics of power transformers, *IEEE Electrical Insulation Magazine,* May/June 2003, Vol. 19, No. 3, pp. 12–18.
45. Saha, T. K., Middleton, R., and Thomas, A. Understanding frequency and time domain polarization methods for the insulation condition assessment of power transformers, *IEEE PES General Meeting,* July 2009.

46. Gafvert, U. Influence of geometric structure and material properties on dielectric frequency response of composite oil cellulose insulation, in *Proc. of International Symposium on Electrical Insulating materials*, June 2005, Kitakyushu, Japan, pp. 73–76.
47. Linhjell, D., Lundgaard, L., and Gafvert, U. Dielectric response of mineral oil impregnated cellulose and the impact of aging, *IEEE Transactions on Dielectrics and Electrical Insulation,* Vol. 14, No. 1, February 2007, pp. 156–169.
48. Koch, M., Kraetge, A., Velasquez, J. Worldwide standardization activities for frequency response analysis and dielectric response diagnostics, *International Conference on Transformers,* TRAFOTECH'10, Mumbai, India, 2010, Session VI, Paper 7, pp. VI 30–35.
49. Bolduc, L., Picher, P., Pare, G., Demers, R. J., and Belanger, J. Detection of transformer winding displacement by the frequency response of stray losses, *CIGRE 2000*, Paper No. 12/33-02.
50. Picher, P. Mechanical condition assessment of transformer winding using frequency response analysis (FRA), *CIGRE WG A2.26 Report*, 2007.
51. Tenbohlen, S. and Ryder, S. A. Making frequency response analysis measurements: a comparison of the swept frequency and low voltage impulse methods, *XIII*th *International Symposium on High Voltage Engineering*, Netherlands, 2003.
52. Badgujar, K. P., Maoyafikuddin, M., and Kulkarni, S. V. Alternative statistical techniques for aiding SFRA diagnostics in transformers, *IET Proceedings-Generation Transmission and Distribution,* Vol. 6, No. 3, 2012, pp. 189–198.
53. Ryder, S. A. Transformer diagnosis using frequency response analysis: results from fault simulations, *IEEE Power Engineering Society Summer Meeting*, Chicago, July 2002, pp 399–404.
54. Abeywickrama N., Serdyuk, Y. V. and Gubanski S. M. Effect of core magnetization on frequency response analysis (FRA) of power transformers, *IEEE Transactions on Power Delivery*, Vol. 23, No. 3, July 2008, pp. 1432–1438.
55. Ryder, S. A. Diagnosing transformer faults using frequency response analysis, *IEEE Electrical Insulation Magazine*, Vol. 19, No. 2, March/April 2003, pp. 16–22.
56. Abeywickrama, K. G. N. B., Serdyuk, Y. V., and Gubanski, S. M. Exploring possibilities for characterization of power transformer insulation by frequency response analysis (FRA), *IEEE Transactions on Power Delivery*, Vol. 21, No. 3, July 2006, pp. 1375–1382.
57. Wang, M., Vandermaar, A. J., and Srivastava, K. D. Improved detection of power transformer winding movement by extending the FRA high frequency range, *IEEE Transactions on Power Delivery,* Vol. 20, No. 3, July 2005, pp. 1930–1938.

58. Rahimpour, E., Christian, J., Feser, K., and Mohseni, H. Transfer function method to diagnose axial displacement and radial deformation of transformer windings, *IEEE Transactions on Power Delivery*, Vol. 18, No. 2, April 2003, pp. 493–505.
59. Sahoo, S. K. and Satish, L. Discriminating changes introduced in the model for the winding of a transformer based on measurements, *Electric Power Systems Research*, Vol. 77, Iss. 7, May 2007, pp. 851–858.
60. Wang, Z., Li, J., and Sofian, D. M. Interpretation of Transformer FRA Responses Part I: Influence of winding structure, *IEEE Transactions on Power Delivery*, Vol. 24, No. 2, April 2009, pp. 703–710.
61. Raghvan, K. and Satish, L. An efficient method to compute transfer function of a transformer from its equivalent circuit, *IEEE Transaction on Power Delivery*, Vol. 20, No. 2, April 2005, pp. 780–788.
62. Pleite, J, Olias, E., Barrado, A., Lazaro, A., and Vazquez, J. Modeling the transformer frequency response to develop advanced maintenance techniques, *14th PSCC*, Sevilla, June 2002. Session 13, Paper 4.
63. Abeywickrama, N., Serdyuk, Y. V., and Gubanski, S. M. High frequency modeling of power transformers for use in frequency response analysis, *IEEE Transactions on Power Delivery*, Vol. 23, No. 4, October 2008, pp. 2042–2049.
64. Picher, P. Mechanical condition assessment of transformer windings using frequency response analysis (FRA), *CIGRE WG A2.26 Report, ELECTRA*, No. 228, October 2006, pp. 30–34.
65. Joshi, P. M. and Kulkarni, S. V. Use of a deformation coefficient for transformer winding diagnostics, *International Journal of Emerging Electric Power Systems*, Vol. 9, Iss. 3, October 2008, Art. 7.
66. Joshi, P. M. and Kulkarni, S. V. Three-phase transformer winding deformation diagnostics using terminal capacitance measurements, *International Journal of Emerging Electric Power Systems*, Vol. 10, Iss. 3, July 2009, Art. 8.
67. Boss, P., Lorin, P., Viscardi, A., Harley, J. W., and Isecke, J. Economical aspects and practical experiences of power transformer on-line monitoring, *CIGRE 2000,* Paper 12-202.
68. Jaeger, N. A. F., Polovick, G. S., Kato, H., and Cherukupalli, S. E. On-line dissipation factor monitoring of high-voltage current transformers and bushings, *CIGRE 1998*, Paper No. 12-102.
69. Breen, G. Essential requirements to maintain transformers in service, *CIGRE 1992*, Paper No. 12-103.

15

Recent Trends in Transformer Technology

In recent times, rapid changes and developments are being witnessed in design, manufacturing and condition monitoring technologies of transformers. The technological leap is likely to continue in the forthcoming years along with increasing power and voltage ratings of transformers deployed in transmission systems. Advanced computational tools are being used at the design stage to meet increasing complexities of power systems on one hand and to optimize the material cost on the other hand for competitiveness. High quality and automated manufacturing processes are essential to supplement design improvements. Hybrid insulation systems are being employed for enhancing the life expectancy of transformers. Distribution transformers are becoming more energy efficient and green. The demand of transformers for wind- and photovoltaic-based generation systems is increasing at a rapid rate. Transformers for such renewable energy applications need to be designed taking into account special site conditions. Power electronics-based distribution transformers may become commercially attractive. The ongoing research in nanotechnology may have considerable impact on some aspects of transformer engineering. There have been considerable research and development efforts for developing state-of-the-art and cost-effective monitoring and diagnostic techniques.

This chapter summarizes the recent and emerging trends in transformer engineering. Applications of new materials are highlighted. The challenges in design and manufacture of the transformers are identified. The chapter gives some pointers to researchers working in the area of transformers.

15.1 Magnetic Circuit

There has been a steady development of core steel materials in the last century from nonoriented steels to scribed-grain oriented steels. Increasing awareness about energy costs has led to specifications with lower no-load loss values. This has resulted in high usage of better and thinner material grades, step-lap joints, and bolt-less constructions. Presently, the lowest thickness of commercially available steel is 0.23 mm. Cores are assembled without the top yoke, coils are lowered and then the top yoke is assembled, thus increasing productivity and reducing handling of the yoke laminations. It is well understood now that cutting and slitting operations, and ill handling of laminations increases the core loss. The effects of overlap lengths at joints, air gaps, number of laminations per layer have also been thoroughly investigated.

Cores built from an amorphous material are used in distribution transformers because of low losses on account of its high resistivity and low thickness. Due to its noncrystalline nature (low anisotropy), the flux distribution is more uniform in them compared to the cores built from CRGO materials. However, the material has low saturation magnetization (~ 1.58 T as compared to 2.0 T of CRGO materials). The maximum operating flux density in the amorphous cores is therefore limited to about 1.35 T. Hence, although the core (no-load) loss is substantially low, the size of the core increases, and the load loss is also higher. Therefore, the use of the amorphous material is attractive when users specify high no-load loss capitalization ($ per kW). The amorphous material is very sensitive to mechanical stresses; the core loss increases significantly with the stresses. Automation of assembling operations is usually essential to improve the performance of a built amorphous core.

The core loss is made up of eddy, hysteresis, and anomalous components. There have been efforts to improve the understanding of the anomalous loss. Better models are being developed for accurate representation of the hysteresis loss, as highlighted in Section 12.7.6. The eddy and anomalous losses affect the hysteresis loop and loss (refer to Figure 12.23). Rotational losses in T-joints in 3-ph 3-limb units are better understood now [1]; a brief discussion on them is available in Section 2.10. FEM is widely used for analysis and optimization of the core loss. Modeling of the core is done through the complex permeability approach for determining the high frequency response of a transformer as elaborated in Section 13.10.3.

15.2 Windings

There has been no significant change in the type of winding conductors used in distribution and power transformers. Rectangular strip or bunch conductors and continuously transposed cable (CTC) conductors are used for windings of power transformers. Foils of either copper or aluminum may be preferred for the LV winding of distribution transformers. The CTC conductor is preferably of epoxy

bonded type for greater short circuit strength. Netted CTC conductors are also used. There have been some attempts [2] to improve the winding space factor significantly by using a cable in which a number of parallel rectangular insulated conductors are bonded edge-to-edge with epoxy. Shielded conductors are increasingly being used instead of an interleaved construction in cases where a moderate increase in the series capacitance of the winding is required.

The use of thermally upgraded paper is practiced to enhance reliability under thermal stresses; the overloading capability and the life expectancy also improve. Hybrid insulation systems (e.g., combination of aramid paper and cellulose-based paper) are also used for the purpose. The aramid paper is used at places where high temperatures are expected. Power ratings can be significantly increased by such measures. Retro-filling with these thermally upgraded papers is also done to extend the life of old transformers.

The design of windings is very complex since there are conflicting requirements for controlling various stresses, e.g., conductor radius (high voltage withstand Vs short-circuit withstand), thickness of paper covering (thermal considerations Vs inter-turn voltage withstand), width of the axial duct at the inside diameter of high voltage windings (thermal considerations Vs dielectric strength), conductor thickness (eddy loss control Vs short-circuit withstand) and width of radial spacers (short-circuit withstand Vs thermal considerations). Hence, judicious selection of winding parameters, based on advanced computations as highlighted in Section 15.4, is necessary.

Superconducting transformers: Advent of high-temperature superconducting (HTS) materials has renewed interest in research and development of superconducting transformers. Previously developed low-temperature superconductors (LTS) required cooling by liquid helium to about 4°K, which was expensive. The development of the technology based on liquid nitrogen (LN_2) at temperatures up to 79°K has reduced the complexity and cost of the superconducting transformers. Some of the most promising HTS materials are based on bismuth compounds (BISCCO) and yttrium compounds (YBCO).

The principal advantages of HTS transformers are much lower winding material content and losses (current densities at least 10 times that of conventional oil cooled transformers can be used), and higher overload capacity up to about 2.0 per unit current. Although HTS transformers have higher overload capacity, they have low through-fault sustaining capability due to their small thermal mass. Due to greatly reduced conductor dimensions, the strength of the superconducting winding against radial and axial short circuit forces is inherently low. The series capacitance also reduces due to reduction in winding dimensions whereas the ground capacitance is not significantly affected. This results into a highly nonuniform voltage distribution. Special countermeasures (e.g., interleaving) need to be taken which increase the complexity of construction. HTS transformers are costly and not commercially viable in conventional transmission and distribution applications with the present state of

the technology; however they have been found attractive for niche applications such as fault current limiters [3]. During a fault condition, the transition from the superconducting state to the normal conducting mode occurs increasing the resistance, which limits the fault current.

For efficient cooling, it is desirable to have direct contact between the LN_2 coolant and the winding conductor; hence in some designs the inter-turn insulation is arranged in such a way that the conductor edges are left bare. The windings of each phase may be kept in a separate cryostat (made of fiberglass) and the tap winding is generally kept outside the cryostat to simplify the overall construction [4]. There is a considerable amount of research and development work currently being done to make the superconducting transformers commercially viable. Second generation YBCO-based HTS technology is being developed [5], which is expected to take the applications of superconducting transformers to the next level.

15.3 New Insulating Liquids

Mineral oil is being used as an insulating liquid since a century due to its low cost and excellent cooling/insulating properties. Its suitability along with pressboard insulation is well proven up to ultrahigh voltages (~ 1000 kV). Its viscosity is low resulting in a higher flow rate which is crucial for naturally cooled transformers wherein the flow is due to thermosyphon action. A low flashpoint temperature and poor biodegradability are its major disadvantages.

***Silicone oil*:** This oil gives an excellent thermal performance. It has a high flashpoint temperature and hence it is used in traction transformers and applications where compact design and high operating temperatures are expected. It is also used in combination with high temperature class aramid paper to make compact transformers for installation in wind turbines. It is thermally stable and fire resistant. Sludge formation is less due to its excellent oxidation resistance. It is mostly used in distribution transformers. Its main disadvantages are poor biodegradability, high cost and inferior cooling due to high viscosity. High capacity pumps may be required due to its viscous nature. Low viscosity silicone oils have also been developed and used.

***Natural esters* (*vegetable oils*):** These oils have a high flashpoint temperature and excellent biodegradability. Their heat conductivity is higher than that of mineral oil, compensating to some extent their inferior cooling properties due to high viscosity. Water solubility in them is many times higher than that in the mineral oil (approximately twenty times [6]), giving higher aging stability because of reduced water content in the cellulose insulation. Natural esters are increasingly being used in distribution and power transformers since 1999 [6].

Their main shortcomings are high cost and accelerated oxidative aging if exposed to atmosphere. Due to its susceptibility to oxidation, the tank is typically hermetically sealed.

***Synthetic esters*:** A high flashpoint temperature, good thermal stability, anti-oxidation properties, good biodegradability, long life are their main advantages. Like natural esters, they are preferred in environmentally sensitive applications. They reduce aging of cellulose due to their very high moisture absorption capacity which is about two times that of natural esters and several times that of mineral oil [6]. The natural and synthetic esters are *polar* fluids giving them the ability to apply a pull on water molecules. They are used in traction and wind applications in combination with aramid papers for designing compact transformers. For retro-filling, synthetic esters are preferred. High cost is their main disadvantage.

The relative permittivities of the esters and silicone oil are between that of the mineral oil and the cellulose insulation. Thus, because of the lower differences between the permittivities of the solid and fluid insulations, dielectric stresses are evenly distributed in insulation systems with the newer fluids compared to that with the mineral oil. Corrosive sulphur problems are absent when these new liquids are used. Due to these advantages, in addition to previously mentioned features (excellent biodegradability, moisture tolerance, and higher flash and fire points), retrofilling with esters is becoming popular. High viscosities of the esters and the silicone oil as compared to that of the mineral oil do not matter much in forced cooling conditions; furthermore their higher thermal conductivities can compensate for any loss in the flow rate due to high viscosity [6].

The disadvantages of silicone oil and esters are that they need to be replaced after aging (since they cannot be treated) and the experience is very limited for high voltage applications. However, there have been efforts recently to qualify the dielectric performance of esters. Streamer velocities and breakdown voltages of esters have been compared with those of mineral oil in [7].

Transformers with silicone oils, natural esters, and synthetic esters are being increasingly specified and used. The monitoring and diagnostic techniques and standards for the transformers with these insulating media need to be evolved and established over a period of time as the experience of working with them grows. Some standards/technical reports have already been talking about it (e.g., DGA of transformers with nonmineral oils in [8, 9]). Mixtures consisting of mineral oil, silicone and synthetic ester oils are being investigated for their use in transformers.

15.4 Advanced Computations

Electromagnetic field computations: Numerical techniques are commonly used for field computations. The finite element method (FEM) has emerged as the most popular technique for the purpose. The boundary element method (BEM) offers some advantages when applied to 3-D electrostatic problems involving insulation studies. It is not easy to analyze stray losses in three dimensions; very small skin depths pose problems. Hence, an additional formulation, such as surface impedance technique, needs to be used in conjunction with FEM. Different formulations based on various scalar and vector potentials are

employed for reducing computational burdens in 3-D calculations. 2-D FEM analysis can be integrated into design optimization program for calculation of winding eddy losses and for checking short circuit withstand. Competence in 3-D analysis is becoming an essential prerequisite for many design and analysis aspects; solution of benchmark problems and a deeper understanding of electromagnetic fields would be essential for the purpose. The challenges and advances in electromagnetic field computations are discussed in Chapters 4, 5 and 12.

Coupled field computations: The current research trends show that many of the complex design problems involving more than one physical field are increasingly being solved by using coupled field formulations. System transients, such as inrush currents and through fault currents, fall under coupled magnetic field–circuit problems in which the transformer forms the field domain and the connected system is the circuit in the formulation. The field and circuit equations are solved simultaneously since the two domains are coupled strongly. Magnetic-thermal problems are usually weakly coupled allowing the tackling of the two domains in a sequential manner; temperature rise problems involving eddy currents in high current terminations typically fall in this category. Deformations of windings/bus-bars due to short-circuit forces require coupling of magnetic and structural domains. Prediction of noise level is a very complex coupled problem consisting of magnetic, fluid, structural and acoustic fields. A detailed discussion on the coupled fields in transformers is available in Chapter 12.

Short circuit withstand: A steady increase in unit ratings of transformers and simultaneous growth of short circuit capacities of networks have made short circuit withstand as one of the most important aspects of the power transformer design. Although static force and withstand calculations are well established, the dynamic short circuit calculations are complicated. Windings are modeled as a mass-spring-damper model and a precise knowledge of dynamic stress-strain characteristics is essential. It is easier to calculate axial and radial electromagnetic forces but the assessment of withstand against various failure mechanisms, viz. buckling, tilting and bending, is not straightforward. Factors of safety can be computed as outlined in Chapter 6. There is ample scope for refining the strength calculations using advanced analytical/numerical techniques and experimental results.

Response to very high frequency transients: Factory and field tests with non-standard waveshapes and terminal conditions as typically observed in the field reveal that transient voltages could be developed between sections/disks/turns significantly in excess of those during the standard tests. Switching operations and line faults at some distance from the transformer terminals are mainly responsible for such overvoltages within the windings. Frequency-dependent parameter values of the core and windings need to be used in the transient

studies to accurately predict the response. Complex permeability based models are used for the purpose as discussed in Chapter 13. Such an approach is also required to determine analytically the response of a winding to a variable-frequency sinusoidal excitation in frequency response analysis based diagnostic studies.

Computational fluid dynamics: A combination of electromagnetic analysis and computational fluid dynamics (CFD) based simulations should help in improving heat transfer efficiencies. Losses and heat generation rates, calculated from the electromagnetic analysis, are used as inputs to the CFD analysis. Oil flow velocities and temperatures in windings can be accurately determined. Commercial CFD solvers are mostly based on the finite volume method of discretization of the governing equations. Computational resources and domain knowledge required are of high order to obtain accurate CFD solutions in a realistic time frame.

15.5 Transformers for Renewable Energy Applications

***Transformers for wind turbines*:** The use of wind turbines, both on land and off-shore, is increasing at a rapid rate. As a source of green energy, the technology is going to play an important role in meeting growing energy requirements across the globe. The transformer, which is an important constituent of a wind turbine, is dry-type/oil-filled. Although its typical rating is around 2 MVA these days, ratings up to 10 MVA may be used in near future. For offshore applications in a corrosive environment, the dry-type transformers may have to be housed in a hermetically sealed enclosure with a heat exchanger equipped with an air filter/dryer. Another option is to use silicone/ester oil-filled transformers, which are environment friendly and can be designed with a simpler cooling system. Transformers with a hybrid insulation system (aramid insulation NOMEX® plus silicone fluid) are used to make them compact and reliable for nacelle and tower installations [10].

The transformer is positioned in one of the three locations. The ground-mounted transformer is generally oil filled; however compact substations consisting of a dry-type transformer and a SF6 circuit breaker are not uncommon [11]. It is located inside the tower close to the ground level for low power units, which makes maintenance easier. In high power units, however, it is preferably located inside the nacelle to reduce the cable length and the associated losses; the adjustment of the nacelle orientation along the wind direction is also easier.

The use of conventional off-the-shelf distribution transformers or generator transformers may not be justified given the following special operating conditions and stresses [10, 11].

- Excessive vibrations due to tall towers, high wind speeds, and fast grid disconnections
- Repeated cycles of thermal stresses with widely fluctuating turbine loads: the direction of air flow may be downwards complicating the situation

- Current harmonics due to the power electronic converter: these cause extra losses and temperature rise in windings
- Voltage harmonics and distortions, particularly, in weak grids
- Overvoltages causing core saturation
- Vulnerability to overvoltages due to proximity of circuit breakers

Transformers in wind energy conversion systems are vulnerable to failures due to these onerous site conditions. Hence, their specifications need to be carefully drafted and they should be designed to take into account specific site conditions and duty cycles. The natural frequency of the transformer should be far away from those of the wind turbines to eliminate mechanical resonances. Special anchoring arrangements are adopted for the transformers located inside the nacelle. There is an upper limit on the weight and dimensions for transformers placed in the tower or nacelle. For those installed in the nacelle, the design of their cooling system is a challenging task because of stringent space restrictions; more losses (due to compact size and harmonics) need to be dissipated in a given space. The wind-turbine generators are generally not disconnected from the grid to maintain stability; the transformers should therefore have *fault ride-through* capability to carry short-circuit currents for a reasonable amount of time [11].

***Transformers for photovoltaic applications*:** Step-up transformers are required to boost the output voltage of large photovoltaic (PV) plants in the range of 400–700 V to 11–50 kV of the medium voltage grid. Their rating is usually selected in accordance with the peak power of the PV plant. However, too large ratings may lead to grid instabilities, and too small ratings may hinder exploitation of the available solar energy. Hence, the rating should be judiciously selected based on the initial and other costs as explained in [12].

Different power electronics-based topologies can be used in PV-based distributed generation applications. A topology proposed in [13] has the following main advantages: small size and weight due to the use of a high frequency transformer, better power quality, and bidirectional power flow.

15.6 Applications of Power Electronics

***Distribution transformers*:** Conventional transformers have the following main issues: voltage variations under varying load conditions, adverse impacts of system disturbances and overloads, overheating due to harmonics, and vulnerability to system faults. Oil-filled transformers pose an additional environmental concern because of poor biodegradability of the insulating liquid. Power electronics-based transformers can be oil free and designed with a built in voltage regulating mechanism. These designs are being proposed and implemented for small distribution transformers deployed in renewable energy applications [14].

There are mainly three types of designs [15]. The first approach realizes the transformer function solely through power electronic devices without any magnetic device; this design is limited to very small transformers because of the lack of magnetic isolation and difficulties in controlling devices connected in series to achieve a desired rated voltage. A high frequency transformer is utilized in the other two approaches. The size of the transformer is small due to a high operating frequency which is typically in the range of 1–10 kHz. In the second approach, single-stage AC/AC converters are employed at the input and output stages for connecting the high frequency transformer in between. The scheme has a few disadvantages such as difficulties in controlling series switches, no possibility of correcting the load power factor, and harmonic distortion. In the third approach, the system has five components: an AC to DC rectifier (input stage), a DC to AC converter, a high frequency transformer, an AC to DC converter, and a DC to AC inverter (output stage). This topology has the following advantages: an ability to correct the load power factor, and prevention of flow of harmonics from the source to the load side and vice versa. Due to DC link capacitors, it can protect loads from temporary power interruptions. Different topologies based on multi-level converters can be used for the third scheme [15].

***Tap changers*:** Mechanisms that utilize electronic switches can be used to realize the function of tap-change. Gate-controlled electronic switches such as insulated gate bipolar transistors (IGBTs) have been used for the purpose. Such tap changers have a number of advantages, viz. better control/flexibility, fast response, performance improvement, and reduced maintenance costs.

There are a few design variants [16]. In one design, switches are connected in an inverse parallel combination across each tap section, eliminating completely the conventional mechanical switches. A wide range of voltage variations can be obtained by connecting or bypassing different switches. Addition of switch pairs can give plus/minus arrangement. The main disadvantage of this mechanism is that it requires more switches, increasing the cost, and the switches have to be designed to carry short circuit currents.

Alternatively, one can have a design in which the switch-pairs, connected across arcing contacts, are made to conduct only during the arcing period. Switches carry the diverted currents from the diverter contacts for a short period of time. Fewer switches with lower current ratings are required. The main issue in this type of design is that the switches, which need to be permanently connected across the conventional contacts, have to withstand reverse voltages in off-periods making them vulnerable to failures.

In order to overcome the disadvantage in the above scheme, the diverter mechanism is suitably modified in the third design so that the switches are introduced across the arcing contact only for a short time period during which the current is either established or interrupted. The solid-state switches need to withstand only inter-tap voltages. Any malfunctioning of the switches does not hamper/damage the tap changer since the conventional contacts take over the

operation.

With the rapid development in power electronics devices and topologies, the costs of the above schemes are expected to reduce in near future. Ensuring reliability of electronic switches is a concern. Topologies have also been suggested in the literature for distribution transformers [17].

***Power flow control*:** As discussed in Chapters 11 and 13, phase-shifting transformers are used to control power flow in networks. As compared to the conventional arrangement shown in Figure 11.12, a complex scheme is proposed in [18] using which any desired angle of the introduced series voltage between two buses in a network can be realized. The secondary winding on each phase is composed of three tap sections which are physically placed on three different limbs. Both real and reactive powers flowing in the line connecting the two buses can be controlled using the scheme, which is economical as compared to sophisticated devices such as unified power flow controller (UPFC).

Response of conventional phase-shifting transformers and the above scheme is slow due to mechanical switches, and the connections between phases (as shown, for example, in Figure 11.13) results in fault modes which are complex. Power electronics-based topologies can be used to augment the performance of the conventional tap-changing mechanisms to have fast control over power flow. One such arrangement has been recently proposed in [19]; a bi-directional AC-AC converter, consisting of two controllable switches, an inductor and a filter capacitor, is used for the purpose. Since the converter is connected across a tap section, the voltage rating of the switches is only a fraction of the rated voltage of the transformer. The mechanism injects a variable series voltage between two buses to achieve the objective of controlling the magnitude and direction of the power flow between them. Since the function is realized by adding an extra device to the existing tap-changing mechanism, the whole scheme is relatively simple and cost-effective as compared to other devices such as UPFC [19]. If the converter fails, it can be bypassed to have the conventional tap-changing mechanism, and the transformer continues to operate normally.

15.7 Other Technologies

Gas-insulated transformers: Unlike the oil-immersed transformers, these have SF6 gas for the insulation and cooling purposes. Initially, SF6 transformers were manufactured in small ratings (10 to 20 MVA). Now, the ratings as high as 275 kV, 300 MVA are common in some parts of the world. SF6 gas has excellent dielectric strength and thermal/mechanical stability. It is nonflammable and therefore the main advantage of SF6 transformers is that they are fire-hazard free; they are preferred in areas with high fire risks. Due to low specific gravity of SF6 gas, they are generally lighter than the oil-insulated transformers. The dielectric strength of SF6 gas is about two to three times that of air at atmospheric pressure and is comparable to that of the oil at about two to three

atmospheric pressure. But as the operating gas pressure is increased, a tank structure with higher strength is required increasing its weight and cost. The challenges while designing SF6 transformers are environmental concerns, sealing problems, lower cooling capability and the present high cost of manufacture. Because of increasing environmental concerns about the gas, there have been efforts to reduce its usage and to find substitutes [20]; SF_6-N_2 and SF_6-CO_2 mixtures are attempted.

***Hermetically sealed power transformers*:** The hermetically sealed construction has been used for a long time in distribution transformers. These transformers do not have a conservator or breather. Because of isolation from the atmosphere, one of the aging processes, i.e., oxidative aging, is eliminated. Furthermore, there is no ingress of moisture from the atmosphere. Vacuum interrupters can be used in OLTCs of these transformers to make them maintenance free. Thus, their main advantages can be summarized as no oxidative aging, no moisture ingress, reduction in depolymerization of cellulose insulation, and an extended service life. Such transformers with ratings above 100 MVA are already in service since 2007 [21].

***Vacuum tap changers*:** A small gap of a few mm in vacuum is enough to achieve high dielectric strength. A shorter arcing time and a high rate of metal vapor recombination reduce contact wear. The number of operations and current rating can be substantially more. Vacuum tap changers are mainly used for hermetically sealed power transformers. They are almost maintenance free and hence are also suitable for special applications such as rectifier transformers, furnace transformers and HVDC converter transformers. Moreover, their use in conventional power transformers is steadily increasing.

***Multi-use transformers*:** Large generating companies try to optimize the cost of spare transformers (usually generator transformers, station transformers, and unit auxiliary transformers) by using a common spare transformer for a number of generating stations. This philosophy requires transformer design in such a way as to have proper compatibility for replacing any of the chosen existing transformers at various sites, having different ratings, voltage ratios, vector groups, frequency, protection schemes, foundations, bus-duct/cable connections, etc. The design of such a spare transformer is really a challenging task which needs a close cooperation between the user and the supplier.

***Applications of nanotechnology*:** The last decade has seen the emergence of nanotechnology which is expected to influence many products and services. Researchers are exploring possibilities of applying it to transformers as well. One of the first applications is the possibility of improvement in heat transfer capability of oil. Suspended nanoparticles in oil can provide larger surface area and they can conduct heat better. Alumina nanoparticles have been attempted [22]. However, the addition of these fillers should not adversely affect the dielectric properties and performance. Self-healing possibilities of nanomaterials may have potential applications. Nanoelectronics-based smart sensors, which may have self-

calibrating and self-diagnosing capabilities could be applied in future. Any application based on the nanotechnology should be cost effective for scale-up. Breakthroughs in basic materials used for active, insulation, and structural components are required to make a major impact on the transformer engineering.

15.8 Trends in Monitoring and Diagnostics

The need for monitoring and diagnostics of transformers has been amply highlighted in Chapter 14. An effective monitoring system based on state-of-the-art instrumentation and diagnosing skills can reduce maintenance costs, utilize transformers in an optimal way, and prevent unplanned outages. Traditional and well-established methods of determining breakdown strength and tanδ of oil, moisture-in-oil analysis, and dissolved gas analysis are used to determine the condition of the insulating liquid and hence the transformers. Online gas analyzers are now commercially available. Most of the research efforts are directed toward development of better tools and algorithms for diagnosis of moisture in solid insulation, localization of partial discharges, and detection of winding deformations.

Time-domain and frequency-domain dielectric response methods are becoming popular to assess the moisture content in solid insulation. There are two time-domain methods, recovery voltage method (RVM) and polarization-depolarization current (PDC) technique; there are some issues with RVM as discussed in Section 14.5. Also, it is a very time-consuming method; hence, the PDC technique is preferred. The frequency-domain method, i.e., frequency domain spectroscopy (FDS), can be effectively used to obtain information about the moisture level in cellulose insulation. These methods require reference experimental data to aid diagnostics. Although the PDC and FDS methods have showed promise, more work is underway to improve interpretation abilities and to understand material behavior. The exact correlation between the estimated dielectric parameters from measured dielectric responses and the fundamental polarization/depolarization processes occurring inside the dielectric is not yet perfectly understood. Hence, simulations of dielectric processes are used for aiding interpretations. It is not easy to comprehend the physical basis of the typical natures of variations in real and imaginary components of the complex permittivity with frequency. These dielectric response methods give information about the average condition of insulation system; on the other hand it is possible to locate defects using partial discharge measurements and the frequency response analysis.

The detection of partial discharges can be done using an electrical method, an acoustic method or a UHF (ultrahigh frequency) method. Detection of partial discharges by electrical measurements is well established. However, this approach is limited by electromagnetic interference problems. Finding locations of discharges is not straightforward since what gets measured is an apparent charge. A number of inexpensive acoustic sensors can be employed to find the PD

location with a reasonable accuracy level. The acoustic approach, however, is limited mainly by signal attenuation. To reduce the influence of noise, a trigger derived from more sensitive electrical or UHF measurements can be used as discussed in Section 14.3. Inherent noise immunity and an online monitoring capability are the attractive features of the UHF method. Special arrangements need to be made for installing UHF sensors. Due to ongoing efforts for developing online monitoring technologies, sensors will be developed to measure oil properties and detect partial discharges. For example, an optical sensor based on MEMS (microelectromechanical system) technology has been proposed in [23] to detect PD induced acoustic signals.

Offline frequency response analysis (FRA) is widely used to detect winding displacements due to short circuits and transport stresses, as elaborated in Section 14.7. There is a growing interest in researchers and practicing engineers to develop online techniques for assessment of the mechanical condition of windings. An online FRA method proposed in [24] uses usual switching operations and transients on the system as the FRA test signal source. In [25], a high-power signal generator is used to inject high-frequency signals at the bushing tap corresponding to the transformer winding under investigation; a circuit to replace the bushing tap short for allowing online monitoring is also elaborated. The main advantage of the method is that no direct connections or measurements on the high-voltage side bus are required. In [26], a low voltage impulse signal is concurrently injected along with the power frequency current during a short-circuit test to monitor any change in winding characteristics throughout the duration of the test. Shifts in resonant frequencies are used as diagnostic signals. The method reported in [27] uses a current deviation coefficient (CDC) derived from terminal current measurements at a selected high frequency (HF) for locating the deformed winding section. Also, any deviations of HF terminal currents from their fingerprint values can be used to determine the extent of the deformation. Procedures for detecting winding deformations in three-phase star- and delta-connected windings are also discussed in the paper.

It is important to identify the key parameters that should be monitored to reduce the cost of the overall monitoring system. Reliability of electronic equipment, performance under adverse field conditions, and inadequate field expertise for some techniques are the issues to be tackled. Users require cost-effective, easy-to-use and portable instruments with an online measurement capability. They should be compatible with other instruments/software for data mining and analysis, and they should be integrated with protection schemes. There is a trend towards the use of online monitoring expert systems that have various modules for monitoring temperatures, moisture and accessories. Global positioning system (GPS)-based monitoring/tracking at site or during transport is another emerging trend.

References

1. Pfutzner, H., Mulasalihovic, E., Yamaguchi, H., Sabic, D., Shilyashki, G. and Hofbauer, F. Rotational magnetization in transformer cores — A review *IEEE Transaction on Magnetics*, Vol. 47, No. 11, November 2011 pp. 4523–4533.
2. Girgis, R. S., Baldwin, C. J., Kennedy, W. N., Monaco, S., Lindgren, S. R., Holm, R. D., and Kothmann, R. E. Design and performance improvements in power transformers using ribbon cable, *IEEE Transactions on Power Delivery*, Vol. 10, No. 2, April 1995, pp. 869–877.
3. Janowski, T., Glowacki, B. A., Wojtasiewicz, G., Kozak, S., Kozak, J., Kondratowicz-Kucewicz, B., Majka, M. and Wozniak, M. Fault current limitation in power network by the superconducting transformers made of 2G HTS, *IEEE Transactions on Applied Superconductivity*, Vol. 21, No. 3, June 2011, pp 1413–1416.
4. Sykulski, J. K, Beduz, C., Stoll, R. L., Harris, M. R., Goddard, K. F., and Yang, Y. Prospects for large high temperature superconducting power transformers: conclusions from a design study, *IEE Proceedings — Electric Power Applications*, Vol. 146, No. 1, January 1999, pp. 41–52.
5. CIGRE A2.4. Power transformers: technology review and assessments, *Electra,* No. 236, 2008, pp. 22–28.
6. CIGRE A2.35 Working Group. Experiences in service with new insulating liquids, 2010.
7. Liu, R., Tornkvist, C., Chandramouli, V., Girlanda, O., and Pettersson, L. A. A. Ester fluids as for mineral oil: the difference in streamer velocity and LI breakdown voltage, Conference on Electrical Insulation and Dielectric Phenomena, 2009, pp. 543–548.
8. United States Department of the Interior, Bureau of Reclamation, *Transformer maintenance*, FIST 3-30, October 2000.
9. Duval, M. The Duval triangle for load tap changers, non-mineral oils and low temperature faults in transformers, *IEEE Electrical Insulation Magazine*, Vol. 24, No. 6, December 2008, pp 22–29.
10. Declercq, J. Transformers for wind turbines: need for new designs or business as usual, *17th International Conference on Electricity Distribution, CIRED,* Barcelona, May 2003, Session 4, Paper No. 25.
11. Ibanez-Mayayo, J., Chamochin-Escribano, R., and Mateo Martinez De Albornoz, C. Wind turbine transformers, *Advanced Research Workshop on Transformers, ARWtr2010,* Santiago de Compostela, Spain, October 2010, pp. 80–86.
12. Testa, A., De Caro, S., La Torre, R., and Scimone, T. Optimal size selection of step-up transformers in PV plants, *XIX International Conference on Electrical Machines, ICEM 2010,* Rome.
13. Hosseini, S. H., Sharifian, M. B. B., Sabahi, M., Hooshi, Z., and Gharehpetian, G. B. A tri-directional power electronic transformer for

photo voltaic based distributed generation application, *IEEE Power and Energy Society General Meeting*, Calgary, July 2009.

14. Bhattacharya, S., Zhao, T., Wang, G., Dutta, S., Baek, S., Du, Y., Parkhideh, B., Zhou, X., Huang, A. Q., Design and development of generation-I silicon based solid state transformer, *Applied Power Electronics Conference and Exposition*, APEC, 2010, palm Springs, CA, February 2010, pp. 1666–1673.
15. Iman-Eini, H., Schanen, JL., Farhangi, Sh., Barbaroux, J., Keradec, JP. A power electronic based transformer for feeding sensitive loads, *IEEE Power Electronics Specialists Conference (PESC 2008),* 2008, pp. 2549–2555.
16. Cooke G. H. and Williams K. T. Thyristor assisted on-load tap changer for transformers, *4th International Conference on Power Electronics and Variable Speed Drives*, July 1990, pp. 127–131.
17. Faiz J. and Siahkolah B. New solid-state on-load tap-changers topology for distribution transformers, *IEEE Transactions on Power Delivery*, Vol. 18, No. 1, January 2003, pp. 136–141.
18. Sen, K. K. and Sen, M. L. Introducing the family of *Sen* transformers: A set of power flow controlling transformers, *IEEE Transactions on Power Delivery,* Vol. 18, No. 1, January 2003, pp. 149–157.
19. Das, D., Divan, D. M., and Harley, R. G. Power flow control in networks using controllable network transformers, *IEEE Transactions on Power Electronics,* Vol. 25, No. 7, July 2010, pp. 1753–1760.
20. Okubo, H. and Beroual, A. Recent trend and future perspectives in electrical insulation techniques in relation to sulfur hexafluoride (SF6) substitutes for high voltage electric power equipment, *IEEE Electrical Insulation Magazine*, Vol. 27, No. 2, March/April 2011, pp. 34–42.
21. Fink, H. and Hofmann, F. New and innovative technologies of power transformers*, International Conference on Transformers, TRAFOTECH 2010*, Mumbai, Session-I, Paper-6, January 2010, pp. I-27-I-31.
22. Patel, H. E., Sundarajan, T. and Das S. K. An experimental investigation into the thermal conductivity enhancement in oxide and metallic nanofluids *Journal of Nanoparticle Research*, Vol 12, No. 3, 2010, pp.1015–1031
23. Wang, X., Li, B., Xiao, Z., Lee, S. H., Roman, H., Russo, O. L., Chin, K. K., and Farmer, K. R. An ulta-sensitive optical MEMS sensor for partial discharge detection, *Journal of Micromechanics and Microengineering*, Vol. 15, 2005, pp. 521–527.
24. Coffeen, L., McBride, J., Woldemariam, N., Benach, J., and van der Zel, L. A summary of NEETRAC on-line frequency response analysis and a new EPRI commercial prototype FRA installation at First Energy, *EPRI Substation Equipment Maintenance, Optimization and Diagnostics Conference*, San Antonio, March 2009.
25. De Rybel, T., Singh, A., Vandermaar, J. A., Wang, M., Mart J. R., and Srivastava, K. D. Apparatus for online power transformer winding monitoring using bushing tap injection, IEEE Transactions on Power Delivery, Vol. 24, No. 3, July 2009, pp. 996–1003.

26. Santhi, S., Jayalalitha, S., and Jayashankar, V. Online analysis of short-circuit tests on windings, *International Conference on Power System Transients* (IPST'05), Montreal, Canada, June 2005, Paper No. IPST05-114.
27. Joshi, P. M and Kulkarni, S. V. A novel approach for on-line deformation diagnostics of transformer windings, *IEEE PES General Meeting*, Minneapolis, USA, July 2010, Paper No. 2010GM1320.

Appendix A: Sample Design

A.1 Introduction

A typical design of a power transformer is discussed in this appendix. It is intended to help students at the undergraduate level to understand broad aspects of the design procedure. For fresh engineers joining a transformer industry, it is expected to provide much needed initial concepts and a flavor of the intricacies of the design. It must be said that the design described is not an optimum one. The values of flux density and current density are on the conservative side. Also, the electrical clearances between windings and insulation coverings on conductors are on the higher side. There is no provision for voltage variation on either the LV or HV winding in the specification (in order to simplify the design). In practice, however, voltage variation is commonly specified for a winding and taps are provided in the body of the winding or through a separate winding. Although a simple design is illustrated, complexities and conflicts that need to be addressed while designing a practical transformer are highlighted at appropriate places.

It should also be emphasized here that the design procedure deals with electrical aspects only. At some places, standard parameter values are used; in actual practice, elaborate electromagnetic field computations, circuit analysis, etc. are required for selecting the values. Thermal and short-circuit strength considerations have considerable influence on many design parameters. Electrical, mechanical, and thermal requirements are often in conflict as will be highlighted while explaining the design procedure. Reference to appropriate chapters is given at many places so that more insight into a particular design aspect can be obtained.

A discussion on design optimization is desirable before we proceed with the elaborated sample design. The main variables are the diameter of the core,

the operating flux density in the core and the current densities in the windings. The selected design should be such that it meets the specified performance figures; the main specifications are the no-load loss, the load loss and the percentage impedance. The optimization is subject to many manufacturing and material-availability constraints. Standardization can come in the way of material cost optimization. However, standardization is often desirable to reduce inventory costs, minimize reworks, and enhance quality, and it is influenced by the adopted technology, the cost of labor, and availability of materials. Standardized design and manufacturing practices have to be revisited periodically to take into account improvements in manufacturing processes and availability of better materials.

What needs to be optimized at the tendering stage is the total owning cost, which consists of the price and the loss cost. The price has the following components: the cost of materials, the cost of overheads, and profit. The loss cost, which represents the running cost to the user, is calculated by multiplying the no-load loss and load-loss values by the corresponding values of per-kW charges given in the specification. These charges are mainly based on prevalent energy costs. For a low-loss design (with lower values of the flux/current densities and higher material content), the material cost (and hence the price) is high and vice versa. Thus, the material cost and the size of the core-winding assembly in the optimized design would vary over a wide range depending on the per-kW charges. The basic design and even the core material can change if, for example, a very high no-load loss charge is specified by the user to improve all-day energy-efficiency as discussed in Section 1.6. In such a case, the amorphous core technology may become an attractive option in small distribution transformers since a higher basic price of the amorphous material and its higher required quantity (due to a lower value of permitted flux density compared to a CRGO steel grade) would be compensated by a much lower loss cost (its no-load loss being about one third of that of a core built from CRGO laminations).

From the above discussion, it is obvious that the transformer design is a constrained optimization problem. Today's computers can process thousands of designs for various combinations of the parameters in a few minutes or even seconds helping designers to arrive at an optimum design with the least capitalized or owning cost. The computer program should have built-in information of various constraints. The program is refined over a period of time because of differing specifications of various users resulting into many design variants. It also takes time to incorporate experienced designers' expertise into the program. It is desirable to have a robust optimization program so that the design at the tendering stage becomes the final one if an order is eventually placed. For this purpose, it may be essential to integrate advanced analytical programs and/or 2-D FEM codes into the optimization program so that the main performance parameters, such as the leakage impedance, winding eddy losses, short-circuit stresses and strength, etc., are accurately calculated.

A final remark about variations in the material cost with various design parameters is desirable. This cost has complex dependence on the parameters. For example, a lower value of the specified leakage impedance increases the short-circuit current and the corresponding stresses, which calls for reducing the current densities, and the cost increases. On the other hand, a higher value of the impedance will increase the leakage field (and the stray load losses); the extra losses then have to be compensated by putting more material in the core and windings. Also, a significantly high impedance value may call for providing a higher gap between the LV and HV windings, thereby increasing the mean diameter and the weight of the HV winding. Thus, the leakage impedance value corresponding to an optimum design is not generally an extremely low or high value but somewhere between the extremes. However, it should be noted that the impedance value is specified by the purchaser, and optimization needs to be done with the specified value as a constraint.

With the above discussion, we can now proceed to design a typical medium rating power transformer. Its specifications are

Rating	: 3-phase, 31.5 MVA, 132/33 kV
Vector group	: Yd1
Frequency	: 50 Hz
Leakage impedance	: 9%
No-load loss	: 26 kW
Load loss	: 146 kW.

Some comments about the specifications are in order. The specification of a practical transformer is usually exhaustive running into several pages. It includes specifications of coolers, voltage variation, control panels, protection devices, breathing arrangement, foundations, size and weight restrictions, etc. The discussions on these details can be found at appropriate places in this book. Here, for the simplified electrical design that is going to be explained, the details are not required. Returning to the given specification, it should be noted that one can specify either a three-phase unit (as in this case) or a bank of three single-phase units. The pros and cons of the two options are discussed in Chapter 2. Different vector groups are elaborated in Chapter 1 and Appendix B. Whether the specified vector group is Yd1 or Yd11, the electrical design is not affected; it decides the type of winding connections at the assembly stage. The frequency specification is country-specific (50 Hz or 60 Hz). For every excess kW in the no-load (open-circuit) and load-loss (short-circuit) tests, there is a penalty charged by the purchaser. Hence, the designed values of the losses should be less than the specified values by an amount that considers manufacturing aberrations and uncertainties of measuring instruments. The leakage impedance is generally given tolerance on both sides (typically, ±10% or ±7.5%).

A.2 Core Design

Let us start the design with selection of the core diameter. Different empirical formulae, relating the diameter mainly to the power rating, are generally used in the industry. Let us choose the diameter as 0.540 m.

Core diameter = 0.540 m.

As the core is assembled from stacked laminations in rectangular steps as shown in Figure 9.5, some amount of magnetic area is lost as compared to the circle area since the number of steps has to be finite in order to limit the number of different widths of laminations that have to be cut and assembled. The nonmagnetic insulation coating on the surfaces of laminations reduces the space factor further as discussed in Chapter 2. The lost area is typically of the order of 10%, giving a space factor value of about 0.9. An additional area is lost when cooling ducts are provided in the core (Figure 9.5) for oil passage. The ducts are generally required for medium and high rating transformers. They, however, are not considered in the present design.

Core area with 0.9 as space factor (A_c) = $0.9 \times ((\pi/4) \times 0.54^2) = 0.2061$ m^2.

The saturation flux density of CRGO steel is of the order of 2.0 T and the knee point at which saturation generally starts to show up is about 1.9 T. The operating point (the peak value of the mutual flux density, B_{mp}) has to be lower than the knee point depending upon the severity of the user-specified over-excitation conditions (as elaborated in Section 2.4).

Let us choose $B_{mp} = 1.7$ T.

EMF equation for transformer is $V = 4.44 \times \phi_{mp} \times f \times N$

$$= 4.44 \times (B_{mp} \times A_c) \times 50 \times N$$

This equation has been derived in Chapter 1. N denotes the number of turns. The voltage per turn (V/N) is thus obtained as

$V/N = 4.44 \times 1.7 \times 0.2061 \times 50 = 77.78$.

Now, let us first choose the number of LV turns. This is generally done because, once an integer number of turns for the LV winding is chosen, the consequently calculated and rounded number of the HV turns does not lead to an unacceptable ratio error. Typically, the ratio error should not be more than 0.5% at any tap position.

A.3 LV Winding Design

It is a delta-connected winding; voltage across any phase winding equals the line-to-line voltage. Therefore, its number of turns corresponds to the line-to-line voltage.

LV winding turns = 33000/77.78 = 424.3 ≅ 424 turns.

Recalculate the flux density on account of rounding of the turns: B_{mp} = 1.701 T ≅ 1.7 T.

Recalculated V/N = 33000/424 = 77.83
Phase current = 31500/(3 × 33) = 318.2 A
Insulation level: 70 kVrms/170 kVp; the former value is the one-minute power frequency (PF) test voltage and the latter is the lightning impulse (LI) test level.

LI level is also called the basic insulation level (BIL). The test levels are specified by users based on guidelines given in standards. A discussion about these test levels can be found in Chapter 8. As the winding voltage class increases, the test levels do not increase in the same proportion. For example, typical values of BIL for 11 kV and 400 kV class windings are 75 kVp and 1300 kVp, respectively; BIL is about 6.8 and 3.25 times the rated voltage, respectively. Correspondingly, the insulation levels of protective devices are chosen. Relatively lower values of insulation levels at higher voltage classes help in reducing cost of transformers.

We have to decide now the winding type. There are mainly two types, layer/helical and disk; the discussion on them is available in Chapter 7. The layer type is generally used for low voltages (and therefore for a fewer number of turns) and/or for high current ratings. In the present design, the number of the LV turns is high enough to have it wound as a disk winding. Let us choose 106 disks and 4 turns/disk to accommodate 424 turns. There can be many other combinations of these two parameters; however, the axial height and the radial depth of the winding, corresponding to the chosen values, fall in a range that is appropriate for the given specification, particularly the leakage impedance value.

Next, a suitable value of the current density has to be chosen. Typically, its value up to 3.5 A/mm^2 can be chosen without exceeding temperature rise limits. If a separate tap winding is present and it is outermost, the current density beyond 4 A/mm^2 can also be chosen due to its well exposed surfaces and lower radial depth. Let us choose 3 A/mm^2 which should help us limit the I^2R loss to a reasonable value in accordance with the specified load loss value.

LV current density = 3 A/mm^2
Cross sectional area of LV turn = 318.2/3= 106 mm^2.

In order to reduce the eddy loss in the winding turns exposed to the alternating leakage field, the winding conductor has to be subdivided into a suitable number of parallel conductors. The eddy loss in any conductor has two components: the loss due to the axial component of the leakage field and the loss due to the radial component of the leakage field; these vary with the square of the conductor thickness and with the square of the conductor width, respectively (refer to Chapter 4 for details). Thus, we need to choose the two dimensions as small as permitted from other design considerations which are generally in conflict with the

aforementioned requirement for the eddy loss control. The thickness has to be sufficiently large to have sufficient strength against short-circuit forces. For the ease of manufacture, the width has to be large enough so that built disks are stable. A very thin conductor may get elongated as the winding is tightly wound. On the contrary, an excessively thick conductor cannot be wound easily, particularly for smaller winding diameters. Thus, the width to thickness ratio has to be between the two extremes from the manufacturing point of view.

It should also be borne in mind that parallel conductors need to be transposed along the winding height so that they have equal resistance and reactance values (refer to Section 4.6). This reduces the circulating current loss to a negligible value. The higher the number of parallel conductors per turn, the higher is the axial space lost along the winding height for doing the required number of increased transpositions, leading to a poor axial space factor.

After due consideration to all the above points, let us choose four parallel conductors per LV turn with the dimensions as 10.6 mm × 2.5 mm:

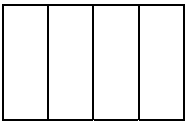

Turn area = $10.6 \times 2.5 \times 4 = 106$ mm^2.

In actual practice, the corners of the conductors are in the form of a small curvature having radius of 0.5-1.0 mm to avoid sharp edges that can cut the insulation paper and to reduce high electric stress levels, and therefore the actual conductor area is slightly smaller than that calculated above.

Now, we need to choose the thickness of the paper covering on the conductor surface. It should be decided based on the voltage difference between touching turns during various high voltage tests (refer to Chapter 8). A higher value of the covering increases the dielectric strength but worsens the thermal gradient between the conductor and the surrounding oil medium. A certain minimum covering is desirable from the mechanical consideration when the conductor is tightly wound on a former during the winding stage. For low voltage windings, the dielectric consideration is not a deciding criterion.

Insulation between adjacent disks is decided based on thermal and dielectric requirements. For low voltage windings the thermal consideration dominates. A certain minimum value of gap between disks is desirable for oil to take away the heat easily through the convection process. A winding with a high radial depth should have larger inter-disk gaps (ducts) to have adequate cooling, particularly in the mid-depth portion; the portions at inside and outside diameters have anyway better cooling conditions due to axial ducts (refer to Figures 9.6 and 9.7).

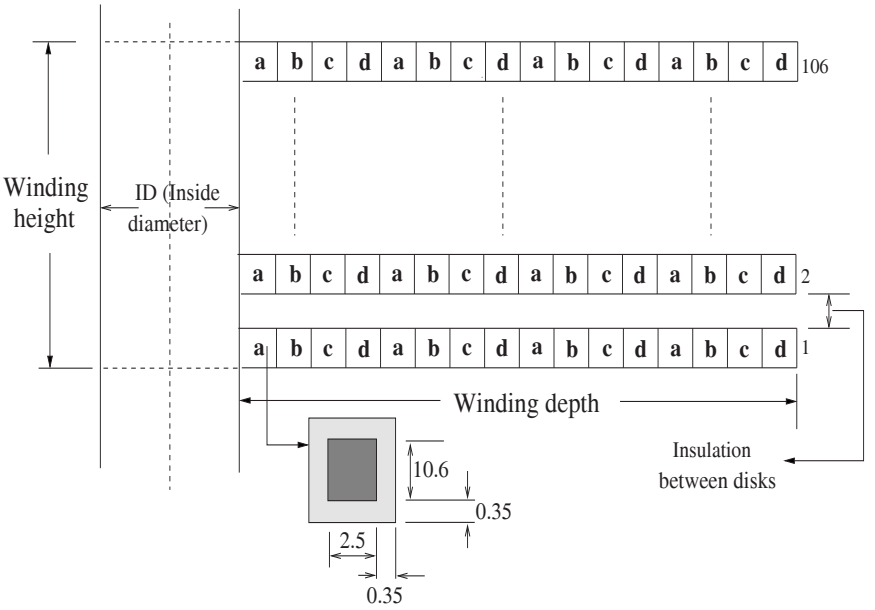

Figure A.1 LV winding details.

Let us choose the insulation on the conductor as 0.7 mm (0.35 mm on one side) and the gap between disks as 3.0 mm. The paper covering of 0.7 mm on the conductor is required from mechanical considerations for the LV disk coil because of the tension experienced by the conductor during the winding operation. For a layer winding of the same voltage class, the paper insulation can be lower based on experience.

Height of the winding = $(10.6 + 0.7 + 3.0) \times 106 - 3.0 = 1513 \approx 1520$ mm
Depth of the winding = $[(2.5 + 0.7) \times 4] \times 4 = 51.2$ mm ≈ 52 mm.

Additional space of 7 mm is considered in the height to take care of variations, if any, in the thickness of the inter-disk insulation spacers. The above calculations can be better understood by referring to Figure A.1, wherein all relevant axial and radial dimensions are marked.

A.4 HV Winding Design

Since the HV winding is star-connected, its phase current equals the line current:

Phase current = $31500/(132 \times \sqrt{3}) = 137.78$ A.

Typical insulation level specification for 132 kV winding is 230 kVrms / 550 kVp.

HV turns = $(132000/\sqrt{3})/77.83 = 979.2 \approx 980$ turns
Choose the number of disks as 98 and the turns per disk as 10
Conductor covering = 1 mm, gap between two adjacent disks = 4 mm.

The conductor covering can be lower by about 20% based on detailed calculations of inter-turn stresses (i.e., working voltage and impulse stresses). The number of disks needs to be chosen in such a way that an appropriate conductor width is obtained as discussed during the design of the LV winding. We have been fortunate here because the rounding of turns from 979.2 to 980 does not lead to any appreciable error in the voltage ratio. In some other cases, if the round-off error is significant the turns have to be electrically dropped along the winding height. For example, if there were 975 turns, instead of rounding the number to 980, 5 turns are dropped when the winding is wound; one way to achieve this is by winding the last turn of every disk shorter by a fraction 5/98, thereby effectively dropping 5 turns when all 98 disks are wound.

The HV winding is also being designed as a continuous disk winding. Disk windings up to 132 kV class are generally designed in this way; shielded-conductor and interleaved windings are used for 220 kV class and beyond to improve impulse voltage distribution, as elaborated in Chapter 7.

The thickness of the paper insulation on the conductor is decided by a continuous working voltage stress value and a worst-case impulse voltage magnitude expected across any two turns. These aspects are discussed in Chapter 8. Cooling considerations and a worst-case voltage magnitude appearing across consecutive disks decide the gap between them. Generally, the inter-disk gaps can be different along the HV winding height; higher gaps are provided at its line end, compared to the neutral end, for withstanding steeply rising overvolatges during high voltage tests. However, here the inter-disk gap is assumed the same throughout the winding height for simplicity. It should be emphasized again that the two parameters are not optimum values for the 132 kV winding. Based on elaborate calculations, as discussed in Chapter 8, these can be reduced.

The height of the HV winding is kept equal to that of the LV winding in the present design. In some special cases, when one would like to reduce short-circuit stresses in a LV layer/helical winding, its height is kept larger than that of the HV winding. In any case, however, the two windings are placed symmetrically about their center line to minimize axial forces as discussed in Section 6.3.2. The radial leakage field at the two ends of the taller winding is less reducing axial forces acting on it; such a design helps the layer/helical winding, which is inherently weak, to withstand axial short-circuit forces.

Bare conductor width = $1520/98 - 1 - 4 \cong 10.5$ mm
For current density of 3 A/mm^2, total conductor area required
$= 137.78/3 = 45.9$ mm^2; choose two parallel conductors as:

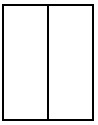

10.5

2 || 2.2

Area of each turn = 46.2 mm^2 which gives the current density of 2.98 A/mm^2

Radial depth of the HV winding = [(2.2 + 1) × 2] × 10 + 1 (tolerance) = 65 mm.

The HV winding, carrying lesser current, required to have only two parallel conductors.

A.5 Overall Dimensions of Core and Windings

Having finalized the design of the LV and HV windings, we are now in position to determine overall dimensions of the windings and the core. The inside diameter (ID), the mean diameter, and the outside diameter (OD) of the windings are given below:

Core diameter		540 mm
Core-LV gap	: 23	563 mm (mean diameter)
		586 mm (LV-ID)
LV radial depth	: 52	638 mm (LV mean diameter)
		690 mm (LV-OD)
LV-HV gap	: 49	739 mm (mean diameter)
		788 mm (HV-ID)
HV radial depth	: 65	853 mm (HV mean diameter)
		918 mm (HV-OD)
Phase-phase gap	: 52	

The previously calculated radial depths of the LV and HV windings, 52 mm and 65 mm, respectively, are used in the above computations. The core-LV gap of 23 mm is required for the 33 kV class LV winding with 70 kVrms/170 kVp insulation level. For a lower voltage class LV winding, the mechanical clearance required for the purpose of proper lowering of the winding onto the core may decide the gap. It should be noted that the transferred surge voltage from the HV winding to the LV winding can be sometimes higher than the specified BIL of the latter winding, necessitating a higher gap between the LV winding and the core. More discussions on such aspects can be found in Chapter 7. The chosen LV-HV gap of 49 mm is considerably higher than today's industry practice for 132 kV windings (the gap can be reduced by about 15% after detailed calculations as elaborated in Chapter 8). The phase-to-phase (ph-ph) clearance, i.e., the gap between the HV windings of any two adjacent phases, should be more than the LV-HV gap.

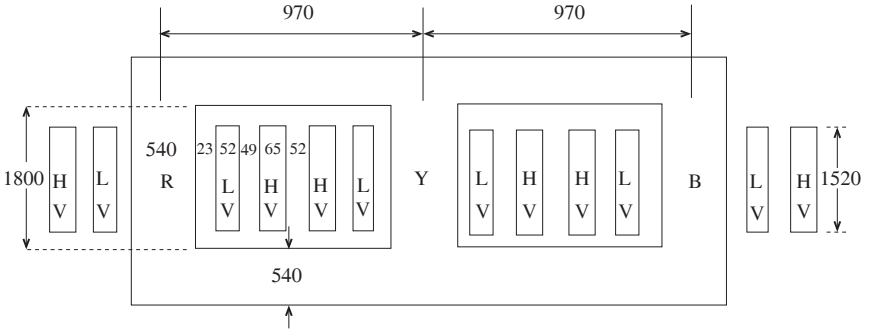

Figure A.2 Dimensions of the core and windings.

Both LV-HV and ph-ph gaps are generally decided by the lightning impulse level of the HV winding; when the lightning impulse test is conducted on the HV winding of any phase, all other windings are grounded. Since the oil ducts in the ph-ph gaps are generally not as small and controlled as in the LV-HV gaps, the ph-ph gaps are kept larger. In some cases, when the switching impulse level is specified, it usually decides the ph-ph gap.

Various dimensions of the core and windings are depicted in Figure A.2. The distance between the centers of adjacent limbs can be calculated as two times the radius of the outermost winding plus the ph-ph gap. In this case, it equals OD of the HV winding plus the ph-ph gap.

Center to center distance of the core structure = 918 + 52 = 970 mm
Windings to top yoke clearance = 200 mm
Windings to bottom yoke clearance = 80 mm
Total end insulation = 200 + 80 = 280 mm
Core-window height = height of the windings + total end insulation = 1520 + 280 = 1800 mm.

The end insulation is decided based on dielectric, thermal, and clamping requirements. The highest of the insulation levels of the ends of all the windings decides the top/bottom end insulation distance. In the present design, the top end of the HV winding is at 132 kV with the corresponding insulation level of 550 kVp and 230 kVrms. The clearance between the windings and the top yoke is therefore determined by this insulation level. Also, three 132 kV leads going to corresponding bushing terminals will also play an important role in deciding the clearance. The windings are usually clamped from the top using a clamping ring. Hence, for transformers with lower voltage ratings (say, 33 or 66 kV HV winding), although dielectrically the insulation clearance required may be substantially less, the clamping arrangement necessitates to have a higher clearance. Sometimes, a clamping ring material with better mechanical characteristics is chosen to increase its mechanical strength; however, it may have inferior dielectric properties thereby increasing the clearance. Furthermore, in

most of the cases, when oil has to be properly directed into and out of the windings at the bottom end and the top end respectively, adequate space has to be allocated for the oil passage.

One may wonder why the clearance of 80 mm has been provided between the windings and the bottom yoke. Since, the LV winding is delta-connected, its top and bottom terminals are of 33 kV voltage class with 70 kVrms/170 kVp insulation level. The neutral end of the HV winding, although grounded under operating conditions, is generally specified with an insulation level of 38 kVrms/95 kVp to take care of any rise in its voltage during certain types of fault conditions. In addition, the windings need to be adequately supported at the bottom; they generally rest on bottom support structures which require some space. With all these considerations, the bottom clearance has to be judiciously chosen. While doing a specific power-frequency overvoltage test, in order to obtain a required voltage at the line terminal of the winding under test, the neutral terminal may have to be raised to a potential which may be higher than its specified insulation level. Such special conditions need to be taken into account while deciding the end insulation clearances. The total end insulation of 280 mm is on conservative side; it can be optimized by using contoured angle rings and by subdivision of the total gap into properly sized oil ducts, as outlined in Section 8.7.

A.6 Core Weight and Loss Calculations

With reference to Figure A.2, the core length is:

Core length = $4 \times (½ \times 540) + 3 \times 1800 + 4 \times 970 = 10360$ mm.

To find the volume, we make use of its area which has been calculated as one of the first few design parameters.

Core volume = $10360 \times 206100 = 2135196000$ mm^3
Core weight = volume × density = 16334 kg
(density of core laminations = 7.65×10^{-6} kg/mm^3).

The core loss has predominantly two components, the eddy loss and the hysteresis loss. These two losses can be evaluated using the expressions given in Chapter 2 if the flux density distribution in the entire core region is known. Since it is impractical and cumbersome to do these calculations, the losses are computed using the curves given by the lamination material supplier, which take into account both components.

W/kg from the supplier's curve at peak operating flux density of 1.7 Tesla = 1.2.

Due to various irregularities (cross-fluxing, saturation, etc.) the loss densities are higher in the joints between limbs and yokes (refer to Chapter 2 for more details). Hence, a penalty has to be imposed for these regions while calculating the losses,

which can be estimated using test results on transformers or using the finite element method (FEM). For simplicity, let us take the penalty factor as 2.0. The weight of all the joints can be calculated from the geometrical details. However, let us assume that the joints contribute 30% of the total core weight. Now, we can determine the core loss:

Weight of the joints = $0.3 \times 16334 \cong 4900$ kg
Core losses = $(16334 - 4900) \times 1.2 + 4900 \times 1.2 \times 2 = 25480$ W $\cong 25.5$ kW

Alternatively, one can determine the losses if we know the building factor of the built core at the operating flux density of 1.7 Tesla. It is the multiplying factor by which the loss of the built core increases compared to the single-sheet loss measured by Epstein's test. The factor is a function of many parameters such as the type of core construction, the type of joints, the operating flux density, the type of the core material, etc. (refer to Section 2.1.2 for more details). Let us take the building factor value as 1.3 meaning thereby that W/kg of the built core is 1.56 (= 1.3×1.2). The factor value is taken on a higher side; it is usually in the range of 1.1 to 1.25 (refer Section 2.1.2).

Core loss = $16334 \times 1.56 = 25481$ W $\cong$ 25.5 kW.

The core loss value is less than the specified value of 26 kW.

A.7 Equivalent Circuit: Shunt Branch

Now we can determine the shunt branch parameters of the transformer equivalent circuit. It should be remembered that the equivalent circuit has per-phase quantities. The shunt branch has two components in parallel: R_c represents the total core loss and X_m denotes the magnetizing reactance.

$$R_c = (132 \times 10^3/\sqrt{3})^2 / (25.5 \times 10^3/3) = 683.3 \text{ k}\Omega.$$

The corresponding loss component of the no-load current is

$$I_c = (132 \times 10^3/\sqrt{3}) / (683.3 \times 10^3) = 0.11 \text{ A}.$$

The quantities are being calculated as referred to the HV side (for more details on the equivalent circuit and its parameters, refer to Chapter 1). It should be noted that a higher value of R_c reflects better core properties; deterioration of the magnetic circuit (e.g., local short-circuits between laminations) will reduce the resistance and increase the loss (for a parallel combination of R and X fed by a voltage source, reduction in R makes the circuit more lossy).

Ideally, the magnetizing volt-amperes (VA) and hence the magnetizing current should be calculated from the flux density distribution in the core obtained using FEM. For every small elemental volume (and the corresponding weight), VA/kg for the corresponding flux density is obtained from the supplier's catalog. The total VA for the entire core can then be estimated by integration over all finite

elements. However, such an approach in practice is cumbersome; designers generally use VA/kg values from test data of built cores. Naturally, these values are higher than the corresponding values for a single lamination due to irregularities at joints. Let VA/kg for the built core at 1.7 Tesla flux density be 9.6, which gives

$$\text{No-load current} = I_0 = (9.6 \times 16334) / (\sqrt{3} \times 132 \text{ x } 10^3) = 0.69 \text{ A (HV side)}.$$

The per-unit (p.u.) value of the no-load current is determined by dividing it by the base current on the HV side,

$$I_0 = 0.69 / 137.78 = 0.005 \text{ p.u.} = 0.5\%$$

$$I_m = \sqrt{(0.69)^2 - (0.11)^2} = 0.68 \text{ A}.$$

The no-load power factor, according to Equation 1.54 is

$$\cos\theta_0 = I_c / I_0 = 0.16.$$

With better lamination material grades, the decrease in I_m can be much higher than the decrease in I_c. Therefore, the no-load power factor value can be higher in today's transformers. The magnetizing component is about 6 times the loss component in this case. The magnetizing reactance can now be calculated as

$$X_m = (132 \times 10^3 / \sqrt{3}) / 0.68 = 112.1 \text{ k}\Omega.$$

The built core has an effective permeability value which is lower than that of a single lamination due to joints. The higher the effective permeability, the lower is the corresponding reluctance and the higher is the magnetizing reactance (since according to Equation 1.39, the magnetizing inductance of a coil is inversely proportional to the reluctance of the magnetic circuit around which it is wound).

A.8 Leakage Reactance Calculation

Chapter 3 contains an elaborate discussion on the leakage field and the corresponding reactance. A formula for the leakage reactance is derived in the chapter. The inductance of a coil having N turns which link flux ϕ can be calculated from any one of the following expressions:

$$L = \frac{N\phi}{i}$$

$$L = \frac{NBA}{i} = \frac{N\mu HA}{i} = \frac{N\mu(Ni/l)A}{i} = \frac{\mu N^2 A}{l}$$

$$L = \frac{\mu N^2 A}{l} = \frac{N^2}{l/(\mu A)} = \frac{N^2}{\Re}$$

where, the relationships $\phi = BA$ and $H = (Ni/l)$ have been used. $\Re$ is the reluctance of the flux path and the other symbols carry usual meanings (refer to Chapters 1, 3, and 12). It should be noted that in the above expressions, the flux ϕ is linked by all the N turns, and l is the height of the coil. More fundamentally, l is the height of a tube containing uniform flux ϕ which links all the turns. However, the leakage field can be uniform only in the gap between the LV and HV windings. It can be observed in Figure 3.1 (a) that approximately half the leakage flux lines in the gap link the LV turns and the remaining lines link the HV turns. Further, if the leakage field is approximated to have only the axial direction (as in Figure 3.2), all the flux lines in the gap link the same amount of ampere-turns, i.e., the LV or HV ampere-turns which are equal since the magnetizing ampere-turns are neglected for calculating the leakage reactance and the lengths (heights) of all the flux lines are equal. Applying Maxwell's ampere-circuital law (Equation 1.12) along any of the lines and remembering that the return path is through the core with (assumed) infinite permeability (i.e., $H_{core} = 0$), the H (and therefore B) value along each of these flux lines in the gap is same. Similarly, any of the flux lines in the LV and HV windings are in the axial direction in Figure 3.2 and return through the core. As one goes into the windings away from the gap, the enclosed ampere-turns reduce, decreasing H and B. Therefore, we have the ampere-turn diagram and the flux magnitude pattern in a trapezoidal form as shown in Figure A.3. For calculating the leakage inductance, we have to integrate flux linkages as done in Section 3.1.1 since the flux magnitude is different at different points along the radial depth of the windings. Consequently, when inductance is defined as $(\mu N^2 A)/l$, the total area A of the flux tube, containing the LV winding, the gap and the HV winding, is contributed more by the gap as compared to the windings; out of the three terms that contribute to A, the terms corresponding to the LV and HV windings have ⅓ as the multiplying factor (refer to Equation 3.17).

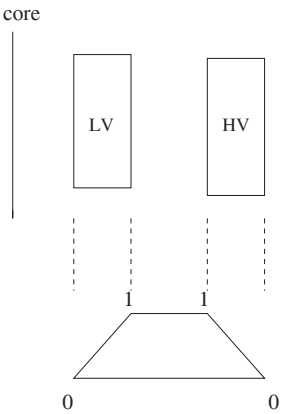

Figure A.3 Ampere-turns diagram.

Also, the term l in the expression is the effective height of the flux tube, which is calculated by dividing the height of the windings by the Rogowski factor (refer to Equations 3.1 and 3.18). The Rogowski factor, being less than 1.0, makes the effective height of the flux tube greater than the physical height of the windings. The factor accounts for the increase in the length of the leakage flux lines due to their fringing at both ends of the windings.

Now, let us proceed with the leakage inductance calculations. Noting that the expression for the cross-sectional area of a winding, through which the axially directed flux passes, is π × mean diameter × radial depth, the effective area of the flux tube can be calculated as

$$A = \pi \times [(52/3) \times 638 + 49 \times 739 + (65/3) \times 853] \times 10^{-6} \text{ m}^2$$
$$= 65751 \times \pi \times 10^{-6} \text{ m}^2 = 0.2066 \text{ m}^2.$$

The terms corresponding to the LV and HV windings are multiplied by ⅓ as explained earlier. The term A equals π times ΣATD given by Equation 3.17. Equation 3.18 gives the Rogowski factor as

$$K_R = 1 - \frac{1 - e^{-\pi H_w / (T_1 + T_g + T_2)}}{\pi H_w / (T_1 + T_g + T_2)} = 1 - \frac{1 - \mathrm{e}^{-\pi \times 1.52/(0.052 + 0.049 + 0.065)}}{\pi \times 1.52/(0.052 + 0.049 + 0.065)} = 0.965$$

and the corresponding effective height of the flux tube according to Equation 3.1 is

l = effective height = 1.520 /0.965 = 1.575 m.

The leakage inductance referred to the HV side can be now be determined as,

$$L = \frac{\mu N^2 A}{l} = \frac{4\pi \times 10^{-7} \times 980^2 \times 0.2066}{1.575} = 0.158 \text{ H (on the HV side).}$$

If we wish to calculate it as referred to the LV side, the value needs to be multiplied by $\left[\left(\text{kV}_{\text{L-L}}\right)_{\text{LV}}\right]^2 \Big/ \left[\left(\text{kV}_{\text{L-L}}\right)_{\text{HV}}\right]^2$, i.e., the ratio of the squares of the line-to-line voltages of the LV and HV windings. The leakage reactance is

$X = 2\pi f L = 2\pi \times 50 \times 0.158 = 49.64\ \Omega$ (referred to the HV side).

The per-unit leakage reactance (refer to Chapter 1) can now be computed by dividing the leakage reactance value by the base impedance value on the HV side.

$$(\text{Base impedance})_{\text{HV}} = \frac{\left[\left(\text{kV}_{\text{L-L}}\right)_{\text{HV}}\right]^2}{(\text{MVA})_{3-ph}} = \frac{132^2}{31.5} = 553.14\ \Omega.$$

$$\therefore \text{Per-unit leakage reactance} = \frac{49.64}{553.14} = 0.0897.$$

Thus, the percentage leakage reactance value is 8.97%. The same value is obtained if Equation 3.15 is used with the following parameter values: $N = 980$, $I = 137.78$ A, $H_{eq} = 1.575$ m, $V/N = 77.83$, and $\Sigma ATD = A/\pi = 65751 \times 10^{-6}$.

A.9 Load Loss Calculations

***I^2R loss in the LV winding*:**

Mean turn length = mean diameter × π = 0.638 × π
Total length of the winding for all three phases with 424 turns in each phase
= 3 × 0.638 × π × 424 = 2550 m
Resistance = (resistivity × total length) / area of turn
Resistivity = 0.0211 x 10^{-6} Ω-m at 75^0C for copper conductors
$R_{LV} = (0.0211 \times 10^{-6} \times 2550) / (106 \times 10^{-6}) = 0.5076\ \Omega$
I^2R loss = $(318.2)^2 \times 0.5076 = 51395$ W ≈ 51.4 kW.

***Eddy loss in the LV winding*:**

The eddy loss occurring in a winding has two components, viz. the loss due to the axial leakage field and the loss due to the radial leakage field. To determine both components, numerical or analytical techniques (as described in Chapter 4) are commonly used. However, it is possible to determine, through a simple expression, the eddy loss in the winding due to the axial component of the leakage field (refer to Section 4.5.1). The eddy loss due to the radial component is assumed to be a part of stray losses for simplicity. The peak value of the flux density in the LV-HV gap is given by Equation 4.98,

$$B_{gp} = \frac{\sqrt{2}\,\mu_0 NI}{H_W} = \frac{\sqrt{2} \times 4\pi \times 10^{-7} \times 424 \times 318.2}{1.52} = 0.1575 \text{ T}.$$

The mean eddy loss per unit volume of the winding due to the axial leakage field is given by Equation 4.99,

$$(P_E)_{mean} = \frac{\omega^2 t^2}{24\rho} \frac{B_{gp}^2}{3} = \frac{(2\pi \times 50)^2 \times (2.5 \times 10^{-3})^2 \times 0.1575^2}{24 \times 0.0211 \times 10^{-6} \times 3} = 10.1 \text{ kW/m}^3$$

$$P_{eddy} = (P_E)_{mean} \times \text{volume of winding} = 10.1 \times 2550 \times 106 \times 10^{-6} = 2.7 \text{ kW}.$$

Provision for transposition of four parallel conductors in the LV winding has to be made as per one of the schemes discussed in Chapter 4, reducing the circulating current loss to a very small value which can be neglected. It should be remembered that the loss cannot be completely eliminated because equalization of impedances between the parallel conductors cannot be perfectly achieved due to the three-dimensional and asymmetric nature of the leakage field, nonuniform interdisk insulation along the winding height, and fringing of flux lines at the

winding ends. Some extra space of a few mm is required in the axial direction at the locations of transpositions. With the circulating current loss neglected, the total losses in the LV winding will be the addition of the I^2R loss and the eddy loss, viz. 51.4 + 2.7 = 54.1 kW.

***I^2R loss in the HV winding*:**

Mean turn length = mean diameter × π = 0.853 × π
Total length of the winding for all three phases with 980 turns in each phase
= 3 × 0.853 × π × 980 = 7879 m
$R_{HV} = (0.0211 \times 10^{-6} \times 7879) / (46.2 \times 10^{-6}) = 3.598\ \Omega$
I^2R loss in HV= $(137.78)^2 \times 3.598 = 68302$ W ≈ 68.3 kW.

***Eddy loss in the HV winding*:**

Following the same procedure as in the case of the LV winding, we have

$$(P_E)_{mean} = \frac{(2\pi \times 50)^2 \times (2.2 \times 10^{-3})^2 \times 0.1575^2}{24 \times 0.0211 \times 10^{-6} \times 3} = 7.8\ \text{kW/m}^3$$

$$P_{eddy} = (P_E)_{mean} \times \text{volume of winding} = 7.8 \times 7879 \times 46.2 \times 10^{-6} = 2.8\ \text{kW}.$$

Assuming, as in the case of the LV winding, that transpositions of two parallel conductors of the HV winding are done, the circulating current loss is zero. Hence, the total losses in the HV winding will be the sum of the I^2R loss and the eddy loss, viz. 68.3 + 2.8 = 71.1 kW.

***Total load losses*:**

The sum of the losses occurring in both windings is 54.1 + 71.1 = 125.2 kW. To these, the stray losses occurring in the structural components (i.e., tank plates, frames, flitch-plates) are added. An elaborate discussion on these losses is available in Chapter 5. Also, the eddy losses in the windings due to the radial leakage field have to be added as stated earlier. The stray losses are caused by alternating flux due to the leakage field from the windings and due to high current leads running parallel to the structural components. Procedures for the calculation of the stray losses are not straightforward. These losses are appropriately referred to as *stray* because of difficulties in estimating them, inability of isolating them experimentally, and impracticability of estimating them in small structural components (e.g., fasteners/bolts). Magnetic and/or electromagnetic shields are employed to shield the structural parts made from magnetic steel to reduce the induced eddy currents and the corresponding stray losses in them. Based on 2-D/3-D FEM analysis, experimental/test data and adopted shielding methods, empirical formulae are generally deduced which can account for the stray losses and the eddy loss in the windings due to the radial leakage field. These empirical formulae depend on design and manufacturing practices. Here, for simplicity, we will assume these losses as 15% of the losses in the windings, i.e., 0.15 × 125.2 kW = 18.8 kW.

Hence, the total load loss = the total winding losses + 18.8 = 125.2 + 18.8 = 144 kW.

The calculated load loss is less than the specified value of 146 kW. The margin of 2 kW is desirable in case manufacturing variations and test-setup errors exist.

A. 10 Calculation of Weights of Windings

Volume of the LV winding = total length of all LV turns × area of one turn
= 2550 m × 106 × 10^{-6} m^2
Density of copper = 8.89 ×10^3 kg/m^3
∴ LV winding weight = 2550 × 106 × 10^{-6} × 8.89 × 10^3 = 2403 kg.

Volume of the HV winding = total length of all HV turns × area of one turn
= 7879 m × 46.2 × 10^{-6} m^2
∴ HV winding weight = 7879 × 46.2 × 10^{-6} × 8.89 × 10^3 = 3236 kg.

A.11 Equivalent Circuit: Series Branch

We have already calculated the shunt branch parameters of the equivalent circuit, which signify the core performance. Now, the series branch parameters will be computed. Remembering again that the equivalent circuit is in terms of per-phase quantities, the load losses are apportioned to the three phases equally. This is an approximation since stray losses in the structural components associated with each phase can be appreciably different due to asymmetrical disposition of the three phases with respect to the components.

Load loss per-phase = 144/3 = 48 kW
Resistance per-phase referred to the HV winding = $(R_{ph})_{HV}$
= (48 × 10^3)/137.78^2 = 2.53 Ω.

This is called the per-phase AC resistance of the transformer, which is greater than the corresponding DC resistance since it is the effective resistance consisting of the DC I^2R losses in the LV and HV windings, and the eddy and stray losses in the windings and the structural parts, respectively, due to the AC currents flowing through the windings.

We have already calculated the per-phase leakage reactance referred to the HV winding as 49.6 Ω, i.e., $(R_{ph})_{HV}$.

Leakage impedance, $(Z_{ph})_{HV}$ =

$$\sqrt{(R_{ph})^2_{HV} + (X_{ph})^2_{HV}} = \sqrt{2.53^2 + 49.64^2} = 49.7\ \Omega.$$

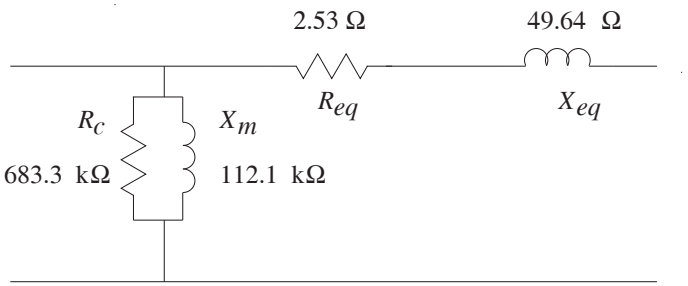

Figure A.4 Equivalent circuit referred to the HV side.

Thus the leakage impedance is almost equal to the leakage reactance, which is generally true for the distribution and power transformers since these are very efficient equipments having low losses. Power transformers are more efficient than distribution transformers and their typical efficiencies are more than 99%.

A.12 Complete Equivalent Circuit

All the computed parameters of the shunt and series branches can now be used to draw the equivalent circuit referred to the HV side as shown in Figure A.4. The parameters can be expressed in terms of p.u. values using the previously calculated base impedance value of 553.14 ohms. The p.u. value of the leakage reactance has already been calculated as 0.0897.

Per unit leakage reactance $\varepsilon_x = 0.0897$

Per unit leakage resistance $\varepsilon_r = \dfrac{2.53}{553.14} = 4.574 \times 10^{-3}$

Per unit shunt resistance $= \dfrac{683.3 \times 10^3}{553.14} = 1235.3$

Per unit magnetizing reactance $= \dfrac{112.1 \times 10^3}{553.14} = 202.66$.

Since the shunt-branch parameters are much higher than the series-branch parameters, the transformer is represented only as series impedance in steady-state analysis of power networks as explained in Section 1.4; in this case, the series impedance is $0.004574 + j0.0897 = j0.0898$ p.u. This is the leakage impedance of the transformer, which is almost equal to the specified value of 0.09 p.u. or 9%.

A.13 Regulation and efficiency

Lastly, we determine the regulation and the efficiency at the full load condition, and also the load at which maximum efficiency occurs, using the formulae given in Section 1.6. The regulation at full load and 0.8 power factor is calculated using Equation 1.63.

$$\text{Regulation} = (0.004574 \times 0.8 + 0.0897 \times 0.6) + \frac{1}{2}(0.0897 \times 0.8 - 0.004574 \times 0.6)^2$$
$$= 0.0574 + 0.0024 = 0.0598 \text{ or } 5.98\%.$$

The efficiency at full load and 0.8 power factor is calculated using Equation 1.68:

$$\eta = \frac{31.5 \times 10^6 \times 0.8}{31.5 \times 10^6 \times 0.8 + 25.5 \times 10^3 + 144.0 \times 10^3} \times 100 = 99.33\%.$$

The load at which the maximum efficiency occurs can be calculated using Equation 1.72:

$$(\text{per unit load})_{\eta_{\max}} = \sqrt{\frac{25.5}{144.0}} = 0.4208 \text{ p.u.}$$

Thus, the maximum efficiency occurs at 42.1% of the full load.

Appendix B: Vector Groups

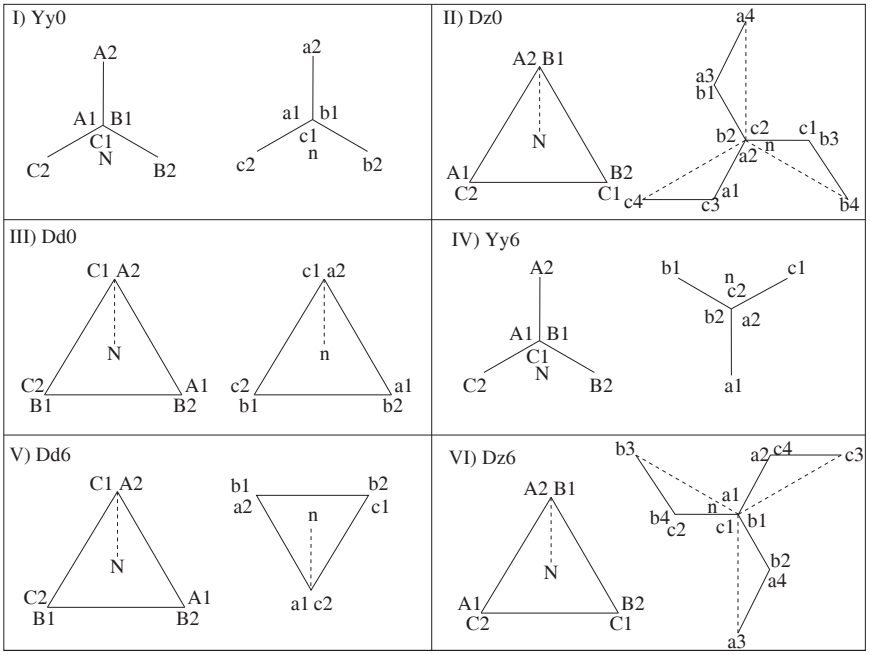

VII) Yd1

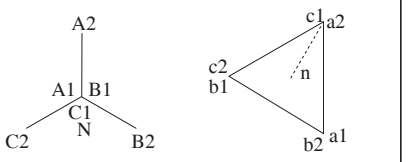

VIII) Dy1

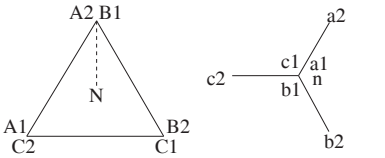

IX) Yz1

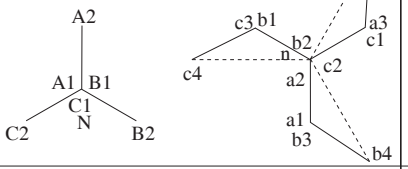

X) Yd11

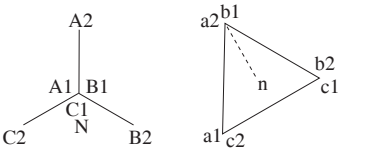

XI) Dy11

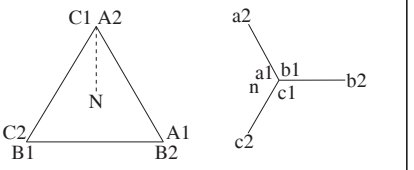

XII) Yz11

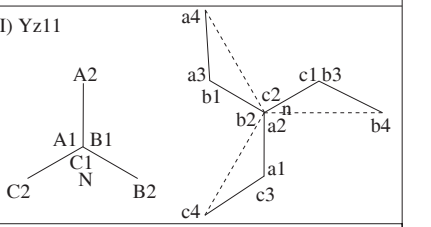

XIII) Yd5

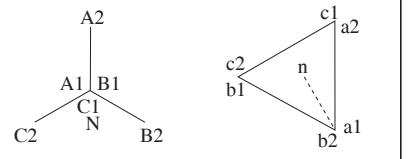

XIV) Dy5

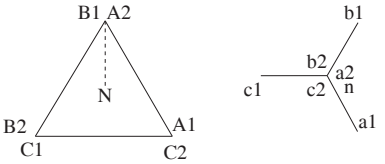

XV) Yz5

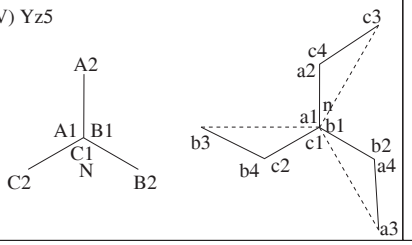

XVI) Yd7

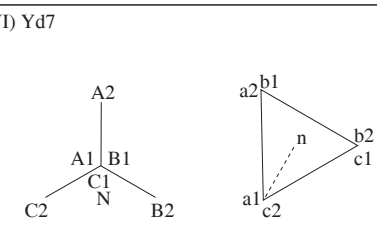

XVII) Dy7

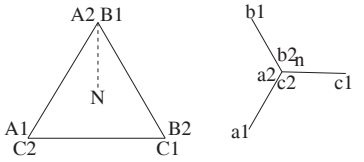

XVIII) Yz7

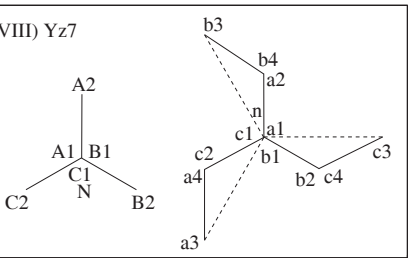

XIX) Dd2

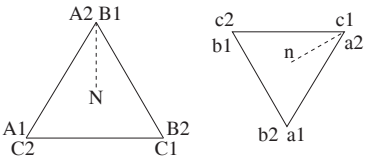

XX) Dz2

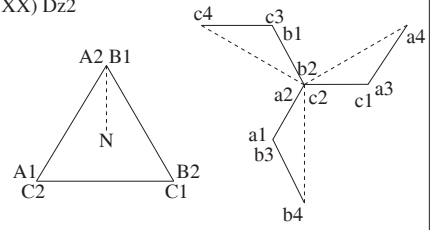

XXI) Dd4

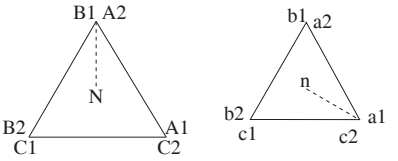

XXII) Dz4

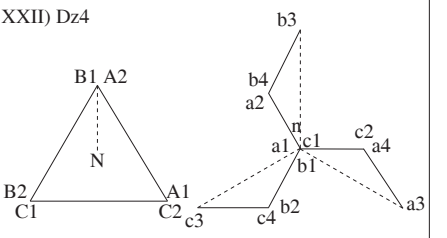

XXIII) Dd8

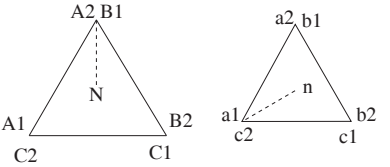

XXIV) Dz8

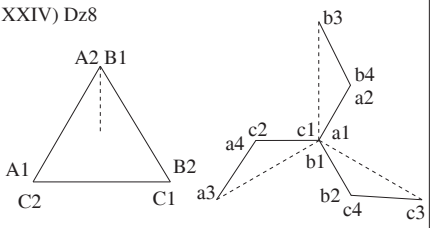

XXV) Dd10

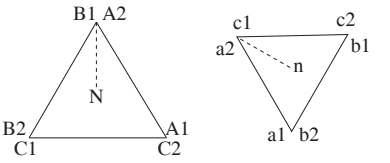

XXVI) Dz10

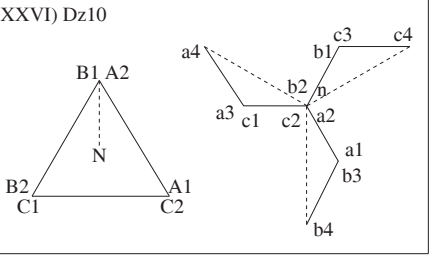

Appendix C: Fault Calculations

In this appendix, asymmetrical fault calculations for a transformer are given. A single-line-to-ground fault on the LV side is considered. The neutral terminals of the LV and HV windings are solidly grounded. Two distinct cases are considered: with and without fault in-feed from the secondary (LV) side. For each of these two cases, two conditions are considered: with and without stabilizing tertiary winding (TV). The effects of omitting the tertiary winding are illustrated with these cases.

Transformer Data

Rating (S) = 25 MVA, Core construction: three-phase three-limb
Voltage ratio: HV/LV/TV, 132/11/11 KV, star/star/delta
Leakage sequence impedances (based on 25 MVA base):

HV/LV : $Z_1 = Z_2 = 12\%,\ Z_0 = 10.2\%$

HV/TV : $Z_1 = Z_2 = 20\%,\ Z_0 = 17.0\%$

LV/TV : $Z_1 = Z_2 = 6\%,\ Z_0 = 5.4\%$

132 KV system fault level (S_F) = 5000 MVA

The positive-sequence system impedance on the HV side is Z_{1HS} = 0.5% (calculated using Equation 6.2). The HV and LV side systems are assumed as effectively grounded (i.e., X_0/X_1 not greater than 3). Here, in particular, the zero-sequence system impedances on the LV and HV sides are assumed to be equal to the corresponding positive-sequence system impedances for simplicity. As mentioned earlier, two alternatives are considered for the 11 KV (LV) system:

(i) Without any fault in-feed from the 11 KV system.
(ii) With fault in-feed from the 11 KV system:

11 KV system fault level (S_F) = 833.33 MVA, which gives the positive-sequence system impedance on the LV side: Z_{1LS} = 3.0% (using Equation 6.2).

The equivalent impedances in the star equivalent circuit can be computed by using the theory given in Section 3.5 as

$$Z_H = (Z_{HL} + Z_{HT} - Z_{LT}) / 2$$

$$Z_L = (Z_{HL} + Z_{LT} - Z_{HT}) / 2$$

$$Z_T = (Z_{HT} + Z_{LT} - Z_{HL}) / 2$$

Therefore, the corresponding positive-, negative- and zero-sequence impedances of the HV, LV and TV windings are computed as follows:

$$Z_{1H} = Z_{2H} = (12 + 20 - 6) / 2 = 13\%\ ,\ Z_{0H} = (10.2 + 17 - 5.4) / 2 = 10.9\%$$

$$Z_{1L} = Z_{2L} = (12 + 6 - 20) / 2 = -1\%\ ,\ Z_{0L} = (10.2 + 5.4 - 17) / 2 = -0.7\%$$

$$Z_{1T} = Z_{2T} = (20 + 6 - 12) / 2 = 7\%\ ,\ Z_{0T} = (17 + 5.4 - 10.2) / 2 = 6.1\%$$

C.1 Asymmetrical Fault with No In-Feed from the LV Side

C.1.1 Delta connected tertiary winding (TV) is present

The equivalent network shown in Figure C.1 corresponds to a single-line-to-ground fault on the LV side. All the impedances are in % values. The network can be derived from Figure 6.3 (a) with impedances Z_{1LS}, Z_{2LS} and Z_{0LS} taken to be effectively infinite since there is no in-feed from the LV side.

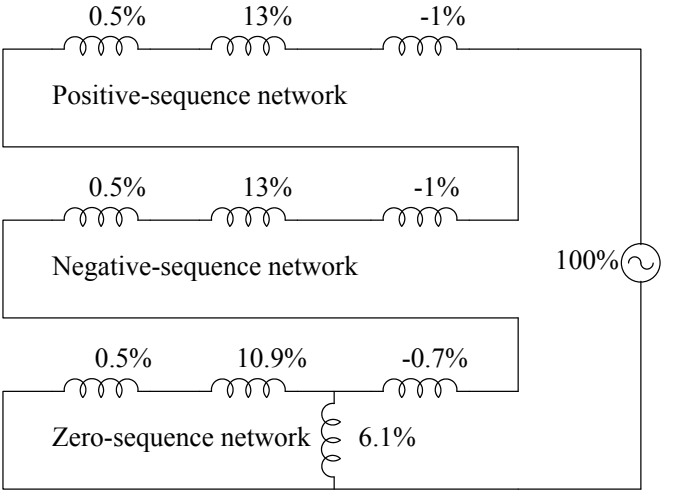

Figure C.1 Sequence network for Case C.1.1.

Total impedance = 2 (0.5 + 13 – 1) – 0.7 + (11.4 // 6.1) = 28.27%.

For a single phase-earth fault, using Equations 6.6 and 6.7 we obtain the values of the sequence components of the fault current as

$I_1 = I_2 = I_0 = 100/ 28.27 = 3.54$ p.u. (i.e., 3.54 times the rated current)

Total fault current= $I_1 + I_2 + I_0 = 3\ (3.54) = 10.62$ p.u.

The fault current in any of the windings is calculated by adding the corresponding sequence currents flowing in them in the three sequence networks. The neutral of the LV and HV windings carries 3 times the corresponding zero-sequence current flowing in them. Therefore,

Current through the HV winding = 3.54 + 3.54 + 3.54 (6.1/17.5) = 8.31 p.u.

Current through the LV winding = 3.54 + 3.54 + 3.54 = 10.62 p.u.

Current through the TV winding = 3.54 (11.4/17.5) = 2.31 p.u.

Current through the HV neutral = 3 × 3.54 (6.1/17.5) = 3.7 p.u.

Current through the LV neutral = total fault current = 3 × 3.54 =10.62 p.u.

C.1.2 Delta connected tertiary winding is absent

The equivalent network shown in Figure C.2 corresponds to a single-line-to-ground fault on the LV side.

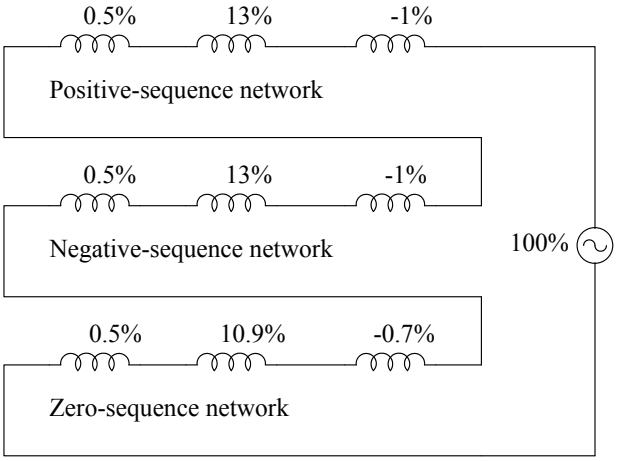

Figure C.2 Sequence network for Case C.1.2.

Total Impedance = 2(0.5 + 13 – 1) – 0.7 + 0.5 + 10.9 = 35.7%

$I_1 = I_2 = I_0 = 100/ 35.7 = 2.8$ p.u.

Total fault current = $I_1 + I_2 + I_0 = 3\ (2.8) = 8.4$ p.u.

Current through the HV winding = 2.8 + 2.8 + 2.8 = 8.4 p.u.

Current through the LV winding = 2.8 + 2.8 + 2.8 = 8.4 p.u.

Current through the HV neutral = 8.4 p.u.

Current through the LV neutral = 8.4 p.u.

It should be noted that the single-line-to-ground fault current in this case (8.4 p.u.) is more than the three-phase fault current (i.e., $1/Z_1 = 1/0.12 = 8.33$ p.u.) due to two reasons. First, the zero-sequence leakage impedance of the transformer is less than the positive-sequence leakage impedance. Second, it is assumed that the positive- and zero-sequence system impedances of the HV side are equal (0.5 p.u.). In many cases, the system zero-sequence impedance is more than the positive-sequence impedance, which will make the single-line-to-ground fault current lower than the three-phase fault current.

It can be observed from the above two case studies that the absence of the tertiary stabilizing winding reduces the total fault current and the current in the faulted LV winding. However, the current in the neutral of the HV winding increases significantly.

C.2 Asymmetrical Fault with In-Feed from the LV Side

C.2.1 Delta connected tertiary winding (TV) is present

The equivalent network shown in Figure C.3 corresponds to a single-line-to-ground fault on the LV side. The network is same as that given in Figure 6.3.

Total positive-sequence impedance = 12.5 // 3 = 2.42%

Total negative-sequence impedance = 12.5 // 3 = 2.42%

Total zero-sequence impedance = [(11.4 // 6.1) – 0.7] // 3 = 1.56%

Total impedance = 2.42 + 2.42 + 1.56 = 6.4%

$I_1 = I_2 = I_0 = 100/ 6.4 = 15.62$ p.u.

Total fault current= $I_1 + I_2 + I_0 = 3\ (15.62) = 46.86$ p.u.

Current through the HV winding

= 15.62 (3/15.5) + 15.62 (3/15.5) + 15.62 (3/6.27) (6.1/17.5)

= 3.02 + 3.02 + 2.6 = 8.64 p.u.

Current through the LV winding = 3.02 + 3.02 + 15.62 (3/6.27) = 13.51 p.u.

Current through the TV winding = 15.62 (3/6.27) (11.4/17.5) = 4.87 p.u.

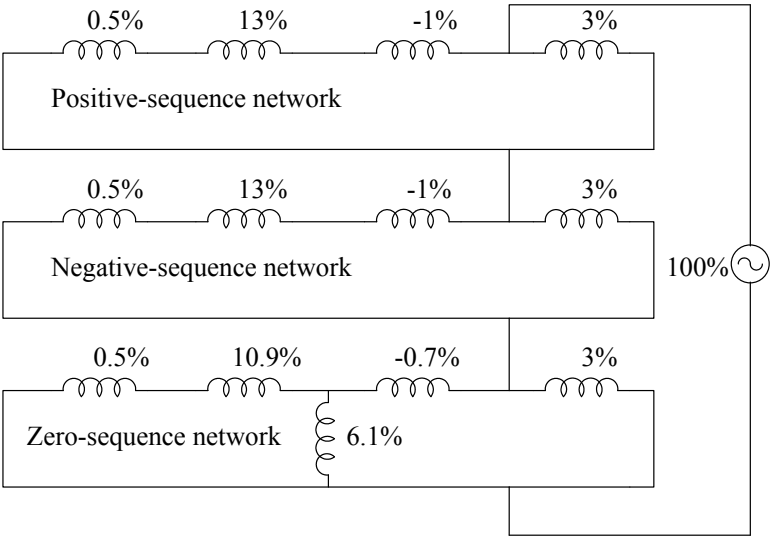

Figure C.3 Sequence network for Case C.2.1.

Current through the HV neutral = 3 × 2.6 = 7.8 p.u.

Current through the LV neutral = 3 × 7.47 = 22.41 p.u.

C.2.2 Delta connected tertiary winding is absent

The equivalent network shown in Figure C.4 corresponds to a single-line-to-ground fault on the LV side.

Total positive-sequence impedance = 12.5 // 3 = 2.42%

Total negative-sequence impedance = 12.5 // 3 = 2.42%

Total zero-sequence impedance = 10.7 // 3 = 2.34%

Total Impedance = 2.42 + 2.42 + 2.34 = 7.18%

$I_1 = I_2 = I_0$ = 100/ 7.18 = 13.93 p.u.

Total fault current = $I_1 + I_2 + I_0$ = 3 (13.93) = 41.79 p.u.

Current through the HV winding

= 13.93 (3/15.5) + 13.93 (3/15.5) + 13.93 (3/13.7)

= 2.7 + 2.7 + 3.05 = 8.45 p.u.

Current through the LV winding = 2.7 + 2.7 + 3.05 = 8.45 p.u.

Current through the HV neutral = 3 × 3.05 = 9.15 p.u.

Current through the LV neutral = 3 × 3.05 = 9.15 p.u.

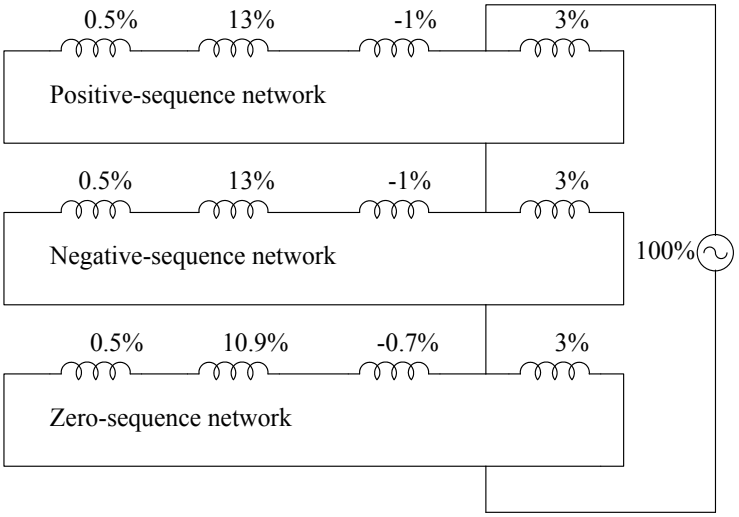

Figure C.4 Sequence network for Case C.2.2.

It can be observed from the above two case studies (in-feed from the LV side) that the absence of the tertiary stabilizing winding reduces the total fault current and the current in the faulted winding (i.e., the LV winding). The current in the neutral of the HV winding increases.

Appendix D: Stress and Capacitance Formulae

In this appendix, formulae are derived for the electric stress and capacitance of two commonly occurring electrode configurations in transformers, viz. a configuration of two round electrodes and a round electrode-plane configuration.

D.1 Stress Calculations

The distribution of the electric field intensity and potential field between two parallel cylindrical electrodes can be determined by considering equivalent line charges. Consider two line charges $+\rho_L$ and $-\rho_L$ (charges per unit length) placed at $x = +m$ and $x = -m$ respectively as shown in Figure D.1. Now, due to single line charge ρ_L, the electric field intensity at a distance *r* is given by

$$E = \frac{\rho_L}{2\pi\varepsilon r} \tag{D.1}$$

where ε is permittivity of medium. The potential reckoned from a distance *R* is

$$u = -\int_R^r E\,dr = \frac{\rho_L}{2\pi\varepsilon}\ln\left(\frac{R}{r}\right). \tag{D.2}$$

The resultant potential at point *A* (in Figure D.1) due to the line charges $+\rho_L$ and $-\rho_L$ is

$$u = \frac{\rho_L}{2\pi\varepsilon}\ln\left(\frac{R}{r_2}\right) - \frac{\rho_L}{2\pi\varepsilon}\ln\left(\frac{R}{r_1}\right) = \frac{\rho_L}{2\pi\varepsilon}\ln\left(\frac{r_1}{r_2}\right). \tag{D.3}$$

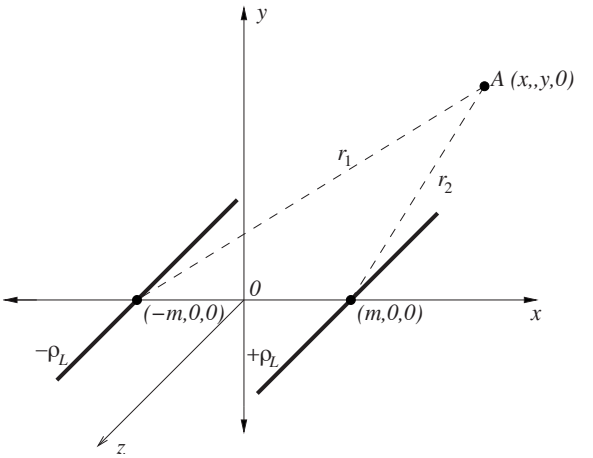

Figure D.1 Two line charges placed at $x = -m$ and $x = +m$.

Let us now determine the nature of an equipotential surface having potential u. From Equation D.3, we have

$$\frac{r_1}{r_2} = e^{\frac{2\pi\varepsilon u}{\rho_L}} .$$

But from Figure D.1, we have $\frac{r_1}{r_2} = \sqrt{\frac{(x+m)^2 + y^2}{(x-m)^2 + y^2}}$.

$$\therefore \sqrt{\frac{(x+m)^2 + y^2}{(x-m)^2 + y^2}} = e^{\frac{2\pi\varepsilon u}{\rho_L}} \quad \text{or} \quad \frac{(x+m)^2 + y^2}{(x-m)^2 + y^2} = e^{\frac{4\pi\varepsilon u}{\rho_L}} .$$

Solving by componendo and dividendo,

$$\frac{(x+m)^2 + y^2 + (x-m)^2 + y^2}{(x+m)^2 + y^2 - \left((x-m)^2 + y^2\right)} = \frac{e^{\frac{4\pi\varepsilon u}{\rho_L}} + 1}{e^{\frac{4\pi\varepsilon u}{\rho_L}} - 1} .$$

$$\therefore \frac{x^2 + y^2 + m^2}{2mx} = \coth\left(\frac{2\pi\varepsilon u}{\rho_L}\right).$$

By algebraic manipulations, we obtain

$$\left(x - m\coth\left(\frac{2\pi\varepsilon u}{\rho_L}\right)\right)^2 + y^2 = \frac{m^2}{\sinh^2\left(\frac{2\pi\varepsilon u}{\rho_L}\right)}. \tag{D.4}$$

This is the equation of a circle with radius $r = \dfrac{m}{\sinh\left(\frac{2\pi\varepsilon u}{\rho_L}\right)}$

and center $(s, 0) = \left(m\coth\left(\frac{2\pi\varepsilon u}{\rho_L}\right), 0\right)$.

Thus, the equipotential surface is a cylinder which intersects the *x*-*y* plane in a circle with radius r and center at (*s*, 0).

From the above expressions for radius and center, we obtain

$$\frac{s}{r} = \cosh\left(\frac{2\pi\varepsilon u}{\rho_L}\right). \tag{D.5}$$

Also, $s^2 - r^2 = m^2\coth^2\left(\frac{2\pi\varepsilon u}{\rho_L}\right) - \dfrac{m^2}{\sinh^2\left(\frac{2\pi\varepsilon u}{\rho_L}\right)} = m^2$. (D.6)

By substituting the value of *m* in the equation for radius, we have

$$\sinh\left(\frac{2\pi\varepsilon u}{\rho_L}\right) = \frac{\sqrt{s^2 - r^2}}{r}. \tag{D.7}$$

Now, from Equations D5 and D7, we obtain

$$e^{\frac{2\pi\varepsilon u}{\rho_L}} = \cosh\left(\frac{2\pi\varepsilon u}{\rho_L}\right) + \sinh\left(\frac{2\pi\varepsilon u}{\rho_L}\right) = \frac{s + \sqrt{s^2 - r^2}}{r} = \frac{r}{s - \sqrt{s^2 - r^2}}.$$

Therefore, the expression for the potential variable is

$$u = \frac{\rho_L}{2\pi\varepsilon}\ln\left[\frac{r}{s - \sqrt{s^2 - r^2}}\right]. \tag{D.8}$$

Now, we will consider two parallel cylindrical conductors of radii R_1 and R_2, placed such that the distance between their centers is 2*s*. The electric field intensity and potential between the two conductors are calculated by considering the corresponding two equivalent line charges as shown in Figure D.2.

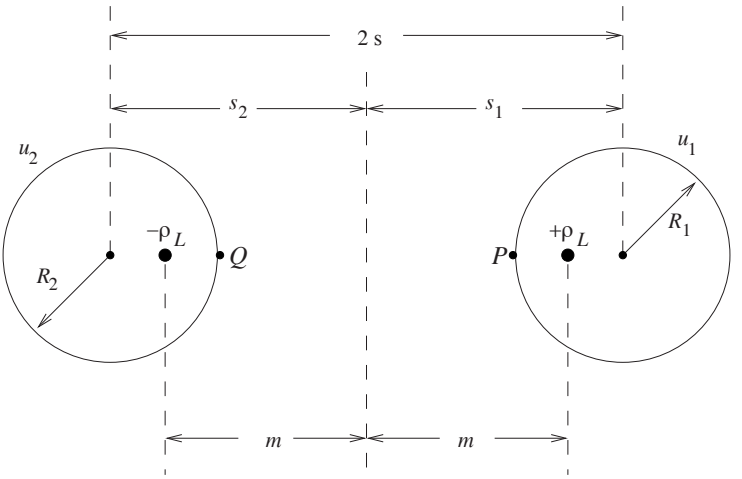

Figure D.2 Configuration of two parallel cylindrical conductors.

Now,

$$s_1 + s_2 = 2s\,. \tag{D.9}$$

Using Equation D.6, we can write

$$s_1^2 - s_2^2 = \left(m^2 + {R_1}^2\right) - \left(m^2 + {R_2}^2\right) = R_1^2 - R_2^2\,.$$

$$\therefore\ s_1 - s_2 = \frac{R_1^2 - R_2^2}{2s}\,. \tag{D.10}$$

By solving Equations D9 and D10 we obtain

$$s_1 = \frac{4s^2 + \left(R_1^2 - R_2^2\right)}{4s} \quad \text{and} \quad s_2 = \frac{4s^2 - \left(R_1^2 - R_2^2\right)}{4s}\,.$$

The electric field intensity at point P on the surface of the conductor on the right side is given by

$$E_P = \frac{\rho_L}{2\pi\varepsilon}\left[\frac{1}{R_1 - \left(s_1 - m\right)} - \frac{-1}{2m - \left(R_1 - \left(s_1 - m\right)\right)}\right] = \frac{\rho_L}{2\pi\varepsilon}\left[\frac{2m}{m^2 - \left(R_1 - s_1\right)^2}\right].$$

Now, by putting the value of $m = \sqrt{s_1^2 - R_1^2}$ in the above equation, we have

$$E_P = \frac{\rho_L}{2\pi\varepsilon\ R_1}\sqrt{\frac{s_1 + R_1}{s_1 - R_1}}\ .$$

By using the expression of s_1 obtained earlier in the above equation, we have

$$E_P = \frac{\rho_L}{2\pi\varepsilon\ R_1}\ \sqrt{\frac{4s^2 + \left(R_1^2 - R_2^2\right) + 4\,s\,R_1}{4s^2 + \left(R_1^2 - R_2^2\right) - 4\,s\,R_1}}\ . \tag{D.11}$$

Now, by using Equation D.8, the potential difference between points *P* and *Q* is given as

$$u_1 - u_2 = \left(\frac{\rho_L}{2\pi\varepsilon}\ln\frac{R_1}{s_1 - \sqrt{s_1^2 - R_1^2}}\right) - \left(\frac{-\rho_L}{2\pi\varepsilon}\ln\frac{R_2}{s_2 - \sqrt{s_2^2 - R_2^2}}\right)$$

$$= \frac{\rho_L}{2\pi\varepsilon}\ln\left[\frac{R_1 R_2}{\left(s_1 - \sqrt{s_1^2 - R_1^2}\right)\left(s_2 - \sqrt{s_2^2 - R_2^2}\right)}\right] = \frac{\rho_L}{2\pi\varepsilon}\ln\left[\frac{R_1\left(s_2 + \sqrt{s_2^2 - R_2^2}\right)}{R_2\left(s_1 - \sqrt{s_1^2 - R_1^2}\right)}\right]$$

By putting the expressions of s_1 and s_2 in the above equation and simplifying,

$$\rho_L = \frac{\left(u_1 - u_2\right)2\pi\varepsilon}{\ln\left\{\frac{R_1}{R_2}\left[\frac{4s^2 - \left(R_1^2 - R_2^2\right) + \sqrt{\left[4s^2 - \left(R_1^2 - R_2^2\right)\right]^2 - 16s^2R_2^2}}{4s^2 + \left(R_1^2 - R_2^2\right) - \sqrt{\left[4s^2 + \left(R_1^2 - R_2^2\right)\right]^2 - 16s^2R_1^2}}\right]\right\}}\ .$$

Putting this expression in Equation D.11, we have

$$E_p = \frac{\left(u_1 - u_2\right)}{\left(2s - R_1 - R_2\right)}\ f_P \tag{D.12}$$

where

$$f_P = \frac{2s - R_1 - R_2}{R_1\ln\left\{\frac{R_1}{R_2}\left[\frac{4s^2 - \left(R_1^2 - R_2^2\right) + \sqrt{\left[4s^2 - \left(R_1^2 - R_2^2\right)\right]^2 - 16s^2R_2^2}}{4s^2 + \left(R_1^2 - R_2^2\right) - \sqrt{\left[4s^2 + \left(R_1^2 - R_2^2\right)\right]^2 - 16s^2R_1^2}}\right]\right\}} \times$$

$$\sqrt{\frac{4s^2 + \left(R_1^2 - R_2^2\right) + 4s\,R_1}{4s^2 + \left(R_1^2 - R_2^2\right) - 4s\,R_1}}$$

is called the nonuniformity factor.

Now, if both electrodes have same radius, i.e., $R_1 = R_2 = R$, then

$$f_P = \frac{2(s-R)}{R \ln\left[\dfrac{4s^2 + \sqrt{(4s^2)^2 - 16s^2R^2}}{4s^2 - \sqrt{(4s^2)^2 - 16s^2R^2}}\right]} \times \sqrt{\frac{4s^2 + 4sR}{4s^2 - 4sR}} = \frac{\sqrt{\gamma^2 - 1}}{\ln\left[\gamma + \sqrt{\gamma^2 - 1}\right]} \tag{D.13}$$

where $\gamma = \dfrac{s}{R}$.

Now, we will consider the other most commonly encountered geometry, i.e., a cylindrical conductor-plane configuration as shown in Figure D.3. The ground plane at point *G* and the round conductor can be replaced by a configuration of the conductor and its image as shown in the figure. From Equations D12 and D13 the electric field intensity, in this case, at point *P* is given as

$$E_p = \frac{(u-(-u))}{2(s-R)} f_P = \frac{u}{(s-R)} f_P. \tag{D.14}$$

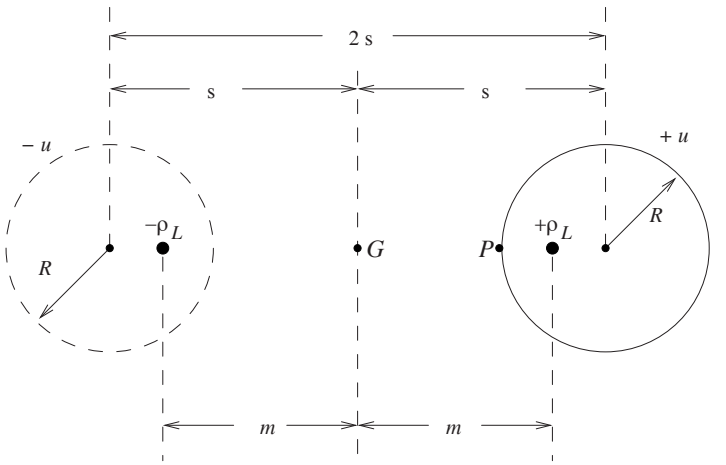

Figure D.3 Cylindrical conductor-plane geometry.

and the nonuniformity factor is

$$f_P = \frac{\sqrt{\gamma^2 - 1}}{\ln\left(\gamma + \sqrt{\gamma^2 - 1}\right)}, \text{ where } \gamma = \frac{s}{R}. \tag{D.15}$$

Now, the electric field intensity at point *G* is

$$E_G = \frac{\rho_L}{2\pi\varepsilon}\left[\frac{1}{m} + \frac{1}{m}\right] = \frac{\rho_L}{\pi\varepsilon\sqrt{s^2 - R^2}} \tag{D.16}$$

where $m = \sqrt{s^2 - R^2}$. Using Equation D.8, the potential at the conductor surface is given as

$$u = \frac{\rho_L}{2\pi\varepsilon}\ln\left[\frac{R}{s - \sqrt{s^2 - R^2}}\right] = \frac{\rho_L}{2\pi\varepsilon}\ln\left[\frac{s + \sqrt{s^2 - R^2}}{R}\right] = \frac{\rho_L}{2\pi\varepsilon}\ln\left[\gamma + \sqrt{\gamma^2 - 1}\right]$$

$$\therefore \rho_L = \frac{2\pi\varepsilon u}{\ln\left(\gamma + \sqrt{\gamma^2 - 1}\right)}. \tag{D.17}$$

Putting this expression in Equation D.16, we have

$$E_G = \frac{2u}{\sqrt{s^2 - R^2}\,\ln\left(\gamma + \sqrt{\gamma^2 - 1}\right)} = \frac{u}{s - R} f_G \tag{D.18}$$

$$\text{where, } f_G = \frac{2(s - R)}{\sqrt{s^2 - R^2}\,\ln\left(\gamma + \sqrt{\gamma^2 - 1}\right)} = \frac{2\sqrt{\dfrac{\gamma - 1}{\gamma + 1}}}{\ln\left(\gamma + \sqrt{\gamma^2 - 1}\right)}. \tag{D.19}$$

The nonuniformity factor f_x for any point between the conductor and ground in the *x* direction (Figure D.4) can be determined now. The electric field intensity at a point with distance of *x* from the conductor center is

$$E_x = \frac{\rho_L}{2\pi\varepsilon}\left[\frac{1}{x - (s - m)} - \frac{-1}{m + s - x}\right] = \frac{\rho_L}{\pi\varepsilon}\,\frac{m}{2sx - (x^2 + R^2)}. \tag{D.20}$$

Now, from Equation D.8 we have

$$u = \frac{\rho_L}{2\pi\varepsilon}\ln\left(\frac{R}{s - m}\right).$$

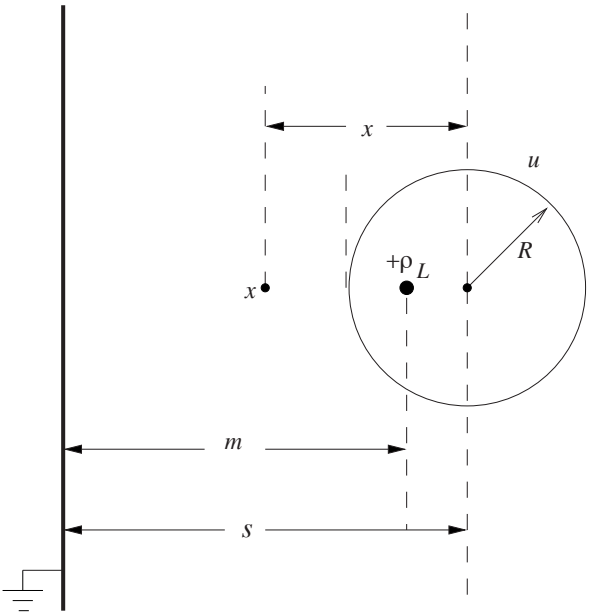

Figure D.4 Stress and voltage at distance x from the conductor center.

$$\therefore\ \rho_L = \frac{2\pi\varepsilon u}{\ln\left(\dfrac{R}{s-m}\right)}. \tag{D.21}$$

Putting this expression in Equation D.20 we obtain

$$E_x = \frac{2u\,m}{\left[2s\,x - \left(x^2 + R^2\right)\right]\ln\left(\dfrac{R}{s-m}\right)} = \frac{u}{(s-R)}\ f_x \tag{D.22}$$

where $f_x = \dfrac{2\,m\,(s-R)}{\left[2s\,x - \left(x^2 + R^2\right)\right]\ln\left(\dfrac{R}{s-m}\right)}$. (D.23)

The voltage at distance x can be calculated using Equation D.3 as

$$u_x = \frac{\rho_L}{2\pi\varepsilon}\ln\left[\frac{m+s-x}{x-s+m}\right] \tag{D.24}$$

where, $\rho_L = \dfrac{2\pi\varepsilon u}{\ln\left(\dfrac{R}{s-m}\right)} = \dfrac{2\pi\varepsilon u}{\ln\left(\dfrac{s+\sqrt{s^2-R^2}}{R}\right)}$ and $m = \sqrt{s^2-R^2}$. (D.25)

D.2 Capacitance Calculations

D.2.1 Capacitance between two parallel cylindrical conductors

From Figure D.2 for the conditions that $R_1 = R_2 = R$ and $s_1 = s_2 = s$, and by using Equation D.8, the capacitance between the two parallel cylindrical conductors per unit length is

$$C = \frac{\rho_L}{u_1 - u_2} = \frac{\rho_L}{\dfrac{\rho_L}{2\pi\varepsilon}\ln\left(\dfrac{R}{s-\sqrt{s^2-R^2}}\right) - \dfrac{-\rho_L}{2\pi\varepsilon}\ln\left(\dfrac{R}{s-\sqrt{s^2-R^2}}\right)}$$

$$= \frac{2\pi\varepsilon}{\ln\left(\dfrac{s+\sqrt{s^2-R^2}}{R}\right) + \ln\left(\dfrac{s+\sqrt{s^2-R^2}}{R}\right)} = \frac{\pi\varepsilon}{\ln\left(\dfrac{s+\sqrt{s^2-R^2}}{R}\right)} . \quad \text{(D.26)}$$

Using Equations D5 and D8 and simplifying we obtain the relation:

$$\cosh^{-1}\left(\frac{s}{R}\right) = \ln\left(\frac{R}{s-\sqrt{s^2-R^2}}\right) = \ln\left(\frac{s+\sqrt{s^2-R^2}}{R}\right). \quad \text{(D.27)}$$

From Equations D26 and D27, we finally have the capacitance per unit length as

$$C = \frac{\pi\varepsilon}{\cosh^{-1}\left(\dfrac{s}{R}\right)} . \quad \text{(D.28)}$$

D.2.2 Capacitance between a cylindrical conductor and a ground plane

Using Equation D.8, the capacitance per unit length between the cylindrical conductor and the ground plane, in Figure D.4, is obtained as

$$C = \frac{\rho_L}{u-0} = \frac{\rho_L}{\dfrac{\rho_L}{2\pi\varepsilon}\ln\left(\dfrac{R}{s-\sqrt{s^2-R^2}}\right)} = \frac{2\pi\varepsilon}{\ln\left(\dfrac{s+\sqrt{s^2-R^2}}{R}\right)} . \quad \text{(D.29)}$$

By using Equation D.27, we obtain the capacitance per unit length between the conductor and ground as

$$C = \frac{2\pi\varepsilon}{\cosh^{-1}\left(\frac{s}{R}\right)}. \tag{D.30}$$

Electrical Engineering

Transformer Engineering

Design, Technology, and Diagnostics

Second Edition

Transformer Engineering: Design, Technology, and Diagnostics, Second Edition helps you design better transformers, apply advanced numerical field computations more effectively, and tackle operational and maintenance issues. Building on the bestselling *Transformer Engineering: Design and Practice*, this greatly expanded second edition also emphasizes diagnostic aspects and transformer–system interactions.

What's New in This Edition

- Three new chapters on electromagnetic fields in transformers, transformer–system interactions and modeling, and monitoring and diagnostics
- An extensively revised chapter on recent trends in transformer technology
- An extensively updated chapter on short–circuit strength, including failure mechanisms and safety factors
- A step-by-step procedure for designing a transformer
- Updates throughout, reflecting advances in the field

A blend of theory and practice, this comprehensive book examines aspects of transformer engineering, from design to diagnostics. It thoroughly explains electromagnetic fields and the finite element method to help you solve practical problems related to transformers. Coverage includes important design challenges, such as eddy and stray loss evaluation and control, transient response, short-circuit withstand and strength, and insulation design. The authors also give pointers for further research. Students and engineers starting their careers will appreciate the sample design of a typical power transformer.

Presenting in-depth explanations, modern computational techniques, and emerging trends, this is a valuable reference for those working in the transformer industry, as well as for students and researchers. It offers guidance in optimizing and enhancing transformer design, manufacturing, and condition monitoring to meet the challenges of a highly competitive market.

K12483

CRC Press
Taylor & Francis Group
an informa business
www.crcpress.com

6000 Broken Sound Parkway, NW
Suite 300, Boca Raton, FL 33487
711 Third Avenue
New York, NY 10017
2 Park Square, Milton Park
Abingdon, Oxon OX14 4RN, UK

ISBN: 978-1-4398-5377-1
90000
9 781439 853771